8th INTERNATIONAL ENGINEERING SYMPOSIUM – IES2019

Faculty of Engineering (Building No.2)

Kumamoto University

March 13-15, 2019

Kumamoto University

Conveners

Shuichi TORII

Professor, Department of Mechanical Engineering & Mechanical Systems
Kumamoto University, Japan

&

Katta VENKATARAMANA

Professor, Department of Civil Engineering
NITK, Surathkal, India

Organized by

Graduate School of Science & Technology
Kumamoto University, Japan

In association with

National Institute of Technology Karnataka,
Surathkal, Mangalore, India

PROCEEDINGS OF

8th INTERNATIONAL ENGINEERING SYMPOSIUM – IES2019

Venue

Faculty of Engineering (Building No.2)
Kumamoto University

Date

March 13-15, 2019

Conveners

Shuichi TORII
Professor, Department of Mechanical Engineering & Mechanical Systems
Kumamoto University, Japan
&
Katta VENKATARAMANA
Professor, Department of Civil Engineering
NITK, Surathkal, India

Organized by

Graduate School of Science & Technology
Kumamoto University
Kumamoto City, Japan

In association with

National Institute of Technology Karnataka
Surathkal, Mangalore, India

PREFACE

The 1st International Engineering Symposium (IES2011), the 2nd International Engineering Symposium (IES2012), the 3rd International Engineering Symposium (IES2013), the 4th International Engineering Symposium (IES2015), the 5th International Engineering Symposium (IES2016), the 6th International Engineering Symposium (IES2017) and the 7th International Engineering Symposium (IES2018) were organized very successfully at Kumamoto University with more than 100 participants each time from India, Japan, Indonesia, Thailand, Taiwan, Vietnam and other countries. With the objective of continuing the interaction between the researchers during these symposia, the 8th International Engineering Symposium (IES2019) has been organized in the month of March, 2018. This symposium provides a common platform for bringing together researchers for expanding academic collaboration.

As part of this symposium, the researchers and the students from abroad have been invited to visit Kumamoto University and get exposed to its educational and research activities. The event focuses on the current R&D of the participating institutions on topics of mutual interest, with a special emphasis on "Science & Technology". The emerging technology and scientific advancements are discussed during the symposium. Presentations feature new and innovative technologies in the relevant fields.

This proceedings volume contains the technical papers presented at the symposium. The topics include a wide spectrum of themes covering major disciplines of science and engineering. The effort put in by the faculty, the staff and the students of Kumamoto University in organizing this event are greatly appreciated.

We sincerely hope that you will find the contents of this proceedings volume useful and productive. We look forward to more intense academic collaborations and research interactions in the coming days, to achieve the common goal of technological advancement for global peace and prosperity.

Shuichi Torii
Katta Venkataramana
Conveners

IES2019 Program Schedule

Venue: Faculty of Engineering, Building No.2

March 13, 2019 (Wednesday)

10:30 – 11:00	Registration
11:00 – 11:30	***Opening Address & Introduction of GSST***
11:30 – 12:15	**Keynote Lecture** *(K1)*
12:15 – 13:00	**Keynote Lecture** *(K2)*
13:00 – 14:00	Lunch Break
14:00 – 17:00	**Campus Tour & Laboratory Visits**
17:00 – 17:30	Free Time
17:30 – 19:00	Welcome Reception

March 14, 2019 (Thursday)

10:00 – 11:30	**Technical Sessions** *(C1,M1,E1,A1)*
11:30 – 11:45	Tea Break
11:45 – 13:00	**Technical Sessions** *(C2,M2,E2,M5)*
13:00 – 14:00	Lunch Break
14:00 – 15:00	**Keynote Lecture** *(K3)* **& Technical Sessions** *(C3,M3,E3,B1)*
15:00 – 15:30	Tea Break
15:30 – 17:00	**Keynote Lecture** *(K4)* **& Technical Sessions** *(C4,M4,C5)*
17:00 – 17:30	Free Time
17:30 – 19:00	Symposium Dinner

March 15, 2019 (Friday)

9:00 – 18:00	**Field visits**

Lunch & Dinner Venue - FORICO Cafeteria

Notations:

K Keynote Lectures
C Technical Sessions (Civil Engineering & Related Fields)
M Technical Sessions (Mechanical Engineering & Related Fields)
E Technical Sessions (Physics, Electrical, Electronics, Computer Science & Related Fields)
A Technical Sessions (Chemistry, Chemical Engineering, Environment & Related Fields)
B Technical Sessions (Management, Finance & Related Fields)

Contents

Keynote Lectures

K1 Fluid-Structure Interaction Problems in Power Plants
Marwan Hassan

K2 "FUREAI" Engineering; A new concept of research field based on Mechanical Bioengineering - *Yoshitaka Nakanishi*

K3 Natural Fiber Reinforced Composites and their Applications
G L Easwara Prasad

K4 Mapping of seismic hazard parameters for Karnataka – a Southern state of India
Shreyasvi C and Katta Venkataramana

Civil Engineering & Related Fields

C1-1 Stiff or Soft – What designers should opt ?
K S Babu Narayan

C1-2 Eco-friendly geopolymer concrete products
S. Thirugnanasambandam

C1-3 Studies on the structural characteristics of laterite blocks and masonry in Puttur area of Karnataka, India
Ganesha Mogaveera and G Sarangapani

C1-4 A comprehensive analytical study on effect of fracture on flexure, shear, bond and torsional strength in SCC
H.C.M. Swamy and G. Prince Arul Raj

C1-5 Studies on effect of near surface mounted (NSM) technique on the dynamic behaviour of RC slab under incremental drop test
Nandeesh M S, Arjun R P Reddy, H N Jagannatha Reddy and R Prabhakara

C1-6 Strength and deformation behaviour of post-tensioned concrete strengthened beams using CFRP laminates with NSM technique
Vathsala, H N Jagannatha Reddy and R Prabhakara

C1-7 Studies on drop test dynamic response of two way HSC slabs strengthened using CFRP strip adopting NSM technique
Arjun R P Reddy, Nandeesh M S, R Prabhakara and H N Jagannatha Reddy

C1-8 Effect on workability and setting time of concrete with aluminium dross as partial replacement for ordinary Portland cement
Panditharadhya B J, Raviraj H Mulangi and A U Ravi Shankar

C2-1 Experimental studies on phenol adsorption potential of soils
Meera Vaeghese and Sunil B. M

C2-2 Numerical analysis of slope stability of geogrid reinforced road embankment
Teena Thomas

C2-3 Application of soft computing techniques in estimation of saturated hydraulic conductivity in spatially variable fields
Paresh Chandra Deka

C2-4 Identification of significant input variables in urban water consumption estimation-case study of Bengaluru
Rumi Thakuria

C2-5 Groundwater investigation using electrical resistivity technique in Karkala Taluk, Udupi district, Karnataka State, India
Shannon Meryl Pinto, Vignesh Bhat, Lokesh K N and Naveenchandra B

C2-6 Spatial Interpolation of Rainfall Data with ArcGIS approach
Ayilobeni Kikon and Paresh Chandra Deka

C2-7 Integrated Study for Delineation of Groundwater Prospect Zones in Hard Rock Terrains - A Review
Venkanagouda B B Patil and Lokesh K N

C3-1 Life cycle analysis of Ferrochrome ash
Krishnamurthy M P and Devatha C P

C3-2 Study on Lateritic Soil Treated with RBI Grade 81 and Aggregate
Amulya S, A U Ravi Shankar, Lekshmy V V and Panditharadhya B J

C3-3 Seismic resistance of precast reinforced concrete shear wall: experimental and analytical study
Shubham Singhal and Ajay Chourasia

C3-4 Pull-out behaviour of headed bars embedded in concrete
Akshat Chourasia, Shubham Singhal and Ajay Chourasia

C3-5 Effect of Sea Water on Strength of Structural Concrete
Vishwanath Okram, Ajith Hebbar and Rashmi H

C4-1 Optimised bus route network design for Bengaluru city
Vinayaka Murthy Vignesh

C4-2 A Comparative Study of Statistical Regression and Artificial Neural Network Approaches in Rainfall–Runoff Modeling
Devika Suresh, Vinayaka Murthy Vignesh and Manna Jacob

C4-3 Short-Term Bus Passenger Demand Estimation Using Time Series Method
Anila Cyril, Raviraj H. Mulangi and Varghese George

C4-4 The influence of land use land cover changes on landslides in Karwar, Uttara Kannada district of Karnataka state, India
Thejashree G, Lokesh K N and Dwarakish G S

C4-5 Interference study between a retaining wall and a closely built strip footing
S Anaswara and R Shivashankar

C4-6 Effect of Manning's N on flow and stage by using HEC-RAS
Pramodkumar, M. K. Nagaraj and Paresh Chandra Deka

C4-7 Effects of oblique weir with an opening on bed morphology and flow structure
Hirotaka Une, Terunori Ohomoto, Kanji Adachi and Hiroto Kondo

C5-1 Effect of SSI on Structural Response of Berthing Structures,
Anjana S Rao, B R Jayalekshmi and Katta Venkataramana

C5-2 Performance Analysis of Coastal vegetation on Wave Transmission using Soft Computing Techniques
Anusha Jain and Subba Rao

C5-3 Growing popularity of cement concrete roads (rigid pavements) : challenges for concrete technologists to give sustainable, greener material
Nagesh Puttaswamy, Arpitha D and Rajasekaran C

C5-4 Behaviour of mortar with partial replacement of fine aggregate by slag in respect to green strength parameters
Arpitha D, Thilak Kumar Y T, Sudarshan V J, C. Rajasekaran and Nagesh Puttaswamy

C5-5 Fracture Behavior of Two Grades of Concrete with Different Percentage of Fibers
Naveenkumar and Prashanth M H

C5-6 Assessment on performance of Steel slag and PGBS as an alternative for fine aggregate – An assertive review
Sudarshan V J, Arpitha D, C. Rajasekaran and Nagesh Puttaswamy

C5-7 Constructive scope on implementation of copper slag as replacement for natural fine aggregate- An overview
Thilak Kumar Y T, Arpitha D, C. Rajasekaran and Nagesh Puttaswamy

C6-1 Effect of varying fibre content and thermal cycles on strength properties of polypropylene reinforced Self Compacting concrete
Deepak G Appaji, Chethan K, S Bhavanishankar and Gopalakrishnan N

C6-2 Experimental study of geocell reinforced monopile foundation under static lateral load
Kishore K and H C Muddaraju

C6-3 Parametric Study on Seismic Response Analysis of Vertical Irregular RC Structures
Shreeneha V S, Chethan K, Ravinesh Kumar and Bhagyashri P

C6-4 Numerical analysis of pile supported railway embankment
Aiswarya S, B R Jayalekshmi and R Shivashankar

C6-5 Torsional behaviour of buildings with vertical stiffness irregularity under earthquake load
Archana J Satheesh, B R Jayalekshmi and Katta Venkataramana

C6-6 A review of experimental studies on geosynthetic reinforced pile supported railway embankments
Sreya M V, B R Jayalekshmi and Katta Venkataramana

C6-7 A Brief review on dynamic response of retaining walls
Amrita, R Shivashankar and B R Jayalekshmi

C6-8 Seismic analysis of elevated intze water tank
Jogi Pranitha and B R Jayalekshmi

C6-9 An overview of dynamic analysis of water tanks
Nimisha P, B R Jayalekshmi and Katta Venkataramana

C6-10 A Review of performance of pile raft system under static and dynamic loading
Vinoda Krishna S and B R Jayalekshmi

C6-11 Buckling strength of thin concrete shells
Krupa Sheela Pattapu and B R Jayalekshmi

C6-12 Performance based seismic evaluation of multistorey rc buildings with concrete miw and user defined hinges
Gaonkar P V, Dyavanal S S and Katageri B G

C6-13 Study on reinforced compressed mud bricks
Sowmya N J and Sucharitha K

C6-14 Nonlinear assessment of building with and without lateral load resisting system
Deepa S, Mithanthaya I R and Venkatesh S V

Mechanical Engineering & Related Fields

M1-1 Corrosion and wear resistance of nano-metal oxide CeO2 daped Aluminum
Harishanand K S, ,Yogish Rao, Hemanth Suvarna, Omprakash B K, Gurumurthy J L and Revati R Kulkarni

M1-2 Study on stress analysis and fatigue damage calculation for civilian aircraft wing attachment bracket
Sagar B S, Satyanarayan and Prashanth N

M1-3 A study on thermal properties and wear characterization of glass fiber hybrid composite materials
Gurushanth B Vaggar and S C Kamate

M1-4 Influence of multiaxial cryoforging on wear properties of Copper-Titanium alloy
Ramesh S and H Shivananda Nayaka

M1-5 Blast Furnace RAFT Calculator
Shaurya Seth, Omkar Barwade and N.N. Vishwanathan

M1-6 Design, implementation of gaits and control of a quadruped robot
Bhavik Parmar and Prajwal B Bharadwaj

M1-7 Review on high-temperature Pb-free solder alloys
Harsha Raj and Satyanarayan

M1-8 Experimental study of solar panel using phase change material
Jameson Keisham and Shankarappa Kalgudi

M2-1 Compressive property of natural fibres treated with alkali solution reinforced with epoxy resin
Pramod V Badyankal, U Gobind and Manjunatha T S

M2-2 Investigation on the performance and emission analysis of Al2O3 nanoparticles as an additive to a B20 blend of lard oil methyl ester on a CI engine
K Raju, K C Sanjay, Madhusudhan Khamitkar, K V Suresha, Peter Fernandes and Joseph Gonsalvis

M2-3 Flexural properties of banana and sisal hybrid fiber composite without treatment
Pramod V Badyankal, Bharathesh Hegde and Manjunatha T S

M2-4 Scope of piezoelectric materials in aviation industry
Omkar Barwade and Shaurya Seth

M2-5 Machinability studies on EN47 Spring Steel of turning process by optimization technique during dry and wet condition
Vasu M and H Shivananda Nayaka

M2-6 Analysis of a Multi-Degree-Freedom PDMS composite cantilever beam for energy harvesting
Sanket Kulkarni, Shivashankar Hiremath and Satyabodh M Kulkarni

M2-7 Tribological characteristics of spray formed Al-Si quaternary alloys
Harish K, Shikhar V Jain, K. Raju

M3-1 Toughness Index Evaluation of T300/914 Composite
Sachin S, Shivananda Nayaka H, Santhosh B and Prasad Krishna

M3-2 Machining performance of AlCrN and AlTiN coated cemented carbide inserts during the dry end milling of maraging steel
Vinay Varghese, Akhil K, M R Ramesh and D Chakradhar2

M3-3 Experimental investigation on Joule Thomson coefficient of air
Akshay S Rao and Rajat A Chandavar

M3-4 Investigations of thermal effects on the response of Polydimethylsiloxane / Carbon black composite
Sushmita, S Hiremath and S M Kulkarni

M3-5 Study on characteristics of emulsion fuel with co-surfactant
Takumi Iwanaga, Shuichi Torii and Keishi Nakamura

M3-6 Investigation of optimum condition to obtain stable emulsion fuel included biodiesel fuel
Keishi Nakamura and Shuichi Torii

M4-1 Study on dynamic characteristics during steam generation by electrode type electric boiler
Taiki Ishimoto and Shuichi Torii

M4-2 Experimental study of graphene oxide nanofluid effect on thermal performance of heat pipe
Masatoshi Matsumura and Shuichi Torii

M4-3 Fabrication of diamond particles coated heating surface by underwater shock wave and effect of diamond particles on pool boiling heat transfer
Kohei Hamahata, Shuichi Torii and Shigeru Tanaka

M4-4 Simplified gasification simulation using zero-dimensional model of empty palm fruit bunch
Priyambodo Nur Ardi and Shichi Torii

M4-5 Effect of nanoparticle motion mechanism on convective heat transfer in turbulent flow
Yuki Kotooka and Shuichi Torii

M4-6 Production of biogas from the co-digestion of chicken wastes and food wastes at different mixing ratios
Huqe Farhana and Shuichi Torii

M4-7 Numerical simulation study on bark combustion in compact combustor
Chong Liu, Shuichi Torii 1 and Xiaoqu Tong

M5-1 Effects of hyper-concentrated sediment on flow mechanism in an open channel with cylindrical roughness
Hiroto Kondo, Terunori Ohmoto, Kanji Adachi and Hirotaka Une

M5-2 Effects of hyper-concentrated sediment on large-scale vortex structures in an open-channel with artificial roughness
Kanji Adachi, Terunori Ohmoto, Hirotaka Une and Hiroto Kondo

M5-3 Investigation on the performance and emission characteristics of a variable compression ratio engine operated with cardanol Ricebran blends with diesel
K V Suresha, Amogh D M, Peter Fernandes and Raju K

M5-4 Effect of injection pressure on performance and emission characteristics of CI engine fuelled with blends of Honge, rice bran hybrid bio fuel with diesel
K V Suresha, Vidish Shetty 2,Peter Fernandes and Raju K

M5-5 Synthesis and characterization of WC ceramic particulates reinforced Al7075 matrix composites via two step melt stirring technique
Gopal Krishna U B, Soufia Shaikh, Ranganatha P, Virupaxi Auradi and Vasudeva B

M5-6 Investigation on the performance and emission characteristics of CI engine fuelled with blends of cardanol, Honge bio diesel with diesel
K V Suresha, Vijaylaxmi P Shivanaguti, Peter Fernandes and Raju K

M5-7 Effect of compression ratio on the performance and emission characteristics of CI engine fuelled with Honge, hybrid bio-fuel with diesel
K V Suresha, Thangjam Seemashwori Devi, Srinivas C S, Peter Fernandes and Raju K

Physics, Electrical, Electronics, Computer Science & Related Fields

E1-1 Effect of soaking time on the structural and morphological properties of Cu2ZnSnS3 (CZTS) prepared using solid state reaction technique
Nagabhushan J Choudhari and Raviprakash Y

E1-2 Synthesis, growth, and characterization of a novel nonlinear optical organic material for optical device applications
Ashwatha Narayana Prabhu and P P Vinaya

E1-3 Radiation profiling of ISM band EM waves at 433 MHz in indoor environment
Harsha M P and N S V Shet

E1-4 Device-free human-computer interfaces for man-machine interaction
Geetha A

E1-5 ModQUIC performance analysis with dynamic packet fragmentation in wireless networks
Prashant Kharat, Shantanu Vijay, Jayanth Putta, Apurva P and M. Kulkarni

E1-6 Prevention of DoS/DDoS attacks in traditional network by migrating it to software defined network
Shivaraj B. Hublikar, Apurva P and Muralidhar Kulkarni

E1-7 Performance of search optimization methods while configuring a voltage impulse Generator
Prabhat K Sonu and Gururaj S Punekar

E2-1 Detection of recognition during operation using electromyogram signals
Masato Tsuchiya, Masahiro Migita, Masashi Toda, Kazuaki Kondo, Junichi Akita and Yuichi Nakamura

E2-2 Extraction of stem and branch in three dimensional point group of Arabidopsis thaliana
Kentaro Inoue, Masahiro Migita, Takumi Higaki and Masashi Toda

E2-3 TLP250 Optocoupler based interfacing circuit for FPGA based BLDC motor drive
Sachin, Harsheeta V, Pavana and Vinatha U

E2-4 Speed control of BLDC motor using pulse amplitude modulation technique
Harsheeta V, Sachin, Pavana and Vinatha U

E2-5 Sensorless speed and position estimation of PMSM using improved sliding mode observer and Phase Lock Loop based technique
Kshitiz Khatri, A Karthikeyan and Prabhakaran K K

E2-6 Distance metric learning for haptic data classification of braille character dataset
Megh Manoj Bhalerao

E3-1 ECG signals denoising using Savitzky-Golay filters
Vrushabh Bhangod

E3-2 Heat-map analysis based formation prediction in field sports
Amitkumar Patel, Mayank Sitapara, Tejas Rafaliya, Shashidhar G. Koolagudi and Pravin B. Ramteke

E3-3 Maximum power generation by shadow dispersion of PV array under variable irradiance using Latin square configuration
Saurabh S Zond, A Karthikeyan and Kshitiz Khatri

E3-4 A frequency reconfigurable antenna for cognitive radio applications
Naveen Jacob, K. Krishnamoorthy and Muralidhar Kulkarni

E3-5 Adaptive parameter choice strategy for fractional Tikhonov regularization method
Kanagaraj K

Chemistry, Chemical Engineering, Environment & Related Fields

A1-1 Photocatalytic treatment of emerging contaminants using ceria-doped TiO2 under solar, UV-C and UV-A irradiation
Manasa M and Hari Mahalingam

A1-2 Pristine *Pteris vittata* L. Pinnae pellets as an adsorbent for the uptake of toxic metals from aqueous solution
Smruthi G Prabhu, Govindan Srinikethan and Smitha Hegde

A1-3 Structure based drug design of PTP-SHP2 Inhibitors using virtual screening of NCI library
Chetan Munegowda, Rakesh Kumar and Dinesh Gupta

A1-4 Solution combustion synthesis of Nickel Ferrite Nanoparticles: Factors of synthesis and comparative study
Wayne Denis Monteiro and Shannon Walter Gonzalves

A1-5 Model predictive control of fluid catalytic cracking process
Avanika B R, Prabhjot Kaur Luthra, Prabhul Pradeep Kumar and Chinta Sankar Rao

A1-6 Effect of synthesis method on facet ratio and its effect on catalytic activity of samarium doped ceria
Prabhjot Kaur Luthra, Praneeth Pichika, Shraya Sapru, Anjana P Anantharaman and Hari Prasad Dasari

A1-7 Batch mode anaerobic co-digestion of food waste and arecanut husk for enhanced biogas production
Adhirashree Vannarath and Arun Kumar Thalla

A1-8 Dust control methods in Iron ore mines of Sandur Schist Belt, Bellary Region, Karnataka, India
Poorva J Kadrolli

Management, Finance & Related Fields

B1-1 Economic and political effects of the transatlantic trade and investment partnership
Ayush Srivastava

B1-2 Non-Performing Assets, their causes and effects on the Indian Banking Sector
Sarang Kalantre, Sai Chaitanya and Suprabha K R

B1-3 Value stream mapping simulation (VSM-sim): methodology to design the lean service systems in India post service industry – A case study
Vadivel S M and A H Sequeira

B1-4 Escaping and falling into poverty in rural Odisha: empirical evidence from panel data
Sunil Khosla and Pradyot Ranjan Jena

KEYNOTE LECTURES

8th International Engineering Symposium - IES 2019
March 13-15, 2019, Kumamoto University, Japan

Fluid-Structure Interaction Problems in Power Plants

Marwan Hassan

School of Engineering
University of Guelph
Ontario, Canada
Email: mahassan@uoguelph.ca

ABSTRACT: Conventionally, power and process plant equipment has been designed and built robustly, and rarely encountered vibrational problems. As the demand for higher production rates and efficiency increased, many types of equipment were built to be more flexible and were subjected to higher flow rates. This has resulted in the emergence of many issues with flow-induced vibrations. One of the major pieces of equipment that suffers from these problems is heat exchangers. These devices contain large numbers of tubes arranged in arrays. The purpose of these devices is to exchange heat between both the internal and external cooling and heating fluids. A great deal of energy is transported in the form of high pressure and heat. If a fraction of this energy is transformed into vibrations, a form of mechanical energy, the tube integrity will be compromised.

Fluidelastic instability (FEI) is the most devastating excitation mechanism, characterized by a critical flow velocity beyond which a very large tube response occurs. These large vibrations will cause devastating failures, and need to be avoided. These failures manifest as fatigue, tube cracking, and fretting wear at the supports. Fretting wear occurs as the result of tubes impacting against their supports.

In the past it was thought that FEI prevails only in the transverse (lift) direction. Design guidelines therefore focused only on designing against instability in the transverse direction. All nuclear steam generators were made using these guidelines. Streamwise (drag) instability was never considered to be of importance in operating steam generators. This belief has been shattered after recent devastating failures in some replacement nuclear steam generators. These steam generators were designed to last for 40 years and instead, lasted for only 11 months. Investigating these failures has confirmed that streamwise (drag) instability was responsible for the damage caused by tube-to-tube fretting wear and failures. The magnitude of these failures sent shockwaves through the academic and the industrial community. In the wake of these incidents, both the research community and industry have made great efforts to understand this phenomenon.

This talk will address some of these issues and will present an overview of the modelling and simulations of these phenomena.

8th International Engineering Symposium - IES 2019
March 13-15, 2019, Kumamoto University, Japan

"FUREAI" Engineering; A new concept of research field based on Mechanical Bioengineering

Yoshitaka Nakanishi
Faculty of Advanced Science & Technology,
Kumamoto University, Japan
Email: y-naka@mech.kumamoto-u.ac.jp

ABSTRACT:
The author innovates "FUREAI" engineering, which is a kind of "Interface Science and Technology" for a multi-scale product design. The basic knowledge comes from Tribology, Surface Engineering as well as Mechanical Bioengineering. By showing the practical applications in a variety of areas, the new concept of research field is explained. The topics below are examples.

1 Artificial joint:
In a polymer-on-hard artificial joint, the bearing parts are typically composed of ultra-high molecular weight polyethylene and Co-Cr-Mo alloy. The wear debris generated from the polyethylene part is considered a major factor in the long-term osteolysis and loosening of an artificial joint because the presence of this debris stimulates macrophage activity, thereby promoting the production of cytokines. The surface profile of Co-Cr- Mo alloy is designed to promote the transfer of a polyethylene film onto the alloy surface and enlarge the size of the wear debris of the polyethylene.

2 Micro-plastics:
Micro-plastics have been discussed in environment concern. The plastic trash in the ocean has been suffered the fragmentation though both ultraviolet light and wave power, finally the size of debris will be in a micro-meter scales. The very small particles might affect living things chemically and physically. My laboratory started to create the quasi-micro-plastic for the related researches using a specially designed a micro-grater.

3 Dental ceramics:
Dental restorations made of lithium disilicate glass ceramics are increasing in popularity due to their high strength and attractive aesthetics. Most of the clinical failures are caused by the fracture extension of surface flaws and chipping. Therefore, eliminating of machining-induced surface damage in CAD/CAM diamond grinding becomes crucial for the long-term reliability. The micro slurry-jet erosion promises to be an effective manufactuing technique for the generation of fracture-free surfaces which are crusial for high-quality monolithic restorations made from the material.

4 Bio-inspired surface:
The biomechanisms of the lotus leaf and moth eye have been explored. In particular, the relationship between their structures and their water-repellency effect and reflection suppression have been elucidated. These studies have contributed to the development of innovative industrial products. The microscopic structure seen on a natural surface is generally created by a nanoimprint method based on semiconductor manufacturing technology, so some limitations must be considered in terms of product size, shape, and material. This study aims to explore surface micromachining, a mechanical material removal process that serves as an alternative to a nanoimprinting, in creating a bio-inspired surface on artificial materials.

8th International Engineering Symposium - IES 2019
March 13-15, 2019, Kumamoto University, Japan

Natural Fiber Reinforced Composites and their Applications

G L Easwara Prasad
Mangalore Institute of Technology and Engineering,
Moodabidri, Karnataka, Mangalore 574225, India.
email: gle.prasad@gmail.com

ABSTRACT: Composite materials are used for various requirements of human beings. Natural fiber reinforced composites are showing the characteristics comparable with those of synthetic/artificial fiber reinforced composites. The increasing demand for environmental friendly materials and desire to reduce the cost of traditional fiber reinforced composites, the natural fiber reinforced composites have been developed. The natural fibers like coir, sisal, jute, banana, basalt, pineapple, hemp and so on are used as reinforcements which are environmental friendly and biodegradable with polymer matrices like polyester, epoxy, vinyl ester, polyethylene and their properties have been reported very much exhaustively. Review of some of the results are presented here.

Keywords*: Natural fiber, Coir, Sisal, Jute, Polymer matrices.*

INTRODUCTION

Composite materials are in limelight nowadays due to their applications ranging from automobile to construction industries. The study of natural fiber has become progressively important in recent years due to the thriving awareness of the need to protect ecological and environmental resources. In recent days, environmental awareness is increased due to high negative impact of synthetic materials [12]. Natural fibers are not only strong and lightweight, but also relatively very economical. Usually, fiber reinforcement is done to obtain high strength and high modulus. Several investigations have been conducted on polymer composites using many types of natural fibers such as coir, sisal, jute, banana, kenaf, hemp, bamboo and so on, to study the mechanical properties of composite materials. Attempts have been made to overcome the problems of durability either by use of fillers to reduce its alkalinity or by treating fibers by some special treatment like using NaoH solution [10]. Natural fiber thermoplastic composites are attractive as they are economical, stiffer, paintable, rot resistant and also can be given the look of wood [18]. Natural fiber composites are attractive to industry because of their low density and ecological advantages over conventional composite with synthetic fibers. These composites are gaining importance due to their non-carcinogenic and biodegradable nature [3]. The use of Natural fiber as reinforcement in polymer-based composites is reviewed here from viewpoints of future expectations of natural bio fibers, properties of natural fiber, fiber surface modifications, physical and mechanical characteristics of natural fiber based polymer composites and hybridization.

COIR FIBER

Coir fiber is extracted from the outer shell of a coconut. The common name, scientific name and plant family of coconut fiber is Coir, Cocos nucifera and Arecaceae (Palm), respectively.

There are two types of coconut fibers, brown fiber extracted from matured coconuts and white fibers extracted from immature coconuts. Brown fibers are thick, strong and have high abrasion resistance. White fibers are smoother and finer, but also weaker. Coconut fibers are commercially available in three forms, namely bristle (long fibers), mattress (relatively short) and decorticated (mixed fibers). These different types of fibers have different uses depending upon the requirement. In engineering, brown fibers

are mostly used. Because of high lignin content coir is more durable compared to other natural fibers and their properties [23] are shown in Table 1.

Fig 1 show a coconut tree, coconut and coconut fibers. Coir fiber can be utilized as a potential reinforcing material for making low load bearing thermoplastic composites.3mm thick coir epoxy composites specimens have shown 17.86Mpa tensile strength, 31.08Mpa flexural strength and 11.49 KJ/m^2 impact strength respectively [8]. Tensile strength of the green coconut fiber reinforced HDPE composite material is greatly influenced by fiber length as well as fiber volume fraction and Tensile strength of the composite material decreases with increase in the fiber length [1]. Alkali treatment of natural fiber also called as mercerization, is the common methods to produce high quality fibers. Mercerization reduces fiber diameter, thereby increasing the aspect ratio, which leads to the development of a rough surface topography that results in better fiber matrix interface adhesion and an increase in mechanical properties [7]. The study of mechanical properties and their prognostication of coir fiber reinforced composite has been extensively reported by considering the variation of fiber volume, laminate thickness, fiber treatment and so on [4,5 & 11].

SISAL FIBER

Sisal fibers obtained from the plants (see Fig 2) after removing the soft tissue and dirt from the stem of sisal plant. The length of the sisal fiber could be up to 3m [12]. Sisal represents the first natural fiber in commercial application, in which it is estimated that in more than half of the total of all natural fibers used is sisal fiber. The Sisal fibers are found commercially in several formats: fabric, cords, strips, wire, rolls, etc…, the properties of sisal fibers[23] are shown in the Table 2.

The feasibility of developing polymer-based composites using sisal fibers is due to low cost of production of composites and amenability of these fibers to winding, laminating and other fabrication processes. The fabrication of these composites was fairly easy and cost of production is also quite low. Tensile strength of sisal epoxy composites is approximately found to be 250-300Mpa, which is half the strength of glass fiber epoxy composites of the same composition [16]. The effect of silane treatment and alkali treatment on mechanical and physical properties of sisal epoxy composites produces stiff and strong composite materials [2]. The impact properties of unidirectionally oriented sisal fiber polyester composites with those of ultra-high-density polyethylene and glass fiber shows sisal composites fracture identical with that of ultra-high modulus polyethylene composites and the toughness of sisal fiber composites is only 25% less than that of glass fiber composites [17]. The comparative study of impact strength of treated and untreated sisal polyester composites exhibited higher impact strength in treated fiber composites than the untreated sisal polyester composites [6].

JUTE FIBRES

Jute fibres are extracted from the ribbon of the stem of the plant by following sequential processes. The properties of jute fiber [23] is shown the Table 3.

The composites reinforced with natural fibers like jute are abundant, cheaper and of low density, biodegradable and carbon dioxide-neutral. Jute fiber has the potential to compete with glass fiber as reinforcing agents in plastics. Jute composites are true substitute of wood.

Researchers have reported the Reinforcement potential of jute for developing thermoplastic and thermo set composites using different techniques, these composite materials have been successful in the semi structural as well as structural applications.

The mechanical properties of jute polyester composites increase with the alkaline treatment of fibers compared to untreated fibers. It is also recorded that the increase in tensile and flexural properties of alkaline treated jute polyester composites with increase in duration of alkaline treatment is because the duration of alkaline treatment increases fiber matrix bonding and also

increases the brittle nature of fibers which in turn decreases the strain [22].
Mechanical properties of jute-coir (1:1) polypropylene hybrid composites with fiber volume percentages of 5%, 10%, 15%, and 20% is reported [20]. They reported the decrease in tensile strength and increase in flexural, impact and hardness properties with increase in fiber percentage.

BANANA FIBER

Banana fiber is a ligno-cellulosic fiber, obtained from the pseudo-stem of banana plant. Banana fiber is a bast fiber with relatively good mechanical properties. Banana fiber has good specific strength properties comparable to those of conventional material, like glass fiber. This material has a lower density than glass fibers. Banana fibers have high strength, light weight, smaller elongation, fire resistance quality and biodegradability.
Banana fiber is used in making products like filter paper, paper bags, greeting cards, lamp stands, pen stands, decorative papers, rope, mats and composite material etc. Polypropylene reinforced with banana fiber is used by automobile companies for making under floor protection panels in luxurious cars like Mercedes [19]. The properties of banana fibers[19] are shown in the Table 4.
NaoH treated banana fiber epoxy composite has been tested to study the tensile, flexural and impact strength with variation in length of fibers. Higher tensile strength is reported with 15mm long fibers, while the flexural strength increased up to a fiber length of 25mm [21].

HYBRID COMPOSITE MATERIALS

The most important criteria for the effective use of natural fiber polymer composite materials are their durability, long-time strength, crack propagation resistance, plasticity reserve at long-term loading, resistance to impact loads, etc. The multifunctionality of the material is of prime importance due to the combination of high elastic and strength properties with resistance to combustion, low smoke emission, non-toxicity and other specific characteristics. The diverse and contradictory requirements for modern composite materials have brought to the forefront the very complex problem of developing new types of composite materials, in which a combination of reinforcing layers from two or more types of fibres the so called hybrid composite materials. Polymer hybrid composite materials (PHCM) have found wide applications in the present time. In terms of fibers, three types of hybridizations are possible, namely
1.Natural/natural FRP
2.Natural/synthetic FRP
3.Synthetic/synthetic FRP
composites constituted of two types of natural fibers are less common, inspite of their high potential for structural applications. Most of the works on natural/natural fiber reinforced composites are experimental works. Finding out two different kinds of natural fibers compatible to each other to be used in the same polymer for reinforcement is the vital task for hybridization. The type of natural fibers to be used as hybrid reinforcement highly depends on the purpose of the composite material and also on the load type [20].
The tensile properties of untreated and treated coir/glass-phenolic composites increase linearly. The tensile strength and modulus of the samples increased linearly with the increase in glass fiber percentage and this attributed to the higher tensile strength and modulus. Increasing the glass fiber content from 0 to 100%, the tensile strength increased from 37 to 350%. A similar trend was reported in the case of treated coir/glass composites. Flexural properties increased with increase in GF content in composites [14].
The carbon fiber and glass fiber reinforced hybrid composites are studied for the evaluation of mechanical properties like micro hardness, tensile and flexural strength of hybrid composites as per ASTM standards. The micro hardness of carbon fiber reinforced composite is higher than the other composites. The inclusion of carbon fiber mat reinforced polymeric composite significantly enhanced the ultimate tensile strength, yield strength and peak load of the composite. The ductility of carbon fiber reinforced

composite is higher than the other composites [9].

The reason behind using a hybrid composite instead of using single fiber composite is to integrate both the tensile strength and the impact strength in the same composite material. There are few factors needed to be considered while choosing fiber combination for hybridization. They are

1. Volume fraction of low elongation (LE) fiber and high elongation (HE) fiber
2. Failure strain ratio for the two fibers
3. Stiffness of the HE fiber [24].

The hybrid effect will be larger when the volume fraction of LE fiber is lower than 50% of the total fiber volume fraction. To get a positive hybrid effect, the failure strain ratio needs to be 2. That means ratio of the failure strain of HE fiber reinforced composite to failure strain of the LE fiber reinforced composites needs to be 2. A ratio even higher does not significantly increase the performance. Finally, more the stiffness of the HE fiber, the more the hybrid effect is. In addition to this, researchers also reported that to get a positive hybrid effect, the layers of the different reinforcements need to be more distinct and segregated [13].

Tensile, flexural and impact properties of plain-woven basalt, plain woven glass and basalt-glass polyester hybrid composites were studied. It was presented that, the hybrid composites exhibited intermediate tensile and flexural properties between plain basalt and plain glass polyester composites while for impact properties for hybrid composite exhibited higher value than plain basalt and plain glass polyester composite. Additionally, it was observed that by controlling the stacking sequence mechanical properties can be improved [15].

APPLICATIONS OF NATURAL FIBER COMPOSITES

The natural fiber composites can be very cost-effective material for following applications:

- Building and construction industry: panels for partition and false ceiling, partition boards, wall, floor, window and door frames, roof tiles, mobile or pre-fabricated buildings which can be used at times of natural calamities such as floods, cyclones, earthquakes, etc.
- Storage devices: post-boxes, grain storage silos, bio-gas containers, etc.
- Furniture: chair, table, shower, bath units, etc.
- Electric devices: electrical appliances, pipes, etc.
- Everyday applications: lampshades, suitcases, helmets, etc.
- Transportation: automobile and railway coach interior, boat, etc…

CONCLUSIONS

From the present review on natural fiber reinforced composites, following conclusions can be drawn.

- Extraction, processing, fabrication and treatment of natural fibers are economical compared to conventional synthetic fibers like glass fiber, carbon fiber and so on.
- NaoH and likewise alkaline treatment enhances the mechanical properties of natural fiber reinforced composites.
- Hybridization on natural and synthetic fibers can enhance the strength of natural fiber reinforced composites.
- Commercial value of the natural fibers can be improved.

REFERENCE

[1] Balarami Reddy (2013), Mechanical performance of green coconut fiber/hdpe composites, Int. Journal of Engineering Research and Applications, Vol. 3, Issue 6, pp.1262-1270.

[2] Bisanda et al., The effect of silane treatment on mechanical and physical properties of sisal epoxy composites, Composites Science and Technology, Oxford, V41, pp 165-178.

[3] Bongarde U S et al., (2014), Review on natural fiber reinforcement polymer composites, IJESIT, Volume 3, Issue 2, pp 431-436.

[4] Easwara prasad et al., (2017), A study on Impact strength characteristics of coir polyester composites, Procedia Engg., 173, pp 771-777.

[5] Easwara prasad et al., (2017), Prediction of Impact strength attributes of raw and alkaline treated coir polyester composites, NCCS 2017, pp 58-69.

[6] Easwara Prasad et al., (2017), Comparative study of impact strength characteristics of treated and untreated sisal polyester composites, Procedia Engg 173, pp 778-785.

[7] Hariprasad et al., (2013), Study of mechanical properties of banana-coir hybrid composite using

experimental and FEM techniques, JMES, V4, pp 518-531.
[8] Harish S et al., (2009), Mechanical properties evaluation of natural fiber coir composites, Elseveir Mater. Charac. V60(1), pp44-49.
[9] Jaganatha T D at al., (2015), Mechanical properties of carbon/glass fiber reinforced epoxy hybrid polymer composites, IJMERR, V4, No.2, pp 131-137.
[10] Jayabal S et al., (2012), Effect of soaking time and concentation of NaoH solution on mechanical properties of coir polyester composites, Bull. Mater. Sci., V35, No.4, pp567-574.
[11] Keerthi Gowda et al., (2015), Probabilistic study of tensile properties of coir fiber polymer matrix composite, IJAMS, V6, no.1, pp7-17.
[12] Kruvilla Joseph et al., (1999), A review on sisal fiber reinforced polymer composites, R. Bras. Eng. Agric. Ambiental, Campina Grande, V.3, n.3, pp 367-379.
[13] Marom, G et al., (1978), Hybrid effects in composites: conditions for positive or negative effects versus rule-of-mixtures behaviour," Journal of Materials Science, Vol. 13, No. 7, pp 1419-1426.
[14] Mithil Kumar N, et al., (2009), Mechanical properties of coir/glass fiber phenolic resin-based composites. J Reinf Plast Comp. V28 pp 2605–2613.
[15] Nayan patel et al., (2018), Investigations on Mechanical Strength of Hybrid Basalt/Glass Polyester Composites, International Journal of Applied Engineering Research, Volume 13, Number 6, pp. 4083-4088.
[16] Paramasivam et al., (1974), The study of natural fiber composites, Fiber Science and Technology, New delhi, V1, pp 85-98.
[17] Pavithran et al., (1988), Impact performance of sisal polyester composites, JMSL, London, V7, pp 825-826.
[18] Rajasekar.K et al., (2015), Design and Analysis of Industrial Safety Helmet using Natural Fibers, IJIET, Volume 5 Issue 3, pp 31-37
[19] Ravi Bhatnagar et al., (2015), A Review on Composition and Properties of Banana Fibers, IJSER, V5, issue 6, pp 49-52.
[20] Siddiki et al., (2013), Physico-mechnical properties of jute-coir fiber reinforced hybrid polypropylene composites, World Academy of science, Engg. and Tech, IJCNMME, V7, Issue 1, pp41-45.
[21] Sumaila M et al., (2013), Effect of fiber length on the physical and mechanical properties of random oriented, non owen short banana (musa balbisiana) fiber/epoxy composites, cellulose 62.
[22] Sutharson B et al., (2012), Effect of chemical treatments on mechanical properties of jute fiber hybrid composite laminates, ARPN Journal of Engineering and Applied Sciences VOL. 7, NO. 6, pp 760-765.
[23] Tara Sen et al., (2011), Application of Sisal, Bamboo, Coir and Jute Natural Composites in Structural Upgradation, International Journal of Innovation, Management and Technology, Vol. 2, No. 3, pp186-191.
[24] Yentl Swolfs et al., (2014), Fibre hybridisation in polymer composites: a review, Composites Part A: Applied Science and Manufacturing 67, pp 181-200.

Table 1 Properties of coir fiber

Specific gravity	1177 Kg/m^3
Water absorption	93%
Tensile strength	95 M Pa -118 M Pa
Modulus of elasticity	8 G Pa

Fig.1 Coconut Tree, Coconut and Coconut fibers

Table 2 Properties of sisal fiber

Specific gravity	1370 Kg/m^3
Water absorption	110%
Tensile strength	347 M Pa -378 M Pa
Modulus of elasticity	15 G Pa

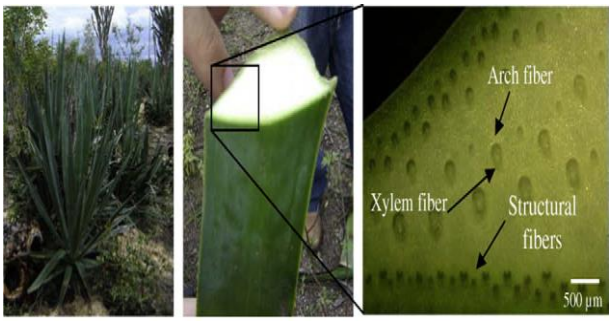

Fig.2 Sisal plant, stem and section

Table 3 Properties of jute fiber

Specific gravity	1460 Kg/m^3
Water absorption	13%
Tensile strength	400 MPa-800 MPa
Modulus of elasticity	10G Pa-30G Pa

Fig.3 Jute fiber

Table 4 Properties of Banana fiber

Specific gravity	950Kg/m^3-750Kg/m^3
Tensile strength	529 M Pa-914 M pa
Modulus of elasticity	27 G Pa-32 G Pa

Fig.4 Banana fiber

Fig.5 Applications of Coconut Fiber Boards in House Construction and Other Utilities

Fig.6 Application of composites in pre-fabricated houses

Fig.7 Sisal fiber cement roofing sheet

Fig.8 Application of composites as door and door frames

8th International Engineering Symposium - IES 2019
March 13-15, 2019, Kumamoto University, Japan

MAPPING OF SEISMIC HAZARD PARAMETERS FOR KARNATAKA – A SOUTHERN STATE OF INDIA

Shreyasvi C [1] and **Katta Venkataramana** [2]

1 *Department of Civil Engineering, National Institute of Technology Karnataka, Surathkal, Mangalore 575025, India. email: shreyasvic@gmail.com*
2 *Department of Civil Engineering, National Institute of Technology Karnataka, Surathkal, Mangalore 575025, India. e-mail: ven.nitk@gmail.com*

ABSTRACT: Karnataka is one of the southerly states of Indian Peninsular characterised by low to moderate earthquakes of intraplate nature. The study attempts to characterise the seismic potential of the region of interest and express the same in terms of hazard parameters. The rate of occurrence (λ), Maximum magnitude (M_{max}), minimum cut-off magnitude (M_{min}) and b-value constitutes the hazard parameters. In order to obtain a reasonable estimate of the parameters, a comprehensive seismic catalogue was compiled from a vast database and available literature. Statistical analysis compliant with the physical phenomena of earthquakes was performed on the regionally compiled catalogue. The study presents maps representing overall seismicity and the hazard parameters. The findings are believed to be useful in the site selection for major infrastructures.

Keywords*: homogenization, declustering, completeness period, maximum likelihood method, intraplate region.*

INTRODUCTION

The rapid growth in population and the emerging urbanization has motivated the engineers to stretch towards more accurate seismic resilient designs. A meticulous seismic design requires explicit estimation of the seismic demand relevant to the region of interest. Seismology coupled with geotechnical engineering aids in providing a reasonable estimate of the seismic demand that can be expected at a chosen site of interest. In this regard, the study aims to determine regional seismicity parameters that are considered to be influential for determining seismic design coefficients.

Karnataka is one of the Southern states of India with an area of 191,791 km^2 and a population of 61,130,704. The state has multiple physiographic features such as malnad (hilly), Maidan (arid) and coastal plains. It has been classified under seismic zone II and III of IS 1893 and is considered as a part of the intra plate region or stable continental region. The study region has witnessed low to moderate earthquakes from time to time with larger spatial extent. Though intraplate earthquakes are rare, they are detrimental in nature. A large earthquake in recent times can have disastrous implications due to increased population and infrastructural development. Hence, thorough understanding of seismicity is necessary for assessing seismic risk of the existing structures as well as safe design of important projects.

The past earthquakes witnessed in the region serve as an index in assessing its seismic potential. The present study attempts to compile a homogenous earthquake catalogue for the whole of Karnataka. The earthquake data collected from multiple sources are further processed. Statistical analyses are performed to extract meaningful results relevant to hazard estimation. The study produces maps of seismicity and seismic hazard parameters. Further, the findings from the study can be utilized for hazard estimation.

METHODOLOGY

The past earthquake records play a major role in understanding the seismicity associated with the study area and its seismic hazard quantification. The study region was divided into 1° X 1° grids and earthquake events within a radius of 300km surrounding each grid point was considered for catalogue compilation. In this regard, a catalogue of past seismic events reported by various researchers and recorded by various global and local agencies was collected and compiled. The data was acquired for a period between 1757 and 2010 from various sources consisting of pre historical, historical and instrumental earthquakes. These data sets consisting of a geographical location of the epicentre, date & time of occurrence, focal depth and its magnitude/intensity were compiled together and multiple reporting of the same event by different sources were being removed manually. The data collected from various sources describe the magnitude of events on different scales such as broadband waveform inversion (Mw), narrow band maximum amplitude data (Ms, m_B, ML) and calibrated from historical data (Intensity scales, e.g.: MMI, MSK, EMS – 98). All these magnitude scales exhibit a saturation level beyond a certain magnitude. However, moment magnitude (Mw) is expressed in terms of the seismic moment which links the dimensions of the fault rupture to the seismic waves generated as given in equation (1) & (2).

$M_0 = \mu AD$ ..... (1)

$$M_w = \frac{\log M_0 - 16.05}{1.5} \quad \text{..... (2)}$$

Moreover, a single earthquake can have multiple valid amplitude magnitudes but only one Mw. Hence, Mw is adopted as the common magnitude scale for the entire compiled catalogue. All the data collected from various sources consisting of events expressed on the different magnitude or intensity scales were homogenised using the formulae given by (Kolathayar et al., 2010) for individual magnitude events and (Musson et al, 2010) for intensity scaled events. After homogenization of the acquired data, the elimination of duplicate data was executed by prioritising the events based on its source characteristics such as reliability, if the data under scrutiny was acquired from the local sources and the size of the seismic network for the data acquired from the global sources. The main sources employed in gathering the data are as follows:

1. International Seismological Centre (ISC).
2. National Earthquake Information Centre, United States Geological Survey (NEIC – USGS).
3. Indian Meteorological Department (IMD).
4. National Disaster Management Agency (NDMA)
5. Incorporated Research Institutions for Seismology (IRIS)
6. Amateur Science Centre (ASC)
7. Events listed by various researchers (Chandra (1977), Rao & Rao (1984), Srivastava & Ramachandran (1985), Bansal & Gupta (1998), K G Raj et al (2001), Rajendran et al (2009), Martin & Szeliga (2010)).

Earthquake catalogue consisted of two components namely, extreme catalogue and complete catalogue. The extreme catalogue is comprised of macro seismic observations such as paleo-earthquakes that are recorded geologically and historical earthquakes that have been described in ancient scriptures. Complete catalogue mainly consists of micro seismic observation wherein even an earthquake of low intensity/magnitude will be recorded by the seismogram and hence, the events are assumed to be The majority of the instrumental data were taken from the global agencies whereas historical earthquake data were taken from local sources and various researchers. In the study, the entire catalogue has been divided into two segments consisting of historical earthquakes (pre – 1970) and instrumental earthquakes (post – 1970).

An earthquake catalogue is composed of independent events (Main shocks) and dependent events (foreshocks and aftershocks). It is necessary to remove the dependent events as they violate the basic assumption of Poissonian distribution which has been extensively adopted in the

study. Aftershocks are identified based on their spatial – temporal proximity to the main shocks and separated by static and dynamic windowing method. In this study, dynamic window method suggested by Gardener & Knopoff (1974) was applied.
The algorithm for Gardener & Knopoff is given as

$$D = 10^{0.1238*M+0.983} \text{ (Km)} \quad \ldots\ldots (3)$$

$$T = \begin{cases} 10^{0.032*M+2.7389} & if\ M \geq 6.5 \\ 10^{0.5409*M-0.547} & else \end{cases} \text{(days)} \quad \ldots\ldots (4)$$

The completeness magnitude (Mc) is the lowest magnitude in the catalogue above which all the earthquake events recorded in a space-time frame are exhaustive. Cumulative Visual Screening (CUVI) method was used to determine the completeness period for various magnitude ranges. CUVI is based on the assumption that occurrence of earthquakes is modelled as a stationary Poisson's process as a result of which the average rate of occurrence of seismic events is constant. Also, it assumes that not all class of magnitudes are complete for the same definite period. In other words, higher magnitude earthquakes have a longer completeness period when compared with lower magnitude earthquakes. It is a graphical procedure of developing plots of a cumulative number of events during the time period of the catalogue in the chronological order for different magnitude classes. The period of completeness for a given magnitude class is considered to begin from the earliest time when the slope of the fitting curve can be fitted by a straight line.

Seismicity parameters are one of the key elements in quantifying the seismic hazard of a region, out of which frequency magnitude recurrence relationship is one of them. The G-R recurrence law also known as power law is given as

$$\log \lambda_m = a - bM \quad \ldots\ldots (5)$$

Where λm refers to the recurrence rate of events with magnitude ≥ M, 'a' gives a general estimate about the seismicity associated with the study area for a period corresponding to the compiled catalogue. A higher 'a' value implies higher seismicity. 'b' represents relative likelihood of large and small earthquakes. A higher 'b' value signifies more number of low magnitude earthquakes and vice- versa. G – R relationship can be interpreted by taking cumulative number of earthquake events of magnitude exceeding a certain threshold magnitude or in the form of a density law, where in number of earthquakes corresponding to a certain magnitude range 'm' is considered. The most commonly accepted approach for determining the seismicity parameters is the maximum likelihood approach proposed by Aki (1965) which gives a formula to estimate the 'b' value as follows.

$$\beta = \frac{1}{\bar{m} - m_{min}} \quad \ldots\ldots (6)$$

Where β = b ln10, $\bar{m}$ = average magnitude and m_{min} is the minimum magnitude of completeness. A Matlab based computer program by name Ha.3 developed by Kijko & smit (2012) was adopted to estimate the seismicity parameters.

RESULTS AND DISCUSSION

The compiled catalogue consisted of 2165 events with a magnitude range of 1 to 6.8 (M_W) and depth up to 80.2km. Fig. 1 shows the seismicity map obtained from the compiled catalogue for the whole of Karnataka and its surrounding areas. The majority of the earthquakes reported and recorded are in the magnitude range of 3 to 4.5 implying that the study area is often subjected to moderate earthquakes and a few higher magnitude earthquakes. Higher seismic activity has been noticed towards the north of Karnataka implying seismic threat to nearby areas of the study region. It can be inferred that the Epicentral density is quite high near Mysore – Bangalore – Kolar region, which could be the resulting aftershocks of the earthquakes originating in the adjoining states such as Tamilnadu and Telangana. Another speculation is that due to the uneven spatial distribution of recording stations throughout the study area, low to moderate magnitude earthquakes might not have been recorded completely. The histogram of the compiled data is shown in Fig.2. It can be clearly stated that the

compiled catalogue consists of more number of aftershocks and earthquakes induced by human activities such as mining (M_w<3). These events are insignificant for seismic hazard estimation based on regional tectonics. Further, the region is subjected to moderate sized earthquakes (M_w = 4 – 6). Fig.3 highlights the usefulness of declustering algorithms. The applied algorithm demonstrates the fact that higher magnitude events are associated with more number of aftershocks and hence the larger difference between as evident from Fig.3. The declustering algorithm identified 238 clusters of events categorising a total of 1095 events as dependent events. the declustered catalogue consisted of 1070 events. Fig. 4 represents CUVI method applied to determine catalogue completeness for events with M_W>5. The catalogue can be considered to be complete over the entire period 1820 - 2015 A. D. for M_W exceeding 5.1 as earthquakes of such magnitude would have made an impact leading to its recording in ancient scriptures as well as instruments in the later period. The completeness period computed using this method has been mentioned in Table 1 for different magnitude ranges. Fig.5 represents the Gutenberg – Richter recurrence relation derived using maximum likelihood approach. The estimated recurrence rate (λ) and maximum magnitude (M_{max}) has been presented in Fig. 6 and 7 respectively.

CONCLUSIONS

In the present study area, an earthquake that occurred in Shimoga on 12th May 1975 has been reported as significant and has spiked interest as no past records of earthquake activity has been reported in this area. The present work is an attempt to understand the regional tectonics and its associated seismicity of Karnataka. The spatial distribution of small to moderate earthquakes has well established the fact that the interior of south Indian shield is continually relieving the strain generated due to tectonic movement in PI. From the compiled catalogue, it can be inferred that most of the shocks are shallow focused in nature with depths conforming within 15km except for few events. A maximum magnitude of earthquake exceeding M_w 6 can be witnessed in central Karnataka stretching towards North. The recurrence rate for events of M_w > 3.5 is higher near Bangalore and Central Karnataka compared to the rest of the region.

REFERENCES

[1] Aki K (1965), Maximum Likelihood Estimate of b in the Formula logN = a - bM and its confidence limits, Bulletin of the Earthquake Research Institute, vol. 43,pp. 237-239.
[2] Bansal, B K, and Gupta, S. (1998), A glance through the seismicity of peninsular India, Geological Society of India, Vol. 52, No. 1, pp. 67-80.
[3] Chandra, U (1977), Earthquakes of peninsular India—a seismotectonic study, Bulletin of the Seismological Society of America, Vol. 67, No. 5, pp 1387-1413.
[4] Gardner, J K and Knopoff, L (1974) Is the sequence of earthquakes in Southern California, with aftershocks removed, Poissonian?, Bulletin of the Seismological Society of America, Vol. 64, No. 5, pp. 1363-1367.
[5] Raj, K G et al (2001), Lineaments and seismicity of Kerala—A remote sensing based analysis, Journal of the Indian Society of Remote Sensing, Vol. 29, No. 4, pp. 203-211.
[6] Kijko, A and Smit, A (2012), Extension of the Aki-Utsu b-value estimator for incomplete catalogs, Bulletin of the Seismological Society of America, Vol. 102, No. 3, pp. 1283-1287.
[7] Kolathayar, S, and Sitharam, T G (2012), Characterization of regional seismic source zones in and around India, Seismological Research Letters, Vol. 83, No. 1, pp. 77-85.
[8] Martin, S, and Szeliga, W (2010), A catalog of felt intensity data for 570 earthquakes in India from 1636 to 2009, Bulletin of the Seismological Society of America, Vol. 100, No. 2, pp. 562-569.
[9] Rajendran, C P et al (2009), Reassessing the earthquake hazard in Kerala based on the historical and current seismicity, Journal of the Geological Society of India, Vol. 73, N o. 6, pp. 785-802.
[10] Rao, B R, and Rao, P S (1984), Historical seismicity of peninsular India, Bulletin of the Seismological Society of America, Vol. 74, No. 6, pp. 2519-2533.
[11] Srivastava, H N, and Ramachandran, K (1985), New catalogue of earthquakes for peninsular India during 1839-1900, Mausam, Vol. 36, No. 3, pp. 351-358.

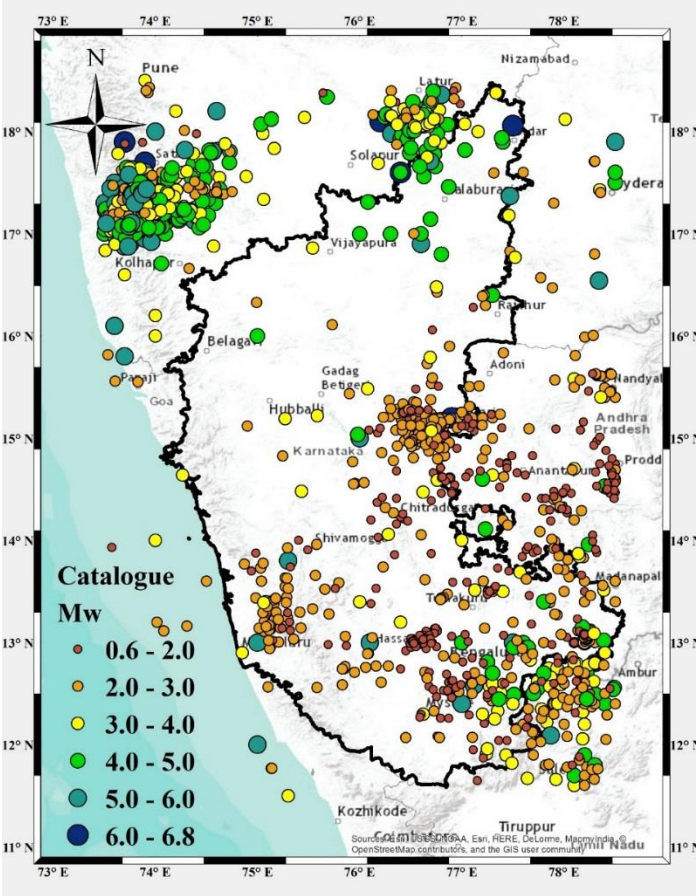

Fig. 1 Seismicity map of Karnataka and surrounding areas.

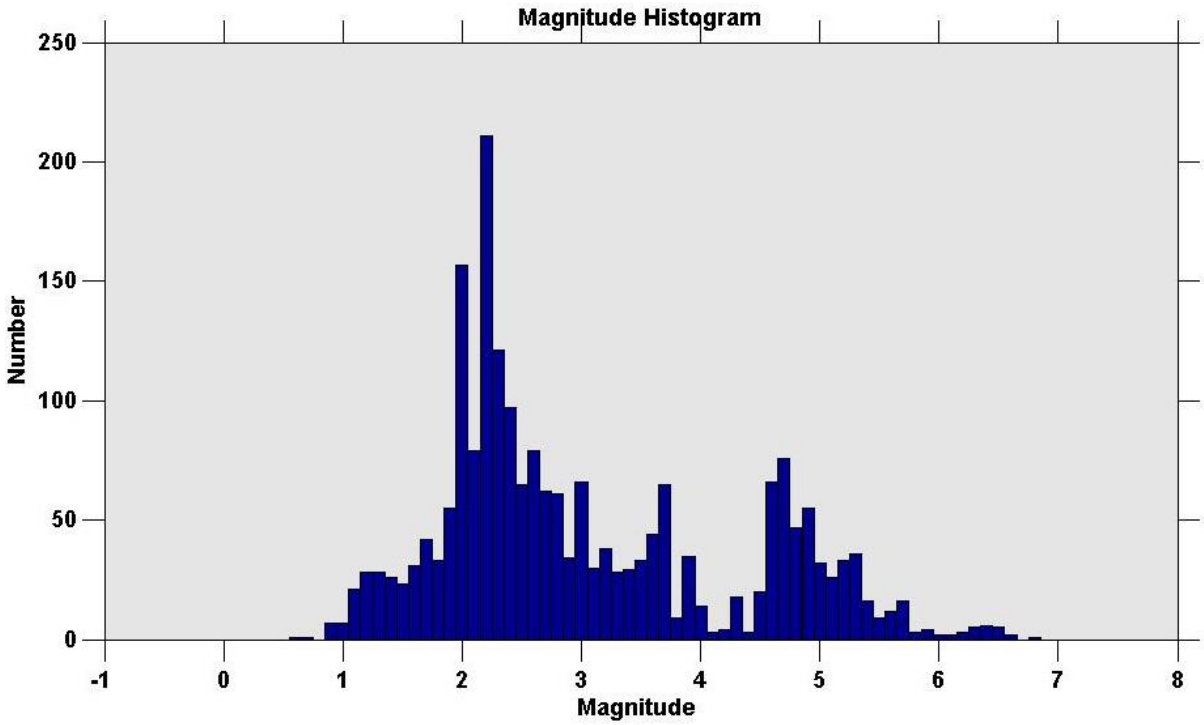

Fig.2 Histogram of the compiled earthquake catalogue.

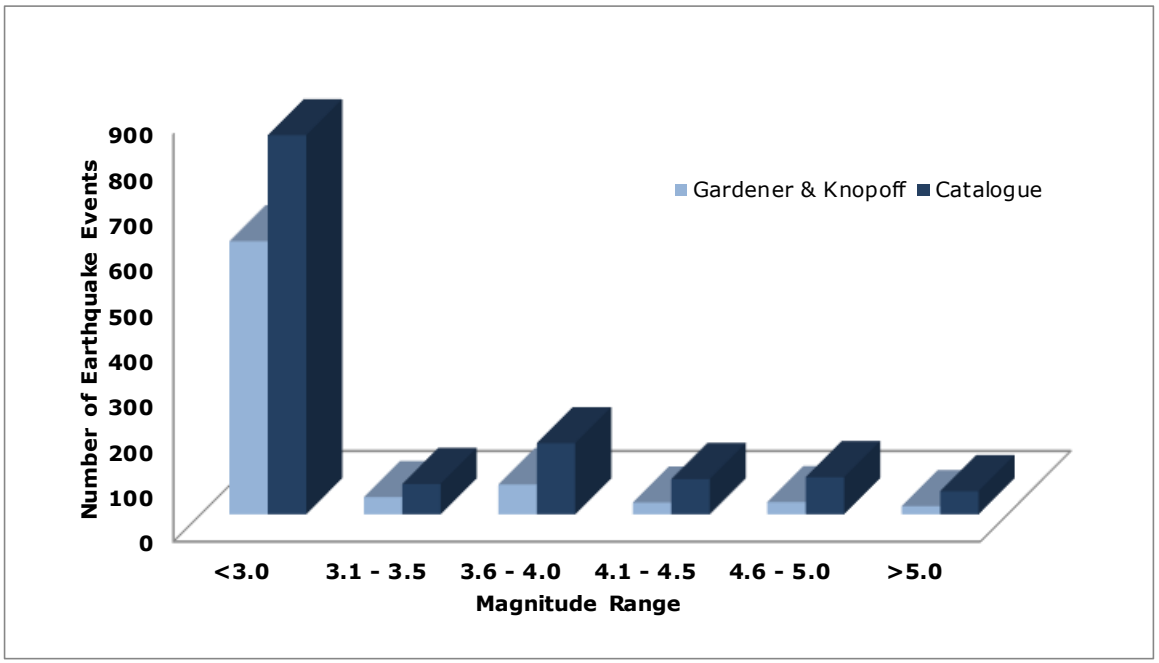

Fig. 3 Comparison of the declustered catalogue with the original catalogue.

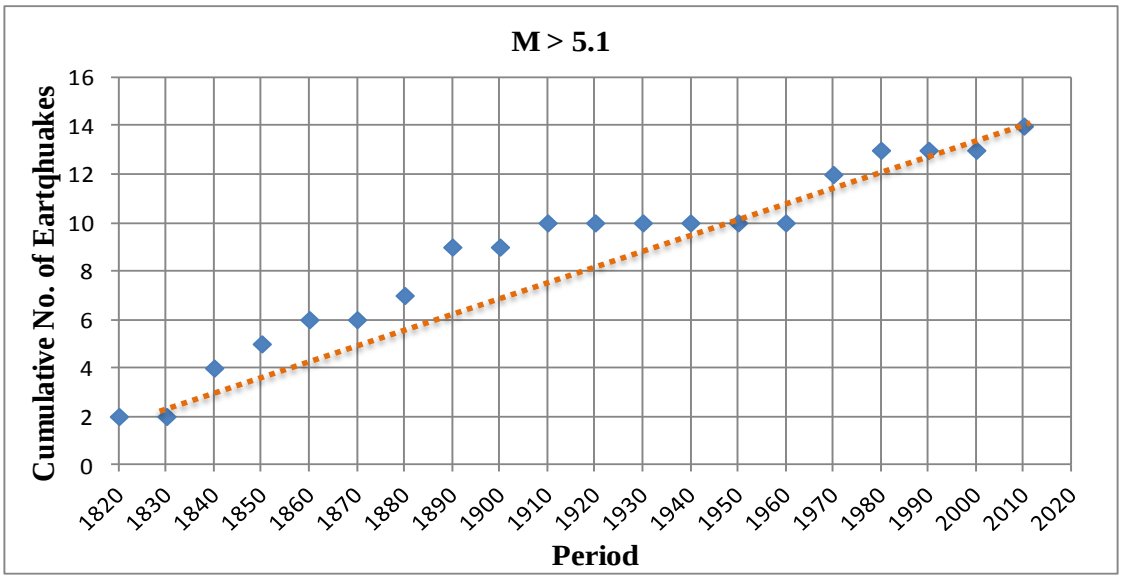

Fig. 4 Cumulative Visual Screening technique applied for events with M_W > 5.1

Table 1: Completeness period computed for various magnitude ranges

Magnitude Class	Completeness Period
<3	45
3.1 – 3.5	60
3.6 – 4.0	65
4.1 – 4.5	70
4.6– 5.0	75
>5.1	185

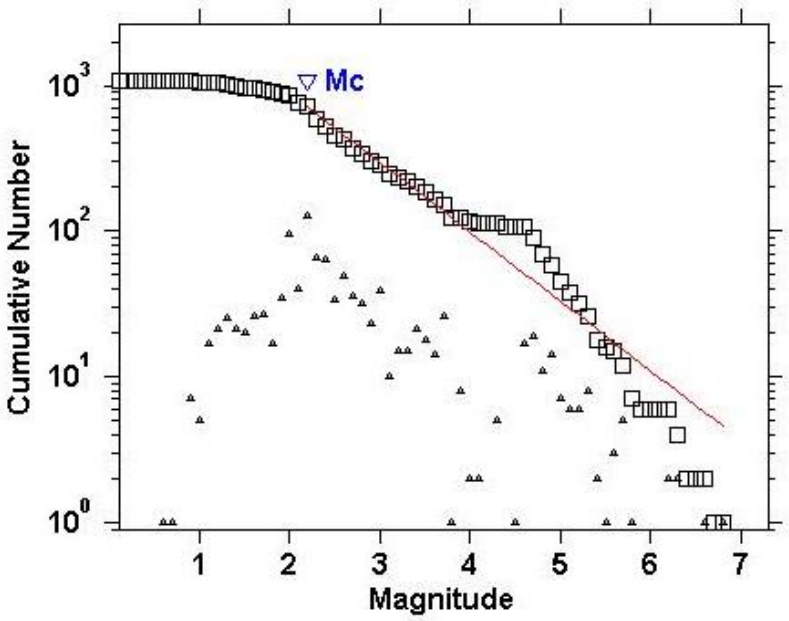

Fig. 5 Estimation of seismicity parameters

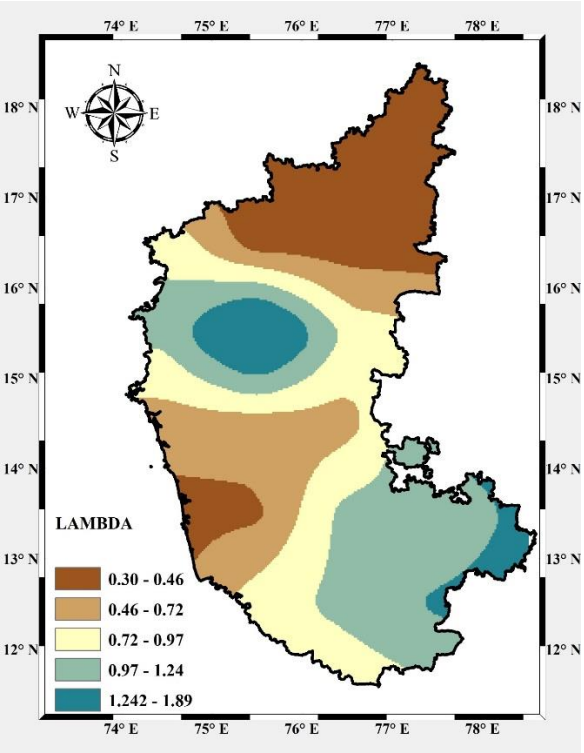

Fig. 6 Map representing the spatial variation of recurrence rate for the entire study region with $M_w > 3.5$.

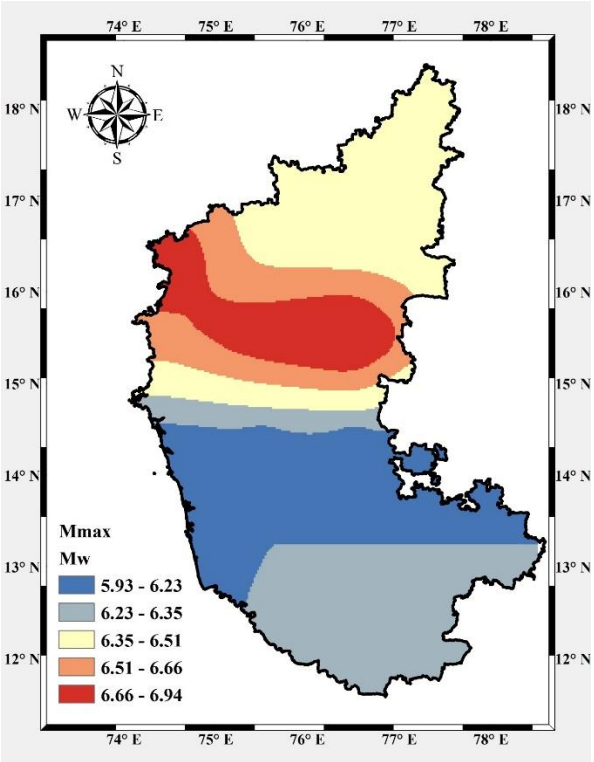

Fig. 7 Map representing the spatial variation of maximum magnitude (M_{max}) for the entire study region

CIVIL ENGINEERING
&
RELATED FIELDS

8th International Engineering Symposium - IES 2019
March 13-15, 2019, Kumamoto University, Japan

Stiff or Soft – What designers should opt ?

K. S. Babu Narayan [1]

1 Professor, Department of Civil Engineering, National Institute of Technology Karnataka, Surathkal, Mangalore 575025, India. email:shrilalisuta@gmail.com

ABSTRACT: Configuration of structural system for channelization of sustained and transient multiple loads to accomplish the best flow and invoke the desired and targeted response is an onerous task. This paper presents the key considerations in analysis, design and detailing of multi hazard resistant structural systems.

Keywords: Stiff, soft, response, frame

INTRODUCTION

Contemplated end use throughout the stipulated utility period, for any structure has to be satisfied and this is termed as functional requirement. In addition to satisfaction of functional requirement the long list of structural requirements includes stability, strength, safety, serviceability and durability at affordable and justifiable costs.

Arrival at the final configuration through which the most efficient load flow is accomplished by proper arrangement of load resisting elements, selection of the most appropriate material of construction, member sizing is a quite challenging and eminently enjoyable exercise for the designer.

A thorough knowledge of loads verses stresses and effects, the nature of loads and the way they act on the structure, the kind of materials of construction employed and their engineering properties like unit weight, elasticity, plasticity, strength, strength to weight ratio, ductility, availability, reliability and sustainability are all issues of great importance and concern. Codes of practice and specialist literature available immensely help the designer in delivering his best.

Selection, performance appraisal, adoption of the right structural system for a situation where multiple loads and their combinations have to be addressed to get the desired structural response is a very complicated exercise that demands tremendous computational efforts and serious engineering judgement. In the section that follows a simple illustration to highlight the designers' dilemma in deciding the stiffness and the softness of structures has been provided.

STIFF OR SOFT ?

Every wind engineer agrees that a structure exposed to winds should be as stiff as possible. Best and targeted response can be obtained by increasing both stiffness and mass of the structure.

Quite conflicting is the requirement of a structure in a zone of high seismicity. For quake resistant design, the structure should be as light and as flexible possible. In a situation where the structure has to be both wind and quake resistant, arriving at the right distribution of mass and stiffness is of paramount importance. A simple example of a single storey single bay RC frame that is unbraced and braced clearly brings this conflict out.

ILLUSTRATIVE EXAMPLE

Fig.1a shows the unbraced frame configuration and the lateral load due to wind. Deformed profile of the unbraced frame is as presented in Fig.1b. The displacement is 27.53 mm and hence the stiffness is approximately 653.85 kN/m.

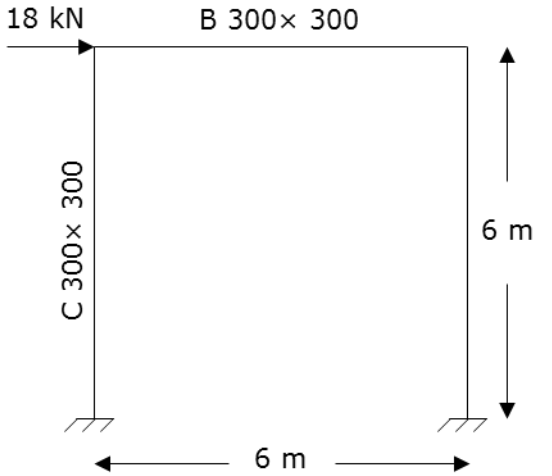

Fig.1a Unbraced frame (Un-deformed)

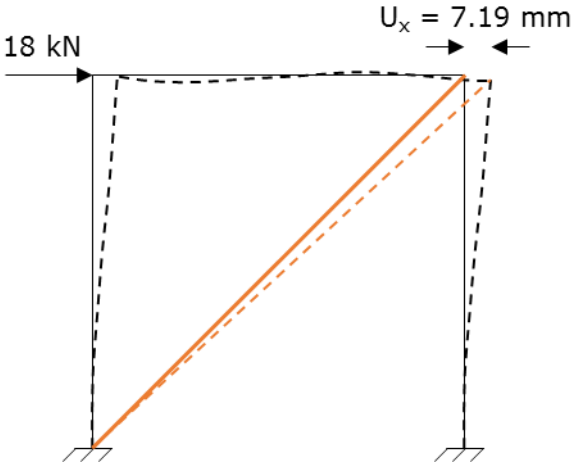

Fig.2b Braced frame (Deformed)

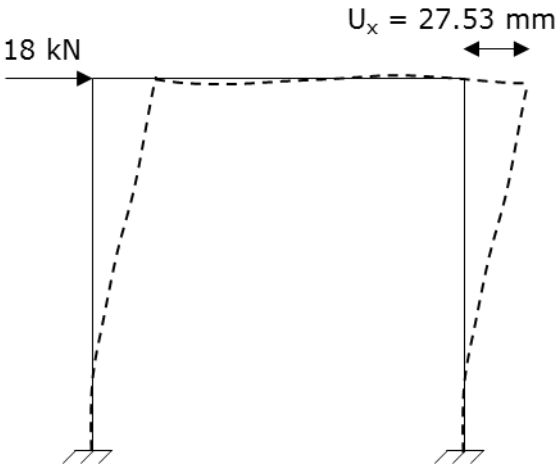

Fig.1b Unbraced frame (Deformed)

Un-deformed and deformed geometry of the same frame with a bracing element are as shown in Fig.2a and Fig.2b respectively.

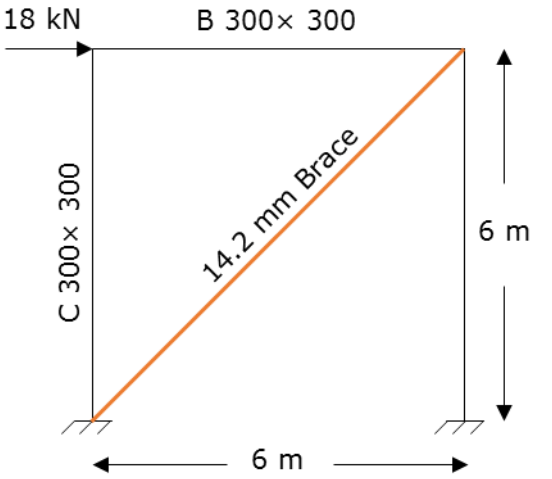

Fig.2a Braced frame (Un-deformed)

The displacement has drastically reduced from 27.53 mm obtained for the unbraced case to 7.19 mm for the braced frame. A reduction of about 74% in drift has been accomplished. The stiffness of the braced frame is 10471.20 kN/m (16 times more stiffer than unbraced).

The stiff frame is very efficient in controlling lateral drift.

The fundamental frequencies and time periods for the unbraced and braced frames considering the whole mass to be capable of motion modelled as inertia force at beam level are 12.58 rad/s, 0.5s and 50.36 rad/s, 0.12s respectively.

For hard soil, IS 1893: 2002 (Criteria for Earthquake Resistant Design of Structures, Part 1: General Provisions and Buildings) suggests spectral accelerations S_a/g as 2.5 for braced frame for which $T<0.4$s and $S_a/g = 1/T$ i.e. $1/0.5 = 2$ for unbraced frame.

It is clearly evident that the stiff braced frame attracts 25% more seismic forces than the unbraced.

This illustration clearly brings out the conflicts in stiffness and softness issues associated with multiple load types.

What works for wind does not work for quake.

CONCLUSIONS

Arrival at the most efficient structural system with appropriate material selection for members and their sizing for accomplishment of load flow to get the desired structural response is a very complicated exercise calling for proper distribution of mass and stiffness through the entire structure.

Multi hazard resistant technologists are seriously considering shape and size optimisation and also auxiliary damping devices and control techniques to make sensitive structures more reliable and habitable. Desired modes of failures are also becoming inherent features of state of the art of structural design.

REFERENCES

[1] Buchholdt, H A and Moossavi Nejad S E (2014), *Structural dynamics for engineers*, 2nd ed., Institution of Civil Engineers, London.
[2] Hemant Gor, (2018), Procedures, Principles and Practices in Tall Buildings, Structural Engineering Digest, Vol. 08, Issue 01, pp 5-11.
[3] Kareem, A et al. (1999), Mitigation of motions of tall buildings with specific examples of recent applications, Wind and structures, Vol.2, No.3, pp 201-251.
[4] Sarkisian, M ,(2016), Designing Tall Buildings: Structure as Architecture, 2nd ed., Routledge, Tylor and Francis, NY & London.

8th International Engineering Symposium - IES 2019
March 13-15, 2019, Kumamoto University, Japan

Eco-friendly Geopolymer Concrete Products

S. Thirugnanasambandam

Department of Civil and Structural Engineering, Annamalai University
Annamalainagar – 608 002, India, Email:agstsai@gmail.com

ABSTRACT: Concrete is one of the most widely used construction materials in the world. It is usually associated with Portland cement as the main constituent for making concrete. The cement industry is responsible for CO_2 emissions, because production of one ton of Portland cement emits approximately one ton of CO_2 into the atmosphere. In view of the serious impact of carbon dioxide on the environment, there is a need to develop an alternative binder to replace cement. It is found that an alkaline liquid could be used to react with the silicon and the aluminium in a source material of by-product materials such as fly ash to produce cementitious binders which is called geopolymer. This paper presents the experimental research work progress of eco-friendly geopolymer concrete structural elements and ferrogeopolymer products.

Keywords: *Geopolymer; Concrete; Beams; Sleepers; Ferrogeopolymer; Roofing Channel.*

INTRODUCTION

Concrete made with Portland cement is the most widely used material on earth. The concrete industry is the largest user of natural resources in the world [Mehta, P. K. (2002)]. Significant increases in cement production have been observed and are anticipated to increase due to the massive increase in infrastructure and industrialization. It is generally agreed that the production of Portland cement clinker is expensive and ecologically harmful [Mehta, P. K. (2001)]. The emissions generated by Portland cement productions are principal contributors to the greenhouse gas (GHG) effect. For instance, the production of Portland cement for concrete accounts for an estimated 5 percent of global anthropogenic carbon dioxide [Karstensen, K. H. (2006)]. The United Nations Intergovernmental Panel on Climate Change (IPCC) has identified the unmindful pumping of CO_2 into the atmosphere is the main culprit for the climate change and highlighted that the "largest mitigation potentials are in the steel, cement and pulp and paper industries…" [IPCC (2007),]. The highest average growth rates in industrial-sector CO_2 emissions are projected for developing countries [Department of Environment and Water (2007)].

In view of the serious impact of carbon dioxide on the environment and the continued anticipated growth of industrialization and urbanization, there is a need to redirect the building industry away from its overwhelming reliance on Portland cement by developing alternative binder systems. The two options which have attracted attention as alternative binders are (i) the partial replacement of cement by industrial by-products like fly ash and slag and (ii) the use of geopolymer binders. The first alternative has been widely researched and abundant information on the fresh and hardened properties of concrete with partial replacement of cement has led to the use of such blended cements [Mehta, P. K. (2004), Stevenson, M. and Panian, L. (2009), Poon, et al (2000), Papadikis, V. G. (1999), Malhotra, V. M. (2002)]. The second alternative, geopolymer binders, is an emerging area of technology. Davidovits [Davidovits, J. (1991)] first proposed that an alkaline liquid could be

used to react with the silicon (Si) and aluminium (Al) in a source material of geological origin or in by-product materials such as fly ash and rice husk ash to produce cementitious binders. Because the chemical reactions that takes place in this case is a polymerization process and the source materials are of geological origin, he coined the term 'geopolymer' to represent these binders.

GEOPOLYMERS

Geopolymers are members of the family of inorganic polymers. The polymerization process involves a substantially fast chemical reaction under alkaline condition on Si-Al minerals, that results in a three-dimensional polymeric chain and ring structure consisting of Si-O-Al-O bonds [Davidovits, J. (1991)]. Research is currently moving from the chemistry domain that includes binder (mortar) composition and properties to engineering, in which mechanical and structural behaviour of geopolymer concretes are studied researched. It has been found that geopolymer concrete has good engineering properties including compressive strength, enhanced tensile strength, bond strength, sulphate and acid resistance and the potential for enhanced durability [Sofy et al (2007), Provis, J.(2007)].

GEOPOLYMER CONCRETE

Coarse and fine aggregates used by the concrete industry are suitable to manufacture geopolymer concrete. The aggregate grading curves currently used in concrete practice are applicable in the case of geopolymer concrete. The alkaline solution is a mixture of sodium silicate and sodium hydroxide solutions. Sodium hydroxide is prepared from the pellets based on the required molarity. The constituents of alkaline solution are shown in Figure 1. The constituents of materials used for hot cured geopolymer concrete are shown in Figure 2 and that for ambient cured geopolymer is shown in Figure 3.

CURING OF GEOPOLYMER PRECAST ELEMENTS

If 100% fly ash is used for the development of geopolymer concrete, then the geopolymer concrete products require steam curing or hot air curing for 24 hours. The geopolymer concrete can be cured under elevated temperature (60 degree in curing chambers). The sophisticated Steam Chamber available at Annamalai University is shown in Figure 4.

PRECAST PRODUCTS DEVELOPED AT ANNAMALAI UNIVERSITY

In our laboratory, We developed strength of geopolymer concrete up to M 60 grade. The details of geopolymer concrete products developed (Figures 5 to 11) and the corresponding strength obtained is given in Table 1.

ENVIRONMENTAL BENEFITS OF THE TECHNOLOGY

The use of fly ash as a source material has environment advantages in addition to those presented by the replacement of Portland cement. The use of the industrial by-products such as fly ash in a high value product like concrete imparts better value-addition to these materials rather than low end usage as landfills and pavement sub-bases.

CONCLUSIONS

From the experimental investigations, the following conclusions are made:

- Geopolymer concrete can be manufactured with low calcium fly ash with different molarities of NaOH.
- Ambient cured Geopolymer concrete elements show better results than conventional cement concrete elements.
- Geopolymer binders have emerged as one of the possible alternative to OPC binders due to their reported high early strength and resistance against acid and sulphate attack apart from its environmental friendliness.
- As geopolymer has better corrosion resistance, evidenced from corrosion tests, it can be used for making precast products like underground pipes, box culverts etc.
- Since it is possible to produce geopolymer concrete of strength

higher than 50 MPa it could be used for prestressed Concrete works.

- Low-calcium fly ash-based geopolymer concrete has an excellent compressive strength and is suitable for structural applications.

ACKNOWLEDGEMENT

We, the authors sincerely acknowledge the support and encouragement provided by the University Grants Commission, New Delhi by sanctioning a research project, *(MRP- MAJOR- CIVIL-2013-36977)* entitled *'Development of geopolymer concrete and testing of elements'* to us.

REFERENCES

1) Davidovits, J. (1991), "Geopolymers: inorganic geopolymeric new materials" Journal of Thermal Analysis, 37, pp. 1633-1656.
2) Department of Environment and Water (2007), "Industrial Process Sector Greenhouse Gas Emissions Projections 2007" available at http://www.climatechange.gov.au/projections/pubs/industrial2007.pdf.
3) IPCC (2007), " Climate Change 2007: Working Group III: Mitigation of Climate Change, Emission Trends (global and regional)" available at http://www.ipcc.ch/publications_and_data/ar4/wg3/en/tssts-ts-7-2-emission-trends.html.
4) Karstensen, K. H. (2006), "Cement Production in Vertical Shaft Kilns in China –Status and Opportunities for Investment" UNIDO Contract RB-308-D40-8213110-2005.
5) Malhotra, V. M. (2002), "High-Performance High-Volume Fly Concrete", Concrete International 24(7): pp. 30-34.
6) Mehta, P. K. (2001), "Reducing the Environmental Impact of Concrete", ACI Concrete International 23(10):pp. 61-66.
7) Mehta, P. K. (2002), "Greening of the Concrete Industry for Sustainable Development", ACI Concrete International, 24(7):pp.23-28.
8) Mehta, P. K. (2004), "High Performance, High Volume Fly Ash Concrete for Sustainable Development" in Proceedings of International Workshop on Sustainable Development and Concrete Technology, Beijing, China, pp. 3-14.
9) Papadikis, V. G. (1999), "Effect of Fly Ash on Portland Cement Systems, Part I: Low-Calcium Fly Ash" Cement and Concrete Research, 29(11), pp. 1727-1736.
10) Poon, C. S., Lam, L. and Wong, Y. L. (2000), "A Study on High Strength Concrete Prepared with Large Volumes of Low-Calcium Fly Ash", Cement and Concrete Research, 30(3), pp.447-455.
11) Provis, J. L., Muntingh, Y., Lloyd, R. R., Xu, H., Keyte, L. M., Krivenko, P. V. and van Deventer, J. S. J (2007), "Will Geopolymers Stand the Test of Time?" Ceramic Engineering and Science Proceedings, 28(9), 235-248.
12) Sofi, M., van Deventer, J. S. J., Mendis, P. A. and Lukey, G. C. (2007), "Bond performance of Reinforcing Bars in Inorganic Polymer Concrete (IPC)", Journal of Materials Science, 42(9), pp. 3107-3116.
13) Stevenson, M. and Panian, L. (2009), "Sustainability through Strength" Concrete International, 31(3), pp. 34:39.

Table 1. Details of Geopolymer Concrete Developed

Sl. No.	Product	Strength obtained
1.	Reinforced Geoploymer Concrete Beams	M 20, M30, M 40, M 50 & M 60
2.	Prestressed Concrete Beams (Post Tensioned)	M 50
3.	Railway Sleepers (Pre tensioned PSC)	M 50
4.	Ferrogeopolymer Products (a) Roofing Channels (b) Domes (c) Pipes	Mortar Strength of 35 - 50
5.	Geopolymer Bricks	5 – 15 MPa

Figure 1. Preparation of Alkaline Activator Solution

Figure 2. Constituents of Geopolymer Concrete (Hot/Steam Curing)

GGBS Fly ash Sand Coarse Aggregate Alkaline Solution

Figure 3. Ingredients of Geopolymer Concrete (Ambient Curing)

(a) Open view

(b) Closed view

(c) Boiler

Figure 4. Steam Curing Chamber

(a) Ambient Curing of Geopolymer Concrete Beam

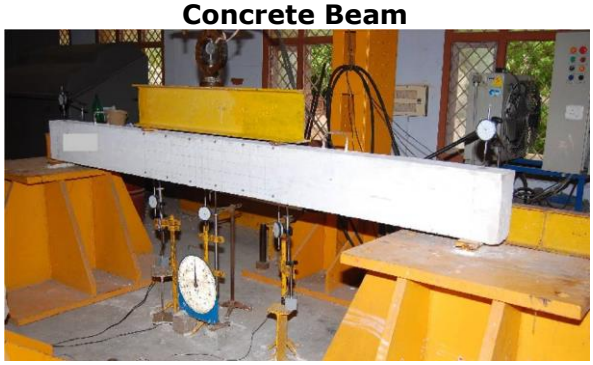

(b) Testing of Geopolymer Concrete Beam

Figure 5. Geopolymer Concrete Beam

a) Casting of Beam

b) Curing of Beam in Steam Curing Chamber

Figure 6. Post Tensioned PSC Beam

c) Ambient curing of GPC Sleeper

Figure 7. Geopolymer Concrete Railway Sleepers

a) Pretensioning of Tendons

b) Anchorage of Tendons with Barrel and Wedges

Reinforcement Grill

Geopolymer Mortar

Test Setup of Ferrogeopolymer Channel

Figure 8. Ferrogeopolymer Roofing Channels

Dome Reinforcement

Outer and Inner Surface of Dome

Testing of Dome

Figure 9. Ferrogeopolymer Domes

Ferrogeopolymer Pipe

Ferrogeopolymer Pipe

Three Edge Bearing Test Setup for Pipe

Figure 10. Ferrogeopolymer Pipes

(a) Casting of Geopolymer Bricks

(b) Ambient Curing of Geopolymer Bricks

Figure 11. Geopolymer Bricks

8th International Engineering Symposium - IES 2019
March 13-15, 2019, Kumamoto University, Japan

Studies on the structural characteristics of laterite blocks and masonry in Puttur area of Karnataka, India

Ganesha Mogaveera [1], G Sarangapani [2]

1 *Dept. of Civil Engineering, Mangalore Institute of Technology and Engineering Moodabidri-574225, Karnataka India, Email: hodciv@mite.ac.in*
2 *Dept. of Civil Engineering, National Institute of Engineering Mysore,Karnataka,India Email: gsp.nie@gmail.com*

ABSTRACT
Laterite blocks are widely used for load bearing masonry. They are used in natural form without any manufacturing process. Several investigators have evaluated the characteristics of laterite blocks and laterite blocks masonry .However the information available on the characteristics of locally available laterite blocks of are scanty. As such a detailed experimental investigation has been made to know the characteristics of laterite blocks masonry constructed using locally available laterite blocks and cement mortars. Three different proportions of cement mortars have been tried. The water transport phenomenon, masonry compressive strength and shear bond strength has been obtained for each case. Compressive strength has been obtained through stack bonded masonry prisms of five block height, whereas the shear bond has been determined through masonry triplets.
***Keywords**: Laterite, Masonry, Shear strength, Prism compressive strength, Water transport*

INTRODUCTION

Masonry units are generally porous and have the tendency of absorbing the water from the mortar due to capillary suction. The rate at which it absorbs water varies with time. Initially it absorbs the water at a very high rate and after sometime the rate of suction slows down. This property of masonry units affects the behaviour of masonry adversely. The mortar in the masonry becomes deficient in water as all the water in the mortar gets transported to the masonry units. This will be very high especially when the masonry units are dry. The water deficiency in the mortar will lead to incomplete hydration. Any incomplete hydration will lead to reduction of strength of masonry.

Bond between the masonry unit and mortar greatly influences the masonry strength. Bond strength is very important especially when the masonry is subjected to in plane and out of plane bending. As the bond strength increases, the masonry compressive strength also increases. A doubling of bond strength can lead to an increase in masonry compressive strength of the order of 40 to 60%.This has been shown by Sarangapani (1998) for bricks with cement mortars and modified lateritic soil cement mortars.

LITERATURE REVIEW

Detailed water transport study has been carried out by G.Sarangapani (1).He has studied the water transport phenomenon using different types of bricks and different types of mortars. He found that the bricks units need to be soaked in water atleast for 15-20 minutes before using it in construction.

ArunkumarBhat et al (2) studied the compressive strength of laterite blocks from DakshinaKannada District gave a strength ranging from 1.04MPa to 3.45MPa.There was a wide variation in strength from place to place. Of the 13 locations studied, 11 locations had strengths below 2.5MPa.It must however be pointed out that laterite blocks have been used for a long time for house construction when the height is limited to two stories.

The use of stone masonry arches in foundations was examined by G.Sarangapani and G.S.Suresh (3). They have concluded that arches in foundations can be effectively used as an alternative to conventional foundation upto two storied buildings located on soils which do not have the tendency of settlements.

Bureau of Indian standard code of practice for laterite blocks (4) specifies an average strength of 3.5 MPa. The standard laterite block is supposed to have a thickness of 190 mm.The minimum strength for burnt brick of 75 mm thickness is also 3.5MPa. It is unrealistic to expect strength of 3.5MPa for a block of 190 mm thickness. The minimum strength specification could probably be brought down to value around 2 to 2.5MPa to take these factors into account.

Kasthurba et al (5) evaluated laterite blocks based on their performance in traditional buildings and also by determining engineering properties of fresh laterite from widely located quarries within Malabar region, Kerala. There is a wide variation in the experimental results (1.3- 4.3 MPa) of compressive strength of commercially available, machine-cut laterite blocks from Malabar region. From a comparison of wet and dry strengths, it is observed that there is a significant reduction in the strength (47-75%) due to saturation.

EXPERIMENTAL INVESTIGATION

Table 1 gives the details of the sources from where the laterite blocks were collected for the test.

All the four sources are in the Mangalore region of western India. They are located between 74° 30’ E to 70° E longitude and 10°N to 12° 30’N latitude. Large volume of mining is done in all the four quarries from where the laterite samples have been collected. Samples were collected at the depth of 1.0 m in all the quarries.

The following sections give the details of tests conducted on laterite blocks and masonry.

Chemical Composition

The properties of the laterite depend on its chemical composition. De creteset (1938) tried to classify the laterite based on the chemical composition. The colour and texture of the laterite block is a function of the chemicals that are present in the block. In this study a detailed chemical analysis has been done to determine the chemical composition of all the four types of laterite blocks that have selected for the study. The procedure given in IS: 2720 (Part XXV) – 1982 has been adopted to determine the chemical composition of laterite blocks to determine the percentage of Silica, Iron oxide and Aluminum oxide.

Compressive strength of laterite blocks and water absorption

Compressive strength of the laterite blocks has been determined as per the guidelines of the IS: 3620-1979, where as the water

absorption have been determined as per the procedure given in IS:1121 (part 1-1974). The size of the blocks used for testing has been taken as 325mm x 220 mm x175mm The compressive strengths have been obtained for all the four types of laterite blocks. As per the procedure given in the code, the two faces are caped using 1:1 cement mortar. The compressive strength has been determined under dry and wet conditions. The wet condition has been achieved by immersing the blocks in water for 72 hours before testing. The blocks are subjected to compressive loading in a compressive testing machine.

Transport of moisture from mortar to laterite block in masonry

This study has been made by considering one type (i.e. type III) of laterite blocks with three types of cement mortars. Cement mortars considered for the study are 1:3 cement mortar, 1:4 cement mortar and 1:6 cement mortar. The simple experiment suggested by Groot (1993) to study the water transport phenomena has been adopted. The steps of the experiment are listed below.

a) The oven-dry blocks used in the experiment are soaked in water for varying duration like 0min, 5min, 10 min, 15min, 20min, 25min, 30 min etc.

b) The partially saturated laterite block is covered with fresh mortar to a thickness of 10mm on top and another similarly saturated laterite block is kept on the mortar.

c) The top laterite block is removed after one hour and the mortar is scooped out and placed in the container to note down the dry weight. This indeed has been used to calculate the moisture content of mortar.

Compressive strength of laterite blocks masonry

The test program consisting of determining the compressive strength of laterite block masonry using various proportions of cement mortars .The various proportions selected for the study were 1:3 cement mortar,1:4 cement mortar,1:6 cement mortar. Laterite blocks used was of type III with a compressive strength of 2.96MPa.The 28 day compressive strength of laterite block masonry has been determined as per the procedure given in IS: 1905-2007.All the blocks were pre-wetted for about 20 minutes before laying. The prisms have been cured under the wet burlap and tested after 28 days. The prisms have been soaked in water for 48 hours prior to testing. A joint thickness of 10mm was maintained for all prisms. Five specimens have been casted for each case. Sand confirming to Zone III and 43 grade ordinary Portland Cement has been used in this program.

Shear bond strength of laterite blocks triplets

Shear bond strength of laterite block masonry has been examined through triplets. A three laterite blocks assembly as shown in figure 1 is used to obtain the shear bond strength of laterite block mortar joints. The arrangements are made in the triplet in such a way that the shear load can be applied at the middle block. The middle block is free to move in the vertical direction, whereas the end blocks are restrained. The shear bond strength is calculated by using suitable formula .

In this investigation the shear bond strength of laterite block masonry triplets with cement mortars have been determined. Laterite blocks used was of type III with a compressive strength of 1.961MPa.The different cement mortars used are 1:3 cement mortar, 1:4 cement mortar and 1:6 cement mortar. 43 grade ordinary Portland cement and sand confirming to zone III was used for preparing mortar. A mortar joint thickness of 10mm was maintained for all the cases. All the triplets were cured for 28 days by keeping in moist condition under wet burlap. Five specimens were tested to obtain an average value of shear bond strength of masonry triplets. All the

triplets were tested in fully saturated condition.

RESULTS AND DISCUSSIONS

Chemical Composition

Table 2 gives the details of the chemical analysis results for laterite blocks tested. From the test results it can be observed that the silica content in the laterite blocks varies from 58 to 76% and iron content varies from 14 to 26%. The alumina content is very less in all the blocks and is in the range of 2 to 8 %. The maximum iron content is for type III blocks at 26 %. For the same blocks the silica content is 58 % and is the lowest among all the blocks tested.

Compressive strength of laterite blocks and water absorption

Table 3 gives the details of the compressive strength and water absorption results of the laterite blocks tested. From the results it can be observed that the dry strength varies from 0.9 MPa to 2.4 MPa and wet strength varies from 0.5 MPa to 0.8 MPa for the blocks tested by applying the load parallel to the grain. The same for blocks tested by applying the load perpendicular to the grains are 1.8 to 2.9 MPa in dry condition and 1.4 to 1.9 MPa in wet condition. In general the wet strength is around 33% to 74% of dry strength. The blocks have higher strength in a direction perpendicular to the grains as compared to that of the strength parallel to the grains. Important information revealed from this study is about relationship between the iron content and compressive strength. In all the cases the compressive strength increases as the iron content increases and silica content decreases. Same types of results have been obtained by Manu *et.al* (2009) and Kasturaba et.al (2007) for the laterite blocks they have tested.

Transport of moisture from mortar to laterite block in masonry

The variation of water-cement ratio of mortar with moisture content of laterite blocks have been plotted in the Figures 1 to 3 for the cement mortars i.e.1:3 cement mortar, 1:4 cement mortar and 1:6 cement. The water-cement ratios of mortar after one hour of contact with the pre-wetted blocks have been considered for the study. From the figures it is clear that if the laterite blocks are dry, most of the moisture in the mortar finds its way into the block within one hour.The value of water cement ratio in the mortar depends on the water retentivity capacity of the mortar. In case of rich mortars (i,e.1:3 and 1:4) the water cement ratio reduces to a value less than 0.5.However for other mortars i.e. 1:6 cement mortar final water cement ratio is around 0.6.If the water cement ratio of the mortar is less than 0.5,setting of mortar will be unsatisfactory and complete hydration will not takes place in mortar leading to lower strengths. To improve the hydration conditions of mortars so as to produce good masonry the only way is to have sufficient moisture content (i.e. around 6%) in the laterite blocks. To achieve 6% moisture content the laterite blocks have to be soaked in water for about 20 to 25 minutes. Masonry in 1:3 cement mortar and 1:4 cement mortar soaking period of around 20 to 25 minutes is required.

Prism Compressive strength

The compressive strength results obtained from the tests conducted on various prisms are presented in table 4 for laterite block masonry in cement mortars. From the test results it can be observed that the compressive strength of laterite blocks prisms in cement mortar varies from 0.657 MPa to 0.83 MPa. The maximum strength is got for 1:3 cement mortars. If the mortar strength is doubled the masonry strength gets increased by 20%.

Shear bond strength

The results of the shear bond strength are presented in Table 5. From the results it

can be observed that the shear bond strength varies from 0.04 to 0.36.It is maximum for 1:3 cement mortar .All the water in the mortar gets transported to laterite blocks leading to deficiency of water in the mortar. Hydration will be incomplete lead to low values of bond strength. Bond strength increases as the mortar strength increases. All the specimens have failed at the interface of laterite block and mortar. The shear bond strength values obtained by Samarasinghe and Lawrence (1992) were marginally higher especially for strong mortars. Walker (1999) reports shear bond strength values of 0.034 MPa to 0.0323 MPa for earth block masonry.

CONCLUSIONS

1.Laterite blocks of type-III has got lesser silica content,higher Iron and Alumina content and also higher compressive strength and hence selected for further test and also for the construction

2.Laterite blocks shall be soaked in water during the construction of laterite block masonry arches. Soaking period shall be around 20-25 minutes to achieve a moisture content of 6 to 10%

3.Strength of mortar is very weekly related to the strength of the masonry.If the mortar strength is doubled the masonry strength gets increased by 20%only.

4. In the construction of laterite block masonry, 6% moisture content is needed in laterite blocks to maintain water cement ratio of 0.5 in the mortar even after one hour of contact for proper hydration.

5.The compressive strength of laterite blocks prisms in cement mortar varies from 0.657MPa to 0.83MPa. The maximum strength is got for 1:3 cement mortar. If the mortar strength is doubled the masonry strength gets increased by 20%.

6.Shear bond strength increases as the mortar strength increases.

REFERENCES

[1] G.Sarangapani, "Studies on the Strength of Brick Masonry using Mud Mortar", Proc of The 4th Int. Seminar on Structural Masonry for Developing Countries, Madras, India, 1992, pp.29-35.

[2] ArunkumarBhat, Study of geotechnical and strength parameters of laterite blocks in and around karkalla taluk′.B.E. Project report,NMAM Institute of Technology,NItte,Karkala.

[3].G.Sarangapani and G. S. Suresh (2002), "Use of Stone Masonry Arches in Foundations", NWABM, IISc, Bangalore.

[4]IS 3620-1979 (Reaffirmed 1998). "Indian Standard Specification for Laterite Stone Block for Masonry", Bureau of Indian Standards, New Delhi, India.

[5]Kasthurba A. K. and Santhanam M."Laterite as a prime masonry material for housing construction in Malabar region of Western India", International Journal for Housing Science and its Applications, Vol. 30, No. 3, pp. 183-194.

Table 1 Details of sources of laterite blocks

Source	Designation
Balnad	Type I
Churipadavu	Type II
Sulliapadavu	Type III
Peruvie	Type IV

Table 2 Chemical analysis

Name of the quarry	Chemical Composition (%)		
	Silica	Iron	Alumina
Type I	76	14	2-4
Type II	71	16	3-5
Type III	58	26	6-8
Type IV	63	21	4-6

Table 3 Compressive strength and water absorption

Quarry Name (Iron content %)	Compressive strength in MPa				Wet/ Dry strength *	Wet/ Dry strength **	Water absorption (%)
	Dry state *	Dry state **	Wet state *	Wet state **			
Type I (14)	0.9	1.8	0.5	1.4	0.55	0.77	22.85
Type II (16)	1.4	2.1	0.55	1.55	0.39	0.74	20.40
Type III (26)	2.4	2.9	0.8	1.9	0.33	0.65	8.5
Type IV (21)	1.8	2.5	0.7	1.7	0.38	0.68	11.80

*- *Loading applied parallel to the grains*
** **- *Loading applied perpendicular to the grains*

Table 4. Compressive strength of laterite blocks prisms for cement mortars

Sl.No.	Type of mortar	Mortar proportions C: Sa (w/c ratio)	Prism compressive strength (MPa)
1	Cement mortar	1:0:3 (0.7)	0.83
2	Cement mortar	1:0:4 (0.8)	0.77
3	Cement mortar	1:0:6 (1.4)	0.66

Table 5. Shear bond strength results of laterite block masonry

Mix proportions	W/C ratio	Mortar compressive strength(MPa)	Shear bond strength (MPa)
1:3	0.7	16.2	0.36
1:4	0.8	11.1	0.32
1:6	1.4	8.92	0.29

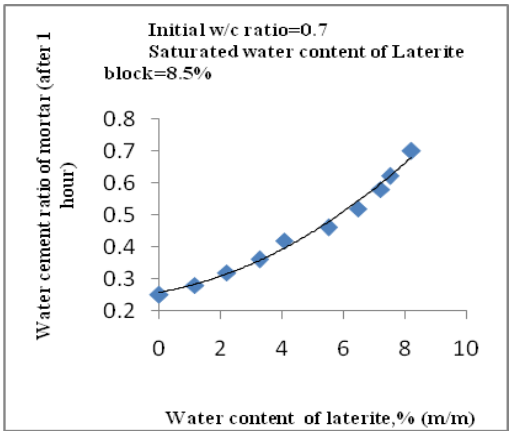

Fig. 1.Variation of water cement ratio of 1:3 cement mortar with water content of laterite block

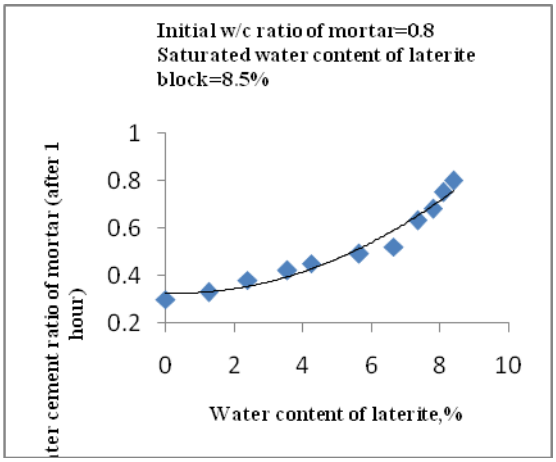

Fig. 2. Variation of water cement ratio of 1:4 cement mortar with water content of laterite block

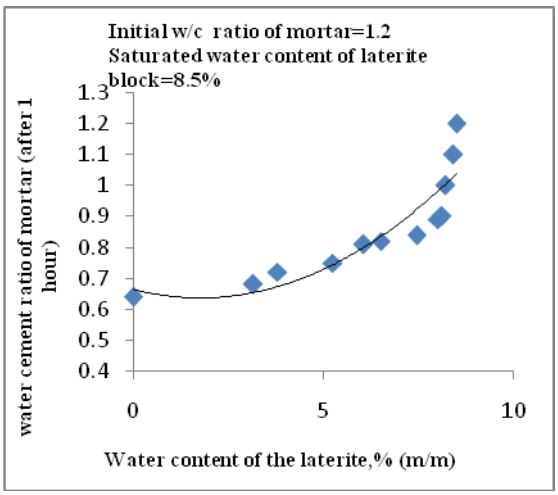

Fig .3. Variation of water cement ratio of 1:6 cement mortar with water content of laterite block

A COMPREHENSIVE ANALYTICAL STUDY ON EFFECT OF FRACTURE ON FLEXURE, SHEAR, BOND AND TORSIONAL STRENGTH IN SCC

H.C.M. Swamy[1,2] and G. Prince Arul Raj[3]

[1.] *Karunya Institute of Technology and Sciences, Coimbatore, Tamil Nadu.*
[2] *Alva Institute of Engineering and Technology, Moodbidri, D.K. Swamy8695@gmail.com*
[3.] *Karunya Institute of Technology and Sciences, Coimbatore, Tamil Nadu.*
princearulraj@yahoo.com

ABSTRACT: Concrete is a brittle material and has very less tensile strength. It contains micro cracks in transition zone, it develops as load increases, and ultimately it fails after it attains maximum tensile strength of concrete specimen. Here a study is proposed to evaluate fracture strength, fracture energy and total strain energy of concrete specimen subjected to flexure, shear, bond and torsion analytically. Here both limit state analysis and fracture analysis are used. Equations are developed and used based on its pre cracking and post cracking analysis. The method follows with classical limit state analysis and brittle fracture analysis. Method is simple and can be applied to all type of structural elements.

Key words: Fracture flexural strength, fracture shear strength, fracture bond strength, fracture torsion strength, strain energy

INTRODUCTION

Concrete is good in compression but weak in tension. So reinforcements are provided at tension zone to cater for its tensile stresses. Here a general method is developed to obtain fracture energy and total strain energy for all type of structural elements subjected to flexure, shear, torsion and bond strength. The study of fracture is classified as plane stress and plane strain fracture models. The post fracture examination of fracture surfaces generally tells about the material behavior. Two types of conditions prevail in fracture, plain stress and plain strain condition. In plain stress condition the post cracking condition can be studied where as in plain strain condition the pre cracking analysis can be justified.

Plane – Strain fracture toughness K_{IC} is a material property just as Young's modulus or yield stress.

Stress intensity factor: Flexure

Plane strain fracture toughness K_{IC} is the material toughness at the onset of fracture. It is measured in terms of stress intensity factor K_I at fracture by standard ASTM test procedure. The measurement of K_{IC} is based on the lowest load at which significant invaluable extension of the crack occurs. Significant invariable extension is defined in terms of a specified deviation from the linearity of the load displacement curve.

The strain energy release rate corresponding to on set of fracture is denoted by G_{IC} and the relationship between K_{IC} and G_{IC} is given by equation as

$G_{IC} = (K^2_{IC}) / E$ for Plane stress
$G_{IC} = (K^2_{IC}) / E (1 - \sqrt{}^2)$ for Plane strain

Case (i) Stress intensity factor given by the equation below: The bend specimen

containing single –edge notched beam loaded by a three –point bending

$K_{IC} = (P S \times f(a / W) / (B W^{3/2})$
Where P = Load
B = Thickness of Specimen, mm
S = Span length, mm
W = Depth of Specimen, mm and
a = Crack length in mm

Case (ii) Compact Specimen for fracture toughness determination in a single edged notched and pin loaded. The stress intensity factor is given by

$$K_{IC} = (P \times f(a / W) / (B W^{1/2})$$

Note: The expression given above was formulated to represent a/W in the range between 0.45 and 0.55 and should not used outside the range.

The analysis of K (Stress intensity factor) and G (Fracture energy) are based on linear theory of elasticity. Linear elastic fracture mechanics (LEFM) cannot be applied to materials which exhibit considerable nonlinearity. Corrections for plastic behavior of materials are needed in order to predict fracture of such materials.

Shear, Bond and Torsion:

Bending is usually associated with shear. Hence R.C. Section should be strong enough to resist the limit state of collapse in shear also. Some of the beams are subjected to torsion also. Hence the designer must know how to assess the strength of R.C. Section in the limit state of torsion. Design of all RC sections is based on the assumption that there is perfect bond between steel reinforcement and concrete. This is possible only if the bond stress is within the limit. Hence designer must be able to asses this bond strength.

In this paper an attempt is made to evaluate analytically and experimentally the Fracture energy and Strain energy of three grades of concrete M18, M30 and M60 (Refer Table 2).The concrete designed is SCC. Now an attempt is made to evaluate shear strength, bond and torsion analytically

Shear Failure:

$$T_v = V_u / (b d)$$
V_u = Design (Factored) Shear force
b = Breadth
d = depth

Rectangular beam of 100 x 100 x600 mm is subjected to shear and the above expression is used and shear stress is calculated.

Torsional Failure

The moment causing twisting of the cross section is called torsional moment. Actually, if rigorous three dimensional analysis of building frame is carried out, it will be observed that all beams are subjected to some torsional moment also. There are many cases in which torsional moment cannot be ignored. Some of the examples are

1. A beam with cantilever slab
2. Balcony girders
3. Ring beams of water tanks resting on columns.

We are familiar with the following torsional equation for circular bars

$$T / J = q / r = G\theta / L$$
Where T = Torsional moment
J = Polar moment of inertia
q = Shear stress due to torsion
.r = Radial distance of the point
G = Modulus of rigidity
θ = Angle of twist and
L = Length of the bar

It should be carefully noted that the above formula is applicable only for the bars of circular section in which warping of the section do not take place. For the members with rectangular section or the built up sections with rectangular components the above equation is used with different meaning for the terms J. J is

called torsion factor. More accurate expression for torsion factor for a rectangular section is given by

$J = b3\, d^3 / (3.58 (b^2 + d^2))$ ……1

$J = b^3 d / 3 \quad (1 - 0.63\, b / d)$ -------2

Equation 1 gives better result for d / b 1 to 1.6 and equation 2 gives better results for d / b > 1.6

In R.C. Structural members, torsion is usually associated with bending moment and shear force. It is also observed that torsion is secondary to flexure. Hence there is no need to study strength of RC members under pure torsion. Based on several research works, all national codes have accepted simple formulae to take care of torsional effect on R.C. moment may be split in to a bending moment of

$M_t = T_u (1 + D/ b) / 1.7$ and a shear force of $1.6\, T_u / b$

D = overall depth of beam.

If M_u is design bending moment and V_u is design shear due to flexure and T_u is design torsional moment, it may be assumed that the beam is subjected to an equivalent moment and shear forces M_e and T_e

Where $M_e = M_u + T_u (1+D/b) / 1.7$

$V_e = V_u + 1.6\, T_u / b$

Then the beam section is designed for the bending moment M_e and shear force V_e

Strain Energy: It is the internal energy which is developed in the material of the body to resist the deformation due to application of load

Bond Strength in R.C Members:

The theory of reinforced concrete is developed with the assumption that there is perfect bond between steel and concrete, in other words, there is no slip. The plane section before bending remains plane after bending also, if and only if, there is no slip. The stress developed between contact surfaces of steel and concrete to keep them together is called bond stress. There is a limit up to which such stress can develop and beyond that there will be slip. The design has to take care of the following two cases of bond failures

1. Flexural Bond
2. Anchorage Bond

Flexural Bond

$\Delta M/\Delta x$ = Rate of change of moment
=Shear

However it is to be noted that the above expression is valid only for mild steel and not for ribbed bars. The reason is in ribbed bars there is considerable increase in resistance to flexural bond due to projection on it. In case of ribbed bars there is no need to check for this flexural bond.

Anchorage Bond :

$L_d = 0.87 f_y \varphi / (4 \tau_{bd})$

Grade of Concrete	M_{20}	M_{25}	M_{30}	M35	M40 and above
Design Bond Stress $\tau_{bd,}$ N/sq mm	1.2	1.4	1.5	1.7	1.9

1. Axial Strain energy:
   $U = P^2 L / 2AE$
2. Shear Strain energy:
   $U = \int_0^L V^2\, dx / 2AG$
3. Flexural Strain Energy:
   $U = \int M^2 ds / 2EI$
4. Torsional Strain Energy:

$$U = \int \tau^2 \, dx \; / \; 2 \, G \, J$$

Where
U = Total Strain Energy
P = Load

L=Length of the Specimen

A = Cross sectional Area

E = Young's Modulus

V= Shear force

G=Shear Modulus = E / 2 (1 + Y)

Table: 1 Stress Intensity Correction Factors for Bend Specimen

a/W	f (a / W)	a/W	f(a/W)
0.45	2.28	0.500	2.66
0.455	2.32	0.505	2.70
0.460	2.35	0.510	2.75
0.465	2.39	0.515	2.79
0.470	2.42	0.520	2.84
0.475	2.46	0.525	2.89
0.480	2.50	0.530	2.94
0.485	2.54	0.535	2.99
0.490	2.58	0.540	3.04
0.495	2.68	0.545	3.09
		0.550	3.15

Table 2: Strain Energy and Fractural Energy

Type of Concrete Mpa	G_F (Experimental) Mpa	G_F (plane Stress) Mpa	G_F (plane Strain) Mpa	U (Strain Energy) Mpa
Ordinary Concrete M18	248.8	256.47	250.669	341.96
Moderate Strength M30	360.7	355.49	363.99	474.39
High strength M60	648.6	654.69	639.96	872.92

Beam Size: 100 x 100 x 600 Dim in mm

CONCLUSION

J = Torsional inertia of the member
Y = Poisson's ratio
M = Moment
Here beams of size 100 x 100 x 600 mm and cubes of 150 x 150 x 150 mm are used. The tests are planned to conduct on 7 days, 14 days and 28 days strengths respectively and the unknown parameters like fracture energy and strain energy by using the above formula are evaluated analytically.

The method is to evaluate the Fracture energy and Strain Energy and also the strength of the members subjected to Flexure, Shear, Bond and Torsion. This strength indicates clearly the values for which a structural member can be loaded safely without causing any damage to the other structural elements. The primary importance of the work is to know, what extent the structure can be loaded beyond the ultimate load and to define its safety against the fracture and usefulness of the structure before fracture. Method is simple and it evaluates all the intrinsic properties of the concrete. By evaluating the above parameters indicates relation between the different force system and the material behavior for the above systems of loading conditions.

Here in all cases the maximum displacement is evaluated experimentally and the material property like modulus of elasticity or yield stress is calculated and the fracture energy and strain energy parameters are evaluated analytically.

REFERENCES

1. Fulton, P.S., Concrete Technology, The Portland Cement Institute, Johannesburg,1977
2. Gambhir, M.L.,Concrete Technology, Tata McGraw-Hill Publishing Company Limited, New Delhi,1986
3. Lydon, F.D.,Concrete Mix Design, Applied Science Publication, London,1972
4. Mclntosh, JU.D.,Concrete Mix Design, 2nd Edn.,Cement and Concrete Association, London,1966
5. Neville. A.M.,Properties of Concrete,3rd Edn, Pitman Publishing Company,1981.
6. Orchard,D.F.,Concrete Technology. Vol. I, 3rd Edn, Applied Science Pyublishers Ltd., London 1973
7. Powers, T.C.,Properties of Fresh Concrete, John Wiley and Sons Inc.,1968.
8. SP:23-1982, Hand book on concrete Mixes, Bureau of Indian Standard, New Deldi,1982

8th International Engineering Symposium - IES 2019
March 13-15, 2019, Kumamoto University, Japan

STUDIES ON EFFECT OF NEAR SURFACE MOUNTED (NSM) TECHNIQUE ON THE DYNAMIC BEHAVIOUR OF RC SLAB UNDER INCREMENTAL DROP TEST

Nandeesh M S[1], Arjun R P Reddy[2], H N Jagannatha Reddy[3] and R Prabhakara[4]

1. *Department of Civil Engineering, M. S. Ramaiah Institute of Technology, Bangalore. Email: nandeeshms@gmail.com*
2. *Department of Civil Engineering, Bangalore Institute of Technology, Bangalore. Email: arjun.rpreddy@gmail.com*
3. *Department of Civil Engineering, Bangalore Institute of Technology, Bangalore. Email: jagannath.priyadhi@gmail.com*
4. *Structural Engineering division, Visvesvaraya Technological University, Belagavi. Email:r.prabhakara@gmail.com*

ABSTRACT: RC slab is an important structural element, which provides the most useful area for working. The effect of impact loads on slabs were not studied effectively due to lot of constraints like lack of experimental setup, cost of sophisticated equipment required for the study among others. Drop weight test on slabs is found to be a simple experimental setup, which aids in measuring the dynamic response of slabs under impact loads with a reasonable degree of accuracy. An experimental study was conducted reinforced concrete slabs, the responses of reinforced concrete slab under three drop heights was investigated for the slabs and a comparison was made between unstrengthened and strengthened by near surface mounting (NSM) technique. The variation of response was studied over different height of impact, change of concrete grade and its variation due to the strengthening technique was recorded using an accelerometer attached at the slab centre on bottom portion. All the slabs were tested as simply supported with the drop weight impacting at the centre of the slab on the top surface. It was observed from this experimental results that the height of the drop and strengthening technique influence the dynamic behaviour of RC slab.

***Keywords**: NSM Technique, drop test, two-way slab, dynamic response, peak acceleration*

INTRODUCTION

Slabs though designed for static loading, will be subjected to sudden impact loads due to various reasons such as dropping of building materials during the construction of structure, accidental events in industrial floor spaces and natural calamities. All these loads induce distress in the slabs for which they are not designed.

The effect of impact loading on concrete is very rarely studied and the assumption of behaviour under impact loading with the information about static behaviour is erroneous and may lead to disastrous results if applied in actual design. The study of impact behaviour of slabs is a complex phenomenon and requires large amount of time and a complex test setup, which has discouraged the widespread study of impact behaviour of concrete slabs.

In the recent days drop test has emerged as an effective way of studying impact behaviour of concrete structures. The main reason for the rising popularity of drop test is its simplicity of test setup and ease of experimentation. The drop test involves, impacting mass onto the structure and recording the impact behaviour of the structural component in terms of the inertial responses, which are recorded as acceleration and velocity signatures and the damage formations which are bound to vary with the changes in impact energy Several parameters influence its impact behaviour such as grade of concrete,

reinforcement, geometry and boundary conditions.

Retrofitting of existing structures is a viable alternative to demolishing and reconstruction of entire structure. NSM technique is one such retrofitting system, which involves embedding of additional reinforcement in form of bars or strips in the groove made in concrete cover. The use of Near-Surface Mounted (NSM) Fibre-Reinforced Polymer (FRP) is the latest method for increasing both flexural and shear strength of deficient Reinforced Concrete (RC) beams and slabs.

In the present study, the study on the acceleration response of the RC slabs with change in grade of concrete from M20 to M70 for different drop heights and how this behaviour is affected by retrofitting the slab by NSM technique.

LITERATURE REVIEW

Hrynk, T D & Vecchio, F J (2014) have studied the behaviour of NSC slabs and steel FRC slabs under high-mass, low velocity impact and concluded that:

- Cracking pattern in normal RC Slabs after first crack was seen to align with reinforcement bar grids on both faces.
- Punching shear cracks under subsequent impacts were seen to form from circumferential cracks form from earlier impacts and occurred around impact area.
- Impact capacity was measured as the total kinetic energy imparted to the slab.
- Impact energy did not have much influence on the slab behaviour with change in longitudinal reinforcement ratio but increase in fibre content increased the impact capacity.
- Displaced shapes of slabs showed distinct punching cones under repeated loading.
- Inertial response of the slab under impact loading was believed to be main cause of punching shear failure.

Ozgur, A et al (2015) have presented an experimental and analytical study on the behaviour of reinforced concrete slabs under impact loading. Both experimental and analytical study considered application of impact loads to the specimens by dropping a standard weighing hammer of 5.25kg from a height of 500mm while varying the support conditions.

- The behaviour of slabs due to impact loads depends significantly on support type and support layout.
- Supports with higher stiffness showed lower acceleration thus leads to lower velocity and displacements.
- Specimens with two opposite sided support layout exhibited better performance compared to two adjacent sided support layout.
- The increase in damage with the number of drops resulted in decrease in accelerations.

Ramanna, N (2012) in his doctoral thesis has shown that the use of near surface mounted carbon fibre polymer (NSM-CFRP) reinforcement such as FRP strips of produces an increase of the flexural strength. In this study, the response of reinforced beams and slabs subjected to static or Impact loads was observed. The experimental work consisted of total 23 number of beams and four slabs for testing. The performance of beams and slabs under impact loads were studied using the acceleration time histories. A single degree of freedom elasto-plastic was developed to capture their dynamic behaviour.

- Retrofitted slab were seen to show two times higher load carrying capacity than the control slab under static loading.
- The deflections in the retrofitted slab was found to be nearly half of the control slab which indicates that the slab was stiffened with the strengthening and thus ductility reduced.
- Retrofitted slab exhibited three times higher stiffness than control slab under dynamic loading.
- Strengthening of the slab was seen to avoid punching shear failure.

OBJECTIVES

- To conduct drop test on slabs to evaluate the dynamic response behaviour of slabs.
- To record the change in dynamic response of different grade of concrete and when slabs are strengthened with NSM technique.

MATERIALS USED IN THE CURRENT STUDY

Materials used in the present investigation was characterized, in accordance with the standard procedure as follows

CEMENT - OPC of 53 grade conforming to IS: 12269-2013.

AGGREGATES - The fine and coarse aggregates confirming to IS 383-1970.

REINFORCEMENT - confirming to IS 1786: 2008.

ADMIXTURE – For the present work, for M70 concrete, Master Glenium Sky 8233 was used and Siri plast was used for producing M20 concrete.

WATER – as per IS 456:2000, for both mixing and curing, potable water confirming was used which was free from injurious salts

CFRP laminates and the epoxy used were "Nitowrap CFP" & "Nitowrap 40" which was sponsored by FOSROC CHEMICALS, Bangalore, for retrofitting both NSC and HSC slabs.

SPECIMEN CASTING AND STRENGTHENING BY NSM TECHNIQUE

The specimen casting was done to carry out the tests for studying the behaviour of slabs in impact loading by varying the grade of concrete for a constant reinforcement ratio. The dimensions and reinforcement details are provided in Fig 1. The slabs without NSM strengthening was identified as control slabs with marking NSM0 and strengthened slabs were designated as NSM1. The strengthening of slabs was done by NSM technique using CFRP strips. The strengthening was done in diagonal direction based of earlier researches [19], a zone of NSM strengthening marked by L/5.31 from the ends of the slab was identified. The typical strengthening system considered and the groove dimensions adopted for this investigation are presented in Fig 2 & 3 respectively. The strengthening was done by cutting a groove on the bottom face of the slab and embedding the CFRP strips in the epoxy, which was filled in the groove cut out earlier to obtain the details as shown in the Fig 4

EXPERIMENTAL SETUP

The Impact test on slab was done by using a drop test. The test setup consists of a drop weight, represented in Fig.5, the loading frame which was used, a pulley and a rope arrangement was fixed to lift the weight as shown in the Fig.6, and a four channel dynamic data acquisition system (DDAS) and accelerometers used to study the response.

EXPERIMENTAL PROCEDURE

All the slabs were dried and white washed, to have a smoother surface, to identify crack formation, propagation of cracks and measuring crack width during testing. The location to fix accelerometer at the centre of the slab and measurements of crack widths were marked on the tension face of the slab and the location of the drop mass striking point was marked on the compression face. The support condition for the slabs to be tested was simply supported on all four edges.

In the present investigation, the drop mass was obtained from the work energy principles for total slab capacity. For the present study the drop mass was worked out to be 70 kg. The height of the drop was varied to give different impact energies to have different range of kinetic energy to the slab and to record variation in the response of slab under different impact energy. For this purpose, the drop weight of 70kg was dropped from the height of 0.67m, 1.33m and 2m respectively on to the different slabs. The total energy impacted due to different drop heights are shown in table 1.

TEST RESULTS

A total twelve number of slabs were cast for impact test, out of which six were control slabs and six were NSM strengthened slab. These slabs were tested in the present investigation and the responses of each slab was obtained from the software "KAMPANA" of data acquisition system where the acceleration, velocity and displacement values were captured from the accelerometer placed at centre of the slab on the bottom portion.

The results from the test are presented in table 2. A graphical representation of the experimental results comparing the

acceleration response of the slabs for different drop heights is as shown in fig 7. The cracks formed on the tension face due to drop impact was measured and a ratio of crack length to area of slab was computed and compared for different test specimen and presented in table 3 and the same is represented in Fig 8 to compare the values easily. A typical crack pattern on tension face of the strengthened slab is shown in Fig 9.

OBSERVATIONS

The following observations were drawn from the experimental results:

1. The acceleration response of unstrengthened slab was observed to increase with increase in concrete grade only for drop height of 0.67m where as it decreased with increase in grade for drop heights of 1.33m and 2.0m.
2. It was recorded that with strengthening, the HSC slabs showed a decrease in acceleration for drop height H1 but it increased for drop heights H2 and H3.
3. Crack length was seen to decrease nominally for all NSC test slabs with strengthening whereas the HSC slabs showed considerable decrease in crack length for drop heights H1 and H2 but increased marginally for drop height H3 with strengthening.

CONCLUSIONS

From the observations made it can be concluded that, for the given reinforcement ratio,

1. The acceleration response of NSC slabs decreased with strengthening for all drop heights.
2. Maximum change in response was recorded for highest impacting energy, where NSC slabs showed a significant decrease in response whereas HSC exhibited the opposite behaviour showing an in increase in acceleration.
3. Crack length per unit area was observed to decrease significantly for HSC slabs when compared with NSC slabs for all cases except highest impact energy considered in the present study.

The study has shown promising results to represent the dynamic response of slabs under impact loads however, further studies need to be conducted to understand the intricacies of the mechanical behaviour to predict the response mechanism of RC slabs under drop test.

REFERENCES

1. Hunchate, S R et al. (2014), "Mix Design of High Performance Concrete Using Silica Fume and Superplasticizer", International Journal of Innovative Research in Science, Engineering and Technology, Vol.3, Issue 3, March 2014
2. Annadurai, A & Ravichandran, A (2014) Development of Mix Design of High Strength Concrete with Admixtures, IOSR Journal of Mechanical and Civil Engineering, Vol.3, Issue 5, Jan 2014
3. Prabhakara, R et al (2006) Ultimate Flexural Strength of High Strength Concrete Beams, Indian Concrete Journal, Oct 2006, pp 40-50.
4. Hrynk, T D & Vecchio, F J (2014), Behaviour of Steel Fibre Reinforced Concrete Slabs Under Impact Load, ACI structural journal, Vol.3, No.5, Sep-Oct 2014.
5. Yoo, D Y et al. (2012), Enhancing Impact Resistance of Concrete Slab Strengthened with FRPs and Steel Fibres. Proceedings of the 6th International Conference on FRP Composites in Civil Engineering, CICE 2012.
6. Fila, A et al. (2015), Perforation Resistance Of Reinforced Concrete Slabs Affected By Low Velocity Drop Loads, SMiRT-23, Manchester, UK- August 10-14, 2015
7. Krauthammer, T and Zineddin, M (1995) Structural Concrete Slabs Under Localized Impact, Fortifikatorisk Notat Nr 211/93, Norwegian Defence Constructive Service.
8. Banthia, N et al. (1988), Impact Testing of Concrete Using Drop Weight Impact Machine. Experimental mechanics Pp 63-69, 1988.
9. Sangi, A J and May, I M (2009) High Mass, Low-Velocity Impacts of Reinforced Concrete Slabs, 7th LS-DYNA Conference, 2009, UK.
10. Ozgur A et al. (2015), Low Velocity Impact Behaviour Of RC Slabs With Different Support Conditions, Construction and Building Materials 2015.
11. Witkowski, H & Kotynia, R (2010), Bond between NSM Reinforcement and Concrete, 8th fib Ph.D. Symposium in Kgs, Lyngby, Denmark, June 20 – 23 2010.
12. Rizkalla, S and Hassan, T (2001), Various FRP Strengthening Techniques for Retrofitting Concrete Structures, 2001.
13. Tavallaee, M & Ted Donchev, T (2014), Bi-Directional Strengthening of Two Way Reinforced Concrete Slabs Using Fibre Reinforced Polymer, New York Science Journal 2014.
14. E. Bonaldo, E et al. (2005), Concrete Slabs Strips Reinforced with Epoxy Bonded Carbon Laminates into Slits, University of Minho, Portugal.
15. Protchenko, K et al (2015), Investigation of Behaviour of Reinforced Concrete Elements Strengthened with FRP, XXIV R-S-P Seminar, Theoretical Foundation of Civil Engineering 2015.
16. Florut, S C et al (2010), Retrofitting Two Way RC Slabs with and Without Cut-Out Opening by Using FRP Composite Materials, Latest Trends on

Engineering Mechanics, Structures, Engineering Geology, July 2010.
17. Florut, S C et al (2010), Efficiency Assessment Of CFRP Retrofitting Solution For RC Slabs With And Without Cut-Out, Latest Trends on Engineering Mechanics, Structures, Engineering Geology, July 2010.
18. Lorenzis, L et al (2000), STRENGTHENING OF REINFORCED CONCRETE STRUCTURES WITH NEAR SURFACE MOUNTED FRP RODS, International Meeting on Composite Materials, Milan, Italy, 2000.
19. Nakul Ramanna (2012) "Static and Impact Load Response of Reinforced Concrete Beams and Slabs with NSM-CFRP Retrofitting" PhD thesis submitted to Old Dominion University, USA.
20. Prabhakara R and Manohara B, (2015) Strength and Ductility Performance of Preloaded HSC Beams Retrofitted with CFRP Strips Using NSM Technique. International Research Journal of Engineering and Technology (IRJET) e-ISSN: 2395 -0056 Volume: 02 Issue: 04| July-2015
21. Sreenivasappa, N et al (2016). Investigations On Effect of CFRP Strips Retrofitted Using NSM Method On Two-Way NSC and HSC Slabs Subjected to Concentrated Load, International Journal of Research in Engineering and Technology eISSN: 2319-1163 | pISSN: 2321-7308 | Volume: 05Special Issue: 14| ICRAES-2016| Sep-2016
22. R P Reddy, A et al (2016). Studies on Strength and Deformation Behaviour of Two-Way NSC and HSC Slabs under Single Point Loading. International Journal of Research in Engineering and Technology eISSN: 2319-1163 | pISSN: 2321-7308 | Volume: 05Special Issue: 14| ICRAES-2016| Sep-2016
23. Bureau of Indian Standards "Plain and Reinforced Cement Code of Practice" IS 456:2000.
25. Bureau of Indian Standards "Design Aid to Reinforced Concrete to IS 456:1978" SP16, 1980.
26. Bureau of Indian Standards "Recommended guide lines for concrete mix design", IS 10262:1982.
27. Bureau of Indian Standards "High Strength Deformed steel bars and wires for concrete reinforcement" IS 1786:2008.

Table 1: Impact Energy on the slabs

Drop Weight 'm' (kg)	Drop Height 'H' (m)		Impact Energy= m x g x H (Joules)
70	H1	0.67	460.01
	H2	1.33	913.31
	H3	2.00	1373.4

Table 2: Response of the test slabs

Unstrengthened Slab	Acceleration (g)	Strengthened Slab	Acceleration (g)
M20/PT1/H1/NSM0	0.718	M20/PT1/H1/NSM1	0.341
M20/PT1/H2/NSM0	0.865	M20/PT1/H2/NSM1	0.43
M20/PT1/H3/NSM0	4.112	M20/PT1/H3/NSM1	0.72
M70/PT1/H1/NSM0	1.826	M70/PT1/H1/NSM1	0.664
M70/PT1/H2/NSM0	0.591	M70/PT1/H2/NSM1	1.455
M70/PT1/H3/NSM0	0.723	M70/PT1/H3/NSM1	3.808

Table 3: Ratio of crack length to slab area

Slab	Crack Length/Slab Area (per m)
M20/PT1/H1/NSM0	2.920
M20/PT1/H1/NSM1	2.790
M20/PT1/H2/NSM0	3.572
M20/PT1/H2/NSM1	3.630
M20/PT1/H3/NSM0	3.443
M20/PT1/H3/NSM1	3.030
M70/PT1/H1/NSM0	2.120
M70/PT1/H1/NSM1	.810
M70/PT1/H2/NSM0	3.470
M70/PT1/H2/NSM1	2.170
M70/PT1/H3/NSM0	3.710
M70/PT1/H3/NSM1	4.130

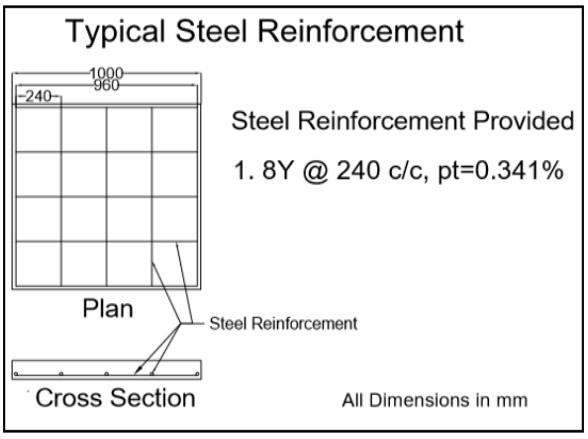

Fig.1: Reinforcement Details of Slab

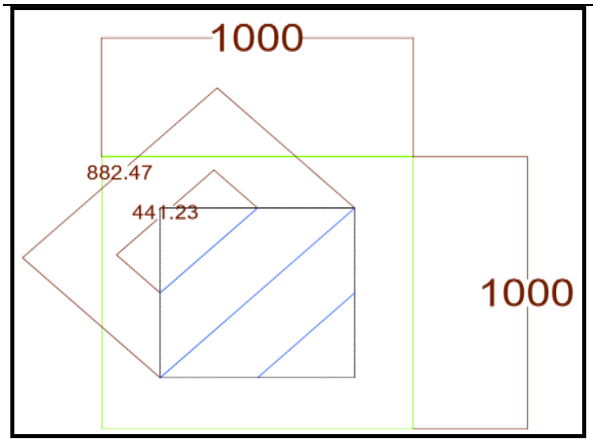

Fig.2: Typical NSM strengthening

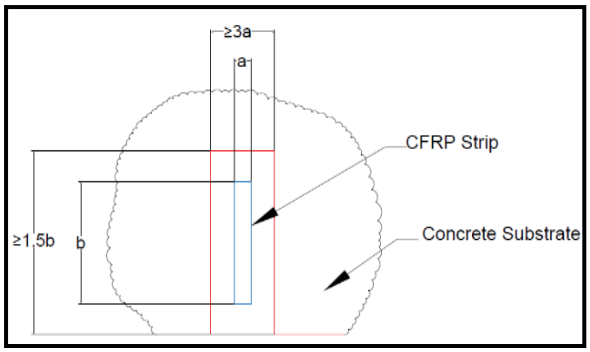

Fig.3: Typical Groove Dimensions

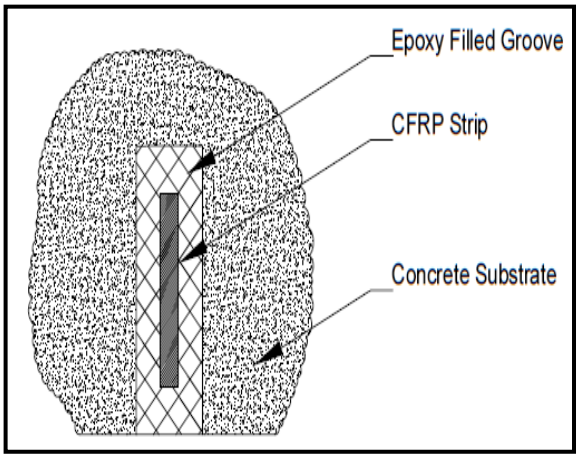

Fig.4: Typical Groove Details

Fig.5: Drop weight of 70kg

Fig.6: Pulley and rope assembly

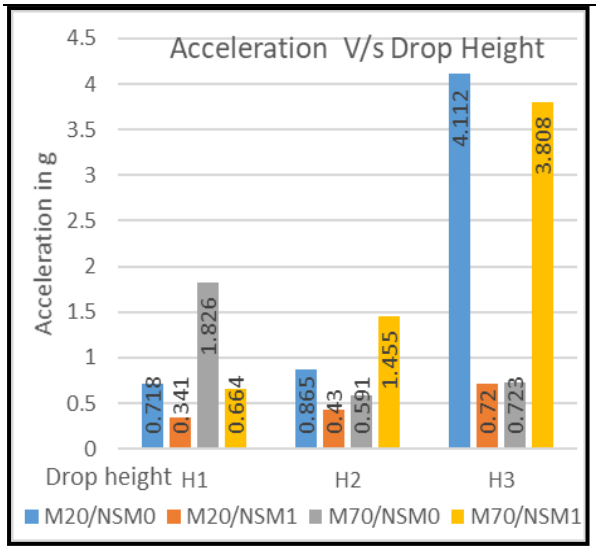

Fig.7: Acceleration V/s Drop Height

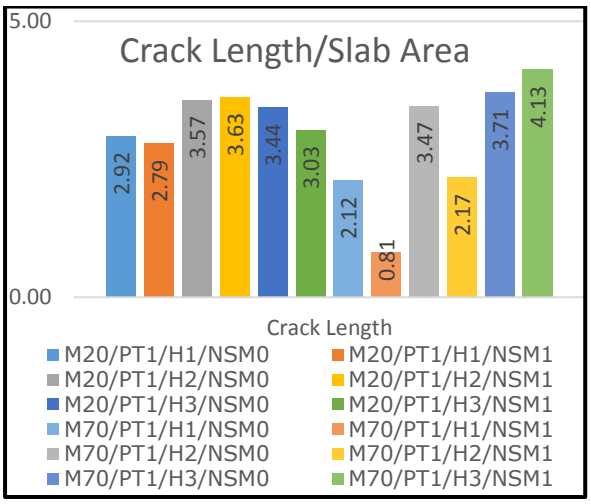

Fig.8: Crack length/Slab Area

Fig.9: Typical crack pattern on tension face of slab

8th International Engineering Symposium - IES 2019
March 13-15, 2019, Kumamoto University, Japan

Strength and Deformation Behaviour of Post-Tensioned Concrete Strengthened Beams Using CFRP Laminates with NSM Technique

Vathsala[1], H N Jagannatha Reddy[2] and R Prabhakara[3]

1 *Dept of Civil Engg. BIT, K R Road, Bangalore-04, India*
Email: vathsalagowda@gmail.com
2 *Dept of Civil Engg, BIT, K R Road, Bangalore-04, India*
Email: jagannath.priyadhi@gmail.com
3 *Structural Engineering Division, PG Center, VTU Belagavi, India*
Email: r.prabhakara@gmail.com

Abstract – Large number of investigations are available on the flexural performance of beams strengthened using several materials and techniques. However, very little information is available on the performance of strengthened post-tensioned (PT) beams. Carbon Fiber Reinforced Polymer (CFRP) strengthening material with Near Surface Mounted (NSM) technique has evolved as the promising material and method respectively due to their superior performance. This paper focused on the strength and deformation behaviour of PT beams, flexural strengthened with NSM technique using CFRP laminate. Four beams were tested in the present investigation, one was regarded as control beam, and remaining three beams with increase over the area of CFRP laminates by a factor 1, 2 and 3 respectively. The aim of the experiment was to demonstrate the strength and deformation behaviour of the PT beams tested under static condition over four points bending. The results revealed that the ultimate load carrying capacity of strengthened PT beams increased linearly compared over control beams. Increase in ductility index with reduction in the deflection at the ultimate load was recorded for the strengthened PT beams.

Keywords- CFRP Laminate, Post tensioned beams, NSM Technique, Ductility Index and Ultimate Load

INTRODUCTION

Pre-Stressed Concrete (PSC) is structural concrete in which internal stresses are introduced to reduce the potential tensile stresses developed resulting from the external loads. This compressive stress is applied by tensioning the high-strength tendons to improve the performance of concrete during service life. The essence of PSC is that once initial compressive stress is applied, the resulting material demonstrates the characteristics of high-strength concrete over the application of subsequent compressive stress. This procedure enhances the structural capacity and serviceability aspects of structural member compared to conventional reinforced concrete.

PSC improved the concrete performance provided over long spans, reduced cross-sectional area of the structural element and realised material savings which resulted in economical construction compared to reinforced concrete. Use of high strength steel in the form of tendons and high strength concrete (HSC) evolved as the good combination in terms of strength and performance of the structural members. Pre-tensioning and post-tensioning are the two distinct methods developed based on the necessary. Post-tensioning (PT) method became very popular compared over pre-tensioning method because of its strong merits.

The performance of PSC structures over several decades has given many problems. It was observed that few PSC structures with high design reliability and maintenance have performed well. However most of the PSC structures have shown distress. This is due to primitive design standards, poor quality of materials and construction, damage due to impact

and exposure to the environmental loads. The state and private agencies realised the effect of those on the economy of the state started the strengthening of the structure with reasonable cost as the complete replacement becomes uneconomical. The knowledge and the knowhow of strengthening or retrofitting of the structures is well developed such as section enlargement, external bonding, warping, jacketing and near-surface mounted (NSM). Many investigations have been documented on the application of strengthening technique to enhance the strength and performance of the conventional structures. However, less information is there on the application of strengthening technique to the PSC structures. This is due to the fundamental fact that the cracking and deformations of PSC structures are slightly different compared over conventional structures.

The critical regions in PSC beams are flexure, shear and anchorage zones, which is strengthened by any method in order to keep structures in operational mode is the main objective. There are several strengthening methods available for the application each one has its own merits and demerits. It has been observed from the available literature that strengthening using FRP has emerged as an effective alternative over others because of the mechanical properties of fibre composites. FRP materials are lightweight, noncorrosive, exhibit high tensile strength and are relatively easy to install.

This paper focused on the strength and deformation behaviour of Post-tensioned (PT) beams, flexural strengthened with NSM technique using carbon fibre reinforced polymer (CFRP) laminate.

REVIEW ON EXPERIMENTAL WORK

Seven decommissioned girders of the Eastern North Carolina bridge were strengthened by NSM techniques with different CFRP systems and studied their performance for fatigue behaviour by **Owen Rosenboom et al., (2006)**

And they concluded that strengthening using CFRP materials reduced stress ratio in the prestressing strands due to their effectiveness in controlling crack widths and increasing stiffness.

Barros et al., (2006) evaluated the efficacies of external bond reinforcement (EBR) and NSM strengthening techniques for concrete beams. CFRP laminates were utilised for NSM technique and CFRP sheets were used with wet lay-up method for EBR technique and the obtained experiment results were compared. From their work, they concluded that for shear strengthening NSM technique was most effective with CFRP laminates. For shear strengthening of beam with more depth, laminates at 45^{o} were more effective than vertical laminates.

An attempt was made by **Bilotta et al., (2011)** to investigate load-slip relationship, mode of debonding and strain distribution of bond between concrete surface and FRP systems in EBR and NSM techniques. For this, they conducted the single shear test on concrete prism strengthened by FRP system.
From their investigation, it was concluded that with higher utilisation factor, NSM technique exploited the tensile strength of FRP materials rather than EBR technique. And also, the authors found that the process of debonding of FRP in NSM was delayed when compared to FRP systems in EBR technique.

Maghsoudi et al., (2017) evaluated the serviceability response of unbonded post-tensioned I beam strengthened by CFRP sheet. From their study they concluded that the strengthening technique had 120% efficiency over the capacity enhancement of the non-strengthened unbonded PT beams under the service state.

EXPERIMENTAL STUDIES

Four numbers of PT beams of size 230mm X 300mm X 3400mm were cast. Out of four beams one beam considered as control beam. All the beams were designed according to IS 1343 specification, and tested under static condition over four points bending. Two bars of 12 mm diameter and two bars of 10 mm diameter of characteristic strength 500 MPa were

provided as bottom and top reinforcements respectively for all beams. Two legged 8 mm diameter bars were provided at a spacing of 170 mm, centre to centre along the length of the beam as shear reinforcement. To achieve unbounded type post-tensioning beams, sheathing pipe was placed at an eccentricity of 106 mm. Two ends of the sheathing pipe were connected to the anchorage system provided at the end of the beam.

A. *Casting of Beam Specimens*

The M40 grade concrete was prepared in a concrete mixer and placed in the moulds where the reinforcement cage was placed. It was then compacted using needle vibrator and the top surface of the beam was properly finished using a trowel. Beams were de-moulded after 24 hrs.

B. *Stressing of Beams*

Post-tensioning was done after 28 days of curing. For post-tensioning, two numbers of high-tensile steel of 12.7 mm diameter were inserted into the sheathing pipe provided at the time of casting the beam. Two tendons of different lengths were placed on each side of the beam, to balance the stress equally on both sides of the beam. The stressing was introduced in three levels; the stressing was done over a span of two hours. Using wedges and barrels, the tendons were anchored to both edges. Stressing force, of about 70% of ultimate strength of high-tensile pre-stressing steel, was applied at the long sides of each tendon provided at the alternative ends. Elongation in each tendon was then measured. The anchorage system used was Gifford-Udall system.

C. *Strengthening of Beams by NSM technique*

After post-tensioning, beams were strengthened by NSM technique. Longitudinal groove of 50 mm width, 25 mm and length of 3000mm depth at the bottom side of the beam was made, to have area of bonding of about 0.15 m^2 for NSM-1. CFRP strip was installed at the clean, epoxy filled groove by maintaining gap of 20 mm between concrete face and laminate. Smooth finish of surface was achieved by uniform application of epoxy. Two grooves of 50 mm width and 25 mm depth each by maintaining the gap of 40mm and laminates were placed inside them to maintain bonding area of about 0.3 m^2 for NSM-2. For the beam NSM-3, three strips were placed in the three grooves by maintaining 20mm spacing between them to achieve bonding area of about 0.45m^2.

D. *Testing of beams*

All the beams were tested for static loading condition, for two point loading case under the frame capacity of 200 ton. The deflection was measured at mid span for each increment of 5 kN up to ultimate load. And development crack were observed and marked on beams.

HISTORY OF FAILURE OF BEAMS

A. Control Beams- CBF

The objective of writing the history of failure of the beam is to understand the cracking and deformation behaviour of the control beam. The first crack was appeared at 62 kN at the bottom of the beam in the mid-span region and the deflection was 2.93mm. As the loading further increased, the identified crack propagated towards the top surface of the beam. Flexural cracks formed at an equidistant and symmetrically spread over the length of the beam. All developed cracks were vertical and secondary cracks were developed originating from the main cracks. Ultimately, the beam failed functionally at the load of 128 kN. The measured maximum central deflection was 24.98 mm. The failure pattern of the beam is shown in fig. 1

B. NSM-1

In NSM-1 beam the first crack was initiated at 88 kN, and corresponding central deflection was 5.54 mm. Number of cracks developed were less compared to control beam. The crack pattern developed was as shown in fig. 2. The crack had developed in the bond between concrete and CFRP laminate. The ultimate load was 180 kN and corresponding central deflection was 18.99 mm.

C. NSM-2

In this beam, the first crack developed at 96 kN and corresponding deflection was

4.37 mm. As loading increased, more numbers of cracks developed which were parallel and the width of cracks increased, as shown in fig. 6. When loading approached ultimate load, a crack had developed at the bottom of the beam, which was between the two laminate strips near the right support, as shown in fig. 3. The ultimate load was 190 kN, and corresponding central deflection was 17.82 mm.

D. NSM-3

In beam NSM-3, even though the bonding area was more compared to NSM-2, the first crack was similar to that of previous beam i.e., 96 kN. The formation of cracks continued as loading proceeded and number of crack were reduced and spacing between them was increased compared to all other beam. As the bonding area was more, at the stage of ultimate load, sudden crack developed at the bottom near the support, as shown in fig. 4. The ultimate load sustained by this strengthened beam was 202 kN and corresponding deflection was 11.69 mm.

LOAD DEFLECTION BEHAVIOUR OF BEAMS

Comparison of load deflection behaviour of three strengthened beams along with control beam has been presented in fig. 5. During the initial stages of loading, strengthened beams were linear compared to control beam. The beam with three strips performed better in terms initial stiffness and load-carrying capacity when compared to other beams. From this, it was observed that as the bonding area increased, load-carrying capacity and stiffness of the beam increased. There was no debonding of laminate occurred in any of the strengthened beams. Failure modes of all three strengthened beams were found to be similar. Development of cracks at the ends of the laminate revealed that the terminating position of the strengthening material played vital role in the enhancement of load-carrying capacity of the beam.

CRACKING, WORKING, ULTIMATE LOADS AND DEFLECTIONS

Load at the first visual crack on the beam was considered as the experimental cracking load (P_{cr}) the deflection corresponding to this load level was noted as deflection (Δ_{cr}) at first crack. The ultimate load (P_u) and corresponding deflection (Δ_u) was also noted. The working load (P_w) was obtained by dividing ultimate load (P_u) by a value of 1.5 and the corresponding deflection (Δ_w) was obtained from load deflection diagram and the values for all the beams are shown in table 1

From table 1, it was observed that initial crack load and ultimate load for NSM-1 were increased by 42% and 40% respectively when compared to control beam and there was a decrease in central deflection of about 24%. In NSM-2, there was increase in the initial crack load and ultimate load by 54% and 48% respectively compared to control beam. In addition, deflection was decreased by 29%. In NSM-3 initial crack load and ultimate load were increased by 54% and 57% respectively compared to control beam. Central deflection was decreased by 53% compared to control beam.

DUCTILITY INDEX

Ductility is expressed in terms of dimensionless ductility factor or ductility index (μ) which is the ratio of ultimate deflection (Δ_u) to the yield deflection (Δ_y) as given by Prabhakara et.al., [33] in equation (1)

$$\mu = \frac{\Delta u}{\Delta y} \qquad (1)$$

Bilinear method has been considered to analyse the ductility of strengthened post tensioned beams. In this method, the yield point is located by equating the area of the actual load deflection diagram to the bilinear system keeping the initial angle same in both the conditions. The ductility index (μ) for control and strengthened post-tensioned beams was calculated and tabulated in table 1. The ductility index ranges from 2.44 to 4.8.

Generally, a high ductility index indicates that a structural member is capable of undergoing large deformations prior to

failure. For beams with ductility index in the range of 3 to 5 is considered imperative for adequate ductility especially in the areas of seismic design and redistribution of moments [33] It has been observed from table 1 that as the bonding area increased, ductility index was decreased.

CONCLUSIONS

Based on the experimental observation, following conclusions are drawn

- There was increase in initial stiffness strengthened post-tensioned beams as compared to control beam.
- The experimental outcomes qualify the application of CFRP in NSM technique, as an effective tool to restore the flexural capacity of post-tensioned beams.
- The Post-Tensioned beam strengthened by laminates with bonding area 0.45m^2 was found to be more effective and the load carrying capacity was increased compared to control beam.

REFERENCES

1. Barros J A O, Dias S J E and Lima J L T (2006). Efficacy of CFRP-based techniques for the flexural and shear strengthening of concrete beams, *Cement and Concrete Composites*, 29(6), 203-217.
2. Bilotta A, Ceroni F, Di Ludovico Nigro E, Pecce M and Manfredi (2011). Bond Efficiency of EBR and NSM FRP systems for strengthening concrete members, *Journal of composites for construction*, 15(5), 757-772.
3. Calvin Reed and Robert Peterman (2004). Evaluation of pre-stressed concrete girders strengthened with carbon fiber reinforced sheets, Journal *Bridge Engineering,* 9(2), 185–192.
4. Dua J S, Francis T.K. Aub, Y.K. Cheungb and Albert K.H. Kwan (2008). Ductility analysis of prestressed concrete beams with unbonded tendons, *Engineering Structures*, 30(1), 13-21.
5. El Meski .F and Harajli (2013). Flexural behavior of unbonded post-tensioned concrete members strengthened using external FRP composites, *Journal of Composites for Construction*, 17(2), 197-207.
6. Hassan T and Rizkalla S (2002). Flexural strengthening of prestressed bridge slabs with FRP systems. *PCI Journal*, 47(1), 76–93.
7. IS 1343-2012: Prestressed concrete - Code of practice
8. Maghsoudi M and Maghsoudi A A(2017). Experimental and Theoretical Serviceability of Strengthened and Nonstrengthened Unbonded Posttensioned Indeterminate I-Beams, *Journal of Bridge Engineering,* 22(7), 05017006
9. Owen Rosenboom, Tare Hassan and Sami Rizkalla (2007). Flexural behavior of aged prestressed concrete girders strengthened with various FRP systems, *Construction and Building Materials*, 21(4), 764-776.
10. Owen Rosenboom and Sami Rizkalla (2006). Behavior of prestressed concrete strengthened with various CFRP systems subjected to fatigue loading, *Journal of Composites for Construction*, 10(6), 492-502.
11. Prabhakara R, K.U. Muthu and R. Meenakshi (2006). Investigations on ultimate flexural strength and ductility behaviour of HSC beams, *The Indian Concrete Journal*, 26(10), 40-50
12. Takács P F and Kanstad T (2000). Strengthening prestressed concrete beams with carbon fiber reinforced polymer plates, *NTNU Report R-9-00*, Trondheim, Norway, 2000
13. Yail J.Kim, Chen Shi and Mark F. Green (2008). Ductility and cracking behavior of pre-stressed concrete beams strengthened with pre-stressed CFRP sheets, *Journal of Composites for Construction*, 12(3), 274-283.

Fig. 1: Crack pattern for CBF

Fig. 2: Crack pattern for beam NSM-1

Fig. 3: Crack pattern for beam NSM-2

Fig. 4: Crack pattern for beam NSM-3

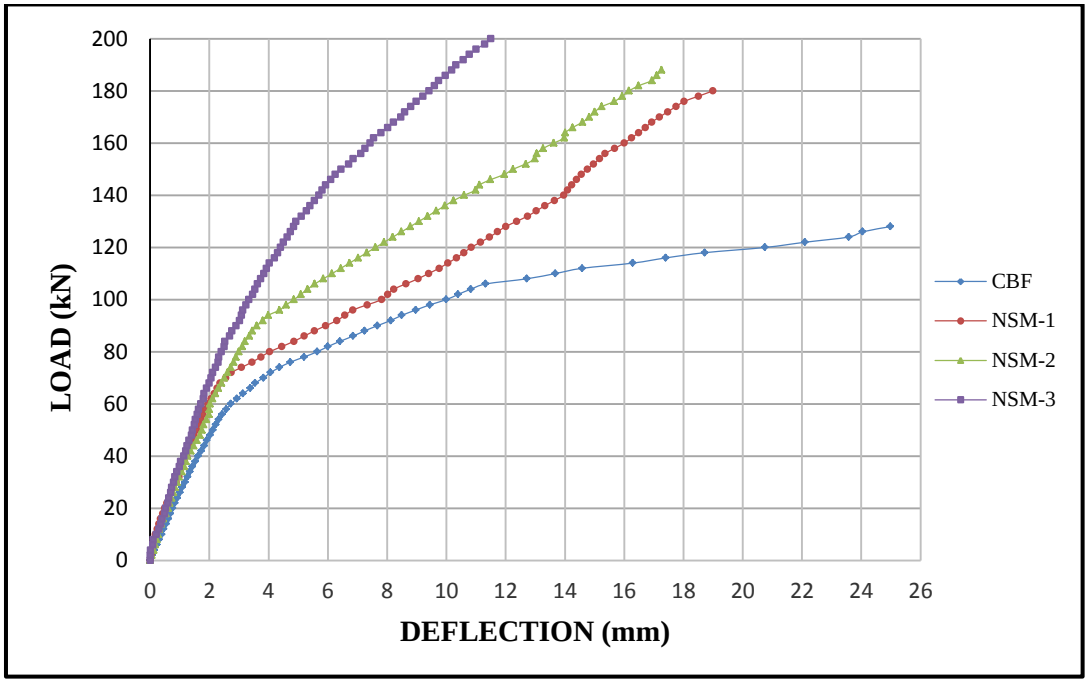

Fig. 5: Combined load deflection diagram of beams

Table 1: Cracking, working, ultimate loads, deflections in flexure and ductility index

Beam	***P_{cr}*** *(kN)*	***Δ_{cr}*** *(mm)*	***P_w*** *(kN)*	***Δ_w*** *(mm)*	***P_u*** *(kN)*	***Δ_u*** *(mm)*	***Δ_y*** *(mm)*	***Ductility index (μ)***
CBF	62	2.93	86	6.85	128	24.98	5.2	4.8
NSM-1	88	5.54	120	10.83	180	18.99	4.2	4.52
NSM-2	96	4.37	126	8.49	190	17.82	4.8	3.71
NSM-3	96	3.12	136	5.39	202	11.69	4.8	2.44

8th International Engineering Symposium - IES 2019
March 13-15, 2019, Kumamoto University, Japan

Studies on Drop Test Dynamic Response of Two Way HSC Slabs Strengthened using CFRP Strip Adopting NSM Technique

Arjun R P Reddy[1], Nandeesh M S[2], R Prabhakara[3] and H N Jagannatha Reddy[4]

1. *Department of Civil Engineering, Bangalore Institute of Technology, Bangalore.*
   Email: arjunreddy.rp@gmail.com
2. *Department of Civil Engineering, M. S. Ramaiah Institute of Technology, Bangalore.*
   Email: nandeeshms@gmail.com
3. *Structural Engineering division, Visvesvaraya Technological University, Belagavi.*
   Email: r.prabhakara@gmail.com
4. *Department of Civil Engineering, Bangalore Institute of Technology, Bangalore.*
   Email: jagannath.priyadhi@gmail.com

ABSTRACT: High Strength Concrete (HSC) slabs are provided as floor slabs in warehouses and industrial flooring. This is because of higher durability factor of HSC. These floor slabs are subjected to higher intensities of loads including drop of objects and accidentally fallen tools and tackles there by subjected to dynamic effect. It has been observed from the literature, the dynamic response behaviour of slabs are obtained with a reasonable accuracy by subjecting the elements to drop test. In the present study, two-way slabs with simply supported end conditions were subjected to drop test. Accelerometer was mounted on the bottom of the slab to record the acceleration time graph and the dial gauge was mounted to record the maximum displacement at the centre. In the current study dynamic behaviour of HSC slabs were evaluated and compared with the same configuration with near surface mounting (NSM) technique strengthened slabs. The change in dynamic response was recorded and studied with the strengthening and found that dynamic parameters such as peak acceleration, displacement and damaged caused by the impact were found to be different. The strengthening technique was effective in reducing the displacement, peak acceleration of slabs.

***Keywords**: NSM Technique, drop test, two-way slab, dynamic response, Acceleration*

INTRODUCTION

Reinforced concrete structures have become majority of existing structures. In designing these structures, various load combinations are used. Slabs being an integral part of a structure and widely used structural member and these are generally designed to withstand static loading but are exposed to other forms of loads like impact loads from the time of their casting to throughout their design life. The impact loads may arise from dropping of building materials like bricks, blocks, formwork materials and cement bags during the construction of structure, accidental events in industrial floor spaces, natural calamities like landslides and rock fall impacts. All these loads induce distress in the slabs for which they are not designed.

Understanding the static behaviour of slabs and extrapolating this information in understanding the impact behaviour is not logical. Experimentations on Impact behaviour of structural elements requires sophisticated test setup and consumes more time, sometimes it will be very sensitive to the results obtained therefore the available literature are less. It has been observed in the recent years drop tests are becoming popular because of their simplicity and less consumption of time.

It is possible to obtain peak acceleration, velocity profile, damping coefficient and acceleration decay from accelerometers used in the drop test. The principle followed in the drop test is based on the energy principle, a fraction of load

obtained from the static analysis is applied on to the slab to observe impact behaviour of slabs.

In the studies conducted, the failure of concrete subjected to impact was under localized effects like punching shear failure, concrete scabbing and perforation. To avoid these ill effects and provide suitable impact resistance HSC are preferred. HSC are gaining wide popularity in the present day field applications due to its advantages like early strength gain, better durability, impact and toughness characteristics. HSC are seen to exhibit better durability and corrosion resistance in comparison to Normal Strength Concrete (NSC). HSC provides higher strength per unit cost, per unit weight and per unit volume thus can lead to reduced size and weight of structures. Higher compressive strength of concrete results in a higher modulus of elasticity and reduced specific creep, and thus increases stability and reduces deflections. These advantages along with high compressive strength of concrete has encouraged the usage of HSC in everyday use.

NSM (Near Surface Mounted) technique, whereby the bar-shaped or strip-shaped FRP (Fiber reinforced polymers) elements are placed as additional reinforcement in the groove made in concrete cover, and they are embedded in epoxy or cement resins (adhesives), which creates adhesion with the concrete, and provides anchoring. The use of Near-Surface Mounted (NSM) Fibre-Reinforced Polymer (FRP) is the latest method for increasing both flexural and shear strength of deficient Reinforced Concrete (RC) beams and slabs.

In the present study, the inertial response due to impact loading on HSC slabs with variation in reinforcement ratio was studied along with its changes when strengthened with NSM technique.

LITERATURE REVIEW

Prabhakara, R et al (2006)

In this study, a mix design procedure for HSC has been provided without use of silica fume. The study was conducted with 20mm down-size aggregate with water content varying between 0.23 to 0.25. Concrete of strength up to 120MPa was obtained. This method provides the best strength with least cement content.

Annadurai, A & Ravichandran, A (2014)

The authors presented the mix design developed for high strength concrete with silica fume and high range water reducing admixture (HRWR). In this work, they selected the 53 grade OPC, 10mm down coarse aggregates and river sand as materials. Using ASTM C 127 standard relative quantities and proportions for M60 grade of concrete was calculated. GLENIUM B233 was used as HRWR. The replacement of cement with 9% of micro silica and 0.9% HRWR gave maximum strength.

Andresson, A (2014)

The load carrying capacity of concrete slabs subjected to concentrated loads are studied considering both static and impact loads. The slabs were casted with reinforcement meshes using shotcrete and some of the slabs were casted with steel fibre reinforced concrete (SFRC). Some slabs were casted with SFRC only, some with SFRC and mesh and one only Normal conventional concrete. Impact loads were performed using a steel mass of 600kg. The free fall height was varied from 1m to 2 m. The peak Impact load varied from 200-250kN and the corresponding impulse load varied from 4kNs- 5.5kNs. The slabs failed in one-way flexure. The concrete fallout was more in the slabs with rebar mesh than the slabs with SFRC. The residual strength after the impact was sufficient to carry the static load of impact test.

Yoo, D Y et al. (2012)

In this study the compressive and flexural behaviour of normal strength concrete, steel fibre reinforced concrete with various fibre volume fractions were determined and further the slabs were strengthened in flexure using externally bonded FRP sheets using AFRP and CFRP and their behaviour under high strain loading was studied. Occurrence of flexure cracks, FRP deboning, spalling etc. reduced the dissipated energy. Strength of concrete

was seen to increase with increase in strain rate and increase in volume of fibres.

RANKOVIC et al. (2010)
Have suggested to use of FRP for enhancing the strength properties by usage of GFRP, CFRP and AFRP and also by using different shapes of bars i.e., square, rectangular which increases the specific reinforcement area of the bar, and circular cross sections which offers ease to anchor during prestressing and by using strips which increase surface coefficient and reduces the risk of adhesion loss and with various surface configurations i.e., smooth , rough with spiral grooves or ribbed grooves choice is based on concrete cover. According to NSM technique, three kinds of failures were observed i.e. separation of adhesive, separation from concrete and tensile failure of FRP.

Ramanna, N (2012)
The use of near surface mounted carbon fibre polymer (NSM-CFRP) reinforcement such as FRP strips holds a high potential for increasing the flexural strength. The studies were focused on response of reinforced beams and slabs subjected to static or Impact loads. . The performance of beams and slabs under impact loads were evaluated using accelerations versus time relationship. A single degree of freedom elasto-plastic was developed to capture their dynamic behaviour. Among four slabs, two were control slabs and two were retrofitted slabs. One control slab was used for static and other for dynamic test similarly each retrofitted slabs was used for static and dynamic test. The drop height calculated for 400lbs steel impactor to impact the slab was calculated using work-energy principles and it should match with the load applied upon the impact and if not it has to be revised. The control slabs experienced bigger cave compared to retrofitted slabs. The load carrying capacity of the retrofitted slab was found to be two times higher than the control slab.

OBJECTIVES
- To obtain the dynamic behaviour of slabs under impact loading.
- To analyse the change in behaviour of the test results over the change in reinforcement ratio and effect of strengthening the slab by NSM technique.

MATERIALS USED IN THE CURRENT STUDY
Materials used in the present investigation have been characterized in accordance with the standard procedure as follows
CEMENT - OPC of 53 grade conforming to IS: 12269-2013 was used.
AGGREGATES - The fine and coarse aggregates used was confirming to the specifications as per IS 383-1970.
REINFORCEMENT - The reinforcing steel was confirming to the specifications as per IS 1786: 2008.
ADMIXTURE – For the present work, for M70 concrete, Master Glenium Sky 8233 was used which is commercially marketed by BASF Construction Chemicals (India) Private Limited.
WATER - Potable water confirming to IS 456:2000 was used which was free from injurious salts for both mixing and curing
FOSROC CHEMICALS sponsored CFRP strips and epoxy used to bond the strips to concrete substrate, that is marketed under the name "Nitowrap CFP" & "Nitowrap 40" respectively was used in the present study for retrofitting the slabs.

SPECIMEN CASTING AND STRENGTHENING BY NSM TECHNIQUE
The specimen were casted to carry out the tests for studying the behaviour of slabs in impact loading by increasing the reinforcement ratio. The dimensions and reinforcement details are given in Fig. 1. The NSM technique with CFRP strips are used to strengthen the slabs. The strengthening was done in diagonal direction based of earlier researches. A zone of NSM strengthening marked by L/5.31 from the ends of the slab was identified. The typical strengthening system considered and the groove dimensions adopted for this investigation are shown in Fig 2 & 3 respectively. The strengthening was done by cutting a groove on the bottom face of the slab and embedding the CFRP strips in the epoxy that was filled in the groove cutout earlier to obtain the details as shown in the Fig. 4.

EXPERIMENTAL SETUP

The Impact testing on slab was carried out by using a drop test. The test setup consists of a drop weight, the loading frame, which was used, a pulley and a rope arrangement was fixed to lift the weight as shown in the Fig.5, and a four-channel dynamic data acquisition system (DDAS) and accelerometers used to study the response.

EXPERIMENTAL PROCEDURE

After a curing period of 28 days, the slabs were then allowed to dry and white washed to have a smoother surface to easily locate crack propagation and pattern. The accelerometer was fixed at the centre of the tension face. Then the specimen was mounted on the loading platform and the slabs were tested for simply supported end conditions.

In the study the drop mass was obtained from the work energy principles for total slab capacity. For the present study the drop mass was obtained as 70 kg. The height of the drop was varied to give different impact energies to have different range of kinetic energy to the slab and to record variation in the response of slab under different impact energy. For this purpose, the drop weight of 70kg was dropped from the height of 0.67m, 1.33m and 2m respectively on to the different slabs. The total energy impacted due to different drop heights are shown in table 1.

TEST RESULTS

Totally twelve number of slabs were cast for impact test, out of which six were control slabs and six were NSM strengthened slab. These slabs were tested in the present investigation and the responses of each slab was obtained from the software "KAMPANA" of data acquisition system where the acceleration, velocity and displacement values were captured from the accelerometer placed at centre of the slab. The accelerometers will capture the response data of the test slab in all three axes.

The results from the test are presented in table 2. A graphical representation of the experimental results comparing the acceleration response of the slabs for different drop heights is as shown in fig.6, fig.7, fig.8 & fig 9.

OBSERVATIONS

The following observations were made from this study:

1. For lower reinforcement ratio the acceleration response of unstrengthened-slab was seen to decrease with increase in drop height from H1 to H2 but increased marginally from H2 to H3 whereas it increased successively for strengthened slabs with increase in drop height as shown in the fig.6.
2. For higher reinforcement ratio both strengthened and unstrengthened slab showed higher response at drop height of H2 and lower at both H1 and H3 as shown in the fig.7.
3. For control slabs with reinforcement ratio of 0.341% the acceleration response decreased for increase of drop height from H1 to H2 and with further increase of drop height to H3 the acceleration increased. This behavior was exactly opposite to that of slabs with reinforcement ratio of 0.789% as indicated in fig.8.
4. It was observed that for strengthened slabs with increase in reinforcement ratio the acceleration response increased for drop height from H1 to H2 however on further increase in drop height to H3 the response of slab with 0.341% reinforcement ratio increased whereas the same decreased for 0.789% reinforcement slab as represented in fig.9.

CONCLUSIONS

1. The slabs with lower reinforcement ratio, strengthening increased the acceleration response for increase in impact energy.
2. For higher reinforcement ratio, the strengthening of slab exhibited lower response when compared with unstrengthened slab for similar impact energy, this may be further examined.
3. For moderate impact energy there was an increase in acceleration response of strengthened slabs for both the reinforcement ratios but in case of highest impact energy considered the same trend was not observed. The reason for this

phenomenon needs to be investigated in detail.

4. The dynamic behaviour of unstrengthened slabs through different drop heights is not showing the trend of expected observation over the increase in reinforcement ratio.

5. Further studies are to be conducted in detail to analyse the parametric studies of strengthened and unstrengthened slabs under impact loading.

REFERENCES

1. Hunchate, S R et al. (2014), "Mix Design of High Performance Concrete Using Silica Fume and Superplasticizer", International Journal of Innovative Research in Science, Engineering and Technology, Vol.3, Issue 3, March 2014

2. Annadurai, A & Ravichandran, A (2014) Development of Mix Design of High Strength Concrete with Admixtures, IOSR Journal of Mechanical and Civil Engineering, Vol.3, Issue 5, Jan 2014

3. Prabhakara, R et al (2006) Ultimate Flexural Strength of High Strength Concrete Beams, Indian Concrete Journal, Oct 2006, pp 40-50.

4. Hrynk, T D & Vecchio, F J (2014), Behaviour of Steel Fibre Reinforced Concrete Slabs Under Impact Load, ACI structural journal, Vol.3, No.5, Sep-Oct 2014.

5. Yoo, D Y et al. (2012), Enhancing Impact Resistance of Concrete Slab Strengthened with FRPs and Steel Fibres. Proceedings of the 6th International Conference on FRP Composites in Civil Engineering, CICE 2012.

6. Fila, A et al. (2015), Perforation Resistance Of Reinforced Concrete Slabs Affected By Low Velocity Drop Loads, SMiRT-23, Manchester, UK- August 10-14, 2015

7. Krauthammer, T and Zineddin, M (1995) Structural Concrete Slabs Under Localized Impact, Fortifikatorisk Notat Nr 211/93, Norwegian Defence Constructive Service.

8. Banthia, N et al. (1988), Impact Testing of Concrete Using Drop Weight Impact Machine. Experimental mechanics Pp 63-69, 1988.

9. Sangi, A J and May, I M (2009) High-Mass, Low-Velocity Impacts of Reinforced Concrete Slabs, 7th LS-DYNA Conference, 2009, UK.

10. Ozgur A et al. (2015), LOW VELOCITY IMPACT BEHAVIOUR OF RC SLABS WITH DIFFERENT SUPPORT CONDITIONS, Construction and Building Materials 2015.

11. Witkowski, H & Kotynia, R (2010), Bond between NSM Reinforcement and Concrete, 8th fib Ph.D. Symposium in Kgs, Lyngby, Denmark, June 20 – 23 2010.

12. Rizkalla, S and Hassan, T (2001), Various FRP Strengthening Techniques for Retrofitting Concrete Structures, 2001.

13. Tavallaee, M & Ted Donchev, T (2014), Bi-Directional Strengthening of Two Way Reinforced Concrete Slabs Using Fibre Reinforced Polymer, New York Science Journal 2014.

14. E. Bonaldo, E et al. (2005), Concrete Slabs Strips Reinforced with Epoxy Bonded Carbon Laminates into Slits, University of Minho, Portugal.

15. Protchenko, K et al (2015), Investigation of Behaviour of Reinforced Concrete Elements Strengthened with FRP, XXIV R-S-P Seminar, Theoretical Foundation of Civil Engineering 2015.

16. Florut, S C et al (2010), Retrofitting Two Way RC Slabs with and Without Cut-Out Opening by Using FRP Composite Materials, Latest Trends on Engineering Mechanics, Structures, Engineering Geology, July 2010.

17. Florut, S C et al (2010), Efficiency Assessment Of CFRP Retrofitting Solution For RC Slabs With And Without Cut-Out, Latest Trends on Engineering Mechanics, Structures, Engineering Geology, July 2010.

18. Lorenzis, L et al (2000), STRENGTHENING OF REINFORCED CONCRETE STRUCTURES WITH NEAR SURFACE MOUNTED FRP RODS, International Meeting on Composite Materials, Milan, Italy, 2000.

19. Nakul Ramanna (2012) "Static and Impact Load Response of Reinforced Concrete Beams and Slabs with NSM-CFRP Retrofitting" PhD thesis submitted to Old Dominion University, USA.

20. Prabhakara R and Manohara B, (2015) Strength and Ductility Performance of Preloaded HSC Beams Retrofitted with CFRP Strips Using NSM Technique. International Research Journal of Engineering and Technology (IRJET) e-ISSN: 2395 -0056 Volume: 02 Issue: 04| July-2015

21. Sreenivasappa, N et al (2016). Investigations On Effect of CFRP Strips Retrofitted Using NSM Method On Two-Way NSC and HSC Slabs Subjected to Concentrated Load, International Journal of Research in Engineering and Technology eISSN: 2319-1163 | pISSN: 2321-7308 | Volume: 05Special Issue: 14| ICRAES-2016| Sep-2016

22. R P Reddy, A et al (2016). Studies on Strength and Deformation Behaviour of Two-Way NSC and HSC Slabs under Single Point Loading. International Journal of Research in Engineering and Technology eISSN: 2319-1163 | pISSN: 2321-7308 | Volume: 05Special Issue: 14| ICRAES-2016| Sep-2016

23. Bureau of Indian Standards "Plain and Reinforced Cement Code of Practice" IS 456:2000.

24. Bureau of Indian Standards "Design Aid to Reinforced Concrete to IS 456:1978" SP16, 1980

Table 1: Energy Impacted on to the slabs

Drop Weight 'm' (kg)	Drop Height 'H' (m)		Impact Energy= m x g x H (Joules)
70	H1	0.67	460.01
	H2	1.33	913.31
	H3	2.00	1373.4

Table 2: Response of the test slabs

Unstrengthened Slab	Acceleration (g)	Strengthened Slab	Acceleration (g)
M70/PT1/H1/NSM0	1.826	M70/PT1/H1/NSM1	0.664
M70/PT1/H2/NSM0	0.591	M70/PT1/H2/NSM1	1.455
M70/PT1/H3/NSM0	0.723	M70/PT1/H3/NSM1	3.808
M70/PT2/H1/NSM0	0.555	M70/PT2/H1/NSM1	0.367
M70/PT2/H2/NSM0	1.26	M70/PT2/H2/NSM1	0.699
M70/PT2/H3/NSM0	0.664	M70/PT2/H3/NSM1	0.468

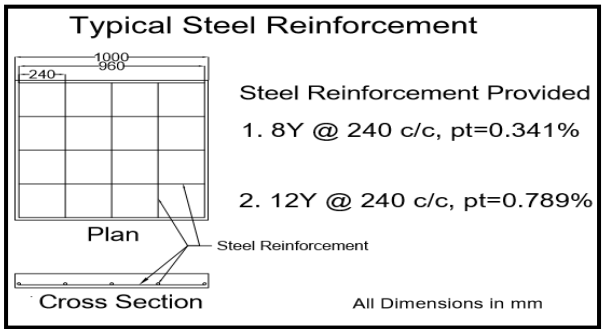

Fig.1: Reinforcement Details of Slab

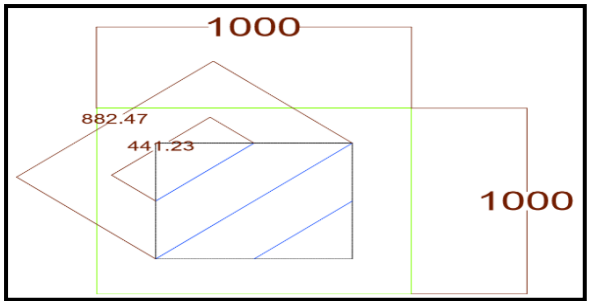

Fig.2: Typical NSM strengthening

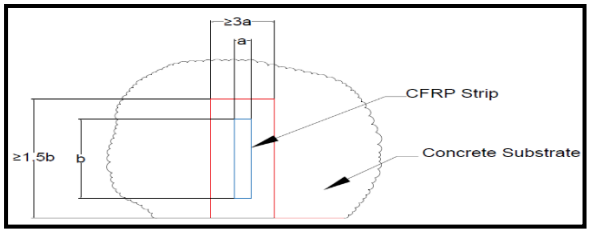

Fig.3: Typical Groove Dimensions

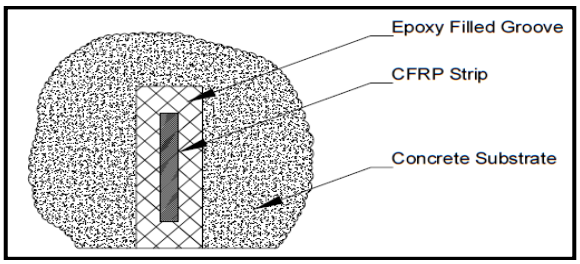

Fig.4: Typical Groove Details

Fig.5: Pulley and rope assembly

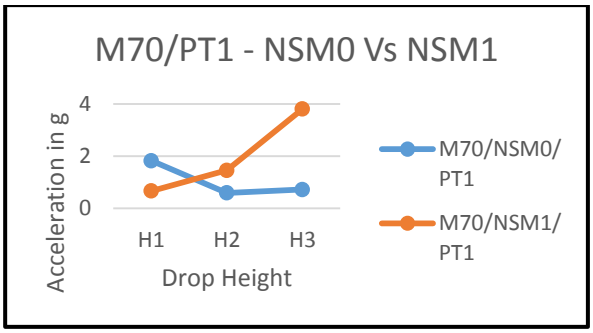

Fig.6: Acceleration V/s Drop Height for PT1 slabs

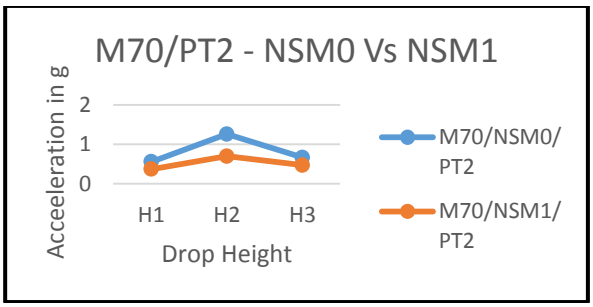

Fig.7: Acceleration V/s Drop Height for PT2 slabs

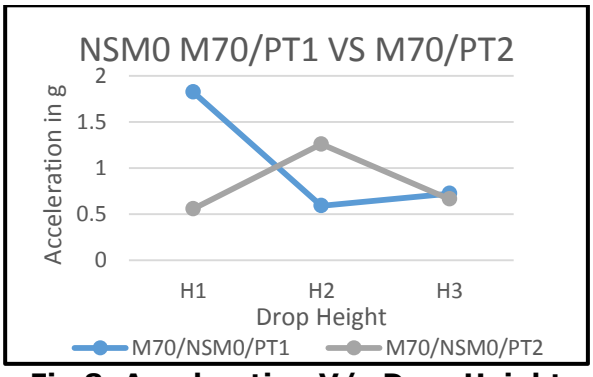

Fig.8: Acceleration V/s Drop Height for slabs

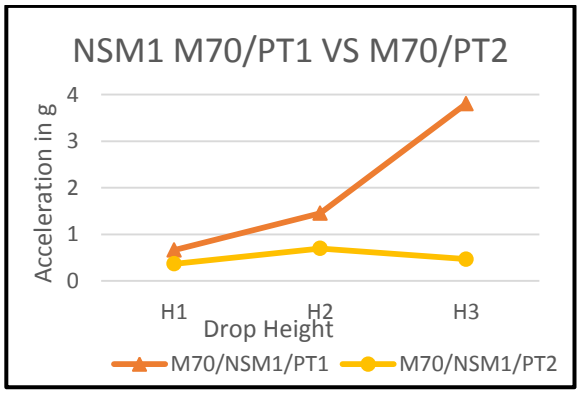

Fig.9: Acceleration V/s Drop Height for slabs

8th International Engineering Symposium - IES 2019
March 13-15, 2019, Kumamoto University, Japan

Effect on Workability and Setting Time of Concrete with Aluminium Dross as partial replacement for Ordinary Portland Cement

Panditharadhya B J[1], Raviraj H Mulangi[2] and **A U Ravi Shankar[3]**

1 *Department of Civil Engineering, National Institute of Technology Karnataka, Surathkal, Mangalore 575025, India. email:pandith23@gmail.com*
2 *Department of Civil Engineering, National Institute of Technology Karnataka, Surathkal, Mangalore 575025, India. e-mail:ravirajmh@nitk.edu.in*
3 *Department of Civil Engineering, National Institute of Technology Karnataka, Surathkal, Mangalore 575025, India. e-mail:aurshankar@gmail.com*

ABSTRACT: Aluminium dross is obtained from aluminium resmelting process which is completely a waste product and hazardous to dispose it into landfills. This is rich in aluminium oxide and having traces of few heavy metals. This makes it interesting to check the feasibility of this material in concrete by replacing it as a binder. Very little studies have been done across the globe and guidelines on the reaction of it in place of cement are not available. In this study, behaviour of replaced aluminium dross in cement paste is evaluated in terms of consistency and setting time. Aluminium dross is replaced by 5, 10, 15 and 20% in the concrete mix and workability is evaluated to understand the behaviour of cement-aluminium dross paste in the concrete. Retarded setting time of concrete with aluminium dross makes it suitable for hot weather conditions.

Keywords*: aluminium dross, consistency, setting time, workability, retardation, hot weather conditions.*

INTRODUCTION

In the construction of concrete structures and pavements, many researches are taking place to give space to the utilization of industrial waste products by recycling them and reutilizing them effectively. Silica fume, fly ash, GGBS (Ground Granulated Blast furnace Slag), etc. are the conventional waste materials or by-products from the industries that are efficiently used in the present construction sector. In the same way, there is generation of various wastes from aluminium refining industries in the form of dross or slag. These wastes are having leachable salts such as KCl and direct dispose of such wastes is an issue to be addressed. Utilizing them for landfills may create a problem to the surroundings as well as to the ground. Still most of part of the dross is being disposed into landfills which causes leaching of toxic metal ions into ground and thereby polluting the ground water (Unger and Beckmann, 1992). Traces of toxic gases like NH3, CH4, PH3, H2, H2S, etc. get released when secondary aluminium dross comes in contact with moisture. Recycling of aluminium waste requires only about 5% of the energy required to manufacture aluminium from bauxite ore which makes it important to consider the concept of recycling it. Also, the cost required for collection of new aluminium source, separation can be reduced with effective recycling of the generated waste. Thus, recycling the aluminium waste and producing an engineered product can solve maximum sustainability problems.

Elinwa and Mbadike (2011) used the waste from aluminium industry for producing concrete with various percentage replacement of cement. They found out that the replacement of cement by 10 %

to 15 % aluminium waste yielded the flexural strength and compression strength nearer to that of the control mix of concrete. Also, they identified retardation in the concrete setting time by addition of aluminium waste material. This makes the concrete suitable for hot weather construction works Elinwa and Mbadike, 2011). In India, there is over 120,000 tonnes of aluminium dross is produced from various industries and if all this can be effectively utilized in the concrete production, there can be noticeable decrease in overall cost of concrete construction works. Also, the carbon foot print in the environment can be reduced with reduced energy consumption in the production of cement. The research works done on concrete produced with secondary aluminium dross as an ingredient in the mix is very less and the utilization of this dross in the construction sector needs more importance. For using the concrete in the road construction sector, suitable concrete mix is designed and its strength properties are determined in this work to know its suitability.

MATERIALS AND METHODOLOGY

Aluminium dross (Al Dross) for the current work was procured from M/s Udyog Alloys (P) Ltd, Mumbai, Maharashtra, India. Sample was in the fine powder form and blackish in colour which was produced when aluminium raw material was burnt at 1900ºC in a furnace. Washing with water is the better solution to make the dross sample free from possible oxide generation and formation of toxic gases (Shriraksha et al., 2017). Aluminium dross sample is shown in Fig. 1. Chemical composition of cement and aluminium dross after washing with water are tabulated in Table 1.

Fig. 1 Al dross sample

Table 1 Composition of Ordinary Portland Cement and Aluminium dross

Composition	OPC (%)	Al Dross (%)
CaO	63.81	0.07
SiO_2	21.45	7.15
Al_2O_3	4.45	63.84
Fe_2O_3	3.07	0.03
MgO	2.42	0.04
P_2O_5	0.11	0.57
TiO_2	0.22	2.0
Na_2O	0.20	0.06
SO_3	2.46	0.03
LOI	0.81	1.81
Insoluble Residue	0.16	2.19

Characteristics of Ordinary Portland Cement (OPC), fine aggregates and coarse aggregates used in the current study are presented in the Table 2 and 3.

Table 2 Characteristics of OPC

Characteristics	Value
Grade of cement used	53
Specific gravity	3.12
Particle size range	50 µm
Compressive strength	49 MPa
Normal consistency	30 %
Initial setting time	50 Min
Final setting time	390 Min

Table 3 Characteristics of fine and coarse aggregates

Characteristics	Fine aggregates	Coarse aggregates
Specific gravity	2.68	2.69
Fineness modulus	2.64	4.04
Water absorption	0.8 %	0.4 %
Grading zone	II	I
Crushing value	-	25 %
Impact value	-	17 %
Abrasion value	-	21 %
Combined flakiness and elongation index	-	29 %

The values obtained are within the requirements of Indian Standards, i.e., IS: 12269 – 1987 (for 53 Grade OPC), IS: 2386, Part III and IV – 1963 (for specific gravity and other mechanical properties of aggregates) and IS: 383 – 2016 (for gradation of aggregates). Fine aggregate belonging to Zone II and coarse aggregates lying under Zone I are taken for the experimental works. The gradation is obtained by sieve analysis test as per IS: 383 – 2016.

RESULTS AND DISCUSSION

In the current work, 5, 10, 15 and 20% of aluminium dross is replaced for cement in a M40 grade concrete mix intended for pavement quality concrete. For highway construction, minimum of M40 strength and 25+/-15 mm slump is required. Setting time and workability of concrete in terms of Slump values are evaluated in this study. Fig. 2 shows the normal consistency of OPC paste at different percentage replacements of aluminium dross.

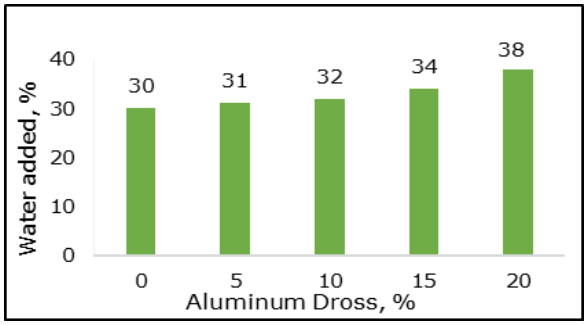

Fig. 2 Consistency of cement paste

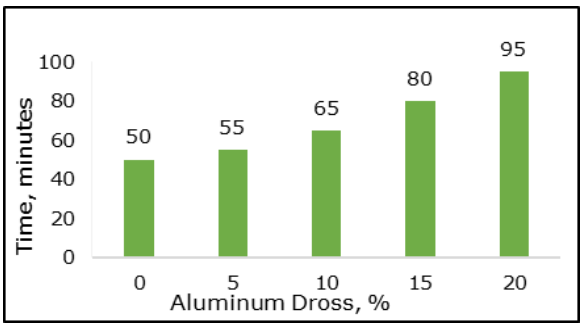

Fig. 3 Initial setting time of cement paste

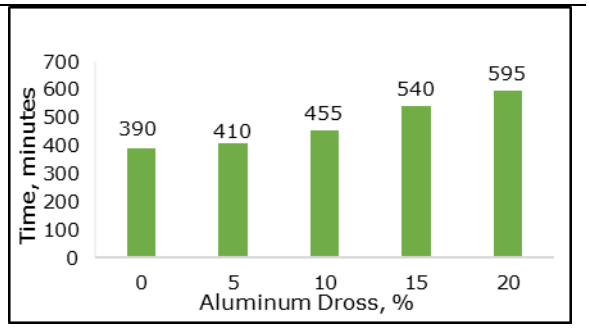

Fig. 4 Final setting time of cement paste

The normal consistency is 34% for 15% replacement of cement by dross and it is 38% for 20% replacement as per the figure shown above. When the replacement is higher, the water demand in the matrix increases due to the increased surface area of the aluminium dross material. When the weather and temperature are considered while laying the concrete in the field practically, there can be variation in the workability of the mix with respect to the aluminium dross replacement levels. This is due to the effect of aluminium dross in retarding the setting time of the mix. Water gets evaporated from the mix when it is exposed to the hot weather making the concrete to undergo thermal cracks due to insufficient water for hydration. Therefore, it is essential to reduce the rate of setting of concrete in the hot whether areas. The concrete produced using aluminium dross as binder has direct influence on the setting time and helps the laying of concrete in the regions with hot weather. Slowdown of hydration of concrete and adsorption of nuclei of calcium hydroxide in the mix makes the concrete to set at a slower rate when aluminium dross is used as partial replacement for cement.

The variation of initial and final setting times with respect to different percentage of aluminium dross replacement is as shown in the Fig. 3 and 4 which represents that the initial and final setting times are getting increased with increase in percentage of aluminium dross. Aluminium dross has certain quantity of silicates and that quantity is the deciding factor in retarding the initial setting time.

Significant amount of water can be absorbed by aluminium dross particles due to the high surface area of nano particles present in aluminium dross. During the hydration of cement, excess of $Ca(OH)_2$ is produced from aluminium dross and it reduces the pozzolanic reaction inside cement matrix (Girish et al., 2016; Panditharadhya et al., 2018). This may become the main reason for retarding effect of the aluminium dross. Hence, aluminium dross is a good material for retarding the rate of setting and it is suitable for hot weather concreting applications.

Ordinary Portland Cement, fine aggregates, coarse aggregates constitute the control mix of concrete which has water to cement ratio of 0.45, named as M1 mix. Aluminium dross contents of 5%, 10%, 15% and 20% by weight of cement are added to the mix and named as M2, M3, M4 and M5 respectively. Slump requirement and quantity of binder is taken as same for all the mix combinations. There was need for adding more water to the mix to achieve required workability/slump of 40+/-15 mm. Water to cement ratio is increased to 0.47, 0.50, 0.52 and 0.55 for M2, M3, M4 and M5 respectively. Properties of fine and coarse aggregates taken for the mix design are as tabulated in table 3. For the control mix of concrete designed for M40 characteristic compressive strength, the proportions of the mix were 1:1.74:3.04 (Cement : Fine aggregate : Coarse aggregate) (IRC: 44 – 2008; IS: 10262 – 2009). For the workability requirement, extra water is added to the other mix combinations. Slump test, Compaction factor test and Vee-Bee consistometer tests were performed as per IS: 1199 – 1959.

Slump cone apparatus is considered for measuring the slump in millimetres wherein the concrete is poured into the specified cone and change in the height of concrete after removing the cone is noted down. The fall in height is measured as the value of slump in millimetres. Fig. 5 represents the slump cone and the slump value being measured.

Fig. 5 Slump cone test

Compaction factor test includes filling the concrete into the hoppers without any compacting effort and releasing it to fill a cylinder placed below the hoppers. The weight of cylinder with concrete is measured and the cylinder is filled with concrete by compacting the concrete in three layers. The ratio of partially compacted concrete to the fully compacted concrete gives the compaction factor value in decimals. The value of compaction factor varies from 0.70 to 0.95, ranged as very low slump (0-25 mm slump) to high slump (100-175 slump). Apparatus used for measuring compaction factor is as given in Fig. 6.

Fig. 6 Compaction factor test

Vee-Bee consistometer measures the slump value in terms of Vee-Bee degree in which the time taken by concrete to adhere uniformly on to the glass plate during vibration is noted in seconds. The graph of Vee-Bee degrees versus slump from IS: 1199 – 1959, gives the value of slump possessed by the concrete mix.

Fig. 7 Vee-Bee consistometer test

Fig. 7 shows the testing of concrete sample for determining the Vee-Bee degree in seconds. The results of these tests to represent the workability of designed concrete mix are as presented in Fig. 8.

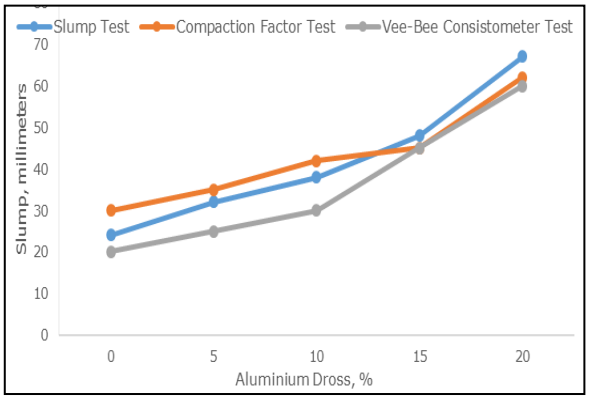

Fig. 8 Workability in terms of Slump from Slump cone, Compaction Factor and Vee-Bee Consistometer tests

Fig. 8 shows that there is a decrement in the value of slump with an increase in the aluminium dross replacement level. Aluminium dross is a finer material compared to cement and tends to adhere to the nuclei of cement particles and hinders the hydration reaction. The formation of $Ca(OH)_2$ in excess quantity lags the pozzolanic reaction in the concrete matrix thereby leaving behind more water in the initial stages of hydration (Panditharadhya et al., 2018). Therefore, more water will be available in the matrix for providing improved workability when the cement is partially replaced by aluminium dross.

The locations having hot weather will allow the water in the concrete matrix to get evaporated quickly during the initial stages of hydration. When exposed to higher temperature in the environment, the water loss become more and reduces the workability of concrete. Even in coastal regions, the more humid climate results in evaporation losses and lessens the water required to provide sufficient workability. Partial replacement of Ordinary Portland Cement (OPC) by small quantity of aluminium dross seems to be a better alternative to increase the flow of concrete to give better workability.

CONCLUSIONS

The following conclusions are deduced from this study:

1) Utilization of aluminium dross, an industrial waste product in concrete reduces the load on the environment and can be said to be a sustainable option to reduce higher energy consumption during cement production and saving of natural raw materials.
2) The issue of disposal of aluminium dross into landfills by utilizing large area as dump sites and its cost are addressed by replacing aluminium dross as an alternative cementitious material.
3) The setting time of cement paste increases with increase in aluminium dross percentage making it suitable for hot weather conditions.
4) Workability of the concrete mix gets increased with an increase in aluminium dross replacement which is due to slower pozzolanic reaction caused in the matrix.
5) Further, the mechanical and durability properties of the concrete with varying aluminium dross percentage has to be evaluated to understand the efficiency of aluminium dross as a binder material for various concreting applications.

ACKNOWLEDGEMENTS

Authors are thankful to the Ministry of Human Resource Development, Government of India for providing fellowship to Mr. Panditharadhya B J and standing as main support for the research work. Also, the research facilities at

National Institute of Technology Karnataka, Surathkal, India deserves a heartfelt thanks for the technical and moral support to the authors. Special thanks to M/s Udyog Alloys (P) Ltd., Mumbai, India for providing aluminium dross free of cost.

REFERENCES

[1] Elinwa, A.U. and Mbadike, E. (2011). "The use of aluminum waste for concrete production." J. Asian Architecture Building Engineering, Vol. 10(1), pp. 217–220.

[2] Girsh, M., Raghavendra, S. N., Sreedhara, B. M., Manu, D. S., Hiremath, P. and Jayakesh, K. (2016). "Investigation of concrete produced using recycled Al dross for hot weather concreting conditions." *REFFIT,* Vol. 2, pp. 68-80.

[3] IRC: 44 – 2008. "Guidelines for Cement Concrete Mix Design for Pavements." *Bureau of Indian Standards*, New Delhi, India.

[4] IS: 10262 – 2009. "Concrete Mix Proportioning – Guidelines." *Bureau of Indian Standards*, New Delhi, India.

[5] IS: 1199 – 1959. "Methods of Sampling and Analysis of Concrete." *Bureau of Indian Standards*, New Delhi, India.

[6] IS: 12269 – 1987. "Specifications for 53 grade Ordinary Portland Cement." *Bureau of Indian Standards*, New Delhi, India.

[7] IS: 2386 (Part III) – 1963. "Methods of tests for Aggregates for Concrete – Specific Gravity, Density, Voids and Bulking." *Bureau of Indian Standards*, New Delhi, India.

[8] IS: 2386 (Part IV) – 1963. "Methods of tests for Aggregates for Concrete – Mechanical Properties." *Bureau of Indian Standards*, New Delhi, India.

[9] IS: 383 – 2016. "Specifications for Fine and Coarse Aggregates." *Bureau of Indian Standards*, New Delhi, India.

[10] Panditharadhya, B. J., Vargala Sampath, Raviraj, H., Mulangi and Ravi Shankar, A. U. (2018). "Mechanical properties of pavement quality concrete with secondary aluminium dross as partial replacement for ordinary portland cement." *IOP Conf. Ser.: Mater. Sci. Eng.,* 431, 032011.

[11] Shriraksha, J., Chandrashekar, A.R., Sujay, R.N., Manu, D.S., Parameshwar, H., Preethi, H.G. and Vinod, K.N. (2017). "Eco-concrete for sustainability: utilizing Al dross and iron slag as partial replacement materials." *Clean Technical Environmental Policy,* Germany.

[12] Unger, T. W. and Beckmann, M. (1992). "Salt slag processing for recycling, light metals." in: E.R.Cutshall (Ed.) *TMS Annual Meeting San Diego California*, 1159-1162.

8th International Engineering Symposium - IES 2019
March 13-15, 2019, Kumamoto University, Japan

EXPERIMENTAL STUDIES ON PHENOL ADSORPTION POTENTIAL OF SOILS

Meera Vaeghese[1] and Sunil B. M[2]

1 *Department of Civil Engineering, National Institute of Technology Karnataka, Surathkal, Mangalore 575025, India.*
2 *Department of Civil Engineering, National Institute of Technology Karnataka, Surathkal, Mangalore 575025, India. email:bmsunil@gmail.com; sunilbm@nitk.edu.in*

ABSTRACT: In the present work the results of a study on adsorption of phenol in lateritic soil and lithomargic clay are presented. Batch adsorption tests were conducted in the laboratory at low concentrations. The interactions of the organic contaminant in lithomargic clay have been studied with respect to the linear and non-linear adsorption isotherms. The coefficient of distribution, k_d, for lateritic soil-phenol interaction is 1.177 L/kg while the corresponding value for the lithomargic caly -phenol interaction is about 1.880 L/kg. From the study it is concluded that the lithomargic clay may be used as a potential soil liner material.

Keywords*: Phenol, adsorption, soils, coefficient of distribution,*

INTRODUCTION

Phenol is an organic compound widely used in various industries such as the manufacture of plastics, lubricants, paints, pharmaceuticals, herbicides and resins. Chemically, phenol is a hazardous substance and if inhaled or absorbed may lead to serious injuries and/or fatalities. Therefore most phenolic compounds are priority pollutants. The Environmental Protection Agency (USEPA) established the drinking water standard for phenol at 1 ppb or less (Acar et al. 1992). Usage of phenol in various industries and its disposal are a cause of concern in wastage management issues.

Adsorption is a phenomenon whereby a solute attaches itself to the surface of a solid material. The more it is adsorbed, the less its migration and less extensive will be the extent of pollution. An important parameter that is used in contaminant transport analytical models, the partition coefficient (k_d), may be directly obtained from adsorption studies. Thus, the ability to retain contaminants by soil for a potential liner material can also be derived from the study on adsorption.

ADSORPTION ISOTHERMS

In this study, the results of batch adsorption tests are analysed using linear and non-linear adsorption isotherms. The parameters used are the amount of contaminant/solute adsorbed, S, and the equilibrium concentration, C_e. When the relationship between S and C_e can be approximated by a straight line, a linear adsorption isotherm is established.

Thus

$$S=k_dCe \quad (1)$$

In Eq. 1, k_d is the distribution coefficient.

Freundlich adsorption isotherm mathematically expressed as in Eq, 2, is used to fit curved relationship.

$$S = KC^{\frac{1}{n}}{}_e \quad (2)$$

where K is the Freundlich adsorption constant, which is a measure of the adsorption capacity and n is an empirical constant. The linear adsorption isotherm is a special case of the Freundlich isotherm

with n=1. Values of n<1 usually indicates unfavourable sorption and with n>1 is said to favourable sorption. The linearized form of Eq. (2) is:

$$\ln S = \ln K + \frac{1}{n} C_e \quad (3)$$

Another useful nonlinear isotherm is the Langmuir adsorption isotherm (Langmuir, 1918) which has been developed based on the concept that a solid surface possesses a finite number of sorption sites. Sorption does not occur if all the sorption sites are filled. Mathematically, this isotherm is expressed as

$$S = \frac{\alpha\beta C_e}{1 + \alpha C_e} \quad (4)$$

where a is an adsorption constant related to the binding energy or the "affinity" parameter (Veith and Sposito, 1977) and β is the maximum amount of solute that can be adsorbed by the soil.

MATERIALS AND METHOD

The organic compound used in the present study is phenol. Phenol (C_6H_5OH) is also known as carbolic acid. The properties of the phenol used in this study are shown in Table 1.

. Table 1 Physical properties of phenol

Formula weight (g/mole)	Boiling point	Melting point	G	Water solubility
94.11 g mo-1	181.7 ° C	40.5 ° C	1.07	8.3 g/100 mL

Sample collection

The lateritic soil and lithomargic clay used in this study are obtained from a natural deposit in coastal district of Karnataka, India. The test soils were collected from about 0.5m -0.6 m depth below the ground surface and transported to geotechnical laboratory at National Institute of Technology Karnataka Surathkal, for further analysis. In the laboratory the test soils are air dried, sieved and stored in small plastic containers for further use.

Properties of test soils

Some of the basic properties of the test soils are shown in Table 2. From Table 2, it is observed that the clay size fraction of lithomargic clay is 16 % and that of the laterite soil is 5%. The pH of the lateritic soil and lithomargic clay are 5.6 and 5.2 respectively (acidic soils). Acidic soils are usually common in tropical climates or humid regions such as in west coast of India, possibly due to heavy rainfall during south-west monsoon. The reaction of rain water with carbon dioxide in the atmosphere makes weak carbonic acid, more available in the soil. These soils also contain large amounts of soluble Al, Fe, and Mn (Gidigasu, 1976).

Table 2 Basic properties of the test soils

Soil type	Parameter			
	G	LL (%)	PL (%)	Clay (%)
Laterite	2.70	44	28	05
Shedi	2.58	46	31	16

Table 3 Chemical properties of soils

Soil type	Parameter		
	pH	EC	CEC
Laterite	5.6	215	4
Shedi	5.2	45	7

Methodology

Phenol solutions with different initial concentrations were prepared using freshly prepared distilled water. Batch adsorption tests on individual soil samples were conducted on soil suspensions where the test soil particles were exposed and available for interaction with the organic contaminant solution. The test procedure followed was shaking of about 10-12 g of soil sample with a series of phenol solutions of different concentrations for 24 h. The mixture was then allowed to equilibrate for 3 days before the final concentrations were analysed using a double beam UV spectrophotometer Systronics Make AU-2701. Detection wavelengths used is 500 nm.

The amount of phenol adsorbed, S, was then calculated using the following equation:

$$S = (C_o - C_e)\frac{V}{M} \quad (5)$$

where C_o is the initial concentration, C_e is the final or equilibrium concentration, V is the volume of solution, and M is the mass of soil used.

Results and discussion

The adsorption test results are shown in Figs. 1 to 3. It is observed that at low concentrations (for initial concentrations C_o < 10 mg/L) the results can be approximated by a linear adsorption isotherm. The slope of the line is the partition coefficient k_d, which is one of the most important parameters in the advective–dispersive model for transport of contaminants in soil. The corresponding values of k_d for lateritic soil and lithomargic clay are about 1.17 L/kg (R^2 = 0.951), and 1.880 L/kg (R^2 = 0.951) respectively. The k_d values of laterite, shedi soil indicated that phenol has a greater affinity to the lithomargic clay (shedi soil). This may be due to the presence of high clay content in the shedi soil and the corresponding greater surface area available for adsorption to take place.

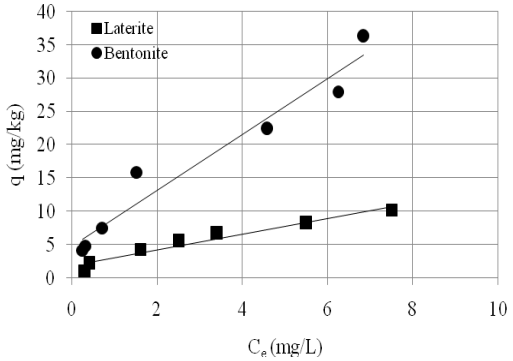

Fig. 1 Linear adsorption isotherm for phenol-soil interaction

The low concentration test results for the Freundlich adsorption isotherm have been plotted in a linearized form in Fig. 2, for the evaluation of adsorption parameters. From the straight lines, the parameters K and n are 3.028 mg/kg and 1.61 kg/L respectively for laterite soil; 5.436 mg/kg and 1.615 kg/L for shedi soil (R^2 > 0.96 in all cases), showing a favourable sorption of phenol on the test soils (i.e. n >1).

The low concentration test results of phenol-soil interaction in the form of linearized adsorption isotherm for Langmuir analysis is shown in Fig. 3. The ȧ and β values for the laterite soil are 0.353 L/mg and 13.16 mg/kg; for shedi soil 0.3116 L/mg and 23.25 mg/kg. Both parameters indicated a more favourable adsorption of phenol onto the bentonite soil. The β values for both soils again prove that the adsorption capacity of lithomargic clay is more than that of laterite soil

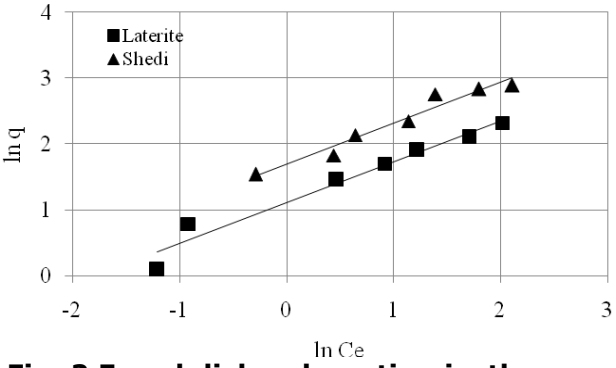

Fig. 2 Frendulich adsorption isotherm for phenol- soil interaction

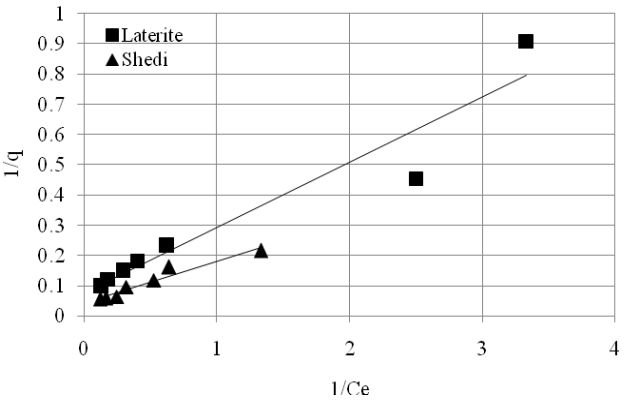

Fig. 3 Langmuir adsorption isotherm for phenol- soil interaction

SUMMARY AND CONCLUSIONS

The interaction of phenol with lateritic soil and lithomargic clay was studied in the laboratory. The experimental results were analyzed using linear and non-linear adsorption isotherms. From the results it was found that lithomargic clay possesses a greater adsorption capacity compared to that of laterite soil. The high adsorption characteristics of lithomargic clay are attributed to the presence of greater amounts of clay size particles and greater surface area. Based on the study results, following are the important conclusions:

- The k_d values for lateritic soil and lithomargic clay are about 1.17 L/kg and 1.880 L/kg respectively.
- The parameters K and n are 3.028 mg/kg and 1.61 kg/L respectively for laterite soil; 5.436 mg/kg and 1.615 kg/L for lithomargic clay (shedi soil).
- The ȁ and β values for the laterite soil are 0.353 L/mg and 13.16 mg/kg; for shedi soil 0.3116 L/mg and 23.25 mg/kg.

REFERENCES

[1] Acar Y.B, Li H, and Gale R.G (1992) Phenol removal from kaolinite by electrokinetics. J Geotech Eng ASCE 118(11):1837–1852.

[2] Caturla, F., Martin-Martinez, J. M., Molina-Sabio, M., Rodriguez-Reinoso, F., Torregrosa, R. 1998. Adsorption of substituted phenols on activated carbon. *Journal of Colloid and Interface Science,* 124, (2) 528–534.

[3] Colella, L.S., Armenante, P.M. 1998. Adsorption isotherms for chlorinated phenols on activated carbon. *Journal of Chemical Engineering Data,* 43, 573–579.

[4] Das, A., Subramanyam, B. 2009. Study of the adsorption of phenol by two soils based on kinetic and isotherm modeling analyses. *Desalination*, 249, pp 914–921.

[5] Freundlich H (1926) Colloid and capillary chemistry. Methuen, London.

[6] Gidigasu, M.D., (1976) "Laterite soil engineering pedogenesis and engineering principles" Elsevier Scientific Pub., Amsterdam, 1976

[7] Langmuir I (1918) The adsorption of gases on plane surfaces of glass, mica and platinum. J Am Chem Soc 40:1361–1382.

[8] Veith JA, Sposito G (1977) On the use of the Langmuir equation in the interpretation of adsorption phenomena. J Am Soil Sci Soc 41:697–702

8th International Engineering Symposium - IES 2019
March 13-15, 2019, Kumamoto University, Japan

NUMERICAL ANALYSIS OF SLOPE STABILITY OF GEOGRID REINFORCED ROAD EMBANKMENT

Teena Thomas

Department of Civil Engineering, Manipal Institute of Technology, Manipal, Mangalore 576104, India. email:annateenathomas@gmail.com

ABSTRACT: The paper discusses the behaviour of road embankment reinforced with geo-grid. In this study the prediction tool utilised is PLAXIS 8.2. In the analysis, three new calculation options were introduced, namely a consolidation analysis, an updated mesh analysis and deformation analysis. This study is focused on conducting a stability analysis for an embankment which is constructed on a soft soil under the application of dynamic traffic loads. In this project two cases were considered for modelling of a road embankment. The first case was an unreiforced road embankment and the second was road embankment with geo-grids. The model defines the most economic design of soil slope reinforced with geo-grids.

***Keywords**: Slope stability analysis, reinforced road embankment, geo-grids, dynamic traffic loads, numerical model*

INTRODUCTION

This paper discusses slope stability analysis of a highway embankment. Stability of slope has always been a difficult task to geotechnical engineers especially when it is built on soft soil because of problems encountered like settlement and instability. It not only results in a weak structure but also increase the construction cost. In the recent days this challenge has been overcome by the use of geosynthetics as reinforcements in embankments. Sadok. et. al. (2015) discusses the membrane strength effect of the geosynthetic and arching effect of the embankment fill which helps in reducing the differential settlement and in turn improving the slope stability. Franz Tschuchnigg. et. al. (2018), deals with long term consolidation and creep settlement which result in long term displacements thereby predicting the embankment behaviour. Also, Murtaza Hasan. et. al. (2017) discusses the substantial improvement in the ultimate load intensity amd stiffness of the ground with the introduction of geosynthtics.

In this attempt, the behaviour of embankment on the application traffic load was studied. The displacement characteristics of the slope under the effect of dynamic traffic loads changes when the embankment is reinforced with geogrids. The change in the load carrying capacity of the embankment with the introduction of the geogrids was also studied.

MODELLING

The numerical modelling of the problem was performed in a finite element software PLAXIS 8.2. Plain strain model with 15 noded element was chosen for the modelling. The finite element method is the most reliable and robust method to determine the factor of safety of slopes as explained in the study of D.V. Griffiths et.al. (1999). The depth of the embankment was 4m which is located above the natural ground of depth 8m. The width of the embankment was 15m at the top. The side slope was assumed to be 1:3 according to the specifications of IRC SP073. The ground water table was located below the embankment at a depth of 8m from the base of slope. The

embankment and the natural ground beneath was made of soft clay. An asphalt concrete pavement was constructed on top of the embankment of thickness 250mm. The properties of soil and asphalt pavement is given in Table 1 and Table 2 respectively. These model parameters were obtained from geotechnical literature. The size of the model was determined based on trial calculations. The mesh was refined until the stress and deformation at the critical zones had stabilised.

In the second part, the model was modified by the introduction of geogrid in the embankment for improving the slope stability. The properties of geogrid is given in Table 3. The geogrids were located beneath the asphaltic pavement, at the bottom of the embankment and also at 1m above the emabankment base as shown in Fig.1.

In this paper the interface boundary between the soil and the geosynthetic was not studied. The traffic loads were considered to be uniformly distributed loads of static load value 4.46kN/m². The dynamic characteristics of the vehicle was obtained from the study of Praznowski K. et. al. (2016), which gives the frequency value to be 10 kHz and amplitude multiplier to be unity. The calculation was performed in two stages. The first stage consists of plastic analysis which involves the analysis of dead load and static loads. The second phase covers the application of dynamic traffic loads. The traffic loads were applied in the second stage and model was tested for a period of one second.

RESULTS AND DISCUSSIONS

In the first stage when the model was developed without considering geogrids, the extreme total displacement was found to be 0.015m. For better understanding of the behaviour of the model three prominent points were chosen i) at the toe of slope ii) on the slope and iii) on the asphalt pavement. Further, the velocity and acceleration of soil particles on the application of dynamic loads were also studied.

In the second stage, geogrids were installed within the model at three depths. With the installation of geogrids, the extreme displacement was reduced to 0.014m. Fig.2 shows the reinforced model which was deformed under the application of traffic loads.

Three parameters; displacement, velocity and acceleration were chosen to understand the behaviourof the soil under the effect of loads. Fig.3, Fig.4 and Fig.5 represents the behaviour of displacement, velocity and acceleration with respect to time for the model without geogrids. Fig.6, Fig.7 and Fig.8 shows the behaviour of soil when reinforced with geogids in terms of displacement, velocity and acceleration respectively. The study was concentrated on three points as explained earlier; at toe of slope, on the slope and on the pavement.

CONCLUSION

The following conclusions were derived from the study:

- The extreme total displacement reduced from 0.015m to 0.014m with the use of geogrids as reinforcement in the embankment. The displcement in reinforced and unreinforced conditions were found to be maximum at midheight of the embankment.
- In the unreiforced model, the velocity of soil particle was observed to be highest on the pavement layer and was found to be 0.025m/s.
- In the reinforced model, the maximum particle velocity was observed at midheight of the embankment and recorded to be 0.021m/s
- In the unreinforced model the maximum acceleration of the soil particle was observed to be 1.55m/s² on the pavement layer and with the inclusion of geogrids, the maximum acceleration was observed to be 1.4m/s² on the slope.

REFERENCES

[1] Brinkgreeve, R.B.J, and Vermeer, P.A, (1998) Plaxis, Finite element code for soil and rock analysis: Professional Version 8, Usage Manual.

[2] D.V.Griffiths, and P. A. Lane (1999), Slope stability analysis by ®nite elements, Geotechnique, Vol. 49, No. 3, pp. 387-403.

[3] Franz Tschuchnigg, and Helmut F. Schweiger (2018), Embankment prediction and back analysis by means of 2D and 3D finite element analyses, Computers and Geotechnics, Vol. 93, pp. 104-114.
[4] IRC SP 073, Two-laning of Highways through Public Private Partnership, Manual of Specifications and Standards, pp. 3- 15, 37- 45.
[5] Murtaza Hasan, and N.K. Samadhiya (2017), Performance of geosynthetic-reinforced granular piles in soft clays:Model tests and numerical analysis, Computers and Geotechnics, Vol. 87, pp. 178-187.
[6] K Prażnowski, and J Mamala (2016),Classification of the road surface condition on the basis of ibrations of the sprung mass in a passenger car, Journal of Scientific Conference on Autom otive Vehicles and Combustion Engines Vol. 148, pp. 105-112.
[7] Sadok Benmebarek, Fouad Berrabah, and Naïma Benmebarek (2015), Effect of geosynthetic reinforced embankment on locally weak zones by numerical approach, Computers and Geotechnics, Vol. 65, pp. 1015-125.

Table 1 Soil properties

Type of soil	Clay
Material model	Mohr-Coulomb
Material type	Drained
Bulk density	16kN/m³
Saturated density	18kN/m³
Permeability	0.001m/day
Young's model	10000kN/m²
Poisson's ratio	0.35
Cohesion	5kN/m²
Friction angle	25⁰

Table 2 Pavement properties

Type of pavement	Ashalt
Material model	Linear elastic
Material type	Non-porous
Bulk density	20kN/m³
Young's model	$2.1x10^6$
Poisson's ratio	0.45

Table 3 Geogrid properties

Material type	Elastic
Axial rigidity	500kN/m
Poisson's ratio	0.25

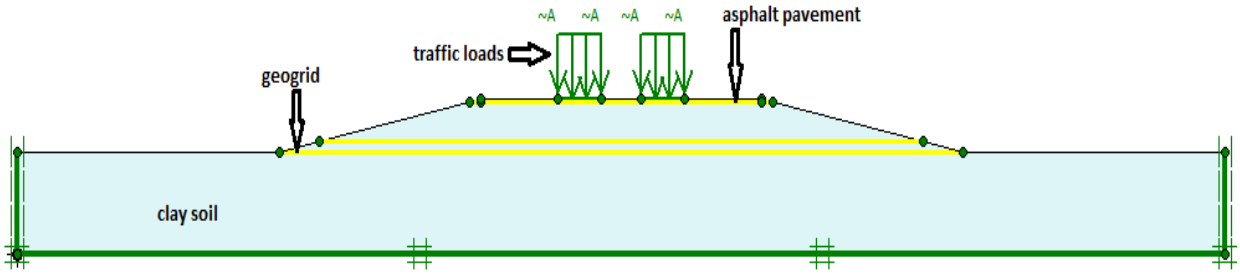

Fig.1 Geogrid reinforced clay soil

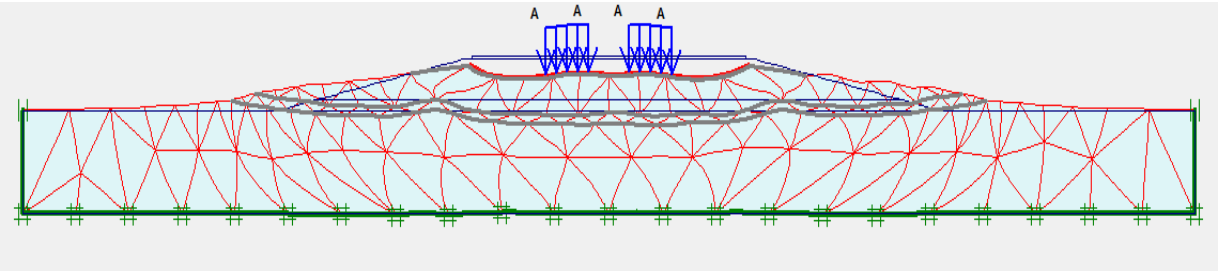

Fig.2 Deformed model

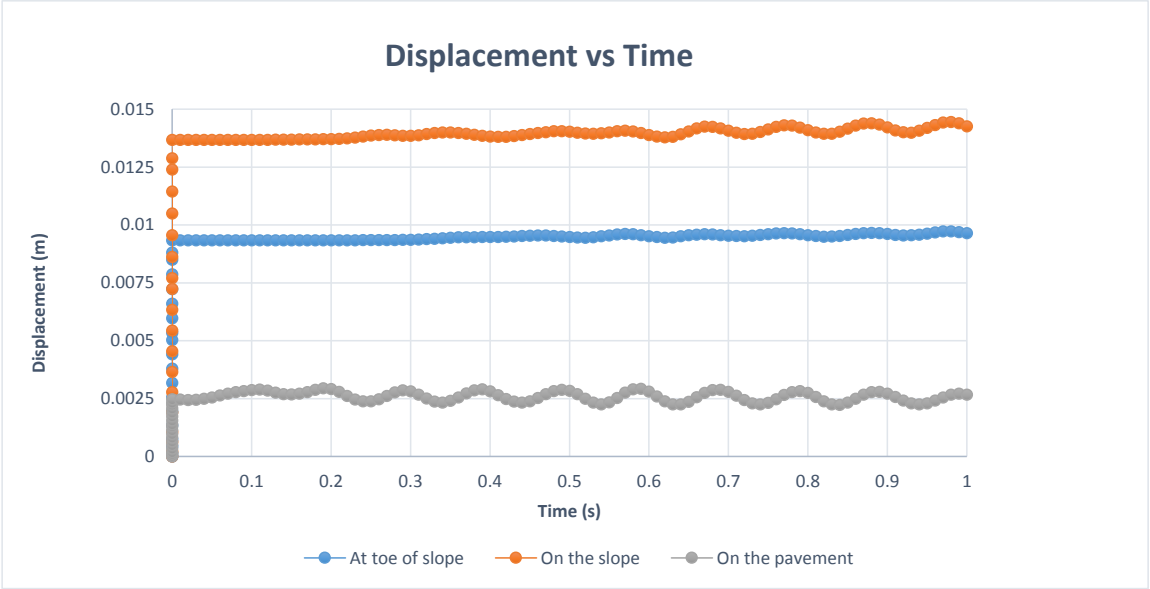

Fig.3 Displacement vs time curve for unreinforced model

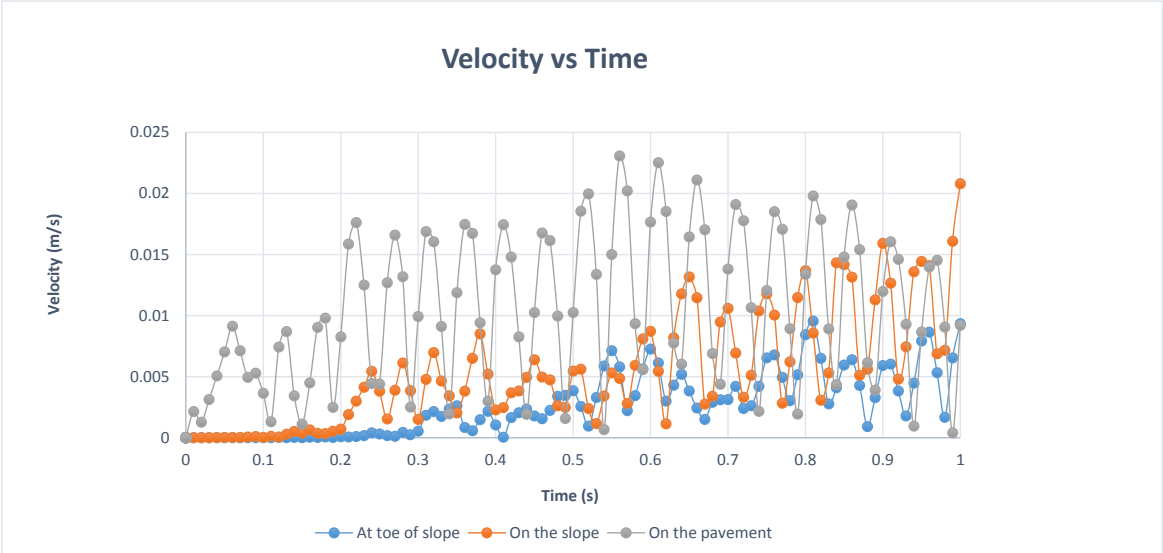

Fig.4 Velocity vs time curve for unreinforced model

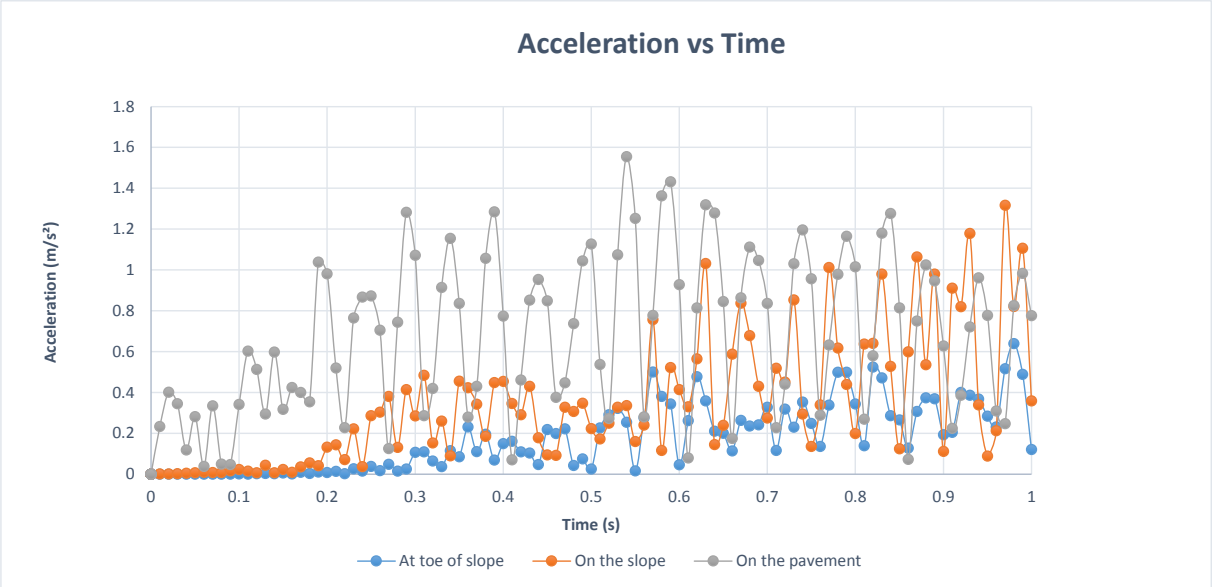

Fig.5 Acceleration vs time curve for unreinforced model

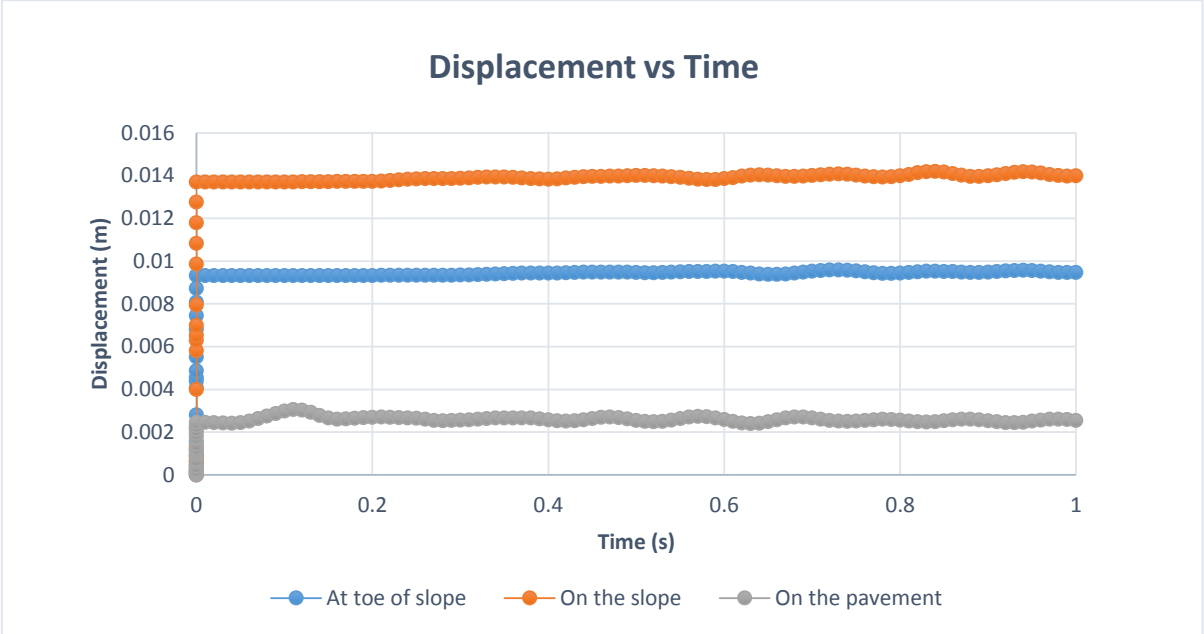

Fig.6 Displacement vs time curve for reinforced model

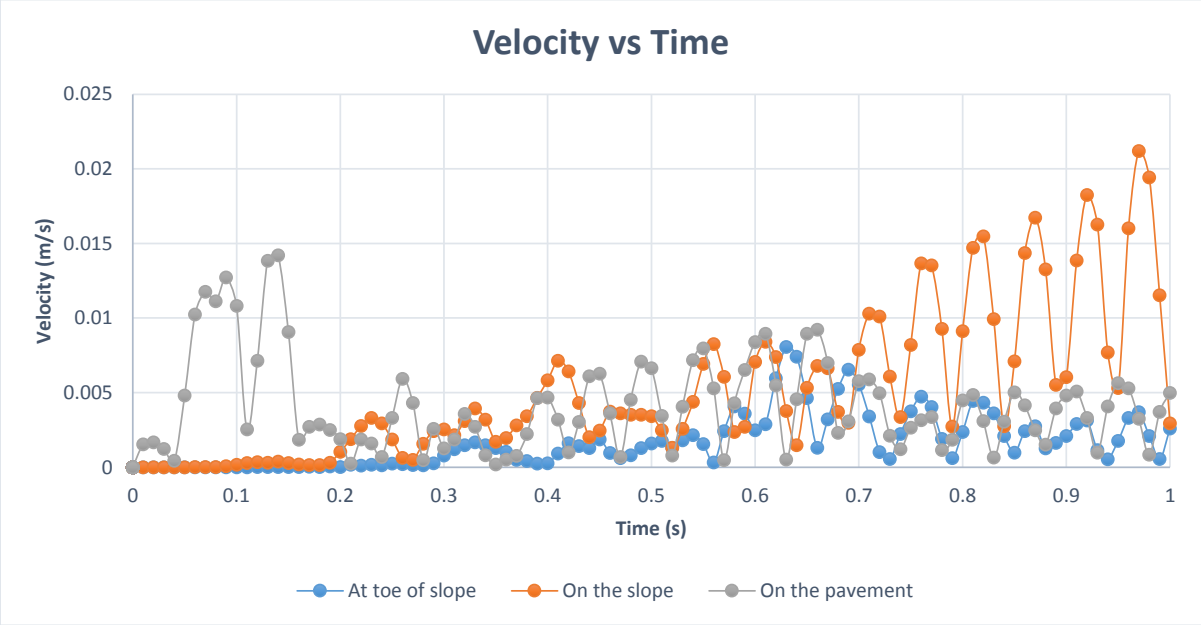

Fig.7 Velocity vs time curve for reinforced model

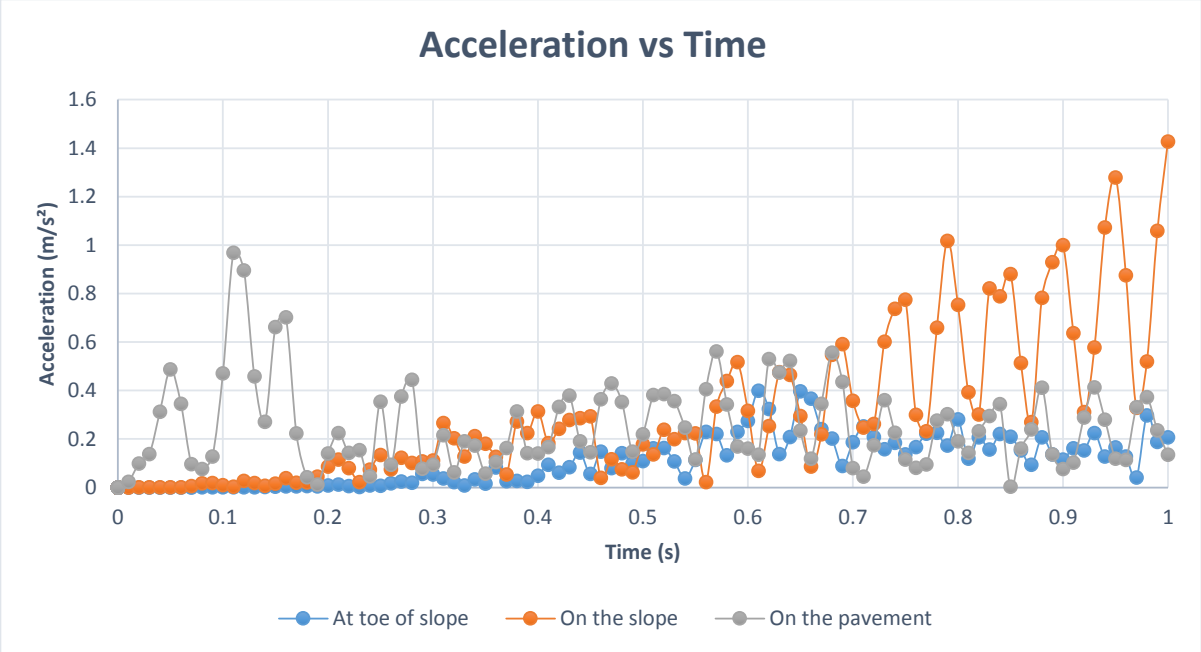

Fig.8 Acceleration vs time curve for reinforced model

8th International Engineering Symposium - IES 2019
March 13-15, 2019, Kumamoto University, Japan

APPLICATION OF SOFT COMPUTING TECHNIQUES IN ESTIMATION OF SATURATED HYDRAULIC CONDUCTIVITY IN SPATIALLY VARIABLE FIELDS

Paresh Chandra Deka
Department of Applied Mechanics and Hydraulics
National Institute of Technology Karnataka-575025
E-mail:dekanitk@gmail.com

ABSTRACT: Objective of this study is to investigate the spatial variability of saturated hydraulic conductivity under different land use land cover by using Guelph permeameter, and to develop PTF(Pedo-Transfer Function) for estimating K_{fs}(Saturated Hydraulic conductivity), from soil index properties, by using soft computing techniques and thus evaluate the performance of these techniques. Study is carried out at Solapur, India. In situ and laboratory tests were carried out to estimate K_{fs} and other basic index properties of soil. Data were pre-processed and then used for modeling purpose. It was found that Porosity has shown strong positive correlation with $K_{fs,}$ whereas bulk density has shown strong negative correlation. Performance of ELM (Extreme Learning Machine) model was found better than other models such as SVM (Support Vector Machine) and ANFIS(Adaptive Neuro-Fuzzy Inference System) .

Keywords*: Saturated hydraulic conductivity, Guelph permeameter, Pedo-transfer function, ELM,SVM,ANFIS*

INTRODUCTION

Saturated hydraulic conductivity is one of the most important physical properties of soil for environmental site characterization such as rate of flow to wells from aquifer, movement of contaminant through soil, performance of landfills, drainage design, irrigation, and in the design of geotechnical engineering projects such as design of slopes, earth dams etc. It is essential to estimate it accurately, so that management and design of various facilities related to flow of fluid can be tackled easily. This property of soil depends on variety of factors related to soil, terrain, land use land cover, pores and their interconnectivity, biological changes that take place under below ground, chemical composition of soil. Number of tests were conducted to account for spatial variability of soil etc.(Bagarello and Geoderno,1999). All these factors affecting saturated hydraulic conductivity will lead to a laborious and costly affair to measure it, so alternative technique is emerged out suggested by various researchers(Parasuraman et al.2006; Kalkhaheh and Kianpoor.2012)to estimate it indirectly by using basic soil properties which are available easily in the database or can be measured; which is called Pedotransfer function (PTF). It is just a functional relation between saturated hydraulic conductivity and basic soil properties. The PTF were developed by various researchers by using linear or nonlinear regression, artificial neural network, fuzzy logic, genetic algorithm, support vector machine and hybrid techniques(Deb and Shukla,2012).

Very few attempts have been made by researchers to develop ELM(Extreme Learning Machine) model to estimate hydraulic conductivity but widely used in other fields (Deo and Sahin., 2014; Patil and Deka., 2016)

This study proposes a recently developed soft computing model,ELM for estimating saturated hydraulic conductivity by using easily measurable soil physical properties such as bulk density, porosity, soil texture etc. To confirm the superiority of ELM model,results were compared with other soft computing model such as SVM(Support Vector Machine) model and ANFIS(Adaptive Neuro-Fuzzy Inference System) model.Further, performances of these models are compared to select the best model for estimating saturated hydraulic conductivity.

STUDY AREA

Study area selected for the work is Solapur as shown in Fig .1, which is geographically located at 17.66^0 N Latitude & 75.90^0E Longitude. Its elevation is 483 m above mean sea level and mean annual rainfall is 723 mm . Due to scanty and non-uniform rain, water scarcity conditions prevail in the district which has adversely affected the socio economic condition of people. In any year,May is the hottest and December is the coldest month.In general, climate is "semi – arid". The soil in this area is derived from basic igneous rock namely basalt and underlain by partially disintegrated rock locally called "murum".
Three sites have been selected for the experimental work, which are Hipparga site (close to college), Mulegaon site and Punanaka site. Hipparga site is having mild downslope followed by undulated terrain with grass cover dominated by blend of silty and clayey soil. Mulegaon site is agricultural harvested land (no crops) with silty soil and Punanaka site is bare land having coarse size soil. These three stations are as shown in Fig.1, distance between college and Punanaka is around 10km. that between College and Mulegaon is 15km and between Punanaka and Mulegaon is 20Km.

METHODOLOGY

Sampling at each site divided in to small grids of 10m X 10m.In-situ saturated hydraulic conductivity was determined by using Guelph permeameter, for which observations were taken at each corner of the grid at a depth of 15cm, 30cm and 45cm. The measurement consisted in estimating a quasi – steady discharge Q of water infiltrating into a vertical borehole of radius a (3cm) in which the water level is maintained at a height H (5cm / 10cm) above the bottom of borehole. Soil sample were collected at all three depths after finishing the observations for permeameter to carry out laboratory analysis these samples are collected carefully in a cylindrical container two in number (100mm diameter and 125mm height). These samples were used for laboratory analysis of soil. Samples from first cylindrical core were used to determine dry bulk density, particle density, and organic matter, and then sample from second core was used to determine soil texture by using hydrometer analysis.

Extreme Learning Machine

Amongst various neural networks, feed forward neural network is favorite one for the researchers due to its inherent advantages such as capability of directly mapping complicated nonlinear data from input samples. Architecture of ELM model is given below in Fig 2.
This network architecture has one input layer, one output layer and hidden layers (one or more). Extreme learning machine is learning algorithm for single layered feed forward network (SLFN) having multiple advantages such as high-speed learning, best generalization, and least error in training with smaller norm weights.
Extreme learning machine were originally proposed for SLFNs and then it was extended to the generalized SLFNs. Essentially ELM trains the SLFN in following stages first it maps the feature randomly and then tends to solve it for linear parameters. The weights are chosen randomly in ELM. On choosing the input weights and hidden layer biases the SLFN can be considered as a linear system and the output weights analytically determined by simple generalized inverse operation of the hidden layer output matrices. This simplified approach makes ELM work faster than the feed forward algorithm.

Adaptive Neuro-Fuzzy Inference System (ANFIS)

ANFIS is developed that used neural network learning algorithm for constructing a set of fuzzy if-then rules from stipulated input output pairs. Fundamentally, ANFIS is a functional equivalent of fuzzy inference systems endowed with neural learning capabilities. An ANFIS model combines the transparent and linguistic representation of a fuzzy system with learning ability of ANN. This allows them to be trained in performing input/output mapping as an ANN model. ANFIS comes with an additional benefit of being able to provide a set of rules on which the model is based.

Support Vector Machine

The Support Vector Machines (SVM) has been gaining popularity due to many attractive features and promising empirical performances. The formulation embodies structural risk minimization (SRM) principle, which has shown better performances than empirical risk minimization (ERM) which is employed by conventional neural networks. SRM minimizes an upper bound on the expected risk, as opposed to ERM that minimizes the error on the training data. It is this difference, which equips SVM with a greater ability to generalize, thus, achieving the goal of statistical learning. SVM comes with an advantage of using kernel trick to minimize both model complexities and prediction errors simultaneously. SVMs were initially developed to solve the classification problems, but recently they have been extended to the domain of regression problems.

RESULTS AND DISCUSSION

Results obtained from the field experimentation and various developed model has been analyzed and discussed here.

statistical analysis:

Statistical analysis of the samples result tested in the laboratory and in the field is done for all samples (900), and subdivided samples for modeling purpose (College, Mulegaon, Punanaka, 15cm depth, 30cm depth and 45cm depth) to know the mean value, standard deviation, minimum and maximum value of each soil parameter being tested.

Maximum value of log saturated hydraulic conductivity (Kfs) was observed (Table 1) at Punanaka (3.842 m yr^{-1}) and minimum value at College site (0.002 m yr^{-1}), standard deviation at college site was more (0.804) as compared to other two sampling stations i.e. 0.598 at Punanaka and 0.621 at Mulegaon.

Correlation coefficient of various soil parameters with the saturated hydraulic conductivity (logarithmic terms) is depicted in Table 2. Porosity shown strong influence with correlation coefficient of 0.9 as compared with other. It is obvious for more flow to take place through a porous media it should have more porosity. Next factor having its dominance in controlling Kfs is bulk density it has negative impact on Kfs with its maximum value of -0.90, density is mass per unit volume. More the density means more number of particles in a given volume thereby reducing the void space and hence conductivity. Other parameters have shown least correlation except sand content which is also positively correlated with the Kfs.

Performance evaluation of models:

Performances of the models were tested by using coefficient of correlation (R), mean relative error (MRE), normalized root mean square error [(NRMSE), close to zero is better] and Nash – Sutcliffe efficiency (NSE).

The performance metrics of training dataset and testing dataset are shown in Table 3 for College site dataset segregated for modeling purpose. Scatter plot between observed and predicted value of the saturated hydraulic conductivity by using ELM, SVM and ANFIS are presented in Fig 3.

R-value for training and testing for ELM model (0.97 and 0.96) performance was found good in comparison to other two models. MRE of ELM in training is 0.02 which (~0) and is less than that for other two models(Table 3). In terms of NSE also

ELM performance is very good during training and testing. NRMSE of SVM and ANFIS are relatively good for training however, for testing it is more in comparison to ELM. The scatterplot of observed v/s predicted Kfs is shown in fig 3 along with 1:1 line. The predicted values of Kfs by ELM methods are close to the 1:1 line in comparison with that of other two methods both during and training and testing phase. Prediction by SVM method during training and testing by SVM were below 1:1 line indicating it fails to predict the Kfs, model is under fitting the values both during training and during testing phase.

CONCLUSIONS

Based on study,following conclusions are drawn:

- Saturated hydraulic conductivity found to vary in vertical direction (along the depth) as well as horizontal direction (lateral / longitudinal).
- In general Kfs was found decreasing with the depth of soil.
- Land use land cover has significant influence on Kfs.
- Kfs found decreasing down the slope.
- ELM model outperformed other two models such as ANFIS and SVM in modeling Saturated Hydraulic Conductivity for the site considered.

ACKNOWLEDGEMENTS

Author acknowledged Mr. S B More, Associate professor,Solapur Engg. College, Maharastra state, India for providing the relevant data.

REFERENCES

[1]Bagarello, V. and G. Giordano. (1999). "Comparison of Procedures to Estimate Steady Flow Rate in Field Measurement of Saturated Hydraulic Conductivity by the Guelph Permeameter Method." *Journal of Agricultural and Engineering Research* 74(1):63–71.

[2]Deb, Sanjit K. and Manoj K. Shukla. (2012). "Variability of Hydraulic Conductivity Due to Multiple Factors." *American Journal of Environmental Sciences* 8(5):489–502.

[3]Deo, Ravinesh C. and Mehmet Şahin. (2015). "Application of the Extreme Learning Machine Algorithm for the Prediction of Monthly Effective Drought Index in Eastern Australia." *Atmospheric Research* 153:512–25.

[4]Kalkhaheh, Yusuf Kianpoor. (2012). "Multiple Linear Regression, Artificial Neural Network (Mlp, Rbf) And Anfis Models For Modeling The Saturated Hydraulic Conductivity (A Case Study: Khuzestan Province, Southwest Iran) Yusef." *International Journal of Agriculture: Research and Review* 2(3):7973.

[5]Parasuraman, Kamban, Amin Elshorbagy, and Bing Cheng Si. (2006). "Estimating Saturated Hydraulic Conductivity In Spatially Variable Fields Using Neural Network Ensembles." *Soil Science Society of America Journal* 70(6):1851.

[6]Patil, Amit Prakash and Paresh Chandra Deka. (2016). "An Extreme Learning Machine Approach for Modeling Evapotranspiration Using Extrinsic Inputs." *Computers and Electronics in Agriculture* 121:385–92.

Table 1: Summary statistics of soil parameters samples at all three sites and all three depths (15cm, 30cm and 45cm)

		Mean	SD	Kurtosis	Skewness	Minimum	Maximum
CO		2.067	0.804	-0.505	-0.231	0.002	3.638
MU	Kfs(m yr^{-1})	2.576	0.621	-1.073	-0.167	0.506	3.647
PN		2.610	0.598	-0.575	-0.330	1.098	3.842
CO		1.622	0.073	-0.954	0.030	1.504	1.761
MU	Porosity (%)	1.668	0.053	-0.962	0.174	1.504	1.773
PN		1.699	0.055	-0.243	-0.292	1.517	1.786
CO		1.265	0.319	-0.453	0.458	0.699	1.944
MU	% sand	1.394	0.281	-0.600	0.636	0.778	1.944
PN		1.492	0.296	-1.043	0.000	0.845	1.940
CO		1.472	0.389	2.108	-1.296	0.000	1.924
MU	% clay	1.407	0.392	0.494	-0.904	0.000	1.914
PN		1.311	0.417	0.034	-0.690	0.000	1.914
CO		1.461	0.305	-0.495	-0.513	0.301	1.903
MU	% silt	1.440	0.313	1.448	-0.935	0.000	1.863
PN		1.415	0.306	1.473	-0.969	0.000	1.863
CO		3.152	0.044	-0.619	-0.785	3.053	3.203
MU	BD ($kg.m^{-3}$)	3.128	0.044	-1.443	-0.162	3.047	3.202
PN		3.099	0.040	-0.690	0.263	3.042	3.201
CO		0.923	0.287	20.751	-3.684	-1.495	1.174
MU	OM(g kg^{-1})	0.981	0.118	6.767	-1.589	0.273	1.144
PN		0.391	0.227	1.002	-1.085	-0.541	0.712
CO		0.396	0.015	-1.194	-0.362	0.370	0.427
MU	G	0.406	0.010	0.493	-0.155	0.369	0.437
PN		0.408	0.017	-1.007	0.561	0.372	0.452

Table 2 Correlation coefficient of various soil parameters with saturated hydraulic conductivity sampled at college (CO), Mulegaon (MU) and Punanaka (PN)

	Kfs (m yr^{-1})	Porosity %	Sand %	Clay %	Silt %	BD ($kg\ m^{-3}$)	OM ($g\ kg^{-1}$)	G
CO	1.00	0.90	0.76	-0.43	-0.14	-0.87	0.28	0.73
MU	1.00	0.88	0.58	-0.42	-0.28	-0.90	-0.05	0.23
PN	1.00	0.70	0.73	-0.59	-0.36	-0.71	0.10	0.58

All soil parameters are in logarithmic terms, CO – college site, MU – Mulegaon site & PN – Punanaka site

Table 3 Performance comparison of models for College (90% training and 10% testing)

Model	Training			Testing		
	ELM	SVM	ANFIS	ELM	SVM	ANFIS
R	0.97	0.77	0.78	0.96	0.52	0.58
MRE	0.02	0.07	0.06	0.18	0.60	0.58
RMSE (myr^{-1})	73.01	257.12	217.52	219.03	771.37	652.55
NRMSE	0.02	0.07	0.06	0.06	0.21	0.18
NSE	0.95	0.16	0.60	0.90	0.18	0.15

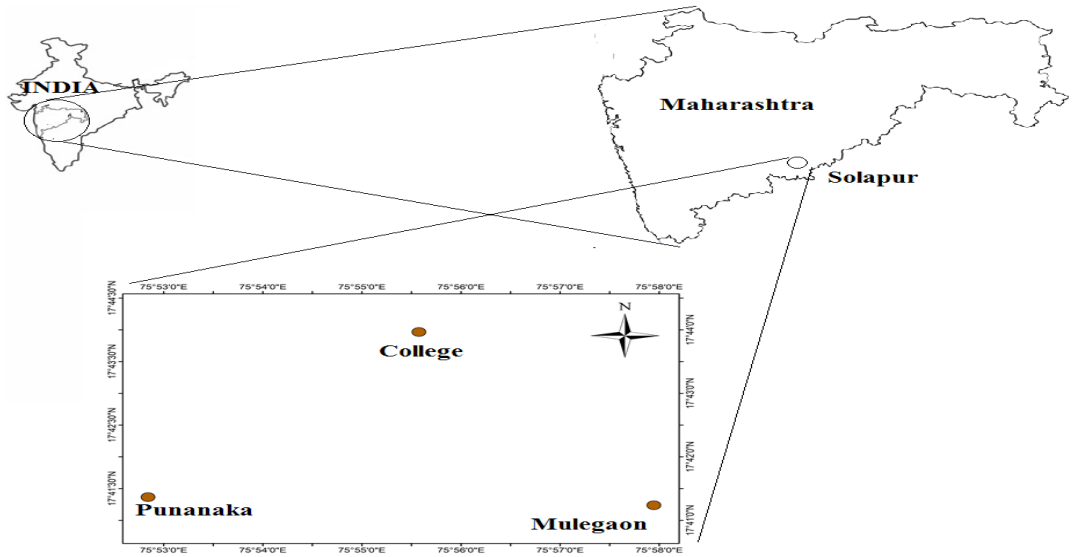

Fig.1 Study area

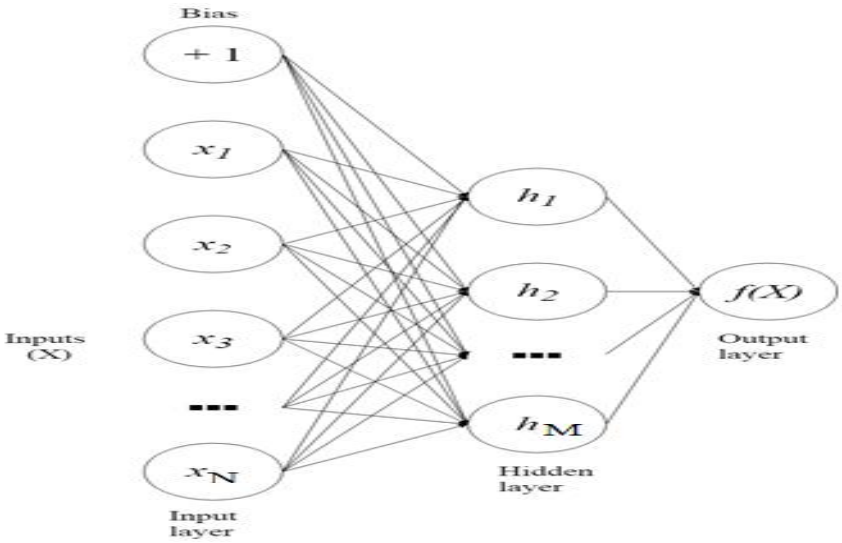

Fig.2 Architecture of ELM model

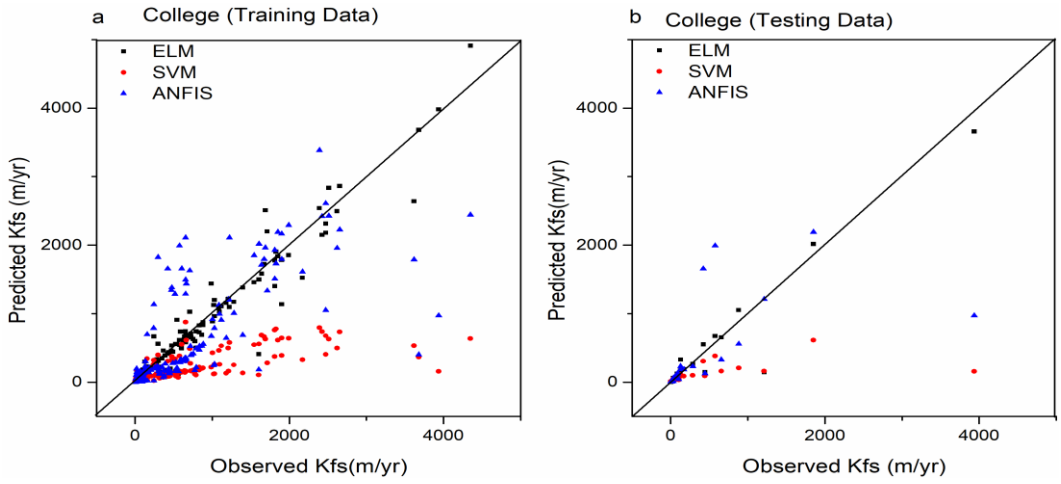

Fig.3 Model performances during training and testing

8th International Engineering Symposium - IES 2019
March 13-15, 2019, Kumamoto University, Japan

Identification of significant input variables in urban Water Consumption estimation-case study of Bengaluru

Rumi Thakuria

Researcher in Social Science,
Commander Glory Apartment, Singapura layout, Bengaluru, Karnataka-560064
E-mail:rumithakuriadeka7@gmail.com

ABSTRACT: The present study aims to address the problem of modeling urban Water Consumption estimation in the perspective of a developing country within Bangalore city,INDIA as the case under investigation. The Influence of Climatic Variables and socio-Economic deforms for residential water Consumption Estimation has been identified by using historical water consumption data and field survey. Selective urban ward was used for field survey using standard questionnaire regarding water consumption pattern linked with various socio-economic scenarios. Regression and ANFIS(Adaptive neurofuzzy inference system) models has been developed and compared the performance accuracy in modeling water consumption using climatic as well as socio-economic variables as inputs. It was found that the ANFIS model outpermed Regression model considering various statistical performance indices.

Keywords*: Urban water, climatic variables, socioeconomic deforms, Regression models, ANFIS models*

INTRODUCTION

The dynamics aspects of water consumption are very difficult to understand since it is associated with many parameters which affect the environment in an urban area. Climatic variation could be the one of the factor which influences the water consumption significantly. The Interlinking between climatic variables and water consumption are crucial in arid and semi arid regions. These climatic variables are time varying in nature and its behavior prediction is one of the challenging tasks to meteorological society all over the world, for proper modeling. To balance the water supply and demand accurate water consumption estimation is necessary, as it can provide a simulated view of future and identify sustainable management alternative.

Most of the research papers addressed the problems of estimating the water consumption using climatic and socio-Economic variables. Babel M.S (2007) developed a model based on the multivariate econometric approach. Randolph.B (2008) discusses the attitude of household to their water consumption
Municipal Residential water consumption pattern has many nonlinear and complex components which is difficult to explain by a linear relationship. Many researchers have been shown the relationship between water consumption and exogenous parameters are nonlinear. However majority of the short term water consumption estimation have treated the water consumption as time series and described the relationship using linear expansion.

Subsequently, for proper understanding of residential water consumption pattern, it is required to identify significant impact of climate variables. The existing literatures indicates that, municipal residential water

consumption is dynamic in nature and proper understanding of drivers of residential water demand are very essential in managing water resources and in the region of limited resources. Hence Residential Water consumption time series in a municipal water distribution system is periodic, time varying and somewhat nonstationary. So, appropriate estimation technique is required in modeling the municipal residential water consumption with higher accuracy.

There are many approaches to water consumption estimation including both mathematical and statistical one. Peng and Hongwei(2007) used an approach for short term forecasting of municipal water consumption based on the largest Lyapunov exponent of chaos theory. These conventional time series technique have served the community for a longer time in modeling the water consumption, but suffer from the assumption of stationary and linearity (Kermani & Teshnehlab,2008), hence reasonable accuracy is obtained from the conventional method. Municipal residential water consumption patterns should be model in a better way apart from the physical process of modeling, due to nonlinearity, periodic and time varying nature, for which conventional methods are weak in obtaining the desired accuracy.

To address complex and highly nonlinear type of data, soft computing technique provides an effective approach. Soft computing is a data-driven technique consists of fuzzy logic, neural computing, machine learning and probabilistic reasoning. Soft computing techniques are capable for analyzing stationary and non-stationary series, due to their good tolerance to uncertainty, partial truth and imprecision. The guiding principle of the soft computing is to exploit the tolerance for imprecision, uncertainty and partial truth to achieve tractability, robustness and low solution cost.

ANFIS is the famous hybrid Neuro-fuzzy for modeling the complex and non-linear systems. ANFIS incorporates the human-like reasoning through linguistic variables consisting of IF–THEN fuzzy rules. ANFIS consist, both the features FL and ANN.

In this work,two models such as regression and ANFIS has been developed to analyze the influence of Climatic variables includes Rainfall, Maximum temperature, Minimum temperature and Relative Humidity on modeling municipal residential water consumption Estimation. The model performance of Adaptive Neuro Fuzzy Inference system and multiple linear regression technique has been compared.

Study area

The present study covers the Fourth ward of Yelahanka city, shown in the figure 1, which is a suburban of Bangalore in the State of Karnataka, India. The city is at a height of about 915m above mean sea level. The city is lush green and has pleasant weather throughout the year. Summer season starts from the beginning of the March month and lasts until the end of May, with a temperature in the range 20^0C to 35^0C results in higher water consumption. At the end of May, the monsoon season starts and lasts until the end of September. Annual rainfall of city is 1140mm. Yelahanka is served by both south west and south east monsoon. Winters are mild and start from the mid of November to the end of February, with a temperature in the range 14^0 C to 24^0C.

METHODOLOGY

Climatic data such as Rainfall, Maximum Temperature, minimum Temperature and Relative humidity were collected on monthly basis from Karnataka state disaster management cell, yelahanka. Similarly water consumption data were collected from Bangalore Water supply and sewage Board (BWSSB) for a period of 10 years from 2004 to 2014. The monthly data set consist of 120 data points out of which 108 data points were used for training and 12 data points were used for testing.

For better understand of water consumption pattern in the proposed study, field survey was carried out with a prepared questionnaire. Questionnaire is handed over to the interested people

participated in the survey process, asking to fill the information containing various factors influencing the water consumption using climatic as well as socio-economic variables. This information was considered in framing the rules for ANFIS modeling. Field survey includes 260 houses of single and attached type. Survey data were divided on the basis of single, attached houses, number of members in family, age group, water bill, maximum usage of water per day.

Multiple Linear Regression Technique

The relationship between dependent and two or more independent variables were determined using multiple relation regression Technique by fitting a linear equation to training data. Each value of the independent variables is connected with the value of the dependent variables.

Based on Linear interval combination, less independent variable can be determined. The Multiple linear regression used to develop the model is shown in the equation below.

$$\beta_0 + \beta_1 x_1 + \beta_2 x_2 + \beta_3 x_3 + \beta_4 x_4 = Y$$

Models were developed using four input and single output combination with limited data, including four years and ten years. In the above equation, Y denotes the target strength and x_1, x_2, x_3 and x_4 represents the independent variables. The above equation is a linear function of unknown parameters, β_0, β_1,β_2,β_3, β_4 called partial regression coefficients..

Adaptive Neuro Fuzzy Inference system (ANFIS) Technique

Adaptive Neuro Fuzzy Inference system (ANFIS) is the famous hybrid approach for modeling the complex non-linear systems, which combines the features of both Fuzzy and Neural Network. The ANFIS having a learning algorithm composed of least square and back propagation method called hybrid learning algorithm. The integration of Fuzzy Logic and neural network has given the path for new hybrid approach. There is no systematic procedure to define the membership functional parameters in fuzzy logic. To construct the fuzzy rule the definition of premises and consequences as fuzzy set is necessary. On the other side Artificial Neural Network has the ability to learn from input and output combination and adapt to it in a better manner. The basic problem in fuzzy system includes, defining the membership function and fuzzy rules is eliminated by using ANFIS. Due to effectively learning capability of Artificial Neural Network, automatic fuzzy rule generation and parameter optimization will be in a better way. (yurdusev & Firat, 2009). Adaptive Neuro Fuzzy inference system has a greater potential to capture the advantage of both Neural network and fuzzy logic in a single frame work.

RESULTS AND DISCUSSION

Table 1 shows the correlation coefficient of various input parameters to output water consumption.The minimum temperature was observed having higher correlation as compared to other parameters.The rainfall is having lowest correlation such as 0.16.The regression analysis results are presented in the table 2.To improve the model accuracy, by increasing the rate of convergence, Adaptive Neuro fuzzy inference system is used for four combined input and single output combination. Due to self rule framing criteria and self learning criteria of ANFIS, rate of convergence will improve, results in better mapping of input-output combination. Model having 243 fuzzy rules were created by grid partition and fuzzy inference system trained by hybrid network. The results obtained were compared with the observed values to find out performance of the models. Table 2, shows the results of ANFIS model. From the overall performance it is found that soft computing methods such as ANFIS shows improved result compared to Regression technique. The results of all the developed models using various techniques for four combined input and single output combination were presented in the table 2. Observed and estimated value of water consumption is shown in the figure 2 for ANFIS. Although developed hybrid ANFIS model performed better, it required higher number of rules for computation and increasing the number of rules leads to slow convergence results in

lower performance in accuracy of the model. Hence developed Single Fuzzy and ANFIS models, may not get the higher accuracy in the case of highly nonlinear data.

Discussion of the Field Survey

In monsoon season, higher rainfall, minimum temperature (< 30^0) and maximum relative Humidity (>87%), leads to more water consumption.
In winter seasons, lesser rainfall, minimum temperature, water consumption is almost same as in monsoon season.
In summer season, higher rainfall (more compare to winter season and less compare to monsoon season), maximum temperature and maximum relative humidity leads to lower water consumption.
Water consumption trend varies irrespective of the seasons.
Most of the responders do not have awareness about the water availability and scarcity.
Results indicate that, only few residents and education institution adopted the rainwater harvesting and recycling methodology.

CONCLUSIONS

In the present research work, Temperature and Rainfall were found to be most important parameters which affect the model performance in estimating the municipal residential water consumption. Whereas Minimum temperature and Relative humidity were treated as significant variables, which improves the model accuracy.
Hybrid Model, Adaptive Neuro Fuzzy Inference system performed better compared to Regression Techniques in modeling water consumption.

ACKNOWLEDGEMENTS
Author acknowledged Dr. H J Surendra, Associate professor, Atria institute of technology,Bangalore,India for providing necessary data.

REFERENCES
[1]Babel, M.S., Das Gupta, A. and Pradhan, P. (2007). "A multivariate econometric approach for domestic water demand modeling: An application to Kathmandu, Nepal". Water resource Management., Vol 21, pp; 573-589.
[2]Kermani, Z., and Teshnehlab, M.(2008). "Using adaptive Neuro fuzzy inference system for hydrological time series prediction". Applied soft computing., no.8, 928-936.
[3]Peng, Z. and Hongwei. Z.(2006). "Short term forecasting of urban water consumption based on the largest Lyapunov Exponent". ISSN 1006-4982, Vol.13, No.3, pp: 191-194.
[4]Randolph. B. and Troy,P.(2008). "Attitude to conservation and water consumption". Environmental science and policy., Vol-11, 441-455.
[5]Yurdusev, A. and Firat, M.(2009). "Adaptive Neuro Fuzzy Inference system approach for municipal water consumption modeling". Journal of hydrology., 265: 225-234.

Table 1 Correlation Coefficient of all the variables

CC	RF(mm)	T-Max (°C)	T-Min (°C)	RH (%)	WC (MLD)
RF	1.00	0.09	0.05	0.34	0.16
T-Max	0.09	1.00	0.42	0.09	0.24
T-Min	0.05	0.42	1.00	0.16	0.66
RH	0.34	0.09	0.16	1.00	0.04
WC	0.16	0.24	0.66	-0.04	1.00

Table 2 results of developed model of all the techniques (Four inputs and one output)

Type	Regression	ANFIS
Correlation Coefficient (CC)	0.49	0.97
Percentage Error (PE) in %	74.00	11.00
RMSE (MLD)	83.22	12.95

Fig.1 Study area

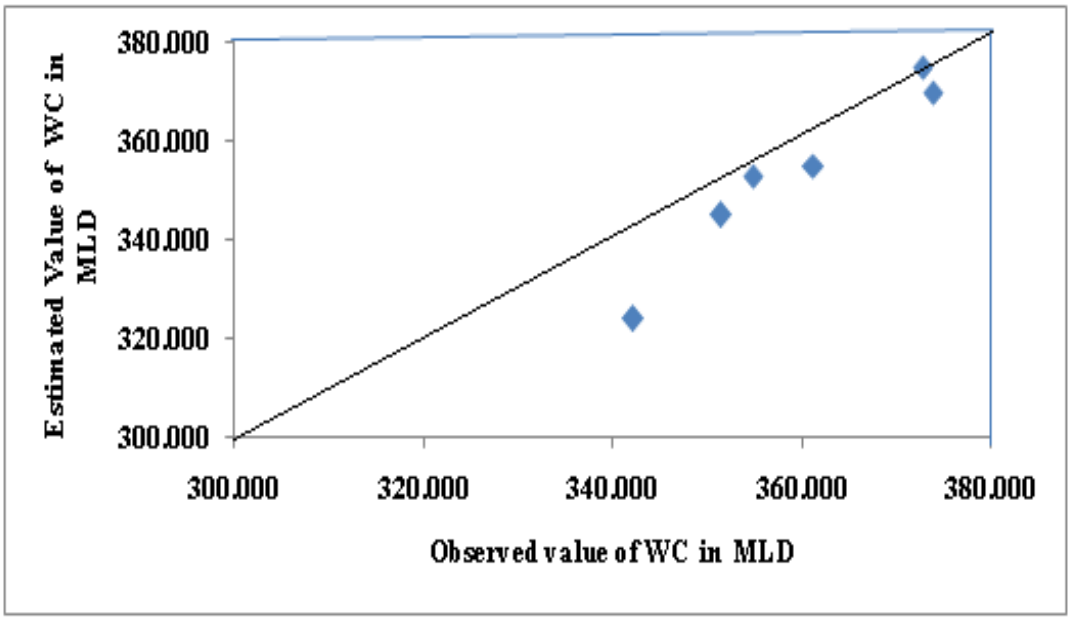

Fig. 2 Model performance of ANFIS

8th International Engineering Symposium - IES 2019
March 13-15, 2019, Kumamoto University, Japan

Groundwater Investigation using Electrical Resistivity Technique in Karkala Taluk, Udupi district, Karnataka State, India

Shannon Meryl Pinto[1], Vignesh Bhat[1], Lokesh K N[2] and Naveenchandra B [3]

1 *Department of Civil Engineering, National Institute of Technology Karnataka, Surathkal, Srinivasnagar Post– 575 025, India Email: shannonmeryl@gmail.com*
2 *Department of Civil Engineering, National Institute of Technology Karnataka, Surathkal, Srinivasnagar Post– 575 025, India Email: knl.lokesh@gmail.com*
3 *Bellare GIS India Pvt. Limited, Serenity Complex, Udupi-576101, India, Email: naveensde@gmail.com*

ABSTRACT: Electrical resistivity survey was carried out in Karkala Taluk of Udupi district to identify potential groundwater zones. The area comprises of laterites, granite and Archean gneisses basement with occasional intrusions of dolerites. A total of 20 Vertical Electrical Soundings (VES) at different locations were carried out using Schlumberger electrode configuration. The measured apparent resistivity values were interpreted by curve matching technique using IPI2WIN software. The resulting curve types are H, KH, HK, QH and HA type. Interpretation of curve type shows that Karkala taluk has a wide range of resistivity variations with the change in litho units and soil layers. From the results it is observed that the occurrence of groundwater is at shallow level in most of the location as the bedrock is encounter at intermediate depth. This paper aims to highlight the application of the VES in investigation of groundwater potential zones using resistivity and its thickness of subsurface layers.

Keywords: *Vertical electrical sounding, Groundwater potential zone*

INTRODUCTION

Our very own survival on planet depends on the basic resource of water, which is nature's valuable gift to mankind. This nature's gift is now becoming a crucial source throughout the world. As groundwater is the largest available source of freshwater, it is a necessity to identify groundwater potential zone for continuous and sustainable development of both socio-economic and agricultural developments.

The electrical resistivity method is considered to be the most suitable and efficient method for groundwater exploration. It is one of the geophysical methods that studies the nature of electrical current passing within the earth and to identify the change in resistance of rock layers beneath the soil surface. This is achieved by passing a direct current (DC current) that has high voltage into the ground. It is based on the concept of subsurface determination, which can yield useful information like the depth to water table, depth to basement rock, structure, composition and water content of the soil (Nwankwo 2011; Panda 2018). The conventional Schlumberger resistivity sounding is extensively used for routine groundwater investigations both in alluvial and hard rock terrain (Rao 2003; Kumar 2012). Hence, an attempt has been made to locate potential zones for groundwater exploration.

STUDY AREA

The study area Karkala taluk falls within Udupi district of Karnataka. The study area lies between 13°5'39.93"N to 13°31'11.712"N latitude and 74°49'25.63"E to 75°12'29.88 "E longitude covering an area of 1062 km^2

(Fig.1). The eastern part the area is covered by the beautiful Western ghats and rest of the area is also lush green because of the agricultural and plantation activities which is the major source of income for the people of this area.

Geology

A detailed information on lithology is most important aspects for classifying the layers because the rocks exhibit a wide range of electrical resistivity (Shenoy & Lokesh 2000). For instance, igneous rocks tend to have the highest resistivity, sedimentary rocks are the most conductive, largely due to their high pore fluid content and metamorphic rocks contain transitional but the overlapping resistivity (Reynolds 2011). The study area lies on the south-western part of Western Dharwar Craton comprising mainly of Precambrian (Archean) Peninsular Gneiss, the Western Ghats Belt of Bababudan group of Dharwar super group, Phanerozoic laterite and the most recent alluvium. The major lithology found in the parts of Western Ghats includes metabasalt, charnockites, granitic gneiss, greywacks and amphibolites. In the study area, laterites form a thick mantle capped over underlying granite. Along with granite, the area also possesses saprolite at places and lateritic soil with lithomargic clay is also present.

METHODOLOGY

Electrical resistivity method has gained considerable importance in the field of groundwater exploration because of its low cost, easy operation. In the present study, about 20 Vertical Electrical Soundings (VES) have been carried out using SSR-MP- ATS, resistivity meter in the study area. The AB/2 separations have measured by Schlumberger configuration. The measured apparent resistivity signals have been interpreted by curve matching technique using this IPI2WIN software. Many researchers have successfully used software technique for prospecting ground water (Yadav et al. 1997; Kumar et al. 2012). The interpretation involves the determination of the geoelectrical layers associated with its true depth, thickness, and resistivity of each layer from the obtained curves (Barseem et al. 2015).

RESULTS AND DISCUSSION

Electrical resistivity method is useful to investigate the nature of subsurface formations by studying the variations in their resistance in flow of electrical current and hence determines the occurrence of groundwater. As the present study area is a hard rock terrain, the response shows high resistivity due to low flow of electrical current. The resistivity values obtained from the plotted curves were processed and interpreted by using curve matching techniques. The true resistivity and thickness of layers of the analysis of VES is represented in Table 1. The various curves types were interpreted and are discussed.

HK type curve

The HK type curve is defined by the resistivity order of $\rho1 > \rho2 < \rho3 > \rho4$. VES 1, 8 and 17 represents profiles having HK curve type (Fig. 2(a)). The top layer of soil has higher resistivity values followed by relatively lower resistivity values in the next layer when compared with topsoil. It reveals the possible existence of laterite and lithomargic clay. The third layer shows a sudden increase in resistivity values with the indication of the presence of massive rock. The fourth layer following lower resistivity value might be due to the fractured rocks capable of yielding moderate groundwater.

H type curve

The H type curve is defined by the resistivity sequence of $\rho1 > \rho2 < \rho3$. VES 3, 4, 5, 12 and 16 represents profiles having H curve type (Fig. 2(b)). The topsoil has higher resistivity values and the second layer with relatively lower resistivity values. It reveals the probable existence of lithomargic clay which can act as better conduits for groundwater movement down to deep aquifers if present or forms shallow aquifers. There is increase in resistivity value of third layer which shows an indication of non weathered rock.

QH type curve

The QH type of curve is defined by the resistivity order of ρ1 < ρ2 < ρ3 > ρ4. The VES 6, 13, 18, 19 and 20 represents profiles having QH curve type, where the resistivity of first, second and third layers are defined by relatively decreasing resistivity. The second layer may also correspond to laterite with thickness varying between 3m to 9m. The fourth layer shows relatively lesser resistivity values indicating highly weathered zones in association with fracture zones. In general a QH type curve indicates good groundwater potential zones. Fig. 2 (c & e) shows the interpretation of VES curves of QH Type.

HA type curve

HA type curve is defined by the resistivity order of ρ1 > ρ2 < ρ3 > ρ4. VES 2, 9, 10, 11 and 15 represent HA curve type. In this curve type, the resistivity of the first layer always exceeds the resistance of the second layer, followed by a progressive increase in the resistivity of successive layers in terms of depth. In most cases, just beneath the third layer, an immediate increase is observed in the resistivity of the fourth layer which can be the sign of a massive hard rock formation. The interpretation of VES curves of HA-Type is shown in Fig. 2(d). The top layer corresponds to soil with high resistivity values, showing signs of sand grains derived from underlying weathered rocks and thickness of the topsoil layer vary from 0.5 m to 1.30 m. The second layer is highly weathered as depicted by fall in resistivity values and followed by a massive rock formation which is indicted by increase in the resistivity of the successive layer. The HA curve type indicates poor groundwater potential area, but in some cases water may stored at shallow depth in such areas.

KH-type curve

The KH type of curves are defined by the resistivity order of ρ1 < ρ2 > ρ3 < ρ4. VES 7 and 14 represents profiles having KH curve type. In the VES profiles belonging to this curve type show highly conductive top soil layer and the thickness of the layers vary between 0.2 to 0.5m. High resistivity is observed in the second layer because of the presence of laterite or gneiss, and a sudden decrease in the third layer indicating the possibility of water saturation in the third layer due to the presence of fractured zones. Fig. 2(f) shows the interpretation of KH- curve type.

From interpretation of sounding curves, it is found that topsoil of Karkala taluk show a high range of resistivity from 600 to 3500 Ohm-m with a thickness of about 0.5-2m. Resistivity of laterites normally varies between 750 Ohm-m and 1500 Ohm-m with a normal thickness range of 4 m to 12 m and nature of laterites induce the infiltrated water to escape as base flow. Laterite is underlain by lithomargic clay which forms the shallow aquifers.

Resistivity of gneisses in Karkala taluk varies from 300 Ohm-m to infinity. From the field curves it is observed that gneisses have deep seated fractures. These fractures are potential zones for groundwater development.

CONCLUSIONS

The VES of Schlumberger configuration survey has effectively enabled to identify the potential groundwater zones in Karkala taluk of Udupi district**.** Based on the VES investigation; interpreted curves belonging to KH and QH type show good groundwater potential under the depths ranging from 4 to 71 m. The HK and H type curve indicates moderate groundwater potential zone below at shallower depths. In HA type curves represent poor groundwater potential zones.

From the results it is observed that the occurrence of groundwater is at shallow level in most of the location as the bedrock is encounter at intermediate depth. This paper aims to highlight the application of the VES in investigation of groundwater potential zones using resistivity and its thickness of subsurface layers.

ACKNOWLEDGEMENTS

The authors would like to thank DST-NRDMS for providing financial support and NITK for providing all necessary facilities and constant encouragements for doing this research work.

REFERENCES

[1] Barseem M S et al (2015), Geoelectrical exploration in the south Al Qantara Shark area for supplementary irrigation purposes–Sinai–Egypt, NRIAG Journal of Astronomy and Geophysics, Vol 4, No. 2, pp. 163-178.

[2] Kumar, T J R et al (2012), Vertical Electrical Sounding for Groundwater Prospecting in Uppodai of Tambaraparani River Tirunelveli and Thoothukudi Districts, Tamil Nadu, India, International Journal of Environmental Engineeringand Management, Vol 3, pp. 147-157.

[3]Nwankwo, L I (2011), 2D resistivity survey for groundwater exploration in a hard rock terrain: A case study of MAGDAS observatory, UNILORIN, Nigeria, Asian Journal Earth Science, Vol. 4, No.1, pp. 46-53.

[4]Panda, K P et al (2018), Mapping lithological variations in a river basin of West Bengal, India using electrical resistivity survey: implications for artificial recharge, Environmental Earth Sciences, Vol. 77, No. 17, pp. 626.

[5]Rao, J P et al (2003), Geoeletrical Data Analysis to Demarcate Groundwater Pockets and Recharge Zone in Champavathi River Basin,Vizianagaram District, A.P., Journal Ind Geophysis Union, Vol. 7, No. 12, pp. 105-113

[6]Reynolds, J M (2011), An introduction to applied and environmental geophysics, John Wiley & Sons.

[7]Shenoy, K N and Lokesh, K N(2000) Electrical resistivity survey for Groundwater exploration in Udupi Municipal area. Journal of Applied Hydrology, Vol. 13, No 3-4, pp. 30-35.

[8]Yadav, G S et al(1997) Fast method of resistivity sounding for shallow groundwater investigations, Journal of Applied Geophysics , Vol. 37, No. 1,pp. 45-52.

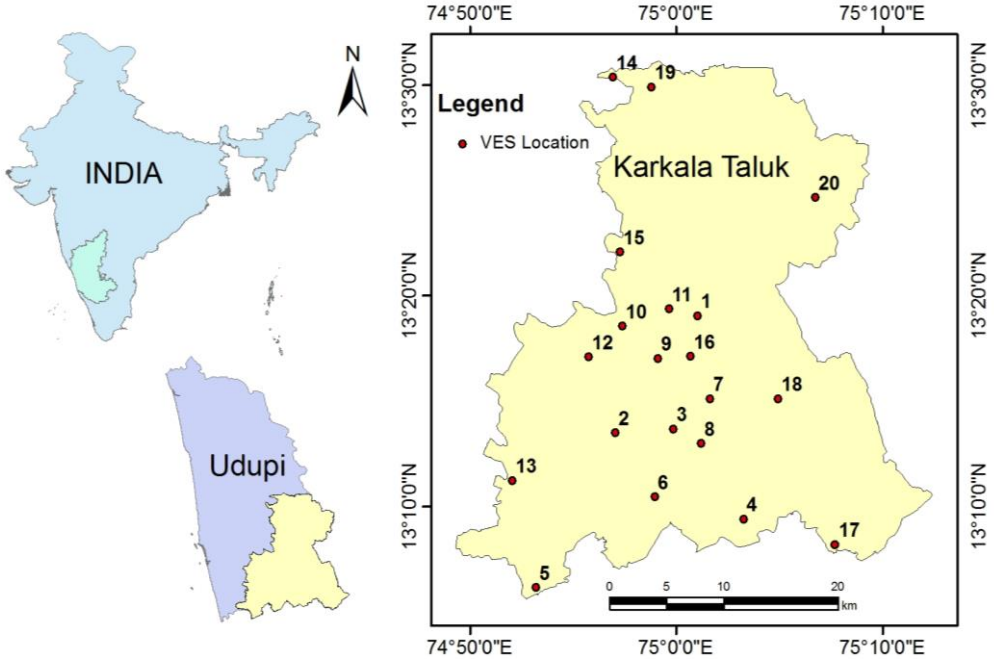

Fig 1: Study area map with VES survey locations

Table 1: Resistivity and thickness of layers for VES

VES no.	Location	Type of Curve	Resistivity (ohm-m)				Layer thickness (m)		
			ρ_1	ρ_2	ρ_3	ρ_4	h_1	h_2	h_3
1	Marna	HK	1169	401	1828	1053	0.5	0.193	12.3
2	Nakra	HA	3616	2421	3598	5237	1.18	1.87	30.2
3	Pervaje	H	631	411	3607		1.74	5.95	
4	Renjala	H	1301	184	1089		7.67	5.34	
5	Sankalkariya	H	1589	382	5294		1.21	16.5	
6	Sanoor	QH	2036	1278	288	5504	0.922	4.5	45.1
7	Dugra	KH	712	1693	257	5412	0.5	15.5	13.3
8	Tellar	HK	1068	356	7357	5153	0.803	1.42	18.8
9	Yennehole	HA	891	368	1365	4591	1.16	0.681	32.1
10	Yeralapadi	HA	2509	1301	2119	6207	0.674	6.8	39.7
11	Ajekar	HA	1850	1679	4290	6467	1.26	3.84	9.66
12	Ballur	H	1558	1051	5837		1.19	24.5	
13	Belman	QH	1952	631	171	1287	1.42	9.86	20.7
14	Belva	KH	1179	5357	957	2131	0.22	1	71.5
15	Yellare	HA	1462	763	1462	5739	1.15	4.82	28.7
16	Hermunde	H	3277	2411	5125		0.632	4.88	
17	Hosmar	HK	1168	550	1568	839	0.906	10.3	1.29
18	Kervashe	QH	2169	1759	1000	3344	0.712	8.3	17.5
19	Belanje	QH	1620	660	114	5577	0.496	12.8	7.32
20	Kudlu	QH	2117	664	77	1257	0.5	3.32	3.56

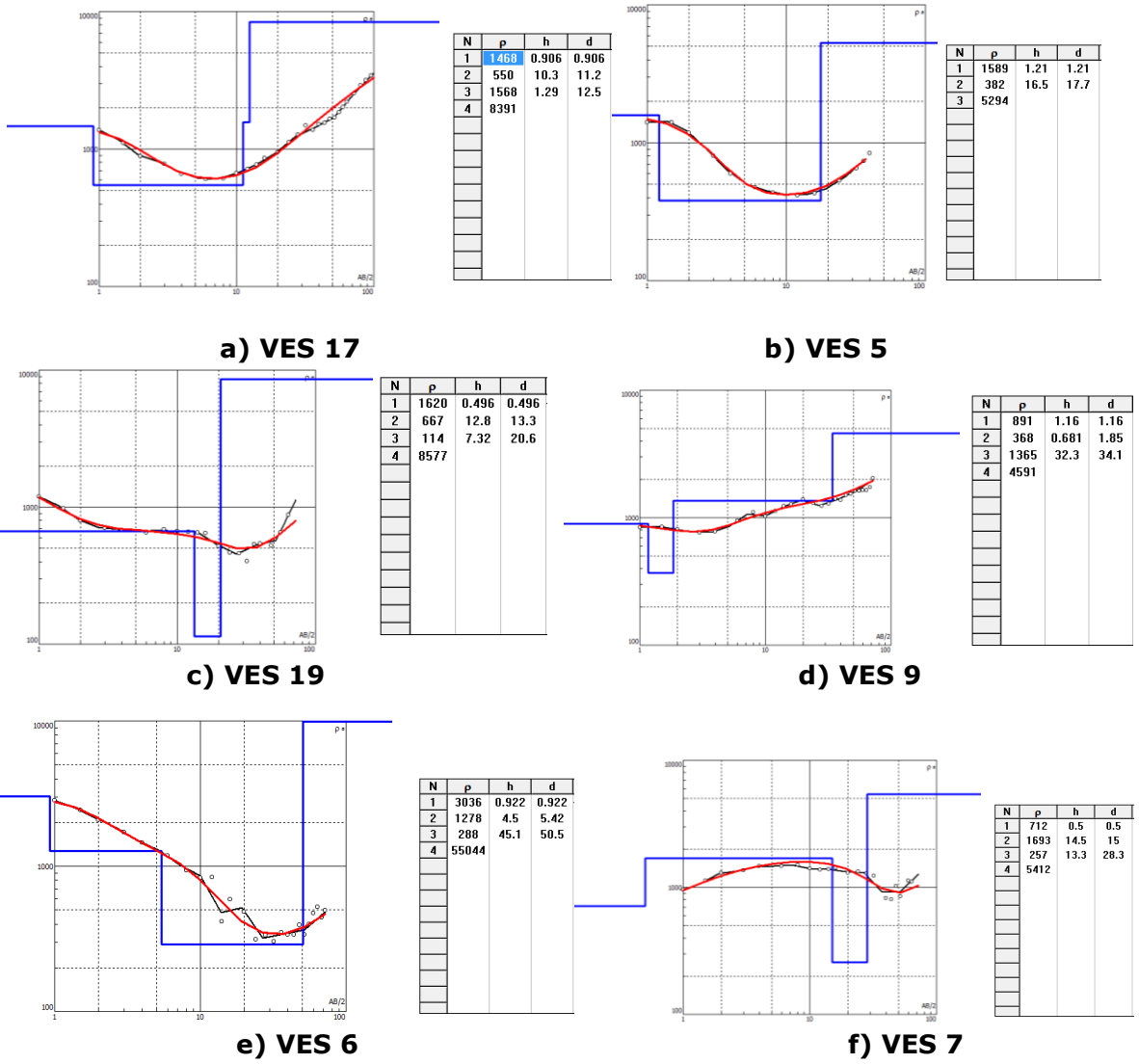

N	ρ	h	d
1	1468	0.906	0.906
2	550	10.3	11.2
3	1568	1.29	12.5
4	8391		

a) VES 17

N	ρ	h	d
1	1589	1.21	1.21
2	382	16.5	17.7
3	5294		

b) VES 5

N	ρ	h	d
1	1620	0.496	0.496
2	667	12.8	13.3
3	114	7.32	20.6
4	8577		

c) VES 19

N	ρ	h	d
1	891	1.16	1.16
2	368	0.681	1.85
3	1365	32.3	34.1
4	4591		

d) VES 9

N	ρ	h	d
1	3036	0.922	0.922
2	1278	4.5	5.42
3	288	45.1	50.5
4	55044		

e) VES 6

N	ρ	h	d
1	712	0.5	0.5
2	1693	14.5	15
3	257	13.3	28.3
4	5412		

f) VES 7

Fig 2: Interpretation of VES curves

8th International Engineering Symposium - IES 2019
March 13-15, 2019, Kumamoto University, Japan

Spatial Interpolation of Rainfall Data with ArcGIS approach.

Ayilobeni Kikon [1], Paresh Chandra Deka [2]

1 *Department of Applied Mechanics and Hydraulics, National Institute of Technology Karnataka, Surathkal, Mangalore 575025, India. email: ayilobeni@gmail.com*
2 *Department of Applied Mechanics and Hydraulics, National Institute of Technology Karnataka, Surathkal, Mangalore 575025, India. email: dekanitk@gmail.com*

ABSTRACT: Accurate measurement of rainfall and understanding its distribution is crucial for water management and planning for future water use. In this study, the Inverse Distance Weighted (IDW) method was used to estimate the rainfall distribution in the Pune District, Maharashtra, India. For the interpolation, five years rainfall data, i.e. 2009-2013 from 16 weather stations were taken into consideration to analyze the rainfall distribution for the given periods both annually and monsoon season. Data from 12 rain gauge stations were used for validation and interpolated to obtain the predicted value. The Root Mean Square Error (RMSE), Mean Relative Error (MRE) and the Coefficient of Determination (R^2) were used as performance indices for evaluation. The analysis gives high correlation coefficient values of over 0.995 which confirms the suitability of IDW method for spatial interpolation to predict the probable rainfall data in the District of Pune and has the potential to be extrapolated to other locations.

***Keywords**: Inverse Distance Weighted (IDW), Spatial Interpolation, Rainfall data.*

INTRODUCTION

Rainfall is one of the most significant meteorological parameters. Rainfall data are recorded as observational data through the designed weather stations (Chen et al., 2012). However, rainfall data are incomplete because of different factors such as the missing rainfall data, insufficient weather stations in the study region. To analyze the problems of the limited rainfall data, a wide range of spatial interpolation techniques has been established. Also, there are better methods which are appropriate and have been used for rapid estimation (Noori et al., 2014).

Spatial interpolation is the process of using the known point values to estimate the values at the other points. It is commonly used in modeling spatial distribution of phenomena such as temperature, precipitation, soil properties, etc. Spatial interpolation has a wide range of applications in Geographic Information System (GIS). Although spatial interpolation is widely used in analyzing and comparing, it becomes difficult to identify an optimum spatial interpolation algorithm (Piazza et al., 2015). The interpolation method has been used in predicting the values of unknown locations collected using the known location data and the methods widely used by researchers are Kriging, Inverse Distance Weighted method, Spline, Trend (Mahalingam et al., 2015). Many types of spatial interpolation techniques have been developed and categorized in different several ways to address the specific applications and for the handling of specific properties of the spatial data (Yang et al., 2015).

The present study has been conducted to analyze the variation of rainfall using Inverse Distance Weighted (IDW) method for a period of five years from 2009-2013 in the study region of Pune District of Maharashtra, India. Rainfall distribution for both yearly (annually) and monsoon period was interpolated using the IDW method.

STUDY AREA and DATA USED

The district of Pune is located between 17° 54′ to 19°24′ North Latitude and 73°17′ to 75°10′ East Longitude of Maharashtra state, India. The district has a geographical area of 15,642 sq. Km covering about 5.10% of the total geographical area of the state. The landscape of Pune district is distributed triangularly in Western Maharashtra at the foothill of the Sahyadri Mountains or Western Ghats. The climate of Pune forms a part of tropical monsoon land and therefore, it shows a significant seasonal variation in temperature as well as rainfall conditions. The climate in the western part of the district is cool whereas the Eastern region is hot and dry. Due to the geographical conditions within the district, the rainfall has been unevenly distributed. Figure 1 shows the study area with locations of the rain gauge stations

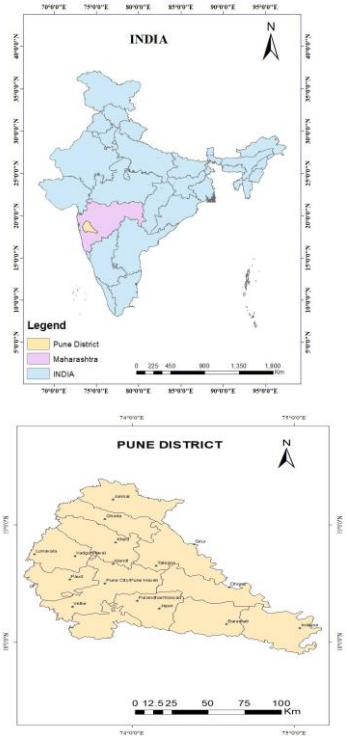

Figure 1. Study area with locations of rain gauge stations.

The names of the rain gauge stations are: Alandi, Baramati, Dhond, Ghoda Ambegaon, Indapur, Jejuri, Junnar, Khed, Lonavala, Paud, Pune city/Pune haveli, Purandhar/Sasvad, Sirur, Talegaon D-Dhera, Vadgaon Maval, Velhe. In this study, 16 rain gauge stations located at different places of Pune District were considered for the analysis. The rainfall data was collected from the archive of the National Data Centre of India Meteorological Department (IMD), Pune. The dataset is extracted using data management tools in ArcGIS. The data period of study was taken from 2009-2013 (5 years). All these 16 rain gauge stations were scattered at different places of Pune District. The yearly and monsoon rainfall distribution from 2009-2013 for the 16 rain gauge stations are shown below:

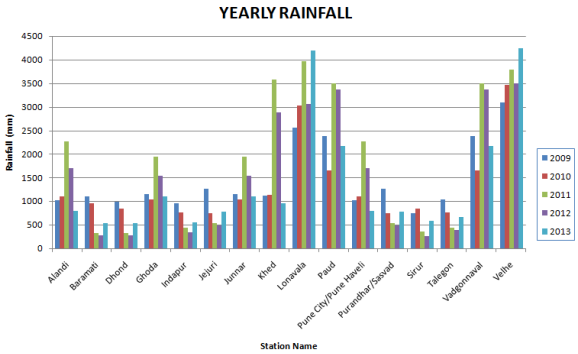

Figure 2. Rainfall distribution for the 16 rain gauge stations yearly from 2009-2013.

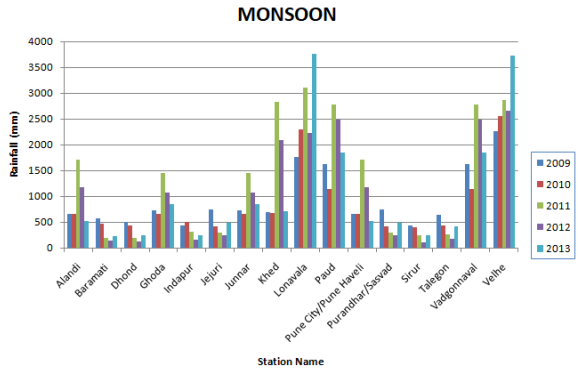

Figure 3. Rainfall distribution for the 16 rain gauge stations for monsoon from 2009-2013.

METHODOLOGY

The Inverse Distance Weighted (IDW) is a part of interpolation method called the

deterministic interpolation. This method allocates the interpolated values to locations because of surrounding measured values and mathematical formulas to create a surface from point data. The monthly and yearly rainfall values was used in the assessment and evaluation using the IDW method. The yearly and monsoon rainfall data at 16 rain gauge station site were sampled for a period of 5 years i.e., 2009-2013 and interpolated using IDW method to know the distribution of rainfall both yearly and for monsoon period in the study region. Also, a validation was done for one-year data i.e., 2013 and the results were compared to check the accuracy and errors in the observed rainfall data. Figure 4 shows the flowchart which shows the different steps that was adopted in the study.

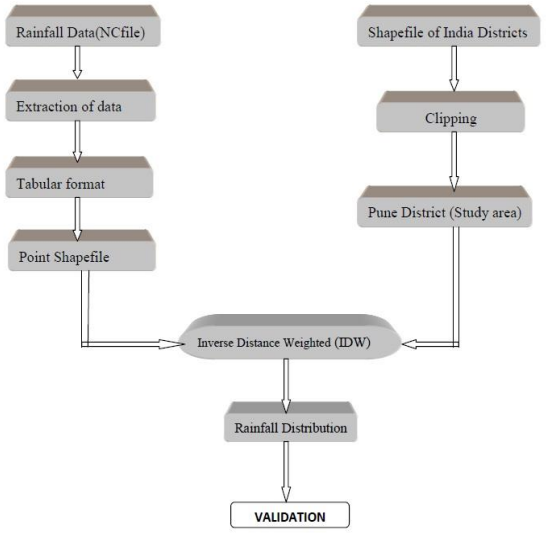

Figure 4. Flowchart showing the different steps adopted in the study.

In this study, rainfall data of 16 rain gauge stations of Pune district of Maharashtra, India were used to interpolate using IDW method and adopted a validation as an appropriate method to assess the accuracy of the spatial interpolated rainfall data. This study had utilized yearly and monthly data for a 5-years period (2009-2013) for the analysis. The rain gauge station location was acquired from IMD Pune. The extracted rainfall data were interpolated by using spatial analyst tools from ArcGIS- IDW method to know the variation of rainfall in different regions of the study area. For one year i.e., 2013 validation was done and compared with the observed rainfall data to estimate the accuracy of the rainfall data yearly and monsoon period. 12 rain gauge stations were interpolated using IDW method to find out the predicted rainfall data which was further use for the calculations in validation. The data interpolated was compared with the observed data.

The Root Mean Square Error (RMSE) and Mean Relative Error (MRE) were calculated to assess the performance of the IDW model. MRE reflects the relative accuracy of the interpolation and RMSE is an indicator of the magnitude of extreme errors. The coefficient of determination (R^2) was also evaluated to check whether the predicted data fits the observed data. To interpolate the unknown rainfall data, 12 known stations were interpolated using IDW method both yearly and monsoon and the interpolated values for the remaining 4 stations were identified and the RMSE, MRE and coefficient of determination for yearly and monsoon were calculated.

Calculation of RMSE value:

The RMSE is also know as Root Mean Square Deviation (RMSD) which is used to measure the values between the observed values and the predicted values. Based on the observed and the predicted data, RMSE values was calculated using the equation:

$$RMSE = \sqrt{\frac{\sum_{i=1}^{N}\left(X_{obs,i} - X_{pre,i}\right)^2}{N}}$$

Calculation of Coefficient of Determination (R^2):

The coefficient of determination is the key output of the regression analysis. It is interpreted as the proportion of the variance in the dependent variable that is predictable from the independent variable. Its value ranges from 0 to 1.

$$R = \frac{N\sum X_{obs} X_{pre} - \sum X_{obs} \sum X_{pre}}{\sqrt{N\sum X_{obs}^{\ 2} - \left(\sum X_{obs}\right)^2} \sqrt{N\sum X_{pre}^{\ 2} - \left(\sum X_{pre}\right)^2}}$$

Calculation of Mean Relative Error (MRE):

The MRE is a residual based measure which indicates whether the model yields positive or negative estimates relative to its observation. MSE is calculated using the equation:

$$MRE = \frac{1}{N}\sum_{i=1}^{N}\left(\frac{X_{pre} - X_{obs}}{X_{obs}}\right)$$

From the above equations, X_{obs} and X_{pre} represents the observed and the predicted values of the rainfall, N represents the total number of data period being used.

Results and Discussion:

From the rainfall distribution maps which has been evaluated using Inverse Distance Weighted method, we can find that the district of Pune has a wide range of rainfall varying from 100mm to 3600 mm during monsoon season for the period of 5 years i.e. from 2009-2013. Most of the region had received rainfall ranging from 100mm to 1200mm in that period of study. Since the western part of the study area is a hilly region and covered with forest, therefore there is a changing pattern of rainfall during the monsoon season which is seen mostly in western part of the region. There is not much variation of rainfall towards the eastern part. The rainfall maps which has been interpolated using Inverse Distance Weighted method showing rainfall distribution for the study region during monsoon for a period of 5 years from 2009-2013 is shown from Figure 5.1 to 5.4

The rainfall distribution was also done on yearly basis using the interpolation method. Here the rainfall distribution varies ranging from 300mm to 4200mm yearly for a period of 5 years (2009-2013). Most of the rainfall had occurred in the western part of the region. There has been a variation of rainfall in the western region but towards the eastern region there is not much variation in rainfall. Also, the eastern region had received less rainfall as compared with the western region.

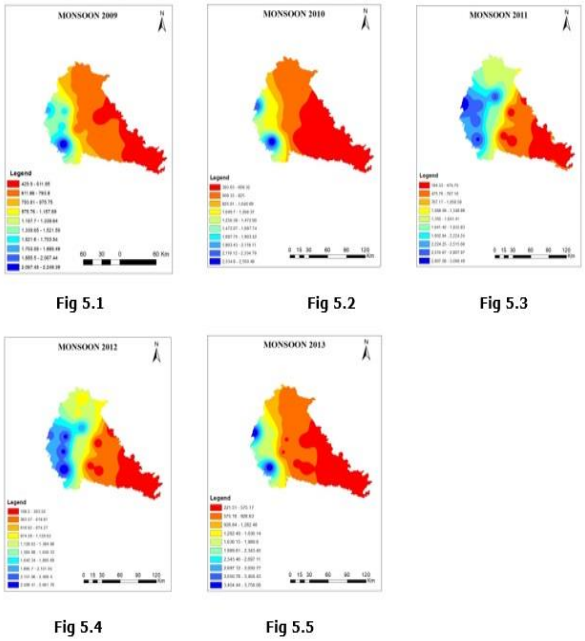

Figure 5.1-5.5 Interpolation maps using IDW during monsoon from 2009-2013

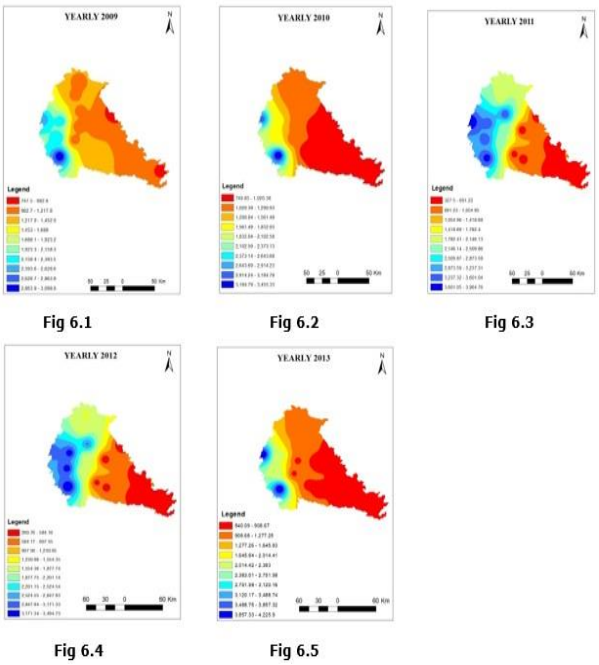

Figure 6.1-6.5 Interpolation maps using IDW for yearly from 2009-2013.

Validation was done for the year 2013 both yearly and monsoon season using the interpolation method of IDW. The validated results were compared with the observed

values and the required calculations were done. Figure 7.1 and 7.2 shows that interpolated maps for the validation both yearly and monsoon (2013) of the study area. The rainfall distribution ranges from 540mm to 4200mm and 200mm to 3700mm respectively for yearly and monsoon.

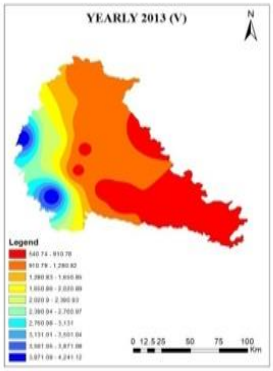

Fig. 7.1

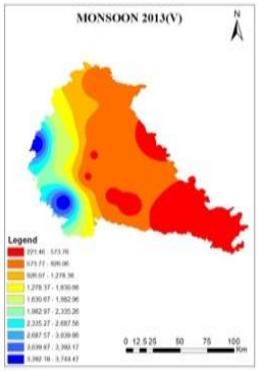

Fig.7.2

Figure 7.1-7.2 Interpolation maps for validation both yearly and monsoon (2013)

Table 1 and Table 2 shows the RMSE, MRE and R^2 providing the range of error.

Table 1. Table showing the RMSE, MRE and R^2 value yearly for 2013

Station Name	Observed	Predicted	RMSE (mm)	Mean Relative Error	Coefficient Determination (R^2)
Dhond	539.9516	884.40655	414.5	.046	0.996
Ghoda Ambegaon	1106.778	1288.80115			
Paud	2174.403	2102.83447			
Talegaon	671.080165	1045.38488			

Table 2. Table showing the RMSE, MRE and R^2 value for monsoon 2013

Station Name	Observed	Predicted	RMSE (mm)	Mean Relative Error	Coefficient Determination (R^2)
Dhond	234.4883	519.415344	82.276	0.01	0.97
Ghoda Ambegaon	846.586	887.107727			
Paud	1836.983	1669.17261			
Talegaon	405.4027	412.316405			

The graph showing the relationship between the predicted rainfall and the observed rainfall for the validated year is shown in Figure 8.1 and 8.2 for yearly and monsoon. The graph shows the comparison of rainfall interpolation with observed rainfall data for the year 2013. It shows that the coefficient of determination (R^2) has high value i.e., 0.996 for yearly and 0.97 for monsoon which indicates a very minimum error.

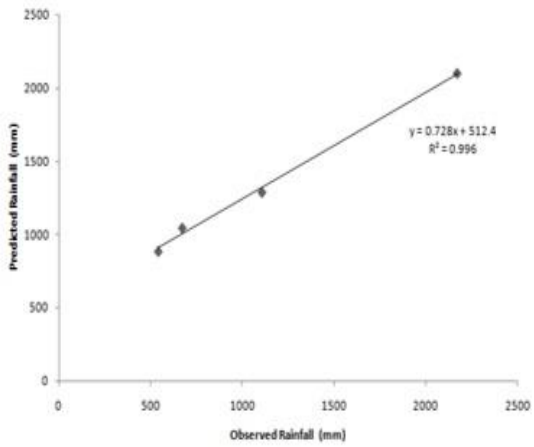

Figure 8.1 Comparison of Rainfall interpolation with observed yearly for the year 2013.

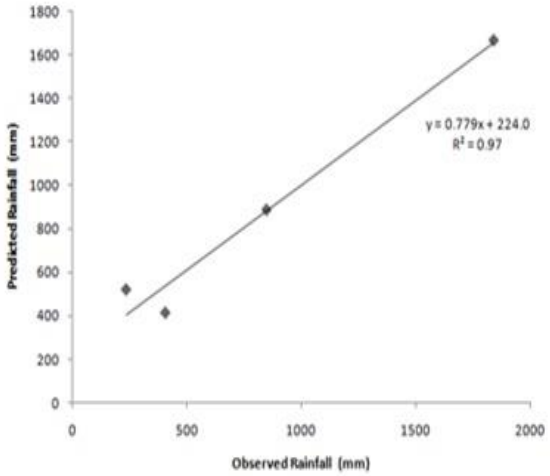

Figure 8.2 Comparison of rainfall interpolation with observed monsoon rainfall for the year 2013.

Conclusion

From the study, we conclude that Inverse Distance Weighted method shows time saving alternative and easy technique producing high accuracy results and is considered as a suitable spatial interpolation method of rainfall. During the period from 2009-2013, there has been a

wide variation of rainfall in the study region. Most important characteristic of the Indian climate is monsoon therefore, rainfall variations during monsoon may have impacts on the vegetation, ecosystems, water resources and hydrology, etc. Since the western part of the study area lies on the windward side, it shows dominance of high amount of rainfall due to the South-West monsoon blowing from Arabian Sea branch. The South-East part of the study area lies on the leeward side or in the rain shadow region and hence receives less rainfall compared to the western part. Most of the South-East parts of the districts shows drought features. The region also has a spatial variability of rainfall and hence the importance of interpolating can be viewed.

References

[1] Chen, F. W., & Liu, C. W. (2012). Estimation of the spatial rainfall distribution using inverse distance weighting (IDW) in the middle of Taiwan. *Paddy and Water Environment*, *10*(3), 209-222.

[2] Noori, M. J., Hassan, H. H., & Mustafa, Y. T. (2014), "Spatial estimation of rainfall distribution and its classification in Duhok governorate using GIS." *Journal of Water Resource and Protection*, *6*(02), 75.

[3] Yang, X., Xie, X., Liu, D. L., Ji, F., & Wang, L. (2015), "Spatial interpolation of daily rainfall data for local climate impact assessment over greater Sydney region." *Advances in Meteorology*, *2015*.

[4] Piazza, A. D., Conti, F. L., Viola, F., Eccel, E., & Noto, L. V. (2015), "Comparative analysis of spatial interpolation methods in the Mediterranean area: application to temperature in Sicily." *Water*, *7*(5), 1866-1888.

[5] Mahalingam, B., Deldar, A. N., & Vinay, M. (2015), "Analysis of selected spatial interpolation techniques for rainfall data." *International Journal of Current Research and Review*, *7*(7), 66.

8th International Engineering Symposium - IES 2019
March 13-15, 2019, Kumamoto University, Japan

Integrated Study for Delineation of Groundwater Prospect Zones in Hard Rock Terrains - A Review

Venkanagouda B B Patil[1] and **Lokesh K N**[2]

1 *Department of Civil Engineering, National Institute of Technology Karnataka, Surathkal, Mangalore 575025, India. email: venkzpatil@gmail.com*
2 *Department of Civil Engineering, National Institute of Technology Karnataka, Surathkal, Mangalore-575025, India. e-mail: knl.lokesh@gmail.com*

ABSTRACT: Groundwater resources are extremely significant in the areas of arid and semi-arid tropics particularly in the hard rock terrains. Recharge of groundwater is extremely low in hard rock terrains due to the low permeability and lack of weathered, fractured and jointed zones in the subsurface. A lesser amount of annual rainfall is also a reason for depletion of groundwater. Chances of failure of bore wells in such areas are high due to lack of groundwater. Prospecting of groundwater in hard rock terrains, arid and semi-arid regions are extremely important for successful exploration and to reduce the number of failures. Electrical resistivity method is one of the most practicing techniques since long to the present time for investigating the availability of groundwater. In addition, with electrical resistivity technique, Remote sensing and GIS approach may increase the accuracy of the investigation. Delineation of groundwater prospect zones can be identified easily with the help of this integrated approach and the success rate of the bore wells can be increased.

Keywords*: Hard rock terrain, remote sensing, groundwater, Electrical resistivity method, Arid- semi arid*

INTRODUCTION

Groundwater is a key source for any activities on the planet earth for all organisms. It is also known as hidden resource since it is beneath the earth surface. Groundwater forms in various conditions and its occurrence and availability is diversified from one place to another. Since the most demanding resource is depleting both in the aspects of quality and quantity and its requirements has made us to think on use of each water droplet. Because of growing industries, agricultural activities, urbanization, diverged rainfall, climate and other anthropogenic activities have made a severe impact on groundwater resources; this in turn has caused depletion of the groundwater all over the world. Availability of groundwater can be at shallower depth in some places which might be influenced by the heavy precipitation and the local lithology of that area. The non accessibility of surface water in some places has led in utilizing groundwater to meet its requirements. There are various traditional techniques to explore the groundwater ever since ages. Surface groundwater investigations are cost effective and has higher success rate. Among various geophysical investigations of groundwater, electrical resistivity method is one of the commonly used techniques where Schlumberger configuration is mostly preferred.

In spite of its significance, the groundwater and its resource management is often ignored since history. Each source of freshwater which is accessible is renewing to some extent each year in the process of the hydrological cycle. It's very difficult to conceptualize the groundwater due its hidden nature. In the present hydrological cycle groundwater plays a vital role since almost entire ecosystem is

depended on it for their survival, Giupponi, (2017). Though there is enough availability of surface water in many forms on the surface of the earth, water crisis still persists due to various reasons caused by both nature and anthropogenic activities as well. Increasing global warming, fluctuation in the precipitation, sea water intrusion, pollution, urbanization, industrial growth, population exploitation are all being a serious cause for diminishing of both quality and quantity of surface water; this is the right time to consider the management and conservation of available fresh water resources. Over last few decades, scientific research on groundwater has gained importance and expanding rapidly, it is also supported by many academicians and a number of journal are emerging in this aspect to spread the knowledge on significance of groundwater and its conservation. This initiation of scientific research on water resources has aided to meet requirements for both industrial and academic sectors. Groundwater study has advanced both in its thematic and cross-cutting areas, Pinder (2012). In groundwater studies, especially to measure aquifer geometry, mapping of the intrusive bodies, electrical conductivity of the subsurface, depth to bedrock, etc. are delineated using geophysical techniques. The geophysical techniques such as magnetic, electrical and electromagnetic have been extensively used since surface investigations are much simpler, fast and cost effective in relative to other methods, Chandra et al. (2008).

Lack in proper approach of groundwater extraction as in case of irregular and haphazard drilling of bore wells may lead into failure. In additional, this kind of exploitation has led in declining of groundwater potential, dropping of groundwater level and also depletion of groundwater quality. Hence it is need of hour to think on the groundwater as vital resource for its sustainable development and management scheme to utilize it properly, which in turn involves the delineation of groundwater potential zones (Prasad et al., 2008).

MATERIALS AND METHODOLOGY

In order to locate suitable site for groundwater extraction, physical properties and subsurface information are determined easily with low cost using geophysical survey such as electrical resistivity method and also for hydrogeological characterization, Sandberg et al. (2002), Sonkamble et al. (2014). Due to the heterogeneity nature of subsurface and associated uncertainties, combination of multiple tools and methods like integrated approaches are used. This includes geophysical survey with remote sensing and GIS which can diminish the ambiguities, Chandra et al. (2006), Sonkamble (2012). The theory and practice of geophysical method for groundwater investigations is nicely documented by Bhattacharya and Patra (1968), Parasinis (1973), Kelly and Mares (1993), etc. Figure 1 illustrates the arrangement and basic measurements for the electrical resistivity survey where MN and AB are potential and current electrodes respectively.

Literatures show that Indian Remote Sensing Satellite (IRS) RESOURCESAT- 1 (LISS-3&4) data were most commonly preferred by Indian authors in their study. The multispectral satellite image from LISS III & IV sensor contains three spectral bands, i.e. green (0.5–0.6 μm), red (0.6–0.7 μm) and near infrared (0.7–0.9 μm). The spatial resolution is 23.5 and 5.8 m for LISS III and LISS IV respectively. Slope and relief maps were generated from the DEM using SRTM, ASTER sensors etc. Similarly, various thematic maps such as geomorphology, soil, lineaments, drainage and land use/land cover were generated using satellite data.

The images were visually interpreted to prepare soil map and land use/land cover based on field knowledge, classification was done in ERDAS imagine software package. Lineaments were recognized from the relief map. Drainage and drainage density, lineament density was prepared using ArcGIS. From the geophysical survey it is possible to know the depth to bed rock and thickness of different subsurface layers. Later the obtained results from Vertical electrical sounding (VES) were converted to raster

maps in ArcGIS and were used as one of the input layer for overlay analysis for delineation of groundwater potential zones by the researchers. The common workflow for locating groundwater potential zones in hard rock terrains is shown in Figure 2. The most preferable source for each thematic layer for Indian scenario is given in Table 1 which may not be suitable and recommended for scenarios.

DEMARCATION OF GROUNDWATER POTENTIAL ZONE

As mentioned in various literatures for mapping groundwater prospect zones, individual thematic maps are prepared from the satellite data, toposheet, field survey and available secondary data. All these thematic layers were converted into raster format and georeferenced to common reference point in the Universal Transverse Mercator plane coordinate system. Later all these layers were integrated with the help of "Spatial Analyst Module" in ArcGIS environment. The integration of various thematic maps describing favourable groundwater zones, into a single groundwater potential map has been carried out through the application of GIS. This is conducted in three steps, they are- (1) Spatial database building, (2) Spatial data analysis and (3) Data integration.

Based on the significance, interrelationships between the occurrences of groundwater and the existing literatures, for each thematic layer, weight and rank are assigned (Table 2 and 3). The high weight value is categorized as the very good or excellent prospect zone and the least weight values as the poor or very poor prospect zone. Though there are various influencing factors for groundwater recharge, some are majorly affects and some are comparatively having low significance in the process of recharge (Figure 3). The weightage and ranking can be observed based on their role and significance (Table 2 & 3) in the groundwater recharge process.

RESULTS AND DISCUSSION

Groundwater potential zone map is much needed in the present scenario especially in hard rock terrains where the failures of bore well drillings are more. Such failures of bore well lead in destruction on both subsurface of earth and economical condition of the human beings. The area falling under hard rock terrains, arid and semi-arid climate are the regions with scanty rainfall which indirectly affects the irregularity in occurrence of groundwater. Lack of rainfall in such areas is leading agriculturists to forcefully drill wells for the crop irrigation and domestic purpose.

Preparing a groundwater prospect zone map is a systematic effort and is done by incorporating various significant governing factors, where there is more influence on soil infiltration and that improve groundwater availability. The outcome map exhibits best locations for groundwater prospecting and exposes the meaningful information for groundwater exploration, Ibrahim-Bathis & Ahmed (2016). Usually the water penetrates to the ground through roots of trees and plants where the area is covered by thick vegetation, tree plantation, and agricultural field and for which high weightage are assigned in the land use theme.

Valley areas and weathered pediplain are given with high weight and rest with relatively low weight in geomorphology theme. Usually groundwater retains within the weathered and fractured part of the hard rock terrains especially in granite and gneiss. Steep slope accelerates the runoff rate after rainfall on the ground surface; whereas the gentle slope area allows the rainwater to percolate and infiltrate to the soil. Therefore, slopes form a prominent influencing factor for groundwater occurrence. So high weight is commonly assigned to flat or gentle slope area and least weight to steep slope areas. Since groundwater is stored in the joints and fractures of hard rock, lineament density is another significant factor in seeking groundwater occurrence. The texture and depth of the soil play a vital role in the process of infiltration and groundwater zone. Commonly the compact clay soil holds the water than to allow permeation whereas more water storage and infiltration can be allowed by gravelly sand particles in the soil. Generally high groundwater potential zones are largely

found along nearly level areas with less than 2% slope, along the lineaments and pediplains. The low groundwater potential zones typically are located in the moderate-to-steep slope area, denudation hills, scrub land and barren land. Moderate potential zones are located in the fallow land and the gently slope areas. Very good groundwater potential zones are commonly exhibited by areas like valley fills and river banks.

Finally, the groundwater potential zones can be classified by considering all the influencing factors and their importance in groundwater occurrence as (1) Excellent/Very good, (2) Good, (3) Moderate, (4) Average (5) Poor and (5) Nil. From the groundwater potential map (Figure 5) it is possible to know how much area is falling under each category to understand the groundwater occurrence in a particular area. The example for final out put map of groundwater potential zones is shown in the Figure 5.

CONCLUSION

The various thematic layers like lithology, geomorphology, drainage, slope, rainfall, land use /land cover, resistivity data can be used to map groundwater potential zones using GIS approach. Based on the field knowledge, weightage are assigned for each layer and classified according to the various literatures. The resultant groundwater potential map after all integration can be classified based on the cumulative weightage assigned to different features of each thematic layer. The resultant groundwater potential zones can be classified as Excellent, Good, Moderate, Poor and very poor zones. This review article provides an insight and knowledge on integrated approach using remoe sening, GIS and electrical resistivity technique for groundwater potential zones investigation. Based on literatures, in the hard rock terrains, weathered, fractured and jointed formation is treated as water bearing zone. GIS method has become most important platform to integrate different thematic layers, which are significant in occurrence and movement of groundwater. The output map from the integrated layers could be advantageous for numerous purposes including development of schemes for sustainability of groundwater along with the delineation of groundwater potential zones for increasing water demands in the human world.

ACKNOWLEDGEMENTS

We are grateful to NITK authorities for extending facilities to carry out the research work.

REFERENCES

[1] Bhattacharya PK and Patra HP (1968), Direct current electrical sounding. Elseveir, Amsterdam.

[2] Chandra, S et al. (2008), Estimation of hard rock aquifers hydraulic conductivity from geoelectrical measurements: a theoretical development with field application. Journal of Hydrology, Vol.357 No. (3-4), pp.218-227.

[3] Chandra, S et al. (2006), Integrated studies for characterization of lineaments to locate groundwater potential zones in hard rock region of Karnataka, India. Hydrogeol J, Vol.14, pp. 767–776.

[4] Giupponi, C. (2017), Integrated groundwater management: Concepts, approaches and challenges. Environmental Modelling and Software, Vol.93, pp. 161-162.

[5] Gnanachandrasamy, G et al. (2018), Remote Sensing and GIS Based Groundwater Potential Zone Mapping in Ariyalur District, Tamil Nadu. Journal of the Geological Society of India, Vol. 92, No.4, pp. 484-490.

[6] Ibrahim-Bathis, K., & Ahmed, S. A. (2016), Geospatial technology for delineating groundwater potential zones in Doddahalla watershed of Chitradurga district, India. The Egyptian Journal of Remote Sensing and Space Science, Vol.19, No.2, pp. 223-234.

[7] Kelly WE and Mares S (1993), Applied geophysics in hydrogeological and engineering practice. Elsevier, Amsterdam, pp. 290.

[8] Marescot, L et al. (2008), Resistivity and induced polarization surveys for slope instability studies in the Swiss Alps. Engineering Geology, Vol. 98, No.1-2, pp.18-28.

[9] Parasinis DS (1973), Principles of applied geophysics, 5th edn. Chapman and Hall, London.

[10] Pinder, G.F., (2012), Groundwater hydrology in 2050. In: Toward a Sustainable Water Future: Visions for 2050. ASCE, pp. 277–287.

[11] Prasad, R K et al. (2008), Deciphering potential groundwater zone in hard rock through the application of GIS. Environmental geology, Vol.55, No.3, pp. 467-475.

[12] Sandberg, S K et al. (2002), An integrated geophysical investigation of the hydrogeology of an anisotropic unconfined aquifer. Journal of Hydrology, Vol.267, No.3-4, pp. 227-243.

[13] Shaban, A et al. (2006), Use of remote sensing and GIS to determine recharge potential zones: the case of Occidental Lebanon. Hydrogeology Journal, Vol.14, No.4, pp.433-443.

[14] Sonkamble S (2012), Integrated approach for demarcating subsurface pollution and saline water intrusion zones in SIPCOT area, Cuddalore, Southern

India. Ph. D Thesis, Osmania University, Hyderabad, India pp. 42–43.
[15] Sonkamble, S et al. (2014), Geophysical signatures resolving hydrogeological complexities over hard rock terrain—a study from Southern India, Arabian Journal of Geosciences, Vol.7, No. 6, pp. 2249-2256.
[16] Yeh, H F et al. (2009), GIS for the assessment of the groundwater recharge potential zone. Environmental geology, Vol.58, No.1, pp.185-195.

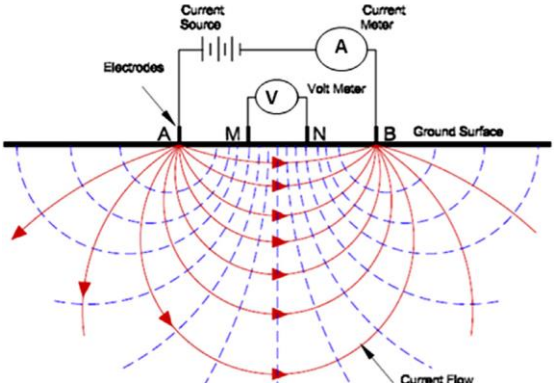

Fig. 1. Illustration of the basic measurements using the method of electrical resistivity (adopted from Marescot et al. (2008)).

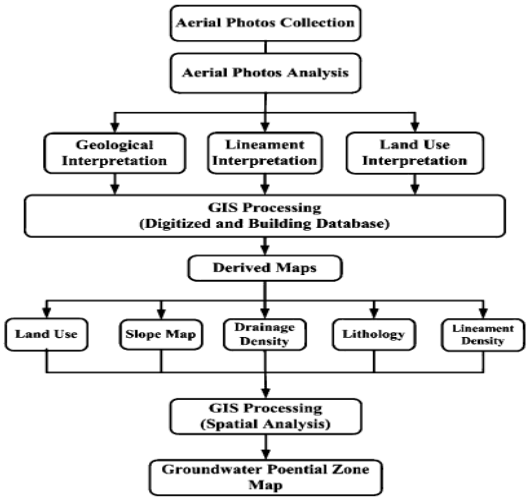

Fig. 2. Methodology flowchart for the groundwater potential zone (Yeh et al., 2009).

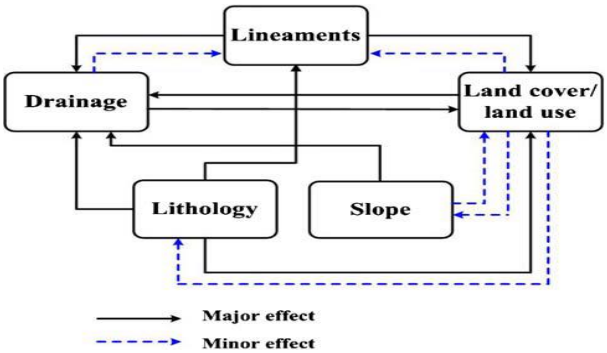

Fig. 3 The interactive influence of factors concerning the recharge property (modified from Shaban et al. 2006)

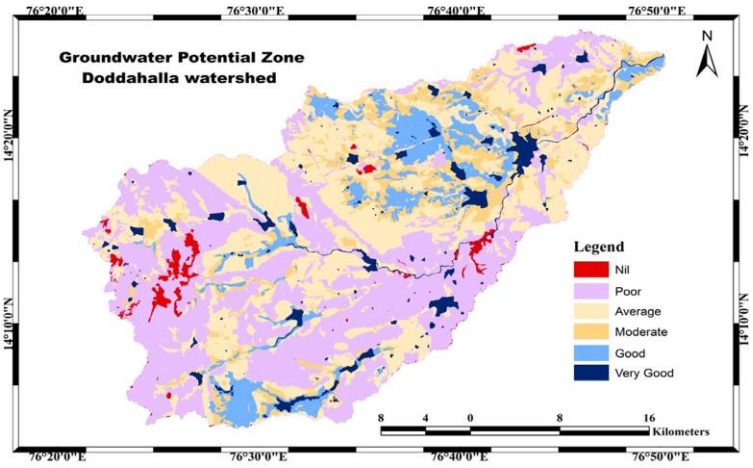

Fig.5 Groundwater potential zone map of Doddahalla watershed (Ibrahim-Bathis & Ahmed, 2016)

Table 1 Thematic layers and their sources for Indian scenario

Sl. No	Thematic layer	Source
1	Contour map	SOI toposheets (1:50000) and SRTM DEM (1Arc Second)
2	Slope map	Will be extracted from DEM
3	Lu/Lc Map	RESOURCESAT-I LISS-IV (Resolution 5.3m)
4	Soil type map	Published by NBSS/LUP or KRSAC
5	Drainage and water bodies map	SOI toposheets (1:50000) and SRTM DEM (1Arc Second)
6	Geomorphology map	Maps published by GSI and KRSAC
7	Lineaments map	Will be extracted from LISS-IV
8	Lithology map	GSI (scale 1:250000) and KSRSAC (scale 1:50000)
9	Soil depth map	Geophysical field survey
10	DEM	Bhuvan Website
11	Depth to bed rock map	Geophysical field Survey
12	Ground water level map	CGWB, MGD and also field Survey
13	Groundwater potential zones map	Geophysical field Survey and other thematic layers

Table 2 Factors taken and assigning weightage with relations to groundwater potential (Gnanachandrasamy et al., 2018).

Thematic map	Weightage Classes	Groundwater Potential
Geomorphology	Pediplain, Upland	Good
	Alluvial Plain, Flood Plain	Moderate
Geology	Sandstone with Clay and lst.	Good
	Fluvial, Fluvio- Marine, Aeolian and marine sediment	Moderate
	Pink migmatite, granitoid gneiss	Poor

Rainfall	High	Good
	Moderate	Moderate
	Low	Poor
Soil	Deep Calcareous Clay soils, Very deep Calcareous soils	Moderate
	Very Deep Calcareous Clay soil, Very deep Clay soils, Very deep Clayey Soils	Moderate to poor
	Very deep Loamy Soils	Good
Slope	Low	High
	Medium	Moderate
	High	Poor

Table 3. Thematic layers with classes assigned ranking and weightage (Gnanachandrasamy et al., 2018).

Thematic map	Classes	Assigned ranking	Weightage
Geomorphology	Alluvial Plain	2	7
	Flood Plain	2	
	Pediplain	3	
	Upland	3	
Geology	Fluvial, Fluvio- Marine, Aeolian and marine sediment	2	6
	Pink migmatite, granitoid gneiss	1	
	Sandstone and Clay	3	
	Sandstone with Clay and limestone	3	
Rainfall	Good rainfall	1	5
	Medium rainfall	2	
	Low rainfall	3	
Drainage density	< 1 (Extremely Low)	3	4
	1 to 2 (Low)	3	
	2 to 4 (Moderate)	2	
	4 - 6 (High)	1	
	> 6 (Very High)	1	
Lineament density	Low lineament density	1	3
	Medium lineament density	2	
	High lineament density	3	
Slope	Gentle slope	3	2
	Moderately sloping	3	
	Moderately steep sloping	2	
	Steep sloping	1	

8th International Engineering Symposium - IES 2019
March 13-15, 2019, Kumamoto University, Japan

Life cycle analysis of Ferrochrome ash

Krishnamurthy M P[1] and Devatha C P[2]

1 *Department of Civil Engineering, National Institute of Technology Karnataka, Surathkal,Mangalore-575025, India. Email: krishna3thymp@gmail.com*
2 *Department of Civil Engineering, National Institute of Technology Karnataka, Surathkal,Mangalore-575025, India. Email: revacp@gmail.com*

ABSTRACT: Ferrochrome ash (FCA) is a discarded material obtained from the ferrochromium industry. More than one metric ton of Ferrochrome ash is produced every year in India and there is a huge demand for dumping site, which is leading to increase in the cost of surrounding land in the industrial areas. FCA dumped without any pollution control measures can cause surrounding soil and water to get contaminated. In the current study, it is focused to understand the usage of FCA in various engineering applications such as replacement for cement, manufacturing of bricks and as an artificial course aggregate. These kind of recycling approaches are necessary to minimize the load on dumping sites and to protect the surrounding environment. In the present study, a light is thrown on life cycle analysis of recycled outputs which reduce environmental ill effects and give economic benefits out of industrial waste management practices.

Keywords: *Vertical electrical sounding, Groundwater potential zone.*

INTRODUCTION

Consciousness of the destructive residues from the industrial incineration plants has tremendously increased in current years. Various treatment methods and characterization of industrial solid wastes were attempted by many researchers worldwide (Lo and Liao 2007; Hykset et al. 2009; Chang et al. 2009; Nowak et al. 2012; Yang et al. 2015). Ferrochromium is one such waste that is formed pyro-metallurgically by reduction of metal oxide consuming carbon as reducing agent at 17000C from chromite ore (FeO.Cr2O3) (Erdem et al. 2005). India is one of the largest ferrochrome producing country(Sahu et al. 2016). FCA used in this study consists of the scrubber deposits collected in the form of ash and stored in dump sites. FCA is a hazardous waste having many toxic constituents such as dioxins and heavy metals in it. Solidification/stabilization is the effective method to reduce the leaching of toxic heavy metals from industrial discarded ash. There are other means to remove heavy metals and to destroy dioxins and furans, namely, extraction/separation and thermal treatment (Saikia et al. 2007; Quina et al. 2008; Rani et al. 2008; Kubonova et al. 2013; Samolada and Zbaniotou, 2014). Since, solidification/stabilization is the cost-effective technique for fulfilling local regulations. The risk assessment of long-term leaching from solidified blocks and the scarcity of land for landfills motivated various researchers to discover the new widespread safe recycling techniques (Hykset et al. 2009). Accordingly, this research aims to compare potential reuse methods of FCA with the traditional landfill disposal for informed decision.

Life cycle assessment framework

IMPACT 2002+ was used as a tool to quantify the environmental impact and it is categorized into four damage categories: 1) human health, 2) ecosystem quality, 3) climate change and 4) resources. Each impact weight was based on the Analytic Hierarchy Process (AHP), considering the suggestions from stakeholders. In this paper, the functional unit was "the

treatment or disposal of one ton of FCA, including the benefits of reusing the products." The boundary of the scenarios contain pre-treatment of FCA, reuse treatment and the final product or disposal.

Impact assessment

Three scenarios are discussed in detail in this section with a flow diagram as shown in Fig. 1:

1) Landfill after solidification,
2) Reuse as cement and
3) Reuse as bricks.

Scenario 1: Landfill after solidification

The most common treatment for FCA in Asia is disposal into landfills after solidification. After the washing process, the FCA is mixed with cement and a chelating agent for stabilization, after which the solidified product is dumped into a sanitary landfill site.

Scenario 2: Reuse as cement after the washing process

After the water wash and chelation, 10% FCA was added to the raw cement materials that include limestone, clay, sand and iron ore. Making cement consists of four processes: extracting raw materials from the mine, blending the raw material with FCA, calcining the product in a rotary kiln, and milling the cement.

Scenario 3: Reuse as bricks after the washing process

After the water wash and chelation, 20% FCA was added to the raw material for making bricks. Making bricks also consists of four processes: clay preparation, moulding, drying, and firing.

Comparison of the environmental impact of the processes in all the scenarios

Landfills had the second largest environmental impact of the three scenarios, but the impact is far less than that of reusing as alkaline. However, landfilling consumes more electricity than that of reusing as alkaline because the FCA is solidified by mixing with cement that has a worse effect on global warming and on renewable resources. The other two scenarios, reuse as cement and bricks, were found to be more environmental friendly and provided the benefits of reusing the products for construction, especially the brick making process. Each impact of the scenario contains a majority ratio of respiratory inorganics owing to the emission of air pollution and the waste water treatment in the washing process. Therefore, the better option would be to reduce the impact of the pollution.

In scenario 1, the greatest impact was the consumption of cement, which was equal to half the amount of FCA. The washing process of the FCA and the use of sodium sulfate for chelation also had a greater effect than the other processes. To improve this treatment option, the consumption of cement and chelating agents must be reduced to moderate amounts.

In scenario 2, the greatest environmental impact was from the air pollution that was caused by the reuse process itself. Global warming and respiratory inorganics are therefore the main categories of impact of this reuse process. The next greatest impact was the pre-treatment of FCA, because of the higher fraction of the total impact. The third greatest environmental impact was the use of electricity in the cement making process. To improve this treatment option, the emission of pollutants like carbon dioxide and nitrogen oxide must be reduced and also there should be reduction in the heavy metals released during the firing process. In addition, the release of heavy metals from the FCA could increase the risks associated with the use of cement in construction.

Scenario 3 had the smallest impact of all the scenarios. The environmental impact was from the reuse process itself and the washing of the FCA. The results for scenario 3were found to be similar with the results for scenario 2. However, the impact of air pollution was much less than it was for the use in cement, because of the lower total impact of reusing FCA as brick material. To improve this treatment option, the treatment of waste water from the washing process must be improved to reduce the pollution from the outflow water. Additionally, the consumption of resources and energy by the waste water treatment must be reduced and the air pollution eliminated.

In this study, the different kinds of reuse treatment for FCA are compared and the environmental impact results are considered. Then the scenario 3, reuse as bricks, is selected as the best and most environmental friendly treatment for FCA. There are two reasons for this choice, the first and most important being that this scenario had the least impact on the environment.

CONCLUSIONS

Based on the environmental impact, this study assessed three kinds of scenarios to find the best treatment for FCA. It is concluded that, out of the three options assessed, the reusing of FCA as brick material was more effective and environmental friendly treatment. In scenario 3, reuse as bricks, the hot spot of impact was in the washing process and pollution emission of the reuse process. Therefore, reducing the air pollution emission and finding a more efficient treatment for wastewater would be crucial to reduce the impact of this FCA reuse method. However, this study cannot be considered as a complete assessment, as only one aspect of reuse treatment was evaluated.

REFERENCES

[1] Chang, C. Y. et al (2009), Characteristics of elements in waste ashes from a solid waste incinerator in Taiwan, Journal of hazardous materials, Vol. 165, No. 1-3, pp. 766-773.

[2] Hyks, J et al(2009), Long-term leaching from MSWI air-pollution-control residues: leaching characterization and modeling Journal of Hazardous Materials, Vol. 162 No. 1, 80-91.

[3] Kuboňová, L et al (2013), Thermal and hydrometallurgical recovery methods of heavy metals from municipal solid waste fly ash, Waste management, Vol. 33, No. 11, 2322-2327.

[4] Lo, H M and Liao, Y L (2007), The metal-leaching and acid-neutralizing capacity of MSW incinerator ash co-disposed with MSW in landfill sites. Journal of Hazardous Materials, Vol. 142, No. 1-2, pp. 512-519.

[5] Nowak, B et al (2012), Heavy metal removal from MSW fly ash by means of chlorination and thermal treatment: Influence of the chloride type. Chemical Engineering Journal, Vol. 179, pp. 178-185.

[6] Quina, M J et al (2008), Treatment and use of air pollution control residues from MSW incineration: an overview, Waste Management, Vol. 28(11), 2097-2121.

[7] Rani, D A et al (2008), Air pollution control residues from waste incineration: current UK situation and assessment of alternative technologies. Waste Management, Vol. 28, No. 11, pp. 2279-2292.

[8] Samolada, M C and Zabaniotou, A A (2014), Energetic valorization of SRF in dedicated plants and cement kilns and guidelines for application in Greece and Cyprus, Resources, Conservation and Recycling, Vol. 83, pp. 34-43.

[9] Saikia, Nt et al (2007), Production of cement clinkers from municipal solid waste incineration (MSWI) fly ash. Waste Management, Vol. 27, No. 9, pp. 1178-1189.

[10] Yang, R et al (2015), Environmental and economic analyses of recycled asphalt concrete mixtures based on material production and potential performance Resources, Conservation and Recycling, Vol. 104, pp. 141-151.

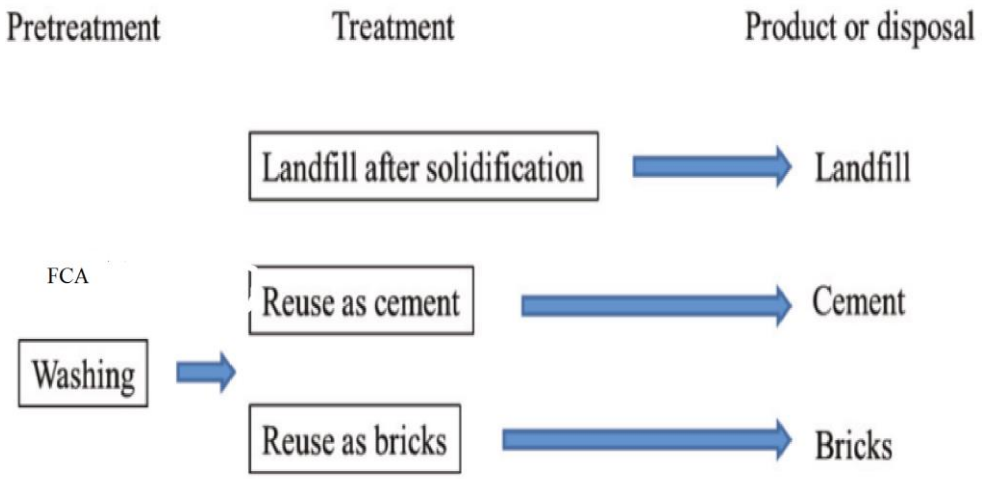

Fig. 3: Three reuse treatment scenarios assessed in the Life Cycle Analysis

8th International Engineering Symposium - IES 2019
March 13-15, 2019, Kumamoto University, Japan

Study on Lateritic Soil Treated with RBI Grade 81 and Aggregate

Amulya S [1], A U Ravi Shankar [2], Lekshmy v v[3] *and* *Panditharadhya B J*[4]

1 Department of Civil Engineering, National Institute of Technology Karnataka, Surathkal, Mangalore 575025, India. e-mail: amulya2mail@gmail.com
2 Department of Civil Engineering, National Institute of Technology Karnataka, Surathkal, Mangalore 575025, India. e-mail: aurshankar@gmail.com
3 Department of Civil Engineering, National Institute of Technology Karnataka, Surathkal, Mangalore 575025, India. e-mail: lekshmyvgopal@gmail.com
4 Department of Civil Engineering, National Institute of Technology Karnataka, Surathkal, Mangalore 575025, India. e-mail: pandith23@gmail.com

ABSTRACT: Road Building International Grade 81 (RBI Grade 81) is a product that was developed for the stabilization of a wide spectrum of soils in an efficient manner. It is an environment friendly, inorganic material which reacts with soil particles. In the present study, the effect of the use of stabilizer RBI Grade 81 on the lateritic soil and lateritic soil – aggregate mix for two different proportions were studied. The soil stabilization was done by adding the RBI Grade 81 from 2 to 6 per cent by weight of soil and soil-aggregates combination was also tried in two proportions such as 50-50 and 60-40% by weight of soil. Optimum Moisture Content (OMC), Maximum Dry Density (MDD), Unconfined Compressive Strength (UCS), durability and California Bearing Ratio (CBR) tests were conducted. Use of RBI Grade 81 resulted in increased UCS to 900% after 28 days curing, un soaked CBR from 140% and soaked CBR to 116% for treated soils after 7 days curing. The stabilized soil beyond 6% RBI Grade 81 is found durable.

***Keywords**: Lateritic soil, Soil stabilisation, RBI Grade 81, Durability, Aggregates, CBR*

INTRODUCTION

The constructed pavement should be durable, economical and safe. Durable pavement can be constructed with the use of granular materials but due to the lack of durable materials such as aggregates (gravel), the usage of locally available materials such as soil is in practice in the present days. Soil alone is not enough to withstand the load imposed on it hence, the strength of the soil has to be enhanced by stabilising it. Stabilisation is a technique where the properties of the source material can be enhanced by adding additives. Stabilization are of many types such as chemical, mechanical stabilisation, stabilisation by bitumen and grouting technique. In the present work, the chemical stabilisation of lateritic soil is done using RBI Grade 81 stabiliser for the construction of pavements in tropical region under heavy rainfall condition.

LITERATURE

Extensive research has been done on the stabilisation of different types of soil using stabilisers such as cement, lime, fly ash, blast furnace slag and pozzolans etc.

Yoder and Witczak (1975) stated that the lateritic soil is rich in iron and aluminium formed due to alternate weathering of the underlying parent rock. Many attempts have been made to stabilise the lateritic soil and Anitha et al. (2009) found that the stabilisation helps to reduce the cost of pavement construction. Naseem et al. (2014), done an experimental work on lateritic soil stabilised with RBI Grade 81 and engineering properties of the soil is verified and found that the plasticity index

decreases, MDD and strength increases is due to the conversion of clay particles into cementitious calcium silicate and aluminium hydrates. Patil and Patil (2013), Manisha et al. (2014), conducted the Differential Free Swell Index (DFS) test on clayey soil stabilised with RBI Grade 81 and found that 4% of RBI Grade 81 reduces the swelling to 35% from 65%. Mamta et al. (2014) made a comparative study in between black cotton soil and lateritic soil stabilised with RBI Grade 81 and found that the stabiliser enhances the geotechnical properties. Lekha et al. (2014) conducted fatigue life test and CBR test under soaked condition and found that the RBI Grade 81 works well with cohesive soils. Madurwar (2013) tried working on soil along with RBI Grade 81 and sodium silicate.

The objective of the present work is to investigate the UCS, CBR and durability of lateritic soil stabilised with RBI Grade 81.

MATERIALS

Following are the materials used in the present investigation.

Lateritic soil

The lateritic soil is the source material used in the present work and is procured from the nearby sites of NITK, Mangaluru, India. The grain size distribution of the soil is tabulated in the table 1.

Table 1 Grain size distribution of lateritic soil

Particle	Percent Present
Gravel	28
Sand	47
Silt	20
Clay	5

Aggregates

The aggregates chosen for this work are 10 mm size down and its sieve analysis result is tabulated in the table 2.

Table 2 Sieve analysis of 10 mm down aggregate

IS Sieve (mm)	Percent Passing (%)
12.5	100
10	91
4.75	21
2.36	5

RBI Grade 81

The stabiliser RBI Grade 81 is an inorganic, odourless, insoluble in water, powdered material. The RBI Grade 81 mainly composed of Calcium oxide (CaO) up to 60%, Silica oxide (SiO2) up to 20%, sulphur trioxide (SO3) up to 10% and few traces of oxides of aluminium, Iron, Magnesium etc. The physical properties are tabulated in the table 3.

Table 3 Physical properties of RBI Grade 81

Properties	Description
Odour	Odourless
pH	12.5
Specific gravity	2.5
Flammability	Non-Flammable
Shelf life	12 months
Bulk density	100g/m^3

Water

The ordinary portable water has been used for the work.

RESULTS AND DISCUSSION

Proctor Tests

The standard proctor test has been conducted only for untreated soil as per IS: 2720 (Part VII), 1980 and found the OMC and MDD as 12.3% and 1.98g/cc respectively. The Modified proctor test is conducted for the soil treated with different dosages of RBI Grade 81 with 2, 4, 6% as per IS: 2720 (Part VIII), 1983 and the soil treated with RBI Grade 81 and the aggregate of proportions 50-50% and 60-40% as per IS: 4332 (Part 3), 1967. The OMC and MDD of the treated soil are tabulated in the tables 4 and 5.

Table 4 OMC and MDD of lateritic soil treated with RBI Grade 81

Sl No	RBI Grade 81 (%)	OMC (%)	MDD (g/cc)
1	0	10.4	2.01
2	2	11.9	2.03
3	4	11.2	2.08
4	6	10.7	2.05

From the table 4, it is observed that when the dosage of stabilizer RBI Grade 81 is increased from 0 to 4%, increase in the OMC and MDD is observed in 8 and 4% is noted, whereas a further increase in RBI

Grade 81 to 6% tends to increase the OMC by 3% and decrease in MDD by 1.5%.

Table 5 OMC and MDD of lateritic soil treated with RBI Grade 81 and Aggregate

Sl No	RBI Grade 81 (%)	Soil-Aggregate Proportion (%) (50-50)		Soil-Aggregate Proportion (%) (60-40)	
		OMC (%)	MDD (g/cc)	OMC (%)	MDD (g/cc)
1	2	9.3	2.1	12.2	2.02
2	4	9.5	2.2	11.2	2.16
3	6	9.9	2.3	11.9	2.2

From the table 5, it is observed that when soil and aggregates are mixed at a proportion of 50-50% and RBI Grade 81 is varied from 2 to 6%, the OMC and MDD keep on increases to 6.5% and 20% respectively. When soil and aggregate is mixed at a proportion of 60-40% and RBI Grade 81 is varied from 2 to 6%, the OMC keep on increases to 10.6% and MDD keep on increases to 10%. From the above values, it can be inferred that as the RBI Grade 81 and Proportion of aggregate increases the MDD also increases.

Unconfined Compressive Strength Test (UCS)

The UCS test is conducted on the soil treated with RBI Grade 81 and different proportion of aggregates as per IS: 2720 (Part 10), 1991. The samples are prepared at modified proctor density and cured for 0, 7 and 28 days. The variation of UCS values of RBI Grade 81 treated soil is shown in the fig.1.

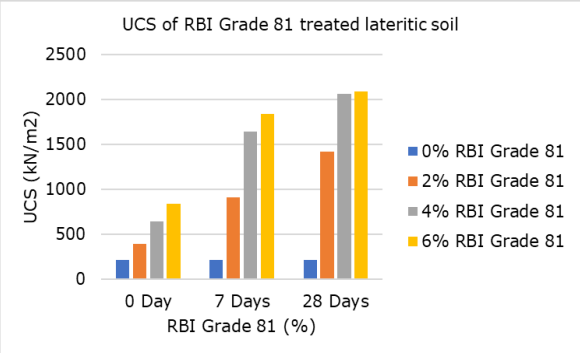

Fig.1 Variation of UCS values of lateritic soil treated with RBI Grade 81

From the Fig.1, it is observed that, when lateritic soil is replaced with varying dosages of RBI Grade 81 from 2% to 6%, the UCS of the stabilized increases to 118% after 0 days curing, 103% after 7 days curing, 47% after 28 days curing. Compared to the untreated soil, at 0, 7 and 28 days curing the UCS of the stabilized soil is increased to 302%, 780% and 900%. This may be due to the formation of cementitious products such as calcium silicate and aluminum hydrates, which helps in binding the clay particles hence gains the strength (www.rbi.com).

California Bearing Ratio (CBR)

The CBR of the untreated soil, soil treated with RBI Grade 81 and soil treated with RBI Grade 81 and different proportion of aggregates is found out as per IS: 2720 (Part 16), 1987. The stabilized soil is cast at modified proctor density and cured for 7 days and both unsoaked and soaked test were conducted after 4 days of soaking. The CBR of soil treated with 2, 4 and 6% of RBI Grade 81 stabilizer, the CBR of the untreated soil with two proportions of 10 mm size aggregates such as 50-50% and 60-40%, the CBR of the soil treated with RBI Grade 81 and two proportions of aggregates are depicted in figures 2, 3, 4 and 5.

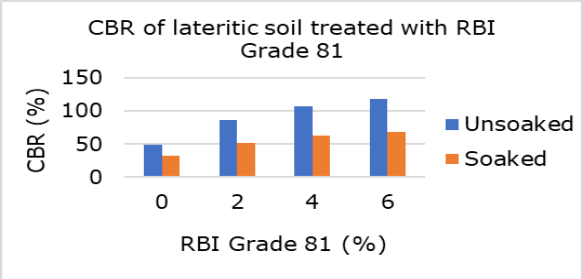

Fig.2 CBR of the lateritic soil treated with RBI Grade 81 after 7 days curing

From the fig.2, it can be observed that when lateritic soil is treated with increased dosages of RBI Grade 81 from 0 to 6%, the CBR increases to 140% at unsoaked condition and 116% at soaked condition compared to untreated soil.

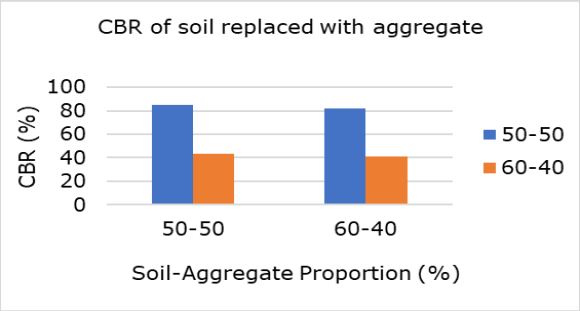

Fig.3 CBR of lateritic soil replaced with different proportion of aggregates

From fig.3, it can be inferred that when lateritic soil is replaced with 50% and 60% of aggregates, the CBR is found more in case of higher aggregate content mixture (50-50%) and a little less in case of 60-40% of proportion.

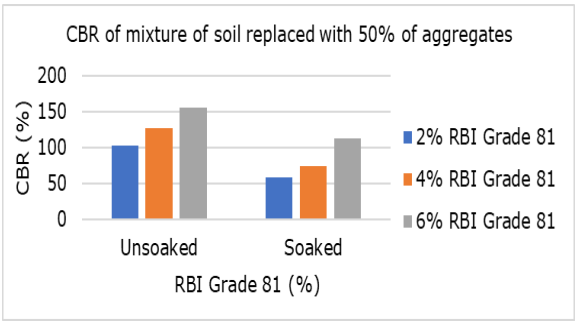

Fig.4 CBR of RBI Grade 81 treated soil replaced with 50% of aggregate

From fig.4, it is found that when lateritic soil is stabilised with RBI Grade 81 and replaced with 50% of aggregate, the CBR is found increases with increasing dosage of RBI Grade 81, and the same trend is observed in case of soaked CBR.

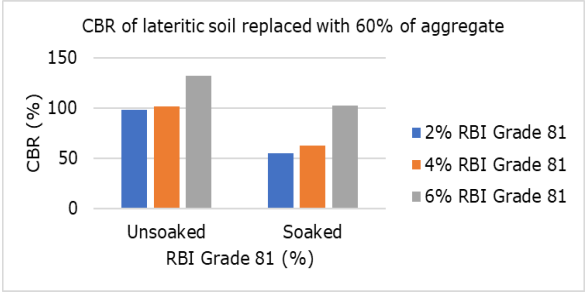

Fig.5 CBR of RBI Grade 81 treated soil replaced with 60% of aggregate

From fig.4, it is found that when lateritic soil is stabilised with RBI Grade 81 and replaced with 60% of aggregate, the CBR is found increases with increasing dosage of RBI Grade 81, and the same trend is observed in case of soaked CBR.

Durability

The roads need to be sustainable at all weather conditions mainly at heavy rainfall and at extreme temperature regions. The two tests such as Wetting and Drying (WD) test and Freeze and Thaw (FT) test are conducted to check the durability of the stabilised soil where the weight loss should not be more than 14% after 12 alternative cycles of WD and FT as per ASTM 559D and 560D. In the present work, the WD and FT test is conducted on the soil stabilised with 0,2,4 and 6% of RBI Grade 81, cured at ambient temperature for 7 days. The untreated soil samples collapse during the first cycle of WD test, whereas it passes all 12 cycles of FT test with weight loss of 12%. The WD and FT test results are tabulated in tables 6 and 7.

Table 6 Percentage weight of RBI Grade 81 treated lateritic soil during WD test

No. of cycles	Percentage weight loss					
	2 % RBI-81		4 % RBI-81		6 % RBI-81	
	Wetting	Drying	Wetting	Drying	Wetting	Drying
1	-2.0	8.9	-1.8	9.9	-2.4	8.9
2	Collapsed		0.7	12.9	-3.3	9.2
3	-	-	collapsed		-2.5	10.7
4	-	-	-	-	-2.2	10.7
5	-	-	-	-	-1.8	11.9
6	-	-	-	-	0.5	13.3
7	-	-	-	-	1.1	14.7
8	-	-	-	-	3.6	20
9	-	-	-	-	9.7	23.5
10	-	-	-	-	12.9	27.7
11	-	-	-	-	Collapsed	
12	-	-	-	-	-	-

Table 7 Percentage weight of RBI Grade 81 treated lateritic soil during FT test

No. of cycles	Percentage weight loss					
	2 % RBI-81		4 % RBI-81		6 % RBI-81	
	Freeze	Thaw	Freeze	Thaw	Freeze	Thaw
1	4.9	4.5	3.4	2.8	1.2	1.0
2	5.3	5.1	4.6	2.5	1.8	1.5
3	5.8	5.5	4.8	2.6	2.5	2.3
4	6.5	6.3	5.8	3.2	2.9	2.5
5	6.9	6.5	6.5	3.3	3.6	3.4
6	7.1	6.9	6.7	4.8	4.3	4.1
7	7.8	7.1	7.1	5.5	4.9	4.2
8	7.9	7.8	7.8	5.8	5.0	4.3
9	8.5	8.2	8.2	5.9	5.2	4.5
10	8.8	8.2	8.5	5.9	5.2	4.6
11	9.2	8.8	8.6	6.1	5.3	4.6
12	10.2	9.7	8.8	6.2	5.3	4.8

From the table 6, it is observed that when the soil is treated with higher dosages of RBI Grade 81 and air cured for 7 days at ambient temperature, the soil samples sustain for 6 cycles of WD and even though it sustains for further cycles, the weight loss is observed to be more than 14%. This shows that the treated soil does not pass WD and hence the RBI stabilized soil is not durable in heavy rainfall region. From table 7, it can be inferred that, the RBI Grade 81 stabilised soil passes all 12 cycles of FT test with weigh loss of 9.7, 6.2 and 4.8% in 2, 4, and 6% of RBI Grade 81 which is less than 14% and hence, the RBI Grade 81 stabilized soil pass in only FT test but not in WD test.

CONCLUSIONS

The following conclusions are made from the present work:

- As dosage of RBI Grade 81 increases in the soil, the OMC keep on increases but MDD increases till 4% of stabiliser and further increase leads to decrease in MDD whereas in case of treated soil with partial replacement of aggregate keep on increases the MDD.
- As dosage of the RBI Grade 81 increases the increase in UCS is observed.
- Increased dosage of RBI Grade 81 and partial replacement of treated soil with aggregate is giving CBR more than 100%.
- RBI Grade 81 treated lateritic soil passes all FT test, but it fails in WD test, hence it is advised to increase the dosage and curing period as well.

REFERENCES

[1] Anitha K R, Ashalatha R, and Johnson A S (2009), Effects of RBI Grade 81 on Different Types of Subgrade Soil, Proceeding of 10th National Conference on Technological Trends (NCTT09), Trivandrum, 165-170.
[2] IS 1498: 1980. Classification and Identification of Soils for General Engineering Purposes. Bureau of Indian Standards, New Delhi, India.
[3] IS 2720 (Part III/SEC - 1): 1980.Methods of Test for Soils (Part III Determination of Specific Gravity). Bureau of Indian Standards, New Delhi, India.
[4] IS 2720 (Part 5): 1985. Methods of Test for Soils (Part 5 Determination of Plastic Limit and Liquid Limit). Bureau of Indian Standards, New Delhi, India.
[5] IS 2720 (Part VII): 1980. Methods of Test for Soils (Part VII Determination of Water Content-Dry Density Relation Using Light Compaction). Bureau of Indian Standards, New Delhi, India.
[6] IS 2720 (Part 8): 1983. Methods of Test for Soils (Part VIII Determination of Water Content-Dry Density Relation Using Heavy Compaction). Bureau of Indian Standards, New Delhi, India.
[7] IS 2720 (Part 10): 1991. Methods of Test for Soils (Part 10 Determination of Unconfined Compressive Strength). Bureau of Indian Standards, New Delhi, India.
[8] IS 2720 (Part 16): 1987. Methods of Test for Soils (Part 16 Laboratory Determination of CBR). Bureau of Indian Standards, New Delhi, India.
[9] ASTM D559. Standard Test Methods for Wetting and Drying Compacted Soil-Cement Mixtures. ASTM International, United States.
[10] ASTM D560. Standard Test Methods for Freezing and Thawing Compacted Soil-Cement Mixtures. ASTM International, United States.
[11] Lekha B M and Shankar A U R (2014), Laboratory Performance of RBI 81 Stabilized Soil for Pavements, International Journal of Civil Engineering Research, vol.5, number 2, 105-110.
[12] Manisha G, Ravichandran P T, Annadurai R, and Divya K (2014), Effect of RBI-81 on CBR and Swell Behaviour of Expansive Soil, International Journal of Engineering Research, vol.3, Issue 5, 336-339.
[13] Mamta and Mallikarjun H (2014), Using RBI Grade 81 A Comparative Study of Black Cotton Soil and Lateritic Soil, International Journal of Research in Engineering and Technology, vol.3, Issue 3, May.
[14] Madurwar K V, Dahale P P and Burile A N (2013), Comparative Study of Black Cotton Soil Stabilization with RBI Grade 81 and Sodium Silicate, International Journal of Innovative Research in Science, Engineering and Technology, vol.2, Issue 2, February.
[15] Naseem A K, Damgir R M, and Hake S L (2014), Effect of Fly ash and RBI Grade 81 on Black Cotton soil as a sub grade for Flexible Pavements, International Journal of Innovations in Engineering and Technology (IJIET), Vol. 4 Issue 1.
[16] Patil B M, and Patil K A (2013), Effect of industrial waste and rbi grade 81 on swelling characteristics of clayey soil, FactaUniversitatis Series: Architecture and Civil Engineering, 11(3), 231-236.
[17] Yoder E J, and Witczak M W (1975), Principles of Pavement Design, John Wiley & Sons, Inc, USA.

8th International Engineering Symposium - IES 2019
March 13-15, 2019, Kumamoto University, Japan

Seismic Resistance of Precast Reinforced Concrete Shear Wall: Experimental and Analytical Study

Shubham Singhal[1] and **Ajay Chourasia**[2,3]

1 *Academy of Scientific and Innovative Research (AcSIR), CSIR- Central Building Research Institute (CSIR-CBRI Campus), Roorkee 247667, India. E-mail: shubham.singhal092@gmail.com*
2 *Structural Engineering Division, CSIR- Central Building Research Institute, Roorkee 247667, India. E-mail: ajayc@cbri.res.in*
3 *Academy of Scientific and Innovative Research (AcSIR), Ghaziabad 201002, India. E-mail: ajayc@cbri.res.in*

ABSTRACT: The paper investigates seismic performance of precast RC shear wall with hollow core filled with the cast-in-situ concrete. The shear wall was subjected to lateral loading and its behaviour was assessed from the standpoint of damage pattern, lateral load capacity and seismic parameters. The wall exhibited competent deformation characteristics owing to its ductile response. No significant damage in the wall was observed, except near the toe region which experienced flexural cracks and severance due to lack of connection between precast panels and raft. A numerical analysis was carried out in Abaqus to speculate the behaviour of developed precast shear wall system, whose results were comparable with the experimental results, thus enhancing confidence to accept and emulate the developed shear wall system, owing to its several advantages over conventional RC shear wall.

Keywords*: shear wall, precast RC wall, precast hollow wall, quasi-static test, seismic resistance, numerical analysis.*

INTRODUCTION

Rapid urbanization and population growth around the globe has resulted in enormous pressure on construction industry, which has evolved a need of speedy and efficient construction technology with safety from different hazards. Precast technology offers speedy and quality construction with the reduced construction cost on mass scale production. Precast structures are beneficial as compared to conventional reinforced concrete (RC) structures in terms of quality, safety, economy, sustainability and pace in construction. In precast construction, the structural components are manufactured in a factory and then transported to the construction site for assemblage, thus vanishing the possibilities of commonly occurring errors at the construction site. They are highly effective in resisting gravity loads, while their seismic performance is unclear. Several earthquakes in the past have demonstrated damage in precast RC buildings. Shear walls increase the seismic resistance of buildings which behave as vertical cantilever beams and adequately transfer lateral loads from the superstructure to the foundation. However, when compared to monolithic shear wall, precast structural walls are rarely used due to their unclear seismic performance and laborious process of handling due to heavy weight. Researchers around the world did significant research on precast shear walls. Parsafar and Moghadam (2017), Sritharan et al. (2015), Todut et al. (2014), Jiang and Kurama (2013),

Pavese and Bournas (2011), Dan et al. (2011), Li and Lim (2010), Smith et al. (2010), Dazio et al. (2009), Orakcal et al. (2009), Greifenhagen and Lestuzi (2005), Holden et al. (2003), Perez et al. (2002) and several others explored seismic performance of precast RC walls. The experimental studies indicate that the base of the precast wall and the region adjacent to the joint are most prone to the stress development. These regions demonstrate damage initiated in the form of cracks, concrete spalling and crushing which later results in extensive slip and permanent deformation at higher loads. Thus, joints are the most crucial part of precast structures that are required to be designed accurately in order to effectively transfer the lateral forces occurring during the event of earthquake. Precast construction is still not very common in the construction industry, attributed to the lack of knowledge on the joint connections, their design acceptability, mass-scale production and competent agencies etc. It is essential to provide RC shear walls in precast construction when adopted in tall buildings in high seismic regions. However, their transportation and handling is a major issue, due to which their adoption in rare in the construction industry. This has led to the requirement of introducing new shear wall systems which can address the issue. This paper experimentally and analytically determines the seismic performance of a shear wall system having two thin precast RC panels connected through steel truss, forming hollow inner core. The developed RC shear wall needs minimal shuttering, have improved buckling resistance and easier handling/ transportation because of lower self weight and adequately connected to achieve monolithic behaviour. Developed precast RC wall system was subjected to lateral loading whose seismic resistance was studied in terms of damage pattern and various seismic parameters as discussed in the paper.

PRECAST WALL DETAILS

A 2.26 m (height) x 1.85 m (length) x 0.3 m (thickness) precast RC shear wall was desinged as per IS 13920: 2016. The wall was designed and constructed as a precast double wall having two 70 mm thick precast RC wall panels encasing 160 mm inner hollow core, which was filled with the cast-in-situ concrete. The wall was constructed on a 3 x 1.8 x 0.25 m raft casted on the strong floor. Vertical rebars were protruded from the raft into the hollow core. Boundary elements of the wall were provided with 3 - 8 mm ø longiudinal rebars in hollow core which were also embedded into the raft. The precast RC panels were connected through three steel truss elements. Concrete strength was M25 and M30 for the raft and precast wall respectively. Reinforcement bars had the yiled strength of 500 MPa.

TEST SET-UP

Fig. 1 shows the view of precast RC wall subjected to reverse cyclic lateral displacements at roof level. The wall were subjected to cyclic lateral displacements with increasing amplitudes. Statically, the frequency of 0.004 Hz (fst) was considered while programming displacement time histories. The lateral load was applied by programmable, two-way acting, 500 kN capacity, ±75 mm stroke length, and servo-hydraulic actuator. The cyclic lateral load from actuator was uniformly distributed through steel plates fixed at both the faces of wall and connected to the actuator plate through steel rods as shown in Fig 1. The displacement response of the wall at critical locations was measured using linear variable displacement transducer (LVDT) and acquired in data-acquisition system at a sampling rate of 200 Hz to capture flexural and shear deformations, base uplift, and relative sliding.

EXPERIMENTAL RESULTS

The lateral load resistance of precast shear wall was evaluated in terms of damage pattern and seismic parameters. Load-displacement curve was obtained to determine seismic parameters. The section discusses the observed response of the tested wall, qualitatively and quantitatively. Based on the observations and physical measurements of lateral load capacity and displacement during the quasi-static test, the seismic performance of the wall is discussed hereby.

Damage Pattern

The behaviour of tested wall was ductile, without showing shear cracks, which prevented shear failure and improved its post-yielding behaviour. The first flexure hairline horizontal crack at toe region of the wall at a displacement cycle of 12 mm. Cracks at the base further expanded in every displacement cycle. Noteworthy damages (widen cracks) at the base of the wall were observed after acquiring maximum lateral load (353 kN at 27 mm displacement). These cracks propagated in the higher cycles, which resulted in separation crack between wall and raft footing as shown in Fig. 2. However, the wall did not show any shear crack. Furthermore, no separation between precast panels and inner core was observed, showing excellent bond between the two.

Lateral Strength

Lateral strength of the wall is defined by minimum resistance offered to lateral deformation during the push-pull loading. A typical average lateral load–displacement hysteresis for tested precast wall is shown in Fig. 3. As can be seen from Fig. 3, that the highest lateral resistance was 353 kN at 27 mm lateral displacement. The limit states, i.e., elastic (crack) limit, maximum resistance and ultimate failure were also considered for studying the seismic behaviour of the precast wall. The control points were derived by trilinear idealization of experimental resistance envelope data. Elastic crack limit state is described at initiation of first significant crack near the base which changes initial stiffness of the wall. Maximum lateral load and corresponding displacement of the wall was obtained on attainment of maximum resistance state. Similarly, ultimate state was determined on attainment of maximum lateral displacement at corresponding resistance lateral load. The wall showed linear response till first crack at a lateral load of 270 kN and 12 mm displacement. Maximum displacement achieved was 63 mm at a load of 295 kN. Table 1 illustrates lateral load and corresponding lateral displacement at different limit states.

NUMERICAL MODELLING

Finite element analysis was performed in Abaqus software with reference to Abaqus manual. 3D tetrahedron continuum solid sections were created for precast panels, cast in-situ core, raft and reinforcement bars were modelled with 3D planar wire sections. Embedded constraint was used to embed the reinforcement bars into the concrete. Interaction between precast panels and cast in situ core region was taken as surface to surface interaction. On the other hand, tie interaction was used reinforcing bars protruded from raft footing into the cast-in-situ core. Encastre boundary condition was given at the base of the raft. The concrete was meshed with 8 noded linear brick and hourglass control elements and reinforcement bars were meshed with 2 noded linear 3D truss elements. Fig. 4 and Fig. 5 show the model and meshing of the wall respectively. The material properties given for concrete and steel were density, poisson's ratio and young's modulus. The plastic properties were eccentricity, dilation angle, k value, f_{bo}/f_{co} and viscosity stated in Table 2. The stress-strain response for concrete was given by damage parameter and cracking strain as per Mander et al. 1988, while response of concrete in tension was given as tension stiffening model as per Nayal and Rasheed (2006). Dynamic explicit procedure was performed on the wall to simulate reverse cyclic lateral loading.

ANALYTICAL RESULTS

Behaviour of precast RC shear wall from FEA was basically examined in terms of stress pattern and lateral strength. Fig. 6 shows numerical model exhibiting substantial stress concentration at the base of the wall as observed in experimental investigation also. Although, numerical model anticipated slight contrast in the response of precast panels and cast-in-situ solid component by foreseeing little prolongation in the cast-in-situ concrete, which was not seen amid the experimental investigation. FEA determined lateral load carrying capacity of 362 kN, which is comparable to 353 kN got from experimental examination. However, lateral displacement obtained through FEA is somewhat lower as compared to the

experimental one. Table 3 shows analytical and experimental results, while Fig. 3 represents the load versus deformation curves of experimental and analytical investigations, which were observed to be fairly comparative.

CONCLUSIONS

Precast double wall system was designed and subjected to lateral loading to examine its seismic behaviour. The following conclusions are deduced from this study:

- The behaviour of tested wall was ductile, without showing shear cracks, which prevented shear failure and improved its post-yielding behaviour.
- No separation between precast panels and inner core was observed, showing excellent bond between the two.
- Substantial stress concentration at the base of the wall was observed in numerical modelling.
- It can be conluded that the concrete grade and reinforcing steel in the precast double wall system was on a higher side, as the wall did not show shear/flexure cracks or any other sign of damage on its surface. Thus concrete grade and amount of reinforcement can be reduced to achieve overall economy.

To conclude, the experimental and analytical results indicate that the precast double wall system is a promising construction technology for precast RC construction in seismic regions. However, further investigations warrant to study the behaviour of the developed precast wall with reference to varying reinforcement and structural configurations; effect of axial load on lateral resistance to strengthen the database and to the develop design guidelines for precast double walls.

ACKNOWLEDGEMENT

The authors are grateful to the Director, CSIR- Central Building Research Institute, Roorkee for giving kind support and encouragement during the research work carried out.

REFERENCES

[1] Dan, D et al (2011), Theoretical and experimental study on composite steel - concrete shear walls with vertical steel encased profiles, Journal of Constructional Steel Research, Vol. 67, No.5, pp. 800-813.

[2] Dazio, A et al (2009), Quasi-static cyclic tests and plastic hinge analysis of RC structural walls, Engineering Structures, Vol. 31, No. 7, pp. 1556–1571.

[3] Documentation, ABAQUS (2010), ABAQUS Analysis User's Manual.

[4] Greifenhagen, C and Lestuzzi, P, (2005), Static cyclic tests on lightly reinforced concrete shear walls, Engineering Structures, Vol. 27, No. 11, pp. 1703–1712.

[5] Holden, T et al (2003), Seismic performance of precast reinforced and prestressed concrete walls, Journal of Structural Engineering, Vol. 129, No.3, pp. 286-296.

[6] Jiang, H and Kurama, Y C, (2013), An analytical investigation on the seismic retrofit of older medium-rise reinforced concrete shear walls under lateral loads, Engineering Structures, Vol. 46, pp. 459-470.

[7] Li, B and Lim, C L, (2010), Tests on seismically damaged reinforced concrete structural walls repaired using fiber-reinforced polymers, Journal of composites for construction, Vol. 14, No. 5, pp. 597-608.

[8] Mander, J B et al (1988). Theoretical stress-strain model for confined concrete, Journal of Structural Engineering, Vol. 114, No. 8, pp. 1804-1826.

[9] Nayal, R and Rasheed, H A, (2006), Tension stiffening model for concrete beams reinforced with steel and FRP bars, Journal of Materials in Civil Engineering, Vol. 18, No. 6, pp. 831-841.

[10] Orakcal, K et al (2009), Shear strength of lightly reinforced wall piers and spandrels, ACI Structural Journal, Vol. 106, No.4, pp. 455.

[11] Parsafar, S and Moghadam, A S, (2017), Development of a rocking R/C shear wall system implementing repairable structural fuses, International Journal of Advanced Structural Engineering, Vol. 9, No. 3, pp. 247-258.

[12] Pavese, A and Bournas, D A, (2011), Experimental assessment of the seismic performance of a prefabricated concrete structural wall system, Engineering Structures, Vol. 33, No. 6, pp. 2049–62.

[13] Perez, F J et al (2002), Lateral Load Behavior of Unbonded Post-Tensioned Precast Concrete Walls, Proceedings of the International Conference on Advances in Building Technology, Vol. 1, 423.

[14] Smith, B J et al (2010), Design and measured behavior of a hybrid precast concrete wall specimen for seismic regions, Journal of Structural Engineering, Vol. 137, No. 10, pp. 1052-1062.

[15] Sritharan, S et al (2015), Precast concrete wall with end columns (PreWEC) for earthquake resistant design, Earthquake Engineering & Structural Dynamics, Vol. 44, No. 12, pp. 2075-2092.

[16] Todut, C et al (2014), Theoretical and experimental study on precast reinforced concrete wall panels subjected to shear force, Engineering Structures, Vol. 80, No. 14, pp. 323-338.

Table 1 Lateral resistance and displacement of the wall

State	Lateral load (kN)	Lateral displacement (mm)	Drift (%)
Elastic limit	270	12.0	0.53
Maximum resistance	353	27.0	1.20
Ultimate state	295	63.5	2.81

Fig. 1 Precast RC wall and test set-up

Table 2 Properties of Concrete and Steel used in Finite Element Modeling

Parameter	Concrete	Steel
Density (kN/m^3)	24	78.5
Young's modulus (N/mm^2)	27386	2×10^5
Poisson's ratio	0.19	0.30
Dilation angle	31	-
Eccentricity	0.10	-
f_{bo}/f_{co}	1.16	-
k	0.667	-
Viscosity parameter	0	-

Fig. 2 Separation of precast panel at the base

Table 3 Comparison of experimental and analytical results

Parameter	Analytical	Experimental
Peak load (kN)	362	353
Load at ultimate state (kN)	200	295
Drift at peak load	0.53	1.20

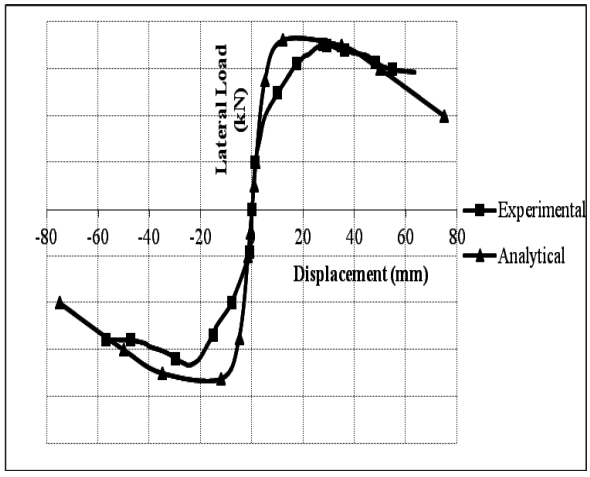

Fig. 3 Lateral-load displacement curve

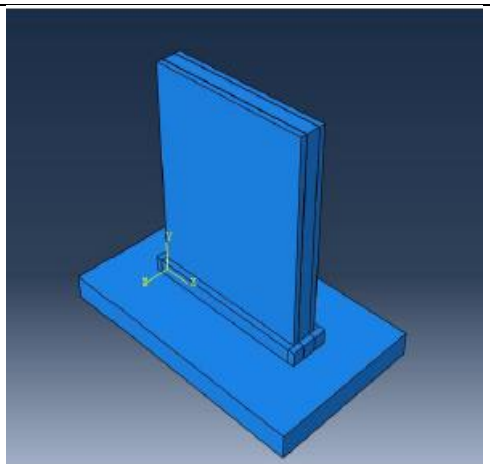

Fig. 4 Modelling in Abaqus

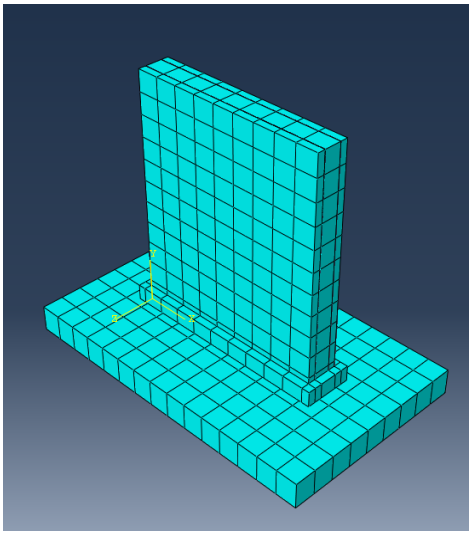

Fig. 5 Meshing of wall

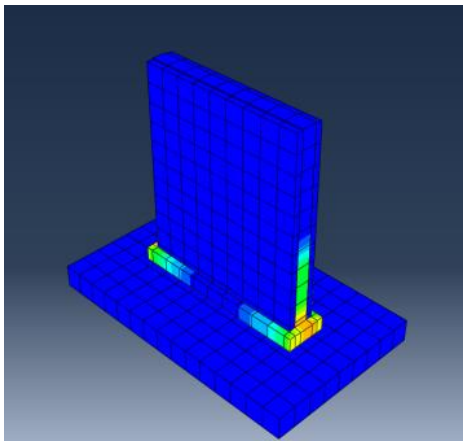

Fig 6. Stess concentration

8th International Engineering Symposium - IES 2019
March 13-15, 2019, Kumamoto University, Japan

Pull-out Behaviour of Headed Bars Embedded in Concrete

Akshat Chourasia[1], Shubham Singhal[2] and **Ajay Chourasia[3]**

1 *Department of Civil Engineering, Manipal Institute of Technology, Manipal 576104, India. E-mail: akshatchourasia03@gmail.com*
2 *Structural Engineering Division, CSIR- Central Building Research Institute, Roorkee 247667, India. E-mail: shubham.singhal092@gmail.com*
3 *Structural Engineering Division, CSIR- Central Building Research Institute, Roorkee 247667, India. E-mail: ajayc@cbri.res.in*

ABSTRACT: The structural behaviour of beam-column joint decides the inelastic performance of the reinforced concrete structure. The bending of beam longitudinal reinforcement into the column increases steel congestion and in many practical cases, the code recommendations are not followed completely due to casting difficulties. The problem can be overcome by providing headed bar reinforcement at the beam-column junction. This paper discusses the bond behaviour of headed bars based on experimental results obtained through pull-out tests conducted on bars embedded into the concrete cuboid. Test parameters considered for headed bars were varying embedment depth, head length and head profile. The results and behaviour of headed bars was compared to that of non-headed bars. The headed bars exhibited slip of bar or concrete failure along with higher bond capacity, whereas non-headed bars showed pull-out failure and lower bond capacity, thus establishing headed bars as potential substitute for conventional hooked bars in beam-column joint.

Keywords*: headed bars, plain bars, grooved bars, ribbed bars, pull-out tests, beam-column joints*

INTRODUCTION

The beam-column joints of reinforced concrete (RC) structure are vulnerable to lateral forces. Therefore, proper design and detailing of joints is recommended in various standards and codes of practise. The bond between the reinforcing bar and concrete plays a major role in achieving the anchorage capacity of the joint. Normally, longitudinal reinforcement bars of beam are bent into the column (hooked bars) up to the required development length to provide anchorage within the column element which creates steel congestion. Many a times, during the concrete casting, steel congestion results in honeycombing, which results in deteriorated joint strength. This may have adverse effect on the structural performance of joints during earthquake. Similarly, bending of large diameter bars is a cumbersome and expensive process in terms of cost and labour. In some cases, the architectural design also constrains the dimension of RC structural members which leads to insufficient development length, which further leads to inadequate shear and bond strength (Goto et al. 2012). These difficulties can be overcome by using headed bars, in which a reinforcement bar with head anchor attached at its end using welding, threading or forging. Headed bar was first used in Europe for construction of offshore oil platform and then expanded to other part of the world with time. It is gaining attention over worldwide due to its simplified design and detailing, lack of congestion, shop fabrication, reduced time and cost. The use of headed bar in the joints allows a very efficient construction

process which eliminates the need of traditional bending and facilitates extremely rapid construction. The head anchors are capable to mobilize full bar strength in tension by larger bearing at the head. ACI 318-08 recommends design provision and limitations for headed bars on various parameters such as grade of concrete, grade of steel, head geometry, embedment length, cover, spacing, confinement reinforcement, etc. Stress mechanism of headed bar relies on the length of embedded bar (friction), deformation on bar (adhesion) and head geometry such as circular, square, rectangle etc. (bearing) (Subramanian 2005). For smooth plain rebars, the bond stress remains zero; whereas in deformed rebars, the deformation enhances the bond capacity, which is mainly governed by mechanical interlocking. Previous research showed that the circular shape is the most effective for uniform distribution of bearing pressure from head base to concrete area. In reinforced concrete structure analysis, the interaction between reinforcement bar and concrete is often termed as bond stress- slip relation. The bond-stress slip relationship expresses the bond stress as a function of slip of a bar against the surrounding concrete. Significant research on bond behaviour of headed bars have been carried out by Berner and Hoff (1994), Choi (2006), DeVries (1997), Hong and Park (2012), Kang et al. (2010), Kang and Mitra (2012), Lee and Yu (2009), Park et al. (2003), Thompson et al. (2005), Wallace et al. (1998), Chun et al. (2017). However, limited research has been performed on the thickness and length of head and its influence on the anchorage capacity. In this research, an experimental investigation was performed on different types of circular headed bars with different profile over the length of head. Fig. 1 demonstrates different types of headed bars used.

EXPERIMENTAL DETAILS

Current research has major significance in design and construction works of joints in reinforced concrete structure. The experimental program was carried out to determine the bond capacity of different types of circular headed bars. In this study, experimental investigations have been performed to evaluate the bond capacity of headed bars with varying embedment depth, length of the head and deformation over the surface of head. The results are compared with that of deformed bar without head anchor. The concrete and reinforcement steel of 20 MPa and Fe 415 grade have been used in the study. A total of 45 different types of specimens with three different profile heads (plain, groove and ribbed) and five different lengths of head (11, 19, 27, 35 and 43 mm) were used in the study. The headed bars were embedded into the concrete cuboid (300 x 300 x 200 mm) at varying embedment depths of $6.25d_b$, $8.33d_b$ and $10.42d_b$ (d_b is bar diameter). The deformed bar was attached to the head using threading technique with minimum head bearing area as four times the area of deformed bar as specified in ACI 318-08. The details of different types of head with notation are given in Table 1. A total of 145 cuboids (45 x 3) specimens were casted for the pull-out test. The free end of headed bar protruded out over a length of 150 mm to ensure proper gripping of bar to conduct the pull out test in Universal Testing Machine (UTM) of 1000 kN capacity. Headed bar was embedded at the centre of the concrete cuboid specimens and arrangement of specimen in UTM is shown in Fig. 2. The specimens were tested monotonically under tension load until the occurrence of failure. In order to prevent the dynamic effects, the bar was subjected to the gradual load. Load and displacement for all the test specimens were measured using the data acquisition system. The pull-out strength obtained from the test is referred as bond capacity or anchorage capacity of the headed bar. The bond stress is calculated on the basis of embedment depth and surface area of the deformed bar in tension.

RESULTS AND DISCUSSION

The pull-out test results are studied from the standpoint of bond capacity, embedment depth, bond stress and slip of bar, which are presented in the form of

graphs and discussed in subsequent sections.

Failure Mode

The failure pattern of headed bar specimens varied with types of head and embedment depth. Concrete cone failure and concrete splitting failure was observed as the failure pattern of plain headed bar of any head length. The bond stress travels along the embedded length of deformed bar and then reaches to the head anchor with the generation of bearing pressure under the base of head, which is distributed uniformly to the surrounded concrete area followed by rebar slip. It was noticed that the tensile load application on the headed bar terminates with the slip of bar, however capacity was still available to resist nearly 30% to 50% more load. In case of plain and grooved headed bars of $8.33d_b$ and $10.42d_b$ embedment depth, yielding of reinforcement bar was observed by virtue of yielding mechanisms. Specimen without head anchor leads to pull-out failure, also termed as bond failure due to insufficient bonding between steel and concrete and found to have no beneficial effect of higher embedment depth. Overall scanning of failure behaviour of different headed bar specimens depicts that ribbed headed bar leads to rebar slip which assure that the presence of bearing capacity of ribbed head anchor is greater than the concrete bearing capacity. The characteristic failure of grooved and plain headed bar influenced with the embedment depth i.e. for $6.25d_b$ embedment depth, concrete cone failure and concrete splitting failure was noticed, whereas for specimens with $8.33d_b$ and $10.42d_b$ embedment depth, yielding and rebar slip was observed.

Influence of Embedment Depth

Among the test variables, the most influential parameter is embedment depth of the headed bar. The measured ultimate tensile bond capacity is plotted against varying embedment depth of different types of headed bar as shown in Fig. 3. It clearly demonstrates the influence of embedment depth, length of head and head profile on the bond capacity. In all the cases, the specimen with higher embedment depth possesses better resistance to the applied load than the specimens with lesser embedment depth. The plain headed bar requires higher embedment depth compared to ribbed and grooved heads. Similar trend has been observed with specimens having grooved head but the bond capacity is more than 40% higher than specimens with plain head. The scenario of specimens with ribbed head is completely distinct and shows exceptionally better resistance to slip and offers better bond capacity than specimen with plain and grooved head. It clearly shows that the need of embedment length can be reduced with the use of ribbed head which can be achieved using higher embedment depths in other cases.

Slip Behaviour of Headed Bars

Slip is a part of bond action. As the load increases gradually, the reinforcement bar is subjected to the interfacial stresses between the reinforcement and surrounding concrete. This results in rebar slip upon weakening of the interface. Fig. 4 demonstrates the influence of head length and profile in resisting the rebar slip. The specimen with plain headed bar experienced much incremental difference in rebar slip with respect to its embedment depth. In case of grooved and ribbed headed bars, the observed difference in slip with respect to the embedment depth is small as compared to plain headed bar specimens. In ribbed headed bar specimens, the average slip is 2% less as compared to the plain and grooved headed bar specimens. The slip reduces with respect to the head length for all the embedment depth. Although the slip value of deformed bar without anchor head is quite similar to the deformed bar with anchor head, the anchorage capacity observed was 30% to 50% more for headed bar. The average slip of headed bar corresponding to ultimate load was estimated between 10 mm to 15 mm for any length or thickness of head.

Influence of Deformation over the Head

The bar geometry and deformation over the surface of the bar governs the general behaviour of the bar to a high degree and

determines the bond resistance. Both grooved and ribbed head were effective enough as compared to the plain head for assurance of bond strength. For headed bar the increase in average bond stress with respect to deformed bar without head for embedment depth $6.25d_b$, $8.33d_b$ and $10.42d_b$ was 69.8%, 30.55% and 26.84%. Similarly, the increase in bond stress of grooved headed bar as compared with plain headed bar for embedment depth $6.25d_b$, $8.33d_b$, and$10.42d_b$ was 15.47%, 11.37% and 3.58%, whereas for ribbed headed bar when compared with plain headed bar the increase in bond stress for embedment depth $6.25d_b$, $8.33d_b$ and $10.42d_b$ were 21.61%, 10.50% and 2.04%. The bond stress decreases with increase in the embedment depth due to increase in surface area whereas bond capacity increases with the same. Ribbed headed bar was found to be more effective when compared to plain and grooved headed bar in terms slip of bar as the slip occurrence was quite less and the bond stress was marginally equal to grooved headed bar.

Influence of Head Length

Head geometry is the key parameter for the proper distribution of full rebar bond stress into the concrete. Other than net bearing area of head anchor, the length of head also has certain amount of impact on the bond stress along the headed bar. From bond stress-slip relationship for varying length of head of different deformation over the length of head, it was found that the length of head influenced the bond stress of headed bar along with embedment depth. On comparing the overall behaviour of 19 mm, 27 mm, 35 mm and 43 mm against 11 mm thick head anchor, results illustrated that mean increase in bond stress was 6.13%, 9.086%, 8.41% and 2.438% respectively. From this, it was clear that 27 mm thick head was effective enough for bond stress resistance.

CONCLUSIONS

The following conclusions are deduced from this study:

- Headed bar is effective enough as compared to traditional anchorage hooked bars.
- The bond capacity of embedment depth $10.42d_b$ is thrice the bond capacity of embedment depth $6.25d_b$. The bond stress value reduces with the increase in embedment depth of headed bar due to increase in the surface area of deformed bar.
- Slip of headed bar is indication of attaining peak bond capacity and passing of further tensile stress to head anchor. Increase in length of head reduces the slip of the headed bar to some extent which prevent pull-out failure of headed bar owing to its bearing capacity.
- Among five different lengths of head, 27 mm head was influential enough for bond stress resistance and 43 mm head for slip of bar.
- All three headed bars (plain, grooved and ribbed) were found to have similar behaviour on initial stage of loading and at the ultimate loading point, the failure pattern differed for each specimen for each embedment depth. Failure pattern was almost similar for plain and grooved headed bar. Ribbed headed bar was found to give better performance in terms of bond capacity and failure pattern as compared to plain and grooved headed bars.

ACKNOWLEDGEMENT

The authors are grateful to the Director, CSIR- Central Building Research Institute, Roorkee for giving kind support and encouragement during the research work carried out.

REFERENCES

[1] ACI Committee, (2008), Building code requirements for structural concrete (ACI 318-08) and commentary, American Concrete Institute.

[2] Berner, D E and Hoff, G C, (1994), Headed reinforcement in disturbed strain regions of concrete members, Concrete International, Vol. 16, No. 1, pp. 48-52.

[3] Choi, D U, (2006), Test of headed reinforcement in pull-out II: deep embedment, International Journal of Concrete Structures and Materials, Vol. 18, 3E, pp. 151-159.

[4] Chun, S C et al (2017), Side-Face Blowout Failure of Large-Diameter High-Strength Headed Bars in Beam-Column Joints, ACI Structural Journal, Vol. 114, No. 1, pp. 161-172.
[5] DeVries, R A, (1997), Anchorage of Headed Reinforcement in Concrete, PhD dissertation, University of Texas at Austin.
[6] Goto, Y et al (2012), Anchorage Failure and Shear Failure of RC Exterior Beam-Column Joint, 15th World Conference on Earthquake Engineering (15WCEE).
[7] Hong, S and Park, S K, (2012), Uniaxial bond stress-slip relationship of reinforcing bars in concrete. Advances in Materials Science and Engineering, Vol. 2012.
[8] Kang, T H et al (2010), D.U. Bar pullout tests and seismic tests of small-headed bars in beam-column joints, ACI Structural Journal, Vol. 107, No. 1, pp. 32-42.
[9] Kang, T H K and Mitra, N, (2012), Prediction of performance of exterior beam-column connections with headed bars subject to load reversal, Engineering Structures, Vol. 41, pp. 209-217.
[10] Lee, H J and Yu, S Y, (2009), Cyclic response of exterior beam-column joints with different anchorage methods, ACI Structural Journal, Vol. 106, No. 3, pp. 329-339.
[11] Park, H K et al (2003), The effect of head plate details on the pull-out behaviour of headed bars, Magazine of Concrete Research, Vol. 55, No. 6, pp. 485-496.
[12] Subramanian, N (2005), Development length of reinforcing bars: Need to revise Indian codal provisions, Indian concrete journal, Vol. 79, No. 8, pp. 39-46.
[13] Thompson, M K et al (2005), CCT Nodes Anchored by Headed Bars-Part 1: Behavior of Nodes, ACI Structural Journal, Vol. 102, No. 6, pp. 808-815.
[14] Wallace, J W et al (1998), Use of headed reinforcement in beam-column joints subjected to earthquake loads, ACI Structural Journal, Vol. 95, No. 5, pp. 590–606.

Table 1 Details of head anchor

Length (m)	No. of grooves /ribs	Plain	Grooved	Ribbed
11	1	P11	G11	R11
19	2	P19	G19	R19
27	3	P27	G27	R27
35	4	P35	G35	G35
43	5	P43	G43	G43

(a)

(b)

(c)

Fig. 1 Different types of Headed bars (a) Plain headed bar; (b) Grooved headed bar; and (c) Ribbed headed bar

Fig. 2 Experimental set-up

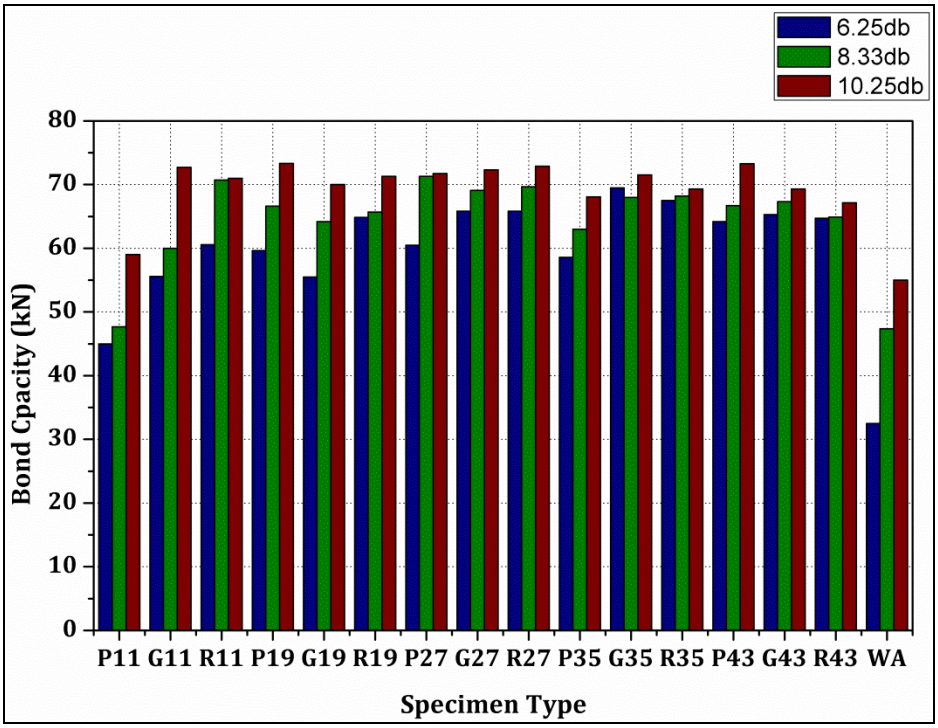

Fig. 3 Ultimate tensile bond capacity versus types of headed bar for varying embedment depth

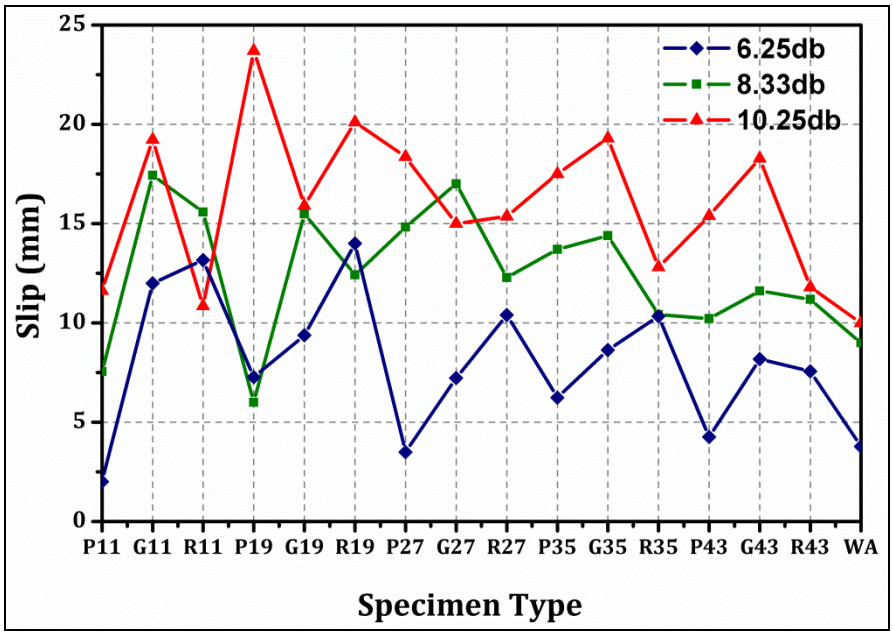

Fig. 4 Ultimate bond capacity versus types of headed bar for varying embedment depth

8th International Engineering Symposium - IES 2019
March 13-15, 2019, Kumamoto University, Japan

Effect of Sea Water on Strength of Structural Concrete

Vishwanath Okram[1], Ajith Hebbar[2] and Rashmi H[3]

[1]Department of Civil Engineering, Alva's Institute of Engineering and Technology Karnataka, Moodbidri, Mangalore 574225, India.
email:vishwanathok@gmail.com
[2]Departmentof Civil Engineering,Alva's Institute of Engineering and Technology Karnataka, Moodbidri, Mangalore 574225, India.
email:ahebbar2@gmail.com
[3]Department of Civil Engineering,Alva's Institute of Engineering and Technology Karnataka, Moodbidri, Mangalore 574225, India.
email:rash.jnnce@gmail.com

ABSTRACT: In this project, the effects of sea water on mixing, curing and strength gaining of different grades of concrete was investigated. Several billion litres of water is annually used for mixing, curing and cleaning in concrete industry. As there is a scarcity of fresh drinkable water around the world, there is a great need to save fresh water and hence possibilities of usage of seawater in concrete industry needs to be investigated seriously. However, most of the reinforced concrete codes do not permit the use of seawater due to risk of early corrosion of reinforcement. In the present study, several concrete cubes prepared using sea water were tested for their compressive strength. The strength of these cubes was observed to be increased till 28 days, but decreased by 15% as compared to the similar concrete specimen made and cured with fresh water at the end of 90 days.

***Keywords**: sea water, compressive strength, concrete, corrosion, curing*

INTRODUCTION

Concrete has an excellent structural performance and durability, but is affected by early deterioration when subjected to a marine environment. The most common cause of deterioration is corrosion of the steel reinforcement, with subsequent sapling of concrete. Therefore the selection of materials, mix design, and proper detailing of reinforcement are essential parameters in producing a durable marine structure concrete.

As the population increases rapidly the world population may be doubled, with the largest growth in developing countries that have experienced in water crisis. In addition more than half population will not be able to get enough drinking water. Increasing infrastructure development is in line with the needs of clean water every year, where sea water has not been used for such things for that reason. Saving of fresh water savings is very seriously needed. In coastal areas, there has always been a deficiency of fresh water as the available water is affected by sea salts. So it is difficult to deliver fresh water for construction works in such location. Also it is economical to use sea water that is available near the construction. But sea water contains large amount of sea salts, which may have unfavorable effect on the properties of concrete.

The durability of concrete is generally regarded as its ability to resist the effects and influences of the environment, while performing its desired function. The chemical deterioration of concrete subjected to seawater has been a topic of interest to concrete researchers in the last few decades, and the findings have revealed some very important facts, but still it remains to be a dynamic subject

for further study and research. The primary chemical constituents of seawater are the ions of chloride, sodium, magnesium, calcium and potassium. In seawater containing up to 35,000 ppm of dissolved salts, sodium chloride (NaCl) is by far the predominant salt. The pH value of seawater varies between 7.4 and 8.4. Corrosion of reinforcing steel occurs below a pH of 11. Therefore, in cases where concrete is subjected to a highly severe environment, the cement must supply alkalinity.

LITERATURE REVIEW

According to this research concludes that both experimentally and analytically, the compressive strength of 7 days and 1 4 days old concrete specimen cured by seawater are higher than those cured by plain water.

The rate of the strength gain in fresh water cubes is slow as compared with the salt water cubes.

MATERIALS REQUIRED

Coarse Aggregate - Crushed angular stone aggregate of maximum size 20mm.

Sand (fine aggregate) -The fine aggregates available at nearby market.

Cement- OPC 43 grade, specific gravity ranging 3.15.

Water - Ordinary clean portable water free from suspended particles and chemical substances from laboratory.

Salt water - On average, seawater in the world's oceans has a salinity of about 3.5% (35 g/L). This means that every kilogram (roughly one litre by volume) of seawater has approximately 35 grams of dissolved salts (predominantly sodium ($Na+$) and chloride ($Cl-$) ions).

EXPIREMENTAL STUDY

The experimental study was carried out using a concrete mixed and cured with fresh water and seawater in order to determine the effects of curing condition for determining the compressive strength.

Concrete mix design

A mix design is prepared for M_{20} concrete. The ingredients of concrete i.e. cement, fine aggregate and coarse aggregate are collected and weigh according to the mix ratio of 1:1.7:2.7. Water cement ratio of 0.45 is used for this mixture. The concrete mix is prepared and casted in the cubes in 3 layers of 35 strokes of tamping rod in a uniform manner over the surface of the layer.

Specimen standards

Eight standard cubes of 150 x 150 x 150 mm^3 were casted and were cured for 7 days, 14 days, 28 days and 90 days. The effect of salt water and fresh water on the compressive strength of concrete is tested using UTM machine.

Effects of Continuous Immersion of Concrete in Sea Water

Concrete that is totally and continuously immersed in water, even if the water contains dissolved salts such as are found in sea water, generally be regarded as being in a protected exposure. Continuous immersion usually provides a uniformity of environment with respect to temperature and moisture content that prevents the immersed concrete from being subjected to such deteriorating influences as frost action, volume change due to wetting and drying, and differential volume change due to moisture content differences between the surface and the interior.

Chemical Attack of Sea Water on Concrete

The potentially aggressive constituents of sea water with respect to concrete are the sulfate, chloride, carbonate, bicarbonate, alkali metal and magnesium ions. The aggressive action of the sulfate ion on concrete is being discussed by other contributors to this symposium. However, since, in sea water, the sulfate component is magnesium sulfate rather than sodium or calcium sulfate, as is more often the case in sulfate-attack situations not involving sea water, the various chemical reactions of magnesium sulfate with several of the constituents of hydrated portland cement are noted subsequently.

RESULTS AND ANALYSIS

After curing the cubes for consecutive days ultimate strength and compressive strength has been determine for each days.

ULTIMATE STRENGTH AND COMPRESSIVE STRENGTH

Type of water	Specimen number	Ultimate Load (KN)	Compression Strength (N/mm^2)	Average Compressive Strength (N/mm^2)
Fresh Water	01 (7days)	597	26.53	30.45
	02 (14days)	661	29.37	
	03 (28days)	738	32.8	
	04 (90days)	745	33.13	
Sea Water	01 (7days	640	28.45	31.26
	02 (14days)	730	32.45	
	03 (28days)	780	34.67	
	04 (90days)	664	29.47	

COMPRESSION STRENGTH GRAPH

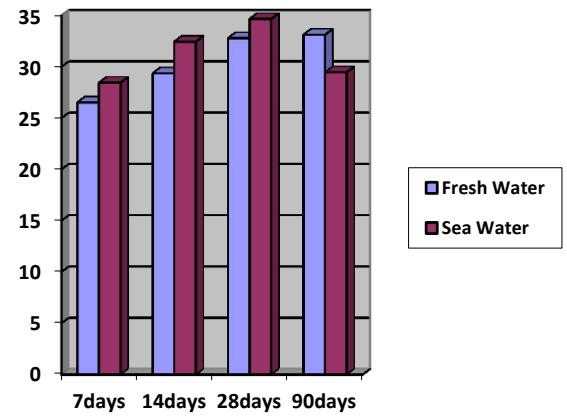

Graph 1: Compression Strength Graph for 7 days, 14 days, 28 days and 90 days (X-axis: Compressive Strength MPa ;Y-axis Water type)

From Graph 1, for M20 grade concrete cubes with Fresh water had given a compressive strength of 26.53, 29.37, 32.8 and 33.13 N/mm^2 at 7, 14 and 28 days respectively.

For M20 grade concrete cubes with sea water had given a compressive strength 28.45, 32.45, 34.67 and 29.47 N/mm^2 at 7, 14, 28 and 90 days. From the tests, we can conclude that using sea water for mixing and curing of the concrete effects the compressive strength due to action of NaCl with the concrete. Thus, sea water can be used if an inhibitor is added to reduce the reaction.

CONCLUSIONS

From this study we have concluded that:

- As sea water increases strength, it reduces with time due to corrosion of steel with sea water.
- The experimental results and discussion, sea water affects the gain in strength of concrete when used for mixing and curing till 28 days and the strength reduces up to 15% at end of 90days. Sea water cannot be used for casting and curing since structures need to hold strength for its design period.
- There is marginal increase in the strength of cubes cast and cured in salt water as compared to those of cast and cured in fresh water at 7, 14 and 28 days ages of concrete. Thus strength decreases due to aging.

REFERENCES

[1] A Review on Strength of Concrete in Seawater by Akshat Dimri, Jay Kr. Varshney, V. K. Verma, Sandeep Gupta, M.Tech Civil Engg and Assistant Professor, Civil Engg G.B.P.U.A&T, Pantnagar, India G.B.P.U.A&T, Pantnagar, India Sandhya R. Mathapati (Guide & Assistant Prof., Department of Civil Engineering, DYPSOET, University of Pune, Pune – 411014)

[2]The Effect of Mixing and Curing Sea Water on Concrete Strength at Different Ages by Qingyong Guo, Lei Chen, Huijian Zhao, Jorge Admilson, and Wensong Zhang.

[3] "Effect Of Salt Water On Compressive Strength Of Concrete" Preeti Tiwari , Rajiv Chandak , R.K. Yadav

[4]IS456:2000 – Indian standards Plain and Reinforced concrete – Code practice.

8th International Engineering Symposium - IES 2019
March 5-7, 2019, Kumamoto University, Japan

Optimised Bus Route Network Design for Bengaluru City

Vinayaka Murthy Vignesh

Department of Civil Engineering, National Institute of Technology Karnataka, Surathkal, Mangalore 575025, India. vigneshvinayakamurthy@gmail.com

Abstract: The objective of this paper is to create or network a bus route transit system for the city of Bangalore by minimizing the operator cost, maximize demand and also minimize the travelling time of a passenger using Genetic Algorithm. Demand in other words is population, and our objective as said is to make the bus route available to as many people as possible thereby most people have access to the bus transport and in turn also increase the profit of the operator.

***Keywords**: Optimisation, Network Design, Bus Network, Bangalore*

INTRODUCTION

Infrastructure plays a key role in the economy and human life. When we talk about infrastructure it refers collectively to the roads, bridges, rail lines and similar public works that are essential for the functioning of industrial economy. Sewage, transportation, communication, water and electric systems are all a part of infrastructure. These systems are high-cost investments and is location specific and cannot be transferred from one place to another.

Transportation and transportation infrastructure are interdependent. Different modes of transportation have various requirements of infrastructure. For air transportation, their infrastructure will be the airport. Port will be the infrastructure for water transportation while infrastructure for land transportation such as public bus will be the bus terminal or bus stop. A bus terminal maybe termed as a station or terminal where multiple routes converge or diverge. It could also act as a junction between 2 routes.

As bus station play a crucial role in reinforcing the volume of traffic as well as in providing service to the citizens, the bus service organizations (especially in the public sector) should improve and encourage the emergence of bus station management system as an independent sector in the field of traffic management.

Investment in public transportation expands service and improves mobility, and if sustained over time can potentially affect the economy by providing:

- Travel and vehicle ownership cost savings for public transportation passengers and those switching from automobiles, leading to shifts in consumer spending
- To further direct travel cost savings for businesses and households
- Business operating cost savings associated with worker wage and reliability effects of reduced congestion
- Business productivity gained from access to broader labor markets with more diverse skills, enabled by expanded public transit service areas and reduced
- Additional regional business growth enabled by indirect impacts of business growth on suppliers and induced impacts on spending of worker wages. At a national level, cost savings and other productivity impacts can affect competitiveness in international markets.

Bangalore (Bengaluru), is a seamless example of peaceful coexistence. Currently Bengaluru has developed and grown

exponentially, while staying true to its base culture. Despite its gradual transformation into a concrete jungle filled with corporates, Bangalore, officially known as Bengaluru is the capital of Karnataka. It has a population of 8.42 million, making it the third most populous city.

For our study, the Bangalore city was divided into 9 zones (table 1 and figure 1) as East Bangalore, Byatarayanapura, Dasarahalli, RR Nagar, Bommanahalli, Mahadevapura, West Bangalore and South Bangalore as per Bruhat Bengaluru Mahanagara Palike (BBMP) the administrative body of Bangalore.

MODEL FORMULATION

Essentially speaking, as stated by Wei Fan and Randy B. Machemehl (2006), the transportation system can be described in terms of "nodes," "links," and "routes." If nodes represent a particular location, links connect them together to form routes. i, j belongs to N centroid nodes i.e., zones; r_k belongs to R routes. For better understanding refer the figure 1 and 2 at the end.

DATA

- R_{max} maximum allowed number of routes for the initial candidate route network;
- N number of centroid nodes in the route network;
- d_{ij} total demand between Centroid Nodes i and j;
- h_{max} maximum headway required for any route;
- h_{min} minimum headway required for any route;
- L_{max} is the maximum load factor for any route;
- P represents the seating capacity of buses operating on the network;
- W is the maximum bus fleet size available for operations on the route Network; C_v per-hour operating cost of a bus in cost/ vehicle/ hr;
- Cm is the of value of time cost/min;
- Ov operating hours for the bus running on any route;
- C_d value of each unsatisfied travel demand in dollars cost/person
- $Q_{r_m}^{max}$ max flow on route r_m
- and C_1, C_2, C_3 are weights reflecting the relative importance of three components including the user costs, operator costs, and unsatisfied total demand costs, respectively. Note that $C_1+C_2+C_3=1$ and It should be pointed out that these three weights are dependent on the planners' experience and expert's judgment.

DECISION VARIABLE FOR THE OBJECTIVE FUNCTION

- M is the number of routes of the current proposed bus transit network Solution,
- r_m is the m^{th} route of the proposed solution, m=1, 2. . . M;
- d_{ij}^{rm} is the bus transit travel demand between Centroid Nodes i and j on Route r_m;
- t_{ij}^{rm} is the total travel time between Centroid Nodes i and j on Route r_m;
- h_{rm} bus headway operating on Route r_m (hour/vehicle); L_{rm} loading factor in Route r_m; T_{rm} round trip time of Route r_m; T_{rm} $=2D_{rm}/V_b$;
- N_{rm} _number of operating buses required on Route r_m; N_{rm} $=T_{rm}$ $/h_{rm;}$
- W says the fleet size available to the operator

OBJECTIVE FUNCTION

$$Z = C_1\left(\sum_{i\in N}\sum_{j\in N}\sum_{r_m\in DR_{ij}} d_{ij}^{r_m} * t_{ij}^{r_m}\right) + C_2\frac{C_v}{C_m}O_v\left(\sum_m^M \frac{T_{r_m}}{h_{r_m}}\right) + C_3\frac{C_d}{C_m}\left(\sum_{i\in N}\sum_{j\in N} d_{ij} - \sum_{i\in N}\sum_{j\in N}\sum_{r_m\in DR_{ij}} d_{ij}^{r_m}\right) \quad \textbf{(1)}$$

CONSTRAINTS

$$h_{r_m}^{min} \le h_{r_m} \le h_{r_m}^{max} \quad \textbf{(2)}$$

$$L_{r_m} = \frac{Q_{r_m}^{max} h_{r_m}}{P} \le L_{max} \quad \textbf{(3)}$$

$$\sum_m^M N_{r_m} = \sum_m^M \frac{T_{r_m}}{h_{r_m}} \le W \quad \textbf{(4)}$$

INITIAL CANDIDATE ROUTE SET PROCEDURE

This procedure i.e, T. M. Murali (2004) is

executed for a set of routes joining different centroid nodes by links that could possibly be the selected paths after optimization. In other words we are choosing routes that could be candidates for optimization to take place. To generate this set we used the Yen's K shortest path algorithm. Yen's K shortest path algorithm is a greedy algorithm that gives us "K" shortest path given an initial point and an end point. The "K" value that we choose is 5 between each centroid nodes, which means that we would have 5 shortest paths from one centroid to another in the candidate set (figure 3)

GENETIC ALGORITHM

Genetic algorithm i.e., Partha Chakroborty and Tathagat Dwivedi (2002); follows Darwin's rule of the survival of the fittest over consecutive generation for the problem to be solved. Each generation entails a population of character strings, analogous to the chromosome in our DNA. Each individual represents a point in a search environment and a probable solution. The individuals in the population go through a series a changes that leads to the drastic change called evolution.

GAs are based on the behavior of chromosomes within a population. They follow the rules given below:

- Individuals in a population compete for resources and mates.
- Those individuals most successful in each 'competition' will produce more offspring than those individuals that perform poorly.
- Genes from `good' individuals propagate throughout the population so that two good parents will sometimes produce offspring that are better than either parent.

Thus each successive generation will become more suited to their environment.

In a GA a population of individuals is maintained and each of these individuals represent a possible solution. The individuals are encoded as vectors of finite length of alphabets or binary codes {0,1}. We can say that the individuals are chromosomes and the variables involved are genes. Hence, a solution (chromosome) is composed of several variables (genes). Each solution is assigned a fitness score. The solution with highest fitness score is considered. The GA uses selective breeding to pick the best solution from the population of solutions by combining different variable values.

The solutions produced for each generation are better than the previous generation's solution. They contain partial solution from the previous generation solution. The populations converges when the solutions are not significantly different from the previous solutions. The algorithm comes to a halt when it has converged to a set of solutions for the given problem.

OPTIMISATIONS

The optimization equation i.e. Wei Fan and Randy B. Machemehl (2006); consists of 3 terms user cost, operator cost and unsatisfied demand cost. Every term is has a time dimension and the objective is to minimize the sum of them. The first term represents the sum of the product of Demand on a route and the time taken to travel by that route. It implies that if time and headway are same on 2 routes, it's easier to transport people on the one with less demand.

The 2nd term consists of the operator cost which includes the number of bus plying on different routes, operator cost per hour per bus and a factor to convert cost to time (value of time).

The 3rd term takes care of the demand not being met, in other words if a route has more number of demands not being met, their objective function value (Z) would be increased and hence that particular route may not be a less ideal route.

Since we have the constraint to plug in the values of maximum and minimum headway there is a need to find the headway for each and every route between 2 given centroid nodes. The idea is to minimize the objective function for a given start and end centroid node combining all the routes.

OTHER REQUIRED DATA

The demand in other words, number of people using that route, was distributed with respect to the population densities in the zones chosen (as shown in figure 1). The round trip time on each route was

calculated by dividing the distance with the average speed of the bus.
Cost values:

- C_v =200 Rupees/Vehicle/Hour
- C_m =70 Rupees/min
- O_v =19 Hours
- C_d =15 Rupees

The headways for each route were adjusted to vary between 10 to 30 minutes in order to provide the best possible service to the citizens that opt for bus transportation.

RESULT

The 2 maps shown in figure 4 and 5 are the first optimized and second optimized paths that need to be implemented in Bangalore for the passengers to have minimum travel time, in order to get better accuracy and realistic path we could introduce more number of zones and exact demands on each routes which would enable us to have an optimized bus network for Bangalore that would help both the citizens and the government or BMTC.

ACKNOWLEDGEMENTS

The internship opportunity I had with Centre for Infrastructure, Sustainable transportation and Urban planning, IISc was a great platform for learning and professional development. Therefore, I consider myself lucky. I am grateful to all the wonderful people who I met during this internship period. I would also like to express my deepest gratitude and special thanks to Dr. Caleb Ronald, who in spite of being busy with his duties, took time out to guide me on the right path and allowing me to carry out my project at their esteemed organization.

REFERENCES

[1] Hiroshi Shimmoto, Jan-Dirk Schmöcker, Fumitaka Kurauchi(2012); "Optimisation of a Bus Network Configuration and Frequency Considering the Common Lines Problem"
[2] Lecture by T. M. Murali (2004); "Computing the k Shortest Paths".
[3] Patricia Jaramillo-álvarez, Carlos a. González-calderón M.s, Guillermo González-calderón (2012-2013); "route Optimization of Urban Public Transportation".
[4] Partha Chakroborty and Tathagat Dwivedi (2002); "optimal Route Network Design for Transit Systems Using Genetic Algorithms".
[5] Steven I-Jy Chien, Branislav V. Dimitrijevic, and Lazar N. Spasovic (2003); "Optimization of Bus Route Planning in Urban Commuter Networks
[6] Wei Fan and Randy B. Machemehl (2006); "Optimal Transit Route Network Design Problem with Variable Transit Demand: Genetic Algorithm Approach".

Table 1: Zone details of Bangalore

S.no	Area	Population	Area (sq.km)
1	East	1695183	30.28
2	Byatarayanapura	578773	49.15
3	Dasarahalli	273622	18.65
4	RR Nagar	404924	33.59
5	Bommanahalli	473205	42.64
6	Mahadevapura	534797	47.61
7	West	1465613	26.42
8	South	1877024	27.54

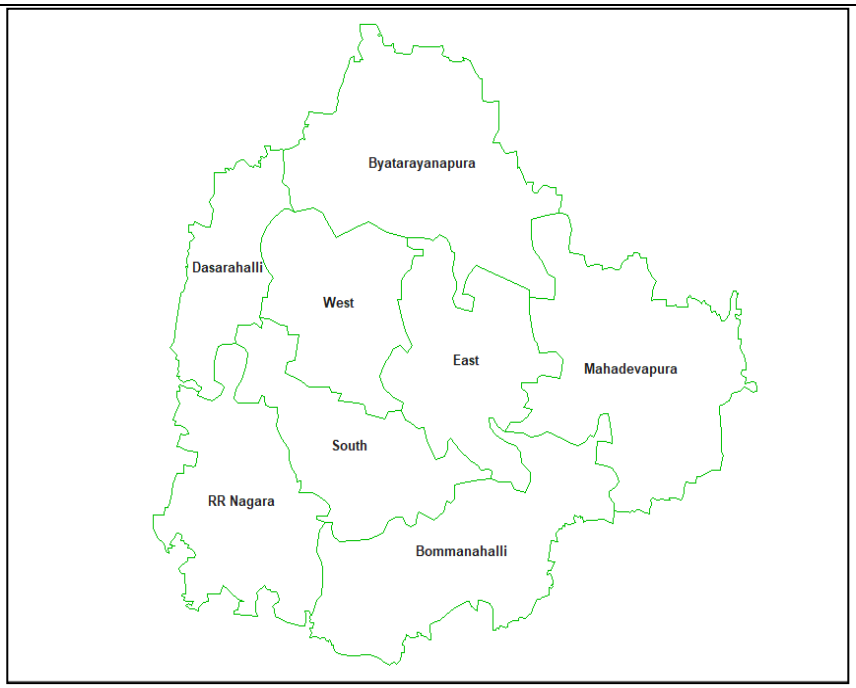

Figure 1: Zone map of Bangalore used for study

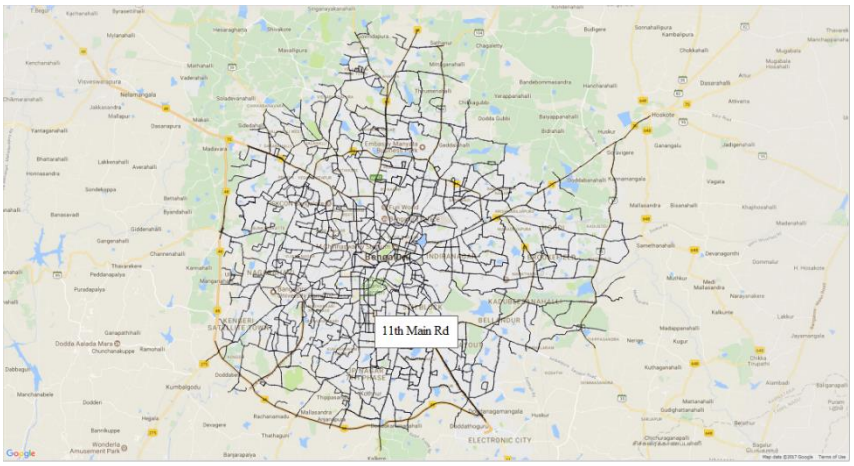

Figure 2: Road network of Bangalore city

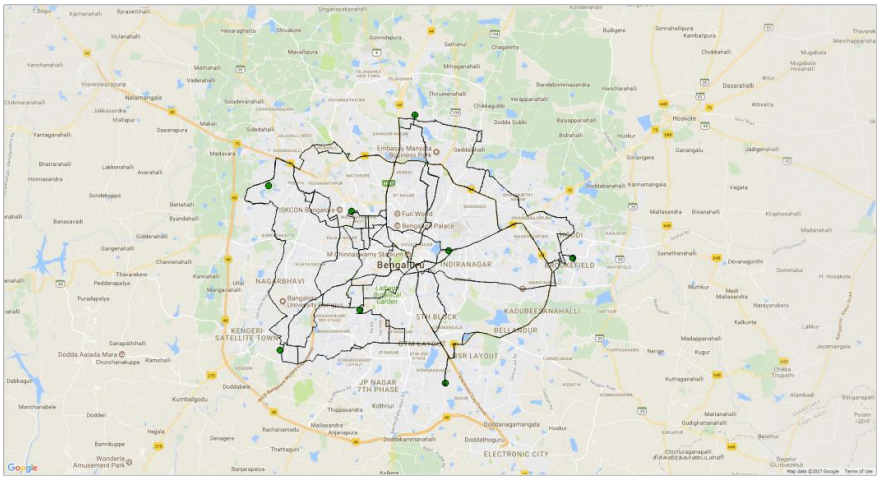

Figure 3: Initial candidate route set

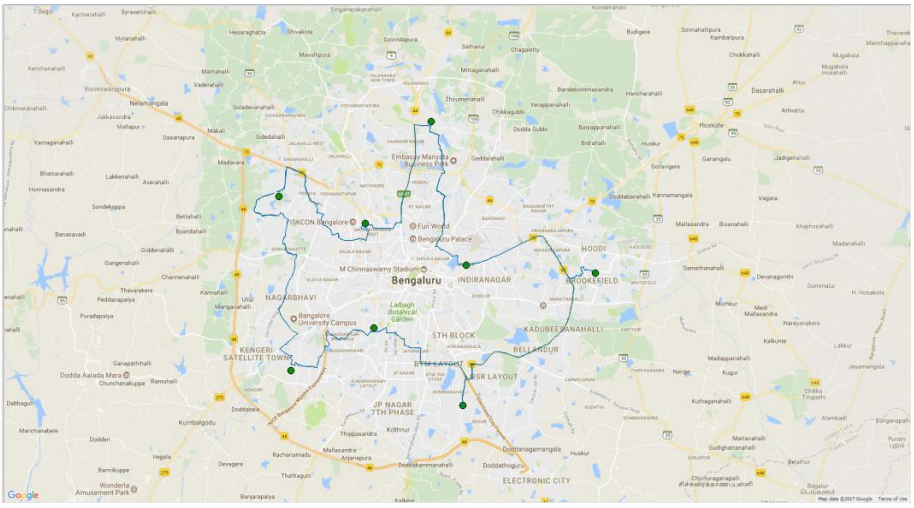

Figure 4: First Optimised Bus route network for Bangalore city

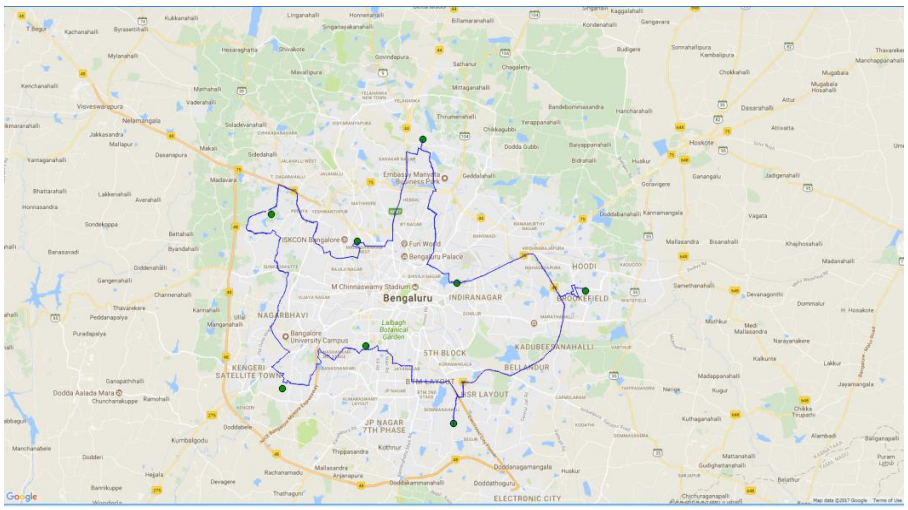

Figure 5: Second Optimised Bus route network for Bangalore city

8th International Engineering Symposium - IES 2019
March 13-15, 2019, Kumamoto University, Japan

A Comparative Study of Statistical Regression and Artificial Neural Network Approaches in Rainfall–Runoff Modeling

Devika Suresh [1], Vinayaka Murthy Vignesh [2] and **Manna Jacob[3]**

1 *Department of Civil Engineering, National Institute of Technology Karnataka, Surathkal, Mangalore 575025, India.*
Email: devikasuresh.nitk@gmail.com
2 *Department of Civil Engineering, National Institute of Technology Karnataka, Surathkal, Mangalore 575025, India.*
Email: vigneshvinayakamurthy@gmail.com
3 *Department of Civil Engineering, National Institute of Technology Karnataka, Surathkal, Mangalore 575025, India.*
Email: mannajacob1997@gmail.com

ABSTRACT: Determining a sturdy relationship between rainfall and runoff for a catchment area has been a challenging task for engineers and hydrologists alike. Through this study, various statistical regression models and artificial neural network (ANN) models have been developed in order to discuss how effectively they reflect complex rainfall-runoff relationships. The models were generated based on the data sets of rainfall and runoff data collected from various catchments located in and around the state of Karnataka in India. This data was collected for a period of a few specific months (Indian Monsoon season) over a number of years. A linear model, a nonlinear model and a lag model are generated for a comparative study in the case of the statistical approach through regression. Similar model architectures with associated independent variables are developed using the ANN approach as well. The output (estimated runoff) from all the models were then tested and compared with the actual runoff data using statistical parameters, such as Root Mean Square Error (RMSE), Coefficient of Determination (R^2) and Coefficient of Correlation (R), as performance criteria. In the recent past, both statistical models and Artificial Neural Network (ANN) models have been used successfully to model complex nonlinear input-output relationships in various interdisciplinary fields. While regression is a more classical approach for modelling hydrological processes, ANN is now considered one of the most promising tools in Hydrology. In this research, our main objective is to conduct a comparative study by analysing both these approaches that are currently being used to model Rainfall-Runoff relationships.

***Keywords**: rainfall-runoff modeling, regression, neural networks*

INTRODUCTION

Water is a life-sustaining natural resource and is under heavy stress due to increased demand and associated limitation of available quantity. Proper water management is the only solution that may offer a squeezed gap between the water demand and its supply. Since human modifications of the environment now occur on scales that significantly affect seasonal and yearly hydrologic variations, a thorough understanding of the different hydrological phenomena is required to study the implications of these changes. Further study of the links, relations and interactions between the phenomena and the related consequences and implications is necessary. Hence, modeling of

relationships between key hydrological components (like rainfall and runoff) become important. This study focuses on the complex relationship between Rainfall and Runoff as together they form the driving forces for most hydrological studies.

Since rainfall is the most widespread mode of precipitation and also the cheapest source of freshwater, many attempts have been made to analyse, model and predict rainfall behavior using various empirical, statistical, numerical and deterministic techniques. However, these attempts fall short if rainfall generated runoff is not taken into account. If the rate of rainfall overreaches the ground infiltration rate then the runoff starts suddenly and hence, it is essential to analyse both rainfall and runoff in a complementary manner to obtain the most accurate results.

RAINFALL-RUNOFF MODELING

A rainfall-runoff model is essentially, a mathematical formulae describing the rainfall-runoff relations of a catchment area. In other words, the model facilitates the conversion of rainfall (independent variable) into runoff (dependent variable). While this kind of conversion between variables might seem simple enough, the problem at hand is that the method of transformation of rainfall to runoff is highly complex, dynamic, nonlinear, and exhibits extreme variability. This is because it is dependent on the local physiographic, biotic and climatic elements.

Hence, rainfall-runoff modeling requires experimentation with different approaches to ascertain which of them will yield relatively more accurate results. In this research, both the statistical approach of regression and the artificial neural network approach have been adopted and the results so obtained have been compared by drawing conclusions, quantitatively and qualitatively.

OBJECTIVES

Overall objective is to develop suitable rainfall-runoff models for four different catchments in Karnataka using both statistical regression and ANN approaches and compare their performances. The following are the specific objectives in order of completion:

1. Acquire the real world data for the model
2. Generate the various models and model architectures using statistical regression and ANN approaches respectively
3. Compare the generated models using various statistical parameters as performance criteria
4. Recommend which approach and model is best suited for each time period and location under study
5. Provide an overall judgement of which approach performs better

PRELIMINARY RESEARCH

Statistical Regression Approach

Regression is a statistical measure used in various disciplines to determine the strength of the relationship between one dependent (or response) variable and one or more independent (or explanatory) variables. Regression models give the simplest representation of the relationship between one or more input functions and corresponding output function. This is why regression models are considered the classical benchmark in hydrological studies. The principle behind them, in the simplest terms, is the minimisation of an objective function defined as the sum of squared deviations between observed data and predicted estimates defined by the regression model equation. This objective function can further be averaged to obtain the statistical parameter Mean Square Error, which is one of the parameters used in our performance analysis.

The three basic types of regression are simple linear regression, multiple linear regression and non-linear regression. In this research, all three types of regression are used to generate three different models, namely: the linear model, the lag model and the non-linear model. Simple linear regression uses one independent variable to explain or predict the outcome of the dependent variable Y, while multiple linear regression uses two or more independent variables to predict the

outcome. At the same time, nonlinear regression uses a non-linear form of the dependent variable(s) to predict the outcome. While simple linear regression models should be enough to effectively represent most relationships, we experiment with both multiple linear regression and non-linear regression as the rainfall-runoff relationship is dependent on multiple variables and has proven to be highly dynamic in nature, as mentioned before.

Artificial Neural Network (ANN) Approach

An ANN is a highly interconnected network of many simple processing units called artificial neurons, which are analogous to the biological neurons in the human brain and nervous system. They form the basic building blocks of an ANN. They receive an input and produce an output, which is to be passed to other neurons in other layers. Neurons having similar characteristics in an ANN are arranged in groups called layers. The neurons in one layer are connected to those in the adjacent layers, but not to those in the same layer. The strength of connection between the neurons in adjacent layers is represented by what is known as connection strengths or weights. An ANN normally consists of three layers: an input layer, a hidden layer and an output layer. Input layer usually receives the input signal values (here, rainfall data) and the neurons in the output layer produce the output signal (here, corresponding runoff data) based on weights assigned in the hidden layer. A neural network can be trained from the previous data to forecast future events without accurately understanding the physical parameters which influences the presents and future events. Hence, it can be trained to find relations between rainfall and runoff data provided to ascertain a best fit neural architecture that can predict runoff, given rainfall, to an acceptable level of accuracy.

Data Collection

The four different catchments in the state of Karnataka on which we have based our research on are the Sitanadi River Basin, the Halkal Catchment, the Vasre Catchment and the Malaprabha River basin (see Fig.1.) The datasets acquired includes monthly total rainfall and monthly total runoff data spread over a number of years (from 7 years to 29 years). Although data for all 12 months were available for certain catchments, the study was focused on the months of June, July, August and September. These months were chosen in particular as these are the predominant monsoon months in India and hence, will yield most accurate results.

METHODOLOGY

Models Developed

Under the statistical regression approach, the following simple linear, multiple linear and non-linear regression models (respectively) were developed and established:

M1: $R_t = a + bP_t$ (1)

M2: $R_t = a + bP_t^2$ (2)

M3: $R_t = a + bP_t + cP_{t-1}$ (3)

where R_t and P_t are total runoff (streamflow) and total rainfall respectively for month t in a particular year and P_{t-1} is total rainfall for the previous month in the same year. Further, a, b and c are the regression coefficients.

M1 is a basic simple linear regression model while M2 is a more complex non-linear regression model. M3 introduces a lag term of the previous month's rainfall in order to improve the predictions and therefore, is a multiple linear regression model. Henceforth, we will reference M1 as the linear regression model, M2 as the non-linear regression model and M3 as the lag regression model in this paper.

Under the ANN approach, the following neural network model architectures were developed based on varying formats of input (rainfall data):

NN1: $R_t = f(P_t)$ (4)

NN2: $R_t = f(P_t^2)$ (5)

NN1: $R_t = f(P_t, P_{t-1})$ (6)

where R and P are total runoff (streamflow) and total rainfall respectively for month t in a particular year and P_{t-1} is total rainfall for the previous month in the same year. Here, NN1 is a basic linear neural network model architecture while NN2 is non-linear in nature. NN3 introduces a lag term of the previous month's rainfall in order to improve the predictions. Henceforth, we will reference NN1 as the linear ANN model, NN2 as the non-linear ANN model and NN3 as the lag ANN model in this paper.

Tools Used

The major software tool used to establish the regression models for the given data sets is Microsoft Excel. The inbuilt functions used include the arithmetic functions to perform summation and averaging operations, Plot function to produce scatter plots and line graphs and most importantly, the Solver Add-In to minimize the error function.

The major software tool used to develop the ANN model architectures for the given data sets is MATLAB, developed by Mathworks. Our research utilised the Neural Fitting Tool feature of MATLAB to develop various neural network architectures with differing number of hidden neurons.

Regression Model Generation

The total estimated rainfalls were calculated separately for each month (June, July, August and September) for each year. Once the initial workable data had been recorded, estimated values of runoff were found for the three different models using the same rainfall data. Errors between estimated runoff (**R**) and observed runoff (**R**obs) were then calculated. These errors were then squared, summed and averaged before its square root was calculated. This value gives us the Root Mean Square Error (RMSE). The solver function is used to minimize the error by setting RMSE as the set objective function and the regression coefficients, a, b and c as variables. This gives us the final minimised estimated runoff.

Further, the Plot function was used to obtain a scatter plot for the Runoff Vs Rainfall data. Both estimated and observed runoff data (ordinate, y axis) is plotted against Rainfall data (abscissa, x axis). **R**obs Vs Rainfall gives a scatter plot whose trend line should convincingly coincide with the line graph of **R**est Vs Rainfall (as shown in Fig.2.). This would show that the error between observed and estimated values of Rainfall has been significantly minimised and the models have succeeded in simulating the real life rainfall-runoff patterns.

Regression Model Generation

To deploy ANN models over MATLAB using the Neural Fitting Tool, initially data was arranged as input and output data sets i.e. observed rainfall and observed runoff sets. MATLAB training of the network automatically stops whenever the recommended output is achieved and is represented in the form of performance plot, training state plot, fit plot, error histogram and regression plot. In the present study, networks were developed using the Neural Fitting Tool in MATLAB. Here, 70% of the data was used for training, 15% for testing and 15% for validation purposes.

Analysis to Compare Performance

Similarly, the selection procedure to choose the best models is based on the following statistical parameters: correlation coefficient (r), coefficient of determination (r^2) and root mean square error (RMSE). The model which gives less mean square error and good regression is selected as best suited calculating runoff.

CONCLUSIONS

In this study, two approaches of Rainfall-Runoff modeling, Statistical Regression and Artificial Neural Network approaches were compared.

The following conclusions were drawn after the analysis was completed:

- In most catchments (three out of four of them), the ANN approach

outperforms the statistical regression approach.

- The anomaly may have arisen due to the limitations of the statistical parameters used to analyse performance. A parameter which would be ideal for one catchment may not be so for another but we are forced to adopt one for the sake of uniformity. Further, the anomalous basin had the smallest of all data sets and it is often seen that regression models work better in such cases.
- Out of the four months under study, the non-linear model outperformed the lag and linear models.
- Therefore, no significant conclusion can be drawn when it comes to which model outperforms the other as there are several factors that come into play when modeling something as complex as rainfall-runoff relationships for multiple catchments. Although, seems to perform marginally better than the other two models, no universal model can be chosen to be the best.

Overall, both techniques have their merits and demerits. ANN models can model intricate relationships and further, no initial specification of the nature of the relationship is needed. However, while ANN models are versatile and more flexible, they pose a "black box" kind of situation wherein it is difficult to qualitatively interpret the possible relationships between parameters. This is in turn means that they are unable to offer any physical interpretation of the phenomenon being modeled and how exactly it is done. While the statistical regression models are quite rigid and primitive, the significance of explanatory (dependent) variables and the qualitative aspect of modeling can be readily explained by these models. Moreover, regression models are simpler and more practical than most ANN models.

ACKNOWLEDGEMENTS

We would like to thank our guide, Dr. Lakshman Nandagiri for his guidance in getting us acquainted with our research topic and reviewing our work on a regular basis. We would also like to thank the Department of Applied Mechanics, NITK Surathkal for providing us with the opportunity to work on this project.

REFERENCES

[1] Kothe Swapnil, Ajay. (2015). Development of Rainfall – Runoff Model using Artificial Neural Network for a Priyadarshini watershed. In college of Agricultural Engineering and Technology.

[2] Nandagiri, L. and Shetty, A. (2003). Streamflow Estimation from rainfall- A Comparison of Statistical and Artificial neural network approaches. In "Advances in Hydrology". Singh VP & RN Yadava (Eds.)

[3] Subramanya, K. (1989). Engineering Hydrology. Tata McGraw Hill Publishing Co. Ltd., New Delhi, 316p.

[4] Yu P, Jeng Y (1997) A study on grid based distributed rainfall runoff models. Water Resources Management 11: 83-99.

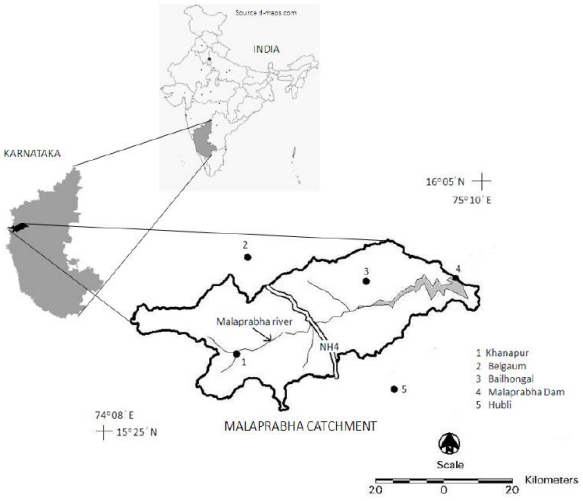

Fig.1. Malaprabha River Basin

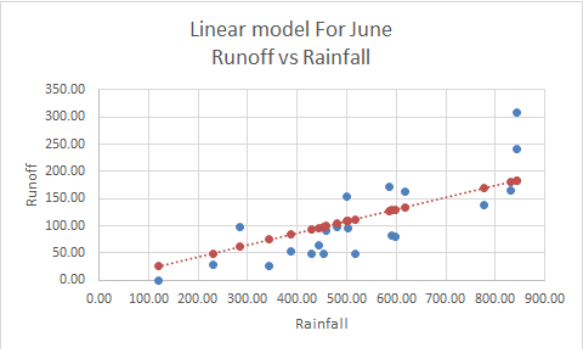

Fig.2. Runoff Vs Rainfall Plot

8th International Engineering Symposium - IES 2019
March 13-15, 2019, Kumamoto University, Japan

Short-Term Bus Passenger Demand Estimation Using Time Series Method

Anila Cyril [1], Dr Raviraj H. Mulangi [2] and Dr Varghese George[3]

1 *Department of Civil Engineering, National Institute of Technology Karnataka, Surathkal, Mangalore 575025, India. email: anilacyril110@gmail.com*
2 *Department of Civil Engineering, National Institute of Technology Karnataka, Surathkal, Mangalore 575025, India. email: ravirajmh@nitk.edu.in*
3 *Department of Civil Engineering, National Institute of Technology Karnataka, Surathkal, Mangalore 575025, India. email: varghese@nitk.ac.in*

ABSTRACT: Accurate prediction of bus transit ridership is necessary for the planning, operation and management of public bus transport system. In this paper, Holt-Winters' time series method is used to forecast the public transport bus passenger demand. The data used in the study is a part of the transaction on ticket sales by Kerala State Road Transport Corporation (KSRTC) maintained at the Trivandrum depot for the period between 2011 and 2013. The accuracy of the developed model is demonstrated in the study by comparing the forecasted values with the actual observed demand. Furthermore, Mean Absolute Percentage Error (MAPE) is used to demonstrate the forecast quality. The results show that the Holt-Winters' method, which uses only historical data of passenger demand, can be used for short-term demand forecasting.

Keywords*: passenger demand; public transport, transit ridership, short-term demand, demand forecasting*

INTRODUCTION

The rapid urbanization and motorization tends to build a great change in connectivity and travel needs of the people. The transportation planners and engineers have to forecast the responses of travel demand due to changes in the attributes of public transportation system and the people using the system. The estimates of public transport demand are important for strategic and operational planning of public transport. In addition, the accurate prediction of traffic loads and proper assignment on the network links are requisite for public transport planning. The developed countries have formulated many approaches for demand modelling and transport planning but developing countries which are becoming significant in the world are still struggling to develop efficient modelling techniques due to lack of sufficient data and allied resources. The researchers in the recent years have focused the attention in identifying and evaluating various approaches for automated data collection (Cui, 1996) and analysis which will curb the cost and time requirements of transportation planning procedures.

Recently in India, most of the public transport operators have installed Electronic Ticketing Machines (ETM) for providing tickets to the passengers and for fare collection. With the use of ETM, large amount of data related to number of passengers, fare collected, operated kilometres and passenger kilometres are generated and stored. This data is available for entire public transport network and fleet. The ETM data can be used to estimate the passenger demand, improve the operational profit and for performance evaluation. The archived ETM data is commonly used for performance evaluation and for improving the operational profit but the potential of the

ticket data for passenger demand estimation and forecasting is not explored.

This paper investigates various aspects related to demand modelling for bus transport systems based on data elicited from Electronic Ticket Machine (ETM). The ETM data has not been explored thoroughly for transportation planning although it is nowadays collected and compiled by public transport undertakings on a regular basis. The data used in the study is part of transactions on ticket sales by Kerala State Road Transport Corporation (KSRTC) maintained at the depots in Trivandrum city for the period between 2010 and 2013.

The data collected through ETM is immensely huge with average monthly passenger transactions of approximately one million. The database can be audited and compiled to determine the passenger demand. It is possible to determine the origin-destination (OD) matrix of the bus commuters by querying the ETM database. The OD data will assist in travel demand modelling, decision-making, and formulation of strategies for future preplanning of the transit system (Cyril, 2017). The work described herein includes description on the use of the time-series approach in short-term demand forecasting using various approaches of Holt-Winters' method. The accuracy of the developed model is demonstrated in the study by comparing the forecasted values of 30 days with the actual demand observed in 2013.

LITERATURE REVIEW

Exponential smoothing methods are one of the widely used time series forecasting methods. The weighted averages of past observations are used for the forecasting of future observations. As the past observations get older the weights assigned is decayed exponentially. In other words, older observations have lesser weights while the recent observations have a higher weight (Hyndman and Athanasopoulos, 2018). The simplicity in model identification, along with minimal effort of computation and better forecast accuracy (Bermudez et al., 2007) are advantageous in the use of exponential smoothing methods in the forecasting process.

Simple exponential smoothing for data with no trend or seasonal pattern, double exponential or Holt's linear method for data with trend and no seasonal pattern and Holt-Winters additive or multiplicative method for data with both seasonality and trend can be used based on the characteristics of the data. The additive method is preferred when the seasonal variations are roughly constant through the series, while the multiplicative method is preferred when the seasonal variations are changing proportional to the level of the series. With the additive method, the seasonal component is expressed in absolute terms in the scale of the observed series, and in the level equation the series is seasonally adjusted by subtracting the seasonal component. With the multiplicative method, the seasonal component is expressed in relative terms (percentages), and the series is seasonally adjusted by dividing through by the seasonal component (Hyndman and Athanasopoulos, 2018).

Holt-Winters' Additive Method

The Holt-Winters' seasonal method comprises the forecast equation ($\hat{y}_{t+h|t}$) and three smoothing equations- one for the level l_t, one for the trend b_t and one for the seasonal component s_t with corresponding smoothing parameters α, β^* and γ. We use m to denote the frequency of the seasonality. The additive formulation of Holt-Winters' method is given by the following equations.

$$\hat{y}_{t+h|t} = l_t + hb_t + s_{t+h-m(k+1)} \quad (1)$$

$$l_t = \alpha(y_t - s_{t-m}) + (1-\alpha)(l_{t-1} + b_{t-1}) \quad (2)$$

$$b_t = \beta^*(l_t - l_{t-1}) + (1-\beta^*)b_{t-1} \quad (3)$$

$$s_t = \gamma(y_t - l_{t-1} - b_{t-1}) + (1-\gamma)s_{t-m} \quad (4)$$

Holt-Winters' Multiplicative Method

The multiplicative form of the Holt-Winters' method is given by the following equations.

$$\hat{y}_{t+h|t} = (l_t + hb_t)s_{t+h-m(k+1)} \quad (5)$$

$$l_t = \alpha \frac{y_t}{s_{t-m}} + (1-\alpha)(l_{t-1} + b_{t-1}) \quad (6)$$

$$b_t = \beta^*(l_t - l_{t-1}) + (1-\beta^*)b_{t-1} \quad (7)$$

$$s_t = \gamma \frac{y_t}{l_{t-1}+b_{t-1}} + (1-\gamma)s_{t-m} \quad (8)$$

Holt-Winters' Damped Additive Method

Damping is possible for both additive and multiplicative models. The damped additive model formulation is given by the following equations.

$$\hat{y}_{t+h|t} = l_t + (\emptyset + \emptyset^2 + \cdots + \emptyset^h)b_t + s_{t+h-m(k+1)} \quad (9)$$

$$l_t = \alpha(y_t - s_{t-m}) + (1-\alpha)(l_{t-1} + \emptyset b_{t-1}) \quad (10)$$

$$b_t = \beta^*(l_t - l_{t-1}) + (1-\beta^*)\emptyset b_{t-1} \quad (11)$$

$$s_t = \gamma(y_t - l_{t-1} - \emptyset b_{t-1}) + (1-\gamma)s_{t-m} \quad (12)$$

Holt-Winters' Damped Multiplicative Method

The model formulation for damped multiplicative method is given by:

$$\hat{y}_{t+h|t} = l_t + (\emptyset + \emptyset^2 + \cdots + \emptyset^h)b_t + s_{t+h-m(k+1)} \quad (13)$$

$$l_t = \alpha \frac{y_t}{s_{t-m}} + (1-\alpha)(l_{t-1} + \emptyset b_{t-1}) \quad (14)$$

$$b_t = \beta^*(l_t - l_{t-1}) + (1-\beta^*)\emptyset b_{t-1} \quad (15)$$

$$s_t = \gamma \frac{y_t}{l_{t-1}+\emptyset b_{t-1}} + (1-\gamma)s_{t-m} \quad (16)$$

METHODOLOGY

Time series is a sequential set of continuous or discrete data points measured at regular intervals arranged in a chronological order. Generally, the time series have main components: trend, cyclic, seasonal and irregular components. Trend is a long term movement in a time series (increasing, decreasing or constant). Seasonality indicates the fluctuations within a year during the season. Cyclic variations indicate the medium term changes caused by circumstances which repeat in cycles. Irregular/random variation in time series is caused by unpredictable influences which are not regular.

For reliable forecasts, it is necessary to fit the Time Series to a suitable model that clearly represent the underlying structure of series and the corresponding parameters are estimated using known values. The procedure of fitting a time series to a proper model is known as Time Series Analysis. It comprises methods that attempt to understand the nature of Time Series and is often useful for future forecasting and simulation. Time series forecasting has application in many fields, often valuable strategic decisions and precautionary measures are taken based on forecast results. The time series is non-deterministic in nature. It is usually assumed that the random variable y_t representing time series is independent and identically distributed, indicating that the observations are normally distributed. But in actual case, they rarely exhibit this property. They follow more or less some regular pattern in long term. It is hence assumed that Time Series forecasting using a proper technique yields results closer to true value. One of the important conditions for Time Series to give reliable forecast is that the model should be stationary i.e., mean and variance of the observation should be independent of time. This is a necessary condition for building up a reliable model, also the mathematical complexity of fitted model reduces with this assumption. Another criterion for time series analysis is Model Parsimony, i.e. it is important to choose a model that gives minimum number of parameters explaining all the underlying properties of the time series data. Model Parsimony reduces over fitting of the data and gives reliable forecasts.

Steps Involved in Holt-Winters Method are as follows:
Step 1: Plot the observation against time to identify the patterns, seasonality, trends and outliers in the data.
Step 2: Seasonal decomposition of time series data.
Step 3: Fitting of the Holt- Winters Model
Step 4: Forecasting the future demand
Step 5: Measuring the forecast accuracy

EMPIRICAL COMPARISON OF RESULTS

The empirical comparison of the results of the methods are done by measuring the forecast accuracy of the models.
The data used in the study is a part of fare transactions of issuing tickets in buses of Trivandrum City Depot. The ticket includes details of the number of passengers, fare, ticket type, route, origin, destination and the time of ticket issued. The data used were daily time series data from 01-01-2012 to 09-10-2013. Figure 1 shows the time series plot for the observed data. It can be observed that the data has a

decreasing trend and outliers. The data from 01-01-2012 to 09-09-2013 was used for model calibration and parameter estimation while the last 30 days data was used for model validation.

The parameters of the model are estimated by maximizing the likelihood value using MLE (Maximum Likelihood Estimation) method. The probability of the data arising from the model is known as likelihood. For a good model, the likelihood value will be larger. In the case of additive model, maximizing the likelihood gives the same result as minimizing the sum of squares. But it is not the same for multiplicative models. The estimated parameters are given in Table 1. The smoothening parameters are α, β, and γ while $\emptyset$ is the dampening parameter. The α governs the amount of change in the successive levels; high value of α lead to rapid changes in the levels while low value of α leads to smooth change in the levels. In the damped method, the smoothing parameter β is having a small value indicating that the slope or trend component change very little over time. Similarly, small value of γ indicates that the seasonal component also changes slowly over time.

The minimum of Akaike Information Criteria (AIC), Corrected AIC (AICc) and Bayesian Information Criterion (BIC) values are used to identify the best model along with Mean Absolute Percentage Error (MAPE). Comparing the AIC, AICc and BIC value of all the four models, it can be observed that Holt-Winters' Damped Additive method have minimum value followed by Holt-Winters' Damped Multiplicative model. But, it can be noted that the standard deviation (σ) of the additive model is very high compared to the multiplicative model. Since, both these models have same number of parameters to be estimated, we can compare the MAPE of the models. The Holt-Winters' Damped Multiplicative model have the least MAPE of 8.29 among all the models. Therefore, it is selected as the best model. To conclude, it can be stated that for a time series data with seasonality, the Holt-Winters' Damped Multiplicative method provides accurate and reliable results.

CONCLUSIONS

This paper studied the application of Holt-Winters' method for short term passenger demand forecasting. Holt-Winters additive and multiplicative model with and without damping have been empirically compared in this study using the real data from route 66 of Trivandrum City depot. The following are the major conclusion from this study:

- Multiplicative models with and without damping outperforms the additive models.
- The MAPE of all the models are almost equal with damped multiplicative model having the least value of 8.29.
- The standard deviations of the multiplicative models are negligible suggesting that the model fit is good.
- Holt-Winters' Damped Multiplicative method provides better forecasts in the case of seasonal data.

REFERENCES

[1] Bermúdez, J, D, Segura, J, V, and Vercher, E, (2007), Holt–Winters Forecasting: An Alternative Formulation Applied to UK Air Passenger Data, Journal of Applied Statistics, Vol. 34, No. 9, pp. 1075-1090.

[2] Cui, A, (1996), Bus Passenger Origin-Desination Matrix Estimation Using Automated Data Collection Systems, M.S Report, University of California at Berkeley.

[3] Cyril, A, George, V, and Mulangi, R, H, (2017), Electronic Ticket Machine Data Analytics for Public Bus Transport Planning. In 2017 International Conference on Energy, Communication, Data Analytics and Soft Computing (ICECDS), pp. 3917-3922, IEEE.

[4] Hyndman, R J and Athanasopoulos, G, (2018), Forecasting: Principles and Practice. OTexts.

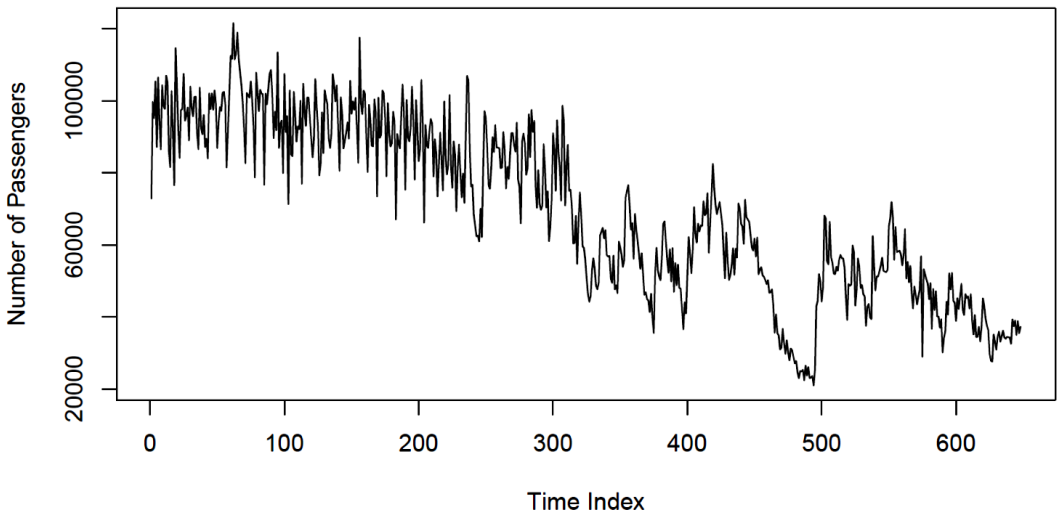

Fig. 1 Time Series Plot

Table 1 Holt-Winters' Parameters Calculated from Calibration Data Set

	α	β	γ	$\emptyset$	σ	AIC	AICc	BIC	MAPE
Holt-Winters' Additive Method	0.472	0.0025	0.084	-	7387.43	14994.18	14994.70	15047.30	8.57
Holt-Winters' Multiplicative Method	0.458	0.0028	0.060	-	0.1141	15048.62	15049.14	15101.74	8.30
Holt-Winters' Damped Additive Method	0.465	1e-04	0.083	0.867	7360.59	14990.67	14991.27	15048.21	8.55
Holt-Winters' Damped Multiplicative Method	0.492	1e-04	0.016	0.975	0.1131	15038.51	15039.12	15096.06	8.29

8th International Engineering Symposium - IES 2019
March 13-15, 2019, Kumamoto University, Japan

The Influence of Land Use Land Cover Changes on Landslides in Karwar, Uttara Kannada District of Karnataka state, India

Thejashree.G[1], Lokesh.K.N [2] and **Dwarakish.G.S [3]**

1 *Department of Civil Engineering, National Institute of Technology Karnataka, Surathkal, Mangalore 575025, India. Email:thejashree217@gmail.com*
2 *Department of Civil Engineering, National Institute of Technology Karnataka, Surathkal, Mangalore 575025, India. Email: knl.lokesh@gmail.com*
3 *Department of Applied Mechanics & Hydraulics, National Institute of Technology Karnataka, Surathkal, Mangalore 575025, India. Email: dwaraki.gs@gmail.com.*

ABSTRACT: Landslides, being a hazardous phenomenon have been a point of concern in hilly regions like the Western Ghats of Karnataka where it is a common occurrence. Karwar lies in part of Western Ghats in Uttara Kannada district of Karnataka State, India. The area is prone to landslides during monsoon season. Land use Land cover (LULC) is one of the factors associated with landslides. In this work, we have attempted to evaluate the influence of land use land cover change on landslides. For the present study LISS III images of 2008 and 2015 are being used to assess LULC changes which play an important role in landslide occurrences. The images were classified using Maximum Likelihood supervised classification method in ERDAS 2014 and mapped using ArcGIS software. Six LULC classes were identified. The results indicate that there is a considerable change in LULC classes from forest and scrub land to agricultural and barren land, and drastic change in built up class which might be the factor for triggering of landslide. The overall accuracy for classification was 86.7% and Kappa coefficient was 0.83.

***Keywords**: LULC, Maximum likelihood classification, Landslide, Karwar*

INTRODUCTION

Landslide occurrence is affected by several factors such as climate, precipitation, geology, geomorphology of the area and human intervention. Human encroachment causes LULC changes which can act as landslide inducing factor at times. Study of LULC change can also help in identifying the spatial distribution of landslides hazard and its mitigation.

Previous researches have established human activity as the biggest contributor to LULC change. Anthropogenic activities such as trade, population settlement, migration etc. can lead to alterations in LULC pattern. Vegetation cover is an important component of the land use affecting the occurrence of rainfall induced landslides. Study of land cover change provides the magnitude of land cover change; spatial locations of the change and also the rate of change (Lambin 1997).

Numerous previous research relating landslides and land cover change are available e.g. (Alcántara-Ayala et al. 2006; Beguería 2006; Glade 2003; Van Beek & Van Asch 2004). Sidle et al. 1985 showed that landsliding is a complex process that can be strongly influenced by attributes of vegetation. Alcántara-Ayala et al. 2006 analysed the distribution of landslides in the context of vegetation fragmentation while Papathoma-Kohle and Glade (2012) also studied landslide hazard with respect to vegetation cover. The studies targeting human induced land use changes and its consequences on stability of slopes in

more populated areas have shown that there is a significant contribution on landslide initiation and reactivation due to human intervention on the sensitive environment (Bruschi et al. 2013; Meusburger and Alewell 2008; Van Den Eeckhaut et al. 2009; Vanacker et al. 2003). In this paper, an attempt is being made to correlate LULC changes caused by impact of humans with the landslide occurrences.

STUDY AREA

Karwar taluk in Uttara Kannada district of Karnataka forms a part of Western Ghats where the range dips into the sea with peaks emerging as picturesque islands. The geographical area is situated between 14°53'44.80"N and 74°06'2.72"E; 14°54'46.42"N and 74°32'0.48"E which lies in Survey of India (SOI) Toposheet no 48J/1 and 48J/5 (Fig. 1).

Geology and Geomorphology

Regionally, the area comprises rocks of Peninsular Gneissic Complex (PGC), older granitoids and rocks belonging to the Chitradurga Group under the Dharwar Supergroup of Archaean age as well as dolerites of Palaeoproterozoic age intruding older rocks. The rocks have undergone intensive chemical weathering resulting in the formation of laterites, a common rock type in humid tropical environment. In the study area, laterites form a thick mantle capped over underlying granite. Along with granite, the area also possesses saprolite at places and lateritic soil with lithomargic clay is also present. Geomorphologically, a number of lineaments are present in the area with high density dendritic drainage pattern where higher stream orders are structurally controlled.

Climate

The area lies on a coastal strip known as the Monsoon Coast. It is surrounded by the Western Ghats and Arabian Sea on east and west respectively. The area possesses tropical climate with hot summers from March to May where temperature can reach as high as 37 °C. Winter starts from December to February and has mild temperatures of 24 °C to 32 °C. The monsoons are experienced in between June and October and receive average annual precipitation of over 3000mm. Most of the rainfall occurs during the peak monsoon period from June to August.

The rainfall in the area includes both Southeast and Northeast monsoons. During peak monsoon period, rainfall is received from southeast monsoon. Retreating monsoon in the area accounts from October to December.

MATERIALS AND METHODOLOGY

This paper aims to relate land cover change to landslide occurrence using vegetation change as an influencing factor. The analysis of the spatio-temporal patterns of land cover will be the base for investigating the landslide risk. Land cover change analysis is done based on satellite images of the same area acquired at different time intervals. These methods make use of reflectance values in various bands of electromagnetic spectrum available in LISS-III imagery.

On October 2nd and 3rd, 2009 numerous landslides occurred in Karwar taluk. On 2nd between 4:15 PM to 4:30 PM a massive landslide occurred in Zariwad locality of Kadwad village, east and south of Karwar town and Kali River estuary respectively. The aggressive landslide that took place killed 19 people and devastated 9 houses. Also, high intensity precipitation of two consecutive days resulted in subsidiary landslides in 21 locations all along the hills obstructing traffic movement on NH-17. The massive slide in Kadwad village was characterized as debris slide. At some locations, it consisted of debris flow, weathered materials and lateritic boulders while at some places rock fall was also witnessed.

Preprocessing

ISRO provides orthorectified LISS-III data in GeoTIFF format for individual tiles in WGS84 coordinate system. This data is radiometrically and geometrically corrected using ground control points and digital elevation model for distortions related to the sensor, satellite and earth (Resourcesat-2 Users Handbook). The individual tiles corresponding to each date

were combined to create a mosaic for the two time instances of observation (Table 1).

Land use Land cover Classification

In this present study, two years' LISS-III images i.e., 2008 and 2015 were compared and assessed using supervised classification technique. Numerous training sites were identified, a supervised classification was performed on both images using Maximum Likelihood algorithm in ERDAS 2014 software. The Maximum Likelihood method is used in classification of the images as it is one of the most commonly used supervised classification algorithms (McIver and Friedl, 2002; Wu and Shao, 2002). It is considered to give very accurate results (Mengistu and Salami, 2007; Reis, 2008). Based on National Remote Sensing Center (NRSC) annexure the following classes were derived using LULC map: 1. Deciduous forest, 2. Evergreen forest, 3. Urban area, 4. Rural/Agriculture, 5. Scrubland, 6. Marshland, 7. Water bodies.

Standard criteria were used to assess the accuracy assessment of the classified image. The user accuracy was defined as the number of the correctly classified pixels in a class to the total pixels that were classified in that particular class. It indicates the probability that a classified pixel actually represents that category in reality. The Overall accuracy was defined as the total number of correctly classified pixels divided by the total number of reference pixels (total number of sample points) as shown by Rogan et al. 2002. Kappa coefficient is defined as a statistical measure of accuracy that ranges between 0 and 1, it measures how much better the classification is compared to randomly assigning class values to each pixel. For example, if Kappa coefficient is of 0.76 this means that the classification accuracy is 76% greater (Miller and Pool, 2002).

RESULTS AND DISCUSSIONS

LULC maps of the Karwar taluk for the year 2008 and 2015 respectively are shown in Fig.2 and Fig.3. Comprehensive data set in terms of the overall LULC changes is tabulated in table 2. The area for each class is calculated by the number of pixels present in each class. The class area was measured by the number of pixel multiplied by spatial resolution (23.5m) of one pixel.

The results show a considerable change in the overall LULC pattern for a period of 8 years. There is a clear indication of increase in urbanisation while there is a general decreasing trend in green areas.

Evergreen forests were the biggest land cover class followed by deciduous forests. Evergreen forests show the steepest decline in area with a reduction of ~4.2%. Similarly, for deciduous forests, a deterioration of about 2.5% is observed. On the other hand, classes such as urban areas and Rural/Agriculture areas show an increasing trend with gains of 2.1% and 1.2% respectively. The overall accuracy assessment for classification was 86.7% and Kappa coefficient was 0.83. Fig.4 shows the change in area for all the classes over the period of 2008-2015.

Locations corresponding to recorded landslides were also mapped as shown in fig. 5.

CONCLUSIONS

This work was carried out to assess landslide affected areas and quantify the LULC change for a period of 8 years. In literature pertaining to landslide research, it is recognized that forested areas favors in stability of terrain. The effect of human induced disturbances such as deforestation, urbanization, quarrying, construction etc and continuous degradation of forested regions along with intense precipitation over a short period of time in the areas with overlying saturated soil might have caused instability of slope leading to landslides. From the classified images, it is evident that landslide occurrences are spatially correlated with forested hillslope areas which have turned into barren areas due to increase in urbanization in the past few years. This information can be utilized by local disaster management authorities for effective avoidance, forecast and mitigation of landslide hazard.

ACKNOWLEDGEMENTS

The authors greatly acknowledge National Institute of Technology, Surathkal, Karnataka for providing financial assistance and facilities for carrying out the research work.

REFERENCES

[1] Alcántara-Ayala, I et al (2006), Landsliding related to land-cover change: A diachronic analysis of hillslope instability distribution in the Sierra Norte, Puebla, Mexico. Catena, Vol. 65, No.2, pp. 152–165.

[2] Beguería, S (2006), Changes in land cover and shallow landslide activity: A case study in the Spanish Pyrenees. Geomorphology, Vol. 74, No.1–4, pp. 196–206.

[3] Bruschi, V M et al (2013), Land management versus natural factors in land instability: some examples in northern Spain. Environmental Management, Vol. 52, No.2, pp. 398–416.

[4] Glade, T (2003), Landslide occurrence as a response to land use change: A review of evidence from New Zealand. Catena, Vol. 51, No.3–4, pp. 297–314.

[5] Lambin, E F (1997), Modelling and monitoring land-cover change processes in tropical regions. Progress in Physical Geography, Vol. 21, No.3, pp. 375–393.

[6] McIver, D K. and Friedl, M A (2002), Using prior probabilities in decision-tree classification of remotely sensed data. Remote Sensing of Environment, Vol. 81, pp. 253-261.

[7] Mengistu, D A and Salami, A T (2007), Application of remote sensing and GIS in landuse/land cover mapping and change detection in a part of south western Nigeria, African Journal of Environmental Science and Technology, Vol. 1, No.5, pp. 99-109.

[8] Meusburger, K and Alewell, C (2008), Impacts of anthropogenic and environmental factors on the occurrence of shallow landslides in an alpine catchment (Urseren Valley, Switzerland). Natural Hazards Earth System Sciences, Vol. 8, pp. 509–520.

[9] Miller, J D and Pool, S R (2002), Mapping forest Post-Fire canopy Consumption in several overstory types using multi-temporal Landsat TM and ETM data. Remote Sensing of Environment, Vol. 82, No.2-3, pp. 481-496.

[10] Papathoma-Köhle, M and Glade, T (2012), The role of vegetation cover change for landslide hazard and risk. The role of ecosystems in disaster risk reduction. UNU-Press, Tokyo, pp. 293-320.

[11] Reis, S (2008), Analyzing land use/land cover changes using remote sensing and GIS in Rize, North-East Turkey, Sensors, Vol. 8, pp. 6188-6202.

[12] Rogan, J et al (2002), A comparison of methods for monitoring multitemporal vegetation change using Thematic Mapper imagery. Remote Sensing Environment, Vol. 80, No.1, pp. 143-156.

[13] Sidle, R C et al (1985), Hillslope stability and land use. American Geophysical Union Water Resources, Washington, DC.

[14] Van Beek, L P H and Van Asch, T W J (2004), Regional assessment of the effects of land-use change on landslide hazard by means of physically based modelling. Natural Hazards, Vol. 31, No.1, pp. 289–304.

[15] Van Den Eeckhaut, M et al (2009), How do humans interact with their environment in residential areas prone to landsliding? A case study from the Flemish Ardennes. In: Proceedings of the international conference on ''landslide processes: from geomorphologic mapping to dynamic modeling, Strasbourg, France, 6–7 February 2009, pp. 19–24.

[16] Vanacker, V et al (2003), Linking hydrological, infinite slope stability and land-use change models through GIS for assessing the impact of deforestation on slope stability in high Andean watersheds. Geomorphology, Vol. 52, pp. 299–315.

[17] Wu, W and Shao, G (2002), Optimal Combinations of Data, Classifiers, and sampling methods for Accurate Characterizations of deforestation. Canadian Journal of Remote Sensing, Vol. 28, No.4, pp. 601-609.

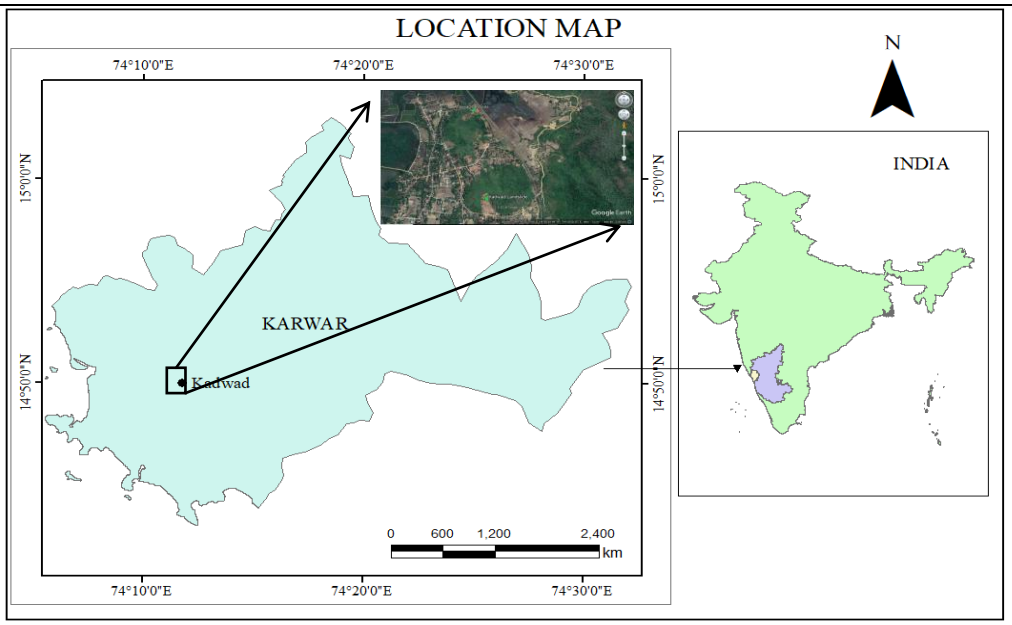

Fig. 1: Location of the study area

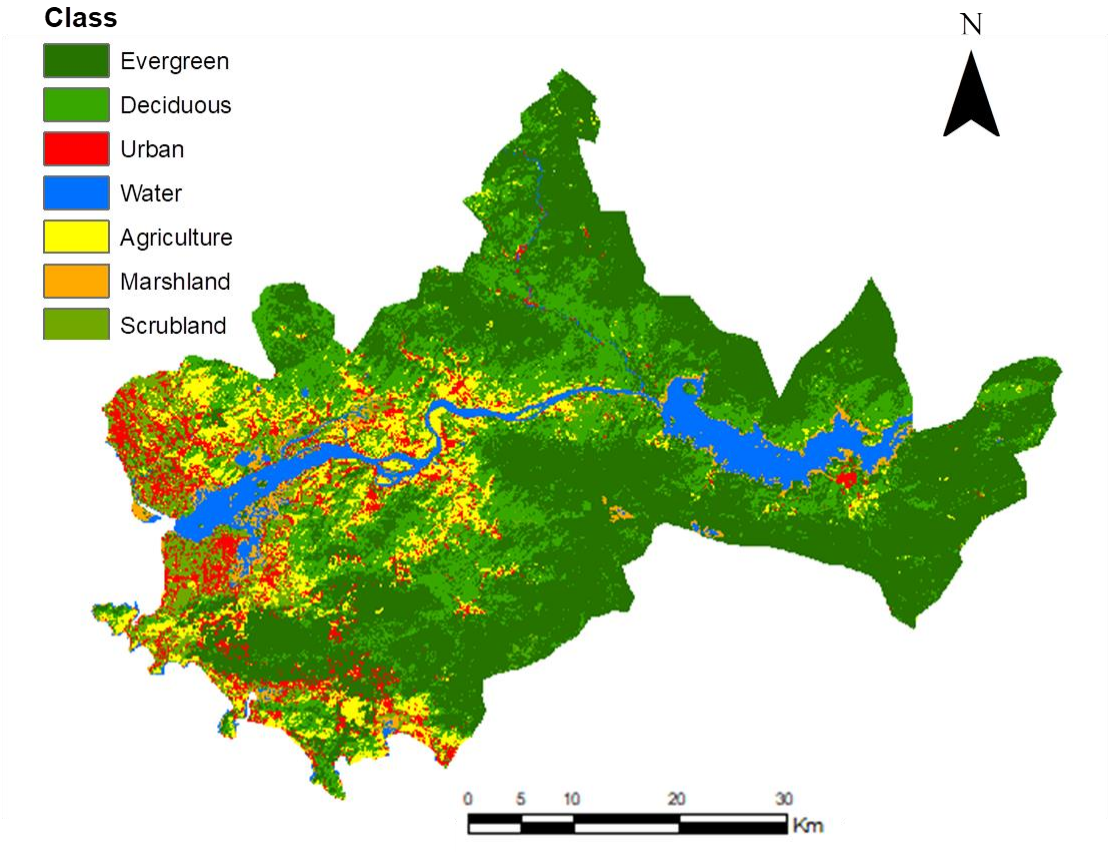

Fig. 2: LULC of 2008

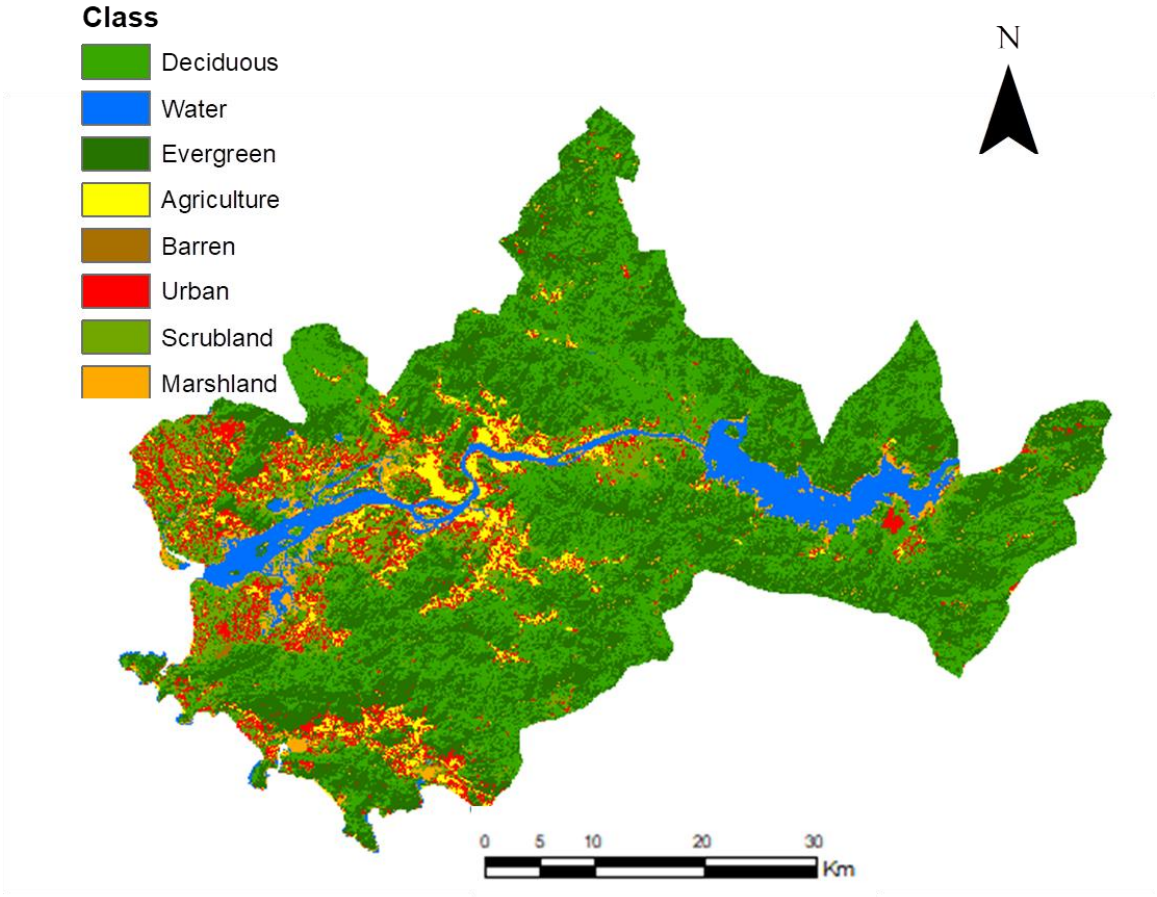

Fig. 3: LULC of 2015

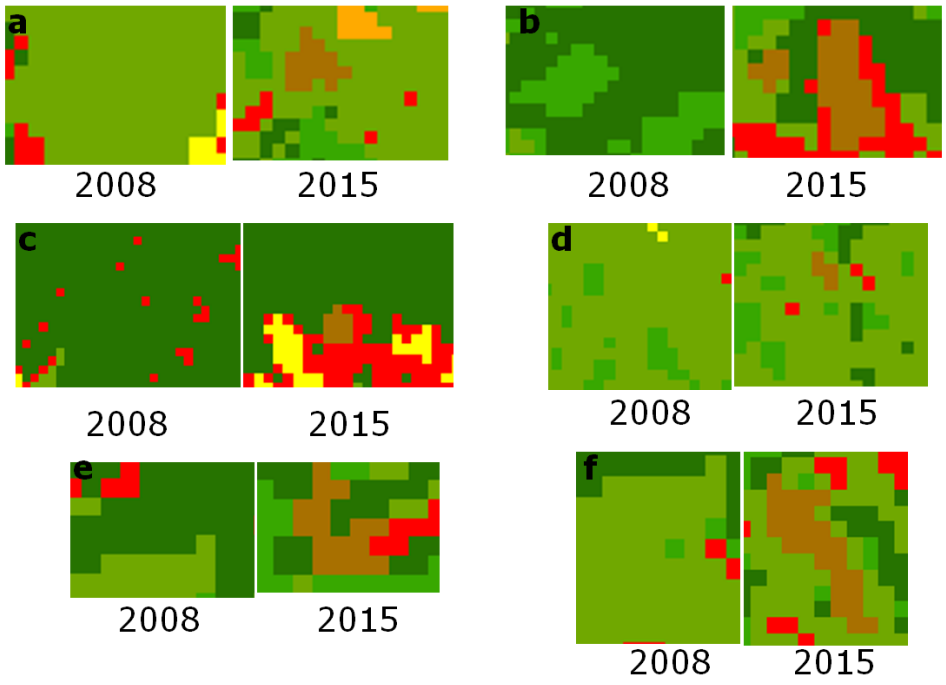

Fig. 5: (a) & (b) Kadwad; (c) Todur; (d) Shirwad; (e) & (f) Arga

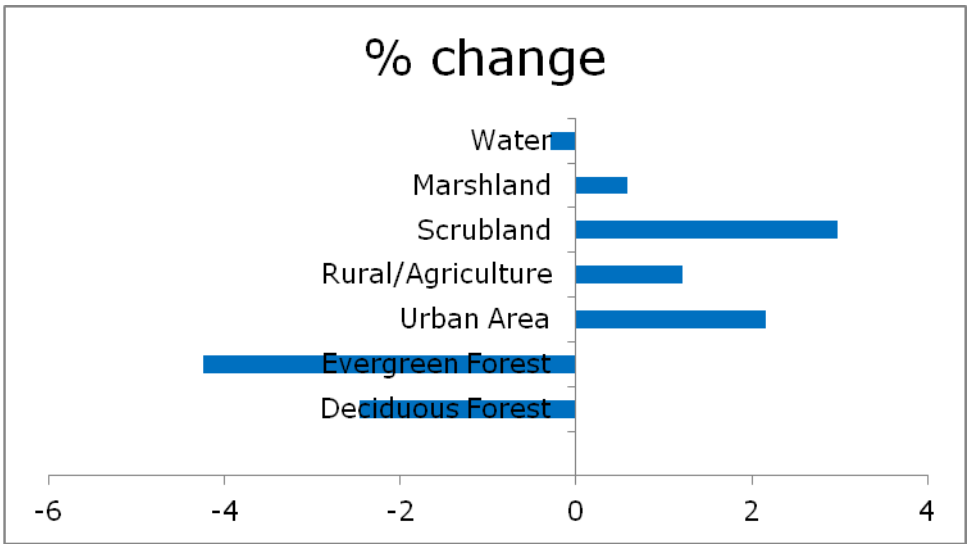

Fig. 4: LULC changed expressed in percentage between 2008 and 2015

Table 1: LISS-III data details

Tile ID	Acquisition Date		Level of Processing
	2008	2015	
D43I01	18-10-2008	03-01-2016	L1
D43I02	18-10-2008	10-12-2015	L1
D43C08	18-10-2008	03-01-2016	L1
D43I05	18-10-2008	03-01-2016	L1
D43I06	18-10-2008	10-12-2015	L1
D43I09	28-10-2008	15-12-2015	L1

Table 2: Change in LULC classes between 2008 and 2015

Land use-Land cover Class	Pixel Count	% of total area	Pixel Count	% of total area	% change
	2008		2015		
Deciduous Forest	263820	21.27096902	233198	18.81408907	-2.456879956
Evergreen Forest	600869	48.44615982	548194	44.22752657	-4.218633253
Urban Area	77300	6.232453587	104051	8.394689412	2.162235824
Rural/Agriculture	97790	7.884497235	112862	9.10554859	1.221051355
Scrubland	91241	7.356472157	128150	10.33896309	2.982490929
Marshland	31246	2.51926578	38568	3.111612394	0.592346614
Water	78016	6.290182394	74463	6.00757088	-0.282611514

8th International Engineering Symposium - IES 2019
March 13-15, 2019, Kumamoto University, Japan

INTERFERENCE STUDY BETWEEN A RETAINING WALL AND A CLOSELY BUILT STRIP FOOTING

S. Anaswara[1], R. Shivashankar[2]

1 *Department of Civil Engineering, National Institute of Technology Karnataka, Surathkal, Mangalore 575025, India. email:anaswaras6@gmail.com*
2 *Department of Civil Engineering, National Institute of Technology Karnataka, Surathkal, Mangalore 575025, India. email: shivashankar.surathkal @gmail.com*

ABSTRACT: The primary function of the foundation of a structure, is to safely transfer the loads from the superstructure to the soil beneath without the occurrence of shear failure and without excessive settlements. Due to rapid urbanisation, very often structures and their foundations are built close to each other. In general, all the footings are rarely isolated, and they do interfere with each other to some extent depending on their relative positions. This numerical study looks into the interference effects between a retaining wall adjacent to a vertical cut and a strip footing closely. A finite element based software-PLAXIS 2D is being used. The parameters varied in this study are the L/B_1 ratio of the shear key provided beneath the retaining wall, where L is the depth of shear key, and B_1 is the width of the base of the L-shaped retaining wall, position of shear keys such as junction and the centre of the base. A surface strip footing is assumed to be placed over a cohesionless soil medium. From the numerical analysis, it is observed that the settlement and tilt are varied by providing the shear key.

Keywords*: interference effect, strip footings, numerical analysis, shear key*

INTRODUCTION

Geotechnical designs of all foundations are based on the limit state of serviceability. Due to rapid urbanisation, very often structures and their foundations are built close to each other. In general, all the footings are rarely isolated, and they do interfere with each other to some extent depending on their relative positions. Owing to the phenomenon of footing interference, the behaviour such as failure mechanism, load-settlement, bearing capacity, settlement, rotational characteristics of each footing is altered compared to that of a single isolated footing.

Interference effect between a (reversed) L-shaped cantilever retaining wall and strip footing is being studied using numerical analysis. Effect of shear key beneath the retaining wall on the interference effect is focused in this study.

The observation of interference phenomenon was first studied by Stuart (1962); the study was carried out using limit equilibrium method on ultimate bearing capacity of two closely spaced strip footings resting on the surface of the cohesionless medium. After that, many researchers have reported on different aspects of the problem.

Salampatoor et al. (2018) have done experimental analysis on unequally and sequentially constructed footings on interference effect. The study shows that settlement and tilting of old footing increases due to a new footing.

PROBLEM DEFINITION

In the first case two similar strip footing with 3m width placed at different spacing ratios. One of the footings representing an already existing foundation is loaded with half of the estimated failure load of isolated footing and adjacent footing loaded up to failure. In the second case, a footing is considered placed adjacent to a

(reversed) L-shaped retaining wall. The ratio between the length of the base (B_1) to the stem height of the retaining wall (H), B_1/H lay between 0.5 and 0.8 is reasonable as far as the equilibrium between rotation and translation of the wall is concerned (Rouili,2013). $B_1/H=0.8$ is selected for this study. Retaining wall height is fixed sas 4m. The base of the retaining wall is maintained 0.8H width and considered to be constructed 1m below from ground surface. The base of the retaining wall is acting as a footing with width B_1. Surcharge of 20 kN/m^2 and 40 kN/m^2 are considered. A shear key having depth (L) $0.25B_1$, $0.5B_1$ and $1B_1$ is included in the retaining wall base at centre and junction between stem and base.

A building is being constructed close to retaining wall. A strip footing with width 3m supporting the building is considered. Interference effect of the base of retaining wall which acts as old footing and strip footing as the new footing is considered. Strip footing of 0.75m thick and 3m width spaced at a spacing ratio (S/B) equal to 0.5 (S clear spacing between the footing, B width of the footing)and retaining wall are considered to be placed on loose sand. The footing is loaded up to safe bearing capacity (Factor of safety is taken as 3).

The footings are loaded unequally and sequentially to simulate the situation like old and new footings. The objective is to determine the magnitude of settlement and tilt of the base of retaining wall before and after the building construction and check the effect of tilt on the new footing.

NUMERICAL MODELLING

In all analyses conducted in the present study, using PLAXIS 2D software, it is assumed that strip footing is located on the ground surface, and the soil is dry. Groundwater condition is not taken into account. Plane strain condition and 15-noded triangular elements are used for the analysis. Material properties are given in Table (1-3). Figure 1 shows the definition of the problem.

RESULTS AND DISCUSSION

From the analysis carried out for two similar and adjacent strip footings without the shear key on loose sand, it is found that the settlement and tilt are maximum at a spacing ratio of 0.5. (Figs.2-3).

An additional element shear key is considered to be added in the retaining wall base at the centre and the junction between the stem and base of the retaining wall. The Parametric study is carried out by varying the L/B ratio of the shear key, where L is the depth of shear key and B is the width of the base.

1. The position of shear key

The shear key is considered to be provided at below junction and below the centre of the base with surcharge 20 kN/m^2. Shear key provided at the junction between base and stem of retaining wall with L/B=1 reduces settlement and tilt by 41% and 60% respectively (Figs.4-6).

2. Surcharge effect

To check the effect of surcharge on backfill, 20 and 40 k N/m^2 were considered to act on the backfill with the shear key placed at the junction between the stem and base. When surcharge increased to 40 kN/m^2 from 20 kN/m^2 settlement and tilt of the base in the presence of new footing increased by 54% and 57% respectively (Figs.7-8). The tilt of new footing in the presence of old footing increases around 3% when surcharge changed to 20 to 40 k N/m^2 (Fig.9).

CONCLUSION

Effect of providing shear key beneath a reverse L shaped cantilever retaining wall in the presence of new footing is studied. Parameters of shear key such as position and depth, surcharge loads on backfill are varied.

- Shear key provided beneath the junction of base and stem of the retaining wall is efficient in reducing tilt and settlement of base of retaining wall in addition to providing better resistance to sliding forces.
- The shear key with $L/B_1=1$ is effective compared to 0.25 and 0.5.
- The tilt of the new footing in the presence of old footing increased to around 3% with the increase in the surcharge of the backfill from 20 to 40 k N/m^2.

REFERENCES

[1] Rouili, A. (2013), Design of rigid L-shaped retaining walls. Int J Civil Environ Struct Constr Architectural Eng, 7, 12.
[2] Salamatpoor S, Jafarian Y, and Hajiannia A (2018), Bearing capacity a ind uneven settlement of consecutively constructed adjacent footings rested on saturated sand using model tests, International Journal of Civil Engineering, pp.1-13.
[3] Stuart J G (1962), Interference between foundations, with special reference to surface footings in sand, Geotechnique, 12 (1), pp 15-22.

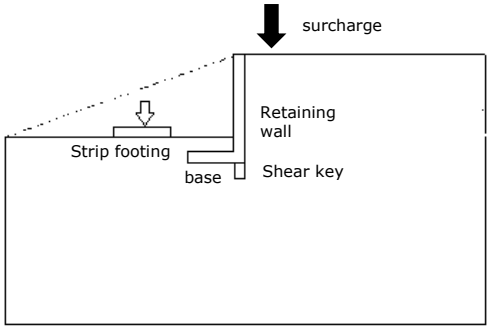

Fig.1 Definition of problem

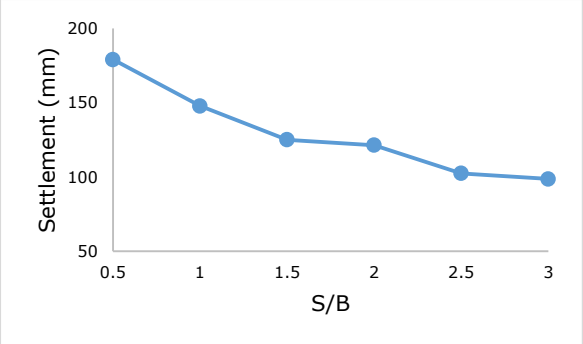

Fig.2 Variation of settlement v/spacing ratio (S/B)

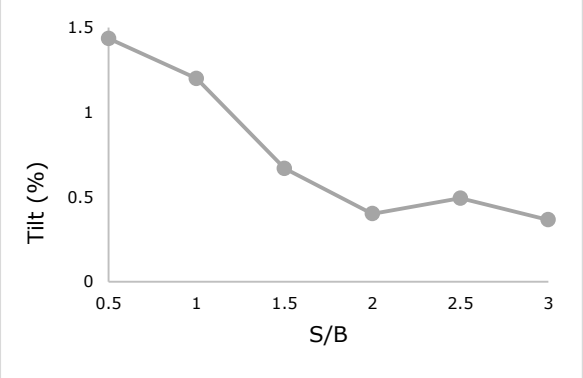

Fig.3 Variation of tilt with respect to the spacing ratio (S/B)

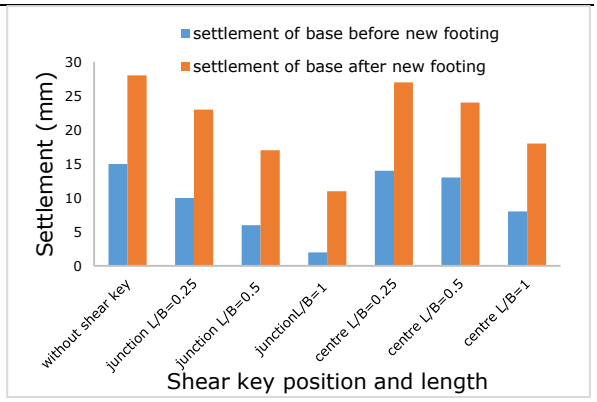

Fig.4 settlement of base of retaining wall before and after the construction of new footing

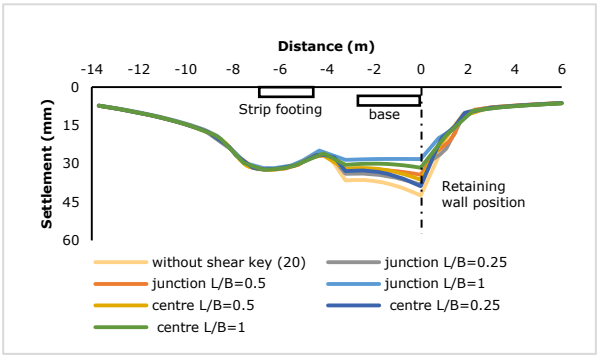

Fig.5 Settlement profile at the level of the base for surcharge 20 k N/m^2

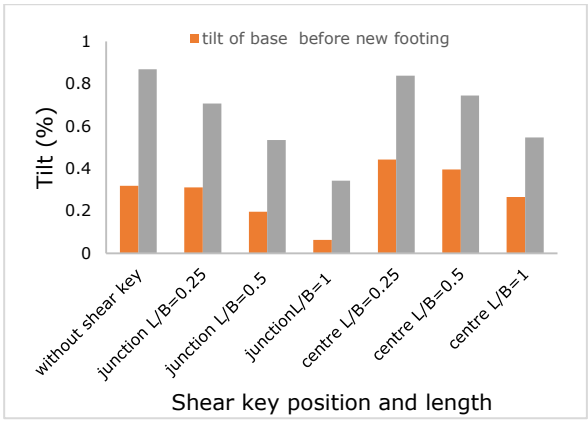

Fig.6 Tilt of base of retaining wall before and after construction of new footing

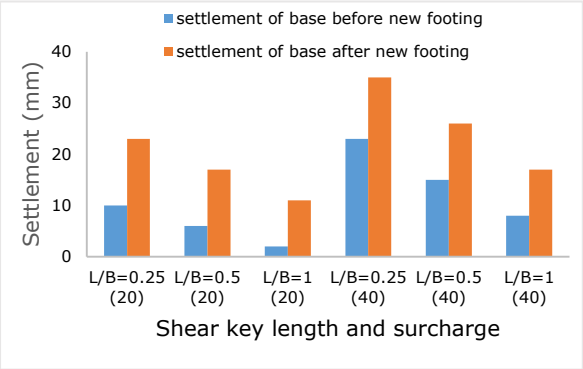

Fig.7 Settlement of the base of retaining wall before and after the construction of new footing with various surcharge loads on backfill (shear key at the junction)

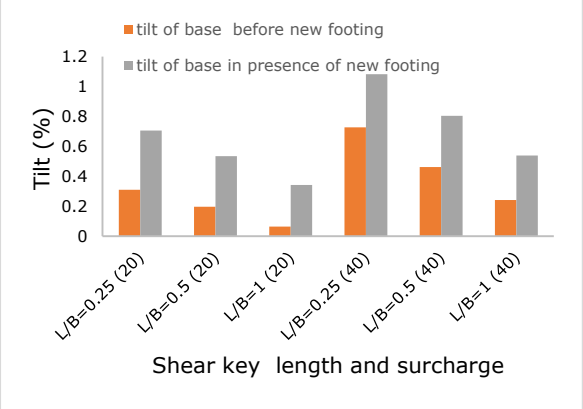

Fig.8 Tilt of the base of retaining wall before and after the construction of new footing with different surcharge loads (shear key at the junction)

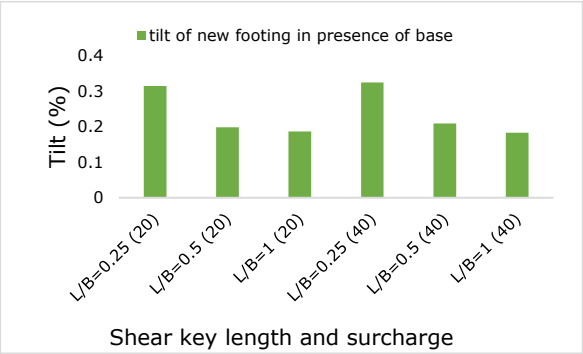

Fig.9 Tilt of the new footing in the presence of a base of retaining wall when surcharge load is increased from 20 to 40 k N/m^2

Table 1 Soil properties

Parameter	Value
Material model	Mohr-Coulomb
Material type	drained
Unsaturated unit weight, γ (kN/m^3)	17.4
Young's modulus, E (kN/m^2)	15000
Poisson's ratio, υ	0.25
Cohesion, C (kN/m^2)	0
Angle of internal friction, φ (^{0})	30

Table 2 Properties of footing

Parameter	Value
Width of footing, B (m)	3
Modulus of elasticity, E (kN/m^2)	25x10^6
Thickness of footing, d (m)	0.75
Poisson's ratio, μ	0.15

Table 3 Properties of shear key

Parameter	Value
Width of shear key, W (m)	0.4
Modulus of elasticity, E (kN/m^2)	25x10^6
Poisson's ratio, μ	0.15
Length of shear key, L (m)	0.25B_1,0.5B_1,1B_1

8th International Engineering Symposium - IES 2019
March 13-15, 2019, Kumamoto University, Japan

Effect of Manning's n on Flow and Stage by Using HEC-RAS

Pramodkumar[1], M. K. Nagaraj[2] and **Paresh Chandra Deka[3]**

1 Department of Applied Mechanics and Hydraulics, National Institute of Technology Karnataka, Surathkal, Mangalore 575025, India. email: Pramodkappadi@gmail.com
2, 3 Department of Applied Mechanics and Hydraulics, National Institute of Technology Karnataka, Surathkal, Mangalore 575025, India.

ABSTRACT: The channel roughness plays an important role w. r. t. the flow variability of the river. In the study, HEC-RAS model was used to simulate the effect of Manning's n on flow and stage for Nethravathi river in Karnataka state, India. The Simulated stages values observed to be in close agreement with observed water levels for the years 2007 and 2008 at Bantwal gauging station. Model results indicated that, the computed stage values increased and the associated peak discharges decreased with the increase in Manning's n. In addition, the stage-discharge rating curves revealed that Manning's n value is relatively more sensitive at higher discharge values. The simulated model is useful to predict flood stage and discharge values for the Nethravathi river basin.

***Keywords**:* Manning's n, HEC-RAS, Flow, Stage.

INTRODUCTION

For flood forecasting, floodplain mapping and flood volume estimation, various hydrodynamic models, based on hydraulic routing, have been developed and applied to different rivers in the past. For flood warning, the discharge and river stage was chosen as the variables along with other hydraulic properties which are associated to each other (Bao, et al.,2009). Among various hydraulic parameters, the channel roughness plays a very important role in the study of open channel flow particularly in hydraulic modeling. Channel roughness is highly variable which depends upon factors such as surface roughness, vegetation cover, channel irregularities, channel alignment etc. (Ramesh, et al., 2000). It is also influenced by factors namely, bed material, vegetation, channel irregularity and alignment, scour and deposition, obstructions, channel size and shape, stage and discharge, seasonal changes, suspended material and bed load (HEC, 2000). Earlier, good numbers of researchers including Parhi et al., (2012) Patrobet al., (2009), Usul et al., (2006), Vijay et al., (2007) and Wasantha Lal (1995) have calibrated channel roughness for different rivers to develop hydraulic model for flood forecasting and floodplain mapping. Ramesh et al., (2000), estimated single channel roughness value for open channel flow using optimization method considering the boundary condition as constraints. Timbadiya et al., (2011), calibrated channel roughness for Lower Tapi River, India using multiple values of Manning's roughness, results highlighted n = 0.035 for upstream and n = 0.025 downstream of Kakrapar weir is suitable for simulation of the future flood in the lower Tapi River. using the HEC-RAS model. Doherty (2010), calibrated the channel roughness for a large number of semiarid rivers in Western Australia with variable channel characteristics for the development of rating curves. In the above context, Parhi, et al., (2013), highlighted need to calibrating the channel roughness coefficient for the Mahanadi River, Odisha which is pertinent severe floods causing huge loss of life and property. In the present study, 1D Saint–Venant equation based HEC-RAS hydraulic model was used to simulate the effect of Manning's Coefficient n on Flow and stage of river flow. The objective of the study is to assess the variation of Manning's n on flow characteristics of the Nethravathi river.

MODEL DESCRIPTION

The Hydrologic Engineering Center - River Analysis System (HEC-RAS) model is based on Saint Venant equations (Eqs. (1) and (2)) formulated primarily for unsteady gradually varied flow in the natural channels (Chow et al., 1988; HEC, 2002).

$$\frac{\partial y}{\partial t} + D_h \frac{\partial v}{dx} + V \frac{dy}{dx} = 0 \quad (1)$$

$$\frac{\partial y}{\partial t} + V \frac{\partial v}{dx} + g\left(\frac{dy}{dx} - S_o + S_f\right) = 0 \quad (2)$$

Where, A = area of flow, V = velocity, Dh =A/B = hydraulic depth, y = depth of flow, Sf = frictional slope, So= channel bottom slope, x = distance along the channel length, g = acceleration due to gravity, t = time. Equations (1) and (2) are solved using the implicit finite difference scheme. This numerical scheme has been shown to be completely non-dissipative but marginally stable when run in a semi implicit form, which corresponds to weighting factor (ϴ) equal to 0.6 for unsteady flow simulation (HEC, 2002). HEC-RAS takes, by default, the weighting factor (ϴ) equals to 1 and allows the users to specify any value between 0.6 to 1. The finite difference scheme has limitation due to its inability to handle transitions between subcritical and supercritical flow, as a different solution algorithm is required for these flow conditions. It has been made possible to overcome the above-mentioned limitation in the present study by using HEC-RAS and using a mixed-flow regime to covering solution in sub reaches (HEC, 2002). HEC-RAS can be effectively coupled with GeoRAS. The GeoRAS software helps in the preparation of input data which can be imported to HEC-RAS. In order to create an import file, DEM of the river system is used. GeoRAS assists in creating a series of points, lines and polygonal layers which are required for HEC-RAS model (Khattak et al., 2016). The important RAS layers are created for flow path, stream centreline, main channel, river bank and cross-section. One can also provide the details regarding bridge, levee, culverts and storage area if any present in the river course. After preparing the input geometric file with the help of HEC-GeoRAS, data are imported to HECRAS. For simulation using HEC-RAS, following input data provided are geometry, resistance, boundary conditions of the channel downstream and upstream.

STUDY AREA AND DATA SET

Nethravathi River

The Nethravathi River is considered for the present study. It is a west flowing River in India, with a total length of 103 km and catchment area of 3657 km2. The length of the river reach of 28 km between the two gauging stations of Uppinangadi and Bantwal is selected based on the availability of hydrological data as shown in Fig. 1. In addition, the Nethravathi River has a simple drainage network with Kumaradhara river as major tributaries, In the context of surface hydrology, the Nethravathi River exhibits significate seasonal fluctuation in river discharge. High flows occur in monsoon, with average monthly discharges ranging between 109 m3/s and 134 m3/s

Data sets

The data required for simulation of flow in HEC-RAS are channel geometry, upstream and downstream boundary conditions and channel. Geometric data of Nethravathi river was extracted from SRTM DEM. The study reach is about 28 km long and has mild slope throughout the length. The effect of meandering has been considered as there is reasonable curvature seen in study reach by providing expansion and contraction coefficient as 0.3 and 0.1 respectively. Discharge hydrograph at Uppinangadi gauging station and friction slope at Bantwal gauging station were considered as upstream and downstream boundary conditions. The Manning's roughness coefficient 'n has been taken as 0.030 to 0.070 for analysis (Chow,1959). The distances between extracted cross sections vary from 1 km to 2 km. Daily discharge data of Uppinangadi gauging station were collected from Karnataka public work department (KPWD), India and Bantwal gauging station were collected from the Central Water Commission (CWC) and used for simulation monsoon period

(June to October) of the year 2007 and 2008.

RESULTS AND DISCUSSIONS

HEC-RAS is used to simulate the stages for flow during years 2007 and 2008. The simulated stage hydrographs were compared with observed stage hydrograph at Bantwal gauging station for duration mentioned in Table 1. The performance of the HEC-RAS model for Nethravathi river is verified using NRMSE and NSE presented in Table 2. Simulated stages from the model are in close agreement with observed water levels for the years 2007 and 2008 at Bantwal gauging station as shown in Fig 2 and Fig 3. The simulated and observed peak discharges for the year 2007 were found to be 3382.54 m^3/s and 3989.68 m^3/s respectively. The simulated and observed peak discharges for the year 2008 were found to be 3752 m^3/s and 5610 m^3/s respectively.

Effect of Manning's N

In Fig. 4 and Fig. 5 it can be noted that there is a significant effect on river stage due to in consistency roughness coefficient. In the main channel, Manning's n is varied from 0.03 to 0.07 with an increment 0.01. The variation of Manning's n shows that an increase in roughness n in the main channel increases the simulated stages and attenuates the associated peak discharges (Fig. 6 and Fig.7). Stage-discharge rating curve was drawn for different Manning's n at Bantwal gauging station for the year 2007 and 2008.

In Fig. 6 shows the loop rating curve. Loops in a rating curve at a given cross section may be due to unsteady flow effects of the hydrograph and Shifts in channel bed forms. Fig. 6 and Fig. 7 shows Stage-discharge curve for different Manning's n. In Fig. 6 the peak stage values were found to be 3.00 m, 3.39m 3.62m 3.93.m and 4.20m for n=0.03, 0.04, 0.05, 0.06 and 0.07 respectively for the considered discharge of 1000 m^3/sec. Whereas for the discharge values of 2500 m^3/sec, the peak stage values were estimated to be 4.48m, 5.31m, 5.81m, 6.17m and 6.64m for n=0.03, 0.04, 0.05, 0.06 and 0.07 respectively for the year 2007. In Fig. 7 the peak stage values were found to be 2.99 m, 3.43m 3.65m 3.93.m and 4.19m for n=0.03, 0.04, 0.05, 0.06 and 0.07 respectively for the considered discharge of 1000 m^3/sec, whereas for the discharge values of 2500 m^3/sec. The peak stage values were estimated to be 4.48m, 5.28m, 5.66m, 6.19m and 6.68m for n=0.03, 0.04, 0.05, 0.06 and 0.07 respectively for the year 2008. From the rating curve, it is very clear that as discharge increases, the effect of manning n on stage relatively increases which shows that roughness is highly sensitive at higher discharges. From Fig. 6 and Fig. 7 it can also be observed that the rating curve is acceptable for 2007 and 2008. The Simulated model is better correlated for the year 2008 compared to 2007.

CONCLUSIONS

The discharge increases, the effect of manning n on stage relatively increases which show that roughness is highly sensitive at higher discharges.

The variation of Manning's n shows that an increase of n in the main channel increases the simulated stages and attenuates the associated peak discharges

Simulated stage hydrographs produced by HEC-RAS model are in close agreement with the observed water levels for the year 2007 and 2008 at Bantwal gauging station. The rating curve is acceptable for 2007 and 2008.

The Simulated model successfully demonstrates the effect of manning's n on the unsteady flow in the Nethravathi river reach using HEC-RAS.

REFERENCES

[1]. Bao, W. M., Zhang, X. Q., and Qu, S. M. (2009), Dynamic correction of roughness in the hydrodynamic model. Journal of hydrodynamics, Vol. 21, No. 2, pp. 255-263.

[2]. Chow, V. T., D. Maidment, and L. Mays (1988), Applied Hydrology, Water Resour. Environ. Ser., McGraw-Hill, Singapore.

[3]. Doherty, R. (2010), Calibration of HEC-RAS Models for Rating Curve Development in Semi-Arid Regions of Western Australia, In AHA 2010 Conference.

[4]. HEC-RAS, "User Manual," US Army Corps of Engineers, Hydrologic Engineering Center, Davis Version 4.0, 2008.

[5]. Khattak, M. S., Anwar, F., Saeed, T. U., Sharif, M., Sheraz, K., and Ahmed, A., (2016), Floodplain mapping using HEC-RAS and ArcGIS: A case study of Kabul River, Arab Journal of Science and Engineering, Vol. 41 No,4, pp. 1375-1390.

[6]. Parhi, P. K., Sankhua, R. N., and Roy, G. P. (2012), Calibration of channel roughness for Mahanadi River, (India) using HEC-RAS model, Journal of Water Resource and Protection, Vol. 4 No. 10, pp. 847.
[7]. Parhi, P. K. (2013), HEC-RAS Model for Mannnig's Roughness: A Case Study, Open Journal of Modern Hydrology, Vol. 3 No. 03, pp. 97.
[8]. Patro, S., Chatterjee, C., Mohanty, S., Singh, R., & Raghuwanshi, N. S. (2009). Flood inundation modeling using MIKE FLOOD and remote sensing data. *Journal of the Indian Society of Remote Sensing*, *37*(1), 107-118.
[9]. Ramesh, R., Datta, B., Bhallamudi, S. M., and Narayana, A. (2000), Optimal estimation of roughness in open-channel flows, Journal of Hydraulic Engineering, Vol. 126, No. 4, pp. 299-303.
[10]. Timbadiya, P. V., Patel, P. L., and Porey, P. D. (2011), Calibration of HEC-RAS model on prediction of flood for lower Tapi River, India, Journal of Water Resource and Protection, Vol. 3 No. 11, pp. 805.
[11]. Usul, N., and Turan, B. (2006), Flood forecasting and analysis within the Ulus Basin, Turkey, using geographic information systems, Natural Hazards, Vol. 39 No. 2, pp. 213-229.
[12]. Vijay, R., Sargoankar, A., and Gupta, A. (2007), Hydrodynamic simulation of River Yamuna for riverbed assessment: a case study of Delhi region, Environmental monitoring and assessment, Vol. 130 No. 1-3, pp. 381-387.
[13]. Wasantha Lal, A. M. (1995). Calibration of riverbed roughness. Journal of Hydraulic Engineering, 121(9), 664-671.

Table 1 Data used for simulation

SL No.	Flow Year	Simulation duration	Gauge station
1	2007	Jun to Oct	Bantwal
2	2008	Jun to Oct	Bantwal

Table 2 Performance of HEC-RAS model

SL No.	Flow Year	NRMSE	NSE	R
1	2007	0.0866	0.884	0.949
2	2008	0.0783	0.842	0.955

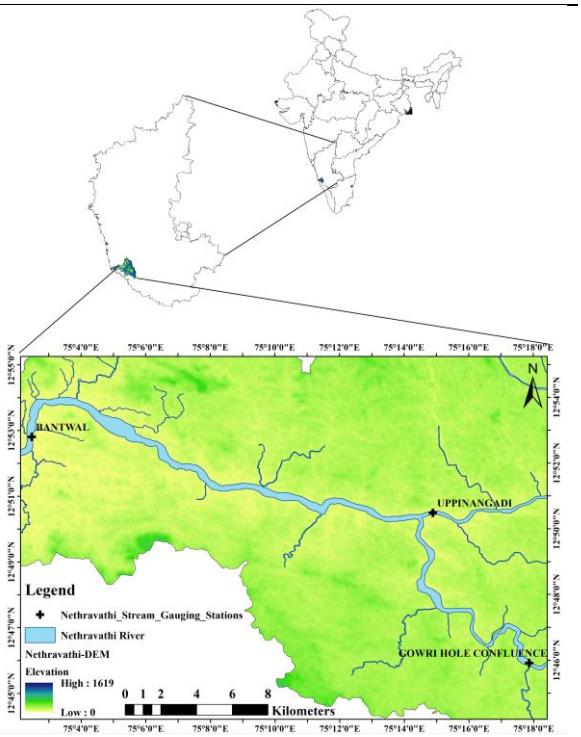

Fig.1 Study area

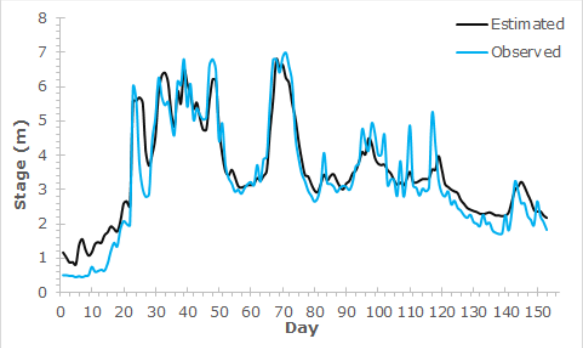

Fig.2 Observed vs estimated hydrograph for the year 2007

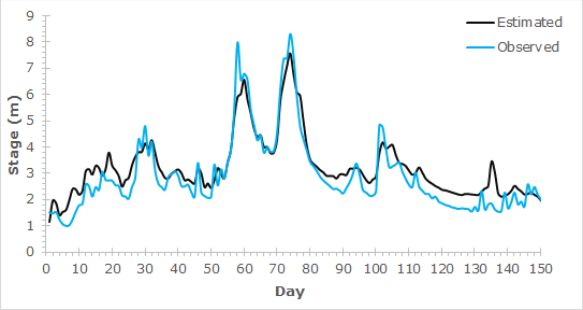

Fig.3 Observed vs estimated hydrograph for the year 2008

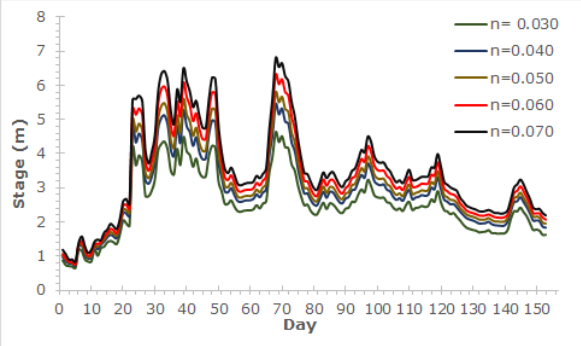

Fig.4 Stage hydrograph for different Manning's n for the year 2007

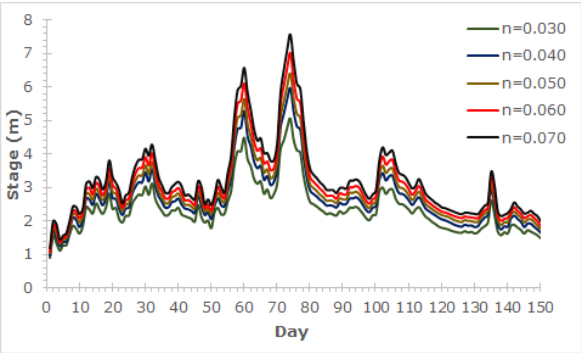

Fig.5 Stage hydrograph for different Manning's n for the year 2008

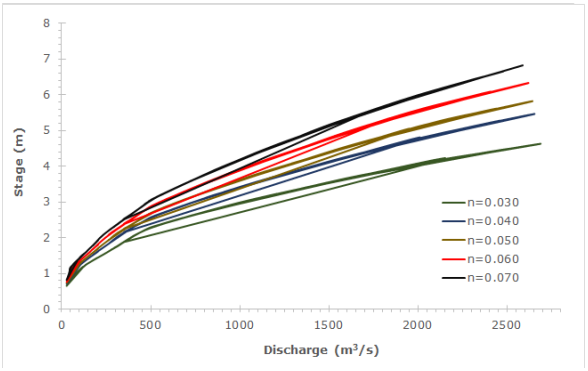

Fig.6 Rating curve the year 2007

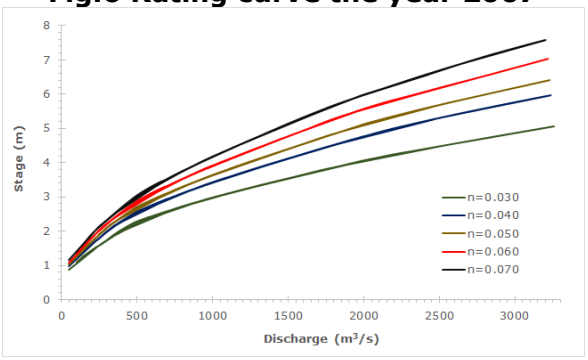

Fig.7 Rating curve the year 2008

8th International Engineering Symposium - IES 2019
March 13-15, 2019, Kumamoto University, Japan

Effects of Oblique Weir with an Opening on Bed Morphology and Flow Structure

Hirotaka UNE [1], Terunori OHOMOTO [2], Kanji ADACHI[3] and **Hiroto KONDO[4]**

1 *Graduate School of Science and Technology, Kumamoto University, 2-39-1 Kurokami, Kumamoto 860-8555, Japan. email: 181d9201@st.kumamoto-u.ac.jp*
2 *Civil and Environmental Engineering, Kumamoto University, 2-39-1 Kurokami, Kumamoto 860-8555, Japan. email: ohmoto@kumamoto-u.ac.jp*
3 *Graduate School of Science and Technology, Kumamoto University, 2-39-1 Kurokami, Kumamoto 860-8555, Japan. Email: 171d8801@st.kumamoto-u.ac.jp*
4 *Graduate School of Science and Technology, Kumamoto University, 2-39-1 Kurokami, Kumamoto 860-8555, Japan. Email: 182d8306@st.kumamoto-u.ac.jp*

ABSTRACT: This paper presents the experimental study on the downstream channel bed due to an oblique weir with an opening, paying attention to the effects of relative overflow depth on local scouring, sand bars and three-dimensional flow patterns. The experiments were conducted under the clear-water scour condition for an equilibrium scour hole. The experimental results show that local scouring and sand bar development at the down-stream of the submerged oblique weir decrease as relative overflow depth decrease and turned out strongly paired cellular secondary currents. In addition, the opening changed the place of strong local scouring from the side to the middle of a channel.

Keywords*: oblique weir with an opening, river bed morphology, local Scouring, sand bar, three-dimensional turbulent flow, cellular secondary currents*

1. INTRODUCTION

River transverse structures such as dams and weirs have been benefiting people for many years in terms of water use and flood control. On the other hand, they interrupt the hydraulic and ecological continuity of rivers and bring about various problems. For example, a fixed weir, which is a transverse river structure, interrupt sediment transport within a river Then the interruption of the sediment transportation, cause the following issues: i) sediment accumulates on the upstream side of the weir, and the original water service function is lowered. ii) Deposit of sediment on the upstream side of the weir increases the water level on the upstream side during flooding, resulting in increased flood risks. iii) On the downstream side of the fixed weir, physical and biological environments disappear and tend to suppress natural disturbance. iv) The river bed in the downstream side is erode because the supply of sediment from upstream of the fixed weir is interrupted by the weir. Iwaya (2006) classified 200 domestic oblique weirs through field survey and literature survey. Miwa (1978) found out that, the curved oblique weir constructed along the crest part of the sand and gravel sediment whose movement was suppressed by the hydraulic model experiment, has a small fluid force at the time of flooding, and hence, because the river bed is at a high position, the scouring of the river bed directly under the weir is small and local deep digging is hard to occur, and insisted on its legitimacy. Otoshi et al. (1998) conducted a hydraulic model experiment on the technical grounds related to the linear determination of the "Miyagawa river" in the Matsuda River flowing through Kochi Prefecture,

which is regarded as the construction of Nonaka Kaneyama from the curved oblique weir . Fukuoka et al.(2001) conducted an experiment in which the rising water level at the dam upstream, the flow at the weir end and the downstream of the weir, and the oblique weirs were installed on the moving bed in the fixed bed flow where the oblique weir was installed and the shape of the river channel and the weir On the river bed fluctuation was investigated.
In the past research, local scouring and flow concentration are discussed along the downstream side shore flow beyond the diagonal weir (Fukuoka et al. 2001), the relationship between the three dimensional structure of flow and river bed variation is unknown. Furthermore, there are few cases of research on countermeasures against oblique weir problems. In this study, we investigated the influence of oblique fixed weir with openings on flow and bed fluctuation as a measure to improve the flood control and environmental problems of oblique weir.

2. EXPERIMENTAL APPARATUS AND METHOD

The experiments were conducted with a 10-m-long, 40-cm-wide, 20-cm-deep variable-slope circulating acrylic flume. As shown in Figure 1, this study uses two kinds of weirs: the oblique weir without opening (non-opening weir) and the oblique weir with opening (opening weir). The angle of the weir was set to 30 ° upstream relative to the right wall. An opening weir with a 10-cm-wide central opening was installed at 5 m from the upstream end of the flume. The 4.5-m-long section upstream of the weir and the 4.5-m-long section downstream of the weir were filled with silicate sand. The mean grain size of the silicate sand is 1.7 mm. A uniformity coefficient to a uniform thickness is 1.50 (ranging from 3 cm to 10.5 cm) according to relative overflow depth. The relative overflow depth was determined by dividing the overflow depth by the height of the weir. The bed

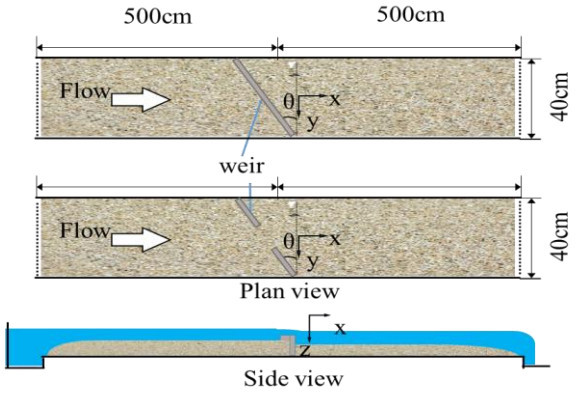

Fig. 1: Experimental channel

Table 1 Weir conditions

Opening conditions	Case	U_m (cm/s)	K_I	H/D_w
Non-opening weir	N1	18.1	0.38	0.60
	N2	20.0	0.47	0.83
	N3			1.0
	N4			1.2
Opening weir	O1			0.22
	O2			0.38
	O3			0.57
	O4			0.83
	O5			1.0
	O6			1.2

elevation on the upstream side of the weir was set to be 1 cm higher than the bed elevation on the downstream side of the weir. In all cases, bed elevation was measured after confirming that the channel bed went into a state of equilibrium after letting the water flow in the flume for 24 hours or longer.
Table 1 shows the conditions of the movable-bed experiments. Because this study focuses on a riverbed in static equilibrium, the flow rate was set to levels below the critical tractive force so that the bed material of mean grain size was not washed out in the upstream and downstream sections beyond the influence of the weir. In the experiments, sand was spread in the flume to a bed elevation needed to meet the relative overflow depth requirements, and the weir at the downstream end was operated at a constant flow rate (Q = 4.3 l/s) and bed slope (I= 1/500). The relative overflow depth was systematically varied at the cross-sectional mean flow velocities of

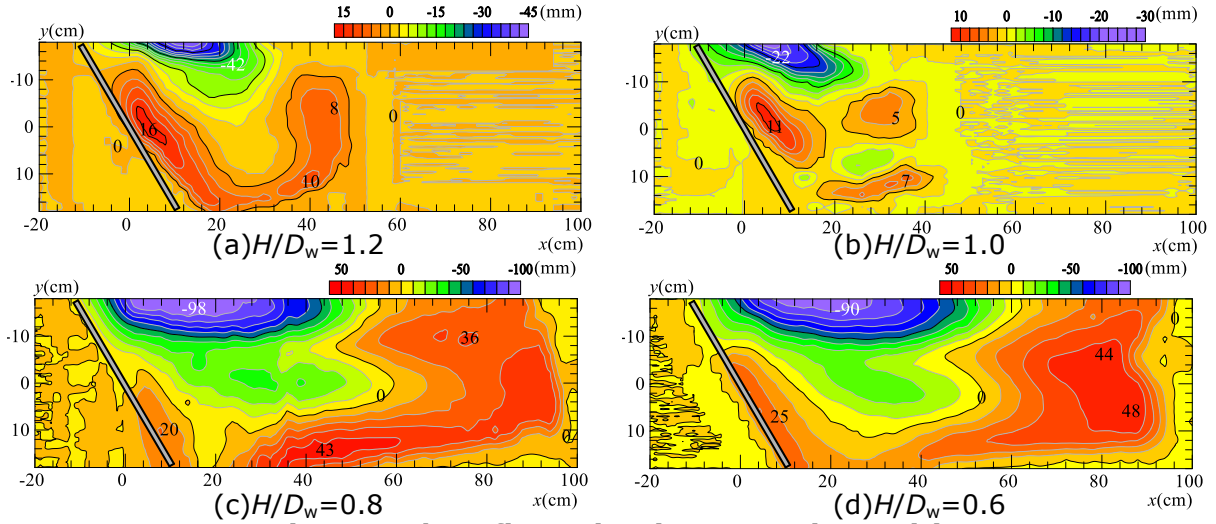

Fig. 2: Bed configuration (Non-opening weir)

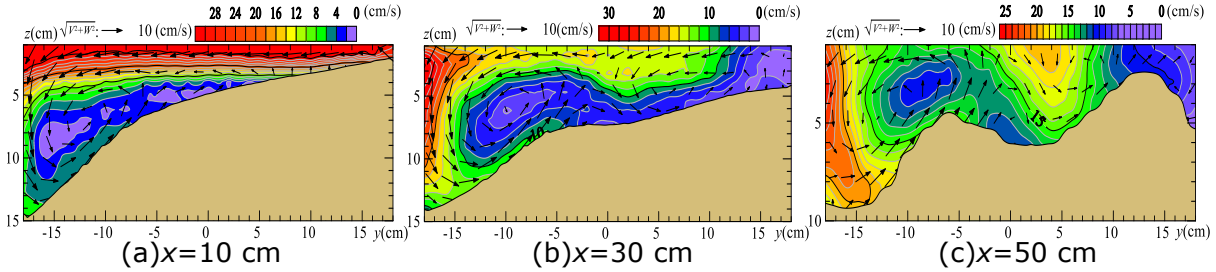

Fig. 3: the vertical flow patterns with synthetic flow velocity |*u*| and secondary flow vectors (Non-opening weir)

about Um=20 cm/s as measured at points beyond the influence of local scouring at the weir. In Table 1, Um represents the cross-sectional mean flow velocity at a distance of 3 m upstream of the weir; H, overflow depth; DW, weir height; H/Dw, relative overflow depth; and KI, the critical flow velocity for initiation of motion of bed material, as distinguished from the cross-sectional mean flow velocity, which corresponds to the flow intensity factor among the K factors proposed by Melville (1997). The maximum scour depth and the maximum deposition of the bed configuration under each weir condition are indicated by ze and zd, respectively. The critical depth hc over top of the non-opening weir can be defined by the following equation:

$$h_c = \sqrt[3]{\frac{Q^2}{g(B/\cos\theta)}} \qquad (1)$$

where hc = the critical depth over top of the non-opening weir; Q = discharge (was 4.3 l/s); g = acceleration of gravity; B =flume width (was 39cm-wide); θ = weir angle (was 30 °). In these cases, flow regime over the weir was submerged overflow because the critical depth hc was 2.1cm.The synthetic flow velocity |u| was defined by the following equation:

$$|u| = \sqrt{U^2 + V^2} \qquad (2)$$

where |u| = synthetic flow velocity; U = the main flow velocity; V = the transverse component of secondary flow.

Water level and bed elevation were measured with a point gauge and an ultrasonic sensor, respectively. To investigate the flow structure, point measurement and multi-point simultaneous measurement of water surface profile and flow velocity were conducted in Case N2 and O4 shown in Table 1. The surface flow measurement was made by the PIV (particle image velocimetry) method using a video camera system capable of multi-point simultaneous measurement of flow velocity. The point measurement of flow velocity was made with I type and L type

two-component electromagnetic current meters.

3. EXPERIMENTAL RESULTS

3.1 Non-opening Weir

3.1.1 Bedform in Static Equilibrium

Figure 2 shows the contour of the riverbed scouring and deposition of oblique weir, with an average flow velocity Um=20 cm/s. In addition, the numerical values of contours are expressed in mm from the initial flatbed bed. The oblique weirs show stronger asymmetry in the transverse direction than the rectangular weir. The scouring at the oblique non-opening weir concentrates along the left bank and the scales and depth of the scouring increases with decreasing relative overflow depth H/Dw. These results indicate that overflow orthogonally to the weir axis as the weir changes flow direction. And as the relative overflow depth H/Dw increases, the cross-sectional area overflowing the weir will increase and the flow velocity will decrease. The maximum scouring depth increases as the relative overflow water depth decreases, and it reveals that it reaches approximately twice the water depth h at H/Dw = 0.60 and H/Dw = 0.83. In addition, the falling distance of scouring is within twice the length of the weir, and it increases as the relative overflow depth H/Dw decreases. Sand bars develop directly in downstream along the oblique weir, the vicinity of the right bank and downstream of the left bank scour and is widely distributed as compared with scouring developed in the left bank. The maximum deposition thickness is about half the maximum scour depth and increases as the relative overflow depth H/Dw decreases.

3.1.2 Local flow in the downstream of non-opening weir

Figures 3 show the vertical flow patterns with synthetic flow velocity |u| and secondary flow vectors measured in 10 cm, 30 cm and 50 cm downstream of the non-opening weir. The magnitudes of the secondary flow vectors show the synthetic flow velocity of transverse component V and vertical component W of secondary flow. At x=10 cm and x=30 cm, the secondary flow vectors near the surface and near the bed show flow toward the left wall and the right wall, respectively. Especially, the secondary flow significantly occurs near the left wall between y=-18cm and y=-5cm. It is assumed that the secondary flow created by bending streamlines. It is classified the first kind secondary flow of Prandtl, it can be seen that the maximum downward flow is extremely strong as 75% of the average cross-sectional flow velocity. At x=30 cm and 50 cm, the secondary flow occurred near the left wall is confirmed although its magnitude is smaller than itself of x=10 cm. At x=50 cm, the upward flow and the downward flow occur over the ridge and trough of the sand bars. A vortex having a direction of rotation opposite to the vortex formed near the left bank is generated between y=-5 cm and y=0cm although it is weaker than the vortex that is formed near the left wall.

For the synthetic flow velocity |u| at x = 10 cm, a high velocity region is uniformly formed in the transverse direction in the range of z = 1 cm to 4 cm near the water surface. The vertical spatial changes in synthetic flow velocity |u| are large under the influence of the weir, and strong shear layers are formed. And in the scour hole, the synthetic flow velocity near the bed is higher than the one of the half water depth. This can be explained by the fact that the high velocity fluid mass is advected by the secondary flow. However, the high synthetic flow velocity |u| region formed near the water surface at x = 10 cm occurs near the left wall at x=30 cm. Therefore, velocity changes in the transverse direction become conspicuous. On the other hand, the synthetic flow velocity |u| near the right wall is extremely small. As the water flow downstream, vertical changes become smaller, and velocity changes in the transverse direction become increasingly conspicuous at x=50 cm. The tendency that the flow velocity near the river bed is larger than that at half depth is more significantly at x=50 cm.

3.2 Opening Weir

3.2.1 Bedform in Static Equilibrium

Figure 4 shows the contour of the riverbed scouring and deposition of oblique weir

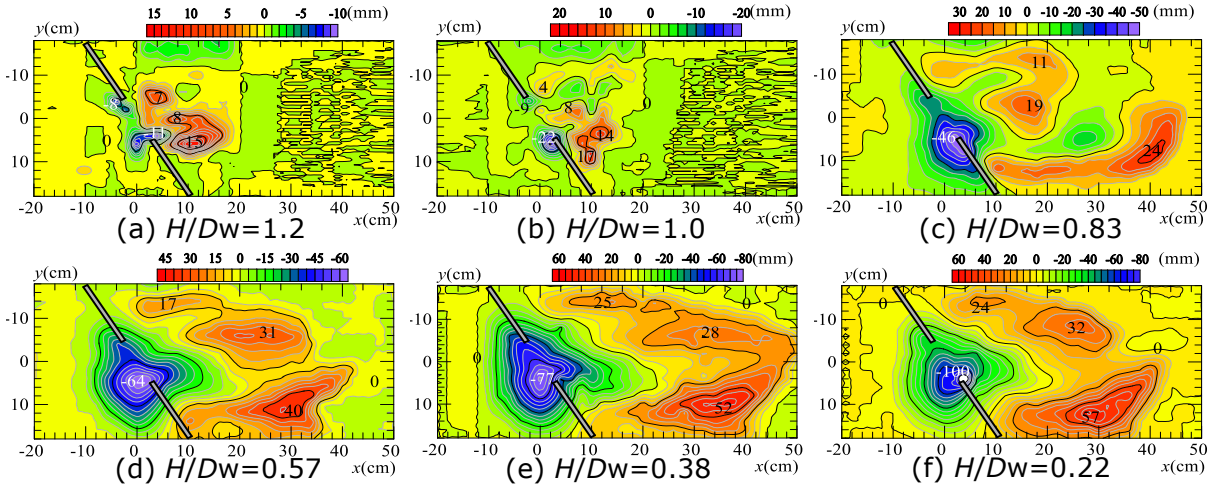

Fig. 4: Bed configuration (Opening weir)

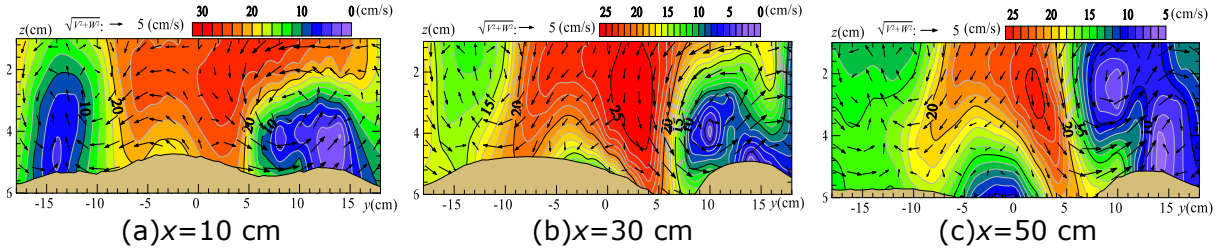

Fig. 5: The vertical flow patterns with synthetic flow velocity |*u*| and secondary flow vectors (Opening weir)

with an opening. The river bed in the oblique weir with an opening has weaker asymmetry than the oblique non-opening weir. The local scouring which occurred near the left bank in the oblique non-opening weir caused the scouring position to shift from near the riverbank to the center of the channel by setting an opening in the weir and the area spread and depth of scouring was relative It increases as the flow depth H/Dw decreases. The position of maximum scouring depth appears at the tip of the weir on the right bank side. It is inferred that descending flow accompanying the horseshoe vortex formed at the front of the weir is stronger at the tip of the weir at the right side and local scouring becomes larger than that at the tip of the left side dam due to the flow field asymmetry. The remarkable sandbar in the oblique opening weir occurs at three places along the center of the descending flow channel and its left bank, and it is similar at any relative overflow depth. In general, the height of the sandbar in the right bank is the largest, which is small in the order of the center of the waterway and the left bank.

3.2.2 Local flow in the downstream of opening weir

Figures 6 show the vertical flow patterns with synthetic flow velocity |u| and secondary flow vectors measured in 10 cm, 20 cm and 30 cm downstream of the opening weir. The magnitudes of the secondary flow vectors show the synthetic flow velocity of transverse component V and vertical component W of secondary flow. The counter rotating cellular secondary flows can be confirmed in the range of y=-18 cm to y=-5 cm and y=18 cm to y=5 cm behind the weir. As shown, the horseshoe-shaped vortex oriented transversely along the weir gradually changes its orientation into a longitudinal vortex oriented in the flow direction as it flows downstream through the weir opening, and longitudinal vortices rotating in the opposite direction are formed around the central vortex. From the magnitudes of the upward and downward flow, it can be inferred that the intensity of those vortices is maximized at x = 10 cm

and becomes somewhat weaker as the water flows downstream.

The magnitudes of counter-rotating cellular secondary flows vector of the left wall side are smaller than ones of the right wall side. The upward flow of the secondary flow cell is located at y=2 cm, y=-13 cm and y=-11 cm located at the peak of the sandbar, the downward flow is located at the valley between sandbars y=-10 cm to y=-6 cm and It is recognized that it occurs in the range of y=4 cm to y=8 cm. On the other hand, downward flows near the left wall also in the oblique opening weir occur similarly to the oblique non-opening weir, but its magnitudes are about 5 cm/s at x=10 cm, whereas at the oblique non-opening weir it is 15 cm/s, which is found to be reduced to about 1/3.

The synthetic flow velocity |u| over weir crests in the sections y=−18 cm to −5 cm and y= +5 cm to +18 cm is relatively low. At x = 10 cm, vertical spatial changes in synthetic flow velocity |u| are large under the influence of the weir, and strong shear layers are formed. As the water flow downstream, vertical changes become smaller, and velocity changes in the transverse direction become increasingly conspicuous. In the sections, y=−18 cm to y=−13 cm and y =7 cm to y=18 cm, flow velocity in the near-surface zone tends to decrease as the water flows downstream. This indicates that low-velocity fluid masses near the bottom were moved up toward the water surface zone by the strong upward flow along the right and left walls.

4. Conclusion

The main results obtained are as follows:

1) Asymmetry in the transverse direction strongly appears in the diagonal non-opening weirs in the transverse direction compared with the rectangular weirs, and the scouring concentrates along the vicinity of the left bank, and sedimentation is directly downward along the oblique weir, in the vicinity of the right bank and in the left bank scour hole Appearing downstream, it is widely distributed compared to scouring developed on the left bank.
2) The opening weir has weaker asymmetry compared to the non-opening weir and the local scouring generated near the left bank of the weir downstream in the oblique non-opening weir has the scouring position shifted from the river bank to the central part of the river way .
3) The secondary flow in both the oblique non-opening weir and the opening weir showed a strong positional relationship with the sandbar in the downstream area, a rising flow on the sandbar and a downward flow converging in the valley between the sandbars.
4) Although descent flow in the vicinity of the left bank occurs similarly to the oblique non-opening weir even if it is inclined opening weir, it is understood that the size is reduced to about 1/3 as compared with the oblique non-opening weir.

REFERENCES

[1]Takao IWAYA.(2007).Functions and Configurations on the Oblique Weir in Japan. Journal of Japan Society of Civil Engineers (JSCE), Journal of Historical Studies in Civil Engineering, Vol.26, pp.45-58. (Japanese press)

Hajime, MIWA (1978). The Rationality of Curved Oblique Weirs on the Basis of the Formations of 'Sarekitai' Transactions of The Japanese Society of Irrigation, Drainage and Reclamation Engineering, Vol. 1978, Issue 76, pp. 61-66,a2 (Japanese press)

Shoji FUKUOKA, Shunichi MISHIRO, Shoji ARATANI, Jun NAKASUKA, Shoji OKADA, Masatoshi Tanaka (2001). THE EFFECT OF WEIR POSITION AND ITS SHAPE ON THE FLOW AND BED TOPOGRAPHY. Journal of Japan Society of Civil Engineers (JSCE), PROCEEDINGS OF HYDRAULIC ENGINEERING, Vol.45, pp.397-402. (Japanese press)

Bruce W. Melville (1997). Pier and Abutment Scour: Integrated Approach. J . Hydraulic Engineering, ASCE, Vol.123, No.2, pp.125-136, 1997

Japan Society of Civil Engineers.(2007). The Special Committee for Technical Evaluation of the Yoshinogawa Dai-ichi Technical Evaluation. http://www.jsce.or.jp/committee/daijyuzeki/photo.shtml (Japanese press)

8th International Engineering Symposium - IES 2019
March 13-15, 2019, Kumamoto University, Japan

Effect of SSI on Structural Response of Berthing Structures

Anjana S Rao [1], B R Jayalekshmi [2] and **Katta Venkataramana[3]**

1 *Dept. of Civil Engineering, National Institute of Technology Karnataka, Surathkal, Mangalore 575025, India. email:anjusrao@gmail.com*
2 *Dept. of Civil Engineering, National Institute of Technology Karnataka, Surathkal, Mangalore 575025, India. e-mail:br.jaya@gmail.com*
3 *Dept. of Civil Engineering, National Institute of Technology Karnataka, Surathkal, Mangalore 575025, India. e-mail:ven.nitk@gmail.com*

ABSTRACT: In order to facilitate berthing and mooring of vessels, loading and unloading of cargo, embarking and disembarking of passengers etc., berthing structures are constructed in ports and harbours. Performance of berthing structures during past earthquakes shows that it is very important to consider the effect of soil-structure interaction during analysis of such structures. In the present study, an existing berthing structure (berth number 18 of New Mangalore Port, India) has been analysed considering the soil-structure interaction and the response is evaluated under static and seismic loading. The width of the berthing structure is 25m and its length is 325m. The analysis is carried out considering all types of static loads on the berthing structure and seismic force corresponding to zone III. The deformations and corresponding bending moment and shear force resulting from the interaction between the structure and the soil, which are not included in conventional design procedures, are investigated. Remarkable difference in structural response has been observed with variation in soil profile, which needs to be taken into account while designing.

***Keywords**: Berthing structure, ports, seismic response, soil-structure interaction*

INTRODUCTION

Berth is a designated location in ports and harbors to provide facilities for berthing and mooring of vessels, embarking and disembarking of passengers and vehicles and for loading and unloading of cargo. In berthing structures, lateral forces are caused by impact of berthing ships, pull from mooring ropes, pressure of wind, waves and floating ice, seismic force, active earth pressure, differential water pressure and live load on the structure. Diaphragm wall and anchor rods are provided in berthing structures in order to enhance their stability. Berthing structures can be classified as open type structures and vertical face type structures. In an open type structure, a rigid deck is supported over vertical piles or over combination of vertical and raker piles. Sheet pile walls, block walls, caissons or diaphragm walls are used in vertical face type structures. Diaphragm walls resist the active earth pressure and the load is absorbed by the tie rods anchored to the diaphragm walls or raker piles.

Most of the civil engineering structures involve some type of structural element in direct contact with soil. Neither the structural displacements nor the ground displacements are independent of each other when the external forces such as earthquake, act on these systems. Soil-structure interaction is a process in which the response of the soil influences the motion of the structure and the motion of the structure influences the response of the soil. Soil-structure interaction effect is usually neglected by conventional design methods.

METHODOLOGY

The berth number 18 of New Mangalore Port (NMPT), India, was considered, for the purpose of the study. The analysis of

the existing berthing structure was done using the software STAAD Pro. 3-D analysis was carried out under static and seismic loading. The response of the structure was evaluated incorporating the soil-structure interaction. This was achieved by modelling soil springs to represent soil stratum.

1. DATA COLLECTION

The various necessary data collected from New Mangalore Port (NMPT), India, includes,

a) Details of sub soil investigation: The different soil layers present in the borehole are silty sand from +4.662m to +3.162m, loose sand from +3.162m to +0.162m, silty sand from +0.162m to -2.838, sandy silty clay from -2.838m to -4.838m, loose sand from -4.838m to -5.838m, dense sand from -5.838m to -10.338m and decomposed granite from -10.338m to -27m. Table 1 shows the soil properties of different soil layers.

b) Details of the berth: The width of the berthing structure is 25m and its length is 325m. The entire length of the berth of 325m is divided into five panels, each of 65m length with expansion joints in between them. Figure 1 shows the plan of a panel of the berth. The berth is supported by a diaphragm wall and piles. The lateral distance of the rows of piles from the berth face is 2.8m, 9.8m, 15.8m and 22.8m. The whole structure is supported by 55 rows of piles in transverse direction having 4 piles in each row. Out of these, 22 rows are of 1300mm diameter piles from seaward end of berth and 33 rows are of 1200mm diameter. The piles have a depth of 30m. The dredge depth is -17 m near the first pile. The thickness of the deck slab of berth is 450mm. The slab is supported on cross beams in the lateral direction and secondary beams in the longitudinal direction. The diaphragm wall is located at 25m from the pile near the sea side. The thickness of diaphragm wall is 1100 mm. The tie rod anchor is inclined at an angle of 45°.

c) Load details: The different loads which act on the structure include self-weight, live load of 55 kN/m^2, mooring force, berthing force, earth pressure and differential water pressure.

2. ANALYSIS

The analysis of the structure was carried out for static and seismic loadings. The different parameters used as input in the STAAD Pro software include the structural details of the different elements, properties of the different soil layers and load details.

The berthing structure was modelled as a single panel of length 65m and width 25m. In order to idealize the supporting soil for piles and diaphragm wall in the horizontal direction, soil springs were modelled at all nodes along the pile and diaphragm wall length. The spring constants were estimated using the modulus of sub-grade reaction, k_s, (Bowles, 1997), as explained below.

$$K_S = A_S + B_S Z^n \quad (1)$$

Where, A_S is the constant for either horizontal or vertical member, B_S is the coefficient of depth variation, Z is the depth of point of interest below ground level and n is the exponent to give k_s the best fit.

$$A_S = C_m\, C\, [cN_c + 0.5\gamma B N_\gamma] \quad (2)$$

$$B_S = C_m\, C\, [\gamma\, N_\gamma] \quad (3)$$

Where, C_m is the size factor, C is the displacement factor, γ is the density of soil, c is the cohesion of soil, N_γ and N_c are Terzaghi's bearing capacity factors.

Spring constant values are obtained using average end area formula,

$$K_{i1} = (BL/6)[2k_{S(i)} + k_{S(i-1)}] \quad (4)$$

$$K_{i2} = (BL/6)[2k_{S(i)} + k_{S(i+1)}] \quad (5)$$

Where, B is the diameter of pile or thickness of diaphragm wall and L is the length of segment.

Spring constant at every node is the average of k_{i1} and k_{i2}.

The different loads considered for the analysis were dead load of the structure, live load of 55kN/m^2, mooring force of 1500kN, berthing force of 1628kN, differential water pressure, earth pressure and seismic forces. Seismic analysis was done corresponding to zone II and zone III.

All the loads were calculated according to IS: 4651 (Part III) and seismic loads were calculated according to IS: 1893.
For static analysis, load combination including dead load of the structure, live load, mooring force, differential water pressure and earth pressure was considered. For seismic analysis corresponding to zone II and zone III, load combination including dead load of the structure, live load, seismic load, differential water pressure and earth pressure was considered.

RESULTS AND DISCUSSION

The present study has been carried out for static and seismic load cases. Table 2 shows the maximum values of displacement, bending moment and shear force in diaphragm wall and pile. The variation of displacement in the diaphragm wall for static and seismic load cases is shown in figures 2 and 3. Diaphragm wall acts like a propped cantilever, in the presence of anchor rod. The maximum displacement of the wall is obtained at -7.5 m depth. The maximum displacement corresponding to seismic zone II load case is 2.21% more than the static load case.
The variation of shear force in diaphragm wall is shown in figures 4 and 5. When the anchor rod is placed at a particular position, the shear force at that point is increased due to the force in the anchor. Since dredging is done till -10.5m, forces due to active earth pressure alone acts on the wall up to a depth of -10.5m. Whereas, beyond -10.5m, forces due to passive earth pressure start acting on the diaphragm wall. The considerable change in the shear force at a depth of -1.5m is due to the change in the characteristics of soil layers. The maximum shear force obtained in seismic zone II load case is 1.29% more than the static load case. Figures 6 and 7 represent the variation of bending moment in the diaphragm wall for static and seismic cases respectively. The maximum bending moments are obtained at a depth of -7.5m. The maximum bending moment obtained in seismic zone II load case is 2.46% more than the static load case. Due to the rigidity of the diaphragm wall, the response is almost same for zone II and zone III load cases.
The variation of displacement in the pile for static and seismic cases is shown in figures 8 and 9 respectively. The maximum displacement is obtained at top of the pile. The maximum displacement corresponding to seismic zone II load case is 6.01% less than the static load case. From figures 10 and 11, it is observed that the maximum shear force in the pile is obtained at a depth of -19m. Up to a depth of -13m, forces due to soil pressure are absent, since dredging is done till -13m near piles. The maximum shear force obtained in seismic zone II load case is 12% less than the static load case. Figures 12 and 13 show the variation of bending moment in the pile. The maximum bending moment obtained in seismic zone II load case is 21.35% less than the static load case.

CONCLUSIONS

The following conclusions are made from the present study:
1) For berthing structures situated in zone II, the static loading with mooring force will govern the design whereas for zone III, seismic loads govern the design. Since the considered berthing structure is situated in zone III, its design considering the seismic effect is proper.
2) The soil profile is to be properly studied for the analysis of the structure as variation in the soil profile influences the response and stability of the structure.
3) SSI has significant effect on the structure as seen by the variation in displacement profile.
4) Variation in soil profile leads to remarkable difference in structural response, which needs to be taken into account while designing.

REFERENCES

[1] Bowles, J (1997), Foundation Analysis and Design, 5th ed., McGraw Hill, New York, pp.935-941.
[2] Kavitha, P E et al (2017), Influence of Soil Structure Interaction in the Structural Behaviour of a Berthing Structure in Sloping Ground, J. Inst. Eng. India Ser. A, Vol. 98, Issue 4, pp.469–476.
[3] Muthukkumaran, K et al (2007), Effect of Dredging and Axial Load on a Berthing Structure, International Journal of Geo-Engineering Case histories, Vol. 1, Issue 2, pp.73-88.
[4] Naidu,G T et al (2017), A Study on Behaviour of Structural Elements of Berthing Structure with Raker Pile and Anchored Wall, International Journal of Civil

Engineering and Technology (IJCIET), Volume 8, Issue 7, pp. 1111–1124.
[5] Subha, I P (2012), Behaviour of an Open Type Berthing Structure under Earthquake Condition - A Numerical Approach, International Journal of Engineering Research and Applications, Vol. 2, Issue 1, pp.036-040.

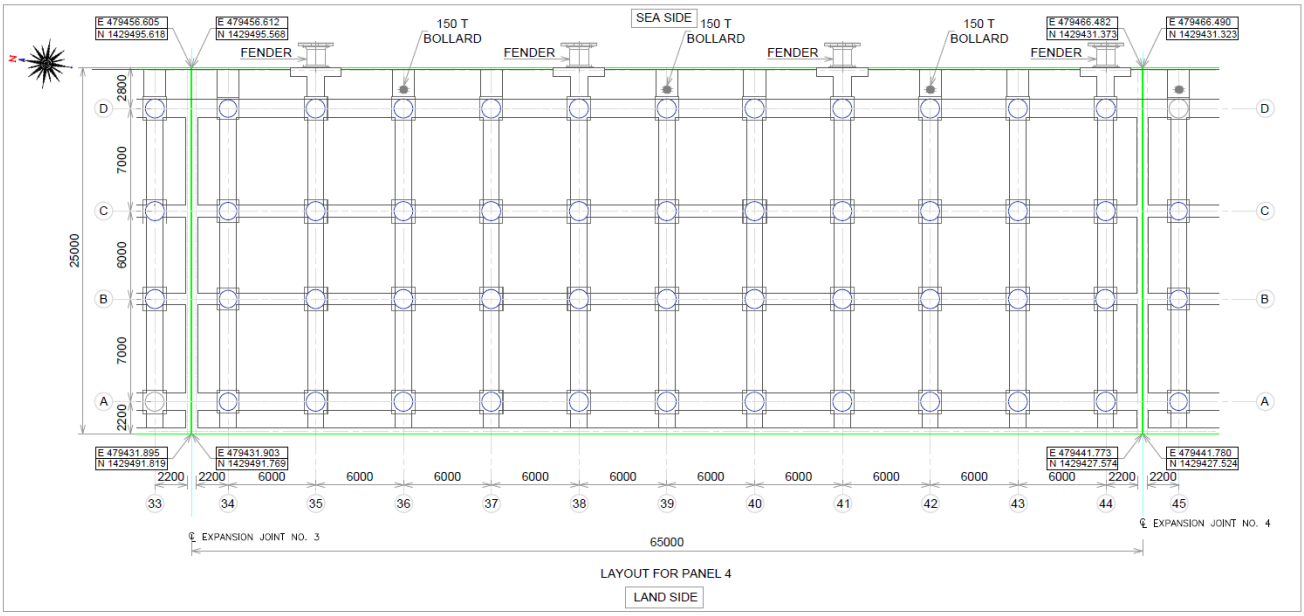

Fig.1 Plan of a panel of the berthing structure

Table 1 Properties of different soil layers

Soil Layer Level (m)		Soil Type	Angle of Internal Friction (degree)	Unit weight of soil (dry/submerged) kN/m^3	Cohesion kN/m^2	Height of layer (m)
Top	Bottom					
4.662	3.162	Silty sand	34	18	50	1.5
3.162	0.162	loose Sand	38	18	0	3
0.162	-2.838	Silty sand	26	9.2	20	3
-2.838	-4.838	Sandy Silty Clay	26	9.37	14.28	2
-4.838	-5.838	loose Sand	26	9.37	0	1
-5.838	-10.338	Dense Sand	26	9.37	0	4.5
-10.338	-27	Decomposed Granite	40	18	0	16.662

Table 2 Maximum values of Displacement, Bending Moment and Shear Force in diaphragm wall and pile

STRUCTURAL ELEMENT	STATIC ANALYSIS			SEISMIC ANALYSIS			
	Displacement (mm)	Shear Force (kN)	Bending Moment (kNm)	Seismic Zone	Displacement (mm)	Shear Force (kN)	Bending Moment (kNm)
Diaphragm Wall	6.52	292.18	700.58	II	6.66	295.96	717.85
				III	6.75	298.3	728.21
Pile	18.44	189.91	1631.9	II	17.33	167.1	1283.54
				III	27.5	265.5	2043.28

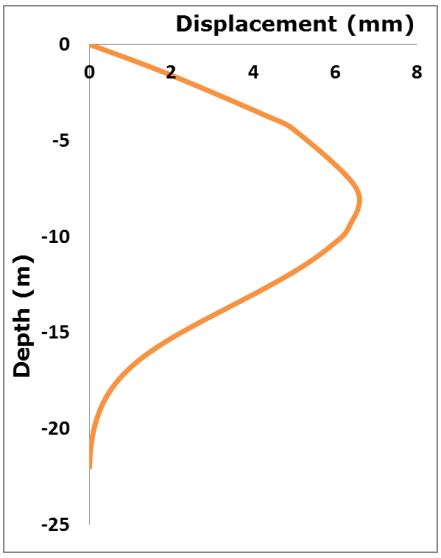

Fig.2 Variation of displacement of diaphragm wall for static analysis

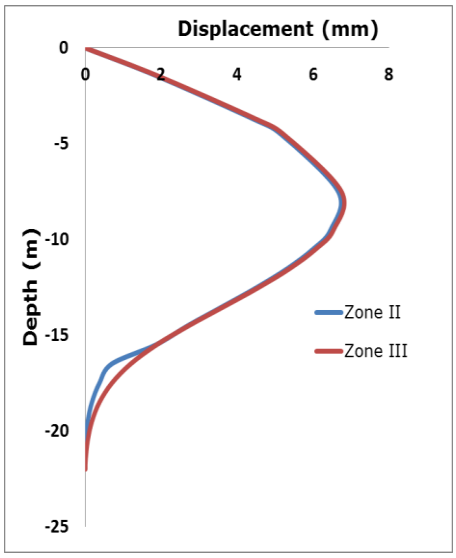

Fig.3 Variation of displacement of diaphragm wall for seismic analysis

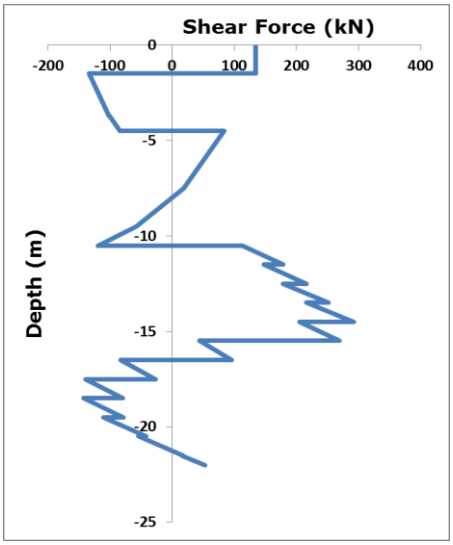

Fig.4 Variation of shear force in diaphragm wall for static analysis

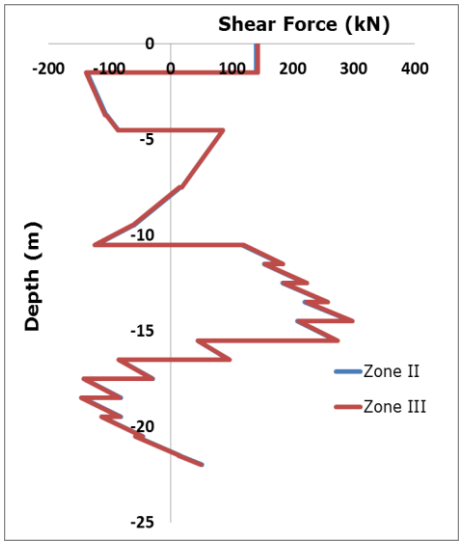

Fig.5 Variation of shear force in diaphragm wall for seismic analysis

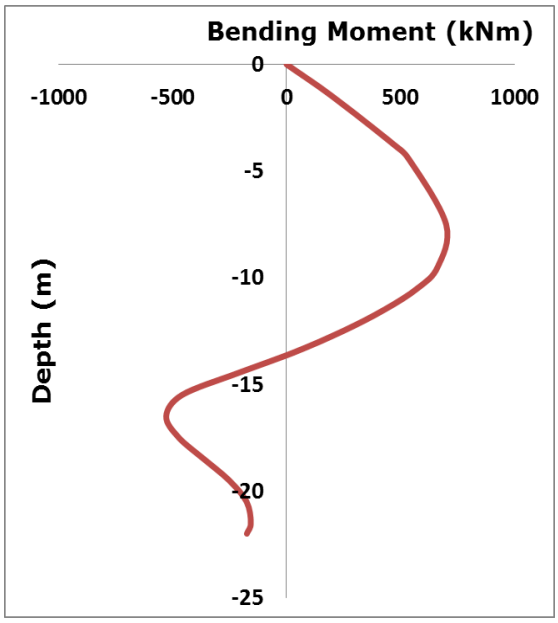

Fig.6 Variation of bending moment in diaphragm wall for static analysis

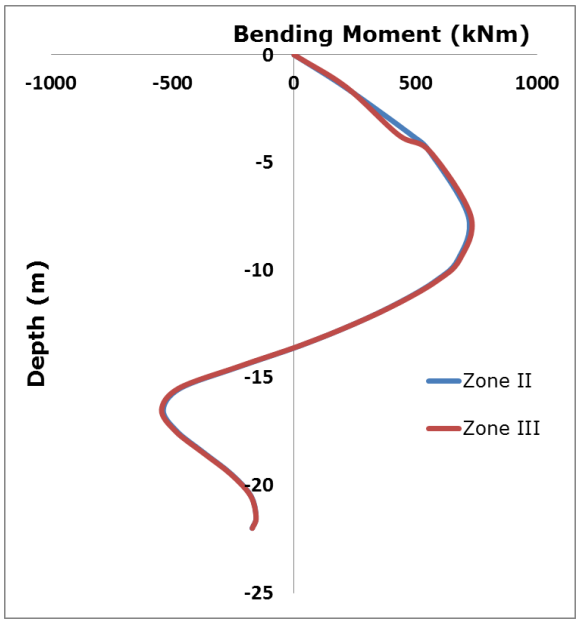

Fig.7 Variation of bending moment in diaphragm wall for seismic analysis

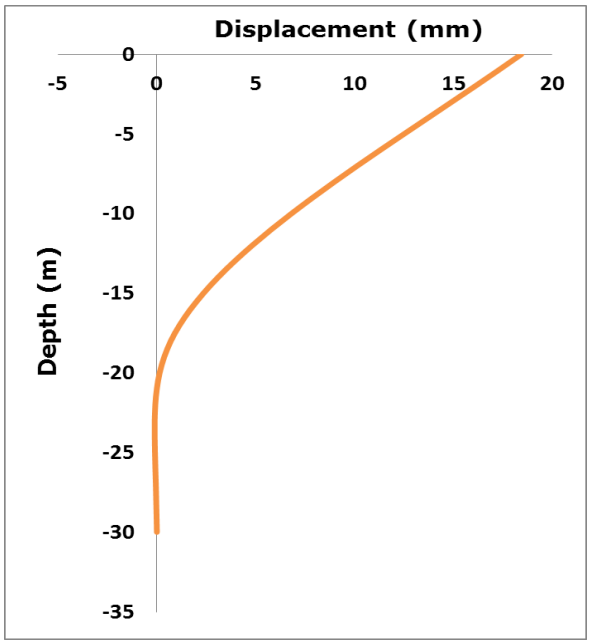

Fig.8 Variation of displacement of pile for static analysis

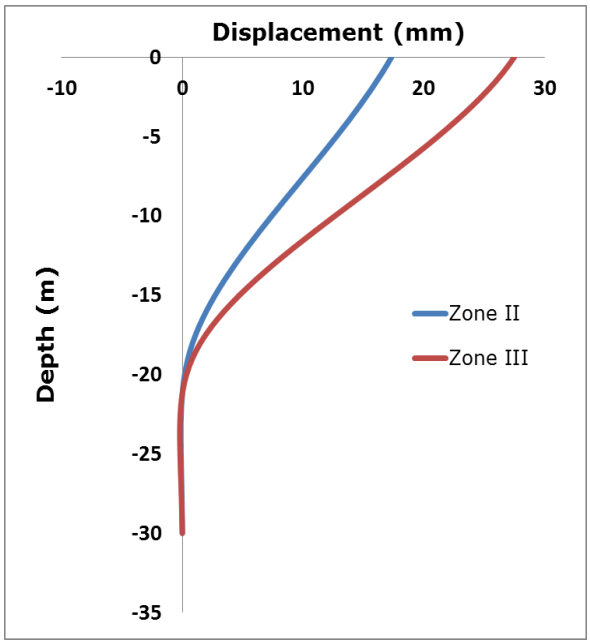

Fig.9 Variation of displacement of pile for seismic analysis

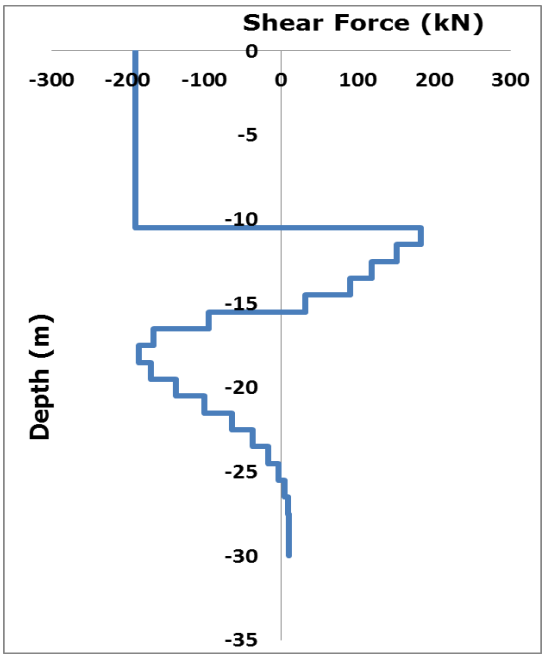

Fig.10 Variation of shear force in pile for static analysis

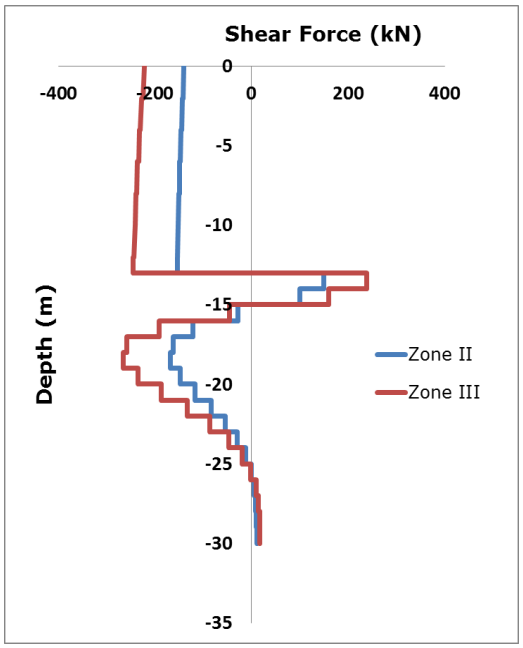

Fig.11 Variation of shear force in pile for seismic analysis

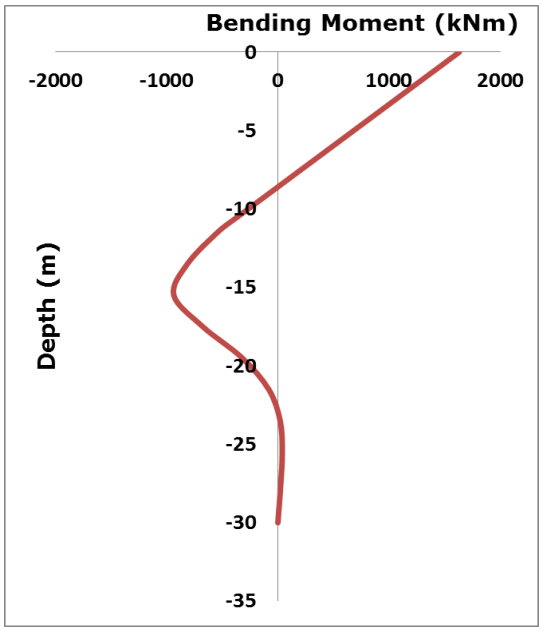

Fig.12 Variation of bending moment in pile for static analysis

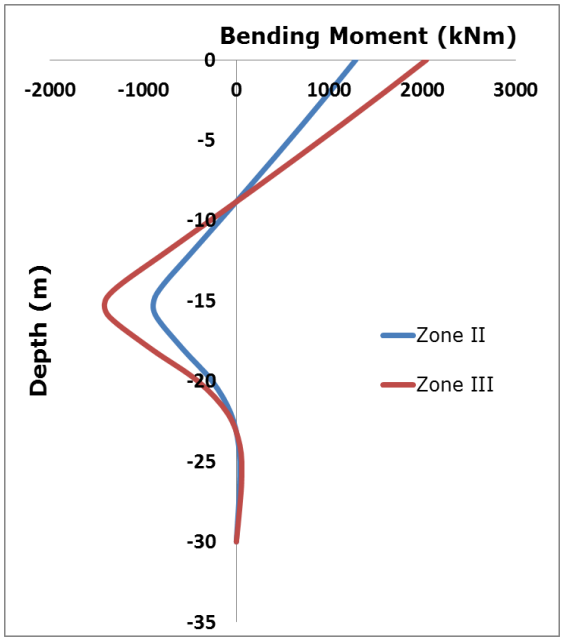

Fig.13 Variation of bending moment in pile for seismic analysis

8th International Engineering Symposium - IES 2019
March 13-15, 2019, Kumamoto University, Japan

Performance Analysis of Coastal vegetation on Wave Transmission using Soft Computing Techniques

Anusha Jain [1] and Subba Rao [2]

1 *Department of Applied Mechanics and Hydraulics, National Institute of Technology Karnataka, Surathkal, Mangalore -575025, India. Email: anushajainp@gmail.com.*
2 *Department of Applied Mechanics and Hydraulics, National Institute of Technology Karnataka, Surathkal, Mangalore -575025, India. Email: surakrec@gmail.com*

ABSTRACT: Coastal vegetation aids in shoreline protection by damping the incoming waves and dissipating the energy. In the present study, the soft computing techniques such as ANN (Artificial Neural Network) and ANFIS (Adaptive Neuro Fuzzy Inference system) are developed using experimental data to predict the wave transmission characteristics of coastal vegetation. The model is trained and tested on the data set obtained from the experiments which were carried out at Marine Structures Laboratory, NITK Surathkal, India. The performance of two models are evaluated using statistical measures namely RMSE (Root Mean Square-Error), CC (Correlation Co-efficient), SI (Scatter-Index) and NSE (Nash-Sutcliff Efficiency). It is found that ANN and ANFIS are very successful in predicting transmission coefficient (K_t) for the vegetation models.

Keywords*: Artificial Neural Network, Adaptive Neuro Fuzzy Inference system, Coastal vegetation, Statistical parameters, Wave transmission.*

1. INTRODUCTION

The environmental stress on the coastal zone is rapidly growing and there is a need to protect the coastal environment. Wave attenuation by vegetation is a function of vegetation characteristics, wave conditions and the water depth. The vegetation characteristics include stem density, leaf structure, geometry, stiffness and the wave conditions include wave period, wave height, water depth and direction. Vegetation penetrates through the layers of varying particle orbital velocities and causes a distortion in the wave orbital velocities, resulting in an increase in turbulence and loss of energy and consequently wave breaking. Hard methods of coastal protection including massive constructions was prevalent during the 19th and 20th centuries, but alternative approaches harnessed from nature or natural resources have gained acceptance in the recent past. Non-structural shore protection measure is cost efficient, aesthetically pleasing, environmentally friendly, and sustainable and are therefore gaining acceptance as opposed to the commonly used "hard" or structural methods. (Beena et.al.,2016)

In order to reduce the cost and time in conducting the experimental work, soft computing techniques such as Artificial neural networks (ANNs), Fuzzy systems (FS), Genetic algorithm (GA), support vector machine (SVM) and hybrid of these models are being applied to solve a wide variety of coastal engineering problems. In practical soft computing techniques are widely used in different fields and accepted as an alternative way to tackle complex problems. Soft computing techniques have an ability to learn from examples and have the capacity to handle noisy and incomplete data. Once the model learns from examples then predictions of the outcome can be done at higher speed.

2.ARTIFICIAL INTELLIGENCE

In recent years, application of artificial intelligence (AI) techniques in modeling coastal processes like structure stability, damage level and wave transmission has received much attention from the researchers. AI algorithms provide explanation of an externally driven process without the need of complex physical models under similar site conditions.

2.1. ARTIFICIAL NEURAL NETWORK (ANN)

ANN in coastal/ocean engineering is commonly used by the researchers to predict ocean wave parameters such as wave height, wave period, impact wave force etc. (Deo and Jagdale, 2003). Apart from this, it has provided promising results in prediction of tidal levels, damages to coastal structures (Mandal et al., 2012), depth of eroded caves in a seawall, seabed liquefaction, storm surges etc. The most significant features of neural networks are the extreme flexibility due to learning ability and the capability of non-linear function approximations. Generally, ANN models do not have any prior knowledge about the problem. The data enters the network through the input layer. The nodes in the input layer are not computational nodes and simply broadcast the data over weighted connections to the hidden nodes (Patil et al., 2012). The ANN are trained with a set of known input and output pairs called the training set.

The typical back- propagation network has an input layer, an output layer, and at least one hidden layer. There is no theoretical limit on the number of hidden layers but typically, there is just one or two hidden layers. Each layer is fully connected to the succeeding layer, as shown in Fig 1. In the present work, the three layers feed forward backpropagation neural network is used to represent the input nodes as first layer, hidden nodes as second layer and output nodes as the third layer. The back-propagation is a supervised learning technique used for training the neural network. The back propagation needs to know the correct output for any input parameters. The number of input nodes depends upon the complexity of the problem and the parameters, which influence the output parameters.

The main objective of back propagation neural network technique is to train the model such that the resultant outputs are nearer to the desired values. Therefore, the error between network output and desired value is minimized. Mathematically, the feed forward artificial neural network is expressed as:

$$Z_k(x) = \sum_{j=1}^{m} W_{kj} \times T_r(y) + b_{ko} \quad (1)$$

$$y = \sum_{i=1}^{n} W_{ji} \times x_i + b_{ji} \quad (2)$$

Where, x is input value from 1to n, W_{ji} - are the weights between input layer and hidden layer nodes and W_{kj} are the weights between hidden layer and output layer nodes. b_{ji} and b_{ko} are bias values of hidden and output layer respectively. m is the number of hidden layer nodes and $T_r(y)$ is transfer function. This transfer function allows a non-linear conversion of summed inputs.

A non-linear transfer function is applied between input nodes and hidden nodes. In the present research work, *Tansig* is used as the transfer function, which is expressed as:

$$T_r(y) = \left[\frac{2}{1+\exp(-2\times y)} - 1\right] \quad (3)$$

Where, y is the summation of input values with weights and biases. The transfer function improves the network generalization capabilities and speeds up the convergence of the learning process. The bias values for both hidden layer (b_{ji}) and output layer (b_{ko}) get adjusted at each time of iterations. The weights between hidden and output layers are calculated using updated Levenberg-Marquardt algorithm. In the present research work, the linear transfer function *purelin* is applied between hidden layer and output layer, and it is expressed as:

$$purelin\,(n) = n \quad (4)$$

The overall objective of training algorithm is to reduce the global error, E, defined as:

$$E = \frac{1}{p}\sum_{p=1}^{p}\left[\sum_{k=1}^{k}\left(d_{kp} - o_{kp}\right)^2\right] \quad (5)$$

Where, p is the total number of training patterns, d_{kp} is the desired value of the k^{th} output and the p^{th} pattern, o_{kp} is the actual value of the k output and p pattern. (Geetha et al.,2017)

2.2. ADAPTIVE NEURO-FUZZY INFERENCE SYSTEM (ANFIS)

ANFIS was first introduced by Jang (1993). ANFIS is a simple structure with effective learning algorithm and high speed (Vairappan et al., 2009). ANFIS training can use alternative algorithms to reduce the error of the training. The advantage of a hybrid approach is that it converges much faster, since it reduces the search space dimensions of the back propagation method used in neural networks. Using the experimental data, ANFIS models are developed using different membership functions. The results obtained will be compared with experimental data for validation.

A general and simple architecture of ANFIS as shown in Fig 2. with nine input variables namely Incident wave steepness (H_i/gT^2), Meadow width parameter (w/L), Relative plant height (h_s/d), gap width parameter (w_{gap}/w), Sea grass density (N_1), Rigid vegetation density (N_2), Trunk density (N_3), Root type I density (N_4), Root type II density (N_5) and the output parameters wave transmission Co efficient K_t is considered.

A conventional ANFIS model consists of five layers and each layer is explained below in brief by Jang et al. (1997).

Layer 1

Every node in this layer is an adaptive node with a node function

$$O_{1,i} = \mu A_i(x), \quad \text{for } i=1,2 \quad (6)$$

$$O_{1,i} = \mu B_{i-2}(x), \quad \text{for } i=3,4 \quad (7)$$

x (or *y*) is the input node and A_i (or B_{i-2}) is a linguistic variable associated with the membership function of a fuzzy setA_1, A_2, B_1, B_2. Typical membership function:

$$\mu A(x) = \frac{1}{1+\left[\frac{c_i}{a_i}\right]^{2b_i}} \quad (8)$$

Where a_i, b_i and c_i is the parameter set. The parameters are called as premise parameters.

Layer 2

Each node in this layer is a fixed node, indicated by π Norm. The output is the product of all the incoming signals.

$$O_{2,i} = w_i = \mu A_i(x).\mu B_i(y), \quad i=1,2 \quad (9)$$

Output signal w_i represents the fire strength of a rule.

Layer 3

Each node in this layer is a fixed node N Norm. The ith node calculates the ratio of the firing strength to the sum of the firing strength.

$$O_{3,i} = \overline{w}_i = \frac{w_i}{w_1+w_2}, \quad i=1,2 \quad (10)$$

Output signal $\overline{w}_i$ is called normalized firing strengths.

Layer 4

Each node in this layer is an adaptive node, indicated by square node with a node function:

$$O_{4,i} = w_i f_i = w_i(p_i x + q_i y + r_i) \quad (11)$$

Where, w_i is the normalized firing strength from layer 3. $\{p_i,q_i,r_i\}$ is the parameter set which is called as consequent parameters.

Layer 5

Each node in this layer is a fixed node, indicated by circle which computes the overall output as the summation of all incoming signals:

$$\text{Overall output, } S = O_{5,1} = \sum_i \overline{w}_i f_i = \frac{\sum_i w_i f_i}{w_i} \quad (12)$$

The different membership functions assigned for input parameters are: Gauss membership function:

$$f(x,\sigma,c) = e^{\frac{-(x-c)^2}{2\sigma^2}} \quad (13)$$

where, x is input parameters, c and σ are mean and variance respectively.

Generalized bell-shaped membership function is given by:

$$f(x,a,b,c)=\frac{1}{1+\left|\frac{x-c}{a}\right|^{2b}} \quad (14)$$

where, x is an input parameter, c locates the centre of the curve.

In this study, a hybrid approach combining least square error and backpropagation methodology is adopted to develop all the ANFIS models. The performance of membership functions (MF) with Gaussian, and generalized bell-shapes are evaluated to determine the most efficient model.

3. DATA COLLECTION

For the present study data from the experiment conducted by Beena (2018) is used. This is the Ph.D. work of Beena titled "Physical model studies on the effect of coastal vegetation on wave attenuation and beach inundation"

4. METHODOLOGY

In the present study, nine input parameters, namely Incident wave steepness (H_i/gT^2), Meadow width parameter (w/L), Relative plant height (h_s/d), gap width parameter (w_{gap}/w), Sea grass density (N_1), Rigid vegetation density (N_2), Trunk density (N_3), Root type I density (N_4), Root type II density (N_5) and the output parameters wave transmission Co efficient K_t is considered. The data is divided into two sets for training (70%) and testing (30%) and the consistency of data is checked by plotting time series data plots. The performance of two models are checked by following statistical measures:

$$RMSE=\sqrt[2]{\frac{1}{N}\sum_{i=0}^{N}(P_{pi}-O_{pi})^2} \quad (15)$$

$$NSE=1-\frac{\sum_{i=1}^{N}(P_{pi}-O_{pi})^2}{\sum_{i=1}^{N}(O_{pi}-\overline{O_{pi}})^2} \quad (16)$$

$$CC=\frac{\sum_{i=1}^{N}(P_{pi}-\overline{P_{pi}})(O_{pi}-\overline{O_{pi}})}{\sqrt{\sum_{i=1}^{N}(P_{pi}-\overline{P_{pi}})^2}\sqrt{\sum_{i=1}^{N}(O_{pi}-\overline{O_{pi}})^2}} \quad (17)$$

$$SI=\frac{\sqrt[2]{\frac{1}{N}\sum_{i=1}^{N}(P_{pi}-O_{pi})^2}}{\overline{O_{pi}}} \quad (18)$$

Where, O_{pi} = observed/actual values, P_{pi} = computed values, N = total number of data points and ($\overline{O_{pi}}$) is the mean of actual data.

5. RESULTS AND DISCUSSION

ANN and ANFIS models are generated for the prediction of wave transmission over coastal vegetation and the performance of these models are evaluated using statistical parameters namely RMSE, NSE, CC, SI.

5.1 Performance evaluation of ANN

The training and testing are carried out using LMA algorithm, 'tansig' as activation function for hidden layer and 'purelin' for the output layer. The hidden layer is kept as one, but the number of neurons is varied from 1 to 8 and the best model is chosen. The network is prepared well using the training data set containing 392 data samples (70%) and then using the weights and biases obtained, the network is then used for predicting the desired output with the testing data set of 168 data samples (30%). It is observed that the performance of ANN model is good from hidden neurons 1 to 8. The training efficiency of 9-3-1 model is giving a very good result with CC for training as 0.99987 and for testing as 0.9959.(Table 1) Also the RMSE value and SI value are close to zero for testing and training and NSE, CC value are close to one. The time taken for simulation of 9-3-1 model is comparatively less when compared to other models with hidden neurons greater than three. Hence 9-3-1 model can be considered to predict transmission coefficient (K_t) for coastal vegetation.

5.2 Performance evaluation of ANFIS

The ANFIS model with eight input parameters and one output parameter is built with different membership functions, fuzzy rules and epoch numbers. In the present study, with 9 input parameters

and 1 output, using Sugeno first order with (2^9) 512 fuzzy rules and 'Gbell (gbellmf)' and 'Gaussian (Gaussmf)' membership functions and 100 epochs the model is trained. Among the membership functions, the ANFIS model with Gaussian membership function performs better than the other membership functions. It is believed that Gaussian membership function has the capacity to handle higher degree of error tolerance compared to other membership functions. The statistical measures obtained for ANFIS model with Gaussian membership function are RMSE= 0.0056, CC= 0.9991. (Table 2)

6.SUMMARY AND CONCLUSION

The soft computing models are built based on the data collected from the experimental study conducted on coastal vegetation by Beena (2018). Non-dimensional input parameters that influence the transmission coefficient (K_t) namely, Incident wave steepness (H_i/gT^2), Meadow width parameter (w/L), Relative plant height (h_s/d), gap width parameter (w_{gap}/w), Sea grass density (N_1), Rigid vegetation density (N_2), Trunk density (N_3), Root type I density (N_4), Root type II density (N_5) are used for developing soft computing techniques. ANN and ANFIS models are assessed and evaluated using model performance indicators in terms of statistical measures such as RMSE, CC, SI and NSE to find the best network.
Based on the present study, the following conclusions are drawn:

- ANN and ANFIS is very successful in predicting transmission coefficient (K_t) for the vegetation models.
- The training efficiency of 9-3-1 model is giving a very good result with CC for training as 0.99987 and for testing as 0.9959. Also, the RMSE value and SI value are close to zero for testing and training and NSE, CC value are close to 1.
- The time taken for simulation of 9-3-1 model is less when compared to other models with hidden neurons greater than three. Hence 9-3-1 model is considered the best model to predict transmission coefficient (K_t).
- It is observed that ANFIS model with Gaussian membership function shows good correlation between the observed and predicted wave transmission for vegetation models.
- Although ANN model shows more precision, the ANFIS training duration is very transient which is advantageous when compared to ANN.

REFERENCES

[1] Beena, M J et al (2016), "Effect of artificial seagrass on wave attenuation nd wave run-up".The International Journal Of Ocean and Climate Systems, Vol. 7, No. 1, pp14-19.
[2] Beena, M J (2018), "Physical model studies on the effect of coastal vegetation on wave attenuation and run-up", Thesis of Doctor of Philosophy.
[3] Deo, M C and Jagdale, S S, (2003), "Prediction of breaking waves with neural networks" J.Ocean Engineering, Vol. 30, pp. 1163-1178.
[4] Geetha, S K et al (2017), "Performance evaluation of ANFIS and SVM in prediction of wave transmission over submerged reef of tandem breakwater" International Journal of Ecology and Development (IJED), Vol. 32, No.2, pp. 141 – 155.
[5] Jang, J S, (1993), ANFIS: adaptive -network-based fuzzy inference system. IEEE transactions on systems, man and cybernetics, Vol. 23, No.3, pp 665-685.
[6] Mandal S et al (2012), "Damage level prediction of non-reshaped berm breakwater using ANN, SVM and ANFIS models". International Journal of Naval Architecture and Ocean Engg, Vol. 4, pp. 112-122.
[7] Patil, S G et al (2012)," Genetic algorithm based support vector machine regression in predicting wave transmission of horizontally interlaced multi-layer moored floating pipe breakwater". J. Advances in Engineering Software, Vol. 45, pp. 203–212.
[8] Vairappan, C et al (2009), "Batch type local search based ANFIS with self- feedbacks for time series prediction", Neuro computing, Vol.72, No.1, pp. 1870-1877.

Table 1 Statistical parameter for ANN models for predicting K_t

Network	RMSE		CC		SI		NSE	
	Train	Test	Train	Test	Train	Test	Train	Test
9-1-1	0.01202	0.01140	0.9932	0.99404	0.02875	0.02620	0.986463	0.98714
9-2-1	0.00736	0.00770	0.9976	0.99779	0.01761	0.00453	0.994920	0.99413
9-3-1	**0.00680**	**0.00825**	**0.9998**	**0.99590**	**0.01624**	**0.01925**	**0.99974**	**0.99965**
9-4-1	0.00682	0.00804	0.9979	0.98377	0.01631	0.01847	0.995644	0.99378
9-5-1	0.00691	0.00786	0.9979	0.99618	0.16538	0.01807	0.995523	0.99405
9-6-1	0.00680	0.00785	0.9979	0.99796	0.01628	0.01804	0.995658	0.99390
9-7-1	0.00670	0.00716	0.9980	0.99827	0.01602	0.01645	0.995796	0.99493
9-8-1	0.00862	0.00742	0.9974	0.99831	0.02062	0.01707	0.993036	0.99454
9-9-1	0.00743	0.00786	0.9976	0.99772	0.01777	0.01808	0.994829	0.99388

Table 2 Statistical parameter for ANFIS models for predicting K_t

Statistical measures	Membership functions	
	Gauss	G-bell
RMSE	0.0056	0.00589
NSE	0.99689	0.9864
CC	0.9991	0.9989
SI	0.0131	0.0156

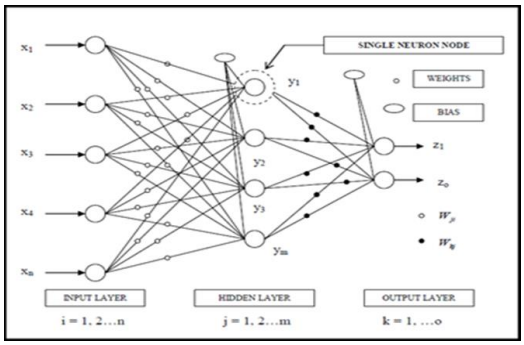

Fig.1 Architecture of feed forward backpropagation network

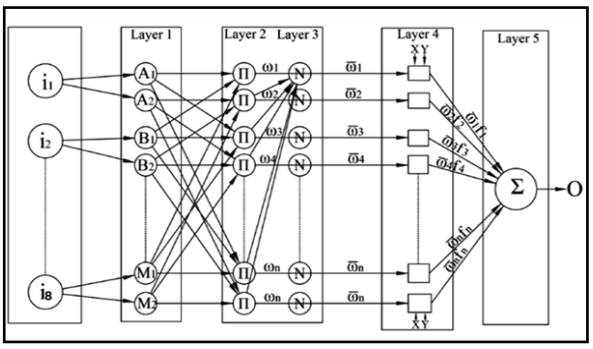

Fig.2 ANFIS structure used in the study

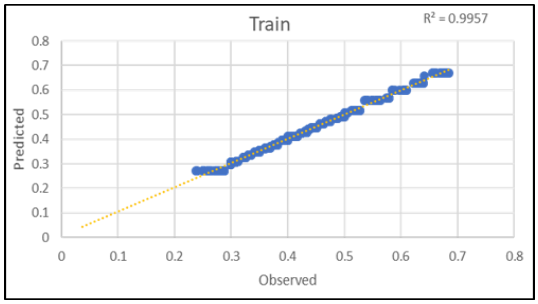

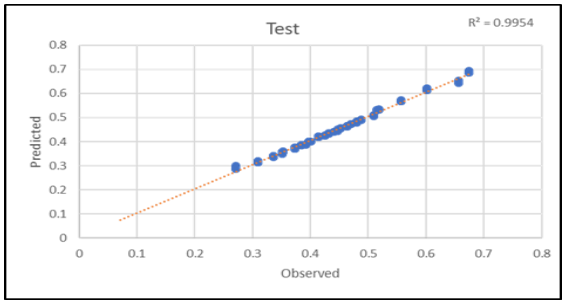

Fig.3 Scatter plot of observed k_t versus predicted K_t for training and testing of ANN 9-3-1 model

8th International Engineering Symposium - IES 2019
March 13-15, 2019, Kumamoto University, Japan

Growing Popularity of Cement Concrete Roads (Rigid Pavements) Challenges for Concrete Technologists to give Sustainable, Greener Material.

NAGESH PUTTASWAMY A[1], ARPITHA D B[2], RAJASEKARAN C C[3]

1 *Regional Head Technical Services, UltraTech Cement Ltd, Bangalore, India. nagesh@nageshp.com*
2 *Department of Civil Engineering, National Institute of Technology Karnataka, Surathkal, Mangalore-575025, India. arpitha.5790@gmail.com*
3 *Department of Civil Engineering, National Institute of Technology Karnataka, Surathkal, Mangalore-575025, India. bcrajasekaran@nitk.edu.in*

ABSTRACT: The thought process of the developing country in looking at the life cycle cost of infrastructure costs rather than today construction has made the construction of Cement Concrete roads popular in many developing countries like India. There are variety of roads depending on the connectivity they create, Traffic intensity, importance, locations from a very remote motor able road to urban centric National highways. The Cement Concrete properties requirement of each of these conditions are requirement is different, like the time v/s strength requirement, to some extent the strength of concrete required itself will vary. The rapid depletion of fossil fuel which is the main source of bitumen for road construction has created scarcity and rapid changes in costing too. Thus the use of cement in road construction has been pushed ahead. Cement being an energy intensive product the Carbon Foot Print is also an issue that the environmentalists raise. There has been a metamorphosis in concrete technology to make concrete greener use of secondary cementitious materials which are industrial by-products is very popular. One of the main criterion in the Cement Concrete for pavement which is popularly known as PQC (Pavement Quality Concrete) is the demand for a minimum flexural strength on the day traffic is allowed on the road. In India the standards specify a minimum of 4.50 MPa flexural strength on the day traffic is allowed, the flexural strength of concrete for design of Mix Proportion is arrived at using an empirical formula available in the *Indian Standard Codes* $Fcr = 0.7 \sqrt{Fck}$ *where Fcr is the flexural strength and Fck is the compressive strength.* This paper is on the experimental study of Mix Proportion Arrived at

1. Using typically available blended cement Fly-ash based to get concrete that is comparable with standard concrete made with Ordinary Portland Cement (OPC) ensuring the required flexural strength but also relatively shorter time.
2. Use secondary material like the GGBS (Ground Granulated Blast Furnace Slag) as a replacement of OPC and still get required properties.

By changing certain ingredients to obtain optimal mix(s) that could be efficient, sustainable and also economical. The Exercise was done in the RMC plants that regularly supply concrete to various road construction work. It is an industry approach to provide the most suitable and economical Mix to various Pavement applications.

Keywords*: Blended cement, flexural strength, GGBFS, Pavement, Sustainable Roads.*

INTRODUCTION

Roads are the life line of any country. The network of roads would define how progressive a country is in terms of economics and this is a vital requirement of developing countries as that would be the primary requirement of the internal business as well as the investment from developed countries for the development of their own.

Basically the there are two type of roads that are generally used

1. Flexible pavement
2. Rigid pavement

Flexible Pavement – binding material is the Bitumen.
Rigid Pavement – binding material is the Portland Cement.

In earlier days the option was the flexible pavement because of the costing and the availability of cement. Cement was preferred to be used in the other developmental works like the dams, bridges and building.

These days the availability of cement has improved and there is a reduction of availability Bitumen which is a petroleum product and its cost also has increased exponentially

The experience has proven that the maintenance cost of Cement Concrete Roads is far less than the bitumen roads which needs periodic maintenance.

Thus the life cycle cost of concrete roads is far less than the Bitumen roads. Life of concrete roads being 30 – 40 years where as the maximum maintenance free life 3-5 years.

Thus there is the concept of cement concrete overlay over bituminous road which is popularly called as white topping which is emerging as viable alternative for upgrading the urban roads.

MATERIALS

Cements: Ordinary Portland cement **(OPC),** and Portland Slag Cement **(PSC)** supplied by UltraTech cement Ltd., were used.
Superplasticizers (SP): Poly Carboxylate Ether (PCE) based Master Glenium sky 8233 were supplied by BASF.
Slags: Iron Slag (SS) of specific gravity 2.6,.
Silica Fume

Governing Codes.

Work carried out as per the Indian codes. Bureau of Indians Standard and Indian Road Congress

1. IS:10262-2009-------Concrete Mix Proportioning Guidelines
2. IRC:15-2002---------Standard Specifications and Code of Practice for the Construction of Concrete Road
3. IS:456-2000----------Plain and Reinforced Concrete – Code of Practice
4. IRC:44-2017---------Tentative Guidelines for Cement Concrete Mix Deign for Pavements
5. IRC 56 2018 guidelines for the design of plain jointed rigid pavements for Highways.
6. IRC – SP 76 2015 Tentative Guidelines For Coventional, Thin And Ultra-thin Whitetopping

IRC*- Indian Road Congress code of practice*
IS *– Indian standard code of practice*

CHALLENGES FACED:

1. Cost of Cement Concrete of Pavement Quality.
2. Time required for conventional concrete construction including the curing period
3. The acceptance criterion is the flexural strength of 4.5Mpa on the day traffic is allowed – as per the codes.
4. Acceptance of Blended Cement or the concrete with secondary blending material like the GGBS in the **Pavement Quality Concrete (PQC).**
5. Challenge of allowing traffic on the concrete roads
6. No direct method available to approach Mix proportioning for flexural strength. All proportioning for the flexural strength is based on the empirical relationship between compressive strength and flexural strength. The relation provided in the relevant codes in India is

   $\mathbf{F_{cr} = 0.7 \sqrt{F_{ck}}}$

Where
F_{cr} – flexural strength of concrete
F_{ck} – compressive strength of concrete

CEMENT CONCRETE

Concrete has been in existence in one form other for over 2000 years and the modern cement concrete is in existence around 100 years.

Lot of work has been done as research and practice for improving concrete performance for various applications. The PQC has some important performance criteria required to accommodate the handing of green concrete by the Paving Machines and other equipment used in the process of Road making.

METHODOLOGY

6.1 Arriving at a mix proportion with only Ordinary Portland Cement, Portland Pozzulona Cement, Portland Slag Cement and specific concrete mix with replacement of cement with GGBS, for specific requirement of Pavement Quality Concrete.

6.2 The mix proportions were arrived at using the guide lines provided by the Indian Road Congress IRC 44 and the Indian Standard code of Practice IS 10262.

1. Control mix with OPC for strength flexural strength requirement of 4.5 Mpa on 3rd, 7th day.
2. Concrete mix to be arrived at for the standard blended cement available in the market in India namely the PSC.
3. Arrive at Concrete mix with 50%, 60% and 70% replacement of OPC by GGBS.

Compare the results with that of the control mix.

As per the codal provisions of IRC and BIS the Mix proportion calculations have been made.

Concrete was made for a slump of the range of 50mm as the requirement of paving equipment that is normally used. Higher end pavers would demand much lesser slump.

The typical test conducted on the cube for compressive strength an beam subjected to 2 point load for flexural strength.

A minimum of 30 sets of results for cubes and beams were done in each case.

Results and Discussion

7.1 study performance of concrete made with Blended cements

The first set of exercise that was carried out is the getting the mix proportion for the off shelf cement that is available namely the OPC, PPC & PSC the mix was arrived at for the relative compressive strength of M45 on the 7th day so that we get the flexural strength of 4.5 Mpa on 7th day

Typically the Mix proportions were arrived as

Cement kgs	CA kgs	FA kgs	Water kgs	Admix. kgs
OPC				
410	1162	775	163.4	2.31
PSC				
410	1162	775	163.7	2.38
PPC				
410	1162	775	160.6	2.37

The typical test results on the cube for compressive strength an beams subjected to 2 point load for flexural strength

Cement Type	Time	Avg comp. strength Mpa	Average flexural strength Mpa
OPC	7 Days	48.06	4.69
	28 Days	57.40	5.30
PSC	7 Days	45.87	4.63
	28 Days	58.40	5.35
PPC	7 Days	46.28	4.38
	28 Days	58.09	5.33

It was observed that there is a slight variation in the mix proportion as per the specific gravity of the cement used, a small variation in the water demand for the required workability.

The results so obtained were also similar except for that the blended cements gave a marginally lesser strength on 7 day and a marginally better strength on the 28 day results.

Study performance of concrete made with replacement of cement by GGBS.

50% replacement of cement by GGBS.

Based on the past experience on the rate of gain of strength of concrete and the requirement of 7-day strength M60 concrete was taken up for studies. Higher end admixture was used to ensure the water cement/binder ratio is controlled below 0.40

Cement kgs	CA kgs	FA kgs	Water kgs	Admix. kgs
0nly OPC				
385	1214	731	153	2.10
Cement (50% OPC+50%GGBS)				
422	1184	711	153	2.25

The results for the compressive and flexural strength obtained are as follows.

Cement Type	Time	Avg comp. strength Mpa	Average flexural strength Mpa
OPC	7 Days	61.556	7.763
	14 Days	65.023	8.175
	28 Days	71.836	8.475
50%OPC 50%GGBS	7 Days	39.778	5.813
	14 Days	48.948	6.487
	28 Days	65.866	8.676

The mix proportion did not have much of a difference except the changes due to the specific gravity of GGBS and slight alteration in the water demand.

The strength of the concrete with OPC indicated early compressive strength better than GGBS replaced concrete. The GGBS replaced concrete exhibited better flexural strength for the same range of compressive strength.

It was observed the GGBS replaced concrete fell short of the indicative compressive strength of 45Mpa hence a set of samples were tested for 15 days also. As the objective of the study was to arrive at the earliest time for the traffic to be allowed on the road.

Cost implications
The performance of the concrete with 50% replacement of cement was matching the required criterion of the pavement quality concrete (PQC) the cost implications were also studied.

Note: all values in Indian rupees

MATERIAL	**COST OPC**	**COST GGBS+OPC**
Cement	3234	1772
GGBS	0	760
M sand	548	533
CA	789	770
Admixture	273	292
Water	9	9
Total	4064	3536
Savings approx..		13%

Thus the GGBS replacing Cement would give a considerable savings especially when we know that roads go long distance and concrete required there would be very high.

CONCLUTIONS

1. The rigid pavement made from Portland cement concrete is gaining popularity as most of the developed countries have realized that the lesser, they spend on maintenance of their roads more money they will have to build new roads.

2. The concrete roads are almost maintenance free almost 20 years and they have a service life of 30 to 40 years theoretically.

3. The Concrete Technologists have taken up the challenge of providing a cost effective sustainable material for construction of Concrete roads.

4. With Emphasis given on sustainability and the greener construction the use of GGBS in concrete without compromising any of the required parameters is a welcome approach towards sustainable road.

5. The cost savings in this approach shall be an added advantage to the infrastructural expenditure of any country especially the developing countries.

PHOTOS

Picture 1. Batching of materials

Picture 2. Dosing of admixture

Picture 3 Specimens cast

Picture 3 Specimens testing

Picture 4 curing of specimen

Picture 5 Feel of concrete

Picture 6 stacking of tested specimen

ACKNOWLEDGEMENTS

The authors acknowledge the support of National Institute of Technology Karnataka, India. Also UltraTech Cement ltd and BASF Bangalore, India.

REFERENCES

1. IRC 44 method for Concrete Mix design
2. IS 10262 guide lines for Concrete Mix proportioning
3. IRC 56 guidelines for the design of plain jointed rigid pavements for Highways.
4. IRC – SP 76 Tentative Guidelines For Coventional, Thin And Ultra-thin Whitetopping
5. NCHRP Synthesis 338, " Thin and Ultrathin Whitetopping"
6. NCHRP Synthesis 204, " Portland Cement concrete Resurfacing"
7. American Concrete Pavement Association publications
8. Guide to Concrete overlay solutions (National Concrete Pavement Technology Centre

8th International Engineering Symposium - IES 2019
March 13-15, 2019, Kumamoto University, Japan

BEHAVIOUR OF MORTAR WITH PARTIAL REPLACEMENT OF FINE AGGREGATE BY SLAG IN RESPECT TO GREEN STRENGTH PARAMETERS

Arpitha D[1], Thilak Kumar Y T[2], Sudarshan V J[3], C. Rajasekaran[4], Nagesh Puttaswamy[5]

1 *Department of Civil Engineering, National Institute of Technology Karnataka, Surathkal, Mangalore 575025, India. arpitha.5790@gmail.com*
2 *Department of Civil Engineering, National Institute of Technology Karnataka, Surathkal, Mangalore 575025, India. tilak8741@gmail.com*
3 *Department of Civil Engineering, National Institute of Technology Karnataka, Surathkal, Mangalore 575025, India. joresudarshan@gmail.com*
4 *Department of Civil Engineering, National Institute of Technology Karnataka, Surathkal, Mangalore-575025, India. bcrajasekaran@nitk.edu.in.*
5 *Regional Head, UltraTech Cement Ltd.Bengaluru, India. nagesh@nageshp.com*

ABSTRACT: Due to extreme urbanization and industrialisation there is increase in the construction, for which the sector is facing greater challenges to serve the two pressing needs of human society namely environmental protection and to meet the infrastructure requirements of growing population. The cement and concrete industries are now slowly becoming aware of the environment and sustainable development issues. Currently sand mining has disastrous environmental impact and this extensive mining of river bed is creating an ecological imbalance which has led to impose ban on mining subsequently escalating its cost by several manifolds, thereby increasing cost of construction. On the other hand, industrial wastes are creating environmental problems, the safe disposal of which is a hurdle leading to find an appropriate measure to mitigate this, some of the waste has potential to be used in the construction sector. These metallic slags can be found its advantages affiliation to sea water and marine constructions. To make sea erosion breakers, jetty piers, retaining walls and other structures exposed to sea water more durable around the shore, concrete is used in some places as a slow sacrificial material. An approach has been made to evaluate the effects of utilization of iron slag as an alternative for fine aggregates in mortars. Also, focussed to understand the compatibility issues and interaction between different combinations of mortar by partially incorporating fine aggregates with slag. The fluidising effect of the admixture on mortar in the presence of mineral additions is studied based on the flow behaviour and compressive strength of mortar. Rheological properties of mortar helps to identify the desirable combinations and thus to carry out further investigations to understand the hardened properties of mortar.

***Keywords**: Iron slag, mortars, compatibility, rheology.*

INTRODUCTION

Today management of industrial wastes is one of the serious issues. The deep rooted complication constitute serious challenges from unified copper and steel industry present in India. The expeditious growth of industries in some of the developed countries have confront to strive in supplying of fine aggregates. The notable importance is to use more and more industrial wastes as ecofriendly materials in construction field. The major criteria is to achieve sustainable construction there by reducing the negative impacts on environment. Identifying the issues, listing out the possible solutions for disposal problems of industrial wastes will reduce

the cost of construction. The by-product from copper industry and steel industry has taken a new step in producing huge quantity of concrete with best quality which is an effective measure to control dumping and landfilling by using these industrial wastes to greater extent as a partial replacement of fine aggregate. High strength and durability characteristics these slags makes its more suitable as a construction material. (Shekarchi et al) observed that the utilization of steel slag as aggregate is advantageous when compared with normal aggregate concrete mixes. The characteristics of river sand and steel slag are similar (Sultan A et al). Steel slag is most suitable for concrete because of its high hardness and strength parameter (Beshr H et al). Deterioration can be controlled due to the presence of refined pore structure, thus provides resistance to concrete (Bouikni A et al). Steel slag has better adhesiveness to cement matrix due to the presence of rough surface texture (R Padmapriya et al). (Chitra et al) Increment in copper slag content as fine aggregate replacement in concrete results in lower rate of water absorption with low chloride permeability values. (Deboucha et al 2015) investigated that the use of blast furnace slag in concrete mix improved the strength and durability properties. (Sheen et al.) Observed that the substitution of stainless steel oxidizing slag is economical in comparison with the engineering properties of control mix from the research work. (Devi et al) Strength property increased with reduced chloride permeability ions by partially replacing fine aggregates with steel slag. (Humam et al) incorporating iron slag as a replacement with river sand at higher level raises the compressive strength of the mortar and improve permeability. It is believed that the blasted copper slag is a technically viable material for application as fine aggregate for concrete mixtures (M.A.G. dos Anjos).

In this work, an attempt is carried out to understand the influence of different dosages of lignosulfonate (L.S), Sulphonated Naphthalene Formaldehyde (SNF) and Poly Carboxylate Ether (PCE) based super plasticizers on the flow behaviour of cement paste and fluidity of mortars made with Ordinary Portland cement (OPC) and Portland Pozzolona Cement (PPC) along with partial replacements of 0% and 50% fine aggregate (FA) by copper slag and steel slag. Concrete mixes were evaluated for workability and compressive strength of mortars. Feasible mechanism of reciprocal action is discussedreference.

Materials

2.1 Cements: Ordinary Portland cement (OPC) and Portland Pozzolona Cement (PPC) of 53 Grade supplied by Ultratech were used.

2.2. Superplasticizers (SP): Ligno Based (LB) Pozzolith 102, Naphtha Based (NB) Rheobuild 1125 and Poly Carboxylate Ether (PCE) based Master Glenium sky 8233 were supplied by BASF.

2.3. Slags: Iron Slag (SS) of specific gravity 2.6, supplied from JSW, Bellary.

Laboratory testing program

Flow table test

The mortars were made for 1:3 cement sand ratio and was mixed in Horbart mixer. Iron slag was incorporated as a partial replacement for fine aggregate at 0% and 50% replacement levels to understand the flow behavior of slags in mortars. Superplasticizers of different dosages at different water cement ratio for different types of cements along with partial replacement of river sand by Iron slag were mixed to measure the fluidity on cement sand mortars.

Cement Mortars

To study the effect of alternative materials to fine aggregate iron slag was substituted at 0% and 50% replacement levels. The mortar specimens (7.05cm* 7.05cm* 7.05cm) were cast for each mix to determine the compressive strength and water-binder ratio was fixed based on the flow test results. Fifteen cubes of three samples for each mix were tested after 3,7,28 days of curing.

Results and Discussion

1)Behaviour of mortar flow for control mix for OPC and PPC without chemical admixture to determine optimum w/c.

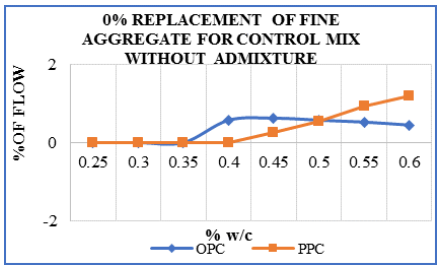

Fig 1: 0% replacement of F.A

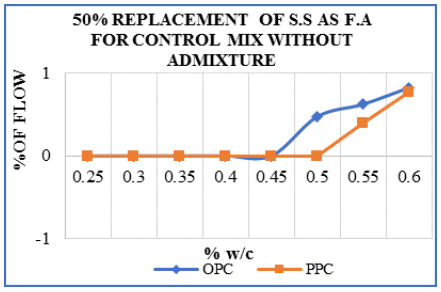

Fig 2: 50% replacement of I.Sfor F.A

The optimum w/c for OPC and PPC control mixes without admixtures is 0.4 and 0.45% respectively as observed from Fig 2. From Fig 3, the w/c for OPC and PPC mixes for 50% replacement of fine aggregate without admixture obtained is 0.45 and 0.50% respectively.

2) Behaviour of mortar flow with partial replacement of iron slag for Fine aggregate

a)Partial replacement of F.A by I.Sconsidering 0.45% w/c for OPC and PPC mixes for various dosage of SP respectively.

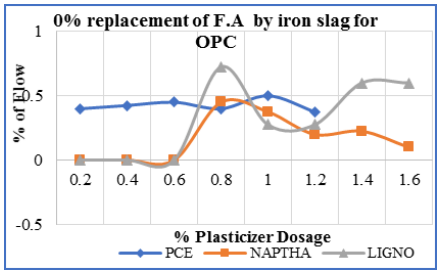

Fig3: 0% replacement of F.A for OPC

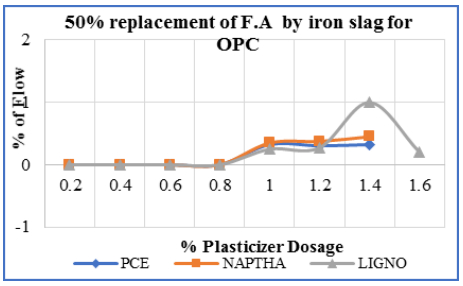

Fig 4:50% replacement of F.A by I.Sfor OPC

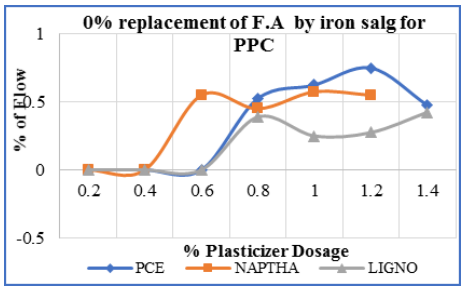

Fig 5: 0% replacement of F.A for PPC

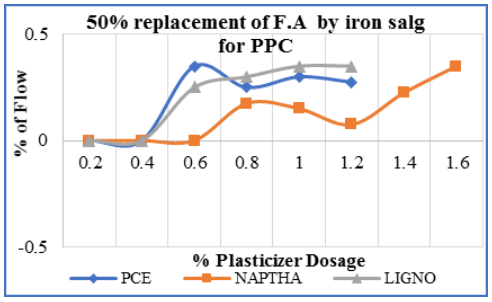

Fig 6:50% replacement of F.A by I.S for PPC

From the Fig 3 and Fig 5, the optimum dosages obtained for PCE based admixtures for OPC and PPC mixes are 0.8% and 0.8% for 0% replacement of fine aggregate. From Fig 4 and Fig 6, for 50% replacement the saturated dosage observed are 1% and 0.6% for OPC and PPC mixes. In case of Naptha based admixture at 0.9% of dosage reliable flow was achieved for OPC mix and at 0.6% of dosage for PPC mix for 0% replacement and 1.0% of dosage reliable flow was achieved for OPC mix and at 0.8% of dosage for PPC mix for 50% replacement. In case of Ligno based admixture at 1.2% of dosage reliable flow is achieved for OPC mix and at 1% of dosage for PPC mix for

0% replacement. The saturated dosage of 1.2% of dosage the reliable flow is achieved for OPC mix and at 1% of dosage for PPC mix for 50% replacement of fine aggregate.

b) Partial replacement of F.A by I.Sconsidering 0.5% w/c for OPC and PPC mixes for various dosage of superplasticizers respectively

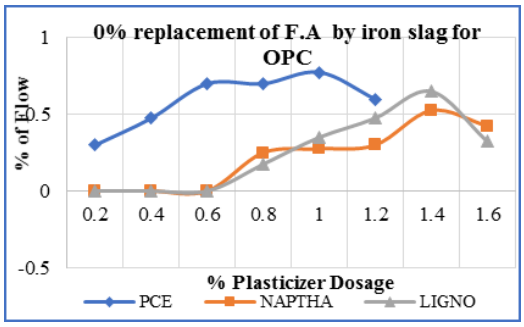

Fig 7:0% replacement of F.A for OPC

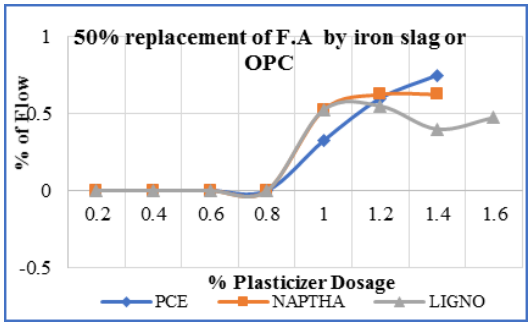

Fig 8: 50% replacement of F.A by I.S for PPC

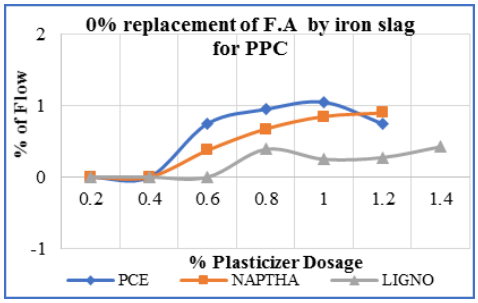

Fig 9:0% replacement of F.A for PPC

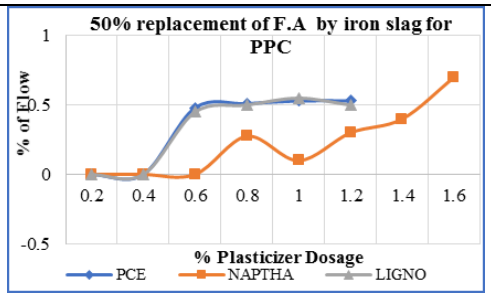

Fig 10: 50% replacement of F.A by I.S for PPC

From the above figures, the optimum dosages obtained for PCE based admixtures for OPC and PPC is 0.6% and 0.8% for 0% replacement. It is observed that the optimum dosage obtained are 0.8% and 0.6% for 50% replacement of Fine aggregate. The optimum dosage for Naptha based admixture obtained is 0.8% for OPC and 0.6% for PPC for 0% replacement. For 50% replacement the saturated dosage is 1.0% for OPC and 0.9 % for PPC. The saturation dosage of 1.2 % and 1.2 % for 0% replacement of OPC and PPC mixes. Optimum Dosages for 50% replacement obtained is 1.4% for OPC and 0.8% for PPC for Ligno based super plasticizers.

3)Behaviour of mortar flow for 0% and 50% replacement of F.A by I.Sfor OPC and PPC mixes for the optimum dosage of PCE to find Optimum w/c.

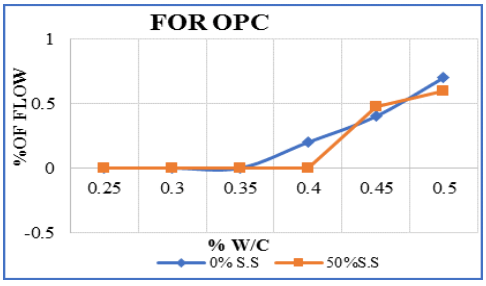

Fig 11: w/c ratio for optimum dosage of PCE for OPC mixes

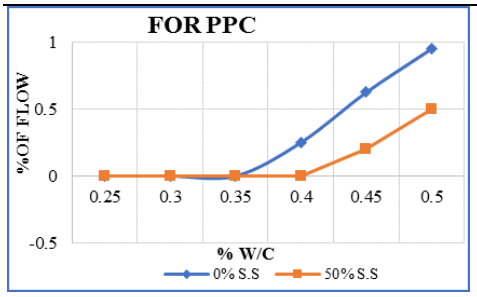

Fig 12: w/c ratio for optimum dosages for PCE for PPC mixes.

The optimum w/c for OPC mixes with 0% replacement of fine aggregate by copper slag for optimum dosage of PCE based admixture of 0.35% is 0.40. It is observed that for 50% replacement of fine aggregate with 0.8% saturated dosage of PCE, the w/c from the Fig 11 obtained is 0.4. Comparatively for PPC mixes, the most favourable w/c for both 0% and 50% replacement of fine aggregates for optimum dosage of super plasticizer of 0.7% and 0.8% is 0.45 respectively as obtained from Fig 12.

Cement Mortars

Cubes of 70.7mm*70.7mm*70.7mm with 1:3 cement to fine aggregate ratio with 0% to 50% replacement of iron slag were casted. .Mortar mix was done using Hobart mixer. Usually compressive strength of mortar is determined by using 2 inch or 50mm cubes as per ASTM C109 / C109M. Mortar is a combination of cement, sand mixed with water. Mix ratio of mortar used is 1:3 of cement to sand ratio in this work.

Effect of super plasticizers and partial replacement of river sand by iron slag on Compressive Strength of cement mortars

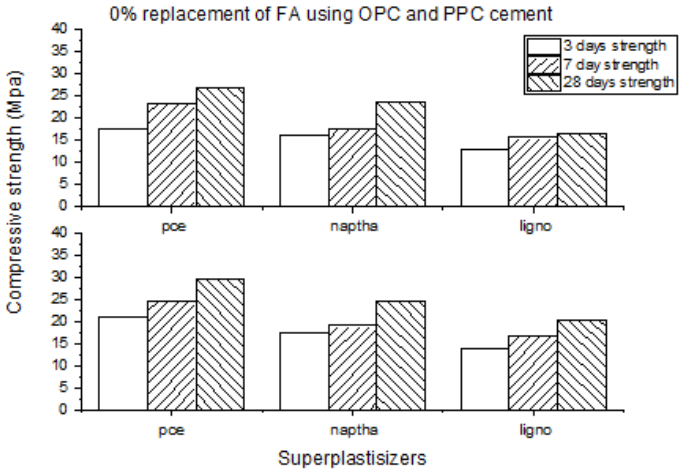

Fig 13**:** Compressive strength of mortars for OPC for 0% replacement of FA using OPC and PPC cement

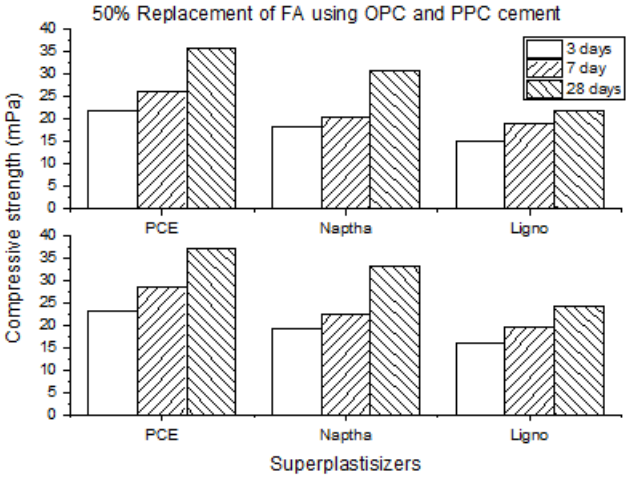

Fig14: Compressive strength of mortars for OPC for 50% replacement of FA using OPC and PPC cement.

The strength behavior of the mortars with and without Iron Slag fine aggregate show similar trends in gain of strength. There is an increase strength of mortar cubes when the PCE based admixture is used and the lowest is observed in case of Ligno based admixture and Naptha coming in between. The mortar with Iron Slag replacement for slag has shown slightly higher strength

than the mortar made with only river sand.

CONCLUSIONS

1. There is no significant difference observed in the flow behavior of cement mortar when the natural sand is replaced with the Iron Slag upto 50%. How ever there is a slight higher demand for admixture dosage – this is because of probable higher water absorption by the Slag as fine aggregate. But the flow pattern was similar to that of the control sample.

2. The mortar strength indicated similarity in gain of strength with the change admixtures. Significant to note that the mortars with natural fine aggregates replaced by iron slag had indicated higher strength than the control sample under all conditions – change in admixture and with respect to time. This could be attributed to the fact that the blended fine aggregates had better particle packing, this is also indicated by the higher density achieved by the mortar cubes made with blended fine aggregates.

3. This experimental study indicates that the iron slag could be used for partial replacement of natural aggregates in the mortars without much difference in performance. The use of Iron Slag as partial replacement of fine will be lead to more sustainable mortar production there by help the cause of environment in the time where Natural Sand especially from rivet is fast depleting, it also clears the earth of probable difficulty of eliminating an industrial bye product.

4. It would take a positive step towards sustainable construction and greener construction.

ACKNOWLEDGEMENTS

The authors acknowledge the support of National Institute of Technology Karnataka, India. Also UltraTech Cement ltd and BASF Bangalore, India.

REFERENCES

1. Beshr H, et al (2003), Effect of coarse aggregate quality on the mechanicalproperties of high strength concrete, Construction and Building Materials., 17, 97-103.
2. Bouikni A, et al (2009), Durability properties of concrete containing 50% and 65% slag, Construction and Building Materials, 23, 2836-2845.
3. M.A.G. dos Anjos, et al (2017), Blasted copper slag as fine aggregate in Portland cement concrete Journal of Environmental Management, 196.
4. Padmapriya R, et al (2015), Study on Replacement of Coarse Aggregate by Steel Slag and fine Aggregate by Manufacturing sand in Concrete, International Journal of ChemTech Research., 8, 1721-1729.
5. Chithra S, et al (2016), The effect of colloidal nano-silica on workability, mechanical and durability properties of high performance concrete with copper slag as partial fine aggregates, Constr. Build. Mater. 113, 794–804.
6. Shekarchi M, et al (2003), Study on electric arc furnace slag properties to be used as aggregates in concrete. In: CANMET/ACI international conference on recent advances in concrete technology, Bucharest, Romania.
7. Sultan A, et al (2014), Effect of using steel slag aggregate on mechanical properties of concrete, American Journal of Applied Sciences., 11(5), 700-706.
8. Human T et al (2013), Properties of mortar incorporating iron slag, Leonardo J. Sci. 23., 53–60.
9. V.S. Devi, et al (2014), Properties of concrete manufactured using steel slag. 12th global congress on manufacturing and management, GCMM 2014, Procedia Eng. 97., 95–104.
10. Deboucha, M.N et al (2015), Effect of incorporating blast furnace slag and natural pozzolana on compressive strength and capillary water absorption of concrete, Procedia Eng. 108 254–261.

8th International Engineering Symposium - IES 2019
March 13-15, 2019, Kumamoto University, Japan

Fracture Behavior of Two Grades of Concrete with Different Percentage of Fibers

Naveenkumar [1] and **Prashanth M H** [2]

1 *Department of Civil Engineering, National Institute of Technology Karnataka, Surathkal-575025. e-mail: naveenbs35@gmail.com*
2 *Department of Civil Engineering, National Institute of Technology Karnataka, Surathkal-575025. e-mail: mh_prashanth@nitk.ac.in*

ABSTRACT: In the present study, the load-deformation behaviour of Steel Fibre Reinforced Concrete (SFRC) beams is carried out by modelling using FEM software, ABAQUS. Two grades of concrete and fibers having different volumetric percentages are considered. Three-point flexural test is performed under displacement control. Fracture properties, such as fracture toughness and fracture energy are determined. The results indicate that presence of fibres show significant improvement in flexural performance of beams.

***Keywords**: Fracture Energy, Fracture Toughness, Steel fibre reinforced concrete beams.*

INTRODUCTION

Concrete is the most versatile material used in the field of Civil Engineering. Concrete is very strong in compression and weak in tension. In tension, large amount of micro-cracks try to open-up leading to failure of specimen. Application of fracture mechanics is important to study the behaviour of concrete under static loading.

Fracture is defined as the separation of a component into at least two parts. Fracture of a material occurs when sufficient stress and work are applied at the atomic level to break the bonds that hold atoms together. The fracture behaviour in concrete is more complicated due to its heterogenous nature and the presence of large size Fracture Process Zone (FPZ) at the crack tip. Failure of a structure usually occurs due to catastrophic growth of cracks resulting in localization of stresses and there by affects the serviceability of the structure.

The present work considers studying of flexural behaviour of concrete by addition of fibers. Fibers are commercially available and manufactured from steel, plastic, glass and other natural materials. In the past three decades, research is being carried to understand the behaviour of fiber reinforced concrete (FRC). The advantages of FRC are - arresting the initiation of micro-crack, control of crack growth and increased tensile capacity. Steel fibers can be defined as discrete, short length of steel having aspect ratio in the range of 20 to 100. Steel fiber Reinforced Concrete (SFRC) offers a solution to the problem of cracking by making concrete tougher and more ductile. Fig.1 shows the steel fibres added to the concrete. The randomly oriented steel fibers assist in controlling the propagation of micro-cracks present in the matrix.

The extent of mechanical strength developed depends on several factors, such as size, shape and volume percentage of fibers added. Plain, straight and round fibres were found to develop very weak bond and hence lower the flexural strength. For a given shape of fibers, flexural strength of SFRC increases with aspect ratio but the workability is adversely affected. Hence aspect ratio is generally limited to an optimum value i.e., 50-70 to achieve good workability and strength. In most of the field applications the diameter of fiber varies from 0.25-1.00

mm, the length varies from 12-60mm, and the fibre contents varies from 0.25 to 2.5% by volume of concrete.

LITERATURE REVIEW

The work carried out by previous researchers on FRC is presented here. Arjun and Divya (2016) carried out fracture study on steel fiber reinforced concrete notched beams for determination of fracture parameters. It is observed that for a fiber content of 0.75 percent, an increase of 37.8% in the ultimate load, 74.8% in fracture energy and 37.5% in fracture toughness were observed compared to that of plain concrete beams.
Chen et al. (2018) studied the fracture energy and fracture toughness of two types of concrete and their interface by three-point bending test. It reveals that the interface causes a great reduction in crack initiation load, peak load, fracture energy and fracture toughness. Ferreira (2007) performed the fracture analysis of a high-strength concrete and a high-strength SFRC. The specimens were subjected to three-point bending configuration. It was observed that the fracture energy and fracture toughness are increased greatly with increase in fibre content as compared to plain concrete. Karadelis and Zhang (2015) investigated the tensile behavior of SFRC by using the finite element analysis software, ABAQUS. They concluded that the analysis could only simulate the macro-scale behavior of SFRC because no fiber bridging law was introduced in the model. Zainab et al. (2016) investigated the steel fiber reinforced concrete beam specimens experimentally and using a numerical 3D modeling, ABAQUS. Good agreement was seen between the experimental and the numerical results in SFRC beam specimens with 0.0, 0.4 and 0.8% volume fractions of steel fiber.

METHODOLOGY

In the present study, finite element software, ABAQUS, is used to analyse and study the fracture properties of Plain Concrete Beam and SFRC Beam. The grades of concrete considered for the study are M25 and M60. The steel fibers having volume fractions of 0%, 0.25%, 0.5%, 0.75% and 1% were considered. The steel fibers used in the study have an aspect ratio of 60 with 30mm in length and 0.5 mm in diameter.
The analysis is carried out considering the mentioned parameters of the beams. The three point bending analysis is carried out on notched beam specimens of size 500mm×100mm×100mm having a span of 400mm. An initial notch of 30mm is provided at the centre of beam.

1. Analysis in FEM Software, ABAQUS

Firstly, the beam is modeled for a dimension of 500mm in length, 100mm in width and 100mm in depth. The size of the steel fiber provided is 0.5mm in diameter and 30mm in length. In the second step, material properties of concrete and steel such as density, modulus of elasticity, Poisson's ratio, etc. are assigned. In the third step, concrete beam and steel fibers are assembled. In the fourth step, time period for the completion of the entire process and number of increments are assigned. For interaction, standard contact between all parts and embedded region for the fibers are assigned. Also, crack in the beam is assigned by using contour integral method. In the fifth step, different boundary conditions (BC) are imposed on the beam model, as shown in figure 2, for the simply supported case. The maximum displacement of 10mm is given in downward direction at the top of mid-section. The displacement is applied in each step and response such as force is measured. Meshing of the beam is done using quadrilateral elements. The analysis is performed to obtain the results.

2. Calculation of Fracture Properties

The fracture properties for different grades of concrete and different percentage of fibres are calculated.

Fracture toughness

The fracture toughness can be determined by using the following equation.

$$K=\frac{3PS}{2BH^2}\ \sqrt{na}\ F(a) \qquad (1)$$

Where,

P is the load applied, S is the span between the supports, B is the width of the beam, H is the depth of the beam, a is the crack length and α=a/H.

The geometric function F(α) for the present case is as follows:

For S/H = 4;

$$F(\alpha)=\frac{1}{\sqrt{\pi}}\frac{1.99-\alpha(1-\alpha)(2.15-3.93\alpha+2.7\alpha^2)}{(1+2\alpha)(1-\alpha)^{3/2}}$$

The notch length (a) can be calculated by using,

$$a.V(\alpha)=\frac{CMOD.B.H.E}{6P.S}$$

Where, E is the Young's Modulus and can be calculated using,

$$E=\frac{6PSa_o}{CMOD.BH}V(a_o)$$

The function $V(a_o)$ for the is given as follows:

For S/H = 4;

$$V(a_o)=0.76-2.28a_o+3.87a_o^2-2.04a_o^3+0.66(1-a_o)^{-2}$$

Fracture Energy

The fracture energy G_F can be calculated by using,

$$G_F=\frac{W_o+2mg\Delta_o}{B(H-a_o)} \qquad (2)$$

Where, W_0 is the area under load-displacement curve, m is the mass of specimen in the range of span S, Δ_0 is the maximum vertical displacement of loading position and a_0 is the initial crack length .

RESULTS AND DISCUSSION

The analysis of plain concrete and SFRC beams are carried out for M25 and M60 grades of concrete.

The variation of displacement in the beam model is shown in figure 3. The gradients of the displacements are symmetrical from the central vertical line of the beam. From the observation, it is seen that displacements are maximum at the centre and are decreasing in a linear trend near to the supports.

Figure 4 and Figure 5 presents the load versus displacement plots for various fibre contents of M25 and M60 grades of concrete respectively. From these figures, it is observed that, up to elastic limit, slopes are linear in the load-displacement plot, but beyond elastic limit, beam with higher percentage of reinforcement shows higher peak load, as indicated in Table 1. In the post peak response, softening part of slopes is decreasing with increase in percentage of fiber content at a particular level of displacement.

The fracture toughness is computed from equation (1) by substituting the peak load from load-displacement curve shown in Figure 4 and Figure 5. The fracture energy is computed from equation (2) by computing the area under the load-displacement curves given in Figure 4 and Figure 5.

The variation of fracture toughness and fracture energy for various fibre contents of M25 and M60 grades of concrete is shown in figure 6 and figure 7 respectively. It is observed that, both fracture energy and fracture toughness increases with increase in grades of concrete and percentage of fiber contents in the beam.

For M25 grade of concrete, the values of fracture toughness and fracture energy for SFRC beam with 1% fiber content are 56.26% and 169.15% respectively, higher when compared to the values of Plain Concrete beam, as shown in Table 2.

For M60 grade of concrete, the values of fracture toughness and fracture energy for SFRC beam with 1% fiber content are 34.20% and 136.5% respectively, higher when compared to the values of Plain Concrete beam, as shown in Table 2.

CONCLUSIONS

The following conclusions are drawn from the present study:

- There is a sustainable increase in ultimate load with increase in grade of concrete and steel fiber content.
- The magnitude of fracture toughness and fracture energy increases with increase in grade of

concrete and steel fiber content when compared to plain concrete beam.

- It is seen that, the percentage increase in fracture toughness and fracture energy is more for M25 grade concrete than M60 grade concrete. Hence addition of fibers results in enhanced fracture properties in M25 (standard concrete) when compared to M60 (high strength concrete).

Table 2 Fracture Toughness and Fracture energy for M25 and M60 grade of concrete

Percentage of fibre	Fracture Toughness (MPa√m)		Fracture energy (N/mm)	
	M25	M60	M25	M60
0.00	11.09	16.87	0.92	1.22
1.00	17.34	22.64	2.48	2.89
Percentage increase	56.26	34.20	169.15	136.50

REFERENCES

[1] Altun, F et al (2007), Effects of steel fiber addition on mechanical properties of concrete and RC beams, Construction and Building Materials 21, pp.654–661.
[2] Arjun, T S and Divya, K K (2016), Fracture Study on Steel Fibre Reinforced Concrete, IOSR Journal of Mechanical and Civil Engineering (IOSR-JMCE), pp. 26-31.
[3] Chen, W et al (2018), Determination of fracture energy and fracture toughness of two types of concrete and their interface, European Journal of Environmental and Civil Engineering, pp.1-13.
[4] Ferreira, L E T (2007), Fracture analysis of a high-strength concrete and a high-strength steel-fiber-reinforced concrete, Mechanics of Composite Materials, Vol. 43, No. 5, pp. 479-486.
[5] Karadelis, J N and Zhang, L (2015), On the Discrete Numerical Simulation of Steel Fibre Reinforced Concrete (SFRC), Journal of Civil Engineering Research, Vol. 5, Issue 6, pp.151-157.
[6] Shah, S P et al(1995), Fracture Mechanics of Concrete - Applications of Fracture Mechanics to Concrete, Rock, and Other Quasi-Brittle Materials, John Wiley & Sons, Inc., New York, USA.
[7] Zainab et al (2016), Experimental and numerical analysis of steel fiber reinforced concrete pavement, Journal of Engineering and Sustainable Development, Vol. 20, No. 06, pp.135-155.

Fig.1 Steel fibres

Table 1 Comparison of ultimate loads for two grades of concrete in different fiber contents

Fibre Content (%)	Ultimate Load (kN)	
	M25	M60
0.00	1.18	1.50
0.25	1.32	1.62
0.50	1.48	1.73
0.75	1.71	1.99
1.00	1.80	2.12

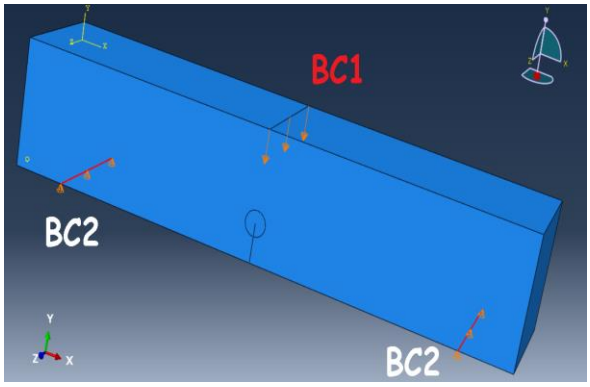

Fig.2 Boundary conditions of the beam model

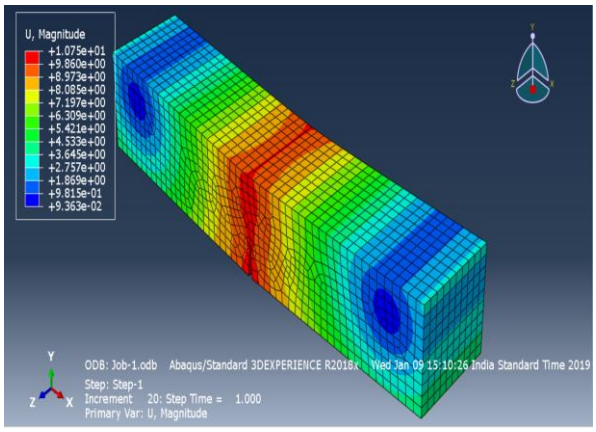

Fig.3 Displacement variation in beam model

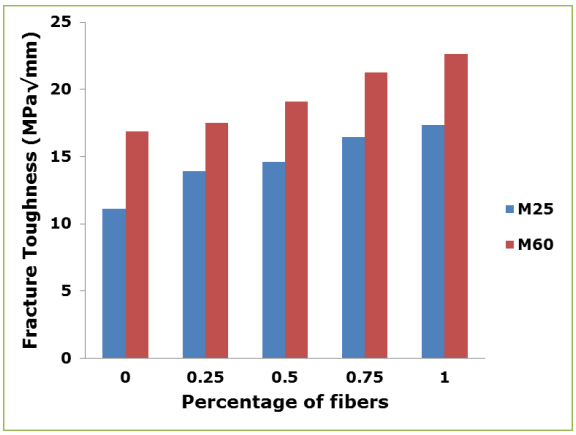

Fig.6 Variation of fracture toughness for various fiber contents

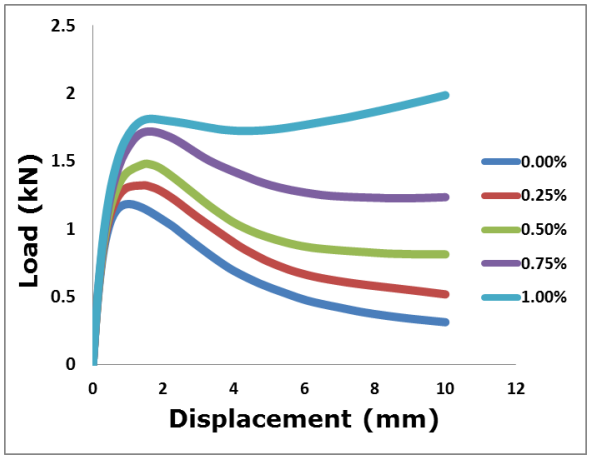

Fig.4 Load versus displacement plots of M25 concrete for various fiber contents

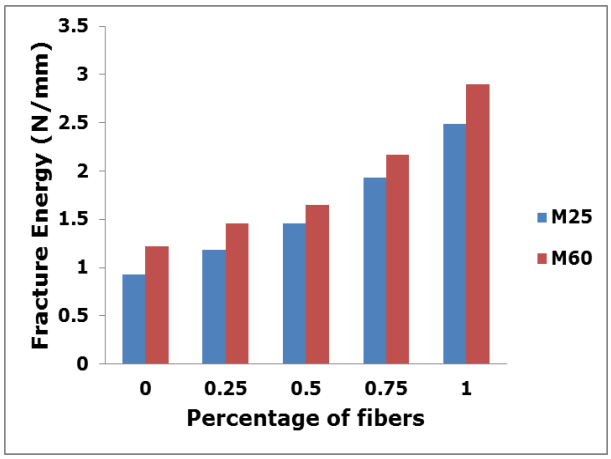

Fig.7 Variation of fracture energy for various fiber contents

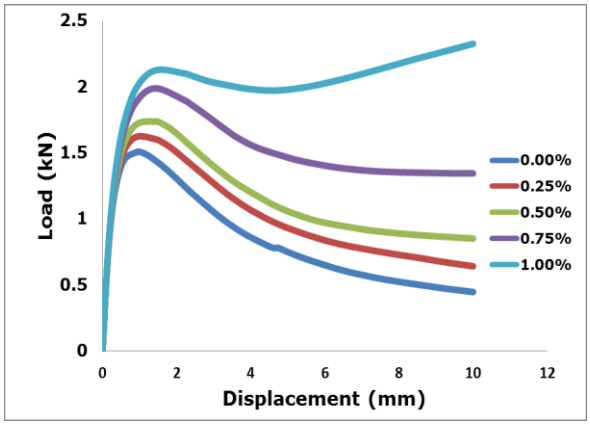

Fig.5 Load versus displacement plots of M60 concrete for various fiber contents

8th International Engineering Symposium - IES 2019
March 13-15, 2019, Kumamoto University, Japan

Assessment on performance of Steel slag and PGBS as an alternative for fine aggregate – An assertive review

Sudarshan V J [1], Arpitha D[2], C. Rajasekaran[3], Nagesh Puttaswamy[4]

1 *Department of Civil Engineering, National Institute of Technology Karnataka, Surathkal, Mangalore 575025, India. Email : joresudarshan@gmail.com*
2 *Department of Civil Engineering, National Institute of Technology Karnataka, Surathkal, Mangalore 575025, India. Email: arpitha.5790@gmail.com*
3 *Department of Civil Engineering, National Institute of Technology Karnataka, Surathkal, Mangalore-575025, India. Email : bcrajasekaran@nitk.edu.in*
4 *Regional Head, UltraTech Cement Ltd.Bengaluru, India : nagesh@nageshp.com*

ABSTRACT: Sand has always been an integral part of construction in our civilization. It has been the most easily available and acceptable source for the same. However, the depletion of river sand availability has started looking at the alternatives including some industrial by-products. One of them is slag obtained from manufacture/refining of metals which would help in the utilization of industrial waste and conservation of natural resources to have a sustainable construction. This paper provides the gist of organised overview involving the evaluation of physical and chemical characteristics, assessment of mechanical and durability properties for the effective utilization of steel slag and processed granulated blast furnace slag (PGBS) that could be modeled from previous researches related to the study. The basic properties of steel slag and PGBS exhibit requisite properties like river sand which is an indication for a possible alternative material to the conventional aggregate. The multiple processing of slag has its influence on strength, durability, and workability of concrete. These recent innovations have made the slag economically viable and environmentally friendly, also profitable salvaging of processed by-product.

***Keywords**:* sustainable construction, steel slag, PGBS.

INTRODUCTION

Concrete is the primary requirement in the construction industry. Currently, due to fast economic growth, rapid urbanization and the demand for construction increased. Therefore, the need for construction materials like cement, sand, aggregate also increased as well. Fine aggregate is taken from the river bed which is getting depleted and exhausted, and its excessive mining has led to the ecological imbalance. As the raw materials are available from natural resources only, it is a serious threat to the environment and can cause sustainable issues. On the other hand, the cost of the construction materials is growing incrementally. This environmental imbalance has created a situation for the people to focus on adoption of innovative technologies and environmentally preferable materials, which will not only preserve the natural resources but also create a productive environment in which human and nature can exist in harmony. To reach this endeavor, one way is to go for eco-friendly concrete made from the products that are generated by mining activities, as waste is certainly a good potential resource.

In concern to this background, this study aims at presenting the use of waste material by partial replacing of natural river sand into concrete and check the feasibility of making concrete and solve environmental problems.

PRODUCTION OF STEEL SLAG

Steel slag is a by-product of steel production. There are different types of slags produced in this process as shown in the table below

Table 1. Categories of Iron/Steel slag

S NO	Steel slags	Manufacturing process	Applications
1	Blast furnace iron slag	Crushing and screening slag, slowly air cooled	Base, Sub base, Concrete aggregate and scour protection
2	Granulated slag	rapidly quenching molten slag with high pressure, high volume water sprays.	Sub base, construction fill, stabilizing binder, glass manufacture
3	Ground granulated slag	Grinding granulated slag to cement fineness	Cement replacement, stabilising binder
4	Basic oxygen steel slag (Caijun shi-2004)	Hot liquid metal is charged to furnace and high-pressure oxygen is injected	Asphalt aggregate, base, sub base, grit blasting
5	Electric arc furnace slag (Caijun shi-2004)	cold steel scraps are charged to furnace, An electrical arc is used to melt the scarp	Concrete aggregate, Sub base, grit blasting
6	Processed granulated blast furnace slag (Satishkumar et al-2016)	Converting granulated slag into PGBS by optimizing granulation parameters and customizing the shaping and screening process	Fine aggregate replacement

MATERIAL PROPERTIES

Physical Properties

Table 2. Physical properties of river sand, Steel slag and PGBS.

Properties	Particle shape	Appearance	Specific gravity	Bulk density g/cc	Fineness modulus	Water absorption
River sand	Irregular	Brownish yellow	2.50-2.81	1.3-1.6	2.58-4.7	1.0 – 3.0
Steel slag	Irregular	Brownish yellow	2.23-3.00	1.0-1.1	3.21	1.2 - 2.5
PGBS	Irregular	Brownish yellow	2.55	1.44-1.63	2.34	<3

(Satishkumar et al.2016, Taehoon Koh et al.2014, Tiwari et al. 2016, Subhatradevi 2014, Anastasiou et al. 2014,)

Physical properties obtained from different authors for steel slag in this study are mentioned in table 2. According to Subhatradevi et al. (2014)and Anastasiou et al. (2014) steel slag exhibit almost similar physical properties as that of river sand and according to Satishkumar et al(2016) PGBS is used as an eco-friendly alternative to 100% replacement of river sand in construction. Tests were conducted to identify the basic properties of Iron slag and PGBS. It is observed that the results fall under the same range as specified in the table 2. A major drawback identified with the use of steel slag in construction is the lesser bulk density in comparison to the of river sand which results in a lower strength of concrete. Higher water absorption and lower specific gravity also contributed to its lower properties. The highly porous structure of earlier granulation slag has improved to the much denser structure resulting in improved density.

Fig 1. Grain size distribution of Steel slag and PGBS

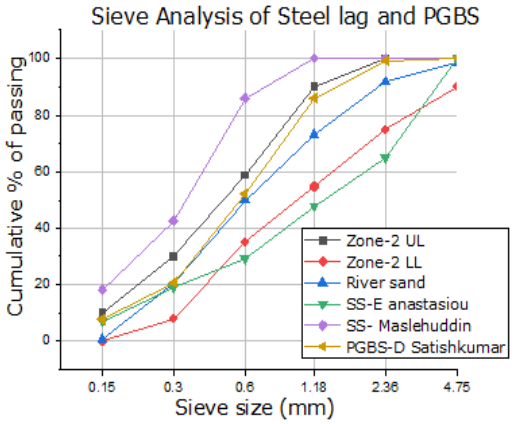

Particle size distribution of steel slag obtained from different authors studied and compared as shown in Fig 1.

Chemical properties

Table 3 shows the range of major constituents in the steel slag. According to the study, iron, silica and calcium content behave as a fluxing agent and is a raw material for clinker. Calcium and magnesium contents capture carbon dioxide. It is noticed that iron and silica content is more. Hence it can be used as a binder in concrete and finer slag can be used to replace with cement or else can be used to manufacture cement.

Fig 2. Chemical compositions of Steel slag

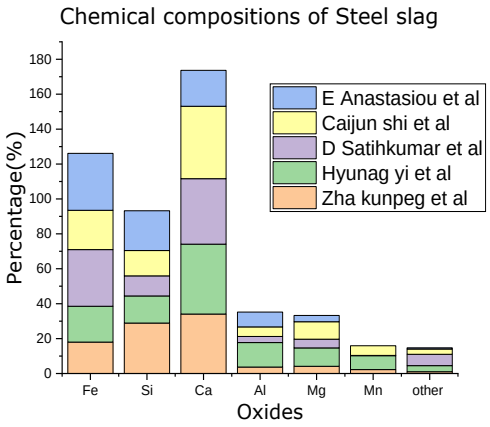

Table 3.Chemical composition of Steel slag

Constituents	Range
Fe_2O_3	18-32.6
SiO_2	11.5-28.92
CaO	20.6-41.5
Al_2O_3	3.5-14
MgO	3.63-10.5
SO_3	0.13-0.15
Mn_2O_3	0.15-8
P_2O_5	0.15-0.2
TiO_2	0.2-0.9
Na_2O	0.15-0.8
K_2O	0.15-1.01

(Hyuang Yi et al. (2012), Satishkumar-(2016), Caijuhn Shi (2004), Anastasiou et al. (2014))

MECHANICAL PROPERTIES

Compressive strength

The compressive strengths presented from the published papers Satishkumar, Maslehuddin et al., wang et al., Caijun shi, Gurupreet Singh and Rafat Siddique, Hisham qasrawi are shown in the Table 4.

Table 4. Compressive strength Data analysis

Sl No	% Slag Replacement	Compressive strength			Author	Remarks
		3 days	7 days	28 days		
1	0% PGBS	-	40	50	Satishkumar et al (2016)	Cement-PSC W/B- 0.38 M 40 grade concrete
	50% PGBS+50% NS	-	39	52		
	50% PGBS+50% MS	-	40.8	52.3		
	50% PGBS + 50% C	-	30.9	49.7		
	100% PGBS	-	42.9	53.3		
2	45% SS	-	-	31.4	Maslehuddin et al (2002)	W/B-0.40 M30 garde concrete
	50% SS	-	-	37.7		
	55% SS	-	-	37.6		
	60% SS	-	-	41.6		
	65% SS	-	-	42.7		
3	0% SS with W/B of 0.5	26	35	48	Wang et al (2013)	W/B-0.35 and 0.5 M40 grade concrete
	15% SS with W/B of 0.5	20	28	45		
	30% SS with W/B of 0.5	12	21	33		
	45% SS with W/B of 0.5	4	10	15		
	0% SS with W/B of 0.35	50	63	73		
	15% SS with W/B of 0.35	40	57	62		
	15% SS with W/B of 0.35	23	50	58		
	15% SS with W/B of 0.35	6	32	38		
4	0% SS	42	61	82	Caijun shi (2004)	Portland SS blast furnace slag cement has been used (HSC)
	10% SS	50	68	92		
	20% SS	49	66	90		
	30% SS	48	64	84		
	100% SS	24	30	36		
5	0% SS	-	23	36	Gurupreet singh, Rafat Siddique (2016)	W/B - 0.44 Self compacting concrete
	10% SS	-	25	38		
	25% SS	-	29	44		
	40% SS	-	30	45		
6	0% SS of grade M25	13	18	26	Hisham Qasrawi et al (2009)	Conventional concrete mixes of 25, 35, and 45 Mpa. All mixes are prepared and adjusted to obtain concrete of medium workability of slump 80 to 120mm Free water content 205Kg/m^3
	15% SS of grade M25	18	27	33		
	30% SS of grade M25	16	24	31		
	50% SS of grade M25	17	26	29		
	100% SS of grade M25	14	19	23		
	0% SS of grade M35	10	27	34		
	15% SS of grade M35	27	37	39		
	30% SS of grade M35	27	35	39		
	50% SS of grade M35	27	35	37		
	100% SS of grade M35	21	28	33		
	0% SS of grade M45	30	38	45		
	15% SS of grade M45	31	43	47		
	30% SS of grade M45	33	43	48		
	50% SS of grade M45	28	38	42		
	100% SS of grade M45	25	37	38		

NS- Natural sand, MS- Manufactured sand, C- Crushed sand, SS- Steel slag, W/B- Water binder ratio

The study explains the strengths of a different grade of concrete with different mixes, different W/C ratios and with different combinations and replacements of steel slag. The compressive strength tends to increase with an increase in the percentage of steel slag in the mix. The mix containing 100% slag produced compressive strengths less than the normal concrete mix. The early age strength gain is higher as compared to later stages if 30% of fine aggregate is replaced by steel slag. According to Hisham Qasrawi et al., lower the grade of concrete, the higher the effectiveness of slag on strength improvement.

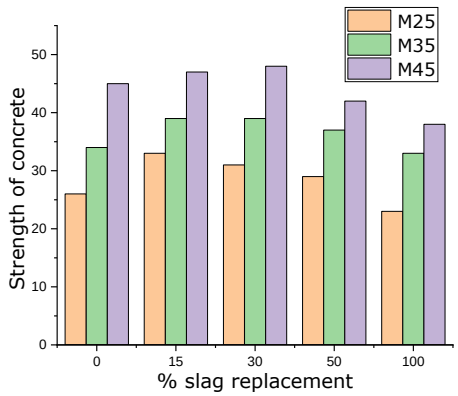

The compressive strength of mortars using PGBS is much higher than the strength of mortar with river sand. The results clearly show that with PGBS as a fine aggregate it is possible to arrive at mix proportion which yields desirable strength and slump and meet the IS 456 requirements.

Tensile strength

According to Hisham Qasrawi et al. (2009), Yung-chin Ding et al. (2017) Steel slag use of slag produced concrete of higher flexural tensile strength. It is observed from the study that up to 50% replacement of steel slag, the flexural tensile strength of concrete increases by the increase in slag ratio. However, the use of a 100% sand replacement by slag was not beneficial when compared to the other replacements in the later strength.

DURABILITY CHARACTERISTICS

Chloride attack

According to Subhatradevi et al (2014), Concrete with GGBS shows moderate chloride penetrability. This is because GGBS has a remarkable ability to decrease the chloride penetrability of concrete but concrete with composite mineral admixture containing a high volume of steel slag can achieve the high chloride penetrability as that Portland cement concrete at later ages.

Sulphate Attack

Gurupreet Singh and Rafat Siddique(2016) conducted tests to study sulphate attack where mass loss and reduction in compressive strength after 28,91 and 365 days was calculated. The specimens were immersed in 50g/l of $MgSO_4$ solution. Spalling and cracks were not found on any concrete specimens during the entire period curing age. No mass loss of specimens was observed, only white deposits were observed after 91 days of immersion period. It is seen that the compressive strength of 10% is better compared to higher percent replacements. The strength loss will be much larger if the concrete is immersed in the solution for a longer period. 10% slag is optimum from the consideration of resistance to sulphate attack.

CONCLUSION

1. Physical properties like specific gravity, particle size and grading of river sand
2. Steel slag appears to be similar.
3. High water absorption and lesser bulk density in comparison to the of river sand results in the lower strength of concrete
4. The highly porous structure of earlier granulation slag has improved the density of the slag.

5. The compressive strength tends to increase with increase in percentage of steel slag. The compressive strength of mortars using PGBS is much higher than the strength of mortar with river sand.

6. It is observed from past researches that up to 50% replacement of steel slag, the flexural tensile strength of concrete increases by the increase in slag ratio. However, the use of a 100% sand replacement by slag was not beneficial when compared to the other replacements in the later strength

ACKNOWLEDGMENT

Author would like to thank all the research articles and the respective authors for providing valuable information and acknowledge the support of National Institute of Technology Karnataka, India. Also, would like to express sincere thanks to JSW, Bellary, India for supplying PGBS required for this study.

REFERENCES

References should be given in alphabetical order. (font to be used: Verdana 8)

[1] Anastasiou, E., Filikas, K. G., & Stefanidou, M. (2014). Utilization of fine recycled aggregates in concrete with fly ash and steel slag. Construction and Building Materials, 50, 154-161.

[2] Devi, V. S., & Gnanavel, B. K. (2014). Properties of concrete manufactured using steel slag. Procedia Engineering, 97, 95-104.

[3] Koh, T., & Hwang, S. (2014). Field evaluation and durability analysis of an eco-friendly prestressed concrete sleeper. Journal of Materials in Civil Engineering, 27(7), B4014009.

[4] Kumar, D. S., Kumar, P., Sah, R., Kaza, M., & Prasad, S. M. R. (2016). Converting Granulated Blast Furnace Slag into Fine Aggregate. Int. J. Civil Eng. Res., 7(2), 91-103.

[5] Maslehuddin, M., Sharif, A. M., Shameem, M., Ibrahim, M., & Barry, M. S. (2003). Comparison of properties of steel slag and crushed limestone aggregate concretes. Construction and building materials, 17(2), 105-112.

[6] Mauthoor, S., Mohee, R., & Kowlesser, P. (2016). Characterisation of electric arc furnace slags as concrete aggregate in a small island developing state: A preliminary study. Construction and Building Materials, 105, 459-464.

[7] Qasrawi, H., Shalabi, F., & Asi, I. (2009). Use of low CaO unprocessed steel slag in concrete as fine aggregate. Construction and Building Materials, 23(2), 1118-1125.

[8] Shi, C. (2004). Steel slag—its production, processing, characteristics, and cementitious properties. Journal of Materials in Civil Engineering, 16(3), 230-236.

[9] Singh, G., & Siddique, R. (2016). Strength properties and micro-structural analysis of self-compacting concrete made with iron slag as partial replacement of fine aggregates. Construction and Building Materials, 127, 144-152.

[10] Tiwari, A., Singh, S., & Nagar, R. (2016). Feasibility assessment for partial replacement of fine aggregate to attain cleaner production perspective in concrete: A review. Journal of Cleaner Production, 135, 490-507.

[11] Wang, Q., Yan, P., Yang, J., & Zhang, B. (2013). Influence of steel slag on mechanical properties and durability of concrete. Construction and Building Materials, 47, 1414-1420.

[12] Yi, H., Xu, G., Cheng, H., Wang, J., Wan, Y., & Chen, H. (2012). An overview of utilization of steel slag. Procedia Environmental Sciences, 16, 791-801.

8th International Engineering Symposium - IES 2019
March 13-15, 2019, Kumamoto University, Japan

Constructive Scope on Implementation of Copper Slag as Replacement for Natural Fine Aggregate- An Overview

Thilak Kumar Y T [1], Arpitha D[2], C. Rajasekaran[3], Nagesh Puttaswamy[4]

1 *Department of Civil Engineering, National Institute of Technology Karnataka, Surathkal, Mangalore 575025, India. thilak8741@gmail.com*
2 *Department of Civil Engineering, National Institute of Technology Karnataka, Surathkal, Mangalore 575025, India. arpitha.5790@gmail.com*
3 *Department of Civil Engineering, National Institute of Technology Karnataka, Surathkal, Mangalore-575025, India. bcrajasekaran@nitk.edu.in*
4 *Regional Head, UltraTech Cement Ltd. Bengaluru, India. nagesh@nageshp.com*

ABSTRACT: This paper communicates organised work on copper slag drawn from scientific literature which comprises of evaluation of physical and chemical characteristics, mechanical and durability properties in the marine environment. Analysis of test data derived from previously available sources reveals that copper slag having similar basic characteristics is an acceptable alternative material to river sand to produce concrete of all grades. The lower water absorption capacity of copper slag is very significant peculiarity which attributes to develop high strength in concrete. The performance of concrete produced using copper slag to the concrete made corresponding to sand component shows identical behavior in the fresh and hardened state. As an aggregate copper slag has the potential to be used as fine aggregate thereby recent advancement in the concrete technology will revolutionise the mixture of various conventional ingredients to uplift the desired properties of concrete to renew its definition, thereby alternative materials to be used as fine aggregate will reduce the burden on the environment which is being extensively investigated all over the world looking to the quantum of requirements, quality, and properties which has been a global consensus on the materials.

***Keywords**: Concrete, Copper slag, Replacement with sand, Review, Waste, Mechanical properties*

INTRODUCTION

Due to the rapid development in construction industries, there is a huge demand for concrete and the world has recorded a rapid increase in the utilization of concrete consistently. Due to the increase in the requirement of concrete, there is a huge depletion of natural resources. This forced civil engineers to think about choosing an alternative material to replace natural resources as an effective, economical and environment-friendly to produce concrete for sustainable development.

However, the sustainable development in the construction sector can only be achieved through various innovative strategies which include choosing appropriate materials, contemporary methods/ techniques for eco-efficient activities, recycling/ reuse of waste materials and so on. Also, according to studies reuse of waste materials can significantly improve the green construction. Copper slag is easily available industrial bi-product obtained during matte smelting process in the production of copper. Approximately 3ton of copper slag is generated for every ton of copper production (Mithun et al. 2015) annually around 24.5million ton of copper slag bi-product generated worldwide (Chang woo et al. 2017) among which 6-

6.5million ton is generated in India (Geetha et al. 2017) and 2million tons generated in Japan (According to Ayano & Sakata 2000).

Concrete consumes around 70% of aggregates, which consists of 40% of sand. The scarcity of sand has increased the cost of construction which is uneconomical. This review works effectively focus on the importance of copper slag as an eco-friendly material for sand that takes a leaping step in creating a new trend in concrete technology.

MATERIAL PROPERTIES

Physical Properties

Table 1 Physical properties of copper slag and sand

Properties	Sand	CS
Particle shape	Irregular	Irregular
Appearance	Brownish Yellow	Black& Glassy
Specific gravity	2.57-2.77	3.36-3.91
Bulk Density (g/cc)	1.71	2.08
Fineness modulus	2.58-4.7	2.61-4.33
Water absorption	1.12-1.5%	0.15%-0.64%
Moisture content	0.50%	0.10%

(Madhavi et al.(2016), KS Al Jabri et al.(2011), Brinda et al.(2011), Mithun et al.(2016), Abmbily et al.(2015), Geetha et al.(2017)

Physical properties of copper slag reviewed from past researches by different authors from different locations are mentioned in table 1. According to Geetha et al.,2017 copper slag exhibit almost similar properties of that River sand hence copper slag can be used as a fine aggregate in concrete. Copper slag observes lesser moisture due to which water-cement ratio can be reduced depending upon the slump required but increase in copper slag workability increases (KS Al Jabri 2009) reduction in w/c ratio effects in the development of higher strength. The specific gravity varies from 3.36 to 3.91 according to the iron content present hence copper slag is denser compared to sand. The hardness of copper slag is 6-7 mohs, and hence it can be used for floors and pavements (Caijuni shi et al., 2008). Using copper slag as Fine aggregate reduces shrinkage of concrete which improves the mechanical and long-term properties of mortar and concrete. Particle size distribution of different samples of CS produced by different location and studied by a different author (Ambily et al. (2015), Al Jabri et al.(2011), Rahul Sharma et al.2017, Mithun et al. 2015). According to the graph, maximum samples fall under zone 2.

Fig 1 Grain size distribution of copper slag

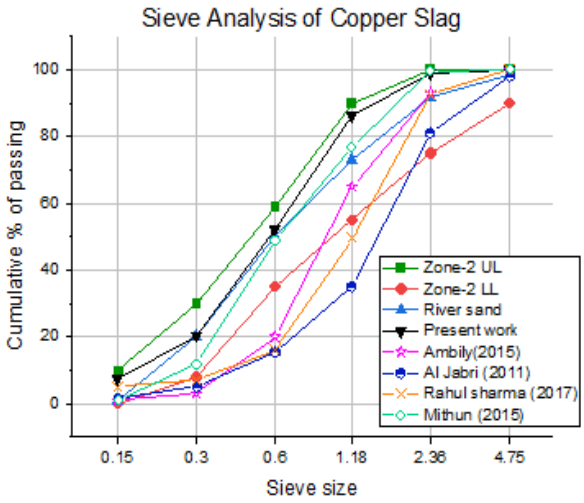

Chemical Properties

Table 2 Chemical compositions of copper slag

Constituents	%Range
CaO	0.15-6.06
Al_2O_3	0.22-6.06
Fe_2O_3	49.3-68.3
SiO_2	25.84-35
MgO	0.2-1.56
Na_2O	0.14-0.95
K_2O	0.03-1.02
SO_3	0.11-1.89
TiO_2	0-0.41
LoI	6.59
Mn_2O_3	0.01-.22
CuO	0.42-1.2

(KS Al Jabri et al. (2011), Brinda et al. (2011), Mithun et al. (2016), Abmbily et al. (2015) , Raja Abhishek et al., Qun lye et al., Rahul Sharma et al.(2017), Geetha et al. (2017)

From table 2 it can be inferred that iron and silica content in the copper slag is more. It is evident that it can be used as a binder in concrete and finer copper slag can be used to replace with cement or else can be used to prepare cement.

MECHANICAL PROPERTIES

Table 3 Statistical Compressive strength and tensile strength data

Sl No	% CS Replacement	Compressive strength (MPa)					ft (MPa)	Author	Remarks
		3 Day	7 Day	28 Day	56 Day	90 Day	28 Day		
1	0	24	42	59			4.22	Mithun et al. (2015)	first sample is 100% OPC all other samples are 100% GGBS
	0	40.5	50.5	62.5			4.78		
	25	39.5	52.5	65			4.81		
	50	41	51	62			4.63		
	75	39.5	53.5	62.5			4.85		
	100	42.5	55	64			4.83		
2	0		36.2	45			3	KS Al Jabri et al. (2011)	OPC Concrete M45 w/c 0.5 1:1.73:2.47
	10		38.8	46			3.5		
	20		40.2	47			3.7		
	40		38.7	47.1			3.8		
	50		38.1	47			4.1		
	60		37.7	46			3.6		
	80		27.8	34.8			3.6		
	100		29	35.1			3.4		
3	0		23	32	35.5		3.3	Rahul Sharma et al. (2017)	SCC OPC 1:1.85:1.27 W/C 0.45 SP 3.85-6.6
	20		23.5	34	38.5		3.45		
	40		26	38.5	43		3.7		
	60		25.5	37	41		3.9		
	80		24.5	36	39		3.5		
	100		23	34	36.5		3.45		
4	0		82	98.5		104.1	5.6	Wei Wu et.al (2010)	High strength 1:1.3:1.3 w/c 0.3 SP 0.27
	20		79.1	96.5		102.6	5.4		
	40		75.7	95.1		99.7	5.4		
	60		74.3	87.7		98.4	5.3		
	80		51.7	69.5		71.2	4.1		
	100		47.9	65		65.5	4.2		
5	0		77	94			5.4	KS Al Jabri et al. (2009)	High Strength 1:1.6:2.68 M85 W/C 0.35 SP 0.79
	10		80	100			5.2		
	20		75	96			6.2		
	40		76	96			6.1		
	50		78	97			61		
	60		69	83			4.8		
	80		64	84			4.7		
	100		63	82			4.4		
6	0			35.11			3.354	Brinda et al. (2011)	1:1.66:3.76 w/c 0.45 M20
	20			43.4			3.961		
	40			46.67			4.576		
	60			39.7			3.924		
7	0		25.6					Madhavi et al. (2016)	1:1.61:2.74 M30 w/c 0.45
	20		25.8						
	40		27.6						
	60		33.3						

ft - tensile strength

Compressive and Tensile strength

The compressive and tensile strengths presented from the published papers (Mithun et al. (2015), KS Al Jabri et al. (2011), Rahul Sharma et al. (2017), Wei Wu et.al (2010), KS Al Jabri et al. (2009), Brinda et al. (2011) and Madhavi et al. (2016)) explains the strengths of different grade of concrete with different mixes, different binder replacement and with different percentage of copper slag replacement. Different authors observed different behavior in strength parameter depending upon the type and location of the copper slag generated. But according to KS Al Jabri et al. (2011), Brinda et al. (2011), Rahul et al. and Mithun et al. (2016) strength of concrete gradually increases with respect to the percentage of replacement of copper slag up to 30-40% (25%-32% of strength increased compared to control concrete cubes), after that there is a decrease in strength development. The split tensile strengths were conducted, and their behavior with CS replacement is very similar to compressive strength and within the permissible limits.

Flexural strength

To find out flexural strength authors cast prisms of size 100x100x500mm (Divya et al. (2017), Geetha et al.(2017), Mithun et al. (2016), KS Al Jabri et al. (2011), Wei Wu et al.(2010) and 70x70x350mm (Ambily et al. (2015)) and tested under third point loading condition.

According to Wei Wu and KS Al Jabri for the high strength concrete, the flexural strength decreases with increase in the percentage of CS beyond 30% replacement due to the porosity induced by the trapped excess water inside the concrete specimen. Geetha et al (2017). explain that the flexural strength increases with an increase in CS (Author studied only up to 20% replacement) for the Marine environment. Author Chang Woo Hong states that up to 60% replacement of CS Flexural strength increases. Mithun et al.(2016), states that CS used with Alkali Activated slag concrete didn't show any differential behavior with respect to Flexural strength when compared to Conventional concrete. But by reducing water to binder ratio, flexural strength can be expected more up to certain CS replacement.

DURABILITY

Chloride attack

Rapid chloride penetration test has resulted that incorporation of CS as a partial replacement of fine aggregate in concrete is suitable for the marine environment and the ingress of chloride ions falls within the acceptable limits when compared conventional concrete (Geetha et al.). The 28day cured 100mm dia, and 50mm thick concrete specimens showed that chloride penetration decreases with the increase in CS percentage replacement. Mithun et al., confirms that Chloride diffusion is much lesser in the case of alkali activated concrete.

Sulphate and Magnesium attack

Concrete samples were immersed under 10% Sodium and 10% magnesium sulphate up to 1Year. The significant increase in the compression strength of alkali activated concrete cubes submerged under sodium sulphate GGBS and CS-based concrete cubes were recorded when compared to OPC based control concrete cubes. On the other hand, GGBS and CS-based concrete cubes showed higher strength loss when compared to OPC based concrete cubes which were immersed in Magnesium sulphate (Mithun et al.).

CONCLUSIONS

1. Basic properties like particle size, grading, lower water absorption, low water demand makes the material most viable alternative to fine aggregates.
2. Due to the decrease in the water absorption, the concrete mix does not demand high water binder ratio. This results in better performance of concrete in both fresh and hardened state.
3. A clear indication has been drawn from previous research works that incorporation of copper slag as a

partial replacement for fine aggregates has improved the durability properties of concrete in concerned to ingression of chloride and sulphate ions.

4. Also, the problem of dumping these waste materials has been overcome, thereby reducing the scarcity of river sand which in turn has made the concrete eco-friendly.
5. The physical and chemical composition of copper slag has shown remarkable results in achieving high strength and high performance concrete.
6. Compressive strength increases up to 30 to 40% of partial replacement thereafter its strength decreases. Hence by studying the strength behavior, IS383-2016 recommends the replacement up to 50%

ACKNOWLEDGMENT

The author would like to thank all the research articles and the respective authors for providing valuable information and acknowledge the support of National Institute of Technology Karnataka, India. Also, would like to express sincere thanks to Sterlite Copper Plant, Tamil Nadu, India for supplying the copper slag

REFERENCES

[1] Geetha, S., & Madhavan, S. (2017). High performance concrete with copper slag for marine environment. *Materials Today: Proceedings*, *4*(2), 3525-3533.

[2] Al-Jabri, K. S., Al-Saidy, A. H., & Taha, R. (2011). Effect of copper slag as a fine aggregate on the properties of cement mortars and concrete. *Construction and Building Materials*, *25*(2), 933-938.

[3] Wu, W., Zhang, W., & Ma, G. (2010). Optimum content of copper slag as a fine aggregate in high strength concrete. *Materials & Design*, *31*(6), 2878-2883.

[4] MITHUN, B., & PALANKAR, N. (2016). Strength Performance of Alkali Activated Slag Concrete with Copper Slag as Fine Aggregate Exposed To Elevated Temperatures.

[5] Brindha, D., & Nagan, S. (2011). Durability studies on copper slag admixed concrete.

[6] Ambily, P. S., Umarani, C., Ravisankar, K., Prem, P. R., Bharatkumar, B. H., & Iyer, N. R. (2015). Studies on ultra high performance concrete incorporating copper slag as fine aggregate. *Construction and Building Materials*, *77*, 233-240.

[7] Krishnan, D., Ravichandran, P. T., & Gandhimathi, V. K. Experimental study on properties of concrete using ground granulated blast furnace slag and copper slag as a partial replacement for cement and fine aggregate.

[8] Al-Jabri, K. S., Hisada, M., Al-Oraimi, S. K., & Al-Saidy, A. H. (2009). Copper slag as sand replacement for high performance concrete. *Cement and Concrete Composites*, *31*(7), 483-488.

[9] Dos Anjos, M. A. G., Sales, A. T. C., & Andrade, N. (2017). Blasted copper slag as fine aggregate in Portland cement concrete. *Journal of environmental management*, *196*, 607-613.

[10] Najimi, M., Sobhani, J., & Pourkhorshidi, A. R. (2011). Durability of copper slag contained concrete exposed to sulfate attack. *Construction and Building materials*, *25*(4), 1895-1905.

[11] Nataraja, M. C., Hatna, S., Rudregowda, S., Majumder, S., Devi, A., Shirahatti, P., ... & Chandan, G. N. (2011). Concrete mix design using copper slag as fine aggregate. *Indian Concrete Journal*, *85*(11), 25-28.

[12] Onuaguluchi, O., & Eren, Ö. (2012). Durability-related properties of mortar and concrete containing copper tailings as a cement replacement material. *Magazine of Concrete Research*, *64*(11), 1015-1023.

[13] Sharma, R., & Khan, R. A. (2017). Sustainable use of copper slag in self compacting concrete containing supplementary cementitious materials. *Journal of cleaner production*, *151*, 179-192.

[14] Abhishek, R., Murari, K., Singh, A., & Gangwa, S. Copper Slag, A Solution and an Alternative to River Sand and in Concrete Manufacturing. *Journal of C*, *4*, 562-8.

8th International Engineering Symposium - IES 2019
March 13-15, 2019, Kumamoto University, Japan

Effect of varying fibre content and thermal cycles on strength properties of polypropylene reinforced Self Compacting concrete

Deepak G Appaji [1], Chethan K [2], S Bhavanishankar [3], Gopalakrishnan N[4]

1 *Department of Civil Engineering, University Visvesvaraya College of Engineering, Bangalore University, Jnana Bharathi Campus, Bangalore 560056, India. email: deepak.g.1013@gmail.com*
2 *Department of Civil Engineering, University Visvesvaraya College of Engineering, Bangalore University, Jnana Bharathi Campus, Bangalore 560056, India. email: k.chethu@gmail.com*
3 *Department of Civil Engineering, University Visvesvaraya College of Engineering, Bangalore University, Jnana Bharathi Campus, Bangalore 560056, India. email: sbhavanishankar@gmail.com*
4 *Department of Civil Engineering, Vijaya Vittala Institute of Technology, Bangalore 560077, India. email: n.gopalakrishnan90@gmail.com*

ABSTRACT: Self compacting concrete (SCC) is being adopted in various application. Addition of fibers to SCC has shown to improve strength and durability of concrete. Concrete structures are subjected to intense solar radiations and alternating temperatures throughout their life time right from the time of casting. The variation in the properties of concrete due to this radiation exposure and thermal cycles of alternating hot and cold temperatures needs to be investigated. The current study presents an investigation on compressive and flexural strength as well weight reduction in polypropylene fiber reinforced SCC at 100°C thermal cycles of 7, 14 and 28 days. Four mixes of concrete with varying percentage of fiber (0%, 0.5%, 1% and 1.5%) are considered. Strength is observed to improve with increase in thermal cycles while the weight is found to reduce.

***Keywords**: Self Compacting Concrete, Fibre Reinforced Concrete, Polypropylene Fibers*

INTRODUCTION

Concrete is the second most consumed material after water and is the most consumed manufactured material in the world. Concrete is a composite material which in its simplest form consists of water, aggregate, and cement. Often, additives (chemical and mineral admixtures) are included in the mixture to achieve the desired physical properties of the finished material.

The popularity and extensive use of concrete for any type of construction has led to requirement of properties like high fluidity, self-compact ability, high strength, high durability, better serviceability and long service life of concrete structures. Manual placing and inadequate consolidation has led to the need for the development of concrete with high fluidity and no segregation. This led to development of a highly engineered concrete that addresses these requirements known as Self Compacting Concrete (SCC). It was developed around 1980 in Japan, to improve the durability of concrete structures.

Fibres when added to SCC, enhances the performance of concrete structures. Fibre reinforced, self-compacting concrete combines benefits of SCC in the fresh state with enhanced performance of fibre reinforced concrete in the hardened state.

The impact of elevated temperature on the properties of concrete is critical for fire resistance and the effect of sustained temperature on strength properties of concrete needs investigation.

LITERATURE REVIEW

Okamura and Ozawa [1] have proposed a simple mix proportioning system for SCC. The coarse and fine aggregate contents are fixed so that self-compact ability can be achieved easily by adjusting the water/powder ratio and super plasticizer dosage only.

K Srinivasa Rao & M Potha Raju [2] investigated the effect of elevated temperatures (up to 950°C) on compressive strength of HSC of M60 grade using fly ash based Pozzolona Portland cement. High strength concrete cube specimens were exposed to different temperatures of 50°C to 950°C in intervals of 50°C for different durations of 1,2 and 3 hours. After exposing the specimens to elevated temperatures, they were tested for their Compressive strength in hot state.

D. B. Kulkarni [3] assessed the effect of sustained temperatures on strength properties of self-compacting concrete. The effect of sustained elevated temperature on the compressive strength, flexural strength, tensile strength & impact strength of self-compacting concrete were tested in laboratory. The specimens were kept in oven at required temperatures (28°C, 100°C, 200°C, 300°C, 400°C, 500°C and 600°C) for 5 hrs at constant temperatures. The results obtained were compared with the corresponding properties of normal concrete with the same water cement and air content.

Arabi N S AL Qadi et al [4] presented an experimental study on optimum amount of polypropylene in self-compacting concrete (SCC) to prevent spalling when exposed to elevated temperatures of 200, 400, and 600°C fixed for 2 and 4 hours. With an increase in percentages of PP fibres segregation resistance decreases. The presence of PP fibres at different dosages does not affect the residual compressive strength at 200, and 400°C, while they considerably increase the residual compressive strength of concretes after exposure to 600°C. Dosage of 0.05% PP fibres by volume can be identified as the optimum amount of PP fibres to use in concretes due to its superior performance during heating.

Slamet Widodo [5] conducted research to evaluate fresh and hardened properties of SCC with polypropylene fibre of 0%, 0.05%, 0.10%, and 0.15% volume fraction. Tests results indicate that polypropylene fibres tend to reduce the flow ability and passing ability but will increase viscosity and segregation resistance of SCC. Compressive strength tends to increase when the fibre added up to 0.05 percent and better splitting tensile strength is observed when the fibre is added up to 0.10 percent. Polypropylene fibre addition also provides positive effects on the impact resistance.

EXPERIMENTAL PROGRAMME

The experimental program included the following steps

- The materials are tested to determine their physical properties.
- Trials mixes using Okamura method of mix design are carried out for the following four mix proportions to achieve the final mixes, which satisfies all the workability properties.
  MIX - 1: SCC with 0% fibres
  MIX - 2: SCC with 0.5% fibres
  MIX - 3: SCC with 1% fibres
  MIX - 4: SCC with 1.5% fibres
- The specimens are cast and cured for 7 & 28 days.
- The specimens are tested for strength values at 7 & 28 days.
- The specimens are subjected to requisite number of thermal cycles at 100^0C as given below:
  7 days cured specimens – 7 & 28 thermal cycles @ 100^0C
  28 days cured specimens – 7 & 28 thermal cycles @ 100^0C
- Change of weight of specimen after each thermal cycle is recorded.
- After thermal cycles, the specimens are tested to know their strength.

Mix design Procedure

The mix design procedure is as follows:

- The coarse aggregate content is fixed in the range of 50 to 60% of the solid volume or 28 to 35% of the concrete volume or 700 to 900 kg/m^3 of concrete.

- The fine aggregate content is fixed in the range of 40-50% of mortar volume.
- The water/powder ratio is assumed in the range of 0.9 to 1.0 (by volume), depending on the properties of the powder (i.e., cement and filler having particles smaller than 0.125mm).
- The super plasticizer dosage and final water/cement ratio are determined through trial mixes so as to ensure self-compactability using U-flow, slump-flow and V-funnel tests. Target values are U-flow of 0 to 30mm, slump-flow of 650 to 800mm, and V-funnel time of 6 to 12 sec.

Material Properties and Mix designations

The specific gravity of materials used in the current study is summarized in Table 1

TABLE 1 SPECIFIC GRAVITY OF MATERIALS CONSIDERED

Material	Specific Gravity
Coarse Aggregate	2.65
Fine Aggregate	2.63
Cement	3.14
Polypropylene Fibres	0.92

The mix designations for the two mixes considered are summarized in Table 2.

TABLE 2 MIX DESIGNATION AND MIX DETAILS

Sl. No.	Mix Naming	Fibres (%)
1.	Mix-1	0
2.	Mix-2	0.5
3.	Mix-3	1.0
4.	Mix-4	1.5

RESULTS AND DISCUSSIONS

The results of fresh properties of self-compacting concrete, as well as hardened properties like compressive strength, flexural strength ad percentage reduction in weight are presented in Tables 3-9.

The obtained results for fresh properties of the SCC mixes are compared with the desired range as per EFNARC 2005 guidelines.

TABLE 3 FRESH PROPERTIES OF MIXES CONSIDERED

Fresh Concrete Property/ Test	Mix 1	Mix 2	Mix 3	Mix 4	Desired Range as per EFNARC (2005) Guidelines
Slump flow (mm)	680	675	670	670	650-800
J-ring (mm)	8	9	9	10	0-10
V-funnel (sec)	10	10	11	11	6-12
L - Box (H_2/H_1)	0.91	0.90	0.89	0.87	0.8-1.0
U - Box (H_1-H_2) (mm)	22	23	24	26	0-30

Compressive Strength for 7 and 28days cured specimens after 100^0C thermal cycles are presented in Tables 4 and 5.

TABLE 4 COMPRESSIVE STRENGTH OF 7 DAYS CURED SPECIMENS AFTER 100^0C THERMAL CYCLES

Mix	Compressive Strength (N/mm^2)		
	No. of Thermal Cycles		
	0	7	28
Mix - 1	20.14	24.29	28.44
Mix - 2	26.86	30.47	31.12
Mix – 3	28.15	36.30	37.41
Mix – 4	21.33	31.10	33.42

TABLE 5 COMPRESSIVE STRENGTH OF 28 DAYS CURED SPECIMENS AFTER 100^0C THERMAL CYCLES

Mix	Compressive Strength (N/mm^2)		
	No. of Thermal Cycles		
	0	7	28
Mix - 1	23.46	25.75	29.87
Mix - 2	31.40	32.58	32.58
Mix – 3	32.89	38.52	39.04
Mix – 4	24.88	28.14	30.51

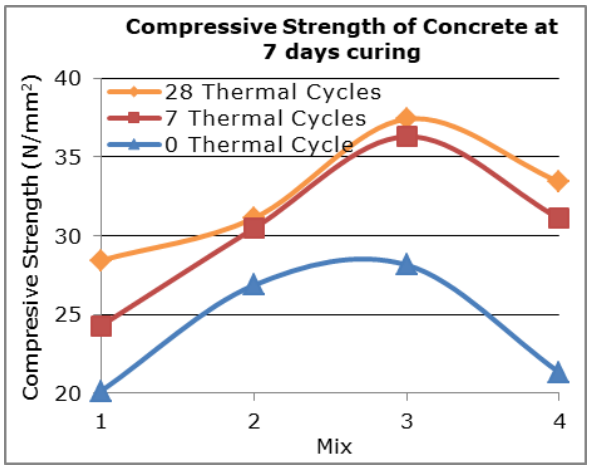

Fig. 1 Compressive Strength of Concrete cubes cured for 7 days subjected to 100°C thermal cycles

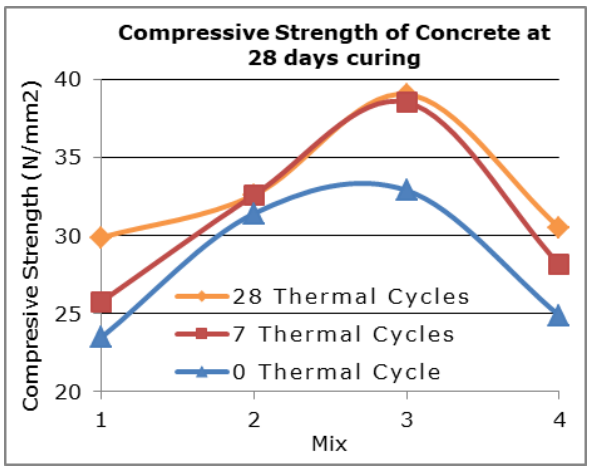

Fig. 2 Compressive Strength of 28 days cured specimens subjected to 100°C thermal cycles

The compressive strength of all specimens with fibers (Mix 2-4) is found to be higher than the compressive strength of mix without fibers (Mix-1) for all thermal cycles as well as for both 7 and 28 days curing. However, Mix-3 (1% of fiber) is found to be the optimum mix in terms of compressive strength.

The percentage increase of compressive strength in case of Mix-3 specimen cured for 7 days is 28.95% when it is subjected to 7 thermal cycle while the corresponding increase is 32.9% for 28 thermal cycles. The increase in compressive strength of 7 days cured Mix-3 specimens as compared to Mix-1 (without fibers) is 39.77%, 49.44% and 31.54% for 0, 7 and 28 thermal cycles respectively.

For 28 days cured Mix-3 specimens there is a 17% and 19% increase for 7 and 28 thermal cycles respectively. There is a large increase of about 30-50% in compressive strength for 28 days cured Mix-3 specimen as compared to Mix-1 specimen without fibers.

The compressive strength increases with increase in fibre content up to 1% beyond which the compressive strength is observed to decrease although the strength is still higher than the concrete without fibers.

Flexural Strength for 7 and 28 days cured specimens after 100°C thermal cycles are presented in Tables 6 and 7.

TABLE 6 FLEXURAL STRENGTH OF 7 DAYS CURED SPECIMENS AFTER 100°C THERMAL CYCLES

Mix	Flexural Strength (N/mm²)		
	No. of Thermal Cycles		
	0	7	28
Mix - 1	6.83	7.53	8.00
Mix - 2	6.83	8.75	9.33
Mix - 3	5.50	7.74	8.17
Mix - 4	6.18	7.16	7.75

TABLE 7 FLEXURAL STRENGTH OF 28 DAYS CURED SPECIMENS AFTER 100°C THERMAL CYCLES

Mix	Flexural Strength (N/mm²)		
	No. of Thermal Cycles		
	0	7	28
Mix - 1	7.89	8.47	8.89
Mix - 2	8.25	9.33	9.58
Mix - 3	7.33	7.78	8.20
Mix - 4	6.83	7.16	7.91

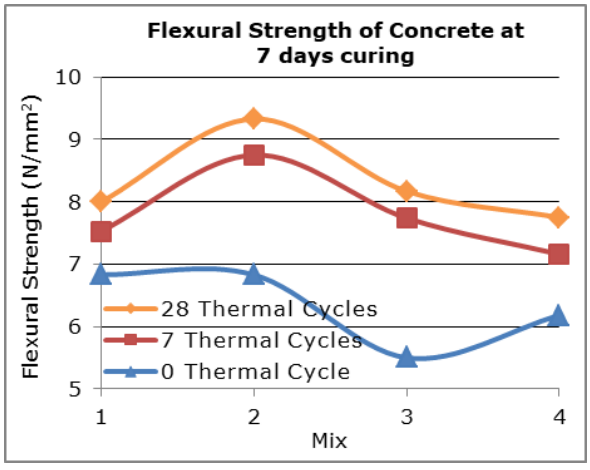

Fig. 3 Flexural Strength of Concrete cubes cured for 7 days subjected to 100°C thermal cycles

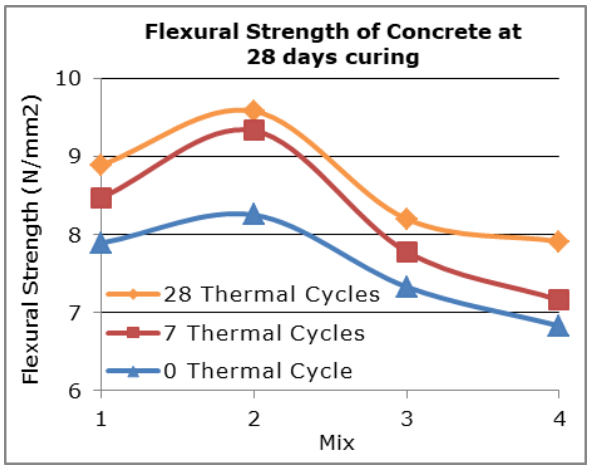

Fig. 4 Flexural Strength of Concrete cubes cured for 28 days subjected to 100°C thermal cycles

The flexural strength of Mix-2 (0.5% fibers) is found to be higher than Mix-1 (without fibers) for all thermal cycles as well as for both 7 and 28 days curing while the flexural strength is lower as fiber content increases i.e. for Mix-3 & Mix-4 as compared to the mix without fibers. Hence, Mix-2 (0.5% of fiber) is the optimum mix in terms of flexural strength.

The flexural strength increases with increase in thermal cycle for both 7days as well as 28 days cured specimens. In case of 7 days cured specimen the rate of increase in strength is much higher than 28 days cured specimens for both 7 and 28 thermal cycles. The percentage increase in flexural strength in case of Mix-3 specimen cured for 7 days is 40.73% when it is subjected to 7 thermal cycle while the corresponding increase is 48.55% for 28 thermal cycles. In 28 days cured Mix-3 specimens, the rate of increase in flexural strength for 7 thermal cycles is 6.14% while the corresponding increase is 11.87% for 28 thermal cycles.

For conventional SCC without fibers (Mix-1) cured for 7 days, the increase in flexural strength for 7 thermal cycles is 10.25% and 17.13% for 28 thermal cycles. For 28 days cured Mix-1 specimens, the flexural strength increases by 7.35% and 12.67% respectively for 7 and 28 thermal cycles.

The increase in flexural strength of 7 days cured Mix-2 specimens as compared to Mix-1 (without fibers) is around 16% for both 7 and 28 thermal cycles while in case of 28 days cured specimen the increase is about 7-10%. For 28 days cured Mix-2 specimens the increase is 13% and 16% respectively for 7 and 28 thermal cycles.

The weight of 7 and 28 days cured concrete prism specimens after 100°C thermal cycles are presented in Tables 6 and 7. The variation in weight of concrete specimens for different mixes with varying percentages of fibers as well as the reduction in weight of concrete prisms with increasing thermal cycles is presented in Fig. 5 to Fig. 6.

TABLE 8 WEIGHT OF 7 DAYS CURED SPECIMENS AFTER 100°C THERMAL CYCLES

Mix	Weight of Prisms (kg)			
	No. of Thermal Cycles			
	0	7	14	28
Mix - 1	11.49	11.35	11.16	11.05
Mix - 2	12.41	12.01	12.00	11.99
Mix - 3	11.93	11.69	11.66	11.61
Mix - 4	12.79	12.23	12.20	12.18

TABLE 9 WEIGHT OF 28 DAYS CURED SPECIMENS AFTER 100°C THERMAL CYCLES

Mix	Weight of Prisms (kg)			
	No. of Thermal Cycles			
	0	7	14	28
Mix - 1	11.97	11.66	11.58	11.45
Mix - 2	12.35	12.16	12.11	12.11
Mix - 3	11.79	11.40	11.25	11.18
Mix - 4	12.03	11.73	11.69	11.69

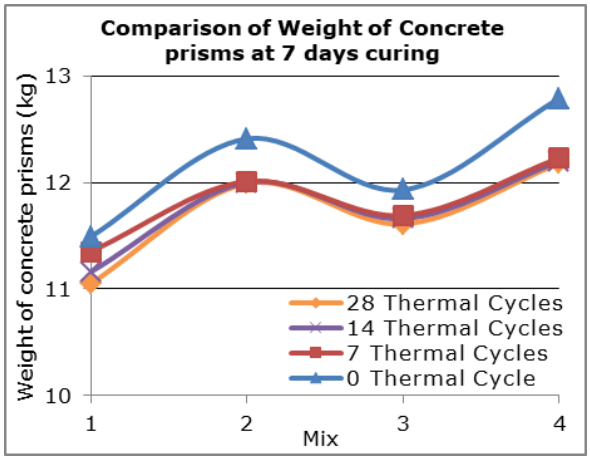

Fig. 5 Comparison of variation in weight of 7 day cured Concrete prisms subject to 100°C thermal cycles

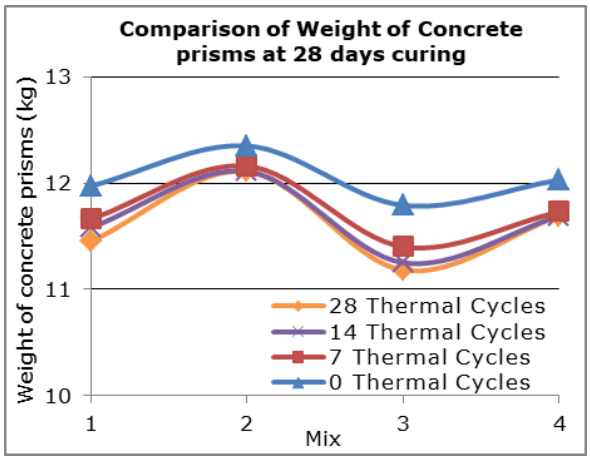

Fig. 6 Comparison of variation in weight of 28 day cured Concrete prisms subject to 100°C thermal cycles

There is a decrease in weight of specimens as thermal cycle increases for both 7 and 28 days cured prisms. For specimens with fibres, the % reduction in weight is not very appreciable beyond 7 thermal cycles.

For 7 days cured SCC specimen without fibers (Mix-1), the weight decreases by 1.22%, 2.87% and 3.83% for 7, 14 and 28 thermal cycles respectively while the corresponding reduction in weight is 2.59%, 3.26% and 4.34% for 28 days cured specimen.

For Mix-2 specimens, the reduction in weight for 7 days cured specimen is around 3% while the reduction in weight is around 1.5-1.9% for 28 days cured specimen.

CONCLUSIONS

- Strength increases as thermal cycle increases for all the mixes although the % increase reduces for 28 days curing.
- The Mix-3 with 1% fiber is found to be optimum in terms of compressive strength while Mix-2 with 0.5% fiber is found to be optimum when flexural strength is considered.
- Weight of the specimens decreases with the increase in no. of thermal cycles. The reduction in weight due to increased thermal cycles is slightly reduced or controlled due to addition of fibers.

ACKNOWLEDGEMENTS

We sincerely thank and acknowledge UVCE, Bangalore University, Bangalore for the successful completion of this study.

REFERENCES

[1] Okamura H, Ozawa K. (1995), Mix design for self-compacting concrete. Concrete Library of Japanese Society of Civil Engineers 25,107-120

[2] K.Srinivasa Rao, M. Potha Raju (2004): A study on variation of compressive strength of high strength concrete at elevated temperatures.25 - 26 August 2004

[3] D. B. Kulkarni and S N Patil (2011): Comparative Study of Effect of Sustained High Temperature on strength Properties of Self Compacting Concrete and Ordinary Conventional Concrete. International Journal of Engineering and Technology Vol.3 (2), 2011, pp. 106-118

[4] Arabi N S AL Qadi, Kamal Nasharuddin Bin Mustapha, Sivakumar Naganathan, and Qahir N. S. Al-Kadi (2011): Effect of polypropylene fibres on fresh and hardened properties of Self Compacting Concrete at elevated temperature, Australian Journal of Basic and Applied Sciences, Vol. 5, Issue 10, pp. 378-384, 2011

[5] Slamet Widodo (2012): Fresh and hardened properties of Polypropylene fiber added Self-Consolidating Concrete, International Journal of Civil and Structural Engineering, Volume 3, No 1, 2012

[6] EFNARC (2005), European guidelines for self-compacting concrete -Specification, Production and Use

[7] H. G. Mundle (2014): Variation in strength of concrete subjected to High temperature. International Journal of Research in Engineering & Technology (IMPACT: IJRET) Vol. 2, Issue 2, Feb 2014, 149-154

[8] M.Benaicha, O.Jalbaud, A.Alaoui Hafidi, Y.Burtschell (2013): Rheological and Mechanical Characterizationof Fibre-Reinforced Self-Compacting Concrete. International Journal of Engineering and Innovative Technology (IJEIT) Volume 2, Issue 7, January 2013

[9] IS 383, "Specification for coarse and fine aggregates from natural source for concrete", Bureau of Indian Standards, 1970.

[10] IS 516, "Methods of tests for strength of concrete", Bureau of Indian Standards, 1959.

[11] IS 2386, "Method of physical tests for aggregates for concrete", Bureau of Indian Standards, 1963.

[12] IS 4031, "Method of physical tests for hydraulic cement", 1996.

[13] IS 12269, "Specification for 53 grades OPC", Bureau of Indian Standards, 1987.

8th International Engineering Symposium - IES 2019
March 13-15, 2019, Kumamoto University, Japan

Experimental Study of Geocell Reinforced Monopile Foundation under Static Lateral Load

KISHORE K [1] H.C. MUDDARAJU [2]

1 *Department of Civil Engineering, UVCE, Bangalore University, Bangalore -560056, Karnataka, India. e-mail:kishore31kk26@gmail.com*
2 *Department of Civil Engineering, UVCE, Bangalore University, Bangalore -560056, Karnataka, India. e-mail:muddu.hc@gmail.com*

Abstract: This paper introduces an innovative use of Geocell as reinforcement in a novel foundation concept, Geocell reinforced Monopile foundation, Where Geocell are used to enhance the lateral resistance of a Monopile foundation. The lateral static behaviour of the monopile foundation was evaluated using a series of reduced scale physical model tests performed on the model foundation installed in soil bed contained in a small size soil container. A one directional loading system was attached to the soil container. A series of lateral static load tests were conducted to investigate the influence of the Geocell reinforcement on the monopile foundation behaviour. The experimental results show that the lateral resistance of a monopile was enhanced by the embedded Geocell reinforcement in the sand bed.

Keywords: *Geosynthetic, Geocell, Reinforced soil, Sand bed, Static Lateral loads, Monopile Foundation, Physical model tests*

Introduction

Poor ground conditions near the surface pose some foundation challenges for design engineers. In many cases, deep foundation systems are sought as the practical foundation option to address the challenges of weak foundation soils. Pile foundations are widely used to transfer both vertical and lateral loads. In many cases pile foundation are expected to resist significant lateral loads. However, the weak subsurface conditions near the ground surface often dictate expensive and time consuming ground replacement, pile inclination or soil stabilization practices in order to enhance the lateral resistance of the pile foundation.

Wind turbines can be constructed using several foundation types. Onshore wind turbine towers are commonly bolted to a concrete slab at soil surface level. Offshore foundations not only transfer wind loads, but also marine loads to the subsoil. The most widely used type of foundation for offshore wind turbines is monopile foundation. With the offshore turbines continuously increasing in size, also the foundation increases.

The use of geosynthetic reinforcement in earth structures have increased significantly over the last two decades. The advantages associated with the use of geosynthetic have been well documented. Some of the typical applications include slopes reinforcement, improvement of embankments foundations, mechanically stabilized retaining structures and subgrade improvement for roads.

Several researchers investigated the use of geosynthetic with geotechnical structures. Piles and geogrid were used together as part of a hybrid system, denoted as the geogrid reinforced and pile-supported (GRPS), to limit total and differential settlements observed in embankments (Liu et al., (2007). Several researchers investigated the (GRPS) system. Maddison et al., (1996); Han and Akins, (2002); Han and Gabr (2002); and Liu et al., (2007) demonstrated its advantages with regard to improving stability of embankments and reducing their settlements. On the other hand, Bathurst and Alfaro (1996), Zhenqi and Bathurst (1995), Sandri (1997), El-Emam and Bathurst (2004) conducted experimental and numerical studies and

showed that the geogrid reinforcement improved the seismic behaviour of earth retaining structures. Similarly S. Bhattacharya et al., (2011), Taha. A et al., (2014) and Vonmaries M.C (2011) conducted experimental and numerical studies on monopile foundation showed that the geogrid reinforcement improved static and dynamic behaviour of monopile foundation. This is attributed to the increased shear resistance due to the friction and interlocking mechanisms at the soil-reinforcement interfaces.

In the present investigation an attempt is made to see how well the Geocell reinforced monopile foundation response to the applied lateral load on sand bed. The pile-soil-geosynthetic interaction of this system will be evaluated using a series of reduced scale physical model tests

Materials and Methods

In order to study the performance of reinforced sand bed under static lateral loading the materials used in the investigation are sand and Geocell reinforcement.

Material Properties

The sand used in the study is collected from the local river. The properties of Sand are given in Table 1.

Table 1: *Properties of Sand*

Properties	Sand
Uniformity coefficient(Cu)	3.15
Coefficient of curvature(Cc)	1.22
Specific Gravity (G)	2.62
Maximum Unit Weight(γ_{max}), e_{min}	17.72 kN/m³,0.48
Minimum Unit Weight(γ_{min}), e_{max}	14.95 kN/m³,0.747
Angle of internal friction (Ø)(phi), degree	38
D_{10}, D_{30}, D_{50}, mm	0.26,0.5,0.82

Reinforcement

High density polyethylene in the form of Geocell is used in the present investigation Table 2 presents the properties of Geocell used.

Table 2: *Properties of Geocell*

Properties	Value
Sheet thickness, mm	1.52
Cell depth, mm	50
Material	HDPE(High Density Polyethylene)
Opening size, mm²	240*210
Seam peel strength, N	710

Monopile

The monopile with L/D ratio of 4.7 is used for the present investigation (Where, L is the length of monopile and D is the diameter of the monopile). The reduced scale physical model of monopile was used for the static lateral load test. The similitude relationship for primary system variables are presented in Table 3.

Table 3: *Similitude relationship*

Mass density	1	Acceleration	1	Length	S
Force	S^2	Shear velocity	$S^{1/2}$	Stress	S
Stiffness	S^2	Time	$S^{1/2}$	Strain	1
Modulus	S	Frequency	$S^{-1/2}$	EI	S^3

S: geometric scaling factor

Table 4: *Properties of model monopile*

Parameter	Model pile	Prototype/Full scale pile
Material	HDPE	Steel
Modulus of elasticity(E)	0.85 GPa	200 GPa
Length	296mm	22m
Outer diameter	63mm	4.4m
Thickness	3mm	90cm

Monopile with L/D ratio 4.7 behave as a rigid pile rather than slender pile. Fig 1

illustrates the behaviour of rigid pile under lateral loading system.

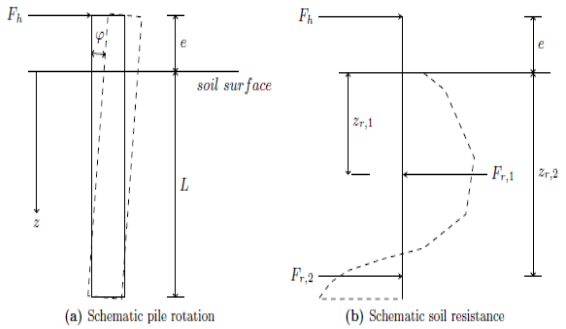

Fig 1: *Behaviour of Laterally Loaded Rigid Pile*

Where F_h is applied lateral load, F_{r1} is the reaction offered above rotation point of pile and F_{r2} is the reaction offered below rotation point of pile

Preparation of sand bed

Rainfall technique is used to achieve reproducible density of compacted sand in the present investigation. The sand is poured in to the tank continuously through a raining box kept at a known height to achieve a particular density. Monopile is vertically placed and sand pouring is continued up to the required height of the tank. This technique of sand pouring is termed as rainfall technique and this technique is reported to achieve good reproducible densities. The sand surface was levelled carefully. This method of sand pouring gave a dry density of 1.68 g/cc corresponding to dense sand state.

The height of fall of sand required to obtain a particular density is determined by trial and error procedure Fig 2, shows a calibration curve obtained for height of fall and density achieved by such procedure

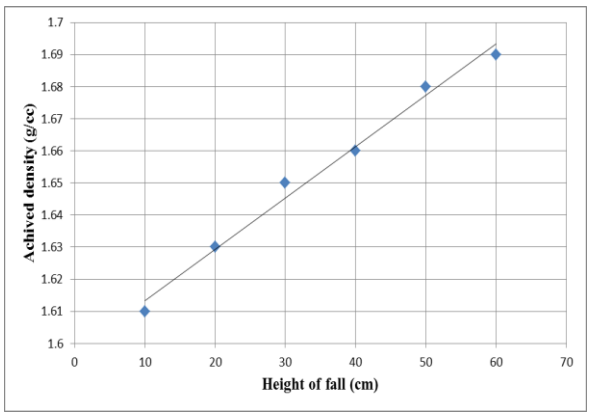

Fig 2: *Calibration curve for height of fall*

Method of Testing

The reinforced and unreinforced sand beds are subjected to static lateral loading in mild steel tank. The load is applied on to the model monopile using proving ring and manually operated Hand winch arrangement. The lateral deformation caused due to the applied lateral load is measured through magnetic mount dial gauge placed on the wall of steel tank. Fig 3 shows the experimental setup used in present investigation.

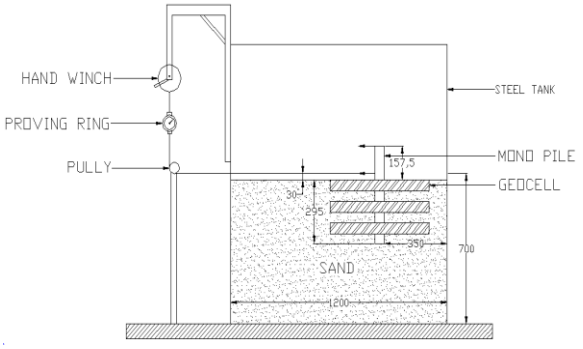

Fig 3: *Experimental setup*

Results And Discussions

To bring out the effect of inclusion of geocell reinforcement on the performance of monopile foundation resting on sand bed, experiments are conducted both on unreinforced and reinforced sand beds under static lateral load, Load is applied at both Mud Level and Head Level of monopile. The results of all such experiments performed are presented in the following sections.

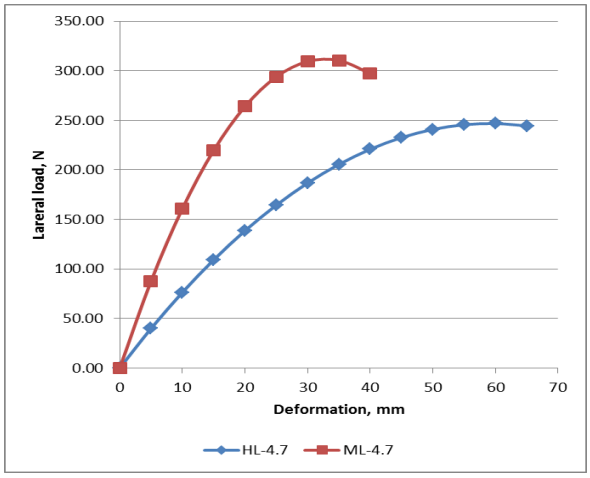

Fig 4: *Performance of monopile resting on unreinforced sand bed under static lateral load*

Fig 4 shows the plot of lateral load carrying capacity of the monopile on the unreinforced sand bed against deformation both at Mud Level (ML) and Head Level (HL).
From the Fig 4 the ultimate lateral load carried by the monopile at the Mud Level (ML) is 311 N and for that at the Head Level (HL) is 247 N and the corresponding deformation recorded are 35mm and 60mm respectively.

Effect of position of reinforcement layers

Fig 4 shows the plot of effect of position of reinforcement layer on performance of the monopile for L/D ration 4.7. From Fig 4, for monopile with L/D ratio 4.7, the reinforcement placed at 0D depth (i.e., at the surface) has better lateral load carrying capacity and shows less deformation, compared to reinforcement placed at 1D depth or 2D depth (where D-diameter of the monopile). For ML the ultimate load carried for reinforcement place at surface is 409N and the corresponding deformation is 30mm. Whereas for the same deformation value of 30mm the ultimate load taken by reinforcement at 1D depth and 2D depth are 383 N and 398 N, thus a reduction in ultimate lateral load capacity by 6.35% and 2.68% respectively is observed.

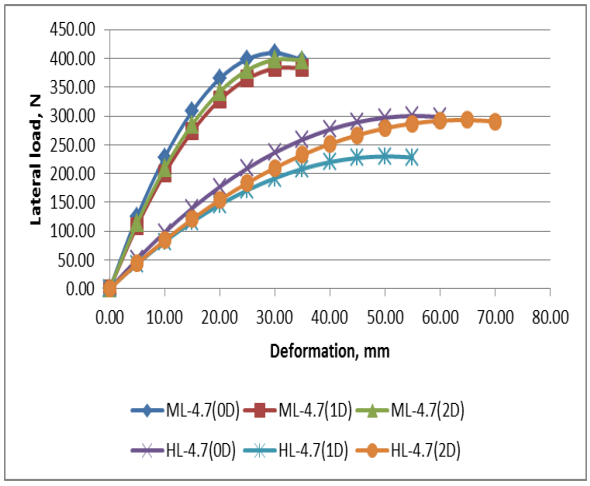

Fig 4: *Effect of position of reinforcement on the performance of monopile resting on sand bed under a static lateral load*

Similarly for HL, The ultimate load carried for reinforcement place at surface is 300N and the corresponding deformation is 55mm. Whereas for the same deformation value of 55mm the ultimate load taken by reinforcement at 1D depth and 2D depth are 283 N and 287 N, thus a reduction in ultimate lateral load capacity by 5.66% and 4.33% respectively is observed.

Effect of position of reinforcement layers

Fig 5 shows the plot of effect of number of reinforcement layer on performance of the monopile with L/D ratio 4.7. *From Fig 5, For* the monopile with L/D ratio 4.7 *It can be seen that N=3 layers show higher lateral load carrying capacity and reduced deformation compared to N=1 and 2 layers. For ML,* the ultimate lateral load carried for 3 layer reinforcement is 533N and the corresponding deformation is 25mm. Whereas for the same deformation value of 25mm the ultimate lateral load taken by 1 layer and 2 layers reinforcement are 398 N and 475 N, thus a reduction in ultimate lateral load capacity by 25.32% and 10.88% respectively is observed. Similarly For HL, the ultimate lateral load carried for 3 layer reinforcement is 403N and the corresponding deformation is 50mm. Whereas for the same deformation value of 50mm the ultimate lateral load taken by 1 layer and 2 layers reinforcement are 297 N and 315 N, thus a reduction in ultimate lateral load capacity by 26.30% and 21.83% respectively is observed.

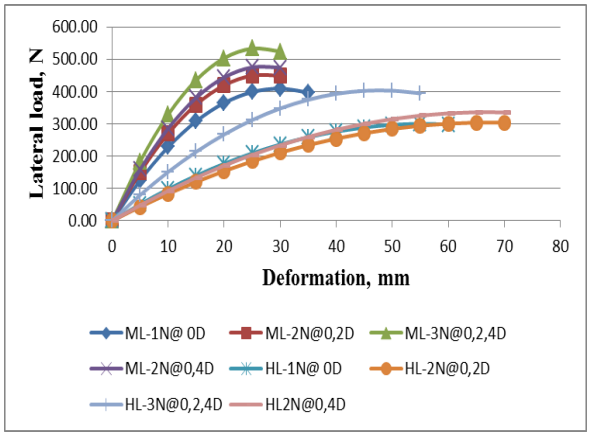

Fig 5: *Effect of number of reinforcement layers on the performance of monopile resting on sand bed under a static lateral load*

Other observation made from the Fig 5 is that, the position of the reinforcement layer in case of N=2 layers is prominent, i.e., the geocell placed at 0D, 4D combination position show better results compared to geocell placed at 0D, 2D combination position.

The comparison between Mud level and Head level

The comparison between Mud level and Head level is further illustrated in Table 5 and Table 6.

Table 5 shows percentage increase of ultimate lateral load and percentage decrease of deformation at Mud level with respect to Head level for placement position of reinforcement.

Table 5: *Variation of parameter at Mud level for placement position of reinforcement*

L/D Ratio	Variation of parameter at Mud Level W.R.T Head level	Placement Position of Reinforcement		
		0D-depth	1D-depth	2D-depth
4.7	% increase in Ultimate lateral load	26.68	26.10	26.38
	% decrease in Deformation	45.54	36.36	53.85

Reinforcement placed at suface of sand bed (i.e., @0D depth) performs better compared to reinforcement at 1D and 2D depth.

From Table 5, the reinforcement placed at surface of sand bed (i.e., @ 0D depth) show 26.68% increase in ultimate lateral load capacity and 45.54% decrease in deformation.

Table 6 shows percentage increase of ultimate lateral load and percentage decrease of deformation at Mud level with respect to Head level for number of reinforcement layers.

2layers of reinforcement combination performs better compared to the 1layer and 3layers reinforcement.

From table 6, the 2 layer reinforcement show 32.44% increase in ultimate lateral load capacity and 45.54% decrease in deformation.

Table 6: *Variation of parameter at Mud level for number of reinforcement*

L/D Ratio	Variation of parameter at Mud Level W.R.T Head level	Number of Reinforcement			
		1N GC @0D	2N GC @0,2D	3N GC @0,2,4D	2N GC @0,4D
4.7	% increase in Ultimate lateral load	26.82	32.44	25.84	29.26
	% decrease in Deformation	45.45	61.54	50	61.54

Conclusion

Based on the results of experiments performed the following conclusions are drawn**.**

- The monopile on reinforced sand beds perform better than the monopile on unreinforced sand beds regardless of the number of reinforcement layers and position of the reinforcement in the sand bed under static lateral loads.
- The Geocell reinforcement configuration greatly influences the performance of monopile subjected to lateral loads.
- The optimum number of reinforcement is found to be 2, since the monopile on 2 layer sand beds showed the highest value of lateral load carrying capacity and lesser deformation.
- The maximum efficiency of the Geocell may be derived when Geocell is placed at 0D depth (i.e., @ surface).

References

[1] *Ahmed M.A Nasr (2013). Experimental and theoretical studies of laterally loaded finned piles in sand. Canadian geotechnical journal 51: 381–393 (2014).*

[2] *Chowdhury Swaraj and Suman Shakti (2015). A reinforced Foundations Review of Studies on Geocell. Research Journal of Recent Sciences Geotextiles and Geomembranes.vol4(ISC-2014),24-30(2015).*

[3] *Chen, R., Sun, Y., Zhu, B. & Guo, W. (2015). Lateral cyclic pile-soil interaction studies on a rigid model monopile. Proceedings of the Institution of Civil Engineers: Geotechnical Engineering, 168 (2), 120-130.*

[4] *Moghaddas Tafreshi, S.N., Dawson, A.R., 2010b. Behaviour of footings on reinforced sand subjected to repeated loading e comparing use of 3D and planar geo-textile. Geotextiles and Geomembranes 28 (5), 434e447.*

[5] *Moghaddas Tafreshi, S.N., Dawson, A.R., 2010a. Comparison of bearing capacity of a strip footing supported on sand reinforced with 3D and with planar geo-textile. Geotextiles and Geomembranes 28 (1), 72e84.*

[6] *S.Bhattacharya.,S.Adhikari(2011). Experimental validation of soil–structure interaction of offshore wind turbines. Soil Dynamics and Earthquake Engineering. 31(2011)805–816.*

[7] *S.Bhattacharya,.D.M Woods., D Lombardi(2011). Similitude relationships for physical modelling of monopile-supported offshore wind turbines. International Journal of Physical Modelling in Geotechnics. 2011, 11(2), 58–68.*

[8] *Udit Shankar Dasgupta(2017). Design of Laterally Loaded Monopile Foundations in Sand for Offshore Wind Turbines. The University Of Texas at Austin.*

[9] *Vonmaries M.C (2011). Static and dynamic response of Monopile for offshore wind turbines. University of Wisconsin-Madison.*

[10] *Taha, A., El Naggar. M. H. and Turan, A. (2014). Experimental and numerical study on lateral behaviour of geosynthetic-reinforced pile foundation system. Geosynthetics International, 21, No.6, 352–363.*

8th International Engineering Symposium - IES 2019
March 13-15, 2019, Kumamoto University, Japan

Parametric Study on Seismic Response Analysis of Vertical Irregular RC Structures

Shreeneha V.S.[1], Chethan K.[2], Ravinesh Kumar[3], Bhagyashri P.[4]

1 *Department of Civil Engineering, University Visvesvaraya College of Engineering, Bangalore University, Jnana Bharathi Campus, Bangalore 560056, India. email:neha4897@gmail.com*
2 *Department of Civil Engineering, University Visvesvaraya College of Engineering, Bangalore University, Jnana Bharathi Campus, Bangalore 560056, India. email: k.chethu@gmail.com*
3 *Department of Civil Engineering, University Visvesvaraya College of Engineering, Bangalore University, Jnana Bharathi Campus, Bangalore 560056, India. email: ravineshkumar2093@gmail.com*
4 *Department of Civil Engineering, Government Engineering College, Ramanagara-562159, India. email: bhagyashriparla@gmail.com*

ABSTRACT With immense loss of life due to earthquakes, the seismic analysis of the structures has become significant. A regular structure i.e.; having mass and stiffness uniformly distributed through its height behave normally. The presence of irregularity in the structures subjected to earthquake load is a matter of concern. Therefore, inelastic static analysis has to be preferred to evaluate the seismic performance of these structures. The objective of this paper is to perform inelastic analysis such as pushover analysis on 3D RC regular and vertical irregular structures using Finite element method and carried out parametric studies to assess their seismic response. 5x 5 bay, ground + ten storied structure is analysed for different seismic zones of India. Modal, Response spectrum and Push over analyses are carried out to find time period, base shear, displacement, storey drift, and performance point and performance level of the structure.
Keywords *Modal, response spectrum, pushover analysis, performance point*.

INTRODUCTION

Earthquake creates violent shaking of ground, which leads to release of high amount of strain energy, and damage to structures depends upon the material that the structure is made up of, type of ground over which structure is constructed, type of earthquake wave (motion) and distribution of mass, stiffness and strength along the height of structure. Past earthquakes indicated in many literatures have revealed that, regular shaped structures perform better during an earthquake event. Many experimental and numerical studies have been carried out towards seismic analysis of regular and irregular structures. Chopra and Kan (1973) had studied the seismic response of series of eight storey shear structures subjected to the earthquake motion data. They had determined the effect of yielding of first storey on upper storeys and found that an ideal plastic mechanism and low yield force are required in the first storey, for safety of higher floors of the structure. Fernandez (1983) found that reduction in storey stiffness resulted in increased storey drift and structures with constant variation of mass and stiffness in vertical direction showed better seismic performance as compared to the structures with abrupt variations. Bariola and Brokken (1991) had determined the effect of strength and stiffness variation on nonlinear seismic response of multistory structure frames and results of analytical study showed that the time period of structure increased during seismic

excitation and this increase is more pronounced in case of weaker structures. Chintanapakdee and Chopra (2004) had evaluated the effects of strength, stiffness and combination of strength and stiffness irregularity on seismic response of multi-storey frames, it was concluded that irregularities in strength and stiffness when present in combination had the maximum effect on the seismic response. Lu et al. (2012) had performed non-linear time history analysis of the tall setback structure and found excessive damage concentration in storeys adjacent to setbacks, and concluded that effect of irregularity depended on extent and location of irregularity. To study further about the seismic response of multi storey irregular structures, in the present work, 3D reinforced concrete (RC) regular and vertical irregular structures are considered and finite element (FE) analyses are carried out.

DEFINITION OF STRUCTURES CONSIDERED FOR FE ANALYSIS

The present study adopts 3D RC structures with different types of vertical irregularity as per IS 1893 -2002 (Part - I). The seismic responses of these structures are been compared with that of the regular RC structure. The base plan size is 5 m x 5 m with five bays in both the horizontal directions. The following are the structures considered:

1. Regular RC structure (RM),
2. Vertical irregular RC structures (IRM1, IRM2 and IRM3).

The structural configuration and material properties considered are given in Table 1.

TABLE 1: STRUCTURAL CONFIGURATION

Type of structure	Special moment resisting RC frame
Grade of concrete	M 25(f_{ck}=25 N/mm^2)
Grade of Reinforcing steel	Fe 500(f_y = 500 N/mm^2)
Number of stories	G + 10
Floor height	3.0 m
Bottom Storey Height	3.0 m
Height of the Structure	33.0 m
Column size	600 mm X 600 mm
Beam size	300 mm X 450 mm
Slab thickness	150 mm
Live Load	2.0 kN/m^2
Floor finish Load	1.0 kN/m^2
Importance factor	1
Zone factor 'Z'	0.1 & 0.36
Response reduction factor 'R'	5

3D RC regular structure (RM)

The plan and 3D view of 3D RC regular structure respectively is shown is Figures 1(a) and 1(b).

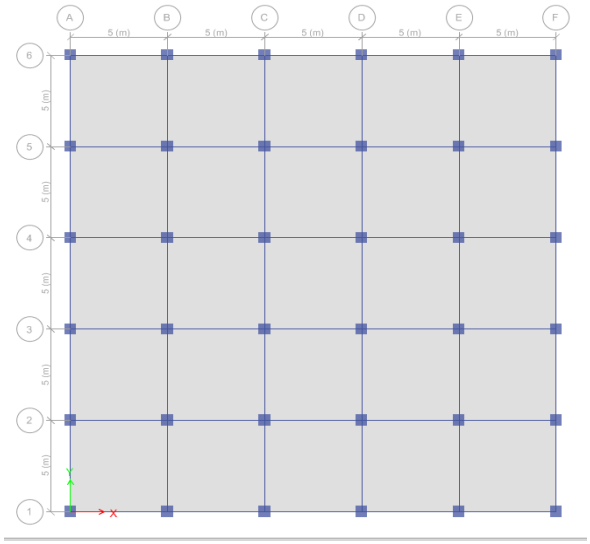

Fig. 1(a) Plan of Regular structure (RM)

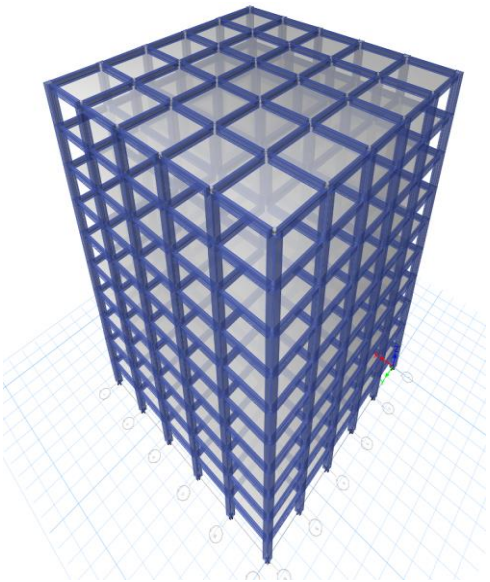

Fig. 1(b) 3D view of Regular structure

Structure with vertical irregularity (IRM1)

The stiffness irregularity limits considered as; the stiffness of the lateral load resisting system is less than 70 percent of that in the storey above or less than 80 percent of the average lateral stiffness of the above three storeys. The ground storey height is increased to 6m to form soft storey which is a type of vertical irregularity as shown in Figure 2.

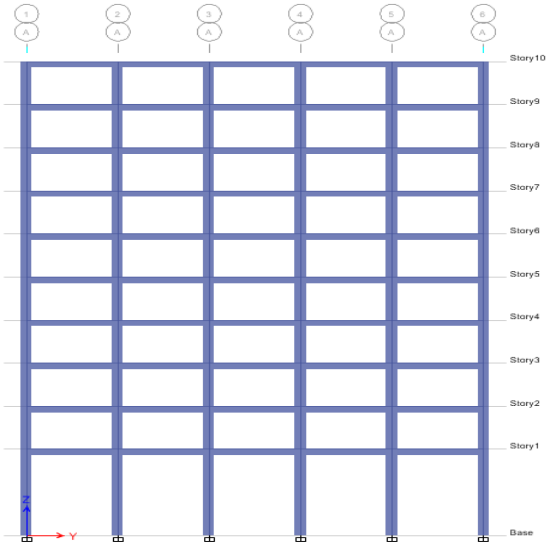

Fig 2 Elevation of Irregular Model (IRM1)

Structure with vertical irregularity (IRM2)

As per IS 1893:2002 the vertical irregularity has been considered when the intermediate storey height is increased to 6m i.e. the third storey height is increased to 6m to form vertical irregularity as shown in Figure 3.

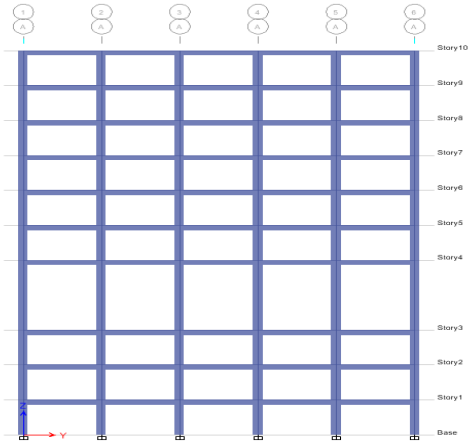

Fig 3: Elevation of Irregular Model (IRM2)

Structure with vertical irregularity (IRM3)

As per IS 1893:2002 the vertical irregularity has been considered by discarding the core beams and columns. The plan and elevation of IRM3 is as shown in Figures 4(a) and 4(b) respectively.

Fig.4 (a): Plan of Irregular Model 3 (IRM3)

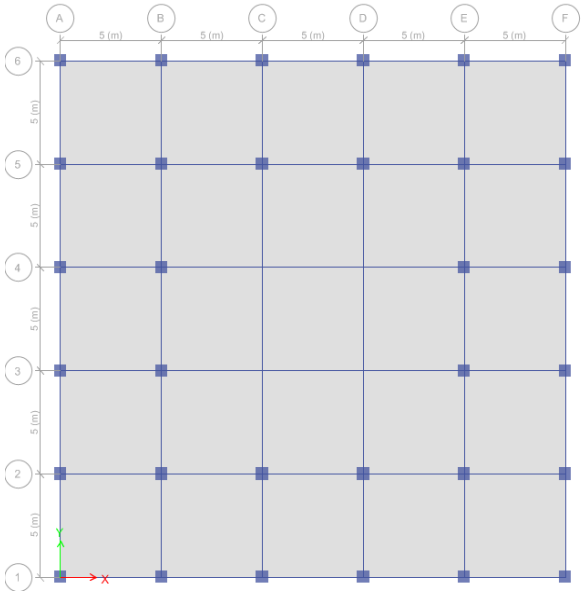

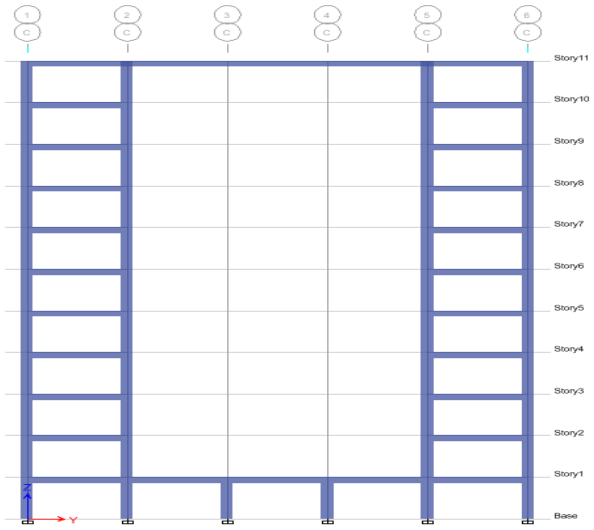

Fig.4 (b) Elevation of Irregular Model 3 (IRM3)

RESULTS AND DISCUSSION

Validation is performed on the previous literature done by Darshale and Shelke, (2016) on seismic response control of

vertically irregular reinforced concrete structure using base isolation. Three dimensional nonlinear response spectrum analyses is carried out by using finite element software for fixed base situation, time period and total base shear are taken into consideration as the comparison criteria.

Modal Analysis

Modal analysis characterizes the earthquake properties of an elastic structure by identifying its mode of vibration. The response of the structure is different at each of the different natural frequencies and these deformation patterns are called mode shapes. The fundamental time period for all models are obtained from the modal analysis and also calculated as per IS 1893:2002 (Part I) as given in Figure 5.

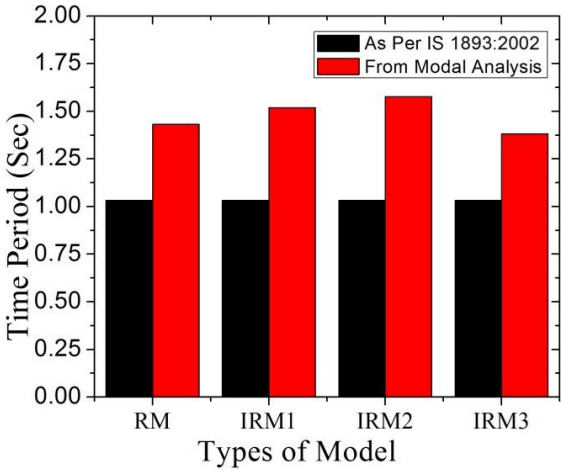

Fig. 5 Time period for different models

Equivalent Static Analysis

Equivalent static analysis converts a dynamic analysis into partly dynamic and partly static analyses for finding the maximum displacement (or stresses) induced in the structure due to earthquake excitation. In the present study it is carried out to obtain static base shear, i.e. an estimate of the maximum expected lateral force that occurs due to dynamic loading. The base shear is a function of mass, stiffness, height, and the natural frequency of the structure. The base shear of structures considered in the analysis is presented in Figure 6. It is observed that base shear of RM is 15.7%, 32% and 25.7% more when compared to IRM1, IRM2 and IRM3 respectively.

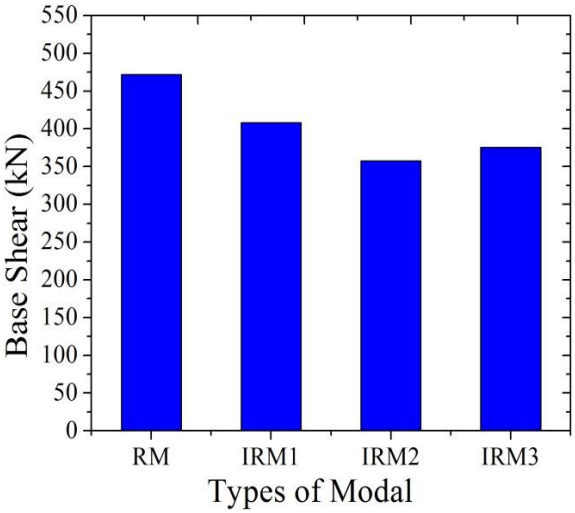

Fig.6 Base shear from equivalent static analysis

Response Spectrum Analysis

Response spectrum analysis of structures are carried out for the seismic Zone II, as per IS 1893-2002, using the response spectrum generated. Dynamic base shear, displacement, inter-storey drift and storey acceleration are obtained. Dynamic base shear obtained due to spectrum loads and scale factors are calculated as given in Table 2. It is observed that base shear of RM is 6.6%, 18.11% and 30.23% more when compared to IRM1, IRM2, and IRM3 respectively.

TABLE 2: SCALE FACTORS

Model	Static base shear	Dynamic base shear	Scale factor
RM	472.09	407.33	1.158
IRM1	407.92	381.92	1.068
IRM2	357.56	344.87	1.036
IRM3	375.54	312.76	1.200

Displacement responses

Displacement of structure is referred as lateral movement of the structure from it equilibrium position in horizontal direction. It is calculated for all the structures and it is observed that, irregular structure (IRM1) displacement is increased by 14.6%, 22.8%, and 16.2% to the

displacements of RF, IRM2, and IRM3 as shown in the Figure 7 highlighting the soft storey effect on the structure.

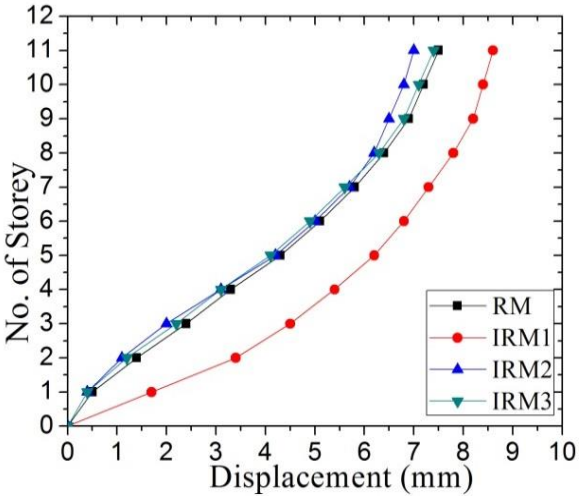

Fig. 7: Displacement variation with storey

Storey Drift responses

The storey drift is obtained for all types of structures and it is observed that, the storey drift is maximum at 'height/2' and all the structures are within the permissible limits i.e 0.004 times the storey height as per IS 1893-2002. Graph showing variation of storey drift with no. of storey is given in Figure 8.

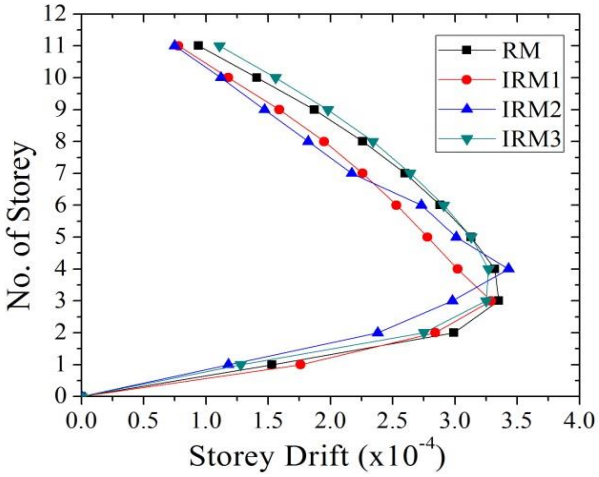

Fig. 8 Storey Drift variation with storey

Storey Acceleration

The acceleration or the rate of change of the velocity of the structure in motion is studied here. Sa/g is a factor (as per IS 1893:2002) denoting the acceleration response spectrum of the structure subjected to earthquake ground vibrations and depends on natural period of vibration and damping of the structure. 5% Damping is considered for the analysis of the structural models. It is observed that the maximum storey acceleration is observed in RM than other structures. The storey acceleration is presented in Figure 9.1

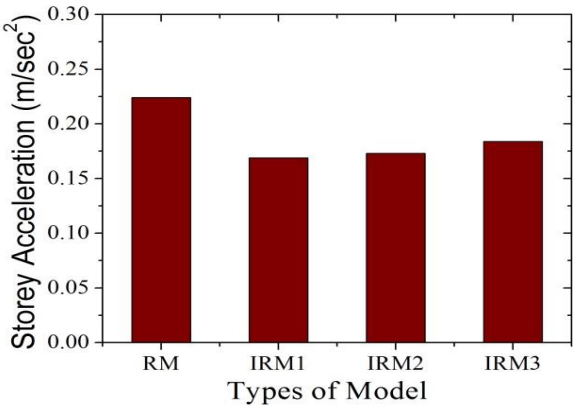

Figure 9: Storey Acceleration

Push over Analysis

Push over analysis is carried out for the regular and vertical irregular RC structures in fixed base conditions for zone II and V. Hinges formation, performance point and the performance level of the structures are tabulated in the Table 3. It is observed that all the structures considered for this study lies in an immediate occupancy level for both seismic zones. Base shear capacity is observed to be greater than the design base shear. Regular structures are having more lateral load capacity i.e. performance point compared to irregular structures due to reduction in flexure and shear demand. Base shear in zone V is more compared to zone II due to change in the zone factors, which predominately affects the base shear of the structure. Displacement in zone V is less compared to displacement in zone II, since capacities of the structures decreases in higher seismic zone, therefore the plot of demand spectrum and capacity spectrum changes as per the respective zones so that displacement of the structure in higher zone also decreases. The comparisons of performance between both the zones are given in Table 3.

TABLE 3: COMPARISON OF PERFORMANCE POINT BETWEEN ZONE II AND ZONE V

	Performance Point		Hinges Formed
Models In Zone II	Base Shear (kN)	Displace-ment (mm)	
RM	4016.076	334.40	1510
IRM1	3454.651	359.00	1340
IRM2	3532.410	365.80	1284
IRM3	3419.929	324.70	1313
Models In Zone V	Base Shear (kN)	Displace-ment (mm)	Hinges Formed
RM	4153.431	283.20	1684
IRM1	3932.045	320.20	1424
IRM2	3945.826	323.20	1630
IRM3	3865.059	283.10	1450

CONCLUSIONS

Time period is same for all the structures as per IS 1893:2002 as there is no consideration of the irregularity in the code and it is based only on the height of the structure. Time period obtained from modal analysis are 38% more as compared to IS 1893:2002. The storey acceleration of the irregular structure is 30- 35% less compared to regular structure. After the pushover analysis it is observed that all the models lies in the immediate occupancy (IO) level in both seismic zones, Zone II and Zone V. Therefore, as a result at this level structural damage is very low, although some minor structural repairs may be appropriate; these would generally not to be required prior to re-occupancy. Vertical irregular structures are having less lateral load capacity i.e. performance point compared to regular structures due to reduction in flexure and shear demand. Base shear in Zone V is more compared to Zone II due to change in zone factors which predominately affect the base shear of the structure. Displacement in Zone V is less compared to Zone II since the capacity of the structures decrease at higher seismic zones.

REFERENCES

1. Bariola V, Brokken S (1991) Influence of strength and stiffness on seismic structural behavior. Bulletin of Seismology and Earthquake Engineering, 23:427-434.
2. Chintanapakdee C and Chopra A K (2004) Seismic Response of Vertically Irregular Frames: Response History and Modal Pushover Analyses. Journal of Structural Engineering, ASCE, 130(8): 1177-1185.
3. Chopra A K, Kan C (1973) Effects of stiffness degradation on ductility requirements for multistorey buildings. Earthquake Engineering and Structural Dynamics, 2(1):35 -45.
4. Darshale S D, Shelke N L (2016) Seismic Response Control of Vertically Irregular R.C.C. Structure using Base Isolation. International Journal of Engineering Research 5(2): 683-68.
5. Fernandez J (1983) Earthquake Response Analysis of Buildings considering the effects of Structural Configuration. Bulletin of the International Institute of Seismology and Earthquake Engineering, Tokyo, Japan, 19:203-215..
6. Lu X, Chen Y, Mao Y (2012) Shaking table model test and numerical analysis of a super tall building with high-level transfer storey. Structural design of tall and special buildings, 21(10): 699–723
7. PankajAgarwal and Manish Shrikhande. Earthquake resistance design of structures, PHI Publication.
8. Varadharajan S, Sehgal V K,Saini B (2014) Fundamental time period of RC Setback Buildings, 5(4), Concrete Research Letters, India.
9. IS: 456-2000 - Code of Practice for Plain and Reinforced Concrete, Bureau of Indian Standards, New Delhi.
10. IS: 1893 (Part – 1) – 2002 - Code of Practice for Criteria for Earthquake Resistant Design of Structures, Part 1: General Provisions and Buildings, Bureau of Indian Standards, New Delhi.
11. IS 13920: 1993, "Indian standard code of practice for ductile detailing of reinforced concrete Structures subjected to seismic forces", Bureau of Indian Standards, New Delhi.
12. IS: 875 – 1987 Code of Practice for Design Loads (other than Earthquake) for Buildings and Structures, Part 1: Dead Loads, Part 2: Imposed Loads, Part 5: Special Loads and Load Combinations, Bureau of Indian Standards, New Delhi.

8th International Engineering Symposium - IES 2019
March 13-15, 2019, Kumamoto University, Japan

Numerical Analysis of Pile Supported Railway Embankment

Aiswarya S [1], B. R. Jayalekshmi [2] and R. Shivashankar [3]

1 *Department of Civil Engineering, National Institute of Technology Karnataka, Surathkal, Mangalore 575025, India. email:aiswaryas950@gmail.com*
2 *Department of Civil Engineering, National Institute of Technology Karnataka, Surathkal, Mangalore 575025, India. email:br.jaya@gmail.com*
3 *Department of Civil Engineering, National Institute of Technology Karnataka, Surathkal, Mangalore 575025, India. email:shivashankar.surathkal@gmail.com*

ABSTRACT: Pile supported embankments are now a days widely used for constructing railway lines as a rapid construction technique to increase the bearing capacity and to reduce the total and differential settlements. In case of piled embankments, major portion of the train loads are carried by the piles, thus causing a considerable reduction in the load carried by the soil. This paper presents a study on the numerical analysis of a piled railway embankment in PLAXIS. The elastic settlements on the surface of the embankment are analysed under static loads considering two types of piles (i) end bearing piles (ii) floating piles. Study reveals that the spacing and diameter of piles can influence the track settlement in a piled embankment.

***Keywords**: Piled Embankment, Railway Track, End Bearing Piles, Floating piles, PLAXIS*

INTRODUCTION

Railway lines usually passes through a variety of terrains and soil profiles. In order to avoid the change in level due to terrain it is essential to raise railway line by providing embankment. When a track passes through poor soils, such as the clays or silts of high plasticity and compressibility it is necessary to provide suitable ground improvement to decrease the settlement.

Large and frequent cyclic train loading from haul and passenger trains often leads to progressive track deterioration. The excessive deformation and degradation of ballast and unacceptable differential settlement of track necessitate frequent and costly track maintenance. A proper understanding of load transfer mechanism and subsequent deformations is the key element for safe and economical design (Indraratna and Nimbalkar 2011).

A well designed piled embankment has the advantage that it requires less construction time and yields little embankment settlement. In order to construct effective and efficient piled embankments, design guidelines are needed. Guidelines for design of piled embankments exist. However, still there are uncertainties and inadequacies in the design guidelines especially for embankments on floating piles. The design of an embankment on floating piles involves complex soil-structure interaction. For such problems, numerical methods such as finite element analysis can be utilised. In the present study numerical analysis of a pile supported railway embankment is done in Plaxis 2D considering two cases (i) end bearing piles (ii) floating piles. The effect of variation in diameter and spacing of piles in varying the settlement has been studied.

PRESENT STUDY

The system is a single lane broad gauge ballasted embankment on soft ground that is improved by RCC driven piles. Figure (1) shows the cross section of the

embankment. The section is taken as per RDSO guidelines. It consists of 2m high embankment with a 9.5m wide crest and a side slope of 1:2, and 0.5m thick ballast layer of slope 1:1.5.The system consists of 1.5m thick coarse grained fill below the embankment. Piles are driven through a very soft clay stratum of 20m depth. Dense strata is available below this. In the present study, the effect of both end bearing as well as floating piles on surface settlement are considered. End bearing piles are driven for a depth of 22m from the bottom of embankment.

In case of floating piles, in order to achieve that the entire embankment load is supported by the floating pile, the pile length l_{crit} should be chosen such that the change in vertical stress at the surface of the soft soil is zero. (Satibi 2009)

$$l_{crit} = \sqrt{\frac{2\, q_{emb}}{\beta \gamma'}}$$

$$q_{emb} = \gamma H$$

$$\beta = \frac{2r}{R^2 - r^2} k \sin\emptyset'$$

$$R = Spacing/2$$

Where, r is the radius of the pile and R is the radius of circular cell. *k* value can be taken as 1 for driven piles. *φ'* is the friction angle for soft soil. H is the height of the embankment. γ' is the effective unit weight of soft soil. Critical length of pile is calculated for pile diameters 0.3m, 0.4m and 0.5m by varying the spacing as 2D, 3D, 4D and 5D, where D is the diameter of pile. The maximum critical length obtained for each diameter of pile among different spacing conditions is taken as critical length of pile for that particular diameter. Thus, the length of floating pile is taken as 10.2m for 0.3 diameter, 10m for 0.4m diameter and 13m for 0.5m diameter pile. RCC driven piles with grade M40 are used. Static loading is given as an axle load of 20t [5].

NUMERICAL MODELLING

Model

A two dimensional plane strain model was created to simulate the behaviour of piled railway embankment using PLAXIS software. The horizontal width of the finite element model was taken as 30m, which is more than 5 times the half of embankment width. Due to the symmetry of the embankment, half of the embankment was modelled for the finite element analysis. The boundary conditions were set as normally fixed on left and right boundaries, while base was restrained in all directions. The top surface of the embankment was free for translation. Analysis was carried out for various pile diameters of 0.3m, 0.4m, and 0.5m. In addition, the spacing for each diameter of pile was varied as 2D, 3D, 4D and 5D. Piles were modelled as embedded beam rows in soil. Rails and sleeper were modelled using plate elements. Rail pad was modelled using rectangular element with a thickness of 8mm. Interface elements were given in between sleeper and soil.

Material Properties

Detailed material properties of soil are shown in table (1). End bearing and skin friction values were calculated separately for each diameter and length of pile. Properties of rail components are as shown in table (2).

RESULTS AND DISCUSSION

End bearing Piles

Figure (2) shows the track settlement pattern for embankment on end bearing piles for different diameter and spacing conditions. The settlement is increasing with increase in spacing as well as for increase in diameter. In case of bearing piles, the total load is transferred at the base to the hard strata which can be considered as an imaginary foundation of same size as that of pile group. As the size of pile and spacing increases, the size of pressure bulb below the pile group is more which increases the settlement. Percentage variation in track settlement with increase in diameter is the least for 3D spacing as seen in table (3). Hence, among different spacing it is seen that the cross sectional size of the pile is less relevant in the 3D spacing configuration.

Floating Piles

Figure (3) shows the track settlements obtained for embankment supported on floating piles. Here, track settlement pattern is different from those on end bearing piles. Settlement is decreasing with increase in spacing between piles. When piles are at closer spacing, pressure bulbs of individual piles may overlap, causing more stress in overlap zones, causing more settlement. Floating piles with close spacing behaves more or less as a raft. But at larger spacing, piles act individually that cause reduction in settlement. From table (4) and figure (3) it can be seen that there is considerable reduction in settlement for 3D spacing as compared to 2D spacing, whereas further increase in spacing has less effect in reducing settlement.

CONCLUSIONS

The following conclusions are deduced from this study:

- Track settlement is more in the case of track supported on floating piles at 2D spacing due to confinement effect of closely spaced piles and 3D spacing is found to be optimum.
- The track settlement is less for closer spacing in embankment on end bearing piles.
- Type of pile, diameter and spacing of piles should be based on the optimum condition of settlement as well as economy point of view.

REFERENCES

[1] British Standard, BS8006-1 (2015), Code of Practise for Strengthened/Reinforced Soils and Other Fills, Section 8.3.3, British Standard Institution.
[2] Indraratna B. and Nimbalkar S. (2011), Implications of Ballast Breakage on Ballasted Railway Track Based on Numerical Modelling, Proc. 13th International Conference of the International Association for Computer Methods and Advances in Geomechanics, Australia, May 9-11 ,pp. 1085-1092.
[3] Plaxis 2D Material Models Manual (2015), Website: https://www.plaxis.com
[4] Plaxis 2D Reference Manual (2015), Website: https://www.plaxis.com
[5] RDSO Guidelines GE: G-5 (2005), Guidelines on soft soil: Stage construction method.
[6] S. Satibi (2009), Numerical Analysis and Design Criteria of Embankments on Floating Piles, Ph.D. thesis, University Stuttgart, Germany, pp.85-92.
[7] Terzaghi, K and Peck, R B, (1987), Soil Mechanics in Engineering Practice, 2nd ed., McGraw Hill, New York, pp.419-440.
[8]Thach P. N. et al (2013), Effect of Pile Method in Mitigating Embankment Vibrations from a High Speed Train, ASCE Journal, Vol. 139, No.12, pp.2-4.

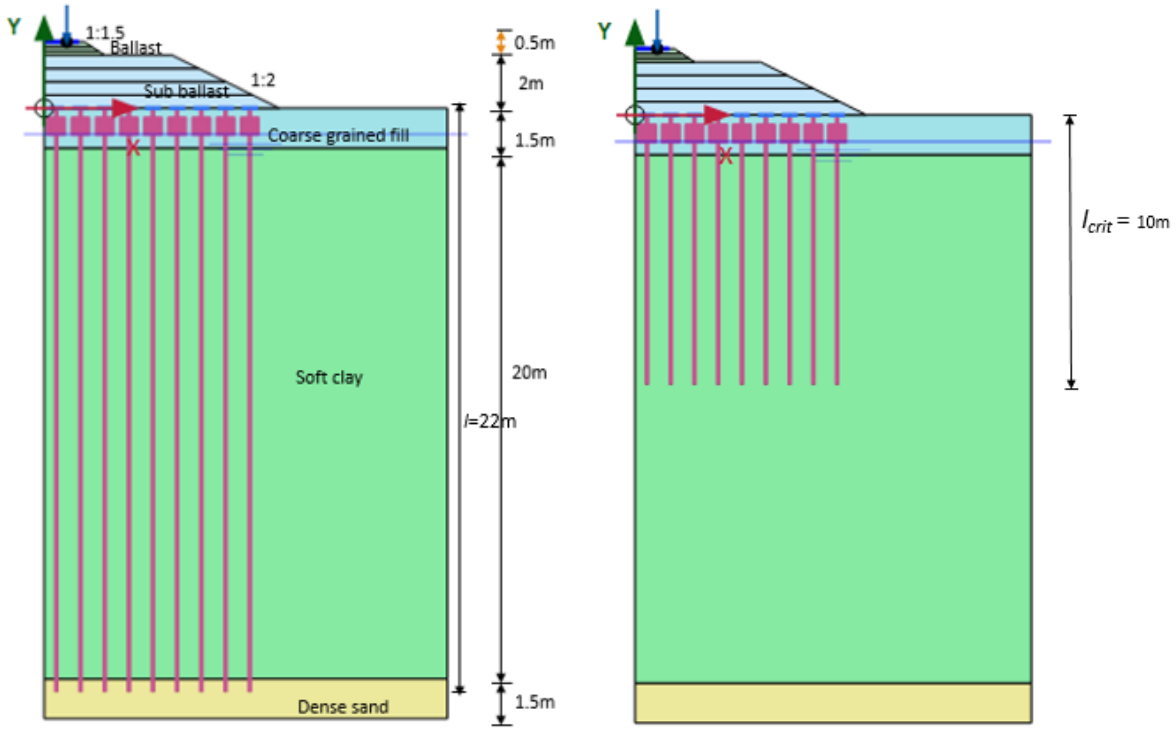

(a) **(b)**

Fig.1 Cross sectional details of the rail embankment with (a) End bearing piles (b) Floating piles (0.4m diameter and 3D spacing)

Table 1 Properties of soil

Soil	Ballast	Embankment	Coarse grained fill	Soft clay	Dense sand
Material Model	Hardening Soil	Mohr-Coulomb	Mohr-Coulomb	HS-Small	Mohr-Coulomb
Unit Weight (kN/m^3)	20	19	19	16	20
Modulus of Elasticity (kN/m^2)	$2.75x10^5$	$1.5x10^5$	$10x10^4$	2000	$1.5x10^5$
Cohesion (kN/m^2)	20	20	20	20	10
Friction angle	50	40	38	20	45
Dilatancy angle	10	0	0	0	10

Table 2 Properties of Rail Components

Properties	Young's modulus	Poisson's ratio	Axial Stiffness(kN/m)	Flexural Rigidity(kNm^2/m)
Rail	210 GPa	0.28	$6.624x10^6$	$6.323x10^3$
Rail pad	0.5GPa	0.495	-	-
Sleeper	50 GPa	0.3	$3.71x10^6$	$12.37x10^3$

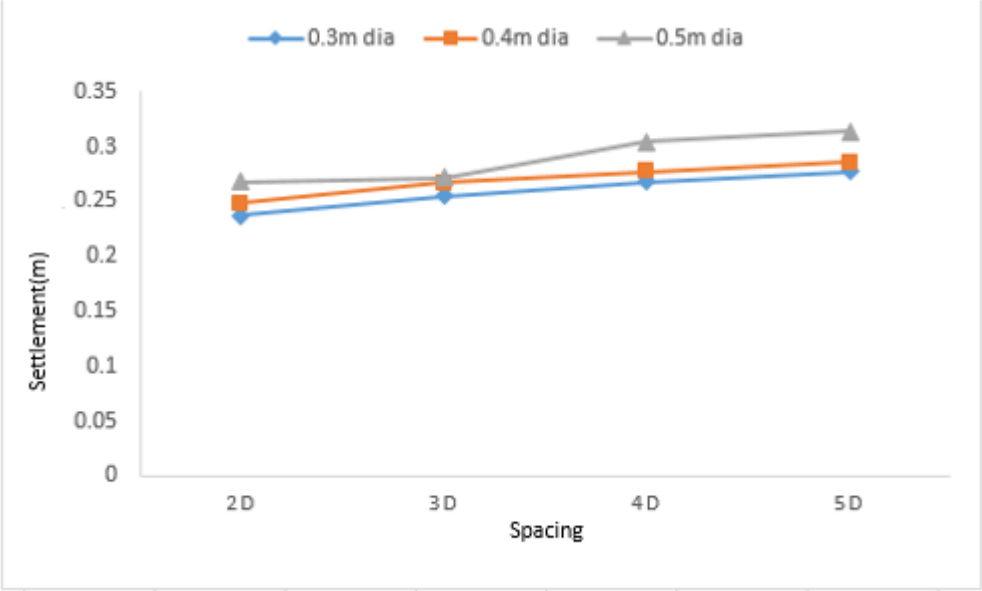

Fig.2 Settlement of Embankment on End Bearing Piles

Table 3 Percentage Variation in Settlement with Different Diameters of End Bearing Piles

Spacing / Diameter(m)	2D	3D	4D	5D
0.3	0.2367m	0.2552m	0.2682m	0.277m
0.4	4.7%	4.4%	3.3%	2.8%
0.5	12.9%	6.4%	13.5%	13.0%

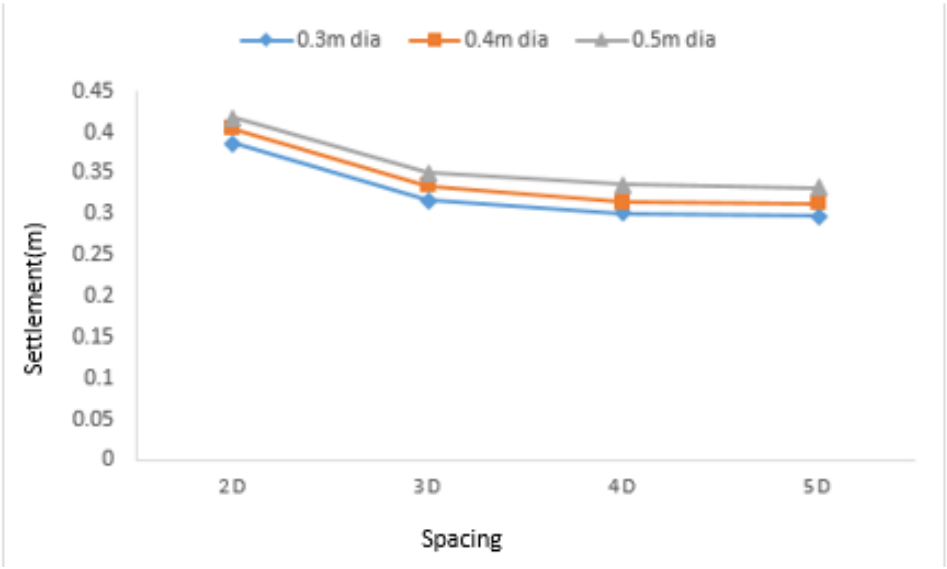

Fig.3 Settlement of Embankment on Floating Piles

Table 4 Percentage Reduction in Settlement with Spacing of Floating Piles

Spacing / Diameter (m)	2D	3D	4D	5D
0.3	0.3867m	17.9%	22.1%	22.9%
0.4	0.4044m	17.2%	22.18%	22.67%
0.5	0.418m	16.14%	19.68%	20.55%

8th International Engineering Symposium - IES 2019
March 13-15, 2019, Kumamoto University, Japan

Torsional Behaviour of Buildings with Vertical Stiffness Irregularity under Earthquake Load

Archana J Satheesh [1], B.R. Jayalekshmi [2] and **Katta Venkataramana[3]**

1 *Department of Civil Engineering, National Institute of Technology Karnataka, Surathkal, Mangalore 575025, India. email:archana.satheesh247@gmail.com*
2 *Department of Civil Engineering, National Institute of Technology Karnataka, Surathkal, Mangalore 575025, India. email:br.jaya@gmail.com*
3 *Department of Civil Engineering, National Institute of Technology Karnataka, Surathkal, Mangalore 575025, India. email:ven.nitk@gmail.com*

ABSTRACT: Torsional effects become significant in irregular buildings when they are subjected to lateral loads such as wind or earthquakes. The present study aims to evaluate the seismic response of vertically irregular 10 storey RC buildings with varying interstorey height or modified stiffness along the height and also with a stipulated amount of in-plan eccentricity. Transient analysis is carried out by subjecting the three dimensional finite element building frames models to El-Centro ground motion and their torsional behavior is evaluated in terms of variation in fundamental natural period, base shear and floor rotation. The results show that the eccentricity of the irregularities has the highest influence on the seismic response when stiffness variation is present in the bottom storey of the buildings.

***Keywords**: Irregularity, Stiffness, Torsion, Transient analysis*

INTRODUCTION

Regular building is more of an idealization and practically, majority of the buildings are irregular in nature. Major seismic codes define structural irregularities into irregularity in plan and in elevation, but quite often structural irregularity is present as a combination of both the types. Irregularity, due to asymmetric placement of mass, stiffness and strength along the plan, causes the most severe damages since it leads to floor rotations (torsional response) in addition to translations as observed from earthquake cases in the recent past making their design for earthquake more complicated This problem has been investigated for over 60 years since the emergence of earthquake engineering as a distinct field of engineering (Anagnostopoulos et al. (2015)). Most of the studies in the past dealt with singe storey idealized models for the study of irregularity in buildings which later paved way for studies on complex multistorey building systems (De Stefano and Pintucchi (2008)). Lin et al. (2001) developed a simplified analysis procedure to consider accidental torsion in building design relative to codes and determined the accuracy by evaluating it against the measured accidental torsion determined from motions of 12 nominally symmetric buildings. Varadharajan et al. (2012) summarized the research works done in the past regarding different types of structural irregularities. Criteria and limits specified for these irregularities as defined by different codes of practice (IS1893:2002, EC8:2004 etc.) were discussed and it was observed that the limits of both plan and vertical irregularities prescribed by these codes were comparable. Dutta et al. (2017) studied the seismic behavior of case studies comprising different configurations of irregular structures analysed by response spectral as well as non-linear time history analyses. The results of the analysis indicate that the irregular

structures may have lesser base shear owing to lesser mass as compared to a similar reference regular structural system. Chance of higher stress concentration as well as higher ductility demand was observed in the members around the irregularity and hence strength enhancement in the vicinity of vertical irregularity may improve the overall seismic performance of the irregular structures. Dimova and Alashki (2003) and D'Ambrisi et al. (2013) proves, that even under small accidental eccentricities or lower values of eccentricity leads to considerable variations leading to irregular behavior of buildings.

A key input in seismic response assessment and a major reason for the asymmetry is the application of appropriate set of ground motions (Chakroborty and Roy (2016) and Bensalaha et al. (2017)). Many studies have been based on the variation of mode properties and frequency of the irregular buildings. Bosco et al. (2013) and Bhosale et al. (2017) described new methods and checked the adequacy of fundamental mode properties and the ratio of uncoupled torsional to lateral frequencies for the quantification of vertical irregularity and comparison with seismic risk indicators. Varadharajan et al. (2014) proposed parameter to quantify mass, stiffness and strength irregularity in terms of both magnitude and location is proposed on the basis of the dynamic characteristics of the building. Ouazir et al (2018) investigated the influence of the coupling of torsional and soft-first-story effects to the seismic behavior of reinforced concrete frame buildings. Similar work was carried out by Archana et al. (2018) on the effect of mass and stiffness irregularities due to change in shear wall positions along the plan of the building. Therefore literature pertaining to the combination of stiffness irregularity along the height of a building and the in-plan eccentricity is limited in general. In this study the seismic response parameters for buildings with a combination of in-plan torsional irregularity and stiffness irregularity along the height of buildings is evaluated in detail.

STRUCTURAL IDEALISATION

Reinforced concrete building frames of 10 storeys high were considered in this study. 3D finite element models of buildings with storey height of 3m and length of each bay as 4m were modeled with 4 bays in each direction. The dimensions of building components were adopted based on structural design as per Indian Standards IS 456:2000 and IS 13920:2016. The beam and column dimensions were taken as 300mm x 400mm and 500mm x 500mm respectively. The thickness of floor slab and foundation slab were taken as 0.15m and 0.5m respectively. The M25 grade concrete and Fe415 grade steel were considered as the materials for structural elements and live loads of 3.0 kN/m^2 and 1.5 kN/m^2 were considered on floor and roof respectively. In the initial set of buildings considered, stiffness irregularities were provided at the bottom and top floors. A change in inter-storey height at the upper and lower levels results in a change in storey stiffness. As per IS 1893-2016, the criterion of vertical stiffness irregularity is considered to exist when stiffness of a storey is less than that of the storey above it. The initial height of storey was taken as 3m. Four inter-storey height variations were provided in the buildings varying from 3m to 4m to give modified storey stiffness K_1 to K_4. K_0 denotes the building configuration with in-plan irregularity without change in the inter-storey height or modified stiffness. The modified stiffness K_1 to K_4 were applied at the bottom and top levels of the buildings by varying the height of the corresponding floor level. Further a second set of buildings were considered in which torsional irregularities are present in addition to the modified stiffness. For incorporating eccentricity, column dimensions were varied in a pattern about a central Y axis, keeping the center of mass constant. Numerous cases with stiffness irregularities along plan were generated in this manner, out of which, a group of 8 configurations IS0-IS8 with increasing eccentricity pattern was

considered in this study as given in Table 1. The dynamic eccentricities (e_d) of the buildings were calculated as per IS 1893-2016 and are represented in terms of the total plan width (L) for the buildings configurations. $IS0_b$ denoted the configuration without in-plan eccentricity but stiffness variation at the first storey level whereas $IS4_t$ denotes the configuration with in-plan eccentricity of 0.14 e_d/L as well as stiffness modification at the top storey. 10R represents the regular building without any kind of irregularity.

Table 1 Building configurations with in-plan eccentricity

Building configuration	e_x (m)	e_d/L
IS0	0.00	0.05
IS1	0.24	0.07
IS2	0.48	0.09
IS3	0.71	0.12
IS4	0.95	0.14
IS5	1.41	0.18
IS6	1.86	0.22
IS7	2.07	0.24
IS8	2.67	0.30

METHODOLOGY

This study attempts to evaluate the response of vertically irregular frames with modified stiffness at the bottom and top floor levels of a building and to identify the effects of torsional coupling on them. Vertically irregular buildings with stiffness variations at the top and bottom of the buildings with eight different plan configurations IS1-IS8 having torsional irregularities as per IS 1893:2016 were considered. In-plan torsional irregularity is said to exist only when the irregularity coefficient which is the ratio of the maximum displacement in the direction of the lateral force at one end of a floor to the minimum horizontal displacement at the far end of the same floor in the same direction is more than 1.5. The torsional irregularity coefficient values of the eight different configurations considered in this study with e_d/L in the varying from 0.05 to 0.3, ranges from 1.317 to 1.862. 130 buildings generated in this manner were modeled in LS Dyna software and were subjected to time history analysis using El Centro 1940 earthquake data. The variation of fundamental natural period, base shear and roof rotation for the buildings with the combination of stiffness irregularity along the height as well as in plan under the effect of earthquake ground motion is evaluated in this study.

RESULTS

The dynamic responses of the group of stiffness irregular buildings in terms of fundamental natural period, base shear ratio and roof rotation and their comparison with respect to that of regular frames are evaluated in this study.

Fundamental Natural Period

Fundamental natural period of vibration is an inherent property of a structure and is determined by carrying out Eigenvalue analyses on building frames. Fig 1 represents the variation of fundamental lateral natural period of the irregular frames with modified storey stiffness K_1 to K_4 at the top and bottom levels. The natural period of the regular buildings, 10R is obtained as 1.07s and that of the IS0 configurations with non-eccentric vertical stiffness asymmetry are in the range of 1.07s to 1.56s. It can be observed with change in stiffness of a storey, the natural period increases. The buildings with modified stiffness at the base of the building, has the highest variation in natural period in comparison with the regular buildings. This variation increases with increase in stiffness from K_1 to K_4. IS0 with the modified storey stiffness K_4 at the top storey level has variation in time period of 28%.

The natural period of IS1-8 configurations with increasing e_d/L due to variation in column dimensions along the plan, are higher compared to the in-plan regular frame buildings. This variation in natural period also increases with increase in eccentricity of the configurations. The natural period in buildings with combination of vertical stiffness irregularity and in-plan irregularity at the lower floor even with lower values of in-

plan eccentricity (less than 0.1 e_d/L), has significant variation with respect to the regularbuildings.

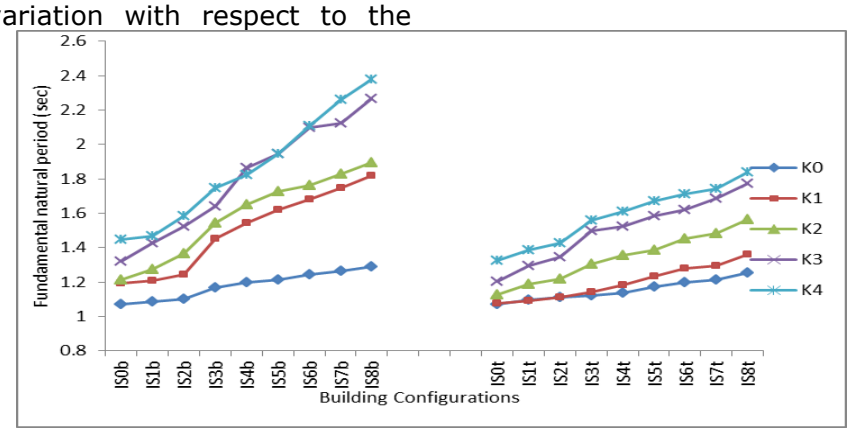

Fig 1 Variation in fundamental natural period

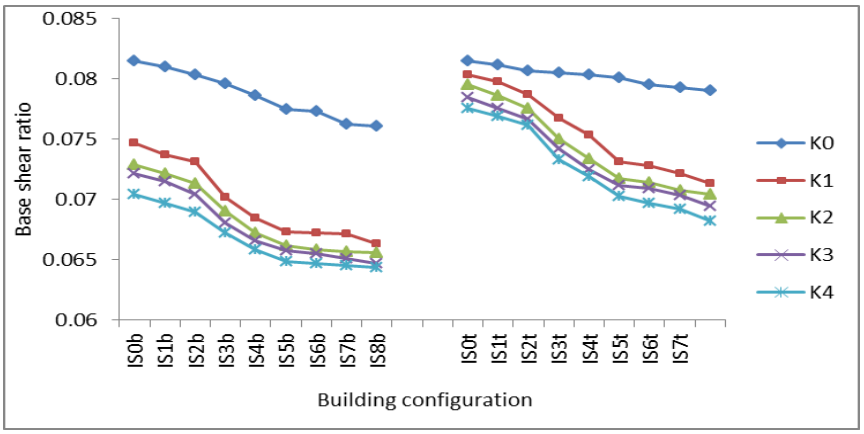

Fig 2 Variation in base shear ratio

$IS8_t$ with modified stiffness of K_3-K_4, has maximum variation in natural period of 33 % with respect to the plan regular IS0 configurations. Hence, due to introduction of eccentricity in the upper levels of stiffness irregular configurations with stiffness reduction also causes considerable variation in its natural period. When the lower storey has reduction in stiffness along with in- plan eccentricity, natural period increases and becomes highest in $IS8_b$ with a stiffness modification of K_4. In this case natural period increases the by maximum 71.8 % in comparison to corresponding IS0 buildings due to high torsional coupling. In the case of irregular frames with stiffness reduction from less than 80% and e_d/L less than 0.13 the variation of natural period is nominal and less than 20%. It can thus be interpreted that with the inclusion of stiffness modification along the height of the building, the natural period increases and reaches a maximum when the variation is present in the bottom levels which is further amplified when in combination with in-plan eccentricity upto 84% with respect to the regular buildings.

Seismic Base Shear

Seismic base shear of buildings with stiffness irregularity in plan as well as elevation, subjected to El-Centro ground motion is as shown in Fig 2. The seismic base shears of the buildings are expressed in terms of their total seismic weight (W). These base shear ratio of the regular configuration was in the range of 0.0815W. It can be observed that with the addition of stiffness irregularity by varying the inter-storey height, there is significant decrease in base shear in comparison to that of the regular frames especially when the stiffness modification is present in the lower floors compared to the presence of stiffness variation in the upper floor levels.

This decrease in base shear occurs due to the increase in natural period in stiffness irregular buildings. While considering the initial set of buildings without eccentricity, due to the presence of the soft storey at the base of the building, base shear ratio decreases by a maximum of 28%.

In the second set of buildings, it can be observed that the base shear decreases with increase in e_d/L. The variation of base shear ratio due to stiffness modification is amplified by the change in eccentricity. The highest variations of base shear of irregular frames with respect to the regular frames are observed $IS8_b$ configurations with modified storey of stiffness K_4 as 29%. The maximum variation of base shear due to eccentricity is obtained in $IS8_b$ as 21% with respect to IS0. Even among buildings with modified storey stiffness K_1, due to in-plan eccentricity at the lower levels, increase of base shear ratio by 20% with respect to regular frames and 21% with respect to IS0 frames is observed.

Roof Rotation

The Roof rotation is estimated by considering the highest storey displacements of the extreme corners of the roof of the building model.

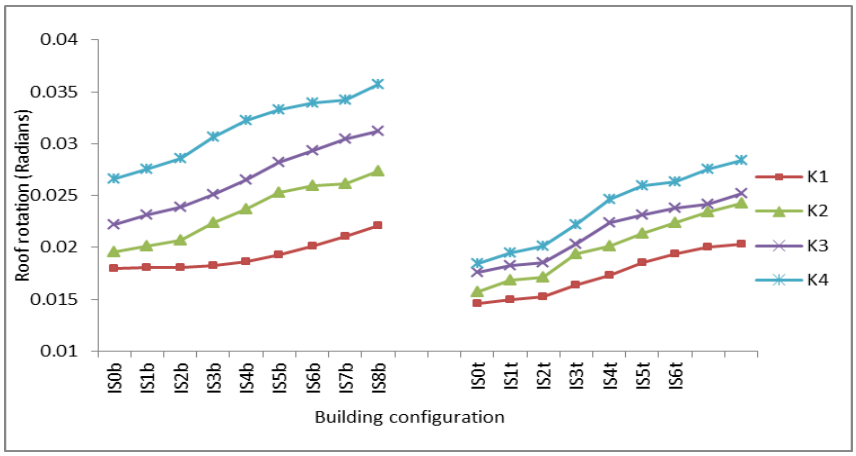

Fig.3 Variation in roof rotation

Roof rotation in radians is obtained by dividing the relative displacement by the width of the building. It can also be seen from Fig 3 that when the longer columns are present in the bottom level of the building, the rotation of the roof is the highest due to the increased flexibility. The roof rotation of buildings with a modified stiffness K_4 at the bottom level increases by 6 times in comparison with that of the regular frames.

Among the second set of buildings with stiffness irregularity along height as well as in-plan, $IS8_b$ with the highest e_d/L has the highest roof rotation, and IS0 without eccentricity has minimal roof rotation. The maximum rotation among all the irregularity combination cases is observed in $IS8_b$ with a stiffness modification K_4 at the lower floor as 0.037 rad; whereas the minimum rotation is observed in $IS1_t$ with a modified stiffness K_1 at the upper floor level as 0.0035 rad. Due to varying e_d/L, a maximum variation of 150% is observed in IS8 configuration with respect to the corresponding plan regular IS0 buildings. $IS8_t$ with a minor stiffness modification K_1 at the upper levels increases the roof rotation considerably by 7% to 34% implying that incorporation of in-plan eccentricity significantly escalates the variation in roof rotation due to stiffness irregularities. When modified stiffness K_1 is present at the bottom half of the buildings combined with the highest eccentricity value, a maximum variation in roof rotation gets doubled in comparison to that of the vertically irregular IS0 buildings.

CONCLUSIONS

The vertically irregular building frames with in-plan stiffness eccentricity were analysed and parametric studies were conducted to determine the effect of in-plan eccentricity on stiffness irregular

frames by considering different inter-storey heights at the bottom and top level of the frames. The seismic responses of structures are expressed in terms of fundamental natural period, absolute maximum responses of base shear and roof rotation. The effects of eccentricity in the considered building configurations were assessed and the following conclusions are drawn,

- Vertical stiffness irregularity at the bottom level of the frames increases the natural period by 6% to 21% in comparison to that of the frames with irregularity at the upper levels. This effect is further amplified due to in-plan eccentricity in the building frames by a maximum of 30.5% with respect to the plan regular IR0 buildings. Even in buildings with stiffness modification K_1 at the upper floor level, there is an amplification of natural period by 45% due to in-plan as well as vertical stiffness irregularity.
- Base shear ratio increases by 9% to 18% with modified stiffness at the upper floor levels in comparison to that at the bottom levels. The base shear ratio increases by 28.9% due to the high in-plan eccentricity at the bottom with respect to IR0 buildings.
- Roof rotation is more when the storey with modified stiffness is at the bottom of the frames by 44% as compared to the change in stiffness at the upper levels. In-plan eccentricity leads to an increase of 125% in roof rotation with respect to plan regular frames. The roof rotation increases by a maximum of 95% due to in-plan eccentricity even in the case of stiffness irregularity due to stiffness modification K1.

REFERENCES

[1]. Anagnostopoulos, S A et al (2015), Earthquake induced torsion in buildings: critical review and state of the art, Earthquakes and Structures, Vol. 8, No.2, pp. 305–377.

[2]. Bensalah, M D (2011), Estimation of the torsion effect on buildings subjected to seismic load, roceedings of the 8th International Conference on Structural Dynamics, EURODYN Leuven, Belgium, 4-6 July, 2751-2756.

[3]. Bosco, M et al (2013), An analytical method for the evaluation of the in-plan irregularity of non-regularly asymmetric buildings, Bulletin of Earthquake Engineering, Vol. 11, No.5, pp. 1423–1445.

[4]. Bhosale, A S et al (2017), Vertical Irregularity of Buildings: Regularity Index versus Seismic Risk, ASCE-ASME Journal of Risk and Uncertainty in Engineering Systems, Vol. 3, No.3, pp. 04017001-9.

[5]. Chakroborty, S and Roy, R (2016), Seismic Behavior of Horizontally Irregular Structures: Current Wisdom and Challenges Ahead, Applied Mechanics Reviews, Vol. 68, No.6.

[6]. D'Ambrisi, A et al (2012), The Effect of Common Irregularities on the Seismic Performance of Existing RC Framed Buildings, Seismic Behaviour and Design of Irregular and Complex Civil Structures, Geotechnical, Geological and Earthquake Engineering, Vol. 24, pp. 47-56.

[7]. De Stefano, M and Pintucchi, B (2008), A review of research on seismic behaviour of irregular building structures since 2002, *Bulletin of Earthquake Engineering*, Vol. 6, No.2, pp. 285–308.

[8]. Dimova, S L and Alas I (2003), Seismic Design of Symmetric Structures for Accidental Torsion, *Bulletin of Earthquake Engineering Vol.* 1, pp. 303–320.

[9]. Dutta, S C, et al (2017), Seismic Behaviour of Irregular Structures, Structural Engineering International, pp. 526-545.

[10]. Ouazir, M et al (2018), Inelastic seismic response of torsionally unbalanced structures with soft first story, Asian Journal of Civil Engineering, Vol. 19, No.5, pp. 571–581.

[11]. Sadashiva, V K et al (2011), Effects Of Coupled Vertical Stiffness-Strength Irregularity Due To Modified Interstorey Height, Bulletin of the new Zealand Society for Earthquake Engineering, Vol. 44, No. 1, pp 31-46.

[12]. Satheesh, A J et al (2018), Torsional Behaviour of Plan Asymmetric Shear Wall buildings under Earthquake Loading, AET 2018, Grenze Scientific Society, pp. 84-90.

[13]. Varadharajan, S et al (2012), Review of different Structural irregularities in buildings, Journal of Structural Engineering, Vol. 39, No. 5, pp. 393-418.

[14]. Varadharajan, S et al (2014), Seismic response of multistory reinforced concrete frame with vertical mass and stiffness irregularities: RC buildings, irregular buildings, mass and stiffness irregularity, The Structural Design of Tall and Special Buildings, Vol. 23, No.5, pp. 362–389.

8th International Engineering Symposium - IES 2019
March 13-15, 2019, Kumamoto University, Japan

A review of Experimental Studies on Geosynthetic Reinforced Pile Supported Railway Embankments

Sreya M V [1], B R Jayalekshmi [2] and **Katta Venkataramana[3]**

1 *Department of Civil Engineering, National Institute of Technology Karnataka, Surathkal, Mangalore 575025, India. email:sreya56vellur@gmail.com*
2 *Department of Civil Engineering, National Institute of Technology Karnataka, Surathkal, Mangalore 575025, India. email:br.jaya@gmail.com*
3 *Department of Civil Engineering, National Institute of Technology Karnataka, Surathkal, Mangalore 575025, India. email:ven.nitk@gmail.com*

ABSTRACT: Construction of embankment over soft soils is a very challenging task due to the risk of bearing failure, excessive settlement and lateral movement of foundation soil. Pile supported embankment is a useful ground improvement method to settle these problems. During the past twenty-five years, biaxial geogrids have been used as reinforcement in the construction of railroad beds and ballasts to improve their performance and structural integrity. In this paper, a review of several published field and large-scale laboratory test findings relating to the reinforcing ability of geogrids and bearing capacity of piles are presented.
***Keywords**: Train-induced vibration, Reinforced mechanism, Geogrid, Geogrid reinforced Pile supported embankments*

INTRODUCTION

Countries such as the United States, China, Canada, Australia and India rely heavily on railways for the transportation of passenger services and bulk commodities. Given the fact that roadways are already saturated and congested, the only viable alternative for the growth of land transportation remains the railways that can either be achieved by the upgradation of existing tracks or by the construction of new ones as per the requirement. These countries have introduced faster and heavier trains in recent years owing to a growing demand from commuters and industry. This has resulted in an increase in track degradation and lateral instability, therefore the frequency and cost of maintenance. This problem becomes more severe under conditions of railroad ballast fouling (Selig and Waters, 1994). Particles of railroad ballast become degraded in railroad tracks under heavy cyclic loading, thereby increasing the overall compressibility (Anderson and Fair, 2008).
In the past, the track superstructure has received major attention; however, the present review is more oriented towards the substructure design, i.e., the design is related to the material and thickness of various base layers of a track. The substructure attains significance because the performance of superstructure is directly dependent on the support provided from beneath.

Train-induced vibration

The response of the rail structure to the wheel axle loads is the source of the largest amplitude of train-induced vibration. The magnitude of these induced waves is influenced by the magnitude of the applied axle load and the rate of application of the load. These waves usually exist in a low frequency band (0-10Hz), and can propagate well beyond the limits of the rail support structure.
In order to quantify and characterize the dynamic motion of the embankment under the loading of a train, it is necessary to measure this motion. The most common instruments used for measuring the displacement of an embankment under loading are accelerometers, geophones and extensometers.
Both geophones and accelerometers carry out the same function although they are

constructed differently. When the geophone moves as a result of vibration, the coil moves through the magnetic field, this produces a voltage which can be measured and interpreted as acceleration. Geophones are very rugged and reliable, but the use of geophones for measurement of low frequency movements (such as 1-2Hz for the loading due to train axles) becomes very expensive (Hall, 2000).

Modelling of Train-induced Displacement

A large quantity of research has been devoted to modelling the effects of dynamic loading, and specifically the modelling of train-induced dynamic loading. Modern modelling follows Finite Element (FE), Finite Difference (FD) and Boundary Element (BE) methods. Finite Element method has emerged as the most common approach and has advantages over analytical modelling. For instance, FE models can be used to determine stress concentrations and for a three dimensional analysis. Despite these benefits, the models are still limited to simplified material model for soil (Hall, 2003).

EXPERIMENTAL STUDIES ON GEO-SYNTHETIC REINFORCED RAILWAY EMBANKMENT

The use of geosynthetics in railroad tracks has been studied in the past, and it has been proven that geosynthetics generally improve track performance by reducing the deformation and degradation of railroad ballast (Indraratna and Salim, 2003). The application of geosynthetics to granular materials both in permanent pavements and for heavy-haul roads is well known, but only limited studies have been conducted on railroad ballast that is significantly coarser (Selig and Waters, 1994; Indraratna et al., 2011).

In addition, only limited studies have focused on the fundamentals of interaction between grids and ballast aggregates under large strain conditions when subjected to cyclic loading. A numerical model that can capture the envelope of the maximum plastic deformations generated during individual load cycles and that facilitates the prediction of accumulated deformation at a large number of load cycles is usually adequate for railroad track practice (Suiker and de Borst, 2003).

Reinforcement Mechanism

Geogrids are used in two ways to reinforce track bed materials. When included at the bottom or within a ballast layer, the primary benefit is an extension of maintenance cycle, i.e., the period between ballast cleaning and replacement operations. In the second way, geogrids are used beneath a rail line is to reinforce the sub-ballast. In this case, the primary purpose of geogrids is to increase the effective bearing capacity of an underlying soft subgrade. Reinforcing mechanism with geogrids is shown in Figs.1 (Perkins, 1999).

Several authors have studied the reinforcement mechanisms associated with the interaction of geogrids and unbound aggregate. Confinement of the aggregate by the geogrid results in a reduction in the amount of lateral spreading and an increase in the lateral stress within the aggregate, thereby increasing its stiffness which reduces the dynamic (recoverable) deformation for each load cycle. An increased modulus of the aggregate results in an improved vertical stress distribution onto the underlying subgrade. The effect is that the surface deformation will be less and more uniform. A reduction in the shear stress within the subgrade leading to lower vertical strain (Perkins, 1999).

It is desirable to optimize performance and provide a background to improve railroad track design. Extensive laboratory experiments were conducted on fresh and recycled railroad ballast under both dry and wet conditions to investigate the effectiveness of three types of geosynthetics using a large-scale prismoidal test chamber (Indraratna and Salim, 2003). Various types of geosynthetic reinforcements placed in unbound ballast have usually improved the performance of rail transportation systems, but unfortunately, the optimal location and number of geogrid layers have not been established. A few studies have attempted to analyze the effects of multiple geosynthetic reinforcement through model studies (Raymond and

Ismail, 2003) and full-scale field trials (Montanelli and Recalcati, 2003).

Indian Railways have recommended a minimum thickness of a sub-ballast layer equal to 1m for tracks laid on fine-grained soil subgrades. Because a sub-ballast layer consists of free draining granular material, this provision becomes uneconomical where the track passes through a long stretch of clayey soil and requires the granular material to be hauled from over a long distance. Use of geosynthetics may provide an economical solution to reduce the sub-ballast thickness under such conditions. The railroad track is one of those few applications where geosynthetics serve multiple functions, namely, drainage, separation, filtration and reinforcement (Chawla S et al., 2016). Model tests provide an alternative way to directly reflect the behavior of the prototype under simulated conditions.

A few studies on reinforced track models available in literature are all based on single sleeper tests (Indraratna et al., 2006; Indraratna and Nimbalkar, 2013). Except for Shin et al. (2002), all of these model studies were conducted to investigate the reduction in ballast degradation due to the provision of a geogrid. Thus, the main focus of these studies was the behavior of the ballast. Accordingly, a thin rubber mat was used in these studies to simulate the subgrade in place of the actual soil. The dimensions of the materials used in the construction of the models such as ballast particles, geogrid apertures, etc. were not scaled down in the study reported by Shin et al. (2002),

Le Pen et al. (2013) demonstrated that there are differences in the shape distributions associated with the different particle size bins of the same material, so that the particle shape distributions do not necessarily scale. However, for a scaling factor of 3, the differences attributable to size effects were less than those between full size ballasts from different sources meeting relevant industry specifications.

Image analysis (Shahu and Yudhbir, 1998; Sowmiya, 2013) has shown the differences in particle shape distribution associated with size to be similarly small. Monotonic drained triaxial tests on scaled and full size ballast showed differences in strength and stiffness between the scaled and full size ballast to be negligible at the range of confining stresses relevant to track loading (Sowmiya, 2013). Thus, from a mechanical point of view, the use of scaled ballast was acceptable. This is inconsistent with the findings of Sevi (2008) and Le Pen et al. (2013). Design and construction protocol of geogrids as reinforcement are well established in this fields (Giroud and Han, 2004).

Brown, Kwan and Thom (2007) reported results of full-scale tests conducted at Nottingham Transportation Engineering Center at the University of Nottingham (UK) that were intended to identify the key parameters that influence geogrid reinforcement of railway ballasts. Repeated loads of 20kN at 2Hz were applied for 30,000 cycles through a loading platen consisting of a section of rectangular hollow steel 250mm wide (0.7 m long) representing the sleeper. This gave a contact stress of 114 kN/m^2 beneath the berm which is about half of the maximum expected on an actual track.

The tests with geocell decreased the vertical and lateral deformation of sub-ballast assemblies at any given frequency (Biabani M M et al., 2016)**.** The discrete element method can provide an insight into the distribution of contact force chains, and average contact normal and shear force distributions, which cannot be determined experimentally. Geosynthetics effectively control the long-term and transient strains in the ballast layer, with the obvious benefit of reducing maintenance costs.

The study of Nimbalkar S et al (2016) showed that the aperture size of geogrids in the range of 1.1 times the mean particle size of the ballast was most effective. The placement of shock mat on a concrete bridge contributed to reduced ballast breakage. The geogrids and geo-composites decreased the settlement of the ballast by almost 35%, a result that would have significant implications on track maintenance. Geocells influenced the sub-ballast behavior under cyclic loading, particularly at low confining pressure and high frequency (Indraratna B et al., 2014).

EXPERIMENTAL STUDIES ON GEO-SYNTHETIC REINFORCED RAILWAY EMBANKMENT WITH PILE SUPPORT

Embankments have been increasingly used to support highways and railways; however, the number of sites with suitable soil conditions has decreased. As a result, more and more embankments have been constructed on land that was previously considered unsuitable. Vertical stiff piles are driven through the soft layers and embedded in a competent substratum beneath to support the granular earth embankment above. The surface and embankment loads are partially transferred to the piles by arching action that occurs in the granular embankment fill material resulting stress reduction on the subsoil.

The inclusion of tensile reinforcement enhances the load transfer mechanism and considerably minimizes the maximum as well as differential settlements (Prasun Halder, 2016) as shown in Fig.2 (Joel A Sloan, 2011). When geotextile layer is used as reinforcement, it is kept at a certain distance above the pile head to avoid the risk of damage through rubbing action. The settlement of the embankment surface reduces with the increasing layers of geotextile having high tensile modulus. The maximum and differential settlements decrease with increase of geotextile stiffness value up to 5000kN/m but further increase in stiffness value does not affect the total as well as differential settlement. The stress reduction ratio also gets increased with the increase of geotextile stiffness but when the stiffness value crosses 6000kN/m, the stress concentration ratio becomes almost constant.

In comparison with some other ground improvement methods, geosynthetic-reinforced pile-supported (GRPS) embankments can be constructed quickly, do not require soft soil replacement and staged construction and meet strict settlement requirements; therefore, they become one of the favored technologies for the construction of embankments on soft soil foundations. A GRPS embankment, consisting of a soft soil foundation, piles, a geosynthetic-reinforced platform (or mattress), and embankment fill, is a complex soil–structure system. The interaction among these components influences the load distribution and the functions of the reinforcement.

The key mechanisms of GRPS embankments have been considered to be soil arching, the tensioned membrane effect, and stress concentration due to modulus difference between piles and soil Han and Gabr (2002) defined soil arching as the phenomenon that differential movement between piles and subsoil induces shear stresses in the fill, which transfer a large portion of the vertical loads to piles and reduce the vertical stresses on the subsoil between these piles. When a rigid platform (e.g. footing) is above piles and subsoil, there are no soil arching and tensioned membrane effect because there is no differential movement but there is still stress concentration on the piles due to their modulus difference between piles and soil.

However, several factors, including the properties of embankment fill, the height of the embankment, the size and layout of the piles (or pile caps), the properties of soft soil, and the properties and number of geosynthetics, play important roles in the performance of GRPS embankments. Piles used in GRPS embankments are mostly end-bearing but some embankments are supported by floating piles. When piles and/or large pile spacing are used, pile caps are often needed to reduce the clear spacing between piles and the differential settlement on top of the embankment (Lai H J, 2016).

Many researchers have carried out experimental studies on pile-supported embankments in the past. But only a few studies are there in the field of railway embankment. Unlike some earlier studies in which only a unit cell of a GRPS embankment or an embankment without any slope supported by four piles (Van Eekelen et al., 2012) was investigated, this study employed a scaled full embankment model with side slopes on piles with pile caps subjected to a vertical load and investigated the influences of the embankment fill (fine sand or fine sand mixed with fibres), the clear spacing of pile

caps, and the pile type on the soil-arching effect and the tensioned membrane effect.
The cohesion of the embankment fill had a significant influence on soil arching, which distributed more loads from the weight of the embankment and the applied pressure to the piles. The embankment fill with cohesion resulted in a larger pile efficacy and smaller settlements of the subsoil between the pile caps and on the crest of the embankment than that without cohesion.
Floating piles also could be used to support GRPS embankments similar to end-bearing piles. Han J (2002) pointed out that with an increase of the applied pressure on the crest of the embankment, the floating piles began to settle thus resulting in re-distribution of the applied load among the pile caps, the geosynthetic reinforcement and the subsoil. Because of the stiffness difference between the piles and their surrounding soil is less than that for end-bearing piles, floating pile results in less arching. Soil arching starts to form at a ratio of the embankment height to the clear spacing of pile caps of 0.5 to 0.7 (Han J, 2002). They got the critical height for full soil arching was at 1.1 to 1.5 times the clear spacing of pile caps. Regardless of fill cohesion, pile type and the clear spacing of pile caps, the vertical earth pressure on the edge of the pile cap comes higher than that in the centre.
Particle breakage and confining pressure have a significant influence on the permanent deformation of ballast. During cyclic loading, breakage was most significant at low and high values of confining pressure, with minimal breakage at some intermediate value. Increasing confining pressure to an optimal range of 30-75kPa results in minimum breakage, which improves the track performance, and reduces the maintenance costs (Indraratna B, 2011).
Subgrade modulus was found to be the most influential track parameter on the overall track responses. The next most important track parameters were depth of sub-ballast, rail moment of inertia, and tie spacing. Reduction in tie spacing and improvement in rail moment of inertia both improve the load-spreading capability of a track structure, reducing the maximum values of stresses and strains inside the track support structure. Subgrade modulus was found to have the greatest influence on overall track responses. The subgrade stresses decreased as the sub-ballast depth increased, reducing the tie deflection and sub-ballast strain significantly and indicating an overall track improvement, which was also reflected in the improvement in the track modulus. However, the stresses and strains in the ballast layer increased marginally (about 10%) and might have some effect on the ballast maintenance cycle.
Centrifugal model test was first conducted to simulate the deformation process of collapsible loess (as 1:100 of the prototype) The settlement of embankment built on collapsible loess foundation without improvement does not meet the post-construction settlement constraint for embankment of ballasted track of high-speed railways (Wang C et al., 2012). The use of rigid piles can significantly reduce embankment settlement and the rate of post-construction settlement. It was also observed that the negative friction developed in the piles varies with pile spacing and pile configurations (Wang C et al., 2012).

CONCLUDING REMARKS

A review of the present state-of-the-art for using geogrids as reinforcement with pile supported railway track bed construction has been presented. Many experimental studies have been carried out so far in the area of railway embankment.
The GRPS techniques can reduce the total, differential and lateral movements. Geogrid reinforcement plays a major role in this, particularly on soft subgrades. Slope stability of the embankment increases with the use of the GRPS system. Construction is faster, since the loading rate not dependent on the rate of consolidation of soil. The elastic deformation of the track for an individual load cycle is reduced due to the stiffening effect of the reinforcement. Geogrid reinforced embankments require less maintenance.

SCOPE FOR FUTURE WORK

- Small scale laboratory tests can be conducted to study the dynamic behaviour of GRPS railway embankment.
- Role of sand drain, to speed up the consolidation and to improve the strength and drainage of subgrade, can be studied.
- Effect of providing suitably spaced sheet or ordinary piles on either side of embankment to reduce the slippage of soil mass can be examined.
- Numerical modelling can also be used to study the effect of different slopes of railway embankment.
- The seismic behaviour of GRPS railway embankment can be investigated.

REFERENCES

[1]. Anderson W F and Fair P (2008), Behavior of railroad ballast under monotonic and cyclic loading, Journal of Geotechnical and Geoenvironmental Engineering, 134(3), 316-327.
[2]. Biabani M M, Indraratna B and Ngo N T (2016), Modelling of geocell-reinforced subballast subjected to cyclic loading, Geotextiles and Geomembranes, 44(4), 489-503.
[3]. Brown S F, Kwan J and Thom N H (2007), identifying the key parameters that influence geogrid reinforcement of railway ballast, Geotextiles and Geomembranes, 25(6), 326-335.
[4]. Chawla S and Shahu J T (2016), Reinforcement and mud-pumping benefits of geosynthetics in railway tracks: Model tests. Geotextiles and Geomembranes, *44*(3), 366-380.
[5]. Giroud J P and Han J (2004), Design method for geogrid-reinforced unpaved roads. II. Calibration and applications, Journal of Geotechnical and Geoenvironmental Engineering, 130(8), 787-797.
[6]. Halder P and Singh B (2016). Effect of Geosynthetic Reinforcement on Pile-Supported Embankment Constructed on Soft Soils.
[7]. Hall L (2000). Simulations and analyses of train-induced ground vibrations, Doktorarbeit, Division of Soil and Rock Mechanics, Royal Institute of Technology, Stockholm, 4, 69.
[8]. Hall L (2003), Simulations and analyses of train-induced ground vibrations in finite element models, Soil Dynamics and Earthquake Engineering, 23(5), 403-413.
[9]. Han J and Gabr M A (2002), Numerical analysis of geosynthetic-reinforced and pile-supported earth platforms over soft soil, Journal of geotechnical and geoenvironmental engineering, 128(1), 44-53.
[10]. Han J, Song S and Xu C (2016), Scaled model tests on influence factors of full geosynthetic-reinforced pile-supported embankments.
[11]. Indraratna B and Salim W (2003), Deformation and degradation mechanics of recycled ballast stabilised with geosynthetics, Soils and Foundations, *43*(4), 35-46.
[12]. Indraratna B, Biabani M M, and Nimbalkar S (2014), Behavior of geocell-reinforced subballast subjected to cyclic loading in plane-strain condition, Journal of Geotechnical and Geoenvironmental Engineering, 141(1), 04014081.
[13]. Indraratna B, Khabbaz H, Salim W and Christie, D (2006). Geotechnical properties of ballast and the role of geosynthetics, Institution of Civil Engineers Proceedings Ground.
[14]. Indraratna B, Salim W, and Rujikiatkamjorn C (2011), Advanced rail geotechnology–ballasted track, CRC press.
[15]. Indraratna B, Tennakoon N C, Nimbalkar S S, and Rujikiatkamjorn C (2013), Behaviour of clay-fouled ballast under drained triaxial testing.
[16]. Indraratna B and Nimbalkar S (2013), Stress-strain degradation response of railway ballast stabilized with geosynthetics, Journal of geotechnical and geoenvironmental engineering, 139(5), 684-700.
[17]. Lai H J, Zheng J J, Zhang R J and Cui M J (2016), Visualization of the formation and features of soil arching within a piled embankment by discrete element method simulation, Journal of Zhejiang University-SCIENCE A, 17(10), 803-817.
[18]. Lai H J, Zheng J J, Zhang R J, and Cui M J (2016), Visualization of the formation and features of soil arching within a piled embankment by discrete element method simulation, Journal of Zhejiang University-SCIENCE A, 17(10), 803-817.
[19]. Le Pen L M, Powrie W, Zervos A, Ahmed S, and Aingaran S (2013), Dependence of shape on particle size for a crushed rock railway ballast, Granular Matter, 15(6), 849-861.
[20]. Madshus C and Kaynia A M (2000), High-speed railway lines on soft ground: dynamic behaviour at critical train speed, Journal of Sound and Vibration, 231(3), 689-701.
[21]. Montanelli F and Recalcati P (2003), Geogrid reinforced railways embankments: design concepts and experimental test results, In IABSE Symposium Report (Vol. 87, No. 6, pp. 1-9), International Association for Bridge and Structural Engineering.
[22]. Nimbalkar S and Indraratna B (2016). Improved performance of ballasted rail track using geosynthetics and rubber shockmat, Journal of Geotechnical and Geoenvironmental Engineering, 142(8), 04016031.
[23]. Perkins S W (1999), Mechanical response of geosynthetic-reinforced flexible pavements, Geosynthetics International, 6(5), 347-382.
[24]. Raymond G, and Ismail I (2003), The effect of geogrid reinforcement on unbound aggregates, Geotextiles and Geomembranes, 21(6), 355-380.
[25]. Selig E T, and Waters J M (1994), Track geotechnology and substructure management, Thomas Telford.
[26]. Sevi A F (2008), Physical modeling of railroad ballast using the parallel gradation scaling technique within the cyclical triaxial framework.
[27]. Shahu J T (1998), Model tests on sands with different angularity and mineralogy, Soils and foundations, 38(4), 151-158.
[28]. Shin E C, Kim D H, and Das B M (2002), Geogrid-reinforced railroad bed settlement due to

cyclic load, Geotechnical and Geological Engineering, 20(3), 261-271.
[29]. Sloan J A (2011), Column-supported embankments: full-scale tests and design recommendations (Doctoral dissertation, Virginia Tech).
[30]. Sowmiya L S (2013), Analysis and experimental investigations of railway tracks with and without geosynthetic reinforcement (Doctoral dissertation, IIT Delhi, India (unpublished)).
[31]. Suiker A S, and de Borst R (2003), A numerical model for the cyclic deterioration of railway tracks, International journal for numerical methods in engineering, 57(4), 441-470.
[32]. Van Eekelen S J, Bezuijen A, Lodder H J, and van To E A (2012), Model experiments on piled embankments Part I, Geotextiles and Geomembranes, 32, 69-81.
[33]. Van Eekelen S J, Bezuijen A, Lodder H J and van Tol E A (2012), Model experiments on piled embankments Part II, Geotextiles and Geomembranes, 32, 82-94.
[34]. Wang C, Zhou S, Guo P, and Wang B (2014), Experimental analysis on settlement controlling of geogrid-reinforced pile-supported embankments on collapsible loess in high-speed railway, International Journal of Pavement Engineering, 15(9), 867-878.

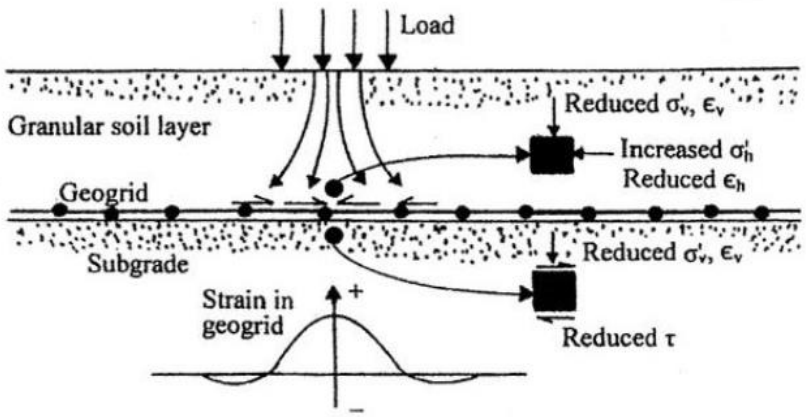

Fig.1 Reinforcement mechanism of geogrid in granular soil over a subgrade (Courtesy - Perkins, 1999)

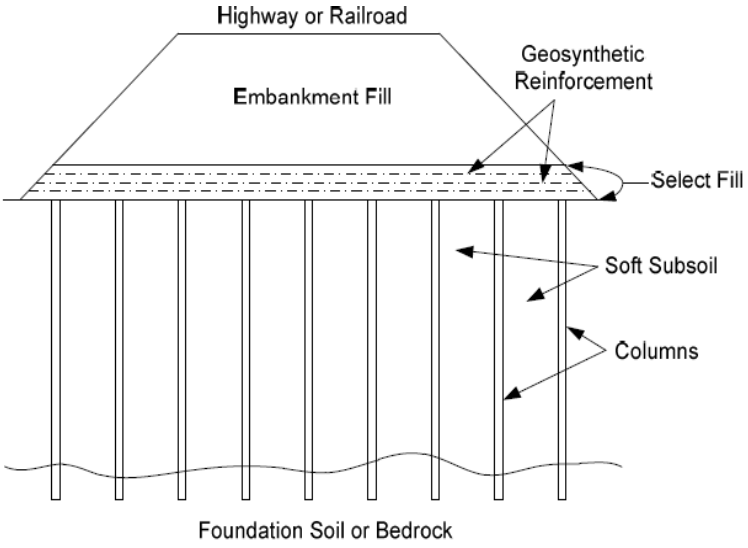

Fig.2 Geosynthetic-reinforced column-supported embankment (Courtesy- Joel A Sloan, 2011)

8th International Engineering Symposium - IES 2019
March 13-15, 2019, Kumamoto University, Japan

A Brief Review on Dynamic Response of Retaining Walls

Amrita[1], R Shivashankar [2] and **B R Jayalekshmi[3]**

1 *Department of Civil Engineering, National Institute of Technology Karnataka, Surathkal, Mangalore 575025, India. email:23amritar@gmail.com*
2 *Department of Civil Engineering, National Institute of Technology Karnataka, Surathkal, Mangalore 575025, India. E-mail: shivashankar.surathkal@gmail.com*
3 *Department of Civil Engineering, National Institute of Technology Karnataka, Surathkal, Mangalore 575025, India. E-mail: br.jaya@gmail.com*

ABSTRACT: A brief review on the response analysis of retaining wall under dynamic excitation is given. There are different approaches available in the literature for the purpose of analysing the behaviour of retaining wall under dynamic conditions. A few theoretical, experimental and numerical approaches carried out by some researchers and descriptions about the results of their studies are described in this paper.

***Keywords**: retaining wall, dynamic excitation*

INTRODUCTION

A retaining wall is a structure which is used for retaining soil mass, known as backfill, laterally so that the soil can be maintained at two different elevations. The lateral earth pressure exerted by retained backfill on the wall and subsequent deformation of soil / wall are two main aspects of engineering design and analysis of retaining walls. So, the stability and the deformation of the wall are main criteria to be analysed. Under dynamic loading the response of such a system also becomes important as the dynamic force developed due to excitation influences the lateral pressure and the deformation of soil / wall. In order to determine the dynamic response of a retaining wall, there are different approaches that can be made use of. These are mainly classified as:

1. Analytical solutions
2. Experimental studies
3. Numerical methods

The analytical approach for the determination of dynamic lateral earth pressure of retaining walls can be carried out by failure wedge equilibrium theory, which is mainly represented as limit equilibrium analysis (plasticity theory or extension of Coulomb's wedge theory) or by sub-grade modulus (elasticity analysis) method, in which the retained soil is considered as elements with stiffness modulus such as shear beams or spring systems.

The experimental investigation are normally conducted using the shaking table test and the results obtained are realistic ways of proposing current theories as well as verifying newly proposed theories. The most advanced shaking table tests are the shaking table incorporated with the centrifuge and large-scale shaking table test.

Nowadays, engineering numerical techniques are developing very fast, which renders numerical methods as a crucial tool in engineering research, design, and analysis.

In the literature, there are quite a number of analytical solutions, experimental investigations and numerical studies that have been conducted to determine the dynamic response of retaining walls with different soil conditions, different wall structures, different dynamic and structural conditions etc. In this review, a very few theoretical developments, experimental findings and numerical modelling techniques have been discussed briefly.

Review

Yogendrakumar et al. [22] carried out the dynamic response analysis of reinforced-soil retaining wall by reviewing the iterative equivalent linear elastic approach and the incremental elastic approach. The finite element programs QUAD4B AND TARA-3 were used and the results were compared with the field test data. The incremental elastic approach used in TARA-3 gave the best prediction of dynamic wall response when compared to the other method. Similar experimental verification of the two limit equilibrium design approaches-NCMA and AASHTO/FHWA was carried out by El-Emam [5]. The response from these design guidelines where compared to the responses from a series of reinforced soil wall models tested on shaking table. It was suggested that the current design methods tend to underpredict the size of the soil failure wedge at different input base acceleration amplitudes and the current equations used to predict the angle of soil slip surface were modified to match measured values. It indicated that the equations suggested to calculate horizontal acceleration coefficient are non-conservative for input base acceleration larger than 0.3g and different modifications have been suggested to reduce conservativeness or to increase the safety of these design guidelines as a whole.

The dynamic response of retaining walls with cohesive sandy materials with up to 30 kPa cohesion value subjected to three different earthquake events, various free field PGAs and different backfill cohesions were studied through a dynamic numerical modelling analysis by Osouli and Zamiran [14] and the results were compared with empirical and analytical solutions of Mononobe-Okabe (MO) method, Seed and Whitman, and NCHRP method for cohesive sandy and cohesionless materials. While taking into account the boundary conditions, a new development to the viscous boundary efficiency to the initially proposed one by Lysmer and Kuhlemeyer (1969) was suggested by Kouroussis et al. [9]. The expressions of the energy ratio were presented in accordance with the original numerical results to minimize the reflected energy of body waves that impinge on the artificial boundary. It confirms the contributions of Lysmer and Kuhlemeyer in wave-propagation modelling in an infinite solid media using the finite-element method.

A finite element analysis of the dynamic response of a geosynthetic reinforced soil retaining wall constructed with dry-stacked modular concrete blocks as the facia system was carried out by Cai and Bathurst [2]. The cyclic shear behaviour of the backfill soil was described using a hyperbolic stress-strain relationship. The reinforcement material was modelled using a hysteretic model and the slip elements were used to simulate the interface shear between wall components. The parameters like wall displacement, cumulative interface shear force and displacement between facing units, tensile forces developed in the reinforcement and acceleration response over the height of the wall were studied. It was found that relative displacement and interface shear force between modular units increased with the duration and magnitude of base excitation during simulated seismic events. A seismic displacement of gravity walls was studied by Ibrahim [8] using conventional static methods for controlled displacement design and it was found that numerical seismic displacements are either equal to or greater than those calculated by using the pseudo-static methods. It was suggested that for empirical estimation of seismic displacement, permissible values calculated by AASHTO can be used. It was found that seismic wall displacement is directly proportional to the positive angle of inclination of the back surface of the wall, soil flexibility and with the maximum ground acceleration. The plain strain numerical analysis was performed using Plaxis dynamic program where constrained absorbent side boundaries were introduced to prevent any wave reflection.

A series of finite element analyses of backfill-cantilever wall-soil/foundation system to study the backfill effects on seismic behaviour of a cantilever retaining wall was conducted by Cakir [3]. The dynamic response was assessed using

ANSYS finite element computer program in which the cohesionless soil was modelled as an elasto-plastic medium with viscous boundary to simulate the wave energy absorption and interface elements were used between the wall and the backfill soil. The magnitudes of lateral displacements and stresses were analysed and was found that the response amplification or de-amplification was highly dependent on the backfill interaction. The relative displacement of the wall with respect to the ground and the stress responses were found to decrease with the decreasing stiffness of the backfill soil. Bakr and Ahmad [1] created a finite element model using Plaxis 2D in which the soil is simulated as a hardening soil with small strain model. It was inferred that the displacement of the retaining wall during an earthquake is independent of the seismic active earth pressure where as it was influenced by the seismic passive earth pressure. Unique design chats were prepared based on the study and it was concluded that the frequency content has a significant influence on above parameter however the seismic active pressure was insensitive to the frequency content of the seismic motion.

Another experimental study was conducted by Candia et al. [4]. The response of a braced basement and a free standing cantilever retaining wall with compacted low plasticity clay backfill was carried out with a series of centrifuge tests. It was found that the seismic earth pressure on walls increases linearly with the free-field PGA and approximately linearly with depth, where the resultant acts near 0.33 times the height of the wall above the footing. It was also concluded that the traditional limit equilibrium methods yield overly conservative earth pressures in areas with ground accelerations up to 0.4g. Whereas the seismic active earth pressure distribution was found to be nonlinear in the analysis conducted by Ghosh and Prasad Sharma [7] and this nonlinearity showed an increasing trend with an increase in the seismicity. The study was on the seismic active earth pressure and its point of application a rigid retaining wall supporting inclined, cohesionless backfill using pseudo-dynamic analysis and a planar failure surface was considered in the analysis.

Three full-scale geosynthetic-reinforced soil walls that were seismically loaded by a shaking table were simulated by Lee et al. [10] using the finite element program LS-DYNA. The backfill was simulated with a cap model with parameters dependent on stress level. It was found that not all the calculated results agree well with the measured data and the seismic wall displacement was found to decrease with decreasing reinforcement spacing. During the study of the seismic response of geogrid reinforced rigid retaining walls with saturated backfill sand using large-scale shaking table test, Wang et al. [20] found that the seismic waves with high acceleration values for a long time from the far field influences the seismic behaviours of the reinforced retaining wall when compared to those from the near field and the presence of geogrid layers decreases the development of excess pore water pressures and also accelerates the dissipation of excess pore water pressures. Ren et al. [17] also simulated a shaking table test on the seismic performance of reinforced-soil segmental retaining wall with dynamic finite element analysis based on a kinematic hardening elastoplastic model. A cyclic mobility model in which the influences of the stress-induced anisotropy, the density and the structure of the soil described in a unified way, was adopted to simulate the backfill soil. In the numerical tests, parametric analyses were conducted to obtain an effective method for improving the stability and controlling the deformation of the wall. It was found that rather than reducing the reinforcement spacing, the reinforcement length can be increased to improve the stability and the compaction degree in the resistant zone should be guaranteed for controlling the overall deformations.

An experimental analysis of flexible cantilever and propped retaining walls were done by Tricarico et al. [19] when subjected to dynamic loading. Centrifuge models of retaining wall embedded in saturated sand were created and the accelerations and pore pressures in the

soil, displacement and bending moment of the walls were determined. The results were compared with the dry sand conditions. Ren et al. [18] also carried out the dynamic assessment of a saturated reinforced-soil retaining wall with the help of centrifuge shaking table test which was simulated using a dynamic finite element program based on finite deformation theory. A kinematic hardening elastoplastic model was created and a numerical method was proposed for the assessment of dynamic behaviour which was tested under practical ground conditions. A representative model of the dynamic behaviour of the soil–retaining wall system in operational conditions with the help of experimental estimates of dynamic behaviour of soil-wall system was created by Rainieri et al. [16]. The measurements of the natural frequencies and the modal shapes of an embedded retaining wall were made utilised and a superposition principle was validated, resulting in a potential a priori estimation of the response of the overall system based on the knowledge of the decoupled responses of different domains bounded by the excavation and the wall.

A new approach was proposed by Li et al. [11] for the seismic stability analysis of gravity retaining walls based on the category of upper bound theorem of limit analysis. For the translational failure mechanism assumed, closed-form solutions were derived that are based on the soil–wall system analysis. The results were found to be consistent with classic limit equilibrium method. They also provided an expression to calculate the critical acceleration factor and it was found that the wall roughness has remarkable influence on the yield acceleration. Another theoretical model was proposed by Liu [13] for the kinematic response of a flexible cantilever retaining wall subjected to harmonic excitation by modal analysis. The seismic response of the wall retaining a semi-infinite viscoelastic soil under plane strain condition was investigated and a continuum solution was developed by considering the soil-wall interaction. Closed-form solutions were derived for the displacement and stress field of the soil-wall system, stiffness in the *m*th mode and dynamic Winkler modulus of the soil, translational and rotational response factors of the wall and the displacement amplification factor at the wall top.
Another pseudo-static approach for the analysis of geosynthetic-reinforced earth retaining wall was proposed by Gaudio et al. [6] in which the seismic coefficient is assumed to be equal to the internal seismic resistance which is calibrated for given levels of seismic wall performance defined by a specified earthquake-induced displacement values. The internal seismic resistance associated with the internal plastic mechanism is kept lower than the external seismic resistance that is associated with the external plastic mechanisms of base sliding, bearing capacity of the foundation and the wall overturning, in order to promote the activation of plastic mechanism during seismic shaking through attainment of maximum strength of geosynthetic reinforcements. A seismic rotational stability analysis of gravity retaining wall resting on rigid foundation supporting dry cohesionless backfill for active case was carried out by Pain et al. [15] using modified pseudo-dynamic method. Stability factor was proposed for the determination of safe weight of the retaining wall against rotational failure under seismic conditions. It was inferred that the wall-soil interaction under various seismic conditions may or may not be in-phase for the entire duration of the input motion and a modified rotating block method was proposed to obtain the rotational displacement in seismic conditions.

CONCLUSIONS

A few theories, experimental findings and numerical studies used for analysis of dynamic response of retaining walls subjected to dynamic excitation have been discussed briefly. The empirical and analytical methods are still in use due to its simplicity however it has got some inherent assumptions that cannot be used in case of a complex practical conditions. They provide a considerable underestimation of total and incremental seismic earth thrust coefficient for

cohesive sandy backfill material [14]. In contrast to the conventional force-based MO theory, it is found that the seismic active pressure force is close to the static earth pressure force for different acceleration levels [1]. The experimental methods give realistic results however the setup is expensive. Many numerical analyses are also used which gives similar results to those obtained from the theoretical one.

These dynamic analyses of retaining walls are carried out with effect of sdifferent soil conditions, different types of retaining walls, different fixity conditions and different structural conditions. And different parameters such as soil cohesion, stresses, deformation of the wall etc. are studied. However the effect of inclined backfill, anchorage facilities would be scope of the study in this area and also the behaviour of soil-wall under dynamic conditions with a significant mechanism taking into account the soil-structure interaction would be an area of future interest.

REFERENCES

[1] Bakr, J. and Ahmad, S.M., (2018). A finite element performance-based approach to correlate movement of a rigid retaining wall with seismic earth pressure. *Soil Dynamics and Earthquake Engineering*, *114*, pp.460-479.

[2] Cai, Z. and Bathurst, R.J., (1995). Seismic response analysis of geosynthetic reinforced soil segmental retaining walls by finite element method. *Computers and Geotechnics*, *17*(4), pp.523-546.

[3] Cakir, T., (2015). Finite Element Based Investigation of Backfill Effects on Seismic Behavior of a Cantilever Wall. *Procedia Earth and Planetary Science*, *15*, pp.231-236.

[4] Candia, G., Mikola, R.G. and Sitar, N., (2016). Seismic response of retaining walls with cohesive backfill: Centrifuge model studies. *Soil Dynamics and Earthquake Engineering*, *90*, pp.411-419.

[5] El-Emam, M.M., (2018). Experimental verification of current seismic analysis methods of reinforced soil walls. *Soil Dynamics and Earthquake Engineering*, *113*, pp.241-255.

[6] Gaudio, D., Masini, L. and Rampello, S., (2018). A performance-based approach to design reinforced-earth retaining walls. *Geotextiles and Geomembranes*, *46*(4), pp.470-485.

[7] Ghosh, S. and Prasad Sharma, R., (2012). Seismic active earth pressure on the back of battered retaining wall supporting inclined backfill. *International Journal of Geomechanics*, *12*(1), pp.54-63.

[8] Ibrahim, K.M.H.I., (2015). Seismic displacement of gravity retaining walls. *HBRC Journal*, *11*(2), pp.224-230.

[9] Kouroussis, G., Verlinden, O. and Conti, C., (2011). Finite-dynamic model for infinite media: corrected solution of viscous boundary efficiency. *Journal of Engineering Mechanics*, *137*(7), pp.509-511.

[10] Lee, K.Z.Z., Chang, N.Y. and Ko, H.Y., (2010). Numerical simulation of geosynthetic-reinforced soil walls under seismic shaking. *Geotextiles and Geomembranes*, *28*(4), pp.317-334.

[11] Li, X., Wu, Y. and He, S., (2010). Seismic stability analysis of gravity retaining walls. *Soil Dynamics and Earthquake Engineering*, *30*(10), pp.875-878.

[12] Lysmer, J. and Kuhlemeyer, R.L., (1969). Finite dynamic model for infinite media. *Journal of the Engineering Mechanics Division*, *95*(4), pp.859-878.

[13] Liu, Q., (2016). Modal analysis for kinematic response of flexible cantilever retaining wall. *Soils and Foundations*, *56*(3), pp.399-411.

[14] Osouli, A. and Zamiran, S., (2017). The effect of backfill cohesion on seismic response of cantilever retaining walls using fully dynamic analysis. *Computers and Geotechnics*, *89*, pp.143-152.

[15] Pain, A., Choudhury, D. and Bhattacharyya, S.K., (2017). Seismic rotational stability of gravity retaining walls by modified pseudo-dynamic method. *Soil Dynamics and Earthquake Engineering*, *94*, pp.244-253.

[16] Rainieri, C., Dey, A., Fabbrocino, G. and de Magistris, F.S., (2017). Interpretation of the experimentally measured dynamic response of an embedded retaining wall by finite element models. *Measurement*, *104*, pp.316-325.

[17] Ren, F., Zhang, F., Xu, C. and Wang, G., (2016). Seismic evaluation of reinforced-soil segmental retaining walls. *Geotextiles and Geomembranes*, *44*(4), pp.604-614.

[18] Ren, F., Zhang, F., Wang, G., Zhao, Q. and Xu, C., (2018). Dynamic assessment of saturated reinforced-soil retaining wall. *Computers and Geotechnics*, *95*, pp.211-230.

[19] Tricarico, M., Madabhushi, G.S.P. and Aversa, S., (2016). Centrifuge modelling of flexible retaining walls subjected to dynamic loading. *Soil Dynamics and Earthquake Engineering*, *88*, pp.297-306.

[20] Wang, L., Chen, G. and Chen, S., (2015). Experimental study on seismic response of geogrid reinforced rigid retaining walls with saturated backfill sand. *Geotextiles and Geomembranes*, *43*(1), pp.35-45.

[21] Yang, S., Chegnizadeh, A. and Nikraz, H., (2013). Review of Studies on Retaining Wall's Behavior on Dynamic/Seismic Condition. *Journal of Engineering Research and Applications, ISSN*, pp.2248-9622.

[22] Yogendrakumar, M., Bathurst, R.J. and Finn, W.L., (1992). Dynamic response analysis of reinforced-soil retaining wall. *Journal of geotechnical engineering*, *118*(8), pp.1158-1167.

a) 1/6 scale reinforced soil model wall

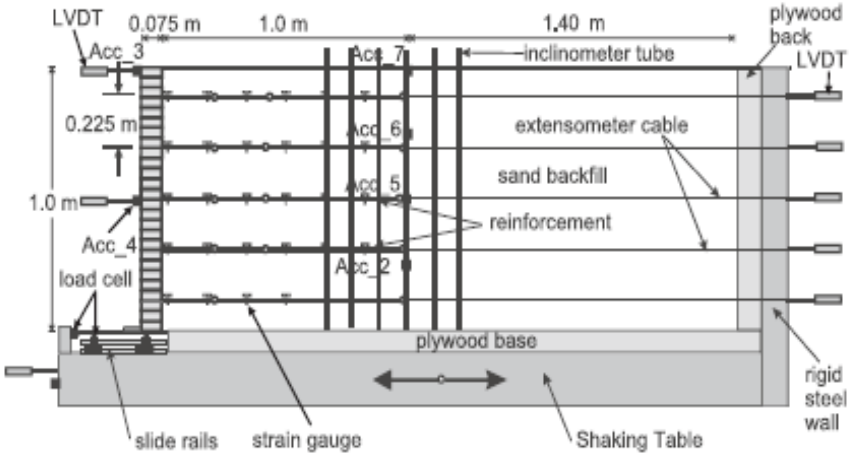

b) Instrumentation layout

Fig.1 General arrangement and instrumentation layout of reduced-scale retaining wall model with vertical full height rigid facing panel
(Courtesy- El.Emam, M.M (2018))

8th International Engineering Symposium - IES 2019
March 13-15, 2019, Kumamoto University, Japan

SEISMIC ANALYSIS OF ELEVATED INTZE WATER TANK

Jogi Pranitha[1] and B. R. Jayalekshmi [2]

1 *Department of Civil Engineering, National Institute of Technology Karnataka, Surathkal, Mangalore 575025, India. email:praneethajogi@gmail.com*
2 *Department of Civil Engineering, National Institute of Technology Karnataka, Surathkal, Mangalore 575025, India. email:br.jaya@gmail.com*

ABSTRACT: Water tanks are one of the important structures which should be functional after the earthquake. In the present study, an R.C.C elevated intze water tank has been analysed by using the response spectrum method. The water tank has a capacity of 7 lakhs litres. A total of 12 models have been generated by considering the tank full, two third full, one third full and empty conditions and supported on different soils. The results show that the base shear and base moment are the highest in tank full condition and when the structure is supported on soft soil.
Keywords*: Elevated water tank, intze tank, response spectrum method, IS 1893, STAAD Pro.*

INTRODUCTION

An elevated water tank is a structure constructed for the purpose of storing water and to hold the water supply level at a definite height to provide sufficient pressure in the water distribution system.

Water tanks should be in working condition after the earthquake to supply water to earthquake-affected localities for drinking as well as fire protection.

Elevated water tanks with circular container are commonly built. However, in the flat bottom, the thickness and reinforcement are found to be heavy. But in the case of intze tanks, in it's domed bottom, the thickness and reinforcement in dome is normal. The main advantages of intze tanks are that the outward thrust from top of conical part is resisted by the ring beam and economical.

Container of the elevated water tank consists of enormous water mass and is placed on a slender staging. Therefore, considering the water tank with staging is the most critical condition in the seismic analysis of water tanks.

It is reported that in circular water tanks, the base shear and base moment is increasing in higher seismicity zones and decreasing with increase in soil stiffness (Raghu K.S et al 2016).

The failure modes observed from the past earthquakes for a reinforced concrete elevated tank with frame staging are shear failure modes in beams, bending shear failure in beams, axial failure in columns, failure due to cracks in connections and torsion failure. (Soheil Soroushnia et al 2011).

The frame supporting structure of elevated water tank must have sufficient strength to resist the axial loads, moment and shear force due to lateral loads. These lateral forces depend on the location of the structure, the type of soil in that location and total weight of the structure. The total weight varies with the water level in the tank container. The present study is to find the critical condition by comparing the seismic response of elevated intze water tank considering different water levels and different supporting soil condition.

PRESENT STUDY

An elevated intze water tank of capacity 700 m^3 is considered in the present study. It has a frame staging with 8 columns and the bracings are located at regular intervals of 7 m and 14 m from base. It is located in zone IV.

The detailed dimensions of each component of the water tank are shown in table 1.

The response spectrum analysis was carried out by considering the provisions from
IS 1893 part I and II with the foundation soil as hard soil, medium soil and soft soil.

MATERIAL PROPERTIES

Concrete of grade M30 and steel of Fe415 grade were used. The density of water is 1000 kg/m^3

METHODOLOGY

Seismic analysis of R.C.C elevated intze tank of capacity 7 lakh litres was carried out. The modeling and analysis of water tank was done by using software STAAD Pro. It is considered as an important structure (I =1.5) and the response reduction factor for water tanks R=2.5 (IS 1893 part II)
Fig 1 shows the rendered view of the water tank. An attempt was made to study the effect of water level and supporting soil conditions in seismic response of water tanks. For this, seismic analysis was done for full water level, 2/3rd water level, 1/3rd water level and tank empty conditions. The dynamic analysis of elevated water tank was carried out by using Response Spectrum method, according to IS 1893-part I considering the foundation soil as hard soil, medium soil and soft soil. The time period for the first mode, base shear and base moment obtained from the analysis were compared. These results are tabulated in table 2.
In order to perform the seismic analysis and design of a structure to be built at a particular location, the actual time history record is required. However, it is not possible to have such records at each and every location. Further, the seismic analysis of structures cannot be carried out based on the maximum values of the ground acceleration as the response of the structure depend upon the frequency content of ground motion and its own dynamic properties. Hence herein the Response spectrum analysis using IS 1893 specifications has been employed.

RESPONSE SPECTRUM METHOD

Response spectrum analysis is a dynamic linear statistical analysis method that assess the contribution of each natural vibration mode to indicate the possible maximum seismic response of an elastic structure. Analysis of the response spectrum provides information on dynamic behavior by measuring acceleration, velocity or pseudo-spectral displacement as a function of the period for a given damping level. There are so many advantages in using the response spectrum method of seismic analysis for the forecast of displacements and member forces in structural systems. The method of analysis involves, calculation of only the maximum values of the displacements and member forces in each mode of vibration using smooth design spectra that are the average of several earthquake motions. The response spectral values depend upon the soil condition, damping in the system and time period of the system
The calculation of base shear is as follows,
Modal mass $\mathrm{M_k}$ of mode k is given by

$$M_k = \frac{[\sum_{i=1}^{n} W_i \emptyset_{ik}]^2}{g \sum_{i=1}^{n} W_i (\emptyset_{ik}{}^2)}$$

Where

$\emptyset_{\mathrm{ik}}$ is the mode shape coefficient at floor i in mode k
$\mathrm{W_i}$ is the seismic weight of floor i of the structure
n = number of floors of the structure
g= acceleration due to gravity

Mode participation factor $\mathrm{P_k}$ of mode k is given by

$$P_k = \frac{\sum_{i=1}^{n} W_i \emptyset_{ik}}{\sum_{i=1}^{n} W_i (\emptyset_{ik}{}^2)}$$

And the peak lateral force Q_{ik} at floor i in mode k is given by

$$Q_{ik} = A_k \emptyset_{ik} P_k W_i$$

Where,

$A_k = \frac{\left(\frac{Z}{2}\right)\left(\frac{S_a}{g}\right)}{\left(\frac{R}{I}\right)}$, A_k is the horizontal acceleration spectrum value using natural period of oscillation T_k of mode k obtained from dynamic analysis
Peak shear force V_{ik} acting in storey i in mode k is given by

$$V_{ik} = \sum_{j=i+1}^{n} Q_{ik}$$

LOADS APPLIED ON THE STRUCTURE

1. Self-weight of the structure.
2. Hydrostatic pressure exerted by water on tank walls and the base of the tank.
3. Earthquake load in horizontal X and Z directions
4. The load combinations considered in the analysis are

- 1.2[DL+ IL ± (EL_X ± 0.3EL_Z)]
  1.2[DL+ IL ± (EL_Z ± 0.3EL_X)]
- 1.5[DL ± (EL_X ± 0.3EL_Z)]
  1.5[DL ± (EL_Z± 0.3EL_X)]
- 0.9 DL ± 1.5 (EL_X ± 0.3EL_Z)
  0.9 DL ± 1.5 (EL_Z ± 0.3EL_X)
- 1.5[DL +IL]

From these load combinations, the maximum values of response quantities are analysed for different water level and foundation soil conditions. Fig 2 shows the deformed shape of the water tank under earthquake load.

RESULTS AND DISCUSSION

An elevated intze water tank was modelled and analysed in STAAD Pro. The results obtained from the study are tabulated and corresponding graphs were drawn. From table 2 it is seen that the tank full condition is more critical. Fig 3 shows the effect of water level in varying the time period of the structure. From fig 4 and fig 5 it is seen that the base shear and base moments are more for the tanks supported on soft soil and with a tank full condition. Therefore, seismic design should be carried for tank full condition incorporating the supporting soil condition.

CONCLUSIONS

The study reveals that,

- The time period is high when the tank is in full condition and it is decreasing gradually with the reduction in water level
- The base shear and base moments are high in tank full condition when compared with 2/3rd, 1/3rd and empty condition.
- The base shear and base moments are high in tanks resting on soft soil.

REFERENCES

[1] IS 1893 (part-1):2016 Indian standard criteria for earthquake resistant design of structures part 1 general provisions and buildings.
[2] IS 1893 (part-II):2014 Indian standard criteria for earthquake resistant design of structures part 2 liquid retaining structures.
[3] Kaviti Harsha (2015), Seismic Analysis and Design of INTZE Type Water Tank, IJSTE, vol 2 September 2015.
[4] Kumara swamy (2016), seismic analysis and design of existing elevated rc intze water tank at pedana as per latest IS provisions, IJTRE, vol 4 December 2016.
[5] Prashant A Bansode and V. P. Datye (2018), Seismic Analysis of Elevated Water Tank with Different Staging Configuration, Journal of geotechnical studies, vol 3, issue 1.
[6] R.Livaoglu, Dogangun,(2006), Simplified seismic analysis procedures for elevated tanks considering fluid–structure–soil interaction, ELSEVIER Journal of fluids and structures 22 (2006) 421-439.
[7] Soheil Soroushnia (2011), Seismic Performance of RC Elevated Water Tanks with Frame Staging and Exhibition Damage Pattern, ELSEVIER, procedia engineering 14 (2011) 3076-3087.
[8] Urmila Ronad et al(2016), Seismic Analysis Of Circular Elevated Tank, IRJET, vol 3 september 2016.

Table 1. Detailed dimensions of various components

Component	Size (mm)
Thickness of Top dome	200
Top ring beam	300 × 500
Thickness of Cylindrical wall	400
Middle ring beam	450 × 600
Bottom ring beam	500 × 1200
Thickness of Bottom interior dome	200
Thickness of Conical dome	400
Horizontal braces	1200 × 350
Diameter of columns	600

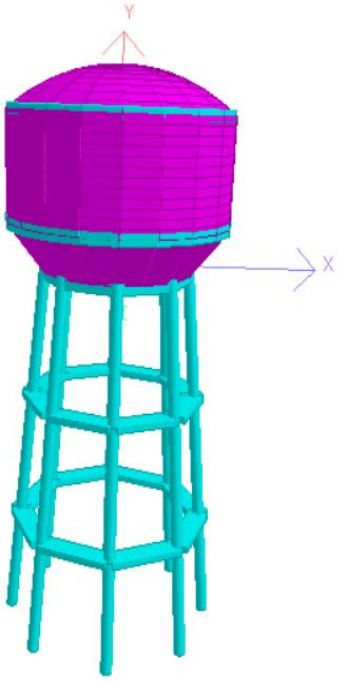

Fig 1. Rendered view of intze tank tank

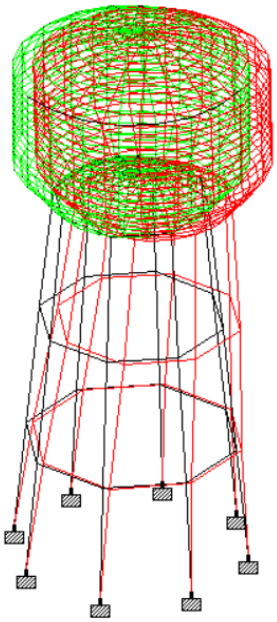

Fig 2. Deformed shape of intze

Table 2. Variation of time period, base shear and base moment for various soil conditions

Soil type	Tank condition	Time period (sec)	Base shear (kN)	Base moment (kN-m)
Soft soil	full tank	2.19	664.78	36009.52
	2/3rd full	2.15	650.46	35011.35
	1/3rd full	1.96	597.9	31192.53
	empty tank	1.29	535.04	27979.41
Medium soil	full tank	2.19	543	29622.09
	2/3rd full	2.15	531.36	28825.52
	1/3rd full	1.96	488.67	25729.04
	empty tank	1.29	436.43	17444.18
Hard soil	full tank	2.19	402.26	22314.05
	2/3rd full	2.15	393.74	21737.29
	1/3rd full	1.96	362.54	19484.78
	empty tank	1.29	322.22	17073.12

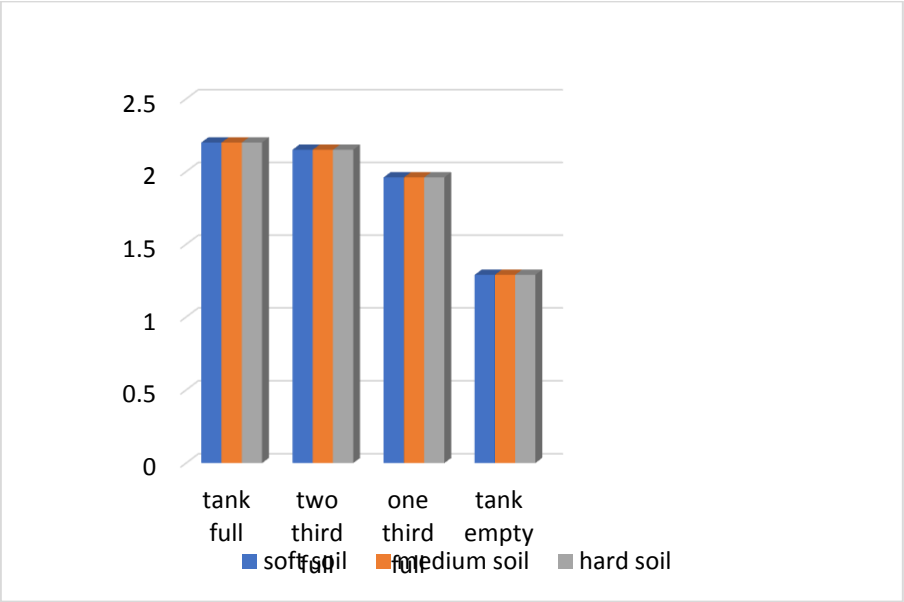

Fig 3. Variation of time period for tanks resting on different soils

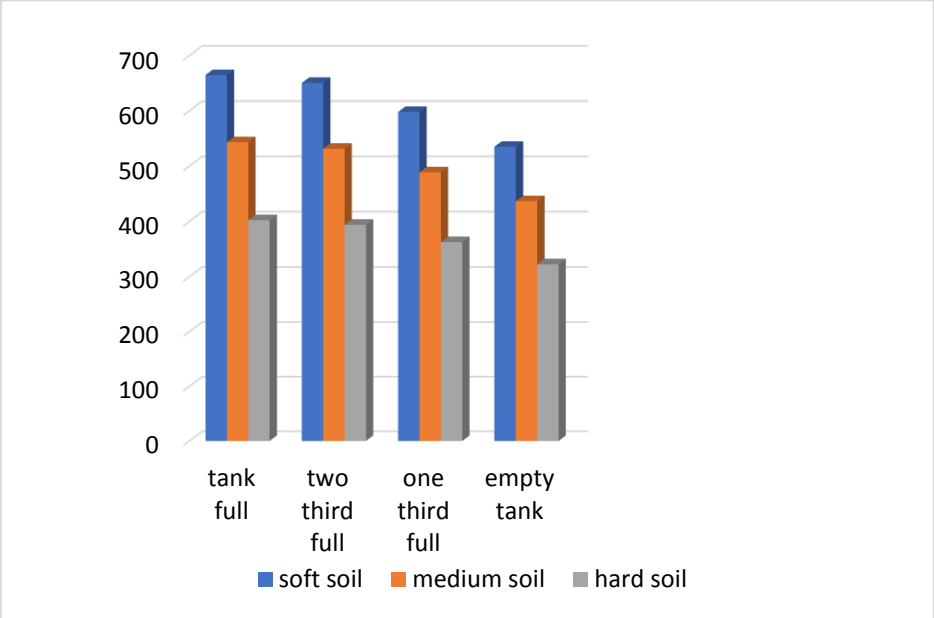

Fig 4. Variation of base shear for tanks resting on different soils

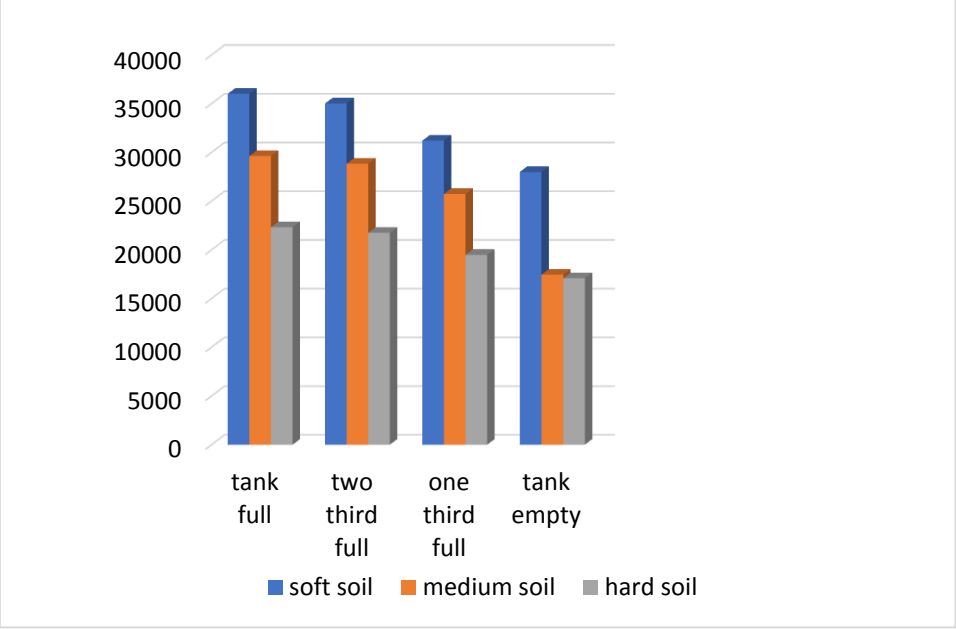

Fig 5. Variation of base moment for tanks resting on different soils

8th International Engineering Symposium - IES 2019
March 13-15, 2019, Kumamoto University, Japan

An Overview of Dynamic Analysis of Water tanks

Nimisha P [1], B R Jayalekshmi [2] and **Katta Venkataramana[3]**

1 *Department of Civil Engineering, National Institute of Technology Karnataka, Surathkal, Mangalore 575025, India. email:nimmigouri@gmail.com*
2 *Department of Civil Engineering, National Institute of Technology Karnataka, Surathkal, Mangalore 575025, India. email:br.jaya@gmail.com*
3 *Department of Civil Engineering, National Institute of Technology Karnataka, Surathkal, Mangalore 575025, India. email:ven.nitk@gmail.com*

ABSTRACT: Water tanks are a very essential part of our infrastructure. They should remain intact during the pre- and post-earthquake period in order to serve the affected public. A number of earthquake damages have been reported in the past due to improper selection of geometry of the structure, incorrect assessment of dynamic effect, insufficient design of staging etc. It is very important to study all the factors affecting the performance of a water tank during earthquake and to design accordingly. This paper aims at highlighting some major works carried so far in this area.
Keywords*: elevated water tanks, earthquake, staging, dynamic effect, sloshing, soil-structure interaction*

INTRODUCTION

Water is an essential prerequisite of our daily lives. Its usage ranges from domestic to the industrial level. We have a number of tanks with different storage capacity. Any damage to these structures may lead to a substantial loss of human life. Therefore it is very important to study in detail and design these kinds of structures properly. Earthquake is a major cause for the damage or even collapse of these kinds of structures, depending on the magnitude and intensity of the earthquake and also on the structural design of tanks. Since we have no control over the magnitude of an earthquake and sometimes its occurrence is beyond our prediction, we have to be very careful during the design of such structures.

Depending upon the location, the tanks are of three types; Elevated tanks, ground supported tanks and underground tanks. Besides this, they can be of different shapes such as rectangular, circular, intze type etc. It can be made of RCC or steel. In elevated tanks, since the water is stored at a high level, it will become more critical during an earthquake due to induced inertia forces. The hydrodynamic effect due to the sloshing of water can intensify the problem. Proper design of staging is also very important in the case of elevated water tanks because a number of collapse of tanks has been reported due to the failure of staging (Soroushnia, 2011) as shown in Fig. 1.

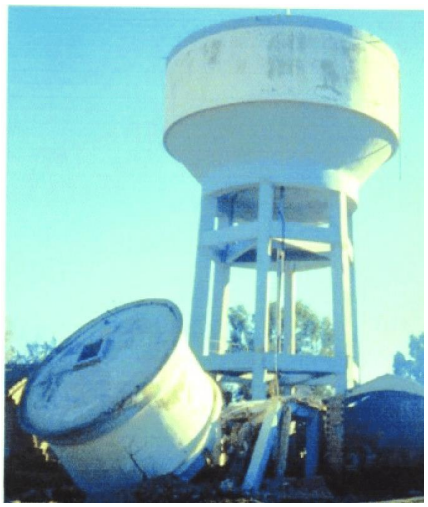

Fig.1 Failure of the reinforced concrete supporting tower of an elevated reinforced concrete water tank during the 1980 El-Asnam Earthquake, Algeria (PEER) (Soroushnia, 2011).

LITERATURE SURVEY

The fluid – structure – soil/foundation interactions make the seismic behaviour of elevated tanks a complex phenomenon. Under tank full condition the elevated tank may be treated as a single-degree-of-freedom system, since the fluid in the tank does not have a sloshing motion (Livaoglu and Dogangun, 2006), but this approach fails when liquid starts to oscillate. Accordingly, the system can be approximated as a single lumped mass model and two mass model (Livaoglu and Dogangun, 2006) as shown in Fig. 2 and Fig 3 respectively. The major parameters affecting the dynamic behaviour of water storage tanks are; sloshing of water in the tank, tank wall flexibility, ground acceleration, soil flexibility, base shear, and soil-structure interaction etc.

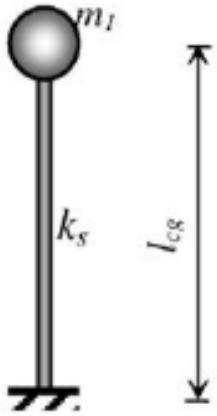

Fig. 2 single lumped mass model (Livaoglu and Dogangun, 2006)

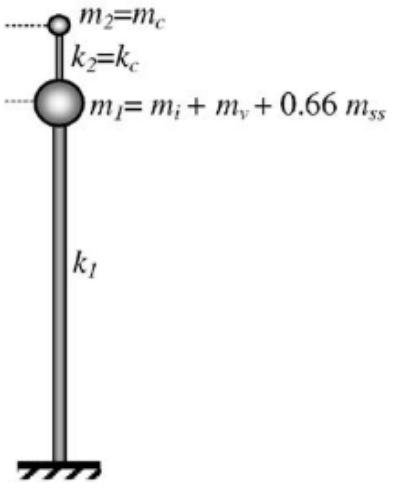

Fig.3 Two mass model by Housner (Livaoglu and Dogangun, 2006)

a) Sloshing of water

The fluid motion with free surface confined inside a tank causes the dynamic load known as sloshing. Tank configuration and seismic characteristics of the applied load, affect the characteristics of sloshing, sometimes resulting in a highly localized pressure on the tank walls (Kumar et al. (2016), Rawat et al. (2019)). The dynamic pressure on the sidewalls of storage tanks, generated by the sloshing, could damage the tanks and/or reduce the building vibration. The amplitude of the sloshing wave and dynamic pressure are dependent upon the tank geometry, liquid depth, amplitude and frequency of the external excitation (Chu et al. (2018)). The sloshing effects in the full-scale tank would occur when the predominant period of the excitation is close to its first period of free oscillations (Radnic et al. (2018)). The sloshing behaviour is most prominent when the ratio of the water level to the height of the water tank is 0.5–0.7 (Kim et al. (2018)).

The seismic behaviour of the tanks was mainly dominated by the impulsive component rather than the convective component. Since the sloshing and impulsive components of the response did not reach their peak values at the same time, the effect of considering convective term on the total response might be either increasing or decreasing (Moslemi and Kianoush (2012)). Unlike the lateral displacement response, the sloshing displacement response does not change for the embedment. So, the effect of embedment on the sloshing response of elevated tanks can easily be ignored during the evaluation or design process (Livaoglu and Dogangun (2007)).

The soil-structure interaction does not have any considerable effects on sloshing responses both for rigid or flexible tanks. After all, for the flexible tank, sloshing displacement is smaller than that for the rigid tank and the embedment causes a little more increase on the sloshing displacement (Livaoglu (2008)). Both impulsive and sloshing behaviour of the tank is practically dominated by its

fundamental modes (Moslemi et al. (2011)). The sloshing behaviour can be simulated by using the linear free surface boundary condition. Due to the large amplitude of sloshing under the strong seismic excitations and turbulence effects in liquid tanks, more complicated boundary conditions on the surface of the liquid are needed to accurately model the convective motions. The sloshing in a tank without any anti-sloshing device is usually damped by viscous forces. For the sloshing behaviour of liquid 0.5% of critical damping is applied (Kianoush and Ghaemmaghami (2011)). The sloshing response increases with the vertical component of ground motions (Shakib and Alemzadeh (2017)). The long-period ground motions can be identified through the damage caused to tanks by liquid sloshing that has been identified repeatedly in the past after major earthquakes. The sloshing height decreases with an increase in the effective frequency.

The effectiveness of seismic isolation of the liquid storage containers increases with the increase of the flexibility of isolation systems. However, the increase of the flexibility of isolation systems is found to have adverse effects on the sloshing height (Hashemi and Aghashirib (2017)). The current provisions may lead to a significant underestimation of the maximum height of the sloshing wave under near-fault conditions. And this may provide an explanation of the extensive post-earthquake damage observed at many tank roofs located in the proximity of active faults (Marina E. Kalogerakou et al. (2017)). The image filter processing technique helps to study the seismic excitation to measure water level response in a liquid storage tank. Under the influence of an external force, a resonance condition may set up in the fluid inside the tank when the frequency of this force gets closer to the frequency of sloshing and it may affect the structural stability of the system. So it is very important to study the physics of sloshing (Kim et al. (2018)). However, the non-linearity of the sloshing wave displacement does not play a significant role while calculating the hydrodynamic pressure distribution on the rigid tank walls (Rawat et al. (2019)).

The baffles can change the natural frequency of the tank and reduce the amplitude of sloshing (Chu et al. (2018)). The convective pressure component is maximum at the top liquid surface, where sloshing occurs (Rawat et al. (2019)). The sloshing behavior of water is highly nonlinear and the assumption of small sloshing amplitude is not applicable. The total pressure mainly consists of the pressure due to liquid sloshing (from the horizontal excitation component) and the pressure induced by the vertical acceleration component (Sadat and Mohammadi (2019)).

The maximum base shear (Vmax) is defined as the maximum shear developed in the structure prior to the onset of stiffness degradation (Ghateh et al. (2015)). The design of elevated tanks based on a fixed base assumption may lead to a wrong assessment of seismic base shear. The underestimation of base shear may lead to unsafe design whereas overestimation may cause uneconomic design (Dutta et al. (2004)). The impulsive mass of water predominantly contributes to the base shear and overturning moment. The increase in base shear due to the effect of soil–structure interaction may be as high as about 33% in tank-full condition (Chandra et al. (2009)). The base shear and base moment values for impulsive modes are higher (increased) in rocking excitation. Whereas, the convective base shear and base moment values will be lower (decreased) during increasing angular motion. This happens due to cancelling out of convective waves already produced due to pure horizontal excitation with waves produced by the increased rocking motion of the tank under consideration (Chaduvula et al. (2013).

b) Flexibility of tank wall

The tank wall flexibility has a considerable effect on seismically induced forces in liquid-filled cylindrical containers subjected to horizontal ground excitations (Moslemi and Kianoush (2012)). The hydrodynamic

pressure in a flexible tank can be significantly higher than the corresponding rigid container due to the interaction effects between flexible structure and contained liquid (Kianoush and Ghaemmaghami (2011), Kumar et al. (2016)). However, it is not worth to consider the wall flexibility effects on sloshing displacements (Livaoglu (2008)). The maximum values of impulsive hoop force, moment, and base shear increase considerably as a result of the wall flexibility effect. On the other hand decrease in associated convective response values due to the flexibility of tank walls will be negligible. This shows that the convective part of the response is almost independent of tank wall flexibility. The maximum impulsive pressure in the flexible shallow tank is about 1.7 times greater than that of a rigid tank (Moslemi and Kianoush (2012)).

Based on the current practice the effect of tank wall flexibility on seismic response cannot be accounted for appropriately and also only the contribution of first sloshing and impulsive modes are included while the effect of higher modes is ignored (Moslemi et al. (2011)). Hashemi et al. (2013) propose a 2-D simplified model to evaluate pressure distribution on the flexible tank wall by developing a mechanical model, which takes into account the deformability of the tank wall. The seismic response of a flexible tank may be substantially greater than that of a similarly rigid tank. By increasing the stiffness of the side tank walls, hydrodynamic forces and hydrodynamic pressures on the side tank walls increase but relative displacements and strains of the tank walls reduce. Increasing the amplitude of the harmonic excitation increases the hydrodynamic force and raises its point of application (Radnic et al. (2018)). Ghateh et al. (2015) suggest the tank size as the critical parameter affecting the seismic response of elevated water tanks. As the length of the tank decreases the hydrodynamic pressure along the wall increases. Under lower tank length, the fluid within the tank has a tendency to rotate, which enhances the hydrodynamic pressure on tank walls (Kumar and Maity (2016)).

c) Ground acceleration

The recent observations of recorded ground motions show that the maximum amplitude of the vertical component of ground acceleration can exceed the peak horizontal amplitude, especially near the epicenter. The fluid surface elevations and hydrodynamic pressures are affected during vertical excitation (Chaduvula et al. (2013)). In seismic areas with thick layers of soft soil and particularly following the peak ground acceleration, the predominant earthquake period may be close to the first period of free oscillations of the liquid–tank system (Radnic et al. (2018)).

The experimental model of a cylindrical steel water tank of 1:4 scale on the shake table facility at CSIR-SERC, Chennai for studying the fluid-Structure-Soil Interaction effect is shown in Fig. 4. The base shear and impulsive base moment values under impulsive and convective modes increase with an increase in earthquake acceleration. But the convective base shear and base moment values decrease with increasing angular motion.

Fig.4 Steel water tank developed at CSIR-SERC, Chennai- Chaduvula et al. (2013)

As tank acceleration increases, the impulsive pressure of tank pressure variation along tank height due to vertical excitation increased. The pressure

variation increases furthermore with added rocking (Chaduvula et al. (2013)).

The frequency characteristics of the earthquake record highly affect the behaviour of the fluid–tank–soil system (Kianoush and Ghaemmaghami (2011)). The site-source distance of the earthquake records also has very much influence on the dynamic behavior of the tank system (Shakib and Alemzadeh (2017)). Under the vertical seismic loading of near-field earthquakes, liquid pressure induced on the tank can be increased and it is strongly influenced by the earthquake peak ground acceleration and also by the spectrum response acceleration at the first sloshing mode, however, its effect on sloshing wave height is negligible (Sadat and Mohammadi (2019)).

The vertical ground acceleration has a more significant effect on the convective part of response than it has on the impulsive part. And also the effect of vertical ground motion on the overall seismic response of the shallow tank is insignificant (Moslemi and Kianoush (2012)). The period of convective motion is very long and it is affected by ground displacement while the period of impulsive motion is relatively short and sensitive to ground acceleration (Masoudi et al. (2012)). The reduction in ground acceleration due to the isolation system leads to a reduction in hydrodynamic pressure for the tank. But the free surface elevation slightly increases because of the lower frequency that characterizes the motion of base-isolated structures (Hashemi and Aghashirib (2017)).

d) Flexibility of soil

The increase in base shear at tank empty condition due to soil-flexibility, even if not very large, may play a crucial role in generating tension in the staging, though this condition is insignificant in the design of staging due to lateral shear only. The soil-flexibility generally causes a decrease in spectral ordinate (Dutta et al. (2004)), offsetting the effect of increased coupling at tank full condition (Dutta et al. (2009)). Neglecting soil-flexibility may lead to overlooking the possibility of tension in one side of the staging (Dutta et al. (2004)) at tank empty condition due to increased tension caused by increased base shear acting simultaneously with a lesser axial stress generated due to lesser dead weight (Dutta et al. (2009)).

The effect of soil-flexibility increases the impulsive lateral period whereas reduces the impulsive torsional-to-impulsive lateral period ratio. The soil-flexibility has a less pronounced effect on seismic base shear with respect to the tanks having lesser aspect ratio. In reality, the elevated tank actually may have its torsional-to-lateral period ratio within a critical range of 0.7–1.25 due to the consideration of soil-flexibility and thus, may undergo a seismic torsional failure even at the tank-full condition ((Dutta et al. (2004)).The finite element model of a tank-foundation-soil system is shown in Fig. 5.

The soil-flexibility is stronger for elevated tanks supported by alternate frame staging configurations with panels of small heights, and a larger number of columns, large column diameter, and stiffer circumferential beams compared to the columns ((Dutta et al. (2004)). The flexibility of the footing-soil system in rocking causes moment magnification and occurs in particular for soils with relatively small shear wave velocity (Haroun and Temraz (1992)).

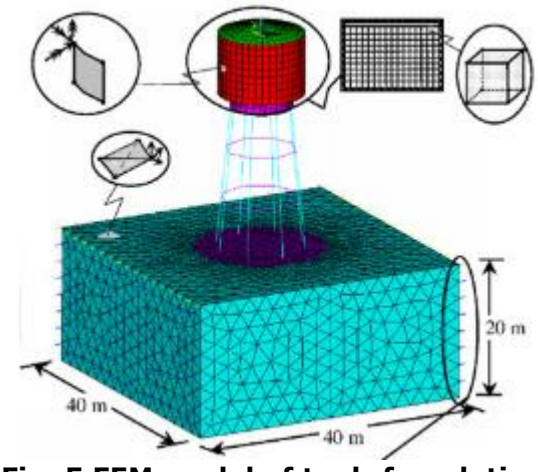

Fig. 5 FEM model of tank-foundation-soil system (Livaoglu and Dogangun (2007)

The tanks having a greater aspect ratio have a smaller container radius. This will result in a larger impulsive mass of water which is perhaps responsible for a less pronounced effect of soil–structure interaction (Dutta et al. (2004)). For columns with small aspect ratio or without adequate shear-resisting reinforcements, shear deformation governs the total response and, finally, leads to unexpected shear or shear-flexure failure (Phan et al. (2017)).

e) Soil-structure interaction

Due to the effect of soil–structure interaction in both tank-full as well as in tank-empty conditions, the base shear may considerably increase (even to the extent of about 30%). This effect is more pronounced in tank-empty conditions for most of the cases. The seismic base shear induces axial compression in half of the staging columns and tension in the remaining ones. The value of maximum axial compression and tension due to seismic base shear are same and occur in two columns located at diametrically opposite sides. In tank-full condition, the axial compressive force due to the weight of container and water is sufficient to counterbalance the maximum axial tensile force. Hence, in this case, all the columns remain under compression. On the other hand, under the tank-empty condition, there remains a possibility of occurring axial tension due to the considerable reduction in axial compression resulting from lesser self-weight (Dutta et al. (2004)). The base shear decreases with the increase of flexibility of the isolation system. This is due to the fact that increased flexibility of the isolation system transmits less acceleration to the tank (Hashemi and Aghashirib (2017)). Livaoglu and Dogangun (2006) suggest a distributed added mass approach for the seismic analysis of elevated tanks in general-purpose structural analysis programs. The lumped mass approach may lead to underestimations of the base shear and the overturning moment.

If soil-structure interaction is ignored in the design, the problem will increase further. Chandra et al. (2009) proposed a simple design procedure for elevated tanks by identifying the deficiencies in the current design. The damping of convective mode is taken as 5% itself instead of 0.5% as indicated in International standards. The study focus on occurrence of tension in the supporting staging, particularly for a tank-empty condition, in contrast to the conventional perception that the design is always guided by tank-full condition.

The frame staging with all kinds of alternate configurations having more number of columns, larger column diameter, less panel heights, and stiffer circumferential beams compared to columns encounter the influence of soil–structure interaction effect (Dutta et al. (2004)). In soft soil, the tank roof displacements were affected significantly by the embedment, however, this effect was smaller for stiff soil types (Livaoglu and Dogangun (2007)).

Masoudi et al. (2012) suggest the idea of having the same response modification factor for both shaft and frame staging. Also the P–Δ effect causes the amplification of seismic induced moment throughout the staging height in the higher modes. So it is important to consider P–Δ effect in the nonlinear analysis of elevated tanks.

Mori et al. (2015) propose two retrofit hypotheses, namely a dissipative bracing system, and a base isolation system for two heritage-listed reinforced concrete (R/C) elevated water storage tanks. Kumar et al. (2016) [14] suggest a design chart to help design engineers in quick dynamic analysis of liquid filled storage tanks. Multiple baffles in the tank alter the natural frequency of the tank and were related to the effective water depth above the baffles. Hydrodynamic force and sloshing height decrease as the baffle height or number increases (Chu et al. (2018)).

CONCLUDING REMARKS

The sloshing effect of water in the tank, tank wall flexibility, ground acceleration, tank aspect ratio, soil flexibility, base shear etc. are some major factors affecting the seismic behaviour of the water storage tank. Also P–Δ effect causes the amplification of seismic induced moment throughout the staging height in the higher modes. So it is important to consider P–Δ effect in the nonlinear analysis of elevated tanks. Apart from this the frequency characteristics and site-source distance of the earthquake record highly affect the behaviour of the fluid–tank–soil system. The seismic base isolation can be an efficient way to reduce seismic responses but it can adversely affect the free surface sloshing height.

Since a number of damages of water tanks have been reported due to the collapse of staging, the dynamic behaviour of staging due to soil-structure interaction under seismic load also need primary attention.

REFERENCES

[1] Chaduvula, U; Patel, D; and Gopalakrishnan, N (2013), "Fluid-Structure-Soil Interaction Effects on Seismic Behaviour of Elevated Water Tanks," Procedia Engineering, vol. 51, no. NUiCONE 2012, pp. 84–91.

[2] Chandra, S; Dutta S; and Roy R (2009), "Dynamic behavior of R / C elevated tanks with soil – structure interaction," Engineering Structures, vol. 31, no. 11, pp. 2617–2629.

[3] Chu, C; Wu, Y; Wu, T; and Wang, C (2018), "Slosh-induced hydrodynamic force in a water tank with multiple baffles," Ocean Engineering journal, vol. 167, no. August, pp. 282–292.

[4] Livaoglu, R; and Dogangun, A (2006), "Simplified seismic analysis procedures for elevated tanks considering fluid – structure – soil interaction," Journal of Fluids and Structures, vol. 22, pp. 421–439.

[5] Dutta, S; Mandal A; Dutta S C (2004), "ARTICLE IN PRESS Soil – structure interaction in dynamic behaviour of elevated tanks with alternate frame staging configurations," Journal of Sound and Vibration, vol. 277, pp. 825–853.

[6] Ghateh, R; Kianoush, M R; and Pogorzelski, W (2015) "Seismic response factors of reinforced concrete pedestal in elevated water tanks," Engineering Structures, vol. 87, pp. 32–46.

[7] Haroun, M A and Temraz, M K (1992), "Effects of soil-structure interaction on seismic response of elevated tanks," Soil Dynamics and Earthquake Engineering, vol. 11, pp. 73–86.

[8] Hashemi, S; and Aghashiri, M H (2017), "Seismic responses of base-isolated flexible rectangular fluid containers under horizontal ground motion," Soil Dynamics and Earthquake Engineering, vol. 100, no. July 2016, pp. 159–168.

[9] Hashemi, S; Saadatpour, M; and Kianoush, M R (2013), "Thin-Walled Structures Dynamic behavior of flexible rectangular fluid containers," Thin Walled Structures, vol. 66, pp. 23–38.

[10] Kalogerakou, M E; Maniatakis, C A; Spyrakos, C; and Psarropoulos, P N (2017), "Seismic response of liquid-containing tanks with emphasis on the hydrodynamic response and near-fault phenomena," Engineering Structures, vol. 153, pp. 383–403.

[11] Kianoush, M R; and Ghaemmaghami, A R (2011), "The effect of earthquake frequency content on the seismic behavior of concrete rectangular liquid tanks using the finite element method incorporating soil – structure interaction," Engineering Structures, vol. 33, no. 7, pp. 2186–2200.

[12] Kim, S; Choi, H; Park, D; Baek, E; and Kim, J (2018), "Water level response measurement in a steel cylindrical liquid storage tank using image filter processing under seismic excitation," Mechanical Systems and Signal Processing, vol. 101, pp. 274–291.

[13] Kumar, K; and Maity, D (2016), "Pressure Based Eulerian Approach for Investigation of Sloshing in Rectangular Water Tank," Procedia Engineering, vol. 144, no. 033, pp. 1187–1194.

[14] Kumar, P D; Alok, A; and Maiti, P R (2016), "Comparative Study of Dynamic Analysis of Rectangular Liquid Filled Containers Using Codal Provisions," Procedia Engineering, vol. 144, pp. 1180–1186.

[15] Livaoglu, R A (2008), "Investigation of seismic behavior of fluid – rectangular tank – soil / foundation systems in frequency domain," vol. 28, pp. 132–146.

[16] Livaoglu, R and Dogangun, A (2007), "Effect of foundation embedment on seismic behavior of elevated tanks considering fluid – structure-soil interaction," vol. 27, pp. 855–863.

[17] Masoudi, M; Eshghi, S; and Ghafory-ashtiany, M (2012), "Evaluation of response modification factor (R) of elevated concrete tanks," Engineering Structures, vol. 39, pp. 199–209.

18] Mori, C; Sorace,S; and Terenzi,G (2015), "Seismic assessment and retro fi t of two heritage-listed R / C elevated water storage tanks," Soil

Dynamics and Earthquake Engineering, vol. 77, pp. 123–136.
[19] Moslemi, M; and Kianoush, M R (2012), "Parametric study on dynamic behavior of cylindrical ground-supported tanks," Engineering Structures, vol. 42, pp. 214–230.
[20] Moslemi, M; Kianoush, M R; and Pogorzelski, W (2011), "Seismic response of liquid-filled elevated tanks," Engineering Structures, vol. 33, no. 6, pp. 2074–2084.
[21] Phan, H N; Paolacci, F; Bursi, O S; and Tondini, N (2017), "Seismic fragility analysis of elevated steel storage tanks supported by reinforced concrete columns," Journal of Loss Prevention in the Process Industries, vol. 47, pp. 57–65.
[22] Radnic, J; Grgic, N; Kusic, M S; and Harapin, A (2018), "Shake table testing of an open rectangular water tank with water sloshing," Journal of Fluids and Structures, vol. 81, pp. 97–115.
[23] Rawat, A; Mittal, V; Chakraborty, T; and Matsagar, V (2019), "Thin-Walled Structures Earthquake induced sloshing and hydrodynamic pressures in rigid liquid storage tanks analysed by coupled acoustic-structural and Euler-Lagrange methods," Thin Walled Structures, vol. 134, no. October 2018, pp. 333–346.
[24] Sadat, F; Hejazi, A; and Mohammadi, M K (2019), "Investigation on sloshing response of water rectangular tanks under horizontal and vertical near fault seismic excitations," Soil Dynamics and Earthquake Engineering, vol. 116, pp. 637–653.
[25] Shakib, H; and Alemzadeh, H (2017), "The effect of earthquake site-source distance on dynamic response of concrete elevated water tanks," Procedia Engineering, vol. 199, pp. 260–265.
[26] Soroushnia, S; Tafreshi, T S; Omidinasab, F; Beheshtian, N; Soroushnia, S (2011), "Seismic Performance of RC Elevated Water Tanks with Frame Staging and Exhibition Damage Pattern", Procedia Engineering, vol. 14, pp. 3076–3087

8th International Engineering Symposium - IES 2019
March 13-15, 2019, Kumamoto University, Japan

A Review of performance of pile raft system under static and dynamic loading

Vinoda Krishna s [1] **B R Jayalekshmi [2]**

1 *Department of Civil Engineering, National Institute of Technology Karnataka, Surathkal, Mangalore 575025, India. email:vinodkrishnasondi@gmail.com*
2 *Department of Civil Engineering, National Institute of Technology Karnataka, Surathkal, Mangalore 575025, India. email: br.jaya@gmail.com*

ABSTRACT: The piled raft foundation system has recently been widely used for many structures, especially high rise buildings. In this foundation, the piles play an important role in settlement and differential settlement reduction, and thus can lead to economical design without compromising the safety of the structure. This paper compiles the details of numerical and experimental studies conducted on the piled raft system.

***Keywords**: Piled raft, Settlement, Load distribution, Dynamic soil structure interaction*

INTRODUCTION

Foundation systems are used to transfer the load safely into the soil ensuring overall stability and serviceability of the superstructures. Raft foundations are used when isolated footings cover more than 70% of the building area under a super structure. A combination between the use of piles and raft foundation is known as piled raft foundation. A typical sketch of pile raft system is shown in fig 1.
It is well known that there are three principal foundation options to transfer heavy structural loads;

1. Raft foundations, where loads are transferred to the ground via a thick rigid concrete slab
2. Pile foundations, where loads are transferred to deeper bearing layers
3. Piled raft foundations, at which the loads are partially transferred by piles and partially by raft.

Piled raft foundations proved to be more economical in case of high rise buildings on clay and can provide safe bearing capacity and serviceability requirements. Piled raft foundations have been widely used for high rise buildings, liquid storage tanks, shipbuilding dock, etc.

The conventional design method for piled raft foundation assumes that the pile carries the whole load without any contribution from the raft. This approach is too conservative as the raft is in direct contact with the soil, and hence it carries a significant portion of load.

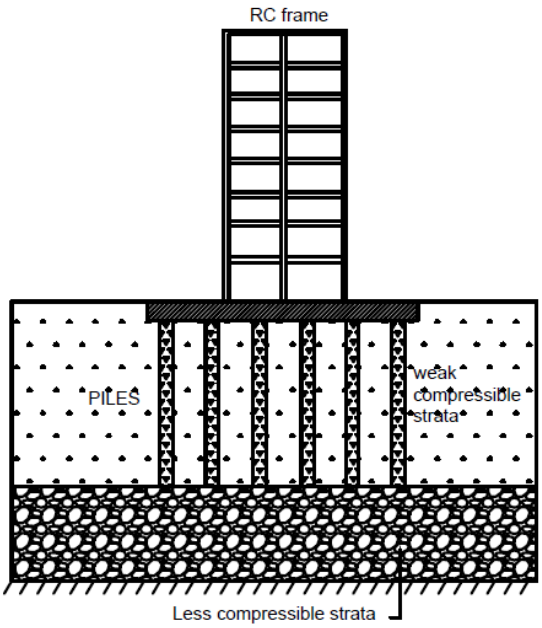

Fig1. Typical sketch of piled raft system

The proper use of piles and careful consideration of the load carried by the raft can reduce differential settlements of the raft and lead to considerable economy without compromising the safety of the structures. Various methods for the analysis of piled-raft foundations have been developed.

NUMERICAL ANALYSIS

Computer-based methods appeared to be effective tools to facilitate the design of such foundation systems, which includes the following broad approaches:

a) The raft is represented by a series of strip footings, and the piles and the soil are represented by springs of appropriate stiffness.
b) Raft is represented by a plate and the piles and the soil as springs.
c) Numerical analyses using Finite Element Method (FEM).

Numerical analyses using FEM usually involve in the detailed design of the piled raft foundation for high-rise buildings. This is necessary in high-rise buildings especially when they become higher and heavier and more complex in configurations. However FEM is very effective tool for analyzing any foundation and structure system. Review of such researches is presented in this section.
It has been reported that the pile group to raft width ratio and pile depth are the most influential elements of system geometry in piled raft system. A width ratio of about one is the most effective to minimize the average displacement, while a width ratio of about 0.5 is the most effective to minimize the differential displacement. To minimize displacements, the width ratio and pile depth have to be determined together by an iteration process. A pile to raft area ratio, which is a combination of pile spacing and pile diameter, of about 5–6% is adequate to minimize the displacements. A smaller pile to raft area ratio would also result in less raft bending moments and a more efficient pile group load transfer mechanism (Prakoso et Al.,2001)

From Finite-element analyses of combined pile raft footing (CPRF) model done by Kumar et al.(2016) for El-Centro 1979, Loma Prieta 1989, Bhuj 2001 and Sikkim 2011 real earthquake pseudostatic loading and real acceleration–time history, the crossover point in the bending moment profile was observed at shallow depths for all cases of loading. The difference in the response of soil just below the raft of the CPRF and at the far field indicated that near-field and far-field ground motions were not in tandem. The normalized horizontal displacement and bending moment profile is maximum at the pile head, which decreased along the length of pile under static and pseudostatic loading conditions for Existing CPRF of Messeturm Tower, Frankfurt am Main, Germany.
Lee et al. (2010) conducted a numerical study using a 3D finite element method which reported that the use of a limited number of piles, strategically located, might improve both bearing capacity and the settlement performance of the raft. And also development of settlements and pile loads for a piled raft is dependent on the slippage at the pile–soil interface and the pile configurations. The average settlements using slip analysis are generally larger than that using no-slip analysis, whereas the maximum pile loads and pile load sharing using slip analysis are smaller than that using no-slip analysis. However, the pile load distributions varied according to the pile spacing, as well as the slippage at pile–soil interface.

For the pile group with rigid cap and the rigid piled raft, the load distribution at the bottom of the raft is related to the size of load acting on the raft. Initially, the load carried by the corner pile is the largest, and the load carried by the central pile is the lowest. As the load acting on the raft increases, finally, all the piles of the group share the same mean load. For the rigid piled raft, as the load increases, the load carried by the piles gradually reach the ultimate resistance of piles while the load carried by the pile cap continue to increase. When a concentrated load is applied and the raft is very flexible, the load is mainly distributed to the vicinity of

the load. It is also seen that when a concentrated load corresponding to the allowable load (the load of the pile group with rigid cap or piled raft at the settlement of 2% of pile diameter) is applied at the center of the raft and the raft is very flexible, the central pile carries the highest of the load. When the raft thickness increases, the corner pile starts to carry a higher proportion of the load (Huang et al.2017).

Ata et al.(2015) investigated the load sharing capacity of the Unconnected piled raft foundation (UCPRF) system using finite element analysis software, ABAQUS. UCPRF is an economical and efficient system where the piles are separated from the raft by a structural fill cushion. The cushion acts to redistribute the load between raft and piles. The maximum axial load in the connected piled raft system occurs at the pile head, and then decreases along the length of the pile. However, in the unconnected system, the location of maximum axial load is shifted downwards to a certain length below the pile head. Beyond the top three meters of the pile, the axial load in the pile starts to decrease following the same pattern as in the connected system.

The study by Haldar et al. (2015) considers one storey system consisting of a mass in the form of a rigid floor slab supported by four columns. The piles are modelled by beam-column element supported by laterally distributed springs and dampers. This simple model used in present study is adequately tuned to exhibit reasonably accurate dynamic characteristics while compared to the existing well accepted methodologies. The study shows that soil-structure interaction leads to considerable lengthening of period though the lateral shear in columns are not significantly changed. However, the shear in piles is significantly increased due to SSI effect as inertia of the considerable foundation mass contributes to this increase in shear of pile. Thus, neglecting SSI may lead to unsafe seismic design of pile

Kumar et al. (2017) studied the soil–structure interaction of a piled-raft foundation which is a part of a raw materials storage building in Vietnam using finite-element-based geotechnical software. Foundation comprises an 81m by 55·5m raft that connects 581 precast hollow concrete piles 20m long with 400 mm outer diameter. Various loading conditions, such as all compartments full to all compartments empty, were considered in the analysis. The results of the analyses indicate the importance of the raft in sharing 23–31% of the total vertical load.

Saha et al.(2015) studied Effect of raft and pile stiffness on seismic response of soil-piled raft-structure system using a simplified model incorporating pile-soil raft and superstructure interaction in very soft, soft and moderately stiff soil. It is observed that pile head shear may significantly increase if the relative stiffness of raft and pile increases and furthermore stiffer pile group has a stronger effect.

The settlement behaviour of a square piled raft in clay soil is investigated by Cho et al.(2012) using numerical analysis. A nonlinear three dimensional finite element analysis with pile–soil slip interface model is performed for various pile positions, pile numbers, pile lengths under the raft and different loading types. It is found that the variation of reduction ratio (ratio of average settlement of raft with pile to the average settlement of raft without pile) of soft clay was relatively greater than that of stiff clay. It is also found that the required pile group-raft area ratio for minimizing differential settlement in soft clay was slightly larger than that of stiff clay in the same pile array.

EXPERIMENTAL STUDIES

Yao et al.(2004) conducted shaking table tests by means of a large-scale laminar box with 4 m in length, 2 m in width and 2 m in height in order to investigate behaviour of a soil-pile-superstructure system in liquefiable ground. A model two-storey structure, supported by a pile group, was set in a saturated sand deposit, and subjected to a sinusoidal base motion with increasing amplitude. Main interests are characteristics of springs used in a sway-rocking model and multi-freedom lumped mass (MFLM) model that

are frequently used in soil–pile interaction analysis. The transient state prior to soil liquefaction is shown to be important in the design of a pile because dynamic earth pressure shows peak response in this state.

Cao et al.(2004) experimentally verified the effectiveness of piles through load tests of model rafts resting on pile-reinforced sand. By varying factors such as raft stiffness, pile length, pile arrangement, and pile number. The loads taken by the piles were found to increase rapidly in the initial loading stage, then to remain at a plateau in subsequent stages. An increase in the rigidity of the model raft led to a decrease of load transferred to the piles. In addition, with the increase of pile length, an increased amount of load was transferred to the piles.

El-Garhy et al.(2013) conducted an experimental program on piled raft model in sand soil. The experimental program is aimed to investigate the behaviour of raft on settlement reducing piles. Three lengths of piles are used in the experiments to represent slenderness ratio (ratio of length of pile to diameter of pile) of 20, 30 and 50, respectively. The dimensions of the model rafts are 30 cm × 30 cm with different thickness of 0.5 cm, 1.0 cm or 1.5 cm. The raft-soil stiffness ratios of the model rafts ranging from 0.39 to 10.56 cover flexible to very stiff rafts. As the number of settlement reducing piles increases, the load improvement ratio increases and the differential settlement ratio decreases.

Saha et al.(2015) studied the distribution of forces at column and pile head in soil-pile raft-structure system due to the incorporation of dynamic soil structure interaction (DSSI) effects is investigated by means of the normalised response of the system, with DSSI versus that obtained in fixed base condition. Results show that the base shear at column may significantly increase due to consideration of DSSI. Such increase can be as high as 1.8 times the fixed base shear for 1 Hz to 10 Hz swept sine motions, and 6.0 times for 5 Hz to 50 Hz motions. Such increase may be due to the fact that lengthening of period results in relatively higher acceleration compared to the fixed base condition for structure in the shorter period range, which is intuitively understandable by the shape of the response spectrum curve available in many codes.

COMBINED EXPERIMENTAL & NUMERICAL STUDIES

Elwakil et al.(2016) studied piled raft system by Experimental and numerical methods, they have been concluded that as the length of piles and number of piles decrease, the load carried by raft increases. Additionally, it is found that the best and the optimal settlement ratio to design the piled raft as settlement reducer is 0.7%. Finally the percentage of load carried by raft at settlement ratio of 0.7% is found to be 39%

Baziar et al.(2009) performed physical model test on a circular rigid raft underpinned with four model piles. Numerical simulation was also carried out on the model test, using FLAC-3D, to show compatibility of the numerical analysis with the test. The obtained results showed very good accuracy of the numerical method used in this study as long as the applied load does not exceed the working load, while the performance of numerical model was relatively good for the loads beyond working load.

The effect of considering the embedment of the pile cap in estimation of piled raft behaviour has been examined for a small scale test and for a full sized structure by Poulos et al.(2011). The calculations for the small scale test indicated that the effect of the soil against the buried cap is quite significant, and therefore to use a conventional pile group analysis where this is neglected will result in a considerable underestimate of lateral load capacity and an overestimate of lateral deflection. The finite element analyses of a full scale building (the Incheon Tower) have shown that by considering the effect of the basement, the estimated lateral deflections are smaller than the deflections of a raft on the surface only. Because the deflections are smaller, the moments in the piles are also smaller, but the effects are relatively modest in this case. A finding of practical importance is that for tall

buildings supported by piled raft foundations with a large number of piles, a conventional pile group analysis may often be adequate, although conservative, for estimating the vertical and lateral behaviour of the foundation and the distributions of pile load and bending moment within the piles in the foundation system

CONCLUDING REMARKS

This study has been carried out aiming to bring in the information regarding the studies on piled raft foundation at one place. Various parameters that affect the performance of piled raft system in terms of load carrying capacity, settlement and lateral displacement in cohesive soil and sand are discussed. Since the piled raft foundation systems are generally provided for high rise structures it is important to know the behaviour of piled raft system under dynamic loading. It is seen that the shear in piles significantly increases due to SSI effect as inertia of the considerable foundation mass contributes to this increase in shear of pile. Thus, neglecting SSI may lead to unsafe seismic design of pile.

REFERENCES

1. Prakoso, W. A., & Kulhawy, F. H. (2001). Contribution to piled raft foundation design. *Journal of Geotechnical and Geoenvironmental Engineering*, *127*(1), 17-24.
2. Kumar, A., Choudhury, D., & Katzenbach, R. (2016). Effect of earthquake on combined pile–raft foundation. *International Journal of Geomechanics*, *16*(5), 04016013.
3. Lee, J., Kim, Y., & Jeong, S. (2010). Three-dimensional analysis of bearing behaviour of piled raft on soft clay. *Computers and Geotechnics*, *37*(1-2), 103-114.
4. Huang, M., Jiu, Y., Jiang, J., & Li, B. (2017). Nonlinear analysis of flexible piled raft foundations subjected to vertical loads in layered soils. *Soils and Foundations*, *57*(4), 632-644.
5. Ata, A., Badrawi, E., & Nabil, M. (2015). Numerical analysis of unconnected piled raft with cushion. *Ain Shams Engineering Journal*, *6*(2), 421-428.
6. Haldar, S., Saha, R., & Dutta, S. C. (2015). Seismic response of soil-pile raft-structure system.
7. Kumar, A., Patil, M., & Choudhury, D. (2017). Soil–structure interaction in a combined pile–raft foundation–a case study. *Proceedings of the Institution of Civil Engineers-Geotechnical Engineering*, *170*(2), 117-128.
8. Saha, R., Dutta, S. C., & Haldar, S. (2015). Effect of raft and pile stiffness on seismic response of soil-piled raft-structure system. *Structural Engineering and Mechanics*, *55*(1), 161-189.
9. Cho, J., Lee, J. H., Jeong, S., & Lee, J. (2012). The settlement behavior of piled raft in clay soils. *Ocean Engineering*, *53*, 153-163.
10. Yao, S., Kobayashi, K., Yoshida, N., & Matsuo, H. (2004). Interactive behavior of soil–pile-superstructure system in transient state to liquefaction by means of large shake table tests. *Soil Dynamics and Earthquake Engineering*, *24*(5), 397-409.
11. Cao, X. D., Wong, I. H., & Chang, M. F. (2004). Behavior of model rafts resting on pile-reinforced sand. *Journal of geotechnical and geoenvironmental engineering*, *130*(2), 129-138.
12. El-Garhy, B., Galil, A. A., Youssef, A. F., & Raia, M. A. (2013). Behavior of raft on settlement reducing piles: Experimental model study. *Journal of Rock Mechanics and Geotechnical Engineering*, *5*(5), 389-399.
13. Saha, R., Haldar, S., & Dutta, S. C. (2015). Influence of dynamic soil-pile raft-structure interaction: an experimental approach. *Earthquake Engineering and Engineering Vibration*, *14*(4), 625-645.
14. Elwakil, A. Z., & Azzam, W. R. (2016). Experimental and numerical study of piled raft system. *Alexandria Engineering Journal*, *55*(1), 547-560.
15. Baziar, M. H., Ghorbani, A., & Katzenbach, R. (2009). Small-scale model test and three-dimensional analysis of pile-raft foundation on medium-dense sand. *International Journal of Civil Engineering*, *7*(3), 170-175.
16. Poulos, H. G., Small, J. C., & Chow, H. (2011). Piled raft foundations for tall buildings. *Geotechnical Engineering Journal of the SEAGS & AGSSEA*, *42*(2), 78-84.
17. Long, P. D., & Vietnam, V. W. (2010). Piled raft—a cost-effective foundation method for high-rises. Geotechnical Engineering, 41(1), 149.

8th International Engineering Symposium - IES 2019
March 13-15, 2019, Kumamoto University, Japan

BUCKLING STRENGTH OF THIN CONCRETE SHELLS

Krupa Sheela Pattapu [1] and **B.R.Jayalekshmi** [2]

1 *Department of Civil Engineering, National Institute of Technology Karnataka, Surathkal, Mangalore 575025, India. email:sheela.krupa@gmail.com*
2 *Department of Civil Engineering, National Institute of Technology Karnataka, Surathkal, Mangalore 575025, India. email:br.jaya@gmail.com*

ABSTRACT: Buckling strength of singly curved circular and parabolic arch dams are investigated considering thin concrete shells with hydrostatic loading on its upstream. The shell may experience buckling because of the internal compressive forces due to the hydrostatic pressure caused by retained water. Hence, Eigenvalue buckling analysis was done considering few factors that influence the critical buckling strength for arch dams that may include the geometry, thickness, rise and width of the shell and hydrostatic loading which gives respective Eigenvalues and Eigenvectors. The present study uses FEM software to study the buckling strength of the concrete shells and the corresponding buckling modes.
***Keywords**: thin shells, buckling , arch dams*

INTRODUCTION

Thin Shell structures are being used in a wide range of applications including aircraft, cooling towers, Liquid storage tanks, foundations, etc. Due to their thinness, buckling is an often a failure controlling mode.
Buckling may occur when a structure is subjected to compressive stresses. Buckling of arch dams is more major subject to buckling of thin shells where the shell may experience buckling because of the internal compressive forces by the water retained due to its hydrostatic pressure.
Ideally, the shell under full load condition should be in a state of pure compression with the negligible bending moments but, it always develops some bending stresses at the boundaries which may lead to buckling. Hence, the critical buckling strength of the shell is to be known for the safety of the dam.

SCOPE OF THE STUDY

The critical buckling strength and their respective buckling modes of singly curved parabolic and circular arch dams using eigenvalue buckling analysis was analysed.The buckling strengths were compared and the difference in buckling modes were checked. In the present study, horizontal-arches fixed in a rectangular valley, with uniform thickness(t) was considered. The chord width and rise are designated as 'a' & 'h'. Keeping the thickness uniform,the effect of the depth(b),width and rise on the buckling strength of the shell were studied. where, depth to width ratio referred to as aspect ratio(b/a) and rise to width ratio as rise ratio(h/a). The dam was considered to be under full load conditions at first. Unit weight of water is $1kN/m^3$.
The parametric study was conducted on the shell in detail, Keeping the parameter thickness(t) fixed with varying aspect ratio from 0.5 to 2.0 with an incremental increase of 0.5, the buckling strengths for both circular and parabolic singly curved arch dam shells for width equal to 75m & 100m with 3 different rise ratios (10%,15%,20%) giving a total cases of 48 models were studied.

The eigenvectors were checked for same aspect ratio and rise ratio for circular and parabolic shells.
The buckling strengths were compared against the hydrostatic pressure caused by the held water under full water load condition.
A complete buckling case was taken from the above cases and compared when water was held at two third full condition.

MATERIAL PROPERTIES AND FEM MODELLING

For the considered concrete arch dam, M30 grade with the material properties as $E = 28 \times 10^6 kN/m^2$ and $\upsilon = 0.15$ .The model properties taken were, thickness(t) of 0.75m, aspect ratios(b/a) from 0.5 to 2.0 with 0.5 increment and rise ratios(h/a) of 10%,15%,20% for widths(a) of 75m and 100m.
The finite element software, ABAQUS was employed for the analysis of the buckling strength of the dams. The edges were considered fully restrained except at the top of the dam, then the eigen value buckling analysis was performed. The triangular variation of loading was applied with zero loading at top and 1kN at the base of the dam.The eigenvalues and eigenvectors were obtained. The buckling strengths, then calculated when eigenvalues were multiplied with the applied loading. The eigenvectors also referred to as buckling modes.

RESULTS

The results were tabulated from the analysis.
Table 1 gives the Critical Buckling strengths for the circular and parabolic singly curved shells for various aspect ratios and rise ratios keeping thickness constant. It shows that the difference in the buckling strengths between circular and parabolic arches are very less, i.e., less than 1.5%. Hence, we further consider circular cylindrical shell for the buckling strength analysis for higher width in Table 2. Table 3 gives the comparison of buckling strengths between full load and 2/3rd full load conditions with the respective hydrostatic pressures.
Fig.1 shows some of the typical buckling modes of the circular arch for a=100m,t=0.75m, b/a =1.0,h/a=0.1 .
Fig.2 shows the difference in first buckling modes of circular and parabolic shells and Fig.3 shows the first four buckling modes under 2/3rd full water conditions. Fig.4 & 5 gives the buckling strengths of the circular shell with various aspect ratios and rise ratios for width(a) equal to 75m and 100m respectively. Fig.6 shows the comparison in buckling strengths under full load and 2/3rd full load conditions.

DISCUSSIONS

From Table 1 and 2, it was seen that the aspect ratio, rise ratio, and width had shown a significant impact on the buckling strength of the shell. When the aspect ratio increases, the buckling increases which results in a decrease in buckling strength and more the rise ratio more the buckling strength, i.e., low buckling. Similarly, the increase in width tends to reduce the buckling pressure for the same rise.
The buckling strengths obtained for circular and parabolic shells are nearly equal but, the mode shapes are different.
Regarding the design consideration, the hydrostatic pressure line has great significance. The points on the plot above this line show that the pressure applied by the water is lesser than the stress that causes buckling which means the point above this line are safe under buckling and below are unsafe.
A case examined which was entirely under buckling and compared with 2/3rd full water load; the buckling tends to be reduced which shows the effect of hydrostatic pressure on the shell.

CONCLUSIONS

From the study, It has been observed that

- The parameters like width, depth and rise has a significant effect on the buckling strength.
- When the eigenvalues and eigenvectors were compared for circular and parabolic curves, there was not much difference in Eigenvalues, but a difference in Eigenvectors were noticed.

- When a case under total buckling under full load conditions compared with 2/3rd full of load, the buckling was seen to be much reduced which shows the impact of Hydrostatic pressure on buckling.

REFERENCES

[1] Da Silva, V.D. and Julio, E.N.B.S., (1997). Computation of membrane shapes and analysis of arch dams. Computers & structures, *64*(1-4), pp.849-855.
[2] Feng, J., Wei, H., Pan, J., Jian, Y., Wang, et al. (2011). Comparative study procedure for the safety evaluation of high arch dams. *Computers and Geotechnics*, *38*(3), pp.306-317.
[3] Li, S., Ding, L., Zhao, L. and Zhou, W., (2009). Optimization design of arch dam shape with modified complex method. *Advances in Engineering Software*, *40*(9), pp.804-808.
[4] Papadakis, G., (2008). Buckling of thick cylindrical shells under external pressure: A new analytical expression for the critical load and comparison with elasticity solutions. *International Journal of Solids and Structures*, *45*(20), pp.5308-5321.
[5] Teng, J.G., (1996). Buckling of thin shells: recent advances and trends. *Applied Mechanics Reviews*, *49*(4), pp.263-274.
[6] Zingoni, A., et al. (2013). Buckling strength of thin-shell concrete arch dams.Thin walled structures, *64*, pp.94-102.

Table 1 Critical Buckling strengths of circular and parabolic singly curved shells for a=75m (under full load conditions)

b/a	b (m)	Hydrostatic pressure, P_{water} (kN/m^2)	Critical Buckling strength , P_{cr} (kN/m^2) for a=75m, t=0.75m					
			h/a = 0.1, h=7.5(m)		h/a = 0.15, h=11.5(m)		h/a = 0.2, h=15(m)	
			circular	parabolic	circular	parabolic	circular	parabolic
0	0	0						
0.5	37.5	367.875	1094	1103	1739.4	1595.4	2254.1	1952.2
1	75	735.75	609.6	621.64	958.23	902.97	1277	1109.8
1.5	112.5	1103.625	471.46	472.17	725.89	709.7	963.88	900.7
2	150	1471.5	409.9	408.2	620.03	612.5	798.38	759.63

Table 2 Critical Buckling strength of circular singly curved shell for a=100m (under full load conditions)

b/a	b (m)	Hydrostatic pressure, P_{water} (kN/m^2)	Critical buckling strength, P_{cr} (kN/m^2) for a=100m, t=0.75m		
			h/a= 0.1, h=10(m)	h/a=0.15, h=15(m)	h/a=0.2, h=20(m)
0	0	0			
0.5	50	490.5	505.95	796.27	1064.1
1	100	981	281.55	453.83	607.91
1.5	150	1471.5	214.75	342.45	458.51
2	200	1962	188.6	310.5	404.42

Table 3 Comparison of Buckling strengths for full load condition and 2/3rd full load for a=100m, t=0.75m, h/a= 0.1.

b/a	b (m)	Hydrostatic pressure, P_{water} (kN/m^2)		Critical buckling strength, P_{cr} (kN/m^2)	
		Full load	2/3rd full load	Dam under full load	Dam with 2/3rd full water
0	0	0	0		
0.5	50	490.5	163.53	505.95	3843.9
1	100	981	326.97	281.55	1022.6
1.5	150	1471.5	490.5	214.75	552.52
2	200	1962	654.03	188.6	410.46

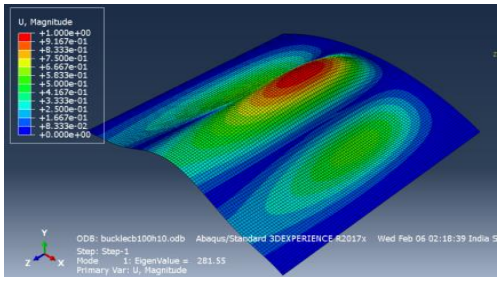
a. first mode

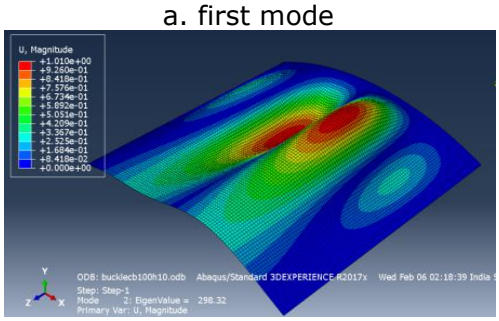
b. second mode

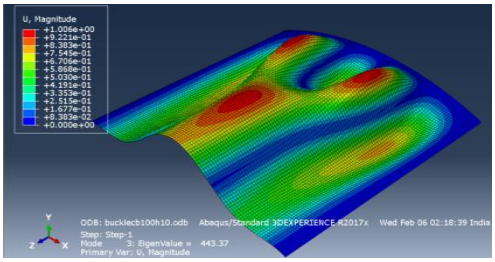
c. third mode

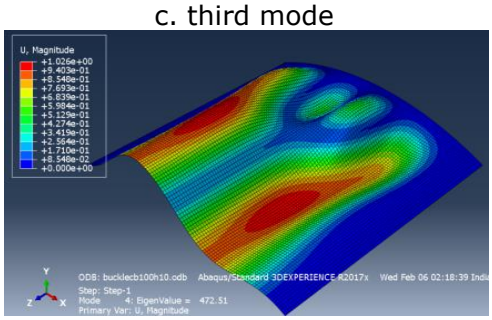
d. fourth mode

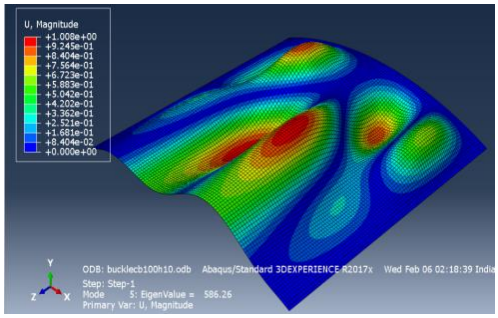
e. fifth mode

Fig.1(a-e) The first five buckling modes of the circular shell with a=100m, t=0.75m, h/a=0.1, b/a=1.0 under full water condition.

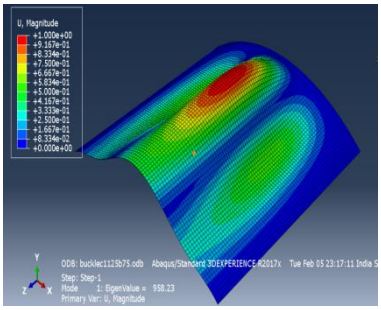
a. Circular shell

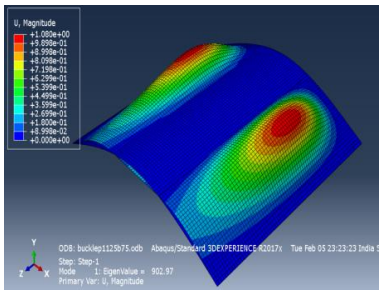
b. Parabolic shell

Fig.2(a&b) The variation in buckling modes for the shells with nearly same buckling strengths.

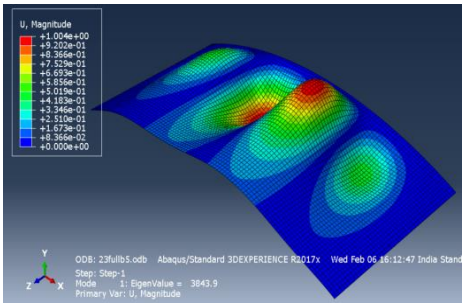
a. first mode

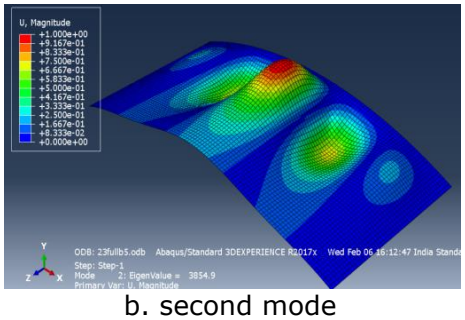
b. second mode

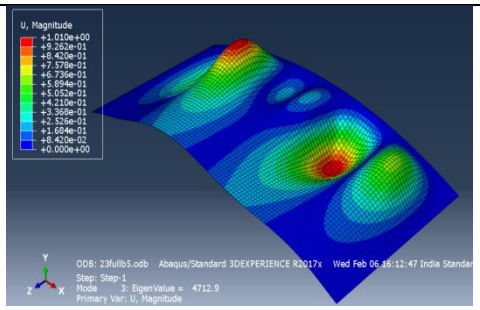

c. third mode

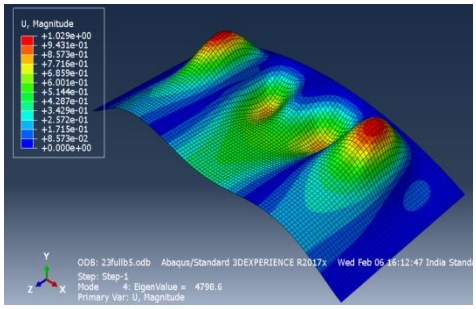

d. fourth mode

Fig.3(a-d) The first four buckling modes of the circular shell with a=100m,t=0.75m, h/a=0.1, b/a=0.5 under 2/3rd full water condition.

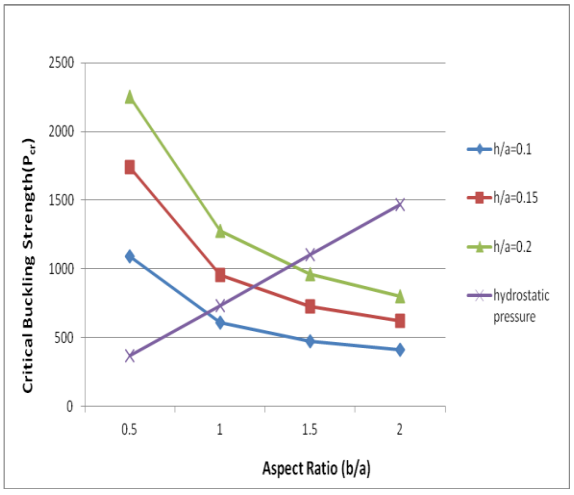

Fig.4 The variation in buckling strengths of the circular shell with aspect ratio for a=75m.

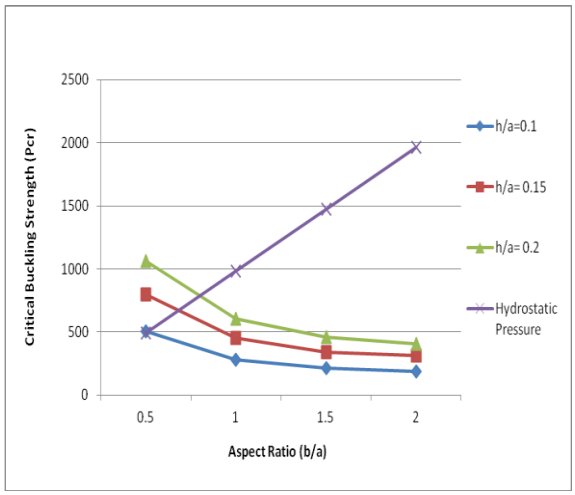

Fig.5 The variation in buckling strengths of the circular shell with aspect ratio for a=100m.

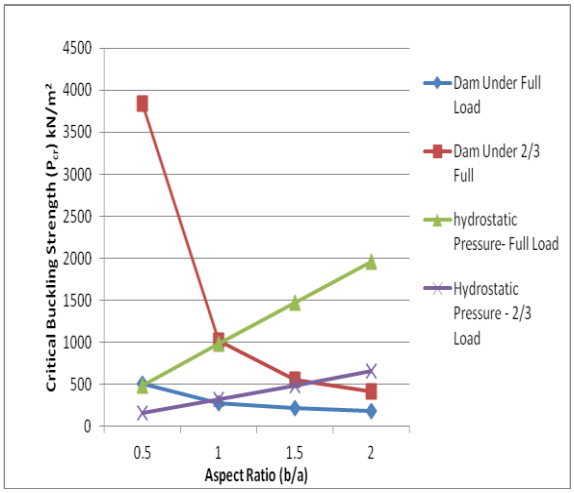

Fig.6 The Comparison of buckling strengths of shells under full and 2/3rd full load conditions.

8th International Engineering Symposium - IES 2019
March 13-15, 2019, Kumamoto University, Japan

PERFORMANCE BASED SEISMIC EVALUATION OF MULTISTOREY RC BUILDINGS WITH CONCRETE MIW AND USER DEFINED HINGES

Gaonkar P V [1], Dyavanal S S[2] and Katageri B G[3]

[1]Dept. of civil Engineering, KLE Technological University, Hubli, priyankagaonkar1510@gmail.com
[2]Dept. of civil Engineering, KLE Technological University, Hubli, ssdyavanal@gmail.com
[3] Dr. M S Sheshgiri Engineering college, Belgaum, basavaraj971@gmail.com

ABSTRACT: In the present paper G+2 and G+5 bare frame and soft storey 2D RC special moment resisting frame buildings built in seismic zone III are investigated. The CIW is modeled as pin-jointed single equivalent diagonal strut as proposed by Stafford and Hendry. Equivalent static, scaled response spectrum, and nonlinear static pushover analyses are performed. User defined hinge properties are assigned to frame elements as per FEMA 440 guidelines. The results are compared with the parameters namely: natural period, base shear, lateral displacement, storey drift, safety ratio, ductility ratio, global stiffness, and hinge status at performance point. The results indicate that, collapse hinges are formed at the few column foundation joints. The soft storey models are retrofitted with CIW at both ends of the ground floor bays and the results reveal that, the retrofitting has successfully enhanced the performance of the soft storey RC buildings to earthquake shaking.

Keywords*: soft storey, equivalent diagonal strut, pushover analysis, hinge status, retrofit*

INTRODUCTION

Rapid urbanisation has created the need for multi-storey buildings construction in urban india and indeed across the world. Majority of buildings are low and medium rise RC buildings. A large number of buildings with open ground storey are constructed in india in recent years (Murty 2004). Most of the buildings have parking facility in the ground storey with no masonry walls between the columns. Presence of masonry infill walls in buildings is advantageous in increasing stiffness and strength of the structure (Das and Murty 2004). The strength normally provided by the presence of walls is absent, making such buildings vulnerable under earthquakes. The presence of masonry infill walls in the upper storeys make them stiffer than the open ground storey. As a result, the upper storeys move almost together as a single block, resulting in most of the horizontal displacement of the building to occur in the open ground storey. If the columns in the open ground storey do not have the required stiffness, strength, and ductility to resist these high stresses, they suffer severe damage. Open ground storey buildings have consistently shown poor performance under moderate and severe earthquakes across the world (Murty 2004).

Majority of buildings in india are designed only for gravity loads and if seismic loads are considered, they are designed as bare frames ignoring the stiffness of infill walls. A number of methods and techniques are available for evaluation and retrofitting of RC buildings (Singh 2003). Generally there are two approaches to enhance the seismic capacity of existing structures. The first approach is a structure- level retrofit, wchich involves global modifications to the

structural system, mainly to enhance the lateral resistance of existing structures. The second approach is a member level retrofit. Seismic vulnerability of open ground storey buildings, mainly the soft storey effect, can be eradicated by increasing the strength and stiffness at ground storey. The retrofit of open ground storey by addition of new MIW between two existing columns in the ground storey is the easiest option to increase the stiffness of the ground storey.

ANALYSIS and MODELING

In the present study 2D RC special moment resisting frames (SMRF) of three and six storey are considered. Seismic analysis is carried out for dead load, live load and seismic load using SAP 2000 v14.2 for bare frame and soft storey structures.

Building Properties

Input data for the building models
Response reduction factor - 5
Type of building use - Official
Material Properties:
Young's modulus of M25 concrete, E_c - 25 x 10^6 kN/m^2
Grade of steel - Fe 415
Member Properties:
Thickness of slab - 0.120 m
Beam size (bare frame) - 0.25 m x 0.5 m
Beam size (soft storey) - 0.3 m x 0.5 m
External column size (bare frame) - 0.4 m x 0.4 m
Internal column size (bare frame) - 0.5 m x 0.5 m
External column size (soft storey) – 0.5 m x 0.5 m
Internal column size (soft storey) - 0.55 m x 0.55 m
Thickness of wall - 0.20 m
Assumed Dead Load Intensities:
Roof finishes - 1.5 kN/m^2
Floor finishes - 1.0 kN/m^2
Live Load Intensities :
Floor - 3.0 kN/m^2
Roof - 0 kN/m^2

Modeling

The buildings are located in seismic zone III proposed for office. In the seismic weight calculations, only 25% of the live loads are considered. The elevations of the building models studied are shown in figure 1-3. The beam-column joint is considered as fully fixed. The rigid zone factor of unity is assigned to beam column joints. CIW are modelled as equivalent diagonal strut.
Models considered in the present study are:
Model 1: Three and six storey buildings modelled as bare frame.
Model 2: Three and six storey buildings have no walls in the first storey and CIW in the upper storeys.

RESULTS AND DISCUSSIONS

Fundamental natural period (FNP)

The natural period obtained for model 1 are longer compared to model 2. These results reveal that the bare frame idealization leads to an overestimation of natural period compared to soft storey model. This result in an underestimation of base shear in bare frame model. On the other hand, it is observed that natural period for retrofitted models are shorter compared to model 2. This leads to the conclusion that retrofitted models can sustain higher earthquake forces since frame sections are designed for higher forces as compared to bare and soft storey models.

Base shear

It is seen that base shear by ESM for models are more than those by RSM leading to overestimation by the analysis. This result in higher factor of safety leading to uneconomical design of buildings. The base shear of model 2 is higher compared to model 1. The reason is stiffness contribution of MIW in bare frame building being ignored. The base shear of retrofitted model increased compared to model 2 with increase in the stiffness at the ground floor.
These results and discussions reveals that, the retrofitting techniques implemented contribute in increasing the base shear of buildings and subsequently are safer to earthquakes.

Lateral displacement

The lateral displacement of a building is a function of the stiffness. The lateral displacement of the building decreases with the increase in the lateral stiffness, hence the displacement of the soft storey model is less than the bare frame. The lateral displacements by ESM in all the

models are slightly higher than those by RSM, indicating over estimation of lateral displacements. This result in ESM estimating lesser global stiffness of building compared to those by RSM. Further it is seen from the tables 6 and 7 that, retrofitting techniques implemented in soft storey buildings are effective in reducing lateral displacements. This results in increasing stiffness thereby reducing vulnerability to earthquake shaking.

Storey drift

Clause 7.11.1 of IS:1893 (Part 1)-2002 code state that the storey drift in any storey of RC framed buildings is limited to 0.004 times the storey height. This permissible limit is equal to 19.2 mm and 14.4 mm at first storey and other storey's respectively. The storey drift for all models are within the limit. The results show that the storey drift at first storey by ESM and RSM are nearly same, while storey drift by ESM are slightly higher than those by RSM from second storey onwards. These results reveal that event though base shears in both the analyses are same, ESM over estimates the storey drift responses marginally. It can be concluded that retrofitting techniques are effective in reducing storey drift within permissible limit thereby reducing vulnerability in soft storey buildings to earthquake shaking.

Performance of building models

From the results shown in tables 12-17 it is seen that, as the stiffness of infill wall is considered in the open ground storey buildings, base force is more than that of the soft storey models. The performance of all the building models is within the life safety range at the ultimate state, as the collapse hinges are few, retrofitting can be completed quickly and economically without disturbing the incumbents and functioning of the buildings. After retrofitting collapse hinges are 2%, 0.9% by equivalent static pushover analysis and 2%, 1.98% by response spectrum pushover analysis for three and six storey building models. Adding MIW at corners in soft storey models are effective in improving the seismic performance.

DR, SR and GS

DR, SR, and GS results are presented in tables 18-21. Ductility ratio of bare frame is lower than the infill frame building models specifying stiffness of infill walls not considered during the analysis. Retrofitting technique exhibited superior ductility behavior to earthquake.

From the results it can be observed that, three and six storey building models with and without infill frame are found safer. Retrofitting technique exhibited superior safety performance to earthquake.

Results from the tables show that the presence of infill wall in building models has increased the global stiffness. Retrofitting technique show higher rigidity and thus are safer to earthquakes during inelastic phase.

CONCLUSIONS

The following conclusions are deduced from this study:

- The models designed considering SMRF exhibit the linear results within the safety limit as per IS: 1893 (Part 1)-2002.
- Stiffness of MIW is to be considered to capture true results of building behavior.
- Retrofitting has successfully increased the performance of the soft storey RC buildings to earthquake shaking.
- Real performance of buildings designed considering SMRF are obtained by linear dynamic pushover analysis.

REFERENCES

[1] Agarwal, P and Shrikhande, M (2006), Earthquake design of structures, Prentice Hall of India Private Limited New Delhi India.

[2] Das, D. and Murty, C.V.R. (2004), Brick Mosonry Infills in Seismic Design of RC Framed Buildings (Part 2), The Indian Concrete Journal, PP 31-37.

[3] Federal Emergency Management Agency, FEMA-440 (2005), Improvement of Nonlinear Seismic Analysis Procedures, California

[4] IS 1893(Part 1):2002, Criteria for earthquake resistant design of structure, General Provision and Building.

[5] IS 456-2000, Code of Practice for Plain and Reinforced Concrete, Bureau of Indian Standards, New Delhi, India.

[6] Murty, CVR (2004), Why are open ground storey Buildings vulnerable in Earthquake, The Indian Concrete Journal, pp 51-52.

[7] Singh, Y (2003), Challenges in retrofitting of RC buildings. Proceedings of workshop on retrofitting of structures, Roorkee, pp 29-44.

Table 1 Codal and analytical natural period for building models

Model No.	Codal (sec)		Analytical (sec)	
	3 Storey	6 Storey	3 Storey	6 Storey
1	0.48	0.78	0.738	1.227
2	0.25	0.48	0.566	0.897

Table 2 Base shear and scaling factor for bare frame building model

Storey	$\overline{Vb}$	V_b	Scaling factor
3	78.27	53.66	1.45
6	113.69	64.82	1.75

Table 3 Base shear and scaling factor for soft storey building model

Storey	$\overline{Vb}$	V_b	Scaling factor
3	121.11	117.44	1.03
6	263.65	158.99	1.65

Table 4 Lateral displacements in longitudinal direction by ESM and RSM for three storey building model in mm

Storey No.	ESM		RSM	
	Model No.		Model No.	
	1	2	1	2
3	8.5	3.9	7.6	3.6
2	6.5	3.5	6	3.4
1	3.6	2.9	3.5	2.8

Table 5 Lateral displacements in longitudinal direction by ESM and RSM for six storey building modle in mm

Storey No.	ESM		RSM	
	Model No.		Model No.	
	1	2	1	2
6	18	11.1	15.3	9.7
5	16.5	10.5	14.2	9.4
4	14.1	9.6	12.4	8.8
3	10.9	8.5	9.9	8.0
2	7.3	7.2	6.9	7.0
1	3.6	5.6	3.5	5.6

Table 6 Lateral displacements in longitudinal direction by ESM and RSM for three storey retrofitted building model in mm

Storey	ESM	RSM
3	1.8	1.6
2	1.4	1.3
1	0.9	0.9

Table 7 Lateral displacements in longitudinal direction by ESM and RSM for six storey retrofitted building model in mm

Storey	ESM	RSM
6	7.0	6.0
5	6.5	5.7
4	5.6	5.1
3	4.5	4.2
2	3.2	3.1
1	1.9	1.8

Table 8 Storey drift in longitudinal direction by ESM and RSM for three storey building model in mm

Storey No.	ESM		RSM	
	Model No.		Model No.	
	1	2	1	2
3	2.0	0.4	1.6	0.2
2	2.9	0.6	2.5	0.6
1	3.6	2.9	3.5	2.8

Table 9 Storey drift in longitudinal direction by ESM and RSM for six storey building mdoel in mm

Storey No.	ESM		RSM	
	Model No.		Model No.	
	1	2	1	2
6	1.5	0.6	1.1	0.3
5	2.4	0.9	1.8	0.6
4	3.2	1.1	2.5	0.8
3	3.6	1.3	3.0	1
2	3.7	1.6	2.5	1.4
1	3.6	5.6	3.5	5.6

Table 10 Storey drift in longitudinal direction by ESM and RSM for three

storey retrofitted building model in mm

Storey	ESM	RSM
3	0.4	0.3
2	0.5	0.4
1	0.9	0.9

Table 11 Storey drift in longitudinal direction by ESM and RSM for six storey retrofitted building model in mm

Storey	ESM	RSM
6	0.5	0.3
5	0.9	0.6
4	1.1	0.9
3	1.3	1.1
2	1.3	1.3
1	1.9	1.8

Table 12 Equivalent static pushover analysis with user defined hinges for bare frame building model

Model	Base force (kN)	Displacement (mm)	AtoB	BtoIO	IOtoLS	LStoCP	CPtoE	Total
3	128.214	58.938	35	4	0	0	5	44
Ultimate	219.356	111.82	35	8	0	0	1	44
6	489.524	87.27	54	9	9	9	3	84
Ultimate	514.316	314.43	54	11	7	11	1	84

Table 13 Equivalent static pushover analysis with user defined hinges for soft storey building models

Model	Base force (kN)	Displacement (mm)	AtoB	BtoIO	IOtoLS	LStoCP	CPtoE	Total
3	1293.35	41.38	40	8	0	0	0	48
Ultimate	1913.57	131.12	34	6	4	2	2	48
6	1660.57	66.09	90	9	0	0	0	99
Ultimate	2166.61	152.53	82	8	5	3	1	99

Table 14 Equivalent static pushover analysis with user defined hinges for soft storey building model after retrofitting

Model	Base force (kN)	Displacement (mm)	AtoB	BtoIO	IOtoLS	LStoCP	CPtoE	Total
3	2115.57	72.57	49	1	0	0	0	50
Ultimate	7402.10	192.99	35	14	0	0	1	50
6	5278.33	112.31	72	29	0	0	0	101
Ultimate	10377.42	240.02	65	26	8	1	1	101

Table 15 Response spectrum pushover analysis with user defined hinges for bare frame building model

Model	Base force (kN)	Displacement (mm)	A to B	B to IO	IO to LS	LS to CP	CP to E	Total
3	116.847	46.87	32	7	0	0	5	44
Ultimate	208.26	108.41	32	11	0	0	1	44
6	468.856	55.52	56	22	0	0	6	84
Ultimate	498.147	182.25	56	27	1	0	0	84

Table 16 Response spectrum pushover analysis with user defined hinges for soft storey building model

Model	Base force (kN)	Displacement (mm)	A to B	B to IO	IO to LS	LS to CP	CP to E	Total
3	1266.86	37.10	40	3	0	1	4	48
Ultimate	1755.627	114.02	40	6	0	1	1	48
6	1545.53	49.45	91	4	1	0	3	99
Ultimate	1998.179	185.78	91	8	0	0	0	99

Table 17 Response spectrum pushover analysis with user defined hinges for soft storey building model after retrofitting

Model	Base force (kN)	Displacement (mm)	A to B	B to IO	IO to LS	LS to CP	CP to E	Total
3	1814.30	48.54	36	12	1	0	1	50
Ultimate	7047.57	168.78	49	1	0	0	0	50
6	4579.93	99.15	44	53	1	1	2	101
Ultimate	9980.28	350.318	51	48	1	0	1	101

Table 18 DR, SR, and GS for three and six storey building models by equivalent static pushover analysis

storey	model	DR	SR	GS
three	1	1.89	2.80	1.66
	2	2.13	8.21	14.2
six	1	2.6	4.52	1.93
	2	3.31	15.79	14.59

Table 19 DR, SR, and GS for three and six storey building models by response spectrum pushover analysis

storey	model	DR	SR	GS
three	1	1.71	2.19	1.47
	2	2.07	7.27	13.39
six	1	2.28	4.28	1.67
	2	3.15	15.14	14.08

Table 20 DR, SR, and GS for three and six storey retrofitted building models by equivalent static pushover analysis

Storey	DR	SR	GS
3	3.16	15.61	38.37
6	3.42	18.65	43.23

Table 21 DR, SR, and GS for three and six storey retrofitted building models by response spectrum pushover analysis

Storey	DR	SR	GS
3	3.07	14.75	29.02
6	3.23	17.11	37.82

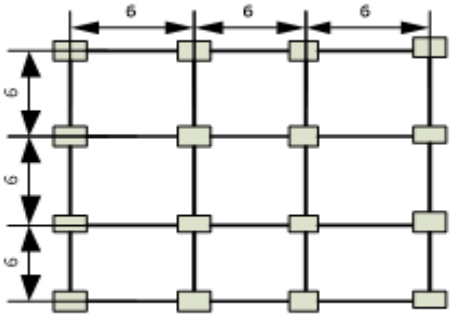

Fig.1: Plan of building model

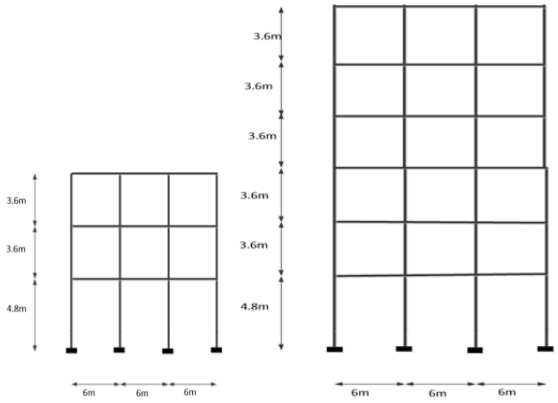

Fig. 2: Elevation of three and six storey bare frame building

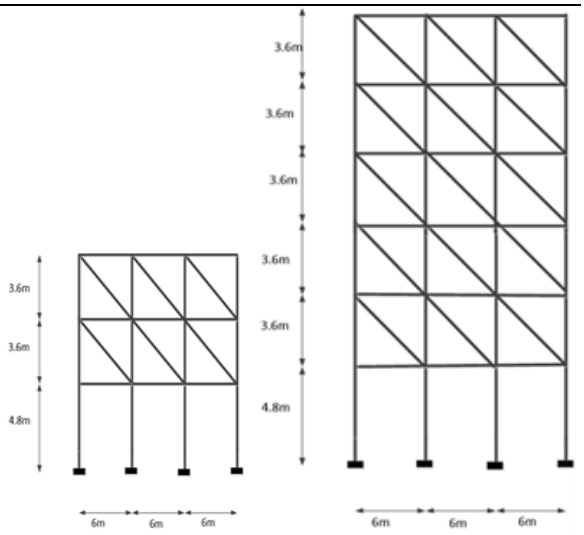

Fig. 3: Elevation of three and six storey building with solid concrete block infill

8th International Engineering Symposium - IES 2019
March 13-15, 2019, Kumamoto University, Japan

Study on Reinforced Compressed Mud Bricks

Sowmya N J[1] and Sucharitha K[2]

1 *Dept. of Civil Engg, Vivekananda College of Engg & Technology,Puttur, 574203, Karnataka, India. email: sowm.shyam@gmail.com*
2 *Dept. of Civil Engg ,KVG College of Engineering,Sullia, 574239, Karnataka, India. email:sucharithakevala9@gmail.com*

ABSTRACT: Soil is one of the cheapest and easily available materials for the house construction. Particularly for the economically weaker section who cannot easily afford the cost of construction. The factors such as population density, economic status, culture etc are changing rapidly in India, resulted increased rate of waste generation and acute problems in disposal of generated waste. Many studies are carried out to utilize the waste in many of the construction in which, bricks have become one of the most superior choices. In this present study the properties of stabilized compressed laterite bricks are investigated by conducting UCC, compressive strength and shape test. The laterite soil is stabilized with different percentages of fly ash (0,10,15,20,25%), coconut coir (0.25,0.5,0.75,1%) and Persea Macrantha gum (5,10,15,20%). The results showed that 20% of flyash in laterite soil with 5% of persea macrantha gives optimum strength and strength increases with the addition of coir content.
.

Keywords: Laterite soil, Fly ash, Coconut coir, Persea Macrantha, UCC, Compressive strength.

INTRODUCTION

In the construction industry bricks are the one of the basic material. Since olden days bricks are being used in great extent even today as building material because of its strength and cost effectiveness

The basic needs for the human beings for the survival is housing, Earth materials are one of the cheapest and easily available materials for the house construction. The various soils like black cotton soil, clay, laterite soil etc are having binding property and easy availability in huge amount can effectively used in making of building materials.

Growth of population, extending urbanisation, improved standards of living due to technological modernization have added to rise in both quantity and variety of solid wastes, generated by industrial, agricultural, mining and domestic activities. Now a day's many studies and researches are carried out for the improvement of bricks by mixing various waste products. In India the solid waste generation from Agricultural and Industrialactivities are about 2600 MT per year(Megha et. al 2015). These wastes are being dumped in large quantity and thus in other hand it converts valuable lands into dumping yards and also increase the cost of management of wastes results in environmental hazards. Only a small fraction of these wastes are being used for various purposes.

Rajendra et. al(2012), Saravanan et. al(2013)and Kunal et. al (2013) were examined the properties of stabilized soil by flyash(FA) varying from 0% to 50% with the increment of 10%. With the addition of FA , they observed the depletion in plastic limit and liquid limit and increase in CBR values up to the optimum dosage. Singh and Mittal(2014) and Shukla et. al(2015) studied the effects of coconut coir (CF) on the behavior of soil

with the addition 0.25%,0.50%,0.75% and 1.0% by the dry weight of soil and observed increase in maximum dry density, CBR and unconfined compressive strength up to the optimum dosage. **Aguwaet.al(2013)** concluded that ,CF has the potential to increase the compressive strength of laterite blocks by ten percent at 28 days of, curing duration, which results in reduction in mass by two percent.

In this study an effort is made to utilize laterite soil which is abundantly available in making of bricks with waste products like Fly Ash(FA) and coconut Fiber(CF). Bonding is the main criteria to improve the strength of bricks. Therefore the gum extracted from Persea Macrantha Gum(PMG) is utilized in addition to FA and CF in soil.

OBJECTIVES OF THE STUDY

The main aim of this work is to study the properties of LS bricks with the replacement of FA and addition of CF of varying percentages. Hence following objectives are framed for the study

- To study the basic properties of the materials used for the manufacture of brick.
- To determine the properties of compressed brick stabilized with different percentages of FA, CF and PMG.
- To determine the optimum dosage of FA and coir required for laterite soil brick

MATERIAL USED

In this study Laterite Soil (LS),Fly Ash (FA), Coconut Fibre (CF),water and Persea Macrantha Gum (PMG) were used to produce the compressed mud bricks.

Laterite Soil

Locally available laterite soil was collected from a a depth of 1m to free from vegetation and organic matter and stored in a dry place. The collected soil sample was tested to know its geotechnical properties(Table 1).

Fly ash

Class F fly ash was obtained from Baikampady, Mangalore .The specific gravity-2.30

Table 1 : Properties of soil

Properties	Laterite soil
Specific gravity	2.65
Gravel (%)	37
Sand (%)	34
Silt and Clay	29
Liquid limit (%)	34.45
Plastic limit (%)	23.52
Plasticity index (%)	10.93
Standard Proctor Test Maximum dry density(kN/m^3) Optimum moisture content (%)	 17.6 20.0
Unconfined compression strength(kN/m^2)	112.9

Coconut coir

Coconut coir is a fibrous material extracted from the locally available husk of coconut. They are sundried and cut in to a smaller length of 1cm before mixing with laterite soil.

Persea Macrantha gum

The plant belongs to Lauraceae family and is about 30m tall tree. In olden days this gum was used for smoothening of earthen wall. To prepare the gum firstly the bark of the tree was removed, cut in to smaller pieces and immersed in water. It was observed that, the higher the dosage, the thicker will be the suspension and the acidity of water is increases as the weight of bark increases(Table 2). To prepare this gum solution about 50 g bark was immersed in one liter water for about 12 hours before casting of brick.

Table 2: The pH of persea macrantha

Dosage of Persea Macrantha	3 days	7 days
50 g	5.44	5.40
75 g	5.26	5.26
100g	5.08	5.08

In this study portable water was used to bind all the materials together.

EXPERIMENTAL INVESTIGATION

First to find the optimum dosage of FA,the properties of soil stabilized with 10, 15, 20 and 25% of FA by weight of soil were studied.The effect of CF on selected dosage of stabilized mix (FA + LS) were determined by adding 0.25, 0.50, 0.75 and 1.0% by weight of soil. The optimum dosage of PMG to the soil was determined by replacing the OMC by 5, 10, 15, 20 and 100%.The properties of CF at various percentages were thendetermined for the optimum dosages of FA and PMG. Bricks were casted for LS + optimum dosages of FA and PMG with varying percentages of CF.

RESULTS AND DISCUSSION

Effect of FA on Atterberg's Limits of Soil

The Fig.1 indicates that FA reduces the plastic properties of soil. This is because the ash content absorbs some quantity of water. FA is the pozzolonic materials which require higher quantity of water for its pozzolonic action.

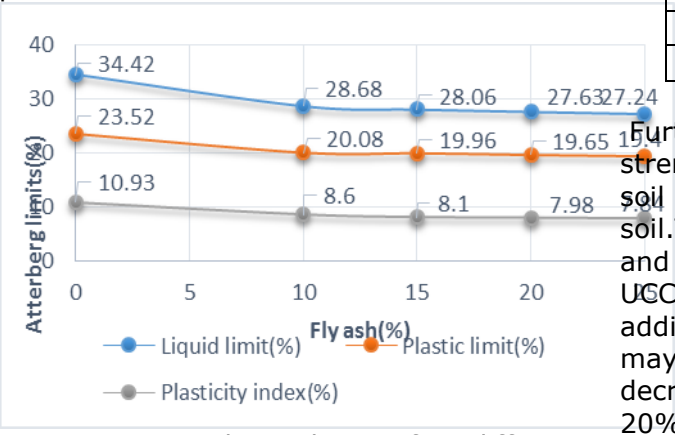

Fig 1: Atterberg limits for different percentages of fly ash

Effect of FA on Density and Water Content

It is clear from the Table 3 that, as the FA content increases the OMC decreases. This is because LS have more resistance to the movement of particles. But with the addition of fly ash the resistance to the movement of particles is reduced which results in reduction in OMC with addition of fly ash.The density is increases because the voids are filled by FA upto 20%, later the density decreases. This is because FA replaces the soil whose specific gravity is lesser than soil

Table 3:OMC and MDD of LS with Varying Proportions FA

FA(%)	OMC(%)	MDD(kN/m^3)
0	19.92	17.6
10	17.18	18.4
15	16.37	18.6
20	15.23	18.8
25	15.29	18.2

.

Effect of FA on Unconfined Compressive Strength of Soil

It is clear from the Table 4 that, as the percentage of FA increases there is an increase in the strength up to 20% replacement.

Table 4: UCC of LS with Varying Percentages of FA

FA (%)	Unconfined Compressive Strength (kN/m^2)		
	(1 day)	(7 days)	(28 days)
0	112.90	209.08	215.64
10	158.50	254.68	259.38
15	182.97	297.43	305.96
20	210.70	323.53	334.67
25	188.24	269.29	270.97

Further the addition of FA results in lesser strength, indicating 20% FA by weight of soil is the optimum content to blend the soil.The pozzolonic reaction between FA and clay mineral of soil leads to increase in UCC up to 20% of FA and further the addition of ash will not react with the soil, may stay as inert material which results decrease in UCC. Based on the results, 20% FA is considered as optimum and used for the further study.

EFFECT OF PMG ON SOIL

It is clear from the Table 5 that, as the dosage of PMG increases, the strength of soil decreases. To study the effect of PMG the OMC of soil is completely replaced by PMG. It is clear that PMG does not accelerate the strength of soil. But increase in strength is observed as the curing days increases. There is no much effect of PMG on soil beyond 10%. Therefore for the further study 5% of PMG by OMC is considered.

Table 5: UCC for Soil with Varying Percentages of PMG

PMG (%)	Unconfined Compressive Strength (kN/m^2)		
	(1 day)	(7 days)	(28 days
100	72.37	124.70	138.48
0	112.90	209.08	215.64
5	77.82	130.99	142.51
10	67.88	126.59	115.51
15	35.47	69.30	118.29
20	23.54	56.40	116.31

EFFECT OF CF ON SOIL STABILIZED FA

It is clear from the Table 6 that, UCC increases with the addition of fibers. The reason is that, the inclusion of fibers improves frictional resistance to deformation under load by interaction of fibers with soil particles.

Table 6: UCC of Soil with 20% FA and Varying Percentage of CF

FA (%)	CF (%)	Unconfined Compressive Strength (kN/m^2)		
		(1 day)	(7 days)	(28 days)
20	0.25	213.57	280.23	289.83
	0.50	249.62	310.66	327.25
	0.75	271.40	331.54	345.62
	1.0	310.90	345.94	350.89

EFFECT OF FA, CF and PMG ON SOIL

It is clear from the Table 7 that, as the curing period increases the strength of FA and PMG in soil also increases. This trend is observed for all dosages of CF. The increase in strength is due to FA and PMG whereas CF is the inert material, it does not increase the strength with curing. Therefore the strength increases only because of FA and PMG.

Table 7: UCC Value for Soil with FA, PMG and CF

FA (%)	PMG (%)	CF (%)	Unconfined compressive Strength (kN/m^2)		
			(1 day)	(7 days)	(28 days)
20	5	0.25	161.2	251.3	262.6
		0.50	180	263.3	280.6
		0.75	193.4	265.6	290.6
		1.0	139.1	240.4	265.5

Compressive Strength of Bricks

It is clear from the Table 8 that, as the curing period increases there is increase in strength of FA and PMG in soil also increases. This trend is observed for all dosages of CF. The increase in strength is due to FA and PMG whereas CF is the inert material, it does not increase the strength with curing period but it acts as a reinforcing material contributing to initial strength.

WATER ABSORPTION TEST

This test was carried out for the cast bricks with constant FA and PMG at varying percentage of CF. But in this study,the specimens are not supportive to perform the test, as they were dissolved.

Table 8:Compressive Strength of Bricks

Mix Designation	Compressive strength(N/mm^2)	
	(7 days)	(28 days)
FA	0.65	0.66
20% FA+5% PMG+ 0.25% CF	0.75	0.87
20% FA+5% PMG+ 0.50% CF	0.95	0.98
20% FA+5% PMG+ 0.75% CF	1.24	1.29

SHAPE TEST

The shape tests were carried for every percentages of bricks. Before keeping it in oven the original size of the brick i.e. 200mmx100mm x100mm was measured and after removing from oven, the brick size was again measured and observed changes in the size i.e. 198mm x 98mm x 98mm.

BRICK PILLAR TEST FOR BRICKS WITHOUT AND WITH PMG

The brick pillar tests were carried out for the bricks with 20% FA and with variation of CF at 0.25, 0.50 and 0.75%.Three number of samples were cast for each percentages.

It is clear from the Table 9 that, the strength increases from 1.14 to 1.49 N/mm^2 at 7 days and 1.20 to 1.52 N/mm^2 at 28 days for the increased CF content and observed no much increase in the compressive strength.

Table 9: Brick Pillar Test Results (Without PMG)

Mix Designation	Compressive strength(N/mm^2)	
	(7 days)	(28 days)
20% FA+ 0.25% CF	1.14	1.20
20% FA+ 0.50% CF	1.33	1.39
20% FA+ 0.75% CF	1.49	1.52

Table 10: Brick Pillar Test Results (With PMG)

Mix Designation	Compressive strength(N/mm^2)	
	(7 days)	(28 days)
20% FA+5% PMG+ 0.25% CF	1.35	1.46
20% FA+5% PMG+ 0.50% CF	1.52	1.64
20% FA+5% PMG+ 0.75% CF	1.62	1.73

Later constant 5% PMG was added to the brick and the brick pillar tests were carried out for 7 and 28 days. It is clear from the Table 10 that, the strength increased from 1.35 N/mm^2 to 1.62N/mm^2,1.46 $N/mm^2$to 1.73N/mm^2 at 7 and 28 days. It is observed that, the strength of brick pillar test with PMG is increased by higher amount as compared to brick pillar test without PMG.

CONCLUSIONS

Based on the experimental study following conclusions are drawn:

- Increase in the percentage of FA in soil decreases the Atterberg's limits.
- Addition of FA decreases the OMC and increases the density.
- Increase in FA increases the UCC value and shows optimum at 20%. The strength of 112.90 kN/m^2increases to 210.70 kN/m^2, 209.08 to 323.53kN/m^2, 215.64 to 334.67 kN/m^2at 1 , 7 and 28 days respectively and it got decreased after 20% FA .
- As the percentage of gum was increased, the strength got decreased and good strength was obtained at 5% of PMG.
- Increase in percentage of CF with 20% FA in laterite soil shows increase in strength in different curing days. Laterite soil with 20% FA and 5% 0f PMG shows good strength at 0.75% of CF at all curing days.
- The compressive strength of 0.65 and 0.66 N/mm^2 for laterite brick with 20% FA at 7 and 28 days respectively. With the addition of 5% PMG and varying percentage of CF, the strength got increased to 1.24 and 1.29N/mm^2 at 7 and 28 days respectively.
- The brick failed during water absorption test indicates that it cannot use for exterior walls.
- The Brick pillar test shows that 20% FA with 5% PMG and varying percentages of CF the strength increases.

REFERENCES

[1] Kunal, A., Awanish, K.S., and Sidharth, S. (2013), "A Comparative Study B/W Black Cotton Soil and Alluvial Soil for Economical Pavement Design by Lime & Fly-Ash Stabilization", International Journal of Engineering Research and Applications, ISSN : 2248-9622, Vol 3, Issue 5,pp: 1609-1620.

[2] Singh, R. R and Mittal, S., (2014), "Improvement of local subgrade soil for road construction by the use of coconut coir fiber", International Journal of Research in Engineering and Technology, Vol 3, Issue 05, pp: 707-711.

[3] Megha K., Garima S., Atul T. (2015), "The Study on Use of Rice Husk Ash", International Journal of Science and Engineering., Vol 3., ISSN: 2347-2200., pp :85-88.

[4] Shukla, D., Rajan, S., Saxena, A.K., and, Jha A.K. (2015), "Soil Stabilization Using Coconut Coir Fibre", International Journal for Research in Applied Science & Engineering Technology (IJRASET), ISSN: 2321-9653, Vol 3 Issue IX, pp: 305-309.

[5] Rajendra, P. H., Agrawal, M.L., and Agrawal, A. (2012), "Use of fly ash in black cotton soil for road construction", Recent Research in Science and Technology, ISSN: 2076-5061, Vol 5, Issue 5, pp: 30-32.

[6] Rama S. K. V and Vikranth J "Application of Coconut Coir and Fly ash in Sub grade strengthening" The International Journal Of Engineering And Science, Vol. 3, Issue 12, December - 2014 , pp.48-54

[7] Saravanan, R., Roopa, S.T., and Merlin, J. (2013) "A study on Soil Stabilization of Clay Soil using Fly ash", International Journal of Research in Civil Engineering, Architecture and Design, ISSN Online: 2347-2855, Vol 1, Issue 2, pp: 33-37.

.

8th International Engineering Symposium - IES 2019
March 5-7, 2019, Kumamoto University, Japan

Nonlinear assessment of building with and without lateral load resisting system

Deepa S[1], I.R.Mithanthaya[2] and S.V.Venkatesh[3]

1 Research Scholar, Department of Civil Engineering, NMAM Institute of Technology Karnataka, Nitte, Udupi, India. email: deepasujayakumar@yahoo.co.in
2 Professor, Department of Civil Engineering, NMAM Institute of Technology Karnataka, Nitte, Udupi, India. e-mail: Mith9999@yahoo.com
3 Professor,Department of Civil Engineering, PES Institute of Technology Bangalor Karnataka, India. Email: svvenkatesh@pes.edu

ABSTRACT: Earlier in the conventional method of analysis the structures were mainly designed for gravity load and less prominence was given to lateral load analysis, under such circumstances the failure of the building occurred when it was subjected to earthquake load. Pushover analysis performance based is one such analysis which predicts the week points in the building. The analysis shows the formation of hinges at various stages which can be strengthened by providing lateral load resisting systems such as shear wall. In the present study an existing 10 storey building is chosen which is designed only for gravity load. The 3D building is modelled using Sap 2000 V19.2 software in severe seismic zone V as per standards IS 1893 (Part-1:2002) and ASCE41-13 and FEMA 440 for nonlinear analysis. Totally 8 models are analysed with three types of soil conditions (Hard soil, Medium soil and Soft soil) and subjected to Equivalent Static analysis with fixed base. The building is latter subjected to Nonlinear Static pushover analysis and the results indicate the week point in the building in the form of hinges. The week points are strengthened by placing Lateral load resisting systems i.e. Shear wall. Further detailed investigation of nonlinear analysis indicate that the bare frame with lateral load resisting system shows better performance and also the building works out to be economical. The results are thoroughly analysed for Base shear, Performance point, Hinge formation.

***Keywords**: Equivalent Static analysis, Nonlinear Pushover analysis, Lateral load resisting system*

INTRODUCTION

"Traditional retrofit design methods assume that buildings respond elastically to earthquakes. In reality large earthquakes can severely damage buildings causing inelastic behavior that dissipates energy. The assumption that buildings remain elastic simplifies the engineers work but obscures a basic understanding of actual performance. The use of traditional procedures for existing buildings can lead to erroneous conclusions on deficiencies and unnecessarily high retrofit costs. More disturbingly they can miss important defects in some buildings. Foundations are a good example. Traditional analysis normally assumes that buildings are rigid at base, which can lead to the prediction of high forces implying extensive retrofitting measures for walls and floors. It also can underestimate the structural displacement that control damage to other parts of the structure, such as columns. In reality, foundations often are quite flexible. Rocking or yielding of the supporting soil material might reduce forces and the need to retrofit the shear walls. The foundation movements, lead to larger displacements which may imply potential collapse of columns. New analysis procedure

described in this document help describe the inelastic behavior of the structural components of a building. Analysis can estimate more accurately the actual behavior of the building during specific ground motion. The document provides extensive guidance on the use of these procedures including properties for concrete components. The analysis procedure tells how to identify which part of the building will fail first. As the load and displacement increases, other elements begin to yield and deform in elastically. The resulting graphic curve is an easy to visualize representation of the capacity of the building. Several alternative technique allow the demand from a specific earthquake or intensity of ground shaking to be correlated with the capacity curve to generate a point on the curve where capacity and demand are equal. This performance point is an estimate of the actual displacement of the building for specified ground motion."

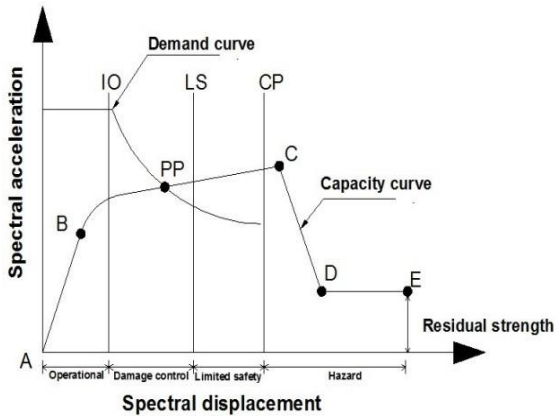

Fig.1

METHOD OF ANALYSIS

A study on 10 storey 3D building is analysed for nonlinear analysis where hinges are assigned for columns and beams as per standards ASCE41-13 and FEMA 440. The vertical loads and lateral loads are applied in corresponding X and Y direction, monitored displacement is opted and pushover analysis is carried out by using Sap 2000 V19.2 software. The bare frame is analysed and the pushover curve is plotted to predict the behaviour of the structure when it exceeds elastic limit. The maximum displacement response during an earthquake denotes the demand of the building. The weak points are highlighted by deformed shape of the structure in the form of hinges which indicate various failure modes. These weak points are strengthened by placing the lateral load resisting systems. The shear wall is placed at these week points and analysed for performance point and also hinge formations. Additionally the analysis is executed by considering the base of the structure to be fixed with 3 types of soil but it was observed that soil type does not change the structures deformed shape so analysis was mainly carried for soft soil and the shear wall was placed starting from 2 stories at ends, middle and in-between by varying the storey height. The shear wall was chosen to place in-between by varying the height as the results of Bare frame showed hinges in the range of C-D was more in middle of the Bare frame so, in order to bring these hinges from C-D to IO-LS range the analysis was performed by placing shear wall at different location for different height.

RESULTS AND DISCUSSION

Results attained after the analysis of a 10 story, bare frame with rigid base subjected to pushover analysis is tabulated as below in Table 1 and Fig.2 and the Shear wall was placed at different locations for different storey height in Fig.3 to Fig.9 also the results obtained by the Lateral load resisting systems at different locations is tabulated in Table2. There is a difference noticed at the performance point where the demand and capacity of the structure meets. The changes in the formation of capacity curve for different models chosen is shown in Fig. 9 to Fig.16 It is noticed that there is not much changes observed in the formation of hinges in different types of soil.

Shape of Pushover Capacity curve

The shape of the Capacity curve for bare frame shows the shape similar to Fig.1 showing all stages of Collapse and also reaching the stage beyond E. By placing the lateral load resisting systems the shape of the curve changes drastically finally showing the elastic states A-B and

B-IO state. This study is mainly to show that when shear walls are placed in critical stage positions of hinges the structure can be brought to life safety range and also it seems to be economical based on height of shear wall wwhen compared to 10 storey placed in between as in Fig. 9 and Fig.16

Hinge formation

The Fig.9 and Fig.16 shows that with the location of shear wall the hinges which were Beyond E range in Bare frame has almost reached elastic state with 1538 hinges in A-B range and 382 hinges in B-IO range. Whereas the Fig.4 to Fig.8 shows number of hinges in A-B and B-IO stage but with more number of hinges in B-IO range compared to the location of shear wall in Fig.9 This shows that the more hinge formation in elastic state is best location of shear wall as in Fig.9

CONCLUSIONS

The following conclusions are deduced from this study:

1.The location of shear wall at critical hinge locations changes the behaviour of structure from Beyond collapse state as in Bare frame to life safety state as with LLRS (refer Fig.9).
2. Variation in length of shear wall shows variation in hinge formation.
3. Variation in height of the shear wall shows the structure to be economical.
4. Variation in location, height and length of shear wall shows drastic variation in capacity curve formation.

REFERENCES

1. Ashraf M, Siddiqi Z.A, Javed M.A, (2008), "Configuration of a multistorey building subjected to lateral forces", Asian Journal of Civil Engineering (Building and Housing) Vol. 9, No.5, pg. 527-537.
2. Bell. D.K. and Davidson. B.J. (2001), "Evaluation of Earthquake Risk Buildings with Masonry Infill Panels", NZSEE 2001 Conference, paper No. 4.02.01, pg. 1 – 9.
3.Can Balkaya, Erol Kalkan, (2003), "Estimation of fundamental periods of shear-wall dominant building structures" Earthquake Engineering and Structural Dynamics 32 (2003) pg. 985 – 998.
4.Diptesh Das and Murthy. C.V.R (2004), "Brick masonry infills in seismic design of RC framed buildings: part 1 – Cost implications", The Indian Concrete Journal, July 2004, pg. 39 – 44.
5.Ghobarah. A, Abou Elfath. H, (2001), "Rehabilitation of a reinforced concrete frame using eccentric steel bracing", Engineering structures 23 (2001) pg. 745 - 755.
6.Hasan kaplan, Salih Yilmaz, Nihat Cetinkaya and Ergin Atimtay (2011) "Seismic strengthening of RC structures with exterior shear walls", Indian Academy of Sciences Sadhana Vol. 36, part 1, February 2011, pg. 17 – 34.
7.Hyun-Su Kim, Dong-Guen Lee, Chee Kyeong Kim (2005), "Efficient three-dimensional seismic analysis of a high-rise building structure with shear walls", Engineering structures, 27 (2005), pg. 963 – 976.

FIGURES AND TABELS

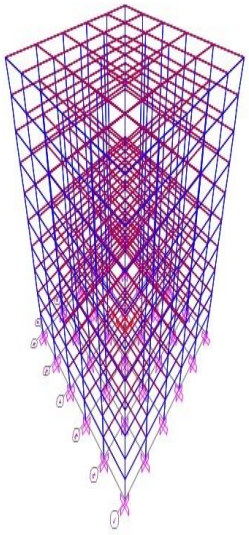

Fig.2BF

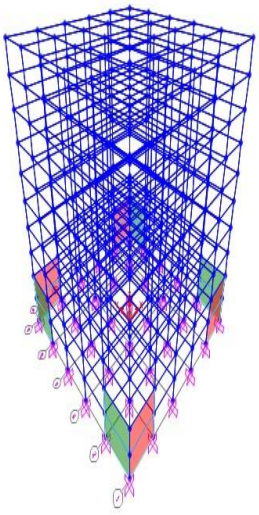

Fig.3 ISWE

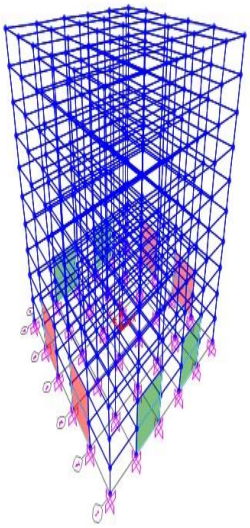

Fig.4 ISWM

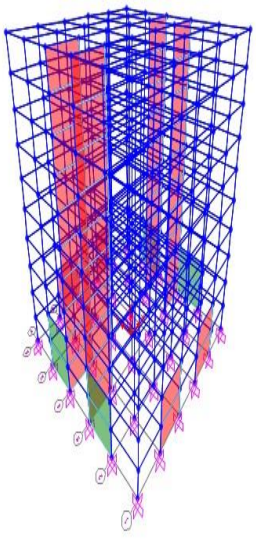

Fig.5 ISXYM-2ST-MX-10ST

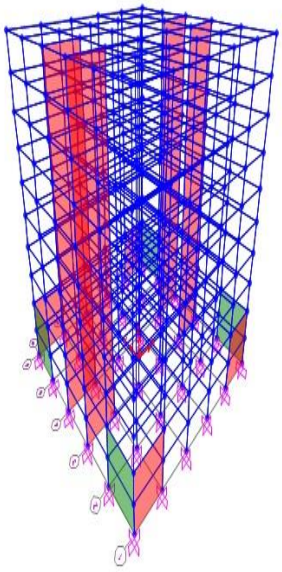

Fig.6 ISXYE-2ST-MX-10ST

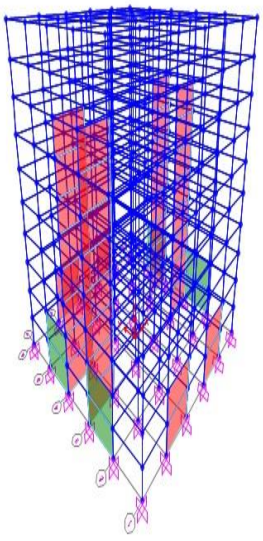

Fig.7 ISXYE-2ST-MX-8ST

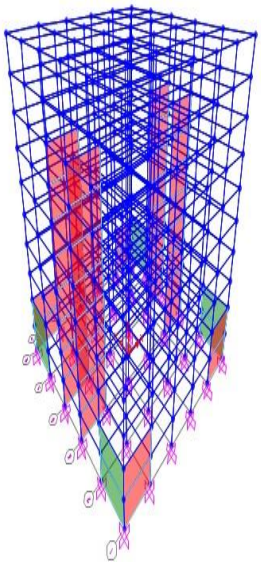

Fig.8 ISXYE-2ST-MX-8ST

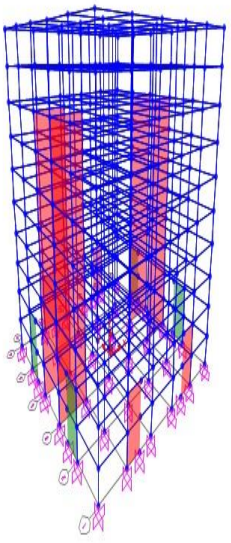

Fig.9 ISXYM-2ST-HALF-MX-8ST

PUSHOVER CAPACIY CURVE

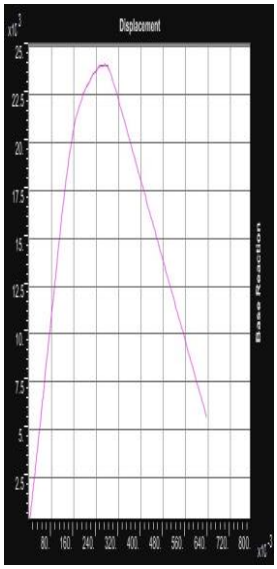

Fig.9 BF

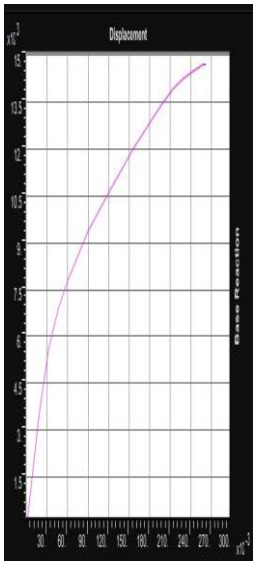

Fig.10 ISWE

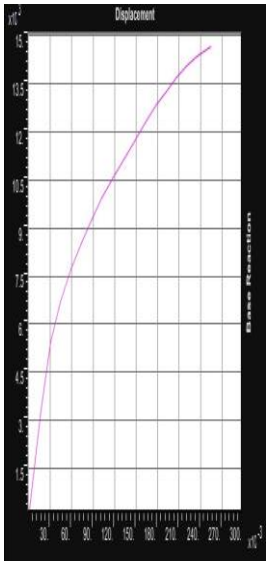

Fig.11 ISWM

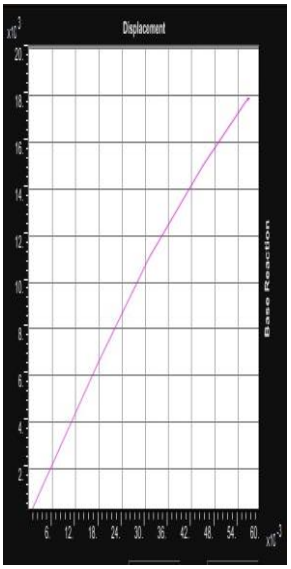

Fig.12 ISXYM-2ST-MX-10ST

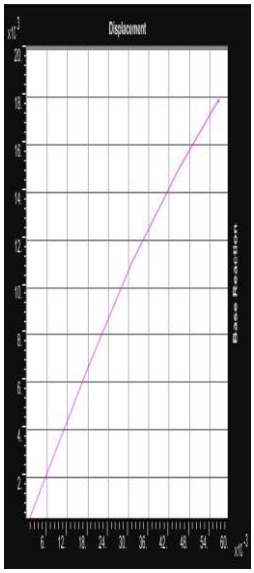

Fig.13 ISXYE-2ST -MX -10ST

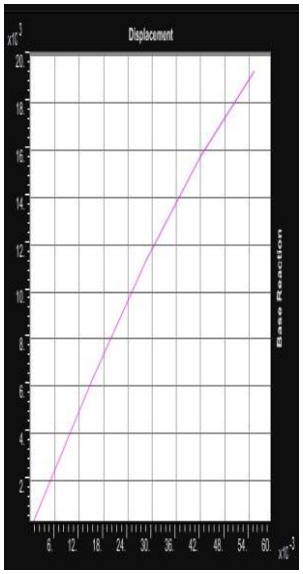

Fig.14 ISXYM-2ST -MX-8ST

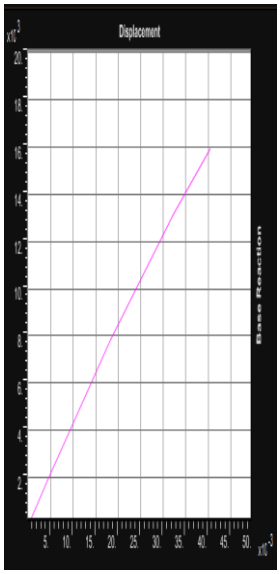

Fig.15 ISXYE-2ST -MX-8ST

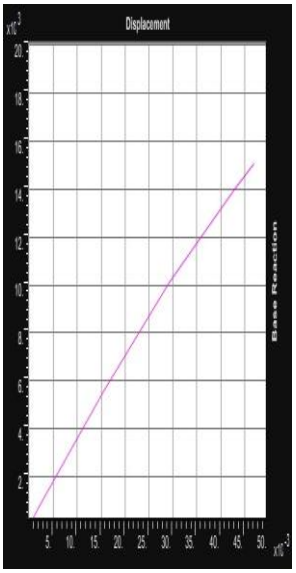

Fig.16 ISXYE-2ST half –MX-8ST

Table 1.Pushover Capacity Curve for Bare frame of 10 story , 5x5 Bay, 5mt in X and Y direction

Step	Displace	Base Force	AtoB	BtoIO	IOtoLS	LStoCP	CPtoC	CtoD	DtoE	Beyo	Total
	ment m	KN								ndE	
0	0.000	0.000	1920	0	0	0	0	0	0	0	1920
1	0.005	693.476	1920	0	0	0	0	0	0	0	1920
24	0.117	16193.425	1914	6	0	0	0	0	0	0	1920
32	0.166	21206.485	1736	184	0	0	0	0	0	0	1920
33	0.171	21501.183	1720	184	16	0	0	0	0	0	1920
36	0.194	22534.267	1632	258	14	16	0	0	0	0	1920
37	0.199	22728.152	1622	260	22	0	0	16	0	0	1920
38	0.204	22880.374	1622	250	28	4	0	16	0	0	1920
119	0.615	6670.899	1554	212	50	4	0	100	0	0	1920
120	0.619	6494.767	1554	212	50	4	0	96	4	0	1920
121	0.619	6494.766	1554	212	50	4	0	96	0	4	1920
122	0.624	6237.134	1554	212	50	4	0	96	0	4	1920
123	0.633	5772.393	1554	212	50	4	0	94	0	6	1920
124	0.635	5666.870	1554	212	50	4	0	92	2	6	1920

Table 2.Pushover Capacity curve for different locations of shear wall for different height

Type of Frame	Step	Displ ac m	Base Force kN	A B	B IO	IO LS	LS CP	CP C	C D	D E	Bey o E	Total
BF	124	0.63	5666.87	1554	212	50	4	0	92	2	6	1920
ISWE	21	0.26	14695.93	1258	418	192	0	0	52	0	0	1920
ISWM	18	0.25	14665.54	1264	414	190	14	0	38	0	0	1920
ISXYE-2ST-MX- 10ST	8	0.06	17873.56	1422	498	0	0	0	0	0	0	1920
ISXYM-2ST-MX-10ST	5	0.05	18859.88	1448	472	0	0	0	0	0	0	1920
ISXYE-2ST-MX-8ST	12	0.06	18656.99	1418	502	0	0	0	0	0	0	1920
ISXYM-2ST-MX-8ST	5	0.06	19347.82	1448	472	0	0	0	0	0	0	1920
ISXYM-2ST 1/2-MX-8ST	5	0.05	15045.55	1538	382	0	0	0	0	0	0	1920

MECHANICAL ENGINEERING
&
RELATED FIELDS

8th International Engineering Symposium - IES 2019
March 13-15, 2019, Kumamoto University, Japan

Corrosion and Wear Resistance of Nano-Metal Oxide CeO_2Daped Aluminum

HARISHANAND K S [1],Yogish Rao[2], Hemanth Suvarna[3], Omprakash B K[4], Gurumurthy J L[5] and Revati R Kulkarni[6]

1. *Department of Mechanical Engineering, Alva's Institute of Engineering and Technology, Moodbidri 574 225, India email:*aietmech08@gmail.com
2. *Department of Mechanical Engineering, Alva's Institute of Engineering and technology, Moodbidri 574225,India email:raoyogish@gmail.com*
3. *Department of Mechanical Engineering, Alva's Institute of Engineering and technology, Moodbidri 574225,India email:hemanth05@gmail.com*
4. *Department of Mechanical Engineering, Alva's Institute of Engineering and Technology, Moodbidri 574 225, India*
5. *Department of Mechanical Engineering, Alva's Institute of Engineering and Technology, Moodbidri 574 225, India*
6. *Department of Mechanical Engineering, Alva's Institute of Engineering and Technology, Moodbidri 574 225, India*

ABSTRACT: Nano Ceria (CeO_2) powder is synthesized by both low temp solution Combustion method and hydro thermal process. The characterization of the product by scanning electron microscope (SEM) and powder X-Ray diffraction (PXRD) is obtained. The composite block of nano-CeO_2/Al is fabricated using powder metallurgy principles. The study on microstructure Micro hardness, Corrosion resistance of the product using, SEM, Vickers microhardness tester, weight loss methods and wear resistance using pin on disc method was carried out. The powder metallurgy samples with nano-CeO_2 content for corrosion resistance, micro hardness, wear resistance and micro structure at varied percentage are evaluated. The result for combustion method shows that micro hardness, micro structure and wear resistance are improved with addition of nano-CeO_2. Wear resistance for the same sample showed greater resistance at 5wt% of nano-CeO_2: Corrosion test proved no loss of mass.

Keywords: *Micro hardness, Microstructure, corrosion resistance, Nano CeO_2, wear resistance.*

INTRODUCTION

The need for coatings with improved resistance to highly aggressive environments is large as a result of a growing demand for extended safe service life of industrial objects. The historic research work as per literatures available suggests that the corrosion and wear resistance of nitrides coatings [1], (TiCr)N and Ti/TiN PVD coatings [2], hard chromium coatings[3], HVOF cermet coatings[4] as well as of composite electrodeposited coatings of nickel and nano-crystals of silicon carbide was studied[5,6].Among the composites, Aluminum matrix composites attract much attention due to their lightness, high thermal conductivity, and moderate casting temperature. Engine pistons, engine blocks and other automotive and aircraft parts operating under severe friction conditions are fabricated from reinforced aluminium matrix composites. Various kinds of ceramic materials, e.g. SiC, Al_2O_3, MgO.

The improvement of corrosion resistance by rare earth elements added to pure Zn has been the purpose of studies by Hilton et.al and Wilson et.al firstly in 1980s. It is suggested that the $CeCl_3$ of 1.0 g/L can make the corrosion velocity of the pure zinc as low as 1/10 of original, and that of the electroplating zinc as low as ½ of original. After the corrosion experiments, there is a layer of yellow film on the surface of both the pure Zn and electroplating zinc. And then Hilton et.al studied the composition and structure of

the film thoroughly, and discovered that the main compositions in the film were CeO_2 and Zn. In this work, the nanoCeO_2/Al powder blends were used to prepare nano-CeO_2/Al blocks by cold pressing followed by sintering, and the performance of the fabricated blocks was studied [3,4].

Preparation of nano-CeO_2/Al powder blends.

Nano-CeO_2 powder produced by combustion method was added to 99.5% pure commercially available aluminium powder with wt% of nanoCeO_2 varying from 0 to 5%. Aluminium powder which was used had average particle size of 74 microns. Powders were mixed for 30 minutes by hand mixing and loaded in metal die for compaction.

Preparation of nano-CeO_2/Al blocks.

Nano-CeO_2 doped Al blocks are fabricated with powder metallurgy technique. Powder blends were cold pressed at 150 MPa to approximately 90% compression and then sintered at 520°C for 1hour. The sintered nano-CeO_2/Al blocks were polished with emery papers with grit size ranging from 200 to 2000 followed by diamond paste polishing for obtaining mirror finish surface on the specimen blocks.

Microstructure analysis of Nano-ceria/ Al blocks.

Light and Scanning Electron Microscopy (SEM) were employed to analyze the microstructure of the polished nano-CeO_2/Al blocks.

Micro-hardness test.

Micro hardness was tested using Vickers Micro-hardness tester with diamond indenter in the form of right pyramid and a square. An optical microscope with up to 400x magnification along with a Micrometer attachment in the eye piece was used to observe and measure the length of the diagonal of indentation. Microscope attachment helps in determining the distribution of nano-CeO_2 dopant in the samples doped at percentages ranging from 0-5%.

Formula used:

$$HV = \frac{2F\sin\frac{136^o}{2}}{d^2} \qquad HV = 1.854\frac{F}{d^2} \text{ approximately} \quad \ldots (1)$$

Where ‘F’ is Load applied in N, ‘d’ is the average diagonal of indentation and ‘HV’ represents Vickers Hardness Number.

Wear resistance test.

Pin on disc apparatus was used to measure the wear resistance of the samples. Nano-CeO_2/Al samples of size 12x12x20 mm^3 were fabricated and mounted on Pin on disk apparatus and made to rub against the rotating stainless steel disk. Area exposed to wear was 12x12 mm^2. Relative velocity of wear test sample with respect to the rotating disk was 2.6 ms-1 and sliding distance was 1.57 km. Mass loss due to wear was calculated for each sample after completion of wear test.

Corrosion resistance test.

Two separate tests were performed to evaluate the corrosion resistance of the nano-CeO_2/Al blocks-

- The specimens were soaked in the spray tank with 3.5% NaCl solution for 40 hr and then were rinsed, dried and weighed. The corrosion resistance was evaluated by the mass loss per area, Δ_m/S (Δ_m is the mass loss and S is the surface area).
- The specimens were soaked in the spray tank with 0.5 mol $MgSO_4$ solution for 6 hr and then were rinsed, dried and weighed.

RESULTS AND DISCUSSIONS

Micro structure analysis of sintered nano-CeO_2/Al blocks:

Nano-CeO_2 particles can be seen well embedded in the grains of aluminium matrix in Fig 2, Fig 3, Fig 6, Fig 7, as a result of which the structure becomes denser and grains compact. Nano-CeO_2 particles are evenly distributed in Al matrix in case of lower doping percentages (0% to 1%) and agglomeration of nano CeO_2 cannot be seen in major part of the Al matrix as shown in Fig.2.

This indicates that the material has uniform structure and steady performance at doping percentages less than 1%. At higher doping percentages (2.5% and 5%), agglomeration of nanoCeO_2 is more common in the Aluminium matrix and the nano-CeO_2 particles are not evenly distributed as shown in Fig .3 and Fig.7.

This uneven distribution and agglomeration of nano-CeO_2 in the Al-matrix leads to density variations from one region of the matrix to another, porosity, non-uniform structure and unsteady performance. Agglomeration of nanoCeO_2 can lead to increase in porosity of the Al matrix around the agglomerations as a result of difference in thermal expansion coefficient from one location in the matrix to another. Porosity is more commonly seen in the sample with 2.5 wt% of nano-CeO_2 and lesser in 1 wt% since pore formation took place mostly around the nano-CeO_2 reinforcement embedded in the host matrix. But due to agglomeration of nano-CeO_2 in the aluminium matrix at high wt%, the porosity in the matrix around sights of agglomeration is high and leads to reduction in uniformity in the matrix.
Non-uniform distribution of the reinforcement material, non uniform grains in the matrix and non uniform thermal expansion coefficient within the sample blocks which results in matrix with uneven hardness from one region to the other.

Overall it can seen from Fig.7 that nano-CeO_2 can be used to increase the micro hardness of aluminium matrix since nano particles get embedded into the grain boundaries, result into uniform and finer grain size in the matrix at the time of sintering. Finer and uniform grain size represents higher micro hardness since grain boundary dislocations are reduced.

Wear Resistance.
Wear resistance of the samples was evaluated in terms of mass loss in samples after the wear test was carried out using pin on disc wear testing machine. The test-rig setup is shown in Fig.8. The test parameters such as load, track radius(500mm), room temperature, speed of disc (500rpm), time(5min) where maintained constant during experiments and results are summarized in Table 1. With the increase in wt% of reinforcement in the samples, mass loss due to wear reduced. Pure Al sample showed highest mass loss of 0.0279 gm where as the sample reinforced with 5 wt% of nano-CeO_2 showed least mass loss of 0.0195 gm. Clearly, it can be seen that increase in wt% of nano-CeO_2 in
Al matrix improves the wear resistance significantly. This increase in wear resistance can be attributed to addition of ultra-fine ceramic reinforcement which possess high hardness, wear resistance and at the same time a strong interfacial bonding with the host matrix.

CONCLUSIONS

The present study demonstrates CeO_2 Nano powder can be synthesized by a low temperature solution combustion method using cerium nitrate and citric acid. Nano-CeO_2 reinforced Aluminium matrix showed improved micro hardness as compared to pure Al matrix. Nano-CeO_2 crystals are well distributed in the Al matrix when doping percentage is increased from 0.1 to 1% and influence their ceramic properties to the matrix like high hardness, and low wear rate due to increased density of the matrix. Optimum wt% of Nano-CeO_2 was found to be 1% with regard to uniform distribution of the reinforcement and highest micro hardness value of 615.32 Hv/0.5kg among all the samples that were considered for evaluation. Increasing trend in wear resistance of samples with increase in wt% of Nano-ceria shows that ceramic particles as Nano-reinforcement can impart superior wear resistance to the host Aluminium matrix. Metal oxide Nano particles are very efficient at imparting their inherent properties to the host matrix like high hardness, refractoriness and strength since they have high surface area to volume ratio. They reduce inter particle spacing in the host matrix and favour the formation of a more compact matrix.

REFERENCES

[1] S.Rossi,L.Fedrizzi,Y.Massiani,F.Vacandio,P.L.Bonora,Mater. Sci.Forum289–292(1998)729.

[2] S.Rossi,L.Fedrizzi,M.Leoni,P.Scardi,Y.Massiani,ThinSolidFilms350(1999)161.

[3] L.Fedrizzi,S.Rossi,F.Bellei,F.Deflorian,Wear253(2002)1173.

[4] L.Fedrizzi,S.Rossi,R.Cristel,P.L.Bonora,Electrochim. Actain press

[5] L.Benea,P-L.Bonora,A.Borello,S.Martelli,F.Wenger,P.Ponthiaux,J.Galland,SolidStateIonics151(2002)89.

[6] L.Benea,P-L.Bonora,A.Borello,S.Martelli,Wear249(2002)995.

[7] S.Psarrou,J.Macheras,C.Kollia,N.Spyrellis,Trans.IMFAssoc. India6(1997).

[8] AnsaryYar, M. Montazerian, H. Abdizadeh, H.R. Baharvandi. Journal of Alloys and Compounds 484 (2009) 400– 404.

[9] Chunyan Tiana, NingLiua, MaohuaLua . Journal of materials processing technology 2 0 5 (2 0 0 8) 411–418

[10] WANG Qian. Trans. Nonferrous. Soc. China 17(2007) s622-s625

[11] Abdulkadir EKSI, SuleymanSARITASTurkish J. Eng. Env. Sci. 26 (2002) , 377 - 384.

[12] I.M. Hutchings, Mater. Sci. Technol. 10 (1994) 513–517.

[13] R.L. Deuis, C. Subramaniun, J.M. Yellup, ―Abrasive wear of aluminium composites—areview‖, Wear 201 (1996) 132–144.

[14] Alpas AT, Zhang J., ―Effect of SiC particulate reinforcement on the dry sliding wear of aluminum–silicon alloys (A356)‖, Wear 1992; 155:83–104.

[15] A. Ibrahim, F.A. Mohamed, E.J. Lavernia, ―Particulate reinforced metal matrix composites—a review‖, J. Mater. Sci. 26 (1991) 1137–1156.

Tables and Figures

Table 1 Comparison of weight Loss during corrosion experiment.

Wt% of Nano-CeO2	0%	1%	5%
Initial Weight (gm)	4.8351	4.7272	4.8621
Final Weight (gm)	4.8072	4.7034	4.8426
Weight Loss (gm)	0.0279	0.0238	0.0195

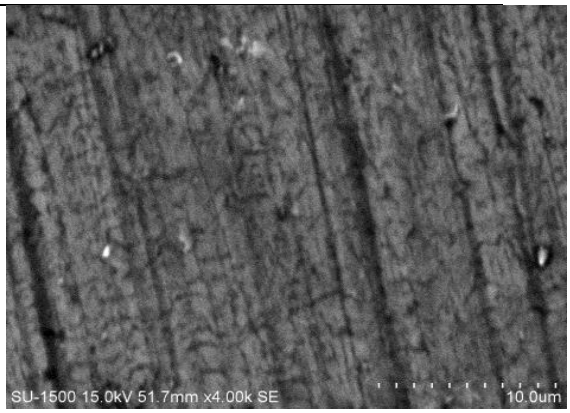

Fig 1: SEM Image of Pure Al matrix

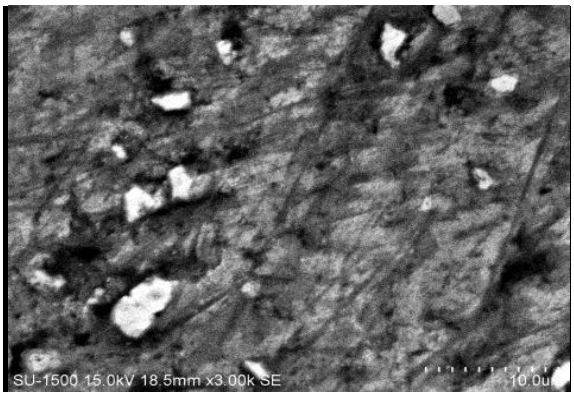

Fig 2: SEM image of 1% ceria doped Al matrix

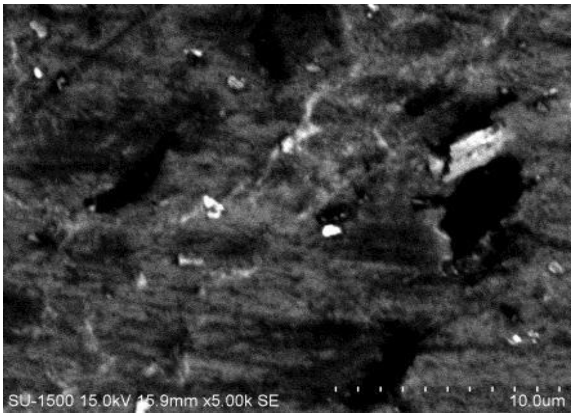

Fig 3: SEM image of 2.5 % ceria doped Al matrix

Fig 4: Optical Microscope Utilized for the study

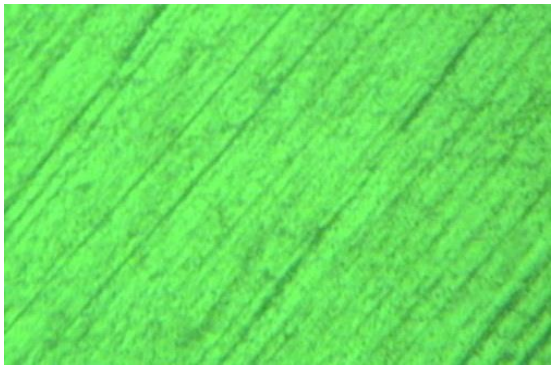

Fig 5: Optical Microscopy of Pure Al matrix(400x magnification).

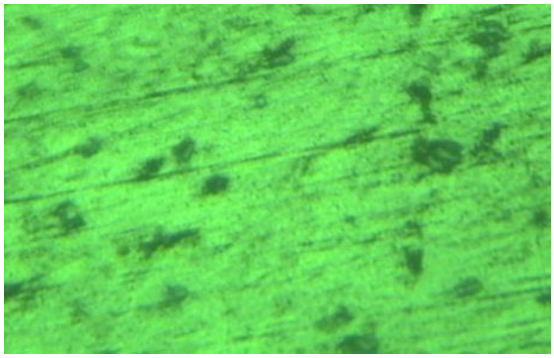

Fig 6: Optical Microscopy of 1% ceria doped Al matrix (400 x magnifications).

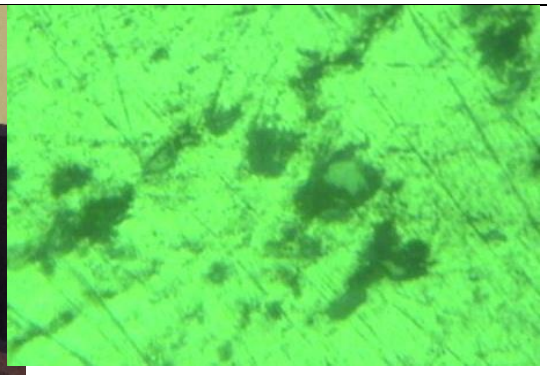

Fig 7: Optical Microscopy of 2.5% ceria doped Al matrix (400 x magnifications).

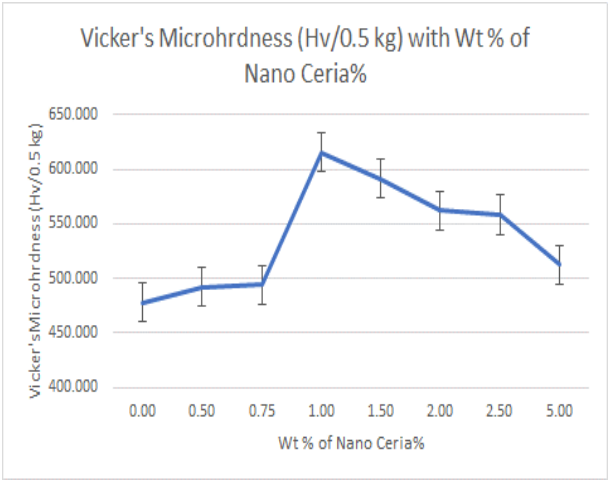

Fig 7: Vicker's Microhrdness (Hv/0.5 kg) with Wt % of Nano Ceria%

Fig 8: Pin On Disc Wear Test-Rig

8th International Engineering Symposium - IES 2019
March 13-15, 2019, Kumamoto University, Japan

Study on Stress Analysis and Fatigue Damage Calculation for Civilian Aircraft Wing Attachment Bracket

Sagar B S[1], Satyanarayan [2] and **Prashanth N[3]**

1 *Department of Mechanical Engineering, Alva's Institute of Engineering and Technology Karnataka, Moodbidri, Mangalore 574225, India. email: sagarbannur@gmail.com*
2 *Department of Mechanical Engineering, Alva's Institute of Engineering and Technology Karnataka, Moodbidri, Mangalore 574225, India. e-mail:satyan.nitk@gmail.com*
3 *Department of Mechanical Engineering, Adichunchanagiri Institute of Technology, Chikmagalur 577102, India. e-mail:prshnth.md@gmail.com*

ABSTRACT: Rarely an aircraft will fail due to a static overload during its service life. For the continued airworthiness of an aircraft during its entire service life, study on fatigue, damage tolerance design, testing and service experience is crucial. In the present investigation, stress analysis and the fatigue damage calculation for the wing-fuselage attachment bracket in a transport airframe was carried out. Also, prediction of damage due to fatigue was calculated using Miner's rule of damage accumulation. Results indicated that maximum tensile stress of 33.6 kg/mm^2 was identified at one of the rivet-holes in the lug. Maximum damage fraction was found to be 0.1727. Concluding that crack will not get initiated for the given load spectrum for another 579 flights. It was also confirmed that, the wing fuselage lug attachment bracket was safe from fatigue considerations.

***Keywords**: Air craft, Stress analysis, Lug, Fatigue, Crack propagation*

INTRODUCTION

The most critical structural elements in aircraft is connected between the wing and fuselage it is known as "wing fuselage lug attachment bracket" [1]. It is usually hard to attach the wing to the fuselage. There is usually a third piece of wing contained within the fuselage. The connection of wings and fuselage are always by way of very strong and heavy bolts. The bolts that are used must be much stronger than necessary, thereby having sufficient lifetime as shown in Figure 1. Stringers are attached to the wing skin, and run span-wise. Their job is to stiffen the skin so that it does not buckle when subjected to compression loads caused by wing bending and twisting, and by loads from the aerodynamic effects of lift and control-surface movement [1-3].

In most aircraft, the wing skin performs several tasks such as It gives it the aerodynamic shape, it carries a share of the loads, it helps to carry tensional loads, it acts as fuel tanks and allows inspection and maintenance [4-5].

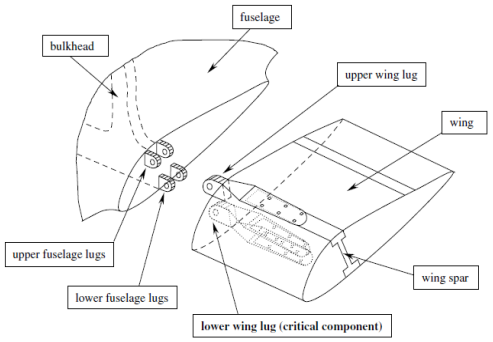

Fig1:Components of typical Wing fuselage attachment connector [6].

Usually the fuel is stored in the wing, which is divided into several tanks, each one usually having its own pumps. This allows fuel to be moved between tanks in flight, which changes the trim of the aircraft to minimize the drag. Flaps are fitted at the trailing edges. Light aircraft usually has simple flaps or none at all. Larger aircraft have the more complex split flap or Fowler flap.

Lug attachment brackets can be some of the most fracture critical components in the aircraft structure, and the consequences of structural lug failure can be very severe (disastrous)that quite a few times the fuselage and wings of an aircraft gets separated).Significant results are obtained which can improve both the understanding of the stress state in a lug and the design of a durable lug [7-8] Therefore, it is important to establish design criteria and analysis methods to ensure the damage tolerance of aircraft Lug attachment brackets.

Brackets are very critical components in the airframe. During the flight when the maximum lift is generated, the wings of the aircraft will undergo highest bending moment. The bending moment will be maximum at the root of the wing, which causes highest stress at this location. The bending moment and shear loads from the wing are transferred to the fuselage through the attachment joints.

In the current study,analysis of wing fuselage attachment bracket using FEA approach was attempted.
Fatigue damage calculation for maximum stress in the lug attachment bracket was also investigated.

Modeling

The parts of wing fuselage attachment bracket were modelled and assembled using CATIA V5 R20 software as shown in Figure 2. The geometry of the lug, tongue, C-sec,I-spar, bulkhead, fork are as shown in the Figure 2.

The lug and other components of the wing fuselage attachment brackets were made of Aluminium 7075-T6 alloy. Mechanical Properties are mentioned in Table 1.

Properties	Unit
Density	27468 N/m^3
Tensile Yield Strength	503 MPa
Ultimate Tensile Strength	572 MPa
Elastic Modulus	73.1 GPa
Poisson's Ratio	0.33
Fatigue Strength	-159 MPa
Fracture Toughness	25MPa-m$^{1/2}$
Bulk Modulus	71.7 GPa
Shear Modulus	26.9 GPa
Shear Strength	331 MPa

Table 1: Material Properties of Aluminum Alloy – 7075 T6 **[3]**

The lug consists of two symmetrical forks having four rows
of rivets of which first row has 10mm diameter and second row of rivets are of 8mm diameter.

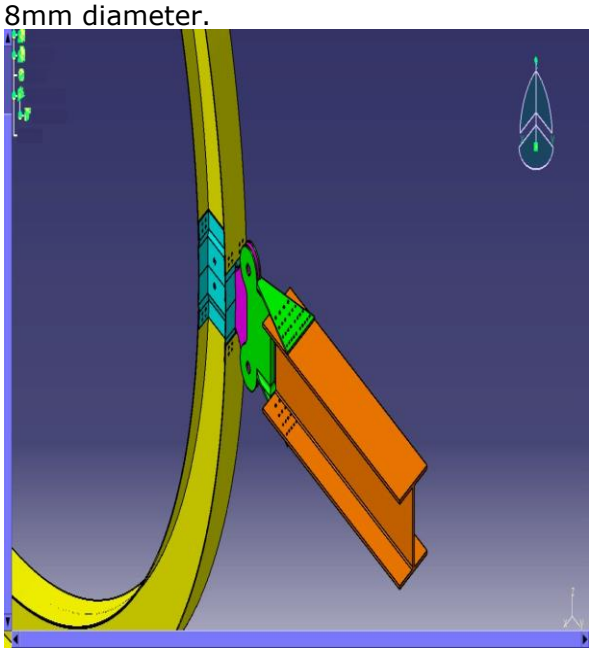

Fig 2 :3D Assembly drawing of wing fuselage attachment bracket

Meshing

The meshed model was filled with nodes and elements. Geometry extraction was the first step involved in the stress analysis procedure. Figure 3 shows the finite elements mesh on wing fuselage attachment bracket using MSc Nastran - Patran

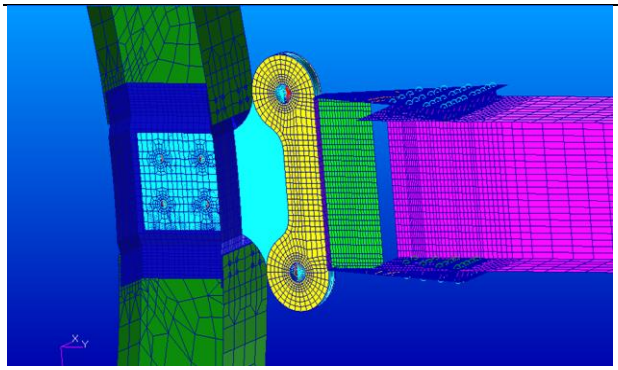

Fig 3: Finite element model of the Wing fuselage attachment bracket

FE model of the wing fuselage attachment bracket , meshing was done by using C-QUAD and C-TRIA elements. Fine meshing was done around the rivet and pin holes and the stress concentrated location; coarse meshing was done at rest of the locations. 1D Beam elements were used to simulate the rivets in the model. Typical four noded 2-D quadrilateral shell element and three noded 2-D Triangular shell elements is as shown in Figure 4. Triangular shell elements were used for the transition between the coarser mesh to finer mesh.

Loads and Boundary Conditions

After completion of meshing of the wing fuselage attachment bracket, loads and boundary conditions were defined as shown in the Figure 4. As in the practical case wings are subjected to bending load like a cantilever beam i.e. one end is fixed & other side transverse load is applied.

Boundary Conditions

Kinematic boundary conditions were usually applied by suppressing or releasing the required degree of freedom. The motion of each element was represented by three displacements T_x, T_y, T_z and three rotations R_x, R_y, R_z co-ordinates. Each direction of motion was termed as degree of freedom.

In this study, the edge nodes connecting the bulkhead of the fuselage were constrained completely and all six degree of freedom at an end of the bulkhead which was connected to fuselage ($T_X=T_y=T_z=0$, $R_x=R_y=R_z=0$), in F.E.M boundary conditions showed by notations 123456 as shown in figure4

For '3g' load condition we have constant bending moment at the lug joint was found to be 1367×10^3 N-mm

Load on each flange of the spar was given by: $1367\times10^3 \div 230 = 5943.48$ kg

Where height of web was =230mm

Therefore total load over a width of each flange was given by:

(5943.48/200)= 29.71kg

Where flange width of the spar was given by: 200mm.

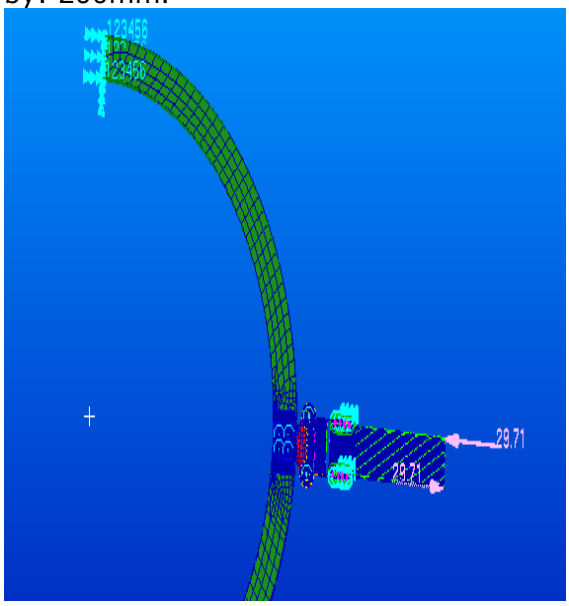

Fig 4:The Finite Element model along with Loads and Boundary Condition

The meshed component with all the material properties specified is as shown in Figure 5

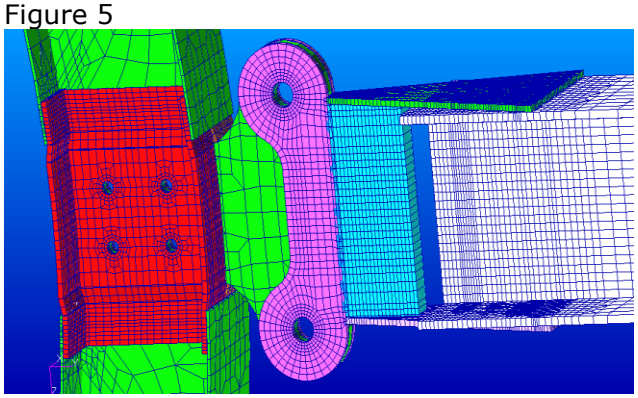

Fig 5:Finite Element Model with Material Properties

RESULTS AND DISCUSSIONS

The stress values at the lug attachment bracket hole is shown in the figures 6 . A maximum stress of 33.6kg/mm^2 was observed at one of the rivet location of top flange on a spar section. So ultimate strength of aluminium Alloy, Heat treated AISI-7075 T6 is 54 kg/mm^2**.** Here max. stress was less than the ultimate strength of structure; therefore structure is safe for applied load. (i.e. load acting on lug attachment bracket is 5943.48 kg). When the Stress is greater than or equal to the ultimate strength of structure than material may fail. The maximum stress value obtained from the analysis is used as the input for the fatigue calculations.

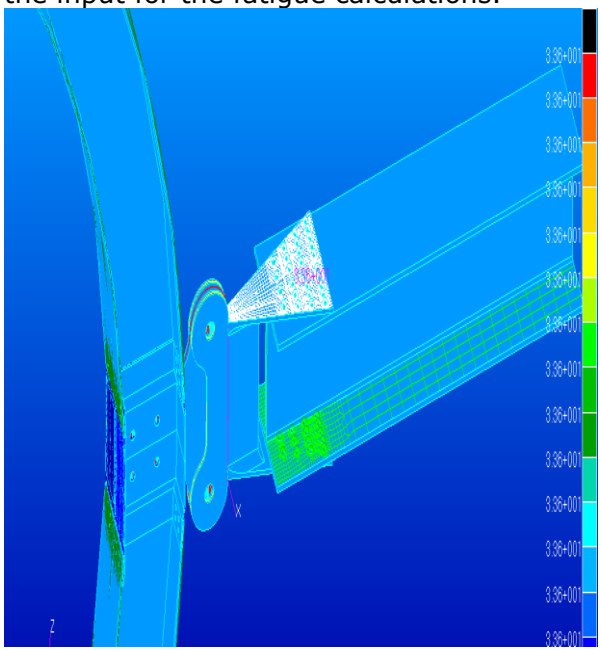

Fig 6 :Max. Stresses in wing fuselage attachment bracket

Fatigue life calculations

From the stress analysis of the lug joint the maximum tensile stress location was identified. A fatigue crack will always initiate from the location of maximum tensile stress. From the stress analysis it was found that such a location is at the pin hole.

Our understanding of fatigue damage problems increased significantly. Simultaneously our tools to tackle problems have been developed to a high potential efficiency. And still, there are problems [9].

Normally aircraft wing experiences variable spectrum loading during the flight. A typical 4 seater aircraft flight load spectrum is considered for the fatigue analysis of the lug joint. Calculation of fatigue life was carried out by using Miner`s Rule.

The damage calculated at different g range with reference from S-N data was tabulated in Table2:

Table2 : The range of "g", the damage accumulated from miner's formula

Range of g	Actual no of cycles(n_i)	Fatigue cycle by using graph(N_f)	Damage accumulated from miner's formula (D_i)
0.5to 0.75	$40x10^3$	∞	∞
0.75 to 1	$55x10^3$	10^7	5.5×10^{-4}
1 to 1.25	$38x10^3$	10^7	3.8×10^{-4}
1.25to 1.5	$25x10^3$	10^7	2.5×10^{-4}
0 to 1.75	500	$9x10^4$	5.5×10^{-3}
0 to 2	300	$6x10^3$	0.05
0 to 2.5	250	$3x10^3$	0.083
-0.5to 1.5	100	$3x10^3$	0.033

Therefore the total damage accumulated by considering the correction factors is

$D_i=D_1+D_2+D_3+D_4+D_5+D_6+D_7+D^8$

$D_i=(5.5+3.8+2.5)+5.5x10^{-3}$

$+0.05+0.0833+0.033$

$\therefore D_i = 0.1727$

Total damage accumulated was 0.1727, which is less than 1. Therefore a crack will not get initiated from the location of maximum stress in the lug for given load spectrum.

Conclusion :

1.Maximum tensile stress of 33.6 kg/mm^2 was observed in the lug.

2.A validation for FEM approach was carried out by SOM approach which was found to be 33.28 kg/mm^2.

3.From the calculations maximum damage fraction was 0.1727 . The value of damage fraction is much less than 1. Hence the crack will not get initiated for the given load spectrum for another 579 flights

REFERENCES

1] Sumanth M H, Ayyappa T Comparative Analysis of aircraft wing fuselage lug attachment bracket., International Journal For Technological Research In Engineering,Volume 5, Issue 11, July-2018.

2]A probabilistic interpretation of the Miner nu mber for fatigue life prediction,30 (2014) 327-339; DOI: 10.3221/IGF-ESIS.30.40

3] http://asm.matweb.com/search/SpecificMaterial.asp?bassnum=ma7075t6 (Accessed on 30/1/2019)

4] Immanuvel D, Arulselvan K, Maniiarasan P, , Senthilkumar S, Stress Analysis and Weight Optimization of a Wing Box Structure Subjected To Flight Loads, The International Journal Of Engineering And Science (IJES) Vol.3 Issue 1,Pages 33-40,2014,.

5] S.Freidrich, J. Schijve.Delft, Fatigue crack growth of corner cracks in lug specimens. university of technology, Department of aerospace engineering, Netherlands.Jan 1983.

6] Witek, Lucjan. "Failure analysis of the wing-fuselage connector of an agricultural aircraft." Engineering failure analysis 13, no. 4 (2006): 572-581.

7] G. S. Wang ,Stress analysis for a lug under various conditions, The Aeronautical Research Institute of Sweden, Bromma, Sweden.

8] J. Vogwell, J. M. Minguez, "Failure in lug joints and plates with holes". School of Mechanical Engineering, University of Bath, Bath BA2 7AY, U.K., Facultad de Ciencias, Universidad Del Pais Vasco, Bilbao, Spain

9] JaapSchijve Fatigue damage in aircraft structures, not wanted, but tolerated,Vol.31, Issue 6,June 2009.

8th International Engineering Symposium - IES 2019
March 13-15, 2019, Kumamoto University, Japan

A Study on Thermal Properties and Wear Characterization of Glass Fiber Hybrid Composite Materials

Gurushanth B Vaggar [1, 2] and **S C Kamate** [3]

1 *Regional Research Centre, Visvesvaraya Technological University, Karnataka, Belagaavi – 590018, India. email: gvgr.aiet@gmail.com*
2 *Department of Mechanical Engineering, Alva's Institute of Engineering and Technology Karnataka, Moodbidri, Mangalore – 574225, India. email: gvgr.aiet@gmail.com*
3 *Hirasugar Institute of Technology, Karnataka, Nidasoshi, Belagaavi – 591236, India. e-mail:Kamateksk@rediffmail.com*

ABSTRACT: Hybrid polymer composite materials (HPCM) are new solution for high thermal resistivity and stability of composites under thermal conditions. In the present study, investigation on thermal properties and wear resistance of silicon inserted glass fiber (GF) hybrid composite materials was carried out. The specimens were prepared by hand layup technique by compression moulding machine. Thermal conductivity (K) and Coefficient of thermal expansion (CTE) of HPCM materials were assessed. Also failure of HPCM was determined using Thermal gravimetric analysis (TGA). The results indicated that K of silicon inserted HPCM increased with increase in percentage of silicon and the value of CTE was decreased with increase in percentage of silicon. TGA indicated that the failure of HPCM occurred at 280^0C for 25 minutes. Further, the wear behaviour of HPCM was studied under varying speeds and percentage of silicon.

Keywords*: Thermal conductivity (K), Coefficient of Thermal Expansion (CTE), Thermal Gravimetric Analysis (TGA), Silicon, Wear.*

INTRODUCTION

Composites are engineered materials made out of two or more components. Most of the composites can be tailored to obtain properties better than individual constituents. A polymer composite reinforced with fibre is called FRP composite. Considering a composite, which involves two or more macro constituent phases, the matrix is referred to as continuous phase and the fibres are called the reinforcing phase. The fibres increase the strength and stiffness, increase thermal and fatigue properties, provide better dimensional stability and electrical resistivity. Whereas the primary function of the resin is to transfer load, to hold the fibres, protect fibres from environment and mechanical abrasion. Matrix also carries transverse loads and interlaminar shear stresses. The advantages of composites include high strength to weight ratio, non-corrosiveness, less maintenance, high electrical resistance, wear resistance, electromagnetic transparency, appeasing appearance etc. Composites can be manufactured in different ways depending upon matrix, reinforcement and application. Different manufacturing methods include Hand-layup, Compression moulding, Resin Transfer Moulding (RTM), Pultrusion, Autoclave and Filament moulding etc. [16].

In the present work a study of thermal properties are carried out to the prepared specimens of silicon inserted hybrid composite materials (on silicon inserted glass – fiber chop strand). The specimens were prepared by hand layup followed by compression molding machine by non-heating molding technique. The thermal properties, 1) Thermal conductivity (K), 2)

Coefficient of thermal expansion (CTE), and 3) Thermo gravimetric analysis (TGA) are found experimentally and specimens and experimental setups are prepared as per the ASTM standards [4]. Thermal properties of any materials decides withstanding and sustainability of that material under variable temperature conditions it may be high temperature or low temperature.

1) Thermal Conductivity (K): The measurements of K carried out under variable heat inputs at ATP condition. According to ASTM E1530 circular slab type HPC specimen diameter 150 mm and thickness 10 mm are used as shown in figure 1. A known value of heat is applied from one side of the composite slab wait till the system reach steady state, the temperature of each interface surfaces were measured by thermocouples. Thermal conductivity determined by using one-dimensional Fourier's law of conduction equation [2]. The conduction equation can be stated as "The rate of heat conduction in a given direction is proportional to the temperature gradient in that direction". This statement can be represented by equation

$$Q = -KA\frac{dT}{dL} = -KA\frac{(T_2 - T_1)}{L}$$

Where,
Q = Heat Supplied (W).
K = Thermal conductivity (W/m $^{\circ}$C).
A = Area (m^2).
L = Thickness of the HPC specimen (m).
T_1= Temperature of lower interface surface of HPC Specimen ($^{\circ}$C).
T_2= Temperature of upper interface surface of HPC Specimen ($^{\circ}$C).
$\frac{dT}{dL}$ = Temperature gradient ($^{\circ}$C/m).

2) Coefficient of Thermal Expansion (CTE): Most solid materials expand by heating and contract when cooled. Thermal expansion is a property of a material is indicative of the extent to which a material expands upon heating. The change in length with temperature for a solid material may be expressed as follows [9].

$$\alpha_1(T_2 - T_1) = \frac{(L_2 - L_1)}{L_1}$$

$$\alpha_1(\Delta T) = \frac{(\Delta L)}{L_1}$$

Where,
L_1 = Initial length
L_2 = Final length
T_1 = Initial temperature
T_2 = Final temperature
α_1 = linear coefficient of thermal expansion
ΔT = Temperature change ($^{\circ}$C)
ΔL= Change in length of the sample (mm)

The CTE test conducted to HPC specimens had length 90mm and thickness 10mm. The CTE tests were done for the temperature range of 25°C to 90°C using temperature controlled muffler furnace. The HPC specimens heated from room temperature to 90°C in the muffler furnace and kept at 90°C for 10 minute.

3) Thermo Gravimetric Analysis (TGA): Thermo gravimetric analysis is one of the method thermal analysis in which the changes in physical and chemical properties of specimens measured with reference to the increase in temperature. The TGA test carried out to the square specimens of size 50mm x 50mm and thickness 10mm. The TGA tests were performed over the temperature range of 30°C to 300°C using temperature controlled muffle furnace. Specimens heated from room temperature to 300°C in the muffler furnace for 20 minutes. After heating specimens check for decompose of hybrid polymer composites and % of loss material in weight is calculated. Figure 2a shows specimen before TGA test and figure 2b shows the decomposed specimen after TGA test.

4) Wear Test: Wear test is conducted as per the ASTM Standards with specimen sizes 10 mm x 10 mm square cross section and length 50 mm the wear testing setup shown in figure 6**.** Wear test conducted for three variable speeds and three different composition hybrid polymer composite specimens [10].

METHOD TO PREPARE HYBRID POLYMER COMPOSITES

Machine moulding is used to prepare hybrid polymer composites by hand layup method. Mould box is prepared as per the size of the HPC with the proper mixture of resin hardener and filler particles pasted on glass fiber layups then pressure applied on mould by using SANTAC compression moulding machine allowed cure for 24 hours under normal atmospheric conditions. This method of preparing hybrid polymer composites is the simplest and economical than other methods.

SPECIMEN COMPOSITIONS

The different specimens with material compositions are given below in table 1.

RESULTS AND DISCUSSION

Variation of thermal properties K, CTE, TGA and Coefficient of friction (μ) for different composition hybrid polymer composite materials are shown in figures 3 to 5 respectively.

In figure 3 it shows that the thermal conductivity value increases as the percentage of silicon filler material increases. The thermal conductivity of silicon is greater than that of epoxy resin hence the coefficient of thermal expansion of hybrid polymer composite decreases with increase in percentage of silicon as shown in figure 4. Thermogravimetric analysis indicated that the failure of HPCM occurred at 280^0C for 25. Figure 5 shows coefficient of friction varies to higher value with increase in % of silicon as well as speed, means the material can sustain more frictional force.

CONCLUSIONS

The following conclusions are inferred from this study.

- Thermal conductivity of hybrid polymer composite materials increases as the percentage of SiC filler material increases.
- The coefficient of thermal expansion decreases as the percentage of filler material SiC increases.
- By Thermogravimetric analysis it shows that the specimens gets decomposed around 275^0C to 280^0C.
- Increase in coefficient of friction with increase in percentage of SiC and speed.
- With the above results it is concluded that hybrid polymer composite materials can withstand high temperatures up to 300^0C. Silicon can be used as filler material in GFER composites successfully.

ACKNOWLEDGEMENTS

The Authors are very much grateful to Dr. K. Devendra, Dept. of Mechanical Engineering, SKSVMACET, Laxmeshwar, Karnataka, India. Dr. Basava T, Dept. of Mechanical Engineering, SDMIT, Ujire, Karnataka, India. Dr. Satyanarayan, Dept. of Mechanical Engineering, AIET, Moodubidire, Karnataka, India for their valuable suggestions, guidance and support.

[1] Malla Surya Teja, M V Ramana, D Sriramulu and C J Rao. "Experimental Investigation of Mechanical and Thermal properties of sisal fibre reinforced composite and effect of SiC filler material". IOP Conf. Series: Materials Science and Engineering 149 (2016) 012095 doi:10.1088/1757-899X/149/1/012095.

[2] Krishnamachar Srinivas, Mysore Siddalingappa Bhagyashekar. "Thermal Conductivity Enhancement of Epoxy by Hybrid Particulate Fillers of Graphite and Silicon Carbide". Journal of Minerals and Materials Characterization and Engineering, 2015, 3, 76-84.

[3] Tahir Ahamad, Rafiq Ahamad, Muhammad Kamran, Bambang Wahjoedi, Imran Ahakoor, Faraz Hussain, Farhad Riaz, Zuhaib Jamil, Sirjeel Isaac, Qaiser Ashraf. "Effect of Thal Silica sand nanoparticles and glass fiber reinforcement on epoxy-based hybrid composite". Iran Polym J (2015) 24: 21-27.

[4] K. Devendra and T. Rangaswamy. "Thermal Conductivity and Thermal Expansion Coefficient of GFRP Composite Laminates with Fillers". ISSN: 2320-2491 (2013).

[5] Alok Agrawal, and Alok Satapathy. "Development of a Heat Conduction Model and Investigation onThermal Conductivity Enhancement of AlN/Epoxy Composites". Elsevier Procedia Engineering 51 (2013) 573 – 578.

[6] Watthanaphon Cheewawuttipong, Daisuke Fuoka, Shuichi Tanoue, Hideyuki Uematsu, and Yoshiyuki Iemoto. "Thermal and Mechanical Properties of Polypropylene/Boron Nitride Composites". Elsevier Energy Procedia 34 (2013) 808 – 817.

[7] Ravi Kumar B N, Ananda.G.K, Shivaappa.D, Mahesh.H.R. "Effect of Fillers on Thermal and Fire Resistance Properties of E-Glass Epoxy Composites". International Journal of Mechanical Engineering Research & Applications (IJMERA) Vol. 1 Issue 4, September – 2013.

[8] MaximeVilliere, Damien Lecointe, Vincent Sobotka, Nicolas Boyard, Didier Delaunay. "Experimental determination and modelling of thermal conductivity tensor of carbon/epoxy composite". Elsevier Composites, part A46 (2013) 60-68.

[9] Yang Hua, Qing-Qing Ni, Atsuhiko Yamanaka, Yoshihiko Teramoto and Toshiaki Natsuki. "The Development of Composites with Negative Thermal Expansion Properties Using High Performance Fibers". Advanced Composite Materials 20 (2011) 463–475.

[10] Basava T, A N Harirao. "Development of Graphite
Particles filled Epoxy Resin Composite Material and its Erosive wear Behaviour". AMAE Int. J. on Manufacturing & Material Science, Vol.01, No.02, November 2011.

[11] Th. Schubert, T. Weibgarber and B. Kieback. "Fabrication and properties of Copper/Carbon composites for thermal management applications". Advanced Materials Research Vol. 59 (2009) pp169-172.

[12] Moran Wanga, Qinjun Kang b, Ning Pan. "Thermal conductivity enhancement of carbon fiber composites". Applied Thermal Engineering 2008.

[13] Dr.Jawad Kadhim Uleiwi, Sura Salim. "Study of Thermal Characteristics of a Composite Specimen Experimentally and by Using Finite Element Method". Eng. & Tech. Vol26, No4, 2008.

[14] Sudarisman, I.J. Davies, H. Hamada. "Compressive failure of unidirectional hybrid fibre-reinforced epoxy composites containing carbon and silicon carbide fibres". Compos. Part A, 38(3) pp. 1070 -1074 (2007).

[15] ZHENG Jing, SONG Wen-juan, MA Guang, JIA Zhi-hua. "Thermal expansion and mechanical properties of Al/Si composites fabricated by pressure infiltration" Science Press Trans. Nonferrous Met. Soc.China 17(2007) s326-s329.

[16] Brian Y. Lattimer, Jason Ouellette. "Properties of composite materials for thermal analysis involving fires" Elsevier Composites, part A37 (2006) 1068-1081.

[17] Bhyrav Mutnuri, "Thermal Conductivity Characterization of Composite Materials". *Morgantown, West Virginia University, 2006*.

[18] Dilek Kumlutas, Ismail H, Tavaman, M. Turhan Coban. "Thermal conductivity of particle filled polyethylene composite materials". Elsevier Composites Science and Technology 63 (2003) 113 – 117.

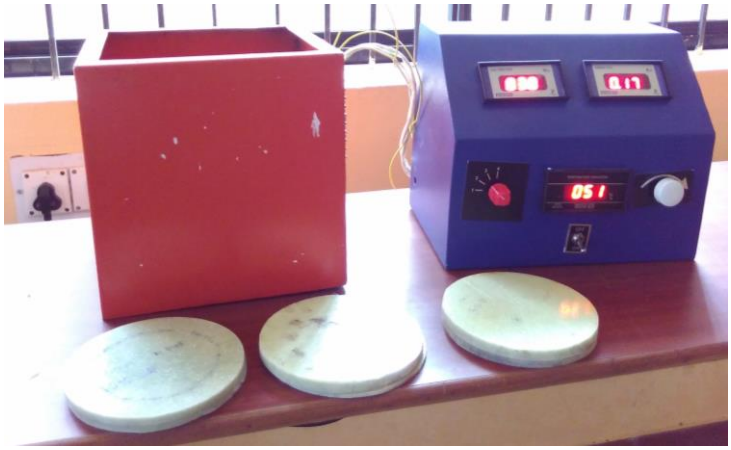

Fig. 1 Thermal conductivity experimental setup.

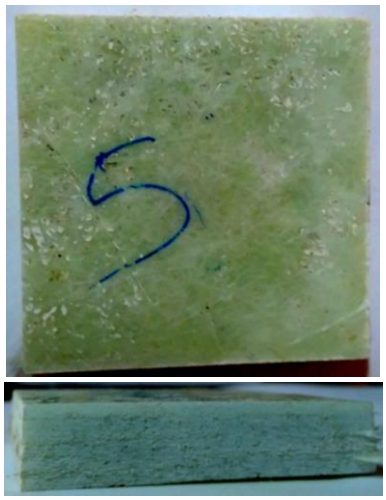

Fig. 2a specimen before TGA test

Fig. 2b specimen before TGA test

Table 1. Specimens with composition of materials

Material Designation	Weight Quantity in Grams			
	Silicon	E-Glass Fiber	Epoxy Resin	Hardener
GE10	0	116.40	291.00	29.10
GE10SI10	24.32	121.60	218.88	21.88
GE10SI20	46.00	115.00	184.00	18.40
GE10SI30	78.18	130.20	182.42	18.242

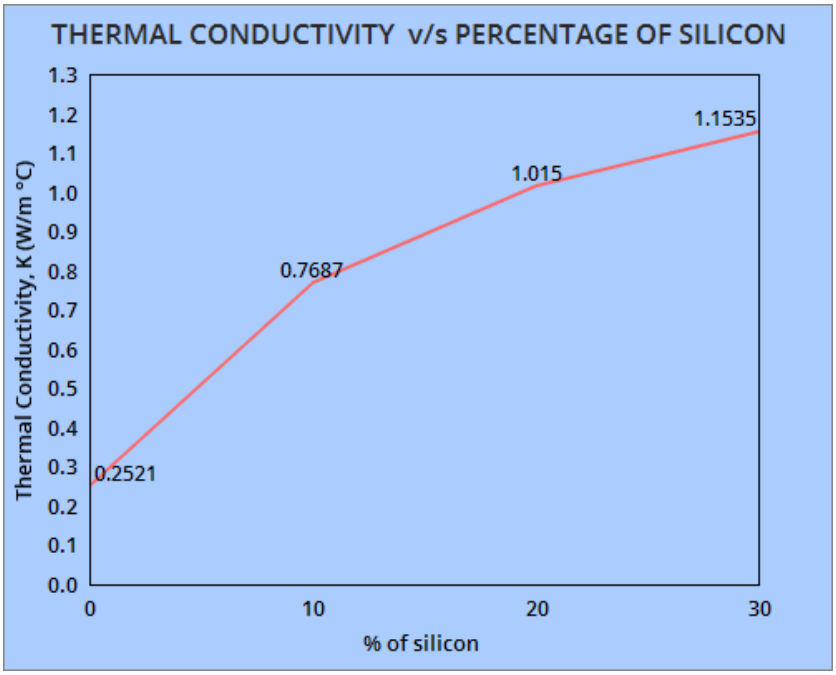

Fig. 3 Variation of thermal conductivity with % of Silicon

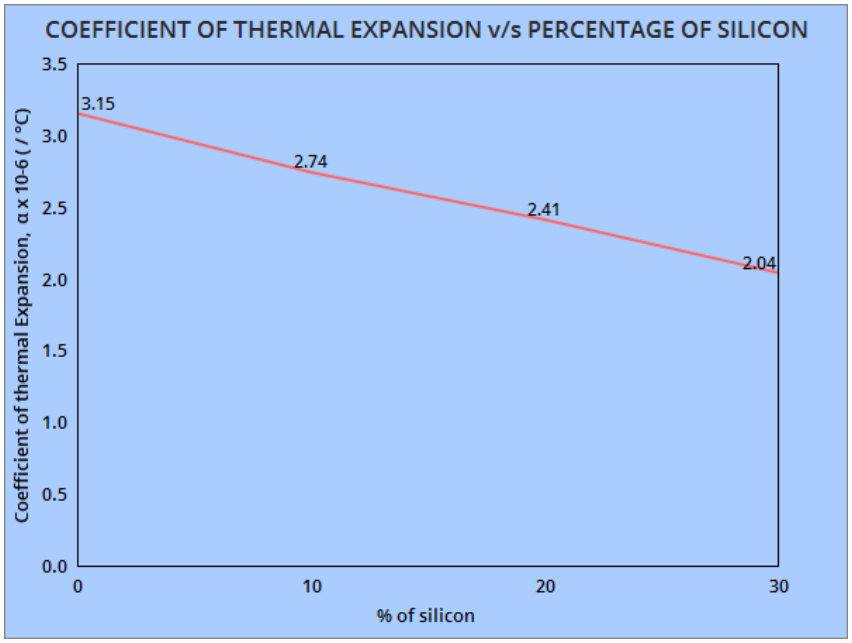

Fig. 4 Variation of Coefficient of Thermal Expansion with % of Silicon

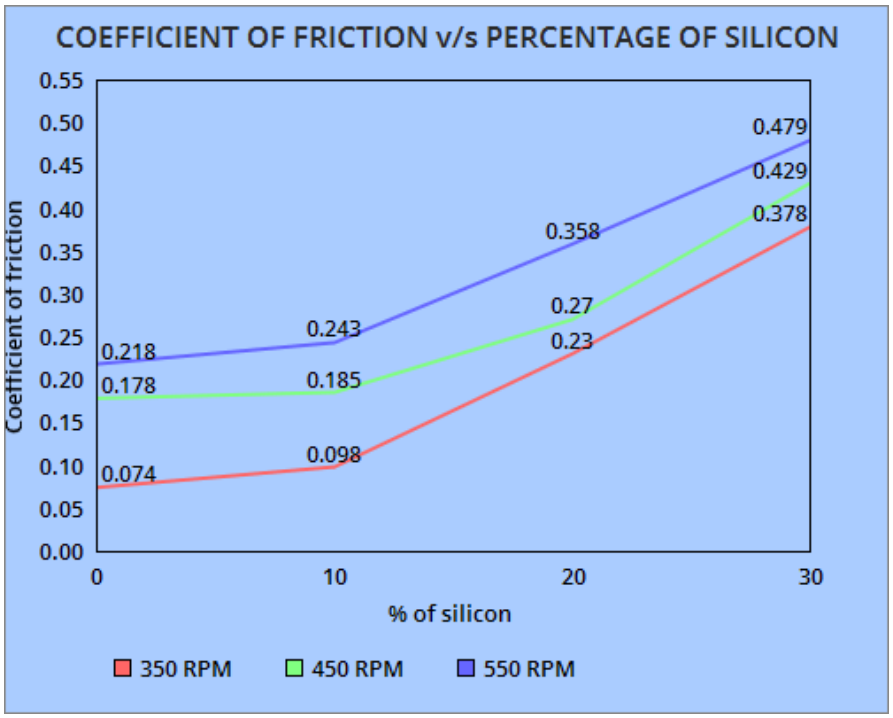

Fig. 5 Variation of Coefficient of Friction with % of Silicon & Speed

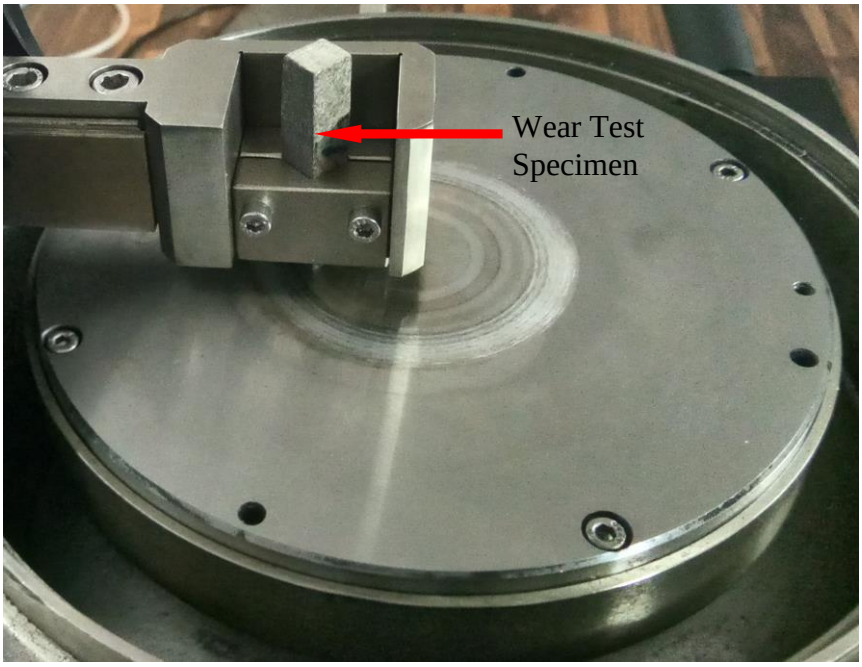

Fig. 6 Wear Test Setup

8th International Engineering Symposium - IES 2019
March 13-15, 2019, Kumamoto University, Japan

Influence of Multiaxial cryoforging on wear properties of Copper-Titanium alloy

Ramesh S [1], H Shivananda Nayaka[2]

1 *Department of Mechanical Engineering, National Institute of Technology Karnataka, Surathkal, Mangalore 575025, India. email:ramaghalli@gmail.com*
2 *Department of Mechanical Engineering, National Institute of Technology Karnataka, Surathkal, Mangalore 575025, India. Email : ramnitk2016@gmail.com, hsn_mech@nitk.ac.in*

ABSTRACT: Cu-3%Ti alloy was processed by multi axial forging (MAF) at cryogenic temperature. Microstructure was analyzed using optical microscope (OM) and electron backscattered diffraction (EBSD). After 3 cycles of MAF, grain size was decreased to 250 mm, as compared to as received sample (80 μm). As number of MAF pass increases, hardness of the sample also increased, due to strain hardening effect. A dry sliding wear test was carried out using a pin on disc wear testing machine. Effect of varying loads of 10 N and 20 N at constant speed 1 m/s with a sliding distance 3000 m were studied. As the number of MAF passes increases wear mass losses decreased and coefficient of friction (COF) decreases with increase in MAF passes and increased with increase the load. Worn surface of the specimen was investigated by using scanning electron microscope (SEM) and micrographs shows clearly worn surface of deformed specimen and wear debris. Energy dispersive analysis (EDAX) shows oxidation along the sliding direction

Keywords*: Multi axial forging ; Cu-Ti alloy; Grain refinement; Microstructure; Hardness ; wear resistance*

INTRODUCTION

Various severe plastic deformation (SPD) processes such as accumulative roll bonding (ARB), multi-axial forging (MAF), constrained groove pressing (CGP), equal channel angular pressing (ECAP), high pressure torsion (HPT) and repetitive corrugation and straightening (RCS) have been developed from past few decades [1-3]. From the above SPD techniques, MAF is the one of the simple SPD technique to produce ultrafine grains. It's a repeated pressing process and suitable for bulk samples for industrial applications. Copper and its alloys are widely used for many applications in automobile industry, electrical applications because of its excellent electrical conductivity, good mechanical properties and high corrosion resistance.

Copper- Beryllium shows the highest strength level in copper groups. It demonstrates good formability good electrical conductivity during hot and cold working [3-5]. Main disadvantages of Cu-Be alloy is toxic and high price. Cu-Ti is the nontoxic substitutes for Cu-Be and it show good mechanical and electrical Properties. Some of the application of Cu-Be alloy was Production of high strength spring as well as element resistant to corrosion, abrasion in electrical connections like contact, relay, gears and electrical wires [6-7]. So that Cu-Ti is best substitution element for Cu-Be alloy.

Some work has been reported on wear behavior of different material subjected through different SPD process. El et al investigated the wear behavior of Al-Cu alloy samples processed through ECAP under dry sliding condition. Wear mass loss decreases as the number of ECAP pass increases and also increased with increases of %Cu [8]. Li, J et al conducted a wear test on Cu-Zr alloy processed by ECAP. Coefficient of friction (COF)

decreases as the number of ECAP pass increase and also wear mass loss and wear depth decreases [9]. Gupta et al examined the dry sliding wear on high leaded tin by MAF process. MAF processed samples show good wear resistance as compared to unprocessed samples for different loading and sliding distances [10]. Padap et al investigated the dry sliding wear of MAF processed AISI 1024 steel at room temperature. The friction coefficient of coarse grain (CG) is higher than the ultrafine grain (UFG) and UFG shows deeper and wider grooves and CG shows shallow grooves [11]. Gopi et al [12] studied the wear properties of ECAP processed AM80 magnesium alloy at 275°C and results shows wear debris, delamination and ploughing decreased with increase in number of ECAP pass, due to increase in hardness. The presence of magnesium oxide leads to oxidation wear. Manjunath et al [13] conducted dry sliding wear tests on Al-Zn-Mg alloy (5%, 10% and 15%Zn with 2 %Mg) processed by ECAP. COF value was decreased when increase the %Zn, load and sliding speed. Micro ploughing, delamination and Scratches were decreases with increase in Hardness.

From the above literature shows less work has been studied wear properties of Copper alloy processed by SPD, nowhere found the wear study on Cu-Ti alloy alloy processed by MAF at cryogenic condition. In the present study, Cu 3%Ti is processed using MAF at cryogenic temperature up to 3, 6 and 9 Pass. Microstructure and mechanical properties were analyzed to study the variation of properties for as-received and MAF processed samples. Pin on disc wear rest set up was used to carried out the wear test and results were analysed using SEM and EDS.

Experimental procedure.

The Cu-3%Ti alloy was obtained with dimension 30 mm × 30 mm × 25 mm from PAHWA metal tech private limited. MAF die was fabricated using HDS steel and CAD model of die shown in fig 1 (a). Die design is based on plane strain condition for deformation. The dimension ratio of 1.3:1.3:1 of the sample was kept inside the liquid nitrogen tank for 20 minutes (till bubble formation stops) to achieve saturation temperature of liquid nitrogen during the first pass of MAF process. After every pass of MAF sample should keep inside liquid nitrogen for 5 minutes to achieve liquid nitrogen temperature. Forging was carried out using a universal testing machine (UTM-200 Ton) with the pressing speed of .03 mm/s. During first pass longest side of the sample (30 mm) consider as a forging axis and keep in the die cavity. After first pass rotate the sample 90° and follow the same procedure like first pass. The notation of MAF process completes one cycle as shown in fig 1

Each pass of MAF imposed a strain of .182 on the sample

Total Cumulative strain from 3 Pass of MAF (1 cycle) is $\varepsilon = 0.546$ every cycle.

Center portion of the Sample was used for microstructural analysis by mechanical polishing using SiC emery papers (800-2000 grit size) and finally cloth polishing was carried out using diamond paste and diamond spryer. Etchant was prepared using a 10 g $K_2Cr_2O_7$, 5 ml H_2SO_4, 2 ml of HCL and 95 ml of distilled water and etched for 3 s. Microstructure was analysed using optical microscope (OM-Zeiss AX10).EBSD data was acquired using scanning electron microscope with an attachment of Oxford instruments Nordlys detector and scanned data were analysed using HKL channel 5 Tango software. Omni-tech (MVH-S-AUTO) microhardness equipment was used to find the Vickers microhardness of the sample by applying a load of 100 g for a dwell time of 15s. Cylindrical pin samples of Ø6 mm and 28 mm length was prepared from as-received and MAF 3, 6 and 9 Pass processed samples as shown in Fig 2. Pin samples made flat on contact surface using 1500 grade SiC emery paper and clean with acetone. To prepare wear specimen samples were taken from center region and prepared as per ASTM G99-05 (Ø6 mm X 28 mm). DUCOM Pin-on-disc wear machine was used to conduct dry sliding wear test at room temperature. Alumina coated disc of 65 HRC hardness is used for wear test against the wear specimen. Wear test was carried out for 10 N and 20 N and sliding distance of 3000 m. Sliding speed of 1 m/s and track diameter of 114

mm is constant for all experiments. Weight loss method was used to measure the wear resistance of the sample. For each trial disc was polished using 1000 grade emery paper and cleaned with acetone to remove wear debris on disc. After wear test the worn surface of as received and MAF processed samples were analyzed using SEM images.

Results and discussion

Microstructural and Hardness analysis

Optical micrograph of as received and MAF processed 3, 6 and 9 pass samples in shown in fig 3. The average grain size of as received sample 80 μm with equiaxed grains as shown in fig 3 (a). After MAF 3 pass large size grains are divided into small and shear bands are formed with elongated grains. As the number of MAF passes increases shears bandwidth decreases and dislocation density increases this is the reason to increases the strength of the material this is called as grain boundary strengthening mechanism. After 6 Pass of MAF grain size was reduced to 14 μm. During first pass grain refinement rate is high as compared to 3 and 6 Pass, because of the high dislocation density. After 9 Pass of MAF grain size was reduced to 2 μm.

OIM of Cu-3%Ti alloy of as received and final pass (9 Pass) MAF sample is shown in Fig 4. As received sample OIM shows clearly grain orientation with different colour as shown in fig 4 (a) and 9 Pass MAF processed samples shows the elongated grains as shown in fig 4 (b). The colors in the stereographic triangle shows corresponds crystallographic plane direction inverse pole figure (IPF) shown in fig 4 (c). Black color pixels shows in the figure are non-indexed points on the sample. As received samples having High angle grain boundaries (HAGB) ,After MAF process strain accumulation increases in sample and grain boundaries are converted from to low angle grain boundaries (LAGB).

Microhardness of as-received, 3 Pass, 6 Pass and 9 Pass MAF samples are represented in Fig.5. hardness of the as received sample is 224 Hv. As number of MAF pass Increases hardness also increases this can be observed in fig 5. After 3 Pass of MAF hardness increased to 340 Hv. Similarly for 6 and 9 Pass was increased to 385 Hv and 410 Hv respectively. Increase in hardness for MAF processed samples due to strain hardening effect because of grain refinement. Hardness increases with decrease in grain size as per Hall-Petch relationship [15]. UTS and YS of as received and MAF processed element of Cu-3%Ti as shown in fig 5.

Wear analysis

3.2.1Coefficient of friction (COF)

As received and MAF processed samples were conducted the pin on disc wear test under 1 Kg and 2 Kg with 3000 m. During wear test constant Sliding velocity 1 m/s and track diameter was maintained throughout the experiment. COF of both as-received and 3 Pass, 6 Pass and 9 Pass MAF processed samples as shown in fig 6. As number MAF passe increases COF value becomes decreases, because of improvement in hardness. Improvement in the COF value was observed when load increases from 10 N to 20 N. After applied 20 N load fluctuation was reduced because of increase in contact between the specimen and steel disc. From the above discussion, it can be observed that MAF process leads to the decrement of COF and it increases wear resistance property [9,12].

Wear mass loss (mg)

Wear test was conducted for as received, 3 Pass, 6 Pass and 9 Pass MAF processed sample for 10 N, 20 N with 3000 m. Wear mass loss of different MAF passes v/s different loading and sliding distance condition as shown in fig 7. In all the cases wear mass loss of as received sample is high and low wear loss observed in the MAF 9 Pass sample. MAF processed samples showed decreased wear mass loss as the number of passes increases. After MDF processed sample wear resistance property was increased due to increase in hardness. This is followed by Archard equation (2) [16].

$$V = K \frac{LF}{H} \qquad (2)$$

Where K is the wear coefficient, L is the sliding distance, F is the applied load, H is the hardness of the sample and V is the total wear mass loss. Wear mass loss is inversely proportional to the hardness and

strength of the sample. After MAF hardness was increased due to grain refinement of the sample.

Wear surface morphology

Fig. 6 shows clearly as the load increases, wear rate also increased for both as received and MAF processed samples. As the MAF passes increases wear mass loss reduces due to increase in hardness of the sample. After MAF sample hardness, increased due to grain refinement. Adhesive wear is the main mechanism and during wear severe plastic deformation occurs on wear surface which results delamination of the worn surface as shown in fig 8. After MAF process Adhesive wear decreases due to decreases in grain size. Fig 6 shows the SEM images of the Cu-3%Ti alloy worn surface of both as received and MAF processed sample under 10 N with sliding distance of 3000 m. Delamination, scratches and micro grooves are observed on the worn surface. This micogroves are formed by ploughing is parallel to the sliding direction. Ploughing exhibits the plastic deformation and also it is directly proportional to hardness of the sample. As the number of MAF passes increases these delamination, scratches and micro groves were decreases, surface become smooth as shown in fig 8. Fig 9 shows the SEM images of the Cu-3%Ti alloy worn surface of both as received and MAF processed sample under 20 N with sliding distance of 3000 m. As the load increases formation of delamination and scratches was more as compared to 20 N load. Initially for as received sample delamination, scratches were more as compared to MAF processed samples is shown in fig 9.

Conclusions

In the present study, wear properties of Cu-3%Ti alloy processed by MAF under cryogenic condition have been studied under 10 N and 20 N with 3000 m. The conclusions are summarized below:

- MAF process was carried out at cryogenic temperature on Cu-3%Ti alloy and grain size was decreased to 2 μm from 80 μm after 9 Pass of MAF.
- Both as received and 3 Pass, 6 Pass, 9 Pass MAF processed samples were subjected to dry sliding wear test to know the COF behavior for different loading condition. COF value decresed with increase in number of MAF pass, due increased hardness of the sample.
- Wear mass loss of MAF processed sample was less as compared to as-received material. Wear mass loss directly depends on the hardness of the material.
- SEM micrograph of worn surface reveals the surface plastic deformation, ploughing and scratches increased with increase load and decreased with increase with number of MAF passes.

REFERENCES

[1] Valiev, R. Z et al (2006). Producing bulk ultrafine-grained materials by severe plastic deformation. Jom, 58(4), 33-39.

[2] Hu, H. et al (2003). Potential magnesium alloys for high temperature die cast automotive applications: a review. Materials and Manufacturing Processes, 18(5), 687-717..

[3] Kulekci, M. K. (2008). Magnesium and its alloys applications in automotive industry. The International Journal of Advanced Manufacturing Technology, 39(9-10), 851-865.

[4] Nagarjuna, S.et al (1997). Effect of alloying content on high cycle fatigue behaviour of Cu□ Ti alloys. International journal of fatigue, 19(1), 51-57.

[5] Nagarjuna, S.et al (1999). On the variation of mechanical properties with solute content in Cu–Ti alloys. Materials Science and Engineering: A, 259(1), 34-42.

[6] Szkliniarz, A.et al (2014). Characteristics of Plasticity of Hot Deformed Cu-Ti Alloys/Charakterystyki Plastyczności Odkształcanych Na Gorąco Stopów Cu-Ti. Archives of Metallurgy and Materials, 59(4), 1307-1312.

[7] Nagarjuna, S. (2004). Thermal conductivity of Cu-4.5 Ti alloy. Bulletin of Materials Science, 27(1), 69-71.

[8] El Aal, M. I. A.et al. (2010). Wear properties of ECAP-processed ultrafine grained Al–Cu alloys. Materials Science and Engineering: A, 527(16-17), 3726-3732.

[9] JLi, J et al (2015). Wear resistance of an ultrafine-grained Cu-Zr alloy processed by equal-channel angular pressing. Wear, 326, 10-19.

[10] Gupta, R.et al (2017). Multidirectional Forging of High-Leaded Tin Bronze: Effect on Wear Performance. Metallography, Microstructure, and Analysis, 6(6), 577-590.

[11] Padap, A. K et al (2010). Mechanical and dry sliding wear behavior of ultrafine-grained AISI 1024 steel processed using multiaxial forging. Journal of materials science, 45(17), 4837-4845.

[12] Gopi, K. R.et al (2017). Wear properties of ECAP-processed AM80 magnesium alloy. Journal of

Materials Engineering and Performance, 26(7), 3399-3409.
[13] Manjunath, G. K et al (2018). Microstructure and Wear Performance of ECAP Processed Cast Al–Zn–Mg Alloys. Transactions of the Indian Institute of Metals, 71(8), 1919-1931.
[14] Vendra, S. L. et al (2017). A study on fracture toughness and strain rate sensitivity of severely deformed Al 6063 alloys processed by multiaxial forging and rolling at cryogenic temperature. Materials Science and Engineering: A, 686, 82-92.
[15] Nieh, T. G., & Wadsworth, J. (1991). Hall-Petch relation in nanocrystalline solids. Scripta Metallurgica et Materialia, 25(4), 955-958.
[16] J. Archard, Contact and Rubbing of Flat Surfaces, J. Appl. Phys., 1953,24(8), p 981–988

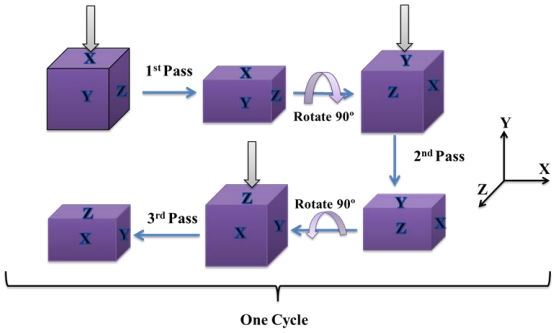

Fig 1 MAF process notation

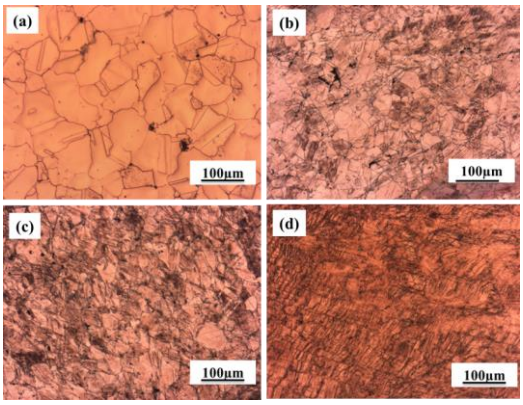

Fig 3 Optical images of (a) as received (b) 3 Pass MAF (c) 6 Pass MAF and (d) 9 Pass MAF processed samples

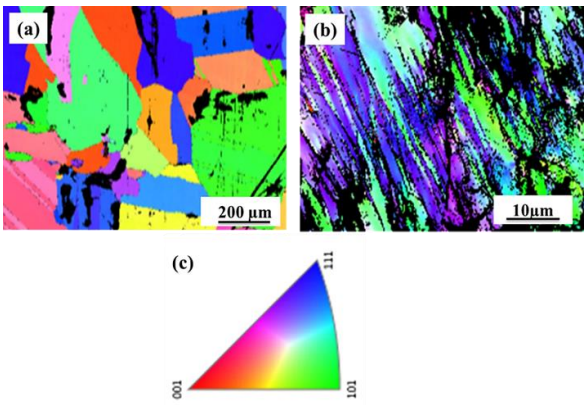

Fig 4 OIM of (a) As received sample (b) 9 pass MAF processed sample (c) IPF

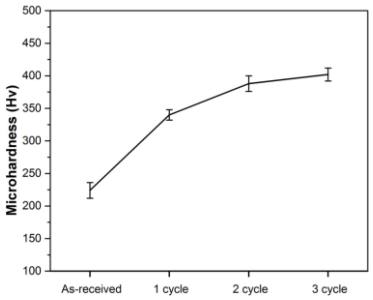

Fig 5 variation of Hardness for different cycles of MAF

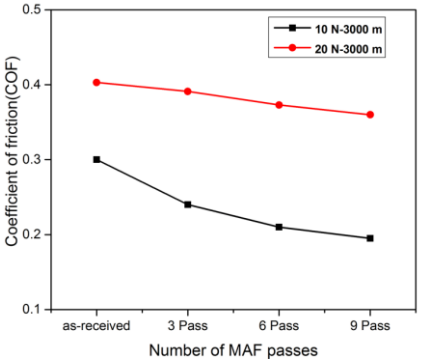

Fig 6 COF versus (a) as-received (b) 3 Pass MAF and (c) 6 Pass MAF (d) 9 Pass MAF processed samples at 10 and 20 N load with 3000 m sliding distance

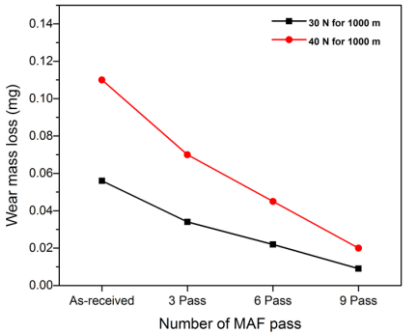

Fig 7 Wear mass loss v/s number of MAF

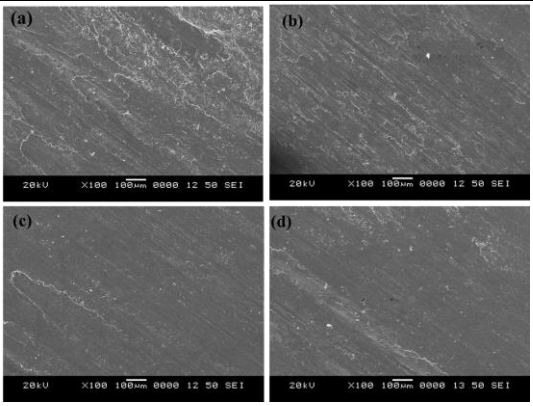

Fig 8 SEM micrograph of the worn surface of (a) as-received (b) 3 Pass MAF and (c) 6 Pass MAF (d) 9 Pass MAF processed samples at 10 N load with 3000 m sliding distance.

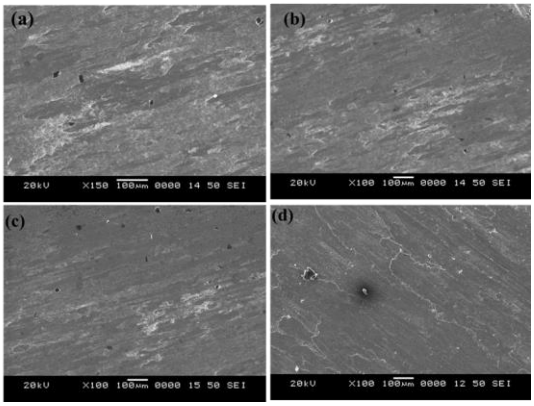

Fig 9 SEM micrograph of the worn surface of (a) as-received (b) 3 Pass MAF and (c) 6 Pass MAF (d) 9 Pass MAF processed samples at 20 N load with 3000 m sliding distance

8th International Engineering Symposium - IES 2019
March 13-15, 2019, Kumamoto University, Japan

Blast Furnace RAFT Calculator

Shaurya Seth [1], Omkar Barwade [2] and **N.N. Vishwanathan[3]**

1 *Department of Metallurgy and Materials Engineering, National Institute of Technology Karnataka, Surathkal, Mangalore 575025, India.*
email:shauryaseth.16mt33@nitk.edu.in
2 *Department of Metallurgy and Materials Sciences, Indian Institute of Technology Bombay, Powai, Mumbai, Maharashtra 400078, India. e-mail:vichu@iitb.ac.in*

ABSTRACT: In an iron blast furnace, there is a certain temperature called as Raceway Adiabatic Flame temperature (RAFT)[1] imperative for the efficient and effective functioning of the furnace. The RAFT is generated near the tuyeres purging hot blast, located above the hearth of the furnace.
The hot blast form tuyeres gushes in at enormous velocities establishing a path for the gases to enter the coke region called as a Raceway. Due to the force, some amount of coke gets entrapped in the raceway and reacts with the hot blast to form carbon monoxide which further elevates the temperature in that region, paving the way for RAFT.
Our project revolves around calculation of RAFT by controlling certain parameters and enforcing them in enthalpy balance equations. The RAFT hereby calculated is then adjusted to a certain influential temperature and the oxygen and moisture content of the blast required for the above adjustment is revealed. Furthermore, the oxygen and moisture content of the blast is chosen accordingly. The above mentioned process is carried out with the help of a computer programming language called python to device a calculator for the same.
Our research concludes that, maintaining RAFT is not only crucial for working of the blast furnace but also for the safety of it. It is important for Steel Industries to first calculate and simulate the parameters associated with RAFT and therefore make a move in their execution.

Keywords*: RAFT, Raceway, Tuyeres, Hot blast, Iron Blast Furnace, Hearth, Coke*

I. INTRODUCTION

Iron Blast Furnace is a tall shaft with a height of around 32 meters and diameter about 10-15 meters employed in the production of molten iron in the form of 'Pig Iron' required for steel making. The output of a blast furnace consists of molten pig iron, slag and blast furnace gases. The product utilizes iron ore mainly Haematite, coke as a source of carbon and energy for carrying out the chemical reactions inside the furnace, limestone and dolomite as flux to slag out the impurities. The molten iron should be of uniform composition and produced at high rates. Temperature is one of the parameters which ensures the aforementioned requirements of the product. The critical hearth temperature of the blast furnace should not be less than 1800 K for tapping iron and the slag in the molten form. There are thousands of blast furnaces in the world with a net productivity of 500 million ton of molten pig iron per year. A schematic of blast furnace operation is given in figure 1.

II. What is RAFT?

The hot blast is provided at the bottom of the furnace from the tuyeres (generally 15 to 40) embedded circumferentially at the hearth. It consists of preheated air made up of nitrogen and oxygen, at a velocity of 200-300 ms^{-1} and a pressure of 2 to 4 atmospheres so that the reducing gases

produced overcome the top pressure of the blast furnace[7] and move against the solid burden. These reducing gases lose heat to the incoming solid charge while ascending and thus cooling themselves in the process.

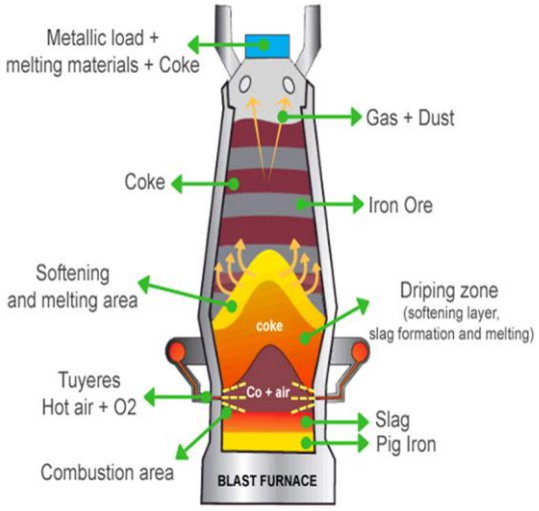

Figure 1 - Blast Furnace Operation

The rapid introduction of preheated air into the hearth (bottommost part of the furnace) of the furnace clears a raceway[5] which extends up to 2 meters inside as shown in figure 2.

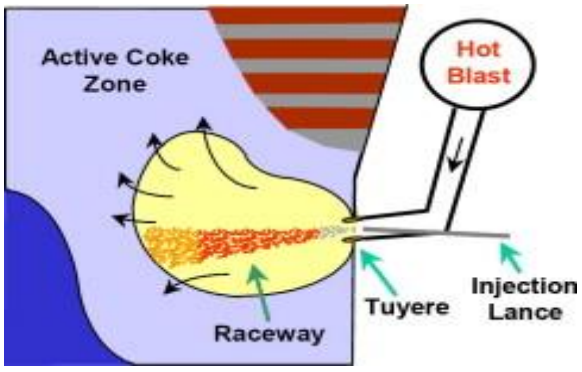

Fig. 2 Raceway schematic

This raceway is surrounded by coke in all directions. The coke is hurtled by the raceway, some coke is engulfed and used in the making of the reducing gas, CO[2]. The whole bed thus gradually moves downward. The formation of carbon monoxide is an exothermic reaction and is produced at the tip of the raceway along with hydrogen, thereby elevating the temperature of raceway and paving the way for RAFT short for Raceway Adiabatic Flame Temperature. The oxygen reacts with the carbon in coke to produce carbon dioxide which manifests carbon monoxide on further reaction with the coke. This is in accordance with the Bernard reaction.

III. Importance of RAFT

RAFT is imperative in the functioning of a blast furnace. Since, temperature is one of the most essential parameters for determining the proper functioning of the blast furnace and it's productivity, there is a suitable range in which RAFT should lie. RAFT is majorly influenced by the critical hearth temperature. Critical hearth temperature hence RAFT should not be less than 1800K otherwise iron and slag cannot be tapped in the molten form. RAFT should be as high as possible for efficient furnace functioning and viscosity reduction of the molten iron for increased flow ability. But certain anomalies can rise up if RAFT is too high.

The refractories start to wear out thereby exposing the blast furnace to abrasion. The permeability of the charge decreases and the descent becomes erratic. The decrease in permeability does not allow sufficient amount of hot gases from the tuyeres to pass through the fusion zone in turn resulting in the low melting slag formation above the fusion zone. These problems can be precluded by generating appropriate RAFT which should not cross 2400 +/- 5K. This can be achieved by manipulating the oxygen enrichment and the moisture content of the blast. The control of RAFT has added advantage of procuring the melt containing constant composition metal.

IV. Factors affecting RAFT

RAFT depends upon the critical hearth temperature as shown in figure 3, because of the fact that the hot blast is being purged and the raceway forms inside the hearth. The hearth consists of the molten slag and iron so, the temperature has to be greater than the melting point of iron. Including the superheat provision the temperature is maintained at 1800K. The salient features of fig. 3 are (a) flame temperature exceeds the critical hearth

temperature (1800 K) when dry blast is preheated to 500 K or more. (b) flame temperature increases proportionally to blast temperature.

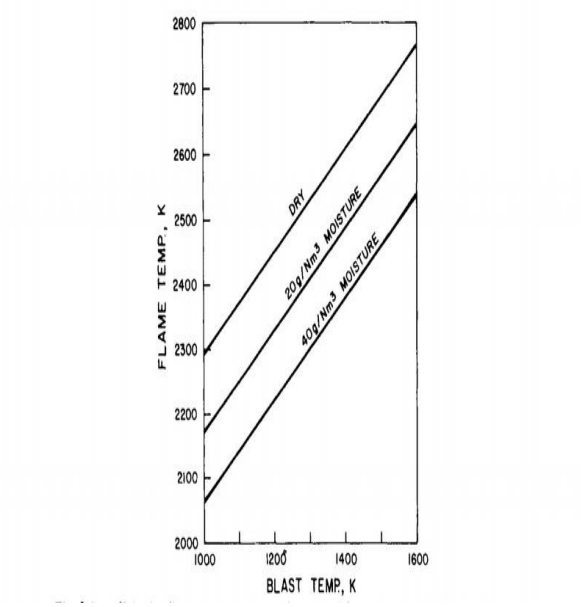

Fig. 3 Flame Temp v/s Blast Temp

Besides critical hearth temperature, amount of oxygen, nitrogen and moisture in the hot blast along with the hydrocarbon injection affects RAFT.
High amounts of moisture is avoided because it decreases RAFT due to the endothermic reaction (1). Hydrocarbon injection also decreases RAFT due to the endothermic nature of dissociation and lower temperature than the incandescent coal.

Importance of RAFT
There is a maximum flame temperature above which the charge descent becomes uncontrollable and erratic and the permeability of the burden also decreases. This is caused by the overheating of the furnace due to the ascent of extensively hot gases from the raceways leading to premature low melting point slag formation above the normal fusion zone. The slag consists of CaO, FeO and SiO_2 with a melting point of around 1400K. The FeO present in the slag is eventually reduced causing it's melting point to increase resulting in freezing of slag and cementing of slag particles over the normal fusion zone.

Excess flame temperatures can also cause abnormally high rates of alkali vaporization in the bosh resulting in

a) Reoxidation products being entrapped in the burden
b) Decrease in burden permeability.

The furnace overheating problems are precluded by generating an appropriate flame temperature (2400 +/- 5K) by manipulating the blast temperature, oxygen enrichment in the blast, humidity and the hydrocarbon injection. An added advantage of adjusting the flame temperature is the continuous, constant and uniform supply of the molten metal.

Equations
$H_2O + C \blacktriangleright CO + H_2 \quad \Delta H_{298K} = +131\,000$ kJ per (kg mole of H_2O). (1)

Table - Calculating oxygen enrichment and moisture content in the blast through tuyeres

Blast Adjust	**No**	**Yes**
Iteration	**100**	**100**
T_HM	**1800**	**1800**
HM_Si	**1**	**1**
HM_C	**4**	**4**
HM_Mn	**1**	**1**
Coke_C	**88**	**88**
Coke_silica	**12**	**12**
T_blast	**1200**	**1200**
Blast_O2_en	**21**	**21**
Blast_moist	**9**	**9**
T_PCI	**298**	**298**
PCI_rate[3]	**150**	**150**
PCI_C	**80**	**80**
PCI_ash	**20**	**20**
PCI_moist	**1**	**1**
Blast_O2[4]	**21**	**23.5819**
Blast_moist	**9**	**9.0**
RAFT	**2181.9957**	**2404.8909**

Result
The raceway adiabatic flame temperature is iterated against the important temperature range 2400 +/- 5K to procure the oxygen amount to be present in the injected hot blast along with the moisture content to maintain the aforementioned

flame temperature.

CONCLUSIONS

The following conclusions can be elicited from this study:

- Raceway Adiabatic Flame Temperature is imperative for the functioning of a blast furnace efficiently.
- For certain crucial reasons regarding the burden descent and the slag solidification, RAFT is adjusted in the temperature range of 2400 +/- 5K.
- Oxygen and moisture content of the injected hot blast from the tuyeres are some of the important parameters which determine the RAFT.

REFERENCES

[1] Blast furnace operation with natural gas injection and minimum theoretical flame temperature by KSA Halim, VN Andronov, MI Nasr - Ironmaking & Steelmaking, 2009 - Taylor & Francis

[2] Fundamentals of coal combustion during injection into a blast furnace by W.P. Hutny, G.K. Lee, J.T. Price

[3] Maximum injection rate of pulverized coal into blast furnace through tuyeres by K Yamaguchi, H Ueno, K Tamura - ISIJ international, 1992 - jstage.jst.go.jp

[4] Numerical investigation of simultaneous injection of pulverized coal and natural gas with oxygen enrichment to the blast furnace by JA de CASTRO, H Nogami, J Yagi - ISIJ international, 2002 - jstage.jst.go.jp

[5] Raceway design for the innovative blast furnace by H Nogami, H Yamaoka, K Takatani - ISIJ international, 2004 - jstage.jst.go.jp

[6] Reducing Net CO_2 Emissions Using Charcoal as a Blast Furnace Tuyere Injectant
John G. Mathieson, Harold Rogers, Michael A. Somerville, Sharif Jahanshahi

[7] The Iron Blast Furnace: Theory and Practice by JG Peacey and WG Davenport.

[8] Theoretical consideration of problems relating to high coal rate injection into blast furnaces by S.Zhang

8th International Engineering Symposium - IES 2019
March 13-15, 2019, Kumamoto University, Japan

Design, Implementation of gaits and Control of a Quadruped robot

Bhavik Parmar [1] and Prajwal B Bharadwaj [2]

1 *Department of Electrical Engineering, Sardar Vallabhbhai National Institute of Technology, Surat 395007, India. email: u14ee067@svnit.ac.in*
2 *Department of Mechanical Engineering, National Institute of Technology Karnataka, Surathkal, Mangalore 575025, India. email: 15me161.prajwalb@nitk.edu.in*

ABSTRACT: This paper describes the kinematic design and control strategy implemented on a quadruped robot. Static and dynamic gaits have been generated for stability of the robot. The locomotion is achieved using a five bar leg mechanism with two active actuators. Inverse kinematics approach is used to generate the motor angles from the trajectory of end effector. Control strategy for stable operation of the robot is elucidated along with embodiment of motor and drive model to generate torque and current waveforms for estimation of hardware parameters. Kinematic simulation is performed in MSC Adams View and control simulations are performed using MATLAB-Adams co-simulation. Stable walking is achieved in co-simulation while turning and trotting are also achieved in motion simulation.

Keywords*: quadruped robot, five-bar inverse kinematics, gait, lower level control*

1 INTRODUCTION

Half of earth's landmass remains inaccessible to tracks and wheels. Bio-inspired robots are indispensable devices in defence applications, forest studies and industrial monitoring. This paper describes the conceptual design and control of a quadrupedal robot to achieve stable motion during straight line walking, turning and trotting, on an even surface. The desired motion of the end point of the leg is achieved using a five bar mechanism with two active actuators.

The problem of making an axisymmetric robot walk with certain regular gaits is addressed by Nilesh Brahme and Kurien Issac(2001). They have developed standard foot trajectories and tables of optimal foot locations which lead to significant reduction in calculations required for gait generation. An important contribution is the procedure for maximizing stroke. Though the discussion is specific to tripod gait, the approach is used for other periodic gaits.

The quadruped robot Minitaur, by University of Pennsylvania uses a five bar linkage for each leg. Each leg has two co-axial motors actuating them directly (Blackman, D. J. et al, 2016).

This paper presents a quadruped working on a five bar leg mechanism actuated by direct-drive motors. However, unlike Minitaur, the motors' axes are parallel. This is done to simplify the geometry of the leg as it reduces the motion of all the components of a leg to 2D space.

A closed loop feedback control system is designed for joint trajectory tracking to produce stable gaits and ensure robustness to distortion generated by system itself. Load disturbance rejection is effectively carried out by proper derivative action (Kristiansson and Lennartson, 2006) and derivative filter coefficient is optimised to supress the derivative effect due to transients in reference trajectories (Visioli, 2006). So, joint trajectory tracking is developed using PID with derivative filter. The model of the motor drive is designed and embedded with, to estimate the mechanical as well as electrical hardware ratings.

2 CONCEPTUAL DESIGN

Fig.1 represents the five bar mechanism where A and B represent the motors while rest of the joints between the links are revolute.

2.i Gaits and stability

Song and Waldron(1989) defined gait as follows: "A gait is defined by the time and the location of the placing and lifting of each foot, coordinated with the motion of the body in its six degrees of freedom, in order to move the body from one place to another".

Static stability is considered when a robot is moving at speeds lesser than one robot length per second. A quadruped robot has stable locomotion if a minimum of three legs are on the ground at any time instant and the centre of gravity lies inside the polygon formed by the toes of the legs. A robot is considered to be statically stable if its centre of gravity remains at a constant height from ground while walking on a flat surface [4]. Dynamic stability is considered when the robot speed is more than one robot length per second. In this condition, lesser than three legs are on the ground at some instants of the cycle. The stroke is reduced to allow the centre of gravity to approximately fall on the line joining the diagonal legs undergoing stance.

Parameters for static gaits: (refer Fig.6)

1. Time period – Time required to complete one cycle of the leg
2. Duty factor (β) – Ratio of stance time to the time period
3. Stroke - Distance covered during stance
4. Φ1 – Phase difference between contralateral legs
5. Φ2 – Phase difference between ipsilateral legs
6. Stability margin(€) – Least distance between side of the triangle and the centre of gravity
7. s1 – Part of the stroke beyond the front edge of the robot
8. d – Offset distance between robot's side edge and the leg

2.ii Trajectory Planning

The following conditions were taken into account while designing the trajectory as mentioned in Nilesh S Brahme. et al. (2001):

1) The toe moves at a constant velocity during stance.
2) The toe continues to move at the same velocity for a small amount of time after and before stance so that slipping is prevented.
3) The curve should be continuous and differentiable at all points.

In Fig.4, 0 to a represents the stance phase, a to b represents velocity extension after stance, b to c represents the polynomial used for continuity, c to d represents the velocity extension before stance.

In Fig.5, 0 to a represents the stance phase, a to b represents the rise of the leg to maximum height during stride, b to c represents the descent of the leg.

2.iii Inverse Kinematics

1) Triangle AED

$$o1 = \cos^{-1}\left(-\frac{r2^2 - r1^2 - b^2}{2 * r1 * b}\right)$$

2) Triangle BCD

$$o2 = \cos^{-1}\left(-\frac{r2^2 - r1^2 - a^2}{2 * r1 * a}\right)$$

3) Triangle ABD

$$g1 = \cos^{-1}\left(-\frac{a^2 - L^2 - b^2}{2 * L * b}\right)$$

$$g2 = \cos^{-1}\left(-\frac{b^2 - L^2 - a^2}{2 * L * a}\right)$$

$$Q1 = -(\pi - g2 - o2) \quad (1)$$

$$Q2 = -(g1 + o1) \quad (2)$$

where Q1 and Q2 are crank input angles.

2.iv Motion Simulation in Adams

Initially, one leg was modelled using primitives present in Adams and under the action of gravity, the motion was observed for similarity with the kinematic simulation performed in MATLAB.

This was followed by modelling of the whole robot with all four legs. Values from MATLAB were exported as tables to Adams to provide motion to the joints. This was used as a preliminary test before control co-simulation in MATLAB-Adams.

Turning was performed by varying the stroke lengths of contralateral legs keeping all other parameters constant. By decreasing the stroke length, increasing the frequency of leg motion and toe compliance, trotting was implemented.

3 CONTROL SYSTEM DEVELOPMENT

3.i Control Architecture Development

As per stable locomotion of the quadruped is concerned, it is necessary to implement the stable gaits and trajectory generated for different gaits to each and every joint in dynamic environmental conditions by means of close loop control. To control here means to determine the torque for each active joints of legs (see Fig. 9) to track the desired trajectory for the desired locomotion and these torques are governed by following equations:

$\boldsymbol{\tau_i} = f(\boldsymbol{\theta d_i} - \boldsymbol{\theta_i})$; Where, $\boldsymbol{i}$ = 1, 2

Where, $\boldsymbol{\theta d1}, \boldsymbol{\theta d2}$ are desired trajectories
$\boldsymbol{\theta 1}, \boldsymbol{\theta 2}$ are current trajectories
$\boldsymbol{\tau 1}, \boldsymbol{\tau 2}$ are the joint torques

Closed loop control model for single joint torque control is shown in Fig.10. PID with derivative filter as shown in Fig.11 is used as controller in this model. Derivative action here is essential for load disturbance rejection [3] where Filter Co-efficient is used to suppress the effect of the derivative gain partially [6] for high fluctuation in reference trajectory.

3.ii Motor Drive Model

As ease of energy storage in batteries and motion control by power electronics drives electrical motors are most commonly used as actuators in the locomotion. It is also important to model the Motor and Drive segment along with the mechanism to augment the nonlinearity due to it and understand model as a whole. This model is used as an integrated part to drive each of the joints of legs and precedes the Mechanical Adams model of the leg in data flow direction succeeds PID controller. Motor Driver converts the PWM signal generated in MATLAB-Simulink to power level to drive the motor. Motor converts the electric power to equivalent torque. During Co-Simulation process Torque data is communicated between Adams and MATLAB over a period of time. This model can be used to monitor electrical characteristics of each motor and drive while controlling the motion of the quadruped robot to predict the hardware specifications for the desired performance. Schematic diagram of the motor drive model is shown in the Fig.12.

3.iii Controller Design in MATLAB

Quadruped model designed in Adams is imported to MATLAB for dynamic co-simulation analysis. Controller designed in MATLAB communicates with the imported Adams model in real time to form a closed loop control system. Mechanical Adams model is provided with joint torques as input and it outputs the angular joint positions accordingly at communication intervals. MATLAB controller estimates the best joint torques to track the desired trajectory based on the current angular joint positions at start of interval and outputs the joint torques at end of interval to the Adams model.

Fig. 13 shows the imported ADAMS model with 4 leg subsystems interconnected. Internal architecture of the leg subsystem is illustrarted in the Fig. 14.

Kinematic Parameters (refer Fig.4)
Length of robot = 400mm
Width of robot = 270mm
Duty factor (β) = 0.9, Stroke = 120mm, Φ1 = +0.5, Φ2 = +0.75,
s1 = Stroke/2 = 60mm, d = 10mm

Control Parameters (refer Fig.11)
P = 0.18, I =5, D = 0.012, N = 45

4.i RESULTS

The given joint angle and torque trajectories traced by the motor is close to the required trajectory as seen in Fig.15. From Fig.16, it can be seen that the variation in elevation of the centre of mass has a range of 15mm while the average speed is close to 150mm/s.

4.ii CONCLUSIONS

This paper has presented the preliminary design and control aspects of a quadruped robot. The following conclusions are deduced:

1. Symmetric stroke of the leg gives the most stable gait when all other gait parameters are kept constant.
2. The leg should have compliance if it needs to exhibit dynamic gaits.
3. It can be seen from the results that the upper range of the torque is 9 Nm which is very high. This torque requirement can be reduced by increasing the time period of the cycle.

4. Derivative action in control is apt for load disturbance rejection and derivative filter can be used for suppression of undesired derivative actions due to transients of reference trajectory.
5. Controller should have capability to adapt to dynamics gaits to conquer over stability issues by cause of momentum and ground impact.

ACKNOWLEDGEMENTS

We would like to thank Prof. K Kurien Issac, under whose supervision this project was carried out during summer internship 2017 in Indian Institute of Space Science and Technology, Thiruvananthapuram.

REFERENCES

[1] Blackman, D. J., Nicholson, J. V., Ordonez, C., Miller, B. D., & Clark, J. E(2016). Gait development on Minitaur, a direct drive quadrupedal robot, 98370I. https://doi.org/10.1117/12.2231105

[2] Kar, D. C., Kurien Issac, K., & Jayarajan, K. (2003). Gaits and energetics in terrestrial legged locomotion. Mechanism and Machine Theory, 38(4), 355–366.

[3] Kristiansson, B., & Lennartson, B. (2006). Robust tuning of PI and PID controllers: using derivative action despite sensor noise. IEEE control systems, 26(1), 55-69.

[4] Nilesh S. Brahme, and K.Kurien Issac,(2001). Gait generation for a six legged walking robot, Proceedings of NaCoMM-01, Khargpur, December, https://doi.org/10.1016/S0094114X(02)00124-6

[5] S.-M. Song and K. J. Waldron,(1989), Machines that walk: the adaptive suspension vehicle. MIT press.

[6] Visioli, A. (2006). Practical PID control. Springer Science & Business Media.

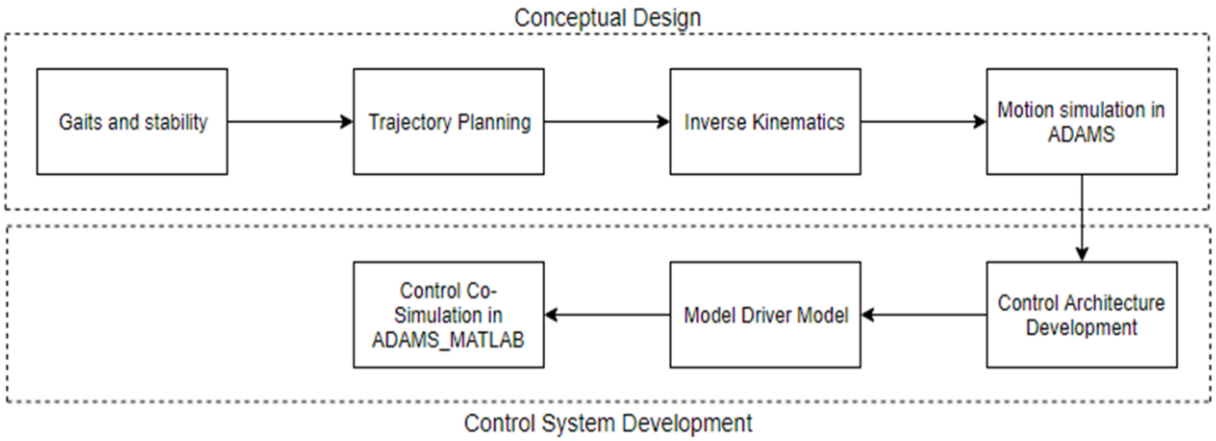

Fig.1 Flowchart of the process

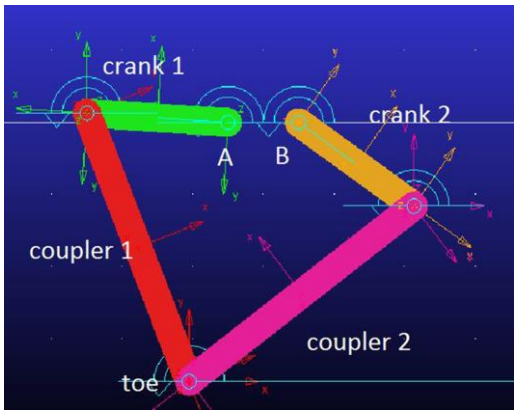

Fig.2 Five bar leg mechanism

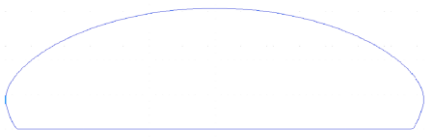

Fig.3 D-shape trajectory of the toe

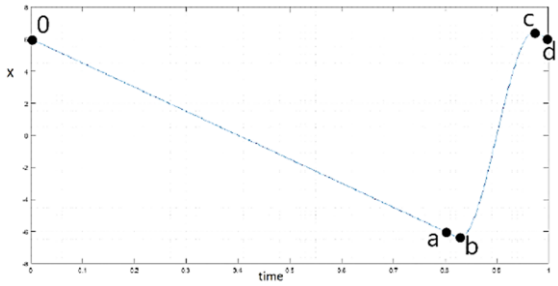

Fig.4 X co-ordinate of the toe vs. time

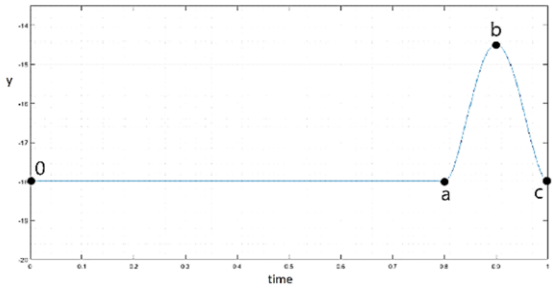

Fig.5 Y co-ordinate of the toe vs. time

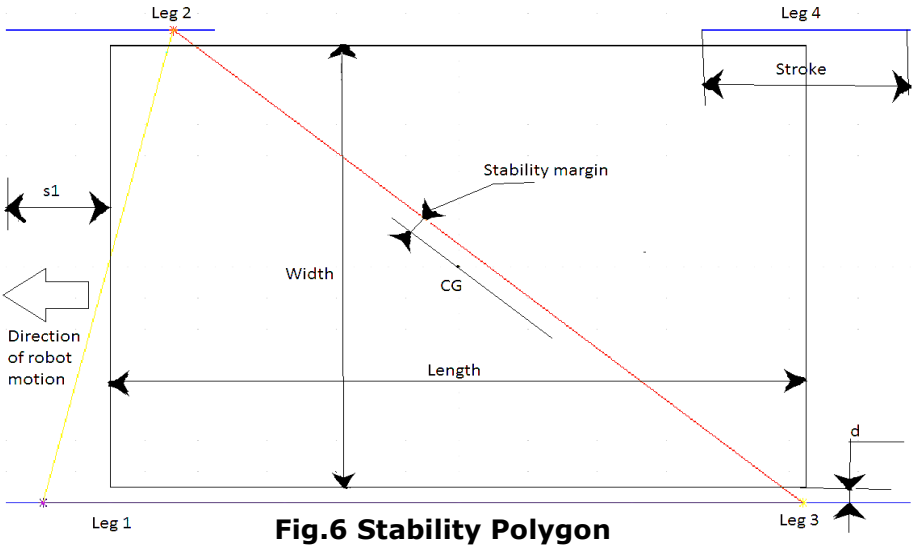

Fig.6 Stability Polygon

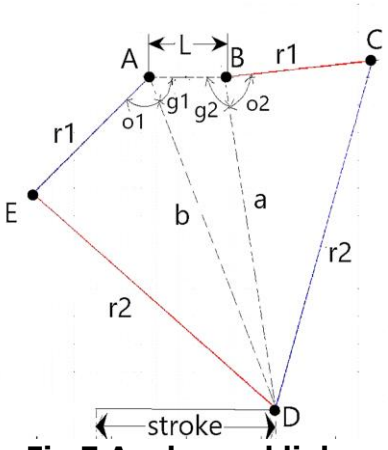

Fig.7 Angles and links

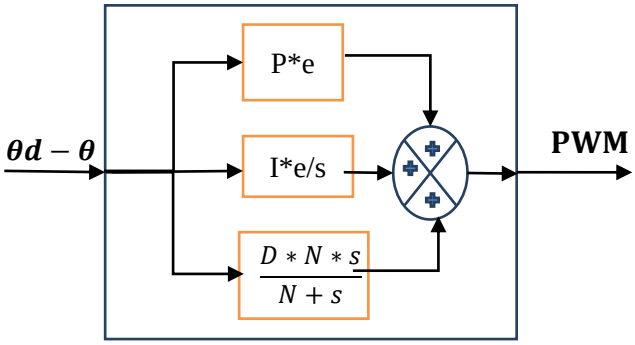

Fig.11 PID controller with derivative filter

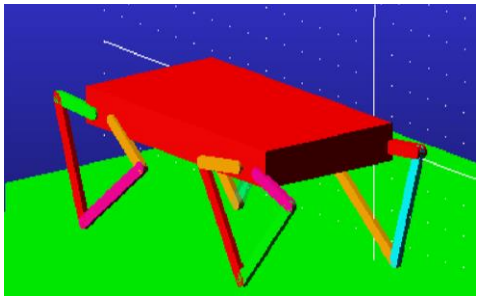

Fig.8 ADAMS model of the robot

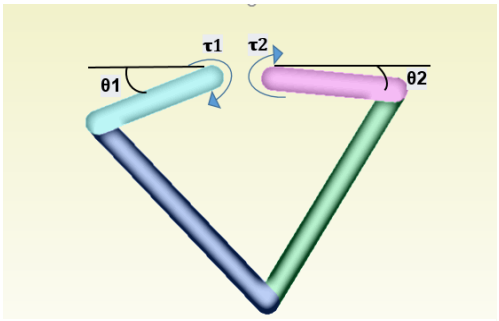

Fig.9 Control parameters of leg

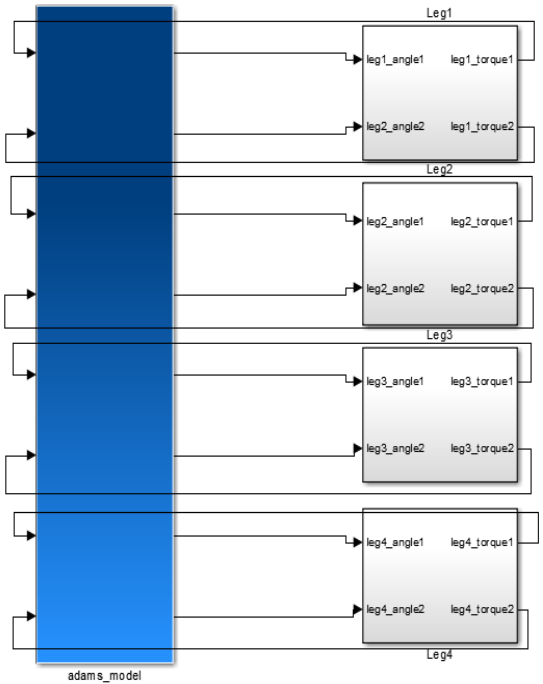

Fig.13 Controller design in MATLAB with imported Adams model

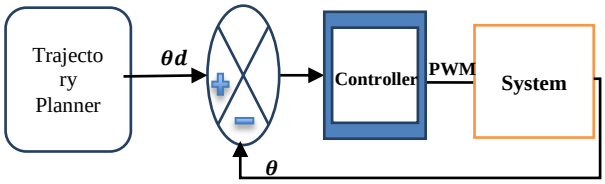

Fig.10 Close loop Control system

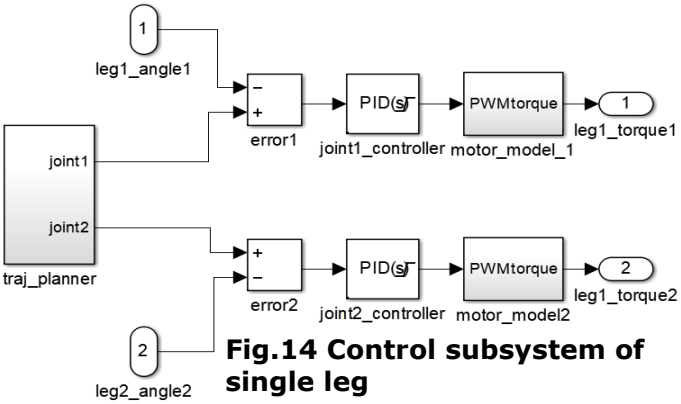

Fig.14 Control subsystem of single leg

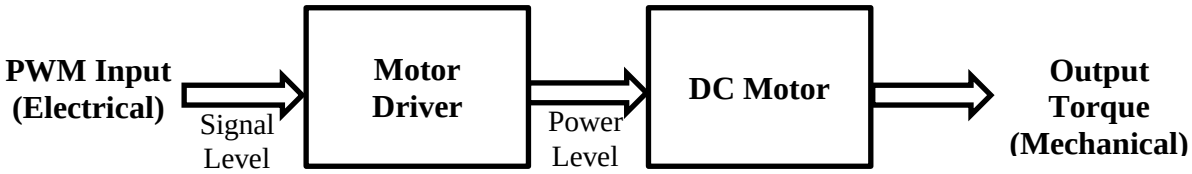

Fig.12 Motor Drive Model diagram for MATLAB-Simulink model

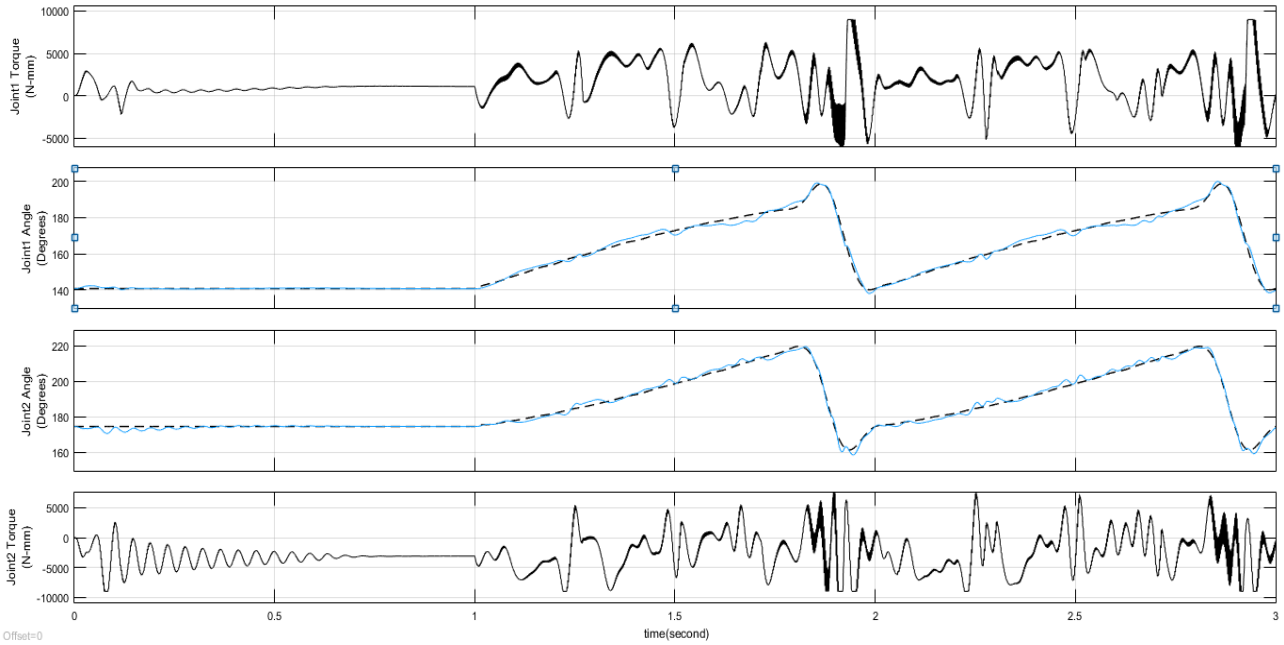

Fig.15 Joint Torque and Angle trajectories

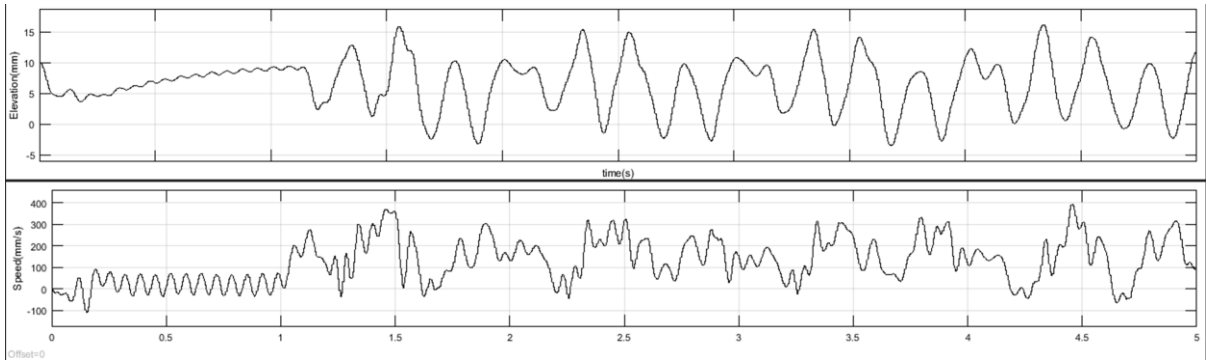

Fig.16 Robot elevation and speed vs. time

8th International Engineering Symposium - IES 2019
March 13-15, 2019, Kumamoto University, Japan

Review on High-temperature Pb-free Solder Alloys

Harsha Raj [1] and **Satyanarayan** [2]

1 *Department of Mechanical Engineering, Alva's Institute of Engineering and Technology Karnataka, Moodbidri, Mangalore 574225, India.*
*e mail:*harsharajpnaik@gmail.com
2 *Department of Mechanical Engineering, Alva's Institute of Engineering and Technology Karnataka, Moodbidri, Mangalore 574225, India.*
e mail:satyan.nitk@gmail.com

ABSTRACT: Due to toxicity of Pb, efforts to develop alternative to Pb-based solders have been increased significantly. In the present paper, a review on selection of Pb free solder alloys to replace traditional Pb based alloys based on availability of literature is carried out. There are limited numbers of Pb-free solder systems exist for high-temperature applications. A discussion on solders for high-temperature applications is highlighted in the current study. Solder systems are discussed with respect to their melting temperature in associated with their use in soldering applications. It is concluded that further development of Pb-free alloys suitable for high-temperature soldering applications is required.

Keywords*: Lead (Pb), Pb-free, Soldering, High temperature, Wetting*

INTRODUCTION

Soldering technology plays a vital role in electronic packaging applications for example flips–chip connection and ball-grid arrays (BGA). Solder joints in the electronic circuits serve as electrical as well as mechanical connections. The solder joints are considered to have failed, when functioning of electrical or mechanical connections is out of service. Currently, there are two soldering technologies employed for mass production first one is plated-through-hole (PTH) and second one is surface mount technology (SMT) soldering [Paul Williams 1999].

At present, the lead (Pb) containing solders mainly eutectic Pb–Sn is used in Printed Circuit Board (PCB) assembly. However, Pb present in the solder material is highly toxic and considered to be hazardous to the environment [Satyanarayan, Prabhu KN 2010]. European Commission directives i.e., WEEE (Waste Electrical and Electronic Equipment), RoHS (Restriction of use of Hazardous Substances) and ELV (End of Life Vehicle) directives have restricted the use of Pb in electronic applications. Even Japan country passed 'Home Electronics Recycle Law'in 1998 [Hwang JS 2005]. These initiatives havelead to the development of novel leadfree solders such as Sn–Bi, Sn–In, Sn–Zn, Sn–Cu, Sn–Ag, Sn–Ag–Zn, Sn–Zn–Bi,Sn–Ag–Cu, Sn–Ag–Bi for electronic applications in which Sn is a major element [Seo SK 2009, Kumar and Prabhu 2007, Mayappan et. al 2007, Chen et al 2000, Kroupa et. 2012]. Legislative initiatives have asked to redesign electronic products using Pb–free components.

It is reported that high lead–bearing solders are still in use even though circuit boards are assembled with middle temperature range Pb–free solders such as Sn–Ag–Cu [web link]. Hence, the establishment of high–temperature lead-free solders is an urgent priority in the electronics industry.

Only few high temperature Pb–free solders are now increasingly being used for the high performance systems. However, there are only a limited number of papers and reports on the research and development for high temperature lead–free alternative solders are available [Prach et al 2015, 13. Gayle et. al 2001, Bae et. al 2015, Kroupa et. 2012]. In the present review paper an attempt has been made to understand the recent development in the area of high–temperature lead–free soldering for electronic packaging applications.

High–temperature solders are used as die–attach solders for assembling optical components, automobile circuit boards and circuit modules etc [Prach et al 2015]. For selecting Pb free–solders for high temperature applications the requirement essential are as follows [Gayle et. al 2001, Bae et. al 2015]

- Melting temperature should be in the range of 260°C to 400°C.
- Minor volume expansion
- Should be drawn as thin wires or sheets
- Good electric and thermal conductivity.
- Good mechanical properties especially fatigue resistance
- Flux less

Among these, major properties for selecting high temperature solders are Melting temperature (°C), the coefficient of thermal expansionCoTE (ppm/°C) and Modulus (GPa). The typical high–temperature solder applications with their major requirements are available in the literature are reported in Table 1. Some properties of selected solders for high temperature applications are given in Table – 2.

As mentioned above, the melting behaviour is an important property to be considered in designing new lead–free high temperature solder alloys. It is essential to consider the proper regime of melting temperature. It is reported that the solidus temperature of the high–temperature solder should be at least 50°C higher than the melting point of the solder used in the second level packaging in order to withstand peak temperatures of the second level soldering [Chidambaram 2010].

The melting point of the commonly used Pb-free solder for second level packaging (Sn–Ag–Cu) is 217°C [Handwerker et al, 2007]. Thus, the preferred melting temperature of a potential high-temperature lead-free solder was by the industries is 270°C. The liquidus temperature of the solder alloy should be below 350°C (In order to avoid thermal degradation of polymers commonly used in the substrate as dielectric materials). Hence, 270°C to 350°C melting temperature range is set by the industries in order to ensure effective process control.

Binary or ternary element additions also increase the melting range and modify certain properties of alloys of solder alloy. For example Nickel (Ni) increases the alloy's strength by forming intermetallic phases with the Sn and increases the melting temperature this is due to marginally soluble in Tin [Miric et. al 2010].

Antimony (Sb) is soluble in tin to increase the alloys strength, and it slightly raises the melting temperature [Miric et. al 2010]. Bismuth (Bi) also soluble in Sn to increase its strength, but decreases the melting temperature enough to compensate for the effects of the Ni and Sb additions [Miric et. al 2010].

Gold (Au)–based solders (hard solders) materials are widely accepted for use in high temperature electronics. It is reported that, among Au–based solders, the Au–Sn based solders are the most widely used for high temperature electronic applications, including microwave devices, laser diodes, RF power amplifiers, and flip-chip bonding applications [Menon et.al 2015]. However, Au–Sn is very stiff and transfers most of the thermo-mechanical stress to the die, making it viable only for small die applications. This solder in its pure state is limited to use at T<280°C [Menon et.al 2015].

The high price of Au has required the development of cheaper and more abundantly available material (such as zinc) that would be conducive for a mass

manufacturing scenario. Zinc (Zn) based alloys are used as high temperature die attach materials and have gained popularity due to their low cost.
By alloying Al and Sn to zinc, the melting temperature of zinc (419.5°C)can be lowered to a suitable range of 300–400°C. The absence of IMCs in the Zn–Sn alloy system results in the Zn–Sn solder alloys being extremely ductile [Menon et.al 2015].

Due to the high costs associated with Au alloys, silver (Ag) offer a possible solution for high temperature applications. Silver has the best electrical conductivity and the second best thermal conductivity. It also demonstrates high temperature stability and has good mechanical properties [Satyanarayan and Prabhu 2013]. At present Sn–Ag–Cu (SAC) are widely used as cheap and best Pb– free solder alloys for high temperature soldering applications. However it is important to note that, as with most SAC solder alloys, too much Cu or Ni can affect the fluidity and wetting characteristics of the liquid alloy. This consideration is particularly important in wave and selective soldering processes, which typically gain Cu and Ni as the metals dissolve from the PWB and component surfaces during processing [Miric et. al 2010].

CONCLUSION

The quest for a replacement of Pb–containing solders for high temperatures appears to be under development. Hence, in the future it is essential to make an attention to design and develop a novel high temperature Pb–free solder alloys (cost effective and better properties in all aspects) for electronic packaging applications in soldering industry.

REFERENCES

Bae, Jee-Hwan, Keesam Shin, Joon-Hwan Lee, Mi-Yang Kim, and Cheol-Woong Yang. "Development of High-Temperature Solders: Contribution of Transmission Electron Microscopy." Applied Microscopy 45, no. 2 (2015): 89-94.

Chidambaram, V. (2010). Development of lead-free solders for high-temperature applications. Kgs. Lyngby, Denmark: Technical University of Denmark (DTU)

Chen YY, Duh JG. J Mater Sci: Mater Electron 2000;11:279–83.
Hu Q, Lee ZS, Zhao ZL, Lee DL. International conference on Asian green electronics; 2005. p. 156–60.

Gayle, F.W., Becka, G., Syed, A., Badgett, J., Whitten, G., Pan, T.Y., Grusd, A., Bauer, B., Lathrop, R., Slattery, J. and Anderson, I., 2001. High temperature lead-free solder for microelectronics. JOM, 53(6), pp.17-21.

Handwerker, Carol, Ursula Kattner, and Kil-Won Moon. "Fundamental properties of Pb-free solder alloys." In Lead-Free Soldering, pp. 21-74. Springer, Boston, MA, 2007.

Hwang JS. Implementing lead-free electronics.McGraw-Hill; 2005. p. 10–90.

Kroupa, Ales, Dag Andersson, Nick Hoo, Jeremy Pearce, Andrew Watson, Alan Dinsdale, and Stuart Mucklejohn. "Current problems and possible solutions in high-temperature lead-free soldering." Journal of Materials Engineering and Performance 21, no. 5 (2012): 629-637.

Kumar G, Prabhu KN. Proc. International conference on advanced materials and composites (ICAMC) Trivandram, India; Oct 24–26, 2007. p. 535–40.

Mayappan R, Ismail AB, Ahmed ZA, Ariga T, Hussain LB. Jurnal Teknologi 2007;46 (C):1–14.

Menon, Sandeep, Elviz George, Michael Osterman, and Michael Pecht. "High lead solder (over 85%) solder in the electronics industry: RoHS exemptions and alternatives."

Journal of Materials Science: Materials in Electronics 26, no. 6 (2015): 4021-4030.

Miric, Anton-Zoran. "New developments in high-temperature, high-performance lead-free solder alloys." Balance 90 (2010): 91-6.

Paul Williams, Surface Mount Council Status Of The Technology Industry Activities And Action Plan, August 1999 https://www.ipc.org/4.0_Knowledge/4.1_Standards/smcstatus.pdf (accessed on 10/12/2019).

Prach, M., & Koleňák, R. (2015). Soldering of Copper with High-Temperature Zn-Based Solders. Procedia Engineering, 100, 1370-1375.

Satyanarayan, Prabhu KN. Wetting behaviour and evolution of microstructure of Sn-Ag-Zn solder on copper substrates with different surface textures, J ASTM Int 2010;7(9):JAI103052.

Satyanarayan and Prabhu, K. N. "Reactive wetting of Sn–2.5 Ag–0.5 Cu solder on copper and silver coated copper substrates." Journal of Materials Science: Materials in Electronics 24, no. 5 (2013): 1714-1719.

Seo SK, Kang SK, Shih DY, Lee HM. J Electron Mater 2009;38(2):257–65.

Web link
https://www.psma.com/ul_files/forums/leadfree/aim_lead_free_guide.pdf (accessed on 10/12/2019)

Table 1. Current high–temperature solders their applications and requirements [Menon et.al 2015].

Solder composition	Melting temperature (°C)	CTE (ppm/°C)	Modulus (GPa)
Au20Sn	280	16	59
Au12Ge	356	13	72
Au3Si	363	12	83
Bi11Ag0.05Ge	262–360	–	–
Ag20In	695	–	–
Zn–(4–6)Al(–Ga, Ge, Mg, Cu)	~380	–	–
Zn–(10 to 30)Sn	360		

Table 2. Few properties of selected high temperature solders [Menon et.al 2015].

Major Solders	Applications	Major Requirements
High Pb alloys	Flip-chip packages	Reflow resistance Low α ray emission
High Pb alloys	Internal connection of passive components	Reflow resistance
High Pb alloys	Quartz device	Reflow resistance Airtightness
High Pb alloys	Heat-resistant vehicle packages	Thermal fatigue resistance Heat exposure resistance
High Pb alloys	Module packages step soldering	Reflow resistance
High Pb alloys Au alloys	Die–attachment of power semiconductors and AISC	Reflow resistance Highthermal/ electric conductivity Thermal fatigue resistance

8th International Engineering Symposium - IES 2019
March 13-15, 2019, Kumamoto University, Japan

Experimental Study of Solar Panel Using Phase Change Material

Jameson Keisham[1] and Shankarappa Kalgudi[2]

[1]Department of Mechanical Engineering, Alva's Institute of Engineering and Technology Karnataka, Moodbidri, Mangalore−574225, India. email:jamson504@gmail.com

[2]Department of Mechanical Engineering, Alva's Institute of Engineering and Technology Karnataka, Moodbidri, Mangalore − 574225, India. email:s.kalgudi2012@gmail.com

ABSTRACT: High operating temperature induces loss of efficiency in solar photovoltaic and thermal panels. The current work investigates the use of phase change material (PCM) to maintain the temperature of panel close to the ambient temperature. The focus of the study was to improve the performance of solar panel by using PCM. For validation process, voltage and current were measured hour by hour and power was calculated from the experimental setup. The solar panel performance was assessed using performance curves. Results indicated that use of a phase change material to the back of the solar panel can maintain the panel's required operating temperature in turn can increase the performance of the solar panel with increase in power production. The maximum temperature was of the panel was reduced from 57.3°C to 53.2°C by cooling with PCM.

Keywords: Phase Change Material, Solar Panel, Temperature, Performance, Efficiency

INTRODUCTION : As the world is facing the problem of energy deficit, global warming and detoriation of environment and energy sources, there is need for an alternative energy resource for power generation other than use of fossil fuels, water and wind. Fossil fuel get depleted in next few decades, hydro power plants are depends on annual rainfall and wind power is also depends on climate changes. Solar energy is one of the comparable candidate for alternate energy source. Solar energy is avery inexhaustible source of energy. The power from the sun intercepted by the earth is approximately 1.8×1011MW which is larger than the present consumption rate on the earth of all commercial energy sources. Thus solar energy could be supply all the present and future energy needs of the world on a continuing basis. This makes it one of the most promising of the unconventional energy sources.

The effeciency of solar panels depends on three factors: the intensity of the solar radiation flux, the quality of the semi conductor in use, and the operating temperature of the semi conductor cell. The variations of solar radiation cannot be ciontrolled. Therefore the ongoing research focuses either on new material like copper, indium diselinium, cadmium tellurium and chalcopyrite's, or on maintaining low operating temperatures. For PV panels, high operating temperatures create a drop in the conversion rate of about 0.5% per celcius degree over the nominal cell operating temperature of 25°C.

The major share of the solar radiation incident on the PV module does not contribute to produce power. Only 5-20% of the incident solar energy is converted into electricity, depending on the PV cell technology. The remaining

energy is converted into heat and affects the current density versus voltage characteristics of the PV module which in turn reduce its electrical efficiency.

Solar panels use light energy from the sun to generate electricity through the photovoltaic effect. The majority of the modules use water based crystalline silicon cells or thin film cells based on cadmium telluride of silicon. The structure member of a module can either be the top layer or the back layer. Cells must also be protected from desired output voltage and/or in parallel to provide the desired current capability. The conducting wires that take the current off the modules may contain silver, copper or other non magnetic conductive transition metals. The cells must be connected electrically to one another and to the rest of the system.

Depending on the construction, PV modules can produce electricity from a range of frequencies of light, but usually cannot cover the entire solar range. Hence much of the incident sunlight energy is wasted by the PV module. Photovoltaic effect occurs due to the absorbtion of photon energy over the band gap. The energy left over after going through the photovoltaic effect thus converts into heat. In contrast, if the photon energy is lower than the band gap energy of the cell, it cannot be converted into electricity and utilized totally to heat up the solar cell. Hence, opposite thermal regulation is indispensable for achieving desired performance from PV power plants. This has projected an increase of efficiency by 50%. The latter solution includes the use of PCM situated in the back of the solar panels.

Another design concept is to split the light into different wavelengths and direct the beams onto different cells tunes to these ranges. This has projected an increase of effeciency by 50%. To lower the ioperating temperature one can improve the back cooling of the panel by the natural and forced convection or to absorb the excess heat by modifying the panel's architecture. The latter solution includes the use of PCM situated in the back of the solar panels.

SUMMARY OF LITERATURE

1) High operating temperature of solar panel has its adverse effect on performance.
2) According to the review of different methods such as air cooling, water cooling can be adopted to maintain the temperature of panel.

MATERIALS AND COMPONENTS: Mono-crystalline solar panel, Digital Multimeter, Digital thermometer, Aluminium plate

METHODOLOGY

For experimental setup and measurements the modification of conventional PV panel with phase change material was made. Chosen conventional PV panel was from company Energy efficient lights was manufactured using a mono-crystalline silicon cell. The PCM was attached on back side of the PV module and enclosed with aluminium plate.

The Final PV-PCM after modification and construction of modified PV-PCM panel and thickness of each layer. PV-PCM are in fact encapsulated and consist of 7 layers of which are tempered Glass, ethylene – vinyl acetate (EVA), Si-solar cells, EVA, PCM and aliminium plate. The detailed electric properties of the PV cell, the thermo physical properties of PCM, which is used in experimental study is noted. The PCM in the modificated PV-PCM panel is paraffinic inorganic type is a pure PCM and this heat storage material utilizing the processes of phase change between solid and liquid to absorb and release large quantities of thermal energy at nearly constant temperature. The phase change material paraffin provide a very effective means of cooling effect by absorbing the heat absorbing the heat and reduces the

temperature of the panel with limited volume of expansion.

The experimental setup consists of PV-PCM panel, PV panel without PCM, three thermocouples for temperature measurement. During the experimental, the temperatures of each of the panel were measured and the surrounding air temperature. The temperature was measured at two points on the front of the panels and surrounding temperature behind the pannels are taken. The solar panel is placed on mild steel frame stand with inclination angle of 45°. The solar panel is connected to the positive and negative terminals of the battery through the voltmeter and ammeter. Battery is discharged with bulb load the data obtained from the measurement were taken for calculations.

EXPERIMENTATION

- Without PCM cooling system the readings of temperature, voltage & current from solar panel with respect to time.
- With PCM cooling system the readings of temperature, voltage & current from solar panel with respect to time.

Comparison of experimental results

The graph ploted (voltage v/s time, temperature v/s time, temperature v/s voltage) shows the comparision between output of the module without PCM and with PCM, it is found from the graph that the current output is higher for system with PCM compared to system without PCM. It is also obserbed that the temperature of module is less compared to that of module without PCM cooling at all intervals. It is also observed that the power output of panels with cooling is greater than the panel without cooling.

CONCLUSION

- The experimental results shows the improvement in the performance of conventional solar panel efficiency on cooling with PCM.
- By decreasing the working temperature of solar module there is a increase in life of the panel cells.
- The experimental results are clear indication of variation of efficiency with panel temperature; hence PCM cooling can increase the efficiency of solar panel.

REFERENCES

1) M Mohamed Musthafa. Enhancing Photoelectric Conversion Efficiency of Solar Panel by Water Cooling, J Fundam Renewable Energy Appl 2015.
2) H.G. Teo a , P.S. Lee b, M.N.A. Hawlader b, An active cooling system for photovoltaic modules, Applied Energy 90 (2012) 309-315
3) Ravindra Kumar, Manoj K. Misra. Phase Change Materials: Technology Status and Potential Defence Applications. Defence Science Journal, Vol. 61, No. 6, November 2011, pp. 576-582

8th International Engineering Symposium - IES 2019
March 13-15, 2019, Kumamoto University, Japan

Compressive Property of Natural Fibres Treated with Alkali solution Reinforced with Epoxy resin

Pramod V Badyankal [1], U Gobind [2] and Manjunatha T S [3]

1 *Department of Mechanical Engineering, Alva's Institute of Engineering and Technology Karnataka, Moodbidri, Mangalore – 574225, India.*
E-mail: pramodvab@gmail.com
2 *Department of Mechanical Engineering, Alva's Institute of Engineering and Technology Karnataka, Moodbidri, Mangalore–574225, India.*
E-mail: gobindukumar@gmail.com
3 *Jain Institute of Technology, Davangere – 577003, India.*
E-mail: drtsma@gmail.com

ABSTRACT: Natural fibres are nowadays considered as a suitable alternative as compared to glass fibres because the main advantages of these fibres are low cost, high strength to weight ratio, environmental friendly, low density etc. In the present work natural fibres such as banana and sisal were used for studying compressive properties. The fibres are treated with alkali solutions for 24 hrs. Fibres were treated with alkali solution of NaOH and washed, rinsed with acetic acid solution. The chemically treated fibres enhanced in mechanical strength as well as dimensional stability of natural fibres. The composition of specimens 20%Sisal 20%banana, 25%sisal 15%banana, 30%sisal 10%banana and 15%sisal 25%banana. The treated fibres were reinforced with epoxy resin [LY-556] and hardener [HY-951] in the ratio 10:1. Compression moulding technique was used for preparing specimens of ASTM D695-02a standard. By treating and increasing the composition of sisal fibres, compressive property of the specimen showed a good result as compared to other composition.

Keywords*: Sisal fibre, Banana fibre, compressive properties, alkali treatment*

INTRODUCTION

Hybrid composites are one of the emerging fields in polymer science that are gaining attention for application in various sectors. Environmental hazards of products have aroused the need for the researchers to develop environmental friendly fibres [2]. In many applications, natural fibre composites are realistic alternatives to synthetic fibre reinforced composites, since the former fibres possess many comparatively recognitions, such as low density, high specific strength, low cost, biodegradability, renewability, good thermal and acoustic insulating properties. The most commonly used plant fibres for polymer reinforcement are sisal, jute, banana, flax, coir, ramie, kenaf, hemp, Palmyra etc [1].

The main objective of this work is to contribute for a better understanding of the dynamic behavior of components made from natural fibre reinforced composite materials. Using natural fibres with polymer based on renewable resources will allow many environmental issues to be solved. In order to investigate the influence of the stacking sequence on the dynamic behavior of the components, experimental study has been carried out.

I.MATERIALS AND METHODOLOGY

a. Materials:

Natural banana and sisal fibres were used to prepare the composite. Epoxy (LY556) and hardener (HY951) were used for the

synthesis of the fibres and as a matrix material, for the chemical treatment the NaOH [Sodium Hydroxide] pallet is used.

b. Methodology:

The sisal and banana fibres were randomly taken from a bundle. Fibre length, fineness, diameter and weight were measured, respectively. Fibres were cut with 2-3 mm in length. The fibres were rinsed in 5% solution of NaOH separately, and left for 24hours. The rinsed fibres were then cleaned with fresh water and further cleaned with 5% Acetic acid solution. Fibres are left to room temperature for drying.

Based on the volume fraction calculation the proper composition of treated sisal and banana fibres with Epoxy resin & hardener in the ratio of 10:1 is used for the preparation of sample using the mould box of 250 mm X250 mm dimension. The fibres are oriented using hand lay-up technique with random orientation of fibres.

c. Experiment procedure:

The proper compositions of fibres based on volume fraction, were mixed to prepare the laminate of desired thickness. The whole material were randomly arranged on a mild steel platform uniformly at utmost care as fibres have a tendency to tangle and clump when laid one on top of other. Then by using compression moulding machine SANTEC – 10 ton is used to compress for the required thickness.

d. Compression testing:

Standard compression testing machine was used to test the specimens and plot a graph of Average load (N) v/s Average displacement (mm). The compression testing analysis was carried out on treated specimens. Four different compositions of banana and sisal fibres (25% banana & 15% sisal, 15% banana and 25% sisal, 20% banana and 20% sisal, 10% banana and 30% sisal) were tested one after the other. The maximum loads taken by the specimens before reaching the failure points were noted down.

The Fig. 1 shows the UTM machine with compression specimen.

Fig. 1 UTM machine

III. RESULTS AND DISCUSSION

The Fig. 2 shows the comparison of different composition. From the result 30S:10B shows a load carrying capacity high as compared to others. It clearly indicates sisal increasing proportion in the composite will increase the mechanical property.

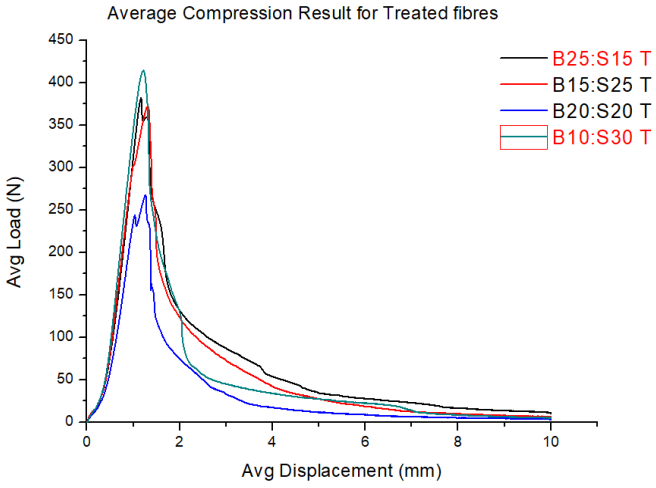

Fig. 2 Avg Load v/s Avg Displacement

IV.CONCLUSION

Natural fibres is available in nature plenty, and can be used for particular application. Compression moulding technique was used to fabricate the natural hybrid composite made by banana and sisal to investigate the results, it was observed that specimen with high in sisal quantity shows good load capacity compared to other composite specimens.

V.ACKNOWLEDGEMENT

The authors gratefully acknowledge the contribution of Mr. Gouvisiddappa, Mr. Krishna Huddar, Mr. Ravindra Nayakar, Mr. Rijvajsab Nagalapur for helping to conduct experimental work.

VI.REFERENCES

1. J.M.PRABHUDASS and K. PALANIKUMAR1, "MECHANICAL & THERMAL PROPERTIES OF SISAL EPOXY/ BANANA EPOXY COMPOSITES- A REVIEW", Applied Mechanics and Materials, Vol. 766-767, 2015, 173-177
2. K. G. Satyanarayana, K. Sukumaran, R S. Mukherjee, C. Pavithran & S. G. K. PiUai, "Natural Fibre-Polymer Composites", Cement & Concrete Composites, Volume 12, 1990, 117-136.
3. A.C.H. Barreto, D.S. Rosa, P.B.A. Fechine, S.E. Mazzetto, "Properties of sisal fibers treated by alkali solution and their application into cardanol-based biocomposites", Composites: Part A, Vol. 42, 2011, 492–500.
4. Easwara Prasad G L, Keerthi Gowda B S, Velmurugan R, "Comparative Study of Impact Strength Characteristics of Treated and Untreated Sisal Polyester Composites", Procedia Engineering, Vol. 173, 2017, 778 – 785.
5. A. Orue, A. Jauregi, U. Unsuain, J. Labidi, A. Eceiza, A. Arbelaiz, "The effect of alkaline and silane treatments on mechanical properties and breakage of sisal fibers and poly(lactic acid)/sisal fiber composites" , Composites: Part A, Vol. 84, 2016, 186–195
6. T.P. Mohan, K. Kanny, "Chemical treatment of sisal fiber using alkali and clay method", Composites: Part A, Vol. 43, 2012, 1989–1998.

8th International Engineering Symposium - IES 2019
March 13-15, 2019, Kumamoto University, Japan

Investigation on the performance and emission analysis of Al_2O_3 nanoparticles as an additive to a B20 blend of Lard Oil Methyl Ester on a CI engine

K. Raju[1], K.C. Sanjay[2], Madhusudhan Khamitkar [3], K.V. Suresha[4], Peter Fernandes[5] and Joseph Gonsalvis[6]

1 *St. Joseph Engineering College, Mangaluru, 575 028, India.*
e-mail: rajuksjec@gmail.com
2 *St. Joseph Engineering College, Mangaluru – 575 028, India.*
e-mail:sanjusanjay523@gmail.com
3 *Alva's Institute of Engg. & Technology, Moodbidri–574225, India.*
e-mail:madhusudhankhamitkar7@gmail.com
4 *Alva's Institute of Engg. & Technology, Moodbidri–574225, India.*
e-mail:kvs_a@yahoo.com
5 *Alva's Institute of Engg. & Technology, Moodbidri–574225, India.*
e-mail: principalaiet08@gmail.com
6 *St. Joseph Engineering College, Mangaluru, 575 028, India.*
e-mail: drjgonsalves@gmail.com

ABSTRACT: In the present study, performance and emission tests were conducted on a CI engine using a blend of B20 Lard Oil Methyl Ester (B20 LOME) without nanoparticles and a B20 LOME blend dispersed with 50, 75 and 100 ppm of Alumina (Al_2O_3) nanoparticles. The experimental results show that at full load, the addition of Al_2O_3 nanoparticles to B20 LOME slightly increases the brake thermal efficiency and decreases brake specific fuel consumption of CI engine as compared to B20 LOME without nanoparticles. The blends of B20 LOME with Al_2O_3 nanoparticles show reduced emission of Hydrocarbons (HC), Carbon monoxide (CO) and smoke as compared to B20 LOME blend without nanoparticles. The NO_X emission is slightly high for B20 LOME blends with nanoparticles at all loads as compared to B20 LOME blend without nanoparticles.

Keywords*: Alumina, Nanoparticles, Lard Oil Methyl Ester, emissions, diesel engine*

INTRODUCTION

Biodiesel is considered as the alternative for the depleting petroleum fuels. It is mainly extracted from vegetable oil and waste animal fats. As the properties of diesel and biodiesel are almost similar, the use of biodiesel in locomotive engines has gained much importance in recent years. The biodiesel has several advantages as compared to diesel such as less sulphur content in the fuel, and lower emission of hydrocarbons, carbon dioxide (CO_2), carbon monoxide (CO) and sulphur dioxide (SO_2) as reported by Patnaik and Acharya (2014). Since biodiesel is prepared from biological resources and has lower emissions compared to petroleum fuel it is considered as eco-friendly. The biodiesel also has some disadvantages such as low calorific value, low oxidation temperature, low volatility and high viscosity which cause severe problem to the engine during operation. The biodiesel is produced by trans-esterification of oil or fats in medium such as methanol or ethanol with NaOH or KOH as catalyst. Methanol is used frequently because of less cost compared to other alcohols as reported by Meher et al. (2006). The scarcity and cost of vegetable oils have made the researchers to show interest in the extraction of biodiesel from waste animal fats. The animal fats are inexpensive and more abundant in nature. The animal fat from beef, pork, chicken and mutton are commonly used in biodiesel production as reported by Rajat et al. (2014), Azjargal et al. (2012), Ejikeme et al. (2013) and Sunil

et al. (2015). Azjargal et al. (2012) have reported that the use of animal fats for producing biodiesel has several advantages such as higher cetane number, high oxidation tendency and good lubricating property. The nano particle metal oxide additives are added to the diesel and biodiesel blend to improve the performance and reduce the emission of harmful gases during combustion. Metal oxides, for example, Al_2O_3, cerium oxide, CuO, MnO, TiO_2 and ZnO are broadly utilized as fuel additive substances.

Basha and Anand (2013) have reported that by adding nanoparticles to biodiesel blend provide a large surface area and higher activity for the decay of hydrogen from water which will increase combustion. The calorific value of fuel increases with increase of nano particle fuel additives which in turn increases the power output. Hence the main aim of this project is to investigate the effect of Alumina (Al_2O_3) nanoparticles as fuel additive on the performance and emission characteristics of CI engine fuelled with a blend of B20 Lard Oil Methyl Ester to reduce emissions without affecting much its performance.

Hence this study is focused on the preparation, testing and comparison of a blend of B20 Lard Oil Methyl Ester mixed with different concentrations of Al_2O_3 nanoparticles and arrive at the optimum blend that would produce least emissions without any considerable reduction in the performance of CI engine.

EXPERIMENTAL DETAILS

Biodiesel is extracted from lard oil by trans-esterification process. The biodiesel blend (B20 LOME) is mixed with different concentrations of Al_2O_3 nanoparticles and they are dispersed in fuel blend by an Ultrasound bath sonicator as shown in Fig.1. The properties of fuel blends are measured according to ASTM standards and performance and emission tests were performed on variable compression ratio (VCR) diesel engine.

Trans-esterification of lard oil

The trans-esterification was done by using a three neck round bottom flask as shown in Fig. 2. One litre of lard oil is measured and transferred to the flask and heated up to 65°C. The solution of methanol with 5.2 g of NaOH is prepared and added to the lard oil at 65°C in the flask. The mixture is maintained at 65°C for 2 Hrs for the chemical reaction to take place. The mixture is stirred at a speed of 600-800 rpm by a magnetic stirrer inserted in the flask during the transfer of lard oil. After 2 Hrs of chemical reaction the mixture is transferred to a separating funnel and kept for 2 Hrs for the settling of glycerine as shown in Fig. 3. The glycerine that has been settled at the bottom of the flask was drained. To recover the methanol the biodiesel (LOME) has been heated up to 75°C. The biodiesel is then washed in hot water so that soap and glycerine are removed from biodiesel. The Lard Oil Methyl Ester (LOME) obtained is further heated to 110°C so that moisture content and water in the biodiesel are eliminated.

Dispersion of Al_2O_3 Nanoparticles in B20 LOME blend

The Al_2O_3 nanoparticles are dispersed in B20 LOME blend by sonication. The sonication process uses ultrasonic sound waves to agitate the Al_2O_3 nanoparticles in the liquid. The Al_2O_3 nanoparticles to be dispersed have been weighed on a weighing scale and added to the B20 LOME blend in the beaker. The beaker is then kept in the water bath so that the ultrasonic sound waves are passed on to the beaker. The blend is agitated for 30 min so that the Al_2O_3 nanoparticles are dispersed uniformly in the blend.

Physico-Chemical properties of fuel samples

The Physico-chemical properties such as higher calorific value, density, kinematic viscosity, flash and fire points are determined as per ASTM standards for biodiesel. The properties of different samples with and without nanoparticles are shown in Table 1.

Details of VCR Diesel Engine Test Rig

The variable compression ratio (VCR) engine test rig consists of a single cylinder four stroke water cooled diesel engine. It has a tilting cylinder block arrangement for varying the compression ratio without changing the geometry of combustion

chamber. The load on the engine can be varied by Eddy Current dynamometer. The specifications of the engine are shown in Table 2. The exhaust gases are analyzed by using gas analyzer and smoke meter.

RESULTS AND DISCUSSION

Performance characteristics

Brake Specific Fuel Consumption (BSFC): The variation of BSFC against load is shown in Fig. 4. From the results it has been observed that the blend of B20 LOME with 100 ppm Al_2O_3 nanoparticles shows 3.7% decrease in BSFC as compared to B20 LOME without Al_2O_3 nanoparticles at full load condition. The calorific value of fuel increases with increase in concentration of Al_2O_3 nanoparticles. The fuel with low calorific value is consumed more to produce the same power output compared to the fuel with relatively high calorific value. The same was reported by Rao and Rao (2015).

Brake Thermal Efficiency (BTE)

The variation of Brake Thermal Efficiency against Load is shown in Fig. 5. From the results it has been observed that BTE of VCR diesel engine increases with the addition of Al_2O_3 nanoparticles to the B20 LOME blend. An increase of 2.4% in BTE has been observed for B20 LOME with 100 ppm Al_2O_3 nanoparticles as compared to B20 LOME blend without nanoparticles at full load condition. The Al_2O_3 nanoparticles act as an oxygen buffer, which helps in complete combustion of B20 LOME blend & thus increase Brake Thermal Efficiency. The same trend has been observed by Rao and Rao (2015), Venkatesan (2015) and Aalam et al. (2015).

Emission characteristics

Hydrocarbon (HC) emission

The variation of Hydrocarbon emission against load is shown in Fig. 6. From the Fig. 6 it has been observed that the emission of HC increases with increase in load. At full load condition, the emission of HC reduces by 65.4% for B20 LOME with 100ppm Al_2O_3 nanoparticles as compared to B20 LOME blend. The addition of Al_2O_3 nanoparticles oxidizes the HC present in the fuel and helps in proper combustion of the fuel. The same has been reported by Aalam and Saravanan (2015).

Carbon monoxide emission

The variation of Carbon monoxide against load is shown in Fig. 7. The emission of CO reduces as the load increases. The CO emission has been reduced by 55.6% for B20 LOME blend with 100 ppm Al_2O_3 nanoparticles as compared to B20 LOME blend. The considerable reduction in CO is due to the high catalytic activity of Al_2O_3 nanoparticles having high contact surface area and proper mixing of air and fuel inside the engine cylinder. The same trend has been observed by Sanjay et al. (2016).

Oxides of Nitrogen (NO_X)

The Fig. 8 depicts the variation of oxides of nitrogen against load. The emission of NO_X is a phenomenon depends mainly on the combustion temperature as reported by Aalam and Saravanan (2015). It has been observed that as the concentration of Al_2O_3 nanoparticles increases in B20 LOME blend, the emission of NO_X also increases and also observed that there is an increase in NO_X emission by 43.5% for B20 LOME blend with 100 ppm of Al_2O_3 nanoparticles as compared to B20 LOME blend**.** High temperature and availability of oxygen are the two primary reasons for high NO_X formation as nitrogen and oxygen respond at higher temperature.

Smoke Opacity

The Fig. 9 depicts the variation of smoke opacity against load. The smoke opacity increases as the load on the engine is increased. The incomplete combustion of the fuel is the key reason for the smoke as reported by Prabhu et al. (2015). The smoke is found highest for the B20 LOME blend and it gets reduced with addition of alumina nanoparticles to the blend. It has been observed that the smoke opacity gets reduced by 34% for B20 LOME blend with 100 ppm Al_2O_3 nanoparticles as compared to B20 LOME blend. The Al_2O_3 nanoparticles dispersed in B20 LOME blend accelerate the combustion process by shortening the ignition delay and reducing the smoke in exhaust gas. The same observation was made by Aalam and Saravanan (2015).

CONCLUSIONS

The following conclusions may be drawn from the present study.

- The Brake Thermal Efficiency has been increased by 2.2% and the Brake Specific Fuel Consumption has been reduced by 3.7% for B20 LOME blend dispersed with 100 ppm Al_2O_3 nanoparticles as compared to B20 LOME blend without nanoparticles.
- The HC, CO and Smoke emissions have been reduced by 65%, 55% and 34% respectively in the exhaust gases for B20 LOME blend dispersed with 100 ppm Al_2O_3 nanoparticles as compared to B20 LOME blend without nanoparticles.
- The NO_X emission has been increased by 43.5% for B20 LOME blend dispersed with 100 ppm Al_2O_3 nanoparticles as compared to B20 LOME blend without nanoparticles.

ACKNOWLEDGEMENTS

The authors are grateful to the Management, St. Joseph Engineering College, Mangaluru for providing the facilities for conducting the performance and emission testing.

REFERENCES

[1] Aalam, C S et al. (2015), Experimental investigations on a CRDI system assisted diesel engine fuelled with Aluminum Oxide nanoparticles blended biodiesel, Alexandria Engineering Journal, Vol. 54, No. 3, pp. 351-358.

[2] Aalam, C S & Saravanan, C G (2015), Effect of nano metal oxide blended Mahua biodiesel on CRDI diesel engine. Ain Shams Engineering Journal, Vol. 8, No.4, pp. 1-8.

[3] Aalam, C S & Saravanan, C G (2015), Performance enhancement of Common-Rail Diesel Engine using Al_2O_3 and Fe_3O_4 nanoparticles blended biodiesel. International Research Journal of Engg. and Technology, Vol. 2, No. 5, pp. 1400-1410.

[4] Azjargal, J et al. (2012), High quality biodiesel production from pork lard by high solvent additive, Science Asia, Vol. 38, No. 1, pp. 95-101.

[5] Basha, J S & Anand, R B (2013), The influence of nano additive blended biodiesel fuels on the working characteristics of a diesel engine, Journal of the Brazilian Society of Mechanical Sciences and Engineering, Vol. 35, No. 3, pp. 257-264.

[6] Ejikeme, P M et al. (2013), Pig-fat (Lard) derivatives as alternative diesel fuel in compression ignition engines. Journal of Petroleum Technology and Alternative Fuels, Vol. 4, No. 1, pp. 7-11.

[7] Karthikeyan, S et al. (2014), Role of Al_2O_3 nano additive in GSO Biodiesel on the working characteristics of a CI engine. Indian Journal of Chemical Technology, Vol. 21, No. 4, pp. 285-289.

[8] Meher, L C et al. (2006), Technical aspects of biodiesel production by transesterification – a review, Renewable and Sustainable Energy Reviews, Vol. 10, No. 3, pp. 248-68.

[9] Patnaik, P P & Acharya, S K (2014), Effect of compression ratio on emission of CI engine using neat karanja oil and karanja oil methyl ester blend, International Journal of Engineering-Transactions C: Aspects, Vol. 27, No. 3, pp. 403-410.

[10] Prabhu, L et al. (2015), Investigation on performance and emission analysis of TiO_2 nanoparticles as an additive for bio-diesel blends, Journal of Chemical and Pharmaceutical Sciences, Vol. 7, No. 1, pp. 408-412.

[11] Rajat, C et al. (2014), Conversion of slaughter house and poultry farm animal fats and wastes to biodiesel: Parametric sensitivity and fuel quality assessment, Renewable and Sustainable Energy Reviews, Vol. 29, pp. 120-134.

[12] Rao, S C & Srinivasa, R M (2015), Performance analysis of DI Diesel engine fuelled with Diesel along with Nano additives, International Journal of Engg. Trends and Technology, Vol. 24, No. 2, pp. 107-110.

[13] Rolvin, D S et al. (2015), Performance and emission characteristics of a CI engine fuelled with diesel and TiO_2 nanoparticles as fuel additive, Materials Today: Proceedings 2, Vol. 2, No. 4, pp. 3728-3735.

[14] Sanjay, K C et al. (2016), Effect of Alumina Nanoparticles on the Performance and Emission Characteristics of CI Engine Fuelled with Lard Oil Methyl Ester Blends, American Journal of Mat. Sci., Vol. 6, No. 4A, pp. 94-98.

[15] Sunil, J D S et al. (2015), Effect of compression ratio on the performance and emission characteristics of blends of lard oil methyl ester and diesel on CI engine, Energy and Power, Vol. 5, No. 1A, pp. 5-9.

[16] Venkatesan, S P (2015), Influence of Aluminum Oxide nanoparticle additive on performance and exhaust emissions of diesel engine, American-Eurasian Journal of Scientific Research, Vol. 10, No. 2, pp. 88-92.

Fig.1 Ultrasound bath Sonicator

Fig. 2 Trans-esterification of lard oil

Fig. 3 LOME kept in the funnel for settling of glycerine

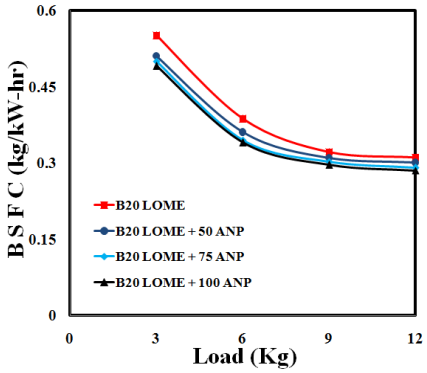

Fig. 4 Graph of Brake Specific Fuel Consumption (BSFC) vs Load

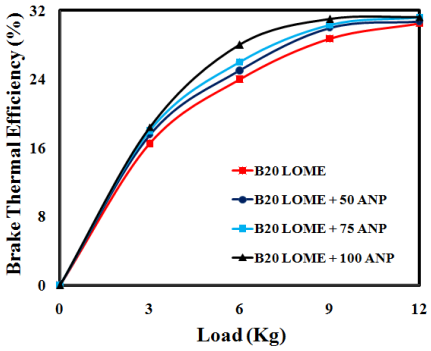

Fig. 5 Graph of Brake Thermal Efficiency vs Load

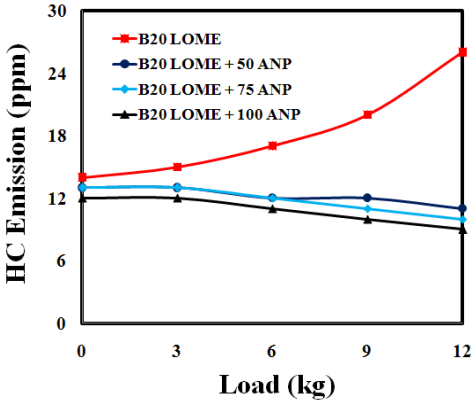

Fig. 6 Graph of HC emission vs Load

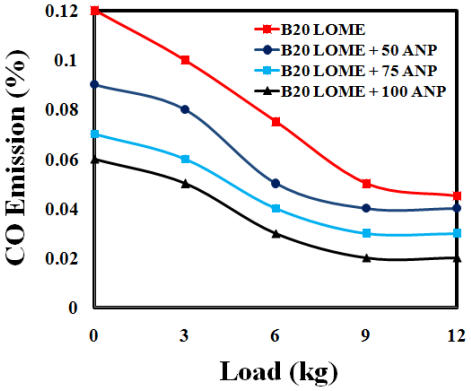

Fig. 7 Graph of CO emission vs Load

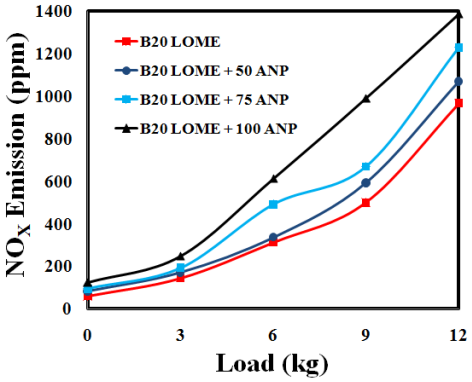

Fig. 8 Graph of NO_X emission vs Load

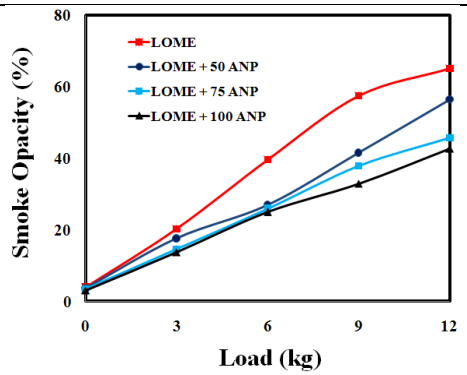

Fig. 9 Graph of Smoke Opacity vs Load

Table 1 Physico-chemical properties of different fuel samples

Properties	Higher Calorific value (kJ/kg)	Density (kg/m^3)	Kinematic Viscosity @ 40°C (cSt)	Flash Point (°C)	Fire Point (°C)
ASTM Standard	D 240	D 4052	D 445	D 92-05a	D 92-05a
Diesel	42000	714.8	2.63	58	63
B20LOME	38932	724.6	3.22	80	82
B20LOME+ 50ANP	38991	725.5	3.42	81	83
B20LOME+ 75ANP	39264	727.2	3.55	82	85
B20LOME+ 100ANP	39537	730.3	3.63	84	87
LOME	27250	750.8	4.12	166	168

Table 2 Specifications of VCR Diesel engine

S. No.	Parameters	Specification
1	Engine	4 Stroke, Single Cylinder, Constant Speed, Water Cooled Diesel Engine
2	Make	Kirloskar
3	BHP	3.5 kW @ 1500 RPM
4	Stroke Length	110 mm
5	Compression Ratio	12:1 to 18:1
6	Connecting Rod Length	234 mm
7	Dynamometer Type	Eddy Current Type with Loading Unit

8th International Engineering Symposium - IES 2019
March 13-15, 2019, Kumamoto University, Japan

Flexural Properties of Banana and Sisal Hybrid Fiber Composite without Treatment

Pramod V Badyankal[1], Bharathesh Hegde[2], and Manjunatha T S[3]

[1]*Department of Mechanical Engineering, Alva's Institute of Engineering and Technology Karnataka, Moodbidri, Mangalore – 574225, India. email: pramodvab@gmail.com*

[2]*Department of Mechanical Engineering, Alva's Institute of Engineering and Technology Karnataka, Moodbidri, Mangalore–574225, India. email: hegde.bharathesh@gmail.com*

[3]*Jain Institute of Technology, Davangere – 577003, India. email: drtsma@gmail.com*

ABSTRACT: Natural fibres bio composites are very important in the field of green composites as they are having benefits such as low density, environmental friendly and high specific mechanical performance. In the present work, the flexural properties of banana and sisal fibres are studied. The banana fibres are extracted from the pseudostem of the banana plant and sisal fiber is extracted by a process known as decortication process. The fibres are cut into 2mm in length, mixed randomly with proper composition using epoxy resin [LY-556] and hardener [HY-951] in the ratio 10:1. The composition of specimens 20%sisal 20%banana, 25%sisal 15%banana, 30%sisal 10%banana and 15%sisal 25%banana. Specimens are prepared according to the ASTM D790-03 standard using 250mm X 250mm mould box of required thickness. The composites are prepared by means of compression moulding technique. By increasing composition of sisal, flexural properties of specimens exhibhited a good result compare to other composition.

Keywords*: sisal fibre, banana fibre, flexural properties*

INTRODUCTION

Composite materials are made with two or more components that differ in shape and chemical composition. Most of the composite materials are made to obtain better properties than individual constituents.

Environmental awareness new rules and legislation are forcing industries to seek new materials that are more environmentally friendly. Over the past two decades, plant fibres have been receiving considerable attention as substitutes for synthetic fibres reinforcement.The mechanical and damage properties of single fibres used in fibrous composite have gained tremendous importance in recent years.[2]

Unlike the traditional synthetic fibres, such as glass and carbon, these lignocelluloses fibres are able to impart certain benefits to the composites including low density, high stiffness, low cost, renewability, biodegradability and a high degree of flexibility during processing.

By the hybridization of banana in sisal mechanical properties got increased and water absorption got reduced [5]. Natural fibres used are available in nature and can be grown. Sisal Fiber is one of the most widely used natural fiber and is very easily cultivated. It is obtain from sisal plant. The plant is known formally as Agave Sisal Ana. These plants produce rosettes of sword-shaped leaves which start out toothed, and gradually lose their teeth with maturity [3]. Banana plant is a large

perennial herb with leaf sheaths that form pseudo stem. Its height can be 10-40 feet surrounding with 8-12 large leaves. The leaves are up to 9 feet long and 2 feet wide (2.7 meters and 0.61 meter) [4].

MATERIALS AND METHODOLOGY

a. Materials:

The sisal and banana are purchased from the local dealer. Epoxy and hardener are purchased from go green, tamil nadu. The epoxy resin with the hardener is used as matrix material. The bending ratio resin with the hardener is 10:1 by weight.

b. Methodology:

The specimens are prepared, by random orientation of fibres [RoHM] with epoxy resin [LY556] & Hardener [HY951], using mould box by compression moulding machine. The specimen is prepare according to ASTM D790-03 standard for testing 3 point bending.[1]

The banana and sisal fibres were randomly taken from a bundle. Fibre length, fineness, diameter and weight were measured, respectively. Fibres were cut with 2-3 mm in length. The composite preparation process was performed in the following order using random mixing technique by hand lay-up.

Based on the calculation of volume friction of mould box as shown in fig.1, a proper composition of sisal, banana and epoxy are used in preparation of specimen.

Mould box made of mild steel of dimension 250X250X5 mm

Fig.1 Mould box

c. Flexural test

The specimen is subjected to 3 point bending test. The load is applied exactly at the centre of the specimen, on the other to side a simply support is placed. The parameters for this test are the support span, speed of loading and the maximum deflection for the test. The fig.2 shows flexural test specimen according to ASTM standard.[1]

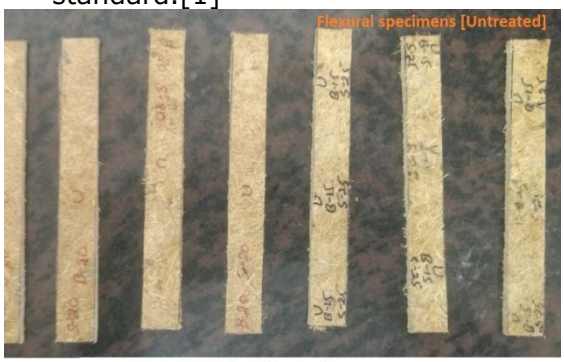

ASTM D790 for Flexural

Fig. 2 Specimens for flexural test

d. Experiment procedure:

UTM machine by MECMESIN of load cell 2500N, along with 3 point bending setup is used for the testing of specimen.

Initially the specimens are marked at different position for the experimental procedure to be carried out as shown in fig.3

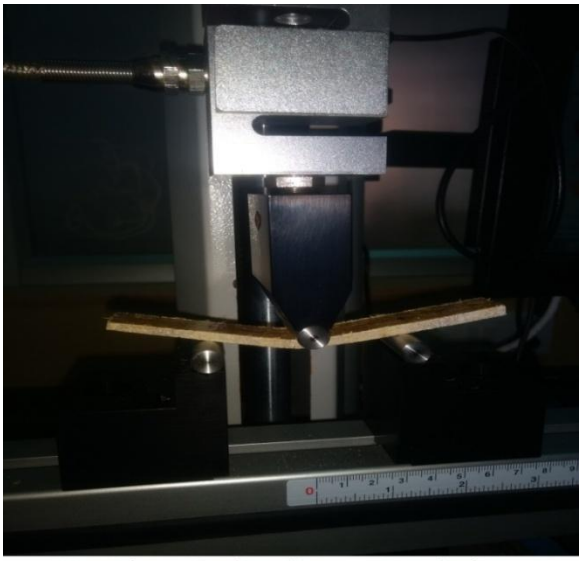

Material starts Bending taking a maximum load

Fig. 3 Load cell with specimen [UTM]

RESULTS AND DISCUSSION

The Fig. 4 shows the comparison of different composition. From the result it is clear that if the composition of sisal in hybrid composite is increased then the load carrying capacity is also keep on increasing. The 30S:10B shows a comparatively good result.

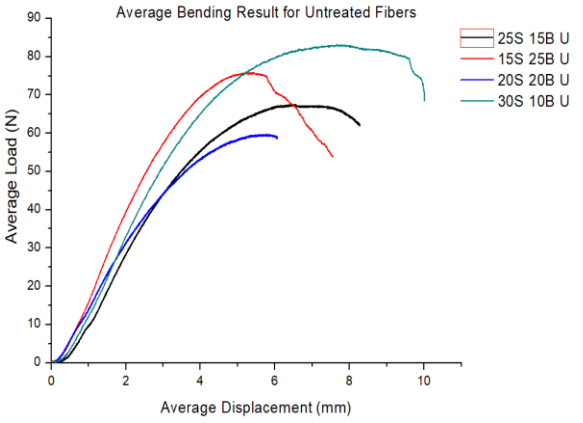

Fig. 4 Avg load v/s Avg displacement

CONCLUSION

Natural fibres are relatively economical to purchase and fabricate. Compression moulding technique was used to fabricate the natural hybrid composite made by banana and sisal to investigate the flexural properties. The flexural property changes with the change in the sisal composition.

ACKNOWLEDGMENT

The authors gratefully acknowledge the contribution of Mr. Gouvisiddappa, Mr. Krishna Huddar, Mr. Ravindra Nayakar, Mr. Rijvajsab Nagalapur for helping to conduct experimental work.

REFRENCES

1. ASTM D790-03: Standard Test Methods for Flexural Properties of Unreinforced and reinforced plastics and electrical insulating Material.

2. Ebisike K, AttahDaniel B. E, Babatope B, Olusunle S.O, "Studies on The Extraction of Naturally-Occurring Banana Fibers", IJES, Volume 2, Issue 9, Pages 95-99, 2013

3. M. M. Owen, C.O. Ogunleye, & E.O. Achukwu, "MECHANICAL PROPERTIES OF SISAL FIBRE-REINFORCED EPOXY COMPOSITESEFFECT OF ALKALI CONCENTRATIONS", Advances in Polymer Science and Technology: An International Journal 2015; 5(3) : 26-31

4. Prasanna Kumar Ilankeeran, Preetamkumar M. Mohite, Sudhir Kamle, "Axial Tensile Testing of Single Fibres", Modern Mechanical Engineering, 2012, 2, 151-156

5. Venkateshwaran,N., ElayaPerumal, A., Thiruchitrambalam, M., 2011. "Mechanical and Water absorption behaviour of banana/sisal reinforced hybrid composite". *Materials and Design,* 32, 2011, 4017-4021.

Scope of Piezoelectric Materials in Aviation Industry

Omkar Barwade and **Shaurya Seth**

Department of Metallurgy and Materials Engineering, National Institute of Technology, Karnataka, Surathkal, Mangalore - 575025, India.
Email : omkarbarwade1198@gmail.com

ABSTRACT: In today's world since the depletion of non-renewable resources for energy has reached a new peak, it is time we focus on generating energy from renewable resources and that is where the piezoelectric materials jump in which generate electricity using the mechanical vibrations. The project focuses on harvesting the electrical energy by using piezoelectric materials utilizing the mechanical stress produced by the people while walking and sitting inside an aircraft and accumulating the energy using a battery for further use. The AC generated is converted to DC using a full bridge wave rectifier. This project mainly focuses on the use of PVdF film or Lead Zirconate Titanate (PZT) for harvesting electrical energy which is cost effective and easy to implement. The project was simulated on Comsol software to find out the amount of electrical energy produced by calculating amount of mechanical stress produced by certain number of people, taking the average weight of people and calculating accordingly. This technology can be implemented in other areas as well and not just aviation industry.

Keywords: *non-renewable resources, energy, renewable resources, mechanical vibrations, piezoelectric materials, aircraft, PVdF*

I. INTRODUCTION

Electrical energy is one of the important forms of energy required for performing various functions in an aircraft. Many subsystems such as avionic system, cockpit control system, engine ignition system use electrical energy which is usually derived by drawing some amount of power from the turbines. But, during mechanical extraction of energy from turbine, there are losses due to low efficiency of reduction gears. Thus, output of turbines is reduced for they not only have to supply energy to the electrical systems but also have to drive compressor through shaft. Also, replacing the batteries is monotonous and costly when the sensor is located in a remote location. These intricacies can be eliminated by the application of energy harnessing devices. The motive of a power

harnessing device is to make use of the energy of a system that is being lost to the environment and transform it into usable energy form as a fuel for electrical devices. Electrical items which do not depend on a definite power source, for instance batteries, can possibly be provided with continuous power by making a good use of this unused energy. In this paper, the focus is on utilization of piezo material as potential energy harvester. A piezoelectric transducer is suggested, which can extricate mechanical vibrations and produce electrical energy in a more definitive, green and efficient way. There are various types of piezoelectric materials available in profuseness such as ceramics and polymers. For this particular operation, Lead Zirconate Titanate (PZT) is more suitable because of its high mechanical Q factor (a dimensionless parameter depicting how underdamped an oscillator or resonator is) and high curie temperature.

II. What are Piezoelectric Materials?

Piezoelectrics produce electricity when exposed to a mechanical stress. They also work in retrograde, producing strain when treated with an electric field. The word 'piezein' arises from a greek word which is defined as 'to press'. It was uncovered in 1880 by Pierre Curie in roschelle salt. Piezoelectrics are a member of a family of materials called the 'ferroelectrics'. In ferroelectric materials, the structure on a molecular level is aligned such that the material manifests a local charge separation, called as an electric dipole. The piezo phenomenon subsists in two domains, first is the direct effect that defines the material's aptness to convert mechanical stress into electrical charge. The other phenomenon being the reverse effect, which is the capability of a piezo material to produce mechanical strain energy pertaining to the applied electric potential. The direct piezo effect is accountable for the material to act as a sensor and the reverse piezo phenomenon is liable for its caliber to work as an actuator.

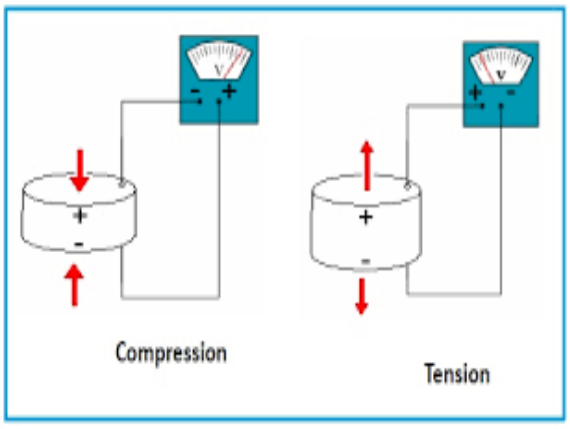

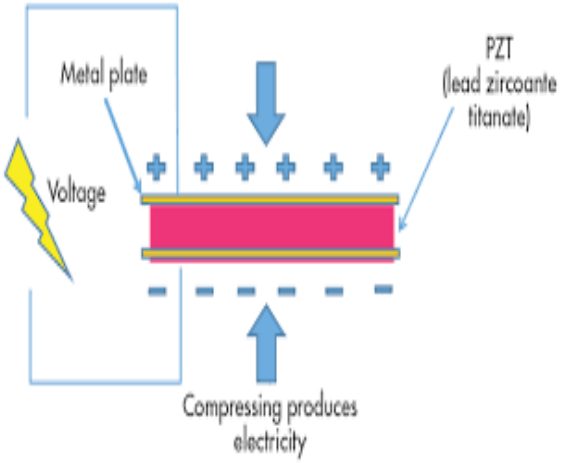

III. Principle of Operation

The piezoelectric material PZT is being used with an intention to extricate the energy departed to the environment while airplane is in motion. Piezo material is situated on high stress places in the airplane such as floor, seats, engine and related parts, luggage compartments, etc. which experience recurrent stress and endures strain to produce electric voltage across its extremities that can be used to generate energy and use it to power other electrical subsystems within the aircraft. The figure shown below shows some of the prime components used for the purpose. PZT strips responds to mechanical vibrations and voltage procured is augmented using a transformer which is then stockpiled in a capacitor. Output voltage is sieved through using a DC filter to eliminate any clamors or oscillations. The system enumerates the required voltage according to the load disparities. The power unit helps in powering of batteries and dispenses back up as a supplementary system.

IV. Mathematical Analysis

Electric power produced from piezoelectric materials is the integrated effect of electrical and mechanical behavior of the substance. The resultant energy can be calculated by the subsequent equation -

$B = d.T + a.E$

B is electric displacement vector, T is the stress vector, a is dielectric permittivity, E is electric field vector, d is the piezoelectric constant.

There are several variants of PZT. Among all types, PZT (III) BM 800 is used because of high mechanical Q factor (a dimensionless parameter depicting how underdamped an oscillator or resonator is) and curie temperature. It has analogously lower charge constant but it is enough to power electrical subsystems of aircraft.

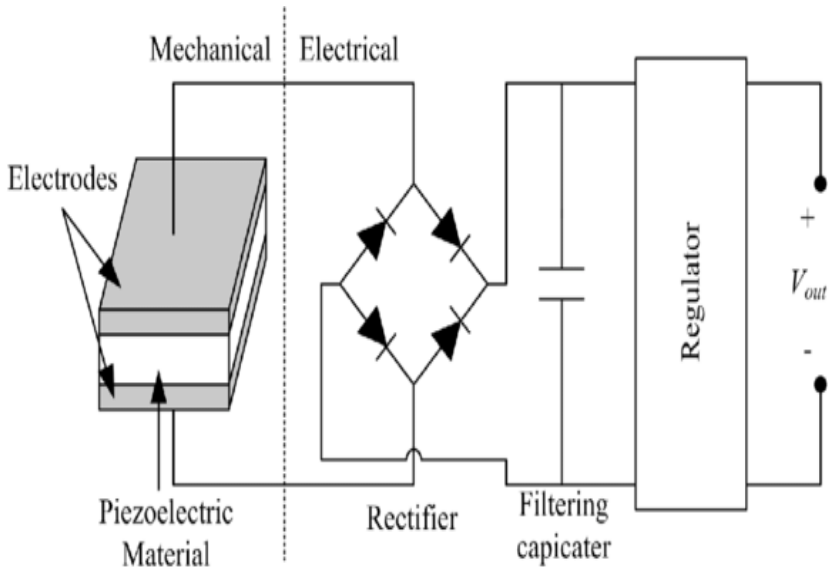

V. Possible Areas of Application

Effectiveness is the main criterion for effective implementation of any equipment. Vibrations can be procured from many coordinates but for acquiring higher voltage out-turn, it is important to position the piezoelectric material at a proper place. Our main purpose is to generate enough voltage from the PZT material which can be utilized to power internal smaller units in an aero plane such as LED, charging points, Air Conditioner, etc. and thus save the energy that we otherwise derive from conventional methods.

Piezoelectric materials sure have a wider range of applications. They are ideal for usage where energy input is less and can be easily derived by mechanical vibrations picked up by piezoelectric materials. We have already seen there application in treadmills and other gym equipments. Piezoelectric materials can be used to run appliances at home by proper placing of these material strips at variable or cyclic stress generating areas. Piezoelectric materials can also be effectively used for LED advertising boards on streets, electric automatic wheelchairs, bicycles, shoes, motorcycles, trucks, tractors, washing machines, etc.

VI. ADVANTAGES

- Highly durable, dependable, green method for harnessing energy.
- Use of piezo ceramics like PZT will also cause vibrational damping as these vibrations are used for producing energy.
- Cost-effective.
- Onboard power generation.
- Uninterrupted and self - charging of batteries.

VII. LIMITATIONS

- Since PZT is brittle, careful handling is required.
- Stability is an issue as loss of polarization of material is a concern and also with time, material performance will decrease.
- High temperature dependence of electromechanical properties.

VIII. CONCLUSIONS

The following conclusions are deduced from this study:

- Piezoelectric materials can be successfully used in many different areas including Aviation Industry which requires huge energy supply.
- Piezoelectric materials prove to be extremely useful for harvesting energy which is being lost in the form of mechanical vibrations.
- Piezoelectric materials are useful to produce electricity in smaller scale for domestic appliances quite easily.

IX. REFERENCES

[1] Damping of structural vibrations with piezoelectric materials and passive electrical networks by NW Hagood and A Von Flotow

[2] A new surface wave in piezoelectric materials by JL Bleustein - 1968.

[3] Linear electro-elastic fracture mechanics of piezoelectric materials by YE Pak , International Journal of Fracture - 1992.

[4] Piezoelectric Ceramic Materials - Processing, Properties, Characterization and Applications - Xinhua Zhu.

[5] Piezoelectric wafer embedded active sensors for aging aircraft structural health monitoring by V . Giurgiutiu, A Zagrai - Structural Health- 2002

[6] Utilisation of smart polymers and ceramic based piezoelectric materials for scavenging wasted energy by I Patel, E Siores , T Shah - Sensors and Actuators -2010.

8th International Engineering Symposium - IES 2019
March 13-15, 2019, Kumamoto University, Japan

Machinability studies on EN47 Spring Steel of turning process by optimization technique during dry and wet condition

Vasu M[1], and H Shivananda Nayaka[2]

1 *Department of Mechanical Engineering, National Institute of Technology Karnataka, Surathkal, Mangalore 575025, India. email: vasu.m.manu@gmail.com*
2 *Département of Mechanical Engineering, National Institute of Technology Karnataka, Surathkal, Mangalore 575025, India. email:shivananda@rediffmail.com*

ABSTRACT: The present work deals with machinability study of EN47 spring steel with SNMG tungsten carbide tool insert to investigates, cutting force (F_z) and surface roughness (R_a) under dry and wet condition. Design of experiments (DOE) Taguchi L_9 orthogonal array (OA) are employed to conduct the experiments. In order to optimize the process parameters of cutting velocity (V_c), feed rate (f) and depth of cut (a_p). The analysis of variance (ANOVA) is employed to know the influencing factor and percentage contribution for each output response. The results reveal that cutting force, are mainly influenced by feed rate and depth of cut and surface roughness is influenced by cutting speed and feed rate. Comparative studies perform with different cutting environments. Hence, improved performance observed with wet machining, cutting force reduced 38.90% and surface roughness improved with 11.95% during wet machining.

Keywords*: Spring steel, DOE, Taguchi, ANOVA, Cutting force, Surface roughness.*

INTRODUCTION

EN47 Spring steel is a hard material having a hardness of 45-48HRC. EN47 material possesses low thermal conductivity and suitable for oil hardening and tempering. Hardened spring steel offers excellent toughness and shock resistance, suitable alloy for automobile applications. (W.H. Yang, and Y.S. Tarng, 1998) investigates machinability characteristics of S45C steel in order to optimize the process parameters by using Taguchi technique. (Iihan Asilturk and Harun Akkus, 2011) employed Taguchi L9 orthoganal array in order to minimize surface roughness by machining of AISI 4140. (Ajay D Jewlikar et al, 2015) studied optimization technique by machining of Bohler K110 Steel in order to optimize process parameters for surface roughness and material removal rate. (S Krishna madhavi et al, 2017) employed Taguchi technique in order to minimize the surface roughness and hardness of the material. Some of the researchers used Taguchi technique to optimize the process parameters. In order to minimize surface roughness, cutting force and tool tip temperature under different cutting environments and different kind of cutting tool inserts. (Vasu. M and H Shivananda Nayak, 2018)

In this present work turning process are carried out on EN47 spring steel with SNMG tungsten carbide tool insert. Design of experiments (DOE) technique Taguchi L9 orthogonal array are used to conduct the experiments. In order to optimize the process parameters cutting speed (V_c), feed rate (f), and depth of cut (ap) on cutting force (F_z) and surface roughness (R_a) are analyzed under dry and wet condition.

EXPERIMANTAION

The present work, deals with machinability study of EN47 spring steel with SNMG tungsten carbide tool insert. The chemical composition of work material is depicted in Table 1. Based on application, workpiece material is chosen. Generally, EN47 spring

steel are used to manufacture leaf spring for heavy vehicles and many other engineering applications such as making of dies, knuckles, shaft and gear manufacturing etc. Dimension of the workpiece (length=170mm and diameter=30mm) For avoiding chatter and vibration of workpiece material L/D ratio maintain less than 10 according ISO 3685. In the current work turning process are carried out under dry and wet condition as shown in Fig 1. In order to identify the main cutting force (F_z) and surface roughness (R_a). Turning process are carried out on precision Panther lathe machine. Kistler dynamometer (Type 9257B) are used to measure the cutting force. Surface roughness was measured by Mitutoyo Talysurf SJ301 roughness tester. For avoiding errors, experiments are conducted thrice and average values are considered for the analysis.

Results and Discussion

Analysis of variance

Analysis of variance (ANOVA) is helped to identify significant terms for output responses and this is a computational technique that allows estimate relative contribution of each input process parameters to the output response. Using mathematical models, the process is validated. Using ANOVA results the significance of the output response is calculated from the probability value (P-value) at 95% confidence level. If the P-value less than 0.05 then obtained model is significant. Table 2 Depicts the experimental plan and corresponding output response.

Analysis of cutting force

Cutting force plays a major role in machinability study. Higher cutting force may affect the productivity as well as increasing the production cost, to overcome this problem DOE technique are used to optimize the process parameters to minimize the cutting force. Some of the literature reported higher cutting force reduces tool life and affects machined surface etc. Design of experiments are used to optimize the process parameters (Vasu. M and H Shivananda Nayak, 2018).

From the ANOVA Table 3 and Table 4 it is observed that cutting force are mainly influenced by depth of cut, followed by feed rate and cutting speed having less significant. From Tables it is noticed that the P-values shows less than 0.05 and depth of cut contributes (47% and 54%), feed rate contributes (39% and 29%) and cutting speed having least significant under dry and wet condition respectively. In Higher depth of cut and feed rate cutting force are increased, this is due to more energy are required to deform the materials. Moreover, frictional force between tool-chip interface hence cutting force are increased (Amel Chabbi et al 2017).

Analysis of surface roughness

Surface roughness is one of the major output response of machinability studies. A better surface finish is eliminating a number of process like honing, lapping and buffing etc. Surface roughness influence coefficient of friction, corrosion resistance, fatigue strength, and wear rate of the machined components.

From the ANOVA Table 5 and Table 6 it is observed that surface roughness is mainly influenced by cutting speed, followed by feed rate and depth of cut having less significant. From Tables it is noticed that the P-values shows less than 0.05 and cutting speed contributes (83% and 85%), feed rate contributes (7% and 7%) and depth of cut having least significant under dry and wet condition respectively. Surface roughness decreased by increasing cutting speed, this is due to in higher cutting speed thermal softening of the workpiece material, which leads improved surface finish. Feed rate increases with increasing surface roughness this is due to in higher feed rate, tool movement forms helical furrows and these furrows are wider and deeper which reduces surface roughness value (R_a) of machined surface similar results was observed by Bensouilah [9].

Main Effects plot

Optimum cutting conditions are identified by a main effects plot, it is a graphical representation for input parameters such as cutting velocity, feed rate and depth of

cut. The highest slope tends more significant for each output response. The optimal cutting conditions are identified by main effect plots as depicted in Table 7.

From the Fig 2 (a-b) it is observed that cutting force are mainly influenced by depth of cut and feed rate, highest slops are identified with both cutting environments as it confirmed from analysis of variance. Cutting speed having less significant. From the Fig 3(a-b) it is observed that surface roughness is mainly influenced by cutting speed, from the plots the highest slope is identified with both cutting environments as it confirmed from analysis of variance. Depth of cut having less significant.

Regression analysis

The regression analysis is used to predict the output response. In the present work a first order linear model are developed by Minitab software. The determination of coefficient (R^2) values should 1 or 100% then obtained models are adequate. Regression equations are mentioned in Equation 1 to 4 for cutting force and surface roughness under dry and wet condition. From the regression analysis predicted values are identified and comparing with the experimental value. From the Fig 4(a-b) and Fig 5(a-b) it is observed that a comparison plots of cutting force and surface roughness under dry and wet condition, predicted values are good agreement with experimental value so developed models are adequate. (Vasu. M and H Shivananda Nayak, 2018).

Regression Equations during dry condition

$$F_z = -31.86 - \left(17.32 \times a_p\right) + \left(0.00204 \times V_c\right) - \left(67.5 \times f\right) \quad (1)$$

$$R_a = -18.05 - \left(0.85 \times a_p\right) + \left(0.01396 \times V_c\right) - \left(27.7 \times f\right) \quad (2)$$

Regression Equations during Wet condition

$$F_z = -28.04 - \left(17.06 \times a_p\right) + \left(0.00067 \times V_c\right) - \left(53.3 \times f\right) \quad (3)$$

$$R_a = -17.92 - \left(1.68 \times a_p\right) + \left(0.01602 \times V_c\right) - \left(30.8 \times f\right) \quad (4)$$

Conclusion

The present work indicates that comparative studies on EN47 spring steel with coated cutting tool insert during dry and wet condition. Experiments are conducted based on design of experiment using Taguchi L_9 orthogonal array. From experimental work some of the conclusion is drawn:

Cutting force are mainly influenced by feed rate and depth of cut, and surface roughness are influenced by cutting speed. This is confirmed by ANOVA tables.

Comparative studies perform with different cutting environments. Hence, improved performance observed with wet machining, cutting force reduced 38.90% and surface roughness improved with 11.95% during wet machining.

From the main effects plot optimum conditions are observed for cutting force (a_p=0.2mm, V_c=796 rpm, f=0.046 mm/rev), (ap=0.2, V_c=1250, f=0.046) and for surface roughness (a_p=0.2, V_c= 1250 f=0.046), (a_p=0.2, V_c= 1250, f=0.046) under dry and wet condition respectively.

From the regression analysis, the developed models are adequate. Predicted and experimental values give satisfactory result for each output response under dry and wet condition.

References

[1] Yang W.H and Tarng Y.S. (1998) Design optimization of cutting parameters for turning operations based on the Taguchi method, J. Mater. Process. Technol. Vol 84, pp122–129.

[2] Asiltürk.I and Akkuş.H (2011) Determining the effect of cutting parameters on surface roughness in hard turning using the Taguchi method, Meas. J. Int. Meas. Confed. Vol44, pp1697–1704.

[3] Jewlikar A.D.et al, (2015) HPT Process Parameter Optimization in Dry Turning of Bohler K110 Steel, Mater. Today Proc. 2 pp2414–2422.

[4]Krishna Madhavi. S et al,(2017) Evaluation of Optimum Turning Process of Process Parameters Using DOE and PCA Taguchi Method, Mater. Today Proc. 4, pp1937–1946.

[5]Vasu.M and Nayaka .H.S, (2018) Comparative study of turning process on EN47 spring steel with different nose radii using statistical technique, Mater. Today Proc. 5, pp16893–16903.

[6]Vasu.M, and Shivananda .N.H., (2018) Comparative study of coated and uncoated tool inserts with dry machining of EN47

steel using Taguchi L_9 optimization technique, in: AIP Conf. Proc.,: p. 020063
[7] Vasu.M, and Shivananda Nayaka.H, (2018) Investigation of machinability characteristics on EN47 steel for cutting force and tool wear using optimization technique, Mater. Res. Express. 5(6), pp066501.
[8]Chabbi.A et al, (2017) Predictive modeling and multi-response optimization of technological parameters in turning of Polyoxymethylene polymer (POM C) using RSM and desirability function, Meas. J. Int. Meas. Confed. vol95, pp99–115.
[9]Bensouilah. H et al, (2016) Performance of coated and uncoated mixed ceramic tools in hard turning process, Measurement. Vol82, pp1–18.
[10] Vasu.M and Shivananda Nayaka. H, (2018), Investigation of Cutting Force Tool Tip Temperature and Surface Roughness during Dry Machining of Spring Steel, Mater. Today Proc. 5(2) pp7141-7149.

Table 1 Chemical composition

Material	C	Mn	Si	S	P	Cr
EN 47	0.45-0.55	0.50-.80	0.50 Max	0.40	0.40	0.80-1.20

Table 2 Cutting condition and output responses

				Dry		Wet	
Sl No	a_p	V_c	f	F_z	R_a	F_z	R_a
1	0.2	625	0.046	91.06	2.81	44.66	2.43
2	0.2	796	0.093	92.77	3.58	45.54	3.21
3	0.2	1250	0.14	138	1.66	85.33	1.27
4	0.4	625	0.093	154.4	3.89	128.4	3.54
5	0.4	796	0.14	175.7	3.58	137.1	3.21
6	0.4	1250	0.046	71.53	1.6	79.69	1.23
7	0.6	625	0.14	339.7	5.4	168.89	5.04
8	0.6	796	0.046	141.5	2.9	98.26	2.53
9	0.6	1250	0.093	265.6	1.2	110.39	0.98

Table 3 ANOVA for Cutting force (F_z) during dry condition

F_z	DF	Seq SS	Adj SS	Adj MS	F-Value	P-Value	Cont%
Reg	3	134.95	134.95	44.99	11.41	0.011	87%
a_p	1	72.033	72.033	72.03	18.27	0.008	47%
V_c	1	2.606	2.606	2.606	0.66	0.453	2%
f	1	60.315	60.315	60.32	15.3	0.011	39%
Error	5	19.717	19.717	3.943			13%
Total	8	154.67					100%

Table 4 ANOVA for Surface roughness (R_a) during dry condition

R_a	DF	Seq SS	Adj SS	Adj MS	F-Value	P-Value	Cont%
Reg	3	132.39	132.39	44.13	15.23	0.006	90%
a_p	1	0.175	0.175	0.175	0.06	0.815	0%
V_c	1	122.02	122.02	122	42.11	0.001	83%
f	1	10.2	10.2	10.2	3.52	0.119	7%
Error	5	14.487	14.487	2.897			10%
Total	8	146.88					100%

Table 5 ANOVA for Cutting force (F_z) during Wet condition

F_z	DF	Seq SS	Adj SS	Adj MS	F-Value	P-Value	Cont%
Reg	3	107.83	107.83	35.94	8.2	0.022	83%
a_p	1	69.836	69.836	69.84	15.94	0.01	54%
V_c	1	0.284	0.284	0.284	0.06	0.809	0%
f	1	37.705	37.705	37.7	8.61	0.032	29%
Error	5	21.906	21.906	4.381			17%
Total	8	129.73					100%

Table 6 ANOVA for Surface roughness (R_a) during wet condition

R_a	DF	Seq SS	Adj SS	Adj MS	F-Value	P-Value	Cont%
Reg	3	173.91	173.91	57.97	18.95	0.004	92%
a_p	1	0.678	0.678	0.678	0.22	0.658	0%
V_c	1	160.67	160.67	160.7	52.53	0.001	85%
f	1	12.563	12.563	12.56	4.11	0.099	7%
Error	5	15.293	15.293	3.059			8%
Total	8	189.2					100%

Table 7 Optimum cutting condition during dry and wet condition

		a_p	V_c	f
Dry	F_z	0.2	796	0.046
	R_a	0.2	1250	0.046
Wet	F_z	0.2	1250	0.046
	R_a	0.2	1250	0.046

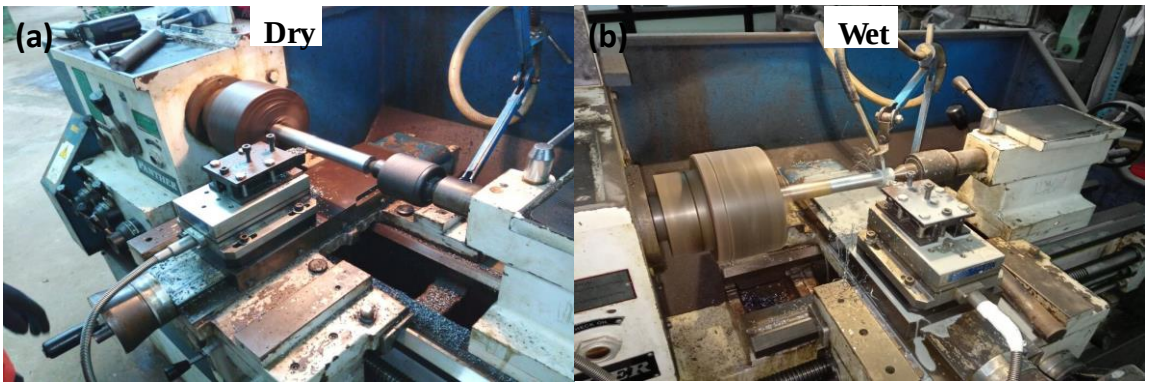

Figure 1 Experimental set during dry and wet condition

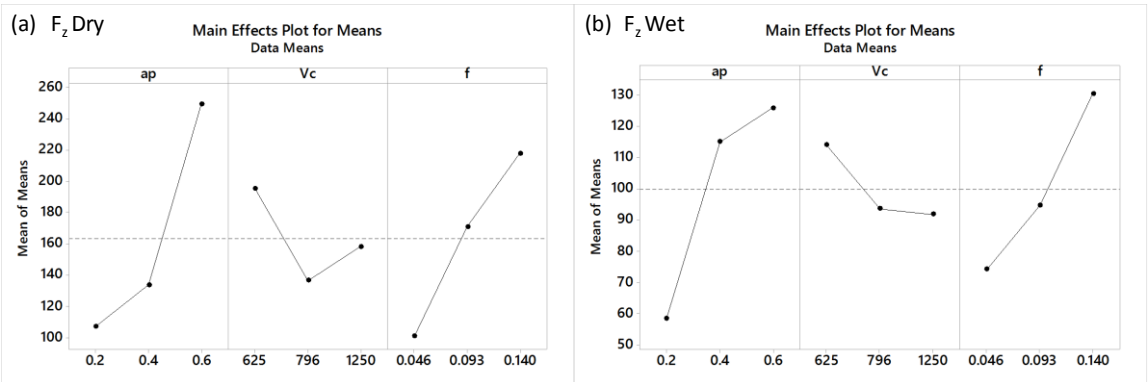

Figure 2 (a-b) Main Effects plot for cutting force during dry and wet condition

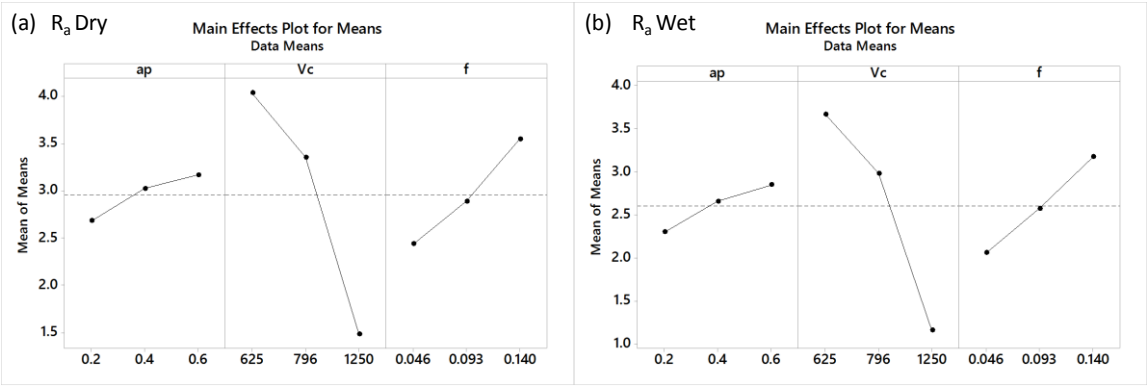

Figure 3 (a-b) Main effects plot for surface roughness during dry and wet condition

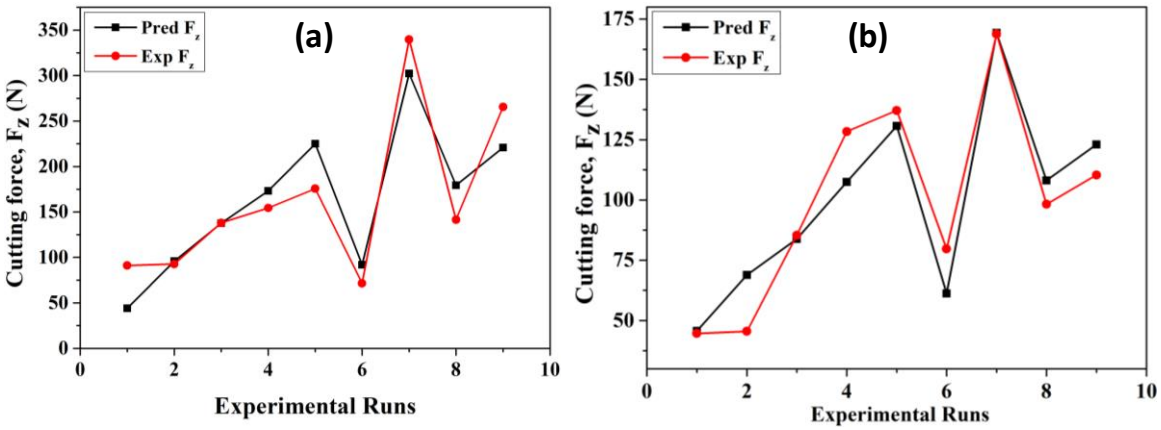

Figure 4(a-b) Experimental vs Predicted for cutting force during dry and wet condition

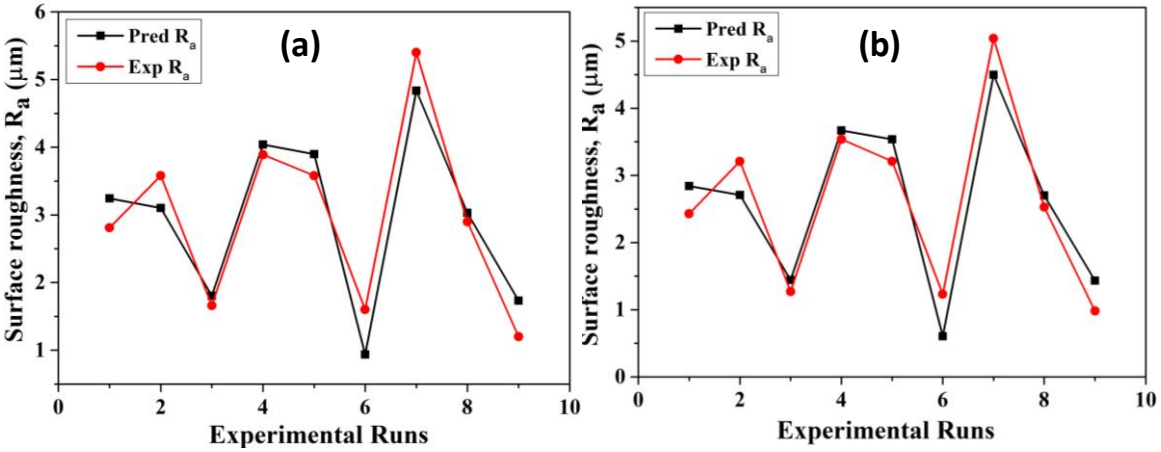

Figure 5(a-b) Experimental vs Predicted for surface roughness during dry and wet condition

Analysis of a Multi-Degree-Freedom PDMS Composite Cantilever Beam for Energy Harvesting

Sanket Kulkarni[1], Shivashankar Hiremath[2] and Satyabodh M Kulkarni[3]

1 *Department of Mechanical Engineering, National Institute of Technology Karnataka, Surathkal, Mangalore 575025, India. email:sanket.16me267@nitk.edu.in*
2 *Department of Mechanical Engineering, National Institute of Technology Karnataka, Surathkal, Mangalore 575025, India. email:sssdait@gmial.com*
3 *Department of Mechanical Engineering, National Institute of Technology Karnataka, Surathkal, Mangalore 575025, India. email:smk@nitk.edu.in*

ABSTRACT: Harvesting energy from moving bodies especially automobiles and its local use to save external energy is the order of the day. Many attempts are made to harvest energy for car vibrations during travel and use it locally to energize devices like tyre pressure monitors, dashboard lighting, etc. Vertical oscillations in a car during travel are with different amplitude and frequencies. A harvester has to deform maximum for each of these, so that more energy can be obtained.

A multi-degree-freedom cantilever made of PDMS-ZnO composite material is proposed and evaluated through Finite Element Analysis for base excitation at different amplitude and frequency. Strain in the beam, which manifests as voltage due to piezo-electric property of the material, is found to be near maximum for most of the amplitudes and frequencies. Potential is obtained and analysed.

***Keywords**: Energy harvesting, PDMS-ZnO Composite, Piezoelectricity, Finite Element Analysis.*

INTRODUCTION

The process of gathering ambient energy surrounding a system, and converting it into usable electrical energy is termed as Energy Harvesting (EH). The main ambient energy sources for EH applications are solar, thermal, mechanical vibration, etc. Additionally, combinations of energy harvesting sources can be used to gather power from different environments. Vibration-based energy harvesting is used in numerous applications ranging from common household devices, transportation tools, industrial machinery and even human motion. In vibration-based EH, the optimal electrical power is achieved within a narrow frequency bandwidth, close to the resonant frequency of the device. (Badr, Delaney, & Dechev, 2015)

Many attempts have been made to analyse the energy harvesting devices based on mechanical vibrations(Farnsworth, Tiwari, & Dorey, 2014). Soft tools based on Finite Element method are used for analysing the above EH devices consisting of simple mechanical structures like cantilever beam(Kundu & Nemade, 2015). Typically to transduce the mechanical energy into electrical energy, piezoelectric materials have found wide applications owing to the efficiency of the conversion, ease of availability/processing and bias-less

operation(Sarma, 2018)(Aparna, Karanth, & Kulkarni, 2018).

Literature on energy harvesting indicates that attempts to improve the performance of harvester include usage of non-traditional geometries(Sunithamani, Lakshmi, & Flora, 2012), particularly thickness-tapered cantilever(Kundu & Nemade, 2015).

Main factors influencing the efficacy of energy harvesters are their lowest natural frequency, deflections/stresses experienced by the vibrating member and the transduction property of the material. Thus researchers have resorted to usage of multi degree freedom piezoelectric structures(Tang & Yang, 2012) to lower the natural frequencies(Inman & Priya, 2009) and attain improved performance in energy harvesting. It could be observed that a complete analysis of piezoelectric structures in multi-dof form is yet to be carried out with an end product in mind.

In the present work a multi-dof cantilever made of PDMS-ZnO composite is studied and an energy harvesting device consisting of up to 4 multi-dof beams is proposed and analysed for the performance in terms of eigenfrequency, displacement and developed potential.

METHODOLOGY

Contemporary research on energy harvesting is directed towards usage of multi-dof piezoelectric members for improved performance. An energy harvesting device consisting of number of PDMS-ZnO composite cantilevers is proposed as shown in Figure 1. Each of these cantilevers in the device are considered to be multi degree freedom structures in order to lower the eigenfrequencies of the device. Different configurations of this device are considered for analysis and are listed in Table 1.

Figure 2 shows the meshed model of a one-dof single cantilever beam made of PDMS-ZnO composites. The piezoelectric ZnO powder is incorporated in the PDMS matrix with a volume fraction of 0.25. The physical and mechanical properties of PDMS-ZnO composite are determined experimentally and are validated through rule of mixture. The properties of the material used in analysis are tabulated in Table 2. The cantilever model is discretised into an extra fine mesh with free tetrahedral isotropic elements. Modal analysis of the cantilever is carried out with base of the cantilever under fixed constraint. Eigenfrequency, displacement and induced potential are determined by solving electrostatic and structural mechanics solvers. Above analysis was repeated for all configurations mentioned in Table 1. Following section presents the results of the analysis.

RESULTS AND DISCUSSION

Results of analysing a 1-DOF single cantilever beam are presented in Figure 3 (a) and (b). These figures represent eigenfrequencies, displacements and induced potentials of 1-DOF single beam configuration respectively. Table 3,4 and 5 summarize the results of analysing all configurations with 2-DOF multi-beam configurations.

Eigenfrequency, displacements and potentials for 2-DOF configurations are plotted in Figures 4,5 and 6. It could be observed that when we go for multi-beam configuration, the eigenfrequency reduces and the device can be subjected to near resonance vibration during the service. Lowest eigenfrequency, highest amplitude and potential are observed for 3 beam configurations.

Tables 6,7 and 8 represent the eigenfrequencies, displacements and potentials of 3-DOF multi-beam configurations. Figures 7,8 and 9 compare the eigenfrequencies, displacements and potentials of 2-DOF and 3-DOF multi-beam configurations.

As observed earlier 3-beam configuration possesses least eigenfrequency and higher displacement (Figure 7 and 8) in 3-DOF system also. In Figure 9, potential induced in different

multi-beam configurations are compared where it could be observed that 3-DOF provides maximum voltage output compared to other configurations.

CONCLUSION

The above conducted analysis brought out the following conclusions. Firstly, it was observed that as the number of degrees of freedom increases, the natural frequency of the cantilever beam reduces. Thus, it becomes easier for the beam to attain resonance and obtain maximum deflection. Due to the increased deflection the stress induced is increased and also the potential developed by the piezoelectric beam increases.

Secondly, as the number of beams increases, the eigenfrequencies decrease thus providing ease of resonance. Also, by using multi-beam configuration, the different beams vibrating at resonance produce respectable amount of electric potential which can be tapped onto and can be used for various purposes.

Thus, by using the proposed design, maximum output can be obtained and it can be acknowledged as an optimum design.

REFERENCES

Aparna, Karanth, P. N., & Kulkarni, S. M. (2018). Modeling of cantilever type piezoelectric polymer actuator. In *2018 3rd International Conference on Control and Robotics Engineering, ICCRE 2018*. https://doi.org/10.1109/ICCRE.2018.8376479

Badr, B. M., Delaney, K. R., & Dechev, N. (2015). Design Piezoelectric Energy Harvesting Using COMSOL for Mice Telemetry Device. In *Proceedings of the COMSOL Conference, Boston* (pp. 1–7).

Farnsworth, M., Tiwari, A., & Dorey, R. (2014). Modelling , Simulation and Optimisation of a Piezoelectric Energy Harvester. *Procedia CIRP*, *22*(December), 142–147. https://doi.org/10.1016/j.procir.2014.07.152

Inman, D. J., & Priya, S. (2009). *Energy Harvesting Technologies*. *Energy Harvesting Technologies*. https://doi.org/10.1007/978-0-387-76464-1_5

Kundu, S., & Nemade, H. B. (2015). Piezoelectric Vibration Energy Harvester Based on Thickness-Tapered Cantilever. In *Proceedings of the COMSOL Conference in Pune* (pp. 5–7).

Sarma, K. (2018). *Energy Harvesting from Vibration Source Using Piezo- MEMS Cantilever*. *Masters Thesis,Asian Intitute of Technology, Thailand*.

Sunithamani, S., Lakshmi, P., & Flora, E. E. (2012). Simulation and Optimization of MEMS Piezoelectric Energy Harvester with a Non-traditional Geometry. Excerpt from the Proceedings of the 2012 COMSOL Conference in Bangalore. *Proceedings of the COMSOL Conference in Bangalore*, *5*.

Tang, L., & Yang, Y. (2012). A multiple-degree-of-freedom piezoelectric energy harvesting model. *Journal of Intelligent Material Systems and Structures*, *23*(14), 1631–1647. https://doi.org/10.1177/1045389X12449920

TABLES AND FIGURES

Table 1 Configurations and their Codes

CONFIGURATION		CODE
Number of Beams	DOF	
One Beam	1	B1D1
	2	B1D2
	3	B1D3
Two Beam	2	B2D2
	3	B2D3
Three Beam	2	B3D2
	3	B3D3
Four Beam	2	B4D2
	3	B4D3

Table 2 Material properties used in FEA

PROPERTY	NAME	VALUE	UNIT
Density	ρ	1294.8[kg/m^3]	kg/m^3
Elasticity matrix	cE	2460[kPa]	Pa
Coupling matrix	eES	{0, 0, 0, 0, 1161…	C/m^2
Relative permittivity	ε_r	4	1
Coefficient of Thermal expansion	α	0.297e-4[1/K]	1/K
Heat capacity at constant pressure	C_P	986.5[J/(kg*K)]	J/(kg.K)
Thermal conductivity	k	0.35[W/(m*K)]	W/ (m.K)
Young's modulus	E	2460[kPa]	Pa
Poisson's ratio	ν (nu)	0.41	1

Table 3 Eigenfrequency Variation

TPYE OF CANTILEVER	**PROPERTIES**		
	Eigenfrequency 1 (Hz)	Eigenfrequency 2 (Hz)	Eigenfrequency 3 (Hz)
Simple	7.038	43.985	52.939
1 Slot, 1 Beam	6.4844	9.7022	18.957
1 Slot, 2 Beam	6.4118	6.4123	9.5435
1 Slot, 3 Beam	5.7067	6.7316	7.2279
1 Slot, 4 Beam	6.2128	6.2137	6.4489

Table 4 Amplitude Variation

TPYE OF CANTILEVER	PROPERTIES		
	Amplitude for E1 (mm)	Amplitude for E2 (mm)	Amplitude for E3 (mm)
Simple	3.429	4.411	3.475
1 Slot, 1 Beam	5.592	6.053	4.952
1 Slot, 2 Beam	7.924	7.838	9.584
1 Slot, 3 Beam	11.9	10.8	11.9
1 Slot, 4 Beam	9.18	9.172	9.121

Table 5 Voltage Variation

TPYE OF CANTILEVER	PROPERTIES		
	Voltage for E1 (V)	Voltage for E2 (V)	Voltage for E3 (V)
Simple	2.00006	2.00011	2.00021
1 Slot, 1 Beam	2	2.00001	2.00017
1 Slot, 2 Beam	2.00281	2.0003	2.00095
1 Slot, 3 Beam	2.01614	2.02515	2.02769
1 Slot, 4 Beam	2.00226	2.00141	2.00217

Table 6

TPYE OF CANTILEVER	PROPERTIES		
	Eigenfrequency 1 (Hz)	Eigenfrequency 2 (Hz)	Eigenfrequency 3 (Hz)
Simple	7.038	43.985	52.939
2 Slot, 1 Beam	6.4705	9.2336	12.151
2 Slot, 2 Beam	6.4016	6.4047	8.9131
2 Slot, 3 Beam	5.6926	6.6254	6.7211
2 Slot, 4 Beam	6.2065	6.2067	6.4405

Table 7

TPYE OF CANTILEVER	PROPERTIES		
	Amplitude for E1 (mm)	Amplitude for E2 (mm)	Amplitude for E3 (mm)
Simple	3.429	4.411	3.475
2 Slot, 1 Beam	5.633	5.994	4.935
2 Slot, 2 Beam	9.31	9.765	10.3
2 Slot, 3 Beam	13.7	12.2	13.2
2 Slot, 4 Beam	10.7	10.7	10.7

Table 8

TPYE OF CANTILEVER	PROPERTIES		
	Voltage for E1 (V)	Voltage for E2 (V)	Voltage for E3 (V)
Simple	2.00006	2.00011	2.00021
2 Slot, 1 Beam	2.00002	2.00002	2.00016
2 Slot, 2 Beam	2.0003	2.00317	2.0001
2 Slot, 3 Beam	2.00214	2.00006	2.00107
2 Slot, 4 Beam	2.00627	2.00249	2.00492

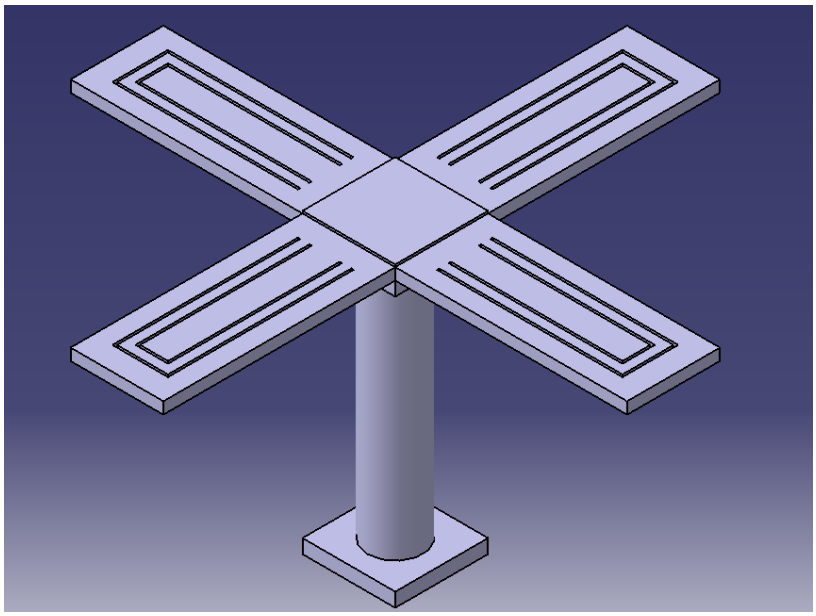

Figure 1 Proposed Energy Harvesting device

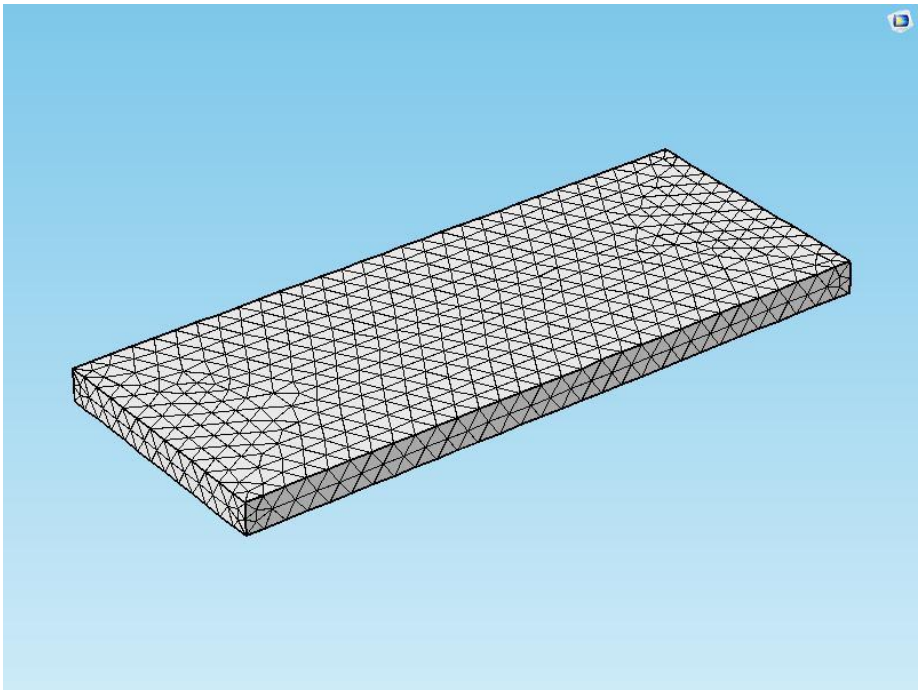

Figure 2 Tetrahedral meshing

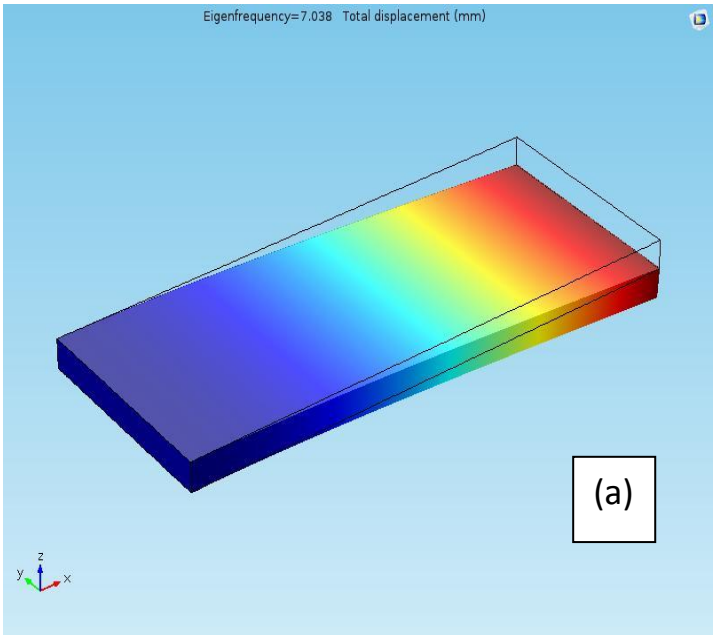

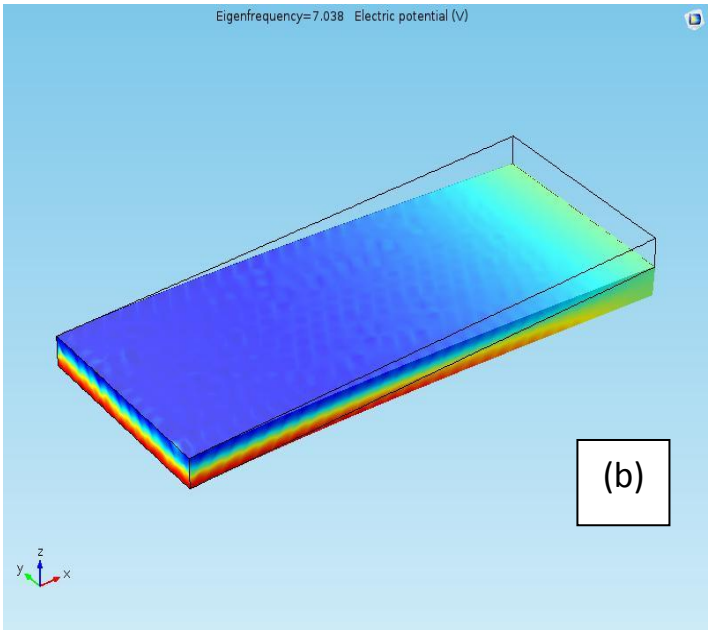

Figure 3 Pictures showing (a)Eigenfrequency and Displacement and (b)Induced potential of 1-DOF cantilever beam

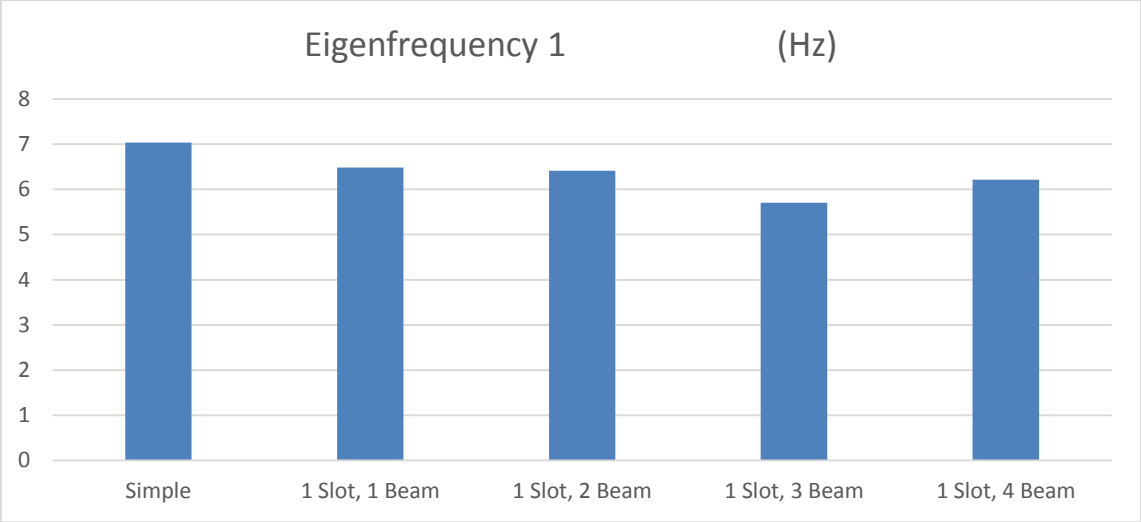

Figure 4 Graph of Eigenfrequency vs Configuration

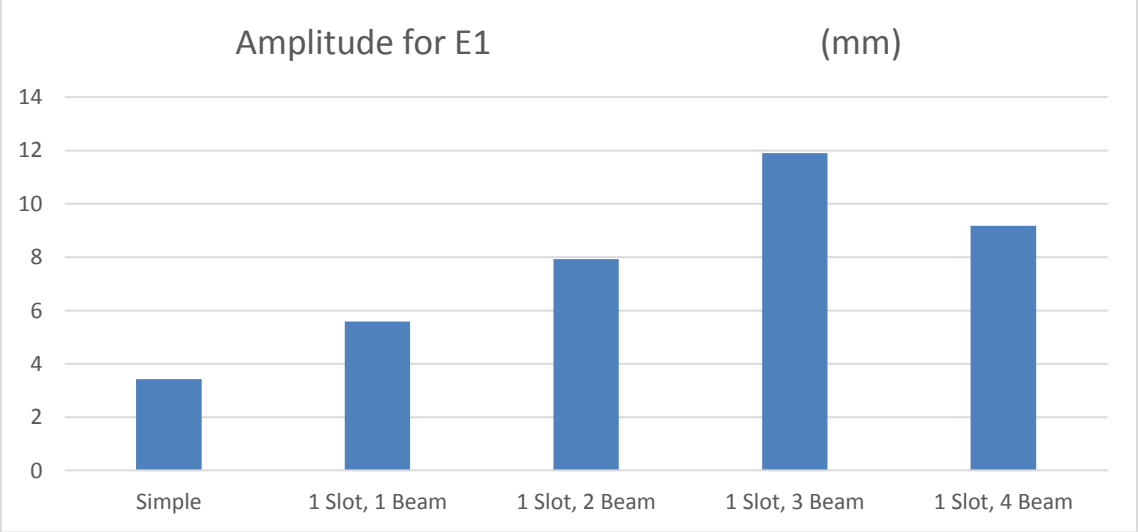

Figure 5 Graph of Amplitude vs Configuration

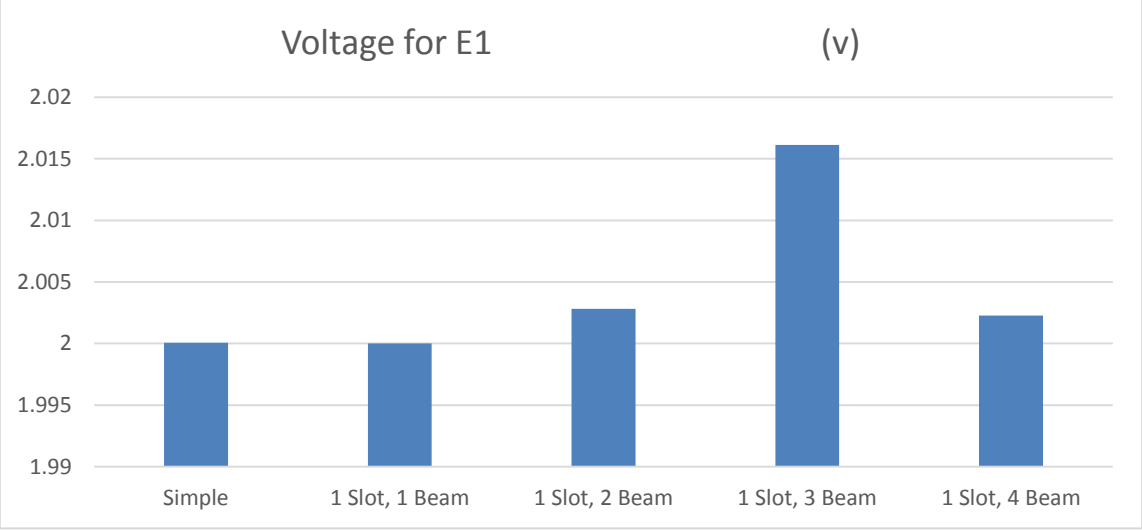

Figure 6 Graph of Voltage vs Configuration

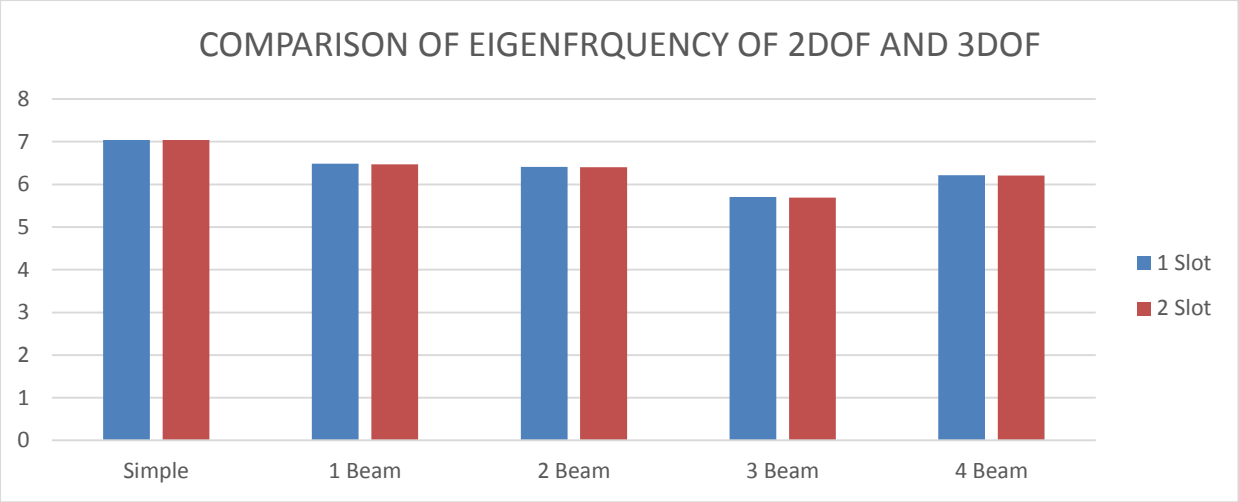

Figure 7

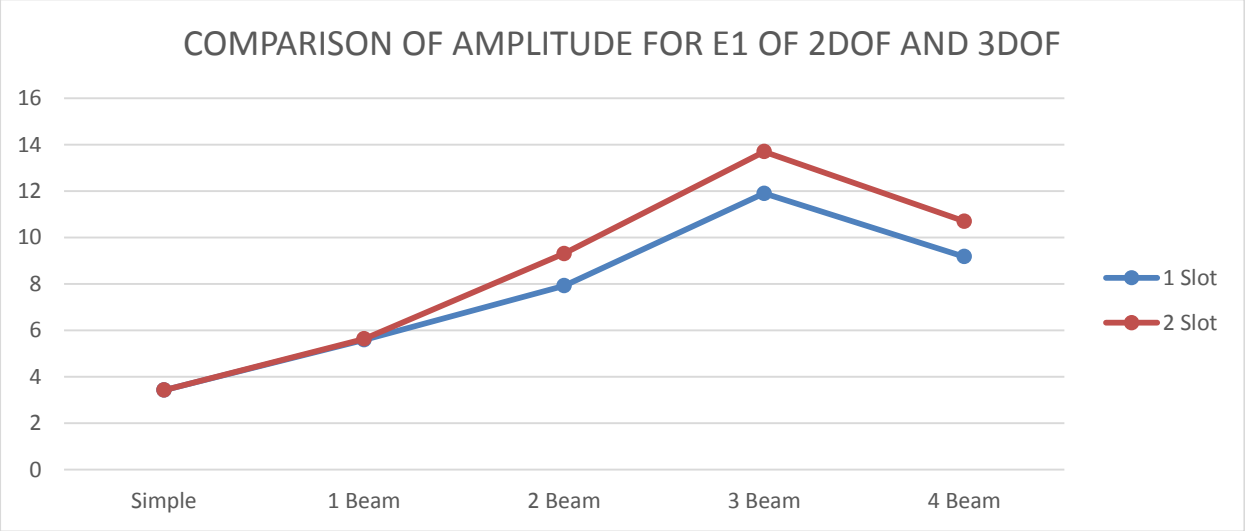

Figure 8

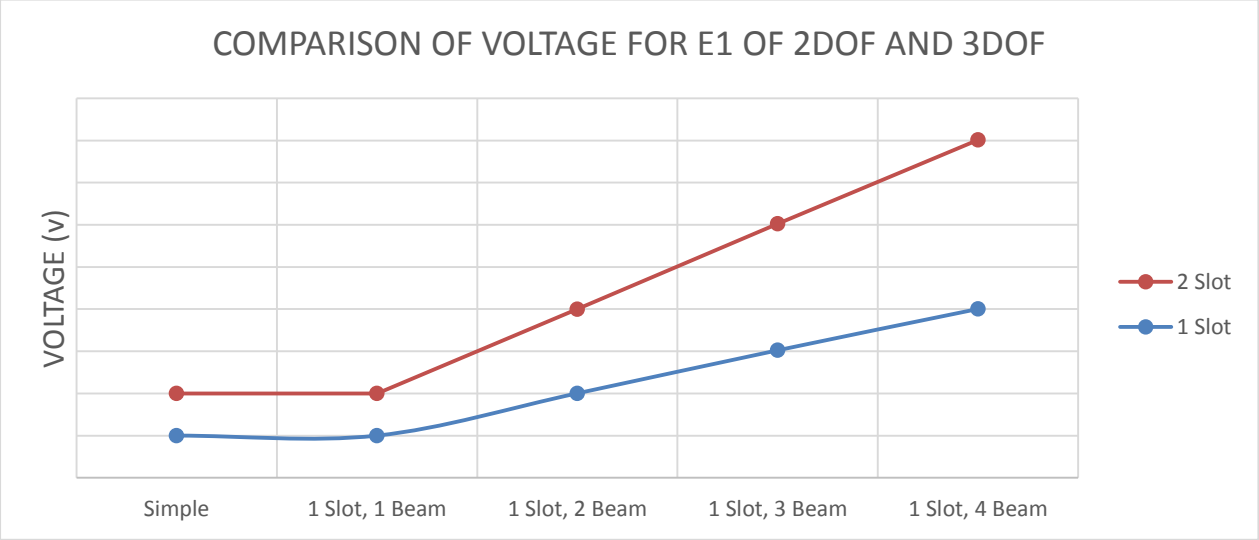

Figure 9

8th International Engineering Symposium - IES 2019
March 13-15, 2019, Kumamoto University, Japan

Tribological characteristics of Spray formed Al-Si quaternary alloys

Harish K [1,2], Shikhar V Jain[3], K. Raju [4]

1 *Department of Mechanical Engineering, AIET, Moodbidri – 574 225, India email:harishaiet@yahoo.com,*
2 *Department of Mechanical Engineering, SJEC, Mangauru – 575 028, India email:harishaiet@yahoo.com*
3 *Department of Mechanical Engineering, AIET, Moodbidri – 574 225, India email:shikharvjainn@gmail.com*
4 *Department of Mechanical Engineering, SJEC, Mangauru – 575 028, India email:rajuksjec@rediffmail.com*

ABSTRACT: In the present study, the preforms of hypo-eutectic, eutectic and hyper eutectic Al-Si quaternary alloys were prepared by spray forming. The wear tests were conducted using pin on disc Tribometer, under varying load conditions. The results indicated that, silicon content has a considerable influence on dry wear properties of spray deposited Al-Si alloys. The wear rate increased as the load increased for all the alloys. However the wear rate of hyper eutectic alloy has been the lowest compared to that of eutectic and hypoeutectic alloys. The better wear resistance of hypereutectic spray formed alloy has been explained in the light of the morphology of its worn out surfaces.

Keywords*: Al-Si alloys, Spray Forming, Wear, Porosity, Coefficient of friction.*

Introduction

The significance and practice of any material process route depend on the prevalence of ensuing microstructure, which in turn decides the material behaviour. In other words microstructure of the material encompasses a strategic partnership between material processing and its final mechanical properties. The morphology of the cast materials is affected by various parameters like cooling rate, alloy constituent phases, porosity, etc. The large size of aluminium-silicon alloy's tribological applications promises, its, much extensive commercial usage. The tribological properties of Al-Si alloys have been decided by the size and distribution of silicon particles, and other additional alloying elements such as magnesium, copper, iron and zinc. Al-Si alloys are widely used in automobile industries due to their low thermal expansion coefficient, density and excellent wear resistance as reported by Zhu et al. (2014). From the work by Shabestari et al. (2011) it is evident that copper addition significantly improves the strength of Al alloys, whereas addition of iron, a transition element enhances the elevated temperature properties by forming thermally stable intermetallic compounds. The coarse plates like iron-based compounds, formed during conventional casting are deleterious to the material strength. These detrimental effects of Fe bearing compounds are effectively minimised by rapid solidification of molten alloy, as investigated by Srivastava et al (2006). Jia et al. (2016) have been favourably recognised that spray forming process, having unique, coupled effects of rapid cooling, refined uniform microstructures and reduced segregation of coarse phases can solve the ill effects of macro segregation.

The wear behaviour of Al-Si alloy containing copper and iron has caught the attention of researchers in recent years. Through spray forming and by optimising of copper and iron content the mechanical properties of the Al-Si were enhanced, and also the adverse effect of Fe-rich

intermetallics on the wear behaviour could be efficiently minimised by rapid cooling as reported by Abouei et al. (2010), Goudar et al. (2013), Wang et al. 2011). In conventional castings, the iron-bearing phases could be seen within the type of Chinese script, needle or petal-like particles. The dimensions and morphology of those particles depend upon the alloy's composition and conditions, this usually becomes finer at faster cooling rates. Combining additional alloying elements such as ferrous and copper to Al-Si alloy systems also showed improvement in mechanical as well as wear properties as reported by Wang et al. (1995), Srivastava et al. (2002), Hou et al. (2010), Wang et al. (2010).

The precipitation of copper-rich phases benefit the mechanical properties by hindering the negative effects of iron-rich phases and effectively inhibit the crack propagation and provide the strengthening effects on the α-Al matrix as reported by Wang et al. (2011). All the investigations on spray forming have confirmed that the spray forming offers faster solidification rate (102–104^0C/s) and produce a fine microstructure with uniformly distributed primary silicon particles (3-10μm). The present study is intended to provide the effect of the Silicon content on dry wear properties of spray deposited hypo-eutectic, eutectic, hyper-eutectic Al-Si quaternary alloys. The correlation between the silicon content and wear behaviour is investigated.

Experimental details

Spray forming

The spray forming process employed in this investigation involved atomization of molten alloy using an annular nozzle. Nitrogen gas at high pressure passed around the straight ceramic melt delivery tube was used as atomization gas.

Three Al-Si alloys containing 7.5, 12.5 and 19.5 wt.% silicon were selected as the experimental materials. In the present work Hypoeutectic (Al-7.5Si-7Fe-2Cu), Eutectic (Al-12.5Si-5Fe-2Cu) and Hypereutectic (Al-19.5Si-5Fe-2Cu) Al-Si alloys were selected for investigation. These alloys were procured from FENFE metallurgical, Bengaluru. The composition selected is given in Table 1.

During each run, about 2.6 kg of Al–Si alloy was heated to a temperature of 960°C in a crucible. The superheated melt was atomized into fine droplets using nitrogen gas at a pressure of 0.45MPa. The droplets were subsequently deposited on a copper substrate at a distance of 350 mm from the Nozzle. The preform was taken out of the substrate after deposition. The deposition was carried out for all the three alloys. The process variables used in the preparation of preforms are given in Table 2.

Porosity measurement

The actual densities of the as-cast and spray formed Al–Si samples were measured by Archimedes principle and thus the volume fraction of porosity was calculated. Initially, the weights of the several polished specimens from various locations within the spray deposited preforms are individually measured in air. Next, the weighing of the same specimens was done when immersed in distilled water. By deriving the actual density from recorded weights and then comparing with theoretical density the volume fraction of porosity was calculated, referring the work of Taylor et al. (1999), Zhang et al. (1993).

Wear testing

Several samples were cut for wear testing from the centre part of the as-spray formed preforms and as-cast alloys. The specimens were machined in a cylindrical configuration with a 30 mm length and 8 mm diameter. All the tests were carried out at room temperature and at dry conditions.

Using a pin-on-disc wear testing machine (Model: TR-20, DUCOM) the wear properties of spray formed alloys were investigated with standard test procedure as per ASTM: G99-05. The surface of the hardened steel disc with a hardness value of 65HRC was cleaned with acetone before each experimental run. The wear property was evaluated at different applied load ranging from 10-40N at a constant sliding velocity of 1.57 m/s. The morphology of worn out surfaces were acquired using

DM750 Optical Microscope (Leica Microsystems Ltd.).

Results and discussion

Volume percent of porosity

The calculated porosity for conventionally cast and spray formed Al-Si quaternary alloys are shown in Figure 1. Approximately 2% porosity was observed in as-cast alloys, whereas 15 to 18% porous structure was observed in spray formed alloys. As reported by Grant (2007), porosity is an undesirable characteristic of spray formed alloys. Suwanpinij et al. (2003), Ye H (2003) and Taylor et al. (2012) reported that, during casting addition of copper and iron found to reduce the liquidus and final solidification temperatures and also the crystallization of Al_2Cu and Al_5FeSi increases with these content respectively. Thus the coarse Fe-rich intermetallic compounds which are formed support pore nucleation and growth, which operate as a stress concentrator or crack initiators and deteriorate mechanical properties. Also, the small quantity of gas that might have dissolved during the melting will be rejected into the matrix upon solidification leading to the formation of pores as reported by Puncreobutr et al. (2014). Srivastava et al. (1998) and Zhang et al. (1993) have reported that, the higher porosity level in the spray deposits can be attributed to, atomising setup, cooling rate and solidification conditions. The processing parameters like gas melt ratio (GMR), flight distance and thermodynamic properties of the materials to be processed also contribute towards the formation of pores within the preforms.

Wear characteristics

The pin on disc wear tests for a range of applied load, at a sliding velocity of 1.57 m/s and a sliding distance of 3400 m were conducted to evaluate the effect of applied load on the wear rate of as-cast and as-spray formed alloys.

The observation of the wear characteristics of hypoeutectic quaternary (Al-7.5Si-7Fe-2Cu) alloys (Figure 2) indicate spray formed alloy offers better wear resistance than the as-cast alloy. This is due to the fact that as-cast alloy becomes more brittle due to the presence of needle or plate-like silicon which acts as stress raisers and further leads to a higher wear rate. The spray forming on the other hand deposit an equiaxed microstructure with α-Al dendrites and fine Si particles that enhance the wear characteristics of the alloys. The wear mechanisms, especially of the spray formed alloy, are different and are attributable to not only the dispersed particles but also the morphology and size. The wear rate of spray deposited as well as as-cast alloys increases with increase in applied pressure makes it clear that due to more intimate contact at higher normal pressure provide more frictional force to shear off the micro welds and leads to increased wear rate. It is depicted that the wear rate of both spray formed and as-cast Al-7.5Si-7Fe-2Cu alloys increases almost linearly with increasing applied load indicating a steady state wear regime condition.

The effect of applied load on the wear rate of as-cast and spray formed eutectic (Al-12.5Si-5Fe-2Cu) and hypereutectic (Al-19.5Si-5Fe-2Cu) alloys is shown in Figure 3 and Figure 4 respectively.

Similar to hypoeutectic alloys the results of the pin on disc wear test analysis for as-cast and spray formed eutectic alloys showed almost a linear increase in wear volume loss of the specimen with applied load. The wear resistance of spray formed alloy is consistently superior as compared to the as-cast alloy. The spray formed alloy shows a constant increase in wear rate during the entire range of applied load. Whereas, the wear rate in as-cast alloy shows a linear trend up to 30 N and attains a swift increase at 40 N. An appreciable improvement in the wear performance of the spray formed Al-Si quaternary alloys have been observed over their as-cast counterparts while the high-silicon content alloys exhibited much better wear performance in the entire range of applied load.

The wear rates of Al-19.5Si-5Fe-2Cu alloy are consistently lower than that for the Al-7.5Si-7Fe-2Cu and Al-12.5Si-5Fe-2Cu alloys. However, the spray formed as well as as-cast hypereutectic alloys initially demonstrate a slow increase in wear rate with increase in applied load and further at

higher loads it increases rapidly. It is evident that a high volume fraction of primary Si phases contributes to good wear resistance. The other important aspect which predominantly affects the wear property of the Al-Si alloys is the homogeneous distribution of primary Si phases in the matrix. The Si particle size, shape and inter-particle spacing, as well as the alloy hardness, are the controlling factors of Al-Si wear rates. Higher silicon content also capable of modifying the wear mechanism of the preform from abrasive to oxidative wear as reported by Chen Z et al. (2007), Raghu Kiran et al. (2015). In addition to silicon content and refined microstructure, the addition of alloying elements such as copper and iron also play a critical role in the enhancement of wear resistance. Goudar et al. (2013) investigated that addition of iron and copper to Al-Si alloy has improved the wear property of the quaternary alloy when evaluated against that of Al-Si binary alloy. The presence of hard β-Al_4FeSi_2 and Θ-Al_2Cu phases in the quaternary alloys provides additional strengthening effect to Al matrix and reduces the removal of Silicon particles off the matrix.

At low loads, the excellent wear resistance of all the spray-deposited quaternary Al-Si alloys over as-cast alloys can be attributed to the primary Si phases that act as load-bearing elements without damaging structural integrity. During this, the shearing force is much below the bonding strength of Si particles and does not cause large volume loss due to the fracture of load bearing particles. At higher applied load the Si particles cannot keep their ability to support the load due to the higher normal force causing surface cracking and high volume loss.

Figure 5 depicts the variation of coefficient of friction with applied load. For all the alloys a high value of coefficient of friction is recorded in the low load regime, followed by a reducing trend for the increase in applied load. The rate of reduction in coefficient of friction is found to be more or less constant for all the alloys. The spray formed hypereutectic alloy has the minimum and that of as-cast hypoeutectic alloy has the maximum coefficient of friction. The higher coefficient of friction at lower loads may be due to roughness locking which occur due to non formation of true contact surface. From the graph it is apparent that the average coefficient of friction is highest for quaternary alloy with low Si content. Thus, it can be concluded that a composition of Si offers reduction in coefficient of friction which in turn leads to minimum wear.

3.3 Morphology of worn-out Surfaces

The topographical features of the worn out surfaces, shown in Figure 6 and Figure 7 exemplify the wear grade of all as-cast and spray formed Al–Si quaternary alloys at an applied load of 40 N. In Figure 6 (a) to (c) the worn-out surfaces of as-cast hypoeutectic, eutectic and hypereutectic alloys have been characterized by several deep, visible grooves and pits on the wear tracks, indicative of a high wear rate. Whereas, in Figure 7 (a) to (c) the worn-out surface of spray formed alloy consists of scoring marks. This ensures uniform distribution and fine interfacial attachment of the reinforcing Si and β phases within the matrix, attained through the spray forming route.

Conclusions

The following conclusions may be drawn from the present study.

- A high porosity level has been observed in spray formed alloys irrespective of Si content.
- The wear characteristics of Al-Si quaternary alloys reveal that wear rate of all the alloys increase with applied load. Wear rates of spray-formed alloys have been compared with that of as-cast alloys and found that spray forming provides wear properties than that of the as-cast alloys.
- The effect of Si content on the dry sliding wear behaviour of spray-deposited Al-Si alloys in a range of applied load has been studied. At low load (up to 30N), the wear rate of all spray-formed as well as as-cast Al-Si alloys declined with increasing Si content.
- The worn-out surfaces of spray formed alloys were found to be less damaged than that of as-cast alloys indicating a low wear rate.

References

[1] Abouei, V., Saghafian, H., Shabestari, S. G., & Zarghami, M. (2010). Effect of Fe-rich intermetallics on the wear behavior of eutectic Al–Si piston alloy (LM13). Materials & Design, 31(7),3518–3524.doi:10.1016/j.matdes.2010.02.015

[2] Chen Z., Teng J., Chen G., Fu D., & Yan H. (2007). Effect of the silicon content and thermomechanical treatment on the dry sliding wear behavior of spray-deposited Al–Si/SiCp composites. Wear,262(3-4),362–368.doi:10.1016/j.wear.2006.05.019

[3] Goudar D. M., Raju K., Srivastava V. C., & Rudrakshi G. B. (2013). Effect of copper and iron on the wear properties of spray formed Al–28Si alloy. Materials & Design,51,383–390. doi:10.1016/j.matdes.2013.04.018

[4] Grant P.S. 2007. Solidification in Spray Forming. The Minerals, Metals & Materials Society and ASM International 2007. DOI: 10.1007/s11661-006-9015-3.

[5] Hou, L. G., Cui, C., & Zhang, J. S. (2010). Optimizing microstructures of hypereutectic Al–Si alloys with high Fe content via spray forming technique. Materials Science and Engineering: A, 527(23),6400–6412. doi:10.1016/j.msea.2010.06.066

[6] Jia Y., Cao F., Ma P., Liu J., Sun J., & Wang G. (2016). Microstructure Evolution and Mechanical Properties of Spray-deposited Al-21. 47Si-4. 73Fe-2. 5Cu-0. 9Mg Alloy. Journal of Iron and Steel Research, International, 23(1), 14–18. doi:10.1016/s1006-706x(16)30004-8

[7] Puncreobutr, C., Lee, P. D., Kareh, K. M., Connolley, T., Fife, J. L., & Phillion, A. B. (2014). Influence of Fe-rich intermetallics on solidification defects in Al–Si–Cu alloys. Acta Materialia,68,42–51. doi:10.1016/j.actamat.2014.01.007

[8] Raghukiran, N., & Kumar, R. (2015). Effect of scandium addition on the microstructure, mechanical and wear properties of the spray formed hypereutectic aluminum–silicon alloys. Materials Science and Engineering: A, 641, 138–147. doi:10.1016/j.msea.2015.06.027

[9] Shabestari S. G., & Parshizfard E. (2011). Effect of semi-solid forming on the microstructure and mechanical properties of the iron containing Al–Si alloys. Journal of Alloys and Compounds, 509(30), 7973–7978. doi:10.1016/j.jallcom.2011.05.052

[10] Srivastava A. K., Ojha S. N., & Ranganathan S. (1998). Microstructural features and heat flow analysis of atomized and spray-formed Al-Fe-V-Si alloy. Metallurgical and Materials Transactions A, 29(8), 2205–2219.doi:10.1007/s11661-998-0045-x

[11] Srivastava A. K., Srivastava V. C., Gloter A., & Ojha, S. N. (2006). Microstructural features induced by spray processing and hot extrusion of an Al–18% Si–5% Fe–1.5% Cu alloy. Acta Materialia, 54(7),1741–1748. doi:10.1016/j.actamat.2005.11.039

[12] Srivastava V. ., Ghosal P., & Ojha S. . (2002). Microstructure and phase formation in spray-deposited Al–18%Si–5%Fe–1.5%Cu alloy. Materials Letters,56(5),797–801. doi:10.1016/s0167-577x(02)00616-x

[13] Suwanpinij P., Kitkamthorn U., Diewwanit I., & Umeda T. (2003). Influence of Copper and Iron on Solidification Characteristics of 356 and 380-Type Aluminum Alloys. Materials Transactions,44(5),845–852. doi:10.2320/matertrans.44.845

[14] Taylor R. P., McClain S. T., & Berry J. T. (1999). Uncertainty analysis of metal-casting porosity measurements using Archimedes' principle. International Journal of Cast Metals Research,11(4),247–257. doi:10.1080/13640461.1999.11819281

[15] Taylor, J. A. (2012). Iron-Containing Intermetallic Phases in Al-Si Based Casting Alloys. Procedia Materials Science, 1, 19–33. doi:10.1016/j.mspro.2012.06.004

[16] Wang E. R., Hui X. D., & Chen G. L. (2011). Eutectic Al–Si–Cu–Fe–Mn alloys with enhanced mechanical properties at room and elevated temperature. Materials & Design, 32(8-9),4333–4340. doi:10.1016/j.matdes.2011.04.005

[17] Wang L., Makhlouf M., & Apelian D. (1995). Aluminium die casting alloys: alloy composition, microstructure, and properties-performance relationships. International Materials Reviews, 40(6), 221–238. doi:10.1179/imr.1995.40.6.221

[18] Wang, E. R., Hui, X. D., & Chen, G. L. (2011). Eutectic Al–Si–Cu–Fe–Mn alloys with enhanced mechanical properties at room and elevated temperature. Materials & Design, 32(8-9),4333–4340. doi:10.1016/j.matdes.2011.04.005

[19] Wang, E. R., Hui, X. D., Wang, S. S., Zhao, Y. F., & Chen, G. L. (2010). Improved mechanical properties in cast Al–Si alloys by combined alloying of Fe and Cu. Materials Science and Engineering: A, 527(29-30),7878–7884. doi:10.1016/j.msea.2010.08.058

[20] Ye H. (2003). An Overview of the Development of Al-Si-Alloy Based Material for Engine Applications. Journal of Materials Engineering and Performance,12(3),288–297. doi:10.1361/10599490377034313 2

[21] Zhang J., Gungor M. N., & Lavernia E. J. (1993). The effect of porosity on the microstructural damping response of 6061 aluminium alloy. Journal of Materials Science ,28 (6) , 1515 – 1524. doi:10.1007/bf00363342

[22] Zhu X., Wang R., Peng J., & Peng C. (2014). Microstructure evolution of spray-formed hypereutectic Al-Si alloys in semisolid reheating process. Transactions of Nonferrous Metals Society of China,24(6),1766–1772. doi:10.1016/s1003-6326(14)63251-9

Table 1: Chemical composition of Al-Si quaternary alloys (wt %)

Sl.No.	Si	Fe	Cu	Mn	Zn	Ti	Al
1.	7.56	7.83	2.91	0.178	0.0860	0.018	Bal
2.	12.67	4.73	2.66	0.125	0.090	0.022	Bal
3.	19.35	5.72	2.50	0.143	0.077	0.026	Bal

Table 2: Process variable used in spray forming

Quantity	2.6 Kg
Temperature	960 °C
Holding time	50 mins
Stand-off distance	350mm
Nozzle size	04mm
Gas pressure	0.45MPa
Mass flow rate	0.024kg/sec

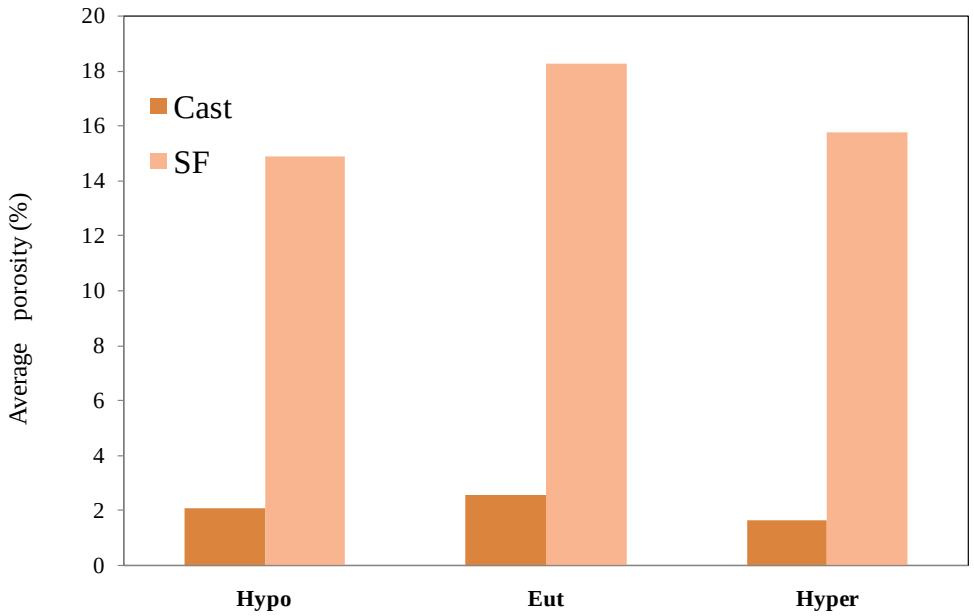

Figure 1: Comparison of porosity of as-cast and spray formed Al-Si quaternary alloys

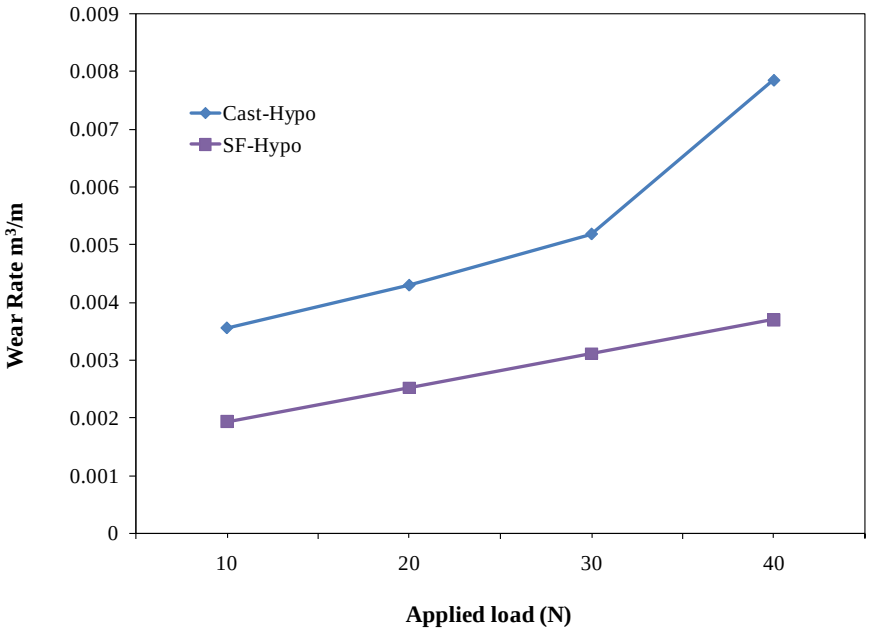

Figure 2: Wear rate Vs Applied load for of Hypoeutectic as-cast and as-spray formed Al-Si quaternary alloys

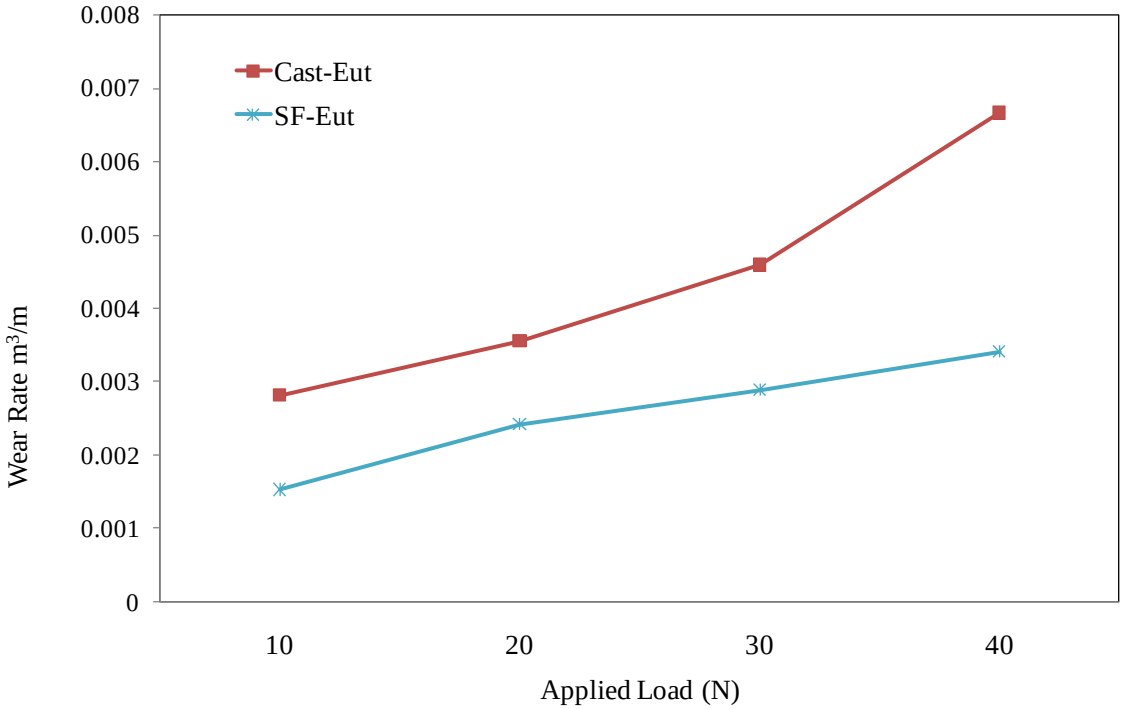

Figure 3: Wear rate Vs Applied load for Eutectic Ascast and Spray formed Al-Si quaternary alloys

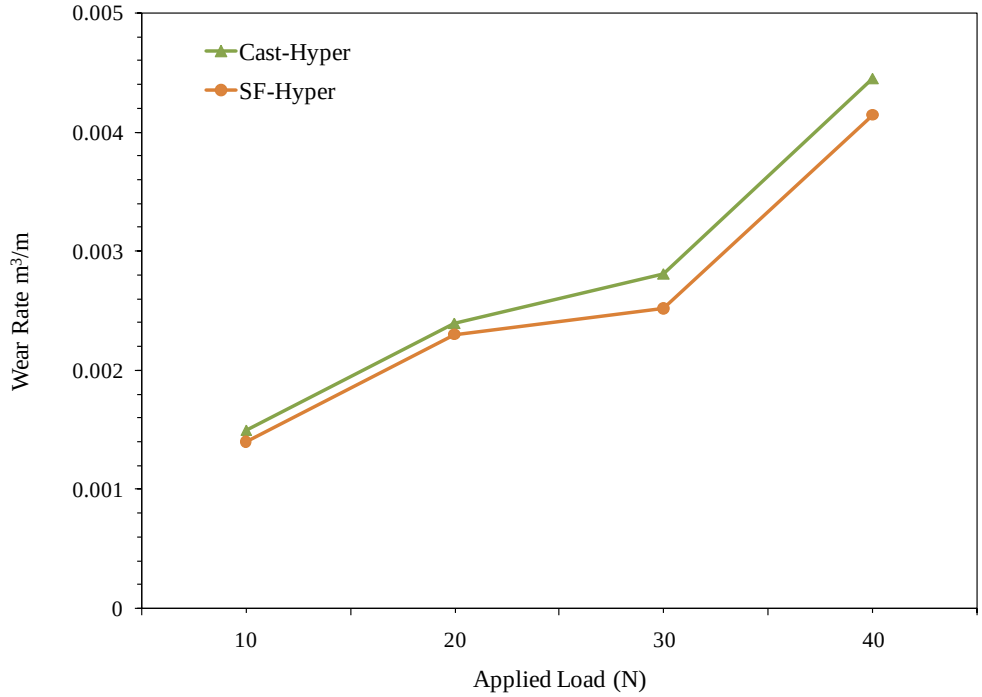

Figure 4: Wear rate Vs Applied load for Hyperetectic As-cast and Spray formed Al-Si quaternary alloys

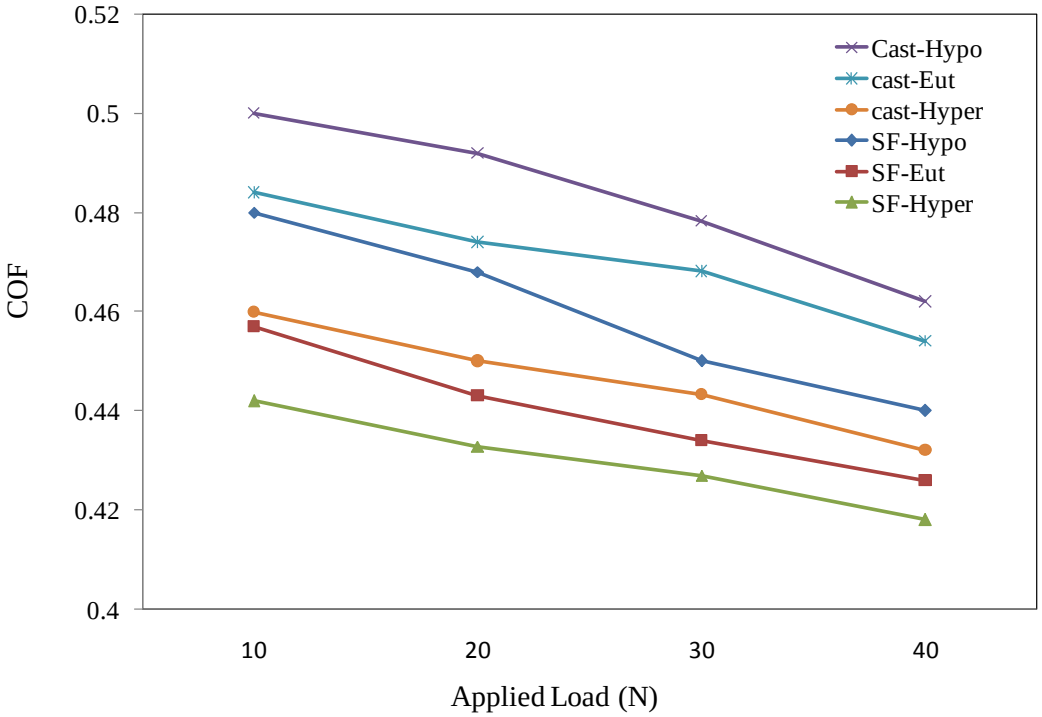

Figure 5: Variation of Coefficient of friction of spray deposited and as-cast Al-Si quaternary alloys w.r.t. load

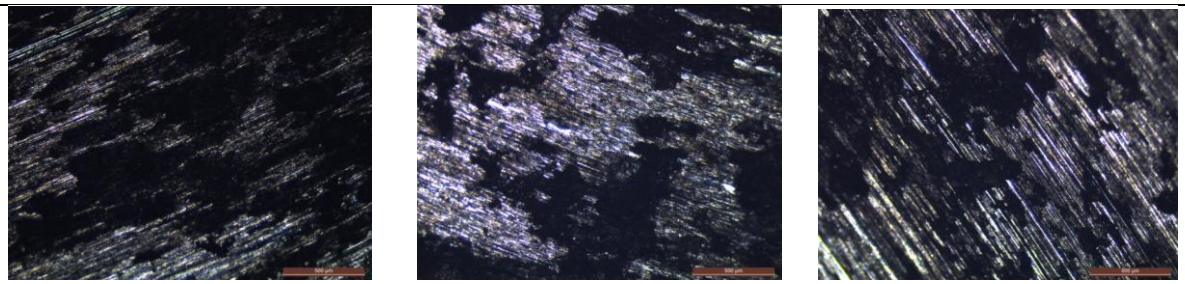

(a) (b) (c)

Figure 6: Worn out surfaces of as-cast Al-Si quaternary (a) Hypoeutectic alloy (b) Eutectic alloy (c) Hypereutectic alloy

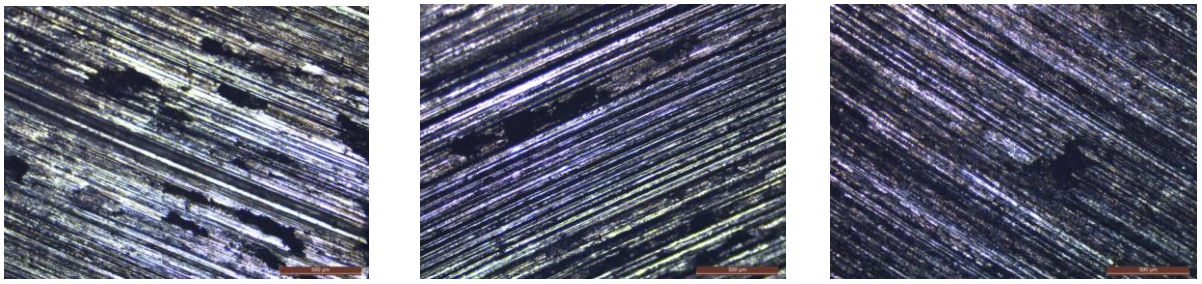

(a) (b) (c)

Figure 7: Worn out surfaces of spray formed Al-Si quaternary (a) Hypoeutectic alloy (b) Eutectic alloy (c) Hypereutectic alloy

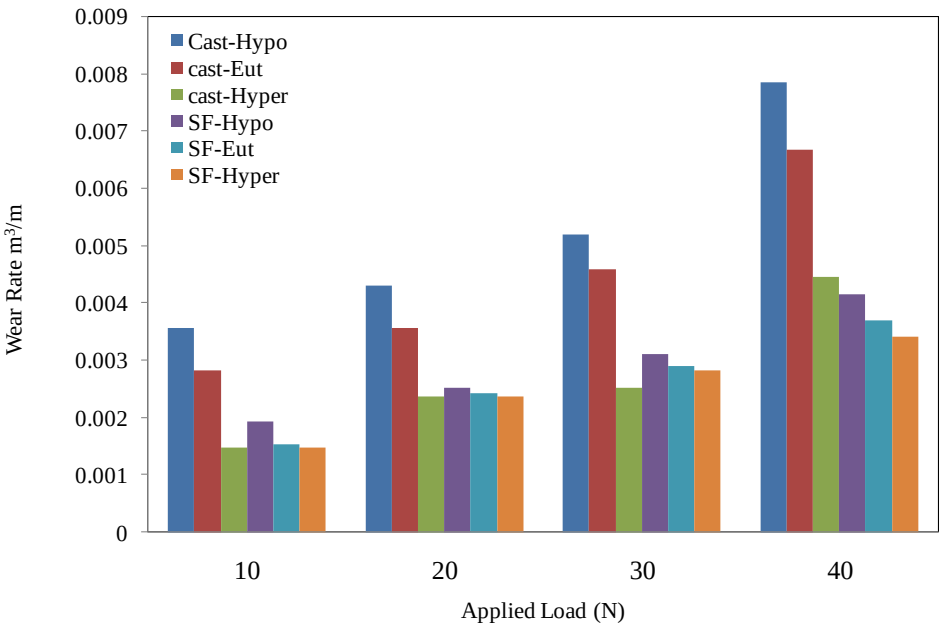

Figure 8: wear rate comparison of As-cast and spray formed Al-Si quaternary alloys

8th International Engineering Symposium - IES 2019
March 13-15, 2019, Kumamoto University, Japan

Toughness Index Evaluation of T300/914 Composite

S Sachin [1], Shivananda Nayaka H[2], Santhosh B[3] *and Prasad Krishna*[4]

1 Dept. of Mechanical Engg., NITK, Surathkal, Karnataka, India [me16f15.sachin@nitk.edu.in]
2 Dept. of Mechanical Engg., NITK, Surathkal, Karnataka, India [hsn_mech@nitk.ac.in,]
3 Vikram Sarabhai Space Center, Thiruvananthapuram
4 Dept. of Mechanical Engg., NITK, Surathkal, Karnataka, India [krishnprasad@nitk.edu.in]

ABSTRACT: Interlaminar fracture toughness tests are carried out on carbon epoxy composite T300/914. The composite has a wide variety of application as a structural material. The considered laminates for tests are fabricated of 48 layers of T300/914 which are stacked in unidirectional sequence to form a laminate of thickness 4.6 mm. ASTM standards are followed to conduct Double Cantilever Beam test to determine the Mode I type of delamination. Mode II interlaminar fracture toughness was found by End Notch Flexure test. Pulse Echo test and C-Scan image of the specimens were taken to detect the defects. The results of mode I and mode II fracture toughness values, after incorporating measures to prevent bonding of release film with laminate during sample preparations, are found to be consistent at 138 J/m^2 and 542 J/m^2 respectively.

***Keywords**: Interlaminar fracture toughness; laminates*

INTRODUCTION

T300/914 is a laminate composite with high modulus of elasticity. They are used in aerospace industry for structural application. Delamination is one of the major causes for failure of laminate composites. A composite laminate with delamination fails in three main modes, Mode I, Mode II and Mode III. Current study deals with investigating delamination failure in T300/914 composites, in Mode I and Mode II by ASTM standards D5528(ASTM, 2014a) and D7905(ASTM, 2014b) respectively.

Tawk et. al conducted end-loaded-split (ELS) to determine Mode I and End-notched Flexure (ENF) tests to determine Mode II interlaminar Fracture toughness on 46 layer T300/914C specimen. These test results were used to validate their proposed simulation model (Tawk *et al.*, 2010). Mohamed Rehan et. al used Multidirectional carbon/epoxy laminates and studied the effect of fiber orientation in each of the ply used in laminate. From the experimental study it was found that the angle of orientation of neighbouring ply had a significant effect on the propagation of crack.,(Bin Mohamed Rehan *et al.*, 2017) . J. Andersons (Andersons and König, 2004) reviewed the literatures on experimental data available for crack growth tests conducted on multidirectional ply oriented laminate. From the study it was derived that the fracture toughness of laminate with multidirectional ply orientation was higher than the laminates that had all the fibers oriented in same direction (i.e unidirectional laminate).

So from the literature it was evident that the laminate with fibers in same direction had lower fracture toughness and showed crack growth at lower loading conditions. Hence a unidirectional laminate was used in this study to determine the fracture toughness of T300/914 laminate.

One of the three methods used for finding the Mode I interlaminar fracture toughness is Modified Beam theory (MBT). It is one of the most widely accepted method to determine the Mode I fracture toughness. MBT method for determining Interlaminar Fracture toughness in Mode I is given by

$$G_I = \frac{3\mathrm{F}x}{2\mathrm{w}(a+\Delta)} \qquad (1)$$

Where, **F** is the applied load

x is displacement of crosshead

Δ is the intercept on abscissa trendline curve fitted to $\mathbf{C^{1/3}}$ versus **a** data.

w is width of specimen,

a length of crack.

C is the compliance

$$\mathbf{C=x/P} \qquad (2)$$

Δ is the intercept on abscissa by extending the straight-line curve fitted to $\mathbf{C^{1/3}}$ versus **a** data.

METHODOLOGY

Interlaminar fracture toughness of aerospace structural composite were investigated in Mode I and Mode II tests. All the tests were conducted as per ASTM standards D5528-01 and D7905/D7905M – 14 respectively.

Laminate fabrication

T300/914 prepreg were used to fabricate the Laminates for the tests. Laminates consist of 48 layers of prepreg. Hand layup process was adopted to construct the required laminate. A high temperature release film was placed at the middle ply of the laminate during fabrication to produce the required delamination region. The release film was placed in a release agent for 24Hrs before placing the film in the laminate. The laminate formed by layup process was bagged and a pressure of negative 0.4 bar was applied in the bag. This setup was then cured for two hours in an autoclave machine at 170 degree Celsius. The cured laminates (as shown in Fig 1 & Fig 2) were then machined to 10 specimens each for Mode I and Mode II tests. For Mode I the dimension of the specimens were 25mm by 165mm (designated as A1 to A10). the specimens used for Mode II tests were of size 190mm by 25mm (designated as B1 to B10.

Piano hinges were attached on the specimens for Mode I test. On both sides of the specimens were covered with white paint. This assists in easy location of the crack front during testing.

For Mode II specimens, the white painted surfaces were then marked with vertical lines for first 5mm at an interval of 1mm and 20mm length with 5mm intervals. These marks were used to identify the progress of the crack during testing.

Loading of Mode I laminate was at a constant rate of 5mm/min. The loading was continued till a stable growth of the crack reached the last vertical marking. During the test the time, load being applied and displacement of the cross head were constantly recorded.

For Specimens of Mode II test, 3 vertical marking were made at distance of 20 mm from crack front and other two marks at an interval of 10mm each from the first line, towards the crack side [6]. Specimens were then placed on a three-point bending test apparatus for loading. The support rollers of the apparatus were placed at a distance of 100 mm as per ASTM standard [6]. Initially calibration loading is performed of the specimens. The specimens are first placed with 20mm calibration line above one of the support rollers. The specimens are then loaded to a predetermined calibration load at constant loading. Same process is then repeated at 40mm calibration line. These calibration loads are withdrawn at a constant displacement rate.

Now, the specimen is loaded to find the critical load of the specimen at the onset of crack growth. This is done by loading the specimen till the crack growth is seen in the specimen.

Above procedures are repeated with new calibration line from the new crack front to get Pre-Cracked readings

RESULTS AND DISCUSSION

DCB and ENF test results performed on T300/914 composite is described. These tests provide the estimate interlaminar fracture toughness of the material under Mode I and Mode II conditions.

MODE I

Fig 4 shows the load at the onset of crack growth. It was noted that load bearing capacity of specimen A5 and specimen A6 were more than other specimens from same laminate. From the C-Scan image (Fig 7) of Mode I laminate, its seen that these specimens were from the section that showed highest density. The high load carrying tendency of the specimen may be caused owing to fact that the better compaction promoted better bonding of laminates and hence the load required to grow the crack through the laminate increased. Hence resulting in an increased interlaminar fracture toughness.
Interlaminar fracture toughness of the fabricated specimens are shown in the Fig 5. By ASTM standard procedure, Mode I fracture toughness of the specimens were evaluated to be 0.138 kJ/m^2

MODE II

From Fig 6, its noted that in the Non Pre-Cracked test, the specimens Z3 and Z4 show higher readings compared to other specimens. Fig 8 (a) shows the position of specimen Z3 in the prepared laminate. It is seen that the region of highest compaction matches with the position of the specimens. Hence it can be concluded that the toughness value depends on the level of compaction of the specimens.

Fig 6 shows average line of Interlaminar Fracture toughness of Non Precracked Mode II specimen. Mode II Fracture toughness of the prepared specimens were estimated as 0.542 kJ/m^2.

CONCLUSIONS

Squeezing out of release agent at higher compaction region caused bonding of the lamina with release film. Hence release film failed to produce delamination if they were not placed in a mould release agent before placing the film in the composite during production process.

The experimental test estimates the interlaminar fracture toughness value of T300/914 composite in Mode I and Mode II to be 0.138 kJ/m^2 and 0.54 kJ/m^2 respectively

REFERENCES

Andersons, J. and König, M. (2004) 'Dependence of fracture toughness of composite laminates on interface ply orientations and delamination growth direction', *Composites Science and Technology*, 64(13–14), pp. 2139–2152. doi: 10.1016/j.compscitech.2004.03.007.

ASTM (2014a) 'D5528-01: Standard Test Method for Mode I Interlaminar Fracture Toughness of Unidirectional Fiber-Reinforced Polymer Matrix Composites 1', *American Standard of Testing Methods*, 03(Reapproved 2007), pp. 1–12. doi: 10.1520/D5528-13.2.

ASTM (2014b) 'Standard Test Method for Determination of the Mode II Interlaminar Fracture Toughness of Unidirectional Fiber-Reinforced Polymer Matrix Composites', *ASTM Book of Standards*, 15.03, pp. 1–18. doi: 10.1520/D7905.

Bin Mohamed Rehan, M. S. *et al.* (2017) 'Experimental study of the influence of ply orientation on DCB mode-I delamination behavior by using multidirectional fully isotropic carbon/epoxy laminates', *Composite Structures*. Elsevier Ltd, 161, pp. 1–7. doi: 10.1016/j.compstruct.2016.11.036.

Tawk, I. *et al.* (2010) 'A multilayered solid element used to model composite delamination', *Advanced Composites Letters*. Elsevier Ltd, 19(1), pp. 23–33. doi: 10.1016/j.compscitech.2009.10.008.

Fig 1 Mode I test laminate

Fig 2 Mode II test laminate

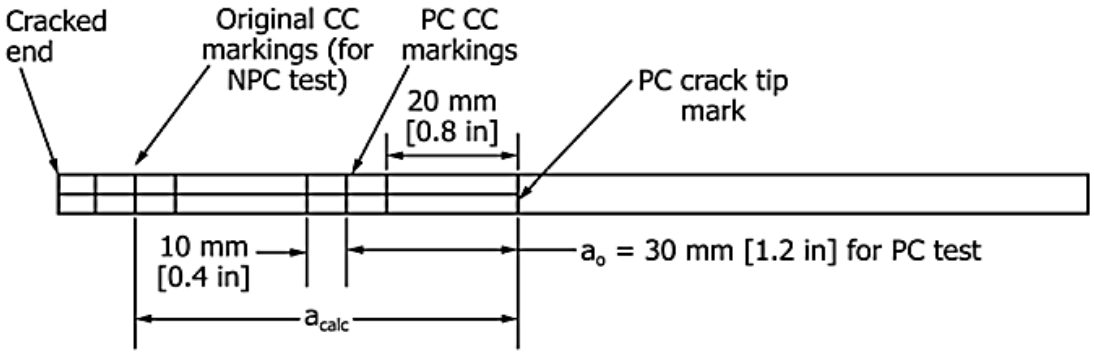

Fig 3 Mode II Position of vertical calibration lines for Mode II test (ASTM, 2014b)

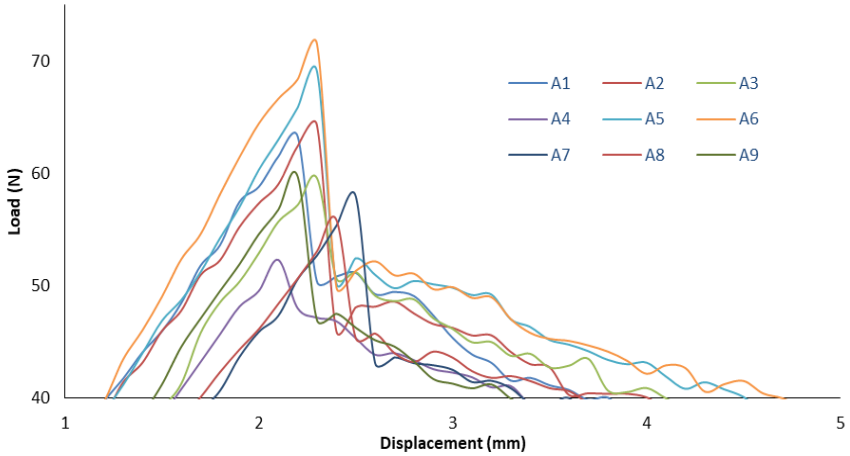

Fig 4 Region of critical Load in Load vs Displacement graph of Mode I specimens

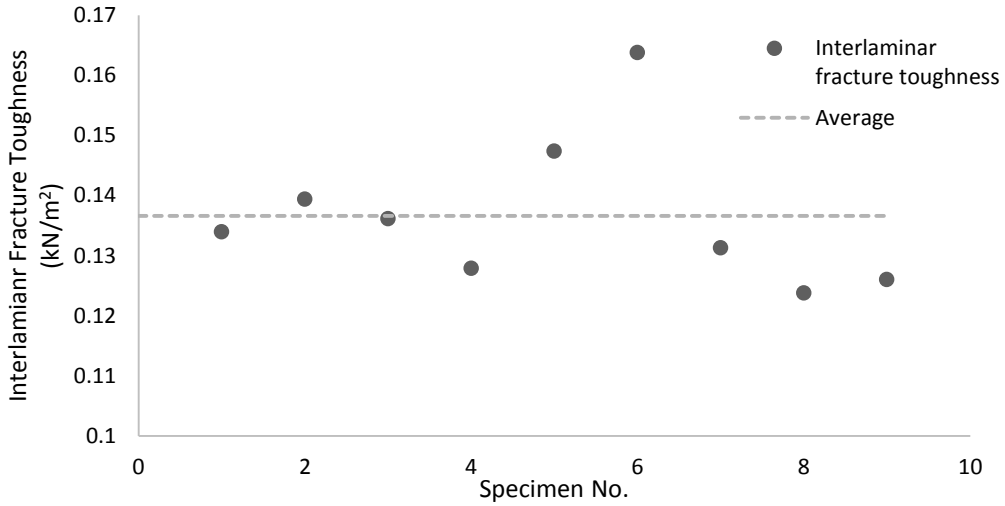

Fig 5 Interlaminar fracture toughness from Mode I

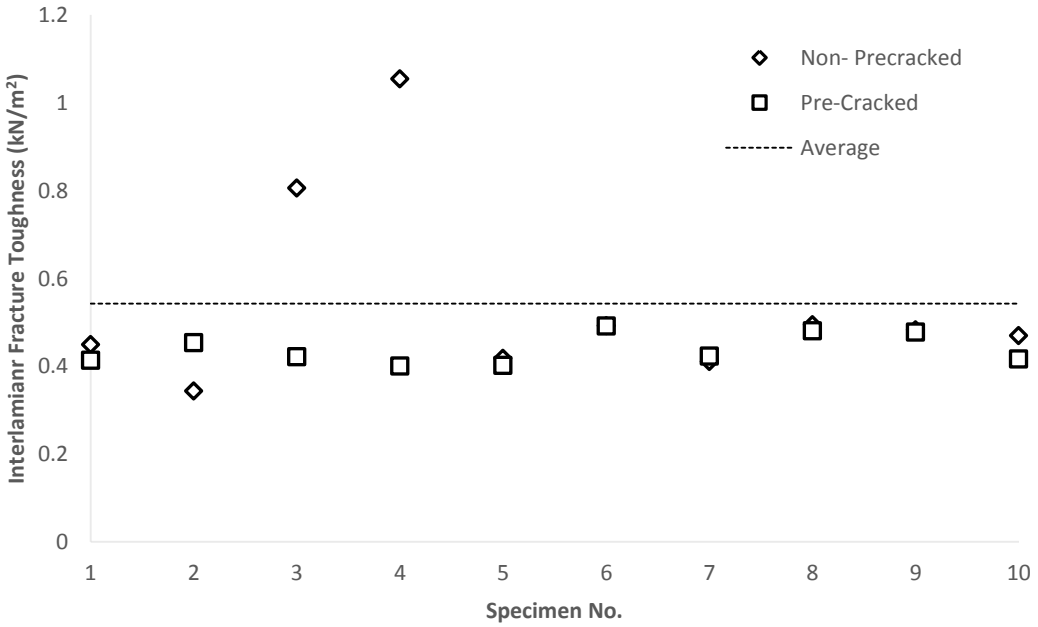

Fig 6 Interlaminar fracture toughness in Mode II for Precracked and Non Pre-cracked specimens.

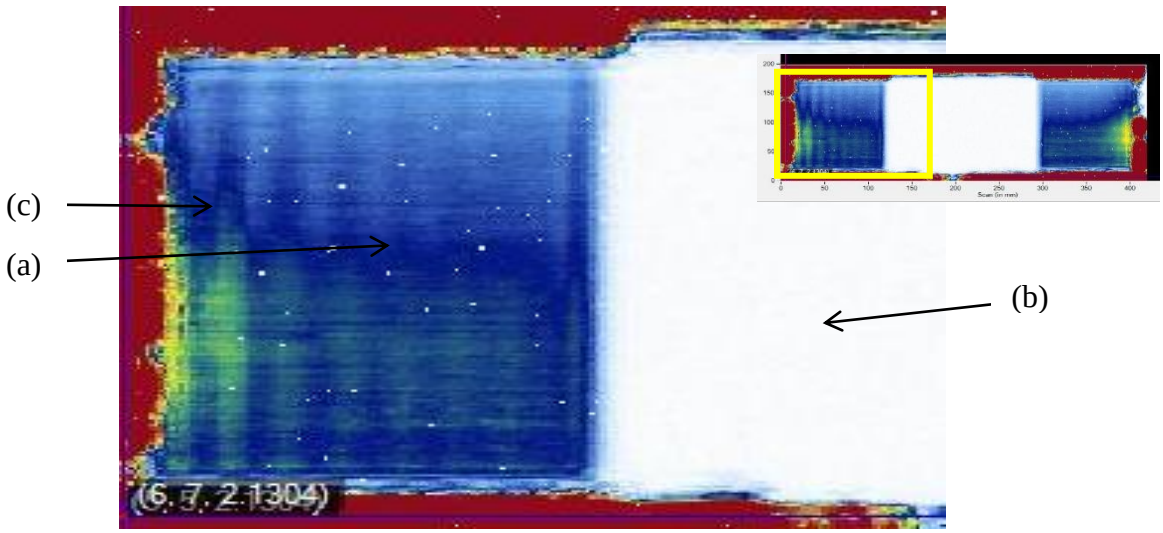

Fig 7 C Scan result of Mode I laminate before machining (a) position of specimen A5 (b) release film region (c) regions of maximum compaction (insert: C Scan image of Mode I laminate)

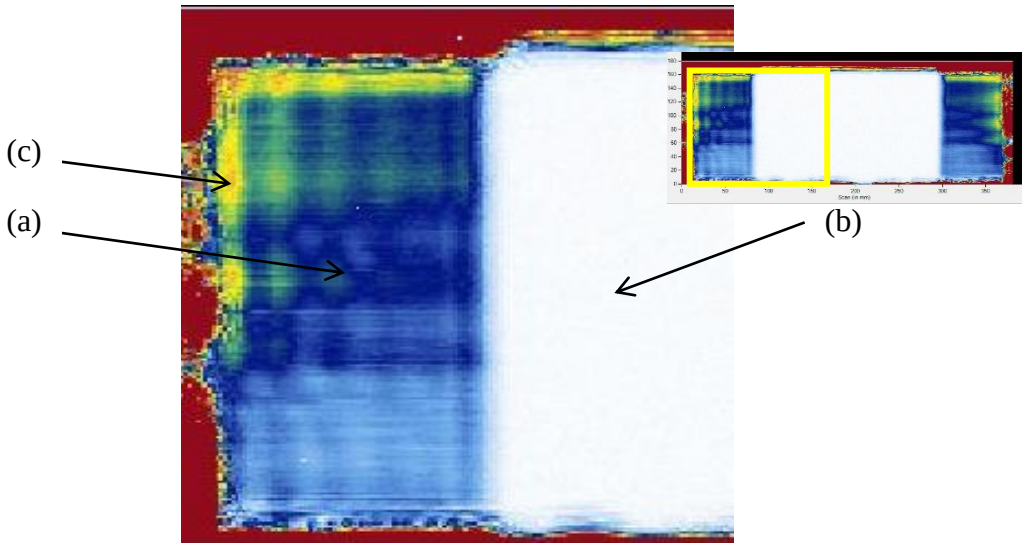

Fig 8 C Scan result of Mode II laminate before machining (a) position of specimen Z3 (b) release film region (c) region od least compaction (insert: C Scan image of Mode

8th International Engineering Symposium - IES 2019
March 13-15, 2019, Kumamoto University, Japan

MACHINING PERFORMANCE OF AlCrN AND AlTiN COATED CEMENTED CARBIDE INSERTS DURING THE DRY END MILLING OF MARAGING STEEL

Vinay Varghese [1], Akhil K.[1], M.R. Ramesh [1] and D. Chakradhar[2]
1.Department of Mechanical Engineering, National Institute of Technology Karnataka, Surathkal, Mangalore- 575025, India, email- vinujavs@gmail.com
2.Department of Mechanical Engineering, Indian Institute of Technology, Palakkad-678557, India, email- chakradhar.dupadu@gmail.com

ABSTRACT: The present study investigate the machining performance of AlCrN and AlTiN coated cemented carbide inserts during end milling of maraging steel MDN 250. The mechanical and metallurgical characterization is carried out to determine the properties of the PVD coatings developed. The end milling experiments under dry environment is carried out using coated inserts at different cutting speeds and compared with uncoated inserts (UC) to evaluate the machining performance in terms of tool wear, surface roughness and cutting forces. The results revealed that a development of PVD coating on the insert is effective in resisting tool wear even at high cutting speeds. The coated inserts showed high tool life, better surface finish and low cutting forces during machining at different cutting speeds. It is found that AlCrN coating had a better wear resistance and machining performance in comparison with AlTiN coating.

***Key words**: Coating technology, cemented carbide, characterization, ends milling, maraging steel, surface roughness, cutting forces.*

INTRODUCTION

Machining is the most widely used material removal process in manufacturing industry since the 18th century. Machining is a process in which the raw material is converted into a desired shape and size by removing the material at a controlled rate. High productivity with low manufacturing cost in addition to better surface finish & dimensional accuracy is the main goal for manufacturing industries. But these things are very difficult to achieve especially when machining difficult to cut materials which are more commonly used in aerospace and aeronautical applications. Excessive tool wear, high heat generation, high power consumption, larger cutting forces, poor surface quality and/or difficulties in chip formation are some of difficulties faced while machining difficult to cut materials. The high cutting temperature developed at cutting zone is the main problem encountered which leads to cutting tool wear and reduced tool life for difficult to cut materials.

Coating of the cutting tools are one of the outstanding strategies developed to avoid the above specified difficulties. The first commercial coating was a TiN physical vapour deposition(PVD) coating developed for a high speed steel drills in 1980's and then on carbide inserts used for milling applications. With the introduction of difficult to cut materials manufacturing industries find excessive application of coatings on the cutting tools in order to achieve the required goals. A large numbers of PVD coatings are developed for milling operations to obtain the higher performances. Al-based coatings find most promising applications in the end milling. B.D. Beake et.al (2015) studied about end milling of H 13 tool steel using PVD coated cutting tools. He found that AlCrN and AlTiN coated tools perform well

under extreme conditions because of their good oxidation resistance, hot hardness and wear resistance at elevated temperatures. J.L. Mo et.al (2013) reported that AlTiN and AlCrN coating shows much higher impact wear resistance and abrasion resistance at higher temperature than CrN coatings. Jiri Nohava et.al (2015) experimental investigation reveals out that AlTiN and AlCrN coating shows good wear resistance from room temperature to 600^0C. J.L. Mo et.al (2008) investigated the behavior of AlCrN coating against Si_3N_4 ball under two sliding conditions. He found out that AlCrN coating has excellent anti-abrasion resistance on both conditions. He concluded that formation of wear resistant and thermally stable oxides due to tribo-chemical reactions of chromium and aluminium are responsible for imparting abrasion resistance.

The current work is therefore undertaken to evaluate the performance of AlCrN and AlTiN coated cemented carbides during the end milling of maraging steel MDN 250 under dry environment. The surface roughness and cutting force are attributes taken to study machining performance of coated tools.

2 EXPERIMENTAL PROCEDURE

The cutting inserts used for coating process were H15 uncoated tungsten carbide- cobalt inserts from Seco.The composition of WC and Co in WC-Co alloy was found to be 90% and 10% respectively. The AlCrN and AlTiN coatings were developed on the WC-Co inserts using Cathodic arc deposition by Oerlikon Balzers, Bangalore. The SEM/EDS analysis of the coatings was done using ZEISS Gemini 500. The crystal structures in the uncoated and coated tools are determined by XRD analysis using Bruker Model: D8 Advance. The Hardness and Young's Modulus of the coatings are measured by using Microtrac Model: Blue Wave. A peak load of 50 mN was applied for nano-identation test to eliminate the effect on measured hardness due to the substrate, by corroborating that resulting pierced depth was within the 10% of coating thickness; around 20 indentations are performed on each sample for ensuring the accuracy of the results. Anton paar's Calo-tester was used to measure the thickness of coated cemented carbides.

A conventional three axis vertical milling machine NAMMILL X6325 is used for milling trials. The cutting conditions encapsulated are: feed rate - 58 mm/min, depth of cut – 0.3 mm, cutting speed- 17 m/min, 22 m/min, 34 m/min. The experimental setup used is presented in the Figure 1.Annealed maraging steel MDN 250 from MIDHANI Ltd. India, dimensions 55×80×30 mm is used to carry out machinability studies. A quartz three component dynamometer KISTLER 9257B was used for measuring cutting forces in three different directions. The average surface roughness (R_a) was measured using a Talysurf SJ 301 with a cut off length of 4 mm at 6 different locations.

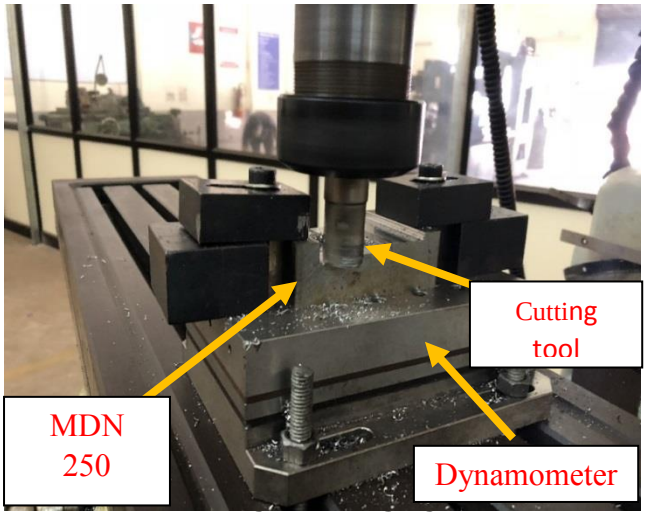

3 RESULTS AND DISCUSSION

The followings facets have been investigated during the milling of Maraging steel MDN 250 using coated and uncoated cemented carbide inserts.

3.1 Characterisation of cutting tools

Before carrying out the machining tests it is necessary to find out physical, electrical, metallurgical and mechanical properties. The SEM images of coated inserts are shown in Figure 2. The SEM images reveals that the AlCrN coating is

much more uniform than AlTiN coatings. Large numbers of macro particles are visible on the surface of AlTiN coating. The macro particles on the surface of coating have important effects on tribological properties. Smoother and uniform surface provides good tribological properties. During machining non uniform coatings provide high coefficient of friction which in turn causes in reduced tool life, higher cutting forces, higher power consumption and poor quality of surface finish.

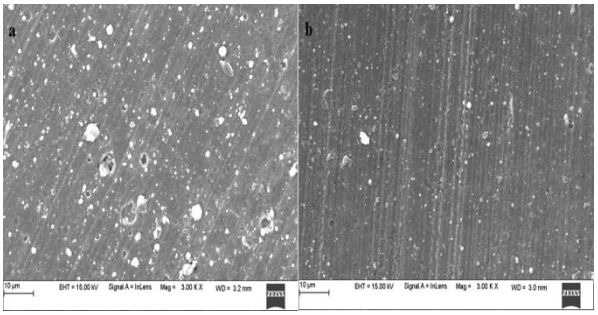

Figure 2. SEM images of a) AlTiN and b) AlCrN coated inserts

Figure 3 shows the EDS spectra for coated and uncoated tools. Figure 4 shows the XRD pattern of coated and uncoated tools. Both AlCrN and AlTiN coated tools shows the presence of AlN. Chromium nitride (CrN) is detected on the coated AlCrN coated samples. Reitera et.al (2005) reported that the presence of CrN in coated samples enhances the tribological behavior of coating. The titanium based phases are unable to identify because of low electro negativity of titanium in comparison with aluminium.The thickness and properties of the coatings are given in Table 1. It can be seen that AlCrN coatings shows improved mechanical properties in comparison with AlTiN coated inserts.The thickness of AlTiN coated samples are around 1.85 times that of AlCrN coated inserts. But the hardness and Young's modulus of AlCrN coatings are much higher compared to AlTiN coatings. Generally cuttings tools requires higher values of hardness in order to avoid the drastic tool wear. Higher H/E values are obtained for AlTiN coatings which is a measure of plasticity. But load bearing capacity (H^3/E^2) of both coatings was found to be quite similar. We can observe from the table that electrical conductivity of coated samples is higher than the uncoated inserts. AlCrN coated samples shows highest electrical conductivity compared to AlTiN coating. According to Wiedemann-Franz-Lorenz Law, the thermal conductivity of materials is directly proportional to electrical conductivity [Sreeramareddy et al. (2005)]. Thus increase in electrical conductivity increases the thermal conductivity of cutting tool thereby improving heat dissipation capacity of cutting tool. Hence reducing the cutting temperature in the machining zone.

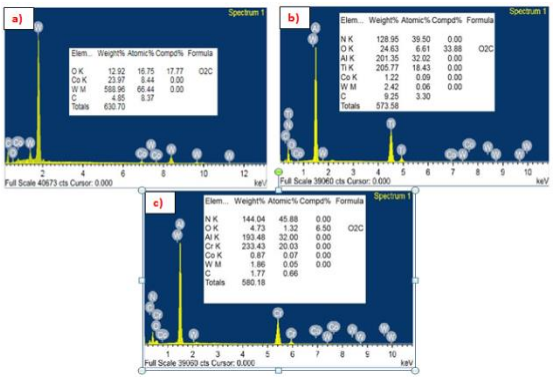

Figure 3. EDS analysis of cutting tool a) Uncoated b) AlTiN coated AlCrN coated inser

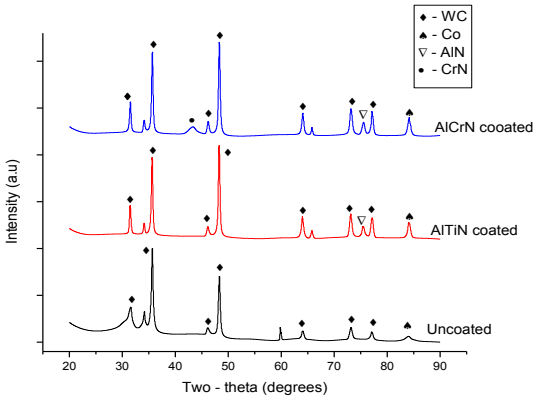

Figure 4. XRD patterns for Uncoated and Coated tools.

Table 1.Properties of AlTiN and AlCrN coatings.

Coatings	Thick-ness (μm)	Surface roughness μm	Electrical conductivity (ohm-m) -1	Hardness (H) Gpa	Young's modulus(E) GPa	H/E Ratio	H^3/E^2 Ratio Gpa
AlTiN	3.654	0.651	1141	28.94±6.44	376.7±59.3	0.076	0.17
AlCrN	1.972	0.547	1259	44.31±12.02	727.5±118.6	0.06	0.16

3.2 Cutting Force

Cutting force is regarded as the measure of power consumption during the machining. The experiments result shows that cutting forces are reduced while using coated tools in comparison with uncoated tools. Figure 5a.depicts the variation of cutting force against cutting speed. It can be seen that coated tool reduces the cutting forces by 20 -30 %than uncoated tools. This is due to higher wear resistance characteristics of coated tools. Higher wear resistance results in reduced tool wear. Because of reduced tool wear the friction between tool and workpiece reduces which in turn lowers the cutting speed. It can be seen that lesser values of cutting forces are obtained with AlCrN coated tools. In comparison with AlTiN coated tools, AlCrN exhibits 5-8% reduction in cutting force. The lower magnitude of force components for AlCrN coated tools is due to minimum friction developed between the applied coatings to the flowing chip.

3.3 Surface Roughness

The surface roughness of machined component has critical effect on the performance and service life of components, especially the components fatigue life. The average values of surface roughness at cutting speed of 17, 22 and 34 m/min are shown in Figure 5b. Cutting force and tool wear are two important factors which affects the surface finish obtained during machining. Figure 5b revealed that coated tools provide better surface finish than uncoated tools. The improved mechanical properties of coated tool produces reduced tool wear and cutting forces which in turn lead to reduced surface roughness. The range of reduction in surface roughness for coatings in comparison with uncoated ones are found to be 12-23%.It can be seen that at cutting speed of 22 m/min, the Ra values are found to be 0.8 and 0.78 μm for AlTiN and AlCrN coated inserts. There was 2.5% reduction in surface roughness using AlCrN inserts compared to AlTiN inserts. This was due to improved tribological properties of AlCrN over AlTiN coatings.

4. CONCLUSION

Machining performance of PVD coated AlTiN and AlCrN milling inserts are studied during end milling of maraging steel MDN 250. The conclusion drawn from the results are discussed below;

- The PVD coated tools can significantly enhance the machinability over uncoated tools by extending tool life, improving surface quality and reducing cutting force.
- The use of coated tool reduces the cutting forces by 20-33%.The AlCrN coated inserts reduces the cutting force by 5-8% in comparison with AlTiN coated inserts.
- The use of coated tool reduces the surface roughness by 20-30%.The AlCrN coated inserts reduces the surface roughness by 4-9% in comparison with AlTiN coated inserts.

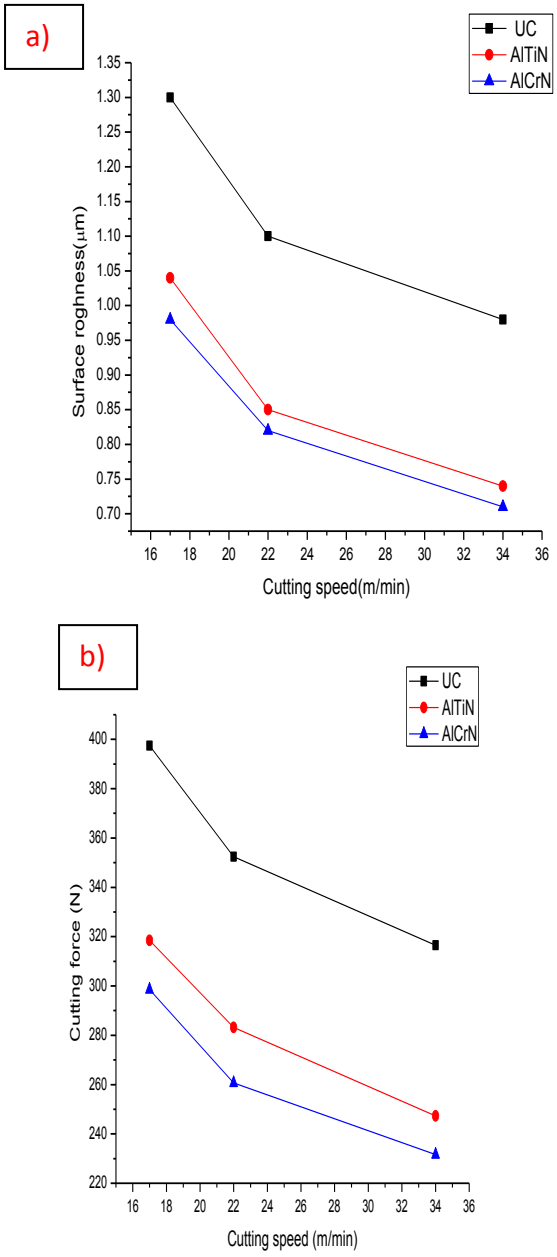

Figure 5. a) Surface roughness Vs. Cutting speed b) Cutting force Vs. Cutting speed

REFERENCES

[1] B.D. Beake, Li Ning, Ch. Gey , S.C. Veldhuis , A. Komarov , A. Weaver, M. Khanna, G.S. Fox-Rabinovich, Wear performance of different PVD coatings during hard, wet end milling of H13 tool steel, *Surface & Coatings Technology*, Vol. 279, pp. 118–125 2015.

[2] J.L. Mo, M.H. Zhu, A. Leyland , A. Matthews , Impact wear and abrasion resistance of CrN, AlCrN and AlTiN PVD coatings, *Surface & Coatings Technology*, Vol. 215, pp. 170–177, 2013.

[3] Jiri Nohava, Pascal Dessarzi, PavlaKarvankova , MarcusMorstein, Characterization of tribological behavior and wear mechanisms of novel oxy-nitride PVD coatings designed for applications at high temperatures, *Tribology International*, Vol. 81, pp 231–239, 2015.

[4] J.L. Mo, M.H. Zhu, Sliding tribological behavior of AlCrN coating, *Tribology International*, Vol. 41, pp. 1161– 1168, 2008.

[5] Reitera,A.E., Derflingera,V.H., Hanselmanna, B., Sartory,B., Investigation of the properties of $Al_{1-x}Cr_xN$ coatings prepared by cathodic arc evaporation, *Surface & Coatings Technology*, Vol. 200, pp. 2114–2122, 2005.

[6] T.V. SreeramaReddy, T. Sornakumar, M. VenkataramaReddy, R. Venkatram, Machining performance of low temperature treated P-30 tungsten carbide cutting tool inserts, Vol. 48, pp. 458-461, 2008.

8th International Engineering Symposium - IES 2019
March 13-15, 2019, Kumamoto University, Japan

EXPERIMENTAL INVESTIGATION ON JOULE THOMSON COEFFICIENT OF AIR

AKSHAY S RAO [1] and **RAJAT A CHANDAVAR [2]**

1 *Department of Mechanical Engineering, National Institute of Technology (NITK), Surathkal, India. e-mail: akshaysrao23@gmail.com*
2 *Department of Mechanical Engineering, National Institute of Technology (NITK), Surathkal, India. E-mail: rajatchandavar1998@gmail.com*

ABSTRACT: In the present study the Joule Thomson(J-T) Coefficient of air has been calculated by setting up and conducting experiment. The experiment is validated by theoretical formula available. Practical usage of Joule Thomson Effect is observed where the temperature drop is required and the measure of this effect is quantitively given by J-T Coefficient. In the experiment the J-T Coefficient of air at room temperature and atmosphere pressure is calculated, since most of the practical usage comes at room temperature and atmosphere pressure and the most frequently used gas is air. At first the best opening of valve for a given inlet pressure is calculated. From the experiment investigation the average value of J-T coefficient is obtained which is calculated for different inlet pressures.
Keywords*: Joule Thomson Coefficient, adiabatic, enthalpy.*

INTRODUCTION

When a real gas is forced through a valve or porous plug at constant enthalpy (adiabatic process) the temperature change takes place. This effect is known as Joule Thomson effect and the process is also called as the Throttling process. This is an irreversible process. To initiate the movement of the gas a pressure difference is required which is generated using a compressor and the ratio of change in temperature to change in pressure gives us the Joule Thomson Coefficient (Equation 2). The value of the coefficient can be positive or negative or zero depending on the state of gas. This effect is useful in the refrigeration process where cooling of the refrigerant is necessary. The effect also comes in handy in the petrochemical industry where liquification of petrol is done.

THEORY

The temperature of a gas depends on the kinetic energy of the gas. During an adiabatic process the temperature changes in two ways, either the internal energy can change (sum of kinetic and potential energies of gas) or just some part of kinetic energy can change into potential energy keeping the internal energy constant. During the Joule Thomson Experiment when the gas is forced from a region of high pressure to region of lower pressure adiabatically (no heat is exchanged between the system and surroundings) and by keeping the enthalpy constant the internal energy changes and hence the temperature changes. But in case of free expansion no change in internal energy is seen and just a part of kinetic energy is converted into potential energy [Goussard, J.-O.; Roulet, B. (1993)].

The equation that represents the Joule Thomson Experiment [M.J. Moran and H.N. Shapiro (2006)] is:

$$\Delta H = \Delta U + \Delta(P \times V) - (1)$$

Where, ΔU is the change in internal energy.

$\Delta(P \times V)$ represents the work done.

Here for adiabatic process enthalpy is constant and therefore, $\Delta H = 0$

And the term $\Delta(P \times V)$ simply becomes $\Delta P * V$ since, $\Delta V = 0$ in the term $\Delta V * P$.

Therefore, from this equation the change in internal energy is equal to work done on the gas or by the gas in magnitude during the process.
Theoretical Vander Waals equation for the Joule Thomson coefficient of a gas can be derived from the Vander Waals state of gas, which is [Atkins, Peter (1997)]:

$$\mu_{JT} = \left(\frac{\partial T}{\partial P}\right)_H = \left(\frac{2a}{RT} - b\right)\frac{1}{C_p} - (2)$$

In the above equation a in $\mathrm{Pa.m^6/mol^2}$ and b in $\mathrm{m^3/mol}$ are the Vander Waals constant.
R is the gas constant in $\mathrm{J/(mol.K)}$.
T is the initial temperature of the gas in K.
And C_p is the specific heat of gas at constant pressure in $\mathrm{J/(mol.K)}$.

EXPERIMENTAL SETUP

The experiment was conducted at IISc, Bangalore in the Cryogenics Department Laboratory as a part of Internship of the authors for a period of one month in June 2017. The apparatus used in the present experiment is shown in Figure.1. The experimental setup consists of 8 bar Compressor (maximum pressure developed is 8 bar), K type Thermocouples-2 (made of Nickel-Chromium alloy), Temperature indicator (Display system), 8 channel switch, needle valve, Copper coil, Steel coil, Water bath and Ball valve. Figure.2 gives the schematic diagram of the setup.
The step by step procedure of the present experiment study is listed below:

1. Connect the 2 thermocouples to the 8-channel indicator and then connect the 8-channel indicator to temperature indicator.

2. Connect the ball valve to air inlet of compressor. Join the copper and steel coil.

3. Connect the compressor outlet to the copper coil. Dip the copper coil in water bath.

4. Connect the needle valve to steel coil.

5. Connect the first thermocouple to inlet coil and second thermocouple to outlet coming from needle valve.

6. Switch on the compressor and temperature indicators. Adjust the ball valve such that we get a constant pressure.

7. Read the values of outlet temperature and make sure that inlet pressure is constant. Wait until the outlet temperature reaches a minimum.

At first the best outlet opening (the outlet for which maximum temperature drop takes place) was decided by changing the needle valve position. The needle valve that was used in the experiment had 9 turns and it is observed that the temperature drop for a fixed inlet pressure (same pressure difference) for different openings. The experiment begins with 0 turns (fully open) and ends with 9 turns (fully closed).

RESULT AND DISCUSSIONS

It is obvious that different openings at outlet leads to different opposing force on the gas that leads to different change in internal energy. Hence the best outlet opening needs to be found first which was found by doing experiment as mentioned above. The result of the experiment is shown in Table.1.

From the Table.1 and Figure.3 it is clear that when the no of turns is 1 maximum temperature drop is obtained. At first there is a positive slope in graph and then the slope becomes negative at 1 and giving the maximum change in temperature in graph. So further we continue our experiments with the needle valve in 1 turn position for different inlet pressure. The atmosphere pressure is 1bar. Different inlet pressure means different pressure drops and hence different temperature drop.

The result is listed down in Table.2.

Table.2 shows the change in temperature for different inlet pressure. The value of μ_{JT} varies slightly in this small pressure

range (7.2bar-2.2bar). Hence, the average value of μ_{JT} needs to be calculated for this small pressure range in order to get μ_{JT} at room temperature and pressure. (The outlet pressure is always 1 bar)
The average value of μ_{JT} can be calculated by plotting graph of ΔT Vs ΔP in Excel.

Figure.4 shows the plot of ΔT Vs ΔP.The best fit line is drawn for the set of data and the slope of the best fit line gives us the average value of μ_{JT}.
Therefore, the value of μ_{JT}=$0.3757 * 10^{-5}$K/Pa or 0.3757 K/bar.
The values of J-T coefficient have been previously calculated by various authors such as Joule-Thomson, Roebuck, Hoxton and Noell at 0 degree Celsius and one atmosphere and got the values 0.275 K/bar, 0.266 K/bar, 0.303 K/bar and 0.278 K/bar respectively. The variation of values occurs is said to have occurred due to variation in methods of measuring temperature, imperfect experiment condition etc. [J.R.Roebuck (1925)]

THEORETICAL VALIDATION

We know the theoretical Vander Waal formula for J-T coefficient is:

$$\mu_{JT} = \left(\frac{\partial T}{\partial P}\right)_H = \left(\frac{2a}{RT} - b\right)\frac{1}{C_p}$$

For air,
a = 0.1358 $\mathrm{Pa.m^6/mol^2}$
b = $0.0365 \times 10^{-3}\mathrm{m^3/mol}$
Cp = 29 $\mathrm{J/(mol.K)}$
R=8.314 $\mathrm{J/(mol.K)}$
T=297.5K
So, from this theoretically the value of $\mu_{JT} = 0.2586 * 10^{-5}$ K/Pa or .2586 K/bar.
The value got experimentally is higher maybe because of imperfect adiabatic condition and due to the manual handling of temperature measurement and pressure control.

CONCLUSION

Based on the present study the following conclusion can be drawn:

- The J-T coefficient is positive in the range of pressure and temperature considered.
- The theoretical value as per validation and the experimental value nearly match

ACKNOWLEDGEMENTS

The authors are thankful to Dr.S.Kasthurirengan for guiding during the experiment and giving an opportunity to work on the experiment. The authors also acknowledge Indian Institute of Science (IISc), Bangalore for providing all necessary experiment setup.

REFERENCES

[1] Atkins, Peter (1997). Physical Chemistry (6th ed.). New York: W.H. Freeman and Co. p. 930. ISBN 0-7167-2871-0

[2] Goussard, J.-O.; Roulet, B. (1993). "Free expansion for real gases". Am. J. Phys. 61: 845–848

[3] J.R.Roebuck, "Proceedings of the American Academy of Arts and Sciences", Vol. 60, No. 13 (Dec., 1925), pp. 537-596

[4] M.J. Moran and H.N. Shapiro "Fundamentals of Engineering Thermodynamics" 5th Edition (2006) John Wiley & Sons, Inc.

Table 1 Temperature Drop for different openings

No. of turns	*Temp Inlet T_{in} °C*	*Least Temp Outlet T_{out} °C*	*T_{in}-T_{out}* $[\Delta T]$
0	23.2	22.1	1.1
1	22.8	20.7	2.1
2	22.9	21.6	1.3
3	22.9	21.8	1.1
4	23	22.1	0.9
5	23.2	22.6	0.6
6	23.2	22.5	0.7
7	23.4	22.9	0.5
8	23.5	22.8	0.7
9	23.5	23.1	0.4

Table 2 Temperature difference for different pressure drop

P_{in} bar	*ΔP (bar)*	*T_{in} °C*	*T_{out} °C*	*ΔT (K)*	*$\mu_{JT} = \Delta T/ \Delta P$ (K/bar)*
2.2	1.2	24.1	23.7	0.4	0.3334
3.8	2.8	24.3	23.2	1.1	0.3928
4.6	3.6	24.3	23.0	1.3	0.3611
5.5	4.5	24.1	22.4	1.7	0.3778
6.5	5.5	23.6	21.6	2	0.3637
7.2	6.2	24.8	22.4	2.4	0.3871

Fig.1 Picture of the actual setup

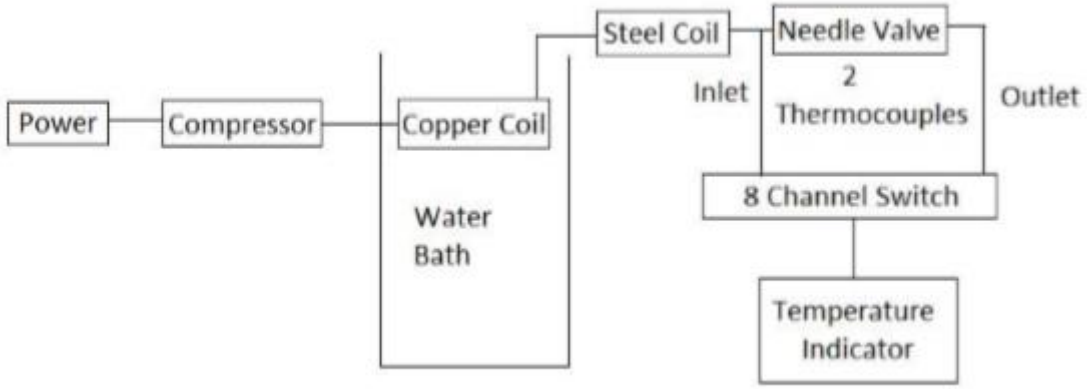

Fig.2 Schematic Diagram of Setup

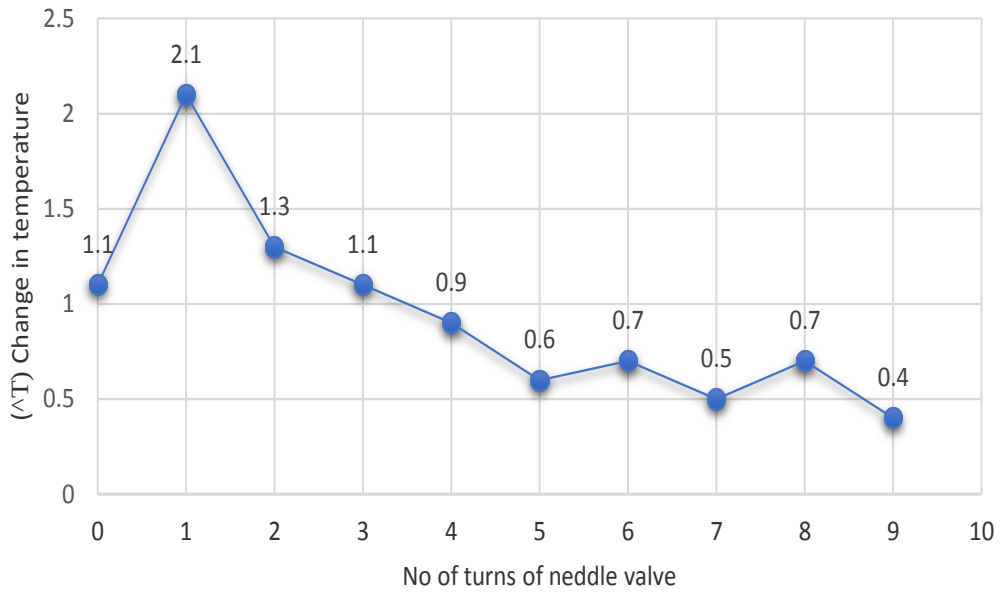

Fig.3 Variation of Change in temperature with No of turns of needle valve

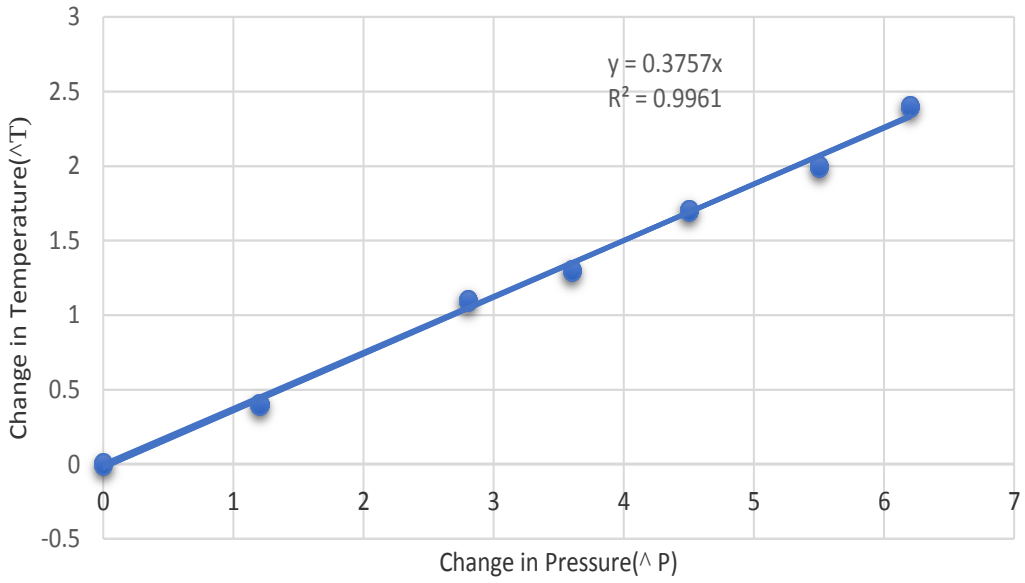

Fig.4 Variation of Change in temperature with change in pressure

8th International Engineering Symposium - IES 2019
March 13-15, 2019, Kumamoto University, Japan

Investigations of Thermal Effects on the Response of Polydimethylsiloxane / Carbon black Composite

Sushmita [1], S. Hiremath [2] and **S.M. Kulkarni[3]**

1 *Department of Mechanical Engineering, National Institute of Technology Karnataka, Surathkal, Mangalore 575025, India. email:sushdesai94@gmail.com*
2 *Department of Mechanical Engineering, National Institute of Technology Karnataka, Surathkal, Mangalore 575025, India. email:sssdait@gmail.com*
3 *Department of Mechanical Engineering, National Institute of Technology Karnataka, Surathkal, Mangalore 575025, India. Email: smkulk@gmail.com*

ABSTRACT: The thermal effects of a polydimethylsiloxane-based polymer containing carbon black as filler are observed. Reinforcement of conductive nano-particles into the polymer leads to increase in conductivity of the material but decrease in heat capacity of the composite. The heat is applied on one surface of the beam for a certain amount of time and conduction through the composite is observed through the rise in temperature on the opposite surface of the beam. The Finite Element (FE) analysis is carried out, where the effect of heat on polymer composite beam is inspected.

The modelling study predicts that as the heat input and percentage of filler content of the composite material increase it leads to a rise in temperature of the polymer based composite. This preliminary investigation is used to design and development of thermal actuators in future.

Keywords*: polymer composite, carbon black, thermal effect, temperature*

INTRODUCTION

For in-plane and out-of-plane motion thermal actuation is a promising solution. Micro-gripper, scanning probes, micro legs, micro positioning liquid drop ejectors, on/off switches and so on are some of the potential applications of these devices. The same has been used by researchers to develop artificial heliotropic systems for solar energy harvesting, Shivashankar et al. (2018)

PDMS (Polydimethylsiloxane) which is a biostable synthetic polymer is widely used in biomedical applications such as drug delivery vehicles and blood-contacting biomaterials. Non-toxicity, biocompatibility, blood compatibility, elasticity, transparency, and durability are some of the unique properties of this elastomeric polymer, Subramaniam A et al. (2014). Also PDMS has the ability to conduct heat. As the Young's modulus of PDMS can be easily modified through simple chemical modifications (more cross linker results in stiffer PDMS) it's ideal to use it as a actuator material, Maleki T et al. (2011).

Different carbon-based nano-materials as reinforcements like Graphene, Nano diamonds, Nano cones/discs and nano horns, Fullerenes and nano tubes, their functionalized forms can be used as sorbent agents. But these materials are found to be very expensive for laboratory work, Zhang et al. (2013)

Thus this paper presents the FE analysis of thermal effects on PDMS based composite beams with carbon black as reinforcement, carbon black (CB) being one of the most economic carbon-based nano-material. The modeling of composite beams are implemented using commercially available

FE software and the temperature variation of the beam surface is observed with varied heat input and reinforcement.

METHODOLOGY

In the present work cantilever beams of PDMS with Carbon black as reinforcement(5,10,15,20 & 25 percentage by volume) are considered for the thermal analysis of the composite material. The dimensions of the beam are considered as 90x14x5 mm^3. Heat is applied for 60s on surface A of the cantilever and the temperature variation is observed. This representation of the analysis is shown in Fig. 1.

MODELLING OF THE CANTILEVER BEAM

The modelling and thermal analysis of the beam is done using the commercially available FE software. For modelling it is assumed that the thickness of the beam is uniform throughout the length and for the thermal analysis it is assumed that the heat is uniformly applied on one surface of the beam. Heat is applied as W/m^2 in the range of 100-1000 W/m^2. For analysis the beam is considered as a cantilever.

MATERIAL OF COMPOSITE

Polymer composites are gaining attention for use in light-weight applications including sports equipment, wind turbines, aircraft composites, and medical implants, Loomis J et al. (2013). The present exertion is to show the thermal abilities of the PDMS based composite beam. Among the polymer-based materials, PDMS is most widely utilized material and additionally is claimed to be suitable dynamic material for sensors and actuator components, Zhi C et al. (2015). Thus in this work PDMS is selected as base material with a reinforcement of carbon black for analysis. The physical and thermal properties of PDMS and carbon black are given in the Table 1. Also Table 2 gives the information about the properties like the density(ρ), conductivity(k) and heat capacity (C_P) of composites which were obtained using rule of mixture. These properties were used to do the FE modelling and analysis.

RESULTS AND DISCUSSIONS

The thermal analysis of PDMS based composite beam is performed by subjecting it to heat source. The simulations were carried out using the commercially available FE software. The simulation models of the composite beams is shown in Fig. 2.

Comparative study of simulation of all the compositions is shown in the Table 3. As shown in Fig. 3 an increment in temperature of the surface B is observed with varied heat input ranging from 100 W/m^2 to 1000 W/m^2 and change in the reinforcement. Also Fig. 4 shows that as the heat input and the percentage of reinforcement increases there is a slight decrease in the temperature of the surface A.

CONCLUSION

On analyzing the simulation results it was found that as the percentage of the reinforcement (carbon black) increases the temperature of surface A comparatively decreases and the temperature of surface B comparatively increases. Thus it can be concluded that the above observed variation in temperature of surface A and B is due to the increase in conductivity and decrease in heat capacity of the composition with increase in the reinforcement.

Thus the beams of these compositions can be used as thermal actuators in applications like on/off switch, micro grippers etc.

References

[1] Loomis, J., Fan, X., Khosravi, F., Xu, P., Fletcher, M., Cohn, R. W., and Panchapakesan, B. (2013). Graphene/elastomer composite-based photo-thermal nanopositioners. Sci. Rep., 3, 1–10.

[2] Maleki, T., Chitnis, G., and Ziaie, B. (2011). A batch-fabricated laser-micromachined PDMS actuator with stamped carbon grease electrodes. J. Micromechanics Microengineering, 21(2).

[3] Shivashankar H and S. M. Kulkarni (2018). Modelling and Analysis of Thermomechanical Behaviour in Composite Bimorph Actuator ISSN: 1662-9752, Vol. 928, pp 209-214.

[4] Subramaniam A. and Sethuraman S. (2014). Biomedical Applications of Nondegradable Polymers. Nat. Synth. Biomed. Polym., Elsevier Inc.
[5] Zhang, B. T., Zheng, X., Li, H. F., and Lin, J. M. (2013). Application of carbon-based nanomaterials in sample preparation: A review. Anal. Chim. Acta, 784, 1–17.
[6] Zhi, C., Shinshi, T., Uehara, M., Matsutani, A., Yuito, I., & Takeuchi, T. (2015). A polydimethylsiloxane diaphragm integrated with a sputtered thin film NdFeB magnet. Microsystem Technologies, 21(3), 675-681.

Table 1 Material Properties

PDMS	Density (ρ)	1030 (kg/m^3)
	Conductivity (k)	0.27 (W/m-K)
	Heat capacity (C_p)	1460 (J/kg-K)
Carbon Black	Density (ρ)	1890 (kg/m^3)
	Conductivity (k)	4-176(W/m-K)
	Heat capacity (C_p)	690.82 (J/kg-K)

Table 2 Material properties of composites used for FE analysis

Percentage of CB	**5%**	**10%**	**15%**	**20%**	**25%**
ρ (Kg/m^3)	1054	1079	1105	1133	1162
K (W/m-K)	0.28	0.29	0.31	0.33	0.35
C_P (J/Kg-K)	1383	1313.7	1251.1	1194.1	1142.1

Table 3 Temperature of surface A and B with heat input

	Heat Input (W/m^2)	**Temperature of surface A after 60s where heat is applied T_1 (°C)**	**Temperature of surface B after 60s initially maintained at room temperature T_2 (°C)**
PDMS + 5% CB	100	26.3	25.3
	500	31.8	27.1
	1000	38.8	29.4
PDMS + 10% CB	100	26.3	25.3
	500	31.9	27.3
	1000	38.9	29.7
PDMS + 15% CB	100	26.2	25.4
	500	31.8	27.4
	1000	38.7	30
PDMS + 20% CB	100	26.2	25.4
	500	31.7	27.6
	1000	38.6	30.3
PDMS + 25% CB	100	26.2	25.4
	500	31.7	27.7
	1000	38.5	30.6

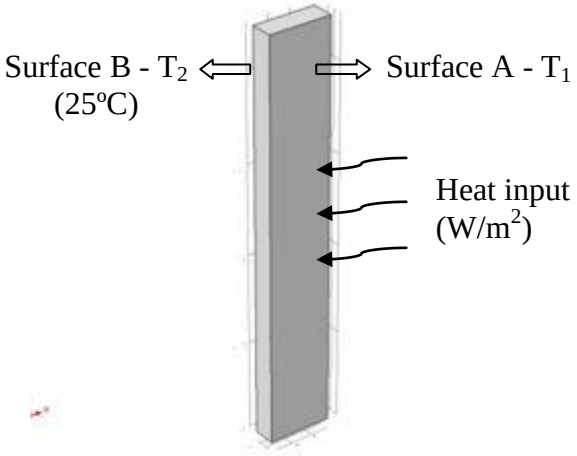

Fig.1 Representation of composite beam with heat input

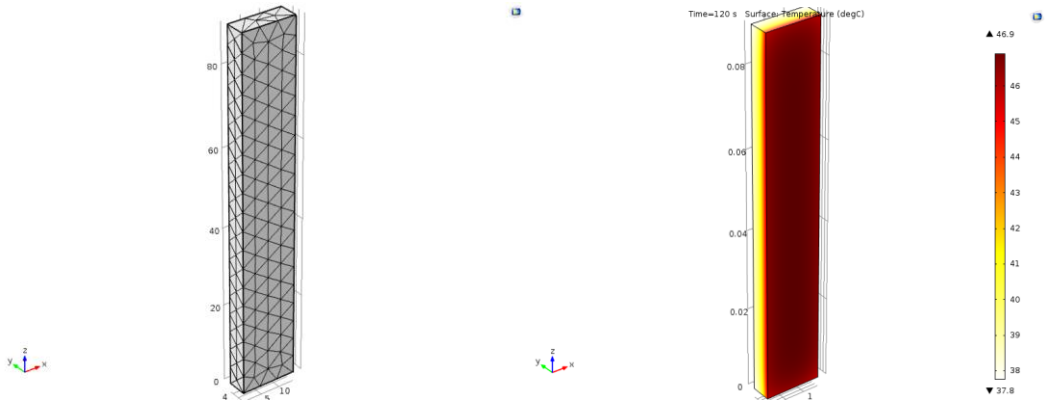

Fig. 2 Mesh generated beam and beam subjected to heat source

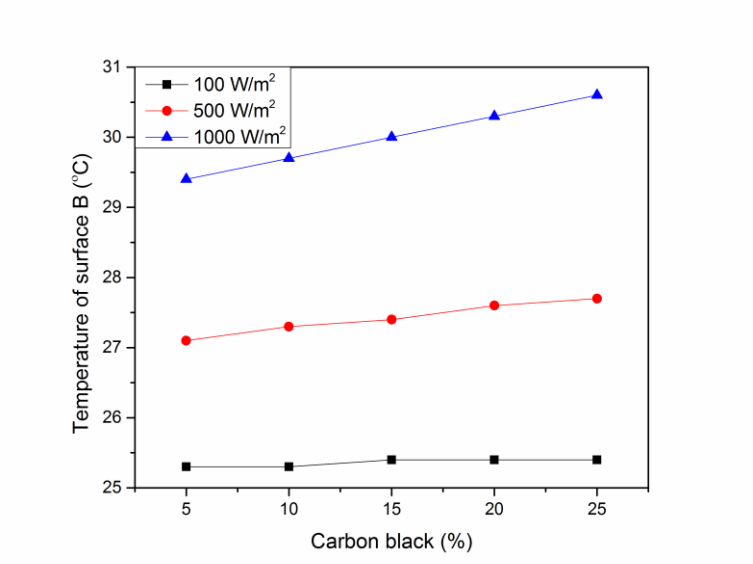

Fig. 3 Temperature of surface B after 60s for different reinforcement

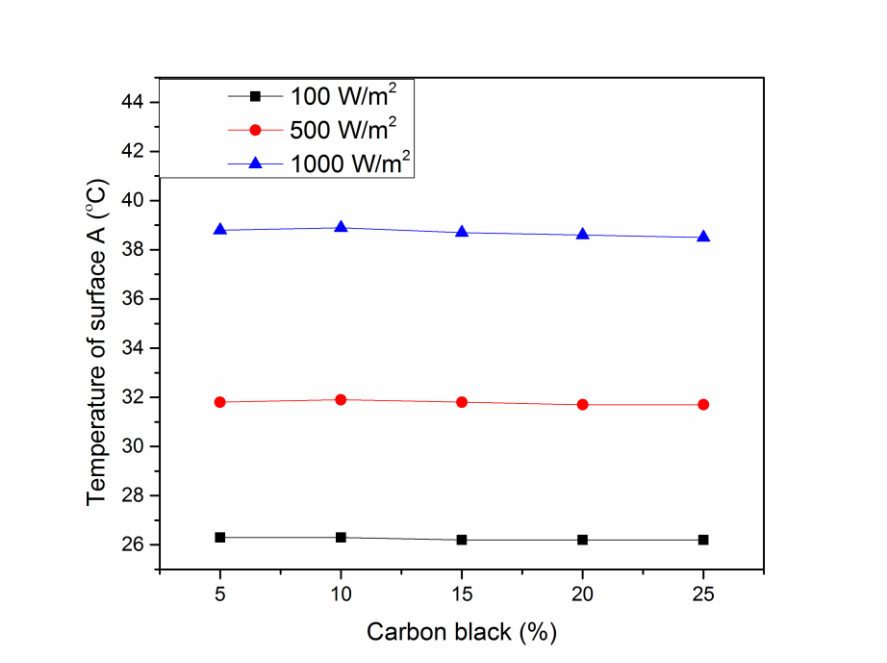

Fig. 4 Temperature of surface A after 60s for different reinforcement

8th International Engineering Symposium - IES 2019
March 13-15, 2019, Kumamoto University, Japan

Study on characteristics of emulsion fuel with co-surfactant

Takumi Iwanaga [1], Shuichi Torii [2] and Keishi Nakamura[3]

1 *Department of Mechanical System Engineering, Kumamoto University, Kurokami, 2-39-1, Kumamoto 860-8555, Japan. e-mail: 181d8453@st.kumamoto-u.ac.jp*
2 *Department of Mechanical System Engineering, Kumamoto University, Kurokami, 2-39-1, Kumamoto 860-8555, Japan.*
3 *Department of Mechanical System Engineering, Kumamoto University, Kurokami, 2-39-1, Kumamoto 860-8555, Japan.*

ABSTRACT: Vegetable oil have most of the properties that is close to diesel. Emulsification is a way to use vegetable oil for diesel engine. Using straight vegetable oil for emulsion fuel are difficulty to keep the stable emulsification for long time if it is made by easy method using only surfactant.
The objective was set to evaluate the property of emulsion fuel using alcohol such as ethanol (99.5) and methanol (99.5) which can affect as co-surfactant in emulsion system in this study. Each sample was evaluated by visual observation. As a result, emulsion of 10wt.% concentration ethanol and 20wt.% concentration methanol has good stability, and the viscosity of 20 wt.% ethanol and methanol emulsion were lower than straight rapeseed oil.

***Keywords**: Vegetable oil, Emulsion fuel, Alcohol, Co-surfactant*

INTRODUCTION

On the current fossil fuels face challenges with regards to environmental hazards and escalating costs. In this regard, the technical researchers are questing for alternative fuels resource. Vegetable oil are renewable and sustainable energy, it has most of the properties that is close to diesel and less polluting than fossil fuels. Vegetable oil is expected as an alternative fuel to diesel. However, if vegetable oil is used directly for a diesel engine, combustion defect occurs because the viscosity is too high[1].
The methods applying directly for diesel engine include preheating, transesterification, and emulsification. When the vegetable oil is heated to about 80 ℃, it has the same viscosity and performance as diesel fuel[2].
Transesterification changes characteristics of vegetable oil. Viscosity is reduced by 90% and cetane number is promoted[3]. A simple way used for diesel engines is a method of emulsifying[4]. Emulsion fuel is obtained by mixing fuel and water.
Emulsion fuel can reduce NOx and PM in the exhaust gas by phenomenon called micro-explosion which is caused due to boiling temperature difference between oil phase and water phase. When rapeseed oil emulsion with a water content of 20% was used in a diesel engine, it was reported that the NOx concentration and the exhaust smoke concentration were lower than when using diesel fuel[5]. However, emulsion fuel which is created using straight vegetable oil are extremely difficult to keep the stable emulsification for long time if it is made by simple emulsification method using only surfactant. Therefore, alcohol was used as a co-surfactant to enhance the stability in this study.
The viscosity of the emulsion fuel can be lowered by adding alcohol[4].
In this study, we try to stabilize the emulsion fuel by using mixture of two kinds of co-surfactant.

Experimental Materials

The emulsion fuel of this study consists of four components. Oil phase used in this experiment was commercial rapeseed oil which was purchased from The Nisshin OilliO Group, Ltd., japan. Sorbitan oleate used in this experiment as surfactant (Span80) was purchased from FUJIFILM Wako Pure Chemical Co., Japan. Distilled water is used as water phase. Co-surfactant used in this experiment was Dry ethanol and Dry Methanol which was purchased from FUJIFILM Wako Pure Chemical Co., japan. The ratio of water and surfactant was constant and experiments were carried out with varied ratio of oil and co-surfactant. Kind of surfactant and co-surfactant are shown in Table 1.

Mechanism of separation

Oil and water separation in the emulsion system depends on the following rate equation[6].

$$v = \frac{2r^2(\rho_0 - \rho)g}{9\eta} \quad (1)$$

Where, v is sedimentation velocity, r is particle radius, g is gravitational acceleration, η is viscosity of continuous phase, ρ_0,$\rho$is density of dispersed and continuous phase. In order to suppress the separation, it is effective to reduce the particle size. Separation can be suppressed also by decreasing the difference in specific gravity between the water phase and the oil phase, increasing the viscosity difference.

Experimental methods

Emulsion fuel is made by rotary homogenizer. Homogenization of the composed liquid is done by the using of rotary homogenizer (Model;AHG-160A, shaft;HT1018, AS ONE Company, Japan). Number of rotations is 8,000 rpm, and it is continued for 3 minutes.

Measurement of viscosity is measured by the viscometer of the BROOKFIELD. All samples were taken 0.5 mL and measured the each viscosity in keeping 40 ℃.
The viscosity was measured three times and averaged. The sheer rate was set in 7.5, 15, 37.5 1/s.

Evaluation of emulsion was carried out by visual observation. In the visual observation, samples are fixed in the motionless environment and are observation the separation between straight rapeseed oil and water.

Experimental conditions are shown in the Table2, Table3 and Table4.

Results and discussion

Fig.1, Fig.2, Fig.3 show the results of visual observation. The emulsion without co-surfactant was separated even 30 minutes later. This separation became bigger 1 day later. The sample as containing ethanol 10wt.% did not showed phase separation 3 weeks later. Samples as containing ethanol 15 wt.% and 20 wt.% were showed phase separation 3 weeks later. The sample as containing methanol 20wt.% did not showed phase separation 3 weeks later. Samples as containing ethanol 10 wt.% and 15 wt.% was showed phase separation 3 weeks later.
Fig.4, Fig.5 show the results of measurement of viscosity. The viscosity of emulsion with ethanol containing 10 wt.%, 15wt.% was higher than straight rapeseed oil. The viscosity of emulsion with ethanol containing 20wt.% was lower than straight rapeseed oil. The viscosity of emulsion with methanol containing 10 wt.%,
15wt.% was higher than straight rapeseed oil. The viscosity of emulsion with methanol containing 20 wt.% was lower than straight rapeseed oil.

As shown in Fig.6, it is considered that the difference in stability between ethanol and methanol is a difference in lipophilicity. Ethanol was dissolved in rapeseed oil and methanol was not dissolved in rapeseed oil. However, ethanol and methanol were dissolved in water. From the Stoke's equation, it is considered that if concentration of ethanol increases, ethanol which was not able to act as co-surfactant dissolves in oil phase, and eventually the emulsion using ethanol make viscosity of oil phase reduce and the separation speed became faster. Generally, adding higher concentration of Amphiphiles(surfactant and co-surfactant) make smaller droplet in emulsion system. However, it is considered

that the emulsion stability was affected that by reducing the viscosity of oil phase more than lowering droplet size in this research.

Conclusions

It was possible to obtain good stability by adding at least 10.0 wt.% of alcohol as a co-surfactant in emulsion using straight rapeseed oil.

The viscosity decreases as the ethanol or methanol content increases. When the content was 20 wt.% or more, the viscosity was lower than straight rapeseed oil that is used as oil phase for the emulsion fuel.

Due to the difference in solubility in oil, Ethanol is stabilized at a low content. On the other hand, methanol is stabilized at a high content.

This result was just focused on the stability and decreasing the viscosity of emulsion. Therefore, it is necessary to examine the working performance of engine and emission gas characteristics when these stable emulsion fuels are actually applied to engine.

REFERENCES

[1]D. Capuano M. Costa S. Di Fraia N. Massarotti L. Vanoli(2017), Direct use of waste vegetable oil in internal combustion engines, ELSEVIER, Renewable and Sustainable energy Review, Volume 69, March, pp.759-770

[2]Narayan LalJain S. L. Soni M. P. Poonia DilipSharma Anmesh K. Srivastava HardikJain, Performance and emission characteristics of preheated and blend thumba vegetable oil in a compression ignition engine, Applied Thermal engineering, Volume 113, 25, February, pp.970-979

[3] Toshiya okazima and Takeru shima. (2015)On the Difference of the Reactivity of Ester-exchange reaction by the Number of Carbon atoms of Alcohols,Fac. Saga Univ. Vol19, No2 pp.235~243

[4]M. Senthil Kumar, M. Jaikumar(2014), A comprehensive study on performance, emission and combustion behavior of a compression ignition engine fuelled with WCO (waste cooking oil) emulsion as fuel Journal of the Energy Institute 87263-271

[5] Kadota, T. and Yamasaki, H. (2002), Recent advances in the combustion of water fuel emulsion, Progress in Energy and Combustion Science, 28(5), pp.385–404.

[6] Teruo H (2010), "Emulsification fundamental theory", J.Soc.Cosmet.Chem.Jpn. overall review, 44(1), pp.2-22

Table 1 properties of used surfactant and cosurfactant

Material	HLB	Source
Sorbitan oleate	4.3	Wako Co. Japan
Ethanol	---	Wako Co. Japan
Methanol	---	Wako Co. Japan

Table 2 Experiment A condition

Experiment A	RO(wt.%)	W(wt.%)	S(wt.%)
76RO20W4S	76	20	4

RO:Rapeseed oil, W:Water, S:Surfactant

Table 3 Experiment B condition

Experiment B	RO (wt.%)	W (wt.%)	E (wt.%)	S (wt.%)
66RO20W10E4S	66	20	10	4
61RO20W15E4S	61	20	15	4
56RO20W20E4S	56	20	20	4

RO:Rapeseed oil, W:Water, E:Ethanol, S:Surfactant

Table 4 Experiment C condition

Experiment C	RO (wt.%)	W (wt.%)	M (wt.%)	S (wt.%)
66RO20W10E4S	66	20	10	4
66RO20W10E4S	61	20	15	4
66RO20W10E4S	56	20	20	4

RO:Rapeseed oil, W:Water, M:Methanol, S:Surfactant

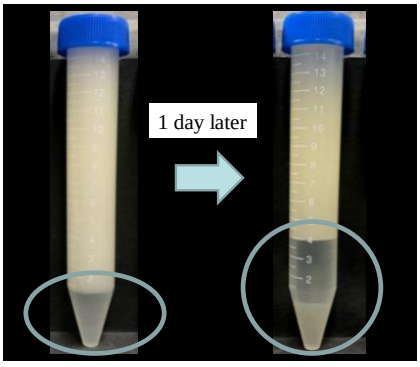

Fig.1 Visual observation of experiment A

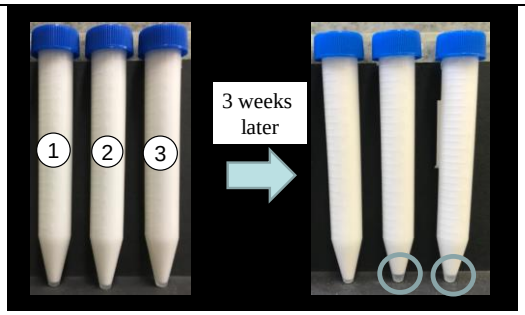

Fig.2 Visual observation of experiment B

Table 5 Containing ethanol

	Containing(wt.%)
1. 66RO20W10E4S	10
2. 61RO20W15E4S	20
3. 56RO20W20E4S	30

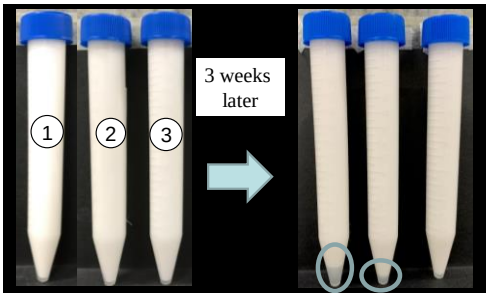

Fig.3 Visual observation of experiment C

Table 6 Containing methanol

	Containing(wt.%)
1. 56RO20W10M4S	10
2. 61RO20W15M4S	20
3. 56RO20W20E4S	30

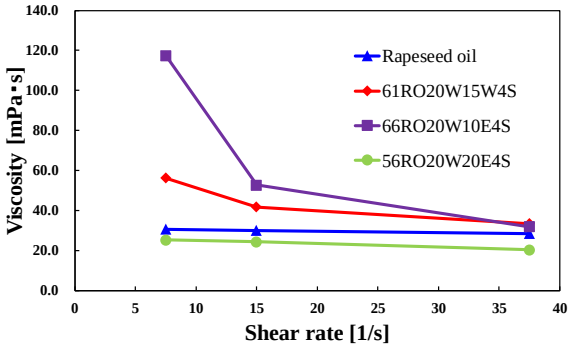

Fig.4 Emulsion sample2: viscosity

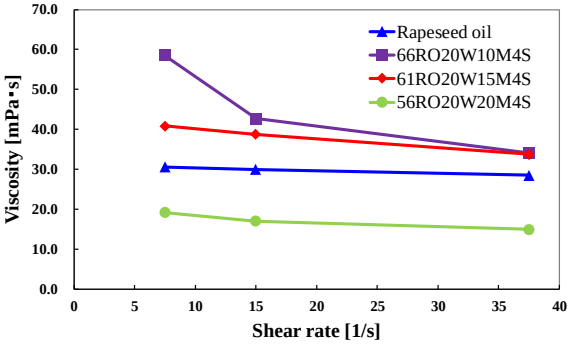

Fig.5 Emulsion sample3: viscosity

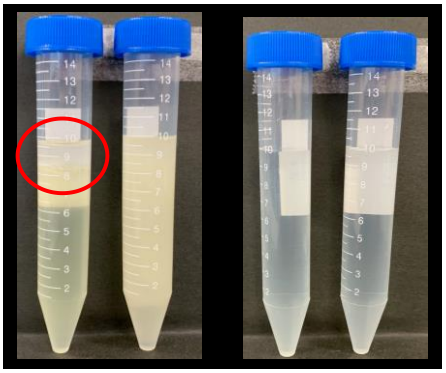

Fig.6 Solubility of ethanol and methanol in oil

8th International Engineering Symposium - IES 2019
March 13-15, 2019, Kumamoto University, Japan

Investigation of Optimum Condition to Obtain Stable Emulsion Fuel Included Biodiesel Fuel

Keishi Nakamura [1], and **Shuichi Torii [2]**

1 *Graduate School of Science and Technology, Kumamoto University 2-39-1 Kurokami, Chuo-Ku, Kumamoto 860-8555 Japan email: 161d8531@st.kumamoto-u.ac.jp*
2 *Graduate School of Science and Technology, Kumamoto University 2-39-1 Kurokami, Chuo-Ku, Kumamoto 860-8555 Japan e-mail: torii@mech.kumamoto-u.ac.jp*

ABSTRACT: Emulsion fuel has been considered as one of the solutions to be able to reduce nitrogen oxide (NOx) and cut particulate matter (PM) in the exhaust gas generated from diesel engine. However, this emulsion fuel has low emulsion stability. The objective of this study was to develop the stability of the emulsion fuel and reveal optimum conditions to obtain stable emulsion. In the experiments for this research, we prepared samples which consist of biodiesel fuel as oil phase, phosphate buffer as water phase and Polyglycerol ester of polyricinoleic acid (PGPR) as emulsifier Each sample was evaluated by visual observation and measuring particle size. Results were determined that emulsion which was consisted buffer of nearly neutral pH, and at least 2.0 wt.% of PGPR shows good stability.

***Keywords**: Emulsion fuel, Biodiesel, Soybean oil, PGPR*

INTRODUCTION

At present, the number of people who are using automobiles has increased due to the promotion of rapid industrialization and air pollution has been getting serious year by year. Air pollution involves various problems such as leading to global warming and damaging the health of the human body. This air pollution is caused by pollutants such as carbon dioxide (CO_2), nitrogen oxide (NO_x) and particulate matter (PM) which are contained in the exhaust gas discharged from the heat engine, and is mainly caused by artificial causes. Therefore, it is necessary to reduce these emissions and improve the fuel consumption.

Emulsion fuel made by emulsifying water and fuel has been considered as one of the solutions to save the fossil fuel and suppress these pollutions. Emulsion fuel is a fuel obtained by homogenizing a fuel and water to make water generate particles and disperse them in the oil phase. Burning this emulsion fuel has the effect of suppressing the generation of nitrogen oxides (NO_x) and particulate matter (PM) as compared with the case when ordinary fuel is burned. In addition, effects of improving combustion efficiency and further reducing the heat loss have been also reported [1], [2]. On the other hand, problems have also been pointed out. It is a low long-term stability of emulsion fuel. In other words, it is very difficult to make an emulsion fuel which does not separate for a long time with water in oil emulsion type (W/O) in which water droplets are evenly dispersed in oil. For the reason, there are instances where the mixture is homogenized just before combustion by devices such as high pressure homogenizer.

Based on the above, the objective of this study is to produce a stable emulsion and determine the optimum condition. As fuel that is an oil layer, biodiesel fuel which is renewable oxygenated fuel, able to contribute to CO_2 reduction due to being thought to be carbon neutral and is promising as a diesel substitute fuel is used.

Experimental Materials

The biodiesel fuel used in this experiment was prepared based on commercial soybean oil which was purchased from AMCO Ltd., Auckland, New Zealand. In the preparation of the biodiesel fuel, a transesterification by using alkali catalyst was used as a production method. As an evaluation for the property, the ester conversion rate calculated from the amount of theoretical glycerin and the amount of reacted glycerin is determined and the measured kinematic viscosity of the obtained biodiesel fuel was compared with the standard of the United States where biodiesel of soybean oil is mainly used. The standard values for kinematic viscosity of biodiesel in countries including the United States are shown in Table 1. The kinematic viscosity was measured by bearing rheometer (AR-G2 Magnetic Bearing Rheometer, TA Instruments Ltd., USA). The actual compared values of kinematic viscosity are shown in Fig. 1. In the three biodiesel fuel produced, the ester conversion rate was as high as 93%, and the measurement results of the kinematic viscosity of these biodiesel fuels were within the standard values of the United States. Therefore, it was judged that the quality was sufficient. Polyglycerol ester of polyricinoleic acid used in this experiment as surfactant (PGPR 4150, Palsgaard Ltd., Denmark) was purchased from Hawkins Watt Ltd, Auckland, New Zealand. Phosphate buffer solution was used for fixing the pH as aqueous phase in this experiment.

Preparation of Emulsion Fuel

Water in oil emulsions (W/O) were prepared by a two-step process with a two stage valve homogenizer (APV 2000, Denmark). Firstly the mixtures were homogenized by rotary homogenizer in condition that speed is 15,000 rpm and time is 3 minutes as pre-emulsification. Secondly, generated emulsions were circulated in two stage valve homogenizer at 150/50 bar (first-stage pressure/second-stage pressure) twice to obtain final W/O emulsion. Emulsion fuels were generated in two different conditions and each condition of materials is shown in Table 2 and 3.

Evaluation of W/O Emulsion

Evaluation of emulsion was carried out by visual observation and determination of average droplet size and particle size distribution. In the visual observation, samples were fixed in the motionless environment and observed whether they are separated or not in room temperature. Concurrently, samples except for being already separated were measured the droplet sizes. In the measurement of droplet size, a Malvern Zetasizer Nano ZS instrument (Malvern Instruments Ltd., Malvern, Worcestershire, United Kingdom) was used to determine them.

There is a phenomenon called creaming in the process of instability of the emulsion structure. This creaming is a phenomenon in which emulsion particles float or settle due to the difference in density between the disperse phase and the dispersion medium. Although this creaming is a reversible process, since the emulsion particles are close to each other, aggregation and coalescence are induced, and finally they are separated. The speed of creaming is given by Stokes' equation (1).

$$v = \frac{2r^2(\rho_0 - \rho)g}{9\eta} \quad (1)$$

Here, v is sedimentation velocity, r is particle radius, g is gravitational acceleration, η is viscosity of continuous phase, and ρ_0, ρ is density of dispersed and continuous phase. Therefore, in order to reduce the creaming speed, measures such as reducing the particle diameter, reducing the density difference between the continuous phase and the dispersion medium, and increasing the viscosity of the dispersion medium are conceivable. In this study, the stability of emulsion fuel was evaluated to measure the particle size [4].

Result and Discussion

· Influence of surfactant concentration on emulsion stability

The experimental results of emulsion fuel produced by changing the concentration of

the surfactant are shown in Fig.2-4. Fig.2 shows the sample one day after stirring (left) and the sample after three weeks (right).Separation (aqueous phase settling) occurred in the sample (0.5, 1.0 wt.%) in which the concentration of the surfactant was low, and it could also be confirmed the separation range widened. On the other hand, samples with high concentration (2.0, 4.0 wt.%) showed good stability for 3 weeks. It is considered that by increasing the concentration of the surfactant, it is possible to increase the packing density of the amphiphilic substance (surfactant) at the interface, which promotes the reduction of the interfacial tension between the water and the oil, and create good stability. Fig. 3 and Fig. 4 shows particle size distribution and the change over time of the average droplet size in the samples (2.0, 4.0 wt.%) which had good stability. As can be seen these results, there was no noticeable change in both result, and at least the concentration of PGPR 2.0 wt.% is enough to obtain stable emulsion.

· Effect of pH of aqueous phase on emulsion stability

Fig.5-7 shows experimental results of emulsion fuel produced by changing pH of aqueous phase. From Fig. 5, it was found that all samples showed good stability for 3 weeks. However, as shown in Fig. 6 and Fig. 7, the sample with acidity (pH 5.0, 6.0) had a relatively large peak of particle size, and remarkable enlargement was confirmed even with time change. On the other hand, in the neutral sample, both the particle size distribution and the change over time of the average droplet size showed the best results. Therefore, although separation was not confirmed in all samples by visual observation, it was confirmed that instability was increased in emulsion fuel with acidity aqueous phase.

Conclusion

In producing emulsion fuel by a two-stage process of pre-emulsification and main emulsification,

- When preparing an emulsion fuel using biodiesel fuel derived from soybean oil as the oil phase, it was possible to increase the stability by using phosphate buffer as the aqueous phase and PGPR as the surfactant.
- As the condition of the surfactant PGPR, emulsion stability could be maintained at the minimum 2.0 wt.%.
- It was found that the stability can be further improved by keeping the pH of the aqueous phase at neutral and the stability drops greatly when it becomes acid.

References:

[1] Debnath, BK, Saha, UK, and Sahoo, N (2015), " A comprehensive review on the application of emulsions as an alternative fuel for diesel engines", Renewable and Sustainable Energy Reviews, 42, pp.196-211
[2] The Chemical Society of Japan (2009), "Basic of modern interfacial colloid chemistry - principle, application and measurement solution", , Maruzen Co., p. 70
[3] Yasufumi Y. and Eiji K (2009), "Applied Technology of Vegetable Oils for Diesel Engines –Use of Biodiesel Fuel-".Journal of the Combustion Society of Japan, Vol.51, pp. 121-128
[4]Teruo H (2010), "Emulsification fundamental theory", J.Soc.Cosmet.Chem.Jpn. overall review, 44(1), pp.2-22

Table.1 Biodiesel specification standards in several countries (Unit [cSt]) [3]

	USA	UK	Australia	Brazil	Japan
Kinematic viscosity (40℃)	1.9 – 6.0	3.5 – 5.0	3.5 – 5.0	3.5 – 5.0	3.5 – 5.0

Table.2 Condition of each sample in experiment (a)

	BDF [wt.%]	Phosphate buffer (0.1M, pH 7.0) [wt.%]	PGPR [wt.%]
Sample 1	79.5	20	0.5
Sample 2	79	20	1.0
Sample 3	78	20	2.0
Sample 4	76	20	4.0

Table.3 Condition of each sample in experiment (b)

	BDF [wt.%]	Phosphate buffer (0.1 M) [wt.%]	PGPR [wt.%]
Sample 1	78	20 (pH 5.0)	2.0
Sample 2	78	20 (pH 6.0)	2.0
Sample 3	78	20 (pH 7.0)	2.0
Sample 4	78	20 (pH 8.0)	2.0

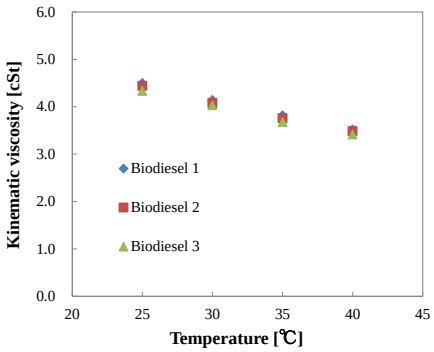

Fig.1 Kinematic viscosity for biodiesel which was made in this experiment

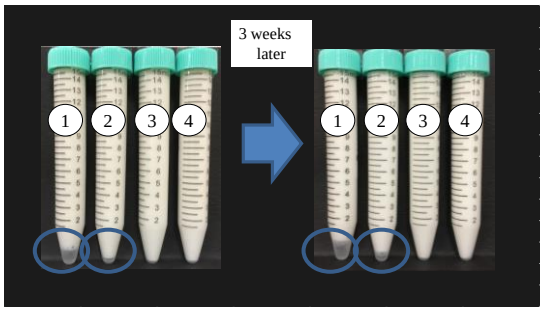

Fig.2 Picture of emulsion as days passed in experiment (a) (left-right : 0.5, 1.0, 2.0, 4.0%, four samples on the left after one day, four samples on the right after 3 weeks)

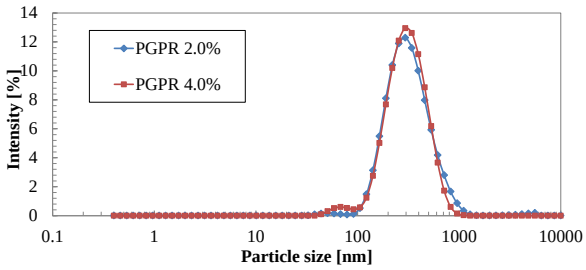

Fig.3 Particle size distribution of experiment (a) (◆ : PGPR 2.0%, ▪ : PGPR 4.0%)

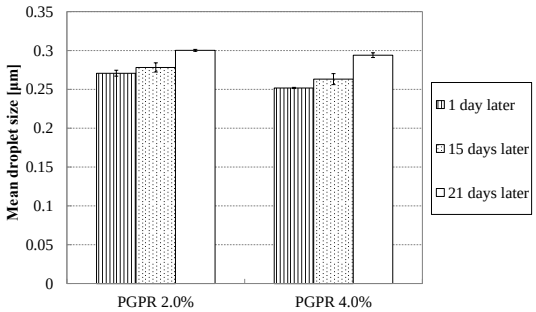

Fig.4 Average droplet size of experiment (a) as days passed (Striped bar : 1 day later, Dotted bar : 15 days later, Plane bar : 21 days later)

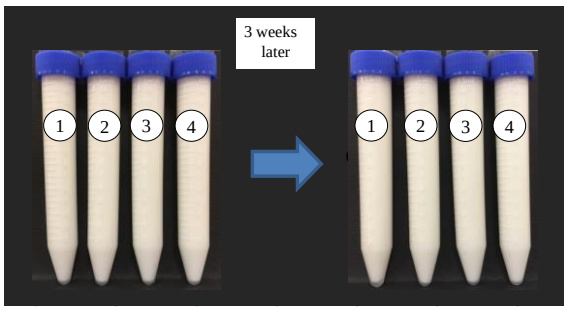

Fig.5 Picture of emulsion as days passed in experiment (b) (left-right : pH 5.0, 6.0, 7.0, 8.0, four samples on the left after one day, four samples on the right after 3 weeks)

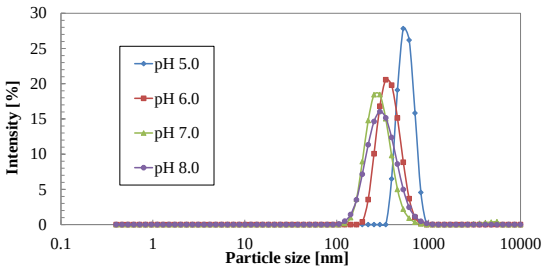

Fig.6 Particle size of experiment (b) (◆ : pH 5.0, ▪ : pH 6.0, ▲ : pH 7.0, ● : pH 8.0)

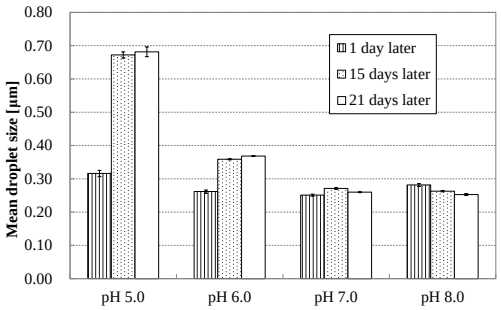

Fig.7 Average droplet size of experiment (b) as days passed (Striped bar : 1 day later, Dotted bar : 15 days later, Plane bar : 21 days later).

8th International Engineering Symposium - IES 2019
March 13-15, 2019, Kumamoto University, Japan

Study on dynamic characteristics during steam generation by electrode type electric boiler

Taiki Ishimoto [1] and **Shuichi Torii** [2]

1 *Student, Department of Mechanical System Engineering, Kumamoto University, Kurokami, 2-39-1, Kumamoto 860-8555, Japan. e-mail: 174d8505@st.kumamoto-u.ac.jp*
2 *Professor, Department of Mechanical System Engineering, Kumamoto University, Kurokami, 2-39-1, Kumamoto 860-8555, Japan. e-mail: torii@mech.kumamoto-u.ac.jp*

ABSTRACT: The boiler of research is an electrode type electric boiler which heats electricity directly to water and heats it. However, it is a special boiler having a plurality of electrodes. Efficiency and superheat degree are important factors for evaluation. The main purpose of this research is to investigate these things. It also heats in a new way. So, it needs to be investigated the internal situation. This boiler can generate steam and hot water steadily with high efficiency. Steam is generated even under 100[℃], and it inhibits current flow. But even then, it can be heated enough. Therefore, this boiler is practical.
***Keywords**: Boiler, Electrode, Electric, Steam*

INTRODUCTION

There are electric boilers as one of high efficiency energy apparatuses. Electric boilers do not exhaust carbon dioxide other boilers. In addition, electric boilers do not have exhaust heat loss because they assume electricity a heat source. From this, electric boilers have been used for various purposes. For example, central heating system, house hot water supply device and high pressure steam washing.
This electric boiler has a new heating method that uses water as a heat source by flowing electricity to water. The boiler consists of a tank that stores water, a pump, two heating tanks with electrodes, and a valve that regulates flow rate or pressure. T The purpose of this experiment is to examine the condition during heating and evaluate the performance.

Method

The schematic of the electric boiler used in this research is shown in Fig.1.
The system consists mainly of two heaters including a water tank, a motor, and an electrode group.
This device is heated by electrode group.
The electrode group generates Joule heat by passing electricity of three phases 200 [V] to liquid water.
Because the liquid water generates heat, it is not necessary to have the heating part like a hot wire type.

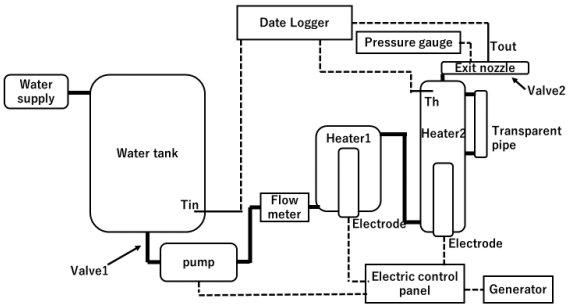

Fig.1 Schematic of electric boiler

This research product produces steam when it is less than a constant flow rate, and generates hot water when it is high. Therefore, experiments are carried out at various flow rates and compared. The experimental flow rates are 2.3[L/min],

2.4[L/min], 3.6[L/min] 4.0[L/min], 4.9[L/min], 7.4[L/min], 8.5[L/min] and 8.6[L/min].
Also, in order to investigate the inside, a transparent acrylic pipe was attached to the heater2 for visualization.

Equations
The electric energy sent from the generator is obtained by the following equation. E is the voltage, and I is the current.

$$W = \sqrt{3} \times E \times I \quad (1)$$

The thermal energy given by the boiler is obtained by the following formula. m is the mass flow of water, h_2 is the specific enthalpy of hot water or steam, and h_1 is the specific enthalpy of water.

$$Q = (h_2 - h_1)m \quad (2)$$

The Efficiency is obtained by the following formula.

$$\mu = \frac{Q}{W} \times 100 \quad (3)$$

The degree of superheat is obtained by the following formula. Tout is temperature of released water. T_b is boiling point.

$$\Delta T = Tout - T_b \quad (4)$$

The Joule heat is obtained by the following formula. R is electric resistance value. T is time.

$$Q_J = \frac{E^2}{R}t \quad (5)$$

Result and discussion
Temperature of released water at each flow rate is shown in Fig.2. The horizontal axis represents elapsed time, and the vertical axis represents temperature of released water.
It also has a stable temperature in about 100 seconds. It is early until steady state is reached.

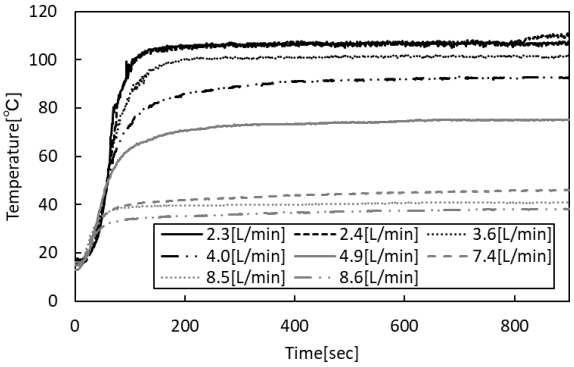

Fig.2 Temperature of all flow rate

The degree of superheat at each flow rate is shown in Fig.3.
The horizontal axis represents elapsed time, and the vertical axis represents degree of superheat.
The lower the flow rate, the higher the degree of superheat.
However, this research product can not produce electricity without liquid water, so it can not make superheated steam inside the heater.
Therefore, the degree of superheat is 0 [℃] at maximum.
When the flow rate is 2.3 [L/min], 2.4 [L/min], 3.6 [L/min], the degree of superheat is 0 [℃]. This means that it is wet steam or saturated water.

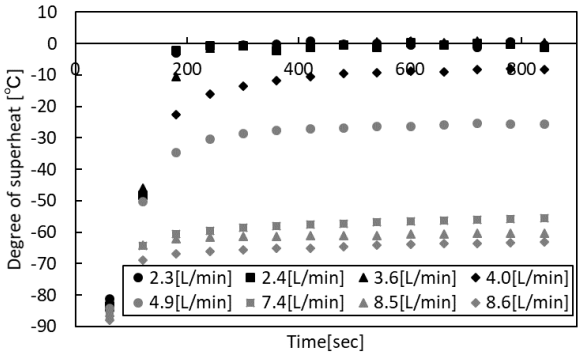

Fig.3 Degree of superheat

Fig.4 and Fig.5 are photographs of visualized acrylic pipe.

Clearly wet steam is generated when the flow rate is 2.4[L/min].
At 3.6[L/min] the degree of superheat is 0 [℃], no steam is generated.
Therefore, it can be inferred that there is a factor hindering the generation of steam.
If steam is generated near the electrode, the steam hinders the flow of electricity.
Therefore, when the flow rate is 2.4 [L/min], it is considered that the following two states are repeated. Fig.6 shows how the current flows.
(Condition: 1) The generated steam hinders the flow of electricity and heat input is decreasing.
(Condition: 2) There is only liquid water, heat input has returned to its original value.
When steam is generated, heat input drops, preventing generation of steam.
Therefore, it is considered that steam did not appear in the visualized part.

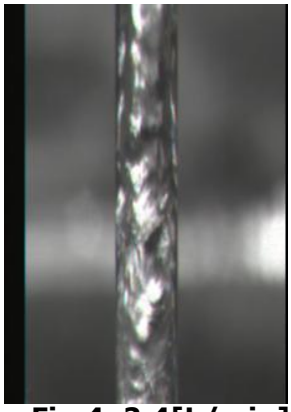

Fig.4 2.4[L/min]

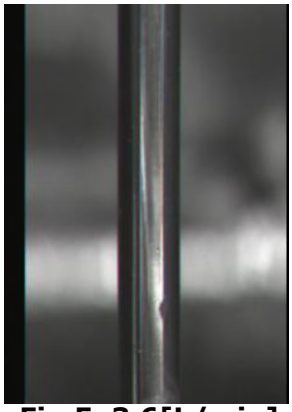

Fig.5 3.6[L/min]

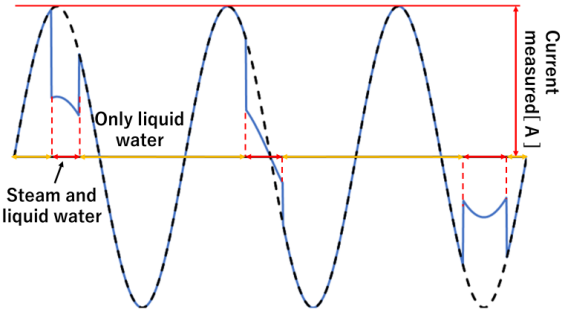

Fig.6 How current flows

Table 1 shows a part of the results of experimental heat input, heat release and efficiency.

When the flow rate is 4.0 [L/min], 4.9 [L/min], 7.4 [L/min], 8.6 [L/min], the lower the flow rate, the greater the heat input.
As the temperature of the liquid water increases, the resistivity decreases. Since the voltage is sent from the generator at 200 [V], the higher the temperature of Tout, the higher the heat input. This is shown by equation (5).
When the flow rate is 4.0 [L/min], the efficiency is lower than the others. This is considered to be caused by temporary generation of steam in the vicinity of the electrode even if the degree of superheat is less than 0 [℃]. That is, it is the state of fig.6.As a result, the current is overestimated. Since the heat input value is calculated to be larger than the actual value, it is considered that the efficiency is calculated low.
Therefore, it is considered that the actual efficiency exceeds 95% in the same way as other experiments.

CONCLUSIONS

The following conclusions are deduced from this study:

- Steam and hot water can be generated steadily and the time to reach steady state is also very short.
- When the flow rate is lowered, the temperature of the discharged water rises.
- Because superheated steam can not be made, the maximum degree of superheat is 0 [℃].
- Reduce flow rate increases heat input. However, when steam is generated in the vicinity of the electrode, the heat input drops.
- The heat input when steam is generated near the electrode may be measured higher than the actual value. Energy efficiency is considered to exceed 95% regardless of the current pattern.

REFERENCES

[1] Akira Kimura, Makihito Kimishima, Naoei Sasaki, Kotaro Tanaka, Yasuyuki Nemoto, Jun Yamada (2014), The way of thinking and how to use by
[2] Haruhiko Yamanaka, Tetsuya Maekima, Yuuto Terumanuma, Kazuhiro Watanabe, Mieko Kashiwagi,

Sumiya Hanada (2014), Measurement of Resistivity Change Characteristics of Pure Water in High Temperature Region, JAEA-Technology 2014-037, pp9.
[3] Japan Boiler Association (1967), Boiler structure, pp131-132.
thermodynamics case, pp170.
[4] Ministry of Economy, Trade and Industry, Agency for Natural Resources and Energy(2015),Annual report on energy in 2015
Website:
http://www.enecho.meti.go.jp/abot/whitepaper/2016 html
[5] Ministry of Economy, Trade and Industry, Agency for Natural Resources and Energy(2018),Annual report on energy in 2018
Website:
www.enecho.meti.go.jp/about/whitepaper/2018pdf/
[6] Miyoshi Hayashi, Yasuhiro Aoki, Hiroaki Sasaki (1999), A Study on Electric Heating in Cold Houses Part 2 Heating System with Electric Boiler, pp975-976.
[7] Tsunekazu Kobayashi (1967), Easy-to-use machine course Boiler and steam turbine, pp55.
[8] Yoshifumi Amemiya (1989), Engineering basic electrical engineering, pp12.
[9] Yu. P. Belyakov and A. G. Zyranov (1993), ADVANTAGE OF HEAT SUPPLY TO CONSUMERS FROM ELECTRIC BOILER HOUSE FED FROM HYDROELECTRIC STATIONS, Gidrotekhnicheskoe Stroitel' No.4, pp 34-36.

Table 1 Efficiency

Flow rate[L/min]	2.3	2.4	3.6	4.0	4.9	7.4	8.5	8.6
State	Wet steam	Wet steam	Wet steam	Hot water	Hot water	Hot water	Hot water	Hot water
Tin[°C]	15.5	15.1	15.8	15.7	14.9	15.3	14.8	13.7
Current[A]	66.5	60.5	71.6	69.5	61.5	47.3	45.5	43.5
Input energy[kW]	23.0	21.0	24.8	24.1	21.3	16.4	15.8	15.1
Output energy[kW]	-	-	-	21.5	20.5	15.7	15.3	14.1
Efficiency[%]	-	-	-	89.4	96.4	95.7	97.1	96.7

8th International Engineering Symposium - IES 2019
March 13-15, 2019, Kumamoto University, Japan

Experimental Study of Graphene Oxide Nanofluid Effect on Thermal Performance of Heat Pipe

Masatoshi Matsumura [1] and Shuichi Torii [2]

1 *Department of Mechanical System Engineering, Kumamoto University, Kurokami, 2-39-1, Kumamoto 860-8555, Japan. email:179d8556@st.kumamoto-u.co.jp*
2 *Department of Mechanical System Engineering, Kumamoto University, Kurokami, 2-39-1, Kumamoto 860-8555, Japan. e-mail:torii@mech.kumamoto-u.ac.jp*

ABSTRACT: Recent study, by using nanofluid to transfer heat, improve the thermal conductivity of heat transfer fluids. [1],[2] Improvement in heat transfer performance of nanofluids has been confirmed, but some problems have also been reported. [3] In this study, graphene oxide nanofluid is used as working fluid. Graphene oxide nanofluid was prepared by Hammers method. The purpose of this study is possibility of using nanofluid as a next generation working medium such as air conditioning equipment. It was revealed that the thermal resistance of graphene oxide nanofluid is reduced compared to pure water.

Keywords*: nanofluid, graphene oxide, thermal resistance, heat pipe*

INTRODUCTION

In various industrial fields such as power generation and air conditioning, conventional working medium such as water and oil is used as a refrigerant of the cooling device. But their heat transfer performance is not so high at present. If such a heat transfer performance of fluid for a refrigerant can be enhanced, it is possible to realize downsizing and high efficiency of the whole device by reducing the area required for heat transfer. In the past, research has been conducted to improve the heat transfer performance of the working medium by using a method of suspending solid fine particles in a working medium.[1] This is because solid fine particles have higher heat transfer performance than water that. And by suspending the solid fine particles in the working medium, the heat transfer performance of the whole fluid is enhanced. In such experiments, it became clear that oxides such as alumina (Al_2O_3) and copper oxide (CuO) with water, oil and ethylene glycol have superior dispersion characteristics and have excellent stability. However, when these researches were previously conducted, some heat transfer performance improvement was observed because particle size of millimeter order or micro order were used. But problems of the flow path, that is, wear of the apparatus and loss of pressure occurred. So it was not put into practical use.[2]

In recent years, nanotechnology advanced and even finer particles "nanoparticles" than microparticles were developed. Nanoparticles are defined as particles with a particle size of 100 nm or less. In the field of thermal engineering, it is desirable to use particles with enormous total surface area because heat transfer occurs on the surface of the particles. Nanoparticles in working medium have bigger area than milli-microparticles. In the case of the same volume, the surface area of the particle is 1,000 times larger for particles with a diameter of 10 nanometer than for particles with a diameter of 10 micrometer. Also, as the particle size becomes nano size, the problem which occurred at the time of millimeter and micrometer was alleviated. The very large surface area of nanoparticles compared with conventional particles not only improves the heat

transfer performance but also increases the stability of the suspension. These nanoparticles suspended in water are called "nanofluid"[3]. It has been found that nanofluids have higher heat transfer characteristics than conventional working media. Various kinds of nanofluids such as alumina nanofluid and copper oxide nanofluid exist. And graphene oxide nanofluid which is suspended in water with graphene oxide can be used as a material for alumina nanofluid and copper oxide nanofluid. It shows relatively high heat transfer characteristics compared to other nanofluids.[5],[6],[7],[8],[9] However, since that results so far have been studied for the case without the phase change, there is doubt about the case where the working medium undergoes a phase change like an air conditioner. Therefore, in this study, we experimentally investigated the change of heat transfer properties before and after phase change using graphene oxide nanofluid. Also, we will clarify the degree of improvement compared to the case of pure water. Graphene oxide nanofluid used in this study, volume fraction of 1 vol% purified by the graphene oxide purification method called the Hummers method. Experimental studies on heat transport performance on phase change will become clear the possibility of air conditioning equipment etc. as a next generation working medium.

GRAPHENE OXIDE

Graphene oxide has a sheet shape, and its thickness is about 1 nm. In addition, raw material graphite is inexpensive, abundantly present and easy to obtain materials. Fig. 1 shows the molecular structure of graphene oxide. The particles of graphene oxide have a sheet-like structure formed by carbon atoms being bonded to each other by an sp2 hybrid orbital and the bonded carbon forms a hexagonal lattice structure and its shape is continuously arranged. Production method of graphene oxide nanofluids differ from alumina nanofluids and copper oxide nanofluids which produced using the PVS method (Physical Vapor Synthesis[4]. In the PVS method, firstly, a raw material (metal) is generated as a vapor of metal atoms by thermal energy, and molecules of metal oxide and clusters are formed by contact with reaction gas (oxygen). After that, it is instantly cooled to produce ultrafine particles that suppress the increase in particle size. As a method for preparing graphene oxide, there is a Hummers method. First, graphite is oxidized and dried to produce sheet-like graphite oxide. Then Graphite oxide separate ultrasonically in a solvent and peeling of each layer one by one. As a method for preparing graphene oxide, Brodie method can be also used. But it includes a chemical reaction which risks explosion in the manufacturing process. In this research, graphene oxide nanofluid was fabricated using Hummers method because of its safety.

The initial volume fraction of the graphene oxide nanofluid used in this experiment was about 0.1 vol%. In addition, the volume fraction of the graphene oxide nanofluid prepared by using decompression boiling on a stirrer was about 1 vol%. The Hummers method is a method that is difficult to reproducibly. It changes the size, nature of the particles, the concentration of the fluid and the like occur depending on various conditions such as the reaction temperature and reaction time. Also, the volume fraction of the graphene oxide nanofluid calculated by comparing the weights before and after the droplet was dried using a moisture content measuring device. As a result of the measurement, it was found that the volume fraction of the graphene oxide nanofluid produced this time is 0.1 vol% and 1 vol%. Since the particle density of graphene oxide has not been clarified, the volume fraction was calculated using the density of graphite (2260 kg / m^3).

Alumina and copper oxide nanofluids are classified as dispersion colloids. Dispersion colloid is a thermodynamically unstable system, and particle agglomeration and sedimentation are likely to occur. Also, graphene oxide nanofluid is classified as molecular colloid. The graphene oxide particles are macromolecules, and most of the molecules contained in the fluid are 1 nm in size. Molecular colloid is thermodynamically stable due to

dissolution of macromolecules and high dispersibility in solvent.

Equations

When the temperature of the liquid on the heating surface is higher than the saturation temperature corresponding to the pressure of the liquid, a phenomenon called boiling occurs. At that time, the phenomenon that heat is transferred from the heating surface to the liquid is called boiling heat transfer. Also, when steam comes in contact with a solid surface at a temperature lower than the saturation temperature, a phenomenon called condensation occurs, and steam releases latent heat and heat is transferred to the cooling surface. The temperature difference of the liquid in this boiling heat transfer and condensation heat transfer can be expressed by the difference between the saturation temperature corresponding to the pressure of the liquid and the temperature of the liquid. Therefore, thermal resistance at boiling heat transfer and condensation heat transfer is expressed by the following equation (1). $\overline{T_{eva}}$ is average temperatures in the heating section and $\overline{T_{con}}$ is average temperature in the cooling section.

$$R = \frac{\overline{T_{eva}} - \overline{T_{con}}}{Q} \quad (1)$$

Heat transfer between the solid surface and the fluid is effected by convection of the fluid. Assuming that the area of the solid surface in contact with the fluid (heat transfer area) A [m^2], the temperature there is T_w [K], and the temperature of the fluid is T_b [K] and the amount of heat transfer Q [W] is expressed by the equation (2).

$$Q = \alpha(T_w - T_b)A \quad (2)$$

As the value of the heat transfer coefficient h[W/(m^2·K)] defined by this equation increases, the heat transfer amount also increases. If the fluid flows along a high temperature solid surface, heat is transferred to the fluid in contact with the solid. The heat is transferred in the direction perpendicular to the solid surface by heat conduction and fluid motion within the fluid. Part of the heat is transferred by the flow in a direction parallel to the solid surface. Since there is no speed in the fluid in contact with the solid surface, here heat is transferred only by thermal conduction. Therefore, the heat transfer amount q_x [W/m^2] per unit area and unit time is expressed by the formula (3) from the Fourier's law.

$$q_x = \frac{dQ_x}{dA_x} = -\alpha\left(\frac{\partial T}{\partial y}\right)_{y=0} \quad (3)$$

Therefore, if the temperature distribution T_x (y) in the y direction of the fluid at an arbitrary position x is known, the heat transfer amount q_x and the heat transfer coefficient α_x at the point x on the solid surface are determined. When Equation (2) is applied to a certain position x, it is expressed by the following equation (4).

$$q_x = \frac{dQ_x}{dA_x} = \alpha_x(T_{wx} - T_{bx}) \quad (4)$$

A_x defined by equation (4) is called the local heat transfer coefficient. Actually, it is sometimes desirable to know the heat transfer amount Q [W] from the entire solid surface. Therefore, considering the average value for the entire heat transfer surface of the area A [m^2], it is expressed by the equation (5).

$$q = \frac{Q}{A} = \alpha(T_w - T_b) \quad (5)$$

Here, T_w [K] is the average value of the heat transfer surface temperature, and T_b [K] is the average value of the fluid temperature. Using the formula (5), the heat transfer coefficient h[W/(m^2·K)] of the heating section can be expressed by the following equations (6).

$$h = \frac{q}{\overline{T_{eva}} - \overline{T_{con}}} \quad (6)$$

Fig. 2 shows a schematic diagram of the experimental equipment used for this experiment to investigate heat transfer characteristics of graphene oxide nanofluid.

Estimated uncertainty using these formulas following Kline's thesis[10]. The uncertainty of each measuring instrument is Table 2. The formula used for calculation is as follows.

$$\frac{\Delta Q}{Q} = \left[\left(\frac{\Delta V}{V}\right)^2 + \left(\frac{\Delta I}{I}\right)^2\right]^{\frac{1}{2}} \quad (7)$$

$$\frac{\Delta R}{R} = \left[\left(\frac{\Delta Q}{Q}\right)^2 + \left(\frac{\Delta(\Delta T)}{\Delta T}\right)^2\right]^{\frac{1}{2}} \quad (8)$$

$$\frac{\Delta h}{h} = \left[\left(\frac{\Delta q}{q}\right)^2 + \left(\frac{\Delta(\Delta T)}{\Delta T}\right)^2\right]^{\frac{1}{2}} \quad (9)$$

(ΔR/R) estimated 5.0%, and (Δh/h) estimated 5.4%

Experimental method

The experimental equipment consists of a cooling device (M & S Instruments Trading Inc. NESLAB RTE – 221), a voltage regulator (YAMABISHI VOLT – SLIDER S – 130 – 20), a data logger (KEYENCE NR – 250), an electromagnetic flowmeter (KYENCE FD – 81 SO (2440)), a small magnet pump (IWAKI MD – 20RM – N), a voltmeter (YOKOGAWA), a vacuum pump, a pressure gauge, a stainless pipe, a heat insulating material, a thermocouple and a water tank.

In the test section, the wall temperature of the outer wall was measured using K-type thermocouple, four in the evaporator section, two in the adiabatic section and three in the cooling section. Also, a water temperature was measured by attaching a K type thermocouple to the cooling water inlet and outlet of the condenser section.

Fig. 3 Shows a schematic drawing of the test part and the mounting position of the thermocouple. A stainless pipe having a length L = 300 mm, an outer diameter D = 9.5 mm, and a wall thickness t = 0.5 mm was used as the test part. Out of the total length L = 300 mm, the evaporator section was set to 85 mm, the adiabatic section was set to 95 mm, and the condenser section was set to 120 mm. Electrodes for applying a voltage are soldered to both ends of the heating section. In order to reduce the heat loss, the heating part is surrounded by heat insulating material. A thin stainless pipe with high electric resistance was used for the test part including the heating part. Thermocouples are all K type thermocouples and distances from the lower end of the test part are T_1: 10 mm, T_2: 35 mm, T_3: 60 mm, T_4: 85 mm, T_5: 115 mm, T_6: 160 mm, T_7: 185 mm, T_8: 240 mm, T_9: 295 mm. Since the temperature becomes high, the temperature sensitive part is used molded type(insulating type) so that the error due to the surrounding influence did not become large. The experiment was conducted the conditions shown in the table 1.

In this experiment, the evaporator part and the adiabatic part are covered with a heat insulating material in order to minimize the influence and error due to the ambient temperature to the measured temperature of the testing part of the experimental apparatus as much as possible. Also, in order to eliminate the measurement error of each thermocouple, before heating the test section, observe the temperature indicated by each thermocouple and measure the temperature of each thermocouple so that they match the inflow temperature of the fluid was corrected.

RESULTS

This experiment was repeated three times and the average was obtained. In this study, thermal resistance and heat transfer coefficient were calculated from values obtained by experiments. And the heat transfer performance on phase change of graphene oxide nanofluid was evaluated. The results of thermal resistance and heat transfer coefficient of the graphene oxide nanofluid measured this time are shown below. Using the calculation formula (1), it is shown in Fig.4 compares thermal resistance with thermal resistance on the vertical axis and thermal load on the horizontal axis. Fig. 5 compares heat transfer coefficient on the vertical axis and heat load on the horizontal axis and compares heat transfer coefficient. Fig. 4 shows that the heat transfer coefficient of graphene oxide nanofluid decreased compared to pure water.

CONCLUSIONS

The purpose of this research is to obtain the thermal resistance and heat transfer coefficient of graphene oxide nanofluid and to clarify whether there is improvement in comparison with pure water. Experimental research on heat

transfer performance on phase change of graphene oxide nanofluid revealed the following.

The following conclusions are deduced from this study:

- The thermal resistance of heat transfer of graphene oxide nanofluid is lower than that of pure water.
- The heat transfer coefficient of graphene oxide nanofluid is higher than that of pure water.

From the above, it became clear that graphene oxide nanofluid has excellent heat transfer performance even on the phase change.

REFERENCES

[1] Maxwell, J.C. (1881): "A Treatise on Electricity and Magnetism, 2nd Ed.". *Clarendon Press*, Oxford, U.K., vol.1, ,pp.435.

[2] S. Zeinali Heris, S.Gh. Etemad., M. Nasr Esfahany (2006): "Experimental investigation of oxide nanofluids laminar flow". *Convective heat transfer International Communications in Heat and Mass Transfer*, Vol.33 pp.529–535.

[3] Choi,U.S. (1995): "Enhancing thermal conductivity of fluids with nanoparticles". *ASME FED* Vol.231, pp. 99–103.

[4] P.Y. Wang, X.J. Chen, Z.H. Liu, Y.P. Liu. (2012): "Application of nanofluid in an inclined mesh wicked heat pipes". *Thermochim. Acta*, 539, pp. 100–108.

[5] H. Q. Yang, T. Kim, T. J. Lu, and K. Ichimiya (2009): "Flow structure, wall pressure and heat transfer characteristics of impinging annular jet with/without steady swirling,". *Int. J. Heat Mass Transf.*, Vol. 53, no. 19–20, pp. 4092–4100.

[6] Kyung Mo Kim, In Cheol Bang. (2016): "Effects of graphene oxide nanofluids on heat pipe performance and capillary limits". *International Journal of Thermal Sciences*, Vol. 100, February, Pages 346–356.

[7] Kyu Hyung Doa, Hyo Jun Hab, Seok Pil Jang. (2010): "Thermal resistance of screen mesh wick heat pipes using the water-based Al2O3 nanofluids". *International Journal of Heat and Mass Transfer*, Vol 53, Issues 25–26, December, pp.5888–5894.

[8] C.Y. Tsaia, H.T. Chiena, P.P. Dingb, B. Chanc, T.Y. Luhd, P.H. Chen. (2004): "Effect of structural character of gold nanoparticles in nanofluid on heat pipe thermal performance". *Materials Letters*, Vol 58, Issue 9, March, pp.1461–1465.

[9] M. Kole, T.K. Dey. (2013): "Thermal performance of screen mesh wick heat pipes using water-based copper nanofluids". *Appl. Therm. Eng*., Vol. 50, pp. 763–770.

[10] Kline, S.J., and McClintock, F.A., (1953), Describing Uncertainties in Single-Sample Experiments, Mechanical Engineering, Vol.75

Table 1 Experimental conditions

Pressure (Mpa)	0.011
Heat load (W)	20,30,40,50
Wick type	120 mesh/inch SUS304
Cooling temperature (℃)	20±1

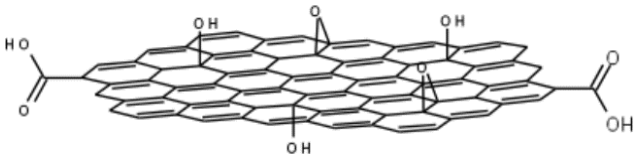

Fig.1 Structure of Graphene oxide

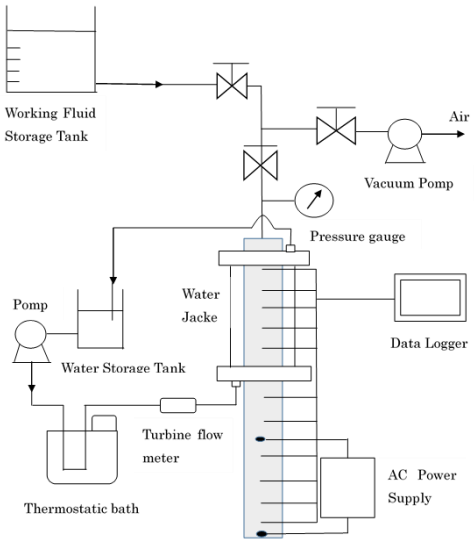

Fig.2 Experimental equipment

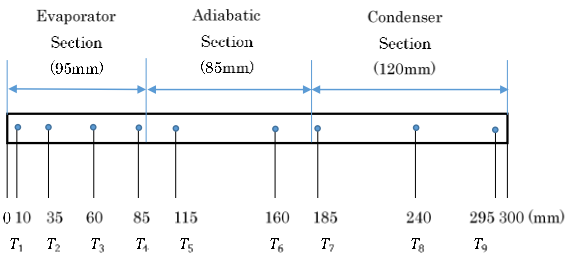

Fig. 3 Test section

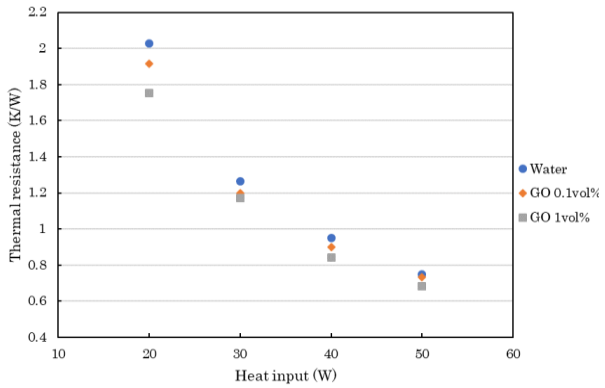

Fig. 4 Thermal resistance

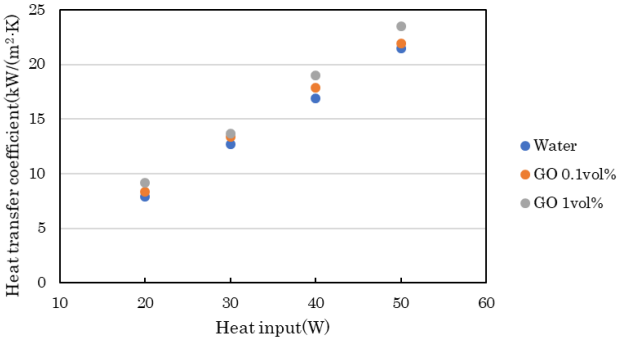

Fig. 5 Heat transfer coefficient

Table2 Uncertainties

Parameter	**Instruments**	**Uncertainties**
Temperature	**Thermocouples**	**0.1%**
Voltage	**Voltmeter**	**0.3%**
Current	**Amperometry**	**0.3%**

8th International Engineering Symposium - IES 2019
March 13-15, 2019, Kumamoto University, Japan

Fabrication of Diamond Particles Coated Heating Surface by Underwater Shock Wave and Effect of Diamond Particles on Pool Boiling Heat Transfer

Kohei Hamahata [1], Shuichi Torii [2] and Shigeru Tanaka[3]

1 *Department of Mechanical System Engineering, Kumamoto University (GGST), Kurokami, 2-39-1, Kumamoto 860-8555, Japan. e-mail: 170d8547@st.kumamoto-u.ac.jp*
2 *Department of Mechanical System Engineering, Kumamoto University, Kurokami, 2-39-1, Kumamoto 860-8555, Japan. e-mail:torii@mech.kumamoto-u.ac.jp*
3 *Institute of Pulsed Power Science (IPPS), Kumamoto University, Kurokami, 2-39-1, Kumamoto 860-8555, Japan. e-mail: tanaka@mech.kumamoto-u.ac.jp*

ABSTRACT: In recent years, heat transfer performance needs to be enhanced because of the heat generation of integrated circuits with improved performance of digital equipment. The microfabrication of heating surface is one of the ways to promote boiling heat transfer. In our research, we tried to promote boiling heat transfer by diamond particles coated heating surface (DPC heating surface). In this study, diamond particles (8-20μm) were embedded in copper block surface by using the underwater shock wave of explosion. From the results of the boiling experiments, it was confirmed that the heat transfer coefficient of the diamond particles coated heating surface in the heat flux = 400 kW/m^2 increased to 1.33 times as compared with smooth heating surface.

***Keywords**: Boiling heat transfer, Diamond particle, Underwater shock wave*

INTRODUCTION

Boiling heat transfer is a heat transfer phenomenon in which boiling bubbles carry thermal energy on the heating surface by phase change. The boiling heat transfer is larger than other heat transfer phenomenon. Many Industrial products such as air-conditioner use it. In recent years, heat transfer performance needs to be enhanced because of the heat generation of integrated circuits with improved performance of digital equipment. The microfabrication of heating surface is one of the ways to promote boiling heat transfer. And it is currently being actively studied [1]. In addition, there are other methods to promote boiling heat transfer, such as the use of nanoflows and alternative CFCs [2] [3]. Boiling bubbles usually generate from the cavity of scratches and cracks on a smooth surface. Boiling bubbles are generated efficiently by increasing the number of artificial cavities with microfabrication of the heating surface and boiling heat transfer is promoted. In our research, we tried to promote boiling heat transfer by diamond particles coated heating surface (DPC heating surface). Diamond has high thermal conductivity and excellent mechanical properties such as wear resistance. In addition, it is considered that boiling heat transfer is promoted by providing the microstructure of diamond particles on the heating surface. Conventionally, it is difficult to manufacture a composite material of diamond and metal by heat treatment or bonding. Therefore, in this study, diamond particles (8-20μm) were embedded in copper block surface by using the underwater shock wave of explosion.

FABRICATION OF DPC COPPER BLOCK

In this study, diamond particles were embedded in copper block surface by using the underwater shock wave of explosion. Fig.1 shows method of coating diamond particles on heating surface. This experimental apparatus was composed of explosive, electric detonator, copper block, diamond particles, stainless steel plate and a sealing vinyl tape. The underwater shock wave of explosion impinges on the steel plate, and the diamond particles is coated on the surface of upper part of the copper block. The experimental conditions as shown in table 1. The experiments were conducted with three explosive attachment distances (D=10, 20, 30mm) as the experimental conditions.

Observation results of DPC surface

The observation results of DPC copper block surface are shown in Fig.2. From Fig.2(b), it is observed on the DPC surface of explosive attachment distance D=10mm that diamond particles were adhered to each other without gaps and successfully bonded. From Fig.2(c), it is observed that diamond particles adhered on the DPC surface (D=20mm) were less amount than the DPC surface (D=10mm). From Fig.2(d), it is observed that diamond particles adhered on the DPC surface (D=30mm) were adhered less amount than the DPC surface (D=10mm) and the DPC surface (D=20mm). Therefore, it was confirmed in fabrication of DPC surface by underwater shock wave that if the explosive attachment distance was smaller, the adhesion amount of the diamond particles on the copper surface increased more. The relationship between the explosive attachment distance and diamond particles adhesion density or peak pressure by underwater shock wave is shown in Fig.3. Where, particle adhesion density is the number of adhered diamond particles per unit area. From Fig.3, it was confirmed that the particle adhesion density and the peak pressure decreased exponentially in accordance with the value of the explosive attachment distance D increased.

Boiling Experimental Method

In this experiment, the boiling condition is saturated pool boiling under atmospheric pressure. The boiling experimental apparatus is shown in Fig.4. This experimental apparatus was composed of boiling vessel, plastic ball, auxiliary heater, DPC copper block, ceramic heater, insulation and voltage converter. In addition, K type thermocouple and data logger used for measurement. The DPC copper block and the ceramic heater were adhered with thermally conductive adhesive. Distilled water was boiled and well degassed for 40 minutes using the auxiliary heater. And, thermal energy is transferred from the upper part of DPC copper block by heat input with the ceramic heater. At this time, the temperature of the saturated water and internal temperature of copper block were recorded using the K type thermocouple and the data logger. Furthermore, details of the experimental conditions are shown in Table 2.

Evaluation Value Equation

The detail of Heating surface is shown in Fig. 5. The heat flux q W/m^2 in boiling heat transfer is given by Eq.1.

$$q = -\lambda \frac{dT}{dx} \quad (1)$$

Where, λ is the thermal conductivity [W/(m·K)] of the copper, T is the internal temperature [K] of copper block , and x is the arbitrary position [m] in the heat transfer direction.

The surface temperature T_W [K] of the heating surface is given by the Eq.2.

$$T_W = T_1 - \frac{q}{\lambda} l \quad (2)$$

Where, T_1 is the internal temperature [K] of the copper block measured at the position closest to the heating surface and l is the length [m] of the thermocouple1 to the heating surface.

The degree of superheat ΔT [K] is given by Eq.3.

$$\Delta T = T_W - T_S \quad (3)$$

Where, T_S is the saturation temperature [K] of water.

The heat transfer coefficient h [W/(m^2·K)] is given by Eq.4.

$$h = \frac{q}{\Delta T} \quad (4)$$

Effect of DPC Surface on Boiling Heat Transfer

The relationship between the degree of superheat ΔT and the heat flux q is shown in Fig.6. According to Fig.6, it was confirmed that boiling heat transfer was promoted by diamond particles coated on the heating surface. It is assumed that this result was got because the artificial cavity increased by diamond particles and boiling bubbles were generated efficiently. In addition, it was confirmed that boiling heat flux increased in accordance with the particle adhesion density more increased. In the DPC heating surface (D=10mm), it can be considered that the saturated water was efficiently supplied to the boiling bubble generation point and boiling heat transfer was most promoted because the capillary force was improved by adhesion of diamond particles.

The relationship between the heat flux q and the heat transfer coefficient h is shown in Fig.7. According to Fig.7, it was confirmed that the heat transfer coefficient of the diamond particles coated heating surface increased in 1.16 times at the q=200 kW/m^2, 1.27 times at the q=300 kW/m^2 and 1.33 times at the q=400 kW/m^2.

CONCLUSIONS

The following conclusions are deduced from this study:

- Diamond particles were adhered to each other without gaps and successfully bonded in the DPC surface of explosive attachment distance D=10mm.
- Fabrication of DPC surface by underwater shock wave that the explosive attachment distance was smaller, the adhesion amount of the diamond particles increased more on the copper surface.
- Boiling heat transfer was promoted by diamond particles coated on the heating surface.
- Boiling heat flux increased in accordance with the particle adhesion density more increased.
- Heat transfer coefficient of the diamond particles coated heating surface increased in 1.33 times at the q=400 kW/m^2.

REFERENCES

References should be given in alphabetical order. (font to be used: Verdana 8)

[1] D. Eok et al., "Review of boiling heat transfer enhancement on micro/nanostructured surfaces", Experimental Thermal and Fluid Science, Vol.66, pp.173-196, 2015.

[2] D.W. Zhou, "Heat transfer enhancement of copper nanofluid with acoustic cavitation", *International Journal of Heat and Mass Transfer*, Volume 47, Issues 14–16, pp.3109-3117, July 2004.

[3] Hitoshi Matsushima and Takuya Saitou, "Heat transfer characteristics of pool boiling under low pressure condition", *Thermal Science & Engineering* Vol.26, No.1, 2018.

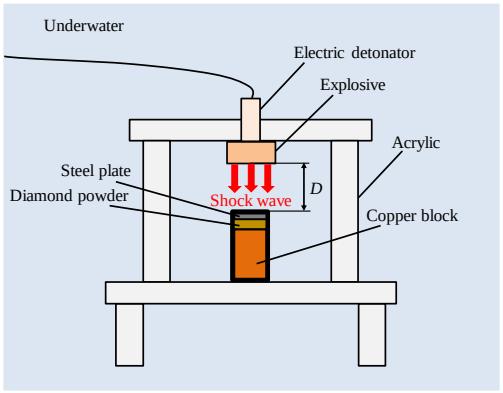

Fig.1 Fabrication method of DPC heating surface

Table 1 Fabrication conditions of DPC heating surface

Copper block size [mm]	15×15×25
Diameter of diamond particle [μm]	8~20
Diamond powder [g]	0.1
SEP explosive [g] (Manufactured by Asahi Kasei Co.)	3
Attachment distance of explosive D [mm]	10,20,30

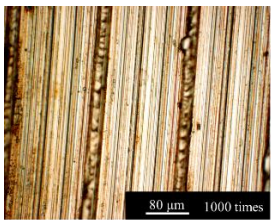

(a) Smooth surface

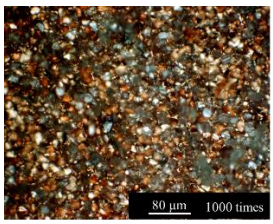

(b) D=10mm

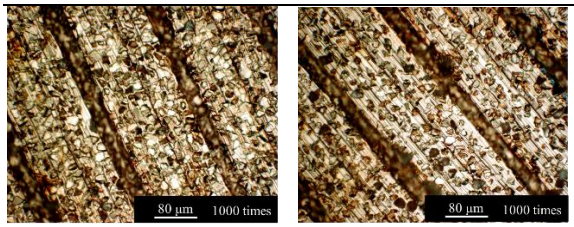

(c) D=20mm (d) D=30mm

Fig.2 Observation results of DPC surface

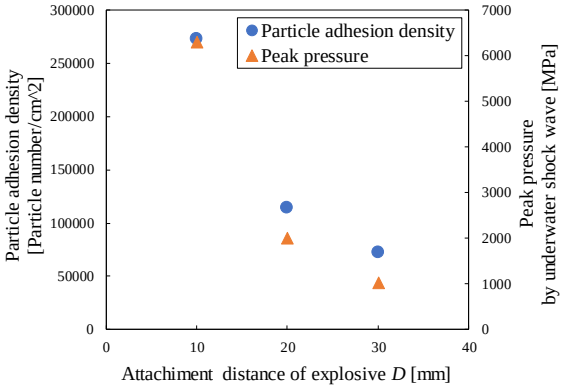

Fig.3 Relationship between the explosive attachment distance and diamond particles adhesion density or peak pressure

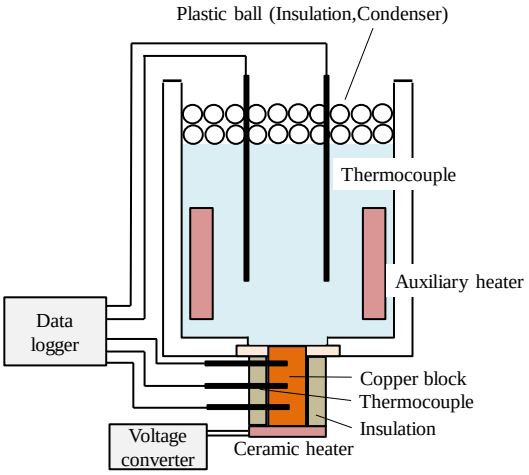

Fig.4 Boiling experimental apparatus

Table 2 Experimental conditions

Input power range [W]	10~90
Heat input of auxiliary heater [W]	200
Volume of saturated water [cm^3]	900~1100
Copper block size [mm]	10×10×17
Condition of heating surface D [mm]	10, 20, 30

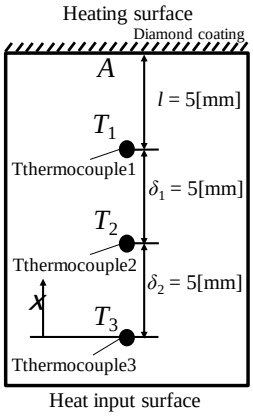

Fig.5 Detail of heating surface

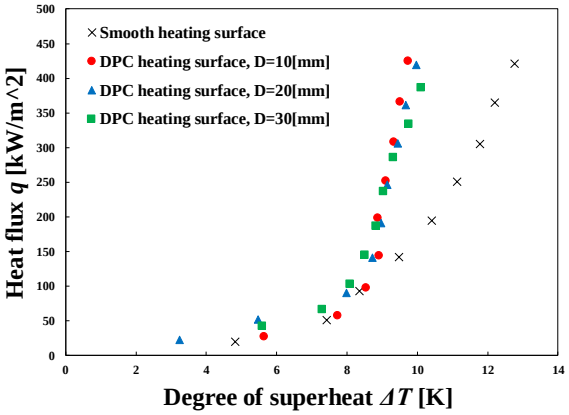

Fig.6 Relationship between the degree of superheat and the heat flux

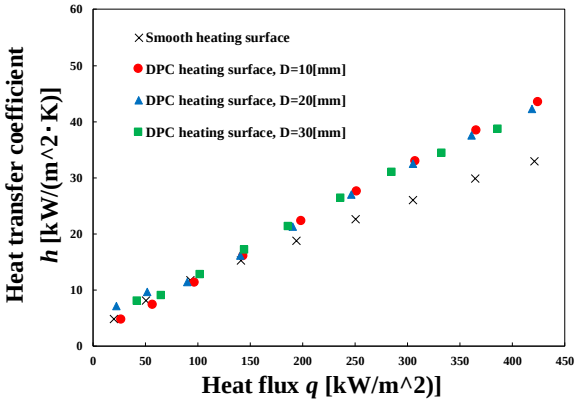

Fig.7 Relationship between the heat flux and the heat transfer coefficient

8th International Engineering Symposium - IES 2019
March 13-15, 2019, Kumamoto University, Japan

Simplified Gasification Simulation using Zero-Dimensional Model of Empty Palm Fruit Bunch

Priyambodo Nur Ardi Nugroho [1,2], and Shuichi Torii [1]

1 *Department of Advanced Mechanical System Engineering, Kumamoto University, Kurokami, 2-39-1, Kumamoto 860-8555, Japan.*
2 *Politeknik Perkapalan Negeri Surabaya, Jl. Teknik Kimia, Kampus ITS Sukolilo, Surabaya 60111, Indonesia. Email: priyambodo@ppns.ac.id*

ABSTRACT:
As one of the most efficient biomass conversions, the gasification process is hard to understand because of its complexity. A simplified gasification simulation using a zero-dimensional model was designed for empty fruit bunch considering its potential in Indonesia. A stoichiometric equilibrium model was applied to simulate the whole gasification process. Global gasification reaction, mass, and energy balance with two independent reactions are integrated to perform the model. Some sets of linear and non-linear equations were solved with the Newton Raphson method in Matlab. The output of the model like syngas composition and the heating value was validated with available experimental data published. Zero-dimensional thermodynamic equilibrium model could be used to predict the maximum performance of gasifier.

Keywords: *Biomass gasification, zero-dimensional model*

INTRODUCTION

Palm oil has been used for centuries ago. Originally from Africa, palm tree (*Elaeis guineensis*) has been naturalized in tropical countries since it grows even better. Palm tree produces crude palm oil (CPO) that could be used in a vast range from cooking oil to biodiesel. CPO become an internationally traded community and is very important for Indonesia as the largest CPO producer.

Along with Malaysia, over 20 million metric tons of CPO produced in the almost 10-million-hectare area. Maitah et al. (2016) reported that CPO production also generates a large amount of biomass. For every 1 kg of CPO, about 4 kg of biomass waste. Most of the waste is oil palm empty fruit bunch; the other is fronds and trunks. Gasification is the thermochemical process that converts carbonaceous material like coal or biomass into valuable gaseous fuel or chemical substance. The history of gasification could be traced back to 1659 when Thomas Shirley discovered gas from a coal mine. In 1739 Dean Clayton successfully distilled coal in a closed vessel followed by Robert Gardner patented its first gasification technique in 1788. According to Basu (2010), Biomass intended not only energy conversion but also the production of a chemical substance as one of the essential commodities.

Similar to gasification, combustion also changes carbonaceous material into product gases. However, there is distinctness like there is no useful heating value in the combustion product gas, in contrast to gasification that possesses beneficial heating value. Combustion release energy in its process, while gasification packs energy into compact chemical bonds. Combustion process occurred in an oxidizing environment and releasing heat, while gasification happened in inadequate oxygen surrounding and demanding heat.

The gaseous medium of gasification is involved in the process of converting either fossil or non-fossil fuel into valuable gaseous fuel or other chemicals. Gaseous mediums example is oxygen, air, steam or mixture of them. The reason behind transforming potential fuel into another form is to increase the heating value of the fuel by releasing non-combustible matter like nitrogen and water. Another motivation is to remove sulfur and nitrogen from the fuel so that this material will not be released into the atmosphere when burning the fuel. An additional motive is to reduce the proportion of carbon to hydrogen ratio in the fuel.

Generally speaking, the more hydrogen contents in the fuel, the lower the vaporization temperature and increases the likelihood of fuel become in the gaseous phase.

Biomass gasification converts solid state biomass into gaseous state fuel or chemicals. The chemical energy contained in the solid biomass is changed into the thermal and chemical energy of the gas. Hence the chemical energy within the product gas is a function of its chemical configuration. In other words, the quality of the product is driven by chemical composition. Htut et al. (2015) reported that the product of gasification is called the syngas in which CO and H_2 are the main gaseous species.

Forecasting performance using thermodynamic computations are commonly used to explain chemical reactions within the gasifier.

Performance prediction of a downdraft gasifier has been made by Zainal et al. (2001) using equilibrium modeling for some biomass materials like wood, paddy husk, paper, and municipal waste. It was found that the heating value of the syngas decrease along with increasing gasifier temperature and also increase in moisture content.

Wu and Chein (2015) have worked on the modeling of biomass gasification with high-temperature inlet as a result of preheating. Combustible species reduction was acknowledged with more than a certain amount of biomass moisture content. Preheated air could enhance gasifier performance; however, the degree of significance was lower than expected.

Align with the great curiosity about the biomass gasification process; it is inevitable to model and foresee the gasifier performance before building the actual one. This paper aims to perform syngas composition and heating value analysis composed of the gasifier with a zero-dimensional equilibrium model.

MATERIALS AND METHODS

Gasification process designed in this paper is illustrated in Fig 1. Biomass enters the gasifier at temperature T_b, while air as the gasifying agent has temperature T_a and pressure P_a. Temperature and pressure inside the gasifier are T_g and P_g respectively. Syngas formed leaving the gasifier at temperature T_s and pressure P_s.

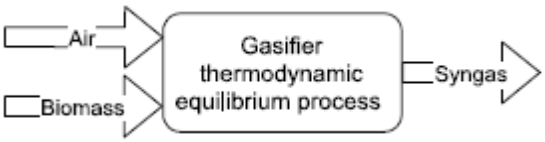

Fig.1 Gasification Process Illustration

Some assumptions according to Wu and Chein (2015) and Htut et al. (2015) were taken into consideration to simplify the analysis.

-thermodynamic equilibrium process and adiabatic (no heat transfer from and to the environment) happens in all gasification reactions.

-thermodynamics properties like temperature, pressure, and species concentration are uniformly distributed within the gasifier.

-steady-state condition is already achieved within the gasifier.

-Biomass from palm empty fruit bunch expressed as $CH_aO_bN_c$. a, b, and c is the number of atoms of hydrogen, oxygen, and nitrogen respectively, derived from the ultimate and proximate analysis in table 1.

-there is no solid carbon remaining after the gasification; all converted into syngas species in the global gasification model.

Table 1. Empty Fruit Bunch Ultimate and Proximate Analysis [8]

Component	%(Wt)	Element	%(Wt)
Volatile	77.46	C	61.51
Fixed Carbon	17.25	H	10.51
Ash	5.29	O	26.00
		N	1.98

-Syngas produced from the gasification process is consisting of H_2O, N_2, H_2, CO, CO_2, and CH_4. Ideal gas law applied to all of the syngas.
Model input required following information
-Biomass chemical composition ($CH_aO_bN_c$), biomass and air initial temperature derived from ambient temperature.
-average gasification equilibrium temperature ranging from 800 to 1000 ^{0}C
-an equilibrium constant (K) used in gasification reaction is from methane forming and water gas shift reaction.
-thermodynamic data for a chemical substance in gasification reactions like enthalpy for formation (H^o_f) and specific heat (C_p) taken from Perry (1984)

Model output is the syngas composition once the equilibrium state achieved, and the syngas heating value calculated from the syngas composition. Cold Gas Efficiency (CGE) and Efficiency (η) are the other two main parameters to determine gasification performance.

$$CGE = \frac{n_{H_2} HHV_{H_2} + n_{CO} HHV_{CO} + n_{CH_4} HHV_{CH_4}}{HHV_{Biomass}} 100\% \quad (1)$$

$$\eta = \frac{E_{product}}{E_{reactant}} = \frac{\Sigma n_i E_i}{E_B + e E_{H2O} + m E_{air}} . 100\% \quad (2)$$

Syngas heating value could be determined from bomb calorimeter, but also could be estimated with the calculation proposed by Reed (1985)

ΔH_c = HHV (kJ/kmol) = 0.2326(146.58 C + 56.878 H – 51.53 O – 6.58 A + 29.45) (3)

Where C, H, O and A are the mass fractions of carbon, hydrogen, oxygen, and ash, respectively, in the dry biomass.

Global biomass gasification for solid biomass $CH_aO_bN_c$ with air as gasification agent could be written with equation (4) below

$$CH_aO_bN_c + wH_2O + m(O_2 + 3.76N_2) \rightarrow n_1H_2 + n_2CO + n_3CO_2 + n_4H_2O + n_5CH_4 + n_6N_2 \quad (4)$$

Where the amount of water pe kmol of biomass is denoted as w, and amount of oxygen per kmol of biomass is denoted as m. The remaining coefficient of a constituent of products is marked as $n_{1\text{-}6}$. w could be calculated from moisture content per mol of biomass, so w become constant once moisture content was identified.
Mass balance is used from the atomic species balance to express the constraints of the gasifier system

C: $1 = n_2 + n_3 + n_5$ (5)
H: $2x + a = 2n_1 + 2n_4 + 4n_5$ (6)
O: $b + x + 2y = n_2 + 2n_3 + n_4$ (7)

Two independent reactions (methane formation and water gas shift reaction) were used to model independent reactions, the case of reactions without the presence of unconverted carbon in the products.

$C + 2H_2 \leftrightarrow CH_4$; and $K_1 = \frac{x_5}{{x_1}^2}$ (8)
$CO + H_2O \leftrightarrow CO_2 + H_2$; and $K_2 = \frac{x_1 x_3}{x_2 x_4}$ (9)

The equilibrium constant for each reaction is expressed as K_1 and K_2, is the function of temperature.

The last constraint is the energy balance as one of the essential equation that occurred in the adiabatic process without transfer of heat or mass of substances between the thermodynamic system and surrounding. Energy is transferred to the surrounding as work only.

$$H^0_{f,bio} + w\left(H^0_{f,H2O(l)} + H_{(vap)}\right) = n_2 H^0_{f,CO} + n_4 H^0_{f,H2O(vap)} + n_5 H^0_{f,CH4} + \Delta T(n_1 C_{pH2} + n_2 C_{pCO} + n_3 C_{pCO2} + n_4 C_{pH2O} + n_5 C_{pCH4} + 3.76 y C_{pN2}) \quad (10)$$

In summary, there are six unknown parameters (n_{1-6}) and six independent relations; three relations from the mass balance reactions (equation 5, 6 and 7), two relations from Independent chemical reactions (equation 8 and 9), and one relation from energy balance (equation 10).

Substitutions and eliminations were used on the mass balance, energy balance and independent reactions to solve the composition of carbon, hydrogen, and oxygen.

After going through the calculation steps, the constant equilibrium K_1 and K_2 for any particular temperature T could be calculated with following general equation for K_1 and K_2

$$lnK_1 = \frac{7082.848}{T} - 6.567\, lnT + \frac{7.466\times10^{-3}}{2}T - \frac{2.164\times10^{-6}}{6}T^2 + \frac{0.701\times10^{5}}{2T^2} + 32.541 \quad (11)$$

$$lnK_2 = \frac{5872.46}{T} + 1.86lnT - 2.69\times10^{-4}T + \frac{58200}{T^2} - 18.0139 \quad (12)$$

The remaining equations are consist of linear and nonlinear equations and solved with the Newton Raphson method and fsolve in Matlab.

RESULTS AND DISCUSSION

The results were validated with some previously developed models, analytical, numerical and experimental models. Root Mean Square Error (RMSE) analysis method was employed to verify which model was better.

$$RMSE = \sqrt{\frac{\sum_{i=1}^{N}(Exp_i - Model_i)^2}{N}} \quad (13)$$

Table 2 shows a comparison between the zero-dimensional model (A) and some available data from the literature. Proposed model (A) has lower RMSE compared with other literature published (A1), hence in comparison with experimental data; hence the zero-dimensional method was relatively close with actual data.

Table 2. Syngas Composition and LHV Comparison

	A1	A	E
H_2 (%)	14.00	14.95	17.50
CO (%)	20.14	20.85	21.30
CH_4 (%)	12.06	16.85	13.30
CO_2 (%)	2.31	2.01	3.10
N_2 (%)	50.79	45.91	44.20
LHV (MJ/m^3)	5.28	5.01	5.69
RMSE	3.44	2.16	

All the models show a good agreement with the experimental data, with syngas composition from the highest to the lowest fraction, are N_2, CO, CH_4, H_2, and CO_2 respectively. Hence the proposed model could be justified because RMSE evaluates the discrepancy between values provided by model and the observed value from the experimental analysis.

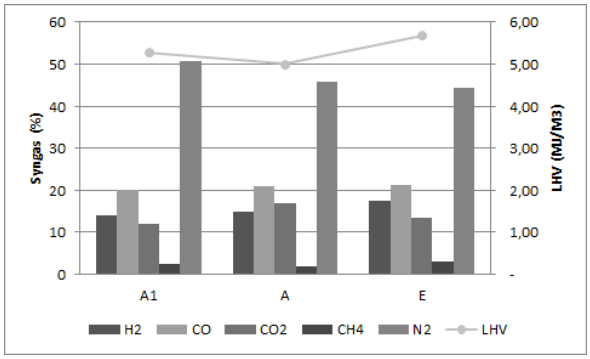

Fig.2 Syngas Composition and LHV

The goal of gasification modeling is to achieve a maximum heating value from syngas. Syngas further usage following the gasification should also be considered. According to Htut (2015), syngas for the internal combustion engine usage will require heating value more than 4.2 MJ/m^3. All of the model and experimental data already meet this requirement.

The effect of gasification temperature on the heating value could be seen in Fig 3. The maximum heating value could be achieved with gasification temperature range 800-900 ^{0}C, or it could be concluded that within gasification range 800-900 ^{0}C maximum syngas fraction of hydrogen, carbon monoxide, and methane was achieved.

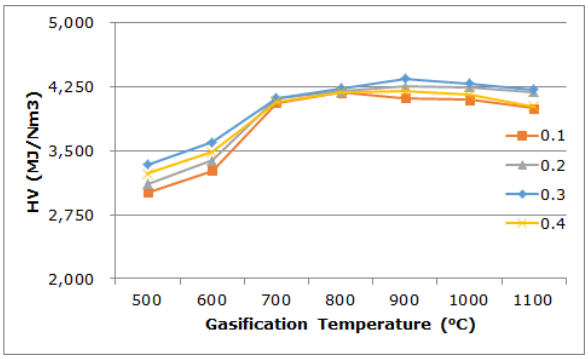

Fig.3 Effect of Gasification Temperature and ER

Equivalence Ratio (ER) variation also affect the Heating Value of syngas produced by gasifier. Lower ER ratio tends to have lower heating value, an increase from 0.1 to 0.2 and reach the maximum heating value at ER 0.3. Higher ER value resulting in a drop in heating value compared to 0.3

CONCLUSIONS

Gasification simulation models could be classified based on the spatial dimension from the complicated three-dimensional models to the simple one-dimensional model.

A zero-dimensional equilibrium model was established and proven its reliability with the experimental data. Thermodynamic computations are unconstrained with the dimension of the gasifier, hence is very useful to analyze the most substantial process parameters.

This model could be used to predict the gasification performance parameter (syngas composition and heating value) with satisfactory precision — the fact that both pyrolysis and syngas products were all need to go through the oxidation zone or the highest temperature in the gasifier. Equilibrium phase could be achieved even in a brief time in the oxidation zone. The advantage of this model is that this model could be able to manage a wide range of biomass source of materials with different operation condition and quite simple to operate.

ACKNOWLEDGMENTS

This research was supported by the Indonesian Endowment Fund for Education (LPDP), Ministry of Finance; and the Directorate General of Higher Education (DIKTI), Ministry of Research, Technology and Higher Education, Republic of Indonesia.

REFERENCES

[1] Andrés Z. Mendiburu, João A. Carvalho and Christian J.R. Coronado, (2014), Thermochemical equilibrium modeling of biomass downdraft gasifier: Stoichiometric models, Energy, vol. 66, issue C, 189-201.
[2] Barman NS, Ghosh S, De S. (2012), Gasification of biomass in a fixed bed downdraft gasifier-a realistic model including tar, Bioresource Technology. 107:505-11. doi: 10.1016/j.biortech.2011.12.124. Epub.
[3] Basu, P., (2010), Biomass Gasification and Pyrolysis Practical Design and Theory, Academic Press, pp.1-4.
[4] Htut, YM., Khine, MM., Win, MM., (2015), Using a simple modeling and simulation scheme for complicated gasification system, International Journal of Scientific and Research Publication, Vol 5, No 6.
[5] Maitah, M., Prochazka, P., Pachmann, A., Šrédl, K., Řezbová, H., (2016), Economics of Palm Oil Empty Fruit Bunches Bio Briquettes in Indonesia, International Journal of Energy Economics and Policy, Vol 6(1), pp.35-38.
[6] Reed TB, Principles and Technology of Biomass Gasification, Advances in Solar Energy, An Annu of Res and Dev, 1985, 2, 125-74
[7] Robert HP, Don WG., Perry's chemical engineer's handbook. Sixth edition.New York: McGraw Hill,1984
[8] Wu KT., Chein, RY., (2015), Modelling of biomass gasification with preheated air at high temperatures, Energy Procedia, 75, 214-219.
[9] Zainal ZA, Ali R, Lean CH, Seetharamu, KN, (2001), Prediction of performance of a downdraft gasifier using equilibrium modeling for different biomass material, Energy Conversion and Management 42(12):1499-1515.

8th International Engineering Symposium - IES 2019
March 13-15, 2019, Kumamoto University, Japan

Effect of nanoparticle motion mechanism on convective heat transfer in turbulent flow

Yuki Kotooka [1], Shuichi Torii [2]

1 *Department of Mechanical Engineering, Kumamoto University, Kurokami, 2-39-1, Kumamoto 860-8555, Japan. email:181d8458@st.kumamoto-u.ac.jp*
2 *Department of Mechanical Engineering, Kumamoto University, Kurokami, 2-39-1, Kumamoto 860-8555, Japan. e-mail:torii@mech.kumamoto-u.ac.jp*

ABSTRACT: As energy demand is increasing around the world, how to use heat in an efficiency way has become a big issue. Nanofluids are known to be excellent replacements for conventional heat transport fluids. Extensive studies on the properties of nanofluids have been conducted in recent decades, but research on the mechanism of improvement in heat transfer rate by using nanofluids is still lacking. In this study, we investigated the heat transfer promoting mechanism of nanofluid. The mechanism of heat transfer promotion of nanofluid was predicted and investigated experimentally. Alumina nanofluid with a volume concentration of 5% were used and Reynolds number is 10000. Experimental results did not give a clear result that nanoparticles actively exchanging heat with momentum transport.

***Keywords**: nanofluid, heat transfer, turbulent flow*

INTRODUCTION

Water and oil well known as a working medium are used in various industrial fields. However, at present, these working media are in a state which the thermal conductivity is low and the heat transfer performance is not very high. Nanofluids are known to be excellent replacements for conventional heat transport fluids. Specifically, there is a report that the convective heat transfer coefficient of water - based carbon nanotube 0.25 wt.% Has increased to 40% compared to pure water in turbulent flow[1]. Heat pipe is applied as actual equipment. Heat pipes have used a wide variety of applications in various heat transfer devices, particularly electronic components. There is a report that heat pipes using 0.1 vol.% carbon nanotubes increased by 10.6% than using base working medium[2]. As described above, many studies have been conducted on heat transfer experiments using nanofluids. However, studies on mechanisms for promoting heat transfer of nanofluids are still in short supply. It is necessary to pay attention to fluid behavior as a factor that promotes nanofluid's heat transfer compared with base fluid. In other words, the theoretical and experimental understanding of the nanoparticle movement mechanism in nanofluids is necessary.

Therefore, it was considered that effect of the motion mechanism of nanoparticle on convective heat transfer.

Nanoparticles and Nanofluid

The nanoparticles have an average particle size of 10 to 100 nm size. For example, carbon nanotubes, copper oxide, and alumina nanoparticles. Alumina nanoparticles are used in this study. The reason for choosing alumina nanoparticles is that the shape of alumina nanoparticles is spherical. This particle was used to make it easy to understand the movement of particles flowing in the fluid. Alumina particles are relatively easy to obtain and have chemically superior stability. In my study, alumina particles and distilled water were mixed to create 5% vol.% Alumina nanofluids. The creation method shows the following procedure.

(1) Prepare accurate amounts of distilled water and alumina nanoparticles.
(2) Mix the prepared water and alumina particles.
(3) Put the mixed alumina nanofluid into ultrasonic machine for 5 hours.
(4) Measure the ph value and the zeta potential to confirm dispersibility.

Three factors are important for nanofluid in the evaluation of dispersibility. It is ph value, zeta potential and particle diameter. Table 1 shows the ph value and zeta potential of my nanofluids. Regarding particle size, the diameter of alumina particles used was observed by SEM in Fig.1. Generally, the zeta potential is said to have high dispersibility between ± 30 and 60 mV [3]. Since the ph value and the zeta potential have a correlation, it is necessary to measure them. In addition, since the particle size of alumina is smaller than 100 nm, it can be determined that my making fluid is a nanofluid having high dispersibility.

The motion mechanism of nanoparticle on convective heat transfer

First consider the flow in a circular pipe under turbulent flow conditions. Generally, when a fluid flows in a circular pipe, it has a velocity distribution. Focusing on the particles flowing through the fluid, the velocity of the particles is shown in Fig.2. When the particle is close to the wall, the flow between the particle and the wall is slower than the particle. There is a speed difference between the velocity of the fluid and the velocity of the particle. As a result, it will cause rotating force acts on the particles. Due to the Magnus effect, a lift force working perpendicularly to the speed direction is generated in the rotating object, so that the lift force is generated toward the center of the circular pipe. Nanoparticles arrive at the center of the pipe, whereby the movement of momentum is actively carried out. At the same time, it is considered that heat transfer promotion of nanofluid has occurred due to heat exchange. Therefore, in my research, experiments were done to show that there are many nanoparticles at the center of a circular pipe.

Experimental apparatus and method

An outline of the experimental apparatus is shown in Fig.3. In order to show that there are many nanoparticles at the center of the pipe, a test section is provided as shown in Fig.4. The pipe on the outside of the test section has an inner diameter of 8 mm and a thickness of 2 mm. The tube inside the test section has an inner diameter of 4 mm and a thickness of 0.5 mm. As the material of the pipe, an acrylic tube and a stainless tube were used respectively. The location of the collecting section is set as point 1 (P1), point 2 (P2).
The experimental method shows the following procedure.
(1) Pump and circulate the nanofluid in the tank.
(2) After circulation, the nanofluids that passed through the test section are collected by collecting parts P1 and P2. In that case also measure the time taken. Fig.5 shows collecting solution.
(3) Dry the collected nanofluids and weigh each.
(4) Based on the mass of alumina after drying, the concentration of nanofluid at the time of collection is determined.
The experimental conditions and the equations used in the experiment are shown below.

Re = 10000

$$M_1(\,Mass\ concentration) = \frac{Mass\ of\ dried\ Al_2O_3}{Mass\ of\ solution} \quad (1)$$

Experimental results and discussion

The experimental results are shown in Fig.6 and Fig7. Experimental results show that there are many nanoparticles on the wall surface inside the circular tube. It was different with my assumption that heat transfer promotion is occurring by the motion mechanism of the particle. It seems that many nanoparticles flowed to the outer pipe (P1) but not the inner pipe (P2). It is necessary to theoretically study the motion mechanism of particles. Specifically, it is necessary to think about shape change when nanoparticles receive heat. Experimental changes due to differences in nanofluid concentrations should also be considered.

Conclusion

- There was no clear cause that the movement of the particles flowing in the circular pipe caused the heat transfer acceleration.
- The shape change by adding heat to the nanoparticles flowing through the fluid is also important factor to be considered.
- The mechanism of particle motion about the difference in heat transfer performance depending on the concentration of nanofluid flowing in the circular pipe still remain unclear.

REFERENCES

[1] A.Amrollahi, A.M.Rashidi (2010), Convection heat transfer of functionalized MWNT in aqueous fluids in laminar and turbulent flow at the entrance region, International Communications in Heat and Mass Transfer, Vol.37, Issue 6, pp 717-723

[2] Paisarn Naphon, teerapong Borirak(2008), Experimental investigation of titanium nanofluid on heat pipe thermal efficiency, International Communications in Heat and Mass transfer, Vol.35, Issue 10, pp 1316-1319.

[3]Saifuddin Jailani, George V. Franks, Thomas W. Healy(2008), ζ Potential of Nanoparticle Suspensions: Effect of Electrolyte Concentration, Particle Size, and Volume Fraction, Journal of the American ceramic Society, Vol.91, Issue 4, pp 1141-1147.

Table 1 My Al2O3 nanofluid

Average	zeta potential [mV]	ph
Al_2O_3 nanofluid 5% vol	45.1	4.51

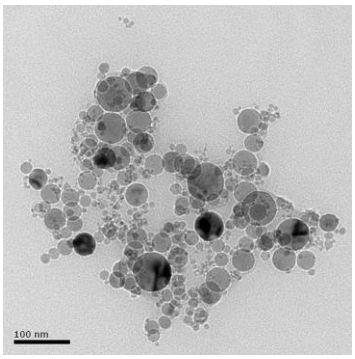

Fig.1 SEM image of alumina particle

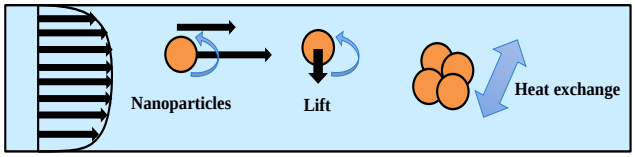

Fig.2 The motion mechanism of nanoparticles in turbulent flow

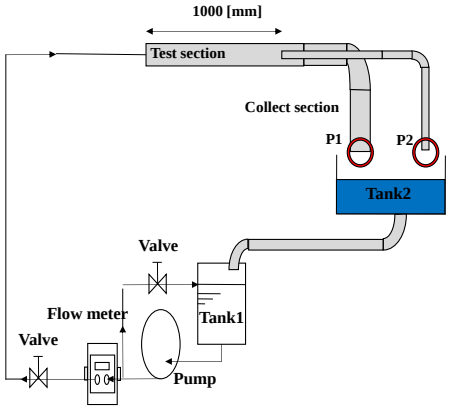

Fig.3 Overall view of experimental apparatus

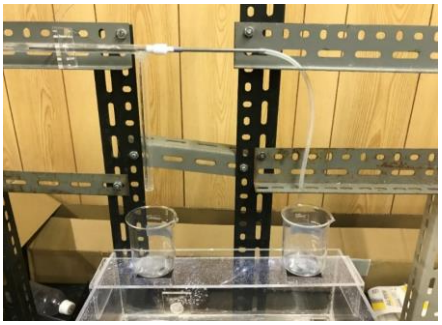

Fig.4 Enlarged view of test section

Fig. 5 The collected nanofluid
Left side: Nanofluid flowing in P1
Right side: Nanofluid flowing in P2

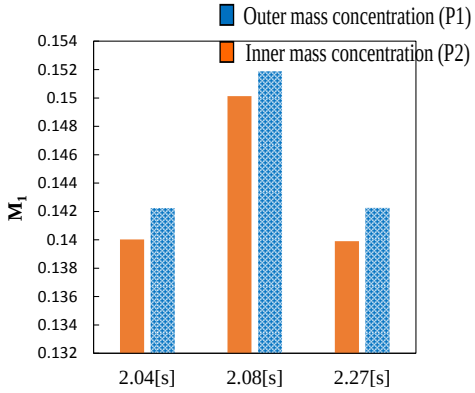

Fig. 6 The difference of mass concentration as collecting for about 2 seconds

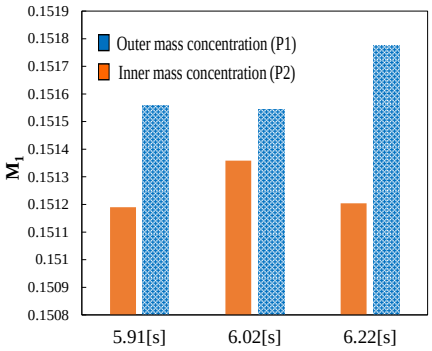

Fig. 7 The difference of mass concentration as collecting for about 6 seconds.

8th International Engineering Symposium - IES 2019
March 13-15, 2019, Kumamoto University, Japan

Production of Biogas from the Co-digestion of Chicken wastes and Food wastes at Different Mixing Ratios

Huqe Farhana [1] and **Shuichi Torii** [2]

1 *Department of Advanced Mechanical System, Kumamoto University, Kurokami, 2-39-1, Kumamoto 860-8555, Japan. e-mail:farhanahuqe@gmail.com*
2 *Department of Advanced Mechanical System, Kumamoto University, Kurokami, 2-39-1, Kumamoto 860-8555, Japan. e-mail:torii@kumamoto-u.ac.jp*

ABSTRACT: Biogas has been used as an entrusted alternative of fossil fuels from a decade ago and anaerobic digestion has been used to produce biogas from organic waste materials. Though this method is useful as it is very cost effective and environment friendly process for utilizing the waste materials, but still now researchers are demanding to find out proper digestion conditions to obtain maximum concentration of methane in the raw biogas. Because, raw biogas produced from anaerobic digestion is mixed with methane, carbon dioxide and other gaseous contents. In such case, co-digestion of the waste materials within appropriate mixing ratio can be a suitable solution to enrich methane concentration in raw biogas. In this paper, we have utilized co-digestion of chicken manure (CM) and food wastes (FW). We have used rotten rice and potato as food wastes. The mixing ratios between the raw materials (CW:FW) were 1:0.5, 0.5:1 and 1:1. During our experiment, we have found that, the faster biogas production was carried out with the mixing ratio of 1:1. Besides, the maximum methane concentration in raw biogas was obtained at the same mixing ratio (54.28%) and the maximum amount of biogas (130mL) was obtained at the mixing ratio of 1.5:0.5.

Keywords*: anaerobic digestion, mixing ratio, daily biogas production, methane concentration*

INTRODUCTION

One of the burning issues faced by the industrialized world today is energy crisis which has been arisen due to lack of proper knowledge of management of solid wastes and change in global climate. Rapid growth of population and uncontrolled and unmonitored civilization are also two major reasons for which these serious problems has been created [5]. Solid disposal treatments such as combustion and pyrolysis have an air pollution problem with high initial investment cost [6]. It is predicted that the conventional (oil, coal, natural gas etc.) energy may last for another ten decades which has lead to global climate change, environmental degradation and human health problems [3]. In this regard, renewable energy resources appear to be one of the most efficient and effective solutions [7]. Biomass has globally remained a renewable energy source derived from plants that use solar energy during the process of photosynthesis. Biogas originated biomass through anaerobic digestion being a source of renewable gas; it has been adopted as one of the best alternatives for conventional fuels in the past two decades. Anaerobic digestion (AD) is a waste-to-energy technology biological process that produces biogas by bacteria under poor or no oxygen conditions [11, 9, 13, 14].Biogas is colourless and flammable and it can be produced from various organic waste materials such as animal manure, plant, human, energy crops, industrial and

municipal wastes amongst others, to give mainly methane (50-70%), carbon dioxide (20-40%) and traces of other gases such as nitrogen, hydrogen, ammonia, hydrogen sulphide, water vapour etc. [10]. It is smokeless, hygienic and more convenient to use than other solid fuels [4]. The digesters are incubated at mesophilic (25–35℃) or thermophilic (45–60℃) conditions for a certain period of time. It is a multi-step biological process where the organic carbon is mainly converted to carbon dioxide and methane [1]. The process can be divided into four steps: hydrolysis/liquefaction, acidogenesis, acetogenesis and methanogenesis. Fig. 1 shows the mechanism pathway of anaerobic digestion process.

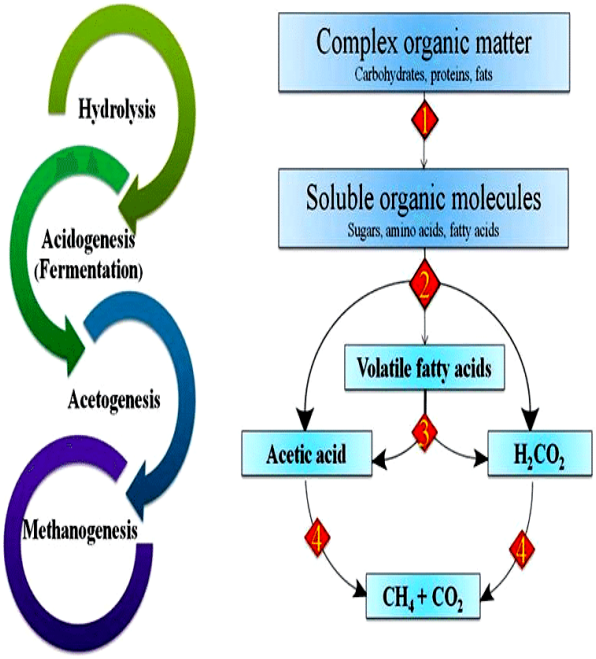

Fig.1 Mechanism of anaerobic digestion for biogas production

Hydrolysis is the first step of anaerobic digestion. In this stage complex organic matters, such as proteins, carbohydrates and lipids are hydrolyzed into sugars, amino acids and fatty acids by extracellular enzyme (cellulase, amylase, protease or lipase) as soluble organic molecules. In the second step acidification or acidogenesis, the soluble organic molecules from hydrolysis are utilized by fermentative bacteria or anaerobic oxidizers to produce volatile fatty acids (acetic acid, propionic acid and butyric acid), alcohols, aldehydes and CO2, H2 and NH3 gases. Acetogenesis is the third step where acidification produced products is converted by acetogenic bacteria into acetic acids, hydrogen, and carbon dioxide. Finally in methanogenesis step, methanogenic archaea converts acetate and H_2/CO_2 into CH_4 and CO_2. Different types of solid wastes result in varying degrees of biogas yields, and thus the effects of mixing various types of waste and their proportions should be determined [8, 12, 2]. The main objective of our study is to obtain better methane concentration and faster biogas production through the co-digestion of chicken wastes and food wastes. In our experiment, we have used rotten rice and potato as food wastes. We have chosen three mixing rations between the chicken wastes (CW) and food wastes (FW) and they are: 1.5:0.5, 0.5:1.5 and 1:1. The waste materials were kept in 2L plastic bottles under mesophilic temperature condition for 14days.

METHODS AND MATERIALS

PREPERATION OF THE SLURRY

The food wastes, that means, the rotten rice and potato were crushed into tiny pieces of 1mm with a mechanical crusher. Then they were mixed with required amount of chicken wastes. After that, tap water was mixed with the raw materials to prepare the slurry for anaerobic digestion. We have chosen three different ratios between the chicken wastes and food wastes and they were: CW:FW= 1.5:0.5, CW:FW= 0.5:1.5 and CW:FW= 1:1. We have used 2L plastic bottle as anaerobic digester and we filled 70% of the plastic bottle with the slurry. The mixing ratio between the raw materials and the tap water was 1:1 every time.

EXPERIMENTAL SET-UP:

Our laboratory scale experimental set-up was consists of three parts: 2.0 L plastic bottle namely digester, water-gas chamber and expelled water collector for every observation. We have used 2.0L plastic bottle as water-gas chamber and 1.0L plastic bottle was expelled water collector. Fig. 2 shows the experimental setup for biogas production.

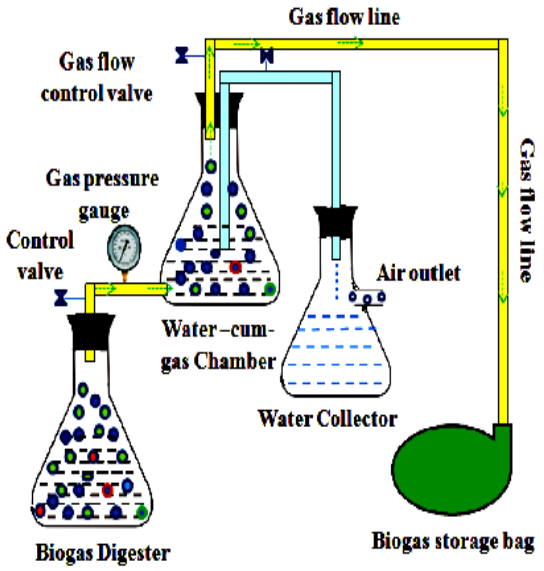

Fig.2 The experimental set-up for biogas production

The digester was connected with the water-gas chamber by a hose pipe. To control the flow of biogas towards the water-gas chamber, a plastic valve was connecter with that hose pipe. The water-gas chamber was connected with the expelled water collector through another hose pipe. Another plastic valve was connected with that hose pipe to control the flow of the expelled water by the raw biogas stored in the water-gas chamber. At the top of the water-gas chamber, a gas collecting bag was connected through another hose pipe of smaller diameter. This gas bag was used for further analysis. All the hose pipes were connected with the respective bottles with corks to maintain airtight system firmly. Silicon glue was used to seal the leakage of the experiment. A thermometer was set with the digester to observe daily temperature of the slurry. The P^H of the slurry was measured before pouring it inside the digester by a digital P^H meter.

DATA COLLECTION AND ANALYSIS:

The Gas composition was analyzed by using a gas chromatography (GC-8AIT / CR8A SHIMADZU Corporation, JAPAN). The pH value was monitored everyday using digital pH meter HM-25R (TOADKK). Moisture content was measured using moisture meter (MOC63u). The moisture content in chicken wastes was 38.27%, in the rotten rice was 57.02% and in potato (with the skin) was 43.28%. Biogas produced by anaerobic co-digestion was measured by water displacement method every day as shown in Fig. 3.

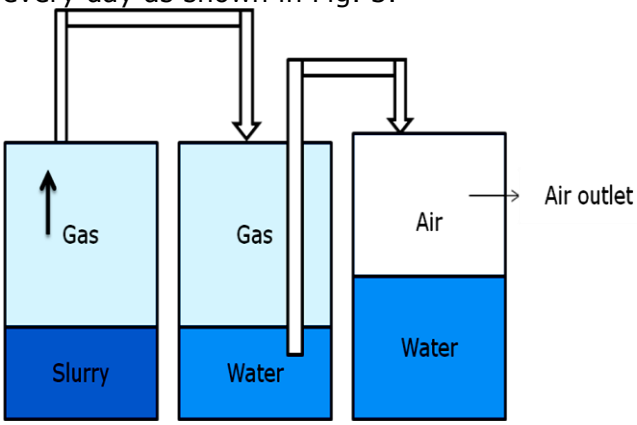

Fig.3 Schematic diagram of water displacement method

OBSERVATION:

In this research, we have arranged three experimental set ups with three different ratios of waste material mixture. Besides, each of these experimental set up was kept for 14day of digestion period. During this retention period, daily biogas production was measured by water displacement method; that means, the volume of raw biogas produced everyday was measured directly by the volume of the water displaced by the gas. Besides, daily methane content was measured from the sampling bag with the gas chromatograph. The P^H of the slurry was measured before pouring it in each bottle. The temperature was measured by the thermometer attached with the digesters. The average temperature of the slurry was 26°C, 28°C and 25°C for the three mixing ratios CW:FW= 1:1, 1.5:0.5 and 0.5:1.5 respectively. Besides, the P^H of the slurry for the above three mixing ratios were 6.4, 6.8 and 6.1 respectively.

RESULTS AND DISCUSSION:

The daily biogas production from chicken waste and food wastes was observed at different mixing ratio for 14days. We have chosen three different mixing ratios for biogas production from chicken wastes and food wastes and they were CW: FW= 1.5:0.5, 0.5:1.5 and 1:1. The waste materials were mixed in these three ratios and then mixed sludge was diluted with tap water with the ratio of 1:1 in every digester. Then the three digesters were

kept for anaerobic digestion. Figure 4 is presenting the graphical presentation of daily biogas production from the chicken wastes and food wastes in three different mixing ratios. In this figure, the green line is presenting the daily biogas production from the mixing ratio CW:FW=1:1, the blue line is presenting the daily biogas production from the mixing ratio CW:FW=1.5:0.5 and the red line is presenting the daily biogas production from the mixing ratio CW:FW=0.5:1.5. From this figure, we can see that, biogas has been started to produce from the first day of digestion in each mixing ratio. Besides, we can observe that, the minimum volume of the raw biogas was found about 17mL/day and the maximum volume of the biogas was found about 130mL/day for the mixing ratio CW:FW=1:1. On the other hand, for the mixing ratio CW:FW=0.5:1.5, the lowest volume of the raw biogas was found to be 8mL/day and the highest volume of the raw biogas was found to be 95mL/day. Additionally, for the mixing ratio CW:FW=1:1, the minimum volume of the raw biogas was 18mL/day and the maximum volume of the raw biogas was 118mL/day. As mentioned before that, the volume of the raw biogas was measured by means of the volume of the water displaced by the biogas daily (water displacement method).

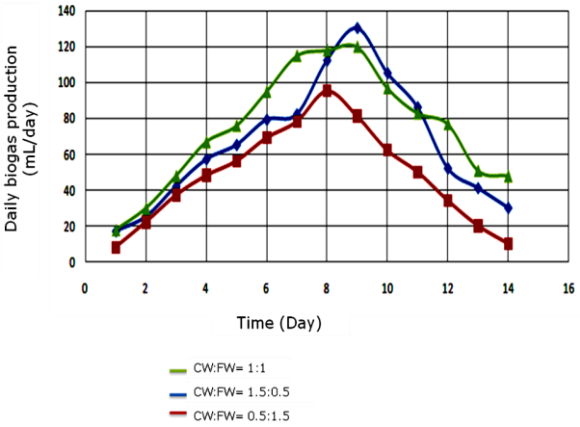

Fig.4 Daily biogas production from chicken wastes and food wastes with different mixing ratios

From these observations, we can say that, if the amount of chicken waste can be higher in the mixed sludge, then the daily biogas production can be enhanced. Besides, if both chicken waste and food waste can be mixed with equal ratio, the biogas production rate can also be accelerated.

Together with the observation of daily biogas production, in our experiment we have also find out the methane concentration present in the raw biogas in daily basis from each of the mixing ratio. Figure 5 is presenting the methane concentration of the raw biogas. Similar with figure 4, the green line is representing the methane concentration of the raw biogas for the mixing ratio of CW:FW=1:1, blue line is presenting the methane concentration in the raw biogas of mixing ratio CW:FW=1.5:0.5 and the red line is presenting the methane concentration in the raw biogas of mixing ratio CW:FW=0.5:1.5.

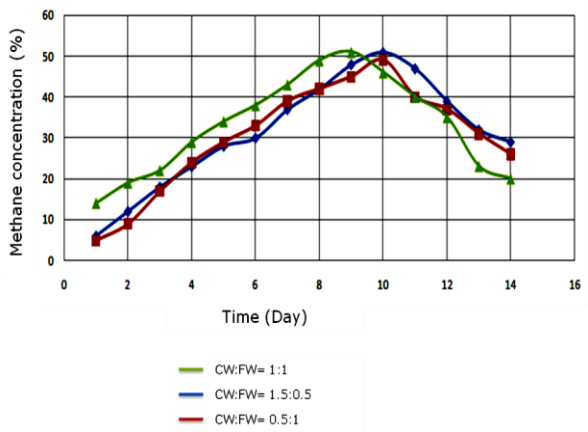

Fig.5 Methane concentration in raw biogas from different mixing ratios of chicken waste and food wastes

From this figure, we can observe that, the highest methane concentration was found in the 8th day of digestion for the mixing ratio of CW:FW=1:1 and the value was 54.28%. On the other hand, the maximum methane concentration in the raw biogas was confirmed at the 10th day of digestion for the mixing ratio of CW:FW=1.5:0.5 and the value was 51.73%. But for the case of mixing ratio CW:FW=0.5:1.5, the highest methane concentration was found at the 9th day of digestion and the value was 46.01%. From these findings, we can say that, the equal ratio between the waste materials generated maximum and sustainable percentage of methane in the raw biogas. May be the nutrition balance in the slurry was well for the digestion in this

mixing ratio. Though the methane concentration in the raw biogas was also good in the mixing ratio of CW:FW=1.5:0.5. May be the higher presence of chicken waste provided the better nutrient for the microorganisms to make a better digestion. These results indicate that, co-digestion of the organic substrates can be used as a method to improvise the daily biogas production rate and to enrich methane concentration in the raw biogas. Because, the co-digestion of the selected waste materials provides better biodegradability with the proper balance of nutrients, increasing the synergistic effects of different microbial populations, or increasing the biodegradability in the digester.

CONCLUSION:

Three different biomasses (chicken waste, rotten rice and potato) were digested properly for biogas production. The results reveal that, these solid organic waste materials have tremendous potential to produce biogas at mesophilc temperature condition. We can also conclude with the fact that, anaerobic co-digestion can be utilize more than single digestion of the solid wastes to enhance biogas production rate. Besides, we can also say that, this technique is also very capable to improve the methane concentration in the raw biogas. We can also observe from the results that, chicken waste can be utilize together with the food wastes to obtain better methane concentration in both medium and large scale anaerobic digesters.

ACKNOWLEDGMENT:

The authors would like to acknowledge the Ministry of Education, Culture, Sports, Science and Technology (MONBUKAGAKUSHO: MEXT for providing the financial support (PhD scholarship) for this research and the extended help of Thermal engineering laboratory under the Department of Advanced Mechanical System Engineering, Kumamoto University, Japan, for providing the facility for experimentation.

REFERENCES:

[1] Angelidaki, I et al (2003), Applications of the Anaerobic digestion Process, Ahring, B.K. Biomethanation II edition. Springer Berlin, pp. 1-33.
[2] Angelidaki, I et al, (2007), Notes for the course 12133: environmental biotechnology, technical university of Denmark, Lyngby, Denmark.
[3] Budiyano, N et al (2010), Increasing Biogas Production Rate from Cattle Manure Using Rumen Fluid as Inoculums, International Journal of Chemical and Basic & Applied Sciences, vol. 10, No. 1, pp. 68-75.
[4] Buren, A V (1979), A Chinese Biogas Manual," Intermediate Technology Publications Ltd.
[5] Dhanalakshmi, S V and Ramanujam, R A (2012), Biogas Generation in A Vegetable Waste Anaerobic Digester: An Analytical Approach, Research Journal of Recent Sciences, Vol. 1, No. 3, pp. 41-47
[6] Elango, D et al (2007), Production of Biogas from Municipal Solid Waste with Domestic Sewage, J. Hazar. Mat., Vol. 141, No. 1, pp. 301-304.
[7] Kamil, K and Abdullah, K (2002), Renewable Energy and Sustainable Development in Turkey, Renewable Energy, Vol. 25, pp. 431–453.
[8] Madigan, M et al (2008), Brockbiology of Microorganisms, Benjamin Cummings, Vol. 12, pp.11-68.
[9] Madsen, M et al (2011), Monitoring of Anaerobic Digestion Processes: A Review Perspective, Renew Sustain Energy Rev, Vol. 15, pp. 3141–3155.
[10] Maishanu, S M et al (1990), Biogas Technology: The Output of The Sokoto Energy Research Centre, Nigerian Journal of Solar Energy, Vol. 9, pp. 183-194.
[11] Rongping, L et al (2009), Anaerobic Co-digestion of Kitchen Waste and Cattle Manure for Methane Production, Energy Sources, Vol. 31, No. 20, pp. 1848-1856.
[12] Salminen, E and Rintal, J (2002), Semi-continuous Anaerobic Digestion of Solid Poultry Slaughterhouse Waste: Effect of Hydraulic Retention Time and Loading, Water research, Vol. 36, pp.3175-3182
[13] Song, Z et al (2012), Comparison of Two Chemical Pretreatments of Rice Straw for Biogas Production by Anaerobic Digestion, BioResources, Vol. 7, pp. 3223–3236.
[14] Weiland, P (2010), Biogas Production: Current State and Perspectives, Appl Microbiol Biotechnol, Vol. 85, pp. 849–860.

8th International Engineering Symposium - IES 2019
March 13-15, 2019, Kumamoto University, Japan

Numerical Simulation Study on Bark Combustion in Compact Combustor

Chong Liu [1,2], Shuichi Torii [1] and **Xiaoqu Tong[2]**

1 *Department of Mechanical System Engineering, Kumamoto University, Kurokami, 2-39-1, Kumamoto 860-8555, Japan. e-mail: 162d9211@st.kumamoto-u.ac.jp*
2 *School of Chemical Equipment, Shenyang University of Technology, Guanghua, No.30, Liaoyang 111003, China. e-mail:351489948 @qq.com*

ABSTRACT: For a variety of reasons, a large amount of biomass fuel is not utilized in our lives. In this paper we focus on bark which is abandoned during logging process and obtain the temperature distribution in the compact combustor, gas emission composition and thermal efficiency by numerical simulation. Then we analysis the bark combustion characteristics and develop a compact combustor. It is found from research that (i) bark can take place self-combustion and maintain a stable combustion temperature in the compact combustor, (ii) combustion temperature distribution appears along the vertical direction in combustor, (iii) the concentrations of nitrogen oxide and sulfur oxides are lower than the discharge standard value. This research is theoretical basis for compact combustor to apply biomass fuel.

Keywords*: Biomass, Simulation, Compact combustor, Stable Combustion*

INTRODUCTION

The exhaustion of fossil fuels and the pollution from their combustion are more and more serious according to Z. ZHOU and W. L. WU (2005). It is an inevitable trend to use renewable energy in the future. Of course, there are many kinds of renewable energy, including biomass energy, wind energy, geothermal energy, solar energy, tidal energy and so on. We are focus on biomass energy. Biomass energy is the fourth largest energy source in the world, after coal, oil and gas according to J. Q. XU et al (2006). But it is the oldest energy source to be used by human. Biomass is the convert the solar energy into chemical energy by plants through photosynthesis according to F. F. MIN and M. X. Zhang (2005). Plants absorb carbon dioxide and emit oxygen in this process, energy is released and carbon dioxide is emitted when the plant is combusted, so the total carbon content on the earth does not increase according to B. LIU et al (2015). In addition, the sulfur and phosphorus components in biomass fuel are very low, so it is almost no pollution to the environment according to J. Y. LIU et al (2001). However, the moisture content in biomass fuel is high, and calorific value is lower than fossil fuel for the same weight according to Z. F. TIAN et al (2014). When considering transportation costs, the cost of biomass fuel is higher than fossil fuel. It is the most important reason to restrict the development of biomass fuel.

It is well known that timber is produced by trunk. Leaves, branch, bark and root will be discard in the logging camps because of the transportation cost. They are considered to be unused biomass. Nearly 2.5 million cubic meter timbers are produced, but more than 20 million cubic meter unused biomass are discarded in the logging camps in Japan. So we focus on bark which is one kind of unused biomass and study combustion characteristics of bark in compact combustor. We hope that stable combustion can be maintain without pollution.

PROPERTY AND APPARATUS

We chose the dry bark as the research object and it was shown in figure 1. The property of dry bark particles was shown as table 1. The element composition of dry bark particles was shown as table 2. So the molecular formula of dry bark particles was $CH_{1.1255}O_{0.475}N_{0.005}X \cdot 0.1937H_2O$. The *X* was impurity, including a variety of trace metal, a variety of trace non-metal, a variety of trace metallic oxide and so on. The chemical equation for bark combustion was shown as:

$$CH_{1.1255}O_{0.475}N_{0.005}X \cdot 0.1937H_2O + 1.043875O_2 \rightarrow CO_2 + 0.75645H_2O + 0.0025N_2 + X \quad (1)$$

The combustion system was consisted of feeder, combustor, heat exchanger, cyclone separator and measurement devices, was shown in figure 2.

Fig.1 Dry bark particles

Table 1 The property of dry bark particles

Property			
Size	Bulk specific gravity	Moisture content	Lower calorific value
5mm under	0.132	12.89%	3498 kcal/kg

Table 2 The elements of dry bark particles

Element	Content
C	44.36%
H	5.63%
O	39.64%
N	0.26%
Others	10.11%

Bark and air were fed by the forced draft fan and combusted in the combustor. The hot combustion gas produced in the combustor was flowed from the top of combustor and the millimetre-sized ash was collected at the bottom of combustor. The hot combustion gas enters into heat exchanger and after the hot combustion gas was cooled in the heat exchanger, the cooled combustion gas flowed through the cyclone separator, resulting in the recovery of the micro-sized ash. At the same time, the hot water was produced in the cyclone separator and the cool combustion gas without ash was discharged from the chimney.

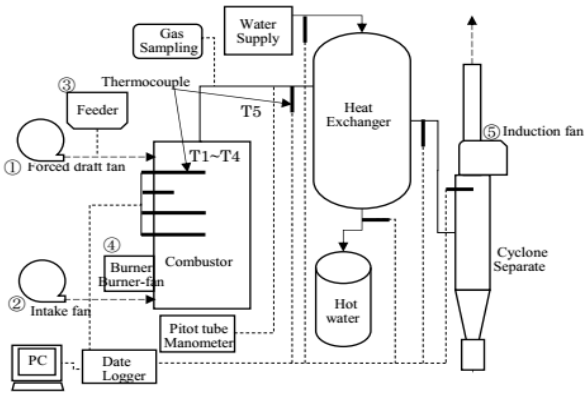

Fig. 2 Combustion system

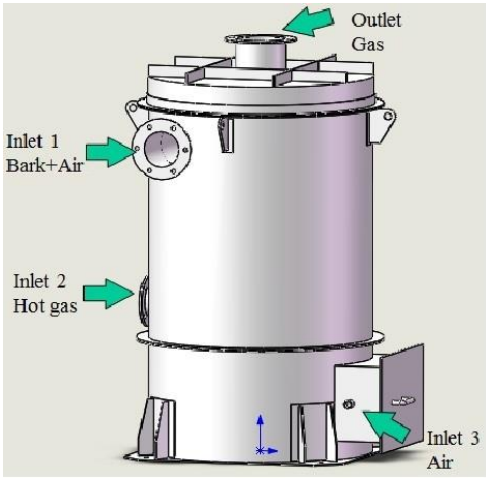

Fig. 3 The external structure of compact combustor

Fig. 3 illustrated the structure of the combustor. The dry bark and air were fed to the upper inlet port of the combustor. The inlet pipe was fixed at the lateral face of the combustor and in the circumferential direction. Thus, the fuel-air mixing flow becomes spiral flow inside the combustor. This structure played an important role in a fuel drying and an extension of combustion time of fuel. The swirling flow yielded a sufficient floating time of the fuel and attenuated the deposition of unburned fuel at the bottom

of the combustor. The combustion gas was exhausted through the top of combustor.

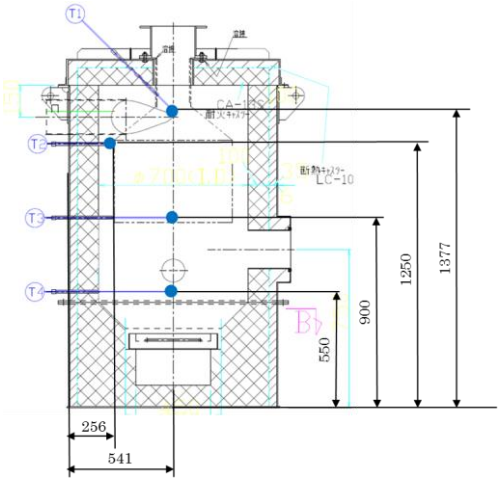

Fig. 4 The internal structure of compact combustor and the positions of four thermocouples

In order to monitor and measure the combustion gas temperature in the different position of combustor, there are four K-Type thermocouples are inserted in the combustor and the corresponding locations (T1, T2, T3, T4) were shown in Fig. 4. T1, T3 and T4 are set in the central axis of combustor, but different heights. T2 is set in the vicinity of the injection port of the fuel-air mixing flow. The combustion gas temperature at the outlet of the cyclone separator is also measured by the thermocouple (named as T5).

NUMERICAL ANALYSIS

1 Geometry

Two numerical modellings were created by Solidworks as shown as figure 3 and figure 5. The only difference between two modes was refractory layer. We did not need to consider heat transfer, so the internal structure modelling was used to analyse the combustion situation.

2 Meshing

Meshing was discretised representation of computational domain which was used by physics solver to provide anumerical solution. We generate mesh with the help of STAR CCM+ meshing tool. The result was shown in figure 5. Surface remesher, polyhedral meshing, and prism layer mesh have been used in our research. The surface remesher was used in order to get quality discretised mesh. For volume mesh, we used polyhedral mesher. It was generated easily and effectively, moreover, Polyhedral mesher provide balance solution for complexed mesh generation problem. Prism layer mesher was used. On the one hand, it was better to simulate the effect of boundary layer, on the other hand, it was better for orthogonality between mesh and surface. Table 3 shows meshing detail.

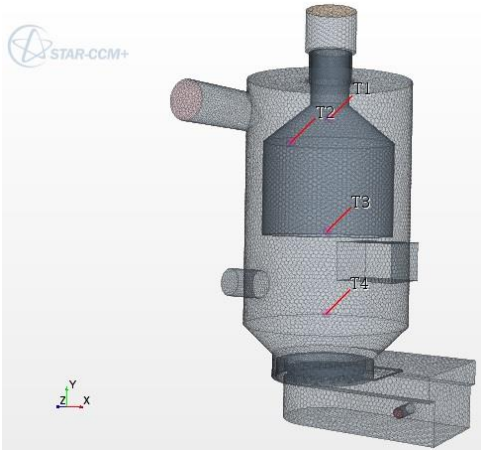

Fig. 5 The internal structure modelling, mesh and the positions of four points

Table 3 The details of meshing

Base size	20mm
Relative minimum size	25% of base size
Relative target size	100% of base size
Prism layer thickness	33.3% of base size
No. of prism layer	2
No. of cell	186083

3 Simulation method and government equation

In my research, the particle of drying bark was fed into combustor by forced draft fan. The drying bark particles were considered as discrete phase while the air was considered as continuous phase during the reaction. The size of drying bark was less than 5mm. Therefore, it was considered as the discrete phase in the combustor. So the Lagrangian multiphase as been used. K-epsilon turbulence used to model turbulent flow. In this method, set of turbulent kinetic energy and turbulent kinetic energy dissipation equation are solved for discrete phase. Eddy break up model used for modelling of drying bark volatilization reaction while Arrhenius equation has been used for chemical kinetics.

3.1 The Governing equation of continuous phase

Continuity equation:

$$\frac{\partial}{\partial t}\left(\alpha_c\{\rho_c\}\right)+\frac{\partial}{\partial x_i}\left(\alpha_c\{\rho_c u_i\}\right)=-\frac{1}{V}\sum_k \dot{m}_k \quad (2)$$

Momentum conservation equation:

$$\frac{\partial}{\partial t}\left(\alpha_c\{\rho_c\}\vec{u}_i\right)+\frac{\partial}{\partial x_i}\left(\alpha_c\left\{\rho_c \vec{u}_i \vec{u}_j\right\}\right)= -\frac{\partial\{p\}}{\partial x_i}+\frac{\partial\{\tau_{ij}\}}{\partial x_i}+\alpha_c\{\rho_c\}g_i-\frac{1}{V}\sum_k v_{k,j}\dot{m}_k-\frac{1}{V}\sum_k \vec{F}_{k,i} \quad (3)$$

Energy equation:

$$\frac{\partial}{\partial t}\left(\alpha_c\{\rho_c\}\vec{u}_i\right)+\frac{\partial}{\partial x_i}\left(\alpha_c\left\{\rho_c \vec{u}_i i_c\right\}\right)= \frac{\partial}{\partial x_i}\left(k_{eff}\frac{\partial\langle T_C\rangle}{\partial x_i}\right)+\alpha_c\{\phi\}-\frac{1}{V}\sum_k v_{k,i}\dot{m}_k-\sum_k \vec{q}_k \quad (4)$$

3.2 The Governing equation of dispersed phase

Particle motion:

$$\frac{dv}{dt}=\frac{F_f}{m}+g \quad (5)$$

The trajectory of particle:

$$\frac{dx_p}{dt}=v \quad (6)$$

The temperature of particle:

$$\frac{dT_d}{dt}=\frac{1}{mc_d}\left(\vec{Q}_d+\vec{m}\,h_L\right) \quad (7)$$

3.3 Turbulence model

The Equation of turbulent kinetic energy:

$$\frac{\partial}{\partial t}(\rho k)+\frac{\partial}{\partial x_i}\left(\rho v_j k\right)= \frac{\partial}{\partial x_j}\left[\mu+\frac{\mu_t}{\sigma_k}\right]\frac{\partial k}{\partial x_j}+G_k+G_b-\rho\varepsilon \quad (8)$$

The equation for Turbulent dissipation rate:

$$\frac{\partial}{\partial t}(\rho\varepsilon)+\frac{\partial}{\partial x_i}\left(\rho v_j \varepsilon\right)= \frac{\partial}{\partial x_j}\left[\mu+\frac{\mu_t}{\sigma_\epsilon}\right]\frac{\partial \in}{\partial x_j}+G_k+\left(1-A_{3\varepsilon}\right)G_b+A_{1\varepsilon}\frac{\varepsilon}{k}-A_{2\varepsilon}\rho\frac{\varepsilon^2}{k} \quad (9)$$

3.4 Species Transport equation

$$\frac{\partial(\rho Y_k)}{\partial t}+\frac{\partial\left(\rho u_j Y_k\right)}{\partial x_j}=-\frac{\partial}{\partial x_j}\left(\rho D_k\frac{\partial Y_k}{\partial x_j}\right)+\dot{\omega}_k \quad (10)$$

3.5 Chemical kinetics

3.5.1 Moisture evaporation of drying bark particles

The biggest difference between biomass fuel and fossil fuel is the high moisture content. Assume that moisture evaporation occur rapidly before the bark particles reaction. The continuity equation for moisture component in particles is given as:

$$\frac{d\alpha_w m_p}{dt}=-r_{wp} \quad (11)$$

3.5.2 Raw bark devolatilization

Devolatilization is a step where the volatile matter gets out of bark particles.

$$Raw\ bark = YY_{pn}\left(volatile\ matter\right)+\left(1-\ YY_{pn}\right)\left(char\right) \quad (12)$$

The continuity equation for raw bark component in particles is given as:

$$\frac{d\alpha_{cp}}{dt}=-r_{cp} \quad (13)$$

The net rate of raw bark consumption given as:

$$r_{cp}=k_{pn}\alpha_{cp} \quad (14)$$

K_{pn} is reaction rate constant calculate using

$$k_{pn}=A_{pn}\,exp\left[-\frac{E_{pn}}{R_u T_p}\right] \quad (15)$$

3.5.3 First order char oxidation:

(char)+ (oxdizer)= (product)

The continuity equation for char component in particle p.

$$\frac{dm_{hp}}{dt}=-r_{hp} \quad (16)$$

The rate of formation of char from particle p

$$r_{hp}=r_{vp}\left(1-\ YY_{pn}\right)/YY_{pn} \quad (17)$$

The rate of reaction is calculated as follows:

$$k_{pl}=A_{pl}T_p^n\,exp\left[-\frac{E_{pl}}{R_u T_p}\right] \quad (18)$$

4 Boundary condition

Preheating was the first step in the operating combustor. Hot gas entered the combustor through the inlet 2. Preheating was defined by the initial condition. After the preheating temperature reached 500°, the bark particles and air entered the combustor through the inlet 1 by the feeder and fan, the Inlet1 was defined as injector. Meanwhile, the air entered the combustor through the inlet 3 by the other fan, the inlet3 was defined as velocity inlet. The combustion gas exited the combustor through the outlet, the outlet was defined as pressure outlet. The surface of modelling was defined as wall. So the initial condition was shown as table 5 and the boundary condition was shown as table 6.

Table 5 The details of initial condition

Initial condition	
Pressure	1atm
Species fraction	N2=0.78 O2=0.22
Velocity	0 m/s
Temperature	500℃

Table 6 The details of boundary condition

Boundary condition	
Inlet 1	
Type of injector	Surface injector
Mass flow rate	0.00786 kg/s
Particle diameter	Normal distribution Maximum=4.9mm Minimum=0.1mm Average=2.5 mm Standard deviation=0.01
Particle temperature	20℃
Species fraction	Rawmaterial=0.77 Moisture=0.1289 Ash=0.1011
velocity	2.03 m/s
Inlet 3	
Type of boundary	Velocity inlet
Velocity	3.4 m/s
Species fraction	N2=0.78 O2=0.22
Static temperature	20℃
outlet	
Type of boundary	Pressure outlet
Pressure	1atm
Species fraction	N2=0.78 O2=0.22
Static temperature	20℃

RESULT AND DISCUSSION

The mass fraction of bark particles gradually declined from high to low in the combustor as shown as figure 6. The bark particles did not combust immediately. The structure of the combustor was designed to prolong the heating time of the particles, on the one hand enhanced the evaporation of water, on the other hand enhanced the mixing of bark particles with hot air.

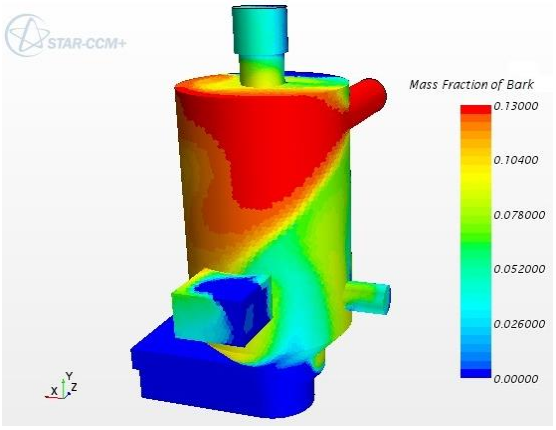

Fig. 6 Mass fraction distribution of bark

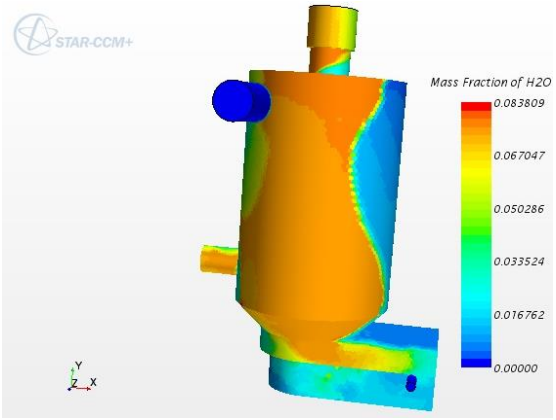

Fig. 7 Mass fraction distribution of H_2O

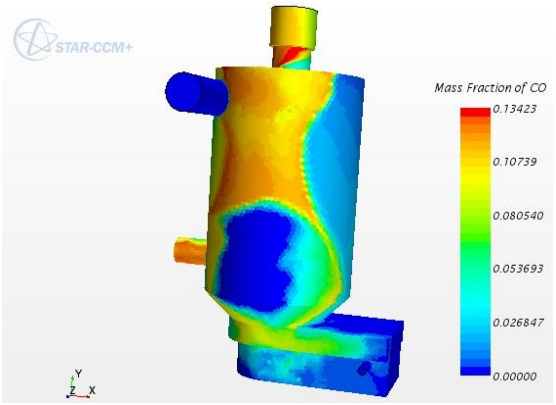

Fig. 8 Mass fraction distribution of CO

The bark particles combusted and generated H_2O and CO as shown as figure 7 and figure 8, then CO reacted with O_2 and generated CO_2 as shown as figure 9. The mass fraction of CO was the lowest, the mass fraction of CO_2 was the highest, the mass fraction of O_2 was the lowest in the lower of combustor as shown as figure 9 and figure 10. Meanwhile the temperature was the highest in this area as shown as figure 11. It was combustion area.

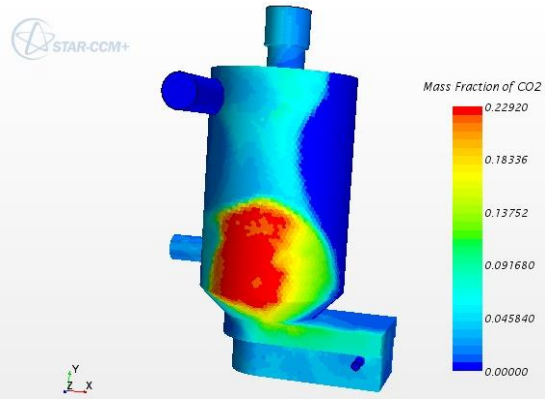

Fig. 9 Mass fraction distribution of CO_2

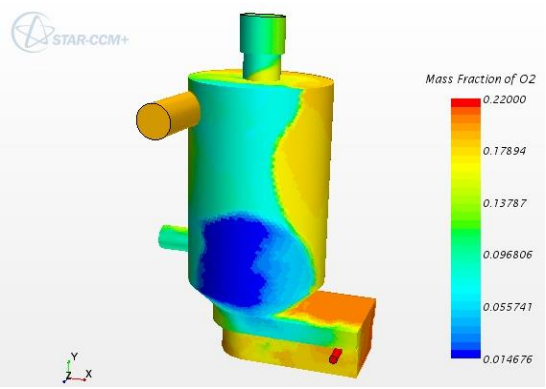

Fig. 10 Mass fraction distribution of O_2

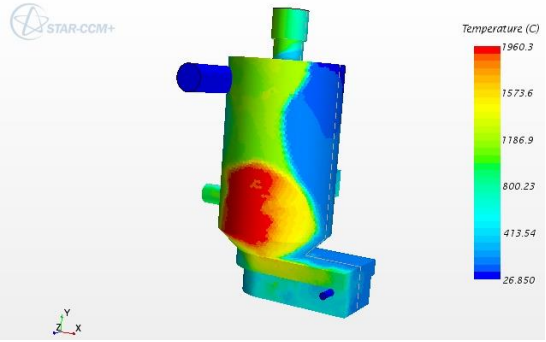

Fig. 11 The distribution of temperature

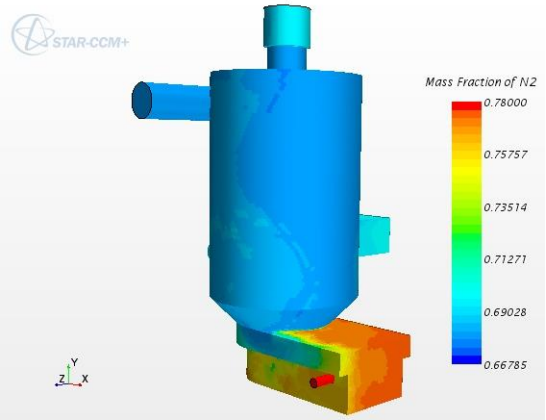

Fig. 12 Mass fraction distribution of N_2

The mass fraction of N_2 was the highest in the bottom of combustor, and lower in the top of combustor. Combustion was considered a process which is the solid phase converted into gas phase. So N_2 was diluted in this process.

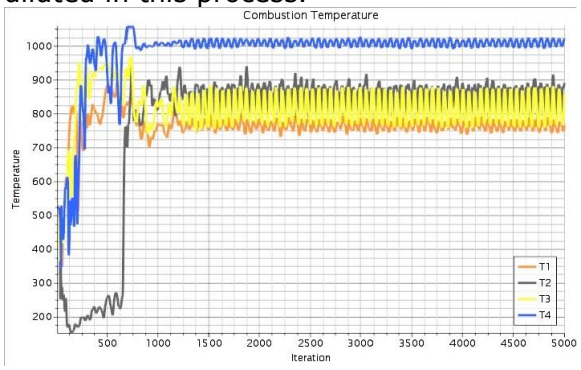

Fig. 13 The temperature distribution of four thermocouples

The temperature of T4 was the highest, about 1000 °C. The temperature of T1, T2 and T3 was in the range from 750 °C to 900 °C. The temperature of T1, T2, T3 and T4 were stable after 1000 iterations. It was considered drying bark particles can combust stably and independently in compact combustor.

CONCLUSION

a. The drying bark particles can combust stably and independently in compact combustor.

b. No pollutant were produced in the combustion process.

c. It was rational design for compact combustor and it was suitable for combusting bark particles.

REFERENCES

[1] B. LIU et al (2015), Combustion characteristics of biomass residue based on thermo gravimetric analysis, Journal of Central South University (Science and Technology), Vol. 46, No.3, pp. 1118-1122.

[2] F. F. MIN and M. X. Zhang (2005), Study on combustion model and combustibility of biomass, Journal of China coal society, Vol. 30, No.1, pp. 105-108.

[3] J. Q. XU et al (2006), Quantity analysis on the biomass of woody bio-energy trees, Journal of Beijing Forestry University, Vol. 28, No. 6, pp. 98-102.

[4] J. Y. LIU et al (2001), Analysis on the characteristics of biomass fuel direct combustion process, Journal of Northeast Agricultural University, Vol. 32, No.3, pp. 290-294

[5] Z. F. TIAN et al (2014), Analysis of Mechanism and the Factors Influencing the Combustion of Biomass Fuels, Journal of Anhui Agri. Sci. , Vol. 42, No.2, pp. 541-543.

[6] Z. ZHOU and W. L. WU (2005), Status quo and prospects of biomass energy, Transactions of the Chinese Society of Agriculture Engineering, Vol. 21, No.12, pp. 12-15.

8th International Engineering Symposium - IES 2019
March 13-15, 2019, Kumamoto University, Japan

Effects of Hyper-concentrated Sediment on Flow Mechanism in An Open Channel with Cylindrical Roughness

Hiroto Kondo [1], Terunori Ohmoto [2], Kanji Adachi and **Hirotaka Une[3]**

1 *Graduate School of Science and Technology, Kumamoto University, 2-39-1 Kurokami, Kumamoto 860-8555, Japan. Email: 182d8306@st.kumamoto-u.ac.jp*
2 *Civil and Environmental Engineering, Kumamoto University, 2-39-1 Kurokami, Kumamoto 860-8555, Japan. email: ohmoto@kumamoto-u.ac.jp*
3 *Graduate School of Science and Technology, Kumamoto University, 2-39-1 Kurokami, Kumamoto 860-8555, Japan. Email: 171d8801@st.kumamoto-u.ac.jp*
4 *Graduate School of Science and Technology, Kumamoto University, 2-39-1 Kurokami, Kumamoto 860-8555, Japan. email: 181d9201@st.kumamoto-u.ac.jp*

ABSTRACT: Hyper-concentrated sediment flow is observed in Yellow River and mud flow. It causes river engineering problems such as local scouring and deposition. Hyper-concentrated sediment flow contains a large amount of clay and /or silt particles, and therefore it has Non-Newtonian properties. Although behaviour of hyper-concentrated sediment flow may be different from that of clear water flow, effect of hyper-concentration sediment flow on fully developed turbulent structure has rarely been investigated. In this context, this study conducted experiments to investigate resistance characteristics and flow structure of hyper-concentrated sediment flow in an open channel with cylindrical roughness. Flow pattern was measured by means of Particle Image Velocimetry (PIV). For the experiments with the PIV, poly sodium acrylic (PSA) solution was utilized to generate hyper-concentrated sediment flow because PSA solved water flow has similar viscous properties to Kaolin suspended flow, and it has an advantage of enabling measurement by the PIV method. The results show that the resistance in the PSA solution of 300mg/ℓ is 0.67 times larger than that in the Clear Water, and the resistance in the PSA solution of 800mg/ℓ is 1.27 times larger than that in the Clear Water.

Keywords*: hyper-concentrated flow, Non-Newtonian properties, PIV, PSA solution, Cylindrical roughness*

INTRODUCTION

Hyper-concentrated sediment flow containing a large amount of fine sediment such as clay and silt has been observed various conditions. For example, it has been observed rivers in the Yellow River basin, and tidal currents containing lagoon sediment near the Rokkaku River estuary at the head of bay in the Ariake sea. In the Shirakawa River in Kumamoto prefecture, it was reported that the volume concentration of sediment showed 10% due to flood disaster on June 26, 1951.

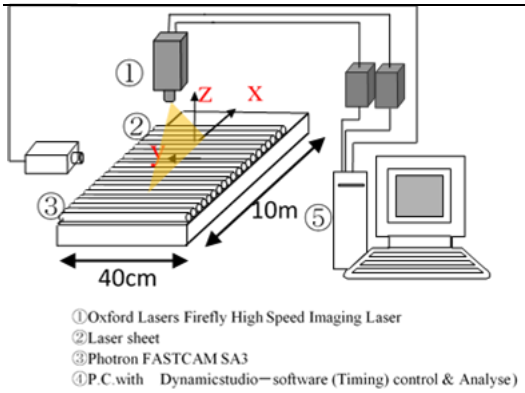

Fig.1 Outline of PIV

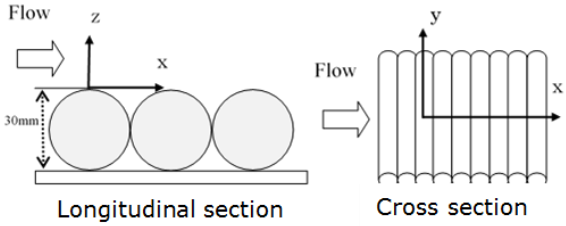

Fig.2 Boundary condition

The definition of hyper-concentrated sediment flow is different from researcher, Z.wang et al [1], the sediment flow with a concentration of 200kg/m^3 and a volume concentration of 8% or more is defined as a hyper-concentrated sediment flow in the Yellow River where sediment containing a lot of minerals flows. Bradley & McCutcheon [2], when the volume concentration is 20% or less, it is a standard water flow which has little influence on density and viscosity, its characteristics appeared when the volume concentration is 20% or more. And especially in the case of sediment flow with clay or silt volume concentration of 5% or more, they revealed that it shows non-Newtonian fluid properties.

From this fact, the dynamic characteristics of the hyper-concentrated sediment flow are greatly different from the clear water, and as the viscosity and the density increase, the turbulence intensity, the distribution of the concentration of the sediment, the resistance characteristic of the flow and the sediment transporting ability change is expected. However, there are many unclear points about its flow mechanism.

As described above, it is necessary to consider the sediment concentration in evaluating the safety level of the flood

Table 1 Experimental conditions

	Case-1	Case-2	Case-3
PSA solution C_w (mg/ℓ)	0	300	800
Discharge Q (ℓ/s)	4.0	4.2	3.6
Channel slope I_0	1/300	1/300	1/300
Flow depth H (cm)	3.23	2.83	3.50
Mean flow velocity U_m (cm/s)	31.37	35.74	28.92
Friction flow velocity U_* (cm/s)	3.25	3.04	3.38
Froude number $U_m/\sqrt{gH}$	0.557	0.678	0.493
Drag coefficient $C_f=2(U_*/U_m)^2$	0.0215	0.0145	0.0274

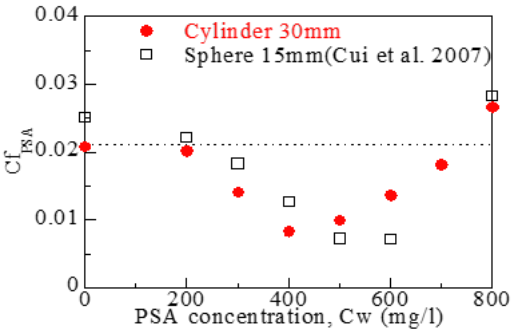

Fig.3 Relationship between flow resistance and PSA concentration

control. Establishment of the resistance law of flow is fundamental in evaluating the safety level of flood control, improvement of prediction accuracy of roughness coefficient is important. Resistance characteristics of flow in real river are defined comprehensively by interaction with riverbed wave, riverbed material, riverbed shape, vegetation community in river way, furthermore river structure and the like. Since it is difficult to calculate the roughness coefficient mathematically or deductively from known boundary conditions, it is currently judged by the apparent roughness coefficient obtained empirically.

Many researches have been conducted in the past, and the resistance law of flow depends on the roughness shape, arrangement and size, and flow conditions. Sufficient research has been done on the resistance law in clear water, but the research on the resistance law in hyper-concentrated sediment flow has not been done sufficiently.

In their experiments, Wang et al. [1] varied the clay concentration of kaolin suspension flow over smooth, gravel and stone beds within a clay concentration by volume of 9%, and showed that as the sediment concentration increased, the resistance coefficient clearly tended to decrease over the gravel and stone beds within the sediment concentration range of 3% to 9% and it tended to increase slightly over the smooth bed. In high sediment concentration flow, however, suspended kaolin particles might be deposited in the spaces between roughness elements, and their paper did not mention the influence of changes in boundary conditions on resistance.

Research on hyper-concentrated sediment-laden flow relies mainly on conceptual models and tends to lack validation because of the difficulty involved in flow measurement. Those models assume that as sediment concentration increases, turbulence is damped rapidly. Experimental research using clay particles such as montmorillonite and kaolin, however, pointed out that transitional turbulent flow exists between laminar flow and turbulent flow. Wang and Plate [3] reported that transitional clay suspension flow is characterized by strong turbulence in the vicinity of the roughness and turbulence damping in laminar-flow regions far from the channel walls. Baas and Best [4] found that in open channel flow using kaolin clay particles over a smooth surface, turbulence structure varied considerably within a volumetric sediment concentration range of 2% to 4%, showing similarity to the transitional flows reported by Wang and Plate [3].

This study investigated the effects of hyper-concentrated sediment on the resistance and flow structure in flow over cylindrical roughness used as two-dimensional roughness elements. The flow structure was examined in detail through comparison with clear-water flow and sediment-laden flow over cylindrical roughness by using a poly (sodium acrylate) (PSA) solution, which viscosity characteristics are similar to those of hyper-concentrated kaolin-laden flow.

EXPERIMENTAL APPARATUS AND METHOD

This flume used in the experiment is a variable-slope, re-cycling straight flume that is 10 m long, 40 cm wide and 20 cm high. The measurement zone is made entirely of acrylic plastic so that laser beam can be radiated from the sidewalls. Table 1 shows the experimental conditions. As shown in Figure.1, a right-handed coordinate system is used for the measurement zone. The direction of flow is x-axis, the transverse direction is the y-axis, and the vertical direction is the z-axis; and corresponding mean velocity components and fluctuating velocity components are U, V and W and u', v' and w', respectively. Figure.2 shows boundary condition.

On the flume in a 9.5 m-long section starting from the upstream end of the flume, aluminum pipe 30mm in diameter were arranged in a close-packed manner. Flow velocity was measured by particle image velocimetry, which is a representative non-contact image processing method. Figure.1 illustrates the measurement system.

An air-cooled double-pulse YAG laser (25mJ) was used as the light source. The laser light sheet thickness was 1mm, and the interval was 2000 μs. For measurement in the xz plane, laser was radiated horizontally through the sidewall. Visualized images acquired by synchronized use of laser and a CCD camera were recorded on the hard disk of a personal computer in the form of 125 fps (frame per second) 1024×1024-pixel, monochromatic video data and were processed by PIV. Lenses with focal of 50 mm and 200 mm were used. The former was used for a shooting range of 50 mm or more, and the latter was used for a shooting range of 15 mm or less to acquire detailed images of near-gravel regions. The minimum pixel size was 0.09 for the 50 mm lens. The velocity sampling frequency was 62.5 Hz. The number of images per measurement plane was 4000, and the measurement time per plane was 32 sec. Nylon particles with a diameter 100 μm and a specific gravity of 1.02 were used as tracers.

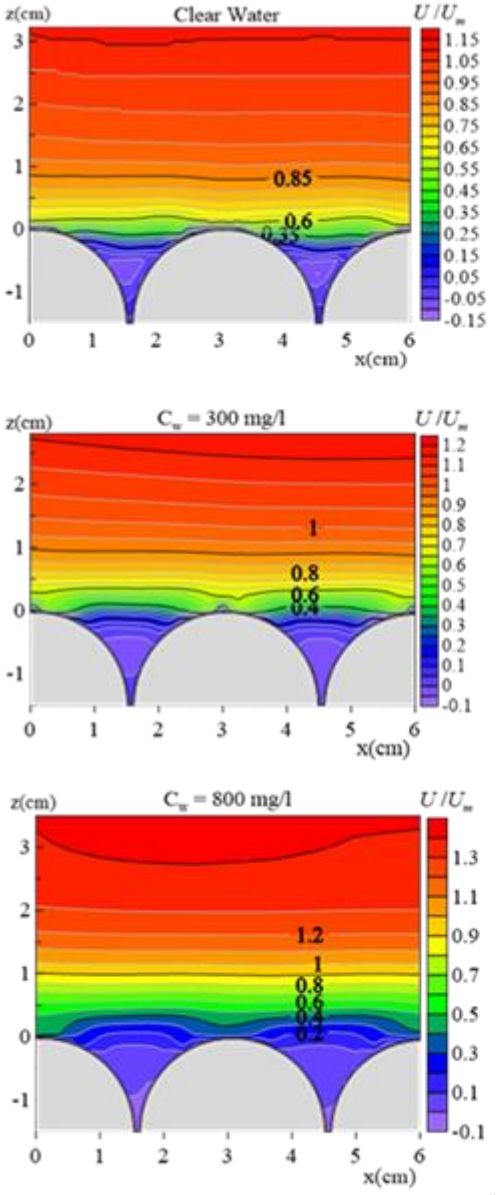

Fig.4 Main flow velocity

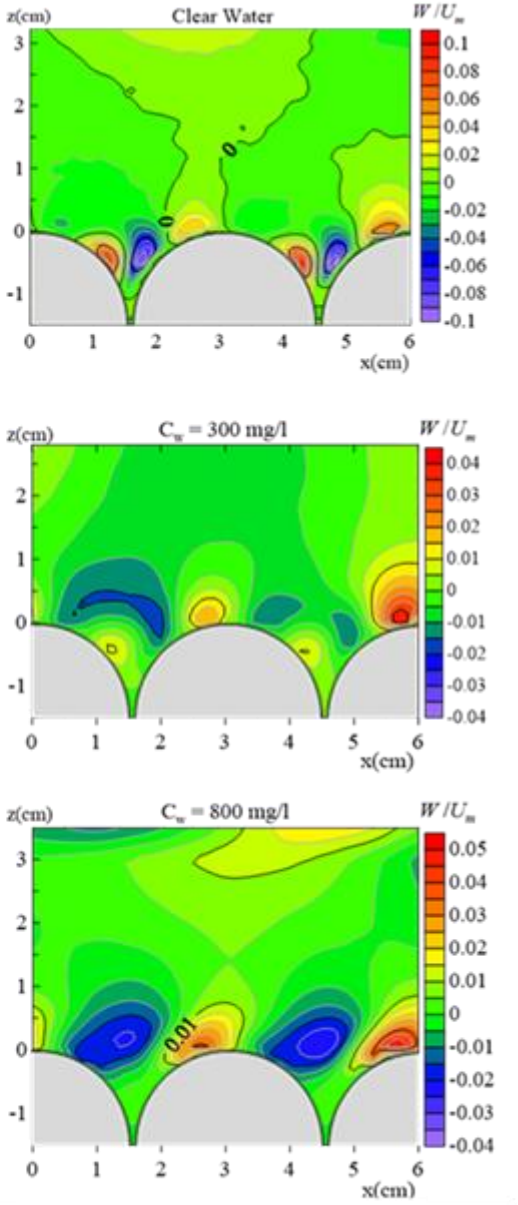

Fig.5 Main flow velocity

EFFECT OF HIGH SEDIMENT CONCENTRATION ON DRAG CHARACTERISTICS

Poly sodium acrylic (PSA) solution as simulated fluid of a hyper-concentrated sediment flow. For the experiment, a uniform flow field was created by letting water flow down the flume at the predetermined rate and adjusting the weir opening at the downstream end of the flume. Uniform flow depth was measured from the top of the spherical roughness using a point gauge. The resistance coefficient was determined from the measured uniform flow depth.

The total drag coefficient is defined as the ratio of total resistance to the inertia of fluid and is expressed by following equation.

$$Cf = 2\left(U_* / U_m\right)^2 \quad (1)$$

where U_* = $(ghi_0)^{1/2}$; g is gravitational acceleration; i_0, flume slope; and U_m, cross-sectional mean flow velocity.

As shown in Fig.3, in the range of PSA solution concentration Cw=200mg/l to 700mg/l, the drag coefficient Cfpsa is clearly smaller than that in Clear Water. At the PSA solution concentration Cw=800mg/l, Cfpsa/Cfw=1.28 and drag coefficient increases. Specifically, the drag

coefficient shows a decreasing tendency in the range of Cw=0 to 400mg/l, and it shows the minimum value when Cw=400mg/l corresponding to Kaolin volume concentration Cv=7%. When Cw=400mg/l, it show an increasing tendency, it becomes equal to the drag coefficient in the clear water around Cw=730mg/l and at Cw=800mg/l it is larger than the drag coefficient in Clear water.

It is considered that this is due to magnitude relationship between the decrease in Reynolds stress and the increase in viscous stress because the viscosity was increasing. It implies that the reason why the uniform flow depth and resistance coefficient at the PSA solution concentration Cw=300mg/l is smaller than them in the case of clear water is that the Reynolds stress decreases and the viscous stress increases with increase in viscosity but the decrease in Reynolds stress is greater than the increase in viscous stress. In addition, it implies that the reason why the uniform flow depth and the resistance coefficient at the PSA solution concentration Cw=800mg/l is larger than them in the case of clear water is that the Reynolds stress decreases and viscous stress increases with increase in viscosity but the increase in viscous stress is greater than decrease in Reynolds stress.

TIME AVERAGE FLOW CHARACTERISTIC

This study covers roughness flow. aluminum pipe with a diameter of 30mm are used as a model of gravel. Poly sodium acrylic (PSA) solution is used as simulated hyper-concentrated sediment flow. In order to know the resistance law and the flow structure of the non-Newtonian flow in spherical roughness flow using the PIV method were examined by comparison with the clear water. The color contours of the main flow velocity U and the vertical flow velocity component W at the clear water, the PSA solution concentration Cw=300mg/l and 800mg/l are shown in the Figure.3 and Figure.4. In addition, as shown in Figure 2, it shows boundary condition. In Figure.1 and Figure.4, the value is divided by mean flow velocity. The origin of the vertical coordinate axis z was the top of roughness as the reference plane. Table 1 shows the experimental conditions for flow velocity measurement.

Figure.3 shows the color contour of the main flow velocity U. From Figure 4, the acceleration zone is seen upstream from the top of the roughness and the deceleration zone is seen in the downstream. It is also confirmed that the change in the vertical direction of the main flow velocity decreases in the vicinity of the water surface at the PSA solution concentration Cw=300mg/l and Cw=800mg/l. Therefore, a plug flow is formed in the vicinity of the water surface at the PSA solution concentration Cw=800mg/l. Plug flow is a flow in which the same speed is bundled.

In Figure.3, the value of the main flow velocity in the vicinity of the roughness is U(CW)= 0.55 at the clear water, U(300mg/l)= 0.45 at the PSA solution concentration Cw=300mg/l and U(800mg/l)= 0.41 at the PSA solution concentration Cw=800mg/l. The magnitude relationship of the main flow velocity was $U(800mg/\ell)<U(300mg/\ell)<U(CW)$. As the viscosity increases, the main flow velocity stabilizes.

Figure.4 shows the color contour of the vertical component W. It was found that the vertical flow velocity component W forms an upward flow at the upstream side of the roughness top and a downward flow at the downstream side. As the concentration of the PSA solution increases, the upward flow and the downward flow become more regularity. Therefore, it was found that the vertical flow velocity component W stabilized as the PSA solution concentration increased. The magnitude relationship of the upward flow is $W_{up}(300mg/\ell)<W_{up}(CW)<W_{up}(800mg/\ell)$, the magnitude relationship of the downward flow is $W_{down}(300mg/\ell)<W_{down}(CW)<W_{down}(800mg/\ell)$.

As shown above, magnitude relationship between the main flow velocity in each PSA concentration is $U(800mg/\ell)<U(300mg/\ell)<U(CW)$. The main flow velocity decreases as the PSA solution concentration increases. The main

flow velocity at the PSA solution concentration Cw=800mg/l in the vicinity of the roughness is generally smaller than the main flow velocity at the clear water and PSA solution concentration Cw=300mg/l. Therefore, since momentum transport by advection is small and momentum transport of turbulence in vicinity of roughness can be neglected, it is recognized that the viscous effect is dominant.

Vertical flow velocity component W shows upward flow and downward flow with high regularity in each PSA solution concentration increases. As the PSA solution concentration increases, the upward flow and the downward flow tend to stabilize.

CONCLUSION

This study investigated the effects of hyper-concentrated sediment on the drag and flow structure in flow over cylindrical roughness used as two-dimensional roughness elements. The flow structure was examined in detail through comparison with clear-water flow and sediment-laden flow over spherical roughness by using a poly (sodium acrylate) (PSA) solution, whose viscosity characteristics are similar to those of hyper-concentrated kaolin-laden flow.

1. The drag coefficient shows a decreasing tendency in the range of Cw=0 to 400mg/l, and it shows the minimum value when Cw=400mg/l corresponding to Kaolin volume concentration Cv=7%. When Cw=400mg/l, it show an increasing tendency, it becomes equal to the drag coefficient in the clear water around Cw=730mg/l and at Cw=800mg/l it is larger than the drag coefficient in Clear water.
2. Magnitude relationship between the main flow velocity in each PSA concentration is U(800mg/ℓ)<U(300mg/ℓ)<U(CW).
3. Momentum transport by advection is small and momentum transport of turbulence in vicinity of roughness can be neglected, it is recognized that the viscous effect is dominant at PSA concentration Cw=800mg/l.

REFERENCES

[1]Wang, Z.Y., Larsen, P., Nesimann, F., and Ditirich, A. , Resistance and drag reduction of flows of clay suspensions: Journal of Hydraulic Engineering, v. 124(1998), pp.41–49.

[2] Bradley,J.B. and McCutcheon,S.C： The effects of high sediment concentrantion on transport processes and flow phenomena, proc. Conf.Erosion,Debris prevention,Japan. 1985

[3] Wang, Z., and Plate, E.J. , A preliminary study on the turbulence structure of flows on non-Newtonian fluid: Journal of Hydraulic Research, v. 34(1996), pp. 345–361.

[4] Baas, J.H., and Best, J.L. , Turbulence modulation in clay-rich sediment-laden flows and some implications for sediment deposition: Journal of Sedimentary Research, v. 72(2002), pp. 336–340.

8th International Engineering Symposium - IES 2019
March 13-15, 2019, Kumamoto University, Japan

Effects of Hyper-concentrated Sediment on Large-scale Vortex Structures in an Open-channel with Artificial Roughness

Kanji ADACHI [1], Terunori OHMOTO [2], Hirotaka UNE[3] and Hiroto KONDO[4]

1 *Graduate School of Science and Technology, Kumamoto University,2-39-1 Kurokami, Kumamoto 860-8555, Japan. e-mail:171d8801@st.kumamoto-u.ac.jp*
2 *Department of Civil and Environmental Engineering, Kumamoto University, 2-39-1 Kurokami, Kumamoto 860-8555, Japan e-mail:ohmoto@kumamoto-u.ac.jp*
3 *Graduate School of Science and Technology, Kumamoto University, 2-39-1 Kurokami, Kumamoto 860-8555, Japan. email: 181d9201@st.kumamoto-u.ac.jp*
4 *Graduate School of Science and Technology, Kumamoto University, 2-39-1 Kurokami, Kumamoto 860-8555, Japan. Email: 182d8306@st.kumamoto-u.ac.jp*

ABSTRACT: The effects of hyper-concentrated sediment flow on flow resistance and flow structure which are essential to estimate the safety level against flood have been investigated by many researchers not only because the hyper-concentrated sediment flow causes serious problems but also shows non-Newtonian properties. It still has questions as to the flow resistance under a certain condition and its turbulent structure. In the present paper, the experiments are conducted in an open-channel with the two-dimensional roughness which is employed to experimentally investigate the effects of the hyper-concentrated sediment flow on the turbulence structure by using Particle Image Velocimetry. The results of another experiment show that the Strauhal number of separation vortex decreases with a decrease of the Reynolds number caused by viscosity increase, and the path lines of vortexes which are obtained by applying vortex identification go through on the area where the shear rate and the turbulence intensity such as the Reynolds stress are great. Also, it found that the separation vortexes resulted from a roughness do not flow in the downstream in the case of high viscosity.

Keywords: *non-Newtonian fluids, PIV, separation vortex, open-channel turblence, identification of vortex*

INTRODUCTION

Hyper-concentrated sediment flow has observed oftentimes under the various conditions, moreover has known that its rheology property has non-Newtonian property. Nevertheless, there are some questions regarding the flow resistance and flow structure because of the difficulty for flow measurement. Therefore, it is extremely meaningful to investigate these questions in regards to hyper-concentrated sediment flow.

Wang et al. [1] varied the clay concentration of kaolin suspension flow over smooth, gravel and stone beds within a clay concentration by volume of 9%, and showed that as the clay concentration increased, the drag coefficient clearly tended to decrease over the gravel and stone beds within the clay concentration range of 3% to 9% and it tended to increase slightly over the smooth bed. In high clay concentration flow, however, suspended kaolin particles might be deposited in the spaces between roughness elements, and their paper did not mention the influence of changes in boundary conditions on drag.

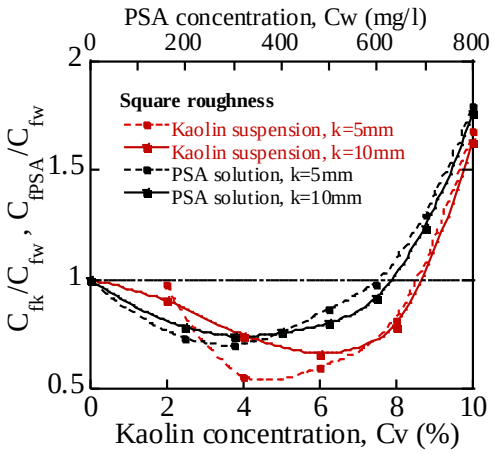

Fig.1 Dependence of flow resistance on sediment concentration (over two-dimensional roughness)

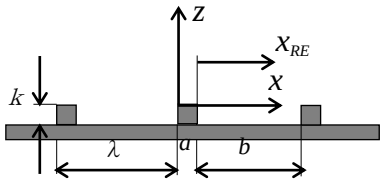

Fig.2 Boundary condition for flow measurement

Table 1 Experimental conditions for Flow Measurement

	Case 1	Case 2	Case 3
PSA concentration Cw (mg/l)	0	300	800
Discharge Q (l/s)	4	4	4
Flow depth H (cm)	7.96	7.19	9.61
Mean flow velocity U_m (cm/s)	12.56	13.91	10.41
Friction flow velocity U_* (cm/s)	3.95	3.75	4.34
Channel slope I_0	1/500	1/500	1/500
Froude number $Um/(gH)^{1/2}$	0.14	0.17	0.11
Reynolds number UmH/ν	10000	-	-

According to Ohmoto [2], as shown in Fig.1, in the open-channel with the two-dimensional roughness, the dependence of the flow resistance coefficient on the sediment concentration shows that the flow resistance coefficient decreases in the range of the sediment concentration by volume Cv <8.5%, conversely, increases in the range of the sediment concentration by volume Cv >8.5%. Additionally, the cause of variation on its flow resistance was revealed in terms of the shear stress and momentum transport that were obtained by measuring the flow structure and calculated. However, the flow resistance under the condition of roughness is essentially characterized by the separation vortex generated from the roughness elements. Yet, the separation vortex generated from the roughness elements at the time flowing the hyper-concentrated sediment flow has not revealed well.

On the other hand, the study employing identification of a vortex has already investigated in an open-channel with the two-dimensional roughness. Yoshimura and Fujita [3] examined the relationship between the separation vortices generated from roughness elements and the water surface fluctuation by numerical analysis. However, there is no mention regarding the relationship between vortices and the mean flow field. Furthermore, to the best of our knowledge, there is no study investigating the effects of hyper-concentrated sediment on large-scale vortex structure.

EXPERIMENTAL APPARATUS AND METHOD

The experimental apparatus and method used are the same as those reported in the preceding paper [2], and the drag coefficient calculation and flow analysis methods are also the same as those reported in the same paper.

The coordinate system has the x-axis representing the stream direction, the y-axis representing the cross-stream direction and the z-axis representing the vertical (upward) direction, and the corresponding flow velocity components are represented by U, V and W, and their fluctuation components by u', v' and w'.

Figure 2 shows the longitudinal and transverse arrangements of square ribs used as roughness elements. The roughness elements were stainless steel elements having a 10 mm (k) by 10 mm (a) square cross-section. The roughness elements were arranged over a length of 6 m on the flume bed from the location at a distance of 2 m from the upstream end of the flume.

For the experiment, a uniform flow field was created by letting water flow down the flume at the predetermined rate and adjusting the weir opening at the downstream end of the flume, and normal depth was measured with a point gauge. The roughness zone is 6 m long, and although the flow in the regions near its upstream and downstream ends is not uniform, flow depth in a 3 m to 4 m long section in between was uniform enough to regard it as a uniform flow field.

Table 1 shows the conditions of the experiment conducted to evaluate the effect of sediment concentration on the flow field. As described later, the concentrations of the poly(sodium acrylate) (PSA) solution simulating hyper-concentrated sediment-laden flow of *Cw* = 300 mg/l and *Cw* = 800 mg/l correspond, if calculated on the basis of comparable drag coefficients and viscosity coefficients, to kaolin concentrations by volume of *Cv* = 6% and *Cv* = 10%. The PSA solution is advantageous for flow measurement by PIV because it closely simulates hyper-concentrated sediment-laden flow in terms of viscosity properties and its colorless transparency enables the use of PIV for flow measurement.

Flow velocity was measured by PIV, a widely used non-contact image processing method.

PIV measurement was made in the uniform flow field 4 m downstream from the upstream end of the roughened surface.

The Q criterion, which utilizes the second invariant Q of the velocity gradient tensor, was employed as a vortex identification. When Q>0, its region is defined as a vortex. The vortices were identified using the measured flow field. The second invariant Q is expressed by the following equation (1).

$$Q = \frac{1}{2}\left(\|\Omega_{ij}\|^2 - \|S_{ij}\|^2\right)$$
$$S_{ij} = \frac{1}{2}\left(\frac{\partial u_i}{\partial x_j} + \frac{\partial u_j}{\partial x_i}\right), \qquad (1)$$
$$\Omega_{ij} = \frac{1}{2}\left(\frac{\partial u_i}{\partial x_j} - \frac{\partial u_j}{\partial x_i}\right)$$

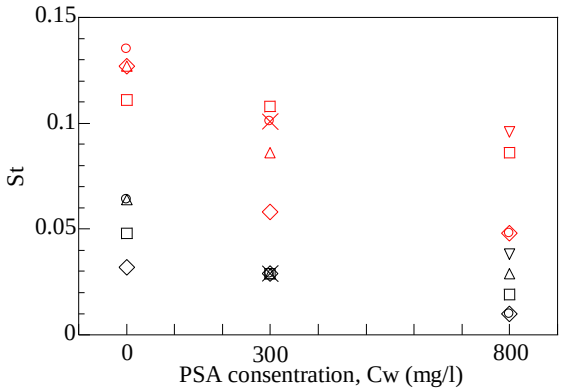

Fig.3 Relationship between the Strouhal number and PSA solution concentration

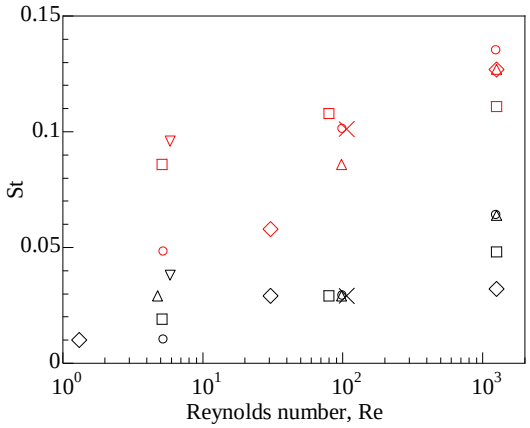

Fig.4 Relationship between the Strouhal number and the Reynolds number

Also, in order to investigate the generation frequency of the vortex, spectral analysis was performed on the fluctuating flow velocity component at designated coordinates, and the dominant frequency was obtained.

EFFECTS OF HYPER-CONCENTRATED SEDIMENT ON TEMPORAL PROPERTY OF LARGE-SCALE VORTEX

Fig. 3 shows the relationship between the Strouhal number and the PSA solution concentration. The Strouhal number here was non-dimensionalized the dominant frequency which was obtained by spectral analysis of the fluctuating flow velocity component at designated coordinates. Then, black dots indicate the first peak in

the power spectrum distribution, and red ones indicate the second peak.

As the PSA solution concentration increases, the dimensionless frequency of the vortex is decreasing.

Figure 4 shows the relationship between the Strouhal number and Reynolds number.

The kinematic viscosity coefficient here at the Reynolds number in the PSA solution was in accordance with Ohmoto et al [4].

It is shown that the Strouhal number is decreasing with the decrease of the Reynolds number due to the viscosity increase by increasing PSA solution concentration.

EFFECTS OF HYPER-CONCENTRATED SEDIMENT ON SPATIAL CHARACTERISTIC OF LARGE-SCALE VORTEX

Figure 5 shows the Reynolds stress distribution and the path line of the center of a large scale vortex at the clear water flow and PSA solution concentration *Cw* = 300 mg/l.

It is shown that the vortex path lines correspond to the region where the Reynolds stress has a large value, which means momentum transportation is great, except in the region of the immediate downstream of roughness.

In addition to that, it is also shown that the vortices pass through the region where has the great value of the shear rate of the main flow velocity.

Also, it is found that the distance of the separation vortex from roughness top that vortices generate to the position where the vortex move up results in longer by the increase of the PSA solution concentration.

Figure 6 shows the appearance frequency of the vortex $P_{Q>Qc}$ ($= n_{Q>Qc}/n$, $n_{Q>Qc}$: the number of satisfying $Q > Qc$, n: the number of time series data, $Qc = 0.4$) at the PSA solution concentration Cw=800mg/l. Here, the broken line shows $d^2U/dz^2 = 0$.

The appearance of vortices was confirmed in the upper layer and the lower layer of the maximum value position of the shear rate.

For *Cw* = 800 mg / ℓ, vortices generated from the roughness top are not confirmed

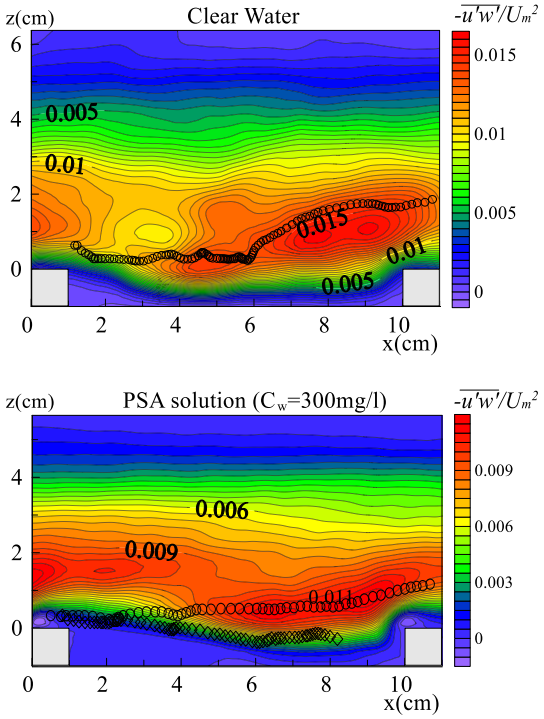

Fig.5 the Reynolds stress distribution and the path line of vortex

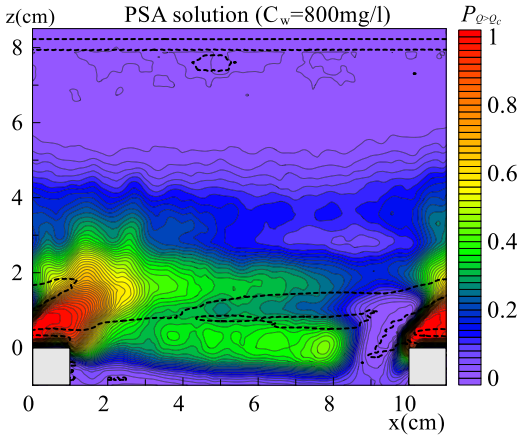

Fig.6 Distribution of appearance frequency of vortex

except in the region of close to roughness. Therefore, it is suggested that the increase in viscosity does not develop the vortices and attenuate vortices.

CONCLUSION

In previous study, under the condition of hyper-concentrated sediment flow, it is implied in the following. The large-scale

vortices generation is restrained. In other words, the frequency of vortex generation decreases with the increase of viscosity due to sediment concentration increases. In addition, it was shown the relationship between the vortex path line and averaged flow fields. That is the vortex path line corresponds to the region where turbulence intensity, the Reynolds stress, and shear rate are great.

REFERENCES

[1] Wang.Z.Y., Larsen.P, Nestmann.F, Dittrich.A : Resistance and drag reduction of flows of clay suspensions, Journal of Hydraulic Engineering, Vol.124, pp.41-49, 1998.

[2] Ohmoto Terunori, Hendratta Liany, Nishi, Shogo: Effects of Hyperconcentrated Sediment on Flow Resistance and Flow Structure in AN Open Channel with Regulaly Arrayed Square Ribs, Journal of Japan Society of Civil Engineers, JSCE,Ser. B1 (Hydraulic Engineering) , vol. 70, issue 4, pp. I_655-I_660, 2014. (in Japanese)

[3] Hideto YOSHIMURAE, Ichiro FUJITA: ANALYSIS OF ASCENDING SEPATARED VORTICES GENERATED FROM A STRIP ROUGHNESS BY USING LES WITH IMMERSED BOUNDARY METHOD, PROCEEDINGS OF HYDRAULIC ENGINEERING, Volume 51 Pages 769-774, 2007. (in Japanese)

[4] Terunori OHMOTO , Zhiying CUI and Yuri KAKIHARAON, RHEOLOGY OF HYPER-CONCENTRATED SEDIMENT-LADEN FLOW, Journal of applied mechanics, JSCE, Vol.7 , pp.979-986,2004 (in Japanese) .

8th International Engineering Symposium - IES 2019
March 13-15, 2019, Kumamoto University, Japan

Investigation on the performance and emission characteristics of a variable compression ratio engine operated with cardanol Ricebran blends with diesel

K.V.Suresha[1,2],Amogh.D.M[3] ,Peter fernandes[4],Raju K[5]

1 *Department of Mechanical Engineering, St. Joseph Engineering college Mangalore, 575028, India.. email:* kvs_a@yahoo.com
2 *Department of Mechanical Engineering, Alva's Institute of Engineering and technology Moodabidri 574225, India. email:* kvs_a@yahoo.com
3 *Department of Mechanical Engineering, Alva's Institute of Engineering and technology Moodabidri 574225, India. email:amogh113@gmail.com*
4 *Département of Mechanical Engineering, Alva's Institute of Engineering and Technology, Moodabidri, 574225, India.email: principalaiet08@gmail.com*
5 *Department of Mechanical Engineering, St. Joseph Engineering colalege Mangalore, 575028, India.email: rajuksjec@gmail.com*

ABSTRACT:
In this study , performance and emission tests were conducted on a four-stroke variable compression ratio 5.2-kW diesel engine using cardanol which is a renewable biofuel was blended with Rice bran oil and diesel as a test fuel in a Volume basis of C5R5 (5% cardanol+5%Ric bran oil+90% diesel),C5R10,C5R15 and C5R20 (5%cardanol+20%Rice bran oil+75% diesel) were prepared and tested at various load like 0%,20%, 40%, 60%, 80%and full load conditions and compared with baseline diesel. From the result it was observed that the brake thermal efficiency of C5R5 is 29.23% comparatively similar to that of diesel 31.05%. The lower emissions of CO, hydrocarbon except NOx are encouraging to recognize Cardanol rice bran blends as an optimized fuel blend for a compression ignition engine. The significant factors of cardanol bio-fuel include its low cost, non-edible, abundance, and it is a by-product of the cashew nut industries this study demonstrates that cardanol Ricebran blends can be used as diesel engine fuel with any engine modification.

Keywords*: Injection Pressure, biodiesel, blends, Cardanol, Rice bran oil, Emission*

INTRODUCTION

Biodiesel is considered as the alternative for the depleting petroleum fuels. It is mainly extracted from vegetable oil and waste animal fats. As the properties of diesel and biodiesel are almost similar, the use of biodiesel in locomotive engines has gained much importance in recent years. The biodiesel has several advantages as compared to diesel such as less sulphur content in the fuel, and lower emission of hydrocarbons, carbon dioxide (CO_2), carbon monoxide (CO) and sulphur dioxide (SO_2) as reported by Patnaik and Acharya (2014). Increasing familiarity with the consumption of non-renewable energy source assets just as their negative natural effect s has activated enthusiasm for the potential benefits of biofuels, for example, biodiesel, which is an elective fuel for diesel motors reported by Pullen J, and Saeed (2011). Vegetable oils contain many fatty acids. Four fatty acids, namely palmitic, stearic, oleic and linoleic acids, present in higher compositions. The variation of fatty acid content in the biofuel affects the performance and emissions in a compression ignition (CI) engine reported by dinesha (2017).Das and Ganesh (2003) studied the methods of extraction of CNSL from cashew nut shell. The authors studied the yield of CNSL at low temperature pyrolysis (CNSL-1) and high temperature pyrolysis (CNSL-2). They did not report

much difference in properties like ash content, moisture, and density. It was observed that the viscosity changed drastically as the temperature rose from room temperature to higher temperature (60 and 80□C). They noticed a slightly higher calorific value and lower flash point in the case of CNSL-2 compared to CNSL-1 and the 100% miscibility with methanol and diesel showed good indication for blending with these fuels Kasiraman et al. (2012) studied the performance, emissions, and combustion characteristics of a single-cylinder four-stroke water-cooled DI diesel engine fuelled with 70% cashew nut shell oil (CNSO) and 30% camphor oil blend (CMPRO 30). They observed that CMPRO 30 blend performs closer to diesel with respect to performance, emissions, and combustion characteristics. The brake thermal efficiency of CMPRO 30 blend was 29.1% at peak load compared to diesel brake thermal efficiency of 30.14%, and 23.1% for neat CNSO. Pushparaj and Ramabalan (2013) conducted experiments a single-cylinder four-stroke DI diesel engine with B20 CNSL blend and ethanol percentages of 5, 10, and 15%. The results showed lower exhaust emissions for 10% ethanol with B20 CNSL blend. NO emissions reduced by 57% compared to B20. Wahome A. et al (2013) conducted engine performance using a single cylinder 4 stroke engine using diesel and Rice bran biodiesel blends. Biodiesel-diesel blends percentage varied by 5%, 10%, 15%, 20%, 25% and 30. Authors concluded that speed of the engine decreases with increase in load for all the blends. As the Biodiesel percentage increased in blends BP also increased. The BP for B5 was found to be 2.636kW while that of B30 it was 2.682kW. This variation was low compared to biodiesel percentage in blend. Engine torque increases with increase in load. When 100% biodiesel was used BSFC was increased by 47%. But, this was reduced to 13.2% when using a 5% blend. BTE was the same for biodiesel, diesel and all blends. This study concluded that Rice bran biodiesel gives similar characteristics as conventional diesel Subbaiah et al(2010) Investigate experimentally the performance and exhaust emission characteristics of a CI engine fuelled with normal diesel fuel, rice bran oil biodiesel, blends of diesel and rice bran oil biodiesel and three blends of diesel-biodiesel-ethanol over the entire range of load on the engine. Here, RBO is taken as additive to diesel-ethanol blends. Authors concluded that the highest BTE was observed with 15% ethanol in diesel-biodiesel-ethanol blends. As the ethanol percentage was increased the exhaust gas According to According to Bora et al. (2012) researched the qualities of biodiesel created by blending three sorts of feedstock (polonga, koroch, and Jatropa curcas) and found that there is a huge improvement in the physicochemical properties of the biodiesel acquired from blended feed stocks compared with those for individual biodiesels. In the present study two biodiesel in particular cardanol and Honge methyl ester were blended in various proportion with diesel and investigate the performance and emission characteristics of single cylinder 4 stroke diesel engine at 1500 rpm..

2. Materials and Methodology

2.1 Transesterification

As indicated by Srivastava and Prasad R (2004) there are four distinctive courses through which non-consumable oils can be converted into methyl esters are transesterification,blending,emulsion and pyrolysis out of which transesterification is ordinarily used.Dharmadhikariet.al(2012) expressed that Free unsaturated fat (FFA) substance should to be known for the crude oil.FFA will be determined by basic chemical titration .Rice bran oil was collected from market and cardanol was collected from Adarsh cashew industry Karkala area

2.2Methodology

One litre of Rice bran oil is warmed in open beaker to a temperature for 100oC to expel water particles present in oil pursued by filtration of oil. The oil is prepared under alkali base based catalyzed transesterification method. Since FFA value was observed to be 0.846%.The oil is blended with300ml of methanol and 6 grams of sodium hydroxide pallets in round bottom flask mixed on a hot plate magnetic stirrer for a one and half hour at 60 ^{o}C and after that

it is permitted to settle down for around 6 to 8hrs to get biodiesel and glycerol. The biodiesel obtained in the process is further washed with water to remove moisture content. Hence Rice bran biodiesel is obtained.

2.3 properties of biodiesel

Haiter and Lenin (2012),Senthil Kumar et.al(2012) expressed that some of the properties like flash point, viscosity, density, specific gravity and calorific value are needed for using the bio-diesel as vehicular fuel. The Physico-chemical properties such as higher calorific value, density, kinematic viscosity, flash and fire points are determined as per ASTM standards for biodiesel. In this study 4 blends are used C5+R5+90D (5%Cardanol+5%Rice bran methyl ester +90%diesel),C5+R10+85D,C5+R15+80D, andC5+R20+75D(5% Cardanol +20% Rice bran methyl ester+75% diesel)were used. The properties of different samples are shown in Table 1.

3. Experimental Procedure

The engine tests were conducted on a computerized single cylinder four four-stroke, water-cooled diesel engine test rig (Fig. 1). It was specifically coupled to a current dynamometer. The engine and the dynamometer were interfaced to a control board, which was associated with an advanced PC, utilized for recording the test parameters, for example, fuel flow rate, temperatures, load and so on. The calorific value and the density of the specific fuel is fed to the software calculating the engine performance. To record the data online, software was logged every time and data stored in the computer hard disk, which can be retrieved when required. The set of experiments were conducted at the designed speed of 1500 RPM and compression ratios of 17.5:1. The experiments were conducted at no-load, 20%, 40%, 60%, 80% and full load with neat diesel and blends Cardanol oil and Methyl ester of Rice bran oil with Diesel as fuel. The exhaust gases are analyzed by using gas analyser and the specifications of the engine are shown in Table 2.

4. Results and Discussion

Initially the experiments were performed for diesel at 205bar injection pressure and 17.5:1. and then 4 blends of cardanol Rice bran methyl ester with diesel were carried out. The engine performance like brake specific fuel consumption, brake thermal efficiency, and emission like HC,CO and Nox were obtained and then compared the performance of blends with those of D100 at 17.5:1 compression ratio. Based on the experimental methodology the following results were obtained

4.1. Brake specific fuel consumption

The variation of BSFC against load for four blends is shown in Fig. 3. From the results it was observed that the load increases the brake specific fuel consumption decreases for the fuel samples used in the test. It is observed that C5+R20+75D blend gives the minimum BSFC of 0.25 kg/kW-hr and minimum BSFC of 0.29 kg/kW-hr for C5+R5+90D blend and which found to be more than diesel i.e. 0.23 kg/kW-hr at full load.BSFC decreases with respect to load and shows close results to diesel. This may be due to improved combustion, low viscosity and high volatility of the test fuels

4.3 Brake Thermal Efficiency

Fig 4.Shows the variation in brake thermal efficiency against load. It was observed that the load increases the brake thermal efficiency also increases for all the fuel samples used in the test fuels. It was observed that the 5C+R20+90D blend gave the maximum brake thermal efficiency of 29.23% at full load which was nearer to the Brake Thermal Efficiency of diesel i.e. 31.05 %.This may be higher heat content, low viscocity,lower density and higher volatility. Since the viscosity and density of that blend nearer to that of diesel ensures finer breakup of fuel droplets at higher compression ratio providing more surface area and better mixing with air.

4.3 Hydrocarbon

Fig 5 shows that the variation of HC with respect to load. It was observed that C5+R5+90D blend shows minimum HC value is 73ppm at full load compared to 70ppm of diesel. The unburnt hydrocarbons emissions are higher at C5+R20+75D blend because low atomization and large droplets are formed

leading to more unvapourised hydrocarbons in the exhaust.

4.3 Carbon monoxide

The Fig. 6 depicts the variation of carbon monoxide against load. From the Fig. 6 it was observed that the emission of HC increases with increase in load. At full load condition, the emission of the HC similar for C5+R5+90D as compared to C5+R20+75D blend and 14.9% increases as compared to diesel. The CO emissions is minimum for all blends because low atomization. Low CO emission of biodiesel at 5C+5H+90D blend and at higher at 5C+20H+75D compared diesel likely due to oxygen content inherently present in the biodiesel which helps in the more complete oxidation of fuel

4.3 Nitric oxides

The Fig. 8 depicts the variation of oxides of nitrogen against load. The emission of NO_X is a phenomenon depends mainly on the combustion temperature. From the result It was observed that maximum Nox value obtained 760ppm at 5C+20H+75D and minimum 680ppm at 5C+5H+90D blend. High temperature and availability of oxygen are the two primary reasons for high NO_X formation as nitrogen and oxygen respond at higher temperature and due to high cylinder pressure and temperature at higher loads

5. Conclusion

The following conclusions may be drawn from the present study.

- Brake Specific Fuel Consumption has been reduced by 13.79% for C5+R5+90D as compared to C5+R20+75D blend. Brake thermal efficiency has been reduced by 5.86% for C5+R5+90D as compared to diesel.
- The HC, CO emissions have been increased by 14.9% for C5+R5+90D compared to diesel.
- The NO_X emission has been increased by 10.5% for C5+R5+90D as compared to C5+R20+75D blend
- By considering the above characteristics C5+R20+75D and C5+R5+90D blend may be used as a vehicular fuel for single cylinder four stroke diesel engines without any modification

REFERENCES

[1] Bora, D.K.et.al(2012).”Performance of diesel engine using biodiesel obtained from mixed feedstock’s”. Renew Sust Energy Rev ,16, 5479-5484

[2] Das P, Ganesh A. Bio-oil from pyrolysis of cashew nut shell—a near fuel. Biomass Bioenergy. ;25(1):113– 117

[3] Dharmadhikari.H.Met.al (2012)” Performance and emissions of CI engine using blends of biodiesel and diesel at different injection pressures. International Journal of Applied Research in Mechanical Engineering (IJARME) ISSN: 2231 – 5950, Vol-2, Iss-2,

[4] Dinesha P et.al(2016)Effect of varying 9Octadecenoic acid (oleic fatty acid) content in biofuel on the performance and emission of a compression ignition engine at varying compression ratio.Biofuels.;DOI:10.1080/17597269.1275491.

[5] Haiter Lenin.A and K. Thyagarajan(2012), ‘Performance evaluation of diesel engine fuelled with methyl ester of pongamia oil’, International Journal of Energy and Environment, Vol. 3, pp. 939-948

[6] Kasiraman Get.al(2012)” Performance, emission and combustion improvements in a direct injection diesel engine using cashew nut shell oil as fuel with camphor oil blending. Energy;47:116– 124.

[7] Patnaik, P P and Acharya, S K (2014), Effect of compression ratio on emission of CI engine using neat karanja oil and karanja oil methyl ester blend, International Journal of Engineering-Transactions C: Aspects, Vol. 27, No. 3, pp. 403-410

[8] Pullen J and Saeed K(2014) ‘Factor affecting engine performance and exhaust emissions- Part II: Experimental Study. Energy;72:17–34

[9] Pushparaj T and Ramabalan S(2013) Green Fuel Design for Diesel Engine, Combustion, Performance and Emission Analysis. Procedia Eng;64:701–709

[10]SenthilKumar.R and R.Manimaran,(2013) ‘Performance and emission characteristics on 4-stroke single cylinder C I engine using cotton seed bio fuels’ Asian Journal of Engineering Research, Vol. 1,Issue II, pp. 1 – 3.

[11] Srivastava A and Prasad R (2004) ”Triglycérides based biodiesel fuels,Renewable and sustainable energy reviews,4,111-133

[11] Subbaiah G V et.al(2010) “Rice bran oil biodiesel as an additive in diesel ethanol blends for diesel engines” *IJRRAS,* Vol.3, No.3, pp. 334-342

[12] Sureshkumar K,(2008). Performance and exhaust emission characteristics of a CI engine fuelled with Pongamia pinnata methyl ester (PPME) anditsblendswith diesel. RenewEnergy.;33(10):2294–2302.

[13] Wahome A(2013) “Performance Characteristics of Blended Rice Bran Biodiesel in a Diesel Engine”, International Journal of Engineering Science Invention, Vol. 2, Issue 5, pp.35-41.

Fig 1 Engine setup

Fig. 2 Trans-esterification of Honge oil

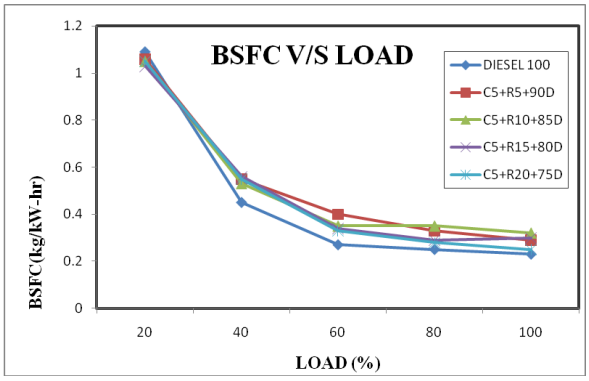

Fig.4 Variation of BSFC against load

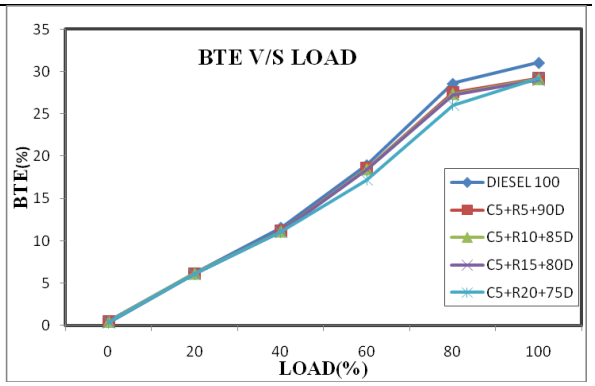

Fig6.Variation of BTE against load

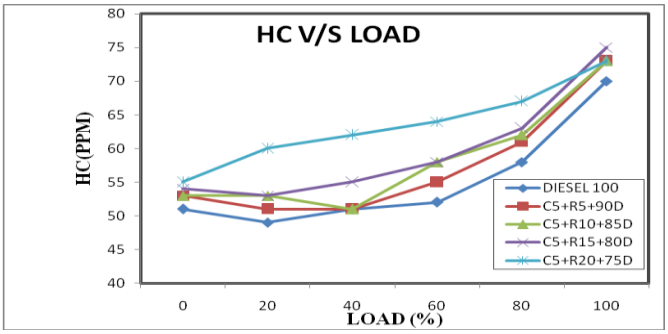

Fig6.Variation of HC against load

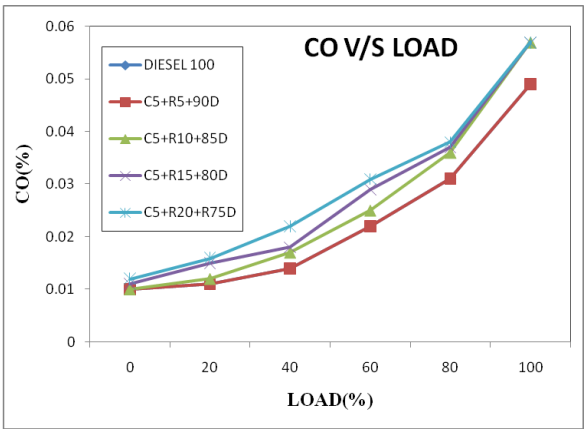

Fig7.Variation of CO against Load

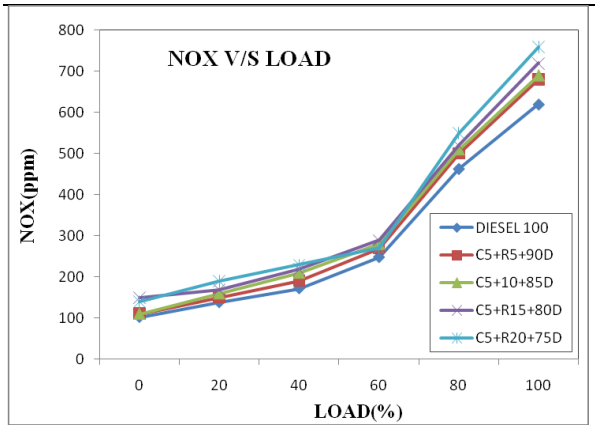

Fig 7.Variation of Nox against load

Table 1 Physico-chemical properties of different fuel samples

Properties	Higher Calorific value (kJ/kg)	Density (kg/m^3)	Kinematic Viscosity @ 40°C (cSt)	Flash Point (°C)
ASTM Standard	D 240	D 4052	D 445	D 93
Diesel	43033	823	2.58	46
Rice bran metyl ester	40850	885	4.40	160
Cardanol	37502	906	6.47	224
C5+R5+90 Diesel	42350	828	2.87	72
C5+R10+85 Diesel	41943	828	3.13	76
C5+R15+80 Diesel	41537	829	3.58	79
C5+R20+75 Diesel	41130	829	3.78	81

Table 2 Specifications of Diesel engine

S. No.	Parameters	Specification
1	Engine	4 Stroke, Single Cylinder, Constant Speed, Water Cooled Diesel Engine
2	Make	Kirloskar,TV1
3	BHP	5.2kW @ 1500 RPM
4	Stroke Length	110 mm
	Bore	87.5mm
5	Compression Ratio	17.5:1
6	Displacement Volume	661cc
7	Injection Pressure	205 bar
8	Lubrication	Forced feed system

8th International Engineering Symposium - IES 2019
March 13-15, 2019, Kumamoto University, Japan

Effect of Injection Pressure on Performance and Emission Characteristics of CI Engine Fuelled with blends of Honge, Rice bran hybrid bio fuel with Diesel

K.V.Suresh[1] Vidish Shetty [2],Peter Fernandes[3] Raju K[4]

1 *Department of Mechanical Engineering, Alva's Institute of Engineering and technology Moodabidri 574225, India. email:kvs_a@yahoo.com*
2 *Department of Mechanical Engineering, Alva's Institute of Engineering and Technology, Moodabidri, 574225, India.email: vidishshetty@gmail.com*
3 *Département of Mechanical Engineering, Alva's Institute of Engineering and Technology, Moodabidri, 574225, India.email: principalaiet08@gmail.com*
4 *Department of Mechanical Engineering, St. Joseph Engineering College Mangalore, 575028, India. email: rajuk@sjec.ac.in*

ABSTRACT: In the present study the performance and emission characteristics of single cylinder 4 stroke diesel engine using Honge and Rice bran oil (RBO) with diesel and its blends . The effect of variation in fuel injection pressure on the performance parameters like brake specific fuel consumption, brake thermal efficiency and emissions characteristic like CO, HC and NOx were studied at constant speed. The test results showed that, the Honge and Rice bran hybrid biodiesel blends at 220 bar injection pressure exhibited better performance and low emission than at 180bar injection pressures except No_x. Results were also showed that performance and emissions of Honge and RBO biodiesel hybrid blends were near to diesel.

Keywords*: Injection Pressure, biodiesel, blends, Honge oil, Rice bran oil, Emission*

INTRODUCTION

The internal combustion engine plays a major role in the power generation sector, power utilised in irrigation, transportation, marine sector, electricity production, transportation, defence, etc. is mainly produced from internal combustion (IC) engines. At present most IC engines are operated by fossil fuels. It is a known fact that the reserves of fossil fuels are depleting at a fast rate, and also the burning of fossil fuels leads to environmental problems such as smog, acid rain, depletion of the ozone layer, global warming, etc.reported by Bora et al (2014).Biodiesel is the name of a clean burning alternative fuel, produced from domestic, renewable resources such as soybeans,Sunflowers,Honge,waste cooking oil, or animal fats. Bio diesel is made through a chemical process called Transesterification in which glycerine is separated from fat or vegetable oil. The depletion of world oil reserves leads to the development of bio fuels since these fuels are promising alternatives to substitute fossil fuels according to Lin et al.(2011),Dharma.et.al(2016).Nowadays, there is great interest in mixing biodiesels produced from different feedstock in order to exploit the benefits of each type of biodiesel. A number of researchers have adopted approach an implemented these fuels in diesel engines as per Kent Hoekman et.al(2012).The biodiesel is produced by trans-esterification of oil or fats in medium such as methanol or ethanol with NaOH or KOH as catalyst. Methanol is used frequently because of less cost compared to other alcohols as reported by Meher et al. (2006). Karanja biodiesel was blended with diesel up to 30% and tested in a constant-speed diesel engine. The B20 blend (i.e. 20% biodiesel and 80% pure diesel) gave high thermal efficiency with low smoke emission compared to the other blends used in that

study by mohite kumar (2016). Saravanan et al.(2010) conducted an experiment to investigate the combustion characteristics of a CI engine using crude rice bran oil methyl ester (B20). The authors reported lower smoke and higher NOx for the biodiesel compared. Kapilan et al. (2006) studied the effect of fuel IP on the performance and emissions of a four-stroke single-cylinder DI diesel engine filled with karanja methyl ester blends (B20) as fuel. At 200 bar IP, B20 presented improved performance and reduced emissions than for other IPs. In addition, there was less CO, HC, NOx and smoke emissions as compared to diesel, and the B20 blend at 200 bar showed BTE similar to diesel As per Bora et al. (2012) investigated the characteristics of biodiesel produced by mixing three types of feedstock (polonga, koroch, and Jatropa curcas) and found that there is a significant enhancement in the physicochemical properties of the biodiesel obtained from mixed feed stocks compared to those for individual biodiesels. In this study two biodiesel namely honge and Rice bran oil methyl ester were mixed in different proportion with diesel and investigate the performance and emission characteristics of single cylinder 4 stroke diesel engine at 3 different injection pressures.

2. Materials and Methodology

2.1Materials

Honge oil is also called Karanja oil. Its botanical name is Pongamia pinnata L, belongs to family of Leguminaceae or papilionaceae. It can grow on most soil types ranging from stony to sandy to clayey. Karanja is a medium sized fast growing evergreen tree, which reaches 40 feet in height and The seeds are usually elliptical,2 cm long and 1.8 cm broad, wrinkled with reddish brown color. The time needed by the tree to mature ranges from 4 to 7 years and depending on the size of the tree the yield of kernels per tree is between 8 to 24 kg and the yield of potential per hectare is 900 to 9000 kg/hectare reported by Yaliwal.V S et.al (2010). Extraction requires passing the seeds through a screw crusher, generally called expellers. The oil is then filtered to make it clean enough for processing stated by C.V. Mahesh (2012) It is found that the maximum yields were obtained by the Solvent extraction method Honge oil was collected locally.

2.2 Transesterification of Honge and Rice bran oil

According to Srivastava and Prasad R (2004) there are four different ways through which non-edible oils can be converted into methyl esters are transesterification,blending,emulsion and pyrolysis out of which transesterification is used commonly reprted by Dharmadhikariet.al(2012) stated that Free fatty acid (FFA) content should be known for the raw oil FFA will be determined by simple chemical titration.

One litre of Honge oil is heated in open beaker to a temperature for 100^{o}C to remove water particles present in oil followed by filtration of oil. The oil is processed under alkali based catalyzed transesterification method since FFA value was found to be 2.76%.The oil is mixed with300ml of methanol and 6 grams of sodium hydroxide pallets in round bottom flask stirred on a hot plate magnetic stirrer for 90 minutes at 60 ^{o}C and then it is allowed to settle down for about 6 to 8hrs to obtain biodiesel and glycerol. The biodiesel obtained in the process is further washed with water to remove acid content and heated above 100^{o}C to remove the moisture. Hence pure honge biodiesel is obtained. Since the FFA Value of Rice bran oil (RBO) was found to be 0.846% Single stage is used.

2.4 Physico-Chemical properties of fuel samples

Haiter LeninK et.al(2012) and Senthil Kumaret.al(2012) stated that some of the properties like flash point, viscosity, density, specific gravity and calorific value are needed for using the bio-diesel as vehicular fuel. The flash and fire points were determined by ASTM Standard using closed cup apparatus, the kinematic viscosity was determined by cannon-fensky viscometer and the calorific value was determined by bomb calorimeter. Bio-diesel can be used in diesel engines either as a standalone or blended with diesel. H100 (Honge methyl ester) R100 (Rice bran oil methyl ester) were used. In this

study 2 blends in the proportion of 10R+5H+85D(10%Rice brain methyl ester +5%Honge methyl ester+90%diesel)and 20R+5H+75D(20%Ricebranmethyl ester +5%Honge and 90%diesel)were used. Table 1 gives the properties of above cited biodiesels

Details of Diesel Engine Test Rig

The engine tests were conducted on a computerized single cylinder four-stroke, water-cooled diesel engine test rig (Fig. 1). It was directly coupled to an eddy current dynamometer The load on the engine can be varied by Eddy Current dynamometer. The specifications of the engine are shown in Table 2. The exhaust gases are analyzed by using gas analyzer. Initially the experiments were performed for diesel at 3 injection pressure like 180bar, 200bar and 220bar and then 10R+5H+85D and 20RBO+5H+75D blends at different injection pressure as mention earlier. The engine performance like brake power, brake specific fuel consumption, brake thermal efficiency, and emission like HC,CO and Nox were obtained and then compared the performance of blends with those of D100 at 220bar.Based on the experimental methodology the following results were obtained

RESULTS AND DISCUSSION

Performance characteristics

Brake Specific Fuel Consumption (BSFC): The variation of BSFC against load is shown in Fig. 4. From the results it has been observed that the blend of 20R+5H+75D gives the minimum BSFC of 0.2667 kg/kW-hr at 220 bar injection in pressure and minimum BSFC of 0.26 kg/kW-hr for 10R+5H+85D blend and which found to be more than diesel i.e. 0.25 kg/kW hr at full load at same 220 bar injection pressures .BSFC values of biodiesel will be always greater than diesel due to Calorific value which is less than diesel.BSFC decreases with respect to load and shows close results to diesel. This may be due to improved combustion, low viscosity and high volatility of the test fuels as compared to diesel at full load but more in low injection pressure at all loads.

Brake Thermal Efficiency (BTE)

As the load increases the brake thermal efficiency also increases for the fuel samples at different injection pressures used in the test as shown in Fig 5. It was observed that the 5H+10R+85D blend at 225bar gave the maximum brake thermal efficiency of 33.32% at full load which was nearer to the Brake Thermal Efficiency of diesel i.e. 34.36 %.This may be higher heat content, low viscocity,lower density and higher volatility. It was observed that the blend at 180 bar injection pressures gave low BTE. Since the viscosity and density of that blend nearer to that of diesel and better spray at 220 bar injection pressure ensures finer breakup of fuel droplets which helps in better combustion process and also providing more surface area and better mixing with air.

Emission characteristics

Hydrocarbon (HC) emission

The variation of Hydrocarbon emission against load is shown in Fig. 6. It has been observed that the emission of HC increases with increase in load. It has been observed that 20R+5H+75D blend gave low HC emission at 220 bar injection pressure similar to that of diesel. The unburnt hydrocarbons emissions are higher at low injection pressures (180bar) and lowest emission at 220 bar injection pressure in all blends at all loads because low atomization and large droplets are formed leading to more unvapourised hydrocarbons in the exhaust. This improper mixing is caused due less surface contact with air and leads to improper combustion and hence more amount of HC is emitted from the engine..

Carbon monoxide emission

The variation of Carbon monoxide against load is shown in Fig.7. It has been observed that 20R+5H+75D blend gave low CO emission at 220 bar injection pressure were 11.35% increased to that of diesel and 16.96% decreased compared to low injection pressure at 180 bar . It shows that the The CO emissions are minimum at 220bar and higher at low injection pressures (180bar) because low atomization. Low CO emission observed the blends of Honge and Rice bran oil methyl esters at 220bar compared diesel likely due to oxygen content inherently present in the biodiesel which helps in the more complete oxidation of fuel

Oxides of Nitrogen (NO_X)

The Fig. 8 depicts the variation of oxides of nitrogen against load. It has been observed that 20R+5H+75D blend gave best Nox value(773ppm) compared to diesel at 180 bar and more (835ppm)at 220 bar injection pressure. The emission of NO_X is a phenomenon depends mainly on the combustion temperature It has been observed that The Nox emissions are more at 220 bar injection pressure compared low injection pressures. However blends at higher Nox are observed at higher injection pressure due to high cylinder pressure and temperature at higher loads**.** High temperature and availability of oxygen are the two primary reasons for high NO_X formation as nitrogen and oxygen respond at higher temperature.

CONCLUSIONS

Based on the above results and discussion the following conclusion is drawn.

* The performance characteristics like brake specific consumption (BSFC), and brake thermal efficiency (BTE) for the hybrid blend 20R+5H+75D at 220 bar injection pressure is better than the low injection pressure (180 bar)
* The HC and CO emission of the hybrid blend 20R+5H+75D at 225 bar gives good result compared low injection pressure except Nox.
* By considering the above characteristics, this blend may be used as a vehicular fuel for single cylinder four stroke diesel engines without any modifications

REFERENCES

[1] Bora BJ et al(2014) Effect of compression ratio on performance,combustion and émission characteristics of a dual fuel diesel engine run on raw biogas. Energy Convers Management;87:1000–1009.

[2) Lin, L.et,al (2011) "Opportunities and challenges for biodiesel fuel". Appl Energy 88, 1020-1031

[3] Dharma, S.et.al(2016a) "Optimization of biodiesel production process for mixed Jatropha curcas–Ceiba pentandra biodiesel using response surface methodology. Energ Convers Manage 115, 178-190.

[4] Kent Hoekman.S et.al (2012) "Review of biodiesl,composition,properties,andspecifications".Renewable and Sustainable Energy Reviews 16, pp 143– 169.

[5] Meher, L C et al. (2006), Technical aspects of biodiesel production by transesterification – a review, Renewable and Sustainable Energy Reviews, Vol. 10, No. 3, pp. 248-68.

[6] Mohite S et.al(2016)"Experimental studies on use of Karanja biodiesel as blend in a compression ignition engine". Int J Renew Energy Res.;6(2):355–360.

[7]Saravanan S.al(2010)."Combustion characteristics of a stationary diesel engine fuelled with a blend of crude rice bran oil methyl ester and diesel. Energy. 2010;35:94–100.

[8] Kapilan N et.al(2006)."Effect of Injection Pressure on the Performance and Emission of Diesel Engine using Blend of Methyl Esters of Karanja Oil and Diesel as Fuel". SAE Technical Paper, 2006-32-0025

[9]. Bora, D.K.et.al(2012)."Performance of diesel engine using biodiesel obtained from mixed feedstocks". Renew Sust Energ Rev ,16, 5479-5484

[10]Yaliwal V.S.et.al(2010)."Production and Utilization of Renewable Liquid Fuel in a Single Cylinder Four Stroke Direct Injection Compression Ignition Engine, International Journal of Engineering Science and Technology, Vol. 2(10) pp. 5938-5948

[11]Mahesh.V.S & E.T. Puttaiah, Studies on Performance and Emission characteristics of non-edible oil (honge oil) as alternate fuel in CI engine, *International Journal of Engineering Research and Applications,* Vol. 2, Issue 3 (2012) pp. 2288-2293

[12]Srivastava A and Prasad R (2004) "Triglycérides based biodiesel fuels,Renewable and sustainable energy reviews,4,111-133

[13] Dharmadhikari.H.Met.al (2012)" Performance and emissions of CI engine using blends of biodiesel and diesel at different injection pressures. International Journal of Applied Research in Mechanical Engineering (IJARME) ISSN: 2231 –5950, Vol-2, Iss-2,

[14] Haiter Lenin.A and K. Thyagarajan(2012), 'Performance evaluation of dieselengine fuelled with methyl ester of pongamia oil', International Journal of Energy and Environment, Vol. 3, pp. 939-948

[15]SenthilKumar.R, and R.Manimaran,(2013) 'Performance and emission characteristics on 4-stroke single cylinder C I engine using cotton seed bio fuels' Asian Journal of Engineering Research, 2013, Vol. 1,Issue II, pp. 1 – 3.

Fig 1 Engine setup

Fig. 2 Trans-esterification of Rice bran oil

Fig. 3 RBO kept in the funnel for settling of glycerine'

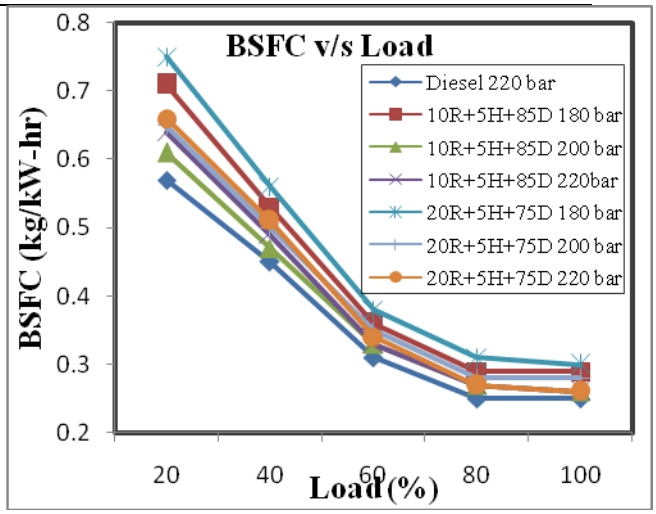

Fig. 4 Graph of Brake Specific Fuel consumption vs Load

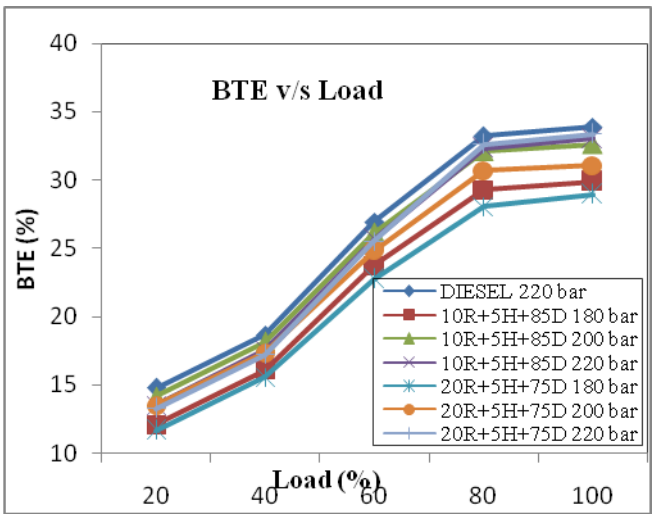

Fig. 5 Graph of Brake Thermal Efficiency vs load

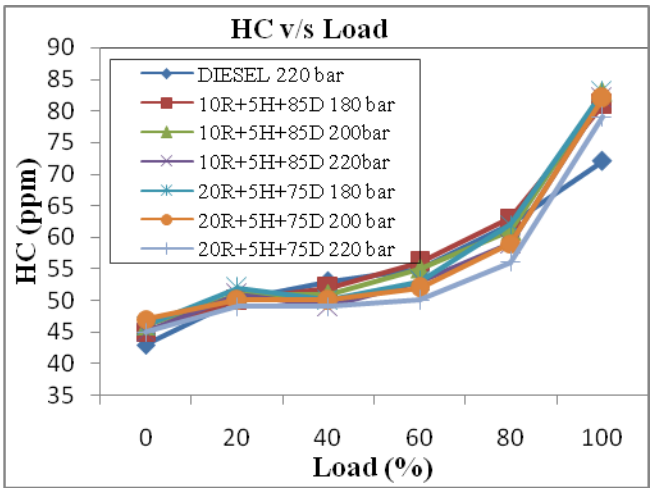

Fig. 6 Graph of HC emission vs Load

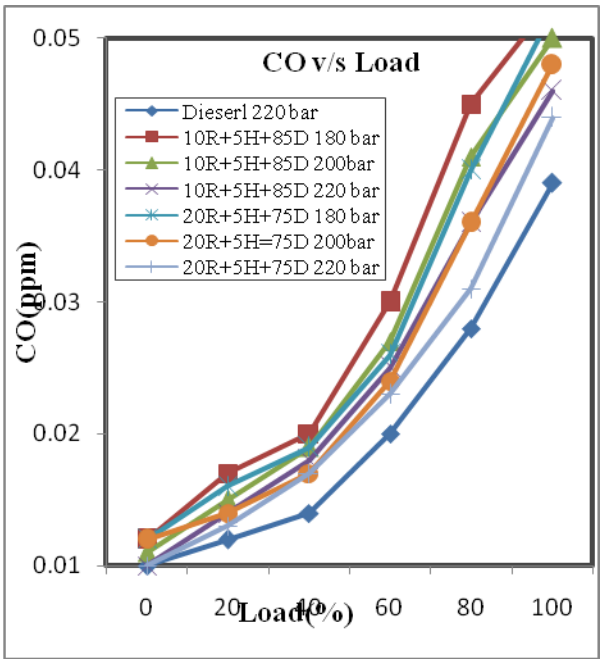

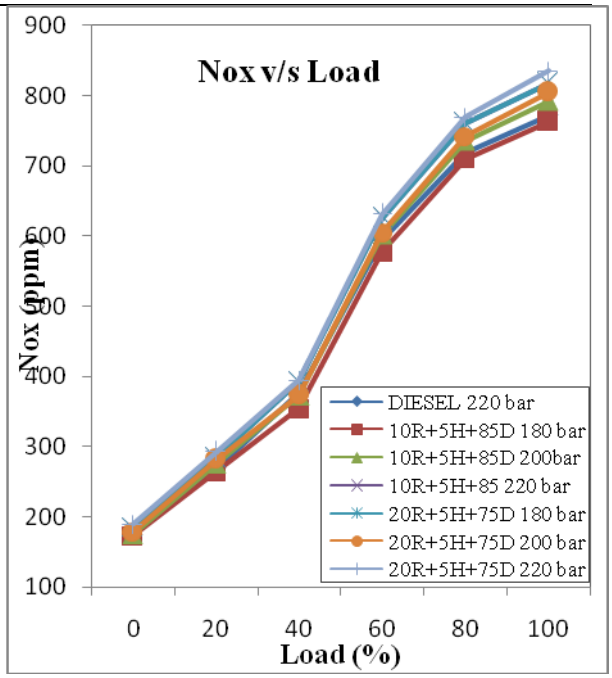

Fig

Fig7 Variation of

Table 1 Physico-chemical properties of different fuel samples

Properties	Higher Calorific value (kJ/kg)	Density (kg/m^3)	Kinematic Viscosity @ 40°C (cSt)	Flash Point (°C)
ASTM Standard	D 240	D 4052	D 445	D 93
Diesel	42850	823	2.63	42
Honge methyl ester H100	34915	834	5.43	203
Rice bran methyl ester R100	40795	873	4.41	178
5H+10R+85 Diesel	42256	771	2.55	49
5H+20R+75 Diesel	42070	764	3.63	50

Table 2 Specifications of Diesel engine

S. No.	Parameters	Specification
1	Engine	4 Stroke, Single Cylinder, Constant Speed, Water Cooled Diesel Engine
2	Make	Kirloskar
3	BHP	3.73 kW @ 1500 RPM
4	Stroke Length	110 mm
5	Compression Ratio	16.5:1
6	Displacement Volume	553cc
7	Starting	Crank Start
8	Lubrication	Forced

8th International Engineering Symposium - IES 2019
March 13-15, 2019, Kumamoto University, Japan

Synthesis and Characterization of WC Ceramic Particulates Reinforced Al7075 Matrix Composites via Two Step Melt Stirring technique

Gopal Krishna U B[1], Soufia Shaikh[2], Ranganatha P[3], Virupaxi Auradi[3] and Vasudeva B[3]

1 *Department of Mechanical Engineering, Alva's Institute of Engineering & Technology, Moodbidri, Dakshina kannada - 574225, Karnataka, India email:gopalkrishnaub@gmail.com*
2 *Department of Mechanical Engineering, Alva's Institute of Engineering & Technology, Moodbidri, Dakshina kannada - 574225, Karnataka, India email: soufiashaikh21@gmail.com*
3 *Research and Development Centre, Department of Mechanical Engineering, Siddaganga Institute of Technology, Tumakuru – 572103, Karnataka, India email:ranganathp9592@gmail.com*

ABSTRACT: Aluminium based metal matrix composites (AMMCs) are advanced materials having the properties of high specific strength and modulus, greater resistance, high elevated temperature and low coefficient of thermal expansion. These composites spread their applications in the field of automobiles, aerospace, defence, cutting tool materials etc. In the present work an attempt has made to synthesis the Al7075 matrix with harder ceramic particulates of Tungsten Carbide (WC). The method used to produce is the low cost efficient stir casting method. To achieve a homogeneous distribution of the reinforcement without any wetting agent a two step introduction of reinforcement was adopted. The prepared composites were subjected to characterization of SEM/EDX which reveals the fair uniform distribution of the ceramic particulates over the matrix.

***Keywords**: AMMCs, WC, Two step addition, SEM*

INTRODUCTION

Many of our modern technologies require materials with unusual contribution of properties that cannot be met by the conventional metal alloys, ceramics and polymeric materials. To satisfy the material property combinations and ranges have been and are yet being extended by the development of composite materials. Metal matrix composites (MMCs) being used to replace conventional materials in many applications especially in automobiles, aerospace industry and machine industries. For engineering applications MMC plays a major role and aluminium is an excellent material in non ferrous family because of its excellent properties like low density, high strength to weight ratio, high thermal and electrical conductivity and fluidity [1]. The major advantages of aluminium matrix composites include high specific strength, stiffness, electrical and thermal conductivity, low coefficient of thermal expansion and wear resistance [2]. The introduction of ceramic material into a metal matrix produces composite materials which gives an attractive combination of mechanical properties which cannot be obtained with monolithic alloys [3]. There is a need for knowledge about the processing techniques and mechanical behaviour of particulate MMCs is view of

their rising production volume and their wider commercial applications. There is an increase in the interest on the particulate reinforced MMCs mainly due to their easy availability of particles and economic techniques adopted for producing the particulate reinforced MMCs [4]. Interest in reinforcing Al alloy matrices with ceramic particles is mainly due to its low density, low coefficient of thermal expansion and high strength of the reinforcements and also due to wide availability [2]. Ceramics like SiC, B_4C, Al_20_3 and WC etc... have been widely used as reinforcements in the preparation of composites. Tungsten carbide has been well known for its exceptional hardness and wear resistance [5].

EXPERIMENTAL DETAILS

In the current work, Al7075 alloy is used as matrix. An atomic absorption spectroscopic analysed composition of Al 7075 is tabulated in Table 1. Ceramic particulates of Tungsten Carbide (WC) particulate with a mean size of 10µm is used as reinforcing material. In the current investigation an attempt is made to synthesize composite at a temperature of 750°C.

PREPARATION OF THE COMPOSITE

Stir casting route is adopted to prepare the composite. To achieve the homogeneous distribution of the reinforcement into the matrix two step methodologies is considered, where the reinforcement is added to the liquid metal of the matrix in twice of equal proportion at the same temperature. Fig.1 shows the stir casting setup.

A batch of 400 grams of Al7075 matrix is kept for melting in a graphite crucible using resistance temperature. Once the temperature of the liquid metal reaches 730°C, solid hexachloroethane tablet of about 2 grams is added and degassing is carried to remove all the gaseous mixture present in the liquid metal. Vortex in the liquid metal is generated at 300rpm using a steel rod stirred which is coated with zirconia (to avoid contamination) for about 10minutes. The formed slag is removed from the melt using a spatula and kept the molten metal ready for adding reinforcement.

The chosen reinforcement of Tungsten Carbide particulates are preheated in an oven at 150°C to. Later the preheated particulates in an equivalent amount of 6Wt% are introduced in two batches with an interval of 30seconds gap into the liquid matrix. The stirring action is carried out for a period of 60 seconds to ensure homogeneous distribution of reinforcement over the matrix.

The cast iron permanent mould (Fig.2(a)) with dimension of 125mm length and Ø15mm diameter is kept ready by preheating and once the liquid melt temperature reaches 750°C the crucible taken out of the furnace and poured into the mould and allowed it to solidify (Fig.2(b)).

Specimen Preparation

To study the microstructure of the specimens were cut and prepared as per the standard metallographic procedure. The specimen surfaces were prepared by grinding through 600 to 1000 mesh size grit papers. Velvet cloth polishing is done for the specimen to get fine surface finish. After that the specimens were etched using Keller's reagent ($HCl+HF+HNO_3$). The microstructures of etched specimens were observed using Scanning Electron Microscope (SEM).

RESULT AND DISCUSSIONS

Microstructure Characterization using SEM/EDAX

The prepared samples are subjected to microstructure analysis. Scanning Electron Microscopy equipped with EDX (Octane Pro Det Model) is employed for observing the presence and distribution of WC particulates in Al7075 matrix. The microstructure image from Fig shows the formation of dendrite precipitates in a matrix of aluminium solid solution and a fairly uniform distribution of reinforcement can be observed in Fig.3(a-d). The

effectiveness of adoption of two stage method to add the reinforcement is observed in the distribution of the reinforcement over the matrix in homogeneous way. Fig.3(e&f) shows EDX spectra taken at the centre of the particle shows the presence of Al, WC, W and C elements.

XRD analysis

X-ray diffraction (XRD) analysis of the Al7075- 6wt% of WC composite was done using XRD Machine-7000; M/s Shimadzu Analytical India Pvt. Ltd. and is presented in Fig.4. The 2θ range was selected such that all the major intense peaks of the phases expected were covered. Analysis of the XRD pattern shows the peaks corresponding to major phases of Al, WC, and minor phases of Al_5W. Probably the Al_5W phase might have been formed at the interface by the reaction between Al matrix and WC particles.

CONCLUSIONS

The following conclusions are deduced from this study:

- Al7075+6Wt% WC composite was successfully synthesized by conventional stir casting method
- Adoption of two stage addition of reinforcement leads to effective mixing of ceramic particulates in liquid matrix.
- Microstructure characterization carried out using SEM/EDX studies have revealed fairly uniform distribution of WC particulates in the Al7075 matrix system
- XRD analysis shows the presence of Al, WC in major phases and Al_5W in minor phases.

ACKNOWLEDGEMENTS

R&D lab, Department of Mechanical Engineering, Siddaganga Institute of Technology, Tumakuru-572103, Karnataka, India for providing opportunity to use the facility and perform the research activity.

REFERENCES

[1] V yuvaraja, n natarajan, k sivakumar, tribological behaviour of heat treated al7075 aluminium metal matrix composites vol. 22, 2015, pp. 51-61.

[2] Ravikumar.bm, dr.sn harish, preetham.bm study on mechanical properties of tib2 reinforced al70775 metal matrix composite materials issue 3 volume 4 2013

[3]Jerry andrews fabian, b.selvim densification behaviour of aluminium reinforced with tungsten carbide particulate metal matrix composite processed by p/m e-issn: 2278-1684, p-issn: 2320-334x pp 24-29

[4]zhang, m.zhu, c.y.wang parameters optimization in the planetary ball milling of nanostructured tungsten carbide/cobalt powder 26 (2008) 329-333

[5] Balaji, V., Sateesh, N., & Hussain, M. M. (2015). Manufacture of Aluminium Metal Matrix Composite (Al7075-SiC) by Stir Casting Technique. *Materials Today: Proceedings*, *2*(4–5), 3403–3408.

Table 1 Chemical Composition of matrix Al7075 used for the experiment.

Chemical Composition	Al7075
Si	0.4 %
Fe	0.5 %
Cu	1.6 %
Mn	0.3 %
Mg	2.5 %
Cr	0.15 %
Zn	5.5 %
Ti	0.2 %
Al	Balance

Fig.1 Stir casting setup

Fig.2(a) Permanent Mould

Fig.2(b) Solidified ascast specimens

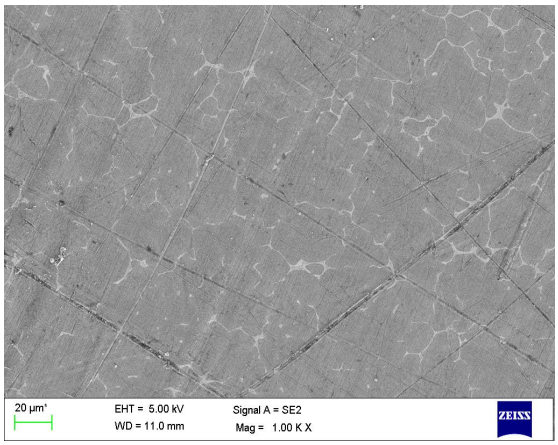

Fig.3(a)

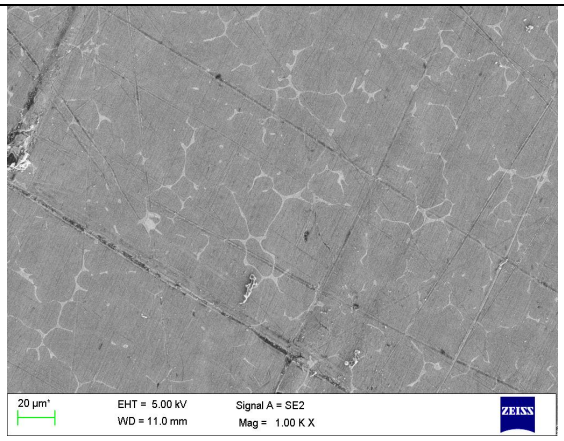

Fig.3(b)

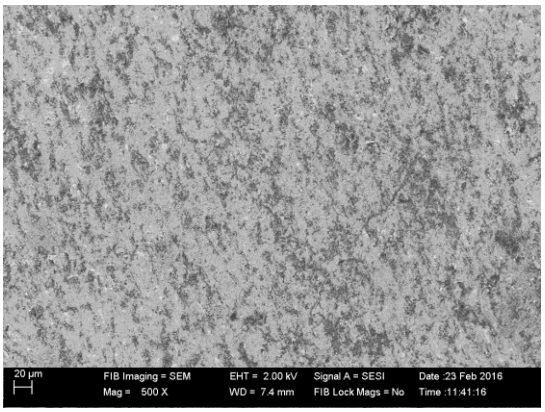

Fig.3(c)

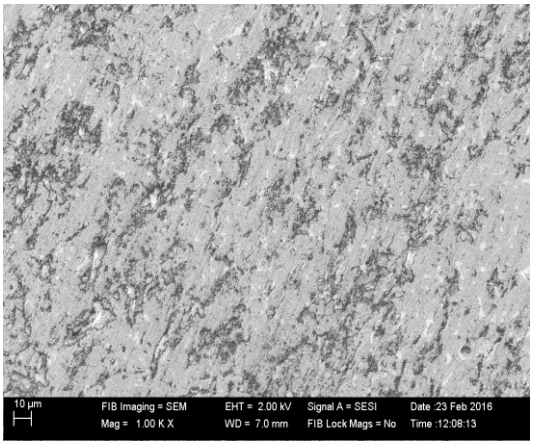

Fig.3(d)

Fig.3 (a-d): SEM micrographs of Al7075+6Wt% WC composite

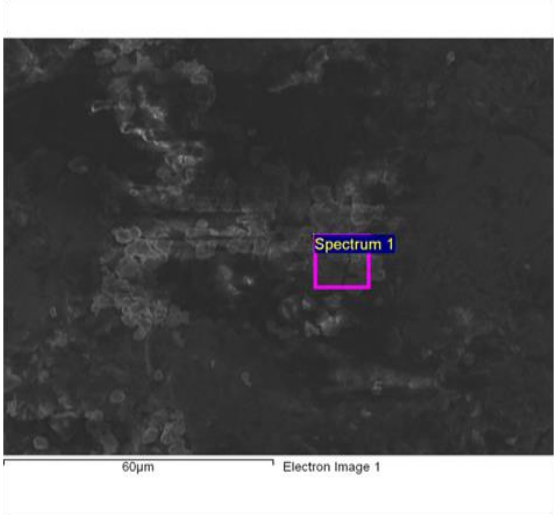

Fig.3(e)

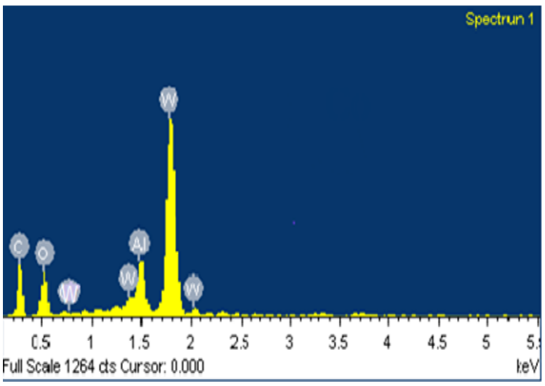

Fig.3(f)

Fig.3(e&f): EDAX Spectrum of Al7075+6Wt% WC composite

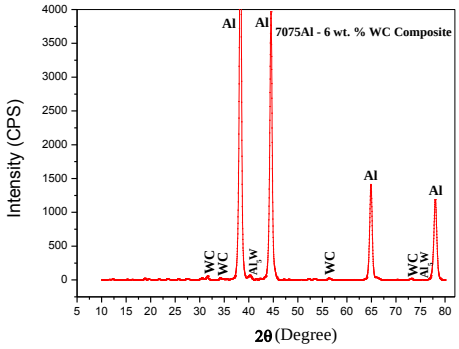

Fig.4: XRD pattern of the prepared composite

8th International Engineering Symposium - IES 2019
March 13-15, 2019, Kumamoto University, Japan

Investigation on the Performance and Emission Characteristics of CI Engine Fuelled With blends of Cardanol, Honge bio diesel With Diesel

K.V.Suresha[1,2],Vijaylaxmi P Shivanaguti[3], Peter fernandes[4],Raju K[5]

1 *Department of Mechanical Engineering, St. Joseph Engineering college Mangalore, 575028, India.email:* kvs_a@yahoo.com
2 *Department of Mechanical Engineering, Alva's Institute of Engineering and Technology, Moodabidri, 574225 India. email:* kvs_a@yahoo.com
3 *Department of Mechanical Engineering, Alva's Institute of Engineering and technology Moodabidri 574225, India. email:shivanaguttivijaylaxmi@gmail.com*
4 *Département of Mechanical Engineering, Alva's Institute of Engineering and Technology, Moodabidri, 574225, India.email: principalaiet08@gmail.com*
5 *Department of Mechanical Engineering, St. Joseph Engineering college Mangalore, 575028, India.email: rajuksjec@gmail.com*

ABSTRACT:
In this study the performance and emissions tests were conducted on a single-cylinder 5.2kW Kirloskar TV1 diesel engine using a non-edible plant-based bio-fuel Cardanol produced from cashew nut shell liquid (CNSL) blend with Honge methyl ester and diesel. The bio-fuel blends 5C5H (5% cardanol+5%Honge+90% diesel),5C10H, 5C15H and 5C20H (5% cardanol+20% Honge+75% diesel) were prepared and tested at various loads (0%,20%, 40%, 60%, 80%and full load conditions) and compared with baseline diesel at 205bar injection pressure and 17.5 compression ratio. The experimental results show that at full load, the brake thermal efficiency of 5C10H is 29.35% comparatively similar to that of diesel is 31.05%. The lower emissions of CO, hydrocarbon except NOx are encouraging to recognize 5C10H as an optimized fuel blend for a compression ignition engine. The significant factors of cardanol bio-fuel include its low cost, non-edible, abundance, and it is a by-product of the cashew nut industries.

Keywords*: Injection Pressure, biodiesel, blends, Cardanol, Honge oil, Emission*

INTRODUCTION

The creating economy combined with population development has added to an exponential interest for energy sources. The disappointment of oil based goods to meet these proceeded with essential demands and pollution related issues as a result of far reaching usage of non-renewable sustainable power sources have required the advancement and the adjustment of inexhaustible and eco-pleasing fuel communicated by Kulkarni BM et.al (2008). Increasing familiarity with the utilization of non- renewable energy resources similarly as their negative characteristic impact has actuated excitement for the potential benefits of biofuels, for example, biodiesel, which is a substitute fuel for diesel engines revealed by Pullen and Saeed (2011). Vegetable oils contain many fatty acids. Four fatty acids, namely palmitic, stearic, oleic and linoleic acids, present in higher compositions. The variation of fatty acid content in the biofuel affects the performance and emissions in a compression ignition (CI) engine reported by Dinesh (2017). Suresh Kumar et al. (2008).Presented their results of performance and emission characteristics of a diesel engine fuelled with blends of Pongamia pinnata methyl ester (PPME) with diesel. The test results revealed that up to 40% biodiesel blend provided better engine performance (BSFC and BSEC) and

improved emission characteristics. The blends B40 and B60 showed lower CO and HC and higher CO2 and NOx emissions due to better combustion of fuel blends Chauhan et al. (2012) tested a Kirloskar single-cylinder diesel engine fuelled with biodiesel Jatropha oil to observe its performance, emissions, and combustion characteristics. They found that Jatropha methyl ester (JME) and its blends gave increased BSEC and NOx emissions, while lowering the BTE, HC, CO, CO2, and smoke emissions as compared to diesel. Das and Ganesh (2003) studied the methods of extraction of CNSL from cashew nut shell. The authors studied the yield of CNSL at low temperature pyrolysis (CNSL-1) and high temperature pyrolysis (CNSL-2). They did not report much difference in properties like ash content, moisture, and density. It was observed that the viscosity changed drastically as the temperature rose from room temperature to higher temperature (60 and 80□C). They noticed a slightly higher calorific value and lower flash point in the case of CNSL-2 compared to CNSL-1 and the 100% miscibility with methanol and diesel showed good indication for blending with these fuels Kasiraman et al. (2012) studied the performance, emissions, and combustion characteristics of a single-cylinder four-stroke water-cooled DI diesel engine fuelled with 70% cashew nut shell oil (CNSO) and 30% camphor oil blend (CMPRO 30). They observed that CMPRO 30 blend performs closer to diesel with respect to performance, emissions, and combustion characteristics. The brake thermal efficiency of CMPRO 30 blend was 29.1% at peak load compared to diesel brake thermal efficiency of 30.14%, and 23.1% for neat CNSO.Mallikappa et al. (2012) conducted an investigation on the performance and emission characteristics of a four stroke double-cylinder CI engine with cardanol biofuel volumetric blends of 0–25%. As the biofuel percentage in the blend increased, reduction in BSEC was obtained. The brake thermal efficiency obtained for cardanol biofuel blends was less than that of diesel. NOx emissions increased with increased proportion of blends and also with higher EGT (exhaust gas temperature). The nominal value of HC emissions was obtained up to B20 and more at B25 due to incomplete combustion. Alcohols like ethanol and methanol are biofuels, which can be used as an alternative in internal combustion engines. Pushparaj and Ramabalan (2013) conducted experiments a single-cylinder four-stroke DI diesel engine with B20 CNSL blend and ethanol percentages of 5, 10 and 15%.The results showed lower exhaust emissions for 10% ethanol with B20 CNSL blend. NO emissions reduced by 57% compared to B20. According to Bora et al. (2012) researched the qualities of biodiesel created by blending three sorts of feedstock (polonga, koroch, and Jatropa curcas) and found that there is a huge improvement in the physicochemical properties of the biodiesel acquired from blended feed stocks compared with those for individual biodiesels. In the present study two biodiesel in particular cardanol and Honge methyl ester were blended in various proportion with diesel and investigate the performance and emission characteristics of single cylinder 4 stroke diesel engine at 1500 rpm..

2. Materials and Methodology

2.1Materials

Honge oil is additionally called Karanja oil. Its plant name is Pongamia pinnata, has a place with group of Leguminaceae or papilionaceae. Karanja is a medium estimated quickly developing evergreen tree. The time required by the tree to develop ranges from 4 to 7 years and relying upon the extent of the tree the yield of portions per tree is between 8 to 24 kg and the yield of potential per hectare is 900 to 9000 kg/hectare reported by V.S.Yaliwal (2010).Extraction requires the seeds through a screw crusher, for the most part called expellers. The oil is then separated to make it clean enough to process as expressed by C.V. Mahesh (2012). Honge oil collected locally and cardanol was collected from Adarsh cashew industry Karkala area Karnataka.

2.2 Transesterification

As indicated by Srivastava and Prasad R (2004) there are four distinctive courses through which non-consumable oils can be converted into methyl esters are transesterification,blending,emulsion and pyrolysis out of which transesterification is

commonly used. Dharmadhikariet.al(2012) expressed that Free unsaturated fat (FFA) substance should to be known for the crude oil.FFA will be determined by basic chemical titration

2.3Methodology

One litre of honge oil was warmed in open beaker to a temperature for 100°C to expel water particles present in oil pursued by filtration of oil. The oil was prepared under alkali base based catalyzed transesterification method. Since FFA value was observed to be 2.41%.The oil was blended with 300ml of methanol and 6 grams of sodium hydroxide pallets in round bottom flask mixed on a hot plate magnetic stirrer for a one and half hour at 60°C and after that it was permitted to settle down for around 6 to 8hrs to get biodiesel and glycerol. The biodiesel obtained in the process was further washed with water to remove moisture content. Hence pure Honge biodiesel was obtained.

2.4 properties of biodiesel

HaiterLenin and thyagarajan(2012),Senthil Kumar et.al(2012) expressed that some of the properties like flash point, viscosity, density, specific gravity and calorific value are needed for using the bio-diesel as vehicular fuel. The Physico-chemical properties such as higher calorific value, density, kinematic viscosity, flash and fire points are determined as per ASTM standards for biodiesel. In this study 4 blends were used 5C+5H+90D (5%Cardanol+5%hongeoil +90%diesel), 5C+1085D,5C+15H+80D and 5C+20H75D (5%Cardanol+20% Honge oil+75% diesel) were used. The properties of different samples are shown in Table 1.

3. Experimental Procedure

The engine tests were conducted on a computerized single cylinder four four-stroke, water-cooled diesel engine test rig (Fig. 1). It was specifically coupled to a current dynamometer. The engine and the dynamometer were interfaced to a control board, which was associated with an advanced PC, utilized for recording the test parameters, for example, fuel flow rate, temperatures, load and so on. The calorific value and the density of the specific fuel was fed to the software calculating the engine performance. To record the data online, software was logged every time and data stored in the computer hard disk, which can be retrieved when required. The set of experiments were conducted at the designed speed of 1500 RPM and compression ratios of 17.5:1. The experiments were conducted at no-load, 10% of full load, 30% of full load, 50%of full load, 70% of full load, and full load with neat diesel and blends Cardanol raw oil and Methyl ester of Honge oil with Diesel as fuel. The exhaust gases are analyzed by using gas analyzer The specifications of the engine are shown in Table 2.

4. Results and Discussion

Initially the experiments were performed for diesel at 205bar injection pressure and 17.5:1 and then 4 blends of cardanol honge with diesel were carried out. The engine performance like brake power, brake specific fuel consumption, brake thermal efficiency, and emission like HC, CO and Nox were obtained and then compared the performance of blends with those of D100 at 17.5:1 compression ratio. Based on the experimental methodology the following results were obtained

4.1. Brake power

Fig 2 shows the variation of Brake power against load for 4 blends. From the results it was observed that as the load increases the brake power also increases for all the fuel samples used in the test. The maximum brake power of 4.93 kW was observed by 5CH+5H+90D blend shows 1.41% decrease in BP compared to diesel at full load. This increase in brake power by the increase in load was attributed by the better air fuel mixture at higher load.

4.2. Brake specific fuel consumption

The variation of BSFC against load for four blends is shown in Fig. 3. From the results it was observed that the load increases the brake specific fuel consumption decreases for the fuel samples used in the test. It was observed that 5C+5H+90D blend gives the minimum BSFC of 0.24 kg/kW-hr and minimum BSFC of 0.26 kg/kW-hr for 5C+20H+75D blend and which found to be more than diesel i.e. 0.23 kg/kW-hr at full

load.BSFC decreases with respect to load and shows close results to diesel. This may be due to improved combustion, low viscosity and high volatility of the test fuels

4.3 Brake Thermal Efficiency

Fig 4 shows the variation in brake thermal efficiency against load. It has been observed that the load increases the brake thermal efficiency also increases for all the fuel samples used in the test fuels. It was observed that the 5C+5H+90D blend gave the maximum brake thermal efficiency of 29.35% at full load which was nearer to the Brake thermal Efficiency of diesel i.e. 31.05 %.This may be higher heat content, low viscocity,lower density and higher volatility. Since the viscosity and density of that blend nearer to that of diesel ensures finer breakup of fuel droplets at higher compression ratio providing more surface area and better mixing with air.

4.4 Hydrocarbon

Fig 5 shows that the variation of HC with respect to load. From the result it has been observed that SC+5H+75D blend shows minimum HC value is 72ppm at full load compared to 70ppm of diesel. The unburnt hydrocarbons emissions are higher at 5C+20H+75D blend because low atomization and large droplets are formed leading to more unvapourised hydrocarbons in the exhaust.

4.5 Carbon monoxide

Fig. 6 depicts the variation of carbon monoxide against load. From the result it has been observed that the emission of HC increases with increase in load. At full load condition, the emission of the HC reduces by 8.93% for 5C+5H+90D as compared to 5C+20H+75D blend and 3.93% increases as compared to diesel. The CO emissions is minimum for all blends because low atomization. Low CO emission of biodiesel at 5C+5H+90D blend and at higher at 5C+20H+75D compared diesel likely due to oxygen content inherently present in the biodiesel which helps in the more complete oxidation of fuel

4.6 Nitric oxides

Fig. 8 depicts the variation of oxides of nitrogen against load. The emission of NO_X is a phenomenon depends mainly on the combustion temperature. From the result it was observed that maximum No_x value obtained 850ppm at 5C+20H+75D and minimum 700ppm at 5C+5H+90D blend. High temperature and availability of oxygen are the two primary reasons for high NO_X formation as nitrogen and oxygen respond at higher temperature and due to high cylinder pressure and temperature at higher loads

5. Conclusion

The following conclusions were drawn from the present study.

- The Brake power has been increase by1.4% for 5C+5H+90D as compared to 5C+10H+85D and 1.4% decrease as compared to diesel.Brake Specific Fuel Consumption has been reduced by 7.69% for 5C+5H+90D as compared to 5C+20H+75D blend. Brake thermal efficiency has been increased by 3.91%for 5C+10H+85D as compared to 5C+20H+75D blend.
- The HC, CO emissions have been reduced by 6.5%, 5.35% respectively for 5C+5H+90 and 5C+5H+90D blend.
- The NO_X emission has been increased by 17.64% for 5C+5H+75D as compared to 5C+20H+75D blend
- By considering the above characteristics, 5C+5H+85D blend may be used as a vehicular fuel for single cylinder four stroke diesel engines without any modification

REFERENCES

[1] Bora, D.K.et.al(2012)."Performance of diesel engine using biodiesel obtained from mixed feedstock's". Renew Sust Energy Rev ,16, 5479-5484

[2] Chauhan BS et.al(2012)"A study on the performance and emission of a diesel engine fuelled with Jatropha biodiesel oil and its blends. Energy.37 (1):616–622

[3] Das P and (2003) Ganesh A. Bio-oil from pyrolysis of cashew nut shell—a near fuel. Biomass Bioenergy. 25(1):113– 117

[4] Dharmadhikari.H.Met.al (2012)" Performance and emissions of CI engine using blends of biodiesel and diesel at different injection pressures. International Journal of Applied Research in Mechanical Engineering (IJARME) ISSN: 2231 – 5950, Vol-2, Iss-2,

[5] Dinesha P et.al(2017) 'Effect of varying 9 Octadecenoic acid (oleic fatty acid) content in biofuel on the performance and émission of a compression ignition engine at varying compression ratio. Biofuels. 2017; DOI: 10.1080/17597269.2016.1275491.

[6] Haiter Lenin. A and K. Thyagarajan (2012), 'Performance evaluation of diesel engine fuelled with

methyl ester of pongamia oil', International Journal of Energy and Environment, Vol. 3, pp. 939-948
[7] Kasiraman G et.al (2012)"Performance, emission and combustion improvements in a direct injection diesel engine using cashew nut shell oil as fuel with camphor oil blending. Energy. ; 47:116– 124.

[8] Kulkarni BM et.al(2008)Investigation of acid oïl as a source of biodiesel. Indian J Chem Techn. 15:467–471

[9]Mahesh.V.SandE.T.Puttaiah(2012)"Studies on Performance and Emission characteristics of non-edible oil (honge oil) as alternate fuel in CI engine, *International Journal of Engineering Research and Applications,* Vol. 2, Issue 3 (2012) pp. 2288-2293
[10]Mallikappa et.al(2012)"Performance and emission characteristics of double cylinder CI engine operated with cardanol bio fuel blends. Renew Energy.;38:150–154.
[11] Pullen J and Saeed K.(2011) 'Factors affecting engine performance and exhaust emissions- Part II: Experimental Study. Energy. 2014;72:17–34
[12] Pushparaj T, Ramabalan S. Green Fuel Design for Diesel Engine, Combustion, Performance and Emission Analysis. Procedia Eng. 2013;64:701–709
[13] SenthilKumar.R and R.Manimaran(2013)" 'Performance and emission characteristics on 4-stroke single cylinder C I engine using cotton seed bio fuels' Asian Journal of Engineering Research, 2013, Vol. 1,Issue II, pp. 1 – 3.
[14] Srivastava A and Prasad R (2004) "Triglycérides based biodiesel fuels, Renewable and sustainable energy reviews,4, 111-133
[15] Sureshkumar K et.al(2008)"Performance and exhaust emission characteristics of a CI engine fuelled with Pongamia pinnata methyl ester (PPME) and its blends with diesel. Renew Energy.; 33(10):2294–2302.
[16] Yaliwal V.S.et.al(2010)."Production and Utilization of Renewable Liquid Fuel in a Single Cylinder Four Stroke Direct Injection Compression Ignition Engine, International Journal of Engineering Science and Technology, Vol. 2(10) pp. 5938-5948

Fig 1 Engine setup

Fig. 2 Trans-esterification of Honge oil

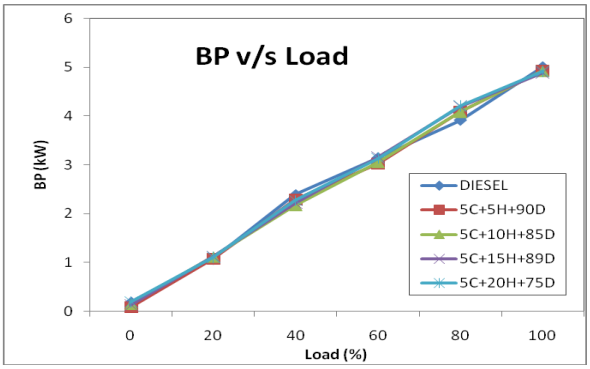

Fig3.Variation of BP against Load

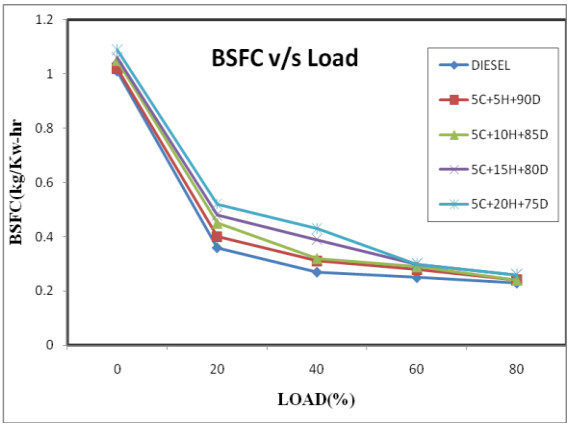

Fig.4 Variation of BSFC against load

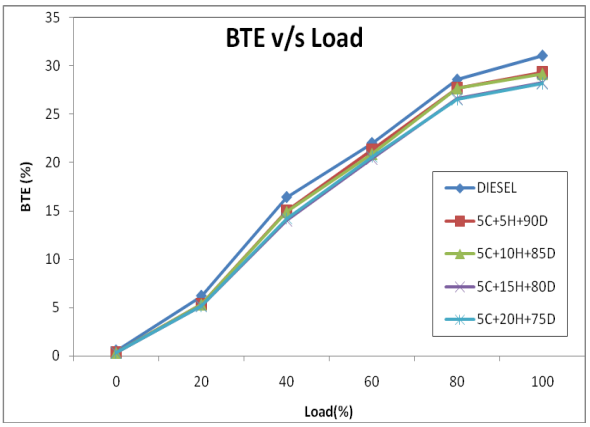

Fig 5.Variation of BTE against laod

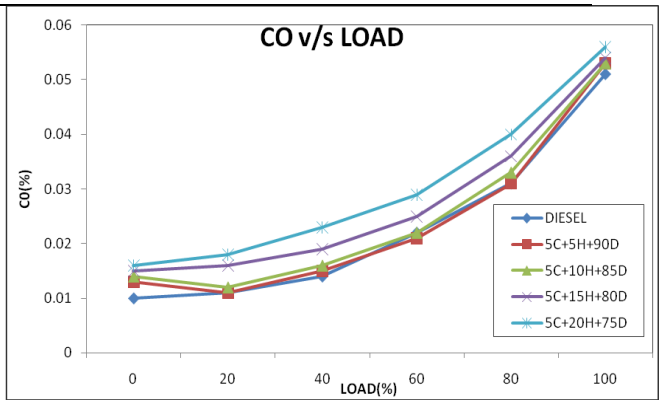

Fig7.Variation of CO against Load

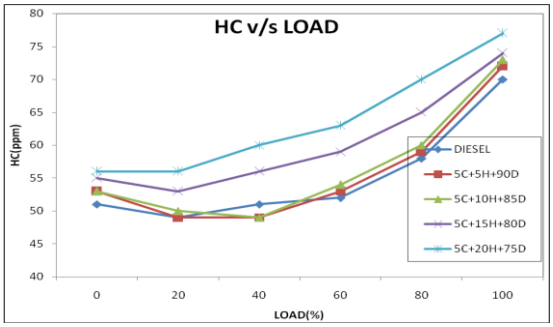

Fig6.Variation of HC against load

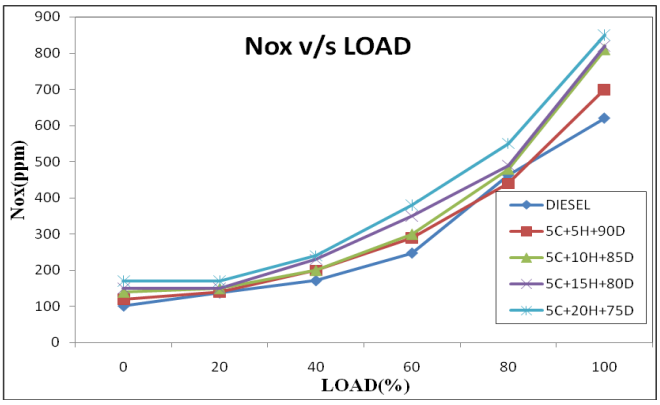

Fig6.Variation of Nox against lo

Table 1 Physico-chemical properties of different fuel samples

Properties	Higher Calorific value (kJ/kg)	Density (kg/m^3)	Kinematic Viscosity @ 40°C (cSt)	Flash Point (°C)
ASTM Standard	D 240	D 4052	D 445	D 93
Diesel	43033	823	2.58	46
Honge	34902	834	5.43	206
Cardanol	37502	906	6.47	224
5C+5H+90 Diesel	42350	828	2.55	69
5C+10H+85 Diesel	41943	828	3.63	76
5C+15H+80 Diesel	41537	829	3.78	79
5C+20H+75 Diesel	41130	829	3.98	81

Table 2 Specifications of Diesel engine

S. No.	Parameters	Specification
1	Engine	4 Stroke, Single Cylinder, Constant Speed, Water Cooled Diesel Engine
2	Make	Kirloskar,TV1
3	BHP	5.2kW @ 1500 RPM
4	Stroke Length	110 mm
	Bore	87.5mm
5	Compression Ratio	17.5:1
6	DisplacementVolume	661cc
7	Injection Pressure	205 bar
8	Lubrication	Forced feed system

8th International Engineering Symposium - IES 2019
March 13-15, 2019, Kumamoto University, Japan

Effect of Compression Ratio on the Performance and Emission Characteristics of CI Engine Fuelled with Honge, Hybrid Bio-Fuel with Diesel

K V SURESHA[1] , THANGJAM SEEMASHWORI DEVI[2], SRINIVAS C. S[3], PETER FERNANDES [4], and RAJU K [5]

1 *Department of Mechanical Engineering, Alva's Institute of Engineering and technology Moodabidri 574225, India. email: kvs_a@yahoo.com*
2 *Department of Mechanical Engineering, Alva's Institute of Engineering and technology Moodabidri 574225, India. email:seemthangjam5@gmail.com*
3 *Department of Mechanical Engineering, Alva's Institute of Engineering and technology Moodabidri 574225, India. email:* srinivasa@aiet.org.in
4 *Département of Mechanical Engineering, Alva's Institute of Engineering and Technology, Moodabidri, 574225, India.email: principalaiet08@gmail.com*
5 *Department of Mechanical Engineering, St. Joseph Engineering college Mangalore, 575028, India.email: rajuksjec@gmail.com*

ABSTRACT: In this present study, the performance and emissions of a single-cylinder Kirloskar diesel engine using a non-edible Honge oil and waste edible oil (WEO) with diesel and its blends were carried out. The bio-fuel blends H5W5 (5% Honge,5%waste edible,90% diesel),H10W5, H15W5 and H20W5 were prepared and tested at various load conditions(0%,30%,50%,70% and 100%of full load) compared with diesel at different compression ratio(14.5:1,15.5:1and 16.5:1). Results indicated that the brake thermal efficiency of H20W5 was 30.75% at 16.5:1 compression ratio comparatively similar to that of diesel (32.36%). The lower emissions of CO, hydrocarbon except NO_x were encouraging to recognize H20W5 as an optimized fuel blend for a compression ignition engine at 16.5:1 compression ratio compared low compression ratio. Results were also showed that performance and emissions of Honge and WEO biodiesel blends were near to diesel.
Keywords*: compression ratio, biodiesel, blends, Honge oil, Waste Edible oil, Emission*

INTRODUCTION

The developing economy coupled with population growth has contributed to an exponential demand for energy resources. The failure of petroleum products to meet these continued vitality requests vulnerability of future supplies and contamination related issues because of widespread utilization of non-renewable energy sources have required the advancement and adjustment to inexhaustible and eco-accommodating fuel expressed by Kulkarni BM et.al (2008) Increasing familiarity with the consumption of non-renewable energy source assets just as their negative natural effect s has activated enthusiasm for the potential benefits of biofuels, for example, biodiesel, which is an elective fuel for diesel engine reported by Pullen J, and Saeed(2011).Sayin and Gumus (2011) investigated the performance and emissions of a DI diesel engine fuelled by biodiesel (5, 20,50, and 100%) blended diesel fuel in relation to CR and injection parameters such as IT and IP. It was observed that an elevation in IP, IT, and CR caused a decrease in smoke opacity, CO, and HC emissions, along with a rise in NOx emissions for all fuels tested. These days, there is extraordinary enthusiasm for blending biodiesels delivered from various feedstocks so as to abuse the advantages of each kind of biodiesel. Various specialists have embraced approach an executed these in diesel engines. According to Kent Hoekman et.al(2012). Srithar et al. (2014) mixed

diesel fuel with Pongamia pinnata-mustard biodiesel at various proportions and found that there is an enhancement in the physicochemical properties increment in the calorific value, specific gravity and viscosity of the blends and furthermore discovered that expanding the biodiesel substance of the mix results in higher brake fuel consumption (BSFC). Be that as it may, there is a slight decrease in the carbon monoxide (CO) and carbon dioxide (CO2) emissions. According to Bora et al. (2012) researched the qualities of biodiesel created by blending three sorts of feedstock (polonga, koroch, and Jatropa curcas) and found that there is a huge improvement in the physicochemical properties of the biodiesel acquired from blended feed stocks compared with those for individual biodiesels. Kannan and Anand (2011) studied the aggregate impact of injection pressure and IT on waste cooking oil found that BTE, in-cylinder pressure, and heat discharge rate demonstrated extensive enhancement alongside diminished emissions of NO, CO, CO2, and smoke for the consolidated impact of higher IP of 240 bar and a advanced IT of 25.5btdc. Anand and Kannan et al(2009) investigated a methyl ester of cottonseed oil mixed with diesel in four different proportions. Tests were led in a single cylinder variable compression ratio diesel engine speed of 1500 rpm.. Most elevated brake thermal efficiency and low specific fuel consumption were found for 5% biodiesel mix for compression ratio of 15 and 17 and 20% biodiesel mix of 19. The 20% biodiesel mix at a compression ratio of 17 had more nitric oxide discharge compared with diesel, decrease in Carbon monoxide emission and smoke in the full range of compression ratio and loads was observed. The results reveal that the biodiesels can be used safely without any modification to the engine. In the present study two biodiesel in particular Honge and waste eatable oil methyl ester were blended in various proportion with diesel and investigate the performance and emission characteristics of single cylinder 4 stroke diesel engine at 3 different compression ratios.

2. Materials and Methodology

2.1Materials

Honge oil is additionally called Karanja oil. Its plant name is Pongamia pinnata, has a place with group of Leguminaceae or papilionaceae. It can develop on most soil types running from stony to sandy to clayey. Karanja is a medium estimated quickly developing evergreen tree, which achieves 40 feet in tallness and The seeds are for the most. The results reveal that2 cm long and 1.8 cm expansive, wrinkled with rosy dark colored shading. The time required by the tree to develop ranges from 4 to 7 years and relying upon the extent of the tree the yield of portions per tree is between 8 to 24 kg and the yield of potential per hectare is 900 to 9000 kg/hectare reported by V.S.Yaliwal (2010).Extraction requires going the seeds through a screw crusher, for the most part called expellers. The oil is then separated to make it clean enough to process expressed by C.V. Mahesh (2012) It is discovered that the most extreme yields were acquired by the Solvent extraction strategy .Honge oil was gathered locally. The Waste Cooking Oil (WCO) was gathered from the adjacent restaurant. Waste oil was gathered from oil processes that are spilled to the floor in huge amount amid the way toward pouring, pressing and exchanging or by spillage and after that these gathered waste oil mix with previously collected waste cooking oil.

2.2 Transesterification

As indicated by Srivastava and Prasad R (2004) there are four distinctive courses through which non-consumable oils can be converted into methyl esters are transesterification,blending,emulsion and pyrolysis out of which transesterification is ordinarily used.Dharmadhikariet.al(2012) expressed that Free unsaturated fat (FFA) substance should to be known for the crude oil .FFA will be determined by basic chemical titration

2.3Methodology

One liter of honge oil is warmed in open beaker to a temperature for 100oC to expel water particles present in oil pursued by filtration of oil. The oil is prepared under alkali base based catalyzed transesterification method. Since FFA value was observed to be 2.41%.The oil is blended with300ml of methanol and 6 grams of sodium

hydroxide pallets in round bottom flask mixed on a hot plate magnetic stirrer for a one and half hour at 60 ^{o}C and after that it is permitted to settle down for around 6 to 8hrs to get biodiesel and glycerol. The biodiesel obtained in the process is further washed with water to remove moisture content. Hence pure Honge biodiesel is obtained. Since the FFA Value of Waste edible oil (WEO) was found to be 5.69% Since the FFA Value of Waste edible oil (WEO) was found to be 5.69%, two stages Transesterification process was used.

2.4 properties of biodiesel

Haiter and Lenin (2012),Senthil Kumar et.al(2012) expressed that some of the properties like flash point, viscosity, density, specific gravity and calorific value are needed for using the bio-diesel as vehicular fuel. The Physico-chemical properties such as higher calorific value, density, kinematic viscosity, flash and fire points are determined as per ASTM standards for biodiesel. In this present study two blends are used 10H+5W+85D(10%Honge+5%wasteedibl eoil+85diesel)and20H+5W+75D(20%Hon ge +5% Waste edible oil+75% diesel)were used, The properties of different samples are shown in Table 1.

3. Experimental Procedure

The engine tests were conducted on a computerized single cylinder four four-stroke, water-cooled diesel engine test rig(Fig. 1). It was specifically coupled to a current dynamometer. The engine and the dynamometer were interfaced to a control board, which was associated with an advanced PC, utilized for recording the test parameters, for example, fuel flow rate, temperatures, load and so on. The calorific value and the density of the specific fuel is fed to the software calculating the engine performance characteristics such as brake thermal efficiency, brake specific fuel consumption, volumetric efficiency etc. Water to motor cooling coat is kept up around 80 lph and water stream strain to Eddy current dynamometer is maintained between 1 to 1.5 bar all through the investigations, this water flow pressure is kept by means of 0.25HP external water pump. To record the data online, software was logged every time and data stored in the computer hard disk, which can be retrieved when required. The set of experiments were conducted at the designed speed of 1500 RPM and compression ratios of 16.5:1. The experiments were conducted at no-load, 10% of full load, 30% of full load, 50%of full load, 70% of full load, and full load with neat diesel and blends of Methyl ester of waste edible oil and Honge oil with Diesel as fuel. Data such as fuel flow cylinder pressure, indicated power, brake power, airflow exhaust temperature, specific fuel consumption, brake thermal efficiency, BP and emission parameter like HC, CO and Nox were recorded at this condition. The engine specifications are given in Table 2.

4. Results and Discussion

Initially the experiments were performed for diesel at 3 compression ratio like 14.5:1, 15.5:1 and 16.5:1. and then 10H+5W+85D and 20H+5W+75D blends at different compression ratio as mention earlier. The engine performance like brake power, brake specific fuel consumption, brake thermal efficiency, and emission like HC,CO and Nox were obtained and then compared the performance of blends with those of D100 at 16.5:1compression ratio. Based on the experimental methodology the following results were obtained

4.1. Brake power

Fig 2 shows the variation of Brake power against load for two blends, it was found that as the load increases the brake power also increases for all the fuel samples used in the test. The maximum brake power of 3.64 kW was observed by 20H+5W+75D blend at 16.5:1 compression ratio at full load. This increase in brake power by the increase in load was attributed by the better air fuel mixture at higher load

4.2. Brake specific fuel consumption

The variation of BSFC against load for two blends is shown in Fig. 3. From the results it has been observed that the load increases the brake specific fuel consumption decreases for the fuel samples at different compression ratio used in the test. It is observed that 10H+5W+85D blend gives the minimum BSFC of 0.26 kg/kW-hr at 16.5:1

compression ratio and minimum BSFC of 0.25 kg/kW-hr for 20H+5W+75D blend and which found to be more than diesel i.e. 0.23 kg/kW-hr at full load.BSFC decreases with respect to load and shows close results to diesel. This may be due to improved combustion, low viscosity and high volatility of the test fuels

4.3 Brake Thermal Efficiency

Fig 4.Shows the variation in brake thermal efficiency against load. It has been observed that the load increases the brake thermal efficiency also increases for the fuel samples at different compression ratio used in the test fuels. It was observed that the 20H+5W+75D blend at 16.5:1 CR gave the maximum brake thermal efficiency of 32.75% at full load which was nearer to the Brake Thermal Efficiency of diesel i.e. 33.26 %.This may be higher heat content, low viscocity,lower density and higher volatility. It was observed that the blend at low CR gave low BTE. Since the viscosity and density of that blend nearer to that of diesel ensures finer breakup of fuel droplets at higher compression ratio providing more surface area and better mixing with air.

4.3 Hydrocarbon

Fig 7 shows that the variation of HC with respect to load. It was observed that 20H+5W+75D blend gave maximum HC value is 70ppm at 16.5:1 compared 76ppm for 14.5:1 CR at full load. The unburnt hydrocarbons emissions are higher at low compression ratio because low atomization and large droplets are formed leading to more unvapourised hydrocarbons in the exhaust.

4.3 Carbon monoxide

Fig 7. variation in CO with load for two blends.The CO emissions is minimum at 16.5:1 CR and higher at low CR (14.5:1)for all blends because low atomization. Low CO emission of biodiesel at higher CR compared diesel likely due to oxygen content inherently present in the biodiesel which helps in the more complete oxidation of fuel

4.3 Nitric oxides

Fig 8.shows variation in Nox against load for two blends. The Nox emissions are more at 16.5:1 for 20H+5W+75D and low at 14.5:1 compression ratio compared to diesel. However blends at higher Nox are observed at higher compression ratio due to high cylinder pressure and temperature at higher loads

5. Conclusion

Based on the above results and discussion the following conclusion is drawn.

* The performance characteristics like brake power (BP), brake specific consumption (BSFC), and brake thermal efficiency (BTE) for the hybrid blend 20H+5W+75D at 16.5:1 CR is better than the low compression ratio.

* The HC and CO emission of the hybrid blend 2H+5W+75D at 16.5:1 CR bar gives good result compared low injection pressure except Nox.

* By considering the above characteristics, this blend may be used as a vehicular fuel for single cylinder four stroke diesel engines without any modification

REFERENCES

[1] Kulkarni BM, Pujar BG, Shanmukhappa S. Investigation of acid oil as a source of biodiesel. Indian J Chem Techn. 2008;15:467–471

[2] Pullen J, Saeed K. Factors affecting engine performance and exhaust emissions- Part II: Experimental Study. Energy. 2014;72:17–34.

[3] Sayin C, Gumus M. Impact of compression ratio and injection parameters on the performance and emissions of a DI diesel engine fueled with biodiesel-blended diesel fuel. Appl Therm Eng. 2011;31:3182–3188.

[4] Kent Hoekman.S et.al (2012) "Review of biodiesl,composition,properties,andspecifications".Re newable and Sustainable Energy Reviews 16, pp 143– 169

[5] Srithar, K., Balasubramanian, K.A., Pavendan, V., Kumar, B.A., 2014. Experimental investigations on mixing of two biodiesels blended with diesel as alternative fuel for diesel engines. J King Saud Univ Eng Scie In Press Corrected.

[6] Bora, D.K.et.al(2012)."Performance of diesel engine using biodiesel obtained from mixed feedstocks". Renew Sust Energ Rev ,16, 5479-5484.

[7] Kannan GR, Karvembu R, Anand R. Effect of metal based additive on performance emission and combustion characteristics of diesel engine fuelled with biodiesel. Appl Energy. 2011;88(11):3694–3703 surface methodology. Energ Convers Manage 115, 178-190.

[8] Anand,R et.al (2009). The performance and emissions of a variable compression ratio diesel engine fuelled with Biodiesel from cotton seed oil. ARPN Journal of Engineering and Applied Sciences. vol. 4, no.9, ISSN 1819-6608, November 2009.

[9] Yaliwal V.S.et.al(2010)."Production and Utilization of Renewable Liquid Fuel in a Single Cylinder Four Stroke Direct Injection Compression Ignition Engine, International Journal of Engineering Science and Technology, Vol. 2(10) pp. 5938-5948

[10] Mahesh.V.S&E.T.Puttaiah,Studieson Performance and Emission characteristics of non-edible oil (honge oil) as alternate fuel in CI engine, *International Journal of Engineering Research and Applications,* Vol. 2, Issue 3 (2012) pp. 2288-2293
[11] Srivastava A and Prasad R (2004) "Triglycérides based biodiesel fuels,Renewable and sustainable energy reviews,4,111-133
[12] Dharmadhikari.H.Met.al (2012)" Performance and emissions of CI engine using blends of biodiesel and diesel at different injection pressures. International Journal of Applied Research in Mechanical Engineering (IJARME) ISSN: 2231 –5950, Vol-2, Iss-2,
[13] Haiter Lenin.A and K. Thyagarajan(2012), 'Performance evaluation of diesel engine fuelled with methyl ester of pongamia oil', International Journal of Energy and Environment, Vol. 3, pp. 939-948
[14]SenthilKumar.R,andR.Manimaran,(2013) 'Performance and emission characteristics on 4-stroke single cylinder C I engine using cotton seed bio fuels' Asian Journal of Engineering Research, 2013, Vol. 1,Issue II, pp. 1 – 3.

Fig 1 Engine setup

Fig. 2 Trans-esterification of Honge oil

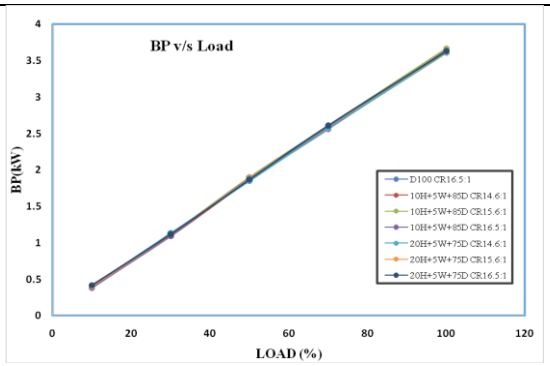

Fig3.Variation of BP against Load

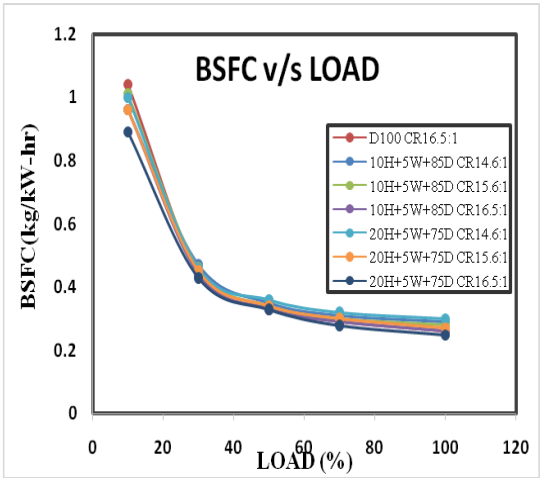

Fig.4 Variation of BSFC against load

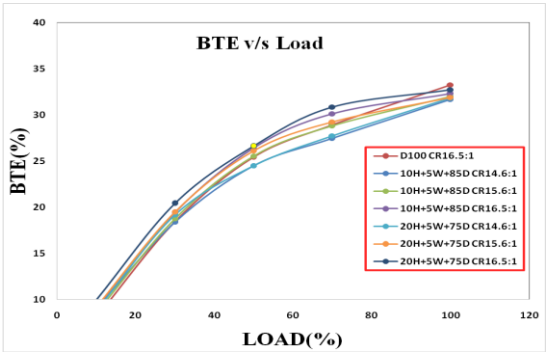

Fig 5.Variation of BTE against laod

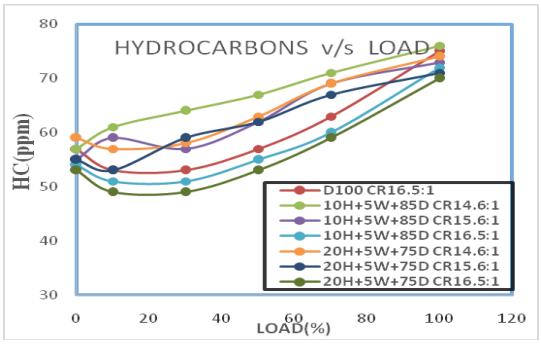

Fig6.Variation of HC against load

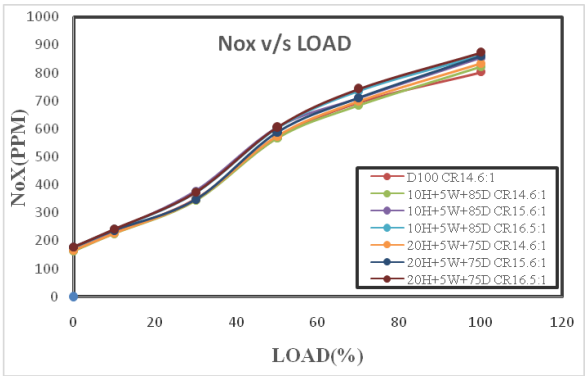

Fig 8.Variation of Nox against load

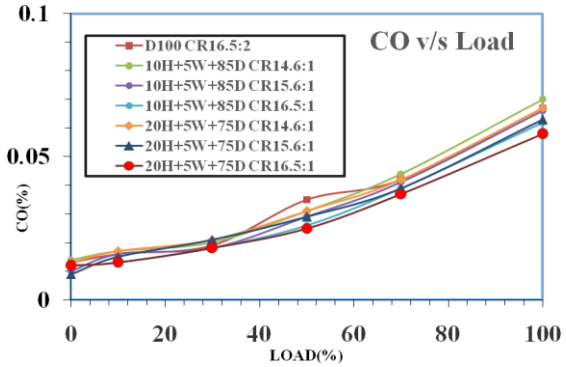

Fig7.Variation of CO against Load

Table 1 Physico-chemical properties of different fuel samples

Properties	Higher Calorific value (kJ/kg)	Density (kg/m^3)	Kinematic Viscosity @ 40°C (cSt)	Flash Point (°C)
ASTM Standard	D 240	D 4052	D 445	D 93
Diesel	42850	823	2.63	42
Honge methyl ester	34915	834	5.43	203
Rice branmethyl ester	40795	873	4.41	178
5H+10R+85 Diesel	42256	771	2.55	49
5H+20R+75 Diesel	42070	764	3.63	50

Table 2 Specifications of Diesel engine

S. No.	Parameters	Specification
1	Engine	4 Stroke, Single Cylinder, Constant Speed, Water Cooled Diesel Engine
2	Make	Kirloskar
3	BHP	3.73 kW @ 1500 RPM
4	Stroke Length	110 mm
5	Compression Ratio	16.5:1
6	DisplacementVolume	553cc
7	Starting	Crank Start
8	Lubrication	Forced

PHYSICS, ELECTRICAL, ELECTRONICS, COMPUTER SCIENCE & RELATED FIELDS

8th International Engineering Symposium - IES 2019
March 13-15, 2019, Kumamoto University, Japan

Effect of soaking time on the structural and morphological properties of Cu_2ZnSnS_3 (CZTS) prepared using solid state reaction technique

Nagabhushan J Choudhari[1] and Raviprakash Y.[2]*

1 Department of Physics, Manipal Institute of Technology, Manipal Academy of Higher Education, Manipal -576 104 India. email:nagabhushanchoudhari@gmail.com
2 Department of Physics, Manipal Institute of Technology, Manipal Academy of Higher Education, Manipal -576 104 India. email: raviprakash.y@manipal.edu *Presenter

Abstract:
The copper zinc tin sulfide Cu_2ZnSnS_3 (CZTS) is a p-type direct band gap material; its elements are non-toxic and earth-abundant. It is a potential solar absorber material which can be used in photo thermal conversion of solar energy and as selective radiation filters on architectural windows. The CZTS compound was synthesized by solid state reaction method. The influence of soaking time on the structural and morphological properties of these films are investigated. Bulk CZTS polycrystals synthesized at various temperature rate profile. X-ray diffraction analysis confirmed the formation of CZTS polycrystals corresponds to the tetragonal phase. Moreover, investigation on the XRD pattern showed that prepared samples do not contain any secondary phases. The crystallite size calculated using Debye-Scherer's formula was found to be in the range of 41.4nm-50.6nm and was found to be increasing with the slower temperature rate. It has been observed that the lattice strain and dislocation density decreases and crystallite size increases with the decrease in temperature rate profile. Compositional analysis using EDAX showed that all the samples were copper rich and sulfur deficient. This is due to the reactivities of different metals during melting and processing temperature profile. It is concluded that slower temperature rate has a significant positive impact on the structure and composition of CZTS compound.

Keywords: Cu_2ZnSnS_3(CZTS), Solar absorber material, Structural and morphological, soaking time

1. INTRODUCTION:

Current photovoltaic market heavily depending on the silicon-based solar cells. Due to the advancements in the thin film technology materials like Cadmium Telluride (CdTe) and Copper Indium Gallium Selenide (CIGS) has acquired a significant share in the photovoltaic (PV) market due to the fact that the power conversion efficiency close to that of the silicon-based solar cells with lesser cost and material usage [1]. The search for a material to cut the cost further and to replace the toxic and scarce elements used in the current thin film PV, resulted in the discovery of earth-abundant, non-toxic and low-cost Cu_2ZnSnS_4 (CZTS), $Cu_2ZnSnSe_4$ (CZTSe) and $Cu_2ZnSn(S,Se)_4$ (CZTSSe) materials. This chalcogenide family of photovoltaic materials emerged as the promising substitution for the existing CdTe and CIGS based thin film solar cells. In order to make it to the market, these materials should cross the mark of 15% conversion efficiency at least. The highest power conversion efficiency achieved so far is 11% for CZTS and 12.6% for CZTSSe which provides ample room to improve the efficiency [2]. For a terawatt(TW)- scale deployment, the current thin film PV technologies like CdTe and CIGS face a severe crisis of the scarcity of the material to meet the future energy demands [2, 3]. CZTS emerges as a solution for this future effect, providing better cost-effective thin film absorber material.

There has been a lot of research focusing on the growth of CZTS thin films and analysis of their properties. But, analysis about the phase evolution towards phase pure growth of CZTS bulk polycrystals at lower processing time regime has not been reported so far. Various techniques have been developed and adopted for synthesizing the CZTS bulk single crystals as well as polycrystals such as iodine vapour transport [4, 5], travelling heater method [6], vertical gradient freeze technique [7], and solid-state reaction method [8]. Due to the possible formation of binary and ternary sulfides during synthesis which depends on the temperature and rate, it becomes challenging to grow phase pure CZTS bulk polycrystals.

In the present work, a detail investigation is made on the phase and structural evolution of CZTS polycrystals where the soaking process is understood with respect to CZTS phases using XRD, Raman EDS techniques. This study aims at the understanding of the lower soaking time on the properties of CZTS material which could be a potential candidate for photovoltaic applications.

2. Experimental Details:

The CZTS bulk polycrystals were synthesized using the solid-state reaction method. A stoichiometric amount of copper, zinc, tin, and sulfur in the ratio 2:1:1:4 having the purity 4N was charged into the quartz ampoule with the diameter of 10mm. The quartz ampoule was evacuated at a base pressure of 2×10^{-5} mbar and sealed in the dynamic vacuum condition. Sealed ampoules were heated in an electric furnace following the four different temperature rate profiles (TRP). The samples were named as T1, T2, T3, and T4 according to the TRP of 3℃/minute, 2℃/minute, 1℃/minute and 0.5℃/minute respectively. The soak time at 300℃ was set to 3 hours and at 1000℃ is set to 5 hours for the homogeneous mixing of the constituent elements to form CZTS. All the samples were cooled to 600℃ as per the respective TRP and later allowed to cool down naturally within the furnace. The optimized sample T3 with TRP of 1℃/minute is chosen to explore the soaking time effect on the properties of CZTS bulk polycrystals. A new set of samples were prepared following the methodology mentioned above but with fixed TRP of 1℃/minute and varying the soaking time. Samples were labeled as S5, S8, S11, and S14 as per the soaking time of 5 hours, 8 hours, 11 hours and 14 hours respectively.

The structural analysis of the synthesized CZTS bulk polycrystals was carried out using X-ray diffraction (XRD) with Cu Kα [λ=1.5405Å] radiation at 40 kV and 15 mA in the 2θ range of 10 – 80° (Rigaku Miniflex 600). Phase formation details were

obtained by raman spectroscopy in back scattering configuration using Ar^+ laser source with 532 nm as excitation wavelength. The laser was directed over an area of 1 X 1 μm^2 with a 1 μm spot size on the sample. The power of the laser was 3 mW. Olympus microscope with the objective lens of 50X (NA 0.75) was used. The elemental composition of the synthesized polycrystals was analyzed by Energy Dispersive Analysis of X-rays (EDAX) (Ziess SEM EVO18).

3. Results and discussion

3.1 Structural analysis

X-ray patterns of CZTS bulk polycrystals prepared under different soak time are shown in the figure 1. All CZTS polycrystals exhibit tetragonal crystal structure with preferred orientation along (112) plane. The diffraction peaks corresponding to the (112), (200), (220), (312), (224) and (332) planes are in good agreement with the reported values (JCPDS No. 26-0575) which confirms the formation of CZTS kesterite structure [9, 10]. For all the samples, lattice strain was found to be decreasing and crystallite size was increasing with the increase in soaking time. Further, there was decrease in the dislocation density with the increase in crystallite size was observed for all the samples (Table 1). It can be noticed that the S14 sample shows better crystallinity as compared to the remaining samples.

Sample	Soak Time (hours)	Average crystallite Size (nm)	Lattice Strain	Dislocation Density (m^{-2})
S5	5	41.40	0.0034	5.83×10^{14}
S8	8	44.14	0.0032	5.13×10^{14}
S11	11	47.07	0.0030	4.51×10^{14}
S14	14	50.56	0.0028	3.91×10^{14}

Table 1: X-ray diffraction data of samples S5, S8, S11, and S14.

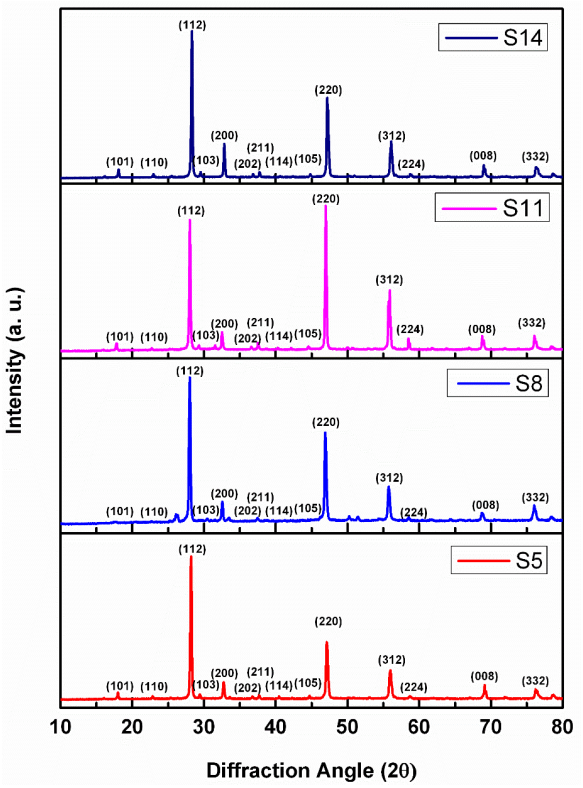

Figure 1. X-ray diffractograms of samples S5, S8, S11 and S14

3.2 Compositional Analysis

The chemical composition of the CZTS bulk polycrystals with different soaking time is compared with the atomic stoichiometry of Cu (25%), Zn (12.5%), Sn (12.5%) and S (50%). The Cu/[Zn + Sn], Zn/Sn and S/Metal ratios were tabulated. A better composition near to stoichiometry with slightly Zinc – rich (1.13) and Copper – rich (1.06) composition has been obtained for the sample S14. Elemental mapping for the sample S14 showed uniform distribution in accordance with the stoichiometry.

Sample	Cu (25%)	Zn (12.5%)	Sn (12.5%)	S (50%)
S5	27.77	13.96	11.50	46.77
S8	26.67	14.18	12.38	46.71
S11	27.98	15.80	11.33	44.88
S14	25.90	13.01	11.42	49.66

Table 2: Chemical composition of CZTS bulk crystals at different soaking time profiles.

3.3 Raman analysis: Disorder and phase identification

To examine the phase purity of the prepared CZTS bulk polycrystals Raman spectroscopy was employed. It is known fact that due to the closeness of the peak positions of Cu_2ZnSnS_4 (CZTS), ZnS and Cu_2SnS_3 (CTS) it becomes difficult to distinguish the CZTS from the binary ZnS and ternary CTS using the x-ray diffractogram alone. Hence, we look into the Raman spectrum to distinguish the CZTS from the above-mentioned phases of ZnS and CTS. Obtained Raman spectrum was fitted with Lorentzian curve and peak positions were determined.

Peaks at 140, 165, 253, 286, 334, 337, 348 and 364 cm^{-1} of the sample S14 are in good agreement with the previous reports [11, 12]. The table 3 shows a comparison of our results with the earlier reports. An additional peak forming a shoulder to the main peak 337 cm^{-1} is observed at 334 cm^{-1}. The full width at half maximum (FWHM) of the shoulder peak is 4.86 cm^{-1}, is wider compared to the main peak. The peak at 334 cm^{-1} cannot be assigned to any of the known possible binaries and ternaries in the CZTS crystal system. The width of 334 cm^{-1} shoulder can be attributed to the disorder in the kesterite phase.

The FWHM of peak P1 in sample S14 reduced drastically to 1.96 cm^{-1} in comparison to the FWHM of peak P1 in samples S5, S8, and S11 which are 9.11 cm^{-1}, 8.56 cm^{-1}, and 8.83 cm^{-1} respectively. This suggests the sudden improvement in the crystalline structure of sample S14 in contrast with others. It can be seen that the main vibrational symmetry mode – A is shifted from 329 – 337 cm^{-1}. The narrowing of FWHM can be attributed to the decreasing degree of disorder and increasing crystallinity. Figure 2 shows the evolution of the Raman spectrum with different soaking time. The peak at 293 cm^{-1} and 354 cm^{-1} of sample S5, 353 cm^{-1} of sample S8, 352 cm^{-1} of sample S11 suggests the presence of copper tin sulfide phase [13] and also the peak at 467 cm^{-1} of sample S8 suggests the formation of copper sulfide phase [14]. In the spectra of sample S14, there is no evidence of binary and ternary phases. However, the peak at 334 cm^{-1} indicates the presence of stannite phase. Calculating the ratio of the area under the 334 cm^{-1} peak (stannite) to that under the 337 cm^{-1} peak (kesterite), we approximate that S14 sample constitutes 89% kesterite and 11 % stannite phase.

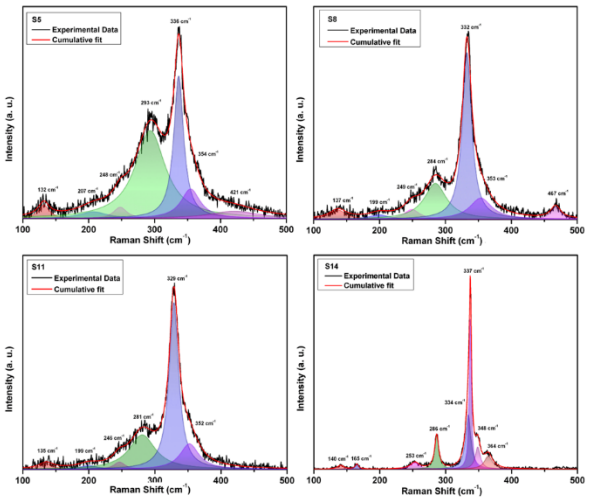

Figure 2. Deconvoluted Raman peaks of sample S5, S8, S11 and S14

Symmetry	Phase	Present work (cm^{-1})	Reported Raman Shift (cm^{-1})
E (TO)	KS	140	139.5
B (LO)	KS	165	164.1
E (LO)	KS	253	252
A	KS	286	287.1
A	ST	334	334.3
A	KS	337	337.5
E (TO)	KS	348	347.3
E (LO)	KS	364	365

Table 3: Obtained peaks, symmetry assignments for sample S14 and reported experimental data.

4. Conclusion

We have demonstrated the time and cost-effective synthesis of CZTS bulk polycrystals which are free from binary and ternary phases from a simple solid-state reaction route utilizing the combination of temperature rate profile and soaking time. Synthesized CZTS polycrystals were obtained with crystallite sizes ranging from 41.40 - 50.56 nm. Structural and compositional investigations pointed towards the formation of near stoichiometric tetragonal kesterite phase with improved crystallinity. Raman studies suggested the evolution of CZTS polycrystals towards being free from undesired phases. This study suggests that in order to obtain a CZTS polycrystal which is free from binary and ternary sulfide phases, an optimum temperature rate profile and a minimum of 14 hours of soaking time are necessary.

5. Acknowledgment

A portion of this research was performed using facilities at CeNSE, funded by Ministry of Electronics and Information Technology (MeitY), Govt. of India, and located at the Indian Institute of Science, Bengaluru.

6. References

[1] M.A. Green, Y. Hishikawa, E.D. Dunlop, D.H. Levi, J. Hohl-Ebinger, A.W.Y. Ho-Baillie, (2018), Solar cell efficiency tables (version 52), Prog. Photovoltaics Res. Appl. 26, pp. 427–436.

[2] S. Abermann, Non-vacuum processed next generation thin film photovoltaics: Towards marketable efficiency and production of CZTS based solar cells, (2013), Sol. Energy, 94, pp. 37–70.

[3] S. Delbos, (2012), Kësterite thin films for photovoltaics : a review, EPJ Photovoltaics, 3, pp. 35004.

[4] D. Colombara, S. Delsante, G. Borzone, J.M. Mitchels, K.C. Molloy, L.H. Thomas, B.G. Mendis, C.Y. Cummings, F. Marken, L.M. Peter, (2013), Crystal growth of Cu_2ZnSnS_4 solar cell absorber by chemical vapor transport with I2, J. Cryst. Growth, 364, pp. 101–110.

[5] K. Tanaka, Y. Miyamoto, H. Uchiki, K. Nakazawa, H. Araki, (2006), Donor-acceptor pair recombination luminescence from Cu_2ZnSnS_4 bulk single crystals, Phys. Status Solidi, 203, pp. 2891–2896.

[6] A. Nagaoka, K. Yoshino, H. Taniguchi, T. Taniyama, K. Kakimoto, H. Miyake, (2013), Growth and characterization of Cu_2ZnSnS_4 single crystals, Phys. Status Solidi, 210, pp. 1328–1331.

[7] S. Das, R.M. Krishna, S. Ma, K.C. Mandal, (2013), Single phase polycrystalline Cu_2ZnSnS_4 grown by vertical gradient freeze technique, J. Cryst. Growth. 381 pp. 148–152.

[8] I.D. Olekseyuk, I.V. Dudchak, L.V. Piskach, (2004), Phase equilibria in the Cu_2S–ZnS–SnS_2 system, J. Alloys Compd. 368, pp. 135–143.

[9] Z. Yan, A. Wei, Y. Zhao, J. Liu, X. Chen, (2013), Growth of Cu_2ZnSnS_4 thin films on transparent conducting glass substrates by the solvothermal method, Mater. Lett., 111, pp. 120–122.

[10] Y.-L. Zhou, W.-H. Zhou, Y.-F. Du, M. Li, S.-X. Wu, (2011), Sphere-like kesterite Cu_2ZnSnS_4 nanoparticles synthesized by a facile solvothermal method, Mater. Lett. 65, pp. 1535–1537.

[11] M. Dimitrievska, A. Fairbrother, X. Fontané, T. Jawhari, V. Izquierdo-Roca, E. Saucedo, A. Pérez-Rodríguez, (2014), Multiwavelength excitation Raman scattering study of polycrystalline kesterite Cu_2ZnSnS_4 thin films, Appl. Phys. Lett. 104 021901.

[12] M.Y. Valakh, V.M. Dzhagan, I.S. Babichuk, X. Fontane, A. Perez-Rodriquez, S. Schorr, (2013) Optically induced structural transformation in disordered kesterite Cu_2ZnSnS_4, JETP Lett. 98, pp. 255–258.

[13] P.A. Fernandes, P.M.P. Salomé, A.F. da Cunha, (2011), Study of polycrystalline Cu_2ZnSnS_4 films by Raman scattering, J. Alloys Compd., 509, pp. 7600–7606.

[14] C.G. Munce, G.K. Parker, S.A. Holt, G.A. Hope, (2007), A Raman spectroelectrochemical investigation of chemical bath deposited Cu_xS thin films and their modification, Colloids Surfaces A Physicochem. Eng. Asp. 295, pp.152–158.

8th International Engineering Symposium - IES 2019
March 13-15, 2019, Kumamoto University, Japan

SYNTHESIS, GROWTH, AND CHARACTERIZATION OF A NOVEL NONLINEAR OPTICAL ORGANIC MATERIAL FOR OPTICAL DEVICE APPLICATIONS

Ashwatha Narayana Prabhu [1], P. P Vinaya [2]

1 *Department of Physics, Manipal Institute of Technology, Manipal Academy of Higher Education, Manipal-576 104, India. email: ashwatha.prabhu@manipal.edu*
2 *Department of Physics, Manipal Institute of Technology, Manipal Academy of Higher Education, Manipal-576 104, India. email: vinayparal@gmail.com*

ABSTRACT: A novel organic nonlinear optical material 4-[(1E)-3-(5-chlorothiophen-2-yl)-3-oxoprop-1-en-1-yl] phenyl 4-methylbenzene-1-sulfonate (TPMS) has been synthesized and grown as a good-quality single crystal by the solution growth method. The grown crystal has been subjected to single-crystal X-ray diffraction studies and cell parameters of the crystal were determined. The optical properties were studied by UV-visible spectroscopy and photoluminescence spectroscopy. The TPMS is thermally stable up to 254°C. The third order nonlinear optical properties of the material were determined using nanosecond laser pulses at 532 nm wavelength by employing Z-scan technique. The large value of third order nonlinear susceptibility (10^{-11} esu) makes the material capable to be used in optical device applications.

***Keywords**: Organic compound, Growth from solutions, Single-crystal growth, Characterization, Nonlinear optical material*

1. Introduction

The research on nonlinear optical (NLO) materials is gaining a tremendous momentum in the last two decades as they are potential candidates in optical communications, optical switching, optical computing, data storage, dynamic holography, optical limiters, harmonic generators and frequency mixing [1]. The NLO properties of organic materials can be tuned by choosing appropriate ingredients during their synthesis. It is well established that a molecule with polarizable electrons i.e., π-electrons over large distances in the molecule exhibit excellent NLO properties [2]. The design, synthesis and characterization of a material with desired NLO property is a challenging task. The derivatives of chalcone are one of the interesting group of materials as they are exhibiting high NLO coefficients and good crystallizability [3]. In this paper we reported experimental results on the synthesis, crystal growth and characterization of a new third order nonlinear optical crystal 4-[(1*E*)-3-(5-chlorothiophen-2-yl)-3-oxoprop-1-en-1-yl] phenyl4-methylbenzene-1-sulfonate (TPMS).

2. Synthesis and growth

The compound TPMS was synthesized by using the general procedure reported in the literature [4]. The purity of the compound was checked by thin layer chromatography and purity of the crystal is enhanced by repeated recrystallization. The TPMS single crystals were grown by solution evaporation technique by using combination of methanol and dimethyl formamide (DMF) (4:1) as solvents. The solution container was covered with a perforated sheet and kept for nucleation at ambient temperature under dust-free atmosphere. The good quality crystals of TPMS were obtained after 15

days. Fig.1 shows the synthesis scheme and grown crystals of TPMS are depicted in Fig.2.

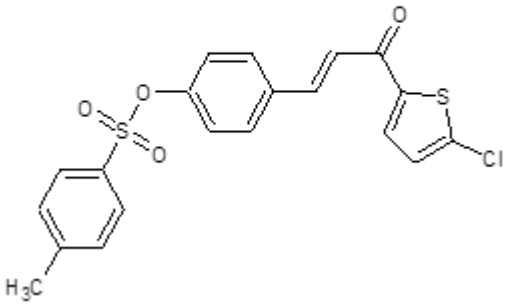

Fig.1: Synthesis scheme of TPMS

Fig.2: Grown single crystals of 4TPMS

3. Result and discussion

3.1 Single crystal XRD

4-[(1*E*)-3-(5-chlorothiophen-2-yl)-3-oxoprop-1-en-1-yl] phenyl4-methylbenzene-1-sulfonate was subjected to single-crystal X-ray diffraction (XRD) using a Rigaku AFC12 Saturn724+ diffractometer. From single-crystal XRD studies, it has been found that the compound crystallizes in inversion symmetry monoclinic system with a space group $P2_1/n$ and Z=4. The unit cell parameters a=11.8004(6)Å, b=5.8540(3)Å, c= 27.8272(13)Å, α=90, β = 98.147(5), γ = 90 and V = 1902.91(16) $Å^3$ [4].

3.2 Optical studies

The UV–Visible absorption spectrum of the crystal was recorded using UV–VIS–NIR SPECTROMETER in the wavelength range of 190 nm-1100 nm, and it shows a good transmittance in the visible region and near IR region as shown in Fig.3. The strong absorbance observed in UV region is due to n–π, n–$π^*$ transition and is attributable to the presence of aromatic ring α,β – unsaturated carbonyl group [5]. The low absorption co-efficient of TPMS in the visible and near IR region can be exploited for NLO applications.

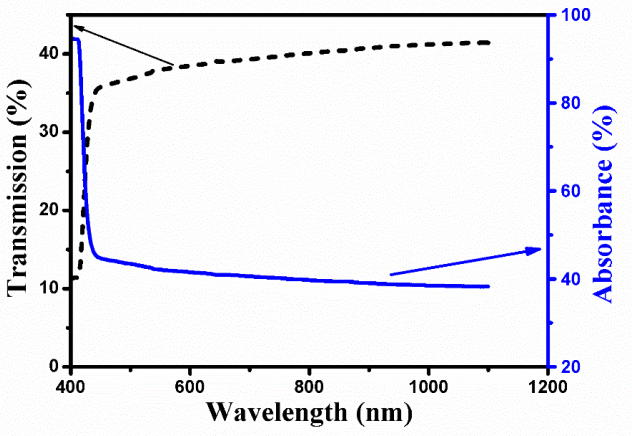

Fig.3: UV-Visible spectrum of TPMS

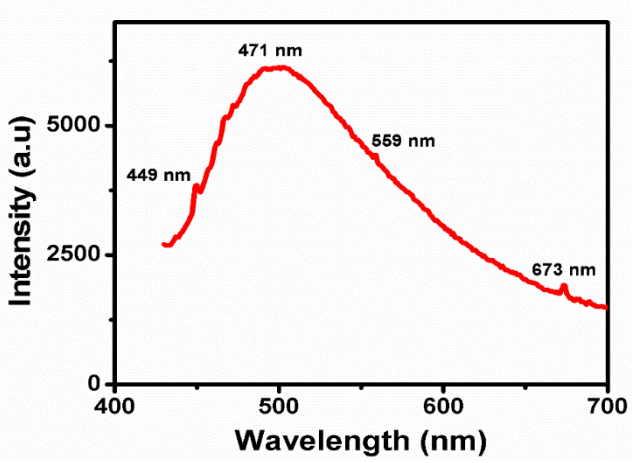

Fig.4: Photoluminescence spectrum of TPMS

The room temperature Photoluminescence (PL) study was carried out using FluoroMax-4CP spectrometer with an excitation wavelength of 410 nm and emission from 430-700 nm as shown in Fig.4. The broad emission peak was observed at 471 nm shows the blue light emission behavior of the sample which involving several transitions below the conduction band. The presence of the defect in the blue wavelength region makes TPMS a promising material for blue LED applications.

3.3 Thermal analysis

The thermal property of the title compound was studied in the powder form by recording the differential scanning calorimetry (DSC) response curve in the temperature range 25 °C to 550 °C, at a rate of 10 °C/ min, in nitrogen atmosphere using SHIMADZU DSC-60.

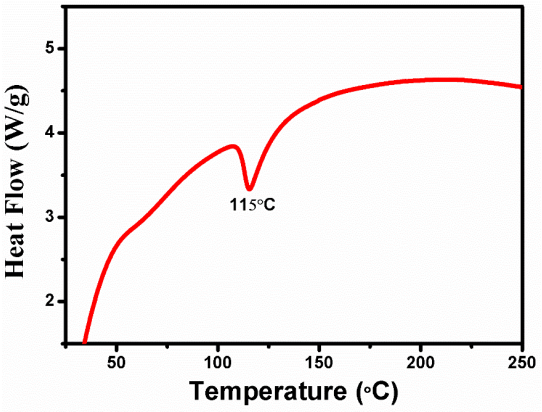

Fig.5: DSC plot of TPMS

The DSC plot [Fig. 5] shows a sharp endothermic peak at 115°C, which corresponds to the melting point of the compound. Also, absence of any endothermic or exothermic peak before the melting point indicates that there is no phase change before the melting point.

3.4 Third order nonlinear optical study

Single beam Z-scan technique [6], was carried out to measure the third-order optical nonlinearities of the sample. This technique enables simultaneous Z-scan measurement was carried out using Q-switched Nd: YAG laser (pulse width 7 ns) operating at 532 nm and pulse repetition rate of 10 Hz. The laser beam is focused to the sample of 10 mm/L solution and transmitted intensity is collected by the pyro electric energy detector.

The third order nonlinear parameters of the title compound n_2, β_{eff}, $Re(\chi^{(3)})$, $Im(\chi^{(3)})$ are compared with

Table.1: Third order nonlinear optical parameters of some organic samples

Sample	nonlinear refractive index(n_2) (10^{-11} esu)	nonlinear absorption coefficient(β_{eff}) (cm/GW)	$Re(\chi^{(3)})$(esu)	$Im(\chi^{(3)})$(esu)
TPMS*	−3.20	5.54	-0.58×10^{-11}	0.17×10^{-11}
DPTF [7]	−2.48	5.11	-0.78×10^{-11}	0.69×10^{-11}
CTDMP [8]	−1.53	3.05	-1.64×10^{-13}	0.47×10^{-13}
DMMC [9]	−2.75	1.7	6.62×10^{-12}	0.93×10^{-12}
Ci3NC [10]	− 4.76	2	0.89×10^{-11}	0.11×10^{-11}
GAL [11]	−4.87 −7.23	3.51 4.86	2.92×10^{-11} 4.51×10^{-11}	1.34×10^{-11} 1.67×10^{-11}
Hydrazones:[12]				
Compound 1	−0.79	1.13	0.72×10^{-13}	0.14×10^{-13}
Compound 2	−0.53	0.44	0.49×10^{-13}	0.05×10^{-13}
Compound 3	−0.69	1.23	0.63×10^{-13}	0.15×10^{-13}

the reported organic materials depicted in Table.1. TPMS is interesting due to the presence the two donor groups tosyloxy and Thiophene, center of carbonyl group (C=O) acts as acceptor. The molecule is arranged in the form of D–π–A–π–D system. As a result, the charge transfer takes place from the donor ends to the acceptor at the middle of the molecule, which produces push-pull behavior. This is well known mechanism for enhanced optical nonlinearity. Similarly, thiophene ring and tosyloxy group at the para position leads to planarity in the molecule which further enhances the third order optical nonlinearity. The large value of $(Re(\chi^{(3)}))$ makes the crystal suitable for all optical switching applications.

Conclusion

TPMS single crystals were grown by slow evaporation solution growth technique. The crystal structure was solved by the single crystal X-ray diffraction method and the lattice parameters were obtained. PL studies revealed that defects are responsible for blue light emission. The good transparency, thermal stability and large value of third order nonlinear susceptibility indicate that TPMS is a promising candidate for optical device applications.

References

[1] D.S. Chemla, J. Zyss, "Nonlinear Optical Properties of Organic molecules and Crystals", Academic Press, New York, 1987.

[2] J.L. Oudar, D.S. Chemla, "Hyperpolarizabilities of the nitroanilines and their relations to the excited state dipole moment", J. Chem. Phys. 66 (1977) 2664.

[3] A.N. Prabhu, A. Jayarama, K Subrahmanya Bhat, V. Upadhyaya "Growth, characterization and structural investigation of a novel nonlinear optical crystal", Journal of Molecular Structure 1031 (2013) 79–84.

[4] P.P Vinaya, A.N. Prabhu, K. Subrahmanya Bhat, V.Upadhyaya "Design, Growth and characterization of D-π-A-π-D based efficient nonlinear optical single crystal for optical device applications," Journal of Physics and Chemistry of Solids, 123 (2018) 300-310.

[5] E.D. D'silva, D. Narayan Rao, Reji Philip, Ray J. Butcher, Rajnikant, S. M. Dharmaprakash, J. Phys. Chem. Solids, 72 (2011) 824-830.

[6] M. Sheik-Bahae, A.A. Said, T.-H. Wei, D.J. Hagan, E.W. Van Stryland, "Sensitive Measurement of Optical Nonlinearities Using a Single Beam", IEEE J. Quantum Electron. QE-26 (1990) 760.

[7] C. S. C. Kumar, T. C. S. Shetty, T. S. Chia, S. Chandraju, S. M. Dharmaprakash, H.K. Fun, C. K. Quah, Mater. Res. Innovations, 21 (2017) 198-205.

[8] A. N. Prabhu, V. Upadhyaya, A. Jayarama, K. Subrahmanya Bhat, Mater. Chem. Phys, 138 (2013) 179-185.

[9] P.S. Patil, S. R. Maidur, S. Venugopal Rao, S. M. Dharmaprakash, Opt. Laser.Technol, 81 (2016) 70–76.

[10] P. S. Patil, P. Ajay Kumar, S. Venugopal Rao, G. Bhagavannarayana, Opt. Laser Technol, 71 (2015) 108.

[11] R. K. Saripalli, N. K. Katturi, V. R. Soma, H. L. Bhat, Suja Elizabeth, J. Appl. Phys, 122 (2017) 223110.

[12] K. Naseema. V.Sujith, K. B. Manjunatha, B. Kalluraya, G. Umesh, V. Rao, Opt & Laser Technol 42 (2010) 741–748.

RADIATION PROFILING OF ISM BAND EM WAVES AT 433 MHz IN INDOOR ENVIRONMENT

MP HARSHA [1], NSV Shet [2]

1) Department of Electronics and Communication Engineering, Nitte mahalinga adyanthaya memorial institute of technology, Nitte, Karkala Tq, India. E-mail ID: parashuramharsha@nitte.edu.in

2) Department of Electronics and Communication Engineering, National institute of technology, Karnataka, Surathkal, India. E – Mail ID: shekar_shet@yahoo.com

Abstract: Satisfactory wireless communication is dependent on the best location for deploying the wireless infrastructure. Thus, a clear knowledge and understanding of the radio signal properties is helpful in deciding on the proper positioning of these technologies in society. Much of the existing research work is either theoretical or simulation based. Practical work and its analysis have taken a backseat. Studies in the past have tried to fit statistical models for the RSSI readings obtained in an indoor scenario, purpose being to better identify the position of an object. The intention of the paper is to answer the following question: Can we identify the position of the transmitter w.r.t the receiver by obtaining the signal strength correlation values between the different locations? Experiments were conducted and the results were analysed to understand its impact.

Keywords: ISM, RSSI, IoT, LOS, NLOS, IPS,LC

1. Introduction

The boom and the interest being generated in the Internet of Things (IoT) has led to the development of new communication standards. The LoRa (Long range) communication standard has characteristics of long range, very low power consumption and low data rate. LoRa is a proprietary wireless communication technology operating in the license free band of frequencies ranging from 433 MHz upto 2.3 GHz (ISM band – Industrial, Scientific and Medical radio band). Here, the frequency chosen is 433 MHz. Since it is very low power technology, output power being maximum of +20 dBm (100 mW), the battery lifetime will improve tremendously. This paper investigates the signal characteristics of LoRa standard for an indoor scenario, viz., a medium sized home. This will give an insight into its particular application for future use. Of course, there are other standards such as the very popular Wi-Fi which are very power intensive. Estimating position or location using accurate techniques like the angle of arrival (AOA) and time of arrival (TOA) were being used for outdoor applications, but due to multiple

reflection problems, they are not very popular in an indoor scenario, P bahl and VN Padmanabhan[3]. Deployment easy technique, the RSSI (received signal strength indicator) based one is being used frequently in indoor cases. Inferring the position of the user can be done by assessing the properties of the signal strength. Here, the LoRa Arduino shield combination is used as the AP (Access point), the transceiver. Statistical properties of a signal are a very important concept which needs to be analysed for better categorizing of the RSSI vector to belong to a particular location.

2. Related Works

Kamol et al [2] studied the signal properties using IEEE 802.11b wireless standard and compared obtained data to see how closely it fits a Gaussian model. They concluded that user's presence has to be factored in because it has a significant effect on signal strength. They also found the distribution of strengths was left skewed, and not Gaussian. But, Wi-Fi based solutions consume larger power. Shukri et al [4] used DFL (device free localization) technique intended for elderly care to track them without causing them any discomfort. This recorded the signal strength attenuation. Then, the attenuation and variance based methods in the AoI (Area of Interest --- i.e., where elderly were present) was applied and the accuracies of the methods were noted. Takens [5] identified and explained different methods in use for RSSI based object identification. A comparison of different RSSI based methods were done with the sole intention of locating and pinpointing the object. Tom et al [6] studied and evaluated performance of existing IPS (indoor positioning systems) considering a modern healthcare scenario. Here, point and room accuracies, latencies of the various methods were computed and recorded. For eg., Wi-Fi gave a relatively good point and room accuracy but latency was high. Amir et al [1] studied the impact of temperature and humidity variations on the RSSI in an indoor case. Signal strength was recorded for different times of the day and signal strengths were noted down. Significant variation in RSSI was observed due to small variations in temperature and humidity levels. All the above papers prove the fact that RSSI measurement technique is quite accurate and popular for indoor positioning systems.

3. Measurement process

The recording system consists of a set of arduino and LoRa shield, both being transceivers. The position of the receiver is fixed and at 1.5 feet above ground at a particular location inside a room. The transmitter location is varied with respect to (w.r.t) the fixed receiver. Also, its height is changed in steps w.r.t the receiver. The change in height of the transmitter w.r.t the receiver and its effect on the RSSI has not been studied in depth by the other authors. Now, RSSI readings are taken at each of the steps. The height of the transmitter is changed in convenient steps from ground level up to 4.5 feet w.r.t the receiver. This is done once, with the antenna in the direction of the receiver, the (LOS --- Line of sight) and all the readings are taken. The other set of

readings are taken with the transmitter antenna position changed arbitrarily in another direction (NLOS – Non line of sight). This procedure is repeated for each position of the transmitter w.r.t receiver in LOS and NLOS condition. The LoRa receiver code is dumped to one card and the transmitter code to the other card. To obtain the readings, the receiver card is connected to the laptop and the received signal strength is measured, the transmitter being powered externally. Measurements are observed on the serial monitor window of the arduino software at the receiver end.

The measurement set up is shown in figure 1. The plan of a medium sized home is shown in figure 2. The various rooms are indicated in the diagram. Measurements are made in the ground floor of the house whose dimension is 1500 square feet. The change in position of the transmitter is indicated and shown as LC1 (location 1), LC2 etc. All measurements are done in rooms which have furniture & metal objects (not necessarily arranged) depicting an actual case of a medium sized house.

Figure 1.

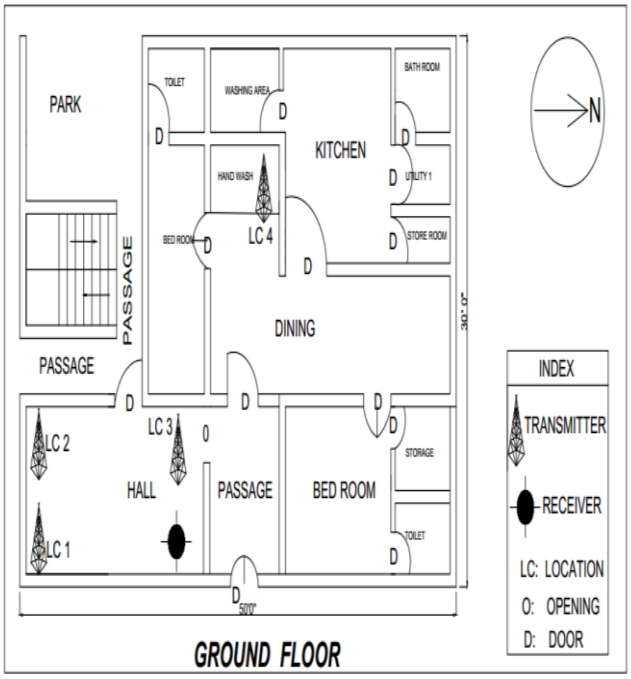

Figure 2.

4. Analysis of RSS data

a) In Location 1, 2 & 3, in LOS case, ground level is the least signal strength area because of the furniture and other obstacles between the transmitter and the receiver. Same is the situation in an NLOS case. Sample RSS values for various changing elevations of the transmitter w.r.t the receiver are indicated below (LOS) case:

Height in feet		0	1.5	2	2.5
RSS (dBm)	LC1	92.5	81.25	77.25	75
	LC2	82	75.5	72.5	73.25
	LC3	90.8	75	72.25	72.5

Table 1 (**Note**: All dBm values are negative)

Sample values for NLOS case for LC's 4, 5 & 7 are indicated below:

Height in feet		0	1.5	2	2.5
RSS (dBm)	LC4	96.75	94.5	91.75	92.25
	LC5	110.7	101	90.75	105.5
	LC7	111	89.5	86.75	86.5

Table 2 (**Note**: All dBm values are negative)

LC's 1, 2 & 3 which are basically the transmitter locations do not encounter a wall thickness as an obstacle, as they are located in a room in which the receiver is housed. The wall thickness is 1 foot. Hence, at ground level, they have higher signal strengths in comparison with the other LC's. The signal strengths at LC's 6 & 8 at ground level are shown below:

Transmitter at ground level (0 feet)		
RSS(dBm)	LC6	95
	LC8	97.6

Table 3 (**Note**: All dBm values are negative)

Comparing Table 1 ground (0 feet) readings w.r.t the other tables clearly indicates the same. But for the above locations (LC6 & LC8), when we observe the other elevation readings, there are changes in the RSS readings. This is because of the effect of two wall thicknesses between transmitter and receiver.

There are 4 samples of RSS readings taken in each location and 8 elevation readings of the transmitter. Considering 8 locations, the total number of readings is 256. In order to improve accuracy, more readings are taken in each of the locations & at different elevations. LC1, LC2 and LC3 (Transmitter locations) are in the same room as the receiver. This is also indicated by the RSSI readings and the positive and high values of the correlation coefficient of these readings w.r.t receiver. This is depicted in the table 4:

Locations (LOS)	Correlation Coefficient
LC1 to LC2	0.778
LC1 to LC3	0.859
LC2 to LC3	0.8851

Table 4

These values of correlation coefficient show that the transmitter and receiver are close by. When the correlation coefficients of LC1 to LC4, LC2 to LC4 were checked, they are of a lower value. This indicates that they are farther away from the receiver.

When we observe the NLOS readings too, a strong correlation exists between RSSI readings of LC1 to LC2, LC1 to LC3 & LC2 to LC3. This indicates the proximity between transmitter and receiver. The correlation coefficient LC1 to LC4, LC2 to LC4 are quite low showing that these locations have more separation distance. As an example, LC1 to LC4 correlation coefficient is 0.06.

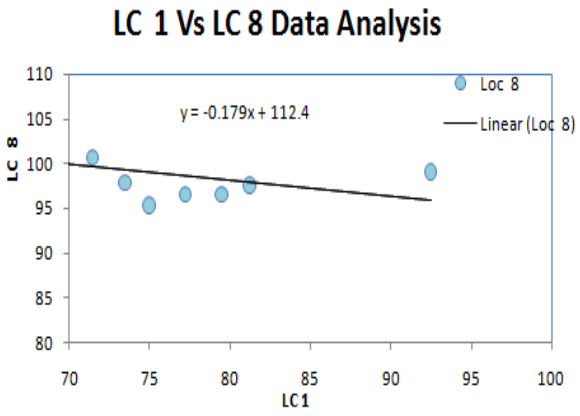

Figure 3

Figure 3 shows the degree of independence of the RSSI readings between locations LC1 and LC8. Here, the correlation coefficient is found to be -0.415, negative. This proves that if the RSSI from LC1 is increasing, same from the location LC8 is decreasing, thus indicating that LC8 is away from the receiver. Interestingly, the correlation coefficient for locations LC1 to LC4 and LC2 to LC4 are 0.06 and 0.009 respectively for the NLOS case even though the separation distance between the locations w.r.t the receiver is fixed. Same is summarised in table 5.

Locations	Correlation coefficient	
	LOS	NLOS
LC1 to LC4	0.6464	0.06
LC2 to LC4	0.7136	0.009

Table 5

Also, when correlation coefficient values were checked for the NLOS case between LC3 to LC4, the value is near 0.5 showing the closeness of the above two locations w.r.t receiver as compared with the low values obtained for LC1 to 4 and LC2 to 4 respectfully. This work can be used as a proximity evaluation tool between transmitter and receiver.

5. Conclusions:

A detailed study of RSSI at a fixed receiver w.r.t the transmitter where its altitude and position is varied has been studied and the following were observed:

- The correlation between transmitter locations which are physically close to the receiver shows a good value both in the LOS and NLOS conditions.
- Also, an interesting factor is that the locations which are not very close have high value of correlation in LOS case and low to very low levels in NLOS case.
- LC 6, LC7 are nearby locations and not widely different in positions w.r.t the receiver. The standard deviations of the RSSI of the two locations have less difference. However, their correlations in LOS and NLOS vary significantly. NLOS case have very low correlation.

References

[1] Amir Guidara, G Fersi et al (2018) Impacts of Temperature and Humidity variations on RSSI in indoor Wireless Sensor Networks, Procedia Computer Science, pp. 1072–1081, 22nd International Conference on Knowledge-Based and Intelligent Information & Engineering Systems.

[2] Kamol Kaemarungsi, Prashant Krishnamurthy (2004) Properties of Indoor Received Signal Strength for WLAN Location Fingerprinting, Proceedings of the First Annual International Conference on Mobile and Ubiquitous Systems: Networking and Services (MobiQuitous'04), IEEE.

[3] P Bahl, VN Padmanabhan, Microsoft Research (2000), Proc. IEEE INFOCOM, pp. 775 – 784, "RADAR: An in building RF – based user location and tracking system."

[4] Shaufikah Shukri, Latifah Munirah Kamarudin et al (2017) RSSI based device free localization for elderly care application, DOI: 10.5220/0006361901250135, In Proceedings of the 2nd International Conference on Internet of Things, Big Data and Security (IoTBDS 2017), pages 125-135, ISBN: 978-989-758-245-5

[5] Simon takens (2010), Master of Science thesis, University of Groningen, department of computer science, Indoor location tracking using signal strength pinpoints.

[6] Tom Van Haute, Eli De Poortre et al (2016), International Journal Of Health Geographics, Performance analysis of multiple Indoor Positioning Systems in a healthcare environment, DOI 10.1186/s12942-016-0034-z.

8th International Engineering Symposium - IES 2019
March 13-15, 2019, Kumamoto University, Japan

DEVICE-FREE HUMAN-COMPUTER INTERFACES FOR MAN-MACHINE INTERACTION

A. GEETHA

Department of Computer Science and Engineering,
Annamalai University, Annamalainagar. India

ABSTRACT: Man-Machine Interaction (MMI) is concerned with the design and implementation of interactive computer systems for human use. Input devices of increasing sophistication are available to mediate the man-machine interaction. Physically disabled and elderly people are important parts of our society and it is necessary to develop easily accessible systems using device-free vision-based interfaces to achieve their inclusion within the new technologies. This technique extracts motion from human interactive modalities like audio, visual and tactile to use verbal and non-verbal interactive signals such as face and body gestures. This interface automatically recognizes gestures within the face region to replace a conventional input device for man-machine interaction.

***Keywords**:* Man-Machine Interaction, device-free vision-based interface, face tracking, non-verbal signals.

INTRODUCTION

Due to the growth of information technology in the world, computer systems have been embedded into our environment to a larger extent. This atmosphere leads to the needs for new types of man-machine interaction with interfaces that are natural and easy to use. In our everyday life, we humans use our vision and hearing as main interfaces to communicate with our environment. Among all the communication channels through which interface information can travel, vision provides a lot of information that can be used for the recognition of human actions and gestures for man-machine interaction purposes Hence an interface based on head movements, face gestures or facial expressions is essential for natural interaction. The proposed work is aimed at developing a man–machine interface based on computer vision technology that automatically detect and track head and facial features in real time environment.

Man-Machine Interaction

Man–machine Interaction (MMI) involves the study, planning, and design of the interaction between users and computers. Man–machine Interaction is important for several reasons. One such important reason is to improve the quality of life by assisting doctors in treating the patients, helping teachers to involve computers for teaching the students, making the disabled individuals use computers etc. The visual based man-machine interaction is the most widespread area in MMI research. Some of the main research areas include Face Tracking, Facial Expression Analysis, Body Movement Tracking, Gesture Recognition, Gaze Detection etc. Hence, automatic detection of human faces and tracking them in a video sequence is a fundamental and challenging problem in the field of human-computer interface to promote entertainments and effective interaction with the computer for man-machine interface applications.

Facial and Head Gestures for MMI

Man-machine interfaces utilize eye, mouth, nose and head gesture measures that allow users to explicitly control themselves. These systems use facial and head gestures to control the cursor position and trigger mouse clicks or other

events. The aim of this work is to find new forms of interactions utilizing facial and head gestures suitable for users.

Applications of Vision-based Interfaces

- Hands-Free Text Entry
- Hands-Free Multimedia Operations
- Hands-Free Printer Operations
- Hands-Free TV Operations
- Hands-Free Browsing
- Hands-Free Interface to Web Applications for Smart Home Environments
- Hands-Free ATM operations
- Hands-Free Computer Games
- Hands-Free Mobile Operations
- Hands-Free GPS Operations

RELATED WORKS

Vijayalaxmi et al. (2016) developed an algorithm to estimate whether eyes are open or closed and fatigue is estimated using PERCLOS method. Disha H. Nagpure et al. (2014) proposed a work that describes eye motion detection using a five stage algorithm to estimate the direction of eye movements to control computer system. The Viola-Jones object detection algorithm is mainly used for head detection. The mouse is controlled by using the movement of cursor with respect to the proportional movement of the eye. Pravin R Futane et al. (2013) have identified an alternative to mouse commands for cursor controlling applications like opening of any note pad, office tools software etc. not by using mouse but by using face and hand gestures. Yo-Jen Tu et al. (2015) developed a face gesture based human computer interaction (HCI) to control the computer. Neha Nikhade1 et al. (2015) developed a HCI that aims to improve the interactions between users and computers by making computers more user friendly. Eye blink detection and head movements were used for communication between man and machine.

PROPOSED WORK

The main objective of the proposed work is to implement a device-free mouse control system using mouth and eye gestures without any special hardware. Human mouth and eye gestures are used to interact with computers for carrying out operations like window open and close, navigation between tabs, zooming etc. The flow diagram of the proposed work is shown in the Figure 1.

Face Detection

Paul Viola et al (2001) proposed a mrthod for face detection that is capable of processing images extremely rapidly while achieving high detection rates. There are three main contributions of this face detection framework. The first step of this method is a new image representation called an *integral image* that allows for very fast feature evaluation. The integral image can be computed from an image using a few operations per pixel. Once computed, any one of the Haar-like features can be computed at at any scale or location in constant time. The second step is a simple and efficient classifier that is built by selecting a small number of important features from a huge library of potential features using AdaBoosting The third step is a method for combining successively more complex classifiers in a cascade structure which dramatically increases the speed of the detector by focusing attention on promising regions of the image.

Eyes and Mouth Detection

The position of the eyes in the face image is found on the basis of certain geometrical dependencies. The located eye region is extracted and further eye tracking is done by means of template matching. Template-Matching is a well-known method for object detection used by T. Palleja et al (2011). In this template matching method, a standard eye pattern is created manually and given an input image, the correlation values with the standard patterns are computed for the eyes. The existence of an eye is determined based on the correlation values. This approach has the advantage of being simple to implement. However, it may sometimes be inadequate for eye detection since it cannot effectively deal with variation in scale, pose and shape.

Feature Extraction
Object Detection using Haar feature-based cascade classifiers is an effective object detection method proposed. Geetha A. et al (2009) preferred Haar-like features that are digital image features used in object recognition. It is then used to detect objects in other images. Initially, the algorithm needs a lot of positive images (images of eye) and negative images (images without eye) to train the classifier. Hence Haar features as shown in Figure 2 are needed to be extracted. They are just like our convolution kernel. Each feature is a single value obtained by subtracting sum of pixels under white rectangle from sum of pixels under black rectangle.

Modelling
The different eye-gestures are classified by using the machine learning models like Support Vector Machine (Christopher J. C. B, (1998)), k-Nearest Neighbor , Radial Basis Function Neural Networks etc (Musavi M T, et al (1992)). The eye-gestures considered are eye open, eye close, eyeball left and eyeball right.

Eye Tracking for Mouse Cursor Movement
The proposed system (Meenakshi K et al (2018)), is aimed at creating an interface between user and the computer using mouth gestures. The mouth and eye regions are tracked for moving the mouse cursor over the computer screen.

Mouth and Eye Gestures for Mouse Click Events
The activation of the mouse buttons use the changes that occur in the mouth region like mouth-open and mouth-close and in the eye region as eye open, eye close, eyeball left and eyeball right .

Interface Creation
The proposed system is aimed at creating an interface (Meenakshi K et al (2018)) between user and the computer using mouth gestures. The mouth and eye regions are tracked for moving the mouse cursor over the computer screen and mouth and eye gestures are detected for mouse click operations as shown from Figures 3 to Figures 11.

PERFORMANCE ANALYSIS
The performance metrics used for analysing the performance of the proposed system are as follows:

- TP – True Positive - No of frames that are correctly detected as eye blinks.
- TN – True Negative - No of frames that are correctly reported as no blinks.
- FP – False Positive - No of frames that are reported as eye blinks but they are not.
- FN – False Negative - No of frames that show eye blinks but they are not detected.
- Precision = TP/ TP+ FP
- Recall = TP/ TP+ FN
- F-measure = 2PR/ P+R

CONCLUSIONS
The following conclusions are deduced.

- The proposed method is found to perform better than the other existing metods
- The proposed method can be extended with other Deep Learning Classifiers.
- Other facial gestures from nose, eye-brows and head can be used for interface creation.
- The interface can be tried for other real-time applications.

REFERENCES

1. Christopher, J C B (1998), "A Tutorial on Support Vector Machines for Pattern Recognition", Data Mining and Knowledge Discovery, Vol. 2, No. 2, pp. 121-167.
2. Disha H. Nagpure et al (2014),"Eye Motion Detection Using Single Webcam for Person with Disabilities," International Journal of Engineering Research & Technology, Vol. 3, pp. 2199-2203.
3. Geetha, A et al (2009), "Facial Expression Recognition—A Real Time Approach", International Journal of Expert Systems with

Applications, Vol. 36, No. 1, pp. 303-308.

4. Meenakshi, K et al (2018), "Mouth Gestures as Human-Computer Interface", International Journal for Science and Advance Research in Technology Vol. 4. No. 4, pp. 503-509.
5. Meenakshi, K et al (2018), Vision-based Eye-controlled Interface for Human-Machine Interaction", International Journal of Advanced Research Trends in Engineering and Technology (IJARTET), Vol. 5, No. 12, pp. 914-921.
6. Musavi, M T et al (1992), "On the Training of Radial Basis Function Classifiers," *IEEE* Transactions on Neural Networks, Vol. 5, No. 4, pp. 595-603.
7. Neha Nikhade1 et al (2015), "Mouse Handling Using Facial Features", International Journal of Advanced Research in Computer and Communication Engineering, Vol.4, No.2, pp. 176-178.
8. Palleja, T et al (2011), "Implementation of a Robust Absolute Virtual Head Mouse Combining Face Detection, Template Matching and Optical Flow Algorithms" Springer, pp. 1479-1489.
9. Paul Viola and Michael Jones (2001), "Rapid Object Detection using a Boosted Cascade of Simple Features" Proceedings of IEEE Computer Society Conference on Compter Vision and Pattern Recognition, Vol. 1, p. 511.
10. Pravin R Futane et al (2013), "Cursor Controlling of Computer System through Gestures", International Journal of Innovative Research in Computer and Communication Engineering, Vol. 1, No. 10, pp. 2304-2318.
11. Vijayalaxmi and Elizabeth Rani, D (2016), "Driver Fatigue Estimation using Image Processing Technique", Information Technology and Computer Science, Vol. 6, No. 2, pp. 66-72.
12. Yo-Jen Tu et al (2015), "Face and Gesture Based Human Computer Interaction", International Journal of Signal Processing, Image Processing and Pattern Recognition, Vol. 8, No. 9, pp. 219-228.

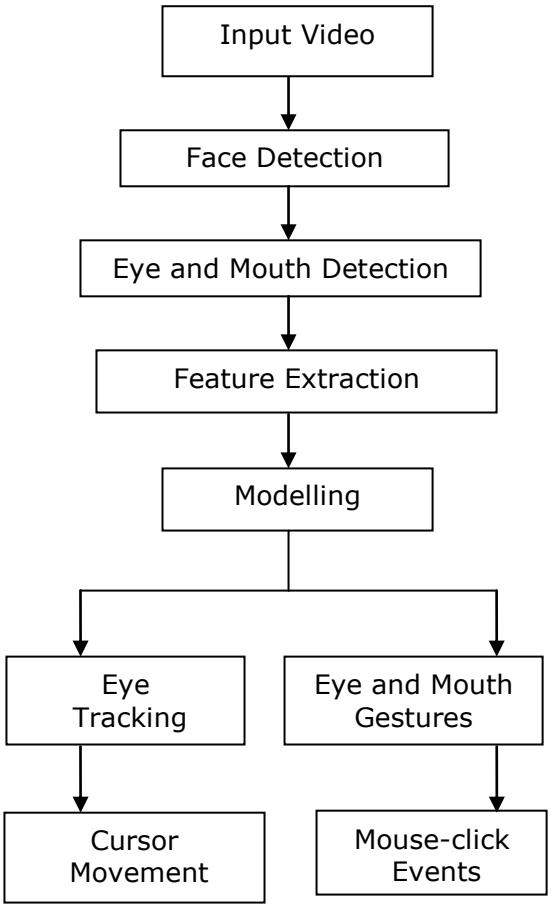

Fig 1. Flow Diagram of the Proposed work

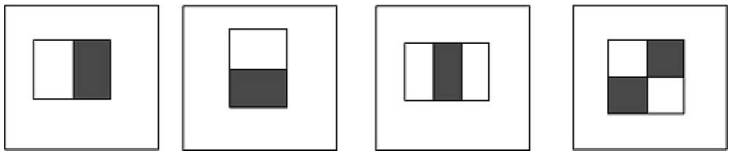

Fig 2. Haar-Features

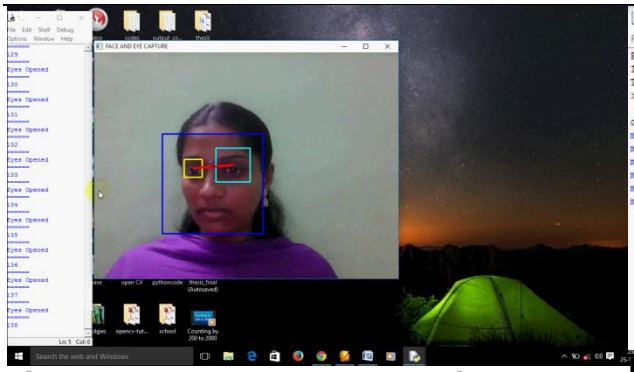

Fig 3. Cursor Movement using Eye-Tracking

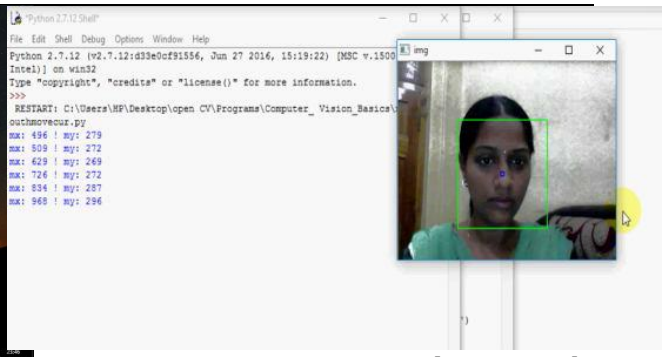

Fig 6. Cursor Movement using Mouth Tracking

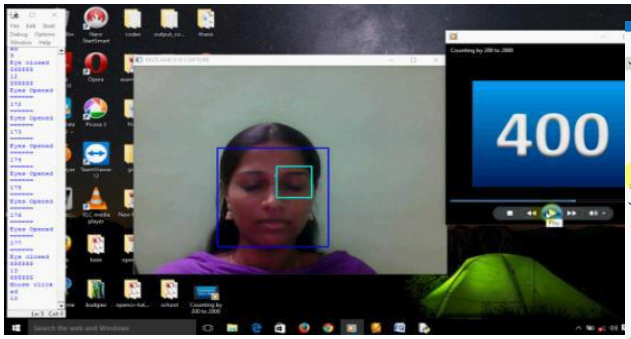

Fig 4. Pausing Windows Media Player by Eye-close Gesture

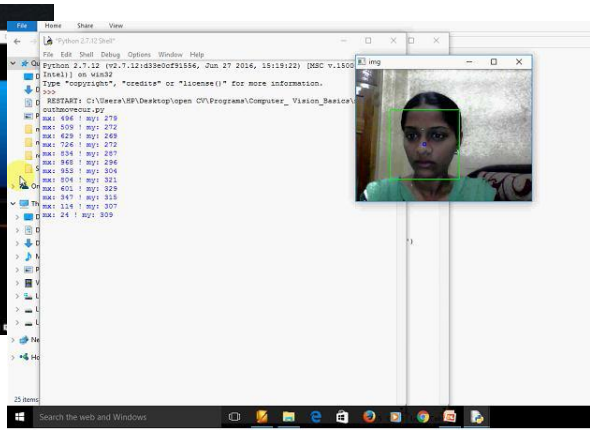

Fig 7. Cursor movement using Mouth Tracking towards Right Side of Screen

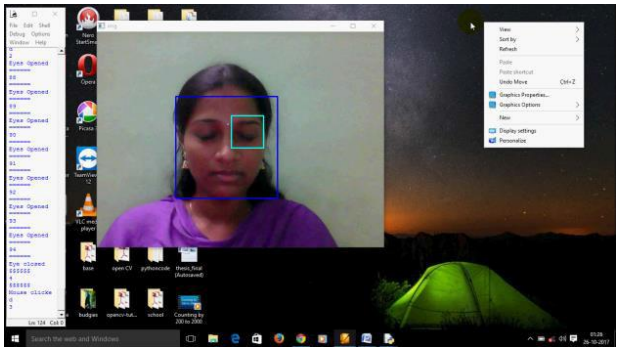

Fig.5. Opening Properties menu by Eye-close Gesture

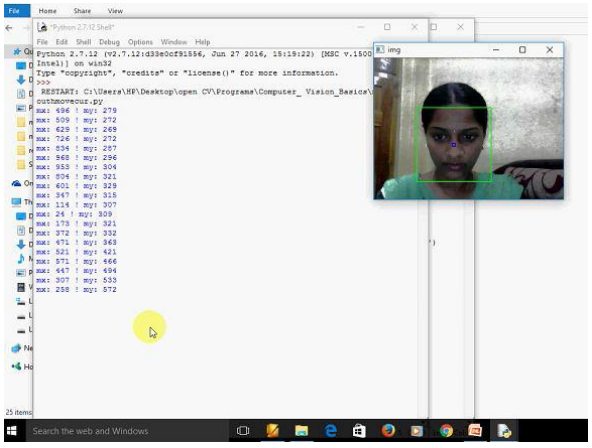

Fig 8. Cursor movement towards Bottom e of Screen using Mouth Tracking

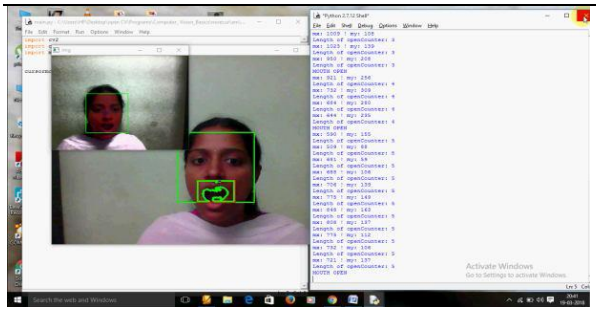

Fig 9. Window Closing by Mouth-open Gesture

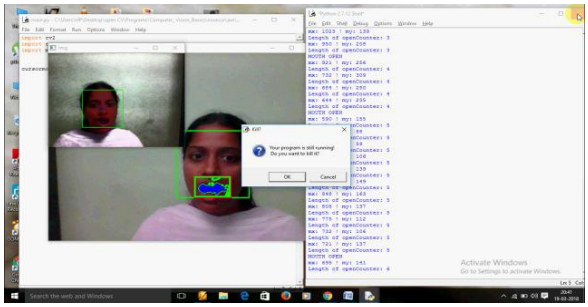

Fig 10. Mouse Left Click by Mouth-open Gesture

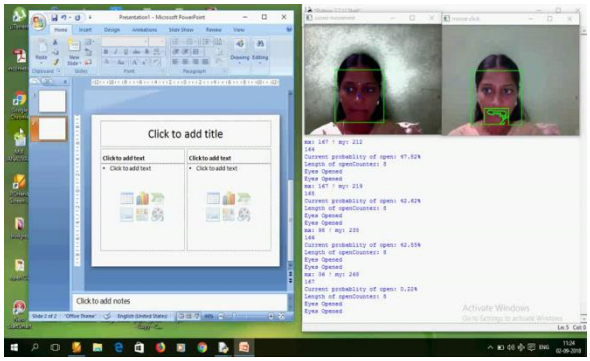

Fig 11. Multimodal Interface

8th International Engineering Symposium - IES 2019
March 13-15, 2019, Kumamoto University, Japan

ModQUIC Performance Analysis with Dynamic Packet Fragmentation in Wireless Networks

Prashant Kharat[1], **Shantanu Vijay**[2], **Jayanth Putta**[3], **Apurva P.**[4] and **M. Kulkarni**[5]

1 *Department of Electronics and Communication Engineering, National Institute of Technology Karnataka, Surathkal, Mangalore 575025, India.*
Email: prashant.kharat@walchandsangli.ac.in

2 *Department of Electronics and Communication Engineering, National Institute of Technology Karnataka, Surathkal, Mangalore 575025, India.*
Email: shantanu.vijay8@gmail.com

3 *Department of Electronics and Communication Engineering, National Institute of Technology Karnataka, Surathkal, Mangalore 575025, India.*
Email: jayanthputta@gmail.com

4 *Department of Electronics and Communication Engineering, National Institute of Technology Karnataka, Surathkal, Mangalore 575025, India.*
Email: apurvap011@gmail.com

5 *Department of Electronics and Communication Engineering, National Institute of Technology Karnataka, Surathkal, Mangalore 575025, India.*
Email: mkulkarni@nitk.ac.in

ABSTRACT: QUIC is an experimental transport-layer protocol, developed by Google. It is built over UDP to compete with TCP's dominance by improving transport layer performance. QUIC provides security equivalent to TLS/SSL along with reduced latency and superior congestion control. As QUIC is developed in the application layer, rapid debugging and testing of QUIC applications is possible. In this paper, we use Mininet (an open-source network emulator) to model a realistic network scenario and test ModQUIC (handshaking mechanism modified by merging window update frame with acknowledgment frame) in a wireless environment to quantify performance metrics such as throughput and latency.

This paper also looks at reducing the number of retransmissions by using packet fragmentation based on available bandwidth. Building upon previous work, we develop an algorithm to fragment packets through a feedback mechanism to avoid packet retransmission. In this method, dynamic fragmentation is implemented based on channel information and fragment transmission bursts. According to the IEEE 802.11 standard, only one threshold is used for fragmentation. Instead, using multiple thresholds can help obtain higher data rates. Our goal is to implement this technique as a part of ModQUIC and provide a thorough analysis of TCP versus QUIC in various scenarios shown through emulation results.

Keywords*: QUIC, Protocol technology, Network performance, Packet fragmentation*

INTRODUCTION

With the rapid evolution of web pages and web applications, there is an enormous increase in global Internet traffic. It is becoming necessary to innovate new technologies to handle this explosive growth. The majority of the Internet currently works over the Transmission Control Protocol/Internet Protocol (TCP/IP) suite of protocols. Google has analyzed the performance of TCP in current networks and observations show that about 25% of all Internet traffic pass through their servers (Megyesi et al., 2016). TCP's counterpart in the protocol world is the User Datagram Protocol (UDP) which is significantly more lightweight than TCP but does not match up in terms of forward

error correction capabilities and general reliability. However, UDP is faster and has significantly lesser control overhead (Hamilton et al., 2016) when compared to TCP which gives it an edge in high bandwidth applications such as gaming and video streaming.

In response to these observations, Google has developed a new network transport protocol known as QUIC (Quick UDP Internet Connections). QUIC runs on top of UDP and is intended as an alternative to TCP. Since TCP is implemented in operating system kernels and middlebox firmware, making significant changes to the protocol is a tedious and time-consuming process. QUIC, on the other hand, is developed in the application layer which allows for a faster development cycle with rapid testing, debugging and deployment (Cook et al., 2017).

One of QUIC's key advantages is that it considerably reduces the number of round-trip handshakes required. While TCP requires a 3-way handshake and an additional handshake for TLS negotiation, this entire process is completed in a single handshake when using QUIC. In fact, if two nodes have communicated in the past, no handshake is required at all, which is the case 75% of the time (Gratzer et al., 2016) in real world applications.

With QUIC, a complete restructuring of the Internet is possible allowing for faster data transfer with encryption equivalent to TLS/SSL and optimizations developed in HTTP/2 (Carlucci et al., 2015). With the rapid development of this protocol, the impact it will have on the Internet will be enormous. Reduced latency, higher bandwidth utilization and enhanced throughput are a few of the improvements that have been demonstrated with this protocol experimentally (Kakhki et al., 2017).

MOTIVATION

Overview

From an experimental protocol, QUIC has grown to have its own working group (Langley et al., 2017) and being used in a range of Google products and services. The protocol is currently responsible for 7% of global internet traffic and is deemed to make certain kinds of webpages load faster (Biswal et al., 2016). Our aim is to introduce two key modifications to the existing QUIC protocol to reduce control overhead and packet retransmission due to packet dropping which will ultimately lead to a reduction in transmission latency.

These modifications are as yet unexplored in any literature and have the potential to significantly improve performance. The first modification is to combine control frames. While this is comparatively minor in terms of its impact, our key focus is on the next modification which involves the use of dynamic packet fragmentation to reduce the number of retransmissions using a rate-adaptive scheme.

Packet Fragmentation

Up until now, there have been many rate-adaptive algorithms developed to increase throughput based on channel conditions. The current IEEE 802.11 standard for packet fragmentation uses one threshold. Our algorithm uses different thresholds based on varying channel conditions and bandwidth to optimize data transfer. A data frame is fragmented according to a threshold calculated based on information collected from the previous transmission as illustrated in the flowchart in Fig.1. This type of algorithm has been proposed in previous literature such as Kim et al. (2005), but not in the framework of the QUIC protocol itself.

METHODOLOGY

Platform

This work will use Mininet, an open source network emulator. This was chosen as the testing platform for a multitude of reasons. The primary reason is that Mininet is a Linux based solution with an extensive Python API. This makes the tool flexible enough to use with both existing protocols and experimental protocols. Mininet can be run as a virtual machine (VM) on any typical desktop and this allows for extended testing to be conducted through remote access on laboratory. Using an emulator also improves the scalability of the testing environment as compared to a hardware testbed.

Data Collection

In order to measure and analyze the performance of the different protocols, specific test cases were developed based on link delay, link bandwidth and packet loss, which are the primary link parameters available in Mininet. A range of values for each of these parameters were selected as shown in Table 1.

All combinations of these parameters were used to generate 120 individual test case specifications using the basic dumbbell topology as shown in the figure below. To maintain uniformity, the link between h1 (host 1) and h4 (host 4) was selected as the test link. All host to switch links have the bandwidth and half the specified delay specified by the test case parameters. The packet loss was maintained as 0% for all links except the s1 to h1 link. This link had the specified delay from the test case. This ensures that the specification describes the overall link between h1 and h4. With regards to the switch to switch link, a Gigabit ethernet link is assumed in order to avoid packet dropping and the bandwidth is set as 1000 Mbps (which is the maximum allowed by Mininet). The delay and packet loss for this link are also set to zero as per the logic above.

These cases are tested to obtain four metrics; packet loss (%), round trip time or RTT (ms), latency (s) and throughput (Mbps). The first two quantities are calculated by sending 50 successive ping requests from h1 to h4. The ping utility itself measures the packet drop rate as well as the minimum, maximum and average RTT and prints it to the terminal after the operation is complete. The other quantities are obtained by attempting a file transfer operation of a with a 10 MB file containing random data from h4 (as client) to h1 (as server). The total time taken and data rate achieved are used to calculate the latency and throughput, respectively. The data transfer will be conducted as 3 trials for each test case to screen for anomalies. The final results from multiple tests will finally be processed to measure speedup in performance and bandwidth utilization which are the relevant figures of merit to measure protocol performance.

Testing

In order to optimize testing, Mininet's Python API was used to automate the generation of the 120 test case definition files based on an initially created sample test case. This sample also included a function call from the Mininet CLI to a testing script in order to automate the actual testing phase and separate this from the topology and link parameter definition. The required tests, trials and storage of results are all specified in a custom test script which can be modified independently of the test cases generated previously.

Unfortunately, it was observed that given the link limitations, testing time was unreasonably long for test cases with high link loss. To avoid lengthy test times, it is recommended to parallelize the process by dividing the test cases into batches which can be executed multiple Mininet VMs running simultaneously on the same host.

Benchmarking

As a basis for comparison, it is necessary to set an initial benchmark. Since TCP currently dominates amongst transport protocols, the first series of tests was intended to set a benchmark and smooth the testing methodology. The first stage of testing was conducted with the ping utility as discussed above. A powerful network troubleshooting tool, iperf (Reeves, 2012), was used to conduct the second phase of testing. The tool was used to open a server on h1 and have h4 act as a client which would transfer the specified 10 MB of data to the server. The results obtained from TCP will be used as the benchmark against which all future performance tests will be measured as well as the base values from which speedup in performance will be calculated.

RESULTS

Packet Loss v/s Link Loss

Link loss is the probability that a packet sent over a link is lost or dropped. This ranged from 0% to 15% in 5% increments in our test cases. Theoretical packet loss is calculated from the assumption that there are two loss scenarios: a ping packet is lost or its acknowledgement is lost. A

simple calculation shows that theoretical packet loss is $2x-x^2$ given a link loss x.

The graph in Fig.3 shows that the average values obtained from testing are very closely related to the theoretical values expected. The significance of this result is that it confirms that the test topology functions as predicted by the model.

Latency and Throughput v/s Link Loss

The graphs in Fig.4 and Fig.5 show the relationship between the latency and throughput of the 10 MB file transfer with the link loss parameter. Data has been grouped according to bandwidth for coherency and the plots are split by delay. The main conclusion here is that as link loss increases, latency and throughput worsen exponentially even over links with high bandwidth. This exponential trend is explained by the fact that TCP's congestion window resets when there is a timeout (Kharat et al., 2018), as would be caused by a packet or its acknowledgement being lost. Link delay does not seem to consistently impact results and link loss appears to dominate.

Latency and Throughput v/s Bandwidth

It was also noted that when link loss was introduced, the impact of bandwidth became quite erratic with no clear-cut trend. This confirms the findings in the above two subsections i.e. the negative impact of link loss on performance is exponential and dominates the impacts of bandwidth and delay. Note that the vertical axes in Fig.5 are on a logarithmic scale.

ModQUIC

ModQUIC is the modification in the existing handshaking mechanism of the QUIC protocol. A proposed frame structure is marked as a modified ACK frame in Fig.6. With respect to working structure of QUIC, window update state is followed by packet ACK state. In the proposed modification, the window update frame is attached with ACK frame to reduce control overhead and window update delay shown in Fig.7. This results in a smooth variation of the congestion window and throughput improvements. The window update size itself varies based on network conditions and application demands.

FUTURE WORK

The next step in this work is to integrate QUIC into the Mininet platform and run the same tests under the same conditions as conducted for TCP. A new development in this work is that QUIC was built from the Chromium source directly on Mininet. The current roadblock is that a socket issue prevents the toy client-server model from being deployed as is. Further work will use Golang libraries to overcome this hurdle. The expectation from this testing is further evidence to support current literature which claims that QUIC's performance will be more tolerant to the exponentially deteriorating links seen with TCP (Srivastava, 2017). The same tests will then be run on ModQUIC along with dynamic packet fragmentation. Finally, a quantitative comparison will be used to analyze the benefits of each of the tested protocols and demonstrate the advantages of ModQUIC and dynamic packet fragmentation, if any.

CONCLUSIONS

The following conclusions are deduced from this study:

- Mininet offers a versatile and convenient testing platform with high automation capabilities
- TCP is severely impacted by congestion in links
- This exponential degradation in performance due to link losses is a serious issue
- Further experimentation against the same benchmark should reflect significant reductions in latency as suggested by existing literature.

ACKNOWLEDGEMENTS

This work is supported in part by AICTE, MHRD under QIP by Government of India. Any opinions, findings, conclusions and recommendations expressed those are of the author(s) only.

REFERENCES

[1] Biswal, P., & Gnawali, O. (2016, December). Does QUIC make the web faster?. In Global Communications Conference (GLOBECOM), 2016 IEEE (pp. 1-6). IEEE.
[2] Carlucci, G., De Cicco, L., & Mascolo, S. (2015, April). HTTP over UDP: an Experimental Investigation of QUIC. In Proceedings of the 30th Annual ACM Symposium on Applied Computing (pp. 609-614). ACM.
[3] Cook, S., Mathieu, B., Truong, P., & Hamchaoui, I. (2017, May). QUIC: Better for what and for whom?. In IEEE International Conference on Communications (ICC2017).
[4] Gratzer, F. (2016). QUIC - Quick UDP Internet Connections. Future Internet (FI) and Innovative Internet Technologies and Mobile Communications (IITM), 39.
[5] Hamilton, R., Iyengar, J., Swett, I., & Wilk, A. (2016). QUIC: A UDP-based secure and reliable transport for HTTP/2. IETF, draft-tsvwg-quic-protocol-02.
[6] Kakhki, A. M., Jero, S., Choffnes, D., Nita-Rotaru, C., & Mislove, A. (2017). Taking a Long Look at QUIC. In Proceedings of the 2017 Internet Measurement Conference.
[7] Kharat, P. K., Rege, A., Goel, A., & Kulkarni, M. (2018, April). QUIC Protocol Performance in Wireless Networks. In 2018 International Conference on Communication and Signal Processing (ICCSP) (pp. 0472-0476). IEEE.
[8] Kim, B. S., Fang, Y., Wong, T. F., & Kwon, Y. (2005). Throughput enhancement through dynamic fragmentation in wireless LANs. IEEE Transactions on Vehicular Technology, 54(4), 1415-1425.
[9] Langley, A., Riddoch, A., Wilk, A., Vicente, A., Krasic, C., Zhang, D., ... & Bailey, J. (2017, August). The QUIC transport protocol: Design and Internet-scale deployment. In Proceedings of the Conference of the ACM Special Interest Group on Data Communication (pp. 183-196). ACM.
[10] Megyesi, P., Krämer, Z., & Molnár, S. (2016, May). How quick is QUIC?. In Communications (ICC), 2016 IEEE International Conference on (pp. 1-6). IEEE.
[11] Reeves, S. (2012, January 30). iperf: A simple but powerful tool for troubleshooting networks. Retrieved from https://www.techrepublic.com/blog/linux-and-open-source/iperf-a-simple-but-powerful-tool-for-troubleshooting-networks/
[12] Sandvine. (2016). Global Internet Phenomena Report.
[13] Srivastava, A. (2017). Performance analysis of QUIC protocol under network congestion (Doctoral dissertation, Master Thesis, Worcester Polytechnic Institute).

Table 1 Test Case Parameters

Delay (ms)	Bandwidth (Mbps)	Packet Loss (%)
20	0.1	0
30	0.5	5
40	1	10
50	10	15
-	50	20
-	100	-

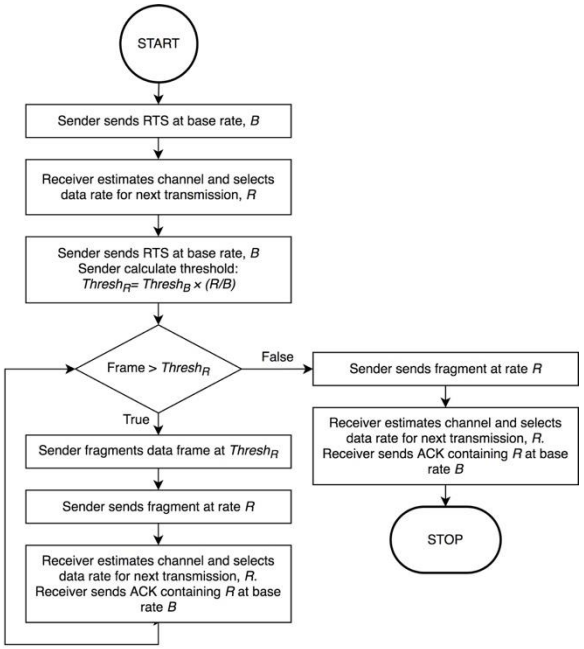

Fig.1 Fragmentation Algorithm

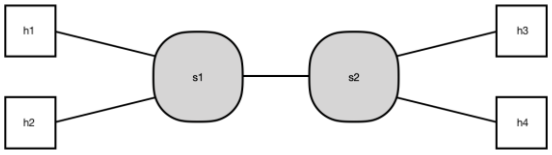

Fig.2 Dumbbell Topology

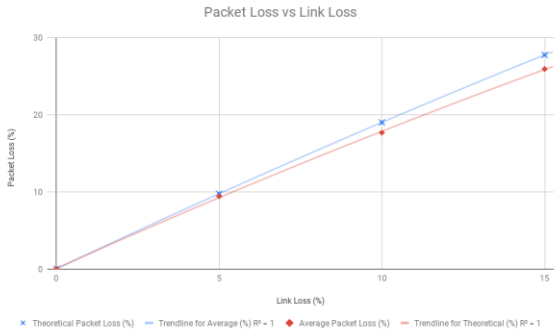

Fig.3 Packet Loss vs. Link Loss

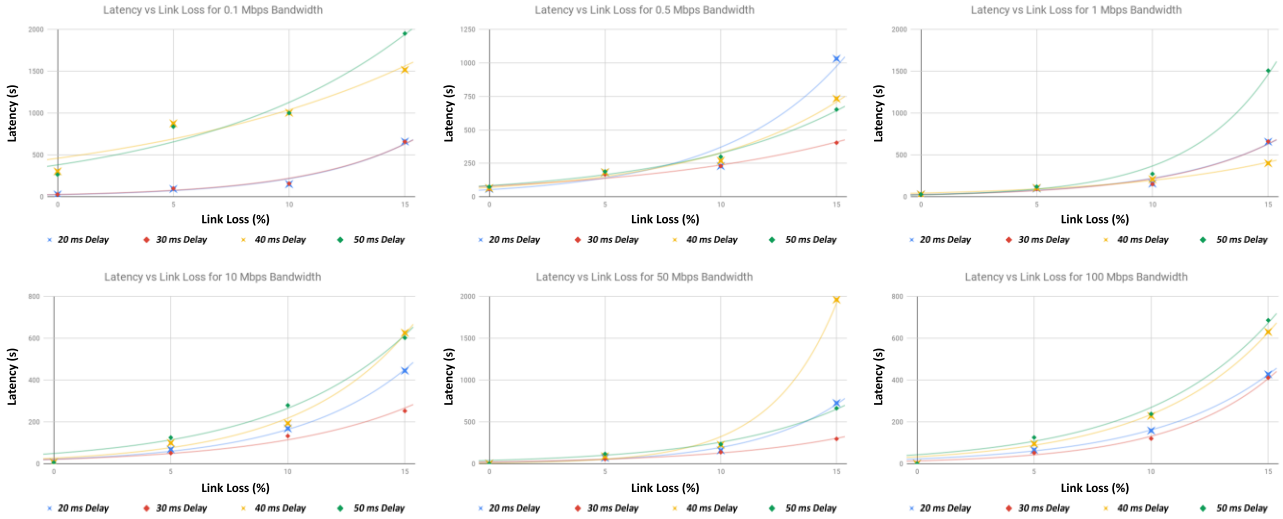

Fig.4 Latency vs Link Loss for Various Bandwidths

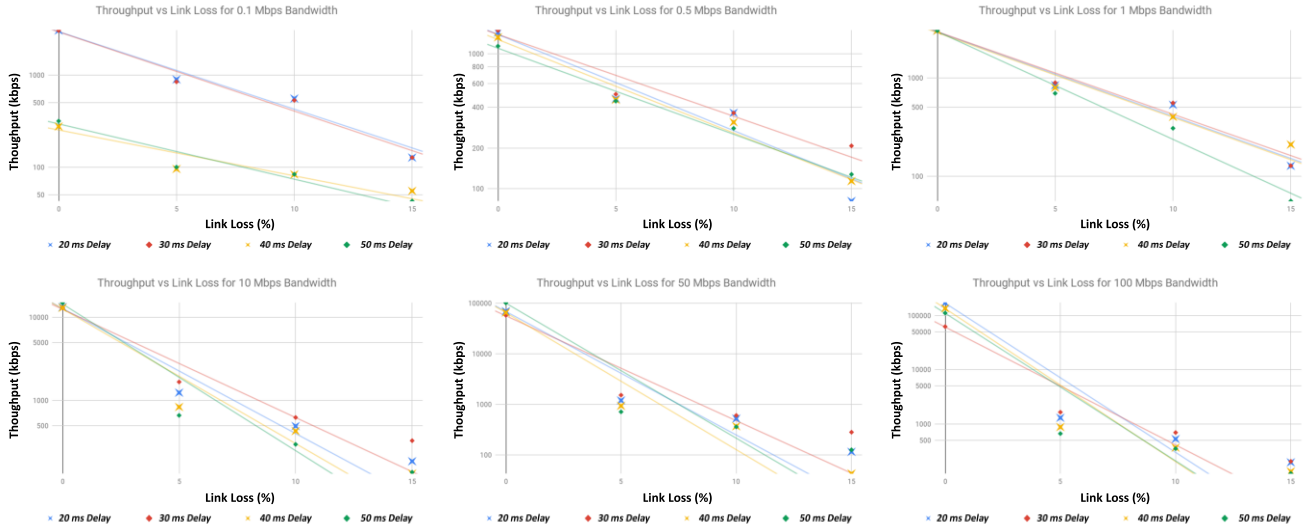

Fig.5 Throughput vs Link Loss for Various Bandwidths

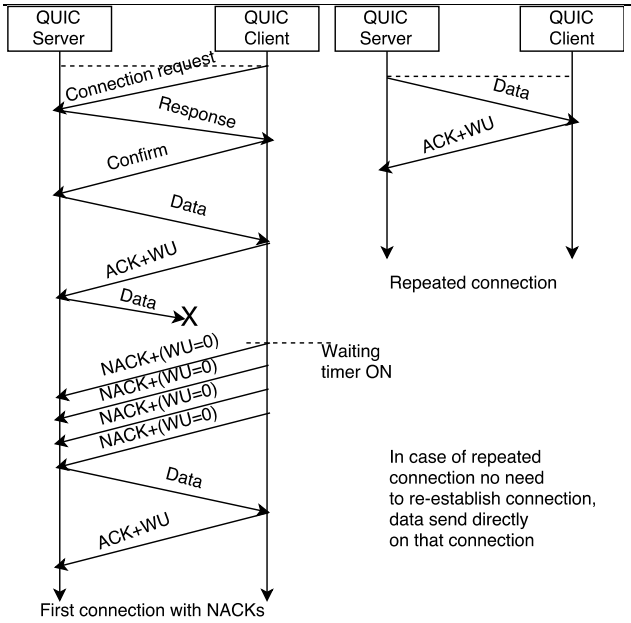

Fig.6 Proposed Acknowledgement with Window Update

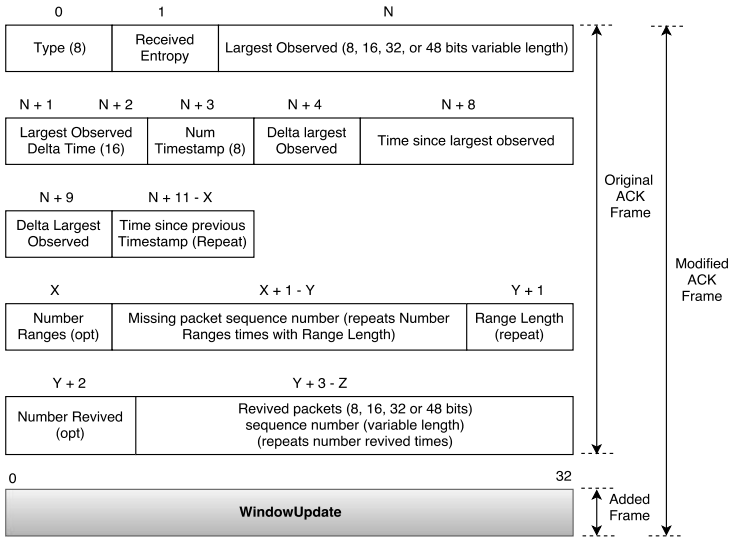

Fig.7 QUIC and ModQUIC ACK Frames

8th International Engineering Symposium - IES 2019
March 13-15, 2019, Kumamoto University, Japan

Prevention of DoS/DDoS attacks in Traditional Network by migrating it to Software Defined Network

Shivaraj B. Hublikar [1], Apurva P [2] and Muralidhar Kulkarni[3]

1 *Department of Electronics and Communication Engineering, National Institute of Technology Karnataka, Surathkal, Mangalore 575025, India. email:shivaraj@bvb.edu*
2 *Department of Electronics and Communication Engineering, National Institute of Technology Karnataka, Surathkal, Mangalore 575025, India. email:apurvap011@gmail.com*
3 *Department of Electronics and Communication Engineering, National Institute of Technology Karnataka, Surathkal, Mangalore 575025, India. email:mkulkarni@nitk.ac.in*

ABSTRACT: Traditional communication networks are vulnerable to DoS attacks due to distributed nature of network control. This leads to initiation of DoS attacks after finding the vulnerabilities in the network. To protect the network from such kind of attacks, Software Defined Network (SDN) switches are deployed, by enabling flow expiry mechanisms. In this context, a preventive solution called the Flow Expiry mechanism is implemented to protect the controller from the DoS attacks. The Flow Expiry mechanism proposed is integrated with OpenFlow protocol to prevent DoS attacks effectively. The switch flow expiry mechanism is run by the switch independent of the controller, based on the state and configuration of flow entries. This paper implements the above stated mechanism to improve the resilience of the SDN network against various DoS attacks by deploying OpenFlow switches and simulating in Mininet emulator.

***Keywords**: SDN, DoS attacks, Flow Expiry*

INTRODUCTION

Software-defined networking (**SDN**) technology is an approach to cloud computing that helps in facilitating efficient network management and enables programmatically efficient network configuration in order to improve network performance and monitoring. SDN is advantageous in achieving better flexibility and easier troubleshooting of current networks as opposed to the static, decentralised and complex architecture of traditional networks.SDN architectures decouple network control and forwarding functions and hence the traffic flow can be dynamically adjusted to the meet various requirements. In a SDN network, the traffic can be shaped using a centralized control console without having to touch the individual switches. The switches are directed to deliver the required network services irrespective of the individual connections between server and devices.

This process is a migration from traditional networks, in which devices have to make traffic decisions based on the routing tables configured. Security, apart from being a benefit, is also a major concern with SDN technology.SDN controller presents a single point of failure which is vulnerable to be targeted by an attacker. This could prove detrimental to the software-defined network. The network is prone to attack quite easily as the attackers can gain unauthorized access either physically or virtually. A host that is already connected to the SDN can be compromised to destabilize the network elements. This could be a type of Denial of Service (DoS) attack.

DDoS, short for distributed denial of service, is an attack where the network or website is made unavailable for its users. In DDoS, the target host is flooded with numerous requests from multiple sources, generally hundreds to thousands of IP

addresses as opposed to DoS attacks where a single user is involved. DDoS attacks are difficult to detect and analyse simply due to large number of devices that are responsible for the attack.

The OpenFlow communications protocol can be used in centrally managed SDN technologies in order to give access to the forwarding plane of a network switch or a router over the network. This helps in simplifying network management, handling all communications between applications and devices to effectively manage and modify network flows. This can be prevented by migrating it to Software Defined Network.

The main goal of this paper is to improve the resilience of an SDN network by integration of Flow Expiry mechanism with OpenFlow Protocol, using Mininet as the emulator.

RELATED WORK

The incoming traffic flooding the victim originates from multiple sources in case of DDoS attacks and effectively makes it impossible to prevent the attack by blocking a single IP address. It is very difficult to make a distinction between legitimate user traffic and attack traffic due to the presence of multiple points of origin. Various schemes have been suggested for the classification of traffic, detection and prevention of DDoS attacks.

Detection of DDoS attacks

TCP packet header can be analysed against the well-defined rules and conditions to discover DDoS attacks. The difference between normal and abnormal traffic can be obtained (Limwiwatkul et al. (2004)). Once the traffic is classified, it becomes important to detect the DDoS attack. The cross-correlation analysis can be used to capture the traffic patterns and decide when and where the DDoS attack possibly occurs as mentioned in J. Yuan & K. Mills, (2005).

Packet filtering

Different approaches to analyse the faulty packets have been proposed in the literature previously.

The hop count and the value of the received IP packet stored in the table built can be analysed. The packet can be discarded when major discrepancies exist between these two values. This is a victim based solution (Wang et al. (2007)).IP address spoofing can be done at the source by using StackPi marks. It is a new marking scheme based on Pi where a packet on its way to the destination is marked by routers Perrig et al. (2003)). Differential Packet Filtering against DDoS Flood Attacks is another method which relies on probabilistic means to determine risky packets. This scheme improves the quality of service and is adaptive to the traffic changes (Tanachaiwiwat et al. (2003))

Prevention of DoS/DDoS attacks

The concept of Secure Overlay Services (SOS) network through which the legitimate traffic is sent can also be used. (Keromytis et al. (2004)) SOS network is used to dynamically modify the overlay topology in order to avoid DDoS attacks. It can survive against the attack of certain key nodes of the network.

Another scheme based on document popularity in which anomaly detector based on hidden semi-Markov model can be used to detect the attacks. However, the Hidden Semi-Markov method poses a problem due to the complexity of the algorithm (Xie et al. (2009))

The click ratio of the web object is defined and the click ratio features are extracted using the cluster method. With the extracted features, the relative entropy is calculated to detect the suspicious sessions. This is a relative entropy based application layer-DDoS detection method proposed by Wang et al. (2010)

Yu et al. (2009) proposed an information theory based detection mechanism in which the distance of the package distribution behaviour among the suspicious flows is used to discriminate mimicking flooding attacks from legitimate accessing. Also websites' log can be analysed to prevent application layer DDoS attacks via human behaviour modelling

which differentiate DDoS bots from human users (Oikonomou et al. (2009))

A system to protect a web cluster from DDoS attacks by CAPTCHAs has also been proposed in previous literature. In this scheme the users have to solve the puzzles to get access to the services can (Kandula et al. (2005))This method assumed that human users can identify the distorted images, but the machine cannot. In DAT (Defense against Tilt DoS attack) scheme, DAT monitors a user's features throughout a connection session to determine whether the user is malicious user or not(Liu et al., (2011))

Most of the available schemes analyze the packet arrival rate, packet header information and so on. This information is used to detect and analyze the attacks precisely in order to prevent them. They treat anomalies as deviations in the IP attributes, for example, source IP address, TTL, and combination of multiple attributes.

PROPOSED WORK

Concept of Flow Expiry Mechanism

Removing the flow entries can be carried out either at the request of the controller or via the switch flow expiry mechanism ("OpenFlow Switch Specification", 2012). The switch flow expiry mechanism is run by the switch independent of the controller. This is based on the state and configuration of flow entries. Each flow entry has idle_timeout and hard_timeout variables associated with it.

hard_timeout, by definition, indicates the number of seconds before the flow entry is removed. It defaults to no timeout. If the hard_timeout field entry is non-zero, then the switch notes the flow entry's arrival time, which might be used to evict the entry later. A non-zero hard_timeout field causes the flow entry to be removed after the given number of seconds, regardless of how many packets it has matched.
idle_timeout, by definition, indicates the number of idle seconds before the flow entry is removed. It defaults to no idle timeout. If the idle_timeout field is non-zero, the switch must note the arrival time of the last packet associated with the flow, which might be used to evict the entry later. A non-zero idle_timeout field causes the flow entry to be removed when it has matched no packets in the given number of seconds. The switch must implement flow expiry and remove flow entries from the flow table when one of their timeouts is exceeded.

Platform

Mininet is a network emulator that provides a simple and inexpensive network test bed for developing OpenFlow applications. It creates a realistic virtual network of hosts, switches, controllers, and links. Mininet hosts run standard Linux network software, and its switches support OpenFlow for highly flexible custom routing and Software-Defined Networking.
The distributed nature of network control makes traditional network more susceptible to DOS attacks. The main goal of this paper is to improve the resilience against DoS/DDoS attacks by migrating it to SDN.

Methodology

Basic hub like functionality is provided in Mininet emulator, wherein it forwards any packet it receives to all the ports except on which it received the packet. To make this work as switch, a learning switch which learns the port number from the source MAC address is created. If there is a packet containing the destination MAC address which is previously learnt and added to the MAC Table, then the switch just forwards the packet to the corresponding output port.

A single switch connected to two hosts is the simplest default topology that Mininet offers. This can be changed to a different topology by passing the parameters using --topo while creating the network using sudo mn command. The switch type used is kernel mode Open vSwitch (OVSK), which comes preinstalled on the Mininet VM. The topology (i.e.Fig.1) can be created by using a simple command and considered for further analysis.

In order to create a learning switch, the

port learning behaviour is added. This is done by fetching the source and destination MAC address. The input port for a given packet is also obtained. The source MAC that was obtained is added to the corresponding input port. A separate act_like_switch method is created for performing the above function. Once the learning switch is created, the input port and the source MAC address can be stored as key-value pair in a dictionary named mac_to_port.

A flow based Switch is created by adding a flow entry to the switch if a packet with known source and destination arrives. If the destination address is present in the MAC table, and if there is an entry, a flow entry is added to the switch. The flow entry tells the switch to forward all the further packets from the output port which is the port corresponding to the destination MAC address.

idle_timeout, hard_timeout and buffer_id parameters are set. The buffer id is a unique value used to track the buffered packet. These parameters affect the duration for which the flow entries are stored. It informs the switch to remove these entries after a certain interval. A list of actions can be performed on matching packets (for example, ofp_action_output). This can prevent attacks on network.

Wireshark is used to verify the flow modification behaviour. Wireshark is a data capturing program that understands the structure of different networking protocols. It can parse and display the fields, along with their meanings as specified by different networking protocols. The idle_timeout, hard_timeout parameters are realised by capturing the OpenFlow packets in Wireshark on the Mininet console.

RESULTS

The result (i.e. Fig.2) clearly verifies that the learning switch added flow entries to the table. From the Wireshark output (i.e. Fig.3) it can be verified that the flow entries are actually deleted. The idle_timeout won't be in effect however the hard_timeout will delete the flow entry. This is confirmed from the captured output (i.e. Fig.3).

It can be noticed that two flow entries that were added at 41s are read at 57 seconds. It shows that the flow entries were deleted in 15s, the hard_timeout.

CONCLUSIONS

The following conclusions are deduced from this study:

- Vulnerabilities in the network may lead DOS/DDOS attack on network.
- To protect the network from such kind of attacks a Software Defined Network (SDN) is deployed by enabling Flow Expiry mechanisms. This prevents DoS attacks on network.

ACKNOWLEDGEMENTS

This work is supported in part by AICTE, MHRD under QIP by Government of India. Any opinions, findings, conclusions and recommendations expressed those are of the author(s) only.

REFERENCES

[1]G.Oikonomou & J.Mirkovic, (2009) "Modeling human be havior for defense against flash-crowd attacks", ICC2009. Computer Science & Information Technology (CS & IT)223

[2]Haining Wang, Cheng Jin & Kang G. Shin, (2007) "Defense Against Spoofed IP Traffic Using Hop-Count Filtering", IEEE Transactions on Networking,vol.15.No.1, pp.40-53.

[3]https://www.networkworld.com/article/2840273/sdn/sdn-security-attack-vectors-and-sdn-hardening.html

[4]Huey-Ing Liu & Kuo-Chao Chang, (2011) "Defending systems Against Tilt DDoS attacks", 6th International Conference on Telecommunication Systems, Services, and Applications.

[5]J. Yuan & K. Mills, (2005) "Monitoring the macroscopic effect of DDoS flooding attacks," IEEE Trans. Dependable and Secure Computing, vol. 2, no.4, pp. 324–335.
[6]Jie Yu, Chengfang Fang, Liming Lu & Zhoujun Li, (2009) "A Lightweight Mechanism to Mitigate Application Layer DDoS Attacks", in Proceedings of Infoscale'2009.
[7]Jin Wang, Xiaolong Yang & Keping Long, (2010) "A New Relative Entropy Based App-DDoS Detection Method", IEEE Symposium On Computers And Communications (Iscc).
[8]Keromytis, A.D., Misra, V., & Rubenstein, D., (2004) "SOS: an architecture for mitigating DDoS attacks", Selected Areas in Communications, IEEE Journal vol. 22, no. 1.
[9]L. Limwiwatkul & A. Rungsawangr, (2004) "Distributed denial of service detection using TCP/IP header and traffic measurement analysis," in Proc. Int. Symp. Commun. Inf. Technol., Sappoo, Japan, Oct.26–29,pp.605–610.
[10] OpenFlow Switch Specification Version 1.3.1 (Wire Protocol 0x04) September 6,2012 Retrieved from https://www.opennetworking.org
[11]Perrig A., Song D, & Yaar A., (2003) "StackPi: a new defense mechanism against IP spoofing and DDoS attacks", CMU technical report.
[12]S.Kandula, D.Katabi, MJacob & A.W.Berger, (2005) "Botz-4-sale: surviving organized DDoS attacks that mimic flash crowds", in Proc. Second Symp. Networked Systems Design and Implementation (NSDI).
[13]Tanachaiwiwat, S. & Hwang, K., (2003) "Differentialpacket filtering against DDoS flood attacks." ACM Conference on Computer and Communications Security (CCS).
[14]Yi Xie & Shun-Zheng Yu, (2009) "Monitoring the Application-Layer DDoS Attacks for Popular Websites", IEEE/ACM Transactions on Networking, Vol. 17, No. 1.

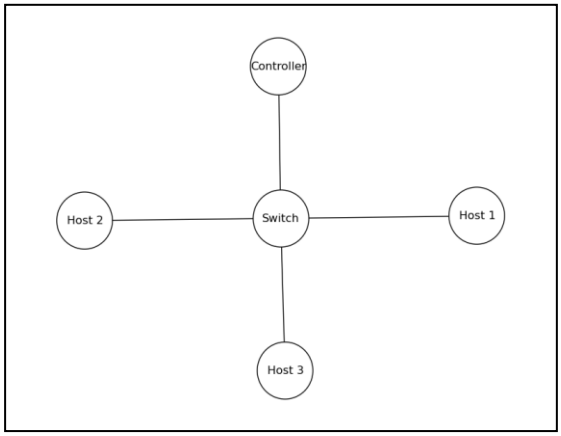

Fig.1: Network topology

```
mininet> sh ovs-ofctl dump-flows s1
NXST_FLOW reply (xid=0x4):
cookie=0x0, duration=2.479s, table=0,
n_packets=3, n_bytes=294,
idle_timeout=10, hard_timeout=15,
idle_age=0,
icmp,vlan_tci=0x0000,dl_src=00:00:00
:00:00:01,dl_dst=00:00:00:00:00:03,n
w_src=10.0.0.1,nw_dst=10.0.0.3,nw_t
os=0,icmp_type=8,icmp_code=0
actions=output:3
cookie=0x0, duration=2.477s, table=0,
n_packets=3, n_bytes=294,
idle_timeout=10, hard_timeout=15,
idle_age=0,
icmp,vlan_tci=0x0000,dl_src=00:00:00
:00:00:03,dl_dst=00:00:00:00:00:01,n
w_src=10.0.0.3,nw_dst=10.0.0.1,nw_t
os=0,icmp_type=0,icmp_code=0
actions=output:1
```

Fig.2: Output with flow entries added

1932	36.80902300(	127.0.0.1	127.0.0.1	OF 1.0	74 of_echo_request
1934	36.82391900(	127.0.0.1	127.0.0.1	OF 1.0	74 of_echo_reply
1982	41.14874600(	10.0.0.1	10.0.0.3	OF 1.0	182 of_packet_in
1990	41.19004500(	127.0.0.1	127.0.0.1	OF 1.0	146 of_flow_add
1992	41.19033300(	10.0.0.3	10.0.0.1	OF 1.0	182 of_packet_in
1994	41.19171000(	127.0.0.1	127.0.0.1	OF 1.0	146 of_flow_add
2259	45.80854300(	127.0.0.1	127.0.0.1	OF 1.0	74 of_echo_request
2261	45.85806000(	127.0.0.1	127.0.0.1	OF 1.0	74 of_echo_reply
2302	50.80860500(	127.0.0.1	127.0.0.1	OF 1.0	74 of_echo_request
2304	50.82566200(	127.0.0.1	127.0.0.1	OF 1.0	74 of_echo_reply
2358	55.80861100(	127.0.0.1	127.0.0.1	OF 1.0	74 of_echo_request
2359	55.84350500(	127.0.0.1	127.0.0.1	OF 1.0	74 of_echo_reply
2385	57.14843800(	10.0.0.1	10.0.0.3	OF 1.0	182 of_packet_in
2386	57.16181400(	127.0.0.1	127.0.0.1	OF 1.0	146 of_flow_add
2388	57.16216000(	10.0.0.3	10.0.0.1	OF 1.0	182 of_packet_in
2389	57.16348600(	127.0.0.1	127.0.0.1	OF 1.0	146 of_flow_add
3043	61.80907200(	127.0.0.1	127.0.0.1	OF 1.0	74 of_echo_request

Fig.3: Wireshark output indicating deleted flow entries

8th International Engineering Symposium - IES 2019
March 13-15, 2019, Kumamoto University, Japan

Performance of Search Optimization Methods while Configuring a Voltage Impulse Generator

Prabhat K Sonu[1], Gururaj S Punekar[2]

1 *Department of Electrical Engineering, National Institute of Technology Karnataka, Surathkal, Mangalore 575025, India. email: sonu.prabhat1@gmail.com*
2 *Department of Electrical Engineering, National Institute of Technology Karnataka, Surathkal, Mangalore 575025, India. email: gsp@nitk.edu.in*

ABSTRACT: The performance of three search-based algorithms, namely, Simplex search method, Particle swarm optimization (PSO) and Genetic algorithm (GA) are compared using an electrical engineering problem of configuring 'voltage impulse generator'. Among these commonly applied numerical methods, PSO and GA are population based parallel search methods. This paper attempts to compare the results of three search optimization methods by applying them to a 'voltage impulse generator' configuration problem. The lightning and switching voltage impulses, used in high voltage impulse testing, are characterized by their time-to-front (t_f) and time-to-tail (t_t). To get the desired values of t_f and $t_{t,}$ for a given impulse generator (generator capacitance) and load capacitance, the wave-shaping resistors (R_s & R_d) of particular value are to be determined. Thus, while configuring the impulse generator, the mathematical model of 'voltage impulse generator' is transformed into a search-problem with an objective. Aim is to minimize the objective function value to get the optimal values of R_s & R_d to achieve the desired wave-shape. The numerical experiments indicate that among these heuristic methods PSO performs better compared to GA and Simplex algorithm.

Keywords*: Genetic Algorithm, Objective function, Optimization, Particle Swarm Optimization, Simplex, Voltage-impulse, Wave-shape.*

INTRODUCTION

Optimization is an engineering tool used to arrive at the best possible solution of any problem. Search-based algorithms are used as optimization tool to solve various engineering problems. In this paper an attempt has been made to compare and find the best among three search-based algorithms, namely, Simplex search method (Wright 2012), Particle swarm optimization (PSO) (Ebehart and Kennedy 1995) and Genetic algorithm (GA) (Mitchel 1999), while configuring a 'voltage impulse generator'. In the process of configuring impulse generator, the mathematical model of 'voltage impulse generator' is converted into a search optimization problem.

'Voltage impulse generator' is characterized by its peak amplitude (V_p), time-to-front (t_f) and time-to-tail (t_t) (IS 2071-1, 1993). To get the intended values of t_f and t_t wave-shaping resistances (R_s and R_d) are to be determined. In an impulse generator, test sample (sample capacitance) is an integral part of wave-shaping circuit (Naidu and Kamaraju 1995). Thus, 'voltage impulse generator' needs to be re-configured for every new sample. In literature efforts have been made to simulate the 'voltage impulse generator' to get desired waveshape for a given generator capacitance (C_g), sample capacitance (C_l) and wave-shaping resistances (R_s & R_d) (Devarajan and Premi 2015, Nair and Prof. Pachori 2013, Pereira et al. 2008, Veisheipl 2016). The worked presented in this paper, while configuring impulse generator, attempts to find out the best values of wave-shaping resistances (R_s & R_d) by three different search algorithms to get intended t_f and t_t for a given C_g and C_l. This is attempted by three optimization techniques. Finally, the

results obtained from these different methods are compared.

VOLTAGE IMPULSE GENERATOR

'Voltage impulse generator' circuit is used to generate very high magnitude of voltage for a short duration with definite wave shape. The basic principle involved is to charge n-number (n is the number of stages) of capacitors in parallel and discharge them in series forming an equivalent capacitance called generator capacitance (C_g). This process of charging and discharging generator capacitance is called sudden DC generation. Such an equivalent circuit of single stage (n=1) 'voltage impulse generator' is shown in Fig.1. The sample or load capacitance (C_l) along with wave-shaping resistances (R_s & R_d) forms the wave-shaping circuit. The impulse generator can be tuned to get intended time-to-front (t_f) and time-to-tail (t_t) by finding appropriate values of wave-shaping resistances (R_s & R_d). The sphere gap (S.G.) shown in Fig.1 acts like a control switch and is used to fire the impulse generator. The sphere gap is adjusted with suitable gap distance to allow breakdown to happen at the desired voltage. This desired voltage is acquired by charging the generator capacitance (C_g) with the help of various types of 'voltage impulse generator' like Marx circuit, Goodlet circuit and modern impulse generator circuit (Naidu and Kamaraju 1995). The output waveform of 'voltage impulse generator' is a double exponential wave as shown in Fig.2. The time-to-front (t_f) and time-to-tail (t_t) shown in Fig.2 corresponds to the peak voltage (V_p) and half the peak voltage ($V_p/2$) respectively (IS 2071-1, 1993).

The mathematical model of the circuit shown in Fig.1 is represented by Eq.1 and Eq.2.

$$\frac{dV_1}{dt} = \frac{1}{R_s C_g}(V_2 - V_1) \quad (1)$$

$$\frac{dV_2}{dt} = \frac{1}{R_s C_l}(V_1 - V_2) - \frac{V_2}{R_d C_l} \quad (2)$$

Where,
V_1 = Voltage across generator capacitor.
V_2 = Voltage across sample/load capacitor.
C_g = Generator capacitor.
C_l = Load or sample capacitor.
R_s = Series resistor (wave-front resistor).
R_d = Discharging resistor (wave-tail resistor).

The solution of Eq.1 and Eq.2 gives the voltage across generator capacitor ($C_{g)}$ and sample capacitor (C_l) respectively. The capacitor C_g will have an initial potential (charged to some voltage). The output voltage (V_2) across the sample capacitor as a function of time is of interest. The t_f and t_t of voltage V_2 is decided by the values of R_s and R_d in conjunction with C_g and C_l. Thus, configuring an impulse generator to get intended t_f and t_t implies finding the appropriate values of R_s and R_d for a given C_g and C_l. Thus, the above mathematical model is transformed into a search problem. The solutions at each step are obtained numerically using the ODE 45 in MATLAB.

SEARCH OPTIMIZATION METHODS

(a) Simplex search algorithm: It is a direct search method based on Nelder-Mead algorithm. There are three key points, worst, lousy and best, involved in this algorithm. Based on the function evaluation at these three points, each iteration involves operations like reflection, contraction, expansion and shrinking (Wright 2012). It is named simplex search as it forms a structure in n-dimensional (n is the number of variables) space, formed by n+1 points that are not in the same plane, called simplex. The Nelder-Mead algorithm starts with a simplex and at each iteration it modifies the simplex depending on the operations involved. The first step in this algorithm is to identify n+1 points of the simplex given an initial guess X_0 of design variables X. After generation of initial simplex, objective function value at each of its vertices is evaluated and three key points are obtained depending on the function value. For a minimization problem, as in our case, worst, lousy and best points are associated with the highest, second highest and lowest function values. The Nelder-Mead algorithm performs listed four operations (reflection, contraction, expansion and shrinking) which generates a new point. And the sequence of

operation to be performed in one iteration depends on the relative value of the objective function at the new point with respect to other key points.

(b) Particle swarm optimization: PSO is a population based stochastic optimization technique developed by Kennedy and Eberhart in 1995 (Ebehart and Kennedy 1995). It is based on swarm intelligence which makes it a bio inspired optimization technique. PSO approaches to the solution based on the global best of the swarm as well as personal best of each individual. Each individual or particle moves towards a new position $x_i(t+1)$ from its current position $x_i(t)$ using three components, namely, personal best $P_i(t)$, its current velocity $v_i(t)$ and the global best $g(t)$. In each iteration the new velocity $v_i(t+1)$ is calculated for each particle using mathematical expression given in Eq.3 (Hasan et al. 2014).

$$v_i(t+1) = Wv_i(t) + C_1\left(\frac{(P_i(t)-x_i(t))}{\Delta t}\right) + C_2\left(\frac{(g(t)-x_i(t))}{\Delta t}\right) \quad (3)$$

Where,
W = inertia factor
C_1 = Self-confidence factor
C_2 = Swarm confidence factor
The new position of the particle is found by implementing Eq.4.

$$x_i(t+1) = x_i(t) + v_i(t+1) * \Delta t \quad (4)$$

PSO is computationally better than other evolutionary algorithms and have high convergence rate in getting the best solution (Hasan et al. 2014).

(c) Genetic algorithm: GA is another population based evolutionary algorithm introduced by John Holland and his colleagues at the university of Michigan in mid-1970's. It is based on the principle of genetics and evolution involving operators like crossover, mutation and elitism (Mitchel 1999). Elite member resembles the survival of the fittest whereas crossover and mutation are two techniques to populate the next generation. The new population is created by evaluating the fitness function or objective function and based on the fitness value, least value for minimization problem, elite members are directly transferred to the next generation. The parents are selected based on the fitness score and are combined to get offspring in crossover whereas children are produced by making random changes to a single parent in mutation. Potentially superior children are produced by extracting the best genes from different individuals in crossover; while mutation adds to the diversity of population thus enabling the algorithm to generate individuals with better fitness value.

SEARCH OBJECTIVE FUNCTION

The objevtive function specific to 'voltage impulse generator is as given in the Eq. 5. The objective function of this two variable optimization problem to get desired values of t_f & t_t, is (see in Eq.5).

$$f_{val} = \left(\frac{t_f - t_{f-desired}}{t_{f-desired}}\right)^2 + \left(\frac{t_t - t_{t-desired}}{t_{t-desired}}\right)^2 \quad (5)$$

The function value (f_{val}) is calculated in each iteration and the function values of present and previous iteration is compared. The algorithms will stop once the difference in function values of two consecutive iterations is less than the set tolerance limit or chosen number of iterations are elapsed (whichever is earlier).

CONFIGURING VOLTAGE IMPULSE GENERATOR

Power system components likely to experience impulse voltages are recommended to be tested with standard impulse voltage wave shapes as specified in the relevant IS standard (IS 2071-1, 1993). Testing of different power system components, for lightning and switching impulse voltages, requires configuration of the impulse generator to get the desired wave shape. Configuring impulse generator implies determining the values of wave-shaping resistors R_s & R_d for given C_g and C_l to get intended t_f and t_t. The wave shape chosen for the present study is a standard lightning impulse wave of 1.2μs/50μs ($t_{f\text{-desired}}/t_{t\text{-desired}}$).
The algorithms involved while configuring 'voltage impulse generator' using three search methods are:
(a) Simplex Search:
Step 1: Input C_g, C_l, $t_{f\text{-desired}}$ and $t_{t\text{-desired}}$.
Step 2: Set function tolerance as 10^{-6}.

Step 3: Calculate approximate values of R_s and R_d using Eq.6 and Eq.7.

$$R_s = \frac{t_f(C_g+C_l)}{3C_gC_l} \quad (6)$$

$$R_d = \frac{t_t}{0.7(C_g+C_l)} - R_s \quad (7)$$

Step 4: Set random initial guess for R_s and R_d using random number generator, in MATLAB, scaled to twice of approximate values of R_s and R_d.
Step 5: Solve Eq.1 and Eq.2 using ODE 45 solver in MATLAB.
Step 6: Obtain t_f and t_t by plotting V_2 and evaluate f_{val} (See Eq. 5).
Step 7: Checking for stopping criteria, (set tolerance and the number of iterations) else go back to step 5.

(b) Particle swarm optimization (PSO):
Step 1: Input C_g, C_l, $t_{f\text{-desired}}$ and $t_{t\text{-desired}}$.
Step 2: Set function tolerance as 10^{-6}.
Step 3: Set swarm size.
Step 4: Solve Eq.1 and Eq.2 using ODE 45 solver in MATLAB.
Step 5: Obtain t_f and t_t by plotting V_2 and evaluate f_{val} (See Eq. 5).
Step 6: Checking for stopping criteria, (set tolerance and the number of iterations) else go back to step 4.

(c) Genetic algorithm (GA):
Step 1: Input C_g, C_l, $t_{f\text{-desired}}$ and $t_{t\text{-desired}}$.
Step 2: Set function tolerance as 10^{-6}.
Step 3: Set population size.
Step 4: Solve Eq.1 and Eq.2 using ODE 45 solver in MATLAB.
Step 5: Obtain t_f and t_t by plotting V_2 and evaluate f_{val} (See Eq. 5).
Step 6: Checking for stopping criteria, (set tolerance and the number of iterations) else go back to step 4.

RESULTS AND DISCUSSIONS

Simplex search algorithm may not give accurate results in every search-runs. Hence, the algorithm is run for ten times and the % error in t_f and t_t obtained in each run is plotted in Fig.3 and Fig.4 respectively. The average value of absolute % error in t_f and t_t for these ten search-runs are 8.3% and 16.3% respectively. Out of ten search-runs, in few runs, % error in t_f and % error in t_t is very large resulting in large standard deviation. So, these erroneous results have to be discarded. This can be done by simple post processing of data using mode as statistical tool. The values of R_s and R_d thus obtained are 198 Ω and 2503 Ω respectively.

The results of PSO vary with swarm size. The % error in t_f and % error in t_t obtained for different swarm sizes are plotted in Fig.5 and Fig.6 respectively. The % error in t_f and t_t decreases with the increase in swarm size (see Fig.5 and Fig.6). It is observed that swarm size of 4 is good enough to get accurate result for this two-variable search-optimization problem. The average value of absolute % error in t_f and t_t obtained with swarm size of 4 in five search-runs are 0.05% and 0.05% respectively. The average values of R_s and R_d obtained in these five search-runs are 198 Ω and 2501 Ω respectively.

The results of GA depend on population size. The dependence of results on population size can be verified from the % error in t_f and % error in t_t plot shown in Fig.7 and Fig.8 respectively. From Fig.7 and Fig.8 it can be seen that GA requires larger population size to achieve a solution with better accuracy. But, with larger population size time taken by the algorithm will also increase. The % error in t_f and % error in t_t for five search-runs with population size of 50 are shown in Fig.9 and Fig.10 respectively. The average value of absolute % error in t_f and t_t obtained from five search-runs of GA with population size of 50 are 0.55% and 2.70% respectively. The average value of R_s and R_d obtained from these five search-runs are 194 Ω and 2575 Ω respectively.

Table 1 contain average and standard deviation of absolute percentage error in t_f and t_t for different search methods. To make the results comparable simplex search algorithm is run for 50 times, PSO with swarm size of 5 is run for 10 times and GA with population size of 10 is run for 5 times to compute average and standard deviation of absolute percentage errors in t_f and t_t.

CONCLUSIONS

- Simplex search algorithm results do not have good precision. Simplex search algorithm requires post processing of data using statistical tool such as 'Mode' to get desired values of R_s and R_d to achieve intended values of t_f and t_t.
- PSO requires minimum population size of 4 to get desired values of R_s and R_d to achieve intended values of t_f and t_t.
- GA requires larger population size to arrive at desired solution. With larger population size it will take more time to get the best values of R_s and R_d.
- Thus, out of the three search optimization methods used for this study, PSO performs better than the two other methods both in terms of accuracy as well as convergence time.

REFERENCES

[1] Devarajan M and Premi V (2015), "Simulation of characteristics of impulse voltage generator for testing of equipment using MATLAB Simulink", International Journal of Advances in Engineering, 1(2), 45 – 50.

[2] Ebehart R. and Kennedy J. (1995), "A New Optimizer Using Particle Swarm Theory", MHS'95. Proceedings of the Sixth International Symposium on Micro Machine and Human Science.

[3] Hassan R. et al. (2004), "A comparison of particle swarm optimization and the genetic algorithm", American Institute of Aeronautics and Astronautics.

[4] IS 2071-1 (1993), "High Voltage test techniques Part 1: General definitions and test requirements".

[5] Mitchel M. (1999), "An Introduction to Genetic Algorithms", MIT Press, Cambridge, Massachusetts, 5th printing.

[6] Naidu M S and Kamaraju V (1995), High Voltage Engineering, textbook published by Tata McGraw-Hill Publishing Company Limited, 2nd edition.

[7] Nair P. and Prof. Pachori A. (2013), "Design of impulse generators for different front and Tail Resistors in Impulse voltage testing of power transformers", International Journal of Enhanced Research in Science Technology & Engineering, ISSN: 2319-7463 Vol. 2 Issue 12.

[8] Pereira C. E. R. et al. (2008), "Simulating High Impulse Voltage Circuits for Testing Winding Type Equipment," 2008 International Conference on High Voltage Engineering and Application, Chongqing, pp. 351-354.

[9] Veisheipl K. (2016), "Simulation of the high voltage impulse generator," 17th International Scientific Conference on Electric Power Engineering (EPE), Prague, pp. 1-5.

[10] Wright Margaret H. (2012), "Nelder, Mead, and the other simplex method", Documenta Mathematica, Extra Volume ISMP 271–276.

Table 1 Average and standard deviation of absolute percentage errors in t_f and t_t for different search methods

Search Methods	Average of absolute % error in t_f	Average of absolute % error in t_t	Standard deviation of absolute % error in t_f	Standard deviation of absolute % error in t_t
Simplex Search	6.517	12.793	10.098	21.290
PSO	0.018	0.018	0.002	0.002
GA	20.472	20.200	17.517	23.055

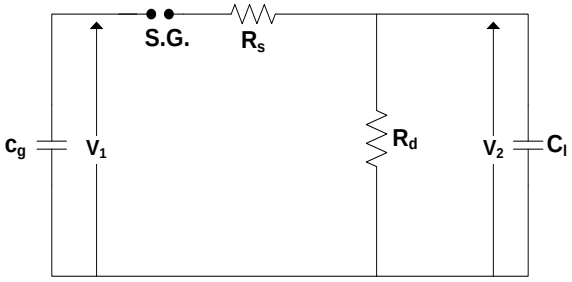

Fig.1 Single stage 'voltage impulse generator' circuit.

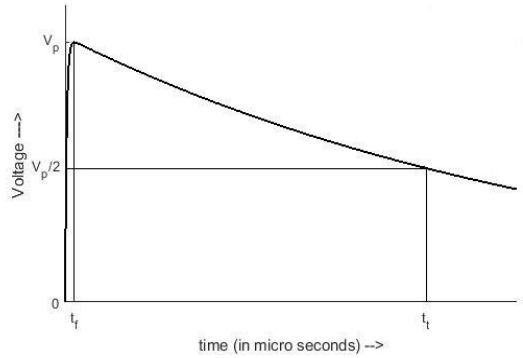

Fig.2 Typical voltage impulse waveform.

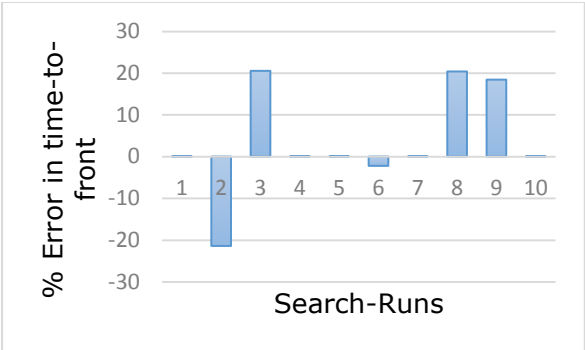

Fig.3 % Error in time-to-front (t_f) in ten-runs of simplex search algorithm.

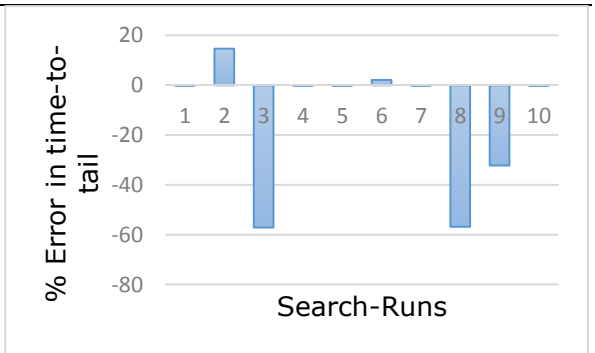

Fig.4 % Error in time-to-tail (t_t) in ten-runs of simplex search algorithm.

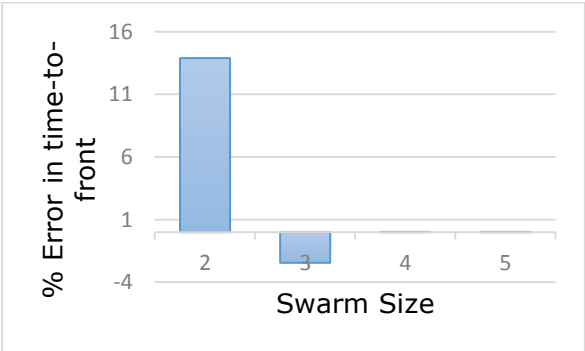

Fig.5 % Error in time-to-front (t_f) for different swarm sizes in PSO.

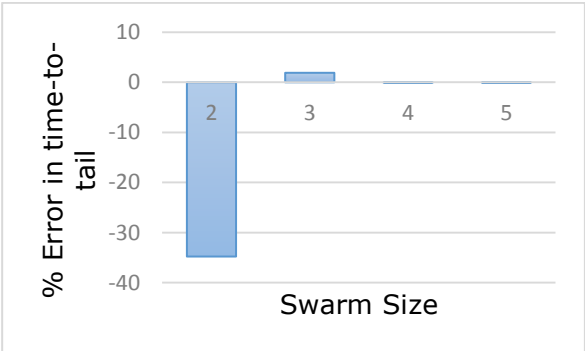

Fig.6 % Error in time-to-tail (t_t) for different swarm sizes in PSO.

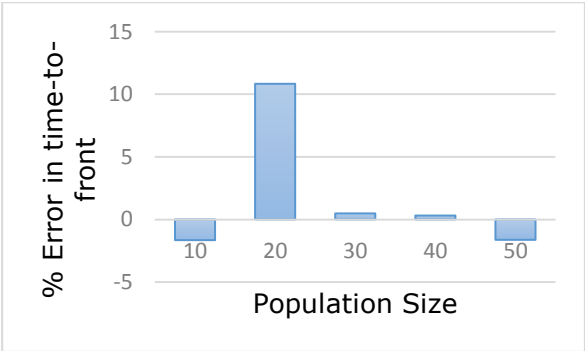

Fig.7 % Error in time-to-front (t_f) for different population sizes in GA.

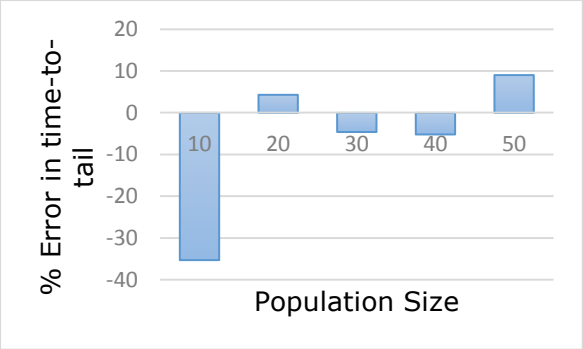

Fig.8 % Error in time-to-tail (t_t) for different population sizes in GA.

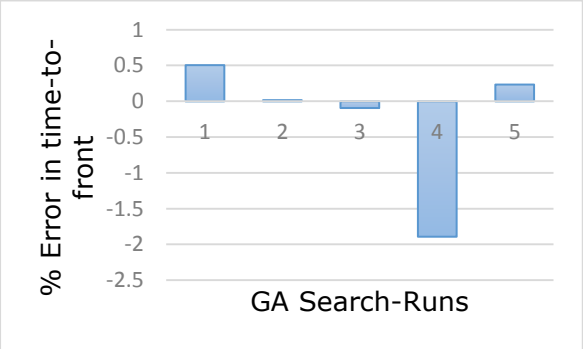

Fig.9 % Error in t_f for population size of 50 in five-runs of GA.

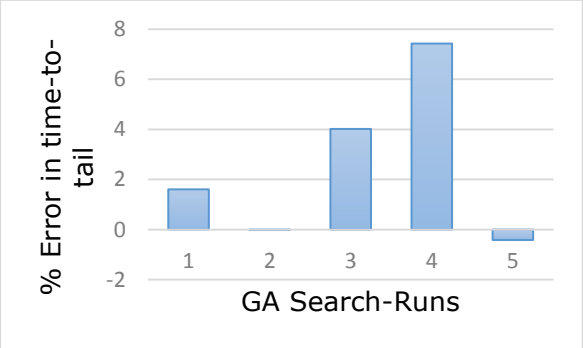

Fig.10 % Error in t_t for population size of 50 in five-runs of GA.

8th International Engineering Symposium - IES 2019
March 13-15, 2019, Kumamoto University, Japan

Detection of recognition during operation using electromyogram signals

Masato TSUCHIYA [1], Masahiro MIGITA [2], Masashi TODA[2]
Kazuaki KONDO [3], Junichi AKITA [4], Yuichi NAKAMURA [3]

1. *Graduate student, Department of Information and Electrical and Electronic Engineering, Kumamoto University, 2-39-1, Kurokami, Kumamoto 860-8555, Japan. email:tsuchiya@st.cs.kumamoto-u.ac.jp*
2. *{Assistant Professor,Professor}, Center for Management of Information Technologies , Kumamoto University, 2-39-1, Kurokami, Kumamoto 860-8555, Japan. e-mail:{migita,toda}@cc.kumamoto-u.ac.jp,*
3. *{Senior Lecturer,Professor} Academic Center for Computing and Media Studies, Kyoto University, Yoshida-honmachi, Sakyo-ku, Kyoto, 606-8501 Japan. email: {kondo,nakamura}@media.kyotou.ac.jp*
4. *Professor, Kanazawa University Graduate School, Kakuma-machi, Kanazawa-shi, Ishikawa, 920-1164 Japan. email: akita@is.t.kanazawa-u.ac.jp*

ABSTRACT: The surface electromyogram signal extracts not only the muscle activity amount but also various features such as the type of motion and its state. For that reason, even if the exercise is at first glance, it is thought that it is possible to distinguish between EMG signals if the circumstances of exercising and the environment are different. Therefore, this time, we used virtual objects and haptic devices to reproduce the seemingly different motion intention. Then, as a result of analysis using muscle activity, we could find features of the same exercise seemingly different in exercise intention. Specifically, it was judged from increase and decrease of each muscle activity degree of the active muscle and antagonist muscle for each virtual object.
***Keywords**:* surface electromyogram signal, Motion intention

1.INTRODUCTION

Biological signals are being studied in various fields due to their high applicability. One of the biomedical signals, the surface electromyogram signal, is also one of the notable interfaces. When a human performs exercise with walking or running, its original driving force is created by muscle contraction. By attaching electrodes on the skin of the surface electromyogram signal, electromyogram potential can be derived through the electrodes and expressed as an electromyogram, and it is possible to know how each of the muscles is active. Since the EMG signal is originally issued from the brain to the muscle, it is thought that it contains human thought information. In other words, even if they are doing the same exercise at the first glance, if the circumstances of the exercise and the circumstances differ, a difference is generated in electromyogram signals and it is considered to be distinguishable. Measurement of muscle activity in motion and response to an object requires reading of "prediction" that human performs during operation. Therefore, the purpose of this research is as follows.

・By seemingly similar operation,

investigate whether human intention of movement can be identified by electromyogram signal

2.Related Work

We introduce studies that estimate exercise intention other than electromyogram signals. The National Institute of Advanced Industrial Science and Technology and the National Center

for Scientific Research jointly work with Brain Computer Interface (BCI), which uses the prediction function of the brain to read exercise (motion intention) envisioned from EEG at high speed and high accuracy) Technology was devised. This technique uses the function of predicting the state of the body (exercise result) after the brain exercises when exercising. We give a stimulus to make the subject's brain an illusionary illusion, and read out deviations of the exercise result which is illusory from the exercise intention predicted from the exercise intention from the brain wave, and estimate the intention of the exercise from that gap [1]. Although high accuracy motion intention estimation has been confirmed in this research, there is a point that it can not make use of the development and measurement ease of the sensor for electromyogram signal as described above.

We introduce studies that estimate the intention of movement using electromyogram signals. Ota and colleagues conducted the following experiments to analyze the change in each electromyogram potential (muscle activity amount) when it was predictable and unpredictable. (Figure 1: Outline of the subject) The subject's task is to keep the basket in the same posture. The experiment organizer may or may not notify the subject when the weight falls. This is a study of two patterns whether it is predictable or impossible of isometric motion [2].

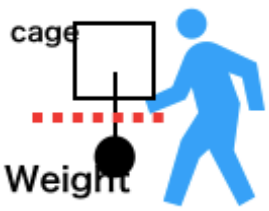

fig.1:Outline of the subject

3.Proposed Method

3.1.Role of muscle

Human beings can adjust delicate motion so as to adjust force adjustment according to the size and strength of the object to be grasped when grasping objects, but the reason why the muscles interact with each other It is because they are meeting each other and adjusting forces. Many of the human muscles exist in pairs, with the active muscle acting in the direction to bend the joint with the bone in between and the antagonistic muscle acting in the opposite direction. For example, when the elbow flexes as shown in Fig. 2, the biceps brachii muscle contracts as the active muscle and the triceps brachii muscle relaxes as the antagonist muscle. On the contrary, when the elbow is stretched as shown in Fig. 3, the triceps brachii muscle contracts as the active muscle and the triceps brachii muscle relaxes as the antagonist muscle. At this time, the antagonist muscle acts according to the speed and strength of the movement of the active muscle, so to speak, it is adjusting the movement of the active muscle. It is also known that there are some lines that support the work of the active muscles called collaborative muscles. In this way, human motion is compounded by each role played by each movement-related role. This is called cooperative movement of the muscle.

fig.2:Elbow flexion

fig.3:Elbow extension

3.2.Analytic method

Muscle activity was used for analysis. Muscle activity is expressed in the form of the sum of the electromyogram of the muscle group. In this research, if we give a simple and stable result, we perform this

conversion using the following equation (1) reported by Nakamura et al.

$$\dot{e} = \frac{u - e}{\tau_{ne}}$$
$$\dot{a} = \begin{cases} \frac{e-a}{\tau_{act}} & (e \geq a) \\ \frac{e-a}{\tau_{deac}} & (e < a) \end{cases} \quad (1)$$

- u ： Electromyogram value after pretreatment
- e ：Intermediate variable
- a ： Muscle activity
- τ_{ne}=40ms,τ_{act} =10ms,τ_{deac} =50ms：Time constant

FIG. 4 shows an example in which the rectified electromyogram signal is converted into the muscle activity degree. In addition, the rectification is to invert the negative waveform and make it a positive waveform.

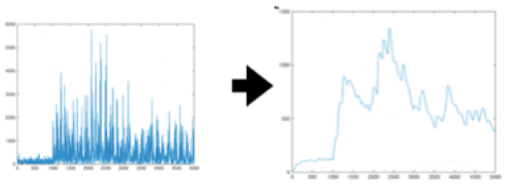

fig.4:Conversion of electromyogram signals to muscle activity

3.3.Using the machine

In this research we use a haptic device "Falcon". (Fig. 5) A haptic device is a device that can be operated by touching a virtual object on a PC. When a virtual object is touched on the screen, the reaction force set for that object is returned by the motor.

fig.5:Haptic device「Falcon」

3.4.Experimental method

The pose of the subject is sitting in front of the desk in the posture as shown in Fig. 6, and the operating part of the back of the hand and the haptic device Falcon of the dominant arm (both of the subjects this time) are fixed. (See FIG. 7) Also, in the open eye state, the examinee views the display of the PC placed in front of the subject. As a task of the subject, elbow extension operation is performed. This motion is easy to measure myoelectric signals because the operation itself is simple and uses the triceps brachii or the biceps brachii muscle etc. in the muscle group to use. In addition, in this case, the triceps brachii muscle strikes the muscle strike described in 3.1, and as the antagonist muscle becomes the biceps brachii muscle, it is a measuring muscle. Instructions such as the timing and speed of elbow extension operation will be described later. The overall view at the time of the experiment is shown in FIG.8.

fig.6:Subject’s pose

fig.7:Fix arm and operating part

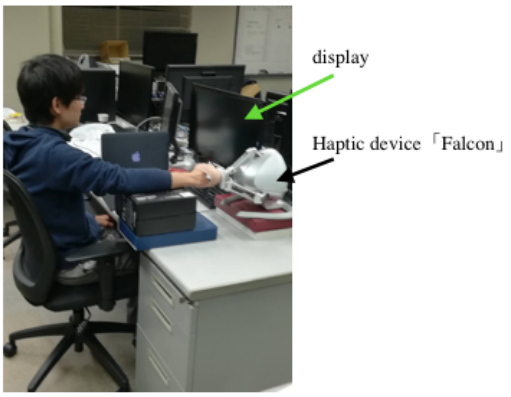

fig.8:Overall view at the time of experiment

Explain the task of the subject in detail. The subject is watching the pointer linked with the operation part of Falcon appearing together with the virtual object displayed on the PC display. The motion of the subject is to move the pointer synchronized with the motion of the right arm of the subject from left to right on the virtual object. At that time, the virtual object has various hardness (resistance). The speed of motion of the subject is specified by following the green object moving from the left to the right of the display. (This green object is referred to as a tracking index) This tracking index moves at a constant speed every time. An example of a display screen is shown in FIG. 9 below.

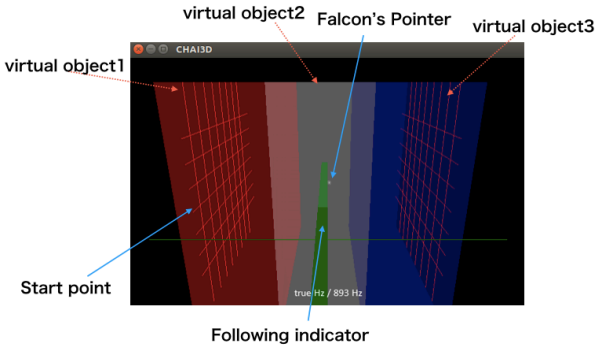

fig.9:An example of display screen

Signals to start the experiment are conveyed to the subject by voice. As tracking indicators start to move along with the signal to start the experiment, the subject elongates the elbow and operates so that the pointer of Falcon follows the following indicator. The sign of the end of the experiment was taken when the follow-up indicator ceased and it took one beat.

One trial was about 4 seconds, and recording was performed at a sampling frequency of 1000 Hz. After that, the measured electromyogram signals were observed, and trials that were considered to be contaminated with electrode contact or hum noise were removed in advance before analysis.

Setting a virtual object will be described. The virtual object created this time is a hard virtual object and a soft virtual object. Also, since it is possible to set colors freely for virtual objects, we created virtual object counts of hardness and color combination in the following three cases as shown in Fig.10. To explain each of the three cases,

Case 1: The boundary is clear, the hardness changes according to the boundary.

Case 2: Hardness changes at a boundary where the subject is unknown. (Grasp of subjects that hardness changes)

Case 3: The boundary is clear, but color and hardness do not match.

fig.10:Model diagram of three cases of virtual objects

3.Results

Experimental Results Indicates the result of discriminating the exercise intention to some extent. I will explain the view of the muscle activity degree diagram. Since the horizontal axis is time, since the sampling frequency is 1000 Hz this time, it is 1 second in horizontal memory 1000 memory. The vertical axis shows muscle activity.

The result of case 1 is as follows. (FIG. 11&FIG.12)

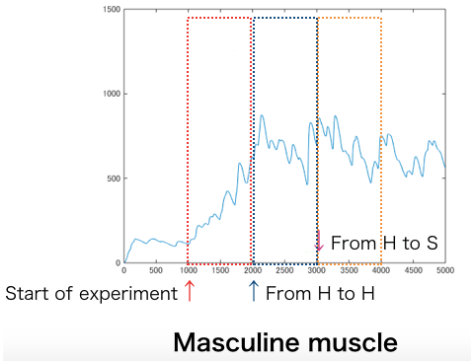

fig.11:Case 1 results(Masculine muscle)

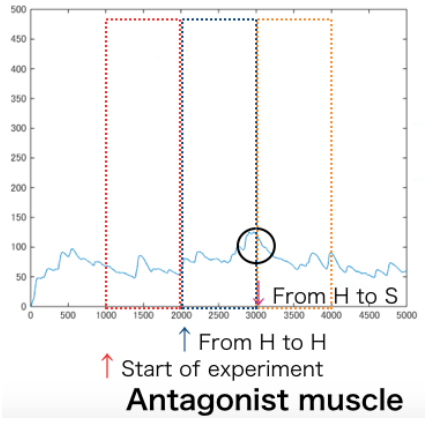

fig.12:Case 1 results(Antagonist muscle)

The result of case 2 is as follows. (FIG. 13&FIG.14)

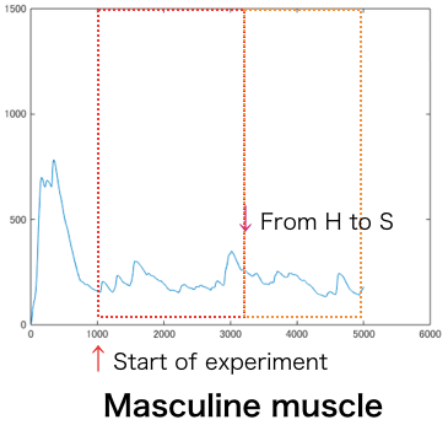

fig.13:Case 2 results(Masculine muscle)

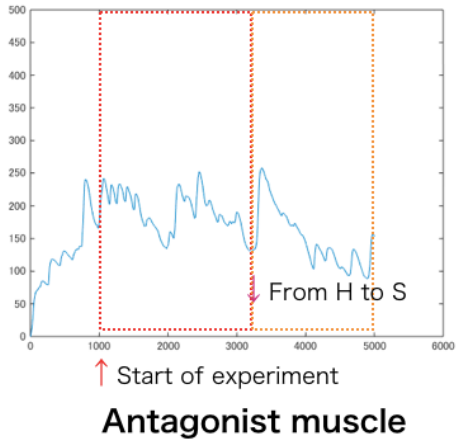

fig.14:Case 2 results(Antagonist muscle)

The result of case 3 is as follows. (FIG. 15&FIG.16)

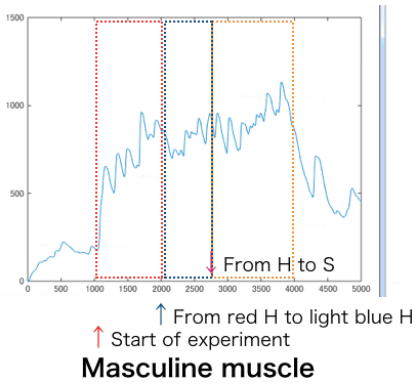

fig.15:Case 3 results(Masculine muscle)

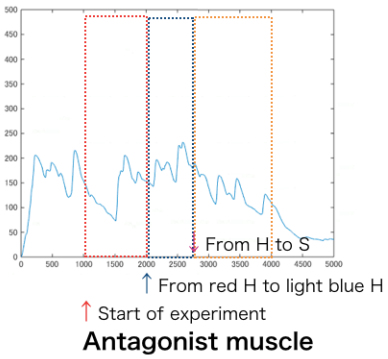

fig.16:Case 2 results(Antagonist muscle)

From the experimental results, we examine how to distinguish between different exercise intentions from the same operation at first glance. Therefore, the characteristic muscle activity change in each case 1, 2, and 3 is confirmed. In Case 1, the antagonist muscle relatively rises just before entering the soft part. In Case 2, the muscle activity of the active muscle when passing through the hard part is lower than in other cases. In Case 3, both the active and antagonistic muscles repetitively perform muscle activity so as to ripple. (It can be said that they have a big cooperative movement) From the above, it can be said that different motions of motion intention which are difficult to distinguish only by viewing angle because of the same operation can find each feature by using EMG signal, and can recognize motion intention.

4.At the end paper

In this research, we are trying to read and model reactions such as prediction when a human performs an action, from the muscle activity, to seek out the purpose, at the first glance, the same motions, whether human exercise intent can be identified by EMG signal I decided to investigate.

By making haptic devices and virtual objects, we conducted experiments by allowing subjects to perform different motions of different intention of motion even at the same seemingly different movements. For the analysis, we confirmed the characteristics at the time of operation by using muscle activity which is easy to understand for knowing muscle tension.

Document

1.Ganesh Gowrishankar , ”Utilizing sensory prediction errors for movement intention decoding: A new methodology” Science Advances 10.1126.

2.Megumi Ota "Effects of prediction on disturbance stimulation on muscle activity of trunk muscles"
Kyoto University Graduate School of Medicine Graduate School of Human Health Sciences Bulletin Health Sciences Vol.5 5 2008.

8th International Engineering Symposium - IES 2019
March 13-15, 2019, Kumamoto University, Japan

Extraction of stem and branch in three dimensional point group of Arabidopsis thaliana

Kentaro Inoue [1], Masahiro Migita [2], Takumi Higaki [3], Masashi Toda [4]

1 *Graduate student, Department of Computer Science and Electrical Engineering, Kumamoto University, Kurokami, 2-39-1, Kumamoto 860-8555, Japan. e-mail:k.inoue@kumamoto-u.ac.jp*
2 *Assistant Professor, Department of Instructional Systems, Kumamoto University, Kurokami, 2-39-1, Kumamoto 860-8555, Japan. e-mail:migita@cc.kumamoto-u.ac.jp*
3 *Associate Professor, International Research Organization for Advanced Science and Technology (IROAST), Kurokami, 2-39-1, Kumamoto 860-8555, Japan. e-mail:thigaki@kumamoto-u.ac.jp*
4 *Professor, Department of Instructional Systems, Kumamoto University, Kurokami, 2-39-1, Kumamoto 860-8555, Japan. e-mail:toda@cc.kumamoto-u.ac.jp*

ABSTRACT: In the research on environmental responses of plants, we will examine how plant hormones affect the growth of plants. Measurement of the plants has conventionally been done by researchers using rulers and protractors. It is cumbersome to measure all of the plants manually and it is a work that requires careful attention so that you do not hurt the plants because it contacts the plants at the time of measurement. In this study, as a preliminary step of acquiring information such as the length and angle of plant stems and branches from the three dimensional point cloud of Arabidopsis thaliana which is often used in research on plant environmental responses, we tried to extract point clouds that consist of the stem and branches.

***Keywords**: point cloud, plants, cylinder detection*

INTRODUCTION

Plants cannot move with their own will, and they have to spend entire life in the place they were born. For that reason, plants have the ability to sense and adapt the surrounding environment. On the ground, stem grow upward for the sun's light while the underground roots grow downward for moisture. In such way, the plant senses the upward and downward direction, and also catches the length of the day and night, and senses which season is now. The function of sensing growth and controlling growth by sensing such environment is called plant environmental response. Plant hormones are involved in environmental response reactions. As plant hormones produced in the body of this plant, auxin, gibberellin, cytokinin, ethylylene, jasmonic acid, abscisic acid, brassinosteroid, salicylic acid, peptide hormone, strigolactone and the like are known. Each works differently. In physiological phenomena of such plants, researches are being actively made to elucidate which protein or gene affects the environmental response. The results of such research are applied to herbicides, growth agents, aging of fruits, promotion of flowering, bulbs and seed dormancy breakdown and so on. Studies on environmental responses of these plants will examine how these plant hormones affect the growth of plants. In the measurements of plants, researchers use ruler for measuring length of stem and use a protractor for measuring angle of the branch. It is troublesome to conduct all the measurements of all the plants manually and it is a work that requires careful attention not to hurt the plants because we contact the plants at the time of measurement. In this research, as a

preliminary step of acquiring information such as the length and angle of plant stems and branches automatically and non-contactly from the 3-dimensional point cloud of the model plant Arabidopsis thaliana which is often used in research on environmental responses of plants, We tried to extract point clouds constituting branches and stems.

METHOD

This time we got a 3D point cloud by using tools from several pictures taken of Arabidopsis thaliana. We attempted to extract the point clouds that make up branches and stems by performing cylinder detection on point cloud that is aquired from tools.

Photographing

In this research, we photographed Arabidopsis thaliana and acquire 3D point clouds using OpenMVG [1,2,3,4,5], OpenMVS [6] which are tools for 3 dimensiona reconstruction. In order to obtain 3D point clouds, this tools need 2d images with what you want to reconstract 3d point clouds in them. So we photographed Arabidopsis thaliana. At the time of photographing, as shown in Fig.1 , photographs were taken from the entire circumference of the plant and the entire Arabidopsis thaliana was photographed. As for the photographing environment, Arabidopsis thaliana to photograph was placed on a round chair as shown in Fig.2 and photographed keeping the distance in the vicinity of the circumference of the round chair.

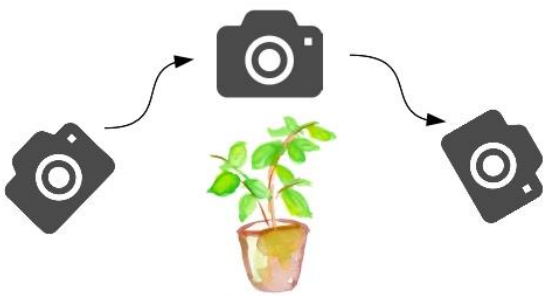

Fig.1 image of photographing

Fig.2 photographing environment

Cylinder Detection

The 3D point cloud reconstructed from the photograph is expressed as a collection of many points and noise is also generated, so it is difficult to grasp which point clouds constitute the stem or brach. Therefore, since the stems and branches have a shape close to a cylindrical shape, a point clouds constituting the stem or branches are extracted by fitting the cylindrical shape. In this research, we implemented cylinder detection using PointCloudLibrary(PCL)[7].

Result

The results of Arabidopsis thaliana reconstruction are shown in Figs.3 and 4. In this study, we focused on the branch part of stem and branch in each point group and verified whether we can acquire the point cloud composed of each part.

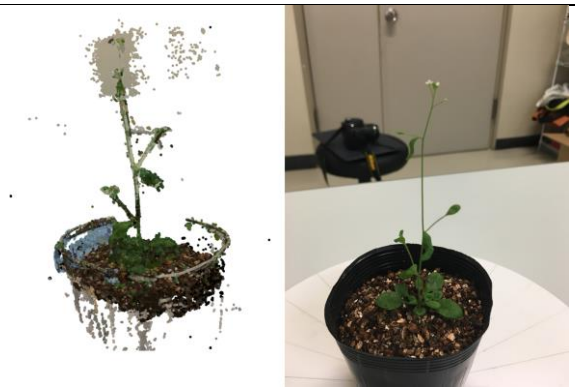

Fig.3 left:result of reconstraction, right: one of the images that was used to reconstruction

Fig.4 left:result of reconstraction, right: one of the images that was used to reconstruction

The results are shown in Fig5, 6. The figure on the right is the point group of interest, the left side is the cylinder detected by the cylinder detection, and the point group belonging to the cylinder.

Fig.5 left:result of cylinder detection, right: regeion of interest in this work from fig.3

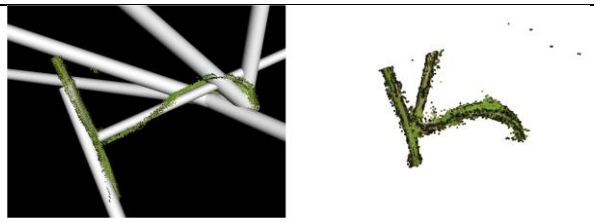

Fig.6 left:result of cylinder detection, right: region of interest in this work from fig.4

In Fig5, a point cloud constituting a branch and a stem can be extracted.
In Fig.6, unlike Fig.5 , a cylinder is detected in the stem and leaf part. It seems that the detection result was pulled out there because there are many point clouds that make up the part of the leaf.

CONCLUSIONS

In this study, we attempted to extract the point clouds that consist the stem and branch by detecting the cylinder in the three dimensional point clouds of Arabidopsis thaliana. In some cases it could be extracted as a result, but the point clouds constituting the leaf part were also detected as cylinders in some cases. Therefore it is necessary to consider a detection method that captures the features of individual parts.

REFERENCES

[1] OpenMVG
Website: https://github.com/openMVG/openMVG .
[2] Moulon Pierre, Monasse Pascal and Marlet Renaud, Adaptive Structure from Motion with a contrario model estimation, ACCV 2012.
[3] Moulon Pierre, Monasse Pascal and Marlet Renaud, Unordered feature tracking made fast and easy, CVMP 2012.
[4] Moisan Lionel, Moulon Pierre and Monasse Pasca, Automatic Homographic Registration of a Pair of Images, with A Contrario Elimination of Outliers, IPOL 2012.
[5] Moulon Pierre, Monasse Pascal and Marlet Renaud, Global Fusion of Relative Motions for Robust, Accurate and Scalable Structure from Motion, ICCV 2013.
[6] OpenMVS
Website: https://github.com/cdcseacave/openMVS .
[7] PointCloudLibrary(PCL)
Website: http://pointclouds.org/ .

8th International Engineering Symposium - IES 2019
March 13-15, 2019, Kumamoto University, Japan

TLP250 Optocoupler based interfacing circuit for FPGA based BLDC motor drive

Sachin[1], Harsheeta V[2], Pavana[3] and Vinatha U[4]

1 *Department of Electrical and Electronics Engineering, National Institute of Technology Karnataka, Surathkal, Mangalore 575025, India. Email :sachin051998@gmail.com*
2 *Department of Electrical and Electronics Engineering, National Institute of Technology Karnataka, Surathkal, Mangalore 575025, India. Email :harsheetamorey@gmail.com*
3 *Department of Electrical and Electronics Engineering, Institute of Technology Karnataka, Surathkal, Mangalore 575025, India. Email : prabhupavana1989@gmail.com*
4 *Department of Electrical and Electronics Engineering, National Institute of Technology Karnataka, Surathkal, Mangalore 575025, India. Email : u_vinatha@yahoo.co.in*

ABSTRACT: This paper presents the implementation of TLP250 optocoupler based interfacing circuit for FPGA based Brushless DC Motor (BLDC) drive. The switching signals generated from the 'Xilinx Basys 3' FPGA are fed to the Voltage Source Inverter (VSI). These signals are necessary to achieve the commutation process. The logic voltage levels of 'Basys 3' - FPGA I/O ports is 0 - 3.3 V. However, the input voltage requirement of SKYPER 32R, the inbuilt gate driver of SEMIKRON VSI, used in the BLDC drive setup is 15 V. This shifting of voltage level from 3.3V to 15V is done by using the 'optocoupler' based level shifting interfacing circuit, to provide the necessary switching pulses for the inverter switches. The optocoupler based interfacing circuit also provides the benefit of opto-isolation between the controller and converter, along with the shift in voltage level. This paper deals with the design and implementation of TLP250 optocoupler based level shifting circuit. The required simulation is carried out in 'Proteus Design Suite' simulation software to obtain the voltage level conversion using TLP250 Proteus model. The circuit is implemented on Printed Circuit Board (PCB) developed using Eagle PCB design tool, in order to avail its utilization in FPGA based BLDC motor drive.

***Keywords**:* Optocoupler, Opto-isolator, TLP250, Brushless Direct Current (BLDC) motor, Voltage Source Inverter (VSI), Field Programmable Gate Array (FPGA), Proteus, Eagle, Printed Circuit Board (PCB)

1. INTRODUCTION

Owing to high efficiency, high torque/inertia ratio, high energy density, low maintenance requirement and wide range of speed control; Brushless DC (BLDC) motors are becoming popular in many low and medium power applications. It is used in many household types of equipment like fans, air conditioners, water pumps, refrigerators, washing machines etc. It also finds application in many industrial tools, medical equipments, heating, ventilation and air conditioning, robotics and precise motion control systems. BLDC motor has a three phase distributed windings on the stator and permanent magnet in the rotor. Owing to electronic commutation, many problems associated with the mechanical commutator such as sparking, wear and tear of brushes and commutator assembly, noise problems, regular maintenance and

electromagnetic interference are eliminated [3].

1.1 ELECTRONIC COMMUTATION

BLDC motors are electronically commutated motors, powered by a DC electric source via an external motor controller. Unlike brushed motors, BLDC motors rely on external controllers to achieve commutation in which hall sensors are used for the rotor position sensing to derive the required commutation state using a voltage source inverter (VSI). Commutation is the process of switching the current in the motor phases to generate motion. Brushed motors have physical brushes to achieve this process twice per rotation, while BLDC motors do not, hence the name [7]. Due to the nature of their design, they can have any number of pole pairs for commutation.

1.2 VSI SWITCHING LOGIC

The rotor of a BLDC motor is influenced by the revolving stator poles, the stator pole position must be tracked in order to effectively drive the 3 motor phases. Hence, a motor controller is used to generate a 6-step commutation pattern on the 3 motor phases. These 6-steps, or commutation phases, move an electromagnetic field which causes the permanent magnets of the rotor to move the motor shaft.

The controller must always know the exact position of the stator in relation to the rotor to maintain accurate control of the motor [5]. The most common methods to achieve this feedback control is through Hall Effect sensors, encoders, or resolvers. Hall sensors are embedded into the stator of the motor to detect rotor position, which is used to switch the IGBTs in the 3-phase bridge to drive the motor. Output signals from the Hall Effect sensor is an indication of rotor position and is used to generate the switching logic for inverter in order to have proper commutation of the motor.

The encoder is used to track position, rotation, speed, and direction with far greater accuracy [2].

1.3 FPGA AS A CONTROLLER

FPGA (Field Programmable Gate Array) is a digital controller used to monitor the feedback circuit and produce the switching logic according to the rotor positions [8]. FPGAs allow designing parallel architectures, based only on the specific needs of the targeted algorithm, which can considerably reduce the execution time and, as a consequence, ensure a quasi-analog treatment. Furthermore, their reprogrammability ensures a good controller flexibility.

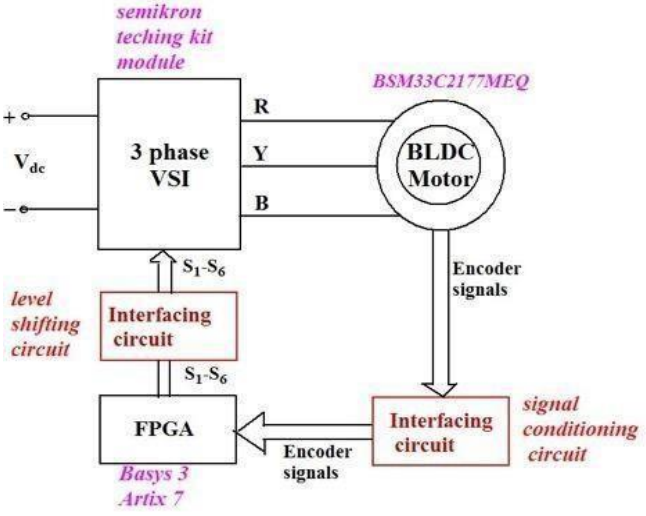

Fig.1 Overview diagram of the BLDC motor drive

2. INTERFACING CIRCUIT FOR FPGA BASED BLDC MOTOR DRIVE

The block diagram of FPGA based BLDC motor drive is shown in Fig.1. The voltage difference problem between FPGA and VSI can be solved by various methods. Usage of op- amps is the simplest solution. This circuit design has certain limitations. It increases the complexity of the circuit. This leads to design a simpler circuit by means of optocouplers. There are various kinds of optocouplers. MCT2E, 6N136 are some examples. TLP250H is used in the design of interfacing circuit as it offers some advantages over other optocouplers like: low propagation delay and less time in switching on the transistor, which justifies its presence in circuit.

2.1 OPTOCOUPLERS

Optocoupler is an electronic component that interconnects two separate electrical circuits by means of a light sensitive optical interface.

Optocoupler, also known as an **Opto-isolator**, consists of an **LED** that produces Infrared light and a semiconductor photosensitive device that is used to detect the emitted infrared beam. Both the LED and the photo-sensitive devices are enclosed in a light-tight body or package with metal legs for the electrical connections. Optocouplers are of four types photo-transistor, photo-resistor, photo-SCR, or a photo-TRIAC.

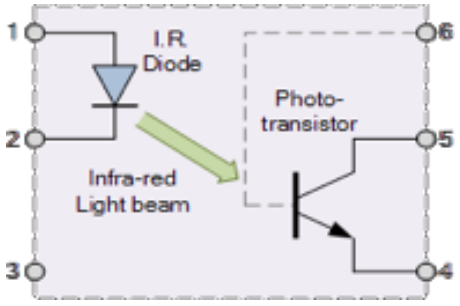

Fig.2 Photo-transistor Optocoupler

The main advantage of optocouplers is their high electrical isolation between the input and output terminal. Control circuits are well protected due to electrical isolation.

2.1.1 TLP250H

The TLP250H is a photo-coupler (photo transistor – refer Fig. 2) in a **DIP** 8 package that consists of a GaAℓAs infrared light-emitting diode (LED) optically coupled to an integrated high-gain, high-speed photo detector IC chips. It has a totem-pole output that can both sink and source current. This IC is ideal for IGBT and power MOSFET gate drive.

Current from the source signal passes through the input (refer Fig.2) LED which emits an infrared light whose intensity is proportional to the electrical signal. The electrical signal being transmitted can be either analog (linear) or digital (pulses).

This emitted light falls upon the base of the photo-transistor, causing it to switch-ON and conduct in a similar way to a normal bipolar transistor.

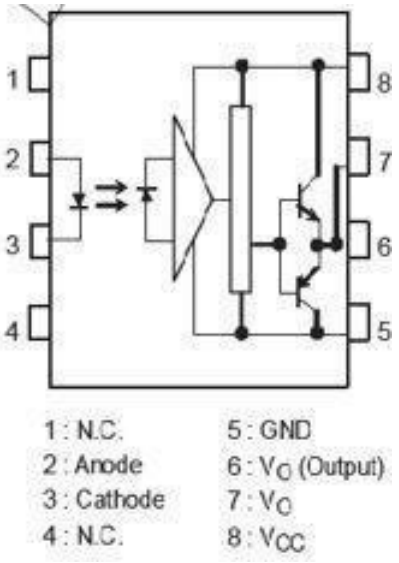

Fig.3 Pin diagram of TLP250H

The base connection of the photo - transistor can be left open (unconnected) for maximum sensitivity to the LEDs infrared light energy or connected to ground via a suitable external high value resistor to control the switching sensitivity making it more stable and resistant to false triggering by external electrical noise or voltage transients. When the current flowing through the LED is interrupted, the Infra-Red emitted light is cut-off, causing the photo-transistor to cease conducting. The photo-transistor can be used to switch current in the output circuit.

3. DESIGN AND IMPLEMENTATION OF TLP250 INTERFACING CIRCUIT

PWMIN is the input drive signal that dictates the output state (referring to Fig.4) which is referenced to the ground (DGND). The TLP250 ground (GND) i.e. VCC is referenced to the power ground and this ground is isolated from the DGND. This clearly illustrates the

isolation in IGBT drive, as the driving signal is isolated from the load supply.

When PWMIN = 1, IGBT is driven from the supply voltage (V_{CC}) – the gate is pulled up to V_{CC} level [1]. IGBT turns on and current flows through the load. Here, V_{cc} is 15V.

Failure to provide this capacitor may impair the switching property. The capacitor should be placed as close to the TLP250 as possible.

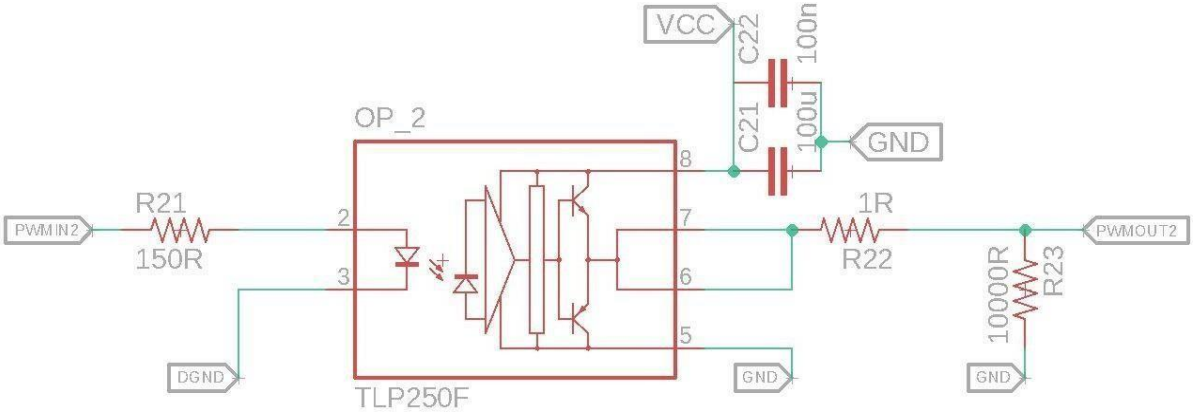

Fig.4 Block diagram of the interfacing circuit using TLP250 H optocoupler

When PWMIN = 0, IGBT is driven low – the gate is pulled down to its source level. IGBT turns off and the load is off.

3.1 DESIGN

The forward current for the LED is taken to be 10mA. The TLP250 is being driven from a Basys 3 FPGA and the amplitude for the signal is 3.3 V. The forward voltage for the LED would typically be between 1.6 V and 1.8V.

So, V = (3.3 – 1.8) V = 1.5V

V = IR.

R = V/I = 1.5V/ (0.01A) = 150 Ω.

R_2 is the gate resistor. R_2 is 1 Ω.

R_3 is the 'gate to source' high value resistor which prevents the current overflow in the circuit. There's no theoretical significance to it. It prevents accidental turn on of the IGBT by external noise usually at startup when the gate is floating. A gate to source resistor acts as a pull-down to ensure a low level for the IGBT. C_1 is the decoupling capacitor (ceramic capacitor) should be connected between V+ (pin 8) and V- (pin 5). This capacitor stabilizes the operation of the high gain linear amplifier in the TLP250H.

3.2 IMPLEMENTATION

Fig.5 shows the required interfacing circuit designed in the Proteus Design Suite.

In the proteus application, a new layout is selected and the circuit is designed. The input given is 3.3 V. Since the V_{CC} is 15 V, the expected output is a wave of amplitude 15 V. The results are obtained from the oscilloscope, as shown in Fig. 6.

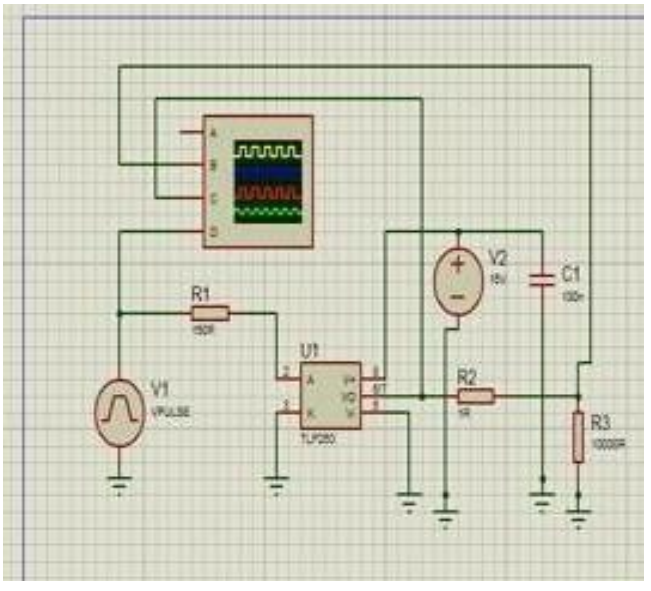

Fig. 5 Interfacing circuit designed in Proteus tool.

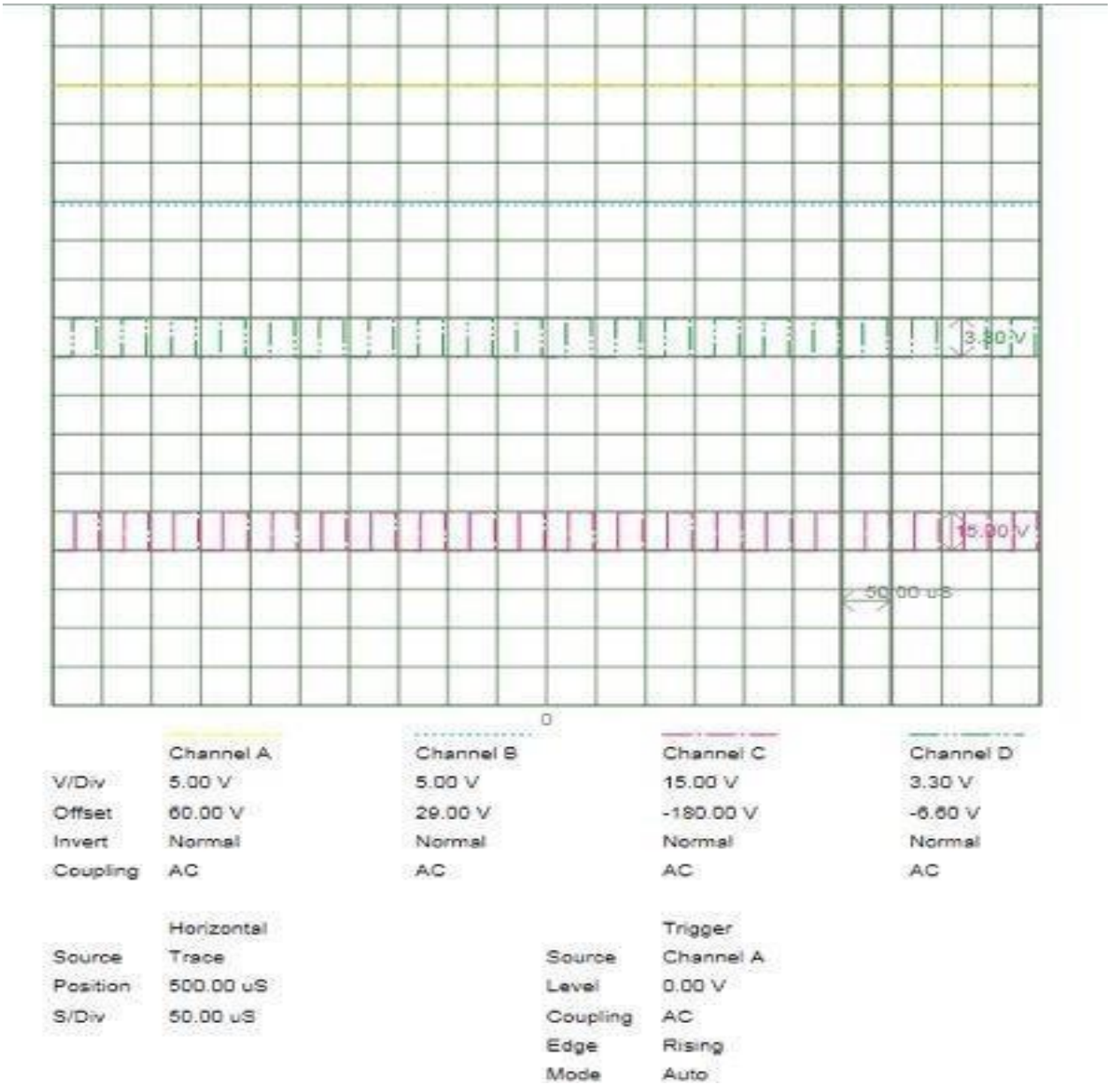

Fig. 6 Graph obtained from the simulation of Proteus file.

3.3 PCB DESIGN USING EAGLE

PCB design in EAGLE is a two- step process. First the schematic is drawn, and then, the PCB is laid out based on the designed schematic.

After installing the Eagle software, a new project has to be created. In this project, the layout contains 6 interfacing circuits.

The designed PCB contains the 6 interfacing circuits, each of them, similar to Fig.4 in a double layer PCB Board. The verified circuit is then converted to Gerber files, and is then sent to the manufacturer for fabrication.

4. RESULT AND DISCUSSION

Fig.6 contains the graph obtained by simulating the proteus model. In the figure, channel D (green curve), channel C (pink curve) indicate the input and output waveforms respectively. The figure clearly shows that the designed circuit could level shift the waveform in phase with the input.

Fig.7 shows a picture of the PCB, designed in eagle with six interfacing circuits in it. The designed PCB could level shift the input from 3.3 V to 15 V. The simulation results are verified.

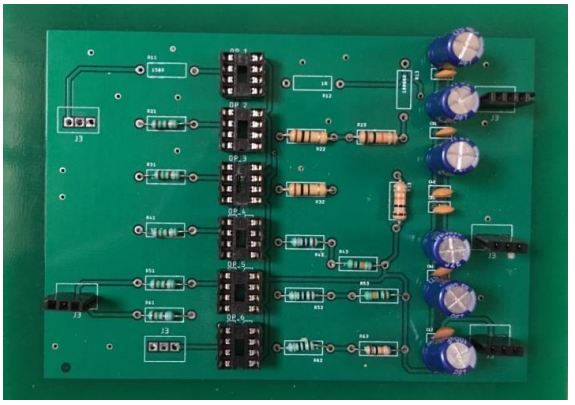

Fig. 7 Picture of the designed PCB

5. CONCLUSION

This work reports an optocoupler based interfacing circuit for an FPGA based BLDC motor drive. Optocouplers are the good choice for an interfacing circuit, when optical isolation is required, and when the input and output levels are different.

From the analysis of the optocouplers, TLP250H was found to be a simple and neat electronic device in interfacing between the FPGA and Skyper32R driver IC.

Electronic design tools such as Proteus suite find their significance in testing a newly designed circuit. Eagle software can be used to design a new PCB. Eagle software provides ease in designing PCB. The results show that the design of TLP250 optocoupler based interfacing circuit performs the level shifting operation effectively.

6. ACKNOWLEDGEMENT

It is our privilege to acknowledge the assistance rendered to us by our mentors of NITK who helped us to complete our project successfully. We are grateful to:

Dr. Prof. B. Venkatesa Perumal,
H.O.D. (EEE Dept.)

Dr. Prof. Mrs. Vinatha,
Assistant Prof. (EEE Dept.)

At last, we would like to thank our family for their constant support and warm blessings.

7. REFERENCES

[1] A. A. Mamun , M. F. Elahi, Design and Implementation of Single Phase Inverter, International Journal of Science and Research (IJSR), India Online ISSN: 2319-7064

[2] Anand Sathyan, Nikola Milivojevic, Young-Joo Lee, Mahesh Krishnamurthy, An FPGA-Based Novel Digital PWM Control Scheme for BLDC Motor Drives, IEEE TRANSACTIONS ON INDUSTRIAL ELECTRONICS, VOL. 56, NO. 8, AUGUST 2009

[3] BIDYUT MAHATO, P.R.THAKURA, Hardware Design and Implementation of Unity Power Factor Rectifiers using Microcontrollers, 978-1-4799-6046-0/14/$31.00 ©2014 IEEE

[4] Blog: Tahmid (2013), Microcontroller and Power Electronics. Website:http://tahmidmc.blogspot.com/2013/05/using-tlp250-for-isolated-mosfet-gate.html

[5]Bo-Chiau Chen, Implementation of Maximum-Power-Point-Tracker for Photovoltaic Arrays, 978-1-4244-8756-1/11/$26.00 c 2011 IEEE

[6]Jason Kelly (2017), Electromechanical Design Engineer, CUI Inc. Website:https://googleweblight.com/i?u=https:// www.digikey.in/en/articles/techzone/2017/feb/what-is-the-most-effective-way-to-commutate-a-bldc-motor&hl=en-IN

[7]Jianwen Shao, Dennis Nolan, and Thomas Hopkins, A Novel Direct Back EMF Detection for Sensorless Brushless DC (BLDC) Motor Drives, 0-7803-7404-5/02/$17.00 (c) 2002 IEEE

[8]Jianwen Shao, Dennis Nolan, Maxime Teissier, A Novel Microcontroller-Based Sensorless Brushless DC (BLDC) Motor Drive for Automotive Fuel Pumps, IEEE TRANSACTIONS ON INDUSTRY APPLICATIONS, VOL. 39, NO. 6, NOVEMBER/DECEMBER 2003

[9]R. Krishnan (2010),*Electrical and Computer Engineering Department Virginia Tech Blacksburg, Virginia, U.S.A., Permanent Magnet Synchronous and Brushless DC Motor Drives*

[10] Padmaraja Yedamale Microchip Technology Inc., Brushless DC (BLDC) Motor Fundamentals, AN885

8th International Engineering Symposium - IES 2019
March 13-15, 2019, Kumamoto University, Japan

SPEED CONTROL OF BLDC MOTOR USING PULSE AMPLITUDE MODULATION TECHNIQUE

Harsheeta V[1], Sachin[2], Pavana[3] and Vinatha U[4]

1 *Department of Electrical and Electronics Engineering, National Institute of Technology Karnataka, Surathkal, Mangalore 575025, India. Email: harsheetamorey@gmail.com*
2 *Department of Electrical and Electronics Engineering, National Institute of Technology Karnataka, Surathkal, Mangalore 575025, India. Email : sachin051998@gmail.com*
3 *Department of Electrical and Electronics Engineering, Institute of Technology Karnataka, Surathkal, Mangalore 575025, India. Email : prabhupavana1989@gmail.com*
4 *Department of Electrical and Electronics Engineering, National Institute of Technology Karnataka, Surathkal, Mangalore 575025, India. Email : u_vinatha@yahoo.co.in*

ABSTRACT: This paper presents the speed control of the BLDC motor using Pulse Amplitude Modulation (PAM) technique. PAM technique can be realised by controlling the DC link voltage of the Voltage Source Inverter (VSI), feeding the BLDC motor. This facilitates the operation of VSI at fundamental frequency and avoids the high frequency switching losses in the VSI. The fundamental frequency switching pulses are generated based on the rotor position signals. The commutation logic of rotor position to switching signals is designed using K-Map technique. Xilinx System Generator (XSG) model based design tool for FPGA is used to model the commutation logic in MATLAB/Simulink environment. The BLDC motor drive fed by the three-phase VSI is implemented in MATLAB/Simulink. Co-simulation with commutation logic modelled using XSG blocksets and the VSI fed BLDC motor modelled using Simulink blocksets is carried out and the speed control of BLDC motor using PAM control technique is evaluated.

Keywords*: Brushless Direct Current motor (BLDC), Voltage Source Inverter (VSI), Pulse Amplitude Modulation (PAM), Direct Current (DC), Field Programmable Gate Array (FPGA), Xilinx System Generator (XSG).*

1. INTRODUCTION

An adjustable speed motor drive can often provide smoother operation compared to a fixed speed mode of operation. They are used in applications in which there are mechanical equipment's powered by motors. These drives provide electrical motor control, so that the motor speeds can be varied precisely, and maintained at the required speed. Several advantages of the adjustable speed motor drive includes controlled starting current, reduced powerline disturbances, controlled acceleration adjustable operating speed, adjustable torque limit, energy savings etc.

Permanent magnet brushless DC motor drives is one such drive. Permanent magnet motors with trapezoidal back EMF have several advantages over the other motor types. They have higher power density that makes them ideal for high torque to weight ratio applications. BLDC motor is becoming popular in various applications because of its higher efficiency, higher power factor, higher torque, simple control and lower maintenance. They are more efficient due to the permanent magnets, which results in zero rotor losses. The absence of commutators and brushes offer several advantages.

Brushless DC motors are electronically commutated motors powered by a DC electric source via an external motor controller. They are widely used in many applications such as motors, sensors,

actuators etc. The only disadvantage of permanent magnet Brushless DC motors is their higher cost and relatively higher complexity due to the power electronic converters, which is used to drive them.

The speed of a BLDC motor can be controlled by either PWM (Pulse Width Modulation) or PAM (Pulse Amplitude Modulation) techniques. The speed control of BLDC motor using PWM control of VSI requires motor current sensors for closed loop control, and has high switching losses. In PAM control of VSI, the speed is controlled by controlling the input DC link voltage of VSI, which eliminates the need for motor current sensors and hence reduces switching losses and the speed performance of the motor is improved using PAM control [5]. This shows that the PAM control is more efficient than the PWM control, and the speed performance of the motor is also improved using PAM control Technique [1].

Microcontrollers have typically been used in motor control applications. For fast and reliable control of PAM signal, Field Programmable Gate Array (FPGA) based speed controller is designed for the operation of the BLDC motor drive. Implementation using FPGA results in better performance as well as cost reduction and can easily control the motor and the switching conditions as well. FPGA is chosen over all other microcontrollers due to its most important feature known as 'Parallel Processing', it can be reprogrammed over and over again for different tasks, making them cost efficient by avoiding recurring expenditure. It also produces large task in less clock cycles [2].

The Xilinx System Generator (XSG) provides complete motor control solutions for electric drives that leverage the benefits with Programmable Logic in FPGA.

2. BLDC Motor Drives with PAM Control

In PAM control, 120-degree commutation control is used in general and the DC-link voltage is adjusted according to the error between speed and its reference. It varies the amplitude of the pulses (DC Link Voltage) at a single side (Input of the Inverter) [4]. Fig.1 shows the block diagram of Voltage Source Inverter (VSI) controlled BLDC motor drive with PAM control. The controller used in this work is FPGA.

The drive consists of an IGBT based voltage source inverter, controller (FPGA), and the hall signals obtained from the drive itself. The voltage source inverter is used to feed the BLDC motor and the exact position of rotor at every instant is obtained with the help of hall sensors mounted on stator. From the hall signals, the switching logic is determined to provide triggering pulses to the inverter switches, using which the speed can be controlled accordingly.

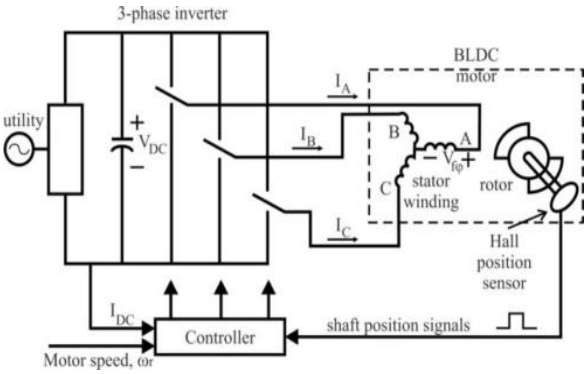

Fig.1 Study of BLDC Motor with PAM control

2.1 Electronic Commutation(EC) (Trapezoidal commutation) Design using K-map

Three phase VSI (acting as electronic commutator) is supplied with switching signals based on the rotor positions.

The switching logic of the VSI is generated using HALL sensing signals as shown in Table 1. The three hall sensors H_a, H_b, H_c are required to detect the position of the rotor, which are mounted at 120 degree intervals on the stator. The ON and OFF conditions of the IGBT switches are indicated by '1' and '0' respectively.

H_a, H_b, H_c represents the HALL sensing signals of phase a, b and c respectively.

S_1, S_2, S_3, S_4, S_5, and S6 represents the IGBT switches. V_{an}, V_{bn} and V_{cn} are the phase voltages across the phase a, b, c, respectively of the BLDC motor with respect to a point n (neutral).

The output voltage of the inverter of Phase 'a', with respect to the potential at point 'n' is given as,

$$V_{an} = V_{dc}/2 \text{ for } S_1 = 1 \quad (1)$$
$$V_{an} = -V_{dc}/2 \text{ for } S_1 = 0 \quad (2)$$
$$V_{an} = 0 \quad \text{for } S_1, S_2 = 0 \quad (3)$$

The voltage values of the other two phases of the VSI feeding BLDC motors (i.e.) V_{bn} and V_{cn}, and the switching pattern of the other IGBT switches(S_3,S_4,S_5,S_6), can be generated in a similar way as can be seen in Table 1.

The commutation logic is obtained by using K-Map technique shown in Table 2, which shows the commutation logic of switches S_1, S_3 and S_5. The switches S_2, S_4, S_6 follow complementary logic of S_1, S_3, S_5 respectively, as follows;

$$S_1 = H_a \, H_b' \quad (4)$$
$$S_2 = H_a' \, H_b \quad (5)$$
$$S_3 = H_b \, H_c' \quad (6)$$
$$S_4 = H_b' \, H_c \quad (7)$$
$$S_5 = H_a' \, H_c \quad (8)$$
$$S_6 = H_a \, H_c' \quad (9)$$

Rotor Position	Hall Sensor H_a	H_b	H_c	Phase	S_1	S_2	S_3	S_4	S_5	S_6
0-60	1	0	1	+ab	1	0	0	1	0	0
60-120	1	0	0	-bc	1	0	0	0	0	1
120-180	1	1	0	+ca	0	0	1	0	0	1
180-240	0	1	0	-ab	0	1	1	0	0	0
240-300	0	1	1	+bc	0	1	0	0	1	0
300-360	0	0	1	-ca	0	0	0	1	1	0

Table 1 Phase voltages and their corresponding switching states based on Hall Effect position sensor signal

H_aH_b \ H_c	0	1
00	0	0
01	0	0
11	0	0
10	1	1

$S_1 = H_aH_b'$

H_aH_b \ H_c	0	1
00	0	0
01	1	0
11	1	0
10	0	0

$S_3 = H_bH_c'$

H_aH_b \ H_c	0	1
00	0	1
01	0	1
11	0	0
10	0	0

$S_5 = H_a'H_c$

Table 2 Switching logic generation from Hall signals

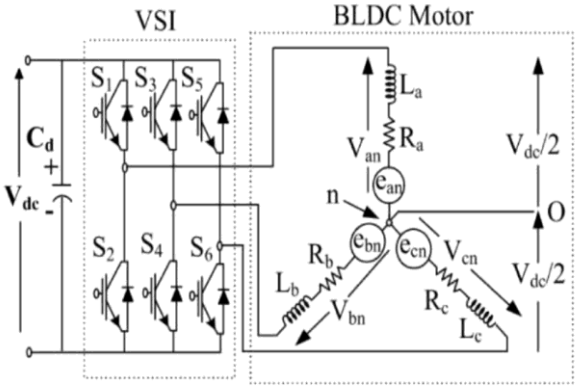

Fig.2 VSI fed BLDC Motor

3. Electronic commutation implementation using Xilinx System Generator(XSG)

Artix7, Basys 3 FPGA by Xilinx manufacturers is chosen for implementing

the control system of the proposed PAM-BLDC drive. This work uses System Generator from Xilinx, that enables the use of model-based Simulink design environment for FPGA Design.

The Simulink model of the BLDC Motor drive is as shown in Fig.3 and consists of the following blocks.

(a) The main power circuit : DC voltage source
(b) The motor : Brushless DC motor of power rating 375W
(c) Electronic commutator : Inverter consisting of driver Skyper32R Semikron device
(d) Measurements : Torque, Speed, Back EMF

The IGBT switches (SKYPER32 circuit) are used for the realization of current commutation of BLDC motors.

Specifications of the motor is given as shown in Table 3 [1].

No of phases	3
Waveform type	Trapezoidal
Voltage constant	78.0005 V/krpm
Torque constant	0.74485 N-m
No of pole pairs	4 pairs
Inertia	0.422e-3
Resistance(Ph-Ph)	14.56 ohm
Inductance(Ph-Ph)	13e-6 H

Table 3 BLDC motor specifications

The Simulink model of the BLDC motor drive is as shown in Fig.3. The Subsystem is designed using the Xilinx block sets as shown in Fig.4, using the equations derived [3].

4. Results and Discussions

The simulation results of the BLDC motor Performance can be evaluated under various input parameters in MATLAB/Simulink environment.

4.1 VSI fed BLDC motor model using Simulink block sets

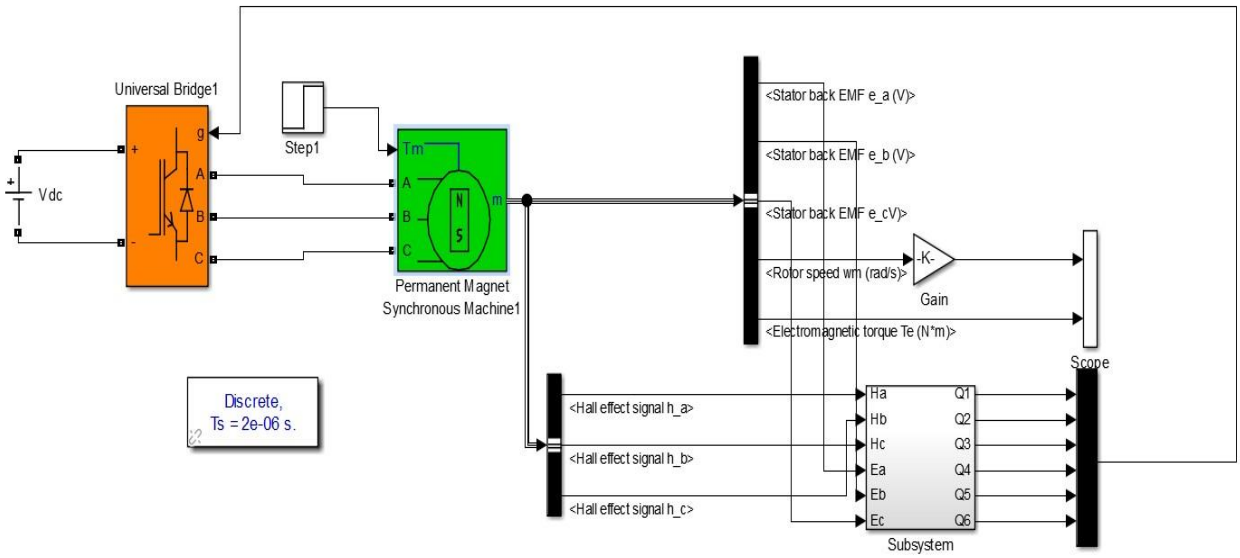

Fig.3 Xilinx System Generator (XSG)

The Load (Torque(Tm)) is varied at a given DC link voltage (for two cases; 320V and 160V) and the respective speed is obtained.

Simulink model

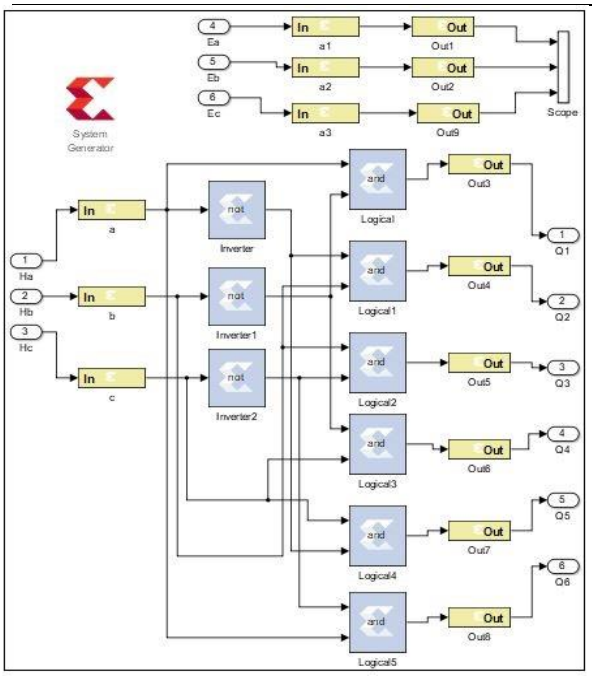

Fig.4 Subsystem of the Motor designed using XSG block sets

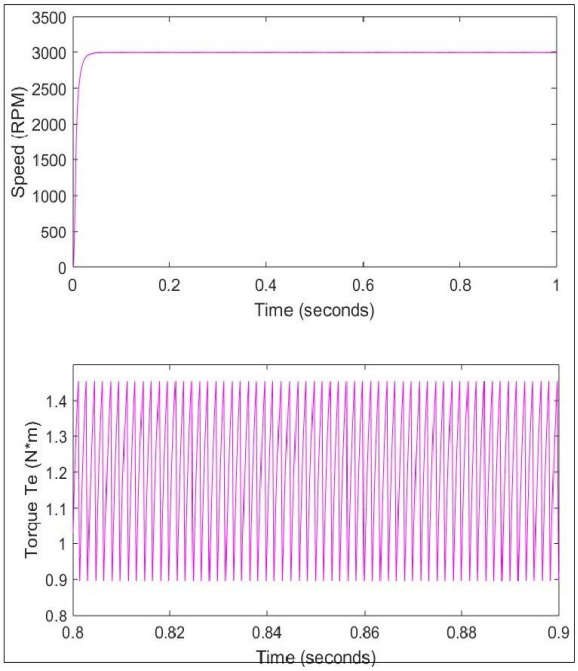

Fig.6 Speed (subplot 1), Torque (subplot 2)

Referring to Fig.5, at a constant load, the speed is higher for an input voltage of 320 V. This is the nature of output that can be predicted from the PAM control method.

The power of any motor can be expressed as

$$P = \tau * \omega \quad (10)$$

Where P is power in Watts, τ is torque in Nm and ω is angular velocity in RPM.

For the rated power, the rated speed of 3000 RPM is obtained at rated load of 1.2 Nm.

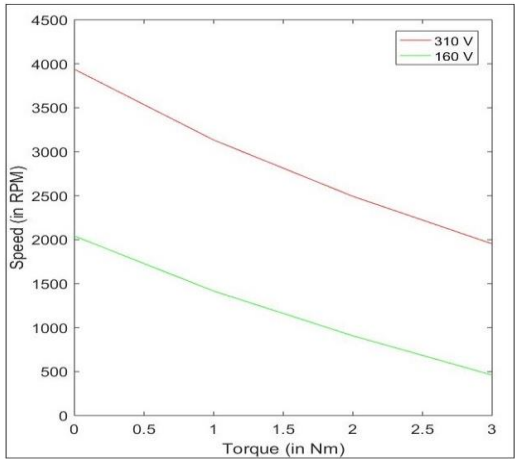

Fig.5 Torque-Speed characteristic for160V, 320V

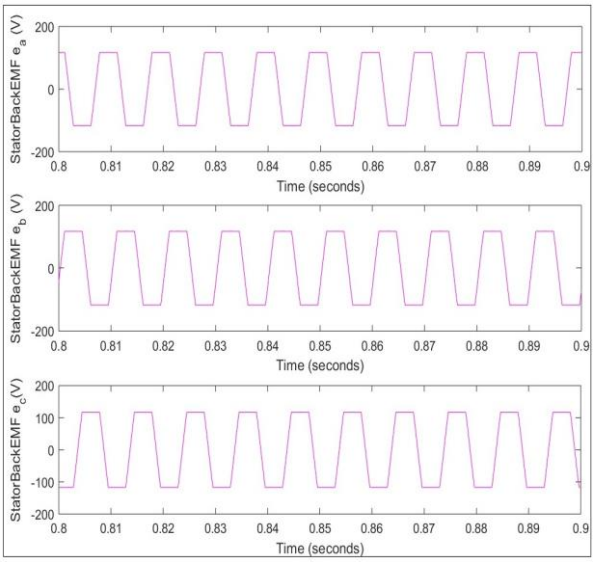

Fig.7 Motor generated Back EMF

The torque ripples generated in Fig.6 is due to the nature of commutation strategy used and is significantly low at high speed.

Fig.7 shows the back EMF pattern of the BLDC motor. The output is a trapezoidal waveform, which is because of the 'six step commutation method', adopted in the design for commutation.

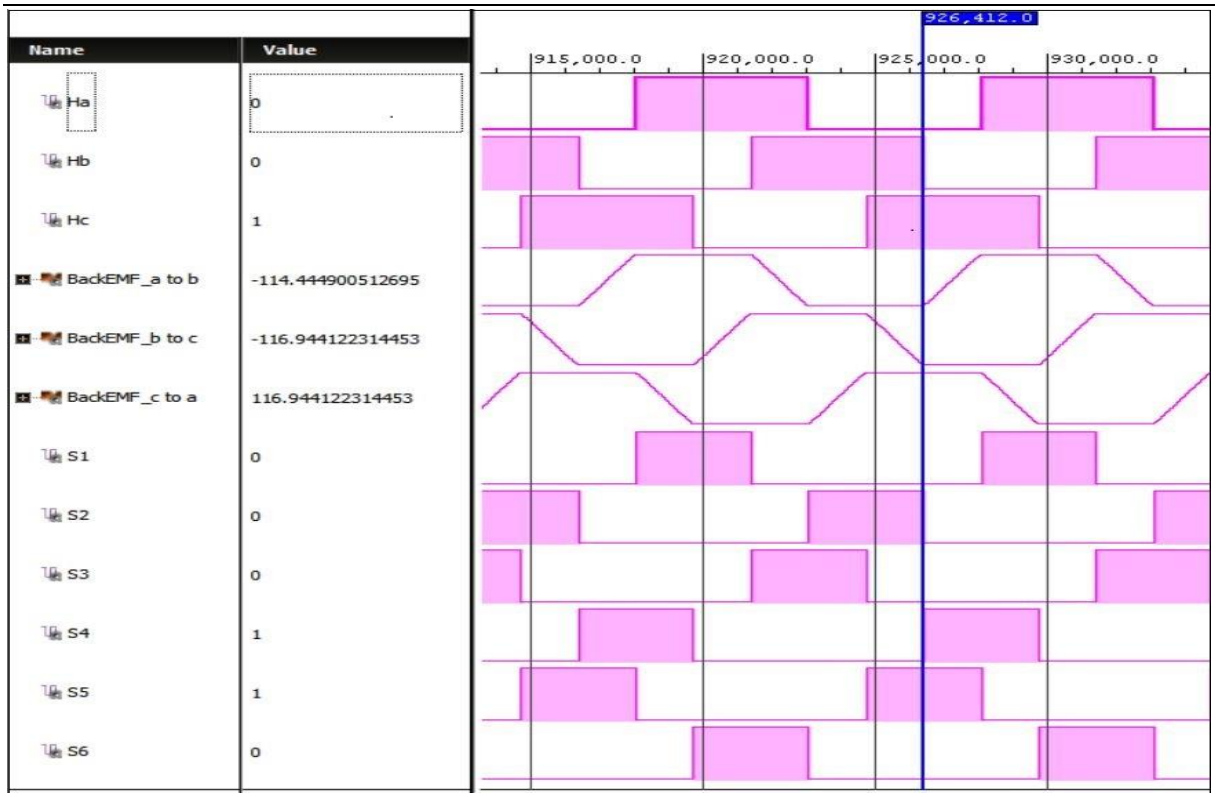

Fig.8 Back EMF profile with respect to rotor sensor signals (60° to 360°)

4.2 Co-simulation with commutation logic modelled using XSG block sets

Fig.8 contains the rotor position signals with respect to the Back EMF profile. The switching logic obtained with respect to Hall sensors using Xilinx System Generator can also be viewed on Xilinx waveform viewer as shown in Fig.8.

5. Conclusion

In this work, the speed control of the BLDC motor drive is realised by PAM control technique. The PAM technique is realised by controlling the DC link voltage of the Voltage Source Inverter (VSI), feeding the BLDC motor. From the analysis, it is seen that the Xilinx System Generator (XSG) model based design tool for FPGA is used to model the commutation logic in MATLAB/Simulink environment. The results suggest that, at a constant load (Torque), the angular velocity of a motor is higher for higher DC source voltage. The trapezoidal commutation generates torque ripples at low speeds and hence is relatively efficient in the high speed range. The results show that the torque ripple produced in PAM approach of speed is of low frequency. It avoids high frequency switching ripples present in PWM approach. The PAM method works more efficiently than PWM by minimising torque ripple.

6. References

[1] A Chenjun Cui, Gang Liu, and Kun Wang (2015), Novel Drive Method for High-Speed Brushless DC Motor Operating in a Wide Range.

[2] B Santhosh Kumar and S. Arockia Edwin Xavier (2015), Brushless dc motor speed control using microcontroller.

[3] Byoung-Kuk Lee and Mehrdad Ehsani (2013), Advanced Simulation Model for Brushless DC Motor Drives, Electric Power Component And Systems, 31:841 – 868.

[4] Dr. T. Vamsee kiran, I.L.B.Sowjanya (2016), Speed Performance of a BLDC Motor Employing PWM/PAM Control Techniques, IJAIEM Volume 5, Issue 5.

[5] P Pillay and R Krishnan (1989), Modelling, simulation, and analysis of permanent Magnet motor drives. IEEE Transactions on Industry Applications.

8th International Engineering Symposium - IES 2019
March 13-15, 2019, Kumamoto University, Japan

Sensorless speed and position estimation of PMSM using improved sliding mode observer and Phase Lock Loop based technique

Kshitiz Khatri [1], A Karthikeyan [2] and **Prabhakaran KK[3]**

1 *Department of Electrical and Electronics Engineering, National Institute of Technology Karnataka, Surathkal, Mangalore 575025, India. email:kshitizkhatri97@gmail.com*
2 *Department of Electrical and Electronics Engineering, National Institute of Technology Karnataka, Surathkal, Mangalore 575025, India. email:jakarthik@nitk.edu.in*
3 *Department of Electrical and Electronics Engineering, National Institute of Technology Karnataka, Surathkal, Mangalore 575025, India. email:k7prabhakaran@gmail.com*

ABSTRACT: The Sliding Mode Observer (SMO) is a non-linear estimation technique that is well known to be robust against variations in parameters and noise that persist over a control system. In conventional SMO to eliminate the chattering phenomenon a low pass filter is needed which introduces a delay in the system. Hence phase compensators are required to eliminate the delay thereby adding extra components to the system. This paper presents an improved sliding mode observer technique for sensor less speed estimation of Permanent magnet synchronous motor (PMSM). The improved SMO incorporates phase locked loop based technique to overcome the aforementioned problems associated with conventional SMO. The simulation studies are carried out through MATLAB/SIMULINK to verify the efficacy of the system.

***Keywords**: Sliding mode observer, Permanent magnet synchronous motor, Phase Lock Loop*

NOMENCLATURE

i_α, i_β	Currents in stationary reference frame
V_α, V_β	Voltages in stationary reference frame
e_α, e_β	Back EMF's in stationary reference frame
R_s	Stator resistance
L_s	Synchronous inductance
ψ_e	EMF constant
ω_e	Rotor electrical speed
θ_e	Rotor position angle

1 INTRODUCTION

In past three decades permanent-magnet synchronous motor (PMSM) drives have been used widely in Industrial Automation, Robotics and cutting edge Aerospace technologies and also in various domestic appliances, like Air-conditioners, Washing machines, Dishwashers etc. The Permanent Magnet Synchronous Motor possesses a blend of characteristics of both an Induction motor (IM) and a Brushless DC Motor (BLDC motor) [5]. The PMSM has a permanent magnet rotor and windings on the stator, akin to the BLDC motor. However, the windings of the stator structure setup a sinusoidal flux density in the air - gap, resembling that of an Induction motor (IM). With same ratings, a PMSM has a higher power density as compared to an Induction motor (IM). This is due to the fact that in a PMSM no part of the stator power is used for magnetic field production. The factors that make PMSM more preferable over Induction motors are it's (i) Brushless construction, (ii) High power density, (iii) High torque-to-inertia ratio, (iv) High Efficiency & (v) High Dynamic performance. With the advancements in technology, the PMSM has become more powerful and small and less dense, leading to the use of the PMSM

in high - efficiency and high - performance motor drive applications.

To attain the field-oriented control of PMSM drive, accurate knowledge of rotor position is needed, speed encoder is required for closed loop operation of any motor drive (Usually optical type sensors are used for IM but for PMSM absolute encoders, resolvers & hall effect sensors are used). An incremental shaft mounted speed encoder is required for close loop speed control. But the presence of such sensors increases the cost and size of the overall drive system and also reduces its reliability and control robustness. Furthermore, it is difficult to install and maintain a position sensor (mechanical shafts) due to the limited assembly space and rigid working environment with severe vibration, humidity and/or high temperature.

Therefore, various position-sensor less [10] control schemes have been developed for the estimation of rotor position and speed. The sensor less rotor speed and position estimation can be classified as follows :- The Fundamental Excitation method & The Saliency and Signal Injection method, the Fundamental Excitation method can be further classified into :- Open and Closed loop estimators, The Closed loop estimation is then further divided into :- State observer based methods and MRAS (Model Reference Adaptive system) method, finally the State observer methods are classified as :- Kalman filter method [3,4], Stator flux based observer method [9] and Sliding mode observer method [1].

Since the state observers of MRAS are usually built on fourth-order permanent magnet synchronous motor (PMSM) models, the convergences of both speed and position estimation method are difficult to achieve under the varying speed/torque conditions

Statur flux based observer methods, fail to work properly at standstill or low speed regions, since it requires the knowledge of machine parameters for estimating speed and position which are affected by noise, error and delay at lower speeds. Though sliding mode observer and extended Kalman filter methods work properly at standstill and low speed conditions they still have their own drawbacks, Kalman filter needs a careful choice of initial value of noise covariance matrices for it to work properly and also the computational complexity involved is very high.

Among different observation methods used, the sliding mode observer (SMO) is an effective technique due to its outstanding robustness properties against motor parameter uncertainties and external torque disturbances, hence a new improved SMO technique is proposed. However, the use of the SMO bring about a small issue that has to be dealt with, the Chattering phenomenon [7]. The discrete switching control brings about the chattering phenomenon. The effect of the chattering phenomenon can only be subdued but not nullified within the boundary of the selected surface. Using a LPF we can reduce the chattering problem, but LPF produces a delay in the circuit, hence an extra compensator is also required to omit delay problem, which makes circuit very complex.

To solve this problem, in proposed technique the traditional on-off function (signum function) is replaced by a Sigmoid function with PLL, in order to weaken the chattering problem and increase the estimation accuracy of rotor position. Further the PLL is used to calculate the rotor position after the back-EMF is estimated from the SMO.

2 PMSM MODELLING

The modelling of the PMSM [2] in stationary reference frame can be done with the use of following equations:-

Current equations can be given by

$$\frac{di_\alpha}{dt} = -\frac{R_s i_\alpha}{L_s} - \frac{e_\alpha}{L_s} + \frac{V_\alpha}{L_s} \quad (1)$$

$$\frac{di_\beta}{dt} = -\frac{R_s i_\beta}{L_s} - \frac{e_\beta}{L_s} + \frac{V_\beta}{L_s} \quad (2)$$

Back-EMF can be represented as

$$e_\alpha = -\psi_m \omega_e \sin\theta_e \quad (3)$$

$$e_\beta = -\psi_m \omega_e \cos\theta_e \quad (4)$$

$$\frac{de_\alpha}{dt} = -\omega_e e_\beta \quad (5)$$

$$\frac{de_\beta}{dt} = \omega_e e_\alpha \quad (6)$$

Flux is produced from stator which acts as a large effective air gap, for the PMSM's with high energy magnets in it's rotor. Because of the these, Inductance of machines get reduced, and since they are heavy, the rotor inertia is also high, the combined effect increases the difference between Mechanical and Electrical time constants, therefore it is moderate to assume that motor mechanical speed changes slowly i.e. ($\dot{\omega}_e \approx 0$).

The voltage V_α, V_β and currents $\hat{i}_\alpha, \hat{i}_\beta$ are the known quantities. Main objective of the paper is to estimate the back EMF's with the proposed Sliding mode observer (SMO) method, using available means of measurement.

3 CONVENTIONAL SMO

In Sliding Mode Observer [8] method the sliding-mode control is used and system structure is changed dynamically to restrict the state variables to be on the sliding surface. The sliding mode control comes under discrete control category where the dynamics of the system are changed by applying a very high frequency switching function. Since it is robust against various system parameter variations it is being widely used for nonlinear system control. This technique is called SMO because the sliding mode controller is adopted for use in the observer design for controlling PMSM in sensor less fashion. The back-EMF is gauged using SMO in stationary frame using current adaptive method. The sliding surface is taken as error between actual and estimated currents; hence the back-EMF is estimated. The state variables converges near the sliding surface in two phases, 'reaching phase' and 'sliding phase' as shown in Fig. 1. During reaching phase, the estimated state variable and the actual state variable approach each other and during sliding phase the estimated state variable converges the actual state variable. In the conventional SMO technique the currents are estimated using machine modelling equations, and then the estimated currents are compared with the actual currents to estimate the back EMF, the block model diagram of the conventional SMO is represented in Fig.2.

4 PROPOSED SMO DESIGN

The architecture of the proposed SMO technique is shown in Fig. 3 which includes a sliding mode current observer, a sigmoid function followed by a PLL [6], for rotor position and speed estimation. In this the command voltages are V_α *and* V_β, input to the sigmoid function is the difference of actual measured current and estimated current i.e. $\hat{i}_\alpha, \hat{i}_\beta$

Output is the rotor position (flux angle) $\hat{\theta}_e$ calculated from the generated back-EMF.
From equations (1) & (2) we know the current equations,
Further the SMO is applied to estimate the currents and formulation is as follows:-

$$\frac{d\hat{i}_\alpha}{dt} = -\frac{R_s i_\alpha}{L_s} - \frac{kH(\hat{i}_\alpha - i_\alpha)}{L_s} + \frac{V_\alpha}{L_s} \quad (7)$$

$$\frac{d\hat{i}_\beta}{dt} = -\frac{R_s i_\beta}{L_s} - \frac{kH(\hat{i}_\beta - i_\beta)}{L_s} + \frac{V_\beta}{L_s} \quad (8)$$

Where $\hat{i}_\alpha, \hat{i}_\beta$ are the estimated voltages in α, β axis, V_α, V_β are the command voltages, k is the gain and $H(x)$ is the sigmoid function which is defined as follows

$$H(x) = \left[\frac{2}{(1+e^{-2\mu x})}\right] - 1 = \frac{1-e^{-2\mu x}}{1+e^{-2\mu x}} \quad (9)$$

where μ is the shape parameter.

On subtracting (1) & (2) with (7) & (8) respectively, the dynamic equation for the estimated current is as follows

$$\frac{d\bar{i}_\alpha}{dt} = -\frac{R_s \bar{i}_\alpha}{L_s} - \frac{kH(\bar{i}_\alpha)}{L_s} + \frac{V_\alpha}{L_s} \quad (10)$$

$$\frac{d\bar{i}_\beta}{dt} = -\frac{R_s \bar{i}_\beta}{L_s} - \frac{kH(\bar{i}_\beta)}{L_s} + \frac{V_\beta}{L_s} \quad (11)$$

And the error in current is defined as

$$\bar{i}_\alpha = (\hat{i}_\alpha - i_\alpha) \quad (12)$$

$$\bar{i}_\beta = (\hat{i}_\beta - i_\beta) \quad (13)$$

Now stability equations of PMSM are used to calculate the rotor angle properly, which are as follows

$$\bar{i}_\alpha \times \frac{d}{dt}\bar{i}_\alpha < 0 \quad (14)$$

$$\bar{i}_\beta \times \frac{d}{dt}\bar{i}_\beta < 0 \quad (15)$$

on substituting (10)&(11) it is obtained that

$$\bar{i}_\alpha \times \frac{d}{dt}\bar{i}_\alpha = (\bar{i}_\alpha \times (e_\alpha - kH(\bar{i}_\alpha)) - R_s \bar{i}_\alpha{}^2)/L_s \quad (16)$$

$$\bar{i}_\beta \times \frac{d}{dt}\bar{i}_\beta = (\bar{i}_\beta \times (e_\beta - kH(\bar{i}_\beta)) - R_s \bar{i}_\beta{}^2)/L_s \quad (17)$$

Further, let

$$e_\alpha = kH(\hat{i}_\alpha - i_\alpha) = kH(\bar{i}_\alpha) = -\omega_e \psi_m \sin\theta_e \quad (18)$$

$$e_\beta = kH(\hat{i}_\beta - i_\beta) = kH(\bar{i}_\beta) = \omega_e \psi_m \cos\theta_e \quad (19)$$

Equations (16) & (17) can satisfy the PMSM stability equations {(14) & (15)} as we know,

$$-\bar{i}_\alpha{}^2 < 0 \quad (20)$$

$$-\bar{i}_\beta{}^2 < 0 \quad (21)$$

Therefore on substituting (18) & (19) in equations (10) and (11) respectively the solution is obtained as follows

$\frac{d}{dt}\bar{i}_\alpha = 0, \bar{i}_\alpha = 0, \frac{d}{dt}\bar{i}_\beta = 0$ and $\bar{i}_\beta = 0$, in the steady state condition

Once the back-EMF $(\hat{e}_\alpha, \hat{e}_\beta)$ are estimated, the PLL is used to calculate the estimate the rotor position as shown in Fig. 3,

Multiply e_α with $\cos(\hat{\theta})$ and e_β with $\sin(\hat{\theta})$ and subtract them to find the error function ε as,

$$\varepsilon = -\hat{e}_\alpha \cos(\hat{\theta}_e) - \hat{e}_\beta \sin(\hat{\theta}_e) \quad (22)$$

To estimate the rotor position, the error should be controlled to zero. Therefore set the parameters of PI controller (k_p & k_i) accordingly such that;

$$\hat{\omega}_r = k_p \varepsilon + k_i \int \varepsilon dt \quad (23)$$

Finally the rotor position can be obtained as;

$$\hat{\theta}_r = \int \hat{\omega}_r \, dt \quad (24)$$

5 RESULTS

The proposed improved SMO with PLL based technique for PMSM drives is simulated in MATLAB/SIMULINK environment. Simulation results of ramp type rotor speed reference with speed reference gradually varied between 0 to 180 rad/s, 180 to -180 rad/s, -180 to 180 rad/s and 180 to 0 rad/s as shown in Fig. 4. It is observed from Fig. 4(a) that the reference and measured rotor speed are matching with respect to each other similarly Fig. 4(b) depicts measured and estimated speed tracks each other simultaneously. From Fig. 4(c) it can be inferred that position tracking is achieved accurately. Fig. 4(d) & Fig. 4(e) shows that speed and position error pertains only during starting, and gradually reaches to zero. The obtained results are efficient.

6 CONCLUSIONS

In this paper an improved Sliding mode observer with Phase locked loop based technique for sensor less speed estimation of Permanent magnet synchronous motor (PMSM) is presented.

The proposed method reduces the chattering problem occurred with conventional SMO and also excludes the use of extra external phase compensators. The system is simulated using MATLAB/SIMULINK and the results proves the high accuracy of estimation and as well assures excellent dynamic performance of the system.

REFERENCES

[1] Danyang Bao, Yi Wang, Xuewei Pan, Xinshuo Wang and Ke Li," Improved Sensorless Control Method Combining SMO and MRAS for Surface PMSM Drives", 2017.

[2] Faa-Jeng Lin and Ying-Chih Hung, "Sensorless IPMSM Drive System Using Saliency Back-EMF-Based Intelligent Torque Observer with MTPA Control", IEEE TRANSACTIONS ON INDUSTRIAL INFORMATICS, VOL. 10, NO. 2, MAY 2014.

[3] Gao Tian, Yang Yan, Wang Jun, Zhou Yu Ru & Zhao Xiao Peng, "Rotor Position Estimation of Sensorless PMSM Based on Extented Kalman Filter",2018 IEEE international conference on Mechatronics, Automation and Robotics.

[4] Kaustubh Shedbalkar, A.P. Dhamangaonkar & A.B. Patil, "Speed Estimation using Extended Kalman Filter for PMSM", International Conference on Emerging Trends in Electrical Engineering and Energy Management (ICETEEEM-2012).

[5] S.Sakunthala, Dr. R.Kiranmayi & Dr. P.Nagaraju Mandadi, "A Study on Industrial Motor Drives Comparison and Applications of PMSM and BLDC Motor Drives", International Conference on Energy, Communication, Data Analytics and Soft Computing (ICECDS-2017).

[6] Sourabh Paitandi & Mainak Sengupta," Design and implementation of sensorless vector control of surface mounted PMSM using back-emf estimation and PLL based technique", 2017 National Power

Electronics Conference (NPEC) College of Engineering Pune, India. Dec 18-20, 2017.
[7] Vasilios C. Ilioudis," Chattering Reduction Based on Equivalent Control Gain Depended Method for PMSM Speed Estimation", IEEE 2015.
[8] Vasilios C. Ilioudis and Nikolaos I. Margaris," PMSM Sensorless Speed Estimation Based on Sliding Mode Observers", IEEE 2008.
[9] Yongsoon Park & Seung-Ki Sul," Sensorless Control Method for PMSM Based on Frequency-Adaptive Disturbance Observer", IEEE JOURNAL OF EMERGING AND SELECTED TOPICS IN POWER ELECTRONICS, VOL. 2, NO. 2, JUNE 2014.
[10] Omer Cihan Kivanc and Salih Baris Ozturk, "Sensorless PMSM Drive Based on Stator Feedforward Voltage Estimation Improved With MRAS Multiparameter Estimation", IEEE/ASME TRANSACTIONS ON MECHATRONICS, VOL. 23, NO. 3, JUNE 2018

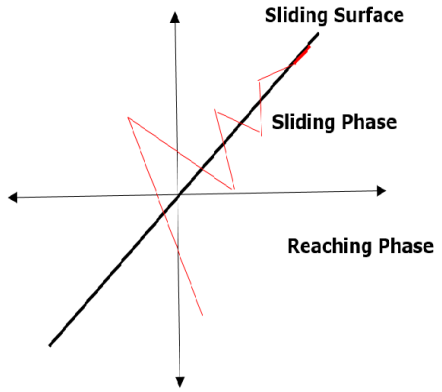

Fig. 1 Reaching and Sliding phase of state variables

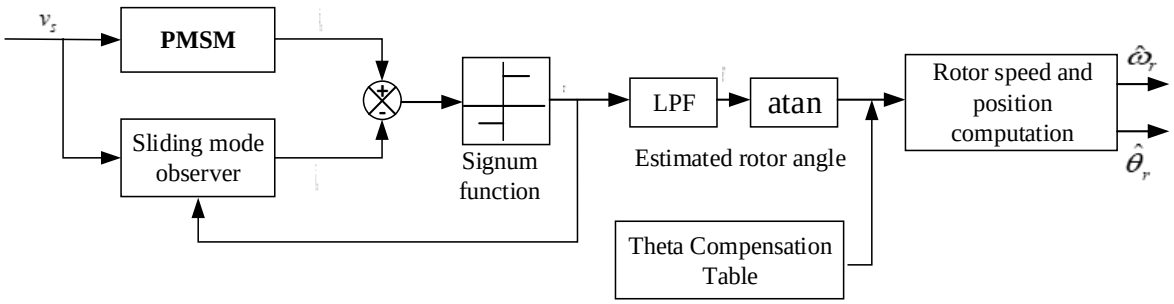

Fig. 2 Block diagram of a conventional SMO

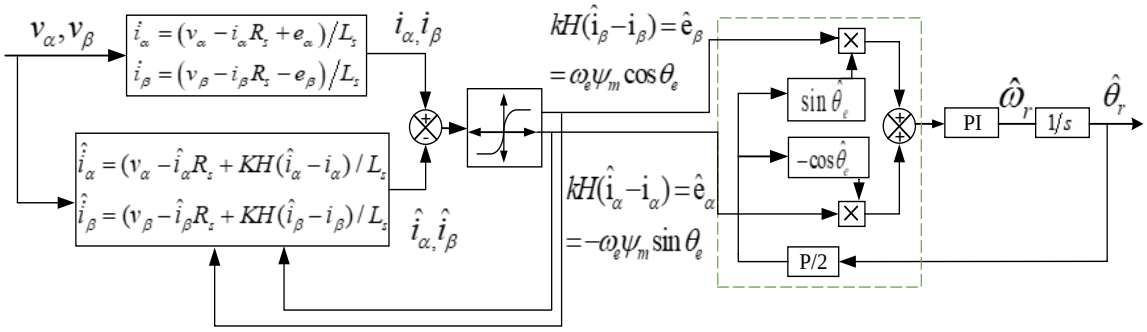

Fig. 3 Block diagram of proposed improved SMO with PLL

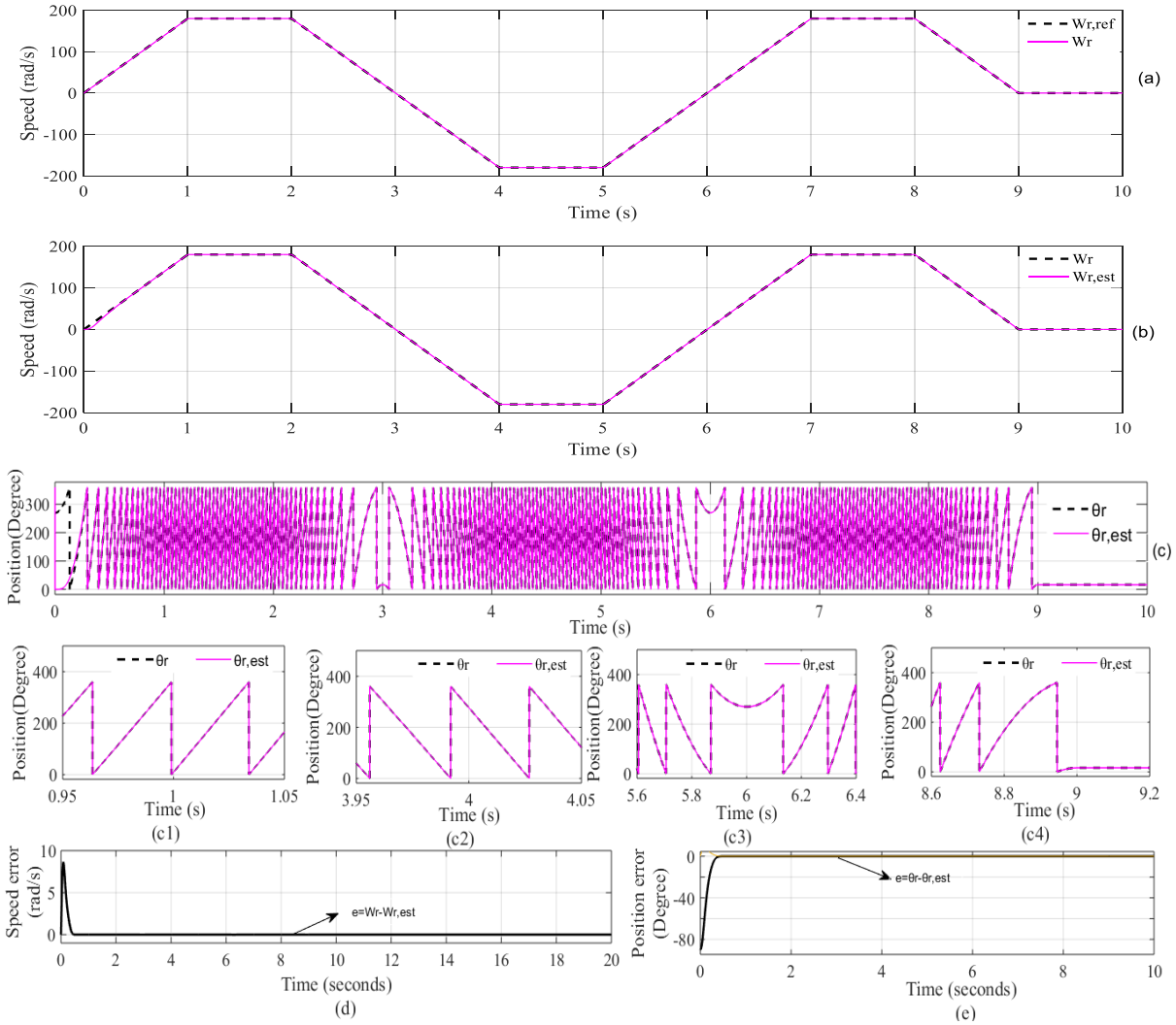

Fig. 4 (a) reference and measured rotor speed, (b) measured and estimated rotor speed (c) measured and estimated rotor position, (c1) magnified around 1s, (c2) magnified around 4s, (c3) magnified around 6s, (c4) magnified around 9s, (d) speed estimation error and (e) position estimation error

8th International Engineering Symposium - IES 2019
March 13-15, 2019, Kumamoto University, Japan

Distance Metric Learning for Haptic Data Classification of Braille Character Dataset

Megh Manoj Bhalerao[1]

1 *Department of Electrical & Electronics Engineering, National Institute of Technology Karnataka, Surathkal, Mangalore 575025, India. email: 16ee234.megh@nitk.edu.in*

ABSTRACT: Machine Learning algorithms such as K-Means Clustering, K-Nearest Neighbors, Support Vector Machines (SVMs) etc. rely on a good metric to be specified over the input data. The standard Euclidean norm between data-points does not always give us a good measure of the relation between data points. Hence, it is crucial to specify a distance metric over the input data. This process of estimating a distance metric by utilizing information inherent to the data is called Distance Metric Learning (DML). Former approaches to DML make the use of class information to learn the distance metric over the dataset. Unlike the previous approaches, our approach makes the use of relative information of similarity or dissimilarity of the data-points rather than defining strict classes to separate the data-points. We obtain the information of similarity and dissimilarity of the data-points by using human perception of the same, and to learn a distance metric so as to mimic this human response. We apply DML upon a Braille Character Dataset and try to reconstruct the Human-Response Confusion Matrix using feature vectors and learned distance metric. We then project our data-points into a new vector space defined by our learned distance metric to minimize the distance between similar pairs and maximize the distance between the dissimilar pairs.

Keywords*: Convex Optimization, Haptics, Distance Metric Learning, Confusion Matrix, Braille Alphabet, Feature Vector*

INTRODUCTION & SCOPE

Distance Metric Learning is generally chosen as a preprocessing step to many machine learning algorithms. Xing et al. showed that the accuracy of K-means and constrained K-Means is brought to 100% after a distance metric is learned over the input data and the data-points are projected into a new vector space based on the learned metric. This aforementioned paper was the beginning of a solid research in DML. Here, DML is applied to the Braille Character Dataset by Jack M. Loomis. The requirements for a distance metric to be learned is a confusion matrix (also called a similarity matrix) and feature vectors corresponding to the data-points (obtained using some feature extraction techniques from the raw data).

The entire problem can be discretized into the following subsections:

1. Apply a least square regression DML algorithm for learning a distance metric on the Braille Character Dataset using different feature vectors corresponding to various Peano curves.
2. Estimate a confusion matrix corresponding to the Braille Character Dataset (using the feature vector and the learned distance metric), i.e. the pairwise distances between the feature vectors of each of the alphabets. Compare the estimated distance matrix with the human response distance matrix.
3. Group the alphabets corresponding to the number of raised dots and

restimate the confusion matrix (dimensions obviously reduce).

THE BRAILLE CHARACTER DATASET

The Confusion (Similarity) Matrix

This data is obtained from Jack Loomis' paper (1985). This confusion matrix is a 26 x 26 matrix where each of the row/column corresponds to a letter of the English alphabet. Let this matrix be called C_b. The entries of this matrix are interpreted as follows:

1. Consider any i^{th} row and j^{th} column of Cb i.e. (i, j) th entry of C_b.
2. C_b (i, j) indicates the fraction of people who responded with the j^{th} alphabet when the stimulus corresponding to the i^{th} alphabet was provided.
3. This tells us that the matrix need not be a symmetric matrix.
4. The matrix is converted to the standard form of a confusion matrix by symmetrizing it.

The Chosen Feature Vectors

The feature vectors are chosen by following various configurations of Peano Curves. Peano Curves are defined as continuous lines between a set of points, starting from a constant chosen point and do not cross each other. Here, Peano Curves are be drawn for the braille characters since they are nothing but a set of 6 points of which some are raised and the others aren't. The feature vectors are chosen according to the following procedure:

1. Peano Curves are drawn with the help of 6 dots of the braille characters.
2. The order in which the dots are connected decide the numbering of the dots in the braille alphabet.
3. The dots of the braille alphabet are numbered accordingly.
4. The feature vector for each alphabet is a six-dimensional vector with 1's at the places where the braille dots are raised and 0 otherwise.
5. Hence, the complete feature vector (say X_b) is a 26 x 6 vector with each row corresponding to the feature vector of one alphabet.

The feature vectors corresponding to Peano Curves of Row Stacking, Column Stacking and U-Shaped Stacking are taken for experimentation and shown below respectively.

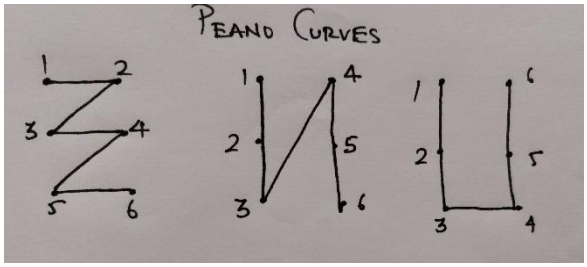

CONVEX OPTIMIZATION PROBLEM FORMULATION

The metric learning algorithm for the Braille Dataset is formulated as a least squares' regression problem of the form:

$$argmin_{M} ||P^T M P - D_b||$$

subject to

$$M \geq 0$$

The terms are defined as follows:

1. P: The vector containing the difference between all the possible pairs of the feature vectors of the Braille Character Set.
2. M: The Distance Metric that is to be learnt.
3. $D_{b:}$ The human response distance matrix.

CONVEX OPTIMIZATION ALGORITHM

As mentioned above the optimization problem here is a least squares regression algorithm and it has a closed form solution which is implemented using the algorithm given below:

Algorithm 1: Learning M using least squares regression - closed form solution

1. Input the feature vector (X_b) and the confusion matrix (Cb). Let the ith and jth entries of X_b be x_{bi} & x_{bj} respectively.
2. Define a Distance Matrix $D_b = 1 - C_b$. Let the (i, j) th entry of D_b be d_{bij}
3. Compute the pairwise distance between all the possible pairs of feature vector i.e. x_{bi} - x_{bj} and store it in a separate variable say P.
4. Our optimization problem is a least squares regression problem of the form

$$\boldsymbol{argmin}_{\boldsymbol{M}} ||\boldsymbol{P^T M P - D}||$$

5. The problem is brought in its standard form by writing it in a slightly different manner i.e.

$$\boldsymbol{argmin}_{\boldsymbol{M}} ||\boldsymbol{Hm - D}||$$

   where m is the unrolled vector of the matrix M.
6. The vector H is the vector containing the pairwise difference between all the possible pairs of the feature vectors.
7. The closed form solution of the above regression problem is given by

$$\boldsymbol{M = (H^T H)^{-1} H^T E}$$

   where E is the unrolled column vector of the lower triangular part of the matrix D.

ACCURACY CHECK

The accuracy of our algorithm is measured by how relatable our estimated distance matrix is to the human response distance matrix. There is no single formula which would give us this measure of closeness/accuracy. Rather, we have to analyze the relation using some graphical approaches. Ideally, the plot of the corresponding cell entries of the estimated distance matrix and the human response distance matrix must be a straight line of inclination of 45 degrees with the allowance for some minor deviations. But the graph we obtain is:

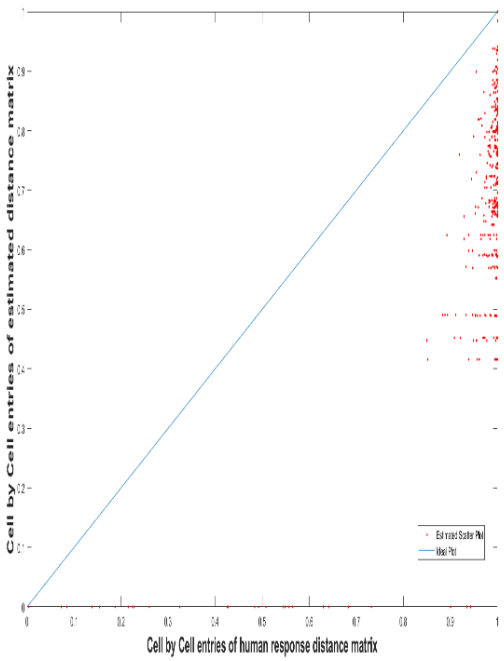

Fig 1: Y and X axes as shown above

The error of our estimate can be measured by how much our estimated data-points have deviated from the ideal plot. A way of doing this is to sum the perpendicular distances of our estimated points from the line. Mathematically it can be expressed as:

$$\epsilon = \sum_{i} \frac{|x_i - y_i|}{\sqrt{2}}$$

where (x_i, y_i) is the coordinate of the ith estimated datapoint.

RESULTS – LEAST SQUARES REGRESSION ALGORITHM

The estimated distance metric obtained using the least squares algorithm is the following: The closeness of the estimated distance matrix and the original human response distance matrix is given by a comparative study of the plots of the distance versus the letter.

The plots are shown below:

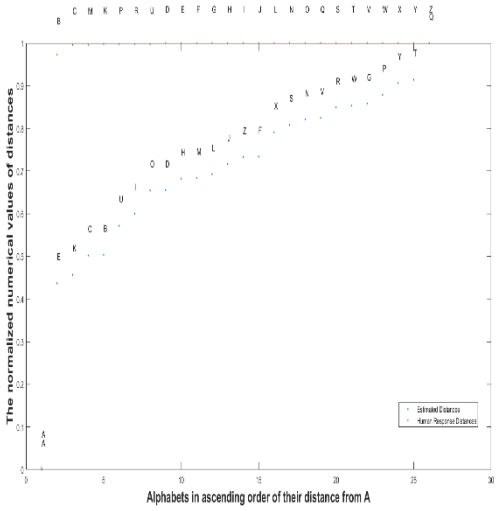

Fig 2: For Row Stacking

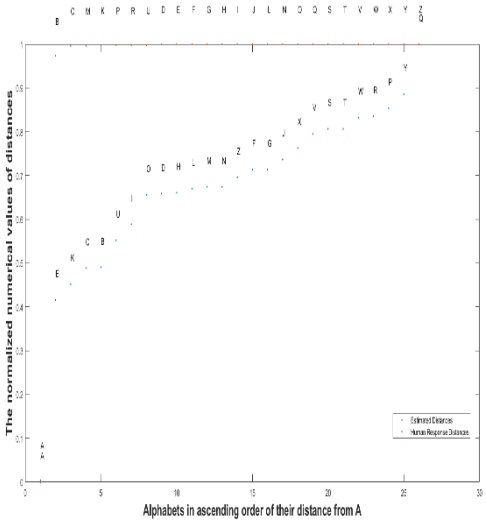

Fig 3: For Column Stacking

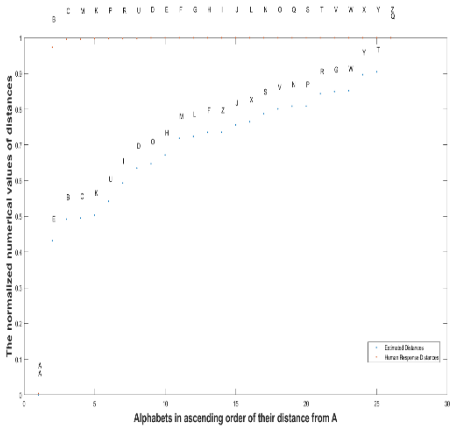

Fig 4: For U-Shaped Stacking

Explanation of the plots shown:

1. The X-axis depicts each letter of the English language spaced at equal intervals.
2. The order of letters is not alphabetical but rather the ascending order of the distances from the reference alphabet.
3. The reference alphabet in this case is the letter A.
4. The Y-axis depicts the numerical value of the distance of the reference letter with respect to the letter written above each of the data-point.
5. The Y-axis distance is normalized by dividing each of the entry in the estimated distance by the sum of entries of that row in the distance matrix to make all entries between 0 and 1.
6. Normalization is done since our human response distance matrix's entries are also between 0 and 1, as it depicts the fraction of people.

A Different Confusion Matrix

An observation of the above plots (of the distance of each character with respect to others) suggests that the similarity perception of the braille alphabet could depend upon different aspects of the alphabets such as:

1. The number of elevated dots
2. The orientation of the dots i.e. vertical or horizontal alignment.

Initially, we convert our 26 x 26 confusion matrix into a 5 x 5 confusion matrix by grouping the rows and columns suitably according to the groups. After that we sum all the entries of the corresponding group as well as one group with the other and place it in the corresponding columns of our new confusion matrix. After this we normalize each of the row of this new matrix so as to make all the entries sum up to 1. We symmetrize this matrix. The new 5 x 5 confusion matrix ($D_f = 1 - C_{f)}$ is given below:

# of dots raised	1	2	3	4	5
1	0.0040	0.9919	0.9993	0.9996	1.0000
2	0.9919	0.0953	0.9021	0.9789	0.9899
3	0.9993	0.9021	0.2893	0.7901	0.9156
4	0.9996	0.9789	0.7901	0.3416	0.5676
5	1.0000	0.9899	0.9156	0.5676	1.0000

# of dots raised	1	2	3	4	5
1	0	0.1541	0.9632	1.0169	1.1209
2	0.1541	0.4821	0.7339	0.8043	0.9567
3	0.9632	0.7339	0.3967	0.7911	0.9834
4	1.0169	0.8043	0.7911	0.3295	0.8694
5	1.1209	0.9567	0.9834	0.8694	0.5357

After constructing D_f, we learn our distance metric M based on D_f and a set of new feature vectors (X_g) which consists of the pairwise distances of one alphabet group with itself and also one alphabet group with the other.

The convex optimization problem is:

$$\boldsymbol{argmin_M} \, ||\boldsymbol{X_{sum}M_u - E}||$$

subject to

$$\boldsymbol{M \geq 0}$$

The terms are defined as follows:

1. X_{sum}: The vector containing the pairwise difference between all the possible pairs of the feature vectors (from different groups as mentioned above) of the Braille Character Set.
2. M_u: The unrolled version of the Distance Metric that is to be learnt.
3. E: The elements of the reduced human response distance matrix arranges such that they correspond to the calculated distance (5 x 5).

The re-estimated distance matrix is the following:

The accuracy of such a methodology can be estimated as follows:

1. Generate all possible triplets (i, j, k) from the grouped-up alphabets such that (i, j) are in the same group and k is from a different group. Let the total number of triplets be N.
2. From all the possible triplets' corresponding feature vectors (x_i, x_i ,x_k) from the alphabet groups count the ones such that $d(x_i, x_j) < d(x_i, x_k)$ where d is the distance between the feature vectors calculated using the learned distance metric M. Let this count obtained be C.
3. The accuracy percentage can be calculated as:

$$\boldsymbol{Acc = \frac{C}{N} \times 100}$$

4. The accuracy obtained by such a method for L2 norm minimization comes out to be around 46.46%

REFERENCES

[1] Xing, E P et al (2004), Distance Metric Learning with application to Clustering and Side Information, NIPS, 2003, pp. 521-528.
[2] Loomis J M, Tactile Recognition of Raised Character: A parametric study, Bulletin of the Psychonomic Society, 1985, Vol 31, No.2, pp. 18 - 20

8th International Engineering Symposium - IES 2019
March 13-15, 2019, Kumamoto University, Japan

ECG Signals Denoising using Savitzky-Golay Filters

Vrushabh Bhangod [1]

1 *Department of Electrical and Electronics Engineering, National Institute of Technology Karnataka, Surathkal, Mangalore 575025, India. email:vrushabh97@gmail.com*

ABSTRACT: In this paper, we discuss the implementation of Savitzky Golay Filters to suppress Additive White Gaussian Noise. This filter performs local least squares polynomial approximation to extract original signal from a noisy environment with significant noise reduction thereby preserving the features of the signals. Noise reduction and feature distortion depend on Impulse Response Length and Order of the filter. In this paper, we provide a detailed derivation of the SG Filters and through examples of ECG signal data derived from physiobank database we show the performance of SG filters.

Keywords*: Savitzky Golay Filter, Order, Impulse Response Length*

INTRODUCTION

Real-time signals are often corrupted by noise. Noise can be moving or stationary. In this paper, we try to employ Savitzky-Golay Filters to smoothen the data points and compute the approximate clean signal from a noisy signal. The filter is based on local least-square polynomial approximation and was formulated by the duo, Savitzky and Golay, hence is the name of this filter. Signal denoising is vital for further signal processing.

SG Filters are Finite Impulse Response, Low Pass and Digital filters. The basic principle behind SG filter smoothing is, to obtain 2n+1 equidistant spaced points so as to represent a polynomial of Order Q. It effectively computes local least square polynomial at every point within the impulse response length P. The duo further proved the fact that[1] local least squares polynomial regression is equal to a discrete convolution with a fixed impulse response assuming that data samples are symmetric about the origin.

Savitzky and Golay have shown that the shape of the signal is preserved and significant noise reduction is observed.SG filters are characterized by the Order(Q) and Impulse Response Length of the filter(2P+1). Schafer[2], provided a detailed paper on the design and frequency domain properties of SG filters. By choosing appropriate Length and Order, noise can be reduced significantly. The aim of this filter is to preserve the salient variation of the signal while eliminating the noise. SG Filters have found applications in Analytical Chemistry, Physics and Geophysical studies etc. They are used for smoothening or differentiation of data. In this paper, we present the derivation and implementation of the filter. We also discuss the variation of various parameters. Mean Squared Error (MSE) is chosen as the parameter for evaluation.

BACKGROUND THEORY

A. Design of SG Filters:

In this context, we assume the noisy signal x[n], clean signal s[n], noise w[n] which is Additive White Gaussian of zero mean and standard deviation of σ and length L. Considering 2P+1 samples centred at n=0 at an instance we determine the polynomial coefficients given by,

$$p(n) = \sum_{k=0}^{Q} a_k n^k \quad (1)$$

where Q is the order of the filter, that yields minimum Mean Squared Error for the input samples under consideration.

In the works of Savitzky and Golay, they showed that the smoothed output value obtained by local least squares polynomial regression is identical to a fixed linear combination of the local set of impulse input samples, all the input impulse samples within the impulse response length interval that is considered for fitting the polynomial.

Hence the output samples can be computed by discrete convolution,

$$y[n] = \sum_{m=-P}^{P} h[m]x[n-m] \quad (2)$$

$$y[n] = \sum_{m=n-P}^{n+P} h[n-m\,x[m] \quad (3)$$

To prove that local ls polynomial regression is equal to the discrete convolution of the noisy signal with the finite impulse response, we need to minimize the cost function in order to determine optimal polynomial coefficients. The corresponding cost function is, $\sum_{n=-P}^{P}(p(n) - x[n])^2$

Hence,

$$\frac{\partial \varepsilon_N}{\partial a_i} = \sum_{n=-P}^{P} 2n^i \left(\sum_{k=0}^{Q} a_k n^k - x[n]\right)^2 = 0 \quad (4)$$

By rewriting the equation(4) we get,

$$\sum_{k=0}^{Q}\sum_{n=-P}^{P} n^{(i+k)} a_k = \sum_{n=-P}^{P} n^i\, x[n] \quad (5)$$

These equations are known as normal equations for least squares approximation problem. We solve the problem by analyzing the equations in the form of a matrix. We define a (2P+1)X(Q+1) Vandermonde Matrix A, given by A = $\{a_{n,i}\}$

$$\alpha_{n,i} = n^i \quad -P \le n \le P, i = 0,..,Q$$

We compute A^TA which is a (Q+1)X(Q+1) symmetric matrix represented by B whose elements are,

$$\beta_{i,k} = \sum_{n=-P}^{P} n^{(i+k)} = \beta_{k,i} \quad (6)$$

If the input sequence is written as a vector x = [x[-M],..x[0],..,x[M]]^T.The polynomial coefficients are written as a vector,

a = [a_{0},a_{1}.....a_{N}]^T. From equation 5, we can write,

$$Ba = A^TAa = A^Tx \quad (7)$$

Hence, the polynomial coefficients are given by,

$$a = (A^TA)^{-1}A^Tx = Hx \quad (8)$$

We need to determine a_{0}, which is the smoothed output value for the group of samples centered at n = 0.

$$y_0 = \sum_{m=-M}^{M} h_{0,m}x[m] = a_0 \quad (9)$$

where $h_{i,n}$ denotes the elements of the (Q+1)X(2P+1) H matrix and $h_{0,m}$ is an element of the zeroth row.

We observe that matrix **H** is dependent solely on order and filter length Q and P respectively. Also, the elements of the zeroth row of H matrix are the flipped impulse response coefficients of the S-G Filter.

B. Mean Squared Error(MSE)

Mean Squared Error (MSE), is the measure of the quality of an estimating model. It is always non-negative and is equal to the average of the squared errors. In dB scale, it is given by,

$$MSE = 10\log_{10}\sum_n (s[n] - y[n])^2 \text{.....dB}$$

EXPERIMENTAL RESULTS

The performance of the above algorithms is provided for the ECG signal sampled at 720Hz, taken from Physio Bank Database. We have added Additive white gaussian

noise for the clean signals. In Fig2. SNR = 3dB.We observe that the MSE is equal to 14.5 dB.

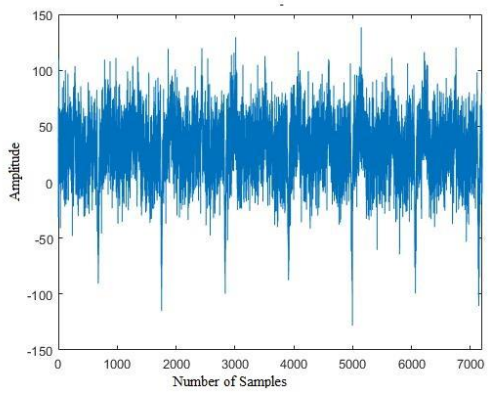

Fig.1 Noisy Signal with 3dB noise

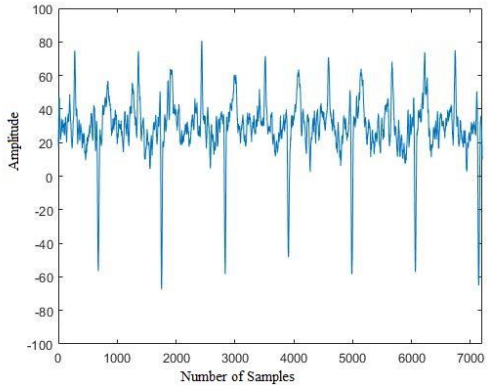

Fig.2 Recovered ECG Signal P=30, Q=4

In Fig.3 we show the variation of MSE with Order of the filter. Least MSE is obtained when the noisy ECG signal is estimated to a 4th order polynomial.

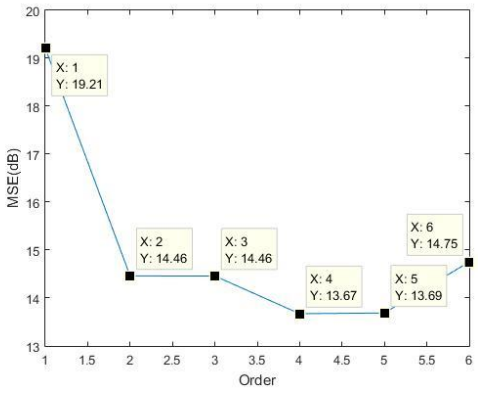

Fig.3 MSE vs Order,P=30 and SNR=5dB

Next, we vary the input SNR and correspondingly compute output SNR.At higher SNRs Input SNR and Output SNR are almost equal.

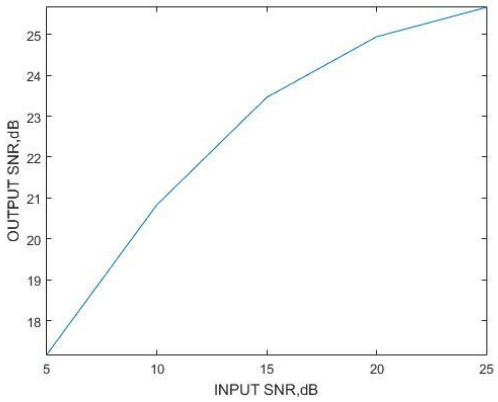

Fig.4 OUTPUT SNR vs INPUT SNR,Q=4,P=61

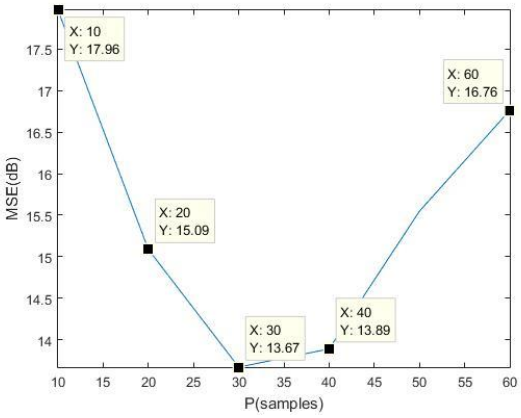

Fig.5 MSE vs P, Q=4,SNR=5dB

In Fig.6 We observe that small order filters preserve smaller scale filter features at the expense of poor noise reduction. While in higher order filters noise is reduced significantly with distortion in smaller scale filter features. The filter performs smoothening without loss of resolution but within limits.

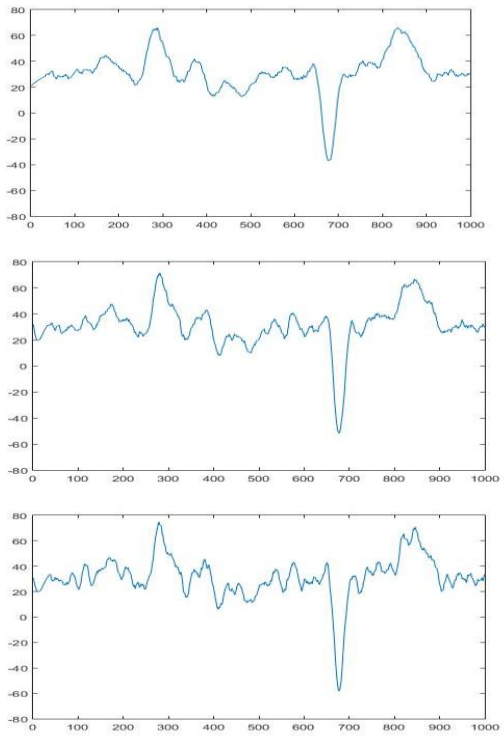

Fig.6 Smoothening by 61 point window with Q=2,4,6 respectively

CONCLUSIONS

SG Filter is one of the advanced filters in the field of signal processing and in our case we have implemented this filter to suppress additive white Gaussian noise applied to ECG signals, further approximating the necessary ECG signal. It is useful in cases where preservation of features is vital.

However, as we observed there is a trade-off between window length and order, we need to implement adaptive algorithms which reconstruct the signal with a unique P and Q for which MSE is minimum using point-wise approach for given sampling rate and signal type.

We have tested the ability of SG filter for denoising purposes on EEG signals and Piece-Wise Regular signals and observed significant noise suppression with reduced feature distortion.

MATLAB functions *polyfit* can be used to evaluate the polynomial coefficients for a given order and window length, in the least squares based approach *polyval* is used to compute the value of the polynomial at each point within the window. These functions can be used effectively to implement the filter on the MATLAB platform.

REFERENCES

[1].Savitzky A, Golay MJE. Smoothing and differentiation of data by simplified least squares procedures. Analytical Chemistry 1964;36;1627–1639.
[2].R. Schafer, What is a Savitzky–Golay filter? [Lecture Notes], IEEE Signal Process. Mag. 28 (2011) 111–117.
[3].Hargittai, S. (2005).Savitzky-Golay Least-Squares Polynomial Filters in ECG Signal Processing. Computers in Cardiology, (32), pp.763-766.
[4] S. Krishnan, C. Seelamantula, On the selection of optimum Savitzky–Golay filters, IEEE Trans. Signal Process. 61 (2013) 380–391.
[5]Physiobank Database [Online] available at https://physionet.org/physiobank/database/aami-ec13/

8th International Engineering Symposium - IES 2019
March 13-15, 2019, Kumamoto University, Japan

Heat-map Analysis Based Formation Prediction in Field Sports

Amitkumar Patel [1], Mayank Sitapara[2], Tejas Rafaliya[3], Dr. Shashidhar G. Koolagudi[4] and **Pravin B. Ramteke[5]**

1 *Department of Computer Science and Engineering, National Institute of Technology Karnataka, Surathkal, Mangalore 575025, India. email:amitpatel111297@gmail.com*
2 *Department of Computer Science and Engineering, National Institute of Technology Karnataka, Surathkal, Mangalore 575025, India. email:mayank.sitapara@gmail.com*
3 *Department of Computer Science and Engineering, National Institute of Technology Karnataka, Surathkal, Mangalore 575025, India. email: trafaliya@gmail.com*
4 *Department of Computer Science and Engineering, National Institute of Technology Karnataka, Surathkal, Mangalore 575025, India. email: koolagudi@yahoo.com*
5 *Department of Computer Science and Engineering, National Institute of Technology Karnataka, Surathkal, Mangalore 575025, India. email: ramteke0001@gmail.com*

ABSTRACT: In field sports, a significant amount of time is invested into preparing players and strategies before advancing into the sport. This involves the analysis of opponents' style of play, strengths and weaknesses. The formation of a team is one of the deterministic factors for the player coordination and performance in the sport. Heat-maps are a map of the frequency of movement of a player or collection of players on the dimensional area for the duration of a game, indicating team formation. This project proposes the deconstruction of aggregate heat-maps of opponent teams over a historical time series using MATLAB and further segregation of the field into sport-relevant zones. The study undertaken on the heat-map datasets available online demonstrates the use of computer graphics and vision library OpenCV in Python to identify potential deficiencies in the opponent player network and generate adaptive strategic formations based on the information obtained and capitalizing on the strengths of the proponent team to increase the likelihood of a favourable outcome.

Keywords*: Heat-map, Formation, Pixel intensities, RGB, Blob detection, Centre-of-Mass*

INTRODUCTION

The business of sports is an ever expanding ecosystem, with teams investing millions of dollars to reach the top and outdo the competition in their respective sport leagues. Field sports have a characteristic of player formation which determines their presence on the field. Football is one such sport which involves two 11-player teams going head-to-head on the field and the result is determined by which team scores the most number of goals. Apart from the on-field effort, teams invest time and research into preparing their players and strategies before going into the game. The analysis of opponent's style of play, strengths and weaknesses is carried out with careful observation in order to prepare the players so that the result is favorable for the team. Although a lot of attention has been directed towards the prediction of the outcome of a match based on previous performances, no in-depth technical analysis has been done to enhance the performance of the players during the game. This is where the analysis of football heat-maps proves useful.

Heat-maps are a map of the frequency of movement of a player or collection of players on the dimensional area for the duration of a game. They indicate the effectiveness of the player in different regions of the pitch. A heat-map is

characterized with a spectrum of intensities, ranging from:

Red region : High activity
Green region : Moderate activity
Blue region : Low activity

Fig.1 Sample Heat-Map

A concentration of red signifies high presence of the player in that part of the field, while concentration of blue signifies the player's absence. The individual/team performances can be scrutinized through the use of heat-maps to obtain the optimum placement of players for a given

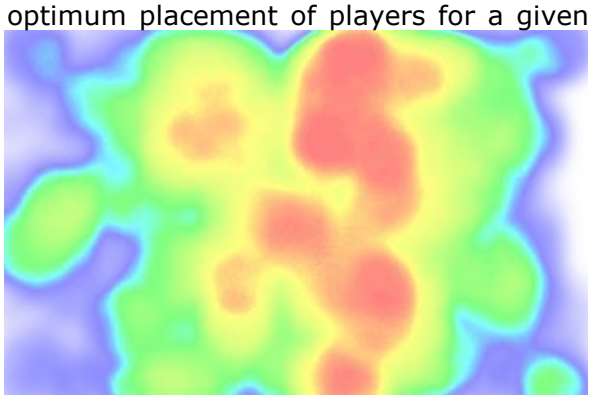

formation for team A when they are about the play against team B. The weak regions of team B can be exploited by team A by strategically positioning their players in the cavities observed in the aggregate heat-maps of team B's past performances.

The objective of this project is to utilize the opponent team's heat-maps and to conduct image analysis on them to obtain useful knowledge about their pattern of play and placement of players. Having obtained this information, the algorithm described in this paper determines the required formation of the team under consideration that will enable them to capitalize on the opponent team's weaknesses while enhancing their own performance.

DATA COLLECTION

The data-set of the project is a collection of heat-maps of a team(s) from matches played throughout the season. The heat-maps comprising the data-set are available on online sources and are generated using proprietary software that use image recognition techniques to allow player's movements to be tracked.

This involves the representation of the football pitch as a grid of pixels and when player movement is detected over a pixel, the intensity of heat increases. Over time, the accumulation of heat over the pixels on the grid over the duration of the map represents the heat-map of a team or player.

The specific heat-maps were collected from whoscored.com. This source provides accurate and reliable information about every match played in top football leagues.

SHAPING OF DATA

Data collected is rarely of correct shape and size for analysis purpose and it needs to be shaped into appropriate form. A single heat-map suggests the team's strategy in a particular game. Teams deploy different strategies in different games, all of which vary by small amount from their basic style of play. To gain better insight into team's overall strategy throughout the season, their aggregate heat-map is required. This aggregation is achieved by the following procedure:

Procedure:

Having gathered data set of N heat-maps of a team from a season, their pre-processing is required before analysis can be carried out. A team may play on either halves of the field over the matches, therefore this needs to be accounted. Processing includes orientation correction through rotational operation in order to align all heat-maps correctly. Aggregate heat-maps of a series of heat-map data collected for a team provides a summarization of the overall performance of the team and its activity and effectiveness in the different parts of the field can be inferred from it.

The code snippet in Fig.2 can be executed in MATLAB to calculate the aggregate

heat-map for a data-set of heat-maps spanning over a series of matches.

Fig.2 Code for Aggregating Heat-maps

The RGB pixel intensities of the image are read as a two-dimensional matrix d. The matrix d is generated for all the images and summed successively as aggregate map to obtain a matrix of total intensity of RGB values for the corresponding pixels.

```
for i=1:dataset_size
     filename=[num2str(i), '.png];
     d=imread(filename, 'png');
     average_map=average_map+double(d);
end

average_map=average_map/i;
average_map=uint8(average_map);

figure;
imshow(average_map);
title('RGB Average');
```

The resultant aggregate heat-map is divided by dataset size to obtain a mean of the RGB intensities for each pixel of the football pitch and converted back to 8-bit integer values.

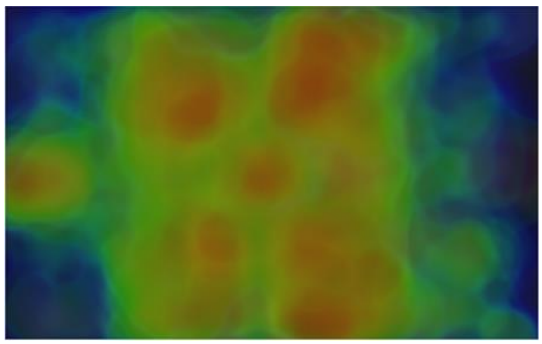

Fig.3 Aggregate Heat-Map

Once the aggregate RGB intensity pixel value matrix is calculated, it can be resulted in an output image to obtain the aggregate heat-map (refer Fig. 3) which is the basis of further analysis of a team's performance on the field.

ANALYSIS OF AGGREGATE HEAT-MAP

Each region of football field has different tactics and strategies involved, due to which each had to be analysed separately. Therefore, the map had to be divided into 3 zones namely: Defence (marked 1 in Fig.4), Midfield (marked 2 in Fig.4) and Attack (marked 3 in Fig.4).

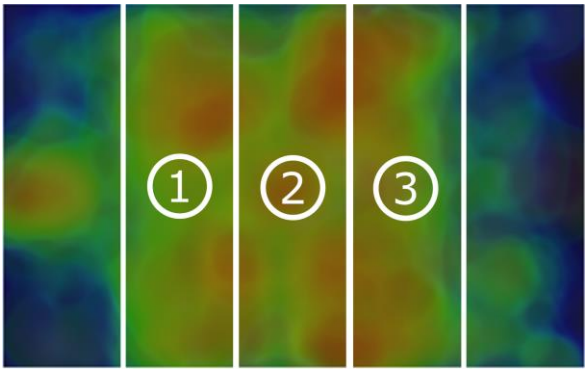

Fig.4 Zone Partition of Aggregate Heat-map

Each zone is further divided into 5 rectangular grids as formations can have up to 5 players in each zone. Hence, the aggregate heat-map consists of 3x5 = 15 grids in total.

The highly active (red) regions are separated from moderate activity (green) and low activity (blue) regions to detect high concentration of player activity of the team. This was implemented by segregating the R (refer Fig. 5) and G (refer Fig. 6) intensities for each pixel in the aggregate heat-map to produce Active Zones and Moderate Zones on the image of the football pitch respectively.

ALGORITHM

The approach to determining formations from aggregate heat-maps is based on the process of blob detection [1] and determination of centre-of-mass of the blob. A blob is a connected component of pixels belonging to that component and having the same colour but the underlying intensity of these pixels may be variable. They analysis can provide information about critical regions in an image [2]. In this application, it will enable the location of candidate player placements.

The centre of mass of a blob depends on the intensity of the pixels that belong to that blob. If the intensity of all the pixels is

the same, then the centre of mass is the set of coordinates that are equidistant from the boundary of the blob. In practical cases, the intensity of the pixels range over a series of values. In such situations, the centre of mass will be placed more towards the pixels having higher intensity values.

There are 3 inputs to the algorithm: the isolated red values of the aggregate heat-map, the isolated green values of the aggregate heat-map, and the aggregate heat-map itself. Each heat-map is divided into a 5x3 grid, and the columns represent the defence, midfield and the attack of the team from left to right. The goal for player placement is such that the formation counters the strengths of the opponent formation (increased presence on pitch) while also exploiting the weaknesses (lack of presence on pitch).

An active filter heat-map (refer Fig. 5) helps locate the strengths of the opponent as it represents the areas where the players have the highest presence. So, the defence can be placed in such a way that it covers the centre of mass of the red blobs, subsequently neutralizing the opponents' strength.

Fig.5 Filtering of Active Regions

A moderate filter heat-map helps locate the weaknesses of the opponent, i.e., the areas where they are lacking presence on the field. Hence, the attacking players of the team can be positioned in such a way that they coincide with the centre of mass of the green blobs, which helps in exploiting the opponents' weakness.

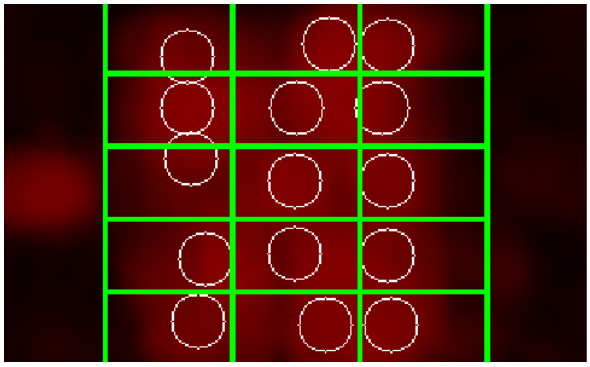

Fig.6 Filtering of Moderate Regions

The midfield however, has a different role, wherein it has to accommodate for the opponents' strengths while also trying to capitalize on the opponent players' relative absence in certain regions of the pitch. Hence, their position is determined by taking the aggregate of the centre of

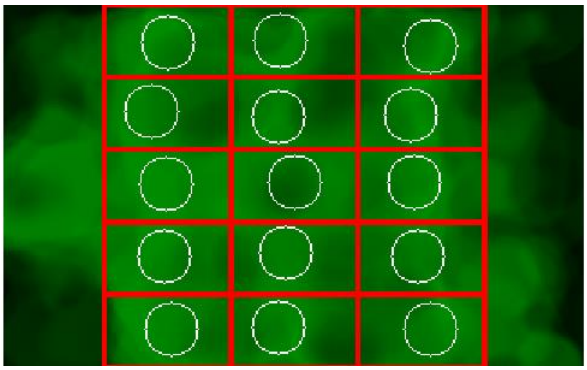

masses of the red blobs and the green blobs which give the players equal opportunities to cover opponents as well as occupy empty spaces. The defence, midfield and attack have 5 positions each. Hence, out of the total 15 positions (refer Fig.7) available, 10 will be selected based on the formation required by the strategist. Whenever less than 5 positions need to be occupied, priority is given to those positions in which the number of pixels in the blob is the highest.

After the formation is selected by the strategist, the algorithm is executed to compute the positions of the players with respect to the formation chosen. The positions are then displayed onto the heat-map using which the results can be compared.

Refer to Fig.6 for the algorithm for Centre-of-Mass Detection in the heat-maps.

1. Set lower and upper bound for red and green pixels to filter out low intensity pixels.

```
redlow=[0,0,100]
redhigh=[90,90,255]

greenlow=[0,100,0]
greenhigh=[90,255,90]
```

2. Traverse the heat-map from left to right, going down the columns.

   For each iteration, detect all blobs present in the tile, and store then in decreasing order of size of the blob.

   Store the center of mass of the biggest blob in a array, along with it's size.

```
for (i=0;i<width;i=i+width/3)
{
    for(j=0;j<height;j=j+height/5)
    {
    frame=cv2.inRange(redlow,redhigh)
    blob = frame>100
    coord[k]=[CenterOfMass(blob),size]
    }
}
```

3. For the green and red pixel array, arrange the blobs in decreasing order of their size, again.

4. Read input formation from the user and decide which positions to place a player in based on the array generated earlier.

Fig.6 Pseudo-code for Centre-of-Mass Detection

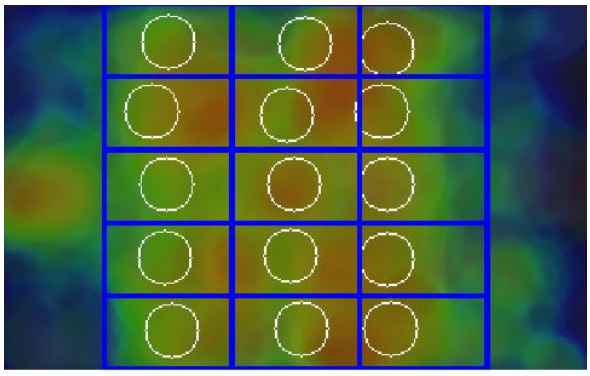

Fig.7 Candidate Blobs for Player Placement

RESULTS

Input given to the code (Isolated active filter heat-map and moderate filter heat-map) is used to compute the position of a player in each tile of the grid. Based on the team strategists' desired formation, the algorithm shortlists the candidate blobs in each zone of the field. The co-ordinates computed for candidate blobs are then used if required based on the formation. The player placement co-ordinates are then displayed onto the heat-map in the form of circular markers (refer Fig.8).

A sample of the results obtained for different formations is shown in Fig. 8. The results obtained are comparable to the position of the players for the same formation in actual football game. This shows that the algorithm produces results that are very close to real life field sport formations and hence, it is viable to use it for strategic analysis of heat-maps.

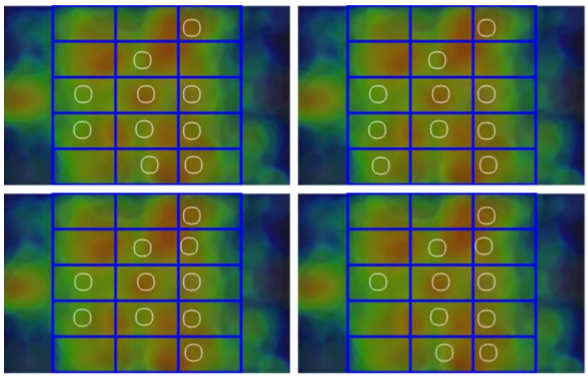

Fig.8 Algorithm Output Formations

CONCLUSIONS

The results obtained from this algorithmic analysis can be used by teams engaged in field sports to enhance their strengths and minimising their team performance weaknesses. Devising algorithms to optimize performance of teams based on heat-maps has the potential to greatly benefit the results of teams and increase the efficiency of the player's movement on the football pitch.

The future line or work in this project can include the analysis of individual players' impact on the team performance and the suggestion of Player Transfers that allow teams to procure players based on their past performance and compatibility with the team. Since Heat-maps are common to many other field sports such as Rugby, Hockey, etc. similar analyses can be

undertaken to understand and improve the chances of winning for a team.

Heat-map generation and analysis has a vast scope for study and research. A digital image-processing approach towards the activity of players and teams can add a technological component to sports and open a multitude of avenues for scientific exploration.

REFERENCES

[1] C. Damerval and S. Meignen, "Blob detection with wavelet maxima lines". IEEE Signal Processing Letters, 14(1):39-42, 2007.
[2] G. Gerig, G. Szekely, G. Israel and M. Berger. Detection and characterization of unsharp blobs by curve evolution. Information Processing in Medical Imaging, 165-176, 1995.

8th International Engineering Symposium - IES 2019
March 13-15, 2019, Kumamoto University, Japan

Maximum Power Generation by Shadow dispersion of PV Array under variable irradiance Using Latin Square Configuration

Saurabh S Zond [1], A. Karthikeyan [2] and **Kshitiz Khatri [3]**

1 *Department of Electrical and Electronics Engineering, National Institute of Technology Karnataka, Surathkal, Mangalore 575025, India.*
email: saurabhzond008@gmail.com
2 *Department of Electrical and Electronics Engineering, National Institute of Technology Karnataka, Surathkal, Mangalore 575025, India.*
email: jakarthik@nitk.edu.in
3 *Department of Electrical and Electronics Engineering, National Institute of Technology Karnataka, Surathkal, Mangalore 575025, India.*
email: kshitizkhatri97@gmail.com

ABSTRACT: Increasing the energy efficiency of photovoltaic (PV) systems has been a challenging task from beginning. One of the main reasons for power reduction in PV array is partial shading. The reduction of power depends on PV array connection and shading pattern. Different types of schemes for PV array connection are given in the literature to reduce effect of partial shading. This paper presents a new method called Latin Square configuration to distribute the effect of shading and enhance the power generation of PV array. The proposed method is compared to conventional configurations for different shading conditions and the MATLAB/SIMULINK results are presented to show the improvement in power extraction from PV array.

***Keywords**: PV systems, Partial Shading, Conventional configurations, Latin Square configuration*

1 INTRODUCTION

Recently renewable sources of energy have become a preferred choice over conventional sources of energy as they are clean and inexhaustible [1], [3]. PV energy being the most prominent solution due to recent developments such as solar photovoltaic technology, in which solar panels trap sun rays and this radiation is transformed into current. The PV material is composed of semiconductor material which uses solar energy to stimulate electron transfer process into direct electric current. This process is clean and sustainable and so greatly preferred over others. As being in its initial phase, it is still under development stage which results in high price of affordability and so more focus is given to increase the efficiency of these PV systems. There are several factors which affect to the solar PV power output such as solar irradiance, solar incidence angle, temperature, shading patterns on PV array, dust etc [2]. Partial shading is one of the major factors for the reduction in power generation. This is caused due to the presence of shadow on PV array of various obstructions such as buildings, towers, trees and passage of clouds [6]. The losses due to partial shading are present due to electrical configuration of the PV modules as due to presence of a shaded module in series with other unshaded modules the series current gets limited and so thereby reducing the maximum power that could be generated by the array [8]. The solar PV array reconfiguration is well known and popular technique being implemented to increase the power output and efficiency of

electricity generation [5]. Different interconnection schemes such as series–parallel (SP), bridge linked (BL) and total cross tied (TCT) are present in the literature [9], [11]. SP configuration is the combination between series and parallel connection of each panel. For BL, the connection of each panel is nearly the same as SP configuration but the connections of some rows between each string will be added. Lastly, for TCT, the connection of each panel is nearly the same as BL but there are connections for all rows between each string. From all the above three configurations of PV array the third type of configuration (i.e.) TCT configuration generates more power than the remaining methods [7]. Another technique was presented, namely Sudoku pattern which showed that the output power from the PV increased by 6% by changing from TCT to Sudoku but has a drawback that it can be performed only on 9X9 array [10].

This paper presents a new configuration method called the Latin Square configuration for arranging the PV modules to increase the power generation even under partial shading. This structure reduces the occurrence of shading in the modules of the same row thereby maximizing the output power from the array. Keeping the electrical connections unaltered and by doing this modification the effect of shadow has been dispersed throughout the array and thereby lowering the influence of partial shading. This configuration is valid for any combination of array thus eliminating the drawback in Sudoku method. The system performance is investigated for different shading patterns on a 4x4 PV array with conventional interconnection schemes and the results reveal that the proposed model exhibits better performance under partially shaded conditions.

2 MODELLING OF PHOTO VOLTAIC (PV) CELL

A PV cell can be modelled as a current source with a diode present in parallel along with a resistance present in parallel and series to the circuit [4]. This can be represented by an equivalent circuit as shown in Fig. 1.

The characteristics of a PV module can be obtained by connecting desired number of such cells in series. The equation for such a PV cell can be given as in Eq.1

$$I_{pv} = I_{ph} - I_o\left[\exp\left(\frac{V_{pv}+R_sI_{pv}}{A}\right)-1\right]-\left[\frac{(V_{pv}+R_sI_{pv})}{R_{sh}}\right] \quad (1)$$

where I_{pv} is the current generated, I_{ph} is the photoelectric current, I_o is the saturation current, V_{pv} is the PV voltage of the module, and A = nkT/q. T represents the temperature of the module in Kelvin, k is the Boltzmann's constant, q is the electric charge, n is the number of cells in series, and R_s is the series resistance. The nonlinear output characteristic of the PV module results in a unique Maximum Power Point (MPP) on its PV characteristics curve.

3 CONVENTIONAL INTERCONNECTION SCHEMES

In a PV array, the interconnection scheme refers to the manner in which modules are interconnected in the array. The three interconnection schemes reported in the literature are the Series Parallel (SP), Total Cross Tied (TCT), and Bridge Linked (BL) configuration. The SP scheme consists of a series of panels in a string and a number of such strings are connected in parallel. For BL, the circuit that includes the bridge connection into the circuit. Finally, TCT is the array connection same as BL but each row of TCT are connected in order to distribute current when they are shaded. Fig. 2. shows different configuration for 4x4 PV array.

4 METHODOLOGY

The losses due to partial shading is not directly proportional to the amount of shading area but depends on the shading pattern. The main objective of the proposed algorithm is to minimize these losses caused due to partial shading by distributing the shaded area over the entire array using Latin Square configuration for different shading patterns considered in the paper. In this, physical relocation of the PV modules is carried out

without changing the electrical connection of the array.

Latin squares are grids filled with numbers, letters or symbols, in such a way that no number appears twice in the same row or column. For e.g., to make a 4x4 Latin Square, only 4 different numbers or letters are required. The following figures in Fig. 3 show Latin Square configuration for numbers 1 to 4 and letter A to D for a 4x4 array.

If the two Latin squares in Fig.3 are combined, a new square with pairs of letters and numbers is obtained. No pair is repeated and the grid formed contains each combination. The new square formed is called a *Euler Square* and two such squares formed are *mutually orthogonal*. From above, a normal PV array is reconfigured using Latin Square method as shown in Fig. 4.

5 RESULTS AND DISCUSSIONS

The simulations are carried out using MATLAB/Simulink environment. All four configurations discussed previously are SP, TCT, BL, and the proposed Latin Square configuration are compared for their power generated under partial shading conditions.

There have been five different shading patterns considered in the text namely, (a) Short and Narrow, (b) Short and Wide, (c) Long and Narrow, (d) Long and Wide and (e) Non-continuous shading condition. For each of the case a comparison has been shown of the shade dispersion for TCT and Latin Square configuration on a 4x4 PV array. The power generated for different shading patterns have been precalculated for above mentioned conventional and Latin Square configuration and are tabulated in table 1 [9].

(a) Short and Narrow shading conditions:

The irradiance value for unshaded module is kept at 1000 W/m^2 with the temperature set at 25^{o}C. The shaded part irradiance is varied as 600 W/m^2 and 300 W/m^2. The dispersion is compared for TCT and proposed method and are as shown in Fig.5 (a). The maximum power was generated by proposed method (3400 W) which was 7.8 percent more than TCT (3156 W). Power generated in SP (2907 W) and BL (3019 W) were found out to be much less in comparison to the Latin Square method.

(b) Short and Wide shading conditions:

In this case, two entire rows are partially shaded with irradiance value of 600 W/m^2 and 300 W/m^2 and rest are kept unshaded. The shade dispersion is as shown in the Fig. 5 (b). The power generated by Latin Square configuration (3213 W) was more than double than TCT (1517 W). TCT, SP and BL configuration generated almost same amount of power.

(c) Long and Narrow shading conditions:

Here four different values of irradiance: 800 W/m^2, 600 W/m^2, 400 W/m^2 and 200 W/m^2 are considered. The shading dispersion for TCT and Latin Square configuration is as shown in Fig. 5 (c). The power generated under the proposed configuration (3091 W) was found out to be more than TCT (2894 W) by 6.8 percent. SP and BL configuration generated 2673 W and 2768 W respectively.

(d) Long and Wide shading conditions:

Most of the modules are shaded for this type of shading and so, power generated is less compared to other shading patterns. Nevertheless, power generated by proposed method (2917 W) was greater than other conventional methods. The shade dispersion is as shown in Fig. 5 (d).

(e) Non-continuous shading conditions:

In this, the shading considered is completely random. The power generated with proposed configuration was more than double as compared to other conventional methods (161 percent increase). The dispersion for TCT and Latin square method is as shown in Fig. 5 (e).

6 CONCLUSIONS

This paper presents a new configuration method namely, Latin Square reconfiguration that aims to increase the power generated by reducing the effect of partial shading. The shaded area is dispersed by physical relocation of the PV modules without any alteration in the electric connection. The simulation of 4x4 PV array under different shading pattern is

performed in MATLAB/SIMULINK for SP, BL, TCT and Latin Square configuration. The power generated for each shading pattern was found out to be maximum for proposed method compared to conventional configurations.

REFERENCES

[1] A. K. Abdelsalam, A. M. Massoud, S. Ahmed, and P. N. Enjeti, "High-performance adaptive perturb and observe MPPT technique for photovoltaic-based microgrids," *IEEE Trans. Power Electron.*, vol. 26, no. 4, pp. 1010–1021, Apr. 2011.
[2] Bidram A, Davoudi A, Balog S. Control and circuit techniques to mitigate partial shading effects in Photovoltaic arrays. IEEE Journal of Photovoltaics, 2012, 2(4): 532–546.
[3] G. Petrone, G. Spagnuolo, R. Teodorescu, M. Veerachary, and M. Vitelli, "Reliability issues in photovoltaic power processing systems," *IEEE Trans. Ind. Electron.*, vol. 55, no. 7, pp. 2569–2580, Jul. 2008.
[4] G. Sreenivasa Reddy, T. Bramhananda Reddy, M.Vijaya Kumar. "A MATLAB based PV Module Models analysis under Conditions of Nonuniform Irradiance", Energy Procedia, 2017.
[5] G. Velasco-Quesada, F. Guinjoan-Gispert, R. Pique-lopez, M. Roman-Lumbreras, and A. Conesa-Roca, "Electrical PV array reconfiguration strategy for energy extraction improvement in grid connected systems," *IEEE Trans. Ind. Electron.*, vol. 56, no. 11, pp. 4319–4331, Nov. 2009.
[6] H. Patel and V.Agarwal, "MATLAB based modelling to study the effects of partial shading on PV array characteristics," *IEEE Trans. EnergyConvers.*,vol. 23, no. 1, pp. 302–310, Mar. 2008.
[7] L. F. Lavado Villa, D. Picault, B. Raison, S. Bacha, and A. Labonne,"Maximizing the power output of partially shaded photovoltaic plants through optimization of the interconnections among its modules," *IEEE J. Photovoltaics*, vol. 2, no. 2, pp. 154–163, Apr. 2012.
[8] Mäki A, Valkealahti S. Power losses in long string and parallel connected short strings of series connected silicon-based photo-voltaic modules due to partial shading conditions. IEEE Transactions on Energy Conversion, 2012, 27(1): 173–183.
[9] P. Srinivasa Rao, G. Saravana Ilango and C. Nagamani, "Maximum Power from PV Arrays Using a Fixed Configuration Under Different Shading Conditions," in *IEEE Journal of Photovoltaics*, vol. 4, no. 2, pp. 679-686, March 2014. Doi: 10.1109/JPHOTOV.2014.2300239
[10] Srinivasa Rao P, Dinesh P, Saravana Ilango G, Nagamani C. Op-timal Su-Do-Ku based interconnection scheme for increased power output from PV array under partial shading. Frontiers in Energy, 2015, 9(2): 199–210.
[11] SREENIVASA REDDY, G; BRAMHANANDA REDDY, T; VIJAYA KUMAR, M. Shadow dispersion of PV Array under variable irradiance for superior power Generation by Magic Square Configuration. International Journal of Engineering & Technology, [S.l.], v. 7, n. 1.8, p. 172-177, feb. 2018. ISSN 2227-524X.

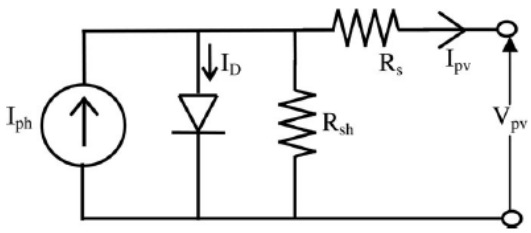

Fig. 1. Equivalent circuit of a PV cell.

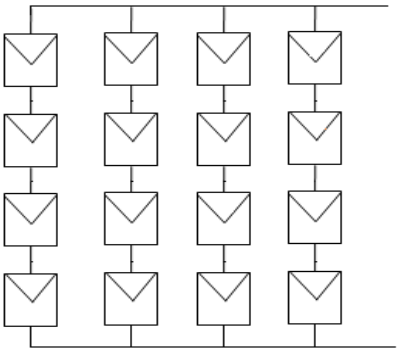

(1) SP Configuration

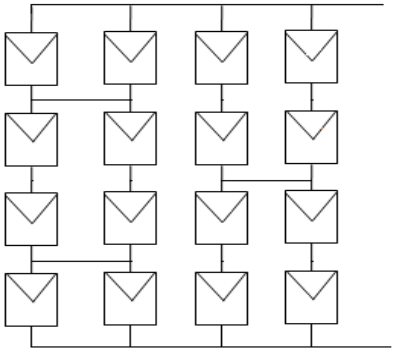

(2) BL Configuration

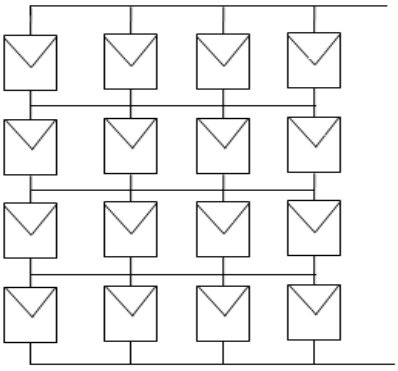

(3) TCT Configuration

Fig. 2. Different configurations shown for 4x4 PV array.

1	2	3	4
2	1	4	3
3	4	1	2
4	3	2	1

A	B	C	D
C	D	A	B
D	C	B	A
B	A	D	C

Fig. 3. Latin Squares for 4x4 array with numbers and alphabets

A1	B1	C1	D1
A2	B2	C2	D2
A3	B3	C3	D3
A4	B4	C4	D4

(a)

A1	B2	C3	D4
C2	D1	A4	B3
D3	C4	B1	A2
B4	A3	D2	C1

(b)

Fig. 4. (a) Normal PV array and (b)After reconfiguration using Latin Square method.

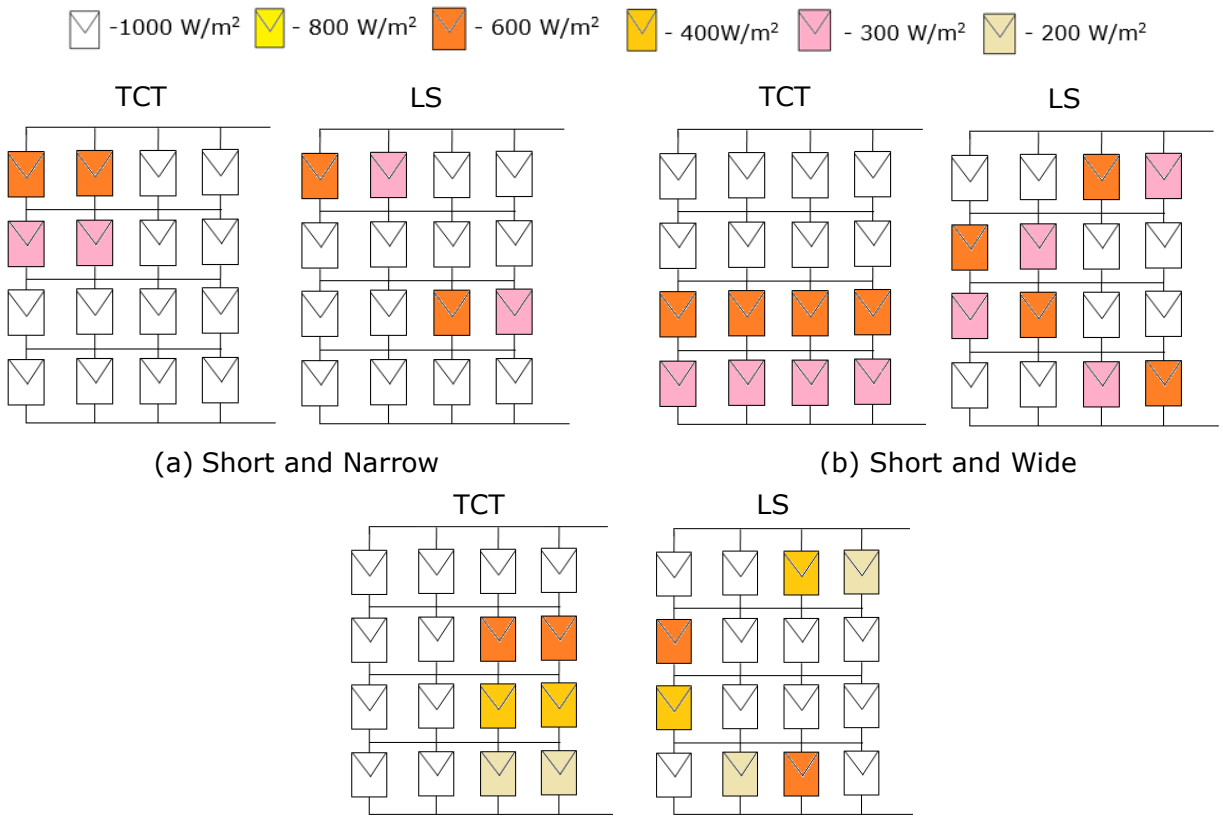

(a) Short and Narrow

(b) Short and Wide

(c) Long and Narrow

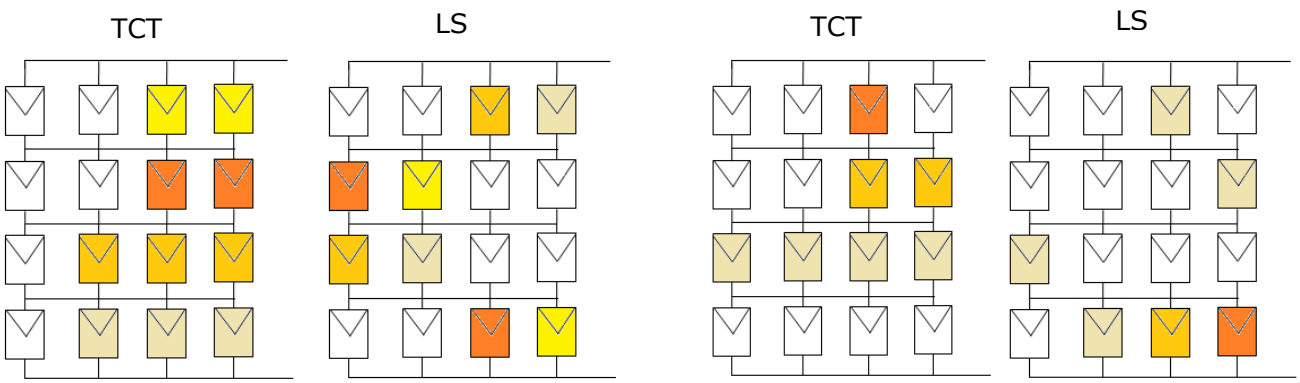

(d) Long and Wide (e) Non- Continuous

Fig. 5. Dispersion of shade shown for TCT and Latin Square configuration respectively for different types of shading pattern.

	SP	BL	TCT	Latin Square
Short Narrow	2907	3009	3156	3400
Short Wide	1516	1516	1516	3213
Long Narrow	2673	2768	2894	3091
Long Wide	1804	1938	1976	2917
Non-Continuous	1018	1019	1022	2676

Table 1 Power generated (W) in a 4x4 PV array for different configurations under different shading patterns.

8th International Engineering Symposium - IES 2019
March 13-15, 2019, Kumamoto University, Japan

A Frequency Reconfigurable Antenna for Cognitive Radio Applications

Naveen Jacob[1], K. Krishnamoorthy[2] and **Muralidhar Kulkarni[3]**

1 *Department of Electronics & Communication Engineering, National Institute of Technology Karnataka, Surathkal, Mangalore 575025, India. email:naveenjacob@yahoo.com*
2 *Department of Electronics & Communication Engineering, National Institute of Technology Karnataka, Surathkal, Mangalore 575025, India. e-mail:krishnak_ece@yahoo.com*
3 *Department of Electronics & Communication Engineering, National Institute of Technology Karnataka, Surathkal, Mangalore 575025, India. e-mail:mkuldce@gmail.com*

ABSTRACT: Cognitive Radio (CR) is designed to achieve intelligent spectrum sensing and sharing, inorder to solve spectrum underutilization problem. Conventional CRs uses multiple/multiport antenna to switch between Ultra Wide Band (UWB) and Narrow Band (NB) frequencies for primary and secondary users. In this communication, we propose a compact frequency reconfigurable single port antenna using PIN diodes, to switch between UWB and NB frequencies. A circular disc monopole antenna with partial ground plane is designed to deliver UWB response. Three Interdigital capacitors are electrically connected to partial ground plane and feed line using PIN diodes. OFF condition of PIN diode will provide the UWB response of 2.7 GHz to 12 GHz and ON condition of diode will result in multiple narrow band frequencies at 1.26 GHz, 2.6 GHz, 3.8 GHz, 4.7 GHz, 5.8 GHz, 6.86 GHz, 7.1 GHz, 8.2 GHz. 8.3 GHz, 10.75 GHz and 11.6 GHz.

Keywords*: Cognitive Radio, Frequency Reconfigurable, Interdigital Capacitor, Monopole Antenna, PIN Diode, Ultra Wide Band*

INTRODUCTION

In modern wireless communication system, different applications with pre-assigned operating frequency bands are integrated to a single system. This requires design and integration of multiple antennas with different operating bands, polarization and radiation pattern diversity on the same device, which results in the increase of complexity, size and cost. Hence the design of single antenna with multi-functional capability which can exhibit different characteristics, as per the requirement, has received lot of research attention. Reconfigurable microstrip antennas are highly accredited solution for this problem and are extensively investigated during last decade. [Hamid Boudaghi et al. (2012)]

One of the major application of reconfigurable antenna is in Cognitive Radio (CR) system, which provides a prospective solution for spectrum underutilization problem. In CR system the primary users are assigned to specific frequency bands of the channel while, secondary users are allowed to use the unoccupied parts of the spectrum by spectrum sensing process, resulting in efficient utilization of spectrum. Therefore a CR requires a "sensing antenna", which must have wide band response to scan full spectrum inorder to identify the unused frequency bands and numerous narrow band "communicating antennas" to operate at specific frequency bands. Conventional CRs uses multiple/multiport antennas for sensing and communicating. [G. P. Jin et al. (2011)]

Several research works are reported on antennas that can be reconfigured to switch between UWB and NB frequencies. A small rectangular patch electrically connected to ground plane of rectangular monopole antenna is reported by James R. Kelly et al. (2010). Two monopole sharing a common ground plane is proposed by Eko Tjipto Rahardjo et al. (2011), where one antenna is used for sensing and other for communication. Optically controlled reconfigurable antenna is proposed by G. P. Jin et al. (2011). A mechanically reconfigured antenna is proposed by Y Tawk et al. (2011). Hamid Boudaghi et al. (2012) presented a monopole antenna which uses switchable slots in ground plane to achieve reconfigurability. K. Kandasamy et al. (2015) utilized the negative permeability of split ring resonators to switch between UWB and NB frequencies. Minakshi Tewari et al. (2016) proposed frequency reconfigurable antenna using pixel ground plane. Mansour Nejatijahromi et al. (2018) proposed a UWB to NB frequency switchable monopole antenna using variable capacitors.

In this communication we propose an antenna to switch between UWB and NB frequency responses by electrically connecting interdigital capacitors to ground plane as well as feed line using PIN diodes.

THEORY AND DESIGN APPROACH

Conventional monopole antennas will inherently deliver narrowband response. Removal of ground plane will result in wideband response due to the reduction in patch capacitance.

If we represent patch antenna in terms of parallel resonant L-C-G network, the quality factor, Q is given by the equation,

$$Q = \frac{\omega C}{G} \quad (1)$$

where, C is the patch capacitance and G is the patch conductance.
Q is related to bandwidth by the following equation: [K. C. Gupta (1988)]

$$BW = \frac{S-1}{Q\sqrt{S}} \quad (2)$$

where, S represents VSWR.

Thus it is clear that the removal of ground plane partially will result in reduction of capacitance, which will reduce the quality factor Q, resulting in the increase of bandwidth. Hence if we can tune the capacitance then the wide band to narrowband conversion can be realized.

ANTENNA GEOMETRY AND DESIGN

Circular disc monopole patch antenna with partial ground plane is selected for the design of UWB antenna. The schematic of the proposed antenna is shown in Fig. 1. All dimensions shown are in mm. The substrate material used is FR4 with ε_r=4.3 with loss tangent=0.025. The height of the substrate is 1.6mm. Radius of circular monopole is 9mm.

Now, for attaining narrow band responses, three interdigital capacitors with different parameters are electrically connected to partial ground as well as feed line using four PIN diodes, D1, D2, D3 and D4.

The equation for capacitance of interdigital capacitor shown in Fig. 2, is given by,

$$C = \left[\frac{\varepsilon_r + 1}{W}\right] L[(N-3)A_1 + A_2] \quad \text{pF/unit length} \quad (3)$$

where ε_r is the dielectric constant of the material, N is the no. of fingers, L is the length of the finger and W is the width of the interdigital capacitor. [Gary D. Alley (1979)]

A_1 and A_2 are given by,

$$A_1 = 4.409 \tanh\left[0.55\left(\frac{h}{X}\right)^{-0.45}\right] \times 10^{-6} \ (\text{pF}/\mu\text{m}) \quad (4)$$

$$A_2 = 9.92 \tanh\left[0.52\left(\frac{h}{X}\right)^{-0.5}\right] \times 10^{-6} \ (\text{pF}/\mu\text{m}) \quad (5)$$

where, h is the height of substrate and X is the finger width of interdital capacitor. [Beeresha R. S. et al. (2016)]

Each interdigital capacitors are designed with different no. of fingers (N), width (W) length (L) and finger width (X) to provide different values of capacitance, so that the effective patch capacitance can be tuned.

SIMULATION AND RESULTS

CST Microwave Studio Suite environment, is employed for the simulation of antenna with different switching configurations of PIN diodes. PIN diode switch is modelled as a resistor. During simulation, the value of diode resistance is set as 1 ohm, for "ON" condition and 10^6 ohms, for "OFF" condition.

When all diodes are in OFF condition, all interdigital capacitors are electrically isolated from the antenna and UWB response results, with a band from 2.7 GHz to 12 GHz. When one or more diodes are in ON condition, the patch capacitance will be varied by interdigital capacitor resulting in multiple narrowband frequency responses.

Reflection coefficient and gain of the antenna for UWB and NB frequency responses, based on different diode switching conditions of PIN diodes are shown in Fig. 3, Fig. 4, Fig. 5 and Fig. 6. Tabulated results are shown in Table 1. E-plane and H-plane radiation patterns at some of the operating frequencies are shown in Fig. 7, Fig. 8, Fig. 9 and Fig. 10.

CONCLUSIONS

A new frequency reconfigurable antenna is presented, which can be tuned to UWB as well as many narrow band frequencies. It comprises of a monopole antenna with partial ground plane and 3 interdigital capacitors connected to ground plane and feed line using PIN diodes. The following conclusions are deduced from this work:

- The antenna can be functioned in "sensing mode" which needs the UWB response.
- The same antenna can be operated in "communicating mode" by switching and selecting any band, out of the 11 narrow bands.

Simulated results shows that the proposed antenna is an impending candidate for cognitive radio applications.

REFERENCES

[1] A. Mansoul et al. (2014), A Selective Frequency-Reconfigurable Antenna for Cognitive Radio Applications, IEEE Antennas and Wireless Propagation Letters, Vol. 13, pp. 515-518.

[2] Beeresha R. S et al. (2016), Design and Optimization of Interdigital Capacitor, International Journal of Research in Engineering & Technology, Vol.5, No.21.

[3] Eko Tjipto Rahardjo et al. (2011), Printed Antenna design for Cognitive Radio Application at 1.8 GHz and 2.35 GHz Spectrum Allocation, Proc. Asia Pacific Microwave Conference, pp. 1881-1884.

[4] Gary D. Alley (1970), Interdigital Capacitors and Their Applications to Lumped-Element Microwave Integrated Circuits, IEEE Transactions on Microwave theory and Techniques, Vol.18, No.12, pp. 1028-1033.

[5] G. P. Jin et al. (2011), Optically Controlled Reconfigurable Antenna for Cognitive Radio Applications, Electronic Letters, Vol.47, No.17, pp. 948-950.

[6] Hamid Boudaghi et al. (2012), A Frequency Reconfigurable Monopole Antenna Using Switchable Slotted Ground Structure, IEEE Antennas and Wireless Propagation Letters, Vol.11, pp. 655-658.

[7] Harish Rajagopalan et al. (2014), MEMS Reconfigurable Optimized E-Shaped Patch Antenna Design for Cognitive Radio, IEEE Transactions on Antennas and Propagation, Vol.62, No.3, pp. 1056-1064.

[8] H. Lalj et al. (2014), Peconfigurable Multi Band Notches Antenna for Cognitive Radio Applications, XXXIth URSI General Assembly and Scientific Symposium, pp. 1-4.

[9] James R. Kelly et al. (2010), Integrated Wide-Narrow Band Antenna for Switched Operation, Microwave & Optical Technology Letters, Vol. 52, No.8, pp. 1705-1707.

[10] K. Kandasamy et al. (2015), Design of SRR Loaded Reconfigurable Antenna for UWB and Narrow Band Applications, IEEE International Symposium on Antennas and Propagation & USNC/URSI National Radio Science Meeting, pp. 1192-1193.

[11] K. C. Gupta (1988), Broadbanding Techniques for Microstrip Patch Antennas - A Review, Scientific Report, University of Colorado.

[12] Mansour Nejatijahromi et al. (2018), Switchable Planar Monopole Antenna Between Ultra-Wideband and Narrow Band Behaviour, Progress in Electromagnetics Research Letters, Vol.75, pp. 131-137.

[13] M. Karmugil and K. Anusudha (2016), Design of Circular Microstrip Antenna for Ultra Wide Band Applications, International Conference on Control, Instrumentation, Communication and Computational Technologies, pp. 304-308.

[14] Minakshi Tewari et al. (2016), Frequency Reconfigurable Antenna: Using Pixel Ground, International Conference on Recent Advances and Innovations in Engineering (ICRAIE), pp. 1-6.

[15] Paritosh Peshwe and Ashwin Kothari (2018), Performance Enhancement of Millimeter Wave Antenna with Integrated Inter-Digital Capacitor Structure, Radio Engineering, Vol.27, No.3, pp. 651-661.

[16] Y. Tawk et al. (2011), Implementation of a Cognitive Radio Front-End Using Rotatable Controlled Reconfigurable Antennas, IEEE Transactions on Antenna and Propagation, Vol.59, No.5, pp. 1773-1778.

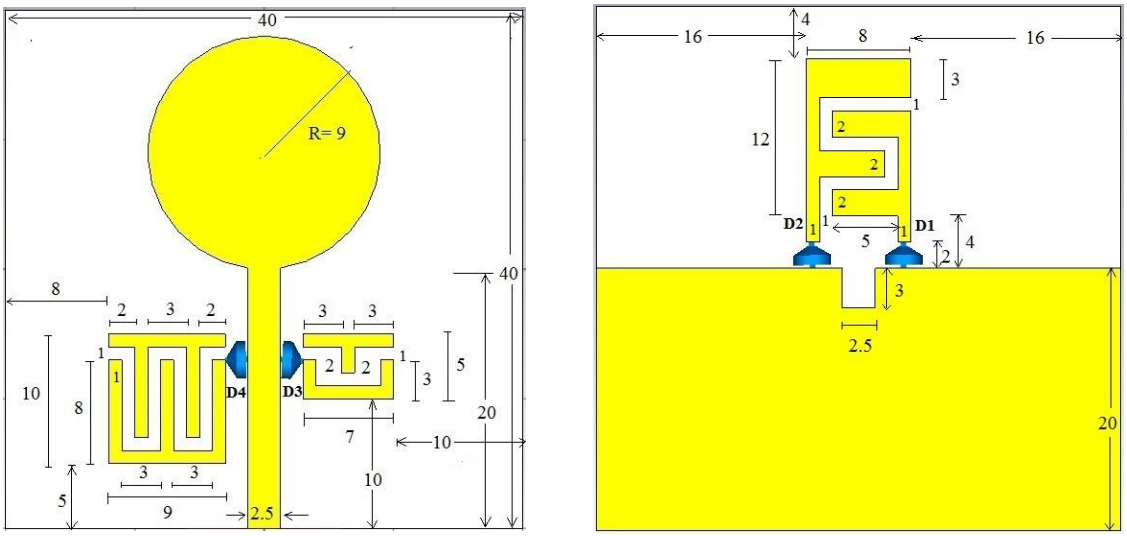

(a) **(b)**

Fig. 1. Schematic of proposed Antenna – (a) Front View (b) Back View (All dimensions are in mm)

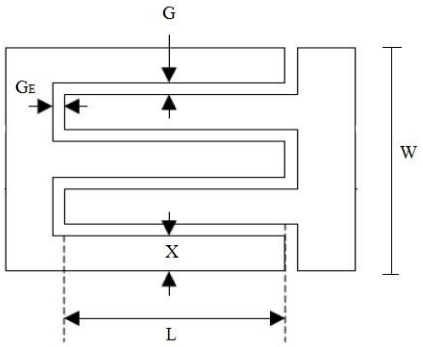

Fig. 2. Interdigital Capacitor

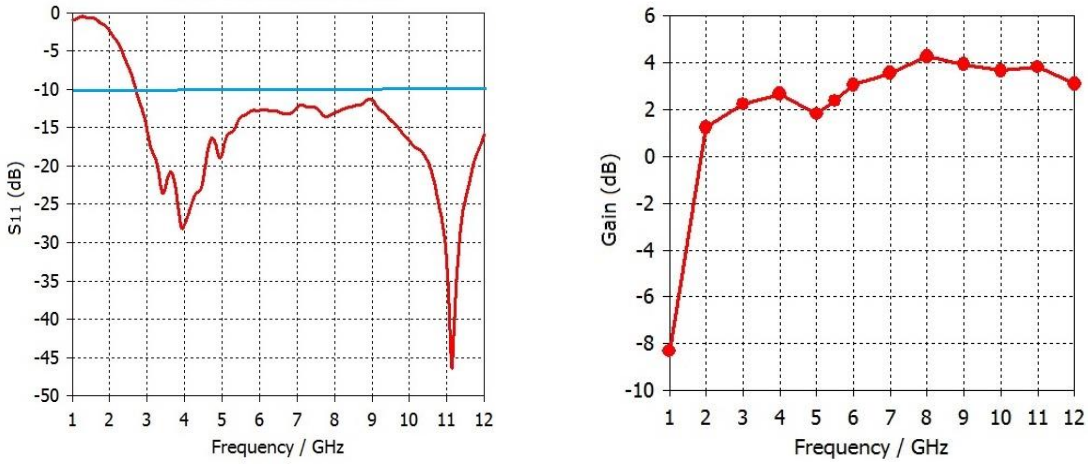

Fig. 3. (a) Simulated S11 (b) Gain - All diodes OFF condition – UWB Response

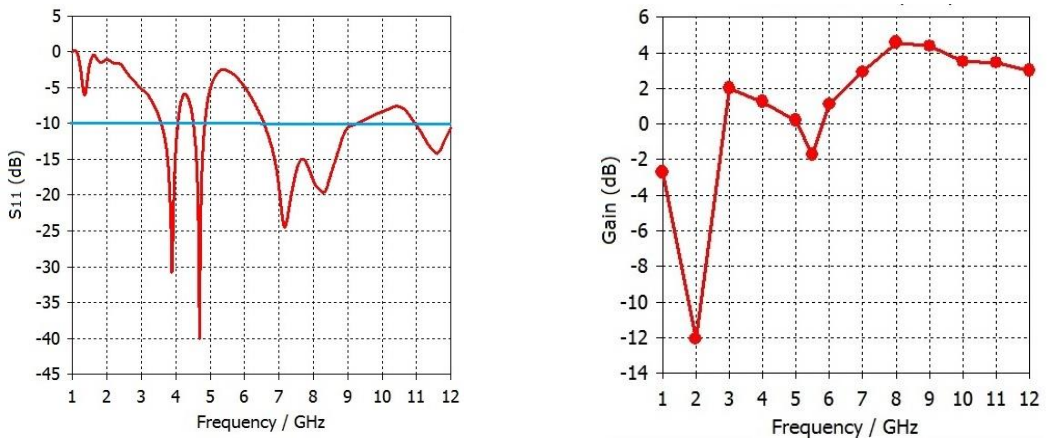

Fig. 4. (a) Simulated S11 (b) Gain - D1, D2 – ON and D3, D4 - OFF condition

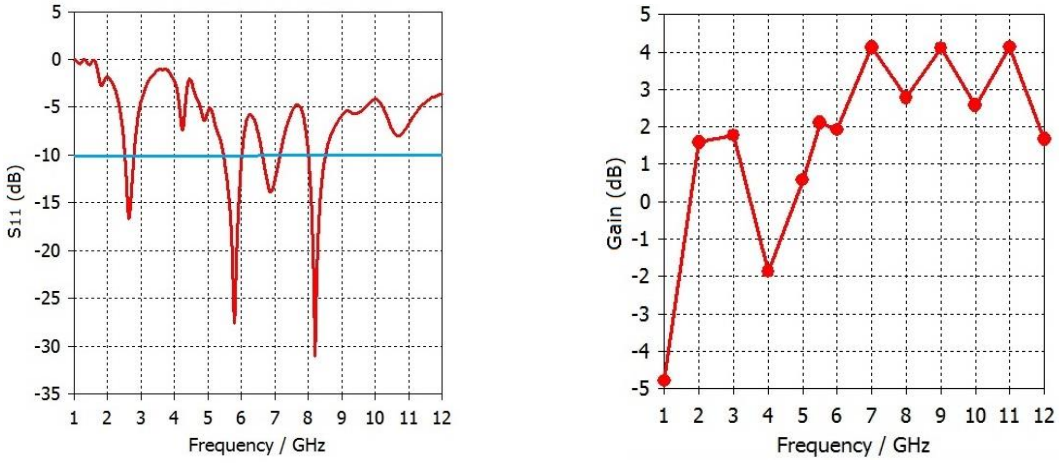

Fig. 5. (a) Simulated S11 (b) Gain - D1, D2 – OFF and D3, D4 - ON

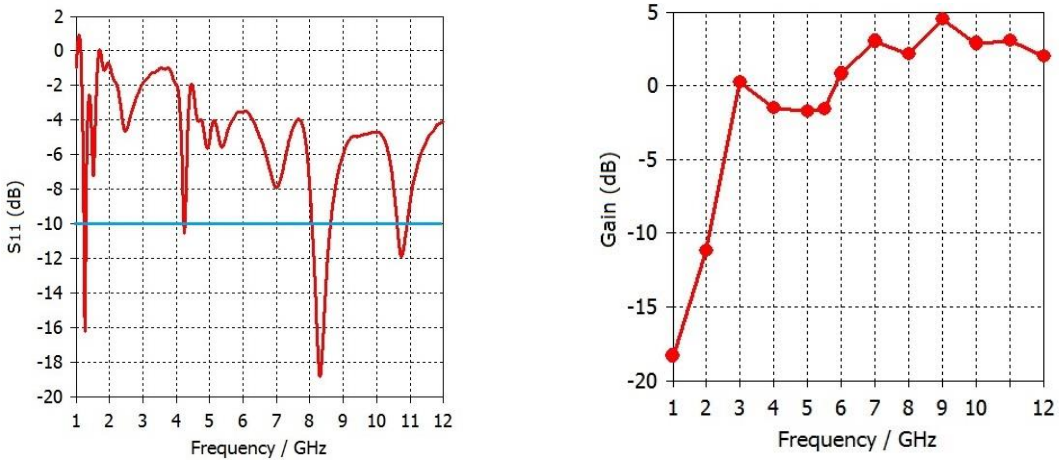

Fig. 6. (a) Simulated S11 (b) Gain - All diodes ON condition

Table 1. Diode Switching Conditions

Diode Condition	Frequency (GHz)	Bandwidth
All Diodes - OFF	UWB Response (2.7 -12)	9.3 GHz
D1, D2 - ON D3, D4 - OFF	3.88, 4.7, 7.1, 11.6	468 MHz, 306 MHz, 2.7 GHz & 2.3 GHz respectively
D1, D2 - OFF D3, D4 - ON	2.6, 5.8, 6.86, 8.2	278 MHz, 541 MHz, 515 MHz & 516 MHz respectively
All Diodes - ON	1.26, 8.31, 10.75	73.7 MHz, 512 MHz & 294 MHz respectively

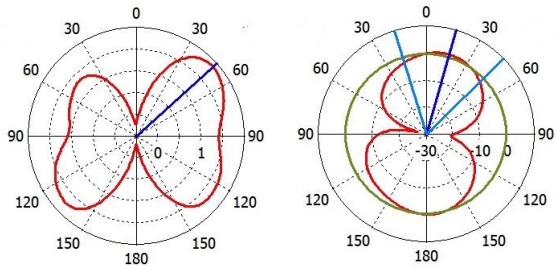

Fig. 7. Radiation pattern at 6 GHz of UWB response – (a) E-Plane (b) H-Plane

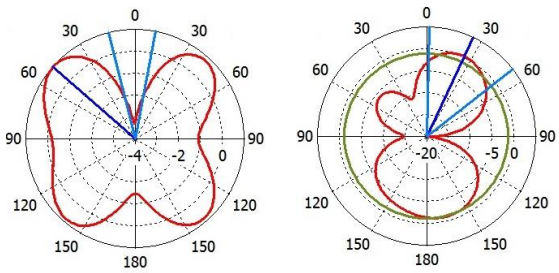

Fig. 8. Radiation pattern at 5.8 GHz – (a) E-Plane (b) H-Plane

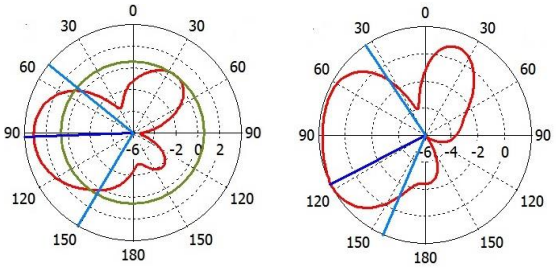

Fig. 9. Radiation pattern at 7.1 GHz – (a) E-Plane (b) H-Plane

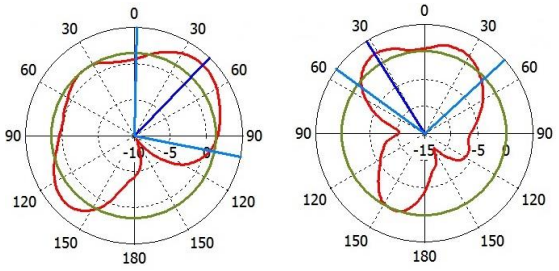

Fig. 10. Radiation pattern at 10.75 GHz – (a) E-Plane (b) H-Plane

8th International Engineering Symposium - IES 2019
March 13-15, 2019, Kumamoto University, Japan

Adaptive parameter choice strategy for fractional Tikhonov regularization method

K. Kanagaraj

Department of MACS, National Institute of Technology Karnataka, Surathkal, Mangalore 575025, India. email: kanagaraj102@gmail.com

ABSTRACT: Fractional regularization method is introduced to overcome over smoothness of the regularized solution. In regularization theory finding a suitable regularized parameter is very crucial part. In this paper we used adaptive parameter choice strategy proposed by Pereverzev and Schock for choosing the regularization parameter in fractional Tikhonov regularization method.

Keywords*: fractional Tikhonov regularization, ill-posed equations, regularization parameter, convergence rate, adaptive method.*

1 INTRODUCTION

Let $T : X \to Y$ be a bounded linear operator between Hilbert spaces X and Y with non-closed range $R(T)$ and $y \in R(T) + R(T)^{\perp}$. We consider the problem of approximating the minimal norm least square solution $\hat{x} = T^{\dagger} y$ of ill-posed operator equation

$$T x = y \qquad (1.1)$$

With the help of well-posed equations [Engl H W.et al. (1996), Groetsch C W (1997), Nair M T (2009)]. Here $T^{\dagger}$ is the Moore-Penrose generalized inverse of T. In practice, the data y is contaminated by noise. Thus, instead of y, we have a noisy data y^{δ} with

$$\|y - y^{\delta}\| \leq \delta. \qquad (1.2)$$

Many authors considered fractional or weighted Tikhonov regularization method [Gerth D. et al. (2015), Hochstenbach M E. et al. (2011), Klann E. et al. (2008), Reddy G D (2018)] for approximating $\hat{x}$ and overcome the over smoothness. In this method the minimizer of the functional

$$J_{\alpha,\omega}(x) = \|T x - y^{\delta}\|_{W}^{2} + \alpha \|x\|^{2} \quad (1.3)$$

is taken as an approximation for $\hat{x}$. Here

$$\|y\|_{W} = \left\| W^{\frac{\beta}{2}} y \right\|_{Y}, \quad \beta \in [-\tfrac{1}{2}, 0] \quad (1.4)$$

with $W = (T T^{*})$ is the weighted semi-norm.

The minimizer of (1.3) with semi-norm (1.4) is given by

$$x_{\alpha,\beta}^{\delta} = \left((T^{*} T)^{1+\beta} + \alpha I\right)^{-1} (T^{*} T)^{\beta} T^{*} y^{\delta}. \quad (1.5)$$

Let

$$x_{\alpha,\beta} = \left((T^{*} T)^{1+\beta} + \alpha I\right)^{-1} (T^{*} T)^{\beta} T^{*} y \quad (1.6)$$

and let

$$\hat{x} \in ((T^{*} T)^{\nu}), \quad 0 < \nu \leq 1 + \beta. \qquad (1.7)$$

We use the following results for our error analysis.

PROPOSITION 1.1 (George S. et al.) Let $x_{\alpha,\beta}^{\delta}$ and $x_{\alpha,\beta}$ be as in (1.5) and (1.6), respectively. Let $\hat{x}$ satisfies (1.7). Then

(i) $\left\|x_{\alpha,\beta}^{\delta} - x_{\alpha,\beta}\right\| \leq C_1 \frac{\delta}{\frac{1}{\alpha^{2(1+\beta)}}}$

(ii) $\left\|\hat{x} - x_{\alpha,\beta}\right\| \leq C_2 \, \alpha^{\frac{\nu}{1+\beta}}$

In particular, we have

$$\left\|\hat{x} - x_{\alpha,\beta}^{\delta}\right\| \leq C \left(\frac{\delta}{\frac{1}{\alpha^{2(1+\beta)}}} + \alpha^{\frac{\nu}{1+\beta}} \right),$$

Where $C = max\{C_1, C_2\}$ and C, C_1 and C_2 are constants.

2.Adaptive selection of the parameter

From above proposition, we have

$$\left\|\hat{x} - x_{\alpha,\beta}^{\delta}\right\| \leq C \left(\frac{\delta}{\frac{1}{\alpha^{2(1+\beta)}}} + \alpha^{\frac{\nu}{1+\beta}} \right). \quad (2.1)$$

Further observe that the error $\frac{\delta}{\frac{1}{\alpha^{2(1+\beta)}}} + \alpha^{\frac{\nu}{1+\beta}}$ in (2.1) is optimal order if $\alpha_{\delta} := \alpha(\beta, \delta)$ satisfies, $\frac{\delta}{\frac{1}{\alpha^{2(1+\beta)}}} = \alpha^{\frac{\nu}{1+\beta}}$. That is $\alpha_{\delta} = \delta^{\frac{2(1+\beta)}{2\nu+1}}$. In order to obtain the optimal

order in (2.1), Pereverzev S and Schock E (2005), introduced the adaptive parameter choice strategy, we modified adaptive method suitably for the situation for choosing the parameter α.

Let $i \in \{0, 1, 2, \cdots, N\}$ and $\alpha_i = \mu^i \alpha_0$ where $\mu > 1$ and $\alpha_0 > \delta$. Let

$$l := \left\{ i : \alpha_i^{\frac{\nu}{1+\beta}} \leq \frac{\delta}{\frac{1}{\alpha_i^{2(1+\beta)}}} \right\} < N \qquad (2.3)$$

and

$$k := \left\{ i : \left\| x^{\delta}_{\alpha_i,\beta} - x^{\delta}_{\alpha_j,\beta} \right\| \leq \frac{4C\delta}{\frac{1}{\alpha_j^{2(1+\beta)}}}, j = 0, \dots, i-1 \right\} \qquad (2.4)$$

THEOREM 2.1

Assume that there exists $i \in \{0, 1, 2, \cdots, N\}$ such that $\alpha_i^{\frac{\nu}{1+\beta}} \leq \frac{\delta}{\frac{\delta}{\frac{1}{\alpha_i^{2(1+\beta)}}}}$. Let assumptions of proposition 1.1 is fulfilled, and let l and k be as in (2.3) and (2.4) respectively. Then $l \leq k$; and

$$\left\| x^{\delta}_{\alpha_k,\beta} - \hat{x} \right\| \leq 6\, C\, \mu^{\frac{2\nu+1}{2(1+\beta)}}\, \delta^{\frac{2\nu}{2\nu+1}} .$$

Proof. To prove $l \leq k$, it is enough to show that, for each $i \in \{0, 1, 2, \cdots, N\}$,

$$\alpha_i^{\frac{\nu}{1+\beta}} \leq \frac{\delta}{\frac{1}{\alpha_i^{2(1+\beta)}}} \Rightarrow \left\| x^{\delta}_{\alpha_i,\beta} - x^{\delta}_{\alpha_j,\beta} \right\| \leq \frac{4C\delta}{\frac{1}{\alpha_j^{2(1+\beta)}}},$$

$$\forall\, j = 0,1,2,\dots,i-1 .$$

For $j < i$, we have

$$\left\| x^{\delta}_{\alpha_i,\beta} - x^{\delta}_{\alpha_j,\beta} \right\| \leq \left\| x^{\delta}_{\alpha_k,\beta} - \hat{x} \right\| + \left\| \hat{x} - x^{\delta}_{\alpha_k,\beta} \right\|$$

$$\leq C \left(\alpha_i^{\frac{\nu}{1+\beta}} + \frac{\delta}{\frac{\delta}{\frac{1}{\alpha_i^{2(1+\beta)}}}} \right) + C \left(\alpha_j^{\frac{\nu}{1+\beta}} + \frac{\delta}{\frac{\delta}{\frac{1}{\alpha_j^{2(1+\beta)}}}} \right)$$

$$\leq 2\, C\, \alpha_i^{\frac{\nu}{1+\beta}} + 2\, C\, \frac{\delta}{\frac{1}{\alpha_j^{2(1+\beta)}}} \leq 4\, C\, \frac{\delta}{\frac{1}{\alpha_j^{2(1+\beta)}}} .$$

Thus, the relation $l \leq k$ is proved. Further note that

$$\left\| \hat{x} - x^{\delta}_{\alpha_k,\beta} \right\| \leq \left\| \hat{x} - x^{\delta}_{\alpha_l,\beta} \right\| + \left\| x^{\delta}_{\alpha_l,\beta} - x^{\delta}_{\alpha_k,\beta} \right\|$$

Where $\left\| \hat{x} - x^{\delta}_{\alpha_l,\beta} \right\| \leq C \left(\alpha_l^{\frac{\nu}{1+\beta}} + \frac{\delta}{\frac{\delta}{\frac{1}{\alpha_l^{2(1+\beta)}}}} \right)$

$$\leq 2\, C\, \frac{\delta}{\frac{1}{\alpha_l^{2(1+\beta)}}}.$$

Now since $l \leq k$, we have

$$\left\| x^{\delta}_{\alpha_k,\beta} - x^{\delta}_{\alpha_l,\beta} \right\| \leq 4\, C\, \frac{\delta}{\frac{1}{\alpha_l^{2(1+\beta)}}}.$$

Hence

$$\left\| \hat{x} - x^{\delta}_{\alpha_k,\beta} \right\| \leq 6\, C\, \frac{\delta}{\frac{1}{\alpha_l^{2(1+\beta)}}}.$$

Now, since

$$\alpha_\delta^{\frac{2\nu+1}{2(1+\beta)}} = \delta \leq \alpha_{l+1}^{\frac{2\nu+1}{2(1+\beta)}} \leq \mu^{\frac{2\nu+1}{2(1+\beta)}}\, \alpha_l^{\frac{2\nu+1}{2(1+\beta)}}$$

it follows that

$$\frac{\delta}{\frac{\delta}{\frac{1}{\alpha_\delta^{2(1+\beta)}}}} \leq \frac{\delta}{\frac{\delta}{\frac{1}{\alpha_l^{2(1+\beta)}}}} \leq \mu^{\frac{2\nu+1}{2(1+\beta)}}\, \alpha_l^{\frac{\nu}{(1+\beta)}}$$

$$\leq \mu^{\frac{2\nu+1}{2(1+\beta)}}\, \alpha_\delta^{\frac{\nu}{(1+\beta)}} + \mu^{\frac{2\nu+1}{2(1+\beta)}}\, \delta^{\frac{2\nu}{2\nu+1}}.$$

This completes the proof.

2.1 Implementation of adaptive choice rule

The balancing algorithm associated with the choice of the parameter specified in Theorem 2.1 involves the following steps:

- Choose $\alpha_0 > 0$ and $\mu > 1$.
- Choose $\alpha_i := \mu^i\, \alpha_0,\ i = 0,1,\dots,N$.

2.2 Algorithm

1. Set $i = 0$.
2. Solve $x^{\delta}_{\alpha_i,\beta}$ by using (1.5).
3. If $\left\| x^{\delta}_{\alpha_i,\beta} - x^{\delta}_{\alpha_j,\beta} \right\| \leq \frac{4C\,\delta}{\frac{1}{\alpha_j^{2(1+\beta)}}}, j = 0, \dots, N$ then take $k = i-1$ and return $x_{\alpha_k,\beta}$.
4. Else set $i = i+1$ and go to step 2.

3. Examples

Example 3.1

We consider Shaw example from the Regularization Toolbox by Hansen P C (2007) with n points. It is defined as follows:

$$[T\,x](s) := \int_{-\pi}^{\pi} k(s,t)\, x(t)\, dt = y(s), -\pi \leq s \leq \pi$$

Where $k(s,t) = (\cos(s) + \cos(t))^2 \left(\frac{\sin(u)}{u} \right)^2$,

$u = \pi\, (\sin(s) + \sin(t))$.

We have introduced random noise level $\delta = 0.05$ and 0.01 in the exact data. Relative error $\alpha := \alpha_k$ obtained using

adaptive method is given in Table 1 for different values of β, n and δ; and the best reconstruction took place at $\beta = -0.15$ and -0.25. Plots of Shaw example are given in Figures 1 and 2.

Example 3.2

We choose Fox good example from the Regularization Toolbox by Hansen with n points. It is defined as follows:

$$[T_1\, x_1](s) := \int_0^1 \sqrt{s^2 + t^2}\;\; x_1(t)\, dt = y_1(s),$$

where $0 \le s \le 1$, $y_1(s) = \frac{1}{3}\left((1+s^2)^{\frac{3}{2}} - s^3\right)$ and solution $x_1(t) = t$. We have introduced random noise level $\delta = 0.05$ and 0.01 in the exact data. Relative error $\alpha := \alpha_k$ obtained using adaptive method is given in Table 2 for different values of β, n and δ; and the best reconstruction took place at $\beta = -0.15$ and -0.25. Plots of Shaw example are given in Figures 3 and 4.

CONCLUSIONS

In this paper we have considered fractional Tikhonov regularization method for ill-posed operator equations in Hilbert spaces. We choose the regularization parameter using the adaptive parameter choice strategy proposed by Pereverzev and Schock (2005) and obtained the optimal order error estimate for $\|\hat{x} - x^{\delta}_{\alpha,\beta}\|$. The numerical results confirm the theoretical results.

ACKNOWLEDGEMENTS

The author would like to thank National Institute of Technology Karnataka, India, for the financial support for to carry out this research and also Kumamoto University for this opportunity to present the paper under Spring Internship program.

REFERENCES

[1] Engl H W, Hanke M and Neubauer (1996), Regularization of Inverse Problems, Kluwer, Dordrecht.

[2] George S, Reddy G D and Kanagaraj K, Parameter choice by discrepancy principles for fractional Tikhonov regularization method leading to optimal convergence rates (Communicated).

[3] Gerth D, Klann E, Ramalu R and Reichel L (2015), On Fractional Tikhonov Regularization, J. Inverse Ill-Posed Probl., Vol.23, No., pp 611-625.

[4] Groetsch C W (1977), Generalized Inverse of Linear Operators: Representation and Application, Marcel Dekker, New York.

[5] Hansen P C (2007), Regularization Tools version 4.0 for Matlab 7.3, Numer. Algorithms, Vol.46, No., pp 189-194.

[6] Hochstenbach M E and Reichel L (2011), Fractional Tikhonov Regularization for Linear Discrete Ill-Posed problems, BIT Numerical Mathematics, Vol.51, No., pp 197-215.

[7] Klann E and Ramalu R (2008), Regularization by Fractional Filter Methods and Data Smoothing, Inverse Problems, Vol.24, No., pp 113-129.

[8] Nair M T (2009), Linear Operator Equations: Approximation and Regularization, World Scientific, Singapore.

[9] Pereverzev S and Schock E (2005), On the adaptive selection of the parameter in regularization of ill-posed problems, SIAM J. Numer. Anal., Vol.43, No.5, pp.2060-2076.

[10] Reddy G D (2018), The parameter choice rules for weighted Tikhonov regularization scheme, Comp. Appl. Math., Vol.37, No.2, pp.2039-2052.

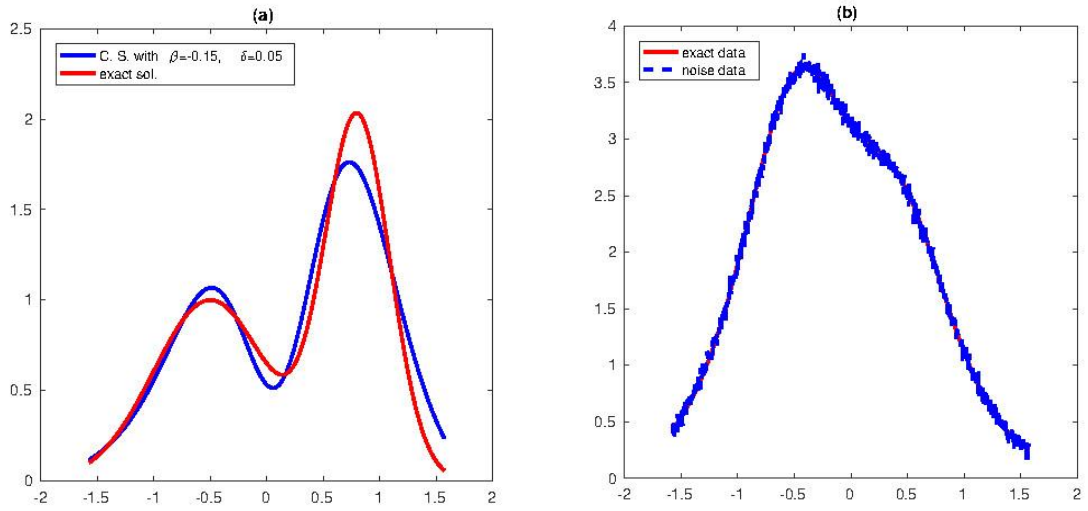

Fig.1: (a) Solution and (b) data of Shaw example with $\beta = -0.25, \delta = 0.05$ and $n = 1000$.

Table.1 Relative errors of Shaw example using adaptive choice rule

β		n=100		n=500		n=1000	
		$\delta = 0.05$	$\delta = 0.01$	$\delta = 0.05$	$\delta = 0.01$	$\delta = 0.05$	$\delta = 0.01$
-0.15	α_k	1.1562e-01	1.0671e-01	4.0526e-02	3.4003e-03	2.7680e-02	2.1113e-03
	$E_{\alpha_k,\beta}$	1.8586e-01	1.2357e-01	1.5553e-01	8.9659e-02	1.4914e-01	7.2042e-02
-0.25	α_k	1.5389e-01	2.5163e-02	7.8974e-02	8.0179e-03	5.9334e-02	5.4763e-03
	$E_{\alpha_k,\beta}$	1.9614e-01	1.3374e-01	1.7088e-01	9.5391e-02	1.6439e-01	8.6191e-02
-0.35	α_k	2.0434e-01	5.3940e-02	1.1562e-01	1.8905e-02	8.6872e-02	1.4204e-02
	$E_{\alpha_k,\beta}$	2.0505e-01	1.4690e-01	1.8085e-01	1.0643e-01	1.6611e-01	9.7066e-02

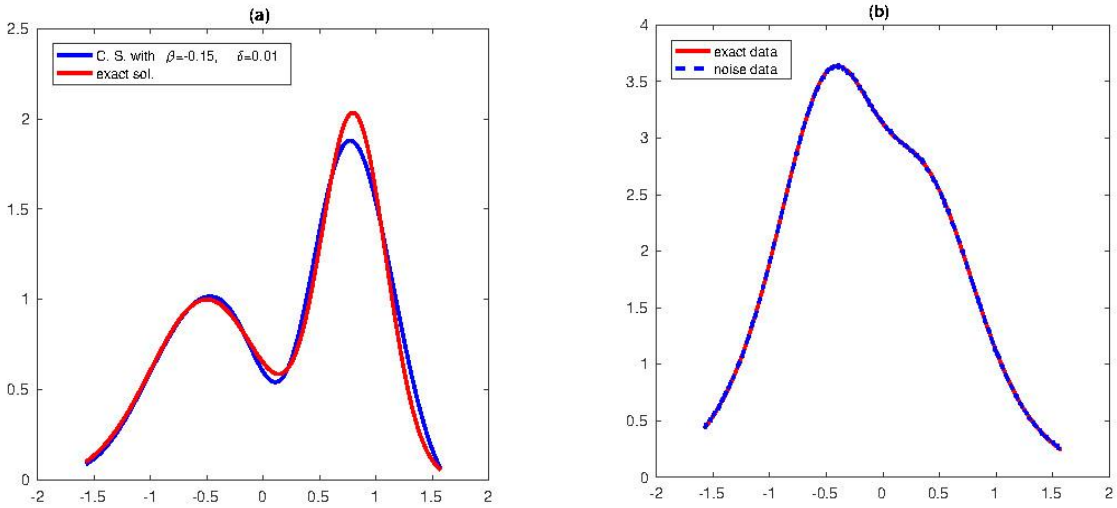

Fig.2: (a) Solution and (b) data of Shaw example with $\beta = -0.15, \delta = 0.01$ and $n = 1000$.

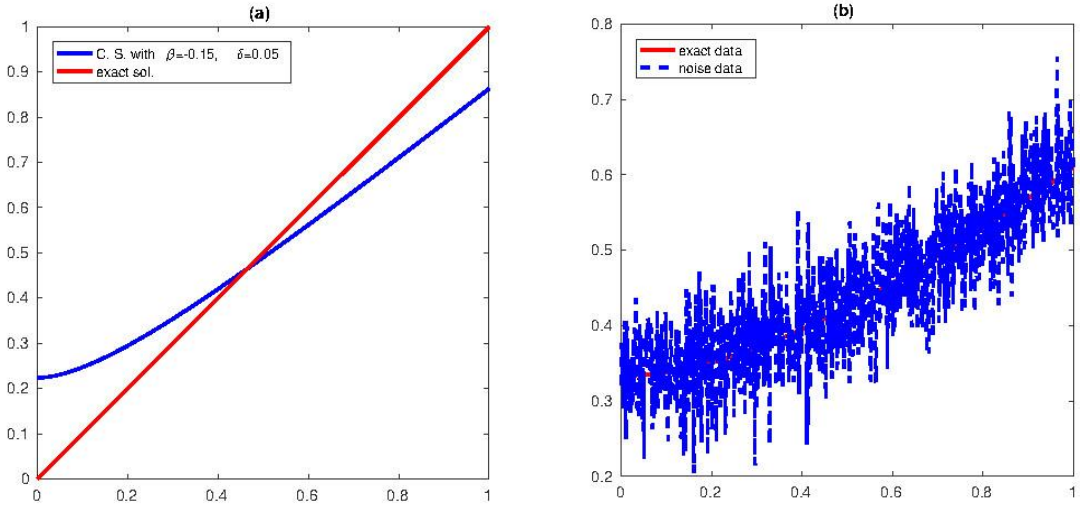

Fig.3: (a) Solution and (b) data of Foxgood example with $\beta = -0.25, \delta = 0.05$ and $n = 1000$.

Table.2 Relative errors of Foxgood example using adaptive choice rule

β		n=100		n=500		n=1000	
		$\delta = 0.05$	$\delta = 0.01$	$\delta = 0.05$	$\delta = 0.01$	$\delta = 0.05$	$\delta = 0.01$
-0.15	α_k	1.1562e-01	1.4204e-02	3.6842e-02	7.2890e-03	2.0796e-02	4.9785e-03
	$E_{\alpha_k,\beta}$	2.7689e-01	1.0924e-01	1.8815e-01	7.5914e-02	1.3114e-01	6.2774e-02
-0.25	α_k	1.5389e-01	2.5163e-02	6.5268e-02	1.2912e-02	4.4579e-02	1.0671e-02
	$E_{\alpha_k,\beta}$	2.9580e-01	1.2150e-01	2.0888e-01	8.5154e-02	1.8300e-01	8.2291e-02
-0.35	α_k	2.0484e-01	4.9037e-02	1.0511e-01	2.5163e-02	7.8974e-02	2.0796e-02
	$E_{\alpha_k,\beta}$	2.9959e-01	1.5805e-01	2.3821e-01	1.0295e-01	2.0145e-01	9.4474e-02

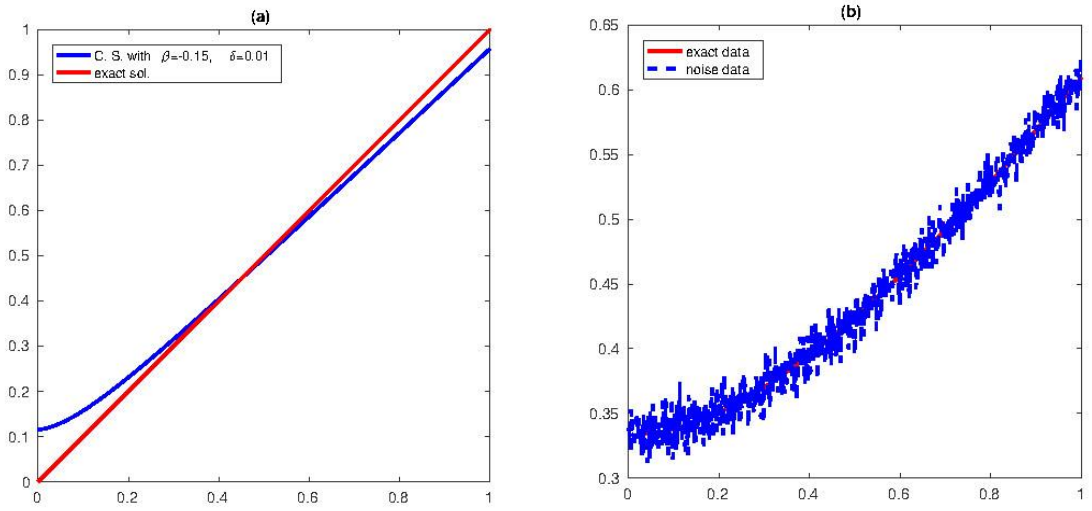

Fig.4: (a) Solution and (b) data of Foxgood example with $\beta = -0.15, \delta = 0.01$ and $n = 1000$.

CHEMISTRY, CHEMICAL ENGINEERING, ENVIRONMENT & RELATED FIELDS

Photocatalytic treatment of Emerging contaminants using Ceria-doped TiO_2 under Solar, UV-C and UV-A irradiation

Manasa M[1] and Hari Mahalingam[2]

1 *Department of Chemical Engineering, National Institute of Technology Karnataka (NITK), Surathkal, Mangalore-575025, Karnataka, India.*
e-mail: mandhan.m@gmail.com
2 *Department of Chemical Engineering, National Institute of Technology Karnataka (NITK), Surathkal, Mangalore-575025, Karnataka, India.*
e-mail: mhari@nitk.edu.in

ABSTRACT: Emerging contaminants are considered as the chemicals having a concentration in the micro-or nano-grams per liter range in drinking water supplies and its risk to human health is highly suspect but yet not quantified with absolute certainty. Antibiotic residues in waterbodies are one of the known emerging contaminants responsible for antibiotic resistance to human pathogens thus posing a definite risk to the overall health of the human population. Cerium-doped TiO_2 (1 at% Ce-TiO_2) is synthesized using a facile, green EDTA-Citrate complexing method and applied in suspended form for the photodegradation of ciprofloxacin under solar, UV-C and UV-A irradiation. A crystallite size of 16.95 nm by XRD (X-ray Diffraction) and bandgap of 2.5 eV by DRS (Diffuse Reflectance Spectroscopy) analysis is observed. For an initial CIP concentration of 10 ppm, under sunlight 91% degradation is achieved within 45 min at an optimum catalyst loading of 0.5 g/L. The performance of the synthesized catalyst under UV-C and UV-A was 93% and 96% respectively within 45 min at an optimum catalyst loading of 1.5 g/L. At longer timeframes of photocatalytic treatment, degradation efficiencies of 93.2% for sunlight and 98.3% for both UV-C and UV-A are observed. These results demonstrate that Ce-TiO_2 can be considered as an effective photocatalyst for the degradation of emerging contaminants.

Keywords: Emerging contaminants, Antibiotic residues, Ciprofloxacin, Ceria doped Titanium dioxide, EDTA-Citrate method

INTRODUCTION

Antibiotics are the primary protectors against various diseases and infections affecting mankind while at the same time, their presence as residues in the environment leads to the evolution of superbugs, hence posing a major threat to the habitat by the evolution of new diseases and infections resistant to traditional lines of antibiotic treatments. Hence, antibiotics are considered as emerging contaminants and must be treated. Ciprofloxacin (CIP), an antibiotic which is used to treat various bacterial infections, is found in the pharmaceutical effluents in the range of 5000-31000 µg/L (Lundborg and Tamhankar, 2017).

Photocatalysis, is one of the significant Advanced Oxidation Processes (AOPs) available for water and wastewater treatment with the generation of powerful oxidizing hydroxyl radicals for the removal of organic contaminants (Munter 2001). It serves as an alternative for the conventional treatment methods of pharmaceutical wastewaters. TiO_2 is the most commonly used photocatalyst, which works effectively only under UV light and it accounts only to 5% of the sunlight. Doping improves the photocatalytic activity by narrowing the bandgap,

utilizing the visible light and reducing the recombination (Huang et al. 2016). This study aims to evaluate the degradation efficiencies of CIP under solar, UV-C and UV-A irradiation using the Ce-doped TiO_2 (Ce-TiO_2) photocatalyst synthesized using the facile EDTA-citrate method.

EXPERIMENTAL METHODOLOGY

Model Pollutant (CIP)

Ciprofloxacin (≥98%, HPLC grade) is purchased from Sigma-Aldrich. The physico-chemical and drug-related information of CIP are listed in Table 1.

Synthesis of photocatalyst

Ce-TiO_2 is synthesized by the EDTA-citrate method (Prasad et al. 2012, Sena et al. 2017). Degussa P25 TiO_2 is procured from Evonik. Cerium nitrate hexahydrate [$Ce(NO3)_3.6H_2O$] is used as source of Ce, EDTA (Ethylenediaminetetraacetic acid), citric acid and ammonium hydroxide solution (NH_4OH) are procured from Sigma-Aldrich. Mole ratio of metal: EDTA: citric acid is 1:1:1.5. EDTA is dissolved in water using NH_4OH. Metal ion solution (Ce and TiO_2) is then added to EDTA solution, followed by the addition of citric acid and pH is adjusted to ~9.0 using NH_4OH. This solution is then heated and continuously stirred until the formation of organometallic gel. The gel is then dried in a hot air oven at 150°C for 24 h, followed by calcination at 350°C for 12 h and 600°C for 5 h. The flowchart of the synthesis procedure is shown in Fig.1.

Characterization

The morphology and structural phases are characterized by scanning electron microscopy (SEM) using (JEOL JSM-6300 LV analytical scanning electron microscope) and X-ray diffraction (XRD) using Cu Kα (λ=0.15418 nm) in the range of 2θ=20-65° with an increment of 0.02° (Rigaku Ultima-IV diffractometer). The bandgap is analyzed through diffuse reflectance spectroscopy-DRS (Varian, Cary 5000). The photodegradation of model pollutant is analyzed by UV-Visible spectrophotometer (GBC CINTRA 103) at λ_{max}=280 nm.

Photodegradation studies under Solar, UV-C and UV-A

The batch studies of degradation of Ciprofloxacin, are carried out in a crystallizing dish (100×50 mm) under Solar, UV-C (18 W, 5 lamps) and UV-A (18 W, 5 lamps) light irradiation. The experiments under sunlight were carried out on sunny days during March and April, 2018 (12p.m.-3p.m.) with an average temperature recorded as 32°C. All the experiments were carried out in duplicates. The effect of catalyst loading in the range of 0.1-2.5 mg/L is studied. 200mL of 10 mg/L CIP solution is irradiated under different light sources for 180 min. Dark condition is maintained for 30 min prior to irradiation, to achieve adsorption-desorption equilibrium. 2 mL of sample is withdrawn at regular intervals and filtered for analysis.

RESULTS AND DISCUSSION

Characterization

The SEM images of TiO_2 and Ce-TiO_2 are illustrated in Fig. 2 (a,b) and Fig. 2 (c,d) respectively. The particles appear to be irregularly shaped with some agglomeration. This confirms the presence of diiferent cyrstallographic planes (Kumar et al. 2013).

The XRD patterns depict the diffraction peaks of anatase and rutile TiO_2, along with CeO_2 (Fig. 3). The 2θ values peak at 25.35°, 36.12°, 37.01°, 37.88°, 48.24°, 54.12°, 55.17° and 62.8° correspond to anatase TiO_2 and 22.86°, 27.48° and 41.39° correspond to rutile TiO_2. The peaks at 28.8° and 56.86° correspond to CeO_2 which is in agreement with the result of Jaiswal et al. (2016).

The crystallite size is calculated using Scherrer's equation for the most intense anatase peak of TiO_2 (Martin et al. 2015). The FWHM, 2θ and crystallite size values are summarized in Table 2.

As mentioned by Ling et al. (2008), Ce^{3+} and Ce^{4+} have an ionic radius of 0.101 nm and 0.087 nm respectively which is higher than that of Ti^{4+} (0.068 nm). Hence, it is difficult for Ce ions to enter into TiO_2 lattice and may exist as Ce-Ti-O or as cerium oxide (Wang et al. 2016). Hence, there is a marginal increase in crystallite size.

The UV-Visible diffuse reflectance spectra of the Ce-TiO_2 is depicted in Fig. 4. Assuming an indirect bandgap, as done by most researchers (Wang et al. 2016) from the Tauc plot (see inset) bandgap of 2.50 eV is obtained. The Ce^{4+}/Ce^{3+} ion exhibits 1.8 eV energy level which extends the absorption edge position to visible region (Wang et al. 2016).

Photocatalytic degradation of CIP under Solar, UV-C, and UV-A

The degradation of CIP under sunlight after 180 min showed 93.2% degradation at a catalyst loading of 0.5 g/L (Fig.5a). As the loading increases, the degradation efficiency is found to be decreasing, which is due to the increase in turbidity of the solution causing hindrance in the light penetration (Allah et al. 2011).

After 180 min of UV-C and UV-A irradiation, CIP degradation of 98.3% was observed at a catalyst loading of 1.5 g/L in both the cases (Fig.5b and Fig.5c). A higher degradation was observed for catalyst loading of 1.5 g/L, due to the generation of more electron-hole pairs. But with an increase in catalyst dosage, the active sites get blocked and hence, decrease in degradation is observed for 2 g/L and 2.5 g/L of catalyst loading (Kumar et al. 2016).

CONCLUSIONS

The Ceria-doped TiO_2 synthesized using EDTA-citrate method showed a crystallite size of 16.95 nm from XRD and a bandgap of 2.5 eV from DRS analysis. From the photocatalytic studies, an optimum catalyst loading of 1.5 g/L is identified with CIP degradation of 98.3% under both UV-C and UV-A. Solar photocatalytic studies showed CIP degradation of 93.2% at an optimum catalyst loading of 1.5 g/L. Focus of most researchers are rapidly increasing towards the treatment of pharmaceuticals and in producing a stable and economically viable photocatalysts. In this regard, immobilizing the photocatalysts onto a suitable inert support helps in the post-treatment recovery and availability of non-toxic photocatalysts for practical applications in the environment. Hence, these photocatalysts serve as a valuable tool for the degradation of emerging contaminants by utilizing solar energy.

REFERENCES

[1] Allah, T A G et al (2011), Photocatalytic oxidation of ciprofloxacin under simulated sunlight, Journal of Hazardous Materials, Vol.186, pp 751-755.

[2] Vieira, G B et al (2018), CeO_2/TiO_2 nanostructures enhance adsorption and photocatalytic degradation of organic compounds in aqueous suspension, Journal of Photochemistry and Photobiology A: Chemistry, Vol.353, pp 325–336. http://dx.doi.org/10.5772/63234

[3] Huang, F et al (2016), Semiconductor Photocatalysis - Materials, Mechanisms and Applications, Influences of Doping on Photocatalytic Properties of TiO_2 Photocatalyst, Intech, chapter 2, 31-80.

[4] Kumar, E et al (2013), Synthesis and Characterization of CeO_2 Nanocrystals by Solvothermal Route, Materials Research, Vol.16, no.2, pp 269-276.

[5] Kumar, J V et al (2016). Fabrication of potato-like silver molybdate microstructures for photocatalytic degradation of chronic toxicity ciprofloxacin and highly selective electrochemical detection of H_2O_2. *Sci. Rep.*, Vol.6, no.1, pp 1-13.

[6] Lundborg, C S and Tamhankar, A J (2017). Antibiotic residues in the environment of South east Asia, BMJ, 358:j2440, pp 42-45. https://pdfs.semanticscholar.org/f0eb/5bcf0aef190b034ef02cacd5aafeaffca5e4.pdf

[7] Ling, Q et al (2008), Visible-light-driven boron/ferrum/cerium/titania photocatalyst, Journal of Photochemistry and Photobiology A: Chemistry, Vol.200, pp 141–147.

[8] Martin, M V et al (2015), The influence of Ce doping of titania on the photodegradation of phenol, Environmental Science and Pollution Research, Vol.22, pp 14291–14298.

[9] Munter, R. (2001). Paper (2001) - ADVANCED OXIDATION PROCESSES .pdf. pp 59–80.

[10] Prasad, D H et al (2012). Synthesis of nano-crystalline $La_{1-x}Sr_xCoO_{3-\delta}$ perovskite oxides by EDTA-citrate complexing process and its catalytic activity for soot oxidation. *Appl. Catal. A Gen.*, Vol.447–448, pp 100–106.

[11] Sena, M S et al (2017), Synthesis and Characterization of Cerium Molybdate Semiconductor Nanoparticles, Materials Research, pp 1-7. http://dx.doi.org/10.1590/1980-5373-MR-2017-0092

[12] Wang, Y et al (2016), Doping TiO_2 with boron or/ and cerium elements: effects on photocatalytic antimicrobial activity, Vacuum, Vol.131, pp 58-64.

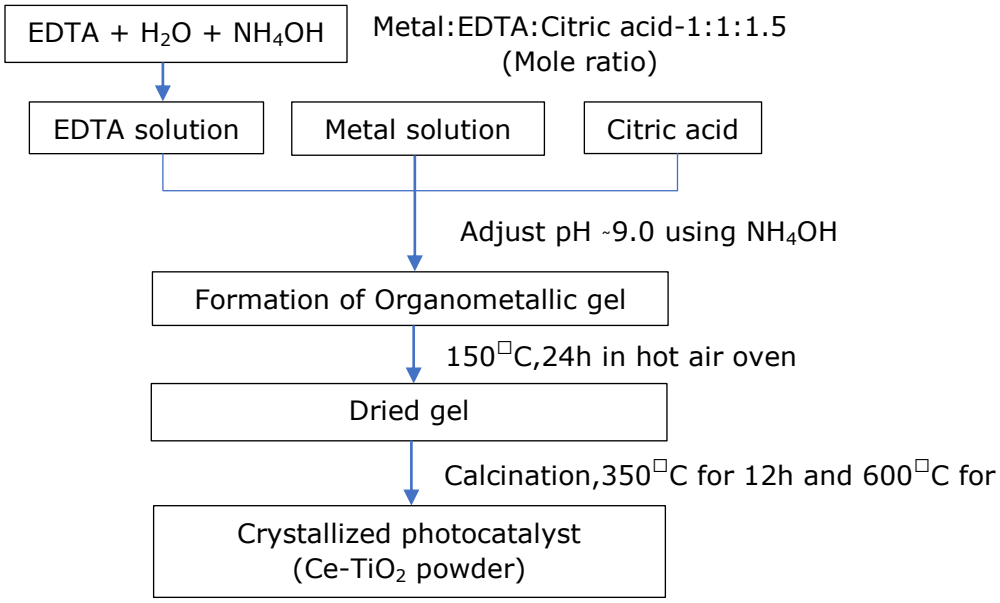

Fig. 1 Flowchart of EDTA-citrate method

Table 1. Physio-chemical and drug information of CIP

STRUCTURE	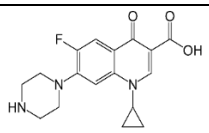
MOLECULAR FORMULA	$C_{17}H_{18}FN_3O_3$
MOLECULAR WEIGHT	331.347 g/mol
DRUG CLASS	Second generation fluoroquinolone antibiotic
MEDICAL USES	Bacterial infections mainly infections of bones and joints, gastroenteritis, respiratory tract (sinus) infections, cellulitis, urinary tract infections
SPECTRUM OF ACTIVITY (Active against)	Gram-negative (mainly *Escherichia coli*, *Klebsiella pneumoniae*, *Legionella pneumophila*, and *Pseudomonas aeruginosa*) Gram-positive (mainly methicillin-sensitive, but not methicillin-resistant *Staphylococcus aureus*, *Streptococcus pneumoniae*, *Enterococcus faecalis*

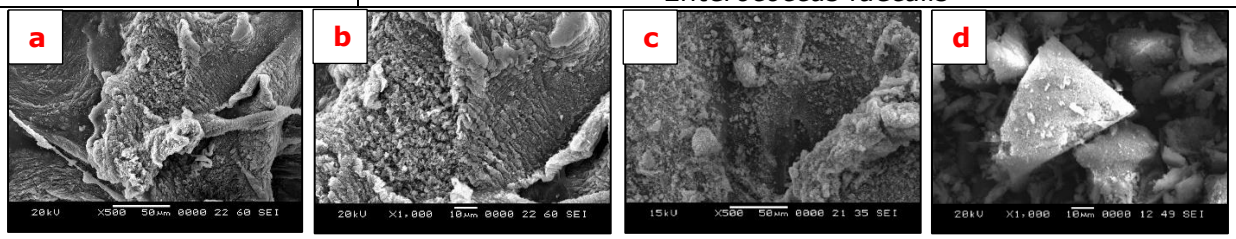

Fig. 2 SEM images of TiO_2 (a,b) and Ce-TiO_2 (c,d)

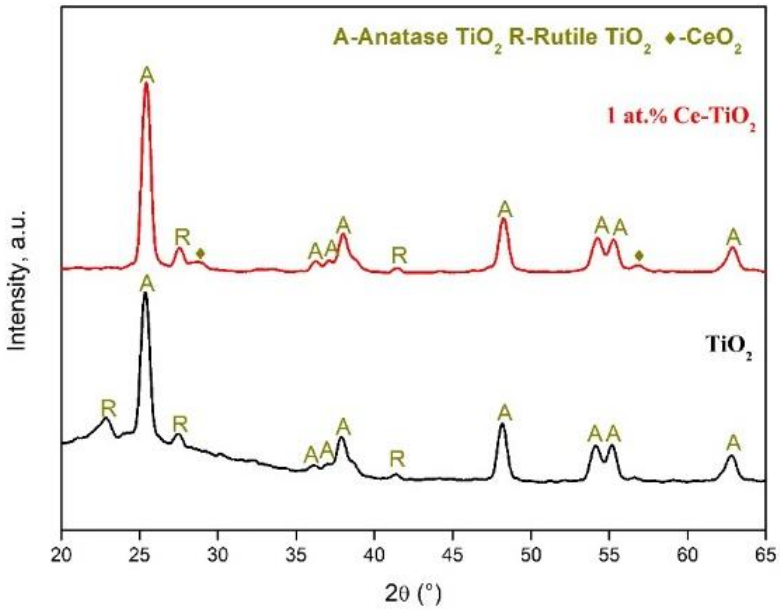

Fig. 3 XRD patterns of TiO_2 and Ce-TiO_2

Table 2. FWHM, 2θ and crystallite size measured from XRD

PHOTOCATALYST	FWHM	2θ	Crystallite size (nm)
TiO_2	0.5094	25.36°	16.70
Ce-TiO_2	0.5020	25.42°	16.95

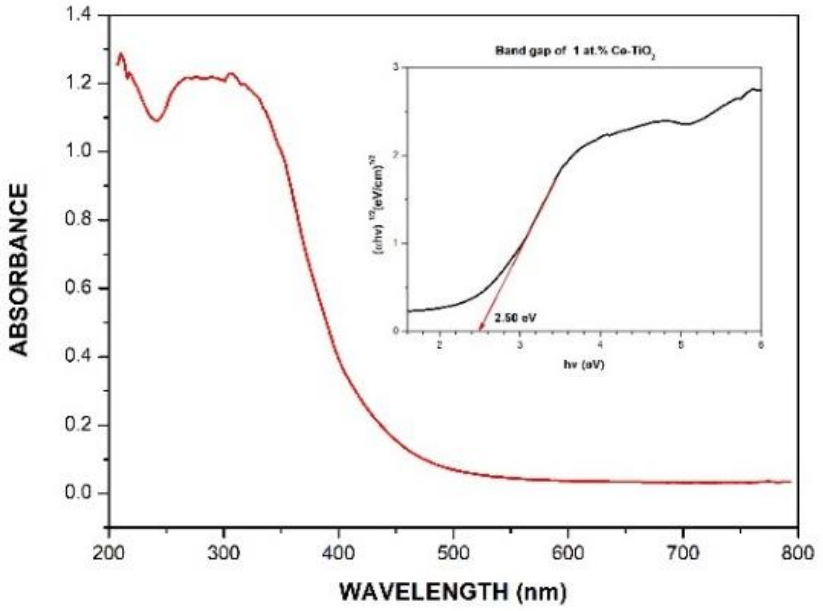

Fig. 4 UV-Visible diffuse reflectance spectra of the Ce-TiO_2

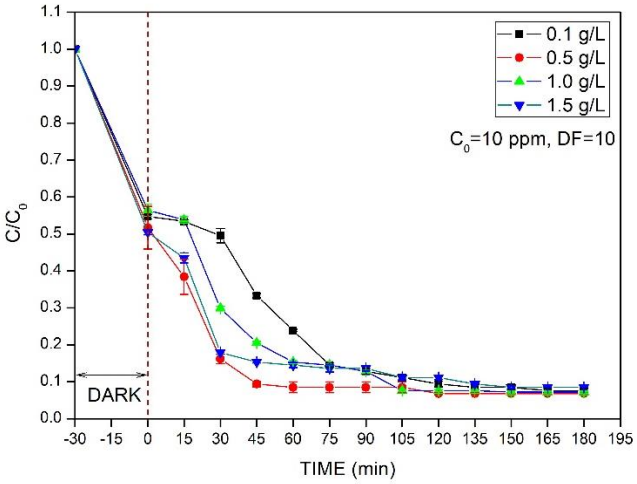

Fig. 5a Photocatalytic degradation of CIP under Solar irradiation

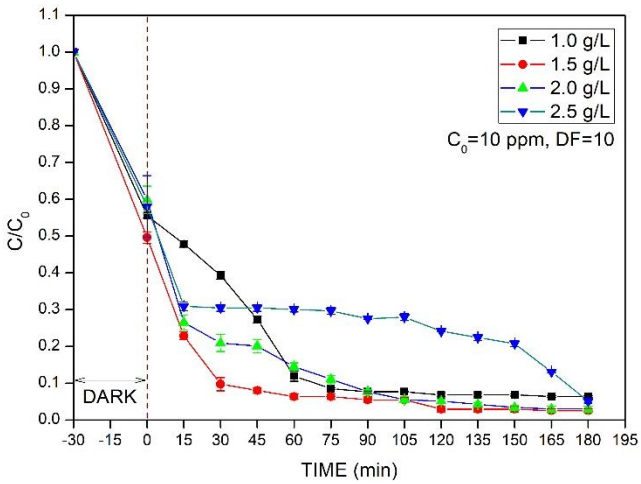

Fig. 5b Photocatalytic degradation of CIP under UV-C irradiation

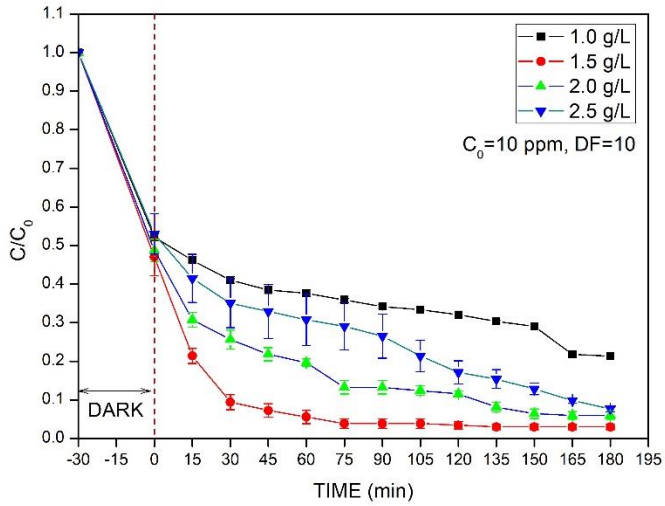

Fig. 5c Photocatalytic degradation of CIP under UV-A irradiation

8th International Engineering Symposium - IES 2019
March 13-15, 2019, Kumamoto University, Japan

Pristine *Pteris vittata* L. Pinnae Pellets as an Adsorbent for the Uptake of Toxic Metals from Aqueous Solution

Smruthi G. Prabhu [1], Govindan Srinikethan[2] and **Smitha Hegde[3]**

1 *Research Scholar, Department of Chemical Engineering, National Institute of Technology Karnataka, Surathkal, Mangalore 575025, India. Email:smruthigp@gmail.com*
2 *Professor, Department of Chemical Engineering, National Institute of Technology Karnataka, Surathkal, Mangalore 575025, India. Email:srinikethan.g@gmail.com*
3 *Professor, Division of Bioresource and Biotechnology, Nitte University Center for Science Education and Research (NUCSER), Paneer Campus, Deralakatte, Mangalore 575018. Email: smitha.hegde@nitte.edu.in*

ABSTRACT: The toxic metals have long-term adverse effects on the environment. Conventional methods for the treatment of wastewater containing toxic methods have their limitations and drawbacks. We propose the use of a pelletized non-living biomass as a simple, yet efficient adsorbent. This paper investigates the pelleting process of *Pteris vittata* L. and its Cd(II) and Cr(VI) adsorption capacity. Compaction of the biomass to stable pellets was achieved using a simple manual pellet-press. The organic binders were narrowed down based upon the stability of the resultant pellets in pH adjusted water. 4.82 mg of Cd(II) and 8.31 mg of Cr(VI) was removed at equilibrium per g of the biomass pellet at a pellet dosage of 10 g/L. The findings indicate *Pteris vittata* L. pellets to be a potential low-cost toxic metal adsorbent.

***Keywords**: Binders, pH stability, pellet expansion, Pteridophyte, Pellet dosage, Isotherm*

INTRODUCTION

The necessity to manage toxic metal pollution is of great importance. Besides the existing conventional techniques of wastewater treatment, passive adsorption using a non-living biomaterial is an alternative method. Several biomaterials including agricultural by-products have been studied as a non-hazardous, economical and effective adsorbent of toxic metals.

Pteridophytes are the non-flowering plants that have generally received limited attention. With a minimal role in the food chain, most often pteridophytes are overlooked as an invasive weed (Prabhu et al. 2016) and are usually destroyed. Besides being not a preferred diet by several living organisms, the invasive growth of pteridophytes is difficult to contain due to reproduction via spores. The appropriate thing to do rather than destroying them would be to put them into an application.

In the present study, *Pteris vittata* L. a small-medium sized pteridophyte with a weedy potential with no seasonal limitations was studied as an adsorbent of toxic metals in its non-living form

(Morajkar et al. 2015). For a stable adsorbent form, *Pteris vittata* L. powder was immobilized by pelleting it. Batch-type sorption experiments have been conducted to screen the adsorption of Cd(II) and Cr(VI) by the pristine *Pteris vittata* L. pinnae pellets.

MATERIALS AND METHODS

The biomass, *Pteris vittata* L. pinnae was collected from Mangalore city and suburbs, India (Coordinates: 12.87°N, 74.88°E).

Preparation of *Pteris vittata* L. pinnae-based adsorbent pellet

Densification of the pristine biomass was conducted in a manual pellet press. Pellets were prepared using various organic binders of concentrations 10% and 15%. Initially, organic binders and the binder concentration required to yield stable pellets were determined. The powdered biosorbent of particle size ≤ 180 µm was selected for pelleting. For pelleting of the biomass, the powdered biomass was mixed thoroughly with the selected binder (viscous) of suitable concentration at 1:1 ratio. The mixture was then transferred into the pellet-press die. An approximate compaction pressure of 44.24 kPa was applied. After pelleting, the pellets were dried in an electric oven at 70 °C for 48 hrs and stored in an airtight container until use.

Determination of pellet stability

The stability of the pellets at pH 2 to 6 was determined by introducing the desired amount of pellets into 100 mL of pH adjusted water. The study was conducted under continuous agitation speed of 150 rpm. The pellets were separated after eight hours, dried at 60 °C and weighed. The difference between the weight of the pellet before and after agitation gives the amount of biomass lost during the study. Pellets with percentage stability of 80% and above were considered to be stable.

Pellet expansion and relaxed density

The length and diameter of ten randomly chosen pellets were measured using a screw gauge immediately after pelletization. The selected pellets were measured again after a week of storage. The density calculated then is the relaxed density.

General procedure for batch scale experiments

The batch scale experiments determined the best-operating parameters like the required pellet dosage, equilibrium time and initial metal concentration. The adsorption of Cd(II) and Cr(VI) by the biomass pellets was conducted at pH 6 and 2, respectively as previously established (Prabhu et al. in press). After equilibration, the solution was filtered using Whatman No. 1 filter paper. The residual metal concentration was analysed using Flame Atomic Absorption Spectrometer (GBC 932 plus, GBC Scientific Equipment Manufacturer PTY Ltd., Australia) at wavelengths 428.9 and 228.8 nm for Cr(VI) and Cd(II) respectively. Controls composed of the metal solution with no pellet were maintained to determine if any change in the initial metal concentration occurred. The amount of metal uptake was calculated from the mass balance Eq. 1.

$$q = {(C_i - C_f)V}/{W} \quad (1)$$

Where V is the volume of the metal solution (L), and W is the mass of sorbent (g).

Data evaluation

The applicability of the kinetics models on the time course data till the attainment of equilibrium was studied using Pseudo-first order and Pseudo-second order model. The data acquired from the biosorption studies were subjected to equilibrium modelling to have a better understanding of biosorption. Langmuir and Freundlich isotherm models were used in the present study to analyse the experimental data.

Statistical analysis

Batch experiments were repeated thrice and the mean values; error bars representing standard deviation are presented. Data gathered were subjected to one-way analysis of variance (ANOVA) at 5% level of significance, to learn if there were any statistically significant differences between the means of the

independent groups. Since the sample size was small, one-way ANOVA option, Welch's ANOVA was applied to determine the significant difference (McDonald 2014). Upon validation of all the assumptions, intergroup mean values were compared using Post Hoc Tukey's Test. If the assumption of equal variance was violated, Games-Howell test was applied to the data for multiple comparisons. Statistical Package for the Social Sciences (SPSS) for Windows software was used for statistical analysis.

RESULTS AND DISCUSSION

Binders and pellet stability

Table 1 displays the stability of the pellets in water excluding the pellets prepared with PVA because the pellets disintegrated upon its contact with water. Statistical tests confirmed no significant difference ($p > 0.05$) in the stability of pellet offered by different binders at various concentrations. The stability of the pellets was affected by the binder and the treating temperature of the pellets. Temperature affects both the binder and the biomaterial. High temperature caused the melting of the components of the biomaterial. Upon cooling, solid bridges are formed between components that strengthen the pellet (Tabil 1996). By the combined interaction of the moisture content and the biomass components (proteins, starch and/ or lignin) at high temperature and pressure, the proteins present in the biomass undergo plasticization/ denaturation and the starch added as binders undergo gelatinization, that promotes better binding of the particles (Tabil 1996; Tumuluru et al. 2016). Also, the waxes and lignins present in the biomass could have undergone a glass transition at 40 °-50 °C and 65 °-75 °C respectively as reported by Stelte et al. (2012). The combined mechanism of glass transition/ plasticization of the biomaterial components and gelatinization of starch-based binder followed by hardening could have played an essential role in binding and improving the strength of the pellets, thus yielding non-significant differences in the stability of pellets offered by different starch-based binders.

Pellet stability in pH adjusted water

Pellets prepared with 15% corn starch binder were tested for stability from pH 2 to 6. The solution pH influenced the stability of the pellets. As the pH was increased from 2 to 6 the stability of the pellets increased from 65.46± 5.06 to 86.53± 0.87% at pH 6. Welch's ANOVA was conducted to compare the effect of pH on the stability of the pellets. The effect was significant with $p< 0.05$, Welch's F (4, 4.79)= 12.515. Tukey's Post Hoc comparisons indicate that water at pH 2 had a significantly lower (p= 0.000) pellet percentage stability (M= 65.46, SD= 5.06) than at pH 3 (M= 88.43, SD= 0.65), 4 (M= 86. 3, SD= 1.01), 5 (M= 86.93, SD= 0.47) and 6 (M= 86.53, SD= 0.87).

Relaxed density and pellet expansion

After densification of the powdered biomass to pellets, the pellets are stored until further use. During its storage, the pellets could expand, having a substantial impact on its quality as a biosorbent. The elasticity of the fibres in the biomass causes the spring back of the pellets resulting in volume expansion and reduced density of the pellets (Si et al. 2016). The pressure applied to the biomass during pelleting is axial; hence, the probability of longitudinal expansion or increased length of the pellet is higher compared to diametric expansion (Si et al. 2016). If the pellet expansion occurs, the quality of the pelletized biosorbent can be improved by increasing the binder concentration. Although a slight increase in relaxed pellet length was observed, the change was insignificant (p= 0.626) compared to compressed pellet length (Table 2). However, there was a significant difference (p= 0.027) observed in the compressed density and relaxed density. However, the lower relaxed density could be attributed to the loss of moisture (wt %) content of the pellets during the heat treatment of the pellets before storage. The pellets thus prepared were suitable to be used as an adsorbent.

Effect of pellet dosage on the uptake of Cd(II) and Cr(VI)

The studied Pellet dosages were 10, 15 and 20 g per litre of metal solution.

Equilibrium biosorption amount (mg/g) of Cd(II) and Cr(VI) on the pelletized biosorbent decreased with the increase in pellet dosage (Fig.1), whereas, the biosorption efficiency of the pellets at equilibrium increased with increase in pellet dosage (Fig. 2). The unsaturated binding sites increase with an increase in dosage resulting in decreased metal uptake amount. On the other hand, the greater availability of the exchangeable sites results in increased percentage removal of heavy metals (Gavrilescu 2004).

Effect of initial Cd(II) and Cr(VI) concentration on its adsorption

The effect of initial metal concentrations was studied from 50 to 200 mg/L with the adsorbent dosage of 20 g/L. With an increase in the metal concentration, the adsorption efficiency decreased. The decrease in adsorption efficiency of Cd(II) and Cr(VI) (Fig. 3) is because of the saturated active sites. The reduced diffusion of the metal ions in the boundary layer of the adsorbent at higher metal concentrations (Pokethitiyook and Poolpak 2016; Sağ and Aktay 2000) contributes to decreased adsorption efficiency. The pellets displayed significant Cr(VI) adsorption efficiency at 100 and 150 mg/L compared to 50 mg/L. The higher Cr(VI) concentration provided an important driving force that helped overcome the mass transfer resistances of the molecules present between the aqueous and the solid phases. Malkoc and Nuhoglu (2007) have reported similar findings.

Adsorption kinetic studies

The controlling mechanism of metal biosorption was investigated by fitting adsorption reaction models, pseudo-first and pseudo-second order model to the experimental data. Pseudo-first order kinetic model with low correlation coefficient suggested that the adsorption of Cd(II) or Cr(VI) on the pelletized adsorbent did not occur onto one site per ion. Moreover, the model is only reliable for an initial period of the adsorption process (Ho and McKay 1999). The pseudo-second order model is relevant for a more extended period. The experimental and theoretical q_e values in pseudo-second order model were found to be substantially close (Table 3). The slight difference is due to the heterogeneous nature of the adsorbent. High correlation coefficients show the rate-limiting step to be chemisorption that is promoted through the sharing or exchange of electrons between the adsorbent and sorbate (Oliveira et al. 2008).

Adsorption isotherm studies

The isotherms represent the amount of metal adsorbed per unit of adsorbent, as a function of equilibrium concentration at a constant temperature. The data was obtained by conducting experiments with varying initial metal concentrations at the best-operating conditions. With a correlation coefficient of 0.936 and 0.911, Langmuir isotherm showed to be the best fit to the data of Cd(II) and Cr(VI) adsorption on adsorbent pellets at 303 K (Table 4). The isotherm indicates the nature of metal ion adsorption to be monolayer on a homogenous surface without any interaction between adsorbed ions (Sarı and Tuzen 2008). Furthermore, the R_L value for Cd(II) and Cr(VI) adsorption were 0.07-0.15 and 0.06-0.01 indicating a favourable biosorption process. The parameters of the isotherm models have been summarized in Table 6.

CONCLUSIONS

The following conclusions are deduced from this study:

- Pelleting was observed to be an efficient technique for the immobilization of the *Pteris vittata* L. powder in the presence of corn starch as the binder.
- Cd(II) was removed easily by the pelletized adsorbent at pH 6, whereas at pH 2 the removal of Cr(VI) was challenging because of the instability of the pellets at the acidic pH.
- The maximum uptake capacity of the adsorbent pellets for Cd(II) was 13.51 mg/g Cr(VI) was 1.66 mg/g as obtained from the Langmuir Isotherm Model.
- The pelletized *Pteris vittata* L. is a potential adsorbent form that can be

- used efficiently for the removal of a metal pollutant from a near neutral aqueous system.
- The metal loaded adsorbent can be directly discarded into the mines as the adsorbent pellet is biodegradable. The metals can be leached out by using bioleaching technology.

ACKNOWLEDGEMENTS
The authors acknowledge Aishwarya Sanjeev Kumar, Bharath Goud Ediga and Uday Krishna Devara for providing help during the research.

REFERENCES
[1] Gavrilescu, M (2004), Removal of heavy metals from the environment by biosorption, Engineering in life sciences, Vol. 4, pp 219-232.
[2] Ho, Y S and McKay, G (1999), Pseudo- second order model for sorption processes, Process Biochemistry, Vol. 34, No. 5, pp 451- 465.
[3] Malkoc, E and Nuhoglu, Y (2007), Determination of kinetic and equilibrium parameters of the batch adsorption of Cr(VI) onto waste acorn of *Quercus ithaburensis*, Chemical Engineering and Processing: Process Intensification, Vol. 46, No. 10, pp 1020–1029.
[4] Morajkar, S et al. (2015), Ferns: A thriving group of urban dwellers, Bionature, Vol. 35, pp 13-21.
[5] McDonald, J (2014), Handbook of Biolological Statistics, 3rd ed., Sparky House Publishing, Baltimore (Maryland), pp 145-157.
[6] Oliveira, W E et al. (2008), Untreated coffee husks as biosorbents for the removal of heavy metals from aqueous solution, Journal of Hazardous Materials, Vol. 152, No. 3, pp 1073-1081.
[7] Pokethitiyook, P and Poolpak, T (2016), Biosorption of heavy metals from aqueous solutions, Phytoremediation: Management of environmental contaminants, Ansari, A A et al. eds., Springer International, Switzerland, pp 123.
[8] Prabhu, S G et al. (2016), Potential of pteridophytes in heavy metal phytoremediation, International Journal of Research in Engineering and Technology, Vol. 5, pp 1-9.
[9] Prabhu, S et al. (in press), Spontaneous Cr(VI) and Cd(II) Biosorption Potential of Native and Dried Pinnae Tissue of Pteris vittata L., a Tropical Invasive Pteridophyte, International Journal of Phytoremediation, doi:10.1080/15226514.2018.1524845
[10] Sağ, Y and Aktay, Y (2000), Mass transfer and equilibrium studies for the sorption of chromium ions onto chitin, Process Biochemistry, Vol. 36, No. 1-2, pp 157-173.
[11] Sarı, A and Tuzen, M (2008), Biosorption of Pb (II) and Cd (II) from aqueous solution using green alga (*Ulva lactuca*) biomass, Journal of Hazardous Materials, Vol. 152, No. 1, pp 302-308.
[12] Si, Yet al. (2016), Effect of Carboxymethyl Cellulose Binder on the Quality of Biomass Pellets, Energy and Fuels, Vol. 30, No. 7, pp 5799–5808.
[13] Stelte, W et al. (2012), Recent developments in biomass pelletization - a review, BioResources, Vol. 7, No. 3, pp 4451–4490.
[14] Tabil, L G (1996), Binding and pelleting charateristics of Alfalfa, Doctoral dissertation, University of Saskatchewan.
[15] Tumuluru, J S et al. (2016), Method to Produce Durable Pellets at Lower Energy Consumption Using High Moisture Corn Stover and a Corn Starch Binder in a Flat Die Pellet Mill, Journaal of Visualized Experiments, Vol. 112, pp 1–13.

Table 1 Water stability study on the pellets using different binders at varied concentration

Binder	% Stability of the pellets at varied binder concentration	
	10 %	15 %
Corn starch	83.75± 0.49	88.35± 0.92
Potato starch	82.90± 0.57	86.65± 2.76
Arrowroot starch	80.65± 1.20	81.05± 0.21

Table 2 Relaxed density (ρ_r) and pellet expansion parameters of the pellets with cornstarch as the binder

Maximum compression density (ρ_m)[a,c], kg/m^3		942.05± 106.21
Relaxed density (ρ_r)[b,c], kg/m^3		769.60± 72.70
Length of the pellets[c] (mm)	Before storage	6.36± 0.70
	After storage	6.80± 0.84
Diameter of the pellets[c] (mm)	Before storage	10.74± 0.57
	After storage	10.52± 0.49

[a] ρ_m was measured as soon as the biosorbent was pelletized, [b] ρ_r was measured after a week of storage and [c] n=8

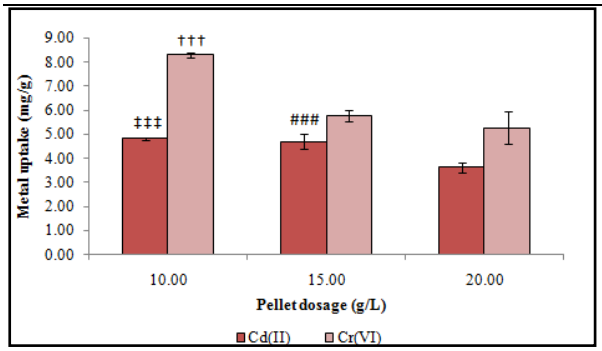

Fig.1 Effect of adsorbent dosage on the uptake of Cd(II) and Cr(VI) by the pelletized adsorbent. Conditions: initial metal concentration of 100 mg/L at 30 °C with an agitation speed of 150 rpm. Values are expressed as Mean±SD. ‡‡‡p=0.000 compared to Cd(II) sorption at 20 g/L, ###p=0.000 compared to Cd(II) sorption at 20 g/L, †††p=0.003 compared to Cr(VI) sorption at 15 g/L

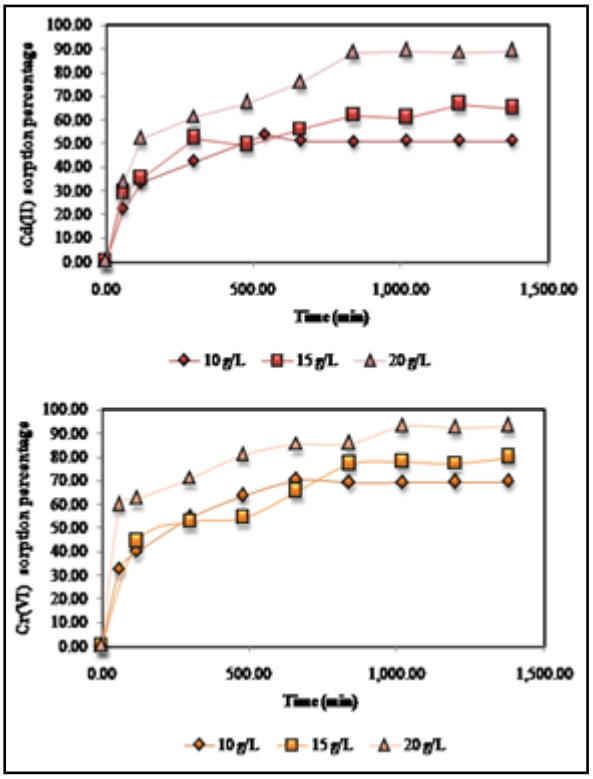

Fig.2 Effect of adsorbent dosage on the Cd(II) and Cr(VI) sorption efficiency of the pelletized adsorbent. Conditions: initial metal concentration of 100 mg/L at 30 °C

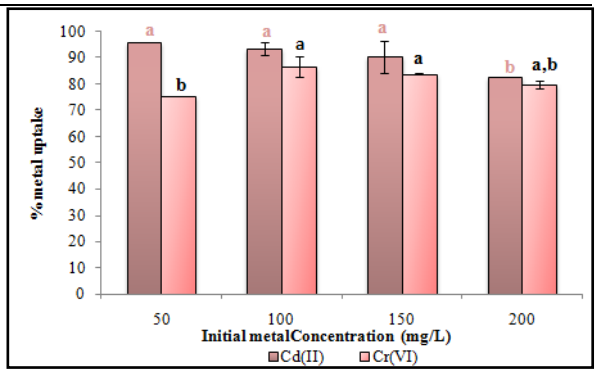

Fig.3 Metal biosorption efficiency of the pelletized biosorbent at varied initial metal concentrations at 840 min and 1020 min for Cd(II) and Cr(VI), respectively. Means that do not share a letter are significantly different

Table 3 Parameters of Pseudo-second order kinetic model for the sorption of Cd(II) and Cr(VI) on the pelletized adsorbent

Pseudo-second order kinetic model $\left({}^{t}/_{q_t} = t\,{}^{1}/_{q_e} + {}^{1}/_{q_e^2 k}\right)$			
Pellet dosage (g/L)	q_e (mg/g)	Theoretical q_e (mg/g)	R^2
Cd(II)			
10	4.82	5.59	0.953
15	4.70	4.97	0.988
20	3.62	4.13	0.985
Cr(VI)			
10	8.31	8.77	0.975
15	5.76	6.17	0.973
20	5.28	5.88	0.996

Table 4 Isotherm model parameters applied to the adsorption of Cd(II) and Cr(VI)

Langmuir Isotherm Model $\left({}^{C_e}/_{q_e} = {}^{1}/_{bQ_o} + {}^{C_e}/_{Q_o}\right)$		
Metal	Cd(II)	Cr(VI)
Q_o (mg/g)	13.51	1.66
b (L/mg)	0.06	0.64
R^2	0.94	0.91
Freundlich Isotherm Model $\left(logq_e = logk_f + {}^{1}/_{n}\log C_e\right)$		
Metal	Cd(II)	Cr(VI)
K_f (L/g)	1.34	0.0625
$1/n$	0.55	1.40
R^2	0.91	0.85

Structure Based Drug Design of PTP-SHP2 Inhibitors Using Virtual Screening of NCI Library

Chetan Munegowda[1], Rakesh Kumar[2] and **Dinesh Gupta[3]**

1 *Department of Chemical Engineering, National Institute of Technology Karnataka, Surathkal, Mangalore 575025, India. Email: mgowdachetan@gmail.com*
2 *Translational Bioinformatics Group, International Centre for Genetic Engineering & Biotechnology, Aruna Asaf Ali Marg, New Delhi 110067, India. Email: dinesh@icgeb.res.in*
3 *Translational Bioinformatics Group, International Centre for Genetic Engineering & Biotechnology, Aruna Asaf Ali Marg, New Delhi 110067, India. Email: dinesh@icgeb.res.in*

ABSTRACT: In this work, structure-based drug designing has been performed to find potential inhibitors of PTP-SHP2 protein in its open and closed conformations. Three dimensional protein-ligand complex structures were obtained from Protein Data Bank and re-docked with AutoDock to get reference data. Docking and virtual screening processes were carried out on chemical compound library against the target proteins (PDB ID: 4RDD and 5EHP). False positives were removed and drug-likeness of the ligands was calculated. Out of 2,84,176 screened compounds 2,276 were identified as probable inhibitors after the virtual screening for closed conformation of PTP-SHP2. Interactions of the ligands with the receptor residues were visualized and analysed. The resulting filtered compounds are predicted as competitive and allosteric inhibitors for open and closed conformations of PTP-SHP2, respectively.

Keywords: *Structure based drug design, PTP-SHP2, 4RDD and 5EHP.*

INTRODUCTION

Cancer is a term used for a large group of diseases that involve abnormal cell growth beyond their boundaries with the ability to invade or spread to other parts of the body. Cancer can affect almost any part of the body and has many anatomic and molecular subtypes that each requiring specific management strategies. According to World Health Organization (WHO), cancer is the second leading cause of death globally and 8.8 million deaths were reported in 2015. India alone has over 2.5 million people living with cancer. And about 71% of the deaths are related to cancer. Lung, prostate, colorectal, stomach and liver cancer are the most common types of cancer in men, while breast, colorectal, lung, cervix and stomach cancer are the most common among women. For many years various combinations of surgery, radiation and chemotherapy have been the main treatment of cancer. Chemotherapy is designed to inhibit cell division of tumour cells, but normal body cells are also affected from this treatment. In the last few decades, targeted therapy is gaining much focus as it can overcome the drawbacks of chemotherapy.

The human body is made up of trillions of cells. Every day some cells die while others divide. To maintain this physiological balance, there has to be a specific signal for cell proliferation, differentiation and apoptosis. Proteins, lipids and other components make up the cell. Proteins present on the surface of

the cells are receptors, which bind to endogenous as well as exogenous substances. Signal transduction is defined as transfer of signal from cell exterior to the interior of the cell with the help of growth factors and growth hormones. Growth factors are naturally found inside the body that is capable of stimulating cell growth, apoptosis and healing. Some examples of growth factors include cytokines and hormones while tyrosine kinase receptors, cytokine kinase receptors, GPCR are some growth receptors.

Cell cycle is characterized by an event of phosphorylation and dephosphorylation of proteins thereby producing a conformational change in the structure of protein tyrosine (Somani, R. et al., 2016). PTPs control protein tyrosine phosphorylation status in concert with tyrosine kinases. Recent studies have indicated significant roles of some PTPs like SHP2, PTP1B, CDC25 and PRL3 in the development of human diseases, particularly in cancer (Chen, C. et al., 2015). SHP2 is the first confirmed bona fide proto-oncogene among the PTP superfamily members. SHP2 is one of the tyrosine phosphatase enzymes which are responsible for the dephosphorylation of tyrosine protein. It was found that the overexpression or inhibition in SHP2 activity may lead to cancer and other diseases, due to abnormal cell signalling (Somani R. et al., 2016). Thus, SHP2 has become one of the novel targets to fight cancer and other diseases.

MATERIALS AND METHODS

Software required

AutoDock 4.2.6 (downloaded from http://autodock.scripps.edu/downloads) was used for docking macromolecules; PyMOL 1.7.4.5 (downloaded from https://www.pymol.org/) was used for visualizing macromolecules; Molecular Graphics Laboratory (MGL) Tools 1.5.6 (downloaded from http://mgltools.scripps.edu/downloads) was used for virtual screening; Open Babel 2.4.1 (downloaded from http://openbabel.org/wiki/Category:Installation) was used for converting structure files into mol2 format; LigPlot^{+} v.1.4.5 (downloaded from http://www.ebi.ac.uk/thornton-srv/software/LigPlus/download.html) was used for visualizing protein-ligand interactions; Microsoft Excel 2010 was used for data analysis. PAINS-Remover (http://cbligand.org/PAINS/) was used to remove false positive ligands. QED (downloaded from http://silicos-it.be.s3-website-eu-west-1.amazonaws.com/software/biscu-it/biscu-it.html#biscu-it) was used to calculate drug-likeness of ligand. MarvinSketch 17.15 was used for displaying and characterizing chemical structures and substructures.

Chemical compounds library

We considered the chemical data available from the National Cancer Institute (NCI) as a library set for searching inhibitors. The 2D chemical structures released as of June 2016 consisting of 2,84,176 compounds were (retrieved from https://wiki.nci.nih.gov/display/NCIDTPdata/Chemical+Data) used as the ligand library to search hits.

Methodology (see **Figure 1**)

The three-dimensional structures of the target proteins were retrieved from Protein Data Bank (https://www.rcsb.org/pdb/home/home.do) in their ligand bound complex (see **Figure 2** and **Figure 3**).

Re-docking of the protein and ligand was done by first separating the protein-ligand complex and preparing target proteins (PBD ID: 4RDD and 5EHP) with AutoDockTools-1.5.6 (Michel F. Sanner, 1999 & Morris, G. M. et al., 2009) by the addition of hydrogen atoms to the target proteins, which is a necessary step for the computation of partial atomic charges. Gasteiger charges were considered for each atom present in the target proteins in AutoDock 4.2.6. Three-dimensional affinity grids were setup for 4RDD and 5EHP with the following atom types: A, C, OA, N, SA and HD for 4RDD and A, C, HD, N, NA, OA and SA for 5EHP representing all probable atom types in the proteins. Genetic Algorithm was used as the search

parameter for both proteins with the default values provided by AutoDockTools-1.5.6 (see **Figure 4**). In addition, a desolvation map and an electrostatic map were also calculated. AutoDock was run several times to obtain various docked conformations and to calculate the predicted binding energy. The docking poses were obtained according to their docking parameters and their corresponding binding pockets.

The ligands set retrieved form NCI database was split into multiple files each containing a set of approximately 10,000 ligands. AutoDock Raccoon tool (Forli, S. et al., 2016) was used for virtual screen generation where the files were converted implicitly from '.mol2' to '.pdbqt'. Virtual screening jobs were generated for 4RDD (open conformation receptor) with appropriate docking parameter files. After the execution of docking jobs conformations produced were summarized and sorted based on ligand binding energy. Only those ligands whose ligand binding energy was less than or equal to -8.00 kcal/mol (with 4RDD) were collected. The resulting set of ligands was made PAINS-free with the help of PAINS-Remover (Baell, J. B., and Holloway G. A., 2010 & Baell, J. B., and Walters, M. A., 2014). QED was calculated for the resulting PAINS-free ligands set (Bickerton, G. R. et al., 2012). Virtual screening jobs were generated for 5EHP (closed conformation receptor) with appropriate docking parameter files. After the execution of docking jobs conformations produced were summarized and sorted based on QED.

RESULTS AND DISCUSSIONS

Table 1 gives the statistical data for each of the processes carried out. The resulting 2276 compounds were sorted based on their QED. Summarized data of the top 3 hits are provided in **Table 2** and **Table 3**.

Figures of ligand, protein-ligand interaction, and protein-ligand docked pose for top 3 hits are shown below.

CONCLUSIONS AND SCOPE FOR FUTURE STUDY

The short listed compounds are putative binders and inhibitors which can potentially act as competitive inhibitor for open conformation and as an allosteric inhibitor for closed conformation of PTP-SHP2 protein thereby controlling its over-expression.

Molecular Dynamics simulations must be carried out on receptor complexes after clustering to identify the protein-ligand complex with most stable bonds. In addition, a Pharmacophore modelling (ligand based drug designing) can be carried out to verify the results from the structure based drug designing.

REFERENCES

[1] Baell, J. B., and Holloway G. A. (2010), New Substructure Filters for Removal of Pan Assay Interference Compounds (PAINS) from Screening Libraries and for Their Exclusion in Bioassays, J. Med. Chem., 53 (7), pp 2719–2740.

[2] Baell, J. B., and Walters, M. A., (2014), *Chemistry: Chemical con artists foil drug discovery*, Nature, Vol 513, 481-483.

[3] Bickerton, G. R., Paolini, G.V., Besnard, J., Muresan, S., Hopkins, A.L. (2012), Quantifying the chemical beauty of drugs, Nature Chemistry, 4, 90-98.

[4] Chen, C., Cao, M., Zhu, S., Wang, C., Liang, F., Yan, L. and Luo, D. (2015), Discovery of a novel inhibitor of the protein tyrosine phosphatase SHP2, Sci. Rep. 5, 17626.

[5] Forli, S., Huey, R., Pique, M. E., Sanner, M. F., Goodsell, D. S., & Olson, A. J. (2016), Computational protein-ligand docking and virtual drug screening with the AutoDock suite, Nature Protocols, 11(5), 905-919.

[6] Michel F. Sanner, Python: A Programming Language for Software Integration and Development, J. Mol. Graphics Mod., 1999, Vol 17, February. pp 57-61.

[7] Morris, G. M., Huey, R., Lindstrom, W., Sanner, M. F., Belew, R. K., Goodsell, D. S. and Olson, A. J. (2009), Autodock4 and AutoDockTools4: automated docking with selective receptor flexibility, J. Computational Chemistry, 2009, 16: 2785-91.

[8] Somani, R., Madan, D. and Rai, P. (2016), Protein tyrosine phosphatase SHP2 as drug target, Mini-Reviews in Organic Chemistry, 2016, 13, 410-420.

Table 1: Statistical data after completion of each process.

Process	No. of ligands
Retrieved from NCI	2,84,176
VSG (4RDD)	2,68,981
Ligand binding energy cut-off (4RDD)	12,640
PAINS-free	10,554
QED/VSG (5EHP)	2,276

Table 2: General information of top 3 hits.

Sl. No	Ligand Name	MF	MW
1	5-Methyl-2-[(4-methylphenyl)sulfonyl]benzoic acid	$C_{15}H_{14}O_4S$	290.34
2	3-[(4-Methylphenyl)sulfonyl]benzoic acid	$C_{14}H_{12}O_4S$	276.31
3	2-[(1-Oxo-1,2,3,6,7,8-hexahydro-as-indacen-2-yl)methyl]benzoic acid	$C_{20}H_{18}O_3$	306.36

Table 3: Ligand binding energy data of top 3 hits.

Sl. No.	Ligand	Ligand binding energy (4RDD), kcal/mol	Ligand binding energy (5EHP), kcal/mol
1.	$C_{15}H_{14}O_4S$	-8.12	-8.99
2.	$C_{14}H_{12}O_4S$	-8.04	-9.83
3.	$C_{20}H_{18}O_3$	-8.84	-10.67

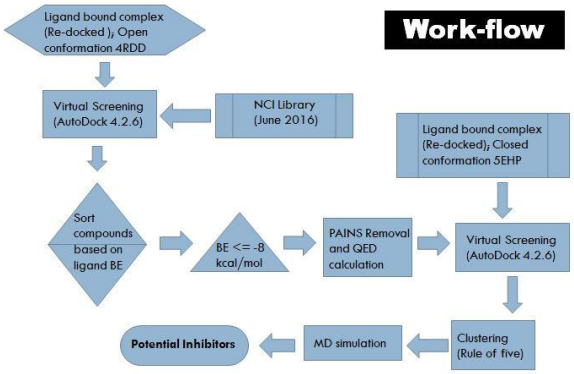

Figure 1: Structure based virtual screening work-flow. (BE = binding energy)

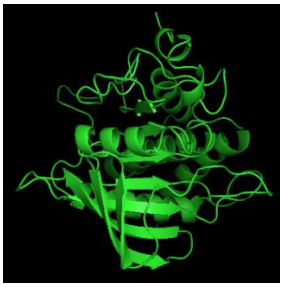

Figure 2: PTP-SHP2 in open conformation; PDB ID: 4RDD.

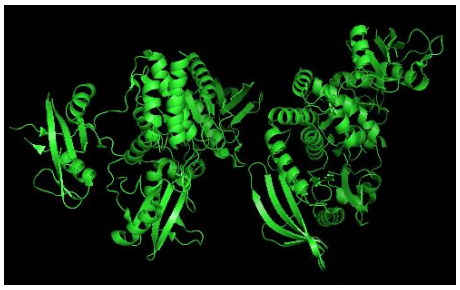

Figure 3: PTP-SHP2 in closed conformation; PDB ID: 5EHP.

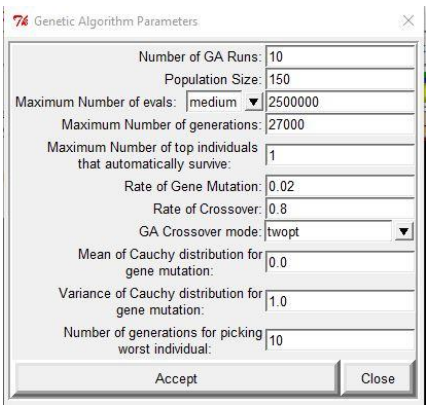

Figure 4: Genetic Algorithm parameters with default values provided by AutoDockTools-1.5.6.

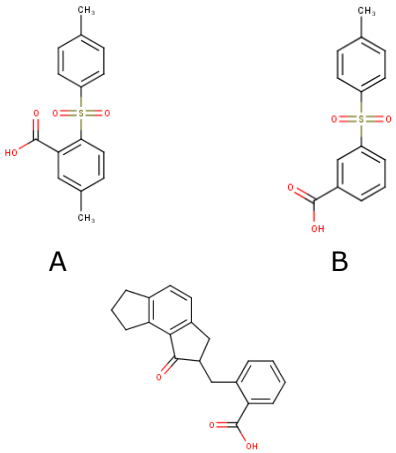

A B C

Figure 5: A, B and C represent ligands 1, 2 and 3 respectively.

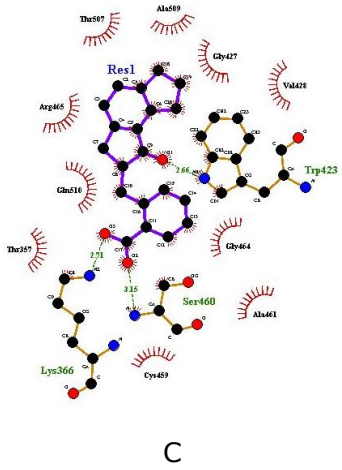

C

Figure 6: A, B and C represent interactions of ligands 1, 2 and 3 respectively with receptor 4RDD.

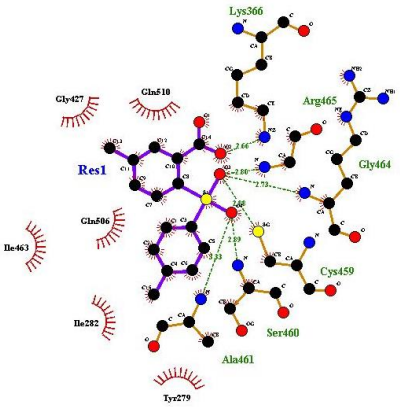

A

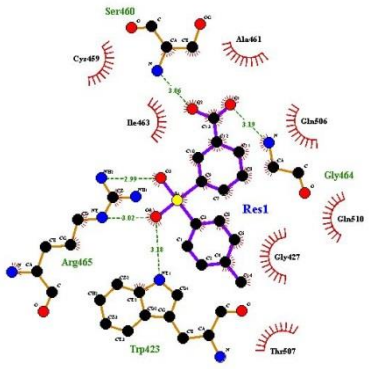

B

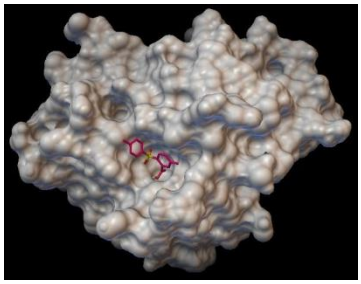

A

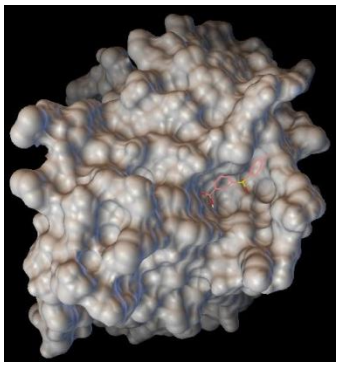

B

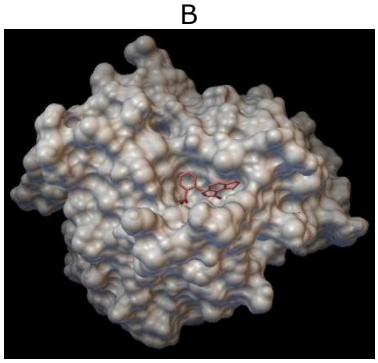

C

Figure 7: A, B and C represent docked poses of ligands 1, 2 and 3 respectively with receptor 4RDD.

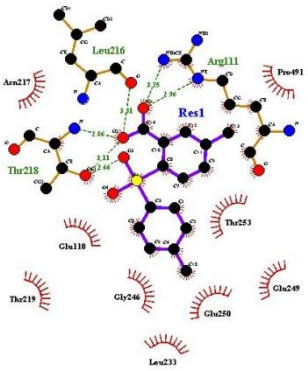

A

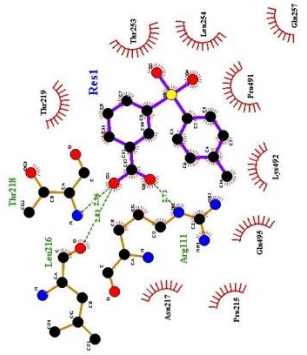

B

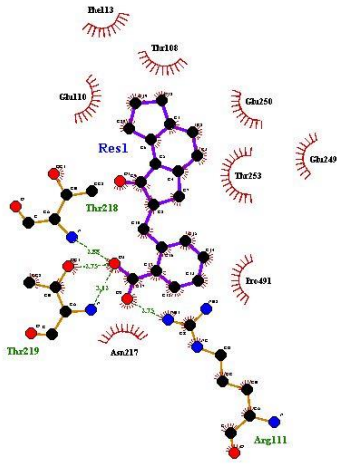

C

Figure 8: A, B and C represent interactions of ligands 1, 2 and 3 respectively with receptor 5EHP.

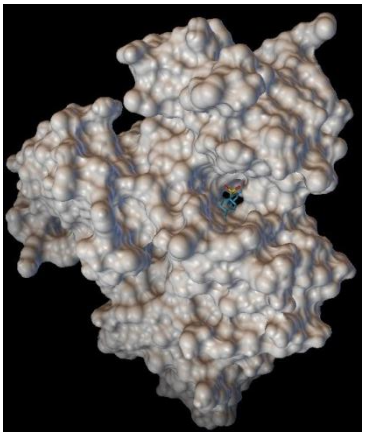

A

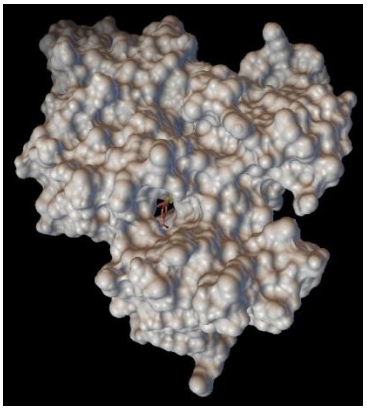

B

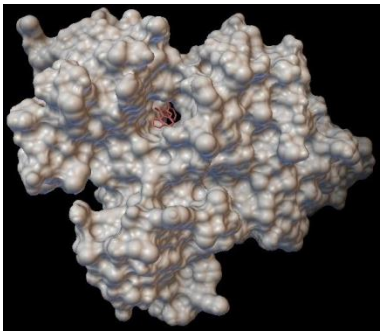

C

Figure 9: (A), (B) and (C) represent docked poses of ligands 1, 2 and 3 respectively with receptor 5EHP.

8th International Engineering Symposium - IES 2019
March 13-15, 2019, Kumamoto University, Japan

Solution combustion synthesis of Nickel Ferrite Nanoparticles: Factors of synthesis and comparative study

Wayne Denis Monteiro [1], Shannon Walter Gonzalves[2]

1 *Department of Chemical Engineering, National Institute of Technology Karnataka, Surathkal, Mangalore 575025, India. email:waynemonteiro97@gmail.com*
2 *Department of Chemical Engineering, National Institute of Technology Karnataka, Surathkal, Mangalore 575025, India. email: shannon6997@gmail.com*

ABSTRACT: Solution combustion synthesis (SCS) is an effective method for the synthesis of nanoscale materials primarily for the production of oxides. SCS makes use of nitrate salts as oxidants and, reducing reagents like organic fuels such as glycine during the combustion reaction. This review explores some of the main factors that govern the production of nickel ferrite nanoparticles which are relevant to various applications. Low flame temperature, high gas generation, appropriate fuel type and optimal fuel/salt concentration produce a narrow size distribution of superparamagnetic nickel ferrite. SCS uses less time and energy as compared to hydrothermal synthesis and produces pure compositionally stoichiometric ferrites as compared to co-precipitation

Keywords: solution combustion synthesis, nanoparticles, nickel ferrite, spinel, superparamagnetic. agglomeration

INTRODUCTION

Nanotechnology, involves the manipulation of matter at sizes of the order of the nanometer. It holds the promise of creating new materials and devices which take advantage of unique phenomena realized at those length scales. This is due to high reactivity caused by the large surface to volume ratio. Application of nanomaterials for the removal of pharmaceuticals and detection of pathogens has come up as an interesting area of research. They exhibit high adsorption efficiency especially due to high surface area and great active sites for interaction with various species. Furthermore, surface modifications have been developed to improve the adsorption and detection ability of these materials. Hence, the high surface area to volume ratio has many added benefits not found in bulk materials (Chaturvedi et al, 2019). Nickel ferrite ($NiFe_2O_4$) is a common spinel magnetic material. Its preparation by the classical solid-state reactions requires a high calcination temperature and hence induces the sintering and aggregation of particles (Costa et al.,2005).

Popular methods of bottom-up synthesis approach are co-precipitation, sol– gel method, microemulsion method, hydrothermal, spray pyrolysis, reverse micelle, precursor, etc. Low production rate is the major drawback of these wet-chemical methods. Sol–gel auto-combustion synthesis method where the chemical sol–gel and combustion process are combined, has shown great potential in the preparation of spinel type ferrite nanomaterials.

SCS offers a way to produce nanoscale materials at low cost and low temperature (compared to alkoxide based sol gel process). Due to molecular chelation there is better control of the stoichiometry. The exothermic nature of the process makes products almost instantly. The process is especially useful for creating multicomponent oxides with single phase and high surface area.

As with any combustion process the production of carbonaceous residue may contaminate the nanoparticles and the possibility of violent combustion reactions needs special production precautions. A deeper understanding of combustion behaviour is needed to perform the controlled combustion in order to get final products with desired properties.

EXPERIMENTAL PROCEDURE USING CITRIC ACID FUEL

Common experimental procedures involve nitrate precursors of analytical grade along with an organic fuel capable of chelation: $Fe(NO_3)_3 \cdot 9H_2O$, $Ni(NO_3)_2 \cdot 6H_2O$, $C_6H_8O_7 \cdot H_2O$ and NH_4OH. Appropriate amounts of metal nitrates and citric acid were first dissolved in a minimum amount of deionized water. The molar ratio of the nickel salt to the iron salt was maintained at 1:2 ratio. Then the aqueous solution of citric acid was added drop by drop into the metal nitrate solution (Kesavamoorthi et al, 2016). Considering fuel propellant chemistry, the molar ratio of nitrates to citric acid may be kept as greater than 2.22, equal to it or lesser than it.
The oxidant to fuel ratio (ψ) thus can be fuel deficient (ψ<1), stoichiometric (ψ =1) or fuel rich (ψ>1) quantifying the quantity of oxygen in-excess, appropriate or deficient. A small amount of ammonia was added to the solution to adjust the pH value at about 7.

Then, the mixed solution was then heated and stirred to transform into a xerogel. Heating temperature can be maintained at around 50-80°C for chelation and evaporation to occur, till xerogel is formed. The xerogel was further heated to ignition. By using these three complexants, glycine, urea, and citric acid, reactions stop at 180°C, 280°C, and 500°C. When ignited points were observed, the dried gel burnt in a self-propagating combustion manner until all the gel was burnt out completely to form loose powder. The powder was then calcined at different temperatures ranging from 500 - 800°C with an average of 650°C for times ranging from 2-8 hrs .

The general chemical reaction involves in synthetic process can be written as $Ni(NO_3)_2 + Fe(NO_3)_3 \cdot 9H_2O + C_6H_8O_7 + NH_3.H_2O \rightarrow NiFe_2O_4 + CO_2 + N_2 + H_2O$

CHARACTERIZATION RESULTS

Crystallite size determined from X-ray diffraction were reported as 18nm and 21 nm by Costa et al (2005) and Kesavamoorthi et al (2016). They also both confirmed single phase cubic spinel nickel ferrite. Annealed samples have more intense peaks than as-prepared samples indicating more crystalline form of nickel ferrite. The temperature of annealing must be well controlled for an optimal particle size distribution, to obtain regular shape and also to prevent multiple phases from forming. Scanning Electron Microscopy Analysis shows the distribution of particle sizes as varied at room temperature and uniform for annealed samples. Magnetic studies of the nanoparticles (Reddy et al, 2017) were measured at room temperature with the applied magnetic field of 20 KOe The magnetic saturation value of 44.36 emu/g, which is lower than the theoretical value of 47.5 emu/g20 previously reported. The lower values of magnetization may be due to small grain size effect of the ferrite nanoparticles. Smaller grains have large surface area on which the magnetic spins are randomly aligned due to increase in surface spin entropy which consequently decreases the saturation magnetization.

PARAMETERS OF SYNTHESIS

1.Flame Type

Solution combustion synthesis, under controlled conditions, generates a smoldering type flame, depending on the employed fuel and oxidizer-fuel ratio, which does not rise and is extinguished in a few seconds. The type of flame in the combustion plays an important role in controlling the particle size of as-synthesized powders.

Fuels like urea act reactively and produce a flame while a fuel like glycine produces a smoldering flame. The reactivity of the combustion reaction is dependent on the ligand groups of the molecules of the fuel and the compositional ratio of fuel and oxidant. (Alves A et al, 2013). It is always better to have a controlled flame because it produces nanoparticles of favorable characteristics

2.Flame Temperature

The combustion flame time and temperature of the synthesis by combustion reaction exerts an important effect on the final characteristics of powders. These parameters depend, mainly of the intrinsic characteristics of each system. For the system $NiFe_2O_4$ the combustion flame time and temperature of reaction reached during the synthesis using urea as fuel, whose obtained experimental values were 11.0 seconds and 622°C (±2°C), respectively. This show that the system led lower temperature and lower combustion time, avoided, this way, the pre-sintering and/or growth of particles (Costa et al, 2008). A higher combustion temperature during SCS usually results in improved crystallinity, larger grain size, more serious agglomeration, and lower specific surface area for the product

3.Gas Generation

It is observed that in combustion synthesis, the powder morphology, particle size and surface area are directly related to the amount of gases that escape during combustion. The evolution of gases break large clusters and create pores between particles. The disintegration of clusters produce more heat, hindering particle growth. The difference in particle size, using different fuels, depends on the number of moles of gaseous products released during combustion. Evolution of gases limits the occurrence of agglomeration

4.Fuel-Oxidant Ratio

A fuel is a reducing agent capable of burning the CH bonds. An oxidant is a substance that helps in burning, providing oxygen. Only intimate mixing of the two can liberate enough heat for the reaction to propagate and produce the particles
Product properties such as crystallite size, surface area, morphology, phase, degree and nature of agglomeration, are generally controlled by adjusting the fuel-oxidant ratio. The fuel-oxidant ratio, however, is not always calculated using a thermodynamic modelling and/or theory of the propellants like done in the experimental procedure reviewed here.

5.Fuel Type

Complexing agents which play the part of fuels too effectively chelate metal ions , which helps in preventing their selective precipitation to maintain compositional homogeneity and stoichiometry.
It has been found that from these three precursors, combustion reaction rate increases in order glycine > urea > citric acid. By using these three complexants, glycine, urea, and citric acid, reactions stop at 180°C, 280°C, and 500°C, respectively (Sutka et al, 2012). Single phased spinel ferrite was obtained when glycine was used, but in case of urea and citric acid traces of impurity phases were detected. Also, by using urea and citric acid, there is higher carbon content after combustion reaction in comparison with glycine, which might be due to incomplete combustion. High phase purity and crystallinity is due to the generation of larger amount of heat during combustion, faster chemical reaction which leads to particle growth and agglomeration. In some instances non-stoichiometry between metal and complexant valences is preferable. Adjustment of the complexant to metal nitrate ratio allows for control of the flame time and its effect on the formation and growth of the phase and on the particle agglomeration rates
With excess of complexant in the gels, the combustion reaction needs oxygen to be supplied externally, thus reaction rate and temperature is reduced because it is limited by oxygen. This inevitably leads to particles having lower crystallinity and

phase purity. Larger volume of gases (primarily CO_2 and NO_2 due to fuel combustion) is produced. This could increase the fraction of super paramagnetic particles which is preferable for specific spinel ferrite applications like bacterial immune-magnetic separations.
For deficient complexant content, the heat generated is not enough due to lack of reductant in the system, and thus reaction rate and temperature are also reduced, resulting in the decrease of particle sizes and the increase of specific surface area. In comparison with complexant excess systems, less amount of carbon content in the final product could be observed due to complete combustion.

6.CHEMICAL COMPOSITION OF PRECURSOR CHEMICALS

Precursor salts should be highly soluble in the medium so that intimate mixing happens at the molecular level. That happens when oxidants and fuels are dissolved in water. The fuel also serves as complexing agent limiting the precipitation of individual precursor components prior to ignition
The addition of an inert salt in a mixture of redox solution for combustion synthesis may result in the formation of well dispersed nanoparticles with a more prominent increase in surface area. The addition of salt should break the three-dimensional porous structure, typical of the resulting powders through combustion and act as an inhibitor of the agglomeration. The inorganic salt is generally low cost when compared with organic salts, readily soluble in water, thermally stable at high temperatures, easily removed from the product-mix as-prepared and recyclable (Alves A et al, 2013).
Nitrate salts are favoured as precursors, because they serve as water-soluble low temperature NO^{3-} oxidant source for synthesis. Metal nitrates possess hygroscopicity; consequently, they easily absorb moisture and become slurry. This variety of the sol–gel auto-combustion is called flash-combustion method (Sutka et al, 2012). However, citric acid is most frequently used in producing in large variety of ferrites with sol–gel auto-combustion method. It is inexpensive and is a more effective complexing agent than hydrazine and glycine in producing fine ferrite powder with smaller particle size.

6.pH

The crystallinity and the average crystallite size are increased as the pH increases. Rapid combustion rates and high flame temperatures attribute to an increase in the crystallite size along with good crystallinity which are both a consequence of the increase in pH.
It was found that Fe^{3+} has achieved complete complexation with citrates only when pH value is approached above 3. From that one could conclude that without ammonia, citric acid works only as a fuel. An imperfect 3D structured gel network could be caused by poor chelation of metal ions with citrates. The drying and auto-combustion processes can help decompose the oxidant nitrate in the xerogel with greater ease. Formation of the desired ferrite compounds is delayed due to the lowered amount of generated heat. Optimal pH value equal to 6 for spinel ferrite formation was found from literature from citric acid as a fuel.

Hydrothermal synthesis and comparison with solution combustion

Hydrothermal synthesis is generally defined as crystal synthesis or crystal growth under high temperature and high-pressure water conditions from substances which are insoluble in ordinary temperature and pressure (<100 °C, <1 atm). The solvent properties for many compounds, such as dielectric constant and solubility, change dramatically under these conditions. The dielectric constant of water decreases with increasing temperature and decreasing pressure and thus its contribution to the reaction rates becomes remarkable based on the electrostatic theory (Hayashi & Hakuta,2010). Thus, the method becomes useful when crystalline phases become unstable at the melting point like in solid-state reactions.
The formation mechanism of metal oxide particles from metal nitrate solution is as

follows: First, hydrated metal ions are hydrolyzed to metal hydroxide. Then, metal hydroxides proceed to precipitate as metal oxides through dehydration.

$M(NO_3)_x + xH_2O = M(OH)_x + xHNO_3$ (1)

$M(OH)_x = MO_{x/2} + x/2\ H_2O$ (2)

When compared with solution combustion (SC) using urea as a fuel (Costa et al.,2005), the average particle size of the nanoparticles is roughly the same (around 20 nm) provided hydrothermal synthesis used lower annealing temperatures (Chandra et al, 2016). Higher annealing temperatures forms larger particles. Therefore, SC provides crystalline nanoparticles without much annealing as compared to the hydrothermal process.

Hydrothermal synthesis leads to water molecules being absorbed by the nanoparticle along with OH^- from the solution during hydrothermal synthesis. While in solution combustion nitrate ions, water and carbon dioxide gas is absorbed too. Hydrothermal synthesis produces minor crystal defects while it is not observed in SC. These are confirmed from FTIR studies. Nanoparticles from both methods exhibit the same magnetization around 45 emu/g conferring similar magnetic properties. (Costa et al.,2005; Reddy et al., 2017)

The advantages of hydrothermal synthesis of nickel ferrite nanoparticles are that it is possible to control particle size and shape using different solvents and hydrothermal conditions. The resulting powders are highly reactive which aid in lowering sintering temperatures. The disadvantages include requiring prior knowledge on solubility of the starting materials in order to optimize the yield. Depending on the precursors the process leads to the formation of mineral acids which are highly corrosive. Since these syntheses use autoclaves at high pressures, accidental explosions could pose a risk. While hydrothermal synthesis is more time and energy consuming, solution combustion requires only a self-propagating energy source provided by the heated solution. It does not produce harmful by-products.

Co-precipitation synthesis and comparison with solution combustion

Co-precipitation and sol–gel techniques have been used to synthesize nickel ferrite nanoparticles. Both the methods produce single phase cubic Ni-ferrite nanoparticles; but sol–gel derived particles annealed at 600C exhibits hematite phase also. Co-precipitation gives particles of very small size with a wide size variation (8– 20 nm) and superparamagnetic nature. Sol–gel combustion produces Ni-ferrite particles of comparatively larger size with small size variation (18–25 nm) and ferrimagnetic nature. As the annealing temperature is increased, particle size and saturation magnetization are found to increase in both the methods. Sol–gel method is better for the preparation of homogeneous, pure and compositionally stoichiometric ferrites while co-precipitation is suitable for the synthesis of ferrites with very small size and superparamagnetic nature. While the homogeneous mixing of reactant precipitates reduces the reaction temperature, the disadvantages are that this process is not suitable for the preparation of high pure, accurate stoichiometric phase. Also, this method does not work well, if the reactants have very different solubility as well as different precipitate rate.

CONCLUSIONS

The following conclusions are deduced from this study:

- Solution combustion synthesis is able to produce nanoscale nickel ferrite that has superparamagnetic nature and is highly crystalline.
- Factors that lead to small sized particles are: smoldering flame, low flame temperature, high gas generation, excess fuel and high pH
- Nickel ferrite is best produced by solution combustion because it produces highly stoichiometric nanoparticles in short periods of time compared to co-precipitation methods and the energy intensive hydrothermal methods

REFERENCES

[1]. A.C.F.M. Costa, A.M.D. Leite, H.S. Ferreira, R.H.G.A. Kiminami, S. Cava, L. Gama (2008) Brown pigment of the nanopowder spinel ferrite prepared by combustion reaction' Journal of the European Ceramic Society,Volume 28, Issue 10, pg 2033-2037,
[2]. Alves, A; Bergmann, C.P; Berutti, F. A. (2013) ` Novel Synthesis and Characterization of Nanostructured Materials' Chapter 2, pg 11-20
[3]. Chandra Babu Naidu, Kadiyala. (2016). Hydrothermal Synthesis of NiFe2O4 nano-particles: Structural, Morphological, Optical, Electrical and Magnetic Properties. Bulletin of Materials Science. 40.
[4]. Chaturvedi S., Dave P. (2019). 'Water Purification using Nanotechnology and Emerging Opportunities' Chemical Methodologies, 3, pg 115-144
[5]. Costa, A.C.F.M. & Gama, L & Morelli, Márcio & Kiminami, R.H.G.A.. (2005). Nickel Ferrite: Combustion Synthesis, Characterization and Magnetic Properties. Materials Science Forum - MATER SCI FORUM. pg 498-499
[6]. Hayashi, Hiromichi; Hakuta, Yukiya. 2010. "Hydrothermal Synthesis of Metal Oxide Nanoparticles in Supercritical Water." *Materials* 3, no. 7
[7]. Kesavamoorthi, R & Vigneshwaran, A.N. & Sanyal, Vijayalakshmi & Raja, C. Ramachandra. (2016). 'Synthesis and characterization of nickel ferrite nanoparticles by sol - Gel auto combustion method'. Journal of Chemical and Pharmaceutical sciences ,9. pg 160-162.
[8]. Khan, Ayaz & Javed, M & Rauf Khan, A & Iqbal, Yousaf & Majeed, Asif & Zahid Hussain, Syed & Durrani, Shahid. (2017). Influence of preparation method on structural, optical and magnetic properties of nickel ferrite nanoparticles. Materials Science-Poland. 35. 10.1515/msp-2017-0006
[9]. Penchal Reddy, M., Shakoor, R., & Mohamed, A. (2017). Auto Combustion Synthesis, Microstructural and Magnetic Characteristics of Nickel Ferrite Nanoparticles. *Indian Journal Of Science And Technology, 10*
[10]. Reddy, M & Shakoor, Rana & Mohamed, A.M.A. (2017).' Auto Combustion Synthesis, Microstructural and Magnetic Characteristics of Nickel Ferrite Nanoparticles' Indian Journal of Science and Technology. 10. pg 1-5.
[11]. Sutka, A. & Mezinskis, (2012)' Sol–gel auto-combustion synthesis of spinel-type ferrite nanomaterials'. Front. Mater. Sci.

8th International Engineering Symposium - IES 2019
March 13-15, 2019, Kumamoto University, Japan

Model Predictive Control of Fluid Catalytic Cracking Process

Avanika B R [1], Prabhjot Kaur Luthra[2], Prabhul Pradeep Kumar[3] and **Chinta Sankar Rao[4]**

1 *Department of Chemical Engineering, National Institute of Technology Karnataka, Surathkal, Mangalore 575025, India. email:avanikabr@gmail.com*
2 *Department of Chemical Engineering, National Institute of Technology Karnataka, Surathkal, Mangalore 575025, India. email:prabhjotkaur090298@gmail.com*
3 *Department of Chemical Engineering, National Institute of Technology Karnataka, Surathkal, Mangalore 575025, India. email:prabhul77077@gmail.com*
4 *Department of Chemical Engineering, National Institute of Technology Karnataka, Surathkal, Mangalore 575025, India. email:csankarrao@gmail.com*

ABSTRACT: Fluidized Catalytic Cracking (FCC) is a complex process. Due to its economic importance, control of FCC is an important problem. A data driven approach is followed to design a Model Predictive Control (MPC) for the FCC unit. MPC is based on multivariate algorithms that use a process model to predict the future behaviour of a process and to maintain the controlled variables close to the set point while handling constraints. A six-lump reaction scheme is developed for the riser part of FCC unit. Model Identification is done using Open Loop Process Reaction Curve and Subspace Identification method. PID and MPC controllers are designed for the Riser and evaluated. The manipulated input variables are the regenerated catalyst flowrate and the flowrate of air to the regenerator. The controlled variables are the temperatures at the top of the riser and in the regenerator bed. The simulation studies show a very good tracking of the set points of the riser and regenerator temperatures despite their changes.

***Keywords**: Fluidized catalytic cracking, Model predictive control, multivariate, constraints, six-lump, Identification*

INTRODUCTION

The FCC unit is a refinery process that converts heavy gas oils especially the vacuum gas oils into more valuable, lighter hydrocarbon products. The FCC unit is capable of converting heavy feed into more valuable products in a few seconds and also is one of the major secondary processes of producing largest volume fraction of gasoline. Hence efficient operation of the FCC unit is essential on both energy and monetary basis. It is a multivariable nonlinear process having a number of operational constraints, thus a very complex process with a number of interactions between yields, reaction rates etc. Thus optimizing and designing an effective controller is the major aim of many researchers currently. [Ellis et al. (1998)].

A FCC unit consists of three major units that include the riser, the separator and the regenerator. The catalytic cracking of the hydrocarbon feed takes place in the riser. The product mixture consisting of oil, gas and catalysts is separated at the outlet of the riser in the separator. Combustion of the coke deposited on the catalysts from the riser reactor takes place in the regenerator, thus reactivating the catalysts. A schematic diagram is presented in Fig.1.

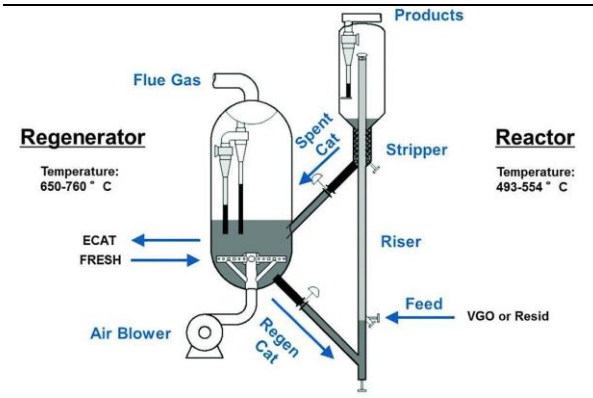

Fig.1 Schematic Diagram of FCC Unit (Vogt and Weckhuysen, 2015)

The FCC process is a complex process due to its feed composition, multiple operating constraints and dynamic mass and heat interactions between its components, which are riser, separator and regenerator. The process also involves complicated hydrodynamics and complex kinetics of the catalytic and coke burning reactions. Hence, control of FCC is a challenging and important problem. By implementing proper control and optimization strategies on the FCC unit, the economic benefits of the refineries can be influenced greatly.

Model Predictive Control (MPC)

Model Predictive Control (MPC) is a class of controller technique derived from Internal Model Control. It is an advanced control technique for multivariate process control. It involves prediction of the output and finding the optimal input for the closed loop response with certain constraints. It is used to control a process with multiple inputs and outputs while satisfying the constraints in these variables. It takes into account the dynamic interactions in the process. It is based on minimizing the deviation of the predicted variables from the reference variables.

The optimal operating point for FCC lies near its constraints. Hence, a control system that operates the process close to the constraints is necessary. The manipulated variables are the regenerated catalyst flowrate and the flowrate of air to the regenerator. The controlled variables are the temperatures at the top of the riser and in the regenerator bed.

FLUIDIZED CATALYTIC CRACKING (FCC) PROCESS

The feed oil is preheated and injected in the bottom of the riser with a small quantity of vapour. This comes in contact with the hot catalyst from the regenerator and gets vaporized. These vapours rise to the top of the riser. They undergo endothermic catalytic cracking as they rise. Coke is a by-product of the catalytic reactions and it gets deposited on the surface of the catalytic particles. This reduces the catalytic activity.

In the regenerator, air blown into the bed is used to burn off the coke from the surface of the catalytic particles. This reactivates the catalyst and also maintains the bed temperature for future cracking. The regenerated catalyst then flows into the riser through another circuit. The heat from the catalyst is used to compensate the heat required for the endothermic reactions in the riser.

MATHEMATICAL MODELLING OF FCC

Riser

The riser is a plug flow reactor. The presence of the high efficiency feed injection systems in modern units justifies this assumption. The residence time of the catalyst and the gases in the riser is assumed to be the same and is a few seconds [Ali et al., 1997].
A lumping strategy is used for the characterization of the cracking reactions. In the lump model, the feed cracks into some lumps like gasoline, diesel etc. as products of these reactions. We have used the 6 lump strategy as shown in Fig.2.

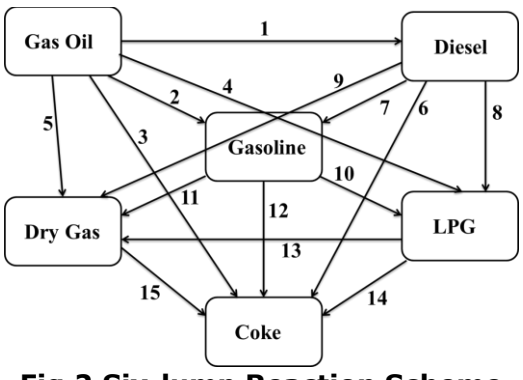

Fig.2 Six-lump Reaction Scheme

The heat of reactions and the kinetic data involved in the six-lump cracking reactions were taken from John et al. (2019). The reaction scheme followed for each component of the six-lump model is listed below.

$$R_{go} = -(k_1 + k_2 + k_3 + k_3 + k_4 + k_5)y_{go}^2 \quad (1)$$
$$R_{dz} = k_1 y_{go}^2 - (k_6 + k_7 + k_8 + k_9)y_{dz} \quad (2)$$
$$R_{gl} = k_2 y_{go}^2 + k_7 ydz - (k_{10} + k_{11} + k_{12})y_{gl} \quad (3)$$
$$R_{lpg} = k_4 y_{go}^2 + k_8 ydz + k_{10} ygl - (k_{13} + k_{14})y_{lpg} \quad (4)$$
$$R_{dg} = k_5 y_{go}^2 + k_9 y_{dz} + k_{11} y_{gl} + k_{13} y_{lpg} - k_{15} y_{dg} \quad (5)$$
$$R_c = k_3 y_{go}^2 + k_6 y_{dz} + k_{12} y_{gl} + k_1 4 y_{lpg} + k_{15} y_{dg} \quad (6)$$

The riser equations are obtained using mass, component and momentum balances and equations 1-6 and are nonlinear ordinary differential equations.

$$\frac{dy_{go}}{dz} = \frac{\rho_c \epsilon_c D \phi_c}{F_g} R_{go} \quad (7)$$
$$\frac{dy_{dz}}{dz} = \frac{\rho_c \epsilon_c D \phi_c}{F_g} R_{dz} \quad (8)$$
$$\frac{dy_{gl}}{dz} = \frac{\rho_c \epsilon_c D \phi_c}{F_g} R_{gl} \quad (9)$$
$$\frac{dy_{lpg}}{dz} = \frac{\rho_c \epsilon_c D \phi_c}{F_g} R_{lpg} \quad (10)$$
$$\frac{dy_{dg}}{dz} = \frac{\rho_c \epsilon_c D \phi_c}{F_g} R_{dg} \quad (11)$$
$$\frac{dy_c}{dz} = \frac{\rho_c \epsilon_c D \phi_c}{F_g} R_c \quad (12)$$

Including changes in temperature along the length of the riser using energy and mass balances, we get the following ODE.

$$\frac{dT_g}{dz} = \frac{\Omega}{F_g C_{pg}} \rho_c \epsilon_c Q_{reac} \quad (13)$$

where Q_{reac} is as follows

$$Q_{reac} = Q_{ygo} + Q_{ydz} + Q_{ygl} + Q_{ylpg} + Q_{ydg} \quad (14)$$

Solving equations 7-13 using *ode45* solver with respect to the height of the riser (47.1m) with feed rate, F_g as 62.5kg/s and a constant regenerated catalyst temperature, T_c of 905K; we obtain the results as shown in Fig.3 and Fig.4.

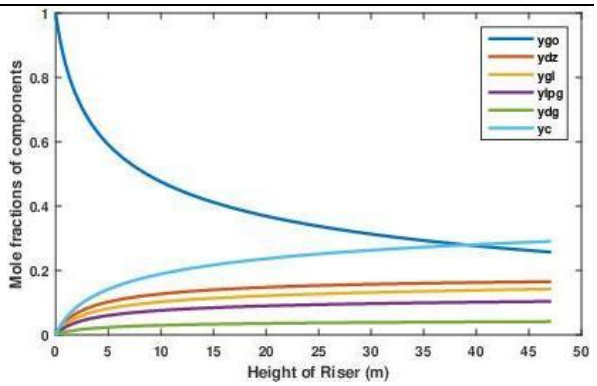

Fig.3 Profile of Riser gas components

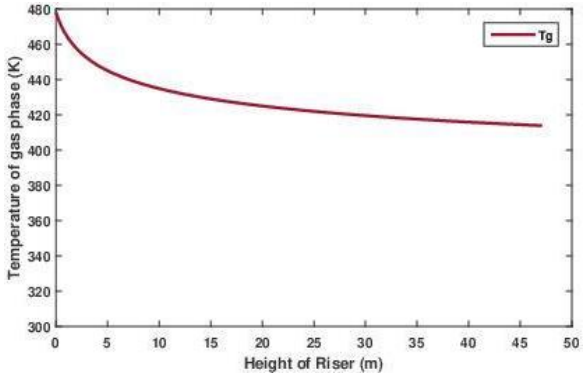

Fig.4 Temperature profile in riser

MODEL IDENTIFICATION

Open Loop Identification Method

Step response of the FCC gives us the process reaction curve for the system. A unit step input is given in gas flow rate and under-damped response is obtained. A SOPTD model is identified as shown in equation 15.

$$G_{cl} = \frac{Ke^{-dS}}{\tau^2 S2 + 2\tau\zeta S + 1} \quad (15)$$

The model parameters are given in Table 1.

Table 1 SOPTD Model Parameters

K	ζ	τ	d
0.037	0.1746	$2.38e^{03}$	$-3.37e^{06}$

The process reaction curve is obtained by a step response of the above transfer function as shown in Fig.5.

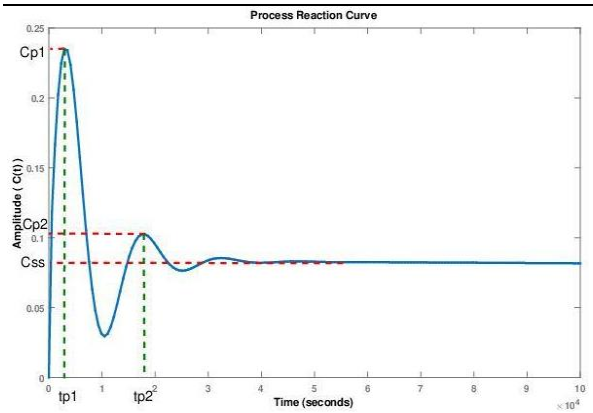

Fig.5 Process Reaction Curve for the Transfer Function

Subspace Identification Method

Subspace identification algorithms do not require an explicit parametrization. The only parameter needed is the system order, input-output dataset, and noise signal if present. The order of the system can be determined using singular value decomposition. Such a method does not require any iteration or parameter optimization thus reducing the complexity of problems.

A white noise signal (with mean zero and variance 0.1) is added to the set point value. In any identification method, the input should be persistently excited of certain order, so that the input should have many distinct frequencies. In order to meet this condition, a white Gaussian noise is added to the steady state point. The output and the input signals shown in Fig.6 are used for the identification.

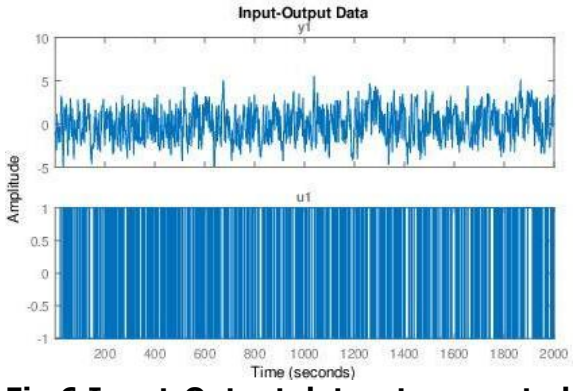

Fig.6 Input-Output dataset generated

The identified model is simulated with the input from the fresh dataset and compare the simulated output with the measured output of the real system. Fig.7 shows the result of the comparison, where the fit is computed as the root of the mean square value of the difference between outputs of the actual system and simulation. Fig.8 depicts the results we received and the best fit order of the system as 3.

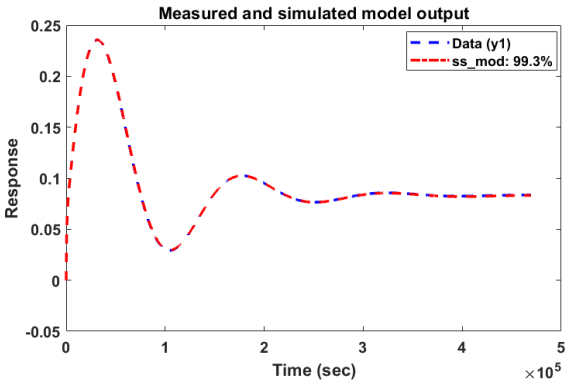

Fig.7 Comparison plot between measured output and predicted output

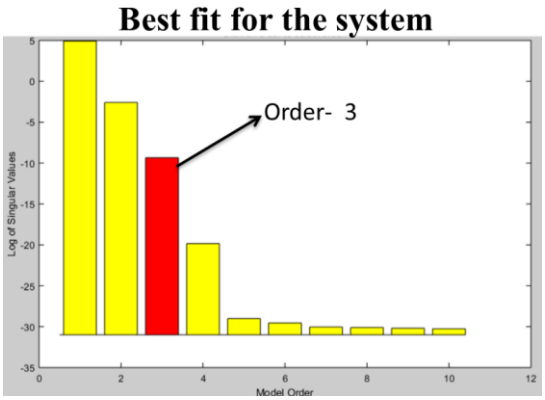

Fig.8 Selection of order of the system from Input-Output Data

CONTROL OF FCC

Controllers are designed based on the identified SOPTD model. There are three types of controllers designed, PID (using Synthesis Method), PID (Ziegler Nicholas Method) and MPC. The basis of all the control strategies are as in Fig.9.

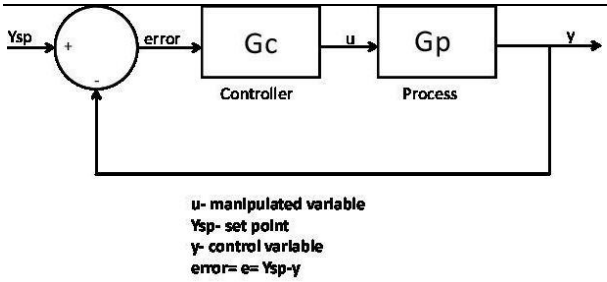

Fig.9 Basic Control Strategy

The design control parameters for each controller are mentioned in Table 2.

Table 2 Design Parameters of Controllers

Controller Strategy	K_c	T_I	T_D	Predictive Horizon	Control Horizon
PID 1	45.45	831	6818	-	-
PID 2	14609	15789	27353	-	-
MPC	-	-	-	10	2

PID Controller

PID control strategy is shown in Fig.10.

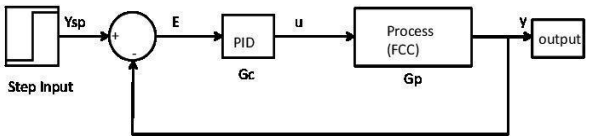

Fig. 10 PID Control Strategy

Synthesis Method

In this approach, an analytical expression for the feedback controller is derived from a process model and a desired closed-loop response. The closed loop response for PID 1 is shown in Fig.11.

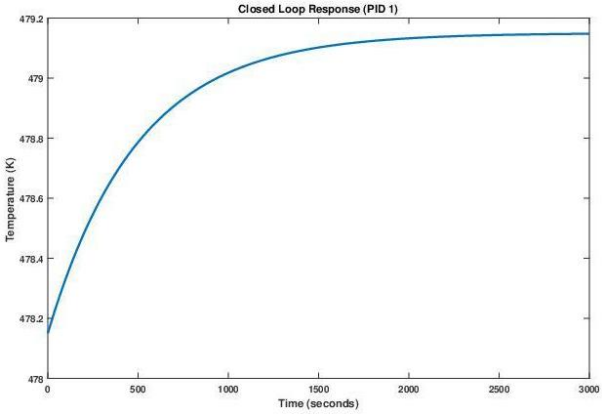

Fig. 11 Closed Loop Response of PID 1

ITAE Minimization Method

The closed loop response for PID1 is shown in Fig. 12.

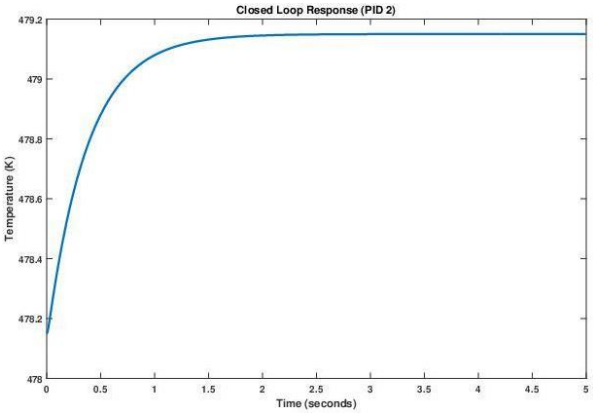

Fig.12 Closed Loop Response of PID 2

Model Predictive Control (MPC)

MPC control strategy is shown in Fig.13.

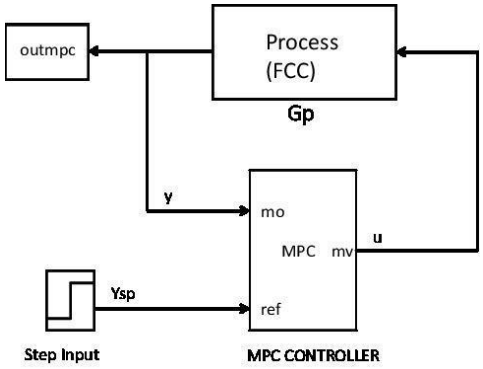

Fig. 13 MPC Control Strategy

The closed loop response for PID 1 is shown in Fig.14.

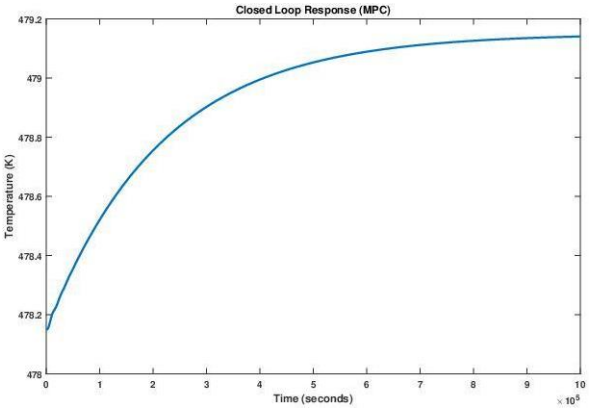

Fig. 14 Closed Loop Response of MPC

The controllers with the above parameters are simulated in Simulink MATLAB and the performance of each controller is evaluated using various performance equations. The results of this simulation are mentioned in Table 3.

Table 3 Error Analysis in Controllers

Controller Type	IAE	ITAE	ISE
PID 1	494.2	2.443E+05	247.1
PID 2	29.24	1.39E+05	0.2227
MPC	9841	5.121E+07	9687

CONCLUSIONS

The following conclusions are deduced from this study:

- The transient response obtained from the mathematical model developed for the riser unit of FCC is in consistence with the results presented in Malay et. al.
- The subspace model identified using various methods generate a stable input for the given corrupted dataset.
- The controllers designed on these identified models show satisfactory results with the output stabilizing in a shorter time.
- Comparing the different control strategies, PID designed using ITAE minimization technique provides better results and smaller error than the one designed using synthesis method.
- As the MPC is not optimized yet, the error values are huge and inconsistent with the predictions.

REFERENCES

[1] Abou-Jeyab, R. A. and Gupta, Y. P. (1996). Control of the fluidized catalytic cracking process using a simplified model predictive controller. Industrial & Engineering Chemistry Research, 35(10):3581–3589.

[2] Aguilar, R., Poznyak, A., Martınez-Guerra, R., and Maya-Yescas, R. (2002). Temperature control in catalytic cracking reactors via a robust pid controller. Journal of Process Control, 12(6):695 – 705.

[3] Ali, H., Rohani, S., and Corriou, J. (1997). Modelling and control of a riser type fluid catalytic cracking (fcc) unit. Chemical Engineering Research and Design, 75(4):401 – 412.

[4] Boum, A. T., Latifi, A., and Corriou, J. (2013). Model predictive control of a fluid catalytic cracking unit. In 2013 International Conference on Process Control (PC), pages 335–340.

[5] Ellis, R. C., Li, X., and Riggs, J. B. (1998). Modeling and optimization of a model iv fluidized catalytic cracking unit. AIChE Journal, 44(9):2068–2079.

[6] Grosdidier, P., Mason, A., Aitolahti, A., Heinonen, P., and Vanhamaki, V. (1992). Fcc unit reactor-regenerator control. 1992 American Control Conference, pages 117–121.

[7] Jia, C., Rohani, S., and Jutan, A. (2003). Fcc unit modeling, identification and model predictive control, a simulation study. Chemical Engineering and Processing: Process Intensification, 42(4):311 – 325.

[8] John, Y. M., Mustafa, M. A., Patel, R., and Mujtaba, I. M. (2019). Parameter estimation of a six-lump kinetic model of an industrial fluid catalytic cracking unit. Fuel, 235:1436 – 1454.

[9] Katayama, T. (2005). Subspace methods for systems identification. Springer, London.

[10] Kealy, T. and O'Dwyer, A. (2002). Closed loop identification of a first order plus deadtime process model under pi control. Proceedings of the Irish Signals and Systems Conference.

[11] Khandalekar, P. and Riggs, J. (1995). Nonlinear process model based control and optimization of a model iv fcc unit. Computers and Chemical Engineering, 19(11):1153–1168.

[12] Malay, P., Rohani, S., and Milne, B. J. The modified dynamic model of a riser type fluid catalytic cracking unit. The Canadian Journal of Chemical Engineering, 77(1):169–179.

[13] Pandimadevi, G., Indumathi, P., and Selvakumar, V. (2010). Design of controllers for a fluidized catalytic cracking process. Chemical Engineering Research and Design, 88(7):875 – 880.

[14] SINGH, B., SAHU, S., DIMRI, N., DASILA, P. K., PAREKH, A. A., GUPTA, S. K., and DAS, A. K. (2017). Seventeen-lump model for the simulation of an industrial fluid catalytic cracking unit (fccu). S¯adhan¯a, 42(11):1965–1978.

[15] Vogt, E. T. C. and Weckhuysen, B. M. (2015). Fluid catalytic cracking: recent developments on the grand old lady of zeolite catalysis. Chem. Soc. Rev., 44:73427370.

[16] Xuemin, T. and Dongbo, F. (2004). Nonlinear model predictive controller for the riser reactor of a fcc unit. In Fifth World Congress on Intelligent Control and Automation (IEEE Cat. No.04EX788), volume 4, pages 3344–3347 Vol.4.

8th International Engineering Symposium - IES 2019
March 13-15, 2019, Kumamoto University, Japan

Effect of synthesis method on facet ratio and its effect on catalytic activity of samarium doped ceria

Prabhjot Kaur Luthra, Praneeth Pichika, Shraya Sapru,
Anjana P Anantharaman[1] and Hari Prasad Dasari[2]

Department of Chemical Engineering, National Institute of Technology Karnataka, Surathkal, Mangalore 575025, India.
[1]email: anjana.pa00@gmail.com [2]email:energyhari@gmail.com

ABSTRACT: In this study, Samarium doped Ceria (SDC) Nano-particles were synthesized using microwave assisted co-precipitation method [1]. Effect of microwave power on SDC nano-particle shape and morphology was studied. The SDC nano-particles exhibited a mixture of spherical and cubic shape and with the increase in microwave power the nano-particles were agglomerated. The crystallite size and BET surface area of SDC nano-particles obtained were in the range of 5~15 nm and 30~75 m 2 /g, decreasing with increase in power. XRD analysis revealed the fluorite phase and Raman spectroscopy analysis showed the F2g (O-Ce-O) structure along with the presence of oxygen vacancy bands. The soot oxidation activity of the obtained SDC nano- particles followed a similar trend and will be presented in detail.

Keywords*: Microwave assisted co-precipitation method; Soot Oxidation; Sm-doped Ceria; X-ray diffraction; Raman Spectroscopy*

INTRODUCTION

Cerium nanoparticles are highly reactive in the presence of atmospheric oxygen hence they normally exists as stable oxides, generally called as ceria (CeO_2). CeO_2 being a versatile material, has wide range of applications especially in the field of catalysts. Ceria nanoparticles are used in catalytic converters in the automotive industry to convert harmful carbon monoxide to less harmful carbon dioxide, which has further applications as Polymer Electrolyte Membrane (PEM) in fuel cells. The semi-conductor industry uses cerium dioxide nanoparticles as fine abrasive and polishing agent in the manufacturing of computer chips. Non-nanoscaled cerium dioxide can improve the light production/output in mantles of gas lanterns as the gas flame produces almost no light itself, whereas burning cerium oxide generates a yellowish-white color. Such wide ranges of uses are due to its ability to store and release oxygen in its n-type fluorite structure. [2–5] This storage of oxygen is possible through oxygen vacancies created in CeO_2 through doping. The amount of self-generated doping is quite less, hence other rare-earth ions, with similar ionic radius are used for increasing the concentration of oxygen vacancies. [6] A number of studies have been performed for the comparison of ceria based electrolytes formed with various rare-earth metal ions and all of them show the superiority of Samarium on structural properties and ionic conductivity.[7,8]

Several techniques are implemented for the synthesis of ceria nanostructures like hydrothermal and solvothermal; microwave assisted hydrothermal; micro emulsion; sol- gel methods, and many more. Hydro or Solvothermal methods are

most commonly used for precise control over shape, morphology and catalytic activity. [9] Studies have been conducted with various solvents[10], dopants at different concentrations[11], by altering the process conditions[12]; and each showed a new way for the synthesis of ceria nanoparticles with better shape control and aimed at minimizing agglomeration. Microwave-assisted hydrothermal method (MAHT) is a new technique for the production of ceria nanostructures and more effective than the traditional hydrothermal method as the microwave irradiation increases the collision rate between the molecules and also provides shape (cubic) control in the synthesis process. But the exact mechanism for the synthesis of nanostructures is still not specified yet[1]. The power of the microwave irradiation can affect the shape, morphology and catalytic activity of the Samarium doped Ceria nanostructures so formed. Hence, to understand such an effect, these nanoparticles were synthesized by Microwave-assisted co-precipitation method at various microwave powers. These synthesized samples were studied thoroughly using different characterization techniques to understand the dependence of microwave power level on the crystallite size, morphology in a strongly basic growth solution used in the microwave-assisted process. The samples were also tested for soot oxidation activity and the correlation with power is presented in detail.

EXPERIMENTAL DETAILS

Material synthesis

Samarium doped Ceria (SDC) samples were synthesized using Microwave-assisted co-precipitation method[1] at various powers namely 540, 720, 900W. And for comparison with traditional method of synthesis, one of the samples was synthesized in an oven. AR grade chemicals were used for the synthesis. Cerium nitrate hexahydrate ($Ce(NO_3)_3.6H_2O$) and Samarium nitrate hexahydrate ($Sm(NO_3)_3.6H_2O$) were used to synthesize these binary metal oxides. 25% of ammonia solution was added dropwise for the precipitation to occur and ceria formation. The precipitated solution was then microwave heated for 30min at specific powers (540/720/900W). The obtained solution was washed and dried at 60°C/3h followed by calcination at 600°C/ 5hr to obtain the corresponding binary metal oxide samples.

Material Characterization

Raman Spectra of the different samples were obtained using Raman spectroscopy (Bruker: RFS 27 Model Raman spectrometer) with a charged-couple device (CCD) detector and a triple polychromator. Nd: YAG laser (λ=1064 nm) was used as an excitation source with a laser power of 10mW on the sample point. These samples were also characterized using X-ray diffraction (XRD), Scanning Electron Microscopy (SEM) and Transmission Electron Microscopy (TEM) techniques. The surface area of these samples was also obtained using the BET method. The instrument details and operating conditions for all these techniques are mentioned in previous reports by the group [11,13,14].

Soot Oxidation Activity

Soot oxidation reaction using different SDC samples as a catalyst is conducted in a TG/DTA 6300 TGA instrument operating at a temperature range of 200–800 °C with a heating rate of 10 °C/min using air as a purge gas at a flow rate of 100 ml/min. The reaction is conducted under tight contact condition with soot: catalyst ratio of 1:4 grounded in mortar and pestle for 30 min. Samples are preheated at around 100 °C to remove moisture content bound on their surface. As described in earlier reports [14].

RESULTS AND DISCUSSION

The SDC samples synthesized via the oven and microwave assisted hydrothermal method were subjected to various characterization tests. The BET Surface Area so calculated for all the samples is

listed in Table 1. With increase in power the BET Surface Area also increases with sample with 720W as the exception. Also we can conclude that surface area obtained using the microwave assisted synthesis procedure is better than oven assisted synthesis procedure. XRD was performed using CuK alpha radiation; the results so obtained are consistent with that of the literature presented in Fig. 6. Analysis for the 111 plane showed, the Dxrd of 12.1 nm and an average crystallite size of 1.807 A for SDC2. And similar calculations were carried out for all samples and listed in Table 1. The SEM samples analysis (Fig 3) revealed a trend of increase in agglomeration as the power they were subjected to be increased. This was consistent with the BET results, with the SDC 2 subjected to 540W power exhibiting the greatest surface area of 72.39 sqm/g. The average nano-particle size calculated for this sample is in the range of 10-15nm.

While, The TEM results (Fig 4) revealed a mixture of spherical and cubic Nanoparticles, with an increase in agglomeration as power was increased. The Raman Spectroscopy gave a clear indication of SDC being present in the form of fluoride structure with certain Oxygen vacancies corresponding to the 456 nm and 580 nm respectively. Soot oxidation activity results showed the higher activity in presence of SDC nanoparticles with SDC 2 showing the highest activity.

CONCLUSIONS

The following conclusions are deduced from this study:

- From XRD study, it was observed that SDC 2 has the highest lattice strain and surface area among the synthesized samples. It also has the lowest crystallite size and low degree of agglomeration.
- SEM and TEM analysis shows the flaky nature of all samples.
- Raman spectrum did not shift much with change in power of microwave.
- SDC 2 showed the highest catalytic activity in Soot Oxidation.

ACKNOWLEDGEMENTS

- Department of Chemical Engineering, NITK
- Department of Metallurgical and Materials Engineering, NITK
- Central Instrumentation Facility, MIT, Manipal, India
- Computational Physics Laboratory, NITK Surathkal, Mangalore, India
- Material Research Facility, MNIT, Jaipur, India
- Sophisticated Test and Instrument Centre (STIC), CUSAT, Kochi, India

REFERENCES

References should be given in alphabetical order. (font to be used: Verdana 8)

[1]O.S. Bezkrovnyi, R. Lisiecki, L. Kepinski, Relationship between morphology and structure of shape-controlled CeO_2 nanocrystals synthesized by microwave-assisted hydrothermal method, Cryst. Res. Technol.51(2016)554–560. doi:10.1002/crat.201600053.

[2]T.X.T. Sayle, S.C. Parker, D.C. Sayle, O. Systems, C. Down, Oxidising CO to CO 2 using ceria nanoparticles, (2005).

[3]Y. Lee, Y. Seo, H. Jeong, Evaluation of Oxide-Chemical Mechanical Polishing Characteristics Using Ceria-Mixed Abrasive Slurry, 8 (2012) 523–528. doi:10.1007/s13391-012-2056-4.

[4]T. Zhu, L. Kundakovic, A. Dreher, M. Flytzani-stephanopoulos, Redox chemistry over CeO 2 -based catalysts : SO 2 reduction by CO or CH 4, 50 (1999).

[5]R. Si, M. Flytzani-stephanopoulos, Zuschriften Shape and Crystal-Plane Effects of Nanoscale Ceria on the Activity of Au-CeO 2 Catalysts for the Water – Gas Shift Reaction **, 2 (2008) 2926–2929. doi:10.1002/ange.200705828.

[6]W. Wattanathana, C. Veranitisagul, S. Wannapaiboon, Samarium doped ceria (SDC) synthesized by a metal triethanolamine complex decomposition method : Characterization and an ionic conductivity study, Ceram. Int. 43 (2017) 9823–9830. doi:10.1016/j.ceramint.2017.04.162.

[7]S. Kuharuangrong, Ionic conductivity of Sm , Gd , Dy and Er-doped ceria, 171 (2007) 506–510. doi:10.1016/j.jpowsour.2007.05.104.

[8] A. Arabaci, Effect of Sm and Gd dopants on structural characteristics and ionic conductivity of ceria, Ceram. Int. 41 (2015) 5836–5842. doi:10.1016/j.ceramint.2015.01.013.

[9]Z. Yang, K. Zhou, X. Liu, Q. Tian, Single-crystalline ceria nanocubes : size-controlled synthesis , characterization and redox property, 185606 (n.d.). doi:10.1088/0957-4484/18/18/185606.

[10]W.J. Khudhayer, N. Kariuki, D.J. Myers, A.U. Shaikh, T. Karabacak, Microstructural evolution of monocrystalline Co-Al-W, Mater. Res. Soc. Symp. Proc. Vol. 1446 (2012) 25–31. doi:10.1557/opl.2012.

[11]A.P. Anantharaman, J. Geethu, M.R. P, H.P. Dasari, J.H. Lee, H. Dasari, G.U. Bhaskar Babu, Ceria-samarium binary metal oxides: A comparative

approach towards structural properties and soot oxidation activity, Mol. Catal. 451 (2018) 247–254. doi:10.1016/j.mcat.2018.01.033.
[12]S. Rajeshkumar, P. Naik, Synthesis and biomedical applications of Cerium oxide nanoparticles – A Review, Biotechnol. Reports. 17 (2018) 1–5. doi:10.1016/j.btre.2017.11.008.
[13]A.P. Anantharaman, H.J. Gadiyar, M. Surendran, A.S. Rao, H.P. Dasari, H. Dasari, G.U.B. Babu, Effect of synthesis method on structural properties and soot oxidation activity of gadolinium-doped ceria, Chem. Pap. 72 (2018) 3179–3188. doi:10.1007/s11696-018-0532-5.
[14]A.P. Anantharaman, H.P. Dasari, J.H. Lee, H. Dasari, G.U.B. Babu, Soot Oxidation Activity of Redox and Non-Redox Metal Oxides Synthesised by EDTA–Citrate Method, Catal. Letters. 147 (2017) 3004–3016. doi:10.1007/s10562-017-2181-7.

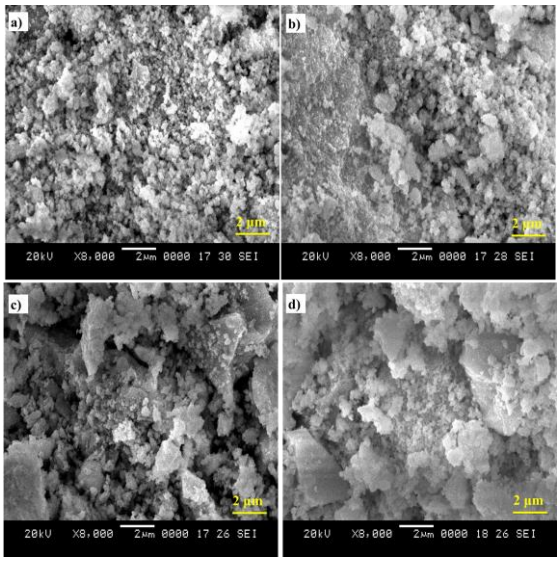

Fig. 1 SEM micrographs

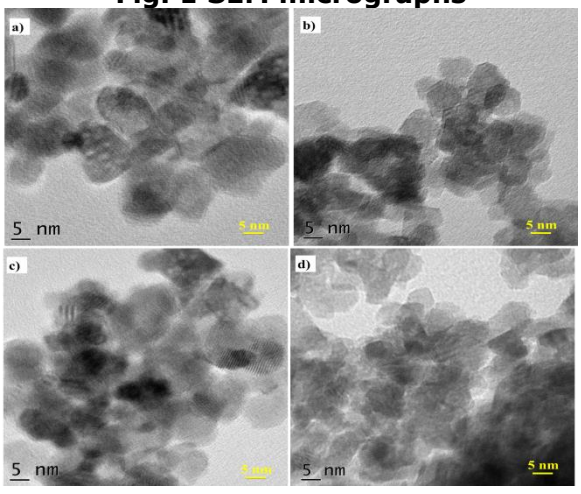

Fig. 2 TEM images – 5nm

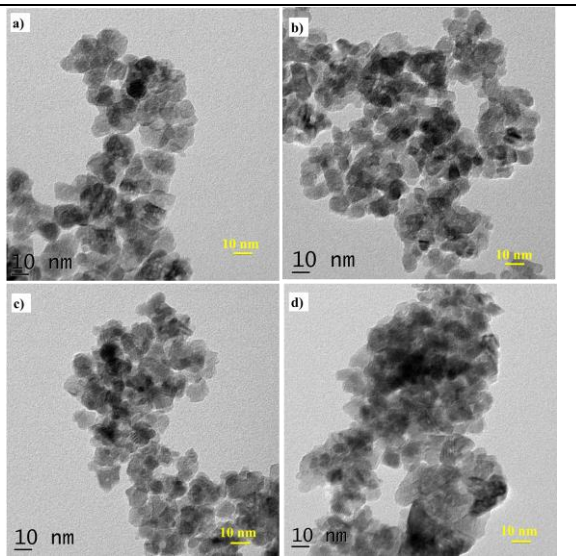

Fig. 3 TEM images – 10nm

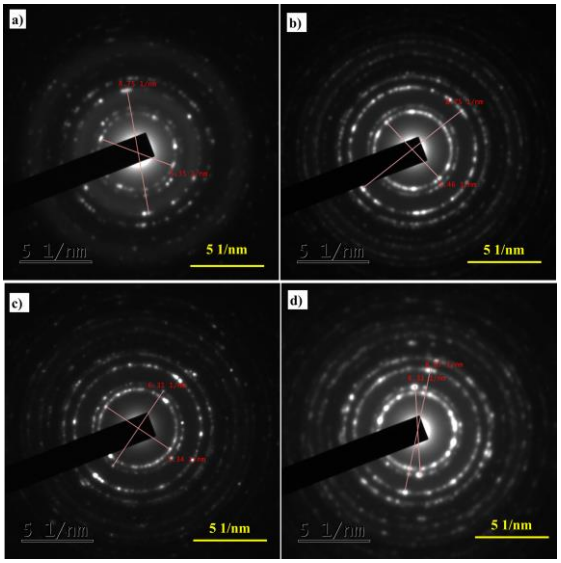

Fig. 4 SAED pattern

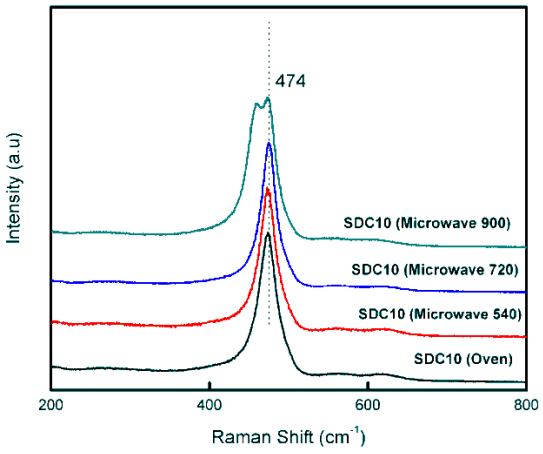

Fig. 5 Raman Spectrum

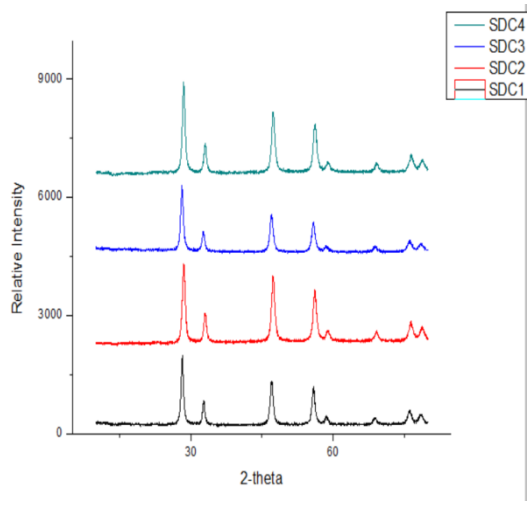

Fig. 6 XRD Results for all samples

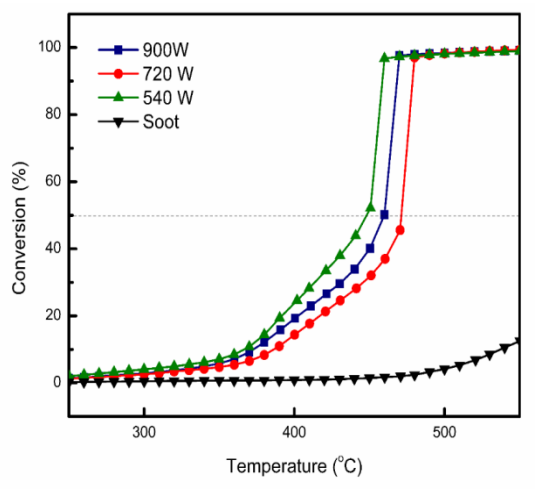

Fig. 7 Soot Oxidation Results

Table 1 BET Surface Area and XRD results for all four samples

SAMPLE	Crystallite size (nm) *	Lattice Constant (Å)	Lattice Strain	BET Surface Area (sqm/gm)	Particle size (nm) **	Degree of Agglomeration (φ)	Plane Intensities (220/111)	Plane Intensities (200/111)
SDC 1	15.11	5.47953	0.0098	53.34	15.57977	1.30109	0.63823	0.359236
SDC 2	12.86	5.41909	0.0114	72.39	11.48142	0.892801	0.846923	0.394744
SDC3	13.77	5.49045	0.0108	29.94	27.75634	2.015711	0.570553	0.329166
SDC4	13.23	5.4213	0.0111	62.19	13.36268	1.01003	0.67344	0.3509787

*Crystallite Size calculated from XRD results
**Particle Size calculated from BET Surface Area

8th International Engineering Symposium - IES 2019
March 13-15, 2019, Kumamoto University, Japan

Batch mode anaerobic co-digestion of food waste and arecanut husk for enhanced biogas production

Adhirashree Vannarath[1] and Arun Kumar Thalla[2*]

1 *Department of Civil Engineering, National Institute of Technology Karnataka, Surathkal, Mangalore 575025, India. email:adhirashree28@gmail.com*
2 *Department of Civil Engineering, National Institute of Technology Karnataka, Surathkal, Mangalore 575025, India. e-mail: thallpce@gmail.com*

ABSTRACT: Lignocellulosic residues are major environmental liabilities in the agricultural sector. So, the conversion of agro-residues to bioenergy is a promising way for future energy requirements. The suitability of arecanut husk (AH) as the co-substrate with food waste (FW) for biogas production was examined in this research. The substrate ratio (AH: FW) was varied as 0:1, 1:3, 1:1, 3:1 and 1:0 in terms of volatile solids (VS) for a batch mode enclosed reactor (1L) at mesophilic (35^{o}C) condition for 34 days. The maximum biogas yield of 330.46mL/gVS was obtained for the optimal VS ratio of 1:1 i.e., an increase in yield of 82.87% and 47.44% than their individual digestion process. Further, the accumulation of volatile fatty acids have inhibited the anaerobic digestion process and acts as a recalcitrant when it is in excess.

Keywords: *lignocellulosic residues, co-digestion, batch mode, biogas yield, inhibitions.*

INTRODUCTION

A hike in energy demand followed by fossil fuel depletion occurred due to rapid urbanisation and industrialisation, and improper solid waste management is the major concerned issues spread worldwide. Researchers are now more focused on implementing a sustainable and clean renewable energy source, replacing conventional sources of energy. The concept of waste to energy conversion can be used to tackle both the problem simultaneously.

Solid wastes include municipal waste (cardboard, paper, broken glasses, etc.), agricultural wastes (leaf trimmings, sheath, husk, stem cuttings, etc.), and industrial wastes. Agriwastes can be widely used because of their immense biomass potential and energy content possessed (Amin et al. 2017; El-mashad and Zhang 2010). Agriwastes consist of cellulose, hemicellulose and lignin and are also called "Lignocellulosic biomass". Cellulose is a major structural component of plant cell walls, which is responsible for mechanical strength while hemicellulose is often repeated polymers of pentoses and hexoses (Singh et al. 2017). Lignin consist of three aromatic alcohols (coniferyl alcohol, sinapyl alcohol and p-coumaryl alcohol) produced through a biosynthetic process and forms a protective seal around the remaining components i.e., cellulose and hemicelluloses (Motghare et al. 2015).

Anaerobic digestion (AD) process can be used as an efficient method for waste to energy conversion in both environmental as well as economic aspect. The organic matter in the solid waste is consumed by the diverse group of the organism producing biogas (CO_2, CH_4 and traces of other gases) (Jayaraj and B. Deepanraj 2014). The process includes four stages, starting from the hydrolysis stage, acidogenesis, acetogenesis and finally methanogenesis stage. Hydrolysis stage is found to be rate limiting step for lignocellulosic biomass. In this step, the complex organic matter gets hydrolysed into smaller and simple molecules that can be consumed by the bacterial consortium.

Table 1 Characteristics of inoculum (Anaerobic sludge) used

	Moisture content (%)	Total solids (%)	Volatile solids (% of TS)	Total carbon (%)	Total Nitrogen (%)	pH	Electric conductivity (µS)
Inoculum	89.18	10.81	40.83	24.32	3.98	7.39	1125

Table 2 Characteristics of AH and FW

	C (%)	N (%)	C/N ratio	Moisture content (%)	Total solids (%)	Volatile solids (% of TS)
AH	54.64	1.09	50.13	11.91	88.09	97.22
FW	48.51	1.63	29.76	81.65	18.35	20.63

In the step of acidogenesis, conversion of these simple molecules to intermediary products such as short-chain fatty acids. In acetogenesis process which is the later step in which acetates are formed. In this accumulation of acetates. Methanogenesis is the last process in which methane-forming bacteria are being formed during fermentation Biogas consist of 55-75% of CH_4 gas and remaining CO_2.

MATERIALS AND METHODS

Substrate and inoculum

The dehusked arecanut husk (AH) is collected from the Central Plantation Crops Research Institute (CPCRI) Kasargod, Kerala, India. The sludge used as the inoculum is from up-flow anaerobic sludge blanket (UASB) digester in a distillery effluent treatment plant, Baikampady, Karnataka, India which have high biodegradability and methanogenic capability. All solutions are prepared from either analytical reagent or laboratory reagent grade chemicals. Raw food waste (FW) was collected from hostel canteens of National Institute of Technology Karnataka, India which mainly contained leftover cooked foods, such as meats, rice, bread, rice and vegetables. The food waste was dehydrated by oven drying, and then the crushing of food waste was done to a particle size of 1-2 mm by an electrical mixer grinder. After being fragmented to uniform size, the raw FW and the raw AH were stored separately at 4ºC. The characteristics of inoculum are presented in table 1. Table 2 shows the characteristic contents in AH and FW.

Biomethane Potential test

The biomethane potentials (BMP) tests were experimentally performed in a 1 L amber coloured bottle at 35ºC (mesophilic condition for a digestion period of 34 days. A total of 12 such bottles were used and performed in duplicates. The first set was added in 500 mL sludge only for a blank experiment. Apart from blank, the substrate ratio (AH: FW) was varied as 0:1, 1:3, 1:1, 3:1 and 1:0 in terms of volatile solids (VS). The working volume of all the experimental sets was 500mL. Nitrogen gas purging was done for all bottles before sealing. There was no addition of macro- or micro-nutrient solutions Biogas produced from each bottle was collected, and measured by water displacement method. Biogas compositions were analyzed using a gas chromatograph equipped with a thermal conductivity detector (TCD) (Balat and Balat 2009; Kaur and Gupta 2016; Rizwan, Yousaf, and Naseem 2015; Tock and Schummer 2017; Yaw, Weng, and Norli 2018).

Analytical methods

The following parameters were analyzed: pH, VFAs, alkalinity, TS, and VS. All samples were analysed in duplicates. Samples were centrifuged at 8000 RPM for 15 min, then, the supernatant was filtered by the 0.45 mm cellulose acetate membrane. Moreover, for this batch mode experiment, parameters were checked for initial (Day 0) and final day (Day 34) (APHA 2012; Jayaraj and B. Deepanraj 2014).

Results and discussion

Stability studies and anaerobic digestion

The pH value is meant to be an indicator of the stability of an AD system. When the pH range is maintained at 6.5–7.5, the system is normal.

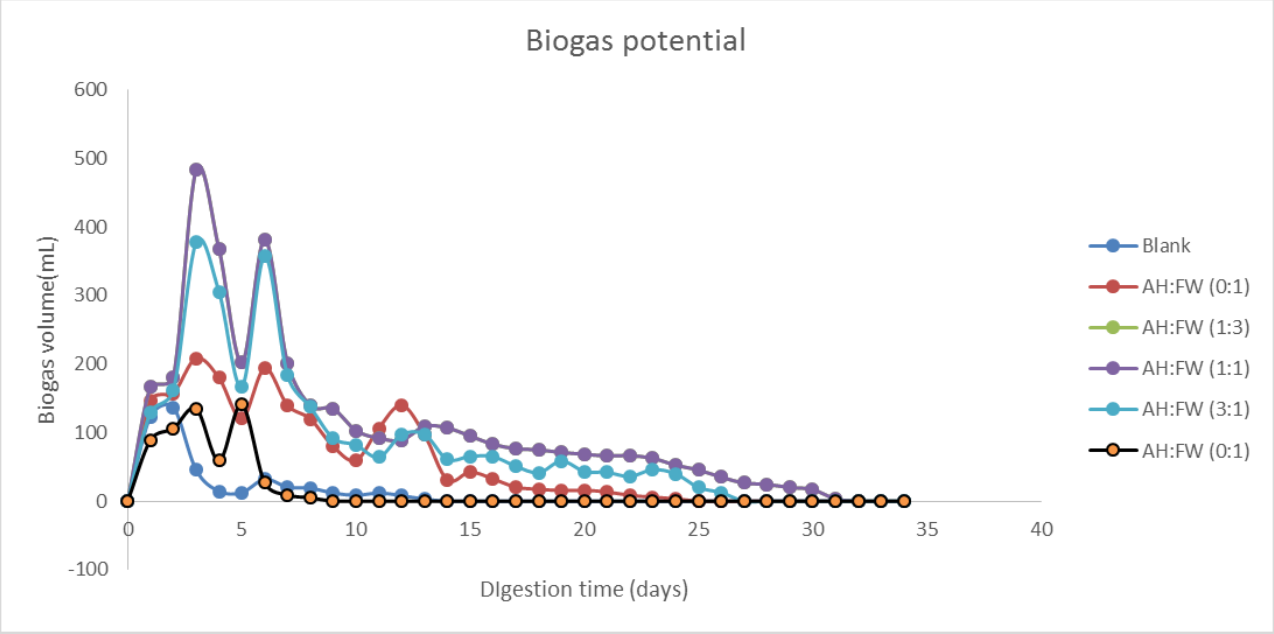

Fig. 1 Biogas potential on daily basis for various substrate ratios

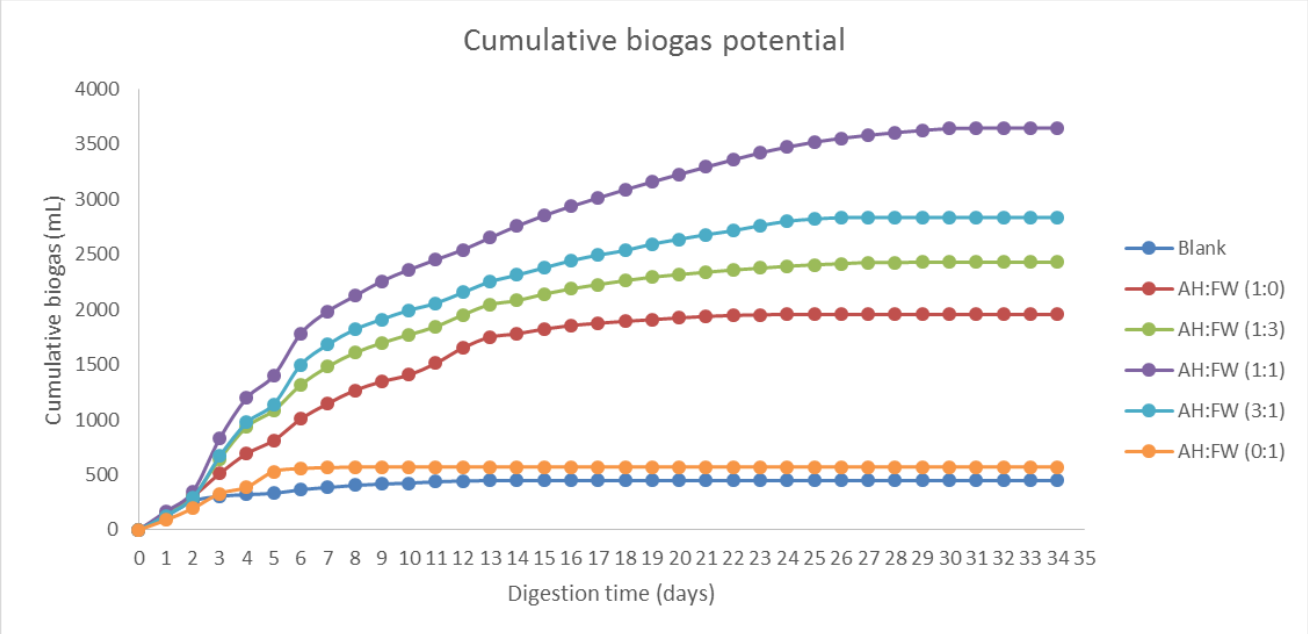

Fig. 2 Cumulative biogas potential for various substrate ratios

In this research, the pH value stabilized at 7.03–7.71 (Siddique and Wahid 2018; J. Zhang et al. 2017; W. Zhang, Zhang, and Li 2015). The pH control of the AD system was done using a buffer system. When the value of VFAs/ALK is less than 0.4, the system is considered stable, whereas when it is between 0.4 and 0.8, the system is unstable. When the VFAs/ALK value is greater than 0.8, the system is severely unstable (Karthikeyan et al. 2017; Kaur and Phutela 2016; Mata-alvarez et al. 2014). In this study, the value of VFAs/ALK was in the range of 0.283-0.387 which is less than 0.4.

Figure 1 shows the biogas obtained for various substrate ratio on a daily basis. The maximum biogas yield of 330.46mL/gVS was obtained for the optimal VS ratio of 1:1 i.e., an increase in yield of 82.87% and 47.44% than their individual digestion process. Similarly, for 1:3 and 3:1 of AH: FW ratio an increase of 34.71% and 25.06%. The cumulative biogas potential curve for each substrate ratio along with the blank is represented by figure 2. Among all, 1:1 AH: FW ratio gave the highest biogas yield which has a close comparison with the biogas produced from other biomass species (Kshirsagar, Arora, and Chandra 2012).

Conclusions

This research determined the feasibility of co-digestion of lignocellulosic biomass (Arecanut husk) along with food waste for the production of biogas using an anaerobic batch mode digester at 35ºC. All the digestion tests were performed for 34 days, which was the time required to achieve the complete digestion of the substrate mix. An AH: FW ratio of 1:1 gave higher biogas yield than other mix ratios confirms the usage of husk as a substrate for fuel generation.

References

[1] Amin, Farrukh Raza et al. (2017), Pretreatment Methods of Lignocellulosic Biomass for Anaerobic Digestion, AMB Express, Vol. 7, No. 72, pp. 1–13.

[2] APHA. (2012), Standard Methods for the Examination of Water and Wastewater, Standard Methods, pp. 541.

[3] Balat, M, and H Balat. (2009), Biogas as a Renewable Energy Source — A Review, Energy Sources, Part A: Recovery, Utilization, and Environmental Effects, Vol.31, pp. 1280–93.

[4] El-mashad, Hamed M, and Ruihong Zhang (2010), Biogas Production from Co-Digestion of Dairy Manure and Food Waste, Bioresource Technology, Vol. 101, No. 11, pp. 4021–28. http://dx.doi.org/10.1016/j.biortech.2010.01.027.

[5] Jayaraj, Simon, and V. Sivasubramanian B. Deepanraj. (2014), Study on the effect of pH on biogas production from food waste by anaerobic digestion, In 9th International Green Energy Conference, pp. 799–805.

[6] Karthikeyan, Obulisamy Parthiba et al. (2017), Pretreatment of Food Waste for Methane and Hydrogen Recovery : A Review, Bioresource Technology, Vol. 9. http://dx.doi.org/10.1016/j.biortech.2017.09.105.

[7] Kaur, Karamjeet, and Urmila Gupta. (2016), Sodium Carbonate Pretreatment : An Approach towards Desilication of Paddy Straw and Enhancement in Biogas Production, Paddy and Water Environment, Vol. 14, pp.113–21. http://dx.doi.org/10.1007/s10333-015-0483-1.

[8] Kaur, Karamjeet, and Urmila Gupta Phutela (2016), Enhancement of Paddy Straw Digestibility and Biogas Production by Sodium Hydroxide-Microwave Pretreatment, Renewable Energy, Vol. 92, pp. 178–84. http://dx.doi.org/10.1016/j.renene.2016.01.083.

[9] Kshirsagar, M P, A Arora, and H Chandra (2012), Estimation of Anaerobic Codigestion Potential of Agri-Waste in India and Comparative Financial Analysis, International Journal of Sustainable Energy, Vol. 31, No. 3, pp. 175–88.

[10] Mata-alvarez, J et al (2014), A Critical Review on Anaerobic Co-Digestion Achievements between 2010 and 2013, Renewable and Sustainable Energy Reviews, Vol. 36, pp.412–27. http://dx.doi.org/10.1016/j.rser.2014.04.039.

[11] Motghare, Kalyani A, Ajit P Rathod, Kailas L Wasewar, and Nitin K Labhsetwar (2015), Comparative Study of Different Waste Biomass for Energy Application, Waste Management, Vol. 3. http://dx.doi.org/10.1016/j.wasman.2015.07.032.

[12] Rizwan, Muhammad, Sohail Yousaf, and Riffat Naseem (2015), Effect of Mixing Ratio of Food Waste and Rice Husk Co-Digestion and Substrate to Inoculum Ratio on Biogas Production, Bioresource Technology. http://dx.doi.org/10.1016/j.biortech.2015.02.105.

[13] Siddique, Nurul Islam, and Zularisam Ab Wahid (2018), Achievements and Perspectives of Anaerobic Co-Digestion : A Review, Journal of Cleaner Production, Vol. 194, No. 1, pp. 359–71. https://doi.org/10.1016/j.jclepro.2018.05.155.

[14] Singh, R D et al (2017), Hydrothermal and Microwave Assisted Alkali Pretreatment for Fractionation of Arecanut Husk, Industrial Crops & Products Vol. 102, pp. 65–74. http://dx.doi.org/10.1016/j.indcrop.2017.03.017.

[15] Tock, Laurence, and Jean Schummer (2017) Sustainable Waste-to-Value Biogas Plants for Developing Countries, Waste Management Vol. 64, pp. 1–2. http://dx.doi.org/10.1016/j.wasman.2017.05.014.

[16] Yaw, Yee, Kian Weng, and Ismail Norli (2018), Strategies for Improving Biogas Production of Palm Oil Mill effluent(POME) Anaerobic Digestion : A Critical Review, Renewable and Sustainable Energy Reviews Vol. 82, No. 01, pp. 2993–3006. https://doi.org/10.1016/j.rser.2017.10.036.

[17] Zhang, Jingxin et al (2017), Three-Stage Anaerobic Co-Digestion of Food Waste and Horse Manure, Scientific Reports, pp. 1–10. http://dx.doi.org/10.1038/s41598-017-01408-w.

[18] Zhang, Wanli, Lei Zhang, and Aimin Li (2015), Anaerobic Co-Digestion of Food Waste with MSW Incineration Plant Fresh Leachate : Process Performance and Synergistic Effects, Chemical Engineering Journal, Vol. 259, pp. 795–805. http://dx.doi.org/10.1016/j.cej.2014.08.039.

Dust control methods in Iron ore mines of Sandur Schist Belt, Bellary Region, Karnataka, India.

Poorva J Kadrolli

Department of Mining Engineering, National Institute of Technology Karnataka Surathkal, India -575025 Email:poorvakadrolli@gmail.com

ABSTRACT: Mineral resources are essential for the economic and industrial development of any nation. Minerals can be extracted out by mining activities going on in the earth's crust wherein dust control has been one of the biggest tasks of concern in various surface mines. Dust emission from the surface mines causes various diseases like silicosis, asbestosis, pneumoconiosis, lung cancer and many more. Almost, every mineral deposit in the Sandur Schist Belt that is being mined out is a hilly terrain deposit and the dust particles tend to fall directly over the agricultural land, nearby villages, residential areas and forest zones (affecting the wildlife and habitat), because of these major issues of dust pollution there could be a stop to the mining activities till a proper solution is drafted out. This paper works on a review of controlling the dust emissions from the drilling and blasting activities, haul roads and crushing and screening plants in the Tunga Iron ore Mines of the JSW Steel Ltd., Sandur Schist Belt, Bellary region, Karnataka, India.

KEYWORDS: Dust emission, drilling, blasting, loading, and transportation, crushing and screening.

INTRODUCTION

Mining is the process in which the mineral resources are extracted out from the Earth's crust through various techniques by different machines. The processes involved in the mining of minerals that eventually lead to dust emissions and further to the contamination of surrounding air, contributing to the air pollution are drilling, blasting, loading, transportation, crushing, screening, overburden dumping, etc releasing gases like NO, SO, NO_2, SO_2, etc. The dust emitted causes a lot of safety and health issues to the people working on site and nearby. Prolonged exposure to dust may eventually damage the lung tissues making the dust-borne particles reach the alveoli, most of the times people are hit with ailments like silicosis, asbestosis, pneumoconiosis, black lung disease etc. Also, air-borne dust generated from the mining activities spreads onto the nearby populated areas, fields, forests, water channels, etc thereby causing a lot of problems for the people surrounding such mines and other issues relating to the water channels and the plants and other species.

Dust Control in Drilling

Since dry drilling results in a lot of dust emissions and the amount of the dust particles generated in the air increases as the depth and the diameter of the hole goes on increasing.

It becomes essential to detect and reduce the large quantities of dust generated due to this mining activity.

Table 1 Quantity of Iron-ore generated at the time of dry drilling and wet drilling in Tunga Mines

Hole diameter (mm)	Dust generated during dry drilling (kg/m)	Dust generated during wet drilling (kg/m)
102	0.685	0.491

Note: 1. mm = millimetre
2. kg/m = kilogram per meter

Table 2 Drill machine details

Specifications	Values and results
The diameter of the drill rod (mm)	100
Length of the drill rod (m)	3.6
Type of the drill bit	Button
Penetration rate (m/s)	0.5
Cost of the drill machine (Cr)	1.83
Manufacturing company	FRD HCR 1200
The quantity of water injected per hole (m^3/s)	0.108
Dust emission rate without wet drilling (kg/m)	0.685
Dust emission rate after wet drilling (kg/m)	0.491

Note: 1. mm = millimetre
2. m = meter
3. m/s = meter per second
4. m^3/s = cubic meter per second

Wet drilling method involves the injection of water through the hole that is being drilled from the centre of the drill steel.

Wet drilling causes problems like jamming, fogging, poor visibility, etc.

Fig.1 Drill machine at Tunga Mines

Table 3 Percentage of dust suppressed after the wet drilling is done per hole

Dust emitted before wet drilling (kg/m)	Dust emitted after wet drilling (kg/m)	% of depressed dust
0.685	0.491	28.32

Dust Control in Blasting

Blasting is the controlled use of explosives to break rock for excavation. Explosive evolution has transformed from gun powder to the modern day use of PETN (Penta Erythritol Tetra Nitrate), resulting in the use of both large density and high velocity of detonation explosives at the mine site. These explosives apart from rock breakage and its displacement emit a lot of dust, noise, fumes, flying rocks and ground vibrations, hence efforts are made in various aspects and perspectives to deduce the ill effects of a blast. Sequential delay blasting, use of shock tube system of initiation and good blast

designs are adopted at various mines in the Sandur schist belt region.

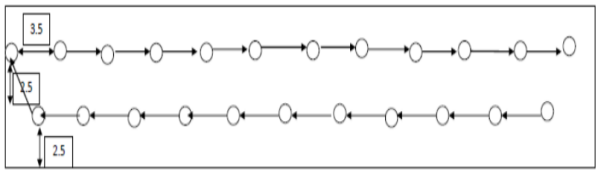

Fig.2 Design of the blast pattern

Table 4 Blasting specifications at Tunga Mines

Specifications	Values
Blast design pattern	Staggered
No. of blast holes	67
Charge per hole (kg)	21.27
Powder factor (m^3/kg)	8.76
Explosive used	1425
Initiating devices	Safety fuse

Note: 1. kg = kilogram
2. m^3/kg = cubic meter/kilogram

Loading and Transportation

Hauling the material by the aid of the backhoe and further dumping it onto the tippers generates dust and so the tippers are often provided with the tarpaulin clothes that are used for covering the loaded tippers to prevent dust emissions into the surroundings while propagation.

Materials used for making the tarpaulin clothes are usually water resistant.

Tarpaulin clothes are made of canvas or polyester coatings and plastics such as polyethylene.

Tarpaulin clothes provide shelter for the loaded material from various environmental elements like; wind, rain and sunlight.

Fig. 3 Tipper with Tarpaulin cloth

Table 5 Tipper details used at Tunga Mines

Waiting time (sec)	Loading time (sec)	Unloading time (sec)	Average cycle time (sec)
60	216	90	366

Note: 1. sec = second

Dust from haul roads gets lifted and floats in the air during the propagation of trucks and leads to the formation of a dust cloud. With an increase in the weight of trucks, speed, and frequency of traffic, the cloud may thus appear to be continuous causing delays and difficulties for the vehicles and other tippers moving on these roads.

During continuous tipper runs, dust loads of surrounding atmosphere build up both vertically and horizontally.

Application of water at frequent intervals with the aid of the water sprinklers is the far the most practical solution for the control of dust on haul roads.

Water applied in a conventional way gets dried up fast, and its replenishment at frequent intervals becomes necessary for effective dust control which adds significant cost.

Fig.4 Dust generation during the time of loading and transportation

Sprinkler systems are used for wetting the ground so as to enhance dust suppression at the time of weighing the loaded and unloaded tippers in front of the weighbridge.

Down Hill Pipe Conveyor (DHCP) system is the best-adopted mode of transport for iron ore material excavated from the mine site to the steel plant. It involves a pipe like covered conveyor transport system through which the material transport is done.

Fig.5 The construction of the DHCP transportation system

The conveyor runs on the idlers across the forest belt supported with large pillars and continuous power supply.

Crushing and Screening unit

Installation of the sprinkler systems at the C&S sites along with the DSS (Dust Suppression System) helps reduce the dry dust dissipation to the various sites, in and around these units.

Plantation of various rare and allied species of flora in and around the mine site also takes care of the dust that is being emitted. It cuts down the transport of the dust particles to over long distances and suspends their motion.

Fig.6 The DSS system installed at the Crushing and Screening unit in the Tunga Mines

Table 6 The DSS unit description

Power supply to run the DSS system (kW)	The rate of water discharge (m/s)
6	25

Note: 1. kW = kilo Watt
2. m/s = meter per second

SUGGESTIONS

1. In order to prevent these problems created by wet drilling, there is an extra addition of soluble oil which creates an emulsion when mixed with water, thereby decreasing the surface tension and improving the drill bit performance and life.

2. Adaptation of pre-splitting, deck charging and controlled blasting for blasting in the mine site can help minimize the dust and associated ill effects with it.

CONCLUSIONS

Dust emissions, identification of the emission sources, tabulating the percentages of emission in each of the mining activities, finding solutions and mitigating measures to eradicate or at least to minimize.

Table 7 The percentage of dust emitted from each of the mining processes

Mining Activity	% of dust emitted
Drilling	15
Blasting	7.5
Loading	30
Crushing and Screening	27
Transportation	20.5

Efforts are being made to reduce the dust emissions at the mine site.

However cent percent elimination is not possible since the particles vary in their size and are truly very tiny.

A stream of propagation of the same is highly unpredictable.

ACKNOWLEDGMENTS

My sincere thanks to the Senior Vice President, Mr. B P Pandey, JSW Steel Ltd., Toranagallu, Bellary, Karnataka, India.

Special thanks to the Junior Managers; Mr. P. Laxmi Chander, Mr. V.S. Sabarish, JSW Steel Pvt. Ltd

My deep sense of gratitude to Dr. A K Tripathi, Department of Mining Engineering, NITK Surathkal.

All photos and data for the above tables are obtained from the fieldwork carried out by me, dated from December 5th to December 10th, 2018.

REFERENCES

1. J. K. Pandey,1997, Dust control practices in the Indian mining industry, 12th Coal Operators' Conference University of Wollongong & the Australasian Institute of Mining and Metallurgy, pp.185-192.

2. M. V. Rudramuniyappa, 1997, Iron ore fines and their impact on the environment in Sandur-Hospet region, Bellary district, Karnataka, India, pp.273-278.

3. Fred N. Kissell, June 2003, Handbook for Dust Control in Mining, NIOSH Pittsburg Research Laboratory, PA, United States of America, pp. 73.

4. John A. Organiscak, 2004-2008, Silica Dust Controls for Surface Mines, National Institute for Occupational Safety and Health, USA.

MANAGEMENT, FINANCE & RELATED FIELDS

8th International Engineering Symposium - IES 2019
March 13-15, 2019, Kumamoto University, Japan

Economic and Political Effects of the Transatlantic Trade and Investment Partnership

Ayush Srivastava
Department of Electronics and Communication Engineering, National Institute of Technology Karnataka, Surathkal, Mangalore 575025, India
Email:ayush.gs1998@gmail.com

ABSTRACT: This paper studies major economic and political effects of the TTIP on the negotiating nations, namely the European Union and the US as well as non-participating countries indirectly affected from this pact. While the ongoing studies have inherently shown that the TTIP will undoubtedly raise profits for the EU and US especially in terms of reduction of non-tariff barriers in trade, it faces issues in the implementation of certain regulations and standards. Many civil societies and trade bodies are concerned about the growth of corporate power and lowering of regulatory rights associated with this. Weather the diplomats behind the treaty will be able to satisfy the key interest groups and forge the cross-issues trade-offs to boil down to a mutual recognition agreement with strict labelling requirement leading to increased customer choices without abandoning their preferences and thus creating a non-discriminatory open regulation, remains to be witnessed.

***Keywords**: Trade, integration, economy, tariff, investment, tariff, regulatory*

INTRODUCTION:

The Transatlantic trade and investment partnership is a proposed trade agreement between the European Union and the United States with the aim of promoting trade and multilateral economic growth. It aims at enhancing market access, reducing regulatory and other non-tariff barriers and contribution to the development of global rules. But it faces certain issues. The last few decades have seen a fragmentation of production processes leading to companies working now in Global Value Chains. In this way the TTIP encompasses regulatory aspects and needs to address issues going beyond the current global trading rules and incentives as laid down in the World Trade Organisation's (WTO) agreements on member state commitments.

The effects of this regional partnership will be discussed in roughly two blocs. The first one talks about the welfare effects: static and dynamic effects. The second one deals in the effects on the global trade. When the welfare effects are studied in a static setting, we can witness both trade creation and trade diversion. Trade creation is clearly positive because the trade barriers having come down, the consumers or producers down the chain can obtain goods and services from one of the members of the agreement instead of relying solely on the domestic producers. On the other hand trade diversion can be seen since the market might shift from the more efficient third-country producer which still faces tariff barriers to maybe a relatively inefficient FTA (Free trade area) producer. The Foreign Direct Investments and other business investments will also be transferred from outside groups to within the FTA eyeing the lowered tariffs. This is not just a problem for third-parties but also for the members of the FTA in terms of productive trade development since trade flow increases but growth doesn't. Trade-deflection may happen if the pact is not a Custom Union causing the external trade partners to introduce goods through the member with lowest barrier entry and then through the zero barriers to the destination. However, dynamic effects

are more significant and long-term than its static counterpart. Dynamic factors include productivity growth, expanded capital accumulation and increase of investments.
In the past few decades, the concept of regional integration has changed significantly. While the 20th century trade model was based on the fact that goods are produced in a country A and shipped to another B, in the 21st century model, the production process has been fragmented. GVCs have come into picture making the discrimination between the outsiders and insiders of the trade agreements much difficult and less likely than the simple 20th century model of trade creation versus trade diversion. In this changing scenario, the concept of dynamic effects to trade becomes increasingly important.

POTENTIAL EFFECTS: The aforesaid theoretical understanding shall be used in making predictions on the outcomes of the TTIP.

Effect on The Two Negotiating Economies

The considerable magnitude of economic integration between the EU and the US, together with relatively similar cost and production structures as well as the generally low tariffs and cross-border barriers to trade makes the policy remarkable. Therefore, one can expect that intra-industry trade and therefore greater specialization will be promoted through TTIP given low border barriers to trade, the chief impacts will arise from decreasing regulatory barriers. The overall effects of a transatlantic trade deal are primarily determined by three characteristics: the huge sizes of both economies, deep level of intra-firm trade between them, and extensive levels of intra-industry trade. As the extent of trade and investments between them is already large, it is by far the largest bilateral economic establishment in the world. Both economies together represent greater than 40 per cent of global GDP. It can thus be expected that the removal of trade barriers would have significant effects both on the participating economies as well on third countries. Main carriers of economic integration between the two economies are foreign affiliates, resulting in a considerably huge amount of intra-firm trade. This is prime for understanding the effects of an FTA since intra-firm trade marks about one third of total transatlantic trade; 50 per cent of all US foreign affiliates are placed in Europe, while 75 per cent of all European affiliates are situated there in the US. This is especially obvious for the German automotive and chemicals plants and industries. In addition to that, the great extent of intra-industry trade is decisive. These sectors mark a Grubel-Loyd-Index of 0.85 which underlines the importace of intra-industry trade.These characteristics are significant for understanding the effects of a transatlantic free trade region. However, effects differ depending on the details of the TTIP. Thus it appears logical to divide this analysis into two sections: border-barriers, and behind-the-border barriers to trade. However, given that most models do not distinguish between different forms of non-tariff-barriers, i.e. subsidies, technical barriers to trade such as standards, sanitary and phytosanitary measures, and other regulations (e. g. Intellectual Property Rights) as behind-the-border-barriers to trade, we stick to the traditional method to distinguish between tariffs and NTBs. For most of the currently traded goods, applied tariffs in the EU and the US are rather low. However, sectoral differences and tariff peaks are clearly evident. Both the economies record significantly higher tariffs on agricultural products along with significant tariff peaks on products such as dairy, beverages and some textiles. Fontagne, Gourdon and Jean estimate that the average tariff protection on EU goods imported by the US amounts to only 2.2 percent, while US goods imported by the EU attract an average tariff of 3.3 percent. Therefore, this tariff liberalisation is rather unlikely to achieve substantial economic gains for either the USA or the EU, with the exception of the removal of duties on a somewhat small number of sensitive products to consider. Calculating the static bilateral trade creation effect in consequence of a tariff elimination, Erixon and Pehnelt find the following results,

which depend on the price import elasticities of the EU and the US: When assuming a rather low price import elasticity, the annual US exports to the EU27 could increase by 2.5 billion Euros. Vice versa, the increase of EU exports to the US would amount to 4.7 billion Euros. However, when assuming high price import elasticity, the results depict an increase of US yearly exports to the EU by 6.4 billion Euros while the EU would record an increase of its exports to the US by 11.7 billion Euros. The estimated trade creation effect would therefore be between seven and eighteen billion Euros. Furthermore, when looking at the sectoral level, the biggest trade creation would happen in the manufacturing sector, chemicals, steel and minerals. By using a general equilibrium model Erixon and Bauer (2010) calculate both static and dynamic effects of the zero-tariff agreement. They predict a static effect on GDP of 0.01 per cent for the EU and 0.15 percent for the US. More importantly, despite the marginal static gains, the dynamic gains, resulting from improved productivity and lowered trade costs, will be considerably higher. For the calculation of dynamic effects, two scenarios are applied that differ in the assumed increase in labour productivity (with one scenario assuming an increase by 2 per cent in goods sectors and the other an increase by 3.5 per cent in sectors with high levels of intra-industry trade and an increase of 2 per cent for other goods sectors) (Erixon and Bauer, 2010). Such dynamic gains would account for somewhat 0.23-0.47 (first and second scenario) percent increase of GDP for the EU and 0.99-1.33 per cent increase of GDP for the US. Considering welfare gains, here measured as national income effects, the authors deduce for the static effect an increase of 3 billion USD for the EU and 4.5 billion USD for the US. For the dynamic gains however, they estimate 58.86 billion USD for the EU and 59-82 billion USD for the US. The change in exports would range between 7 per cent (static) and 18 per cent (dynamic) for the US, between 8 per cent (static) and 17 per cent (dynamic) for the EU. Calculating the static bilateral trade creation effect in consequence of a tariff elimination between the EU and the USA, Erixon and Pehnelt (2009) find the following results, dependent on the price import elasticities of the EU and the US: When assuming a rather low price import elasticity, US exports to the EU27 could increase by 2.5 billion Euros (about 1.51 percent) while the increase of EU exports to the US would amount to 4.7 billion Euros (about 1.95 percent). However, the results show an increase of US annual exports to the EU by 6.4 billion Euros (3.76 percent), while the EU would record an increase of its exports to the US by 11.7 billion Euros (4.89 percent). The estimated trade creation effect would hence be between 7 and 18 billion Euros (Erixon and Pehnelt, 2009). Furthermore, when looking at the sectoral level, the biggest trade creation would occur in the manufacturing sector, chemicals, steel and minerals. By employing a computable general equilibrium model, Erixon and Bauer (2010) calculate both static and dynamic effects of a zero-tariff agreement. They calculate a static effect on GDP of 0.01 per cent for the EU and 0.15 percent for the US. More importantly, despite the marginal static gains, the dynamic gains, resulting from improved productivity and reduced trade costs, will be considerably higher.

Agreement on trade in services

Services represent a big portion of the transatlantic economy. In 2012, 28.9 per cent of all EU services imports were from the US, while 26.3 per cent of all EU services exports were directed for the US. For the US, the EU is the chief destination for services exports. In 2010, 31.8 per cent of all US services exports were destined for the EU. However, some services in both economies are still considerably restricted. For both the US and the EU, the share of output which were characterized by 'a substantial level of protection' according to the OECD's Product Market Regulation Index 5, represents 20 per cent of GDP (Messerlin and van der Marel, 2009). A product market regulation index which was greater than average was recorded by the following sectors: electricity, renting

machinery, business services, transport and storage, and financial services. However, the US services sectors are comparatively more open than the EU's (Messerlin and van der Marel, 2009). An assessment and subsequent rearranging of certain product market regulations would yield significant direct and indirect effects, as well as static and dynamic gains. This is of special relevance since most of the highly regulated sectors are 'backbone services' which reveal an overall importance for the whole economy. Through major inter-sectoral linkages, the improved productivity in the course of market liberalisation would yield substantial overall economic results (Erixon and Brandt, 2011). Moreover, Draper, Lacey and Ramkolowan (2014) stated that the most systemically important gains are likely to be made in areas such as financial services, professional services, education services, telecommunications services, express delivery and e-commerce (Draper, Lacey and Ramkolowan, 2014). These sectors are crucial to the operation of GVCs. Messerlin and van der Marel (2009) pointed out the importance of a bilateral services agreement that could potentially become a plurilateral agreement. It would only need eight more countries to join the agreement in order to reach a mass of 80 per cent of world trade. Those countries may include Japan, China, India, Brazil, Russia, Canada, Korea and Mexico. This may enforce a multi-lateralisation of services agreements, complementing the TISA which is the most significant development for trade negotiations at the plurilateral level. TISA negotiations cover almost seventy per cent of world services trade, and include major trading partners, like Canada, the EU, Japan, the Republic of Korea and the United States. With China expressing an interest to join recently, further dynamics can be induced to this project (Marchetti and Roy, 2013). However, Marchetti and Roy (2013) note that the TISA negotiations are not likely, as currently constructed, to deliver new market access gains in services since the parties only effectively agreed to bind their best market access levels as offered through their own PTAs. A TTIP that goes further shall offer the possibility of deeper liberalization at the multilateral level.

Effects on Third countries:

Effects of a reduction or elimination of non-tariff barriers

A reduction of non-tariff barriers can affect third countries in many ways, depending on the extent of the reduction and the initial divergence of regulations. In case of a partial alignment of regulations, standards and other non-tariff measures, countries outside of the agreement face particular scenarios: It is either possible that non-member countries which struggle to comply with the existing or new requirements are damaged since they face a loss in their relative competitiveness. Or countries and existing exporters somehow maintain the standards and regulations set by the EU and the US and may be able to withstand competitive pressures from members of the agreement (Draper, Lacey and Ramkolowan, 2014; Felbermayr and Larch, 2013b). However, a differing effect occurs in case standards that are mutually recognized between the US and the EU. Countries outside of the mega-economic agreement will then face two competing effects: Where requirements, standards and regulations are made stricter, non-member states will face higher compliance and trade costs in all markets implementing the common framework, potentially implying more competition from exporters within the mega-regional block (Draper, Lacey and Ramkolowan, 2014). If a third country is able to meet the standards in either one of the economies with an admission to sell its products to the foreign market, it could be automatically qualified to export to the other partner economy as well. Hence, in the case of a harmonization of standards between the EU and the US, third countries may profit if they manage to meet the standard requirements and can export to both the economies. Therefore, the harmonization and mutual appreciation of standards is not discriminating if third countries are capable of utilizing them as

well. A transparent definition and certification system of mutual EU-US standards would hence be preferable. Following the scenario of harmonized standards, another feature is the expectation that common transatlantic standards could gain worldwide acceptance which would subsequently lead to an overall improvement of product standards worldwide, enforcing consumer and environmental protection. This in turn would yield a general growth stimulus in the regions of competition, labour and environmental policies. It is clear that the reduction of non-tariff measures between members of megaregional agreements can be both beneficial and destructive to non-member countries. The extent to which changes in non-tariff measures are beneficial for non-member states depends on both the level of stringency of the new measures implemented by the mega-regional agreement and the extent to which harmonisation of these non-tariff measures and regulatory standards across members of the mega-regional agreement occurs.

Effect of a zero tariff agreement

Since the tariff level is already quite low for most manufactured goods, trade diverting effects from extra-transatlantic to the transatlantic are not so likely (Felbermayrand Larch, 2013a; Erixon and Pehnelt, 2009). Moreover, remaining tariff peaks of the EU and the US are primarily in labour-intensive consumer goods and some goods which are mainly exported by developing and emerging economies. Hence, there is a rather small potential of transatlantic trade to be substitutable to these goods categories. Rollo et al (2013) highlights that "there is practically no similarity between, on the one hand, the structure at HS 6 Digit level (around 5000 product categories) of the non-fuel exports of the LIC (low income countries) to the EU and US, and on the other hand, the exports of the EU to the US, and of the US to the EU". Furthermore, Baldwin (2014), notes that if complementarities are high, as is the case with African Caribbean Pacific (ACP) – EU and ACP – USA trade, then if the TTIP results in trade growth for the member states it is likely that this would suck in imports from the ACP in order to supply expanding production plants in the signatory states. This means increased traditional exports, particularly of resources, and therefore intensification of current comparative advantage patterns. Depending on one's view of comparative advantage this could be positive (more exports, more foreign exchange, more jobs etc) or negative (lock-in effect, marginalization from global value chains, etc). Selected ACP countries within specific product categories may nevertheless face substantial preference erosion and increased competition resulting in a trade diversion from countries participating in mega-regional agreements. Rollo et al (2013) note that low-income country product exports such as textiles, clothing and footwear, and specific agricultural products like fish, bananas and sugar, encounter preference erosion in both the EU and US markets with the implementation of the TTIP. Hence, while it is reasonably clear that the overall effects of the TTIP on low-income countries is likely to be small, some developing countries are likely to face significantly higher levels of competition in a specific set of products.

CONCLUSION: Following conclusions are deduced from this study:
The envisaged TTIP is a promising political undertaking, which may substantially benefit both its partners as well as third countries. However, it needs some serious steps to overcome numerous obstacles, mainly in the lines of regulations and standards. One way to deal with such standards is to conclude MRAs with strict labelling requirements, leading to more choices for consumers without undermining domestic consumer protection preferences. It could be expected that Europeans who dislike GMOs will not purchase them. In order to not divert trade and to not disadvantage third country producers, these mutually recognized standards should also be open

for them. In other words, they can choose which of the standards to follow. Such a non-discriminatory regulatory regime can be beneficial for the global trading order since the transatlantic partners have the chance to maintain their high standards without discriminating against third parties, since they are already used to these standards and do not have to adjust to a new one. However, the path towards the TTI P contains some serious loopholes to be dealt with, such as the European dislike of GMOs and US insistence on complete freedom of data flows. As mentioned earlier, governments on both sides of the Atlantic will also confront many civil society lobbies concerned about the growth of corporate power and alleged diminution of regulatory prerogatives associated. So much depends on the willingness of the transatlantic negotiating partners to remedy the obstacles. This will require concerted political will and focus, substances that are scarce in beleaguered Western democracies still confronting the fallout of the worst financial crisis since the 1930s. It becomes the call for the hour that the democratically elected leaders overcome key interest groups, and forge the cross-issues trade-offs in their full complexity to create radical changes.

REFERENCES

[1] Baldwin, *R. (1993), A Domino Theory of Regionalism, NBER Working Paper, 4465.*

[2] Baldwin, *R. (2013), Multilateralising 21st Century Regionalism, Geneva, mimeo.*

[3] Baldwin, *R. (2014), The Impact of Mega-Regionals, forthcoming, mimeo.*

[4] Baldwin, *R. and E. Seghezza (2007),Are Trade Blocs Building or Stumbling Blocks? New Evidence, Geneva, mimeo.*

[5] Conway, *P.; **Janod,** V. and G. **Nicoletti** (2005), Product Market Regulation in OECD Countries: 1998 to 2003, OECD Economics Department Working Papers No. 419.*

[6] Davies, *M.; **Draper,** P. and H. **Edinger** (2014), Changing China, changing Africa: Future contours of an emerging relationship, Asian Economic Policy Review, 9(2), xxx-xxx (forthcoming).*

[7] Erixon, *F. and G. **Pehnelt** (2009), A New Trade Agenda for Transatlantic Economic Cooperation, ECIPE Working Paper No. 09/2009.*

[8] Messerlin, *P. and E. **van der Marel** (2009), Leading with Services: The Dynamics of Transatlantic Negotiations in Services, Paris: Grouped 'Economie Mondiale/Sciences Po.*

[9] United States Trade Representative *(2011) "Outlines of the Trans-Pacific Partnership Agreement",*
November 12. Available on the USTR website: http://www.ustr.gov/about-us/pressoffice/ fact-sheets/2011/november/outlines-transpacific-partnership-agreement (visited on 14 December 2013).

8th International Engineering Symposium - IES 2019
March 13-15, 2019, Kumamoto University, Japan

Non-Performing Assets, their causes and effects on the Indian Banking Sector

Sarang Kalantre [1], Sai Chaitanya [2] and **Suprabha K.R.[3]**

1 *Department of Electronics & Communication Engineering, National Institute of Technology Karnataka, Surathkal, Mangalore 575025, India. email: kalantre.sarang@gmail.com*
2 *Department of Electronics and Communication Engineering, National Institute of Technology Karnataka, Surathkal, Mangalore 575025, India. email: b.saichaitanya98@gmail.com*
3 *School of Management, National Institute of Technology Karnataka, Surathkal, Mangalore 575025, India. email: suprabha@nitk.ac.in*

ABSTRACT: Non-Performing assets and failure to recover advances have proved to be a menace for the Indian Banking Sector in the near past. Dedicated provisions for bad loans have had a direct impact on the profitability of the public as well as private sector banks. This invariably has led to the discovery of various leniencies in granting loans to individuals as well as corporations. This paper attempts to study Non-Performing Assets, their causes and their subsequent effects. Ratio analysis of Secondary Data obtained from RBI Statistics further reveals the specific impact on private and public sector banks taking into account the provisions made to tackle these Stressed Assets. Further, the paper touches upon the Sector-wise default analysis and Composition of Ownership of Deposits.

***Keywords**: Non-Performing assets, Ratio analysis, Stressed Assets.*

INTRODUCTION

All financial institutions including banks pay the account holders interest for depositing money. They also lend loans to corporations or individuals. The interest rate on loans is significantly kept higher than that for deposits. The difference in margin of these rates becomes the profit for these financial institutions. Hence it is evident why banks have a tendency to give away advances to become more profitable.

After the World Financial Crisis in 2008, the regulators felt the need to boost the economy by pumping capital into the system. Hence, banks were encouraged to grant loans. This facilitated growth but evidently highlighted the weak post credit approval monitoring and unestablished effective legal framework. These issues combined to give rise to what we call Non-Performing Assets today which inevitably hurt banks' profitability.

CLASSIFICATION OF TYPES OF ASSETS

Assets are entities which are capable of earning an individual or an organization capital.

Based on the Income Recognition and Asset Classification (IRAC), Assets are classified into four types.

1. **Standard Asset:** Revenue generating assets are Standard Assets.
2. **Sub-standard Asset:** Assets that have not yielded any interest for a period of 12 months or less.
3. **Doubtful Asset:** These assets are further characterized into three categories and stand for assets that have not yielded any income for 12 months or more

4. **Loss Asset:** When a borrower is in no situation to pay back the debt he owes, the asset is characterized as a loss asset.

All assets which are not 'standard' and have not generated any income for more than 90 days are called as 'Non-Performing Assets'.

SIGNIFICANCE OF NPA AND CLASSIFICATION

Knowing that the financial institutions will take risks to increase profitability that might erode the general public deposit, regulators have mandated to keep aside a certain portion of the profit of the bank to account for losses that might come from Non-Performing Assets. These are called provisions. Higher provisions are made for more doubtful assets or loss assets. To take into account the provisions Non-Performing Assets are classified into two different categories:

1. **Gross NPA:** It is the total sum of the initial principal amount which is not generating any income after a period of three months.
2. **Net NPA:** Net NPA is the sum obtained after subtracting the provisions from the Gross NPA. Thus, Net NPAs give a clearer idea about the burden on the bank.

The level of non-performing loans/assets is considered a critical indicator to assess a Bank's health. Ideally, a bank should average zero Net NPAs i.e. the provisions should cover for all the losses from the Non-Performing Assets.

A higher value of Gross NPA indicates larger provisions to be made from Profit before Tax. This has a direct impact on the bank's profitability. In a worse case, lack of provisions can hamper depositors' savings.

Net NPA Ratio and Gross NPA ratio are calculated to have a measure rise/fall in NPAs.

$$Net\ NPA\ Ratio = \frac{Net\ NPA}{Net\ Advances}$$

similarly,

$$Gross\ NPA\ Ratio = \frac{Gross\ NPA}{Gross\ Advances}$$

CAUSES OF RISING NPA

There are various internal as well as external factors which have had significant to minimal impact on the rise of NPAs. (Sulanga Das et al 2014)

Internal Factors:

1. Improper Credit Analysis: It is highly essential to analyse before granting an advance whether the borrowing individual or corporation will be able to pay back the loan timely.
2. Era- Inappropriate Technology: In the world of digital media and electronics, there is a necessity to make all bank records and transactions on computer systems. Failure to keep a track of dues payable and make real-time decisions hasn't helped to control rising NPAs.
3. Lack of Physical Contact between Bank and Borrower: A wilful defaulter is most likely to pay his dues when contacted frequently by Bank Officials. Lack of this practice has led to an increase in Wilful Defaults.

External Factors:

1. Natural Calamities: Destruction of crop fields, construction projects due to natural calamities like earthquakes, tsunamis or floods can render the borrowing individual or institution helpless and unable to pay the debt owed.
2. Wilful Defaulters: Individuals having the means to pay back loans and yet not making timely payments give rise to NPAs.
3. Recession: Loss of Jobs can leave common individuals without any means to pay back the loans.
4. Changing Government Policies: Loan Waivers and changing initiatives of Government can sometimes give rise to NPAs.
5. Improper Project Handling: Projects started with the backing of loans are sometimes mishandled leading to delayed completion of the same. This may hamper with the earning capacity of the project itself.

TRENDS IN GROSS NPA

Public Sector banks are majority lenders of advances. Foreign banks have a very insignificant contribution to the statistics of all Scheduled Commercial Banks (SCBs) combined which is dominated by Public Sector Banks. (Fig. 1)

1. Public Sector Banks: PSBs have been hit the most with 15% advances in FY17 being stressed. % Gross NPA has also increased with passing years.
2. Private Sector Banks: These banks have done relatively well when compared to Public Sector Banks with a controlled 5% in stressed assets. However, there is no hiding from the fact that the % Gross NPA in Private Sector Banks has also increased steeply over the years.
3. SCBs: The Gross NPAs for all SCBs has increased over the years. While this may seem natural taking into account the Time Value of Money, the % Gross NPA has also steeply increased almost three times in the last four years.

TRENDS IN PROVISIONS MADE

1. Public Sector Banks: The percentage provisions when calculated against the Gross NPAs has declined slightly over the years. Since the Financial Crisis, Public Sector Banks have failed to have provisions more than 50% of their stressed advances. (Fig. 2)
2. Private Sector Banks: The provisioning in Private Sector banks have declined drastically over the last seven years. This has invariably resulted in higher values of Net NPAs. (Fig. 2)
3. All SCBs: Overall, for all Scheduled Commercial Banks, the provisions as a ratio to Gross NPAs have declined steadily which has resulted in higher Net NPA ratios over the years.

TRENDS IN PROVISION TO ASSET RATIO

Provision to Asset Ratio is defined as,

$$Provision\ to\ Asset\ Ratio = \frac{Provisions\ Made}{Total\ Assets} \times 100$$

Over the last six years, the percentage of ratio of provisions to Assets of Public Sector Banks has become five-fold (Fig. 3). While there is a slight increase in the ratio for Private Sector Banks, there is a dominant overall impact seen on all Scheduled Commercial Banks with Provisions Covering 2.5% of the total Assets.

This ratio clearly suggests that the increase in Provisions made has had a direct impact on the banks' assets and hence profitability. Constantly and steadily increasing ratio suggests hazard.

TRENDS IN NET NPA

In both Public and Private Sector Banks, the Net NPAs have increased over the years. The increase in provisions made for stressed assets has failed to arrest the growth of % Net NPA which continues to rise in Public as well as Private Sector Banks.

COMPOSITION OF NPA IN PUBLIC SECTOR BANKS

Three sectors classified as Priority Sector, Non-Priority Sector and Public Sector combine to form all NPAs in Public Sector Banks. Priority Sector includes all loans given to Agriculture and Allied Activities, poor people for housing, students for education, etc. Non-priority Sector includes all other loans apart from the ones given towards the benefit of Public Sector or Government.

There is a steady increase in the loans given to both Priority and Non-Priority Sector, however, in recent years the majority % NPA in Public Sector banks has come from Non-Priority Sector which was relatively lower seven years back. (Fig. 4)

COMPOSITION OF OWNERSHIP OF DEPOSITS

In March 2018, the percentages of deposits owned by various categories of Sectors is shown in Table 1. As can be deduced from the table, with a rise in NPAs and threat to deposits, the Household Sector will be the most affected since it naturally has a greater number of individuals when compared to any other sector.

SECTOR-WISE MAJOR CONTRIBUTORS TO NPA

In recent years, sectors in India like Steel, Power, Telecom, Infrastructure and Textile have been the major contributors to Non-Performing Assets. The Retail Sector has delivered the least percentage (when calculated against the advances given in Retail) of NPAs in recent years.

CONCLUSIONS

The following conclusions are deduced from this study:

- Various Internal, as well as External Factors in addition to higher Inflation Rates and Higher Repo Rate, have given rise to Non-Performing Assets in the Indian Banking System.
- The percentage of assets kept as provisions has increased considerably over past years yet failing to curb the growing % Net NPA in Public as well as Private Sector Banks.
- Majority of NPAs have come for Industries which fall under the Non-Priority Sector. Following this, The Government of India has encouraged banks to lend more to Priority Sector.

REFERENCES

[1] Ashly Lynn Joseph, Dr.M. Prakash (2014), A Study on Analysing the Trend of NPA Level in Private Sector Banks and Public Sector Banks, International Journal of Scientific and Research Publications, Volume 4, Issue 7

[2] Ayub Ahamed KS, Vishwanath Panwar (2016), A Comparative study of NON-PERFORMING ASSETS (NPA) in Private Sector Banks and Public Sector Banks in India, IRACST-International Journal of Commerce, Business and Management (IJCBM), Vol. 5, No. 6.

[3] Dr.K.ShreeLatha Reddy, M.V. Sivaram Naidu (2017) A Comprehensive Study of NPAs of Scheduled Commercial Banks, IOSR Journal of Business and Management PP 28-34.

[4] Dr. Ujjwal M Mishra, Jayant R Pawaskar (2017) A Study of Non-Performing Assets and its impact on Banking Sector, Journal for Research, Volume 03, Issue 01.

[5] Sulagna Das, AbbijitDutta (2014) A Study of NPA of Public Sector Banks in India, IOSR Journal of Business and Management, Volume 16, Issue 11, ver. 1, PP 75-83.

Table 1 Ownership of Deposits

Sector	% Deposit
Government	13.5
Private (Non-Finance)	10.1
Finance	5.9
Household	63.3
Foreign	7.2

Source: RBI Data

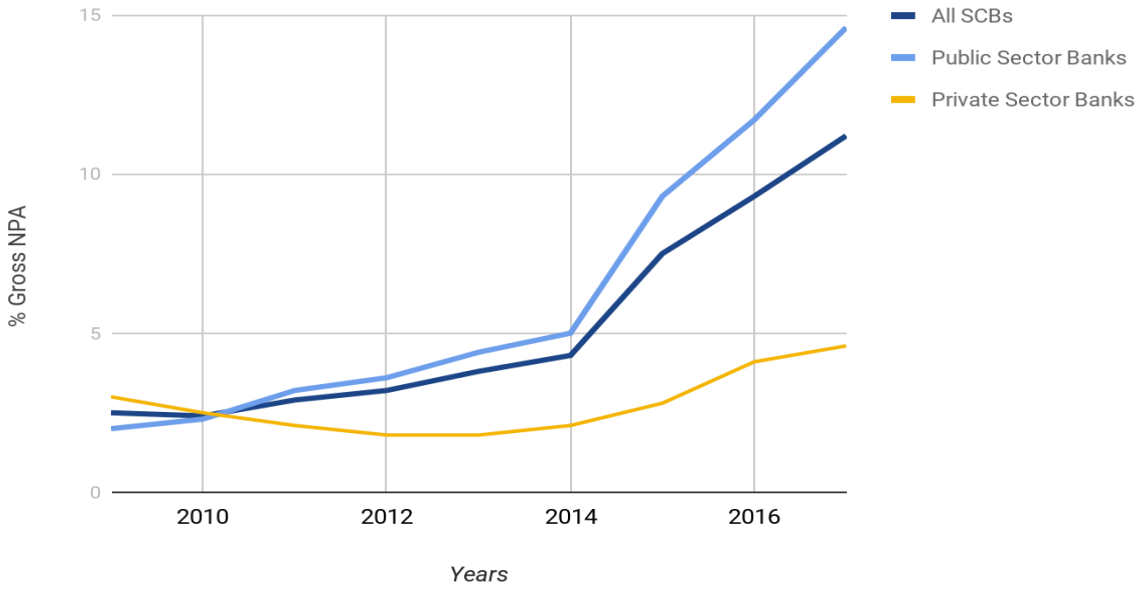

Fig 1. Percentage (%) Gross NPA*

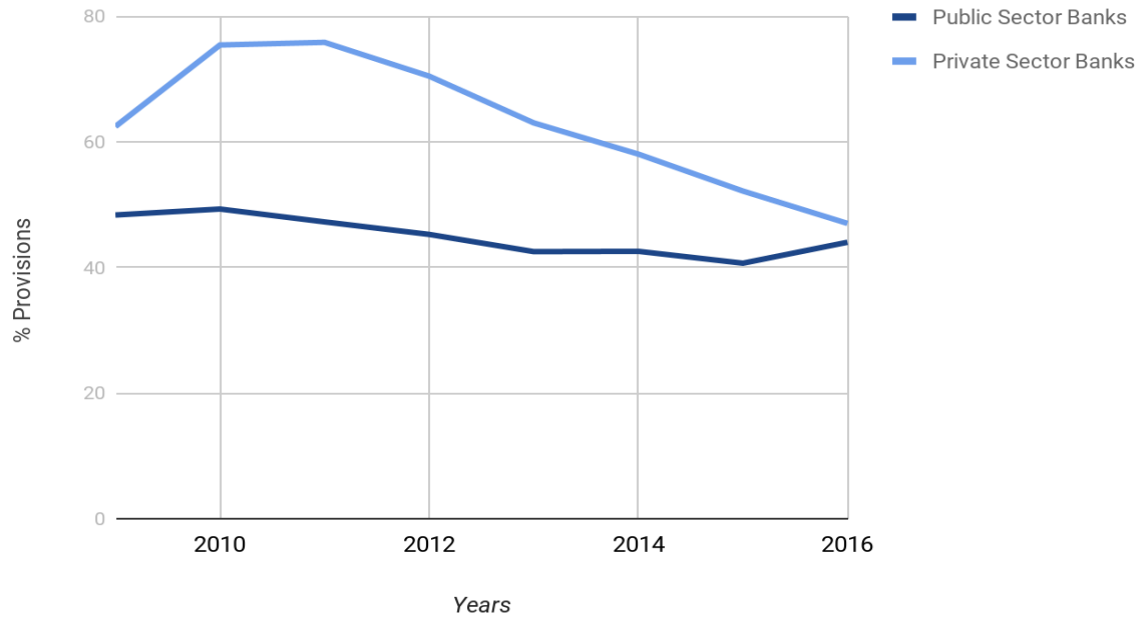

Fig 2. Percentage (%) Provisions*

*Source: RBI Data

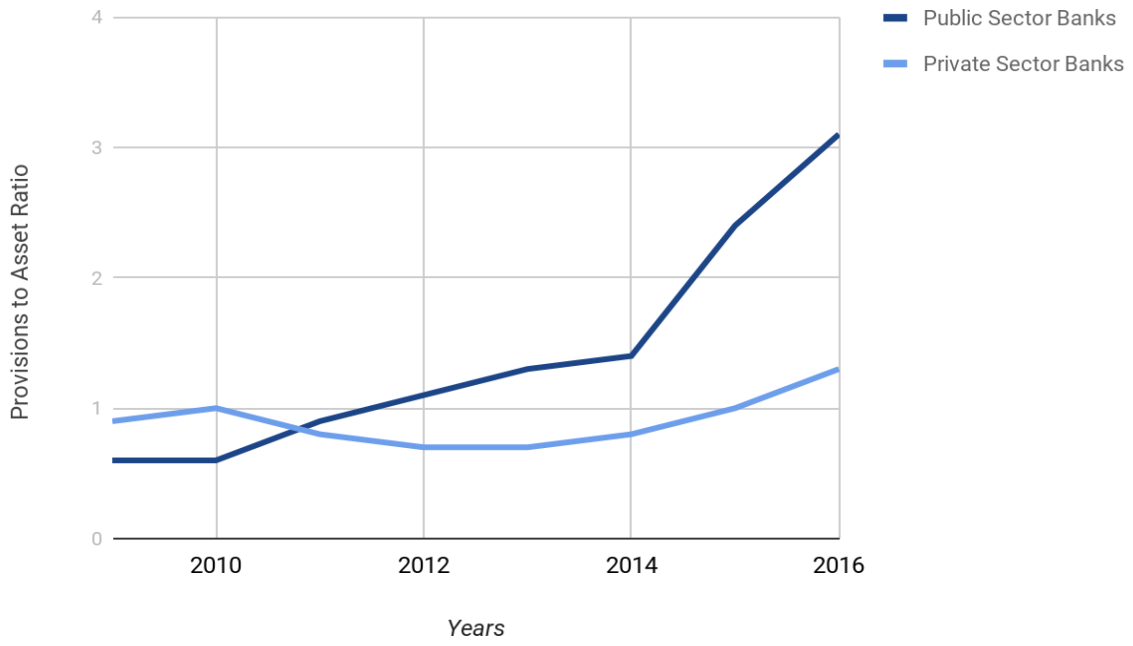

Fig 3. Provisions to Asset Ratio*

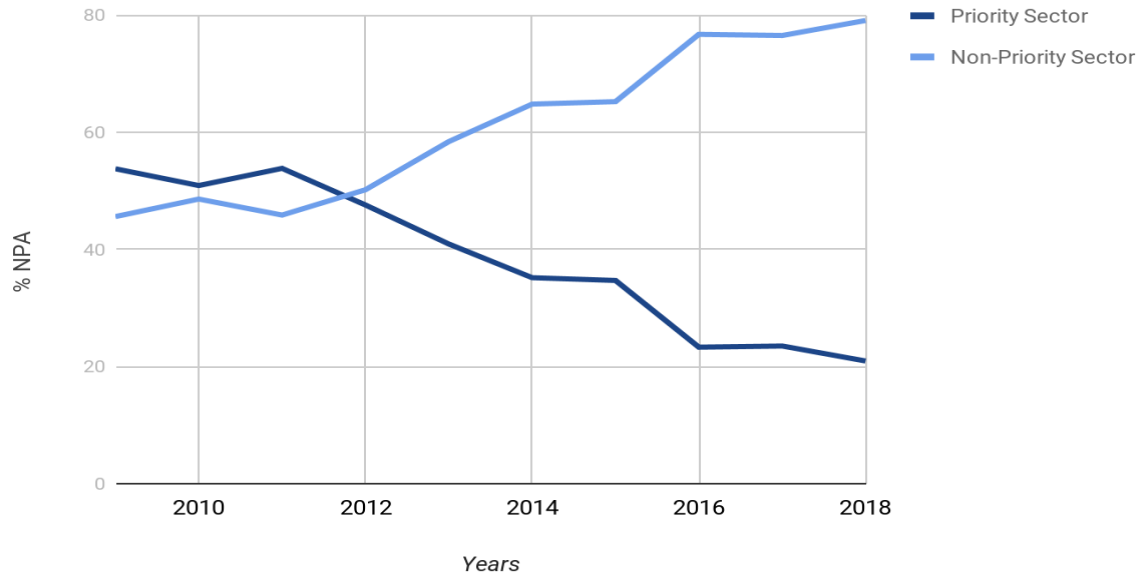

Fig 4. Composition of NPAs in PSBs*

*Source: RBI Data

8th International Engineering Symposium - IES 2019
March 13-15, 2019, Kumamoto University, Japan

Value Stream Mapping Simulation (VSM-Sim): Methodology to Design the Lean Service Systems in India Post Service Industry – A Case Study

Vadivel S M [1], A H Sequeira [2]

1 *School of Management, National Institute of Technology Karnataka, Surathkal, Mangalore 575025, India. email:ph.dvadivel@gmail.com*
2 *School of Management, National Institute of Technology Karnataka, Surathkal, Mangalore 575025, India. email: aloysiushs@gmail.com.*

ABSTRACT:

Purpose – Generally, lean service (LS) implementation starts from value stream mapping development. Here, we have recommended VSM along with simulation. The goal of this study is to present an application of VSM with simulation to design the lean service systems (LSS) in India postal case study in National sorting hub (NSH) Mangalore, Karnataka, India.
Design/methodology/approach – Simulation models software called Arena simulation used for the case organisation after implementing various LS elements.
Findings – Simulation studies taken as two perspectives such as "before LS" (current state VSM) and "after LS" (future state VSM). It was found that the case organisation can achieve significant improvement in the operational performance.
Originality/value – No case study exists in the literature that discusses the application of VSM with simulation in India post service industry.

Keywords: *Lean service, Mail processing operations, Computer Simulation, Value stream mapping, Performance measures.*

1`Introduction

The postal industry governed by central government and it comes under Indian public sector. It is a main service industry exploits the labour advantage for the rigorous work in India. It aims to provide better service to the people with the integration of airways, railways and roadways. India post has a wide-ranging postal network of 1,54,939 post offices and it is the vast network in the world. They are handling mails, parcels, logistics service, retail and financial services across nation. They are playing a significant role in bolstering the socio-economic development. In India, total postal department has 1,54,866 post offices, out of that 1,39,040 were in rural 15,826 in semi-urban and urban areas.

Daily postal department receiving more than 40,000 articles which require more space and efficient sorting process methods. Hence, postal departments need to re-think purposefully from the traditional to non-traditional way in order to enhance the operational performance. In reality, most of the operational performance related problems can be resolved with common sense approaches with low investments. Lean Manufacturing (LM) is one of the techniques to find and eliminate the waste and provides an opportunity to enhance the operational performance with the employees' coordination.

1.1 Statement of the Problem

In recent years, postal service has facing tumbling demand, unbalanced workforce, with low skill level and lack of human resource management. In current state, C2C mail is on the decreasing side, whereas B2B and B2C mail are in increasing side simultaneously. Problems such as inadequate facilities, logistic management, warehouses facilities prevent growth further.

At present, postal service industry faces many challenging tasks with e-communication mail processing operations. In the postal service operations, on-time delivering mails are very important and critical one. Regularly, postal department operates thousands of mails in the back-end operations (without customer involvement). The postal departments need to improve their operational performance in order to maintain or retain the customer as per the current needs. LS focuses on 8 forms of wastes in terms of excess transportation, keeping inventory mails, unwanted human motions, over processing, over production, waiting in line, service defects and underutilization of skill. This research objective is to find and eliminate 8 types of waste in speed postal service and improve the operational performance through simulation.

2.0 Theoretical Background

Firms either manufacturing or service should observe on continuous improvement with the help of five lean principles to improve their operation. These principles already mentioned by Womack (1991) such as specifying the value, the value stream, flow, pull systems which are described by the following:

i. Specifying the value from customer point of view. Manufacturing companies has not only focused on their manufacturing products but also develop their product portfolio based on understanding of customers' requirements.

ii. The organization has to organize the processes starting from raw materials and ends to final customer based on customer point of view rather than what departments wants. (i.e.) reinforced their supply chain from supplier to customer.

iii. Creating value flow from people, open culture and their processes in order to avoid the waste and increase value to the products.

iv. Leverage pull system to avoid excess production by focusing on the demands of customers.

v. Seeking perfection which involves employees' coordination on the focusing goals with no compromise on quality as well as elimination of waste.

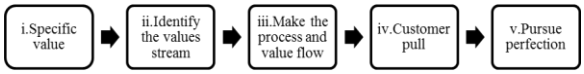

Source: Womack & Jones, 1998

Figure 1. The five principles of lean

There are five principles originally developed for manufacturing, but it can be applied in service industries also. From Figure 1 showed the five principles adopted in postal service. The second principle is vital one which emphasized identification of value stream in manufacturing and "mail flow "in postal service. Remaining principles remain same manufacturing as well as service sector.

Lean concepts mostly implemented and succeeded in manufacturing sector. However, lean in service sector called "lean service" concepts evolved recently. Though the concepts of lean thinking are the same, there are few differences in the service sector implementation. The main differences are the difficulty in definitions and standardizations since the variability in service sector is higher than the manufacturing sector (Arbós, 2002).

Considering lean service application in this study where we apply the lean concepts in the India speed post service at the backend operations. Although there are some lean studies in mail processing service industries, these are generally related to lean implementation success and failed practices in public sectors. In particular, in this study, we consider the manual sorting process in the National Sorting Hub (NSH) Mangalore, South Karnataka. Identifying the value-added and non-value-added activities, then, elimination of the non-value-added

activities to decrease cycle time, and enhance the operational performance by using lean service techniques. Here, value-adding and non-value-adding activities using VSM used for the current state conditions and also future state conditions with the help of simulation. To see the effects of the recommended improvements on this system, it is simulated and various aspects are analysed.

The remaining paper is organized as follows. Section 2, provides the literature review. Section 3 describes the case study problem reflected in our study. In Section 4, the details of the proposed methodology are presented, and then VSM and simulation studies are discussed. Section 5 describes our results, and final section presents the conclusions of this research work.

2. Literature review

There are few examples of lean applications in service organizations in the literature. First, lean service applications were mostly used in the healthcare sector. Initially, lean concepts applied in manufacturing sector, then it is started to apply in service sector. Some lean applications applied in government/public sector also.

Although VSM is mainly used in manufacturing sector, recently it has used in service sector applications especially in healthcare services. Solding and Gullander (2009) and Shararah et al. (2011) showed that, how VSM and simulation can be used together systematically. There are few studies in service sector combining VSM and simulation discussed in table 1.

Table 1. Brief literature review

Author, year	Description
Abo Hamad et al. (2012)	Combined VSM with simulation to identify value added and non-value-added activities and to assess the gains of proposed improvement strategies in healthcare facilities. The recommended methodology is used only for the drug round process and to illustrate the gains of proposed improvement strategies.
Robinson et al. (2012)	Proposed the "SimLean" approach integrated simulation with lean in healthcare and showed how simulation could be used together with lean to increase the productivity of these systems.
Tobail et al. (2013)	Integrated simulation and VSM method to improve the delivery of healthcare to patients.
Swallmeh et al. (2014)	Integrated VSM and simulation to minimize the patient waiting time and decrease the service time and capacity for an emergency department.
Doğan and Unutulmaz (2016)	Used a simulation-based VSM method to identify waste and design new processes in the physical therapy and public hospital rehabilitation department.

The main contribution of this study is to implement the lean concepts by using VSM map and simulation tools in postal service sector, specifically, for the back end operations in NSH Speed post, Mangalore. According to the best of our knowledge, this is the first study in that particular area (NSH Speed postal services) which combines VSM and simulation for the implementation of the lean concepts in a postal service industry.

3. Case Study: Problem definition

In this section, presented a case study in NSH Mangalore. The following problems had been observed in the manual sorting centre on October, November, 2017: Time and interval of the shift, variety of the mail, reliability of the equipment's and allocation of the work force. The method of data collection was quantitative and duration was two months. There were two shifts running in a day. The postal employees have to produce 8,000 articles per day. There were 5 sections includes deposit section, scanning, sorting, sealing and dispatch sections as shown in figure 2 as a process flow diagram.

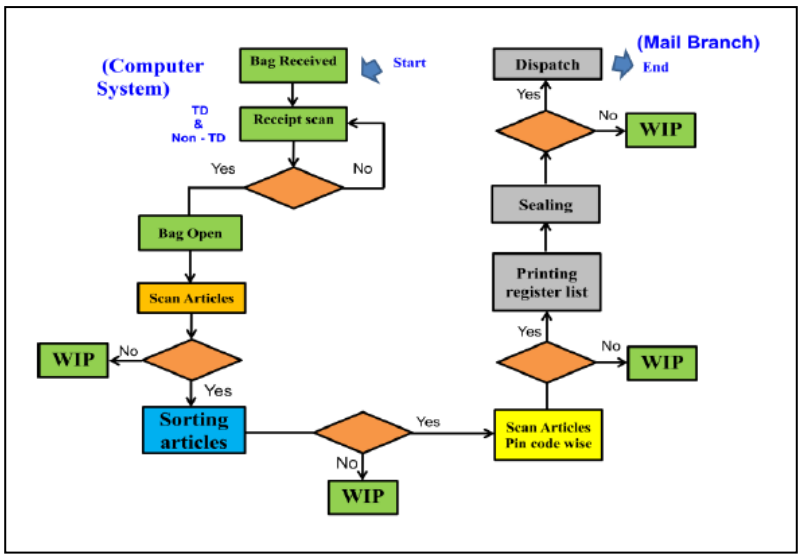

Figure 2. Process flow in NSH Mangalore

Cycle time for one article, layout working area, floor space, and equipment's (bin, basket, table, sorting case) sizes were noted during the data collection. Factors that lead to visual ergonomics in postal sorters and workplace environmental problems noted down from the questionnaire study. It comprises the effects of machinery-paced work, bad workplace environments (noise, cramped conditions, poor lighting and poor ventilation), system break-downs and associated problems. Generally postal sorting work itself may be a cause stress with different time patterns.

4. Proposed Methodology

4.1 Value Stream Mapping

The VSM map provides the information about mail flow, information flow inside the NSH. We can measures the performance through cycle time, process ratio, takt time, productivity, value added time, production lead time, cycle time and setup time etc. as shown in Figure 4. We have proposed the research methodology as shown in Figure 3. From the current conditions of VSM map, we found out that non-value added activities are eliminated through simulation model with different time patterns in Arena 15.1 package and incorporate operational performance layout in future state conditions.

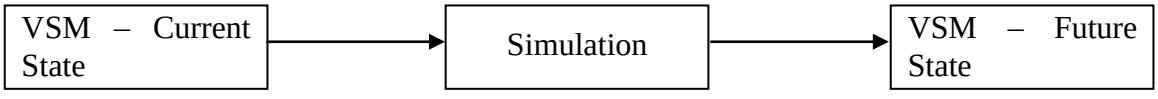

Figure 3. Proposed methodology

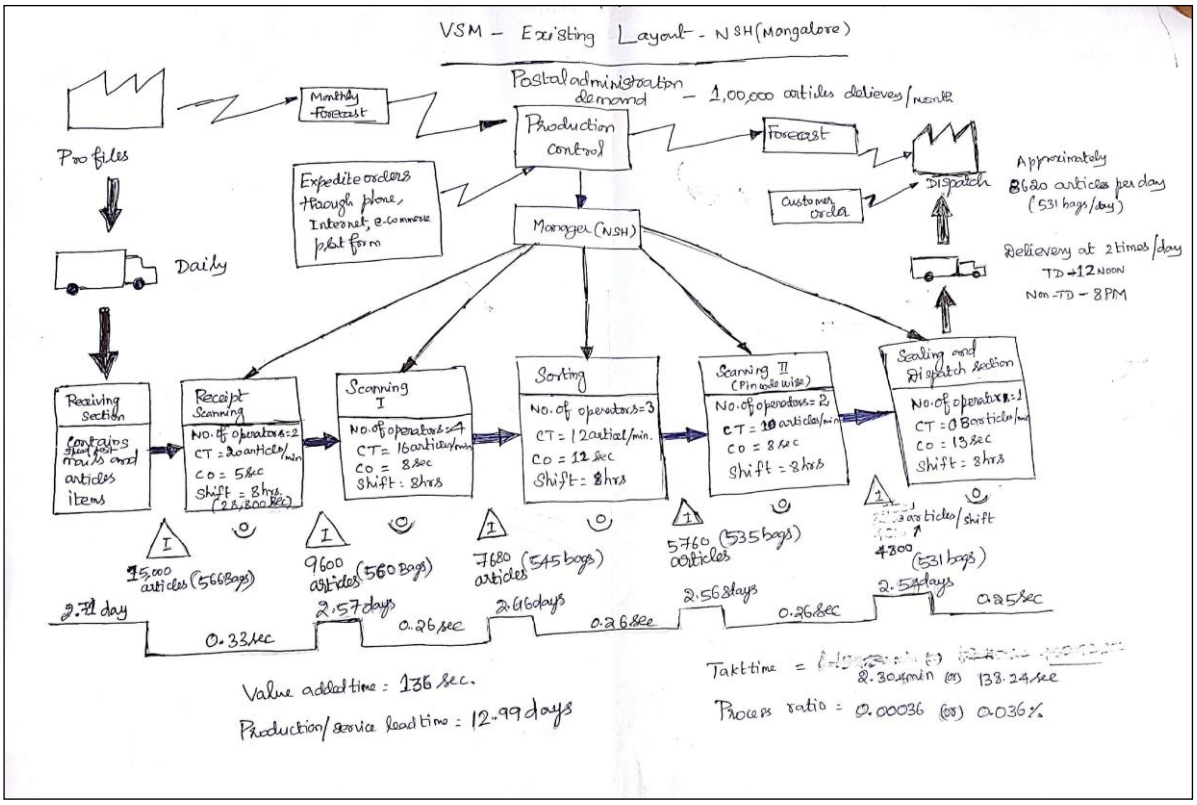

Figure 4. Current state VSM for Mail processing operations

4.2 Simulation Models

This section explains the details of the simulation models. The simulations of the current system as well as the suggested system design corresponding to the future state to be found out from the model. Arena software package (version 15.1) (Rockwell Corporation) is used to build logic and systematic building blocks models. We have performed 50 replications of 8 hours' time to run the model. There were 8 different operations in our simulation model as shown in figure 5 (as a single server queuing system, the queue and the server).

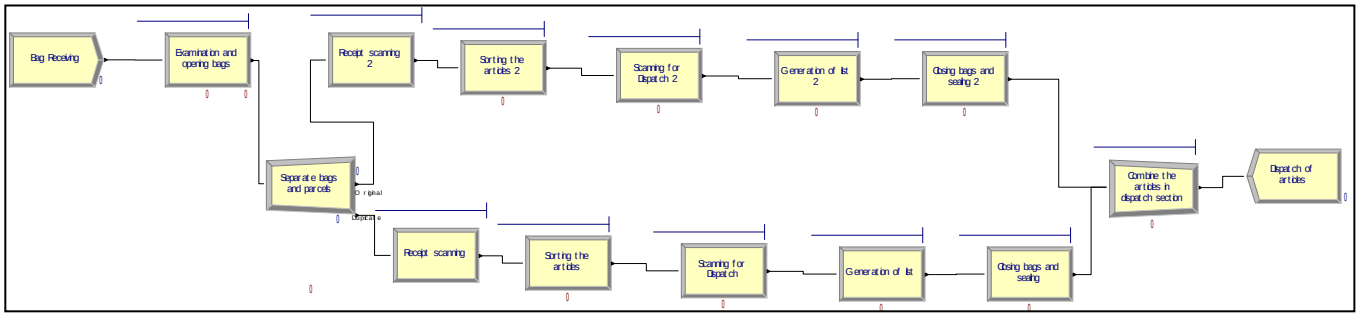

Figure 5. Simulation model for Mail processing operations

5. Results and Discussions

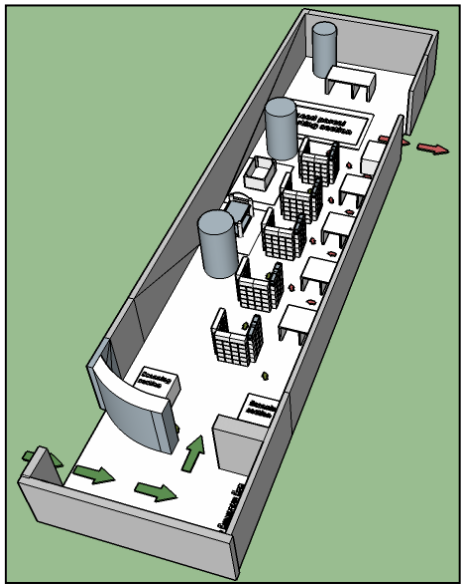

Figure 6 Implemented Feasible layout –NSH Mangalore. Green arrows indicate receiving the mails, while red arrows indicate dispatch of mails.

From Table 2 presents a summary of results for the resource utilizations. As it is expected, we note a significant decrease in each resource's utilization value in the simulation model results. The scanning and sorting process decrease the cycle time because of fixed scanning method and tag readability change. Conclude that, the workloads of the office employers significantly decrease in the future state situation.

Table 2 Production performance metrics

Descriptions	Existing layout	Implemented layout	Improved observed in weeks
Processing time per person/day	8620	9450	9450/day (9.62%)
Flow rate / hr.	568.97	623.76	565.24/hr. (9.62%)
Cycle time	171.00 sec	157.32 sec	157.32 sec (7%)
Synchronizing ratio	0.86	0.94	1.03 (7.29%)
Space occupied	416 sq.	389 sq.	389 sq. (6.4%)
Line efficiency	27.02%	27.25%	0.20%

6. Conclusion

This study leads to development of methodology which incorporates VSM and simulation methodology in India Speed post at NSH Mangalore. From the results, we can infer that new future layout can increase productivity by 10% with same manpower by modifying sorting and process methodologies. The future layout has many advantages such as improving operational performance, better workplace environment and improved ergonomic conditions. Based on postal administration expectations alternative possibilities of worker allocation, deployment of workers and layout optimization can be made using simulation software model. Incorporating VSM and simulation methodology in postal service sector can be easily adopted to improve the productivity by providing safe workplace environment for the employees.

ACKNOWLEDGEMENTS

The authors gratefully acknowledged the support and co-operation extended by India Post authorities, especially the Post Master General, South Karnataka region and the authorities of NSH Mangalore Speed post services.

REFERENCES

[1] Abo Hamad et al (2012), towards leaner healthcare facility: application of simulation modelling and value stream mapping, International Workshop on Innovative Simulation for Healthcare (I-WISH), Vienna.

[2] Arbós, L.C. (2002), Design of a rapid response and high efficiency service by lean production principles: methodology and evaluation of variability of performance, International Journal of Production Economics, Vol. 80 No. 2, pp. 169-183.

[3] Doğan, N.Ö., Unutulmaz, O. (2016), Lean production in healthcare: a simulation-based value stream mapping in the physical therapy and rehabilitation department of a public hospital, Total Quality Management & Business Excellence, Vol. 27 Nos 1-2, pp. 64-80.

[4] Robinson, S et al (2012), SimLean: utilising simulation in the implementation of lean in healthcare, European Journal of Operational Research, Vol. 219 No. 1,pp. 188-197.

[5] Sharara h, M.A et al (2011), Value stream map simulator using ExtendSim, Proceedings of the World Congress on Engineering, London, pp. 755-758.

[6] Solding, P.,Gullander, P. (2009), Concepts for simulation based value stream mapping, Proceedings of the 2009 Winter Simulation Conference (WSC), IEEE, Austin, TX, pp. 2231-2237.

[7] Swallmeh, E et al (2014), Integrating simulation modelling and value stream mapping for leaner capacity planning of an emergency department, Sixth International Conference on Advances in System Simulation, SIMUL 2014, Nice, pp. 256-262.

[8] Womack, J.P., Jones, D.T. and Roos, D. (1990), Machine that Changed the World, Simon and Schuster, New York, NY.

8th International Engineering Symposium - IES 2019
March 13-15, 2019, Kumamoto University, Japan

Escaping and Falling into Poverty in Rural Odisha: Empirical Evidence from Panel Data

Sunil Khosla [1], and **Pradyot Ranjan Jena [2]**

1 *School of Management, National Institute of Technology Karnataka, Surathkal, Mangalore 575025, India. email:sunilkhosla1993@gmail.com*
2 *School of Management, National Institute of Technology Karnataka, Surathkal, Mangalore 575025, India. email:jpradyot@gmail.com*

ABSTRACT: The paper examines the poverty dynamics and its determinants in rural Odisha. Using panel data from 1353 rural households for the period of 2004-05 and 2011-12, we find that 25.26% households were chronic poor, 45.24% of households were transient poor, and remaining 29.50% households were non-poor. Further, it was observed that 37.04% households were ascended out of poverty between 2004-05 and 2011-12 and 8.20% households were descended into poverty simultaneously. Using multinomial logistic regression model, the most influential factors for household remain non-poor are shown to be: the level of education, household engaged in salary job, and the level of assets holding. The factors that have the largest impact on impending a household escaping poverty are the large family, the proportion of dependency ratio, and engaged in the farming sector. The government may consider paying more attention to rural infrastructure development, improve access to good quality education, and family planning.

Keywords*: Poverty dynamics, Determinants, Multinomial logistic regression, falling into poverty, Escaping poverty, Odisha*

INTRODUCTION

Since 1990, the main goal of the world community has been to end poverty. The Millennium Development Goals (MDGs) have achieved the broader target of reducing half of world poverty rate by 2015. The post-2015 global development agenda is called Sustainable Development Goals (SDGs), targets zero poor in the world by 2030. Apart from this, with respect to poverty reduction, most countries have wide-ranging anti-poverty programs on fostering education, job creation, asset building and advocated policies to support the people who are poor. Although there is a significant reduction in poverty, still countries like sub-Saharan Africa and other underdeveloped areas of many parts of the world endure high poverty rate (United Nations, 2015[a]). In addition, the SDGs report reveals that 1 in 8 persons, that is, 766 million poor are battling for their basic needs (United Nations, 2016). Further, increasing the poverty line from $1.25/day to $2.50/day will increase the proportion of poor to 2.7 billion (United Nation Development Program (UNDP), 2014). Hence, it is understood that the poverty rate is still large and makes it alarming to give careful consideration to the issue.

A number of studies have been conducted on the subject of poverty reduction but limited studies have conducted on understanding the dynamics of poverty reductions. It is observed that people are escaping poverty due to various positive events (income diversification, credit facility, insurance, government support) but at the same time, many people are falling into poverty due to various negative events (illness, the death of a breadwinner, job loss, unemployment,

disability, loss of residential and commercial property, crop failure etc.). The research on poverty recently suggested two different sets of the program to eradicate poverty effectively; one set of programs to uplift the households that are already poor and are likely to stay poor and the another sets of program to help households that are at risk of becoming poor (Krishna A. 2010). To formulate such effective different set of policies, it makes necessary to identify the households that need the set of programs to overcome poverty and the households that need programs for building their resilience to minimize the likelihood to fall into poverty. The households are basically distinguished from chronic poor and transient poor (Humle and Shepherd, 2003). The chronic poor is the households who have been poor for a certain period of time that is their income/consumption remains below the poverty line in every survey year whereas moving into and out of poverty is called the transient poor (Humle, 2003; chronic poverty report 2004-05; Chiwaula L S. et al., 2011; Stampini M. et al., 2016). Panel data assistances in distinguishing the chronic poor and transient poor, however, this type of analysis has been limited largely because of data deficiency in the developing countries (Stampini M. et al., 2016).

In the recent past, there have been several studies in poverty and poverty reduction in Odisha. Hatlebakk M. (2014) studied the household vulnerability to poverty using the retrospective life-histories method to 800 household samples from Kalahandi and Cuttack districts in Odisha. The findings show that Schedule Tribe (ST) households are more trapped in poverty in rural Odisha. Datta D. et al., (2014) using the participatory poverty assessment (PPA) studied the poverty and vulnerability in highland forest regions of Odisha. The study finds that 47% were critically poor and 22% were the chronically poor. Rahman A. (2016) examined the impact of PDS in households' poverty level by using 800 households from KBK (Koraput, Balangir, and Kalahandi) region Odisha. The study found that PDS has improved the living standard of the targeted people. Patnaik and Das (2017) studied the development intervention on households' vulnerability using the 800 household data from Balangir and Kalahandi districts in Odisha. The study found that the positive impact of the intervention. However, very little attention has been paid to understand the poverty dynamics at the state level in Odisha.

In this study, we take the advantage of household panel data from Indian Human Development Survey (IHDS) and distinguish households into chronic and transient poor. The panel data enable to identify the households that have escaped poverty and the households that have descents into poverty over the specified period. Thus in this study, we attempt to study the following two objectives: 1. To understand the change in poverty status (chronic poor, transient poor, and non-poor) in rural Odisha between 2004-05 and 2011-12 and 2. To understand the influencing factors that increase the chance of being chronic poor, ascend out of poverty and descend into poverty.

The remainder of the paper is structured as follows. Section 2 outlines the methodology used in the study. Section 3 presents the results and discussions. The last section provides the conclusion.

RESEARCH METHODOLOGY

Data Source: The current research paper used the household panel data from the Indian Human Development Survey for the period between 2004-05 and 2011-12. The households panel data were collected by the National Council of Applied Economic Research (NCAER), New Delhi. The surveys cover 41,554 households in 2004-05 and 42,152 households in 2011-12 across the nation. The IHDS data provides a wealth of information on household demography, health, economic status, education, asset level, government benefits, ethnicity, marriage, fertility, employment, a range of community-level infrastructures, and social capitals. It separately provides the individual data, special to women data, village level data, and school characteristics data. The household samples were drawn using the stratified sampling method. In particular, the IHDS data contains valuable

information on household income and consumption data, therefore, either one can be used to estimate the poverty dynamics. The present study has extracted the desired data for Odisha (both 2004-05 and 2011-12). IHDS-II reports that 83% of the households are re-interviewed in 2011-12. After the attrition, the panel data for our study is comprised to 1353 for both the survey years 2004-05 and 2011-12.

The Predetermined Poverty Line for the Poverty Measurement: To measure the poverty level, a predetermined poverty line has to be fixed. The present study assessed poverty dynamics using household consumption per capita. Indian planning commission defines state-specific poverty line for the nation. The present study adopts the poverty line defined by Suresh Tendulkar committee for the period of 2004-05 and 2011-12. The predetermined poverty line for rural Odisha is 407.78 and 695 for the period of 2004-05 and 2011-12 respectively (Planning commission India, 2009*)*.

The Study Area: Odisha, one of the east coast states of India is one of the poverty-stricken and most vulnerable states in the world (Kunte P D. et al., 2014; Kumar and Kunte, 2012). The state is located between 17º49'N and 22º34'N latitudes and 81º27'E and 87º29' E longitudes. The state has a total population of 41.94 million and a population density of 269 with the coverage area of 156,000 km2 (Census report, 2011).

In order to understand the economic status at the regional and disaggregated (districts) level, National Sample Survey (NSS) has been divided the state (Odisha) into three geographical divisions. The southern region comprises 12 districts; the coastal region consists of 9 districts; and the northern region includes 9 districts (NSS, 2009*)*. The same classification has been used in the present study to understand the poverty dynamics at the regional divisions and at the disaggregated level.

MODEL SPECIFICATION

Defining Chronic and Transient Poverty: The theoretical description of the paper is based on the chronic poverty report 2004-05, which defines poverty dynamics into three main poverty categories from the five specified poverty groups. The five specified poverty groups are as follows: (1) Always poor: households that the income/consumption per capita each period remains below the predetermined poverty line. (2) Usually poor: households that the income/consumption per capita overall remains below the predetermined poverty line. (3) Fluctuating/churning poor: households that the income/consumption per capita fluctuates around the predetermined poverty line. (4) Occasionally poor: households that the income/consumption per capita some periods fall below the predetermined poverty line. (5) Non-poor: households that the income/consumption per capita always remains above the predetermined poverty line, presented in figure 1.

The broad three categories of poverty are defined as 1. Chronically poor, which includes both always and usually poor 2. Transient poor includes fluctuating poor and occasionally poor and 3. Non-poor with the income/consumption always remain above the predetermined poverty line.

The present study has adopted this categorization. Since the Indian Human Development Survey (IHDS) has two waves (2004-05 and 2011-12) of panel data, four categories of change in poverty status are possible, presented in table 4.

MULTINOMIAL LOGISTIC REGRESSION

The present study utilizes the multinomial logistic model to understand the determinants of poverty dynamics. The outcome variable in the study was four distinct variables (chronic poor, ascended out of poverty, descended into poverty, and non-poor).

The multinomial logit model determines the probability that a household i experiences one of the J mutually exclusive outcomes. This probability is given by

$$P_{ij} = P(Y_i = j) = \frac{e^{\beta_j x_i}}{\sum_{k=1}^{j} e^{\beta_k \chi_i}}$$, j= 1…. j

Where, Y_i is the outcome experienced by the household i, β_κ are the set of

coefficients are to be estimated and χ_i includes the various covariates. As suggested by Greene (2000), to identify the model, one of the β_j must be set zero (the base category), and all other sets are estimated in relation to this benchmark. For this study one of the β_j is set to be zero, so the above probability function can be written as:

$$p_{ij} = P(Y_i = j) = \frac{e^{\beta_j \chi_i}}{1 + \sum_{k=1}^{j} e^{\beta_k \chi_i}}$$

, for j= 0,1, 2…, j and $P_{i0} = (P(Y_i = j) = \frac{1}{1 + \sum_{k=1}^{j} e^{\beta_k \chi_i}}$

In the present study, J=4, $P(Y=0)$ is the probability of a household escape poverty, $P(Y=1)$ is the probability of a household being chronic poor. $P(Y=2)$ is the probability of a household being non-poor, and $P(Y=3)$ is the probability of a household falling into poverty.

Thus, the specific model applied in the present study when standardizing β_0 equals zero give as

$$P_{ij} = P(Y_i = j) = \frac{e^{\beta_j \chi_i}}{1 + \sum_{k=1}^{3} e^{\beta_k \chi_i}}$$

, for J=1, 2, 3,

$$P_{i0} = P(Y_i = 0) = \frac{1}{1 + \sum_{k=1}^{3} e^{\beta_k \chi_i}}$$

and

One further step of estimating marginal effects was performed for the ease of interpretation. The marginal effects are estimated as

$$\frac{dP_{ij}}{dx_i} = P_{ij}(\beta_j - \sum_{k=1}^{3} P_{ik}\beta_k)$$

RESULT AND DISCUSSION

The main objective of the paper was to understand the change in poverty status in rural Odisha. The findings show that one-fourth of rural households were chronic poor i.e. 25% of households were poor in both 2004-05 and 2011-12. Previous studies on poverty have observed that lack of human capital, the demographic composition of households, location of residence, lack of ownership of physical assets, and low-paid labour are the characteristics of the chronic poor (McKay and Lawson, 2002). However, it is also observed that the reasons for being chronic poor differ from place to place and the local poverty reduction strategies need to be adopted for the effective poverty reduction (Krishna A. 2007). The change in poverty status for rural Odisha was observed that more than 37% of households have escaped from poverty in 2011-12 but at the same time, more than 8% of households have fallen into poverty. The remaining 29.50% households were non-poor regardless of the negative extreme events. It appears from the findings that only one-fourth households in rural Odisha were able to remain in above the poverty line. However, more than 70% of households were living on the edge of poverty (table 1).

Table 2 shows the change in poverty status at the regional level. The chronically poor households were found to be more in the coastal region followed by the southern region. The households from the coastal region are subject to face frequent extreme events such as floods and cyclones. Perhaps the impacts of the extreme events on rural households are severe and that made about 30% of households to remain below the poverty line. The southern region is known for the hunger, drought, and malnourishment. Majority of the households belongs to the tribal community those are the marginal disadvantage group in the state. Since the literacy rate is low in the tribal and marginalized groups, most of them remain in chronic poor and transferred the poverty to the future generation.

The result shows that the chronic poor households were found to be less in the northern region but the households that descents into poverty were comparatively more in the region. In addition, although chronic poor households were more in the coastal region, comparatively the households fallen into poverty was found to be less than the other regions.

However, the southern region continues the second rank in both escaping and descents into poverty.

Interestingly, the non-poor households were found to be more in the southern region followed by the northern region. Although most of the southern districts are covered by the IAP program, it is hard to understand the factors that helped those households to remain in above poverty line. Therefore, understanding the factors that are related to escape and descents into poverty will shed light on poverty reduction.

FACTORS INFLUENCING CHRONIC POOR, ASCENDED OUT OF POVERTY, DESCENDED INTO POVERTY, AND NON-POOR

Factors influencing chronic poverty:

Household size: The results from the model show that household size appears to be significantly associated with chronic poverty in the rural Odisha. Increasing household size is likely to put an extra burden on the household expenditure pattern and hence larger family were more likely to stay in poor for the longer period. It shows that an addition of new member in the household increases the probability of being chronic poor by 14.3% rural Odisha respectively (table 4).

The proportion of dependency ratio: Similar logic applies to the proportion of dependency ratio of children and elder in the household, shows that an increase in one dependent person in the household will lead to increase the probability of being chronic poor. However, the household size square shows the negative association with chronic poverty. It appears that for small families, larger family size may actually be enabling them to overcome the labour shortage in the agriculture sector and help to generate more income for the household.

Gender of the head: It was observed that there is no association between gender of the head and change in poverty status in the aggregate as well as the rural model.

Age of the head: Similarly, the age of the household head was not significant for the chronic poverty.

Level of education: Education has been the main determinant of poverty reduction. A household head having higher education helps him engaged in the formal sector which increases the household income and improves the living standard. It was also seen that more educated households are better able to cope up with the adverse events. The result shows that an additional year of schooling of the household head would decrease the probability of being chronic poor in rural areas.

Asset ownership: In the case of asset ownership, it appears a negative association with chronic poverty in the rural Odisha. It shows that households having more assets were more likely to be non-poor. Keeping other things constant, it suggests that the addition of one productive asset reduces the risk of being chronic poor by 5.1% for rural areas.

Land ownership: As expected, land ownership was statistically significant and has a negative association with chronic poverty. Since it has been the most important asset for rural households, acquiring an additional unit of land reduces the probability of being poor by 1.5% for the rural households. However, the land size square has a positive association with chronic poverty, shows the diminishing returns from the factor.

Economic activity: Economic activity is important correlates with chronic poverty. A household member working in the farm sector and salary job did not turn out to be statistically significant while a further step of marginal effect was performed.

Location: Location of the household is, in fact, plays a crucial role in the household living standard. A location with more opportunities for economic activities will help the household to manage a normal living, however, a location in remote areas, as well as danger of various adverse events, leads more fluctuations of income. The list of adverse events affects Odisha is more than the country faces (Directorate of Economics and Statistics (DES), Odisha, 2013). The dummy coastal region has a significant and negative association with chronic poverty suggests that being in the coastal region reduces the probability of being chronic poor. However, the probability of being chronic poverty reduces is quite more than other regions if households belong to the southern region.

Factors influencing remain non-poor: Household size: Table 4 presents the factors that help to remain non-poor and fall into poverty. The results show that large household size has a negative association with the escaping poverty.

Age of the household head: It shows that increasing age of household age increases experience and hence increases the probability of remain non-poor.

Economic activities: It was also found that education level, engaged in salary job and assets levels were positively associated with remain in non-poor.

Location: the result shows that household staying at southern region has more chances of remain non-poor than other region

Factors influencing descended into poverty: Gender of the head: the gender variable has a negative association with descends into poverty, being a male household in rural areas reduces the probability of falling into poverty by 6.7%.

Age of the head: Age of the head has a positive association with falling into poverty in rural Odisha. In the rural areas most of the household heads are engaged in the unskilled work and increasing age will decrease the work capability. Further, lack of nutrient food and very hard work will not allow many households to productive work in the old days. The result shows that household has a more chance of falling into poverty if the head grows older.

Level of household asset: Asset level has a negative association with falling into poverty. In the rural areas, people use to sell their land, livestock, and jewelry to meet their critical situation and hence having more assets protect them from the fluctuation of income. It shows that additional household asset reduces the probability of falling into poverty by 1.2%.

Large family size: Similar logic applies to household size. It suggests that increasing household size increases the probability of falling into poverty.

CONCLUSION

The following conclusions are deduced from this study:

- The findings show that 25.26% households were chronic poor, 45.24% of households were transient poor, and remaining 29.50% households were non-poor. Further, it was observed that 37.04% households were ascended out of poverty between 2004-05 and 2011-12 and 8.20% households were descended into poverty simultaneously.
- It appears that the most influential determinants helping households to remain non-poor are the level of education, the level of asset holding, and households engaged in salaried job.
- The factors that have the largest impact on impeding an escape from poverty are large family size, female household head, and proportion of dependency ratio.

REFERENCES

[1] Chaudhuri, S et al (2002), Assessing household vulnerability to poverty from cross-sectional data: A methodology and estimates from Indonesia, Vol. 102, pp. 52. Discussion paper.

[2] Chiwaula, L S et al (2011), An asset-based approach to vulnerability: The case of small-scale fishing areas in Cameroon and Nigeria, The Journal of development studies, Vol. 47, No. 2, pp.338-353.

[3] Chronic Poverty Research Centre, (2004), The chronic poverty report 2004–05. CPRC.

[4] Desai, Sonalde, and Reeve Vanneman and National Council of Applied Economic Research, New Delhi. India Human Development Survey-II (IHDS-II), 2011-12. ICPSR36151-v2. Ann Arbor, MI: Inter-university Consortium for Political and Social Research [distributor],2015-07-31. http://doi.org/10.3886/ICPSR36151.v2.

[5] Desai, Sonalde, Reeve Vanneman, and National Council of Applied Economic Research, New Delhi. India Human Development Survey (IHDS), 2005. ICPSR22626-v8. Ann Arbor, MI: Inter-university Consortium for Political and Social Research [distributor], 2010-06-29. http://doi.org/10.3886/ICPSR22626.v8.

[6] Odisha Economic Survey (2013-14), Planning and Coordination Department, Directorate of Economics and Statistics, Government of Odisha, Bhubaneswar.

[7] Patnaik U, and Das P K (2017), Do development interventions confer adaptive capacity? Insights from rural India, World Development, Vol. 97, pp.298-312.

[8] Rahman, A (2016), Universal food security program and nutritional intake: Evidence from the hunger prone KBK districts in Odisha, Food policy, Vol. 63, pp.73-86.

[9] Thorat, A et al (2017), Escaping and falling into poverty in India today, World development, Vol. 93, pp.413-426.

[10] UNDP (2014), Human development report: sustaining human progress, New York, NY: United Nations.

[11] United Nations (2015_a), Millennium Development Goals Report 2015, New York: United Nations.

[12] United Nations (2016), The sustainable development goals report, New York.

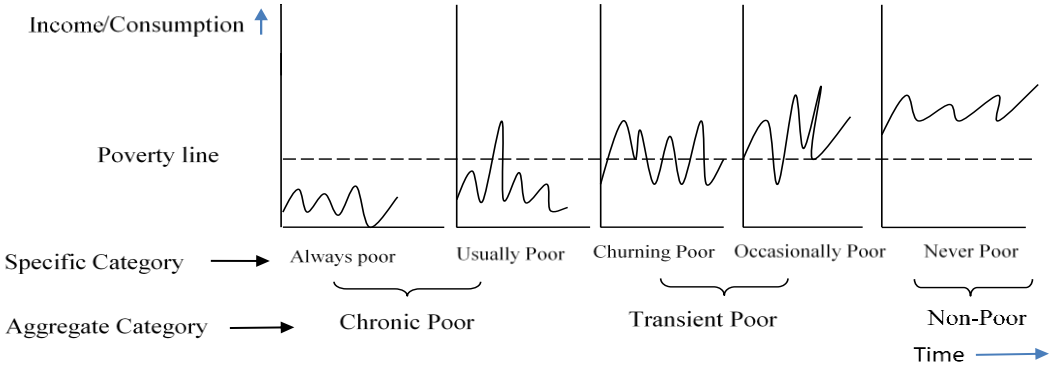

Fig. 1 Poverty Categorization
Source: Chronic poverty report 2004-05

Table 1 Classified poverty groups for the analysis

Types of poor based on IHDS panel data (2004-05 and 2011-12)	Description	Classified poverty for the analysis of the present study
Always poor	Remain poor in 2004-05 and 2011-12	Chronic poor
Escaped poverty	Poor in 2004-05 but became non-poor in 2011-12	Transient poor
Descents into poverty	Non-poor in 2004-05 but became poor in 2011-12	
Non-poor	Remain non-poor in 2004-05 and 2011-12	Non-poor

*Source: Authors classification based on the chronic poverty report 2004-05*Table

Table 2 State-level poverty Dynamics

Change in poverty status between two rounds 2004-05 and 2011-12	Households (%)
Chronically poor	25.26
Escaped poverty	37.04
Descent into poverty	8.20
Transient poor (Escaped + Descents)	45.24
Non-poor	29.50

Source: The statistics are based on data for the 1353 households in each year

Table 3 Regional Level Poverty Dynamics

Region	Change in poverty status in regional level between two rounds 2004-05 and 2011-12 (%)				
	Chronic poor	Transient poor (Escaped + Descents)	Escaped poverty	Descents into poverty	Non-poor
Coastal	29.04	46.39	39.18	7.21	24.56
Northern	21.71	51.68	42.38	9.30	26.87
Southern	24.09	38.71	30.32	8.39	37.20

Source: The statistics are based on data for the 1353 households in each year

Table 4 Results from Multinomial Logistic Regression Model

Outcome variable: Change in poverty status, 0= Ascended out of poverty, 1= Chronic poor, 2= Non-poor, 3= Descended into poverty	Chronic Poor	Non-poor	Descended into poverty
	Coefficient (Standard Error)	Coefficient (Standard Error)	Coefficient (Standard Error)
Head gender	-.006 (.059)	-.018 (.055)	-.067**(.032)
Age of the household head	-.002 (.001)	.003** (.001)	.003** (.001)
Years of schooling completed by the head	-.015** (.005)	.017*** (.005)	.004 (.003)
Ownership amount of land	-.011** (.004)	.001 (.003)	-.000 (.002)
Land size square	.000** (.000)	-.000 (.000)	5.022 (.000)
Asset level	-.051***(.006)	.046*** (.005)	-.012***(.003)
Household size	.143*** (.026)	-.144*** (.025)	.029** (.015)
Household size square	-.006*** .002)	.007*** (.001)	-.001 (.001)
Number of member in salary job	-.066 (.058)	.105** (.042)	.022 (.029)
Number of member in agriculture sector	.009 (.015)	-.004 (.017)	-.003 (.010)
Proportion of dependency ratio (child + elder)	.053** (.016)	-.003 (.017)	.011 (.010)
Household is member in saving group	-.145* (.081)	.036 (.062)	-.001 (.044)
Household is member in Social group	-.076* (.040)	.023 (.038)	.019 (.023)
Coastal region	-1.427*** (.045)	-0.987*** (.042)	-3.447 (.027)
Northern region	-1.52 (.055)	-0.106** (.048)	-3.438 (.032)
Southern region	-1.601** (.707)	-1.175**(.566)	-3.453***(.922)
Observation	966		
Pseudo R^2	0.2420		

Source: The statistics are based on data for the 1353 households in each year